University of Rochester
Laboratory for Laser Energetics

DOE/
NA/3856-1799
September 2023

LLE 2022 Annual Report

October 2021 – September 2022

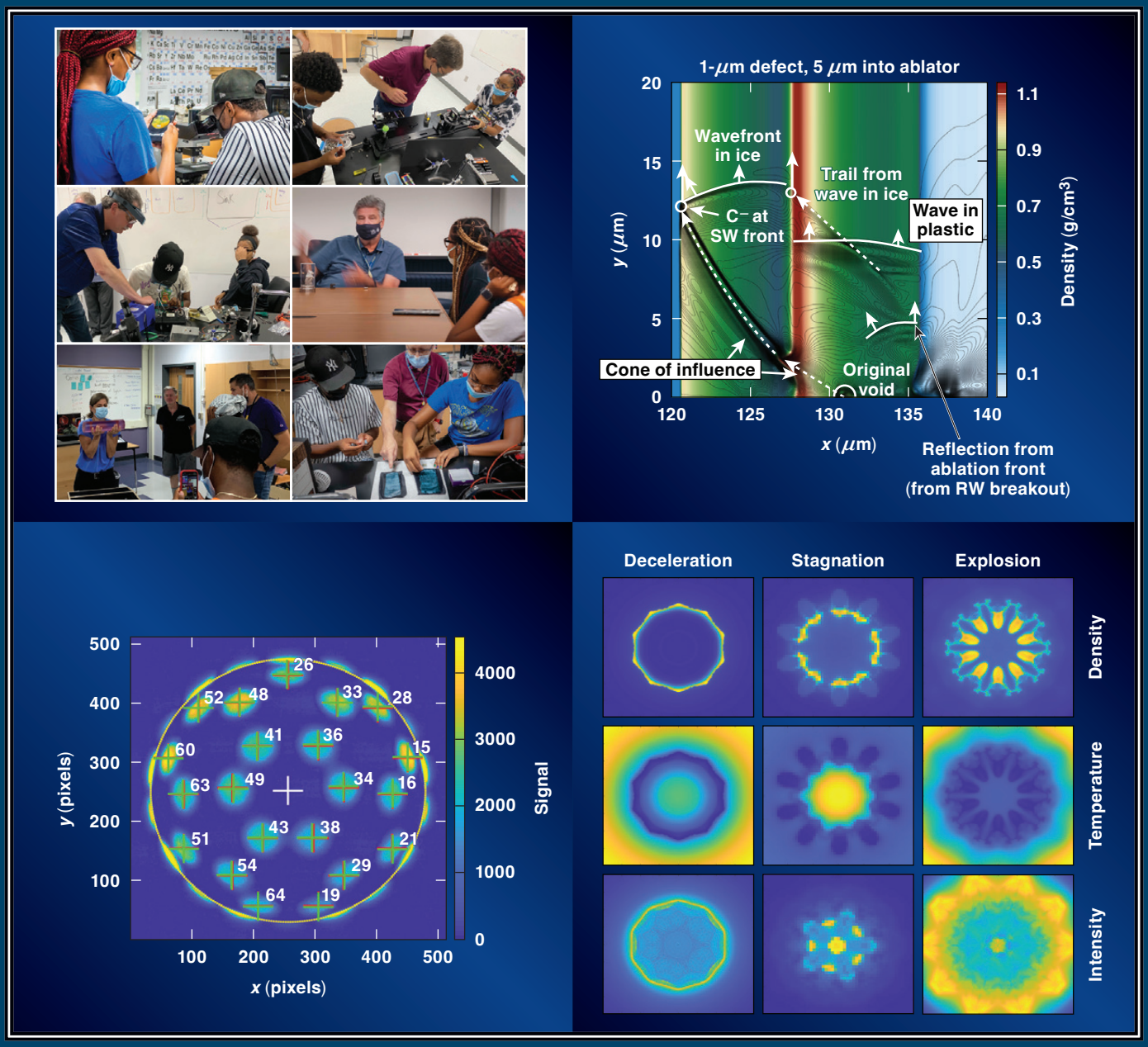

UNIVERSITY OF ROCHESTER
LABORATORY FOR LASER ENERGETICS

Volume 169
October–December 2021
DOE/NA/3856-1700

LLE Review

Quarterly Report

About the Cover:

The high school students and teachers who participated in the 2021 Broad Exposure to Science and Technology (BEST) Research Program are shown engaging in various aspects of science and technology that support LLE's laser research program. They explored microscopy, spectroscopy, electronic technology, lasers, optical design, liquid crystals, and holography. The importance of continued STEM education in research, was emphasized by former LLE director, Mike Campbell, to highlight the extensive teamwork required to make advancements in laser development and scientific applications.

The BEST program was carried out at East High School within the Rochester City School District during the summer of 2021. The participants of the BEST program (shown left to right) include East High teachers Trent Russell and Gavin Jenkins, East High students Yusuf Gazali, Reganae Walters, Taiasia Gibson, and Ramir Wearen, and program coordinator Terry Kessler, LLE Diversity Manager.

LLE mentors exposed the BEST students and teachers to the key technologies that are central to the construction and operation of the OMEGA Laser System. Electronic circuits were explored by dissecting computer systems and practicing the microsoldering techniques. Lasers were brought into the classroom for demonstration and exhibition. Both interferometry and holography were experimentally explored to manufacture diffraction gratings and holographic 3-D images. In addition, liquid crystal materials were used to manufacture polarization optics and color-tuned paints. The philosophy that underpins the BEST program is that multiple early exposures help guide students in their pursuits of STEM fields and encourages them to explore the next generation of related jobs and careers.

I3113JR

The work described in this volume includes current research at the Laboratory for Laser Energetics, which is supported by New York State Energy Research and Development Authority, the University of Rochester, the U.S. Department of Energy Office of Inertial Confinement Fusion under Cooperative Agreement No. DE-NA0003856, and other agencies.

For questions or comments, contact Nickolaos Savidis, Editor, Laboratory for Laser Energetics, 250 East River Road, Rochester, NY 14623-1299, (585) 275-3413.

www.lle.rochester.edu

Printed in the United States of America
Available from
National Technical Information Services
U.S. Department of Commerce
5285 Port Royal Road
Springfield, VA 22161
www.ntis.gov

UNIVERSITY OF ROCHESTER
LABORATORY FOR LASER ENERGETICS

Volume 169
October–December 2021
DOE/NA/3856-1700

LLE Review

Quarterly Report

Contents

In Brief

This volume of LLE Review 169 covers the period from October–December 2021. Articles appearing in this volume are the principal summarized results for long-form research articles. Readers seeking a more-detailed account of research activities are invited to seek out the primary materials appearing in print, detailed in the publications and presentations section at the end of this volume.

Highlights of research presented in this volume include:

- R. C. Shah *et al.* report on a new continuum x-ray measurement to characterize hot-spot x-ray yield and hot-spot electron temperature of a series of implosions typical of current best cryogenic designs, comparing x-ray production relative to neutron production and assessing the ratio of hot-spot mix (p. 1).
- Y. Lawrence *et al.* show lowering the central density by a factor of 5 or more compared to the vapor density of deuterium–tritium (DT) at triple point can aid in achieving small hot-spot size without excessive amplification of deceleration-phase Rayleigh–Taylor instability, possibly enabling ignition and high gains in laser-direct-drive designs using lower energies (p. 5).
- D. A. Chin *et al.* experimentally identify three x-ray phases consisting of the corona, core stagnation, and afterflow using temporal, spatial, and spectral x-ray emission of implosion glow-discharge polymerization shells on OMEGA EP (p. 9).
- K. Weichman *et al.* demonstrate that the generation of underdense, relativisitically thermal plasma can be realized with currently available laser and magnetic-field–generation capabilities by leveraging two regimes of magnetically assisted direct laser acceleration (p. 12).
- R. K. Follett *et al.* create an independent-hot-spot model to predict multibeam instability behavior (p. 16). The model is applied to the absolute two-plasmon–decay instability and is shown to provide an improved description of laser–plasma instability behavior over the common-wave approach.
- S. Ressel *et al.* present the full uncertainty distributions inferred from radiography analysis in high-energy-density systems (p. 20). They demonstrate the importance of a full treatment of uncertainties, done here through Bayesian analysis, which is critical to avoid overconfidence in parameter estimates in this system due to the correlations between parameters and multiple maxima in the likelihood function introduced by typical experimantal noise sources.
- M. C. Marshall *et al.* use data from two OMEGA EP experiments to demonstrate that the chemical and thermodynamic conditions inside ice giant planets, which have inner ice layers dominated by CH_4, NH_3, and H_2O, are suitable for diamond formation (p. 23).
- V. V. Karasiev, D. I. Mihaylov, and S. X. Hu address exchange-correlation (XC) dependence thermal modeling in density-functional-theory simulations of warm dense matter and high-energy-density plasma effects by developing a thermalization framework for XC functionals and XC additive correction at the GGA level, improving simulation accuracy and agreement to experimental results (p. 26).
- S. Zhang *et al.* perform simulations from first principles and analyzed the structure, electron density, and thermodynamic properties of liquid SiO_2 at high-energy conditions to gain insights into the nature of the bonded-to-atomic transition (p. 29).
- H. Poole *et al.* conduct a feasibility study of using spatially integrated, spectrally resolved, x-ray Thomson-scattering measurements to diagnose the temperature, density, and ionization of the compressed DT shell of a cryogenic DT implosion at two-thirds convergence for both low- and high-adiabat implosions (p. 31).

- S. F. Nwabunwanne and W. R. Donaldson discuss the design and fabrication of $Al_xGa_{1-x}N$-based photodetectors with rectangular and circular asymmetric, interdigitated electrode geometries GaN/AlGaN semiconductors with an interest in high-efficiency detectors targeting semiconductor-driven ultrafast laser pulse characterization and plasma diagnostics (p. 34).
- J. Musgrave and J. Bromage investigate signal phase accumulation from pump wavefront errors and the potential impact on signal pulse compression, offering an approach to determine the suitability of a given pump laser to ensure there are no spatiotemporal pulse-broadening effects that degrade the laser's peak intensity (p. 37).
- G. W. Jenkins, C. Feng, and J. Bromage demonstrate a new method of contrast improvement that allows both contrast improvement and temporal compression in a single step—divided-pulse nonlinear compression (p. 40).
- C. Feng *et al*. develop a simple and cost-effective tool to reduce pump-induced temporal contrast degradation up to 15 dB by applying a pump-seed delay optimization and pump-to-signal noise transfer of a two-stage ultra-broadband optical parametric chirped-pulse amplifier (p. 43).
- C. Dorrer and M. Spilatro demonstrate broadband, spectrally incoherent nanosecond pulses with closed-loop pulse shaping, inspired by laser–plasma instability mitigation and improving target to high-energy laser pulse interactions (p. 46).
- S.-W. Bahk *et al*. analyze the effect of the pump beam wavefront phase and amplitude transferred to the idler and signal beam phase and amplitude using the analytic optical parametric amplifier (OPA) phase solution, wave-vector picture, and experimentally measured OPA phase using the MTW-OPAL laser (p. 50).
- T. Z. Kosc *et al*. develop and experimentally validate a modeling capability to evaluate large-aperture optics, applicable for minimizing transverse stimulated Raman scattering gain during crystal-cut optimization, predicting maximum operational fluence, and helping to develop novel designs with complex polarization control (p. 56).
- T. J. Kessler reports on the BEST Program, designed to engage underrepresented high school students and their teachers in various aspects of science and technology that support LLE's laser science and applications research (p. 58).
- J. Puth *et al*. summarize operations of the Omega Laser Facility during the first quarter of FY22 (p. 63).

Nickolaos Savidis
Editor

Bound on Hot-Spot Mix in High-Velocity, High-Adiabat Direct-Drive Cryogenic Implosions Based on Comparison of Absolute X-Ray and Neutron Yields

R. C. Shah,[1] D. Cao,[1] L. Aghaian,[2] B. Bachmann,[2] R. Betti,[1] E. M. Campbell,[1] R. Epstein,[1] C. J. Forrest,[1] A. Forsman,[2] V. Yu. Glebov,[1] V. N. Goncharov,[1] V. Gopalaswamy,[1] D. R. Harding,[1] S. X. Hu,[1] I. V. Igumenshchev,[1] R. T. Janezic,[1] L. Keaty,[2] J. P. Knauer,[1] D. Kobs,[2] A. Lees,[1] O. M. Mannion,[1] Z. L. Mohamed,[1] D. Patel,[1] M. J. Rosenberg,[1] C. Stoeckl,[1] W. Theobald,[1] C. A. Thomas,[1] P. Volegov,[3] K. M. Woo,[1] and S. P. Regan[1]

[1]Laboratory for Laser Energetics, University of Rochester
[2]Lawrence Livermore National Laboratory
[3]Los Alamos National Laboratory

Here we report on new continuum x-ray measurements to characterize hot-spot x-ray yield and hot-spot electron temperature of a series of implosions typical of current best cryogenic designs.[1] The objective of these measurements is to consider the consistency of x-ray production relative to neutron production and assess if this ratio implies hot-spot mix. Because of the insufficient time for equilibration given plasma parameters in these high-velocity implosions, there are significant differences between the hot-spot electron and ion temperature, which can influence the comparison of the x-ray and neutron yields. Based on the measured neutron yield and both hot-spot temperatures, the expected x-ray yield (assuming a pure-DT hot spot) is determined for each implosion and then compared to the measured x-ray yield. The x-ray and neutron yields are found to be consistent without invoking hot-spot mix within an estimated sensitivity corresponding to ~2% by atom, fully ionized carbon–deuterium plastic.

The x-ray yield and electron-temperature measurements were newly developed for this experiment. Approximately 30 images of each implosion were generated using an array of differentially filtered circular apertures and recorded on an absolutely calibrated image plate (IP).[2] The imaging apertures make it possible to distinguish the hot-spot x rays from a background of neutrons and coronal x rays (the spatial identification of hot spot as compared to coronal x rays was corroborated with simulation data). The x rays were filtered with Al foils in order to have four data channels. After accounting for IP response, the mean recorded energies of the channels ranged from 10 to 18 keV. In this range, the dense fuel was optically thin, and the signal level was within the dynamic range of a single scan read of the IP (consistent with the calibration). The channel measurements were used to constrain an isobaric hot-spot model, and the hot spot (assumed static) was used to calculate the volume integrated bremsstrahlung x-ray continuum using the free–free emissivity for hydrogen. [Figures 1(a)–1(c) show examples of the data, measured and modeled channel signals, and inferred spectrum for shot 96806.] Finally, a neutron-weighted electron temperature (T_e) was calculated to parameterize the hot-spot electron temperature on similar footing as the ion temperature. For the simulations, post-processed x rays were spatially and temporally selected to isolate the hot-spot contribution. The hot-spot x rays from the simulations were then filtered by the experimentally used channel responses and analyzed using the same procedure as for the data.

The measured hot-spot electron and ion temperatures for five cryogenic implosions of 25 February 2020 that are typical of current best performing designs, as well as the values from 1-D simulation, are shown in the bar plot of Fig. 2. In contrast to the x-ray yield and electron temperature, neutron yield and ion temperature are routinely measured in inertial confinement fusion experiments on OMEGA. The hot-spot ion temperature (T_i) is inferred based on the temporal width of the neutron time of flight (nTOF), which, under ideal circumstances, characterizes a neutron-weighted ion temperature. This inferred T_i will be inflated by flows, which, if anisotropic, will result in variations of the inferred value as observed from different lines of sight.[3] In our experiments, there were five independent nTOF's and shown are the maximum and minimum values of T_i for each shot. The range between the extremes was large for only the first shot, for which a target defect was observed and believed to cause a large

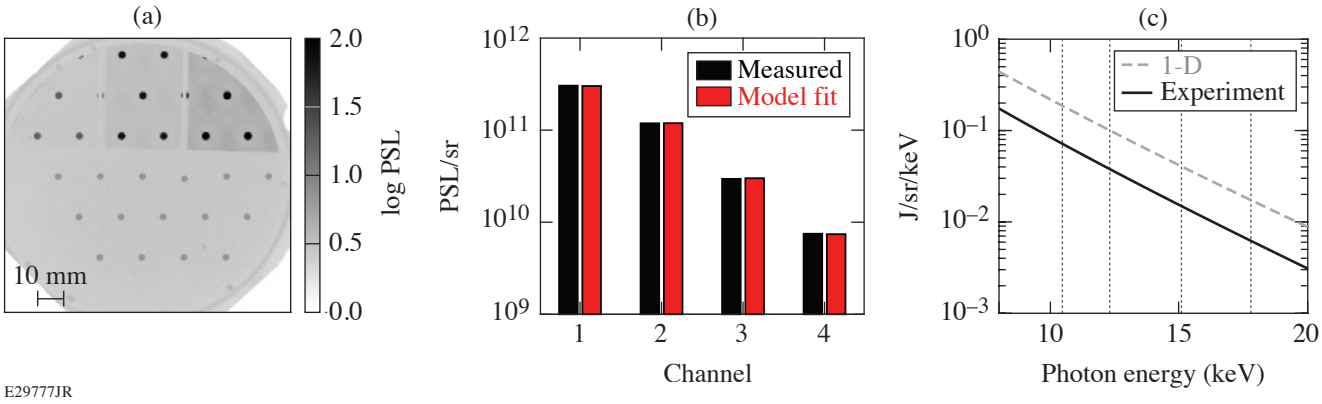

Figure 1
(a) Image-plate data for shot 96806 with image intensity reported in units of photostimulated luminescence (PSL). (b) Measured and fit channel signals. (c) The hot-spot model x-ray spectrum determined from the channel data. Dotted vertical lines indicate the mean recorded energy of each of the four imaging channels. For reference, the hot-spot model x-ray spectrum obtained from the identical analysis of the 1-D simulation is also plotted.

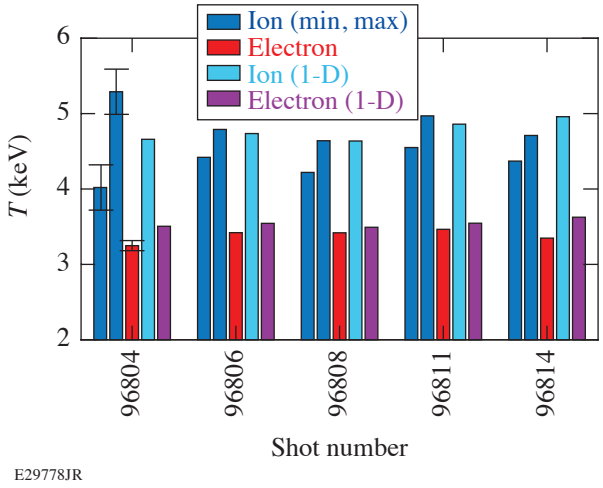

Figure 2
The measured hot-spot T_e is typically ~75% of the minimum T_i obtained from five independent lines of sight. The result is similar to what is obtained from 1-D simulations.

flow. In that case, the minimum T_i takes its lowest value. We have used the minimum nTOF T_i as the value best representative of the ion thermal conditions. Note that for the x-ray and neutron yield ratio comparison, an inflated value of T_i will increase the estimated hot-spot mix; therefore, in this sense the inferred mix quantification will be an upper bound estimate. Figure 2 also shows that the measured T_e value is typically ~75% of the minimum T_i. This degree of equilibration is similar to what is obtained in the 1-D simulation.

The predicted x-ray yield (Y_x) for a hot spot in the absence of mix is calculated using these temperatures as well as the measured neutron yield (Y_n). This result, along with the measured Y_x, is plotted in Fig. 3(a). There is a generally positive correlation of the measured x-ray and neutron yields contrasting what was reported by Ma *et al.*[4] in indirect-drive implosions of the National Ignition Campaign and for which mix was identified as a prominent issue. Additionally, since the measured and mapped values of Y_x do not significantly deviate, there is no measurable indication that mix is consistently present across these implosions. This is more explicitly shown in Fig. 3(b) as the ratio of the measured to mapped values, or x-ray enhancement. In this plot, the variability observed in the application of the model to a set of test simulations is indicated by the shaded region, and we interpret it as an estimate of the sensitivity by which we can measure an enhancement due to mix. The dashed lines in Fig. 3(b) indicate the value of the x-ray enhancement estimated for specified fractions of mix in the hot spot, accounting for the increase in both bremsstrahlung and recombination emission due to the carbon atoms. The measurement sensitivity is compromised by both the

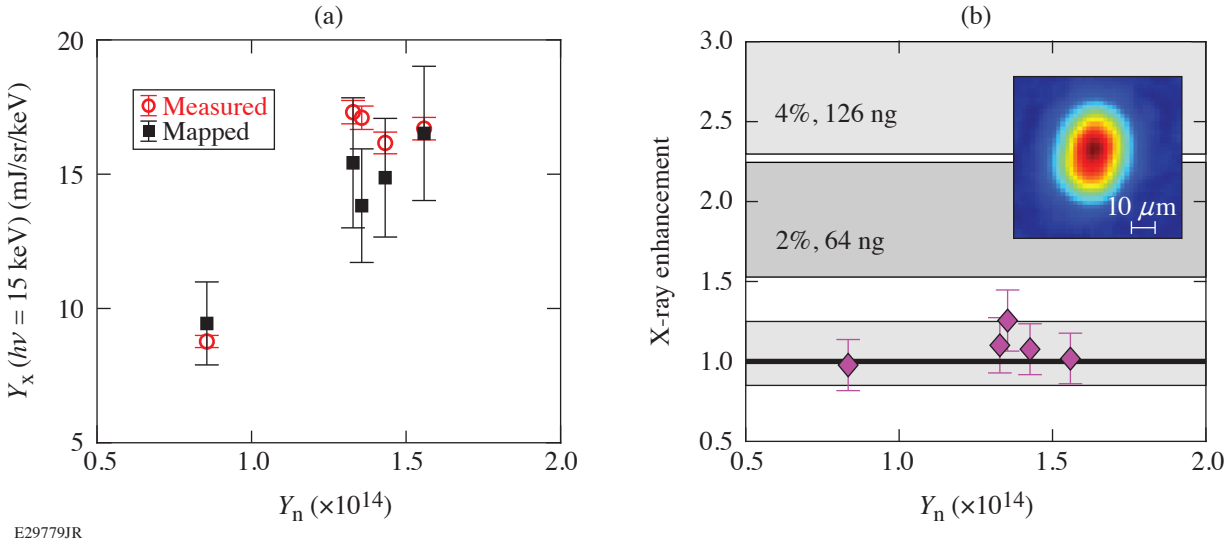

Figure 3
For each implosion, the measured Y_n, T_i, and T_e are used to calculate a mapped x-ray yield that is compared to the measured x-ray yield. (b) The x-ray enhancements fall within the systematic errors observed for the mapping (as determined by tests on a simulation database) indicated by the shaded gray region of the plot. The percentage values refer to percent-by-atom levels of CD mix required to cause the indicated level of x-ray enhancement. The inset shows the recovered hot-spot image from channel 1 for shot 96806.

error propagation (dominated by the hot-spot temperatures and indicated with error bars) as well as the model errors (indicated by the shaded region). We find no indication of hot-spot mix within the combined effect of these errors or an approximate sensitivity limited to ~2% by atom carbon–deuterium (64 ng, assuming a typical 1.2-μg hot spot). We have also extracted the hot-spot images from image-plate data using an established approximation to tomographic analysis,[5,6] applicable to the precisely machined circular apertures (General Atomics, San Diego). The inset of Fig. 3(b) shows the image with an estimated 8-μm resolution obtained from channel 1 for shot 96806. Typical of all the implosion and other channels, we do not identify the sorts of bright features which have been associated with mix in other experiments[7] in hot-spot images of these and similar implosions. It is plausible that decompression, peripheral bubbles, and residual motions, observed in multidimensional simulations[8] and also previously proposed based on experimental signatures,[9] dominate the hydrodynamic degradations without creating hot-spot mix.

In summary, measurements were presented of the x-ray yield and hot-spot electron temperature for direct-drive cryogenic implosion experiments. The comparison of the electron temperature with the ion temperature routinely characterized in the experiments was consistent with the prediction that ions and electrons remain substantially unequilibrated in the high-velocity, high-adiabat designs of present interest. The independently measured electron and ion temperatures of the hot spot with the D–T fusion neutron yield were used to estimate a corresponding x-ray yield expected from the nonequilibrium DT hot spot, assuming the absence of mix. The comparison of the measured and expected x-ray yields is consistent within the estimated sensitivity of the technique and therefore indicates that hot-spot mix, if present in these implosions, is at levels less than what the yield comparison can detect.

This material is based upon work supported by the Department of Energy National Nuclear Security Administration under Award Number DE-NA0003856, the University of Rochester, and the New York State Energy Research and Development Authority.

1. V. Gopalaswamy *et al.*, Nature **565**, 581 (2019).
2. M. J. Rosenberg *et al.*, Rev. Sci. Instrum. **90**, 013506 (2019); 029902(E) (2019).
3. T. J. Murphy, R. E. Chrien, and K. A. Klare, Rev. Sci. Instrum. **68**, 610 (1997).
4. T. Ma *et al.*, Phys. Rev. Lett. **111**, 085004 (2013).
5. B. Bachmann *et al.*, Rev. Sci. Instrum. **87**, 11E201 (2016).
6. G. Di Domenico *et al.*, Med. Phys. **43**, 294 (2016).

7. A. Pak *et al.*, Phys. Rev. Lett. **124**, 145001 (2020).
8. D. Cao *et al.*, "Understanding Origins of Observed Fusion Yield Dependencies," to be submitted to Physical Review Letters.
9. A. Bose *et al.*, Phys. Rev. E **94**, 011201(R) (2016).

Mitigation of Deceleration-Phase Rayleigh–Taylor Growth in Inertial Confinement Fusion Implosions

Y. Lawrence,[1,2] V. N. Goncharov,[2] K. M. Woo,[2] W. Trickey,[2] and I. V. Igumenshchev[2]

[1]University of Chicago
[2]Laboratory for Laser Energetics, University of Rochester

In inertial confinement fusion (ICF), small hot spots are desirable because they lower the threshold hot-spot energy required for ignition, $E_{\rm hs} > 16$ kJ $(R_{\rm hs}/50\ \mu{\rm m})^2$ (Refs. 1–4). However, they generally lead to greater implosion asymmetry due to the growth of the Rayleigh–Taylor (RT) instability on the inner shell surface during the deceleration phase. A challenge then arises of how to attain a high convergence ratio (CR, defined as the ratio of the initial inner shell radius to the hot-spot radius at peak compression), without excessively high RT growth. In this study we show that lowering the central density [by a factor of 5 or more compared to the vapor density of deuterium–tritium (DT) at triple point] has the greatest leverage in achieving small hot-spot sizes without excessive amplification of deceleration-phase RT.

First, we review some basic aspects of deceleration-phase RT growth. During the deceleration phase, initial perturbations on the inner shell surface grow exponentially because the less-dense hot spot pushes against the denser shell. Neglecting convergence effects and including only the instability drive term, $\Gamma_{\rm drive} = \int \sqrt{A_T k g}\, {\rm d}t$, where A_T is the Atwood number, g is the inner surface acceleration, and $k \cong \ell / R_{\rm hs}$ is the effective wave number ℓ [the inner surface perturbations are decomposed in spherical harmonics with the mode number ℓ (see also Ref. 5)] and $R_{\rm hs}$ is the position of the shell's inner surface. We postpone defining A_T until later in this summary and assume for now that $A_T \cong 1$. Evaluating this integral from the start of the deceleration phase until peak compression (when the hot-spot radius reaches its minimum value $R_{\rm hs,m}$), it can be shown that $\Gamma_{\rm drive} = \sqrt{2\ell}\,{\rm arcsinh}\left(\sqrt{{\rm CR_d} - 1}\right)$, where ${\rm CR_d} \equiv R_{\rm hs0} / R_{\rm hs,m}$ is the maximum hot-spot convergence ratio during shell deceleration and $R_{\rm hs0}$ is the hot-spot radius at the beginning of deceleration. So, to decrease the instability drive term, ${\rm CR_d}$ should be decreased, but to reduce the ignition threshold, $R_{\rm hs,m}$ must also be reduced. This means that the deceleration phase should start later (i.e., at a smaller radius); therefore, $R_{\rm hs0}$ needs to be reduced as well as ${\rm CR_d}$.

Now we turn to scaling laws for ${\rm CR_d}$ and $R_{\rm hs0}$ to identify the target design parameters that can achieve these desired reductions. It can be shown (following from Ref. 3) that

$$ {\rm CR_d} \sim \frac{v_{\rm imp}^{2/3}}{\alpha_{\rm inf}^{1/5} p_{\rm sh0}^{2/15}}, \tag{1} $$

where $v_{\rm imp}$ is the peak implosion velocity, $\alpha_{\rm inf}$ is the in-flight shell adiabat, and $p_{\rm sh0}$ is shell pressure at the onset of deceleration. Also,

$$ R_{\rm hs,m} = \frac{R_{\rm hs0}}{{\rm CR_d}} \sim R_0 \frac{p_0^{1/5} \alpha_{\rm inf}^{1/5}}{p_{\rm sh0}^{1/5} v_{\rm inf}^{2/3}}, \tag{2} $$

where R_0 is the initial inner surface radius and p_0 is the initial vapor (central) pressure of the target. Equations (1) and (2) show that CR_d and R_{hs0} can be reduced by lowering the initial vapor pressure p_0 and/or increasing the shell pressure at the start of deceleration p_{sh0}. The remaining reduction in RT growth for the lower-central-density design comes from the increase in the ablative stabilization and reduction in the Atwood number.

Mass ablation from the inner shell surface, characterized by an ablation velocity v_a, reduces RT growth since the hot spot preferentially ablates the RT spikes that contact the hot spot at higher temperature gradients. It can be shown (following from Refs. 6 and 7) that

$$v_a \sim \frac{\alpha_{inf}^{0.5} v_{imp}^{2.2}}{R_0 p_0^{0.2} p_{sh0}^{0.13}}, \quad \frac{v_a}{R_{hs,m}} \sim \frac{\alpha_{inf}^{0.3} v_{imp}^{2.85}}{R_0^2 p_0^{0.4} p_{sh0}^{0.07}}. \tag{3}$$

As with the deceleration-phase convergence ratio and hot-spot radius at the onset of deceleration, the mass ablation velocity v_a increases with a lower initial vapor pressure. Meanwhile, density scale lengths L_m that are higher correspond to lower Atwood numbers A_T. Following from the previously written scaling laws and Ref. 6, it can be shown that

$$L_m \sim R_0 p_0^{0.2} p_{sh0}^{0.27} \alpha_{inf}^{0.8} v_{imp}^{0.54}, \quad \frac{L_m}{R_{hs,m}} \sim v_{imp}^{1.2} p_{sh0}^{0.33}. \tag{4}$$

Equation (4) shows that L_m is larger in designs with increased shell pressure at the onset of deceleration, p_{sh0}. Taken together, the scaling laws in Eqs. (1)–(4) for CR_d, R_{hs0}, v_a, and L_m show the beneficial stabilizing effects of reducing the initial vapor density and increasing the shell pressure at the start of the deceleration phase. This is accomplished most efficiently by reducing the initial vapor pressure p_0. A lower initial vapor pressure leads to extra convergence of the central region necessary to build up its pressure and begin shell deceleration; then, because of the convergence effects, the shell pressure p_{sh0} at the beginning of deceleration increases as well. Furthermore, as will be shown in an upcoming paper, 1-D simulations in *LILAC*[8] show that low-central-density designs experience reduced CR_d and R_{hs0}, as well as increased v_a and L_m. However, the fairly weak dependence of the hot-spot convergence ratio and stabilizing terms on the initial vapor density requires that it must be significantly reduced (factor of 5 or more). While this is not feasible with nominal cryogenic targets, the new dynamic shell formation concept can achieve this reduction by controlling the strength of the blast wave and the duration of the target expansion phase.[9]

To validate these predictions, we use 2-D hydrodynamic simulations in *DEC2D*[10] to study perturbation amplification during shell deceleration for two dynamic shell designs driven by shorter and longer laser pulses. In Ref. 11, one can find details of the target dimensions and pulse shapes that produce central densities of 0.6 mg/cm^3 and 0.12 mg/cm^3, respectively. Figure 1 shows density maps for the two dynamic shell designs taken at times when the neutron production reaches $\dot{N} \cong 5 \times 10^{26}\,s^{-1}$. The perturbation amplification is significantly reduced in the lower-central-density design [Fig. 1(b)] compared to the high-central-density design [Fig. 1(a)], despite the smaller hot-spot size, in agreement with the scaling arguments described earlier. Similarly, Fig. 2(a), which shows the mode $\ell = 20$ growth for the two dynamic shell designs, again confirms larger stabilization effects in the lower-density design. Figure 2(b) compares even-mode spectra for the two designs. The greatest RT growth suppression for the lower-density design occurs at mid- and higher-mode numbers, while the improvement for the low-mode numbers is slightly more modest.

Motivated by various scaling laws, we have demonstrated with 2-D simulations that reducing the initial central density in ICF targets leads to smaller hot spots (reducing hot-spot energies required for ignition) and, at the same time, suppresses deceleration RT growth. The required central-density reduction can be achieved using the new dynamic shell-formation concept. These results show a promising path to achieving ignition and high gains in laser-direct-drive designs at moderate laser energies $E_{laser} \sim 1$ MJ.

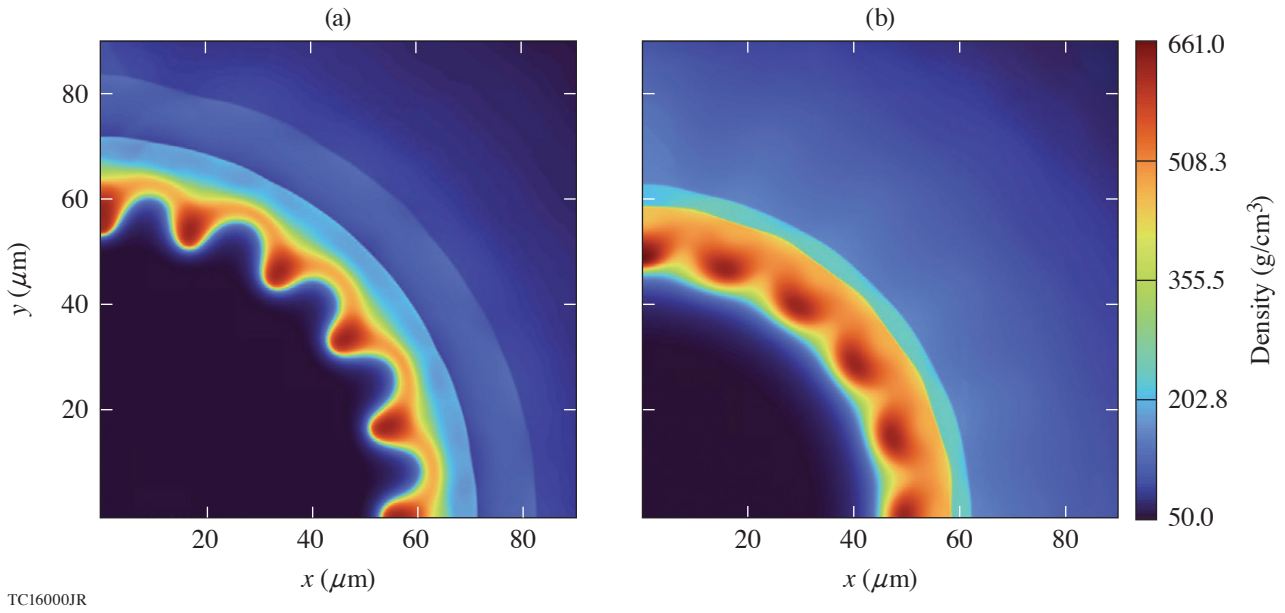

Figure 1
Two-dimensional density maps from mode $\ell = 20$ *DEC2D* simulations for the dynamic shell designs with (a) higher and (b) lower central densities (as described in Ref. 11), near stagnation at times of an equal neutron-production rate of $\dot{N} \cong 5 \times 10^{26}$ s^{-1}.

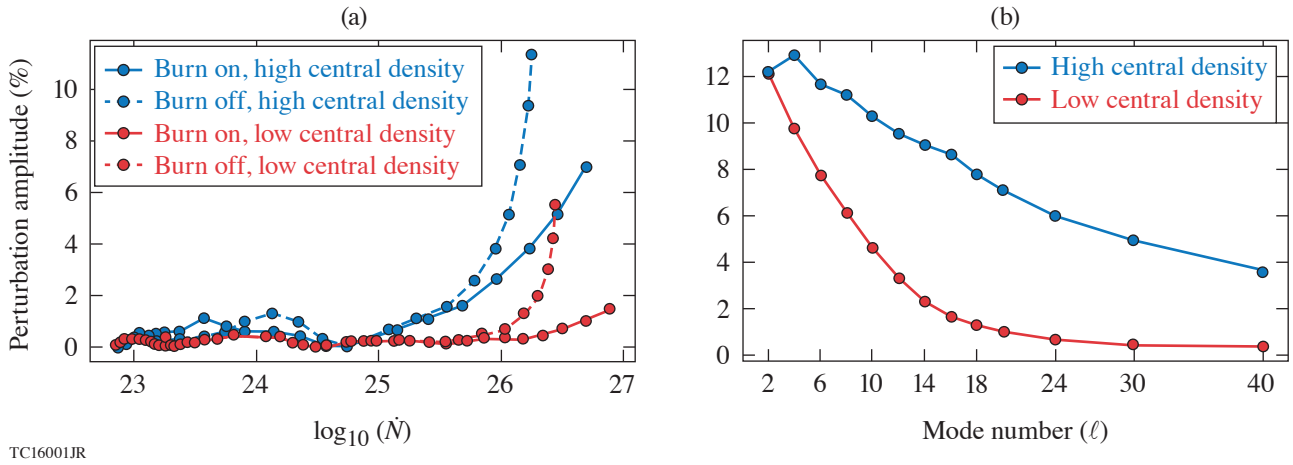

Figure 2
(a) Deceleration RT mode $\ell = 20$ evolution for dynamic shell designs with high/low central densities and alpha heating turned on or off. (b) Deceleration RT mode spectra with alpha heating turned on, taken at a neutron-production rate of $\dot{N} \cong 5 \times 10^{26}$ s^{-1} for the dynamic shell designs with high/low central densities. (Lines are used to guide the eye and do not represent fits.)

Funding was provided by the ARPA-E BETHE Grants No. DEFOA-0002212 and DE-AR0001272 and DOE OFES Award No. DE-SC0017951. This material is based upon work supported by the Department of Energy National Nuclear Security Administration under Award Number DE-NA0003856, the University of Rochester, and the New York State Energy Research and Development Authority.

1. J. D. Lindl, *Inertial Confinement Fusion: The Quest for Ignition and Energy Gain Using Indirect Drive* (Springer, New York, NY, 1998).
2. S. Atzeni and J. Meyer-ter-Vehn, *The Physics of Inertial Fusion: Beam Plasma Interaction, Hydrodynamics, Hot Dense Matter*, 1st ed., International Series of Monographs on Physics, Vol. **125** (Oxford University Press, Oxford, 2004).
3. V. N. Goncharov *et al.*, Phys. Plasmas **21**, 056315 (2014).
4. V. N. Goncharov *et al.*, Plasma Phys. Control. Fusion **59**, 014008 (2017).
5. V. N. Goncharov *et al.*, Phys. Plasmas **7**, 5118 (2000).
6. R. Betti *et al.*, Phys. Plasmas **8**, 5257 (2001).
7. C. D. Zhou and R. Betti, Phys. Plasmas **14**, 072703 (2007).
8. J. Delettrez *et al.*, Phys. Rev. A **36**, 3926 (1987).
9. V. N. Goncharov *et al.*, Phys. Rev. Lett. **125**, 065001 (2020).
10. K. M. Woo *et al.*, Phys. Plasmas **25**, 052704 (2018).
11. W. Trickey *et al.*, Front. Phys. **9**, 784258 (2021).

Emission Phases of Implosion X-Ray Sources for Absorption Spectroscopy

D. A. Chin,[1,2] J. J. Ruby,[1,2] P. M. Nilson,[1] D. T. Bishel,[1,2] F. Coppari,[3] Y. Ping,[3] A. L. Coleman,[3] R S. Craxton,[1] J. R. Rygg,[1,2,4] and G. W. Collins[1,2,4]

[1]Laboratory for Laser Energetics, University of Rochester
[2]Department of Physics and Astronomy, University of Rochester
[3]Lawrence Livermore National Laboratory
[4]Department of Mechanical Engineering, University of Rochester

At LLE's Omega Laser Facility, thin plastic shells were directly driven with ~20 kJ, resulting in a time-integrated x-ray yield of ~10^{12} ph/eV/sr at 7 keV. Using temporally, spatially, and spectrally discriminating diagnostics, three x-ray emission phases were identified: corona emission produced by the laser ablation of the shell, core stagnation, and afterglow emission due to the expanding hot material after stagnation. The newly measured corona and afterglow emission phases account for ~25% of the total x-ray signal and produce x-ray emission at a different time or larger radius than previously considered. The resulting implications of this additional emission for x-ray absorption fine structure (XAFS) spectroscopy are discussed.

This work presents a comprehensive measurement of the temporal, spatial, and spectral x-ray emission of implosion GDP (glow-discharge polymerization) shells on the OMEGA Laser System and identifies three experimental x-ray emission phases consisting of the corona, core stagnation, and afterglow. During the corona phase, the laser illuminates the shell, producing x-ray emission and driving a shock through the shell, causing the material to release inward. When the remaining material reaches the center, it stagnates, reaching Gbar pressures and producing a bright x-ray flash. After stagnating, the remaining material decompresses at Gbar pressures, remaining hot enough to emit x rays for a brief period of time. A schematic of each x-ray emission phase is shown in Fig. 1. To characterize the different emission phases, x-ray emission models were verified using a hydrodynamic simulation and fit to experimental data. The details of each emission phase are shown in Table I.

Table I: Fraction of the total emission in each phase obtained by fitting the streaked spectrum. The fractions are shown along with the 68% credible interval, which was calculated from uncertainty in the fit along with the variability between shots. The time duration was also calculated from the fit and represents the time interval that contains 95% of the signal. Lastly, the diameter was estimated from the time-integrated and time-resolved imaging.

	Corona	Core	Afterglow
Signal fraction	12^{+2}_{-2}	76^{+7}_{-6}	12^{+7}_{-6}
Time duration (ns)	0.2 to 1.1	1.0 to 1.1	1.1 to 1.4
Diameter (μm)	~850	~50	~300

The different spatial profiles of the x-ray sources directly impact the spectral resolution of the XAFS measurement. Using the Rowland (Yaakobi) x-ray spectrometer (XRS) as an example XAFS spectrometer, the impact of these three phases on the XAFS measurements can be estimated. An iron synchrotron absorption spectrum[1] was assumed to be the spectrum for a point source. To simulate the XAFS spectrum for the different source sizes, the point-source absorption spectrum was convolved with a Gaussian

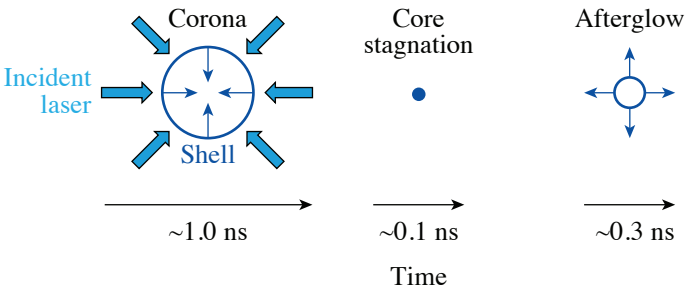

Figure 1
The x-ray emission occurs in three different phases: First, the incident laser causes the shell to emit x rays as the shell is ablated. Second, when the shell material stagnates in the center, there is a bright flash of x-ray emission. Finally, the remaining shell material expands and continues to emit x rays. The estimated time scale corresponds to an 865-μm-outer-diam, 9-μm-thick GDP shell.

function[2] whose full width at half maximum corresponded to the spectral resolution of each emission phase. The total signal was estimated by adding the signals from all three sources in transmission space while including the fractional weights from Table I.

The x-ray absorption near-edge spectroscopy (XANES) spectrum for each of the three phases along with the total signal is shown in Fig. 2(a). While the core spectrum is able to capture the majority of the features of the XANES spectrum, the corona and afterglow phases cannot. This is reflected in the total signal, which is not able to duplicate all of the features in the XANES spectrum. For example, the total spectrum loses the modulation, highlighted with the red arrow (in the inset plot), which can be used to distinguish structural changes and melting in iron.[3] Furthermore, the slope of the total spectrum is decreased, which must be accounted for when extracting the electron temperature.[4] Figure 2(b) shows the degraded extended x-ray absorption fine structure (EXAFS) spectra with each of the three phases and the total spectrum. Temperature can be extracted from the damping in the EXAFS modulations, and, under the harmonic approximation, this damping is given by $e^{-2k^2\mathrm{DWF}}$, where DWF represents the Debye–Waller factor.[5] Fitting[6] the point source and total signal spectra with this harmonic EXAFS approximation, the total signal spectrum has a DWF that is 16±6% larger. It should be noted that other spectrometers will have different spectral resolutions for each emission phase and will be impacted differently. Finally, these spectra represent a sample in a single thermodynamic state for the duration of the backlighter emission. If the material was not in a uniform thermodynamic state, each emission phase could potentially probe the material at a different density, temperature, or crystallographic structure resulting in shifting, amplifying, or decreasing XAFS modulations in unexpected ways.

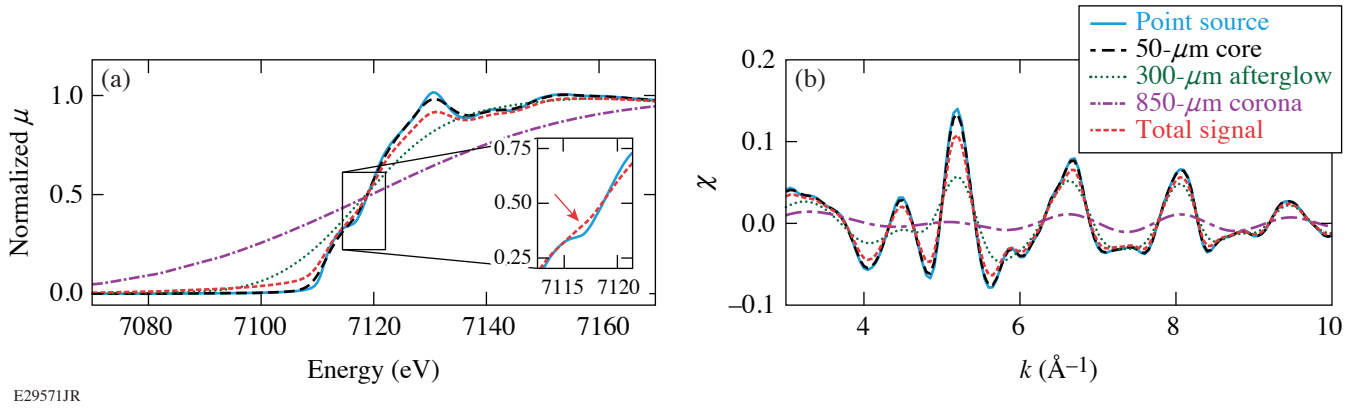

Figure 2
Iron XAFS spectra degraded with the three source sizes, assuming the XRS spectral resolutions. Iron synchrotron data[1] are assumed to give the point-source spectra. (a) XANES spectra as the normalized absorption coefficient (μ). The inset plot compares the point source and total signal with the other lines removed for visibility. The red arrow highlights a modulation that can be used to distinguish structural changes or melting in iron.[3] (b) The EXAFS data as $\chi(k)$ with E_0 = 7118 eV (Ref. 2).

This material is based upon work supported by the Department of Energy National Nuclear Security Administration under Award Number DE-NA0003856, the University of Rochester, and the New York State Energy Research and Development Authority. The support of DOE does not constitute an endorsement by DOE of the views expressed in this paper. D. Chin acknowledges

DOE NNSA SSGF support, which is provided under Cooperative Agreement No. DE-NA0003960. This collaborative work was partially supported under the auspices of the U.S. Department of Energy by Lawrence Livermore National Laboratory under Contract No. DE-AC52-07NA27344.

1. International X-Ray Absorption Society: Fe Data, IXAS X-Ray Absorption Data Library, Accessed 10 May 2021, https://xaslib.xrayabsorption.org/elem/.
2. B. Ravel and M. Newville, J. Synchrotron Rad. **12**, 537 (2005).
3. M. Harmand *et al.*, Phys. Rev. B **92**, 024108 (2015).
4. B. Kettle *et al.*, Phys. Rev. Lett. **123**, 254801 (2019).
5. E. Sevillano, H. Meuth, and J. J. Rehr, Phys. Rev. B **20**, 4908 (1979).
6. B. Ravel and M. Newville, J. Synchrotron Rad. **12**, 537 (2005).

Underdense Relativistically Thermal Plasma Produced by Magnetically Assisted Direct Laser Acceleration

K. Weichman,[1,2] J. P. Palastro,[1] A. P. L. Robinson,[3] and A. V. Arefiev[2,4]

[1]Laboratory for Laser Energetics, University of Rochester
[2]Department of Mechanical and Aerospace Engineering, University of California, San Diego
[3]Central Laser Facility, STFC Rutherford Appleton Laboratory
[4]Center for Energy Research, University of California, San Diego

The discovery of special relativity in 1905 transformed the fields of electromagnetism and charged-particle kinetics that, some 20 years later, would coalesce into the field of plasma physics. Predictions have continually emphasized the importance of special relativity in plasmas where the majority of electrons are relativistic regardless of reference frame, but, even today, experimental verifications of these predictions remain relatively rare. The laboratory generation of these relativistically thermal plasmas is needed to address open questions in astrophysics regarding shock acceleration and the origin of cosmic rays,[1] fast radio bursts,[2,3] and γ-ray bursts.[4] Relativistically thermal plasmas also feature a substantially modified response to electromagnetic radiation relative to the nonrelativistic or nonthermal cases, which is of significant interest in basic plasma physics,[5] laboratory astrophysics,[6,7] and laser-plasma physics.[8–11]

It is challenging, however, to produce relativistically thermal plasma in the laboratory with sufficient volume and duration for subsequent probing. Pulsed-power and microwave sources, while capable of igniting thermal plasma over large volumes, are incapable of reaching relativistic electron temperatures. Laser pulses with relativistic intensity ($I_0 \gtrsim 10^{18}$ W/cm^2 for $\lambda_0 = 1$-μm wavelength) are capable of imparting substantial energy to electrons, but they are conventionally unable to create persistent, large-volume plasma where the majority of electrons are relativistic. Configurations involving opaque plasma ($n_e > n_c$, where $n_c \approx 10^{21}$ cm^{-3} is the critical density for $\lambda_0 = 1$ μm),[12,13] near-critical density plasma,[14] or acceleration by the plasma (wakefield) electric field[15,16] typically leave the majority of electrons cold in either momentum or configuration space. In the underdense regime ($n_e < n_c$), laser pulses can volumetrically accelerate electrons to high energy,[17,18] but the plasma does not remain hot after the laser pulse passes due to the reversibility of the acceleration process. This reversibility is disrupted, however, by the addition of a uniform static magnetic field, enabling dramatic plasma heating.

We propose the first method to volumetrically generate relativistically thermal, underdense plasma. Our approach leverages two regimes of magnetically assisted direct laser acceleration, as illustrated in Figs. 1(a)–1(c). First, a $+x$-propagating, y-polarized relativistic short (20-fs) laser pulse interacts with electrons in an underdense (10^{-3} n_c) plasma with an embedded transverse magnetic field $B_0\hat{z} = 500$ T, imparting net energy as electrons slip through the full pulse duration [Fig. 1(b)]. Second, a longer (0.8-ps) laser pulse with the same propagation and polarization directions interacts with these preheated electrons, delivering half-laser-cycle energy kicks that promote the electron to higher-energy cyclotron orbits [Fig. 1(c)]. The short (subscript "s") and long (subscript "ℓ") laser pulses have peak normalized electric-field amplitude ($a_0 = \left| e \right| E_0 / mc\omega_0$, where ω_0 is the laser frequency) of $a_s = 5$ and $a_\ell = 1$. Simulations were conducted in 2-D using the particle-in-cell code *EPOCH*.[19]

The interaction of the two laser pulses with the target creates multi-MeV average electron energy over a large volume (e.g., $r < w/2 = 25$ μm, where w is the HWHM laser spot size), which persists for picoseconds following the interaction [Fig. 1(d)]. The corresponding momentum spectrum is 2-D isotropic (in p_x and p_y) with a flat energy spectrum. While the plasma can be heated somewhat by the short laser pulse and magnetic field alone, significant relativistic heating requires all three elements of

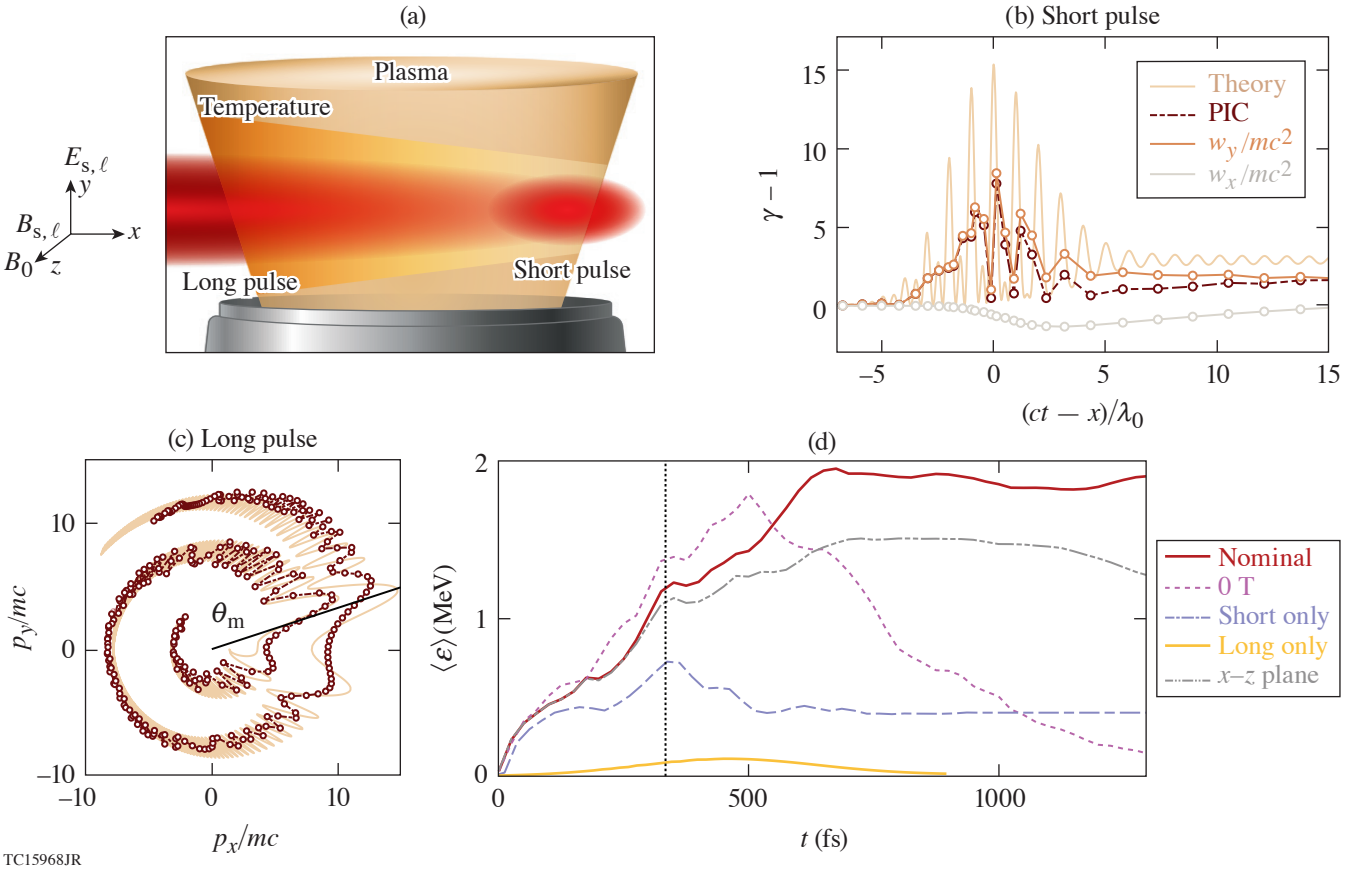

Figure 1
Generation of relativistic underdense plasma via magnetically assisted direct laser acceleration. (a) Illustration of laser and magnetic-field configuration. [(b),(c)] Example of the energy-gain process for a representative electron interacting with (b) the short pulse, and (c) the long pulse. w_y (w_x) is the work done by the transverse (longitudinal) electric field. (d) Average energy of all electrons in $r < 25$ μm. Vertical black dotted line: the time the peak of the short pulse leaves the plasma slab. The long-pulse intensity has dropped to a_ℓ/e at the right edge of the slab at the final time shown. The nominal case corresponds to both laser pulses and $B_{z0} = 500$ T, simulated in the x–y plane.

the short laser pulse, long laser pulse, and applied magnetic field [c.f., cases in Fig. 1(d)]. Unlike conventional laser-based heating methods, more than half of the electron population is heated to $\gamma \geqslant 2$, i.e., the plasma is relativistically thermal.

These observations are explainable as volumetric heating by magnetically assisted direct laser acceleration in the two distinct regimes covered by the short pulse and the long pulse. The energy retained following electron interaction with the short laser pulse through multicycle magnetically assisted direct laser acceleration[20] is used to catalyze subsequent heating by a long (picosecond) laser pulse via half-cycle magnetically assisted direct laser acceleration.[21] The latter process is capable of imparting higher net energy than the former; however it requires preheating of electrons, which in our case is provided by the short pulse.

The generation of relativistically thermal plasma is robust to increased electron density (up to $10^{-2}\,n_c$), finite laser spot size in the magnetic-field direction, and lower applied magnetic-field strength (e.g., 200 T). The average electron energy can additionally be increased by increasing the plasma size and the laser pulse duration, as shown in Fig. 2.

Our results demonstrate that the generation of underdense, relativisitically thermal plasma can be realized with currently available laser and magnetic-field–generation capabilities. With a 200-T magnetic field, we anticipate multi-MeV average electron energy under gas-jet–relevant conditions ($n_e \sim 10^{18}$ cm^{-3}, few-millimeter plasma size) using kilojoule-class laser pulses with a

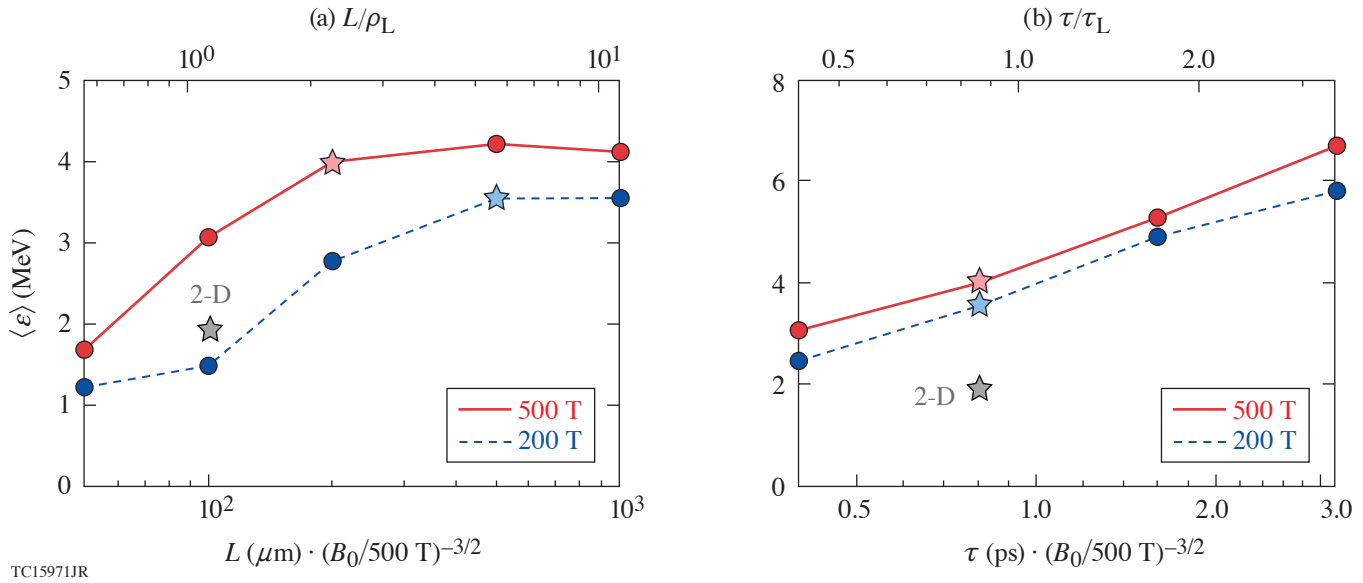

Figure 2
Strategies for improving average electron energy in 1-D particle-in-cell simulations. (a) Scan over plasma size near $L/\rho_L \sim 1$ with fixed duration. (b) Scan over long-pulse duration near $\tau_\ell/\tau_L \sim 1$ with fixed plasma size. ρ_L and τ_L are the Larmor radius and cyclotron period associated with the maximum energy that can be delivered in a half-cycle energy kick $\Delta\gamma \sim 2^{3/2}a^{3/2}_\ell\,(\omega_0/\omega_{c0})^{1/2}$. The starred points are shared between (a) and (b). The peak of the short pulse is kept coincident with a_ℓ/e on the rising edge of the long pulse. $\tau_s = 50$ fs for the 200-T cases.

few-hundred-micron spot size and 50-fs/multipicosecond duration. Our approach is thereby anticipated to offer the first practical access to the relativistically thermal plasma regime, enabling experimental verification of longstanding, foundational predictions in basic plasma physics, laboratory astrophysics, and laser-plasma physics.

We thank R. Bingham (STFC Rutherford-Appleton Laboratory) for useful discussions. This material is based upon work supported by the Department of Energy National Nuclear Security Administration under Award Number DE-NA0003856, the University of Rochester, and the New York State Energy Research and Development Authority, and the DOE Office of Science under Grant No. DESC0018312. A. V. Arefiev was supported by NSF Grant No. 1903098. The support of DOE does not constitute an endorsement by DOE of the views expressed in this paper. Particle-in-cell simulations were performed using *EPOCH*,[19] developed under UK EPSRC Grant Nos. EP/G054940, EP/G055165, and EP/G056803. This work used HPC resources of the National Energy Research Scientific Computing Center (NERSC), a U.S. Department of Energy Office of Science User Facility operated under Contract No. DE-AC02-05CH11231, and the Extreme Science and Engineering Discovery Environment (XSEDE),[22] which is supported by National Science Foundation grant number ACI-1548562, under allocation TG-PHY190034 on the Texas Advanced Computing Center (TACC) at The University of Texas at Austin.

1. R. Blandford and D. Eichler, Phys. Rep. **154**, 1 (1987).
2. R. Bingham *et al.*, Astrophys. J. **595**, 279 (2003).
3. B. D. Metzger, B. Margalit, and L. Sironi, Mon. Not. R. Astron. Soc. **485**, 4091 (2019).
4. P. Kumar and B. Zhang, Phys. Rep. **561**, 1 (2015).
5. J. Bergman and B. Eliasson, Phys. Plasmas **8**, 1482 (2001).
6. M. Lontano, S. Bulanov, and J. Koga, Phys. Plasmas **8**, 5113 (2001).
7. T.-Y. B. Yang, J. Arons, and A. B. Langdon, Phys. Plasmas **1**, 3059 (1994).
8. D. J. Stark *et al.*, Phys. Rev. Lett. **115**, 025002 (2015).
9. G. Li, W. B. Mori, and C. Ren, Phys. Rev. Lett. **110**, 155002 (2013).
10. Y. Zhao *et al.*, Phys. Plasmas **21**, 112114 (2014).
11. J. S. Ross *et al.*, Phys. Rev. Lett. **104**, 105001 (2010).

12. M. A. Purvis *et al*., Nat. Photonics **7**, 796 (2013).
13. S. M. Weng *et al*., Sci. Rep. **6**, 22150 (2016).
14. G. Li *et al*., Phys. Rev. Lett. **100**, 125002 (2008).
15. T. Tajima and J. M. Dawson, Phys. Rev. Lett. **43**, 267 (1979).
16. E. Esarey, C. B. Schroeder, and W. P. Leemans, Rev. Mod. Phys. **81**, 1229 (2009).
17. J. Krüger and M. Bovyn, J. Phys. A **9**, 1841 (1976).
18. F. V. Hartemann *et al*., Phys. Rev. E **51**, 4833 (1995).
19. T. D. Arber *et al*., Plasma Phys. Control. Fusion **57**, 113001 (2015).
20. A. P. L. Robinson and A. V. Arefiev, Phys. Plasmas **27**, 023110 (2020).
21. A. Arefiev, Z. Gong, and A. P. L. Robinson, Phys. Rev. E **101**, 043201 (2020).
22. J. Towns *et al*., Comput. Sci. Eng. **16**, 62 (2014).

An Independent-Hot-Spot Approach to Multibeam Laser–Plasma Instabilities

R. K. Follett, H. Wen, D. H. Froula, D. Turnbull, and J. P. Palastro

Laboratory for Laser Energetics, University of Rochester

In laser-driven inertial confinement fusion (ICF), a millimeter-scale cryogenic capsule of deuterium–tritium fuel with a thin outer ablator is imploded by either direct laser illumination (direct drive) or focusing the lasers onto the interior walls of a hohlraum to generate an x-ray bath (indirect drive).[1] In both cases, the many high-intensity laser beams overlapping in underdense plasma can drive various laser–plasma instabilities (LPI's) that can severely inhibit implosion performance.[2,3]

Analytic results for instability behavior are typically limited to the case of a single plane-wave laser driving instability in the linear regime. ICF experiments, however, involve multiple overlapping laser beams, each using a phase plate that generates a complex speckle pattern in the plasma,[4] and accurate predictions of instability behavior require a description that accounts for their combined interaction.[5] Analytic theories for instability behavior in a single speckled beam have been developed using the independent-hot-spot model, where a statistical description of the speckle intensity is combined with the single-speckle instability behavior to predict the global instability behavior.[6,7] Multibeam interactions have historically been described using the common-wave model, where wave-vector matching considerations are used to show that overlapping laser beams can couple to a shared daughter wave propagating along the drive-beam axis of symmetry.[8–13] However, recent experiments and simulations of multibeam LPI's have shown that the common-wave description often fails to predict instability behavior. In particular, laser beams that do not satisfy the geometric requirements imposed by the common-wave matching conditions can still contribute to instability growth.[14–16]

Here we develop a multibeam hot-spot model that provides a more-predictive description of LPI behavior than the widely used common-wave approach. The model is extended to include absolute instability in an inhomogeneous plasma and applied to the two-plasmon–decay (TPD) instability. The excellent agreement with multibeam *LPSE* simulations demonstrates its utility and shows that there is an important qualitative difference between 2-D and 3-D single-speckle instability thresholds that is not present in the plane-wave case and results in lower instability thresholds in 2-D. This approach leads to a new understanding of multibeam instability behavior that can be used to make better quantitative predictions for improving the design of experiments and future laser facilities.

Given a collection of N speckles, the absolute instability threshold occurs when the peak speckle intensity is equal to the single-speckle threshold, $I_M = I_{\text{thr,speckle}}$. Introducing the average laser intensity I_0 and ensemble averaging over speckle realizations, this can be written as

$$I_{\text{thr}} = \frac{1}{\left\langle I_M / I_0 \right\rangle} I_{\text{thr,speckle}}, \tag{1}$$

where we have defined the expected average intensity at threshold $I_{\text{thr}} \equiv \left\langle I_0 \right\rangle$. Accordingly, evaluation of the expected threshold in the independent-hot-spot model is reduced to the evaluation of $\left\langle I_M / I_0 \right\rangle$ and $I_{\text{thr,speckle}}$. The expected peak speckle intensity can be written in terms of the probability that every speckle intensity is less than u:[17]

$$\left\langle I_M / I_0 \right\rangle = \int_0^\infty \left[1 - P\left(I / I_0 < u\right)^N\right] \mathrm{d}u. \tag{2}$$

Reference 18 derives speckle distributions that are valid for high-intensity speckles but behave badly at low intensities. Accordingly, we use exponential distributions at low intensities to generate probability distributions that behave well at all intensities:

$$P\left(I/I_0 > u\right)_{2\text{-D}} = \begin{cases} e^{-u/\mu_2}, & u < u_{s2} \\ A_2\left[\left(\frac{1}{2}+\frac{\pi}{4}\right)u+\frac{1}{2}\right]e^{-u}, & u > u_{s2} \end{cases}, \tag{3}$$

$$P\left(I/I_0 > u\right)_{3\text{-D}} = \begin{cases} e^{-u/\mu_3}, & u < u_{s3} \\ A_3\left[u^{3/2}-\frac{3}{10}u^{1/2}\right]e^{-u}, & u > u_{s3} \end{cases}, \tag{4}$$

where the μ_i are parameters and the A_i and u_{si} are chosen to make the distributions and their first derivatives continuous. Here $\mu_2 = \mu_3 = 4$ was chosen on the basis of comparison to simulations, which gives $A_2 = 1.185$, $u_{s2} = 0.944$, $A_3 = 1.848$, and $u_{s3} = 2.210$.

Incorporating Eqs. (3) and (4) into Eq. (2), using the binomial theorem, and integrating gives

$$\left\langle I_M/I_0\right\rangle_{2\text{-D}} = \sum_{a=1}^{N}\binom{N}{a}(-1)^a\left[\frac{\mu_2}{a}\left(e^{-au_{s2}/\mu_2}-1\right)-A_2^a a^{-1-a}e^{2a/2+\pi}\left(\frac{2+\pi}{4}\right)^a\Gamma\left(1+a,\frac{2a}{2+\pi}+au_{s2}\right)\right], \tag{5}$$

$$\left\langle I_M/I_0\right\rangle_{3\text{-D}} = \sum_{a=1}^{N}\binom{N}{a}(-1)^a\left[\frac{\mu_3}{a}\left(e^{-au_{s3}/\mu_3}-1\right)-A_3^a\sum_{k=0}^{a}\binom{a}{k}\left(-\frac{3}{10}\right)^k a^{k-1-3a/2}\Gamma\left(1-k+3a/2,au_{s3}\right)\right], \tag{6}$$

where $\Gamma(s,x)$ is the incomplete gamma function.

To determine N, we restrict our discussion to instabilities that are spatially localized by plasma inhomogeneity such that N is the number of speckles in a cross section of the laser field (i.e., the interaction region is not significantly longer than the speckle length). Accordingly, N is approximately the laser power divided by the mean power in a speckle, $N = P_L/\langle P_s\rangle$. The laser power is the average intensity times the cross-sectional area ($P_L = I_0\sigma_b$). To determine the mean power in a speckle, we first average over the probability density of speckle intensities to obtain the mean speckle intensity $\left\langle I/I_0\right\rangle = \int_0^\infty uP(u)\mathrm{d}u$, where $P(u) = -\partial P\left(I/I_0 > u\right)/\partial u$. Equations (3) and (4) give

$$\left\langle I/I_0\right\rangle_{2\text{-D}} = \mu_2 - (\mu_2+u_{s2})e^{-u_{s2}/\mu_2} + A_2e^{-u_{s2}}\left[4+\pi+(4+\pi)u_{s2}+(2+\pi)u_{s2}^2\right]/4, \tag{7}$$

$$\left\langle I/I_0\right\rangle_{3\text{-D}} = \mu_3 - (\mu_3+u_{s3})e^{-u_{s3}/\mu_3} + A_3\left[\frac{3\sqrt{\pi}}{5}\operatorname{erfc}\left(\sqrt{u_{s3}}\right)+e^{-u_{s3}}\sqrt{u_{s3}}\left(u_{s3}^2+\frac{7}{10}u_{s3}+\frac{6}{5}\right)\right], \tag{8}$$

where $\operatorname{erfc}(x)$ is the complementary error function. For speckles with a Gaussian transverse profile $\left[I(r) = Ie^{-\left(2\sqrt{\log 2}\,r/w_s\right)^2}\right]$ and full width at half maximum (FWHM) w_s, integration over r gives the mean power in a speckle, $\langle P_s\rangle_{2\text{-D}} = \left\langle I/I_0\right\rangle_{2\text{-D}} I_0 w_s\sqrt{\pi/\log 2}$ and $\langle P_s\rangle_{3\text{-D}} = \left\langle I/I_0\right\rangle_{3\text{-D}} I_0 w_s^2\pi/(4\log 2)$. Finally, the expected number of speckles in 2-D and 3-D, respectively, is

$$N = \frac{\sigma_b}{w_s\left\langle I/I_0\right\rangle_{2\text{-D}}}\sqrt{\frac{\log 2}{\pi}}, \tag{9}$$

$$N = \frac{\sigma_b}{w_s^2 \langle I/I_0 \rangle_{3\text{-D}}} \frac{4\log 2}{\pi}. \tag{10}$$

The single-speckle threshold ($I_{\text{thr,speckle}}$) generally depends on the speckle size, plasma conditions, and the instability under consideration. An analytic approximation can be obtained by constructing a spatially localized solution out of the linear eigenmodes for a plane-wave drive laser,[19] but it is not sufficiently accurate for quantitative applications. Here we take a semi-analytic approach where the speckle statistics are given by Eqs. (5) and (6), while $I_{\text{thr,speckle}}$ is taken from single-speckle *LPSE* simulations.

Figure 1 compares Eq. (1) to various speckled-beam *LPSE* calculations. The thresholds are normalized to the threshold for a single plane-wave drive beam, $I_{\text{thr,TPD}}$ (Ref. 19). Figure 1(a) shows 2-D calculations using a single beam with a varying *f* number at $L_n = 200\ \mu$m, $T_e = 2$ keV, and $L_n = 400\ \mu$m, $T_e = 4$ keV, which are similar to the conditions in direct-drive ICF experiments on the OMEGA[20] and National Ignition Facility[15] lasers, respectively. The thresholds are higher in the longer-scale-length calculations because, for a given speckle width, the single-speckle threshold increases with increasing temperature and scale length. The non-monotonic nature of the thresholds is a result of the competition between the increasing thresholds with decreasing speckle size and the increased number of speckles with decreasing *f* number.

Figures 1(b) and 1(c) show 3-D instability thresholds for $L_n = 200\ \mu$m, $T_e = 2$ keV and $L_n = 400\ \mu$m, $T_e = 4$ keV, respectively, for three different beam configurations: (1) a single beam with varying *f* number; (2) six *f*/6.7 beams uniformly distributed on a cone relative to the *x* axis with polar angle θ and azimuthal angle for the *m*th beam $\varphi_m = 2\pi m/6$; and (3) eight *f*/6.7 beams organized into two four-beam cones with polar angles θ and $\theta/2$ and azimuthal angles $\varphi_m = 2\pi m/4$ and $\varphi_m = 2\pi m/4 + \pi/4$, respectively. For the multibeam cases, the horizontal axis corresponds to an effective *f* number given by the cone angle, $f_{\#} = 1/(2\tan\theta)$ and the beam polarizations were aligned. All three beam configurations give the same threshold to within statistical variations and are in good agreement with the semi-analytic model. This shows that the instability behavior is predominantly determined by the smallest (and highest intensity) speckles and justifies the treatment of the cones of beams as a single beam with a small effective *f* number.

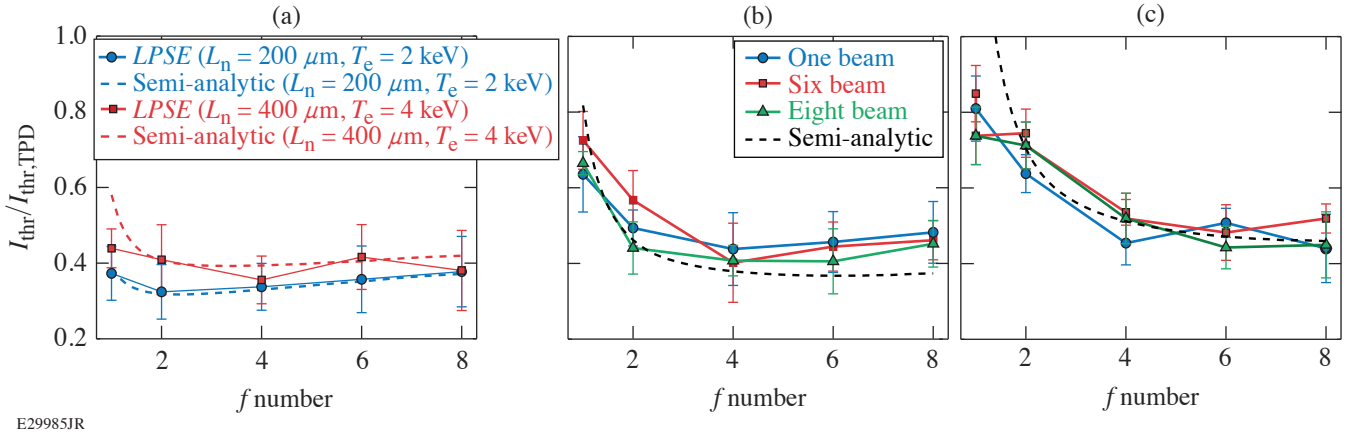

Figure 1
Absolute TPD instability thresholds for speckled beams (normalized to the plane-wave threshold). (a) Two-dimensional *LPSE* calculations at $L_n = 200\ \mu$m, $T_e = 2$ keV (blue circles), and $L_n = 400\ \mu$m, $T_e = 4$ keV (red squares). [(b),(c)] Three-dimensional *LPSE* calculations show $L_n = 200\ \mu$m, $T_e = 2$ keV and $L_n = 400\ \mu$m, $T_e = 4$ keV, respectively, for one beam (blue circles), six beams (red squares), and eight beams (green triangles). The dashed curves show the corresponding semi-analytic results. The error bars correspond to the standard deviation from an ensemble of 20 (5) speckle realizations in 2-D (3-D).

This material is based upon work supported by the Department of Energy National Nuclear Security Administration under Award Number DE-NA0003856, ARPA-E BETHE grant number DE-FOA-0002212, the University of Rochester, and the New York State Energy Research and Development Authority.

1. S. Atzeni and J. Meyer-ter-Vehn, *The Physics of Inertial Fusion: Beam Plasma Interaction, Hydrodynamics, Hot Dense Matter*, 1st ed., International Series of Monographs on Physics, Vol. 125 (Oxford University Press, Oxford, 2004).
2. W. L. Kruer, *The Physics of Laser Plasma Interactions, Frontiers in Physics*, Vol. 73, edited by D. Pines (Addison-Wesley, Redwood City, CA, 1988).
3. R. S. Craxton *et al*., Phys. Plasmas **22**, 110501 (2015).
4. Y. Kato *et al*., Phys. Rev. Lett. **53**, 1057 (1984).
5. C. Stoeckl *et al*., Phys. Rev. Lett. **90**, 235002 (2003).
6. H. A. Rose and D. F. DuBois, Phys. Rev. Lett. **72**, 2883 (1994).
7. V. T. Tikhonchuk, C. Labaune, and H. A. Baldis, Phys. Plasmas **3**, 3777 (1996).
8. D. F. DuBois, B. Bezzerides, and H. A. Rose, Phys. Fluids B **4**, 241 (1992).
9. D. T. Michel *et al*., Phys. Rev. Lett. **109**, 155007 (2012).
10. P. Michel *et al*., Phys. Rev. Lett. **115**, 055003 (2015).
11. J. Zhang *et al*., Phys. Rev. Lett. **113**, 105001 (2014).
12. D. T. Michel *et al*., Phys. Plasmas **20**, 055703 (2013).
13. J. F. Myatt *et al*., Phys. Plasmas **21**, 055501 (2014).
14. R. K. Follett *et al*., Phys. Plasmas **24**, 102134 (2017).
15. M. J. Rosenberg *et al*., Phys. Rev. Lett. **120**, 055001 (2018).
16. R. K. Follett *et al*., Phys. Rev. E **101**, 043214 (2020).
17. B. Eisenberg, Stat. Probab. Lett. **78**, 135 (2008).
18. J. Garnier, Phys. Plasmas **6**, 1601 (1999).
19. A. Simon *et al*., Phys. Fluids **26**, 3107 (1983).
20. T. R. Boehly *et al*., J. Appl. Phys. **85**, 3444 (1999).

Density Reconstruction in Convergent High-Energy-Density Systems Using X-Ray Radiography and Bayesian Inference

S. Ressel,[1,*] J. J. Ruby,[1,2,†] G. W. Collins,[1,2,3] and J. R. Rygg[1,2,3]

[1]Laboratory for Laser Energetics, University of Rochester
[2]Department of Physics and Astronomy, University of Rochester
[3]Department of Mechanical Engineering, University of Rochester
[*]Currently at Department of Atmospheric Sciences, University of Washington
[†]Currently at Lawrence Livermore National Laboratory

X-ray radiography is a technique frequently used to diagnose convergent high-energy-density (HED) systems, such as inertial confinement fusion (ICF) implosions, and to provide unique information that is not available through self-emission measurements. We investigate the scope and limits of that information using a radiography simulation combined with Bayesian inference workflow. The accuracy of density reconstruction from simulated radiographs of spherical implosions driven with 20 kJ of laser energy is assessed, including the increase or decrease in accuracy due to the addition of Lagrangian marker layers, Poisson noise, and improved prior information. This work is the first to present the full uncertainty distributions inferred from radiography analysis in HED systems and demonstrates the importance of constructing the full posterior probability density, as opposed to a point estimate, due to the modal structure of the likelihood surface introduced by typical experimental noise sources. This general methodology can be used for both robust analysis of radiographic data and improved design of radiography experiments by modeling the full experimental system.

The inference workflow was tested on realistic data generated from the 1-D radiation-hydrodynamic code *LILAC*, where a single spherically converging shock wave was simulated in a solid hydrocarbon sphere (CH) driven by 27 kJ of UV light using the *SESAME* 7592 EOS table and Los Alamos's astrophysical opacity tables. The resulting radial density profiles are used to generate a simulated radiograph, using a straight-line ray trace to simulate the optical system of an x-ray streak camera with a slit imager, to determine how much density-profile information is encoded in the lineout and to what extent the density profile can be reconstructed from lineout data.

The parameterization used to represent the *LILAC* density profile is similar in form to previous work[1] and is given by

$$\rho(r) = \rho_0; r < r_s,$$

$$\rho(r) = \rho_s + (\rho_p - \rho_s)(r - r_s)/(r_p - r_s); r_s < r < r_p,$$

$$\rho(r) = \rho_p \cdot \exp\left[-(r - r_p)^2/(2\sigma^2)\right]; r_p < r < r_e,$$

$$\rho(r) = \rho_e \cdot \exp\left[-a(r - r_e)\right]; r_e < r,$$

$$\text{and } \sigma = \sqrt{-(r_p - r_e)^2/2\ln(\rho_e - \rho_p)}. \quad (1)$$

where r_s, r_p, and r_e are the radial locations of the shock, peak density, and tail, respectively; ρ_0, ρ_s, ρ_p, and ρ_e are the densities of the material in ambient conditions, immediately after being shocked, at its maximum due to converging flows, and at the tail of the density profile, respectively; and α is a scale parameter that determines how quickly the density reduces to zero in the tail.

The results of using Bayesian inference to construct the posterior probability densities for the parameters in the density profile (shown in Fig. 1) demonstrate that some additional information is needed to constrain the inferred shock compression. Figure 2(a) shows the uniform prior distribution (green) for the shock compression, alongside the posteriors from inference including an additional constraint and including noise. A defining feature of the inference from these cases is the upper limit placed on the shock compression, which can be used in combination with outside information to further constrain the posterior.

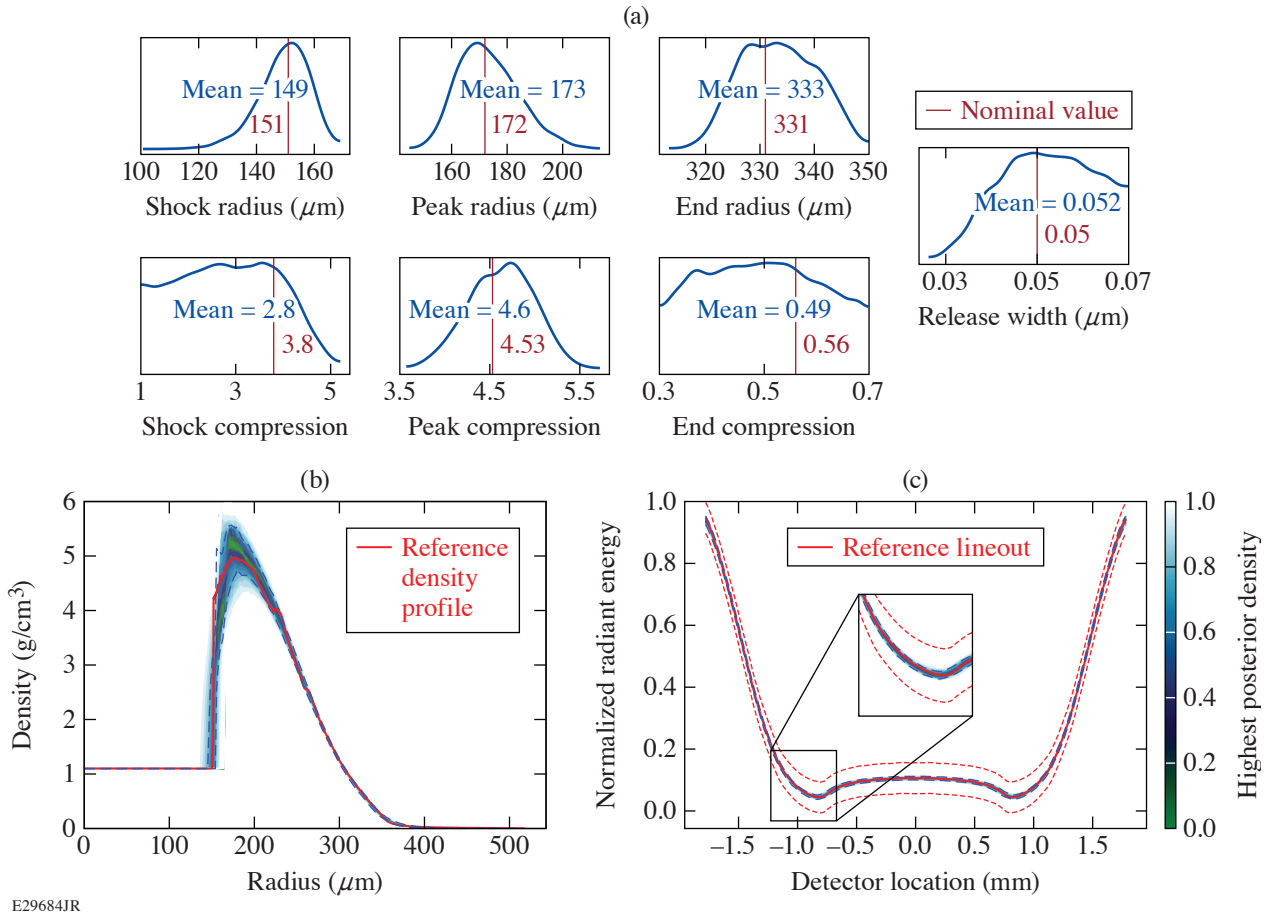

Figure 1

(a) Posterior distributions for each of the seven parameters of the model given in Eq. (1), as well as (b) posterior predictive distributions (PPD's) of the density profiles and (c) lineouts generated from said posterior distributions. A number of the parameters are well constrained, as shown by a single narrow peak in their posterior distributions, including the location of the shock, the location of the peak density, and the peak compression, and they all recover the underlying nominal value, given by the vertical red line, which is the least-squares best fit value recovered by fitting the simulated density profile with the assumed model. Notably, the posterior distribution for the shock compression (ρ_s/ρ_0) is not well constrained, presenting an upper bound of about 4, but roughly equal probability density across all values below 4. This can also be seen in (b), which is well matched to the reference density profile outside the region of the shock. Despite this, the PPD's of the lineouts in (c) are converged from the inference and well matched to the reference information, even around the feature due to the shock limb highlighted in the inset.

The simplest way to introduce this outside information is by using a more-informed prior distribution—for example, one that introduces a lower limit on the shock compression. A naive implementation is shown in Fig. 2(b) where the data-informed prior (orange) is simply a uniform distribution with a lower bound set by the maximum compression measurement of 3.39 (Ref. 2)

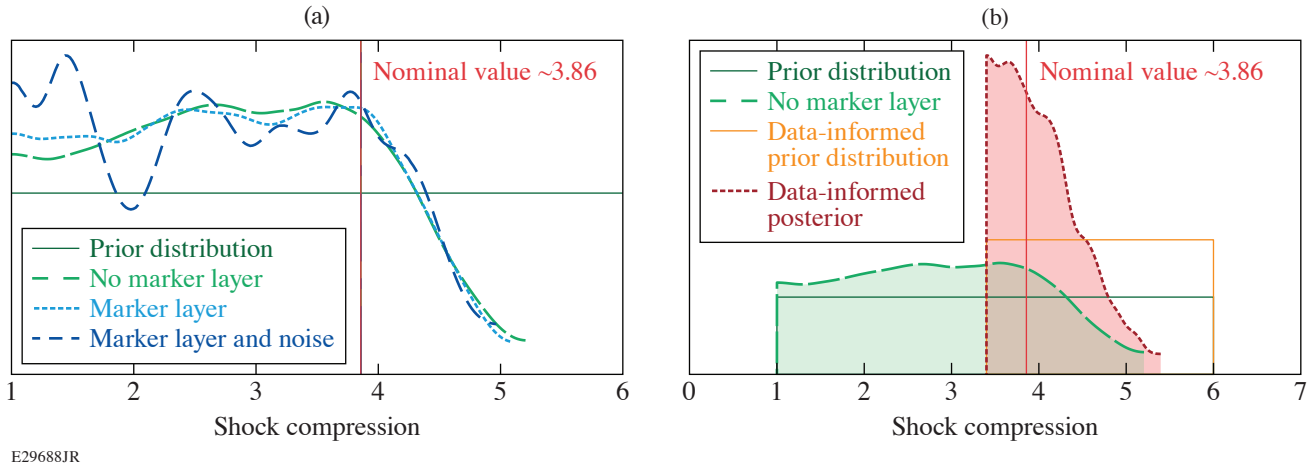

Figure 2

(a) Posterior distributions of the shock compression (ρ_s/ρ_0) for the cases with no noise and no Lagrangian marker layer (dashed green curve), no noise with a Lagrangian marker layer (dotted light blue curve), and with noise and a Lagrangian marker layer (dashed dark blue curve). Also shown are the prior used for each case (solid green, horizontal line) and the nominal value from the *LILAC* density profile (solid red, vertical line), given as ~3.86. All of the distributions show the same general trend that above a compression of 4 the probability density drops sharply, due to the peak compression behind the shock being well constrained and the shock jump necessarily being smaller, effectively giving an upper bound on the shock jump. There is little constraint on the lower end of the compression where the probability density is effectively flat between 1 and 4. The case with noise shows modal structure that, if point estimates are used, can give the impression of constraint while being only a local maximum in probability density. (b) The posterior for shock compression (dashed green curve) for the case with a broad uniform prior (solid green line) and posterior (dotted red curve) for the case with a narrow uniform prior (solid orange line) truncated at the low end at the location of previous measurements.[2] This demonstrates how Bayesian inference allows additional information to be leveraged to constrain a quantity that is otherwise unconstrained. The combination of the prior informing a lower limit of compression and the radiograph constraining upper limits of compression results in a nicely peaked posterior probability density that captures the proper underlying value (solid red line). The axes are expanded to demonstrate how the priors enforce that there is zero probability density outside of their bounds. Note that the data-informed posterior is largely asymmetric, although it presents a strongly peaked result that recovers the nominal value.

from previous data along the Hugoniot of CH up to 8.74 Mbar performed in planar geometry using a different methodology. Figure 2(b) also shows the posterior for shock compression given the new prior (red), which is now significantly more peaked than the previous results (green), meaning that there is a well-defined region of high probability density.

Although the shock compression is not strongly constrained by the radiograph alone, the density profile is well constrained by the radiograph measurement. In particular, the areal density (ρR) is very well constrained and is a quantity of particular interest within the ICF community. The findings here are in excellent agreement with previous radiography measurements taken on shells for the purpose of diagnosing metrics relevant to ICF modeling.[3] This work can be seen as an extension of those efforts with additional insight into the uncertainties associated with such reconstructions. Additionally, the peak density achieved within the bulk of the material behind the shock, which has a great effect on the propagation of the outgoing shock wave, is well constrained. Radiography measurements of this kind contain a great deal of information that can be used in combination with other measurements to develop a full picture of implosion experiments, including how materials respond to strong converging shock waves. This work can be used as a foundation to develop further investigations about the information contained in measurements of this type.

This material is based upon work supported by the Department of Energy National Nuclear Security Administration under Award Number DE-NA0003856, the U.S. Department of Energy, Office of Science, Office of Fusion Energy Sciences under Award No. DE-SC001926, the University of Rochester, and the New York State Energy Research and Development Authority.

1. D. C. Swift *et al.*, Rev. Sci. Instrum. **89**, 053505 (2018).
2. M. A. Barrios *et al.*, Phys. Plasmas **17**, 056307 (2010).
3. D. G. Hicks *et al.*, Phys. Plasmas **17**, 102703 (2010).

Diamond Formation in Double-Shocked Epoxy to 150 GPa

M. C. Marshall,[1] M. G. Gorman,[2] D. N. Polsin,[1,3] J. H. Eggert,[2] M. K. Ginnane,[1,3] J. R. Rygg,[1,3,4] G. W. Collins,[1,3,4] and L. D. Leininger[2]

[1]Laboratory for Laser Energetics, University of Rochester
[2]Lawrence Livermore National Laboratory
[3]Department of Mechanical Engineering, University of Rochester
[4]Department of Physics and Astronomy, University of Rochester

The formation of diamond from carbon-based polymers, compounds, or other carbon polymorphs (i.e., graphite) under extreme pressures has been actively researched for many decades.[1–12] Diamond can form by extreme heating and compression of some plastics,[1] methane,[2,3] and explosive materials.[10,12] For example, cubic diamond was detected from double-shocked polystyrene (CH) at 139 to 159 GPa using *in-situ* x-ray diffraction in experiments at the Linac Coherent Light Source (LCLS), indicating that breaking of the carbon and hydrogen bonds and restructuring of the carbon into diamond can occur over only nanosecond time scales.[1] The results presented here indicate that cubic diamond also forms from Stycast 1266 epoxy (C:H:Cl:N:O ≈ 27:38:1:1:5) (Ref. 13) doubly shocked to 80 and 148 GPa. These results demonstrate that the chemical and thermodynamic conditions inside ice giant planets, which have inner ice layers dominated by CH_4, NH_3, and H_2O, are suitable for diamond formation.

Two experiments were conducted on the OMEGA EP Laser System,[14] where laser beams were used to shock compress the target comprising an epoxy sample and a LiF window with a reflective Ti coating between them to measure the interface velocity using a velocity interferometer system for any reflector (VISAR).[15] When the shock wave is incident on the higher-impedance LiF interface, a return shock (reshock) is launched back through the epoxy, which approximately doubles the pressure. The target was probed with x rays, and the resulting diffraction pattern was measured using the powder x-ray diffraction image-plate diagnostic[16] when the epoxy was in the reshocked state. Diffraction consistent with cubic diamond was observed for both shots (Fig. 1). The pressure and temperature state during the x-ray exposure time were determined using hydrodynamic simulations matched to the measured epoxy/LiF interface velocity.

The results are compared to previous works in Fig. 1(a), where CH (Ref. 1), polyethylene (CH_2) (Ref. 5), methane (CH_4), (Refs. 2 and 3), and methane hydrate (MH) (Ref. 4) were also probed *in situ* at high pressures and temperatures to study diamond formation. Diamond formation from methane and methane hydrate is observed over ~10 to 80 GPa and ~2000 to 4000 K in laser-heated diamond-anvil cell experiments, where the samples are compressed and heated over seconds to hours.[2–4] At these conditions and compression rates, diamond formation is largely temperature dependent and the temperature threshold at which it occurs is lowered by the addition of oxygen as suggested by the methane hydrate experiments.[4] Diamond formation is not observed in singly shocked CH (Ref. 1) and CH_2 (Ref. 5) when they are compressed over nanoseconds at similar temperatures and pressures. While diamond still does not form in doubly shocked CH_2, it does form from doubly shocked CH and epoxy at ~80 to 200 GPa pressures and ~2000 to 6000 K temperatures. Diamond formation at these fast nanosecond times scales is not purely pressure or temperature dependent and is affected by the initial material composition and thermodynamic compression path (e.g., single versus double shock). These differences in behavior among all the experiments collectively suggest that the kinetics associated with the vastly different time scales, the thermodynamic path, and the chemical composition of the initial material play an important role in diamond formation at extreme conditions.

(a)

Diamond	No diamond	Initial material	Experiment type, time scale	
◆		Epoxy (C,H,O,N,Cl)	Laser shock, ~1 to 15 ns	Marshall (this work)
◆	+	CH	Laser shock, ~1 to 10 ns	Kraus[1]
	+ +	CH_2	Laser shock, ~1 to 10 ns	Hartley[5]
◆	+	MH (C,H,O)	LHDAC, ~10 to 120 min	Kadobayashi[4]
▭		CH_4	LHDAC, ~1 to 15 min	Benedetti[2]
▭		CH_4	LHDAC, ~10 s to 15 min	Hirai[3]

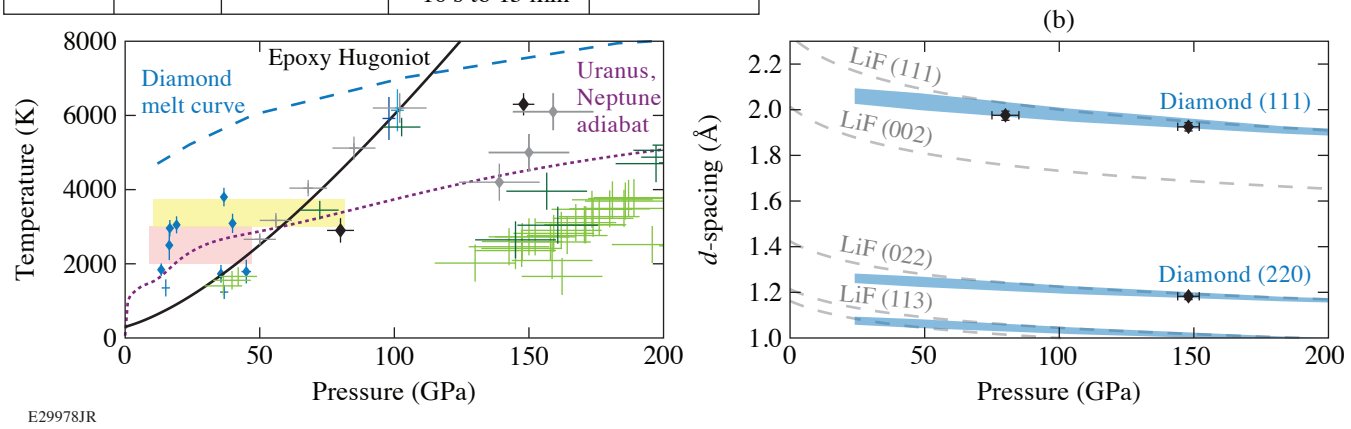

Figure 1
(a) Phase diagram showing diamond-formation results from compressed and heated epoxy, polystyrene (CH), polyethylene (CH_2), methane hydrate (MH), and methane (CH_4). Data points on singly shocked CH and CH_2 lie close to the epoxy Hugoniot (*SESAME* 7602). Data points from this work and all points above 120 GPa on CH and CH_2 are on doubly shocked samples. (b) Lattice *d*-spacing results from this work compared to predictions for compressed diamond (spanning the cold curve[17] to the melt curve[18] to encompass all possible temperature effects) and shocked LiF.

This material is based upon work supported by the Department of Energy National Nuclear Security Administration under Award Number DE-NA0003856, the University of Rochester, and the New York State Energy Research and Development Authority. This work was performed under the auspices of the U.S. Department of Energy by Lawrence Livermore National Laboratory (LLNL) under LLNL's Laboratory Directed Research and Development (LDRD) Program under Grant No. 18-SI-004. Lawrence Livermore National Laboratory is operated by Lawrence Livermore National Security, LLC, for the U.S. Department of Energy, National Nuclear Security Administration under Contract DE-AC52-07NA27344.

1. D. Kraus *et al.*, Nat. Astron. **1**, 606 (2017).
2. L. R. Benedetti *et al.*, Science **286**, 100 (1999).
3. H. Hirai *et al.*, Phys. Earth Planet. Inter. **174**, 242 (2009).
4. H. Kadobayashi *et al.*, Sci. Rep. **11**, 8165 (2021).
5. N. J. Hartley *et al.*, Sci. Rep. **9**, 4196 (2019).
6. D. Kraus *et al.*, Nat. Commun. **7**, 10970 (2016).
7. E. B. Watkins *et al.*, Sci. Rep. **12**, 631 (2022).
8. D. G. Morris, J. Appl. Phys. **51**, 2059 (1980).

9. F. H. Ree, J. Chem. Phys. **70**, 974 (1979).
10. M. van Thiel and F. H. Ree, J. Appl. Phys. **62**, 1761 (1987).
11. W. J. Nellis *et al.*, J. Chem. Phys. **75**, 3055 (1981).
12. J. B. Donnet *et al.*, Diam. Relat. Mater. **9**, 887 (2000).
13. We provide only an estimated C:H:Cl:N:O ratio for the final cured Stycast 1266 mixture, obtained by combining the listed components in the safety data sheets for Parts A and B by the quoted mix ratios and assuming a closed system. The exact composition of the Stycast 1266 Part A and B may vary from the quoted percentages or are trade secrets.
14. D. D. Meyerhofer *et al.*, J. Phys.: Conf. Ser. **244**, 032010 (2010).
15. P. M. Celliers *et al.*, Rev. Sci. Instrum. **75**, 4916 (2004).
16. J. R. Rygg *et al.*, Rev. Sci. Instrum. **83**, 113904 (2012).
17. A. Dewaele *et al.*, Phys. Rev. B **77**, 094106 (2008).
18. X. Wang, S. Scandolo, and R. Car, Phys. Rev. Lett. **95**, 185701 (2005).

Meta-GGA Exchange-Correlation Free Energy Density Functional to Increase the Accuracy of Warm-Dense-Matter Simulations

V. V. Karasiev, D. I. Mihaylov, and S. X. Hu

Laboratory for Laser Energetics, University of Rochester

High-energy-density physics includes a complicated warm-dense-matter (WDM) domain of state conditions that is characterized by elevated temperatures (from few to hundreds of eV) and pressures to 1 Mbar or greater. Accurate knowledge of equation of state, transport, and optical properties describing possible phase transitions (e.g., insulator-to-metal transition) across a warm dense regime plays an important role in planetary science, astrophysics, and inertial confinement fusion.[1–6] Currently, the vast majority of density-functional-theory (DFT) simulations of WDM and high-energy-density plasmas use the zero-temperature (ground-state) exchange-correlation (XC) functionals without explicit temperature dependence, which were developed by the condensed-matter physics and quantum chemistry communities, leading to neglect of thermal XC effects and degraded accuracy of predictions. The use of a ground-state XC functional is justified only at low electronic temperatures not exceeding a few tenths of the Fermi temperature or in the high-temperature limit when the XC contribution to the total free energy is negligible.[7–10] Recent development of the temperature-dependent Karasiev–Sjostrom–Dufty–Trickey (KSDT)[11] local-density approximation (LDA) (see Ref. 12 for the corrected set of parameters corrKSDT), the generalized gradient approximation (GGA)–type XC functional "KDT16" (Ref. 12), and the thermal hybrid KDT0[13] have shown that thermal XC effects are very important to increasing the accuracy of simulations at extreme conditions and improving agreement with experimental measurements as compared to the standard zero-temperature Perdew–Burke–Ernzerhof (PBE)[14] calculations. The way to improve overall accuracy of the thermal GGA XC functional is to use the next rung approximation at zero temperature and construct thermally extended meta-GGA XC.

In this work, we address this problem by developing a thermalization framework for XC functionals at the meta-GGA level of refinement and realization of a simple scheme via universal thermal XC additive correction at the GGA level of theory, which is applied to an accurate at low-T, ground-state meta-GGA XC. Thermal correction is applied to the ground-state deorbitalized, strongly constrained, and appropriately normed semilocal density functional (SCANL)[15–18]—to date, one of the most-accurate meta-GGA XC functionals, which, for example, is capable of accurately describing the liquid–liquid insulator-to-metal transition of warm dense hydrogen.[3] The resulting thermal meta-GGA XC functional, referred to here as T-SCAN-L, inherits the precision of the ground-state meta-GGA SCAN-L at low T, and most of the thermal XC effects are captured at the GGA level of theory, providing overall a much higher accuracy across the temperature regimes spanned by the WDM domain.

With increasing temperature, the electron density approaches the slowly varying regime. The KDT16 GGA functional, by construction, recovers the finite-T gradient expansion. Thermal XC corrections beyond the GGA level are expected to be small; therefore, in the following we propose a simple perturbative-like self-consistent approach via a universal thermal additive correction treated self-consistently, similar to the idea used in Ref. 19 to construct GGA XC with additive thermal LDA correction. The KDT16 XC free energy in the zero-T limit reduces to the ground-state PBE by construction:

$$\lim_{T\to 0} \mathcal{F}_{\mathrm{xc}}^{\mathrm{KDT16}}\left[n,T\right] \approx E_{\mathrm{xc}}^{\mathrm{PBE}}\left[n\right], \tag{1}$$

a choice driven by popularity of the PBE functional and by availability of pseudo-potentials and projector augmented wave (PAW) data sets generated by using the PBE XC. Given the quality of SCAN-L functional at zero temperature, we propose a simple temperature-dependent meta-GGA

$$\mathcal{F}_{\mathrm{xc}}^{\text{meta-GGA}}[n,T] = E_{\mathrm{xc}}^{\text{meta-GGA}}[n] + \Delta\mathcal{F}_{\mathrm{xc}}^{\mathrm{GGA}}[n,T], \tag{2}$$

with the additive thermal correction defined as follows:

$$\Delta\mathcal{F}_{\mathrm{xc}}^{\mathrm{GGA}}[n,T] := \mathcal{F}_{\mathrm{xc}}^{\mathrm{KDT16}}[n,T] - E_{\mathrm{xc}}^{\mathrm{PBE}}[n] \tag{3}$$

and meta-GGA = SCAN-L. An explicit functional form defined by Eqs. (2) and (3) is used in standard fully self-consistent DFT calculations with local XC potential calculated as a functional derivative of $\mathcal{F}_{\mathrm{xc}}^{\text{meta-GGA}}[n,T]$ with respect to electron density n.

Ab initio molecular dynamics (AIMD) simulations that demonstrate the superior accuracy of the new T-SCAN-L meta-GGA functional are for dense helium. Figure 1 compares relative errors for total pressures obtained from DFT simulations with four XC functionals and high-quality path-integral Monte Carlo (PIMC). PIMC is an efficient *first-principles* simulation technique for quantum systems at finite temperature that accurately takes into account the Coulombic interaction between electrons using pair-density matrices, so it therefore can be used to benchmark approximate XC density functionals at elevated temperatures.[7] Both ground-state functionals (PBE and SCAN-L) systematically overestimate the total pressure: the relative error with respect to the reference PIMC data is between 4.2% and 5.8% at T = 10.77 eV. In contrast, the T-SCAN-L total pressures are in excellent agreement with the PIMC values, demonstrating unprecedented accuracy between 0.05% and 0.35% for this range of densities. Relative differences between the KDT16 and PIMC values are larger as compared to the T-SCAN-L values and range from 0.4% to 1.4%. These comparisons show that T-SCAN-L calculations can improve the DFT simulation accuracy for He at these warm dense conditions by a factor of ~3 to 10 over the widely used XC functionals (PBE, SCANL, and KDT16). This clearly demonstrates that the T-SCAN-L meta-GGA functional can accurately capture combined XC thermal and nonhomogeneity effects. When temperature increases to 21.54 eV, the relative error of the ground-state functionals reduces to the range between 1.3% and 3.6% (because the XC contribution becomes less important as compared to the noninteracting free-energy term at high T), while the relative difference between T-SCAN-L and PIMC values is still less than ~1%.

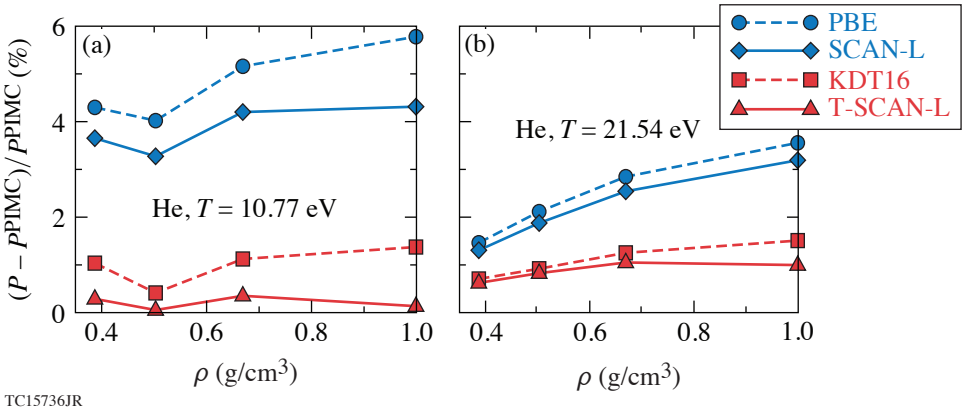

Figure 1
The relative error of total pressure from AIMD simulations of warm dense He using PBE, SCAL-L, KDT16, and T-SCAN-L XC functionals calculated with respect to the reference PIMC results and shown as a function of material density for two temperatures.

The simplest thermalization scheme, which uses a universal additive thermal correction and a perturbative-like self-consistent approach, has been implemented, leading to thermal T-SCAN-L functional. The nonempirical T-SCAN-L meta-GGA density functional takes into account combined thermal and nonhomogeneity effects at the meta-GGA level, providing a significantly higher accuracy for DFT to better predict material properties in the WDM regime, as compared to the thermal KDT16, and to the ground-state PBE and SCAN-L XC functionals. In the zero-temperature limit, T-SCAN-L reduces to its ground-state counterpart, therefore preserving the SCAN-L meta-GGA level of accuracy at low T.

This material is based upon work supported by the Department of Energy National Nuclear Security Administration under Award Number DE-NA0003856 and U.S. National Science Foundation PHY Grant No. 1802964. This research used resources of the National Energy Research Scientific Computing Center, a DOE Office of Science User Facility supported by the Office of Science of the U.S. Department of Energy under Contract No. DE-AC02-05CH11231.

1. J. J. Fortney and N. Nettelmann, Space Sci. Rev. **152**, 423 (2010).
2. W. Lorenzen, B. Holst, and R. Redmer, Phys. Rev. B **84**, 235109 (2011).
3. J. Hinz *et al*., Phys. Rev. Research **2**, 032065(R) (2020).
4. C. A. Iglesias, F. J. Rogers, and D. Saumon, Astrophys. J. Lett. **569**, L111 (2002).
5. S. X. Hu *et al*., Phys. Plasmas **22**, 056304 (2015).
6. V. V Karasiev and S. X. Hu, Phys. Rev. E **103**, 033202 (2021).
7. V. V. Karasiev, L. Calderín, and S. B. Trickey, Phys. Rev. E **93**, 063207 (2016).
8. V. V. Karasiev, S. B. Trickey, and J. W. Dufty, Phys. Rev. B **99**, 195134 (2019).
9. K. Ramakrishna, T. Dornheim, and J. Vorberger, Phys. Rev. B **101**, 195129 (2020).
10. M. Bonitz *et al*., Phys. Plasmas **27**, 042710 (2020).
11. V. V. Karasiev *et al*., Phys. Rev. Lett. **112**, 076403 (2014).
12. V. V. Karasiev, J. W. Dufty, and S. B. Trickey, Phys. Rev. Lett. **120**, 076401 (2018).
13. D. I. Mihaylov, V. V. Karasiev, and S. X. Hu, Phys. Rev. B **101**, 245141 (2020).
14. J. P. Perdew, K. Burke, and M. Ernzerhof, Phys. Rev. Lett. **77**, 3865 (1996); **78**, 1396(E) (1997).
15. J. Sun, A. Ruzsinszky, and J. P. Perdew, Phys. Rev. Lett. **115**, 036402 (2015).
16. H. Peng *et al*., Phys. Rev. X **6**, 041005 (2016).
17. D. Mejia-Rodriguez and S. B. Trickey, Phys. Rev. A **96**, 052512 (2017).
18. D. Mejia-Rodriguez and S. B. Trickey, Phys. Rev. B **98**, 115161 (2018).
19. T. Sjostrom and J. Daligault, Phys. Rev. B **90**, 155109 (2014).

Unveiling the Nature of the Bonded-to-Atomic Transition in Liquid SiO_2 to TPa Pressures

S. Zhang,[1] M. A. Morales,[2,3] R. Jeanloz,[4] M. Millot,[3] S. X. Hu,[1] and E. Zurek[5]

[1]Laboratory for Laser Energetics, University of Rochester
[2]Center for Computational Quantum Physics, Flatiron Institute
[3]Lawrence Livermore National Laboratory
[4]Departments of Earth and Planetary Science and Astronomy, University of California, Berkeley
[5]Department of Chemistry, State University of New York at Buffalo

SiO_2 is an important compound for theory, basic science, and technology, including as a laboratory standard for high-energy-density experiments. As a key constituent of Earth, terrestrial, and even giant planets, the response of SiO_2 to dynamic compression helps to determine (1) how planets form through giant impacts and (2) the high pressure–temperature material properties that control, for example, how the deep interiors of planets evolve.

Laser and magnetically driven experiments and first-principles calculations over the past two decades[1–12] have provided important constraints on the high-temperature phase diagram and properties of SiO_2 and established it as a standard for impedance matching at up to 1.2 TPa. Questions remain, however, about the liquid structure of SiO_2 at extreme conditions,[8,13–15] the understanding of which not only helps to clarify phase transitions and metallization that generally occurs in materials under significant compression but can also shed light on material transport properties (e.g., electrical and thermal conductivity) critical to modeling the dynamics of the magma ocean and magnetic-field generation in early Earth and super-Earth exoplanets, as well as for numerical simulations of giant impacts.

We have performed extensive simulations from first principles and in-depth analysis of the structure, electron density, and thermodynamic properties of liquid SiO_2 to gain insights into the nature of the bonded-to-atomic transition. Our results show that a heat capacity anomaly happens at 2 to 3×10^4 K (1.5 to 2.5 eV) over the pressure range of 0.1 to 1 TPa, coinciding with conditions where the lifetime of Si–O bonds equals 50 fs. This corresponds to bonded-to-atomic liquid transition temperatures that are lower and more sensitive to pressure than previous estimates based on laser-driven Hugoniot measurements (black line with diamonds versus gray dashed curve in Fig. 1). These results render a new bonded-to-atomic boundary of liquid SiO_2 that overlaps with the conditions of interest to giant-impact simulations, which indicates more-complex variations (i.e., a decrease and then an increase with temperatures) in heat capacity than that considered previously. This can rebalance the dissipation of irreversible work into temperature and entropy in events of giant impact, necessitating reconsideration of predictions by simulations that are based on empirical equation-of-state (EOS) models.

Furthermore, our calculated Hugoniots show overall agreement with experimental ones (see Fig. 1) and are similar to previous calculations using similar methods.[4,8,9,14] The discrepancies between theory and experiment in the stishovite temperature–pressure Hugoniot near melting, together with the previously shown inconsistencies at 1.0 to 2.5 TPa, emphasize the need for further development in both numerical simulations and dynamic compression experiments to improve constraints on the phase diagram, EOS, and properties of SiO_2 in regions off the Hugoniots of α-quartz and fused silica and elucidate the exotic behaviors affecting matter at extreme conditions. These include simulations that overcome the increased limitations of pseudopotentials and computational cost for reaching convergence at the high density/temperature conditions or go beyond LDA/GGA (local density approximation/generalized gradient approximation) for the exchange-correlation functional, as well as more in-depth experimental

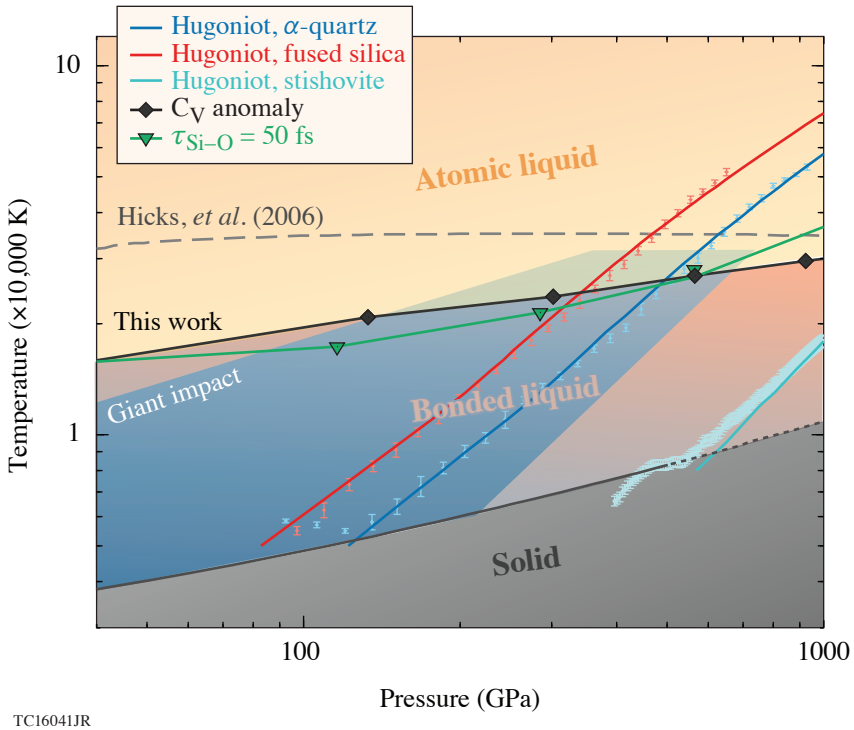

Figure 1
Phase diagram of SiO_2 featuring the bonded-to-atomic liquid transition determined in this work (black curve with diamond symbols) as compared to a previous estimation (Hicks *et al.*,[1] gray dashed curve). Also shown are the conditions for Si–O bond lifetime equaling 50 fs (green line with triangles), Hugoniots from this work (solid curves in red, blue, and turquoise for fused silica, α-quartz, and stishovite, respectively) in comparison to experiments[1,2] (lighter-colored symbols), the melting curve (solid dark-gray curve: measured; dashed dark-gray curve: extrapolated) from Millot *et al.*,[2] and the conditions of interest (blue shaded area) to giant impacts.[16]

studies, currently lacking benchmarking u_s–u_p data for stishovite between 0.2 and 1.2 TPa and relying on pyrometry and a gray-body approximation for temperature estimation.

This material is based upon work supported by the Department of Energy National Nuclear Security Administration under Award Number DE-NA0003856, the University of Rochester, and the New York State Energy Research and Development Authority.

1. D. G. Hicks *et al.*, Phys. Rev. Lett. **97**, 025502 (2006).
2. M. Millot *et al.*, Science **347**, 418 (2015).
3. M. D. Knudson and M. P. Desjarlais, Phys. Rev. B **88**, 184107 (2013).
4. T. Qi *et al.*, Phys. Plasmas **22**, 062706 (2015).
5. M. D. Knudson and R. W. Lemke, J. Appl. Phys. **114**, 053510 (2013).
6. C. A. McCoy *et al.*, J. Appl. Phys. **119**, 215901 (2016); **120**, 235901 (2016).
7. M. C. Marshall *et al.*, Phys. Rev. B **99**, 174101 (2019).
8. S. Root, J. P. Townsend, and M. D. Knudson, J. Appl. Phys. **126**, 165901 (2019).
9. T. Sjostrom and S. Crockett, AIP Conf. Proc. **1793**, 050010 (2017).
10. M. Li *et al.*, Phys. Rev. Lett. **120**, 215703 (2018).
11. M. Guarguaglini *et al.*, Nat. Commun. **12**, 840 (2021).
12. F. Soubiran and B. Militzer, Nat. Commun. **9**, 3883 (2018).
13. R. G. Kraus *et al.*, J. Geophys. Res. Planets **117**, E09009 (2012).
14. R. Scipioni, L. Stixrude, and M. P. Desjarlais, Proc. Nat. Acad. Sci. **114**, 9009 (2017).
15. E. C. R. Green, E. Artacho, and J. A. D. Connolly, Earth Planet. Sci. Lett. **491**, 11 (2018).
16. R. M. Canup, Icarus **168**, 433 (2004).

A Case Study of Using X-Ray Thomson Scattering to Diagnose the In-Flight Plasma Conditions of DT Cryogenic Implosions

H. Poole,[1] D. Cao,[2] R. Epstein,[2] I. Golovkin,[3] T. Walton,[3] S. X. Hu,[2] M. Kasim,[1] S. M. Vinko,[1] J. R. Rygg,[2] V. N. Goncharov,[2] G. Gregori,[1] and S. P. Regan[2]

[1]Department of Physics, University of Oxford
[2]Laboratory Laboratory for Laser Energetics, University of Rochester
[3]Prism Computational Sciences

The design of inertial confinement fusion ignition targets requires radiation-hydrodynamic simulations with accurate models of the fundamental material properties (i.e., equation of state, opacity, and conductivity). Validation of these models are required via experimentation. A feasibility study of using spatially integrated, spectrally resolved, x-ray Thomson-scattering (XRTS) measurements to diagnose the temperature, density, and ionization of the compressed DT shell of a cryogenic DT implosion at two-thirds convergence was conducted. This study involved analyzing the x-ray scattering data produced by targets with very different adiabats, specifically 2.8 and 8.0, to determine if their conditions were distinguishable.

Synthetic scattering spectra were generated using 1-D implosion simulations from the *LILAC* code[1] that were post-processed with the x-ray scattering model, which is incorporated within *Spect3D*.[2] To model the x-ray emissivity, a 1-kJ laser with a 10-ps pulse length and a source diameter of 50 μm was used to produce a Gaussian x-ray source, with a FWHM of 10 eV (Ref. 3). The scattering geometry is shown in Fig. 1. The detectors captured scattering data at $\theta_F = 40°$ and $\theta_B = 120°$. Two x-ray photon energies, 2 keV and 3.5 keV, were considered.

Using the output spectra from *Spect3D*, synthetic experimental data were produced by assuming a detector efficiency of $\Gamma_{det} \sim 10^{-5}$ and a spectral resolution of 3 eV/bin, which gives ~300 inelastically scattered photons resolved by the detector. Synthetic experimental noise was added by removing the uniform background signal and using the Poisson statistic, which estimates the noise as $\sim 1/N_t$, where N_t is the number of photons per spectral resolution element.

Before extracting the plasma parameters from the spatially integrated simulated spectra, the inverse problem instability must first be addressed, which implies that the same measured spectra could be fitted equally well by very different plasma parameters. Bayesian inference, using Markov–Chain Monte Carlo (MCMC) to sample the multidimensional space, is a more-robust approach to exploring the behavior of the complex multiparameter simulations.[4]

The MCMC exploration fit the entire spectra, assuming two weighted uniform plasma regions, one containing DT and the other CH. The cost function used to determine the appropriateness of each MCMC spectrum calculates the maximum percentage error to allow equal weighting of the fitting to the elastic and inelastic peaks between the MCMC spectrum I_{fit}, and the synthetic experimental spectra I_{raw},

$$\beta_{cost} = \max\left(\frac{I_{fit} - I_{raw}}{I_{raw}} \frac{1}{\sqrt{2}\,\sigma}\right)^2,$$

where σ is the standard deviation representative of the noise of the synthetic scattering spectra. The σ is selected such that the noise of the scattering signal falls comfortably within the spread of the accepted fits. A value of 0.075 was chosen. The forward-

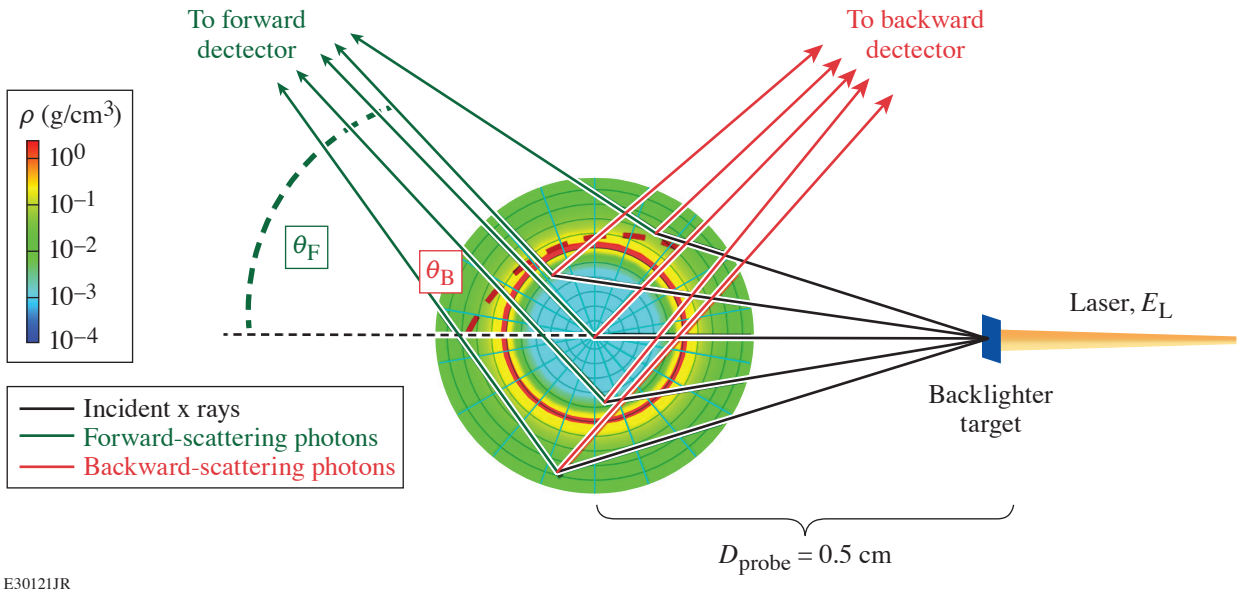

Figure 1
A sketch of the proposed experimental setup, with a laser of energy E_L incident on a backlighter target, producing x rays with a conversion efficiency of η_x. The scattering x rays are shown incident on the 3-D inferred density profile from *Spect3D* using the 1-D simulation data produced by the *LILAC* code. A schematic of the scattering events, recorded on the detector by *Spect3D*, from different zones throughout the implosion, is shown. The scattering geometry is demonstrated and not drawn to scale.

and backward-scattering spectra were analyzed separately, and their parameter distributions were combined to produce an overall distribution for each plasma parameter. The distributions for each adiabat and x-ray photon energy are shown in Table I.

Good agreement was found between the mass-averaged simulation parameter values and the MCMC distributions. There is, predictably, very little information regarding the CH plasma. This is due to its lower density compared to the DT compressed shell, meaning it does not contribute to the overall shape of the scattering. Overall, the optimum analysis presented in this summary to resolve the plasma conditions in the compressed shell, using a realistic laser probe from OMEGA EP, is performing MCMC analysis from spectra produced using a backward fielding detector. Since the collective forward-scattering detector is not required for sufficient convergence on the DT compressed shell parameters, either a 2-keV or 3.5-keV x-ray photon energy probe could be used. Better agreement may be achieved between the MCMC parameters and the simulations if a narrower bandwidth probe beam could be used.

Table I: The full spectral analysis of MCMC DT fitting parameters compared to the mass-weighted parameters from the *LILAC* 1-D simulations, focused on the compressed DT shell, for each adiabat and each probe.

DT parameter	T_e	n_e (cm^{-3})	Z
Adiabat = 2.8			
Simulation	25	5.5×10^{23}	0.97
MCMC 2 keV	33±8	$(5.2\pm0.6) \times 10^{23}$	0.94±0.03
MCMC 3.5 keV	25±3	$(5.0\pm0.3) \times 10^{23}$	0.95±0.03
Adiabat = 8.0			
Simulation	38	3.7×10^{23}	0.97
MCMC 2 keV	50±6	$(2.6\pm0.4) \times 10^{23}$	0.88±0.07
MCMC 3.5 keV	56±6	$(3.2\pm0.5) \times 10^{23}$	0.87±0.05

In summary, spatially integrated XRTS spectra for 1-D *LILAC*-simulated conditions of low- and high-adiabat, DT cryogenic implosions have been calculated at two-thirds convergence. Markov–Chain Monte Carlo analysis was performed for two different scattering setups. Information on the compressed shell conditions was obtained since it has been shown to be possible to use the spectral resolution in a spatially integrated measurement to discriminate between different regions in the plasma. Fielding just one detector in the noncollective scattering regime produces good agreement with the compressed shell mass-averaged parameters from the simulation. This technique can be used to resolve both the low- and high-adiabat implosions. In the future, similar analysis will be performed on the conditions at stagnation, the effect of mixing in the implosion, as well as investigations into 2-D and 3-D simulations using *DRACO* and *ASTER*.

This material is based upon work supported by the Department of Energy National Nuclear Security Administration under Award Number DE-NA0003856, the University of Rochester, and the New York State Energy Research and Development Authority.

1. J. Delettrez *et al.*, Phys. Rev. A **36**, 3926 (1987).
2. I. Golovkin *et al.*, High Energy Density Phys. **9**, 510 (2013).
3. C. Stoeckl *et al.*, Rev. Sci. Instrum. **85**, 11E501 (2014).
4. M. F. Kasim *et al.*, Phys. Plasmas **26**, 112706 (2019).

Interdigitated Electrode Geometry Variation and External Quantum Efficiency of GaN/AlGaN-Based Metal–Semiconductor–Metal Ultraviolet Photodetectors

S. F. Nwabunwanne and W. R. Donaldson

Laboratory for Laser Energetics
Department of Electrical and Computer Engineering, University of Rochester

Efficient and ultrafast $Al_xGa_{1-x}N$-based ultraviolet (UV) photodiodes are suitable candidates for UV photodetection because of their highly mobile carriers. The characteristics of $Al_xGa_{1-x}N$, a group III–V compound that has endeared it to the optoelectronics community, consist of a tunable direct band gap, superior electrical stability, elevated thermal resistivity, and robust performance in hazardous environments like inertial confinement chambers and space environments. $Al_xGa_{1-x}N$-based photodiodes (PD's) offer an important feature that permits the selection of a desired spectral window by simply altering the percentage composition of Al in the $Al_xGa_{1-x}N$ compound.[1,2]

AlGaN-based PD's produce the best response speed in the metal–semiconductor–metal (MSM) configuration because in this design, the response time is limited by the carrier transit time between the interdigitated fingers. Furthermore, in the MSM setup, the capacitance due to the interdigitated fingers is extremely small, of the order of 20×10^{-15} F, which leads to an ~1-ps resistor capacitor time constant for a 50-Ω external coupling circuit.[3]

Here, we discuss the successful design and fabrication of $Al_xGa_{1-x}N$-based photodetectors with rectangular and circular asymmetric, interdigitated electrode geometries GaN/AlGaN semiconductors. The thin films were grown on commercially available sapphire substrates via metal-organic chemical vapor deposition by KYMA Technologies.[4] The best-performing devices yielded a scope-limited pulse duration of 62 ps with a 29-ps rise time. The bias-independent external quantum efficiency of the devices was >70% for intrinsic devices at 60 V and >400% at 10 V. The main goal of this investigation was to establish the bias voltage that saturates the external quantum efficiency (EQE) of these devices.

Figure 1 depicts the device's epitaxial structure for both metals that were employed in the detectors. The experimental setup is shown in Fig. 2. UV light was produced by Astrella and an optical parametric amplifier (OPA) by a fourth-harmonic–generation technique. Astrella is an 800-nm Coherent laser operating at 1 kHz and possessing a 30-fs pulse duration. The 800-nm visible

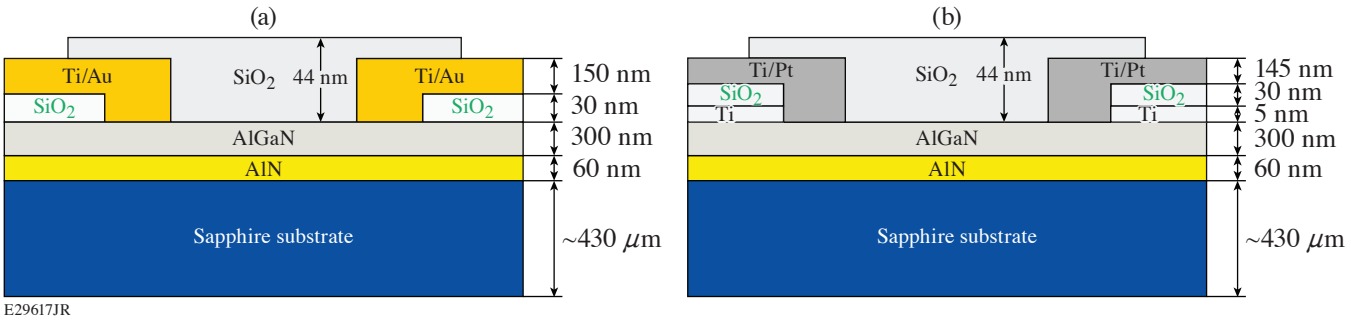

Figure 1
Epitaxial stack of the fabricated (a) Au and (b) Pt AlGaN-based MSM UV PD's for efficient and ultrafast UV detection.

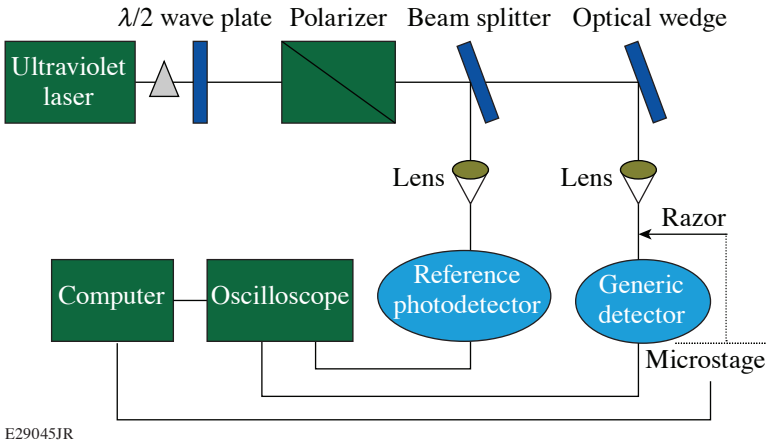

Figure 2
Experimental setup for ultrafast testing of AlGaN PD's at 262 nm (Ref. 1).

light output of Astrella served as the input pump laser to the OPA, which changes it to 262 nm of UV light using fourth-harmonic generation. The output energy per pulse from the OPA at 262 nm is 40×10^{-6} J, but only 0.749×10^{-9} J reached the detector under test. The reference detector was a 200- to 1100-nm Thorlab Det10 Si-biased detector.

Figure 3(a) posits the photocurrent of Pt intrinsic $Al_{0.2}Ga_{0.8}N$ with the circular asymmetric contact device as a function of bias voltage. The Schottky contact blocks current from –3.5 V to +3.5 V.

Figure 3(b) depicts the ultrafast impulse response function of Au $Al_{0.1}Ga_{0.9}N$ and Pt $Al_{0.2}Ga_{0.8}N$ intrinsic MSM UV photodiodes at 20-V bias voltage. The Au PD recorded a 29-ps rise time with 62-ps pulse duration, while the Pt PD showed a 34-ps rise time and 72-ps pulse width. The Au device exhibited the best response characteristics with a 29-ps rise time with 62-ps full width at half maximum; this response is not the intrinsic response time of the device due to the bandwidth limitation of the oscilloscope.

$$\mathrm{QE}(\eta) = \frac{I_{\mathrm{ph}}/e}{P/hv}. \tag{1}$$

The efficiency of the devices was computed using Eq. (1) and the results for Pt $Al_{0.1}Ga_{0.9}N$ *n*-doped circular asymmetric (CA) and Pt $Al_{0.2}Ga_{0.8}N$ intrinsic rectangular asymmetric (RA) detectors are plotted in Figs. 3(c) and 3(d), respectively.

The interdigitated electrode geometries of $Al_xGa_{1-x}N$ MSM UV photodiodes were redesigned as rectangular asymmetric and circular asymmetric fingers. These were successfully implemented and tested to establish their UV response profiles. Investigations were done to obtain the bias voltage that saturates these devices to find the detector's bias-independent EQE. The alterations of electrode geometry in addition to fewer electrodes on the devices reduced the effects of electrode shadowing and allowed about 34% more UV light to be absorbed. A combination of these factors resulted in the recorded bias-voltage–independent EQE of our devices. Establishment of the efficiency of these detectors will improve the quest for semiconductor-driven ultrafast laser pulse characterization and plasma diagnostics.

This material is based upon work supported by the Department of Energy National Nuclear Security Administration under Award Number DE-NA0003856, the University of Rochester, and the New York State Energy Research and Development Authority.

1. S. Nwabunwanne and W. Donaldson, Proc. SPIE **12001**, 120010F (2022).
2. E. Monroy *et al.*, Appl. Phys. Lett. **74**, 3401 (1999).
3. Y. Zhao and W. R. Donaldson, IEEE J. Quantum Electron. **56**, 4000607 (2020).
4. AlGaN Templates, Kyma Technologies Inc., Raleigh, NC 27617, accessed 10 June 2022, https://kymatech.com/products-services/materials/gan-related-iii-n-materials/499-algan-templates.

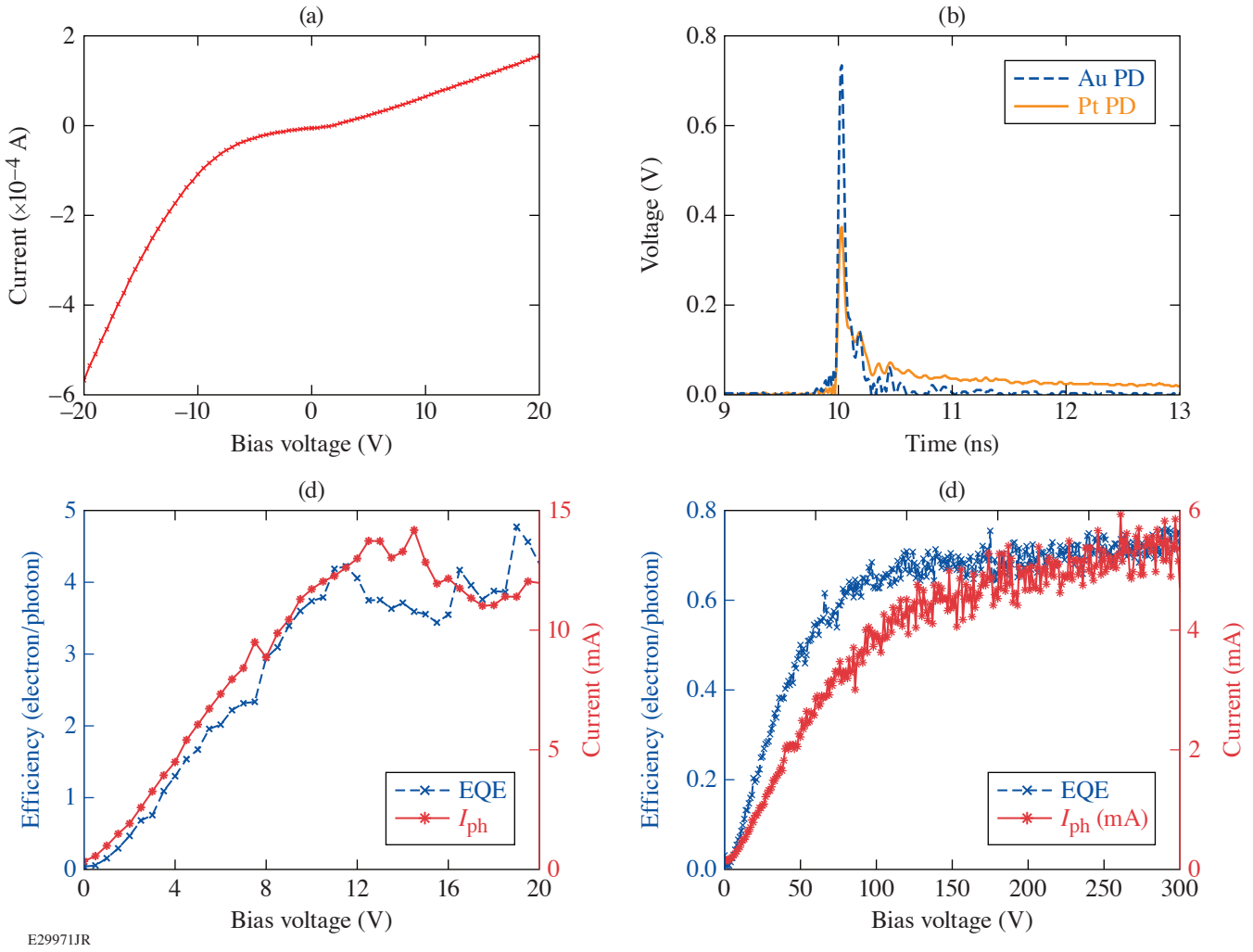

Figure 3
(a) Pt intrinsic $Al_{0.2}Ga_{0.8}N$ MSM UV photodiode I–V curve under dark conditions. (b) Au $Al_{0.1}Ga_{0.9}N$ and Pt $Al_{0.2}Ga_{0.8}N$ intrinsic MSM UV photodiodes' impulse response function at 20-V bias voltage. The Au PD yielded a 29-ps rise time with 62-ps pulse duration, while the Pt PD produced a 34-ps rise time and 72-ps pulse width. External quantum efficiency and photocurrent as a function of bias voltage. (c) Pt $Al_{0.1}Ga_{0.9}N$ *n*-doped CA device (saturation began at 10 V). (d) Pt $Al_{0.2}Ga_{0.8}N$ intrinsic RA device (saturation began at 60 V).

Impact of the Optical Parametric Amplification Phase on Laser Pulse Compression

J. Musgrave[1] and J. Bromage[2]

[1]Institute of Optics, University of Rochester
[2]Laboratory for Laser Energetics, University of Rochester

Optical parametric chirped-pulse amplification (OPCPA) has been widely used to provide high gain over broad bandwidths suitable for sub-20-fs pulses with multijoule energies, corresponding to petawatt peak powers.[1–3] Precise control and measurement of a system's spectral and spatial phases are required for Fourier transform–limited pulse compression and diffraction-limited focusing, respectively. Phase accumulated during optical parametric amplification (OPA) can degrade the compressibility and focusability of the pulse, reducing peak intensity. OPA is a three-wave mixing process where energy is transferred from a strong pump wave to a weak signal wave with the production of a third wave, called the "idler," to conserve energy and momentum. For efficient energy transfer, this process must be phase matched. Significant phase mismatch leads to reduction in gain and, as shown by Bahk,[4] can lead to signal phase accumulation. In this summary, we investigate signal phase accumulation from pump wavefront errors and evaluate the potential impact on signal pulse compression.

Broadband phase matching can be achieved by matching the group velocity of the signal and idler pulses using the amplifier material's birefringence and a noncollinear angle between the pump and signal.[5,6] Figure 1 shows relative orientation of the pump, signal, and idler k vectors to the crystal axis (O), with a noncollinear angle α.

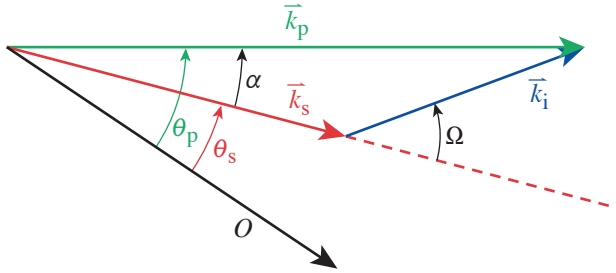

Figure 1
Phase matching between the wave vectors of the three beams: pump, signal, and idler. O is the optical axis of the nonlinear crystal.

The phase mismatch in the z direction is given by Eq. (1):

$$\Delta k = k_p \cos(\alpha) - k_s - \sqrt{k_p^2 \cos^2(\alpha) - k_p^2 + k_i^2}\,. \tag{1}$$

The sensitivity to pointing, caused either by global angular errors or local from wavefront aberrations, is given by the derivatives with respect to θ_p or θ_s for the pump and signal, respectively.[7] The resulting signal phase errors can be expressed analytically for the small-signal case or calculated numerically for higher-efficiency amplifiers.[7] In particular, modification of the signal spectral phase $\phi_s(\omega)$, an important parameter for determining pulse compression, can be evaluated for a range of pump and signal angular deviations from the optimum phase-matched condition.

As a test case, we chose the final amplifier of the Multi-Terawatt optical parametric amplifier line (MTW-OPAL), all-OPCPA system.[3] This amplifier uses 70% deuterated potassium dihydrogen phosphate (DKDP) crystals pumped by the second harmonic

of MTW to amplify 1.5-ns pulses centered at 920 nm with 140-nm bandwidths up to 11 J before recompression to sub-20 fs. For amplification, the pulse is chirped before the amplifier to 100,000× the Fourier transform limit; therefore, the interaction between the pump and the 140-nm-wide signal at a given time is essentially monochromatic. The sensitivity of the signal phase for this amplifier for a given angular error of the signal or pump is shown in Figs. 2(a) and 2(b), respectively. Curves for deuteration levels ranging from 70% to 100% are shown—the maximum range suitable for this system; they can be adjusted during the crystal growth with the relative amounts of hydrogen and deuterium. Changing the deuteration level requires changing the noncollinear angle α for optimum phase matching.[8] This, in turn, affects the phase-mismatch sensitivity and therefore the sensitivity of the signal phase to angular deviation. In the case of pump deviation [Fig. 2(a)], reducing the deuteration level causes an increase in pump-deviation sensitivity; for signal deviation [Fig. 2(b)], the opposite holds.

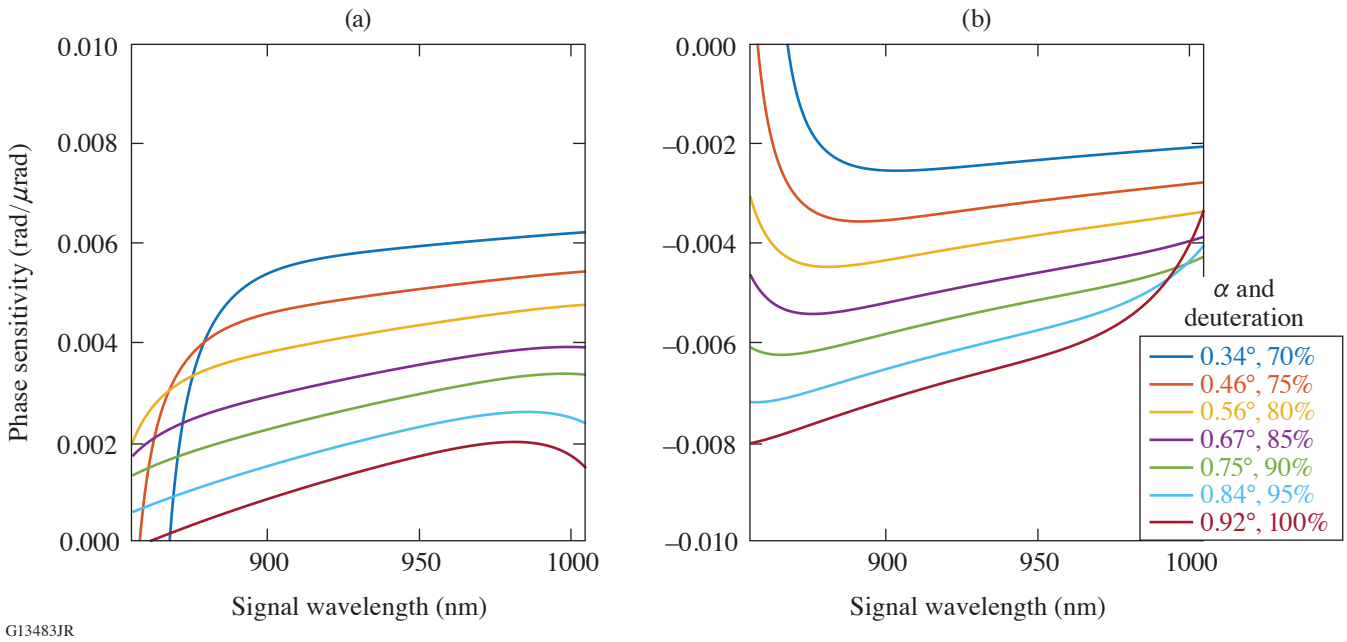

Figure 2
(a) Pump and (b) signal phase sensitivity across the signal wavelength for different deuteration levels and corresponding noncollinearity.

One point to note is that the phase sensitivity (in units of radians per microradian) is small but not zero and, in particular, can vary significantly across the signal bandwidth from 830 to 1010 nm. This variation in phase—a spectral phase error—can be problematic when it also has a spatially varying component, as would happen if the pump or signal angles vary locally. A number of cases were evaluated,[7] one of which is shown in Fig. 3, where the pump wavefront produces a local angular error of 500 μrad. This would produce a reduction in gain by ~50%, leading to local beam profile distortion. It would also change the local pulse (as shown in Fig. 3) with a shift of ~5 fs that, averaged over the beam profile, could cause a pulse broadening in the focal plane. Thankfully, in the case of the MTW-OPAL Laser System, wavefront slopes of this magnitude are not present and phase plates must be added to produce these effects.[9] Nonetheless, this analysis is valuable in determining the suitability of a given pump laser to ensure there are no spatiotemporal pulse-broadening effects that degrade the peak intensity achieved by the laser.

This material is based upon work supported by the Department of Energy National Nuclear Security Administration under Award Number DE-NA0003856, the University of Rochester, and the New York State Energy Research and Development Authority.

1. A. Dubietis, G. Jonusauskas, and A. Piskarskas, Opt. Commun. **88**, 437 (1992).
2. V. V. Lozhkarev *et al.*, Laser Phys. Lett. **4**, 421 (2007).
3. J. Bromage *et al.*, High Power Laser Sci. Eng. **9**, e63 (2021).
4. S. W. Bahk, Opt. Lett. **46**, 5368 (2021).

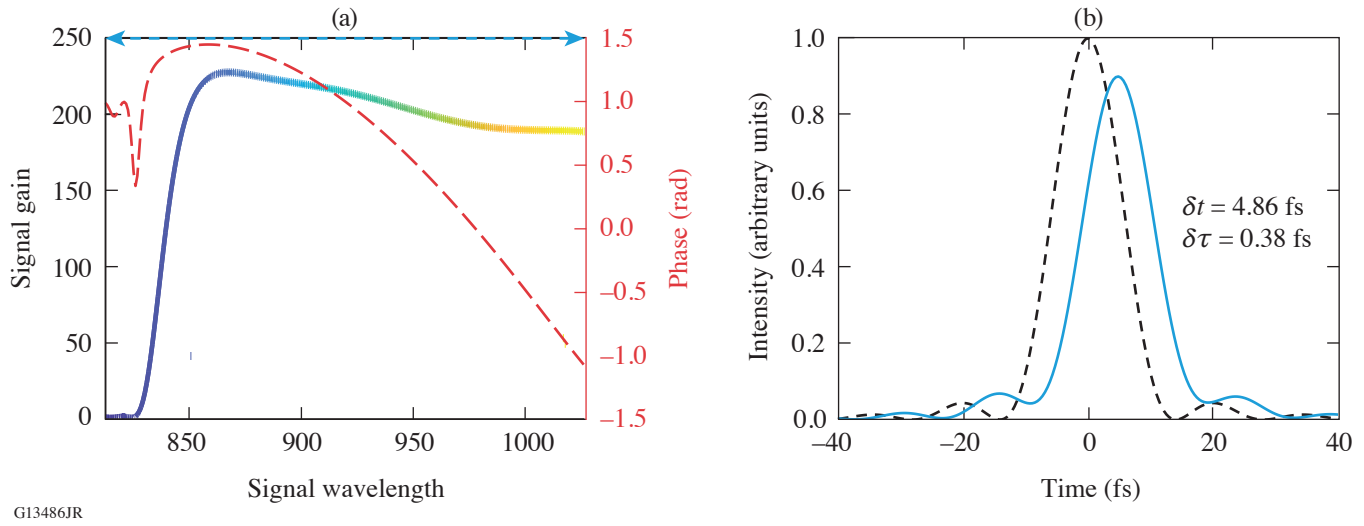

Figure 3
(a) Impact of angular error on signal gain and spectral phase. (b) Impact on the compressed pulse assuming equivalent gain across the spectrum (to show spectral phase effects). δt is the temporal shift of the peak, and $\delta\tau$ is the change in pulse full width at half maximum from the nominal 13 fs.

5. G. M. Gale *et al.*, Opt. Lett. **20**, 1562 (1995).
6. G. Cerullo and S. De Silvestri, Rev. Sci. Instrum. **74**, 1 (2003).
7. J. Musgrave and J. Bromage, Appl. Opt. **61**, 3838 (2022).
8. K. Fujioka *et al.*, J. Appl. Phys. **117** (9), 093103 (2015); **119**, 249902(E) (2016).
9. S. W. Bahk *et al.*, Opt. Express **30**, 12,995 (2022).

Simultaneous Contrast Improvement and Temporal Compression Using Divided-Pulse Nonlinear Compression

G. W. Jenkins,[1,2] C. Feng,[1] and J. Bromage[1]

[1]Laboratory for Laser Energetics, University of Rochester
[2]Institute of Optics, University of Rochester

Temporal contrast is an increasingly important specification for high-energy, ultrafast lasers because prepulses with only a fraction of a percent of the main pulse's energy can ionize the laser's target and modify experimental conditions before the main pulse arrives. To remove the prepulses, many temporal contrast improvement methods have been developed. We are particularly interested in methods such as nonlinear ellipse rotation (NER)[1] that allow simultaneous contrast improvement and spectral broadening.[2,3] Yb laser technology suffers from relatively long pulses (of the order of hundreds of femtoseconds to picoseconds) and requires temporal compression to efficiently pump many applications of interest. With NER, both contrast improvement and temporal compression can be accomplished in a single step.

In this summary, we demonstrate a new method of contrast improvement that allows both contrast improvement and temporal compression in a single step—divided-pulse nonlinear compression (DPNLC). In DPNLC, a high-energy pulse is divided into multiple low-energy pulses that are spectrally broadened through self-phase modulation (SPM) in gas, as illustrated in Fig. 1. After spectral broadening, the low-energy pulses are coherently recombined back into a high-energy pulse and the recombined pulse is compressed to its new transform limit. We have been developing DPNLC to overcome gas-ionization problems encountered at high energies but have found that the ability to apply an unequal nonlinear phase to the low-energy divided pulses allows us to use the method for contrast improvement as well.

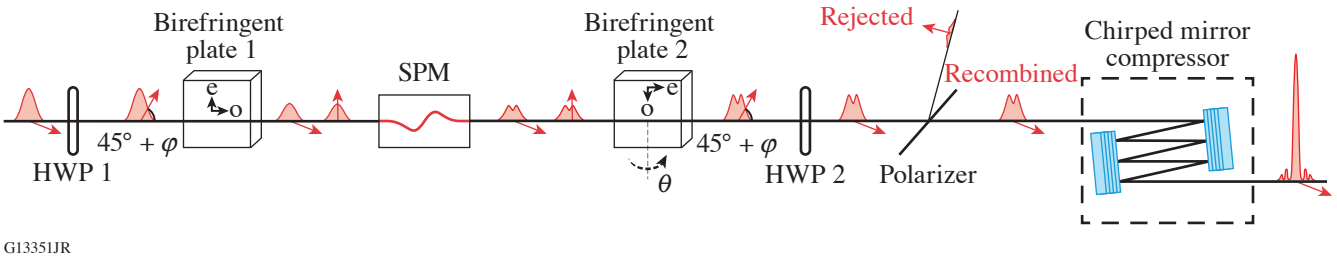

Figure 1
Apparatus for DPNLC. Birefringent plates with extraordinary axis "e" and ordinary axis "o" are used to divide one pulse into two low-energy, orthogonally polarized pulses. Red arrows indicate the pulse's polarization, and the distorted pulse shape after the SPM stage indicates an arbitrary reshaping by nonlinear processes in the SPM stage. After recombination, the polarization is cleaned with a polarizer and the pulse is compressed to a shorter duration with chirped mirrors. The angles φ and θ represent angular alignment errors in polarization and crystal angle of incidence, respectively. HWP: half-wave plate.

In our previous work,[4] we analyzed the alignment tolerances for DPNLC. The final result of our analysis was an expression for the pulse power in each polarization after the recombination step. The output is written as a Jones vector, where the top row is the power in the $\hat{p} = 45° + \varphi$ polarization and the bottom row is the power in the $\hat{m} = 45° + \varphi$ polarization:

$$\bar{P}_{\text{out}} = \frac{e^{-T^2}}{2\sqrt{\pi}} \begin{bmatrix} 1 + \sin^2(2\varphi) + \cos^2(2\varphi)\cos\left[2\phi_{\text{NL}}\sin(2\varphi)e^{-T^2} + \Delta\phi(\theta)\right] \\ \cos^2(2\varphi)\left\{1 - \cos\left[2\phi_{\text{NL}}\sin(2\varphi)e^{-T^2} + \Delta\phi(\theta)\right]\right\} \end{bmatrix}, \tag{1}$$

where we have normalized the expression so integrating over time gives a total energy of 1. In Eq. (1), the two most important alignment angles are the incoming polarization error (φ) and the angle of incidence (AOI, θ) on the second birefringent plate. The nonlinear phase accumulated in the SPM stage is represented by ϕ_{NL}, and $\Delta\phi(\theta) = \phi_2(\theta) - \phi_1$ is the difference in retardance between the two calcite plates. We developed a similar equation that describes a typical prepulse after recombination:

$$\bar{P}_{\text{pre}} = \frac{e^{-T^2}}{2\sqrt{\pi}} \begin{bmatrix} 1 + \sin^2(2\varphi) + \cos^2(2\varphi)\cos\left[\Delta\phi(\theta)\right] \\ \cos^2(2\varphi)\left\{1 - \cos\left[\Delta\phi(\theta)\right]\right\} \end{bmatrix}. \tag{2}$$

These equations indicate a simple method to improve the temporal contrast of the pulse train. Equation (2) shows that if the retardance difference $[\Delta\phi(\theta)]$ is set to zero, the entire prepulse will be found in the $\hat{p}$ polarization. Then we can apply a polarization alignment error (φ) to rotate the main pulse into the $\hat{m}$ polarization. Finally, we use a polarizer to pass the $\hat{m}$ polarization and reject the $\hat{p}$ polarization, thereby rejecting all of the prepulses.

We successfully demonstrated and quantified contrast improvement using these steps. Our laser system is a homebuilt Yb-doped, thin-disk regenerative amplifier that emits 1.2-ps pulses at a wavelength of 1030 nm, a repetition rate of 1 kHz, and an average power of 10 W. The pulses are coupled into a 1.8-m-long, 500-μm-inner-diam, hollow-core fiber (HCF) filled with 1.7 bar of argon for spectral broadening. The pulses accumulate 8.4 rad of nonlinear phase in the HCF. A 12-mm-thick, x-cut calcite plate divides the pulses in two before the HCF, and an identical plate recombines the pulses after the HCF, as previously illustrated in Fig. 1. A half-wave plate (HWP1) is placed before the first birefringent plate to carefully control the incoming polarization error φ, and a second HWP (HWP2) is placed after the last birefringent plate to select either the $\hat{p}$ or $\hat{m}$ polarization for transmission through the recombination polarizer.

First, we measured the original contrast of the laser system. The apparatus in Fig. 1 was aligned with zero alignment errors and measured near-perfect recombination into the $\hat{p}$ polarization (97.3% limited by a 2.5% p-polarization reflection on the polarizer). With this alignment, both the main pulse and prepulses are transmitted by the polarizer with maximum efficiency. The original contrast of the laser was measured by attenuating the beam with a set of neutral-density (ND) filters and then focusing it onto a photodiode. On the photodiode, both the main pulse and prepulses could clearly be seen, as shown in Fig. 2. The maximum prepulse height is 1.9 mV, while the main pulse is 2.3 V; therefore, the initial contrast of the laser is $\sim 10^{-3}$.

Next, we applied a polarization angle error to improve the contrast. We rotated HWP1 until the energy of the main pulse in the $\hat{m}$ was maximized (found at a HWP angle of 3°). Then we rotated HWP2 to transmit the $\hat{m}$ polarization and reject the $\hat{p}$ on the polarizer. We made the same photodiode measurement and found that the prepulses were rejected to below our measurement sensitivity, as shown in Fig. 2. The main pulse was transmitted with high efficiency and measured at 1.7 V.

To quantify the contrast improvement, we removed the ND filters until the prepulses became visible again. We removed 3.5 optical density of the ND filters; we then made fine adjustments to the AOI of calcite plate 2 and the angle of HWP2 to minimize the prepulses and measured a prepulse signal of 0.7 mV. This puts the new contrast of the pulse train at $\sim 10^{-7}$—an improvement of four orders of magnitude.

Finally, we compressed the contrast-improved pulse using a series of chirped mirrors (–43,000-fs group-delay dispersion) and measured the compressed pulse in a second-harmonic frequency-resolved optical gating system. The measured pulse was excellent, compressed with a FWHM pulse duration of 187 fs, close to its transform limit of 180 fs. The compressed pulse with-

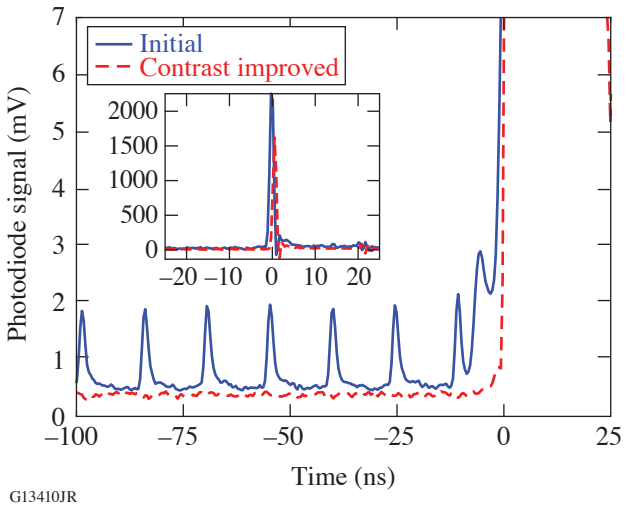

Figure 2
Captured photodiode signals from the pulse train. A train of prepulses with a maximum signal of 1.9 mV is clearly seen before the main pulse, which starts at time = 0. After the HWP's are rotated to improve the contrast, the prepulses are rejected and completely unmeasurable. At the same time, the height of the main pulse is reduced only from 2.3 V to 1.7 V, as shown in the inset.

out contrast improvement was compressible to a similar duration (186 fs with a transform limit of 185 fs) with the same chirped mirrors. Therefore, the contrast improvement method enables temporal compression equivalent to standard HCF operation.

In conclusion, we demonstrated a new method for temporal contrast improvement—divided-pulse nonlinear compression. By slightly misaligning the calcite plates used for pulse division and recombination, we rotated the polarization of the main pulse and rejected problematic prepulses on a polarizer. We measured four-orders-of-magnitude temporal contrast improvement and 72% efficiency for the main pulse, values comparable with other state-of-the-art temporal contrast improvement methods. Simultaneously, we compressed the pulse from 1.2 ps to 187 fs.

This material is based upon work supported by the Department of Energy National Nuclear Security Administration under Award Number DE-NA0003856, the University of Rochester, and the New York State Energy Research and Development Authority.

1. D. Homoelle *et al.*, Opt. Lett. **27**, 1646 (2002).
2. N. Smijesh *et al.*, Opt. Lett. **44**, 4028 (2019).
3. N. G. Khodakovskiy *et al.*, Laser Phys. Lett. **16**, 095001 (2019).
4. G. W. Jenkins, C. Feng, and J. Bromage, J. Opt. Soc. Am. B **38**, 3199 (2021).

Analysis of Pump-to-Signal Noise Transfer in Two-Stage Ultra-Broadband Optical Parametric Chirped-Pulse Amplification

C. Feng, C. Dorrer, C. Jeon, R. G. Roides, B. Webb, and J. Bromage

Laboratory for Laser Energetics, University of Rochester

Optical parametric chirped-pulse amplification (OPCPA) provides the most viable route for the development of tens to hundreds of petawatt peak-power laser systems.[1] In OPCPA, different mechanisms introduce either isolated pulses or a slowly varying pedestal before the main pulse, therefore degrading its temporal contrast, which is defined as the ratio of the peak power of the main pulse to the power of the light in some predetermined temporal range. When the laser beam is focused to interact with the target, the intensity of the light present before the main pulse can exceed a threshold for irreversible modification of the target (e.g., ~10^{12} W/cm^2) and have a detrimental effect on laser–matter interaction. Therefore, understanding the origins of contrast degradation and maximizing the temporal contrast are essential for the development of ultrahigh-peak-power laser facilities.

Pump temporal modulation is one mechanism that can degrade the temporal contrast of the recompressed signal because it induces high-frequency spectral modulation on the chirped signal spectrum during parametric amplification.[2] Pump modulation is commonly introduced by the interference between the main pump pulse and the amplified spontaneous emission (ASE). This modulation is broadband with its bandwidth proportional to the spectral bandwidth of the ASE. Spectrally filtering the ASE of the pump pulse using a narrowband filter is an effective way to reduce the high-frequency pump noise and, therefore, the pump-induced contrast degradation.[3]

In this work, we have investigated, for the first time to our knowledge, the pump-to-signal noise transfer in a two-stage ultra-broadband OPCPA and demonstrated a novel mechanism based on pump-seed delay optimization to reduce the pump-induced temporal contrast degradation by as much as 15 dB (Ref. 4). The results are widely applicable to support the design and development of OPCPA-based ultrahigh-peak-power systems, for which maximizing the temporal contrast is a high priority.

The experimental demonstration was performed in a two-stage ultra-broadband OPCPA system (Fig. 1), which is a subsystem of the Multi-Terawatt–pumped optical parametric amplifier line (MTW-OPAL), i.e., a 0.5-PW, 20-fs, all-OPCPA system.[5] The subsystem consists of an ultra-broadband front end (UFE), two noncollinear optical parametric amplifiers (NOPA4a and NOPA4b), a single pump laser for pumping both NOPA stages, and a grating compressor. In high-power OPCPA systems, it is common to use a single laser to pump several optical parametric amplification stages to reduce experimental complexity and cost. In such a system, the signal amplified in the first stage carries the pump modulations, and amplification in the second stage occurs with a pump pulse having the same modulations. The temporal modulations of the amplified chirped signal and the temporal contrast of the compressed signal pulse, therefore, depend on the difference in pump-seed delay t in different stages, as illustrated in Fig. 1.

We investigated pump pulses with two types of dominating noise, either a 30-GHz sinusoidal modulation or a broadband ASE modulation with ~40-GHz-bandwidth full width at half-maximum (FWHM). Figure 2 plots the experimental and simulation results obtained when NOPA4a and NOPA4b were in the linear amplification regime. The sinusoidally modulated pump pulse represents the case of a multilongitudinal-mode pump laser and was used to facilitate the identification and analysis of the pump-induced contrast degradation. As shown in Fig. 2(a), when the pump-seed delay τ at NOPA4b was equal to zero or to the sinusoidal modulation period T (i.e., T = 33.3 ps), and therefore the pump and seed modulations were in phase, the pump sinusoidal modulation introduced an isolated prepulse (postpulse) at –(+)0.64 ps in the cross-correlation signals of the NOPA4b

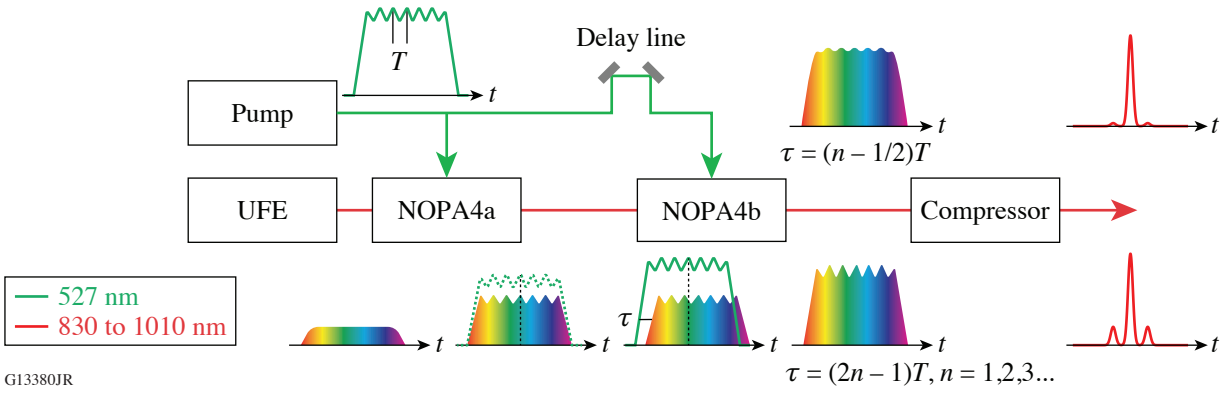

Figure 1
Experimental layout of the two-stage ultra-broadband OPCPA together with the illustrative pump and signal pulses propagating through the system. The delay line controls the pump-seed delay τ with <50-fs temporal resolution.

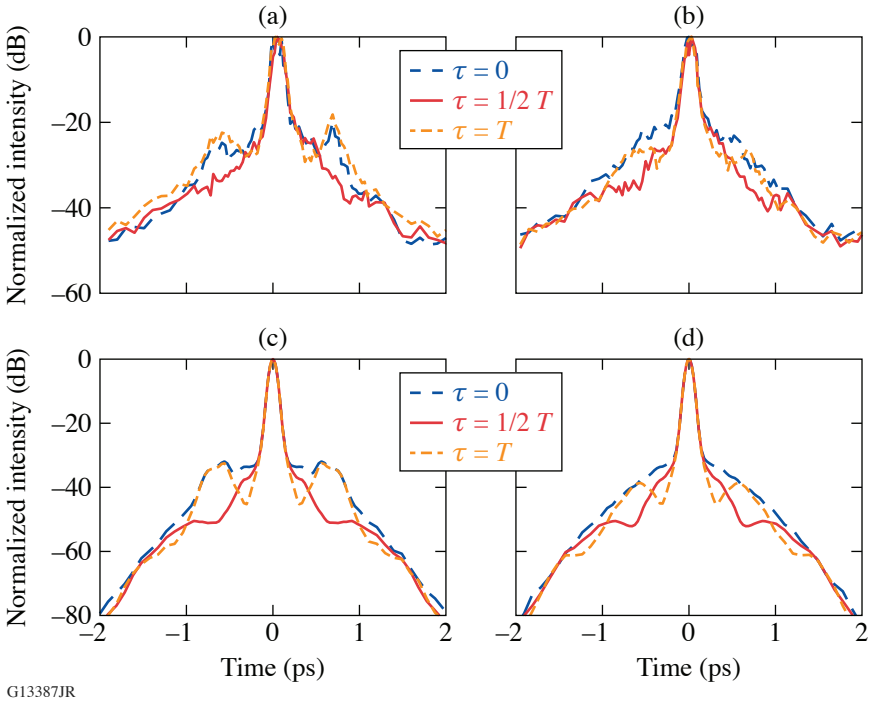

Figure 2
The [(a),(b)] measured and [(c),(d)] simulated cross-correlation signals of the compressed NOPA4b pulses at different pump-seed delays, when both NOPA4a and NOPA4b were operated in the linear regime. T = 33.3 ps corresponds to a modulation frequency equal to 30 GHz. [(a),(c)] The case of a pump pulse with both ASE and 30-GHz sinusoidal modulations; [(b),(d)] the case of a pump pulse with ASE modulation only.

compressed pulses. When the pump-seed delay was set to half the modulation period (i.e., 1/2 T = 16.7 ps) such that the pump and seed modulations had a π phase shift, the pre- and postpulse were strongly suppressed, resulting in the reduction of contrast degradation up to 15 dB. In the more-general case of a pump with broadband ASE modulation, a slowly varying broad pedestal was observed in the compressed pulse and a 10-dB reduction of the contrast degradation at τ = 1/2 T [Fig. 2(b)] was obtained. The simulated cross-correlation signals [Figs. 2(c) and 2(d)] well reproduced the pump-seed-delay–dependent effect.

When NOPA4a and NOPA4b were operated closer to saturation, the measured cross-correlation signals [Fig. 3(a)] showed negligible dependence on the pump-seed delay, which was reproduced by the simulations [Fig. 3(b)] where the limitations in spectral acceptance of the second- and third-harmonic generations in the high-dynamic-range scanning third-order cross-correlator (SEQUOIA®, Amplitude Technologies) were taken into account. These simulations also confirmed, however, that the negligible dependence on pump-seed delay is due to the limited spectral acceptance of the cross-correlator. In the absence of spectral band-

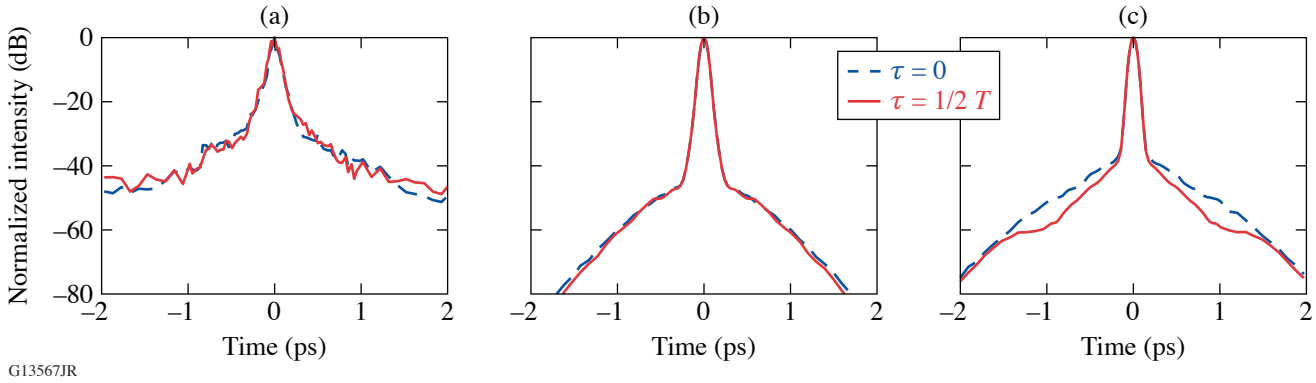

Figure 3
The (a) measured and [(b),(c)] simulated cross-correlation signals of the compressed NOPA4b pulses, when both NOPA4a and NOPA4b were operated closer to saturation and with pump ASE modulation. The spectral acceptance of the third-order harmonic generation in the cross-correlator was limited to 90-nm FWHM using a tenth-order super-Gaussian spectral filter to obtain the results in (b) or kept at >180 nm for the full signal bandwidth for getting the results in (c). Results obtained with only two, instead of three, pump-seed delays are presented for easier visualization of the delay-dependent contrast effect.

width limitation, both cross-correlation signals [Fig. 3(c)] and compressed pulses (simulation not shown) from simulations revealed the delay-dependent contrast effect. Therefore, the pump-seed delay can serve as a simple and cost-effective tool to minimize the pump-induced contrast degradation in a multi-stage OPCPA, even when parametric amplifiers are operated in saturation.

This material is based upon work supported by the Department of Energy National Nuclear Security Administration under Award Number DE-NA0003856, the University of Rochester, and the New York State Energy Research and Development Authority.

1. C. N. Danson *et al.*, High Power Laser Sci. Eng. **7**, e54 (2019).
2. N. Forget *et al.*, Opt. Lett. **30**, 2921 (2005).
3. C. Dorrer *et al.*, Opt. Lett. **32**, 2378 (2007).
4. C. Feng *et al.*, Opt. Express **29**, 40,240 (2021).
5. J. Bromage *et al.*, High Power Laser Sci. Eng. **7**, e4 (2019).

Spectral and Temporal Shaping of Spectrally Incoherent Pulses in the Infrared and Ultraviolet

C. Dorrer and M. Spilatro

Laboratory for Laser Energetics, University of Rochester

Laser–plasma instabilities (LPI's) hinder the interaction of high-energy laser pulses with targets. Simulations show that broadband, spectrally incoherent pulses can mitigate these instabilities. Optimizing laser operation and target interaction requires controlling the properties of these optical pulses. We demonstrate closed-loop control of the spectral density and pulse shape of nanosecond, spectrally incoherent pulses after optical parametric amplification in the infrared (~1053 nm) and sum–frequency generation to the ultraviolet (~351 nm) using spectral and temporal modulation in the fiber front end.[1] The high versatility of the demonstrated approaches can support the generation of high-energy, spectrally incoherent pulses by future laser facilities for improved LPI mitigation.

Temporal and spectral shaping are demonstrated on the fourth-generation laser for ultrabroadband experiments (FLUX) test bed, which is composed of a fiber front end, an optical parametric amplification (OPA) stage, a sum–frequency generation (SFG) stage, and a frequency-doubled Nd:YLF laser system generating the pump pulse for the OPA and SFG stage (Fig. 1). The fiber front end generates the broadband spectrally incoherent OPA seed and the coherent seed for the pump laser using a single high-bandwidth arbitrary waveform generator. The pump laser generates a sequence of two pulses to pump the OPA stage (second pulse) and the SFG stage (first pulse), with a relative delay set to compensate for the optical path difference at 1ω and 2ω between these two stages. Spectral shaping is implemented using a programmable filter (WaveShaper, II-VI). Temporal shaping is implemented using a Mach–Zehnder modulator (MZM) driven by a programmable arbitrary waveform generator (AWG70001, Tektronix).

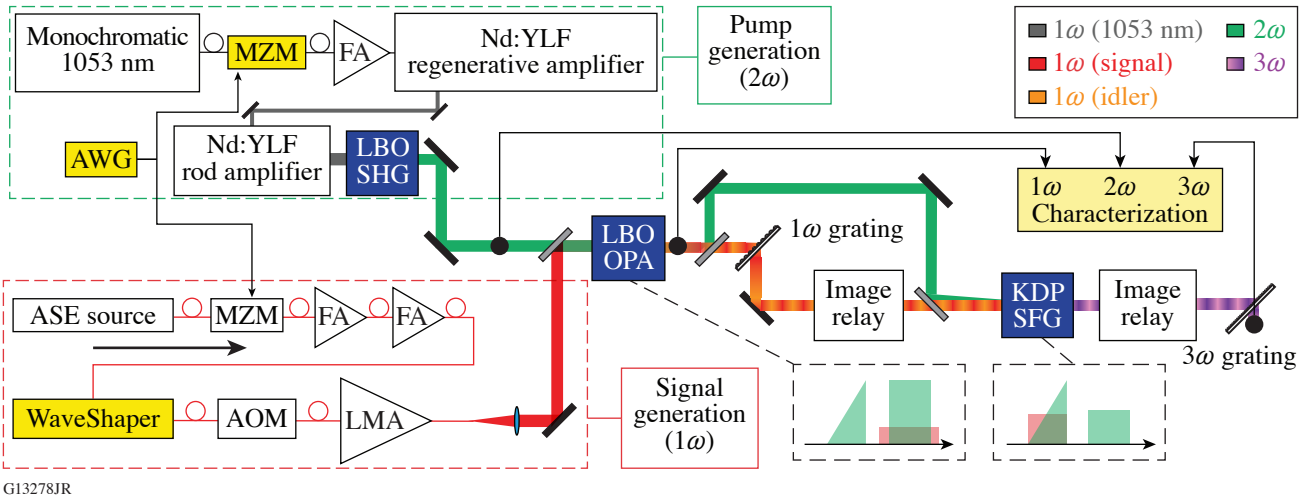

Figure 1

Experimental setup showing the signal generation at 1ω, pump generation at 2ω, amplification in the LBO OPA stage, and frequency conversion in the KDP SFG stage. The properties of the 1ω, 2ω, and 3ω pulses are measured after the OPA, SHG, and SFG stages, respectively. The insets represent the timing configuration for the 1ω pulse (in red) and the 2ω pulses (in green) within the OPA and SFG stages. SFG: sum frequency generation; SHG: sum-harmonic generation; ASE: amplified spontaneous emission; FA: fiber amplifier; AOM: acousto-optic modulator; LMA: large mode area.

The spectrum of the amplified signal measured after the OPA is shaped by controlling the spectrum of the input seed using the programmable spectral filter in the front end. Such shaping can precompensate the wavelength-dependent gain variations in the Yb-doped fiber amplifiers and OPA, although the latter are not expected to be significant, considering that a lithium triborate (LBO) OPA with that length has a bandwidth larger than 100 nm. Without spectral shaping, the OPA output spectrum peaks at ~1032 nm and has a full width at half maximum equal to 7 nm. The wavelength-dependent filter transmission is iteratively modified to decrease the error between the measured spectrum and target spectrum S_{target} (both peak-normalized to 1) using closed-loop control following

$$T_{n+1}(\lambda) = T_n(\lambda) + \eta\left[S_n(\lambda) - S_{\text{target}}(\lambda)\right], \tag{1}$$

where T_n and S_n are the transmission and spectrum as a function of wavelength λ at iteration n, respectively. For stability, the feedback is implemented with η typically equal to –0.1. Initial conditions correspond to a fully transmissive spectral filter [$T_0(\lambda) = 1$] and the resulting spectrum $S_0(\lambda)$. The wavelength axes of the spectral filter and spectrometer are precisely mapped by generating and measuring narrow Gaussian spectra. Figure 2 presents spectral-shaping examples for which S_{target} has been set to a 10-nm flattop profile with a central wavelength ranging from 1032 to 1044 nm [Figs. 2(a)–2(d)] and to the same flattop profiles modulated by a parabolic term [Figs. 2(e)–2(h)]. This simulates spectral shaping for operation at different central wavelengths with precompensation of spectral gain narrowing in subsequent amplifiers.

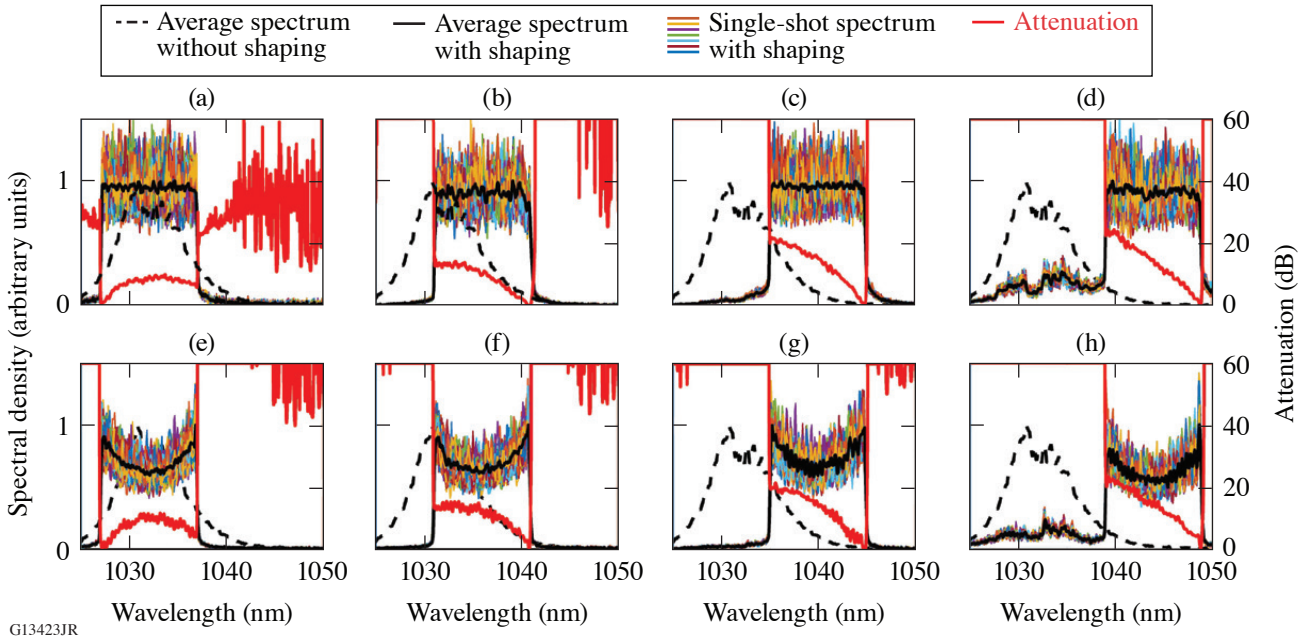

Figure 2
Spectral shaping of the OPA output signal. In the first row, S_{target} is a 10-nm flattop spectrum centered at (a) 1032, (b) 1036, (c) 1040, and (d) 1044 nm. In the second row [(e)–(h)], S_{target} is set to a 10-nm flattop spectrum with parabolic modulation centered at the same wavelengths. In all plots, the spectra averaged over 100 acquisitions without and with shaping are plotted using a dashed black line and solid black line, respectively. The spectra acquired over 100 successive shots are plotted with thin colored lines. The transmission of the spectral filter, in dB, is plotted with a thick red line.

The spectrally shaped 1ω pulses from the OPA are converted to spectrally shaped 3ω pulses using SFG with a narrowband 2ω pulse in a noncollinear angularly dispersed geometry.[2] SFG with a monochromatic field translates the input field along the frequency axis; i.e., it leads to identical spectral features for the input 1ω wave and output 3ω waves if the spectral acceptance is large enough. Figure 3 compares the 1ω and 3ω spectra, where the two wavelength ranges have been set to cover the same frequency range. For Fig. 3(a), the spectral-filter transmission is constant, whereas closed-loop control with various target spectra

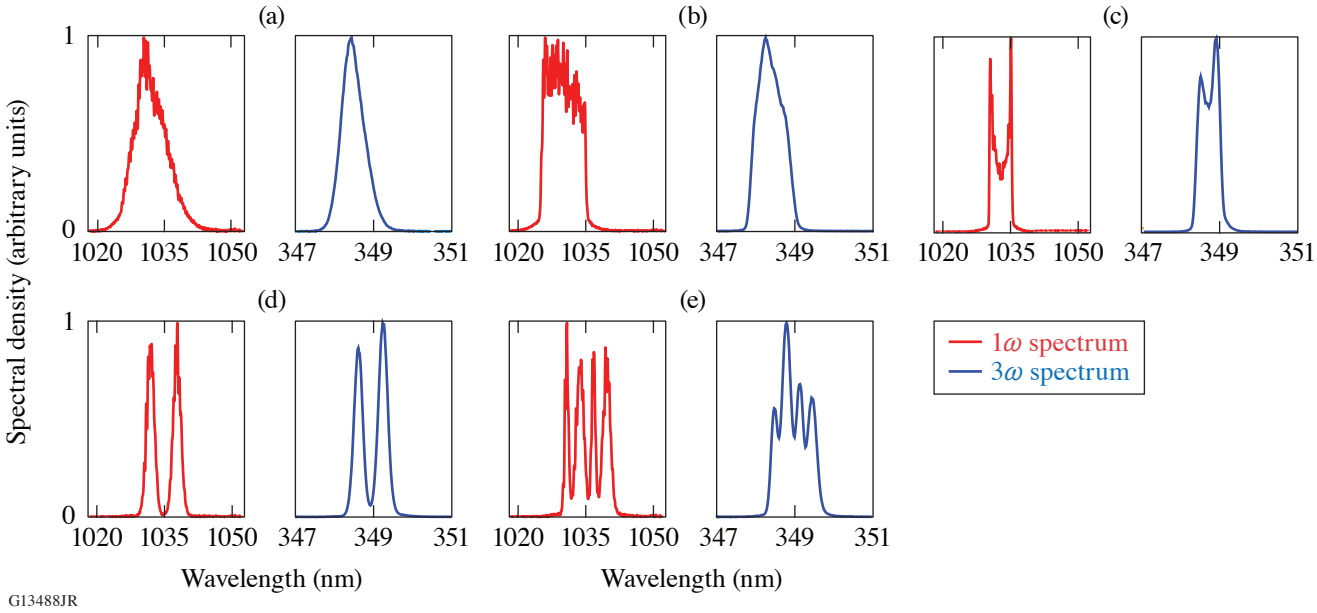

Figure 3
Spectral shaping of the SFG output signal corresponding to a shaped OPA output signal. Plots (a)–(e) show the 1ω spectrum (red line) and the 3ω spectrum (blue line), which are plotted over wavelength ranges that correspond to the same frequency span (10 THz).

was used for the results shown in Figs. 3(b)–3(e). There is generally good agreement between the measured spectral shapes at 1ω and 3ω, although the latter have broader features because of the lower resolution of the UV spectrometer compared to the IR spectrometer (0.25 THz versus 0.05 THz).

Closed-loop pulse shaping has been implemented between the AWG-driven MZM in the fiber front end and the 2ω pulse shape after SHG. A preliminary calibration based on the generation of short Gaussian pulses at different times within the injection window of the regenerative amplifier maps out the linear relation between the time base of the AWG and oscilloscope. Saturation in the fiber amplifiers and Nd:YLF amplifiers leads to significant square-pulse distortion; i.e., the gain at earlier times is significantly higher than at later times within the pump pulse, while the gain observed at a given time depends on the energy that has been extracted at earlier times. Square-pulse distortion in the laser amplifiers, the nonlinear transfer function of the MZM relative to its drive voltage, and the nonlinear second-harmonic generation makes the temporal shaping of the output pulse a complex task. Closed-loop control to generate the pulse shape P_{target} is implemented as follows:

$$W_{n+1}(t) = W_n(t) + \eta\left[P_n(t) - P_{\text{target}}(t)\right], \tag{2}$$

where W_n and P_n are the time-dependent waveform and power at iteration n, respectively. The AWG and MZM are set to implement a monotonic relation between voltage and transmission, while operation at a reference voltage corresponds to the null transmission of the MZM. The shaped pulses, composed of the high-order super-Gaussian OPA pump pulse and the user-defined SFG pump pulse, are routed after convergence to the OPA and SFG stage. Figure 4 displays the shaped 2ω pulse and the resulting 3ω pulse for various user-defined profiles. A super-Gaussian OPA pump pulse (second pulse) is consistently obtained, allowing for temporally uniform OPA saturation. This leads to a flat-in-time amplified 1ω signal, and transfer of the SFG pump pulse shape (first pulse) from 2ω to 3ω via SFG.

This material is based upon work supported by the Department of Energy National Nuclear Security Administration under Award Number DE-NA0003856, the University of Rochester, and the New York State Energy Research and Development Authority.

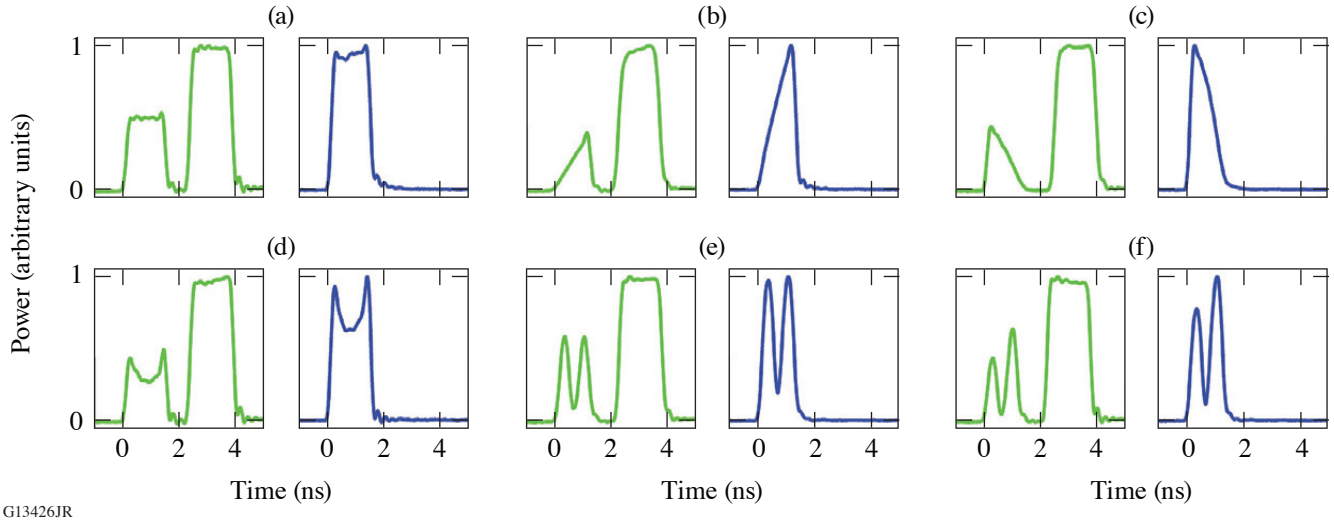

Figure 4
Temporal shaping of the 2ω pump pulse (solid green line) and resulting 3ω pulse shape (solid blue line) for target profiles equal to (a) a super-Gaussian pulse, (b) a positive ramp, (c) a negative ramp, (d) a modulated super-Gaussian pulse, (e) a pair of short pulses with identical amplitudes, and (f) a pair of short pulses with unequal amplitudes. The 2ω pulse is composed of the SFG pump pulse (first pulse) and the OPA pump pulse (second pulse).

1. C. Dorrer and M. Spilatro, Opt. Express **30**, 4942 (2022).
2. C. Dorrer *et al.*, Opt. Express **29**, 16,135 (2021).

Effect of the Pump-Beam Profile and Wavefront on the Amplified Signal Wavefront in Optical Parametric Amplifiers

S.-W. Bahk, I. A. Begishev, R. G. Roides, C. Mileham, R. Cuffney, C. Feng, B. M. Webb, C. Jeon, M. Spilatro, S. Bucht, C. Dorrer, and J. Bromage

Laboratory for Laser Energetics, University of Rochester

Optical parametric chirped-pulse amplification (OPCPA) is known to have advantages over conventional chirped-pulse amplification based on population inversion gain medium.[1] The bandwidth can be extended more than 100 nm without being limited by gain narrowing. The angle between pump and signal beams can be adjusted to provide an even-broader gain bandwidth than collinear geometry. The thermal effect is minimal due to instantaneous energy transfer from pump to signal. The temporal contrast is, in general, better because fewer amplifiers are required and the parametric fluorescence is confined within the pump pulse duration. The OPCPA scheme is a practical way to amplify ultra-broadband pulses to kilojoule energies using commercially available large potassium dihydrogen phosphate (KDP) crystals and existing high-energy nanosecond driver lasers in laser fusion facilities.[2] Deuterated potassium dihydrogen phosphate (DKDP)-based OPCPA systems have been demonstrated on the PEARL laser at the Institute of Applied Physics in Russia[3] and LLE's Multi-Terawatt optical parametric amplifier line (MTW-OPAL).[4] OPCPA lasers based on lithium triborate (LBO)[5,6] or yttrium calcium oxyborate (YCOB)[7] crystals show promising performance at the 800-nm central wavelength seeded by a Ti:sapphire oscillator.

The amplified signal intensity in an optical parametric amplifier (OPA) is a nonlinear function of pump intensity. In general, a flattop pump profile at a fixed intensity is optimal for good conversion efficiency from the pump to signal. In this regime, the amplified signal-beam profile and spectrum are saturated following the pump-beam profile and the pulse shape. The amplification-induced signal phase or "OPA phase" exhibits a phase shift similar to the one observed in a population inversion system.[8] Several authors have investigated the effect of pump on the OPA phase. Ross *et al*. concluded that the OPA phase is a function of pump intensity. They have formally shown that the pump-beam phase impacts the idler phase but does not affect the signal phase.[9] Li *et al*. have experimentally shown that astigmatism in the pump beam is transferred to the idler beam.[10]

Others, however, found that the OPA phase is affected by the pump phase as well. Wei *et al*. have numerically shown that the pump-beam walk-off introduces phase transfer from pump to signal and suggested a walk-off–compensated geometry to mitigate this effect.[11] The same group later experimentally demonstrated the mitigation effect.[12] Chen *et al.* gave a qualitative description of the pump-to-signal phase transfer effect being proportional to the pump wavefront derivative.[13]

Authors in Refs. 10–13 studied the effect of input beam wavefronts on the OPA phase using wave equations and numerical simulations. We analyze this effect using the analytic OPA phase solution and the wave-vector picture. The phase solutions of the three waves in an OPA process have been studied by several researchers[9,14] and were recently presented in closed form in Ref. 15. The main results for the case of zero idler input are summarized here for convenience:

$$\phi_s(L) = \phi_s(0) + \psi_s\left[\Delta k, I_s(0), I_p(0), L\right], \tag{1}$$

$$\phi_i(L) = \pi/2 - \phi_s(0) + \phi_p(0) - \Delta kL/2. \tag{2}$$

The function ψ_s is an additional phase introduced in the signal beam by the OPA process and will be equivalently called the "OPA phase." The ψ_s is a function determined by four independent parameters and has a term made of the incomplete elliptic integral of the third kind [for the detailed expression of ψ_s, refer to Eq. (17) of Ref. 15]. I and ϕ denote intensity and phase with the subscripts "s, i, p" indicating signal, idler, and pump, respectively; L is the crystal thickness. The OPA phase is determined by the input signal and pump intensities, the wave-vector mismatch (Δk), and the crystal thickness (L). The dependence on the input signal's intensity is weak for the normal OPA regime, where $I_s(0) \ll I_p(0)$.

Equation (2) shows that the phases of the input signal [$\phi_s(0)$] and input pump [$\phi_p(0)$] are all directly transferred to the output idler phase. Although this is mostly true, the OPA phase ψ_s is not entirely immune to input phase aberrations. The subtlety lies in the fact that the wave vector is normal to the input phase front in a spatially coherent beam; therefore, the spatial phase variation is accompanied by variation in Δk, which in turn impacts ψ_s. (We assume here a regime where diffraction is negligible over the length of the crystal.) The OPA phase also depends on the input pump intensity independently from the input phase.

The OPA phase is linear with respect to Δk within amplification bandwidth. The OPA phase in the linear regime can be approximated as

$$\psi_s \sim -\frac{\Delta k}{2} L\left\{1 - \frac{1}{a\sqrt{I_p(0)L}} \tanh\left[a\sqrt{I_p(0)L}\right]\right\}, \tag{3}$$

where $a\left(d_{\text{eff}}/c\right)\sqrt{2\eta_0\omega_s\omega_i/n_s n_i n_p}$ (Ref. 15). One can numerically show that $a\sqrt{I_p(0)}L \sim 1.16\log_{10}(\text{gain}) + 1.36$ in the depletion regime with perfect phase matching, where gain is defined as the ratio of output to input signal intensities [$I_s(L)/I_s(0)$]. For a 20-dB gain, $a\sqrt{I_p(0)}L \sim 3.68$, and Eq. (3) in terms of relative phase can be further approximated to

$$\Delta\psi_s \sim -0.36\Delta(\Delta k)L. \tag{4}$$

The local wave vectors of pump and signal waves are normal to their phase front. The wave-vector mismatch is a function of pump and signal phase slopes or derivatives. $\Delta(\Delta k)$ can be written as

$$\Delta(\Delta k) = \left(-\rho_{p,x} + \frac{k_{s,0}}{n_i k_{i,0}} a_{x,0}\right)\frac{\partial\phi_{p,0}}{\partial x} + \left(-\frac{k_{p,0}}{n_i k_{i,0}} a_{x,0}\right)\frac{\partial\phi_{s,0}}{\partial x} + \left(\frac{k_{s,0}}{n_i k_{i,0}} a_{y,0}\right)\frac{\partial\phi_{p,0}}{\partial y} + \left(-\frac{k_{p,0}}{n_i k_{i,0}} a_{y,0}\right)\frac{\partial\phi_{s,0}}{\partial y}. \tag{5}$$

The Δ notation in the above equations denotes relative change across two points in space. The incident pump and signal phase terms here are residual phases that do not include tilt terms corresponding to the incidence angles. Equation (5) shows that the noncollinear interaction angle allows both seed and pump-beam wavefront gradients to be transferred to the OPA phase. On the other hand, the birefringence term ($\rho_{p,x}$) always enables the pump wavefront transfer-to-OPA phase even with the collinear geometry. It is possible to mitigate the birefringence-induced OPA phase by choosing the sign of the noncollinear angle in order to cancel the coefficient of the pump phase gradient, which is the first term in Eq. (5). This was attempted by Wei and Yuan,[11,12] but the cancellation of the pump gradient term increases the signal gradient term, only shifting the problem from the pump to the signal side. Such cancellation is also a trade-off with other considerations that typically constrain the relative angle between pump and signal, e.g., bandwidth requirements and mitigation of parasitic second-harmonic generation.

Equations (4) and (5) show good agreement with the wave-equation approach of Refs. 10–13 in the absence of diffraction except that the small spatial positions shift in the beams coming from birefringence and the noncollinear angle does not appear in the wave-vector approach.

The spatial variation of the pump-beam amplitude can also affect the OPA phase. Figure 1 shows the OPA phase variation with respect to pump intensity using the more-accurate OPA phase expression in Eq. (17) of Ref. 15. Equation (4) is not accurate enough at pump intensities below what is required for depletion or at comparable signal and pump intensities. These plots were

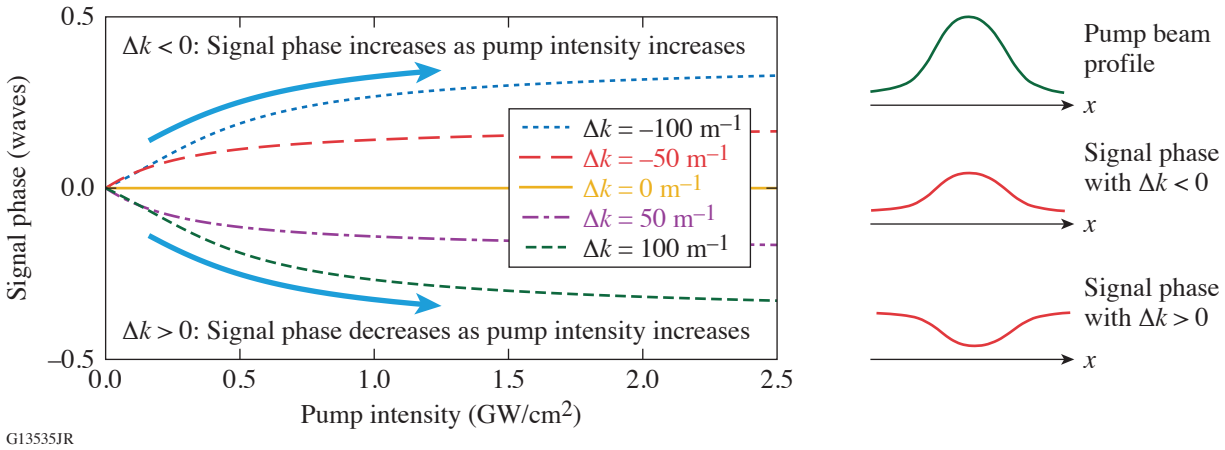

Figure 1
Effect of pump-beam intensity on the signal phase at different wave-vector mismatches.

generated using a 1-MW/cm^2 signal at 920 nm and a pump intensity at 527 nm from 0 GW/cm^2 to its depletion intensity, which is 2.5 GW/cm^2 for a 52-mm-long crystal. Unlike the phase effect, the amplitude effect depends on the sign of Δk. With positive Δk, the signal phase decreases with increasing pump intensity, whereas the trend is the opposite for negative Δk. When the phase mismatch is not equal to 0, the pump-beam shape is imprinted onto the signal phase. This qualitative behavior is illustrated on the right-hand side of Fig. 1 for a Gaussian-like pump beam.

It is interesting to note that this is similar to the intensity-dependent nonlinear effect with a sign dependency on phase matching as in cascaded nonlinearity.[15,16] The sign and amplitude change for spectral variations in Δk implies chromatic aberrations depend on the way Δk varies across the spectrum. Wang *et al*. described the chromatic effects in more detail.[17] With the linear dependence of Δk on frequency and a Gaussian-profile pump beam, this results in a radial group delay. The relative strength of the dispersion terms of Δk can easily change, depending on the phase-matching conditions and may exhibit more-complicated spatiotemporal coupling. On the other hand, chromatic effects induced by the pump phase are not significant because the signal phase's response is linear with the same slope wherever Δk is within the amplification bandwidth.

We conducted experiments to verify the prediction of pump wavefront and amplitude effect on the OPA phase in the final amplifier of the MTW-OPAL laser. Details about the MTW-OPAL system and the final pump laser are provided in Refs. 4 and 18. We specifically study the pump phase's effect in a collinear amplification geometry and the pump amplitude's effect. The amplifier, called NOPA5 being the fifth noncollinear OPA in the system, is based on a 52-mm-long, 70%-deuterated KDP crystal. The pump-signal angle for an optimum amplification bandwidth depends on the deuteration level.[19] The amplifier is currently configured in a collinear geometry because this configuration is optimal for the 70% DKDP crystal. The seed beam is a 100-mJ, 42-mm square beam. The seed pulse has a 150-nm bandwidth stretched to 1.2 ns. The pump beam is a 50-J, 40-mm square beam with a 1.7-ns pulse width. Beam size, pulse width, and bandwidth are estimated at 20% of the peak. The pump and signal are combined with a broadband dichroic mirror. The input pump wavefront and the output signal wavefront were sampled through leaky mirrors and measured with wavefront sensors after down-collimation and imaging. The signal wavefront was measured with a 930-nm bandpass filter. The inherent aberrations in the signal beam imaging system are estimated to be 0.16 waves peak to valley (p–v) based on a double-pass retro measurement. The design aberrations in the pump beam's imaging system are 0.2 waves p–v but no special effort was taken to measure the pump beam's diagnostic aberrations. The spectra of the input and output pulses are sampled by fiber-coupled diffusers and transported to a multichannel spectrometer. The energies of the pump and signal pulses are either measured directly with calorimeters or indirectly in the diagnostics beam path with calibration factors. The crystal is angle tuned using a precision rotation stage. We induce specific phase modulations on the pump beam using a phase plate after the main pump amplifiers or specific amplitude modulation upstream before the amplifiers using a programmable beam-shaping system.[20]

A high-order phase plate with ~2.5 waves (p–v) transmitted wavefront at 526 nm was inserted in the pump-beam path to introduce a more-complex phase profile, as shown in Fig. 2(a). The resulting signal intensity and wavefront, with bandpass filtration at 930 nm, are shown in Fig. 2(b); the calculated counterparts are shown in Fig. 2(c). The measured wavefront is a relative wavefront referenced against the amplified signal wavefront without the phase plate. The amplitude and overall shape of the measured and calculated wavefronts, in particular local extrema, are in excellent agreement.

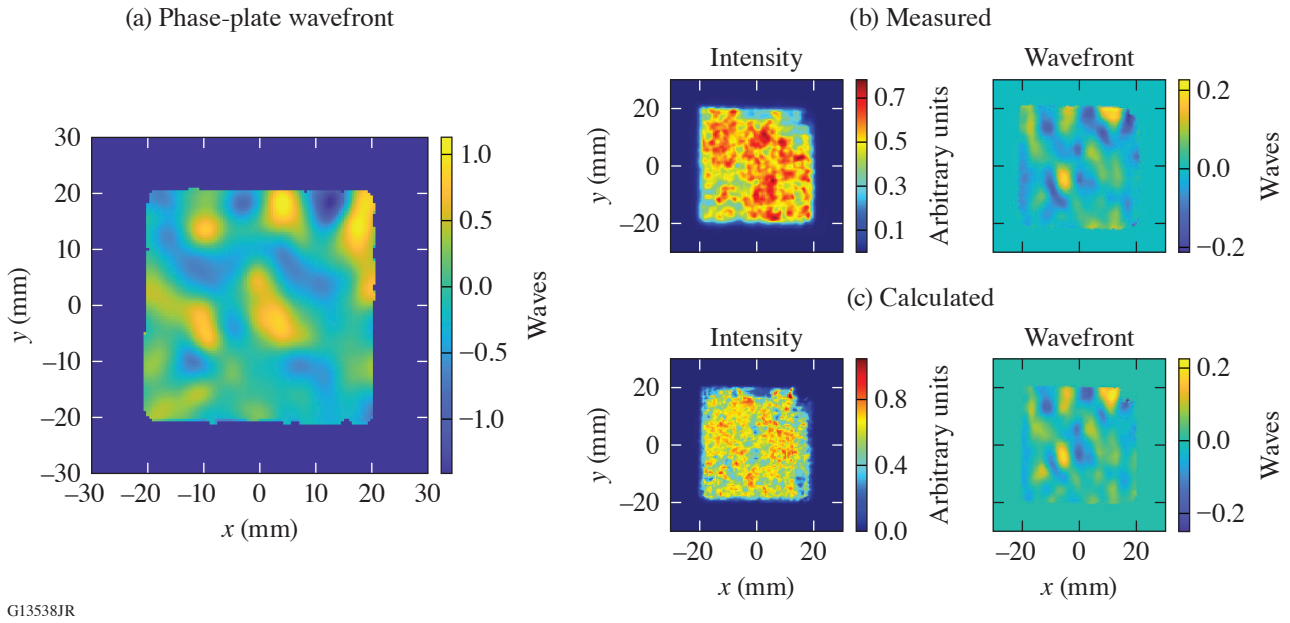

Figure 2
(a) Transmitted wavefront of the phase plate, (b) measured intensity and wavefront, and (c) calculated intensity and wavefront at 930 nm.

To investigate the amplitude effect, the beam-shaping system[20] for the pump beam was used to produce a cylindrical Gaussian-like beam as shown in Fig. 3(a). The crystal angle was detuned ±0.017° to change the sign of Δk and demonstrate its sign sensitivity on the induced wavefront. The lineouts of the measured and calculated wavefronts at 930 nm are shown in Fig. 3(b) as solid and dashed lines, as shown in the legend. The lineouts are averaged over 80% of the central region of the beam in the y direction. This comparison shows a good agreement in the overall quadratic shape following from the pump-beam profile. We also measured the wavefronts at three wavelengths (890 nm, 930 nm, and 990 nm) using bandpass filters installed in front of three separate wavefront sensors as shown in Fig. 3(c), which directly show chromatic effect.

We presented a detailed theory of the OPA phase produced by the pump and signal wavefronts and measured the OPA phase from the pump wavefront. The main theoretical result is that the OPA phase is proportional to the derivative of the pump and signal wavefronts in the phase-matching direction. The birefringent walk-off and noncollinear interaction geometry couple the phase derivative terms to phase mismatch and therefore to the OPA phase. The effect of the pump-beam profile has also been investigated. Our expressions showed the OPA phase depends on the pump intensity and the sign of the phase mismatch. The signal wavefront modulation caused by the pump-intensity modulation is more sensitive at a lower pump intensity. A small amount of chromatic aberrations following the shape of the pump profile is expected.

We performed experiments demonstrating both the phase and amplitude effect of the pump beam on the OPA phase using a broadband OPA amplifier in a collinear geometry. The pump wavefront effect was investigated by adding a high-order phase plate in the pump beam. The experiment confirmed that the induced signal phase is related to the pump phase gradient in the phase-matching direction. The OPA phase due to the pump beam profile was measured for different phase-matching conditions

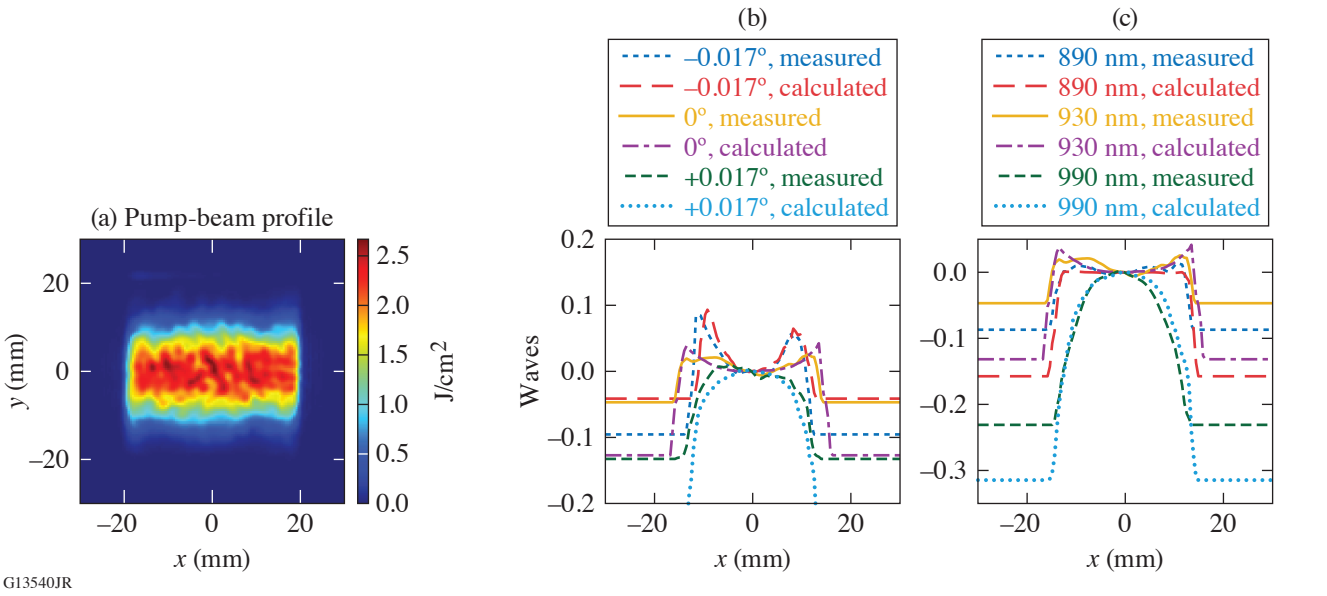

Figure 3
(a) Vertically nonuniform pump-beam profile; (b) measured and calculated wavefront-averaged vertical lineouts at different crystal tuning angles; (c) measured and calculated wavefront averaged lineouts at three wavelengths at 0°.

obtained by slightly detuning the crystal. The measurements confirmed that the amplitude-induced OPA phase depends on the sign of the phase mismatch and the pump-beam profile.

The traditional understanding of the general behavior of the pump-beam wavefront being transferred to the idler beam is, in general, correct in the sense that the OPA phase introduced by the pump-beam wavefront is generally an order of magnitude smaller than the pump wavefront directly transferred to the idler beam. The transfer to the signal beam can be non-negligible, however, for a larger system with large wavefront errors. The experimental verification of the pump and signal phase effect for noncollinear geometry will be discussed in subsequent publications. We expect the considerations presented in this summary will play an important role for future construction of a scaled-up high-energy broadband OPCPA system, where the wavefront becomes difficult to control as the beam size increases.

This material is based upon work supported by the Department of Energy National Nuclear Security Administration under Award Number DE-NA0003856, the University of Rochester, and the New York State Energy Research and Development Authority.

1. G. A. Mourou, T. Tajima, and S. V. Bulanov, Rev. Mod. Phys. **78**, 309 (2006).
2. C. N. Danson *et al.*, High Power Laser Sci. Eng. **7**, e54 (2019).
3. V. V. Lozhkarev *et al.*, Opt. Express **14**, 446 (2006).
4. J. Bromage *et al.*, High Power Laser Sci. Eng. **9**, e63 (2021).
5. L. Xu *et al.*, Opt. Lett. **38**, 4837 (2013).
6. M. Galletti *et al.*, High Power Laser Sci. Eng. **8**, e31 (2020).
7. S. Yang *et al.*, Opt. Express **28**, 11,645 (2020).
8. R. S. Nagymihaly *et al.*, Opt. Express **27**, 1226 (2019).
9. I. N. Ross *et al.*, J. Opt. Soc. Am. B **19**, 2945 (2002).
10. W. Li *et al.*, Appl. Phys. B **123**, 37 (2016).
11. X. Wei *et al.*, Opt. Express **16**, 8904 (2008).
12. P. Yuan *et al.*, High Power Laser Sci. Eng. **2**, e30 (2014).
13. Y. Chen *et al.*, Adv. Condens. Matter Phys. **2018**, 5731938 (2018).

14. H. J. Bakker *et al.*, Phys. Rev. A **42**, 4085 (1990).
15. S. W. Bahk, Opt. Lett. **46**, 5368 (2021).
16. R. DeSalvo *et al.*, Opt. Lett. **17**, 28 (1992).
17. Y. Wang *et al.*, Opt. Lett. **46**, 5743 (2021).
18. I. A. Begishev *et al.*, Appl. Opt. **60**, 11,104 (2021).
19. K. Ogawa *et al.*, Opt. Express **17**, 7744 (2009).
20. S.-W. Bahk, I. A. Begishev, and J. D. Zuegel, Opt. Commun. **333**, 45 (2014).

Evaluation of Transverse Raman Scattering in KDP and DKDP in Geometries Suitable for Beam Polarization Control

T. Z. Kosc, H. Huang, T. J. Kessler, and S. G. Demos

Laboratory for Laser Energetics, University of Rochester

KDP and DKDP are particularly suitable materials for polarization control due to their ability to grow in large sizes and their inherent birefringence. However, their performance in large-aperture, high-fluence systems at 351 nm is hindered by the generation of transverse stimulated Raman scattering (TSRS)[1,2] seeded by the strong symmetric A_1 Raman mode. This process transfers energy to parasitic transverse beams and thereby limits the maximum power output in order to avoid damage to the optic and its mount. The intensity of the TSRS signal is governed by the propagation length (optic size) L; the laser intensity I_{pump}; and the Raman-gain coefficient g, where the latter is directly proportional to the spontaneous Raman-scattering cross section, $d\sigma/d\Omega$:

$$I_{\text{TSRS}} \sim \exp\left(gI_{\text{pump}}L\right), \text{ where } g = \left(8\pi cM \big/ \hbar\omega_s^3 n^2 \Delta\bar{\nu}\right) \cdot \left(d\sigma \big/ d\Omega\right).$$

The strength of the Raman-scattering cross section in a given orientation is related to the mode's Raman polarizability tensor which was only recently ascertained with high accuracy (due to the presence of numerous measurement artifacts mainly arising from depolarization of the pump beam and Raman signal during propagation in these birefringent materials) for both KDP and 70% DKDP.[3]

The goal of this work is to develop a modeling capability to evaluate the TSRS risk and its directional dependence in geometries relevant to polarization control. This ability, in turn, will enable optimization of the design (such as the crystal-cut orientation) of KDP or DKDP polarization control optics and guide the design of future laser systems. To support this modeling effort, a detailed experimental study of the transverse Raman scattering was conducted to validate the model accuracy. Experiments were performed using a novel setup detailed in Ref. 4 that utilized spherical samples to enable accurate measurements at relevant excitation geometries. A complete set of data was acquired by varying three parameters: (1) the angular position θ of the optic axis (OA) with respect to the vertical pump beam between 0° and 90°, (2) the angular alignment α of the pump-laser polarization relative to the vertical plane containing the OA, and (3) the transmission axis of the signal analyzer (parallel and orthogonal with respect to the beam-propagation direction). The data shown in Fig. 1 were obtained for an excitation and signal collection geometry suitable for polarization control (angle between OA projection on transverse plane and laser polarization $\alpha = 45°$). The signal intensity is normalized to the signal corresponding to the orientation that produces the maximum spontaneous Raman-scattering cross section in each material. The signal detected using the parallel analyzer arises mainly from polarization artifacts, which also cause the complex peak and valley features detected when using the orthogonal analyzer. As Fig. 1(c) demonstrates, the model is capable of reproducing the experimental results fairly accurately when considering the experimental conditions (a 32-mm-diam sphere, an ~0.5° incident half-angle, and a 5.7° collection half-angle).

The ray-tracing model tracks the spontaneous Raman emission using geometrical optics. Rays are generated from each point source (with initial intensity determined according to the relevant tensor products) and propagate in all directions as either ordinary (o) or extraordinary (e) components acquiring different phases. In the cross-section simulations, the source volume contains a large number of such source points and the collected Raman o and e photons are considered mutually incoherent. The corresponding experimental results (with the analyzer parallel and perpendicular to the pump laser) are estimated as the sums of the projections of the o and e components.

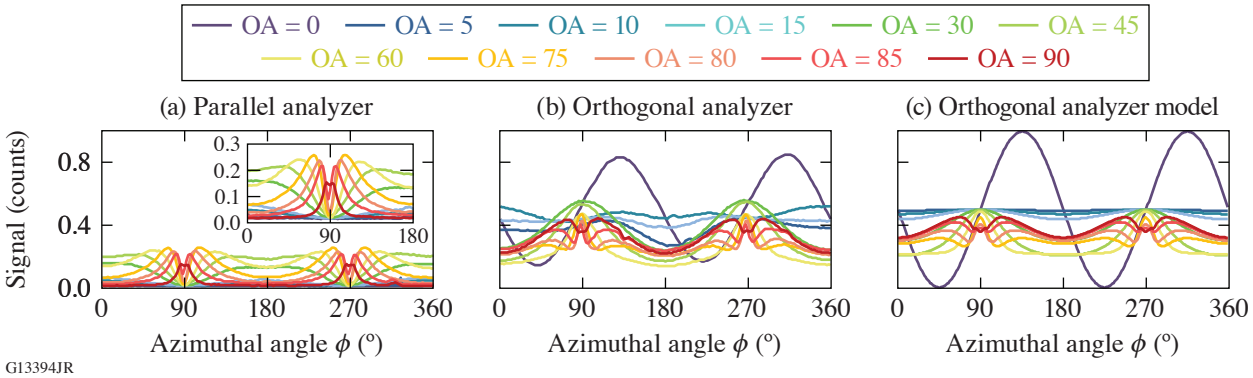

Figure 1
Data acquired using the KDP spherical sample with the Raman signal analyzer aligned (a) parallel and (b) perpendicular to the pump laser. (c) Ray-trace modeling reproduced experimental data, including polarization rotation artifacts. The pump polarization was set at $\alpha = 45°$ with respect to the vertical plane containing the crystal OA, whose position is varied between 0° and 90° with respect to the beam-propagation direction.

The ray-trace modeling also confirmed that the polarization rotation artifacts decrease as the collection aperture size is reduced. If we assume a collimated beam propagating though the crystal and the Raman scattering detected over an infinitely small collection angle, the signal with the analyzer perpendicular to the pump beam will converge the shape of the total signal (sum of the two analyzer positions). This behavior is shown in Fig. 2, which includes the (a) experimental and (b) modeling results.

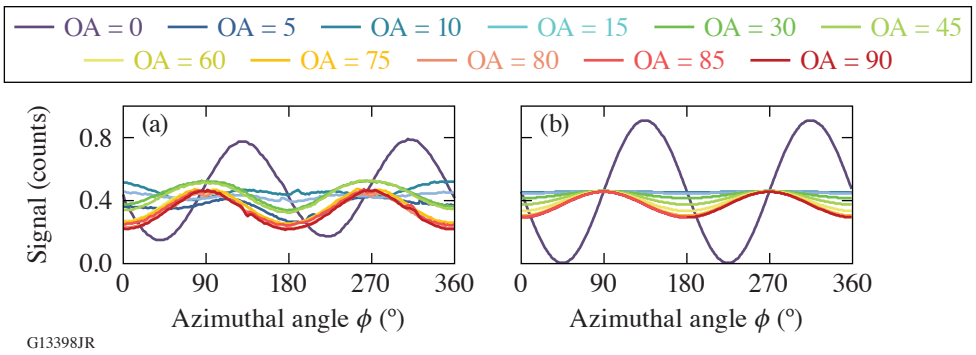

Figure 2
The sum of the parallel and perpendicular polarizations is shown as the total Raman signal for (a) experimental data and (b) the model. The polar angle varied between 0° and 90°, and the profile color coding is the same as in Fig. 1.

The results discussed above can be directly applied for the assessment of the TSRS risk in large-aperture laser systems. The validation of the model and methodology by the experimental results provides confidence on its use to guide crystal-cut optimization needed to minimize TSRS gain, to predict maximum operational fluence, or to help develop novel designs with complex polarization control properties in large-aperture optics. Future work will consider the design of specialized optics and include the ray paths contained by total internal reflection or retroreflected conditions that introduce longer gain paths.

This material is based upon work supported by the Department of Energy National Nuclear Security Administration under Award Number DE-NA0003856, the University of Rochester, and the New York State Energy Research and Development Authority.

1. C. E. Barker *et al.*, Proc. SPIE **2633**, 501 (1995).
2. S. N. Dixit *et al.*, J. Phys. IV France **133**, 717 (2005).
3. T. Z. Kosc *et al.*, Sci. Rep. **10**, 16283 (2020).
4. T. Z. Kosc *et al.*, Rev. Sci. Instrum. **91**, 015101 (2020).

LLE BEST Student and Teacher Research Program: Broad Exposure to Science and Technology

T. J. Kessler

Laboratory for Laser Energetics, University of Rochester

The primary goal of the Broad Exposure to Science and Technology (BEST) Research Program is to engage underrepresented high school students and their teachers in various aspects of science and technology that support LLE's laser science and applications research. This broad exposure helps guide students in their pursuit of STEM fields and encourages them to explore the next generation of related jobs and careers. Teacher participation equips educators with knowledge and experience that can be brought back to their schools to enhance science and technology curricula during the school year. The BEST program was carried out at East High School within the Rochester City School District (RCSD) during the summer of 2021. Four high school students and two teachers participated in the pilot program (Fig. 1). This research experience occurred over a six-week period during the months of July and August.

I3044JR

Figure 1
The participants of the BEST program in 2021 included (from left to right) East High teachers Trent Russell and Gavin Jenkins, East High students Yusuf Gazali, Reganae Walters, Taiasia Gibson, and Ramir Wearen, and program coordinator Terry Kessler, LLE Diversity Manager.

The teachers and students were exposed to different areas of science and technology research such as optical microscopy, optical testing and design, holography, liquid crystals, the Omega Laser Facility, and technical communications. The importance of engineering support for research, including chemical, electrical, mechanical, optical, computer, and workspace engineering, were emphasized to highlight the extensive teamwork required to make advancements in these fields. Students and teachers were given tours of LLE's laser science and technology laboratories during the program period.

The BEST team attended LLE Zoom presentations and discussions each week. They carried out science and technology research at East High School using temporarily relocated LLE equipment including microscopy, interferometry, and holography systems. Some examples of the many experimental activities are shown on the screen located in the middle of the white board (Fig. 1). The white board or "Google Board" displays each day's goals and the many questions generated by the students and teachers during lectures, demonstrations, and laboratory investigations.

Large scientific institutions, such as UR/LLE, employ many different types of professionals to carry out their research activities. Each of the many research and support activities requires teams consisting of these professionals. This matrix relationship shown in Fig. 2 is what allows LLE to maintain a successful research program. Exposure to this science and technology matrix provided the students and teachers with an understanding of the broad diversity of research activities as well as the rich diversity of individual professionals that enable the research to flourish.

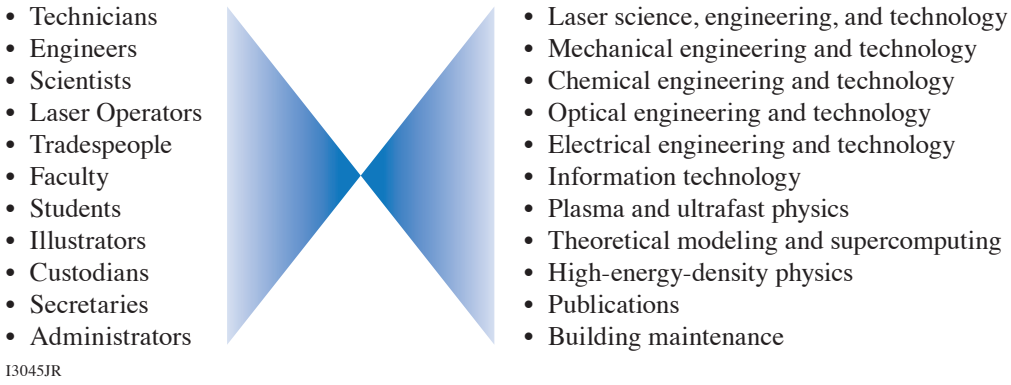

Figure 2
The BEST students and teachers were introduced to the many employment positions (left) that constitute the workforce at LLE. These positions support the wide variety of activities (right) needed to maintain the thriving science and technology research at LLE. Exposure to the LLE workforce provides guidance for students to choose their education and training experiences.

A team of LLE volunteers worked with the BEST students and teachers in a variety of science and technology fields (see Fig. 3). Each volunteer spent between one and four days at East High school over a six-week period. The program coordinator provided backup in order for the team members to maintain a flexible schedule during the summer months. Each volunteer, being an expert in their research field, was able to bring detailed information, coupled with hands-on opportunities, into the high school laboratory environment. For future summer programs, it is envisioned that the students and teachers will be exposed to additional fields of science and technology including laboratory operations, light–matter interaction, publications, and the technology trades that support all research activities at LLE.

LLE mentors exposed the students and teachers in the BEST Program to various technologies that are critical to the design and operation of the OMEGA 60 and OMEGA EP Laser Systems (see Fig. 4). Circuit board technologies were explored by dissecting computer systems, studying hardware design, and practicing the microsoldering techniques used to assemble electronic components. Laser hardware, such as alignment lasers and laser amplifier materials, were brought into the classroom for demonstration and exhibition. In addition, the phase transitions of liquid crystal materials were investigated, while optical components used to control the polarization and color of light were manufactured. This broad exposure highlighted the technologies that connect electronics, optics, and chemistry to laser systems.

I3046JR1

Figure 3
A team of nine LLE participants [(shown left to right) Terry Kessler, lasers/holography; Karen Cera, laboratory safety; Stavros Demos, spectroscopy/microscopy; Tanya Kosc, light polarization; Mike Krowl, electronics technology; Ken Marshall and Nate Urban, liquid crystals; Brian Kruschwitz, grating applications; and Nickolaos Savidis, optical design] worked with the BEST students and teachers in a variety of science and technology fields including laboratory safety, holography, spectroscopy, microscopy, light polarization, mechanical systems, electronics technology, liquid crystals, chemistry, diffraction gratings, and optical system design and prototyping.

(a)

(b)

(c)

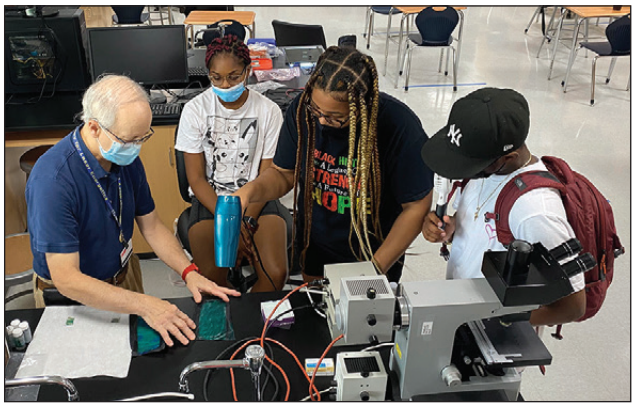

I3047JR

Figure 4
(a) Tanya Kosc, Optical Materials Technology Group Scientist, is shown exhibiting a neodymium-doped laser amplifier rod. (b) Mike Krowl, Electronics Group Technician, is shown instructing the students and teachers in circuit board technology including computer components and microsoldering techniques. (c) Ken Marshall, Optical Materials Technology Senior Research Engineer, is shown working with students on techniques to apply layers of liquid crystal to flexible fabrics.

A holographic interferometer was constructed at East High to record array-generating diffraction gratings. The number of reconstructed spots (orders) was plotted as a function of the development time in seconds (Fig. 5). Students view the multicolor orders by looking through the diffraction grating at a white-light source. The array of multicolor spots was photographed showing the characteristic blue to red angular shift for each order. This activity provided the hands-on experience to understand how gratings and grating spectrometers work. LLE mentors built on this experience to instruct the students and teachers on the basic concepts of chirped-pulse amplification and smoothing by spectral dispersion, two important laser schemes to produce high-intensity short pulses and uniform focal spots, respectively.

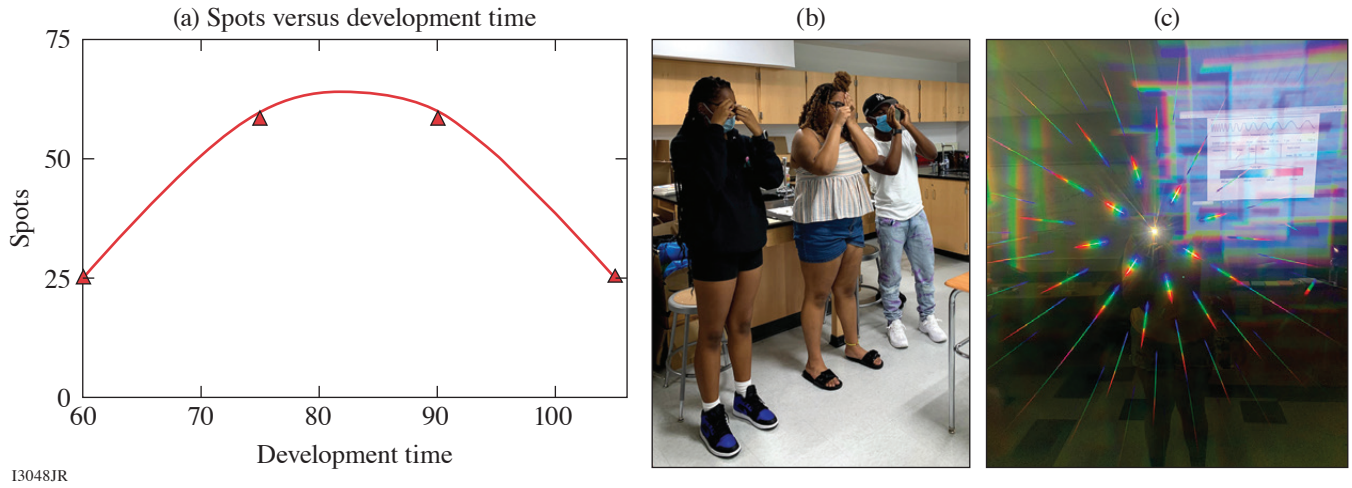

Figure 5
(a) The number of reconstructed spots from a multi-order diffraction grating was plotted as a function of the development time in seconds. (b) Students view the multicolor orders by looking through the diffraction grating at a white-light source. (c) The array of multicolor spots shows the characteristic blue to red angular shift for each order.

Spectroscopy is the study of the absorption and emission of light and other radiation by matter. There are numerous applications of spectroscopy at LLE including optical material composition analysis, light-scattering investigations, and the study of laser–matter interaction. Brian Kruschwitz, Group Leader of OMEGA System Science, worked with students to construct a grating spectrometer in a chemistry classroom at East High School. Stavros Demos, Group Leader of Optical Materials Technology, brought a spectrometer into the classroom to measure the wavelength transmission of optical filter glass. Using a color scale on a large classroom monitor, the students were able to make visual assessments of the filters' transmissions in order to compare objective and subjective spectral analyses (Fig. 6).

Due to COVID 19, the BEST participants visited LLE for only one day during the last week of the summer program to tour the OMEGA and OMEGA EP lasers, optical manufacturing facilities, and other support laboratories (Fig. 7). Together, the students and teachers were exposed to elements of science and technology that underscored the importance of their normal high school curricula. In addition, this group participated in tours of optics and imaging-related departments at Monroe Community College, the Rochester Institute of Technology, and the University of Rochester.

An important aspect of the BEST program involves the students' roles as ambassadors for outreach to other students enrolled at East High and other RCSD high schools. Two projects were completed for this purpose. First, the students and teachers created a PowerPoint presentation showing the broad range of science and technology topics included in the program. Second, a photomontage video was created to show the relationship between the BEST program and the work carried out at LLE. This video was accepted as an Innovative Spotlight in the 2022 University of Rochester Equity, Diversity, and Inclusion Leadership Summit. In planning for the 2022 BEST program, students from several RCSD high schools including East High, Young Women's College Prep, Monroe Upper High, and Rochester Early College others are being invited to participate.

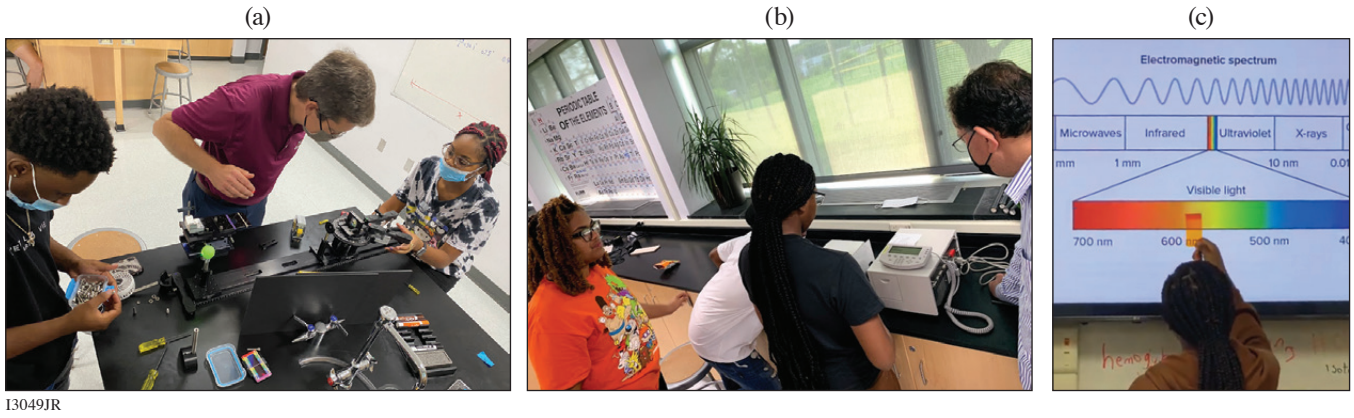

Figure 6
(a) Brian Kruschwitz, System Science Group Leader, is shown working with Ramir Wearen and Taiasia Gibson to construct a grating spectrometer. (b) Stavros Demos, Optical Materials Technology Group Leader, is shown demonstrating the procedure for operating a spectrometer to measure the wavelength transmission of optical filter glass. (c) Taiasia is shown visually comparing a glass filter to a large spectral scale.

Figure 7
The BEST students and teachers visited various LLE laboratories. (a) Amy Rigatti, Optical Manufacturing Group Leader, explains the work carried out in the coating facility. (b) Mike Campbell, LLE Director, discusses science and education with East High students Reganae Walters and Taiasia Gibson.

FY22 Q1 Laser Facility Report

J. Puth, M. Labuzeta, D. Canning, and R. T. Janezic

Laboratory for Laser Energetics, University of Rochester

During the first quarter of FY22, the Omega Facility conducted 233 target shots on OMEGA and 207 target shots on OMEGA EP for a total of 440 target shots (see Tables I and II). OMEGA averaged 10.4 target shots per operating day, averaging 91.3% Availability and 88.9% Experimental Effectiveness. OMEGA EP averaged 9.0 target shots per operating day, averaging 95.3% Availability and 94.9% Experimental Effectiveness.

Table I: OMEGA Laser System target shot summary for Q1 FY22.

Program	Laboratory	Planned Number of Target Shots	Actual Number of Target Shots
ICF	LLE	104.5	104
	LANL	11	12
	LLNL	11	6
ICF Subtotal		126.5	122
HED	LLE	11	8
	LANL	11	9
	LLNL	22	23
HED Subtotal		44	40
LBS	LLNL	22	21
LBS Subtotal		22	21
AIBS		22	17
APL		11	14
NLUF		22	19
Grand Total		247.5	233

AIBS: Academic and Industrial Basic Science
APL: Applied Physics Labs (Johns Hopkins University)
NLUF: National Laser Users Facility

Table II: OMEGA EP Laser System target shot summary for Q1 FY22.

Program	Laboratory	Planned Number of Target Shots	Actual Number of Target Shots
ICF	LLE	14	13
	LLNL	21	26
	NRL	7	9
ICF Subtotal		42	48
HED	LLE	14	16
	LANL	7	8
	LLNL	21	27
HED Subtotal		42	51
LBS	LLNL	10.5	18
	LLE	7	14
	PPPL	7	6
LBS Subtotal		24.5	38
CMAP		7	10
CEA		7	8
NLUF		31.5	39
Calibration	LLE	0	13
Grand Total		154	207

CMAP: Center for Matter at Atomic Pressures
CEA: Commissariat à l'énergie atomique et aux énergies alternatives

Publications and Conference Presentations

Publications

S.-W. Bahk, "Analytic Phase Solutions of Three-Wave Interactions," Opt. Lett. **46**, 5368 (2021).

I. A. Begishev, V. Bagnoud, S.-W. Bahk, W. A. Bittle, G. Brent, R. Cuffney, C. Dorrer, D. H. Froula, D. Haberberger, C. Mileham, P. M. Nilson, A. V. Okishev, J. L. Shaw, M. J. Shoup III, C. R. Stillman, C. Stoeckl, D. Turnbull, B. Wager, J. D. Zuegel, and J. Bromage, "Advanced Laser Development and Plasma-Physics Studies on the Multiterawatt Laser," Appl. Opt. **60**, 11,104 (2021).

M. D. Bergkoetter, B. E. Kruschwitz, S.-W. Bahk, and J. R. Fienup, "Measurement of Chromatic Aberrations Using Phase Retrieval," J. Opt. Soc. Am. A **38**, 1853 (2021).

A. F. A. Bott, L. Chen, G. Boutoux, T. Caillaud, A. Duval, M. Koenig, B. Khiar, I. Lantuéjoul, L. Le-Deroff, B. Reville, R. Rosch, D. Ryu, C. Spindloe, B. Vauzour, B. Villette, A. A. Schekochihin, D. Q. Lamb, P. Tzeferacos, G. Gregori, and A. Casner, "Inefficient Magnetic-Field Amplification in Supersonic Laser-Plasma Turbulence," Phys. Rev. Lett. **127**, 175002 (2021).

J. Bromage, S.-W. Bahk, M. Bedzyk, I. A. Begishev, S. Bucht, C. Dorrer, C. Feng, C. Jeon, C. Mileham, R. G. Roides, K. Shaughnessy, M. J. Shoup III, M. Spilatro, B. Webb, D. Weiner, and J. D. Zuegel, "MTW-OPAL: A Technology Development Platform for Ultra-Intense Optical Parametric Chirped-Pulse Amplification Systems," High Power Laser Sci. Eng. **9**, e63 (2021).

Y.-Y. Chang, X. Cheng, A. Hannasch, M. LaBerge, J. M. Shaw, K. Weichman, J. Welch, A. C. Bernstein, W. Henderson, R. Zgadzaj, and M. C. Downer, "Faraday Rotation Study of Plasma Bubbles in GeV Wakefield Accelerators," Phys. Plasmas **28**, 123105 (2021).

A. Colaïtis, I. Igumenshchev, J. Mathiaud, and V. Goncharov, "Inverse Ray Tracing on Icosahedral Tetrahedron Grids for Non-Linear Laser Plasma Interaction Coupled to 3D Radiation Hydrodynamics," J. Comput. Phys. **443**, 110537 (2021).

C. Feng, C. Dorrer, C. Jeon, R. Roides, B. Webb, and J. Bromage, "Analysis of Pump-to-Signal Noise Transfer in Two-Stage Ultra-Broadband Optical Parametric Chirped-Pulse Amplification," Opt. Express **29**, 40,240 (2021).

P. Franke, D. Ramsey, T. T. Simpson, D. Turnbull, D. H. Froula, and J. P. Palastro, "Optical Shock-Enhanced Self-Photon Acceleration," Phys. Rev. A **104**, 043520 (2021).

V. Gopalaswamy, R. Betti, J. P. Knauer, A. Lees, D. Patel, A. R. Christopherson, I. V. Igumenshchev, D. Cao, K. S. Anderson, A. Shvydky, D. H. Edgell, O. M. Mannion, C. Thomas, W. Theobald, C. Stoeckl, S. P. Regan, V. N. Goncharov, R. C. Shah, and E. M. Campbell, "Using Statistical Modeling to Predict and Understand Fusion Experiments," Phys. Plasmas **28**, 122705 (2021).

S. Heidtfeld, R. Adam, T. Kubota, K. Takanashi, D. Cao, C. Schmitz-Antoniak, D. E. Bürgler, F. Wang, C. Greb, G. Chen, I. Komissarov, H. Hardtdegen, M. Mikulics, R. Sobolewski, S. Suga, and C. M. Schneider, "Generation of Terahertz Transients from $CO_2Fe_{0.4}Mn_{0.6}Si$-Heusler-Alloy/Normal-Metal Nanobilayers Excited by Femtosecond Optical Pulses," Phys. Rev. Research **3**, 043025 (2021).

J. Jeet, A. B. Zylstra, M. Rubery, Y. Kim, K. D. Meaney, C. Forrest, V. Glebov, C. J. Horsfield, A. M. McEvoy, and H. W. Herrmann, "Inertial-Confinement Fusion-Plasma-Based Cross-Calibration of the Deuterium-Tritium γ-to-Neutron Branching Ratio," Phys. Rev. C **104**, 054611 (2021).

G. W. Jenkins, C. Feng, and J. Bromage, "Alignment Tolerance Analysis for Divided-Pulse Nonlinear Compression," J. Opt. Soc. Am. B **38**, 3199 (2021).

V. V. Karasiev, J. Hinz, S. X. Hu, and S. B. Trickey, "On the Liquid–Liquid Phase Transition of Dense Hydrogen," Nature **600**, E12 (2021).

D. I. Mihaylov, V. V. Karasiev, S. X. Hu, J. R. Rygg, V. N. Goncharov, and G. W. Collins, "Improved First-Principles Equation-of-State Table of Deuterium for High-Energy-Density Applications," Phys. Rev. B **104**, 144104 (2021).

S. F. Nwabunwanne and W. R. Donaldson, "Boosting the External Quantum Efficiency of AlGaN-Based Metal–Semiconductor–Metal Ultraviolet Photodiodes by Electrode Geometry Variation," IEEE J. Quantum Electron. **57**, 4000608 (2021).

A. M. Saunders, C. V. Stan, K. K. Mackay, B. Morgan, J. A. K. Horwitz, S. J. Ali, H. G. Rinderknecht, T. Haxhimali, Y. Ping, F. Najjar, J. Eggert, and H.-S. Park, "Experimental Observations of Laser-Driven Tin Ejecta Microjet Interactions," Phys. Rev. Lett. **127**, 155002 (2021).

A. Shvydky, A. V. Maximov, V. V. Karasiev, D. Haberberger, S. X. Hu, and V. N. Goncharov, "Ionization State and Dielectric Constant in Cold Rarefied Hydrocarbon Plasmas of Inertial Confinement Fusion," Phys. Rev. E **104**, 045207 (2021).

A. Tentori, A. Colaïtis, W. Theobald, A. Casner, D. Raffestin, A. Ruocco, J. Trela, E. Le Bel, K. Anderson, M. Wei, B. Henderson, J. Peebles, R. Scott, S. Baton, S. A. Pikuz, R. Betti, M. Khan, N. Woolsey, S. Zhang, and D. Batani, "Experimental Characterization of Hot-Electron Emission and Shock Dynamics in the Context of the Shock Ignition Approach to Inertial Confinement Fusion," Phys. Plasmas **28**, 103302 (2021).

W. Trickey, V. N. Goncharov, I. V. Igumenshchev, A. Shvydky, T. J. B. Collins, and E. M. Campbell, "Central Density and Low-Mode Perturbation Control of Inertial Confinement Fusion Dynamic-Shell Targets," Front. Phys. **9**, 784258 (2021).

C. A. Williams, R. Betti, V. Gopalaswamy, and A. Lees, "High Yields in Direct-Drive Inertial Confinement Fusion Using Thin-Ice DT Liner Targets," Phys. Plasmas **28**, 122708 (2021).

Forthcoming Publications

P. T. Campbell, C. A. Walsh, B. K. Russell, J. P. Chittenden, A. Crilly, G. Fiksel, L. Gao, I. V. Igumenshchev, P. M. Nilson, A. G. R. Thomas, K. Krushelnick, and L. Willingale, "Measuring Magnetic Flux Suppression in High-Power Laser–Plasma Interactions," to be published in Physics of Plasmas.

T. J. B. Collins, C. Stoeckl, R. Epstein, W. A. Bittle, C. J. Forrest, V. Yu. Glebov, V. N. Goncharov, D. R. Harding, S. X. Hu, D. W. Jacobs-Perkins, T. Z. Kosc, J. A. Marozas, C. Mileham, F. J. Marshall, S. F. B. Morse, P. B. Radha, S. P. Regan, B. Rice, T. C. Sangster, M. J. Shoup III, W. T. Shmayda, C. Sorce, W. Theobald, and M. D. Wittman, "Causes of Fuel–Ablator Mix Inferred from Modeling of Monochromatic Time-Gated Radiography in OMEGA Cryogenic Implosions," to be published in Physics of Plasmas.

M. F. Kasim, D. Watson-Parris, L. Deaconu, S. Oliver, P. Hatfield, D. H. Froula, G. Gregori, M. Jarvis, S. Khatiwala, J. Korenaga, J. Topp-Mugglestone, E. Viezzer, and S. M. Vinko, "Building High-Accuracy Emulators for Scientific Simulations with Deep Neural Architecture Search," to be published in Machine Learning: Science and Technology.

R. G. Kraus, R. J. Hemley, S. J. Ali, J. L. Belof, L. X. Benedict, J. Bernier, D. Braun, R. E. Cohen, G. W. Collins, F. Coppari, M. P. Desjarlais, D. Fratanduono, S. Hamel, A. Krygier, A. Lazicki, J. Mcnaney, M. Millot, P. C. Myint, M. G. Newman, J. R. Rygg, D. M. Sterbentz, S. T. Stewart, L. Stixrude, D. C. Swift, C. Wehrenberg, and J. H. Eggert, "Measuring the Melting Curve of Iron at Super-Earth Core Conditions," to be published in Science.

N. R. Shaffer and C. E. Starrett, "Dense Plasma Opacity via the Multiple-Scattering Method," to be published in Physical Review E.

R. Sobolewski, "Optical Detectors and Sensors," to be published in the Handbook of Superconducting Materials.

G. F. Swadling and J. Katz, "Novel Design for a Polarizing DUV Spectrometer Using a Wollaston Prism and Its Application as a Diagnostic for Measuring Thomson Scattering Data in the Presence of Strong Self-Emission Backgrounds," to be published in the Review of Scientific Instruments.

W. Theobald, D. Cao, R. C. Shah, C. A. Thomas, I. V. Igumenshchev, K. A. Bauer, R. Betti, M. J. Bonino, E. M. Campbell, A. R. Christopherson, K. Churnetski, D. H. Edgell, C. J. Forrest, J. A. Frenje, M. Gatu Johnson, V. Yu. Glebov, V. N. Goncharov, V. Gopalaswamy, D. R. Harding, S. X. Hu, S. T. Ivancic, D. W. Jacobs-Perkins, R. T. Janezic, T. Joshi, J. P.

Knauer, A. Lees, R. W. Luo, O. M. Mannion, F. J. Marshall, Z. L. Mohamed, S. F. B. Morse, D. Patel, J. L. Peebles, R. D. Petrasso, P. B. Radha, H. G. Rinderknecht, M. J. Rosenberg, S. Sampat, T. C. Sangster, W. T. Shmayda, C. M. Shuldberg, A. Shvydky, C. Sorce, C. Stoeckl, M. D. Wittman, and S. P. Regan, "Enhanced Laser-Energy Coupling with Small-Spot Distributed Phase Plates (SG5-650) in OMEGA DT Cryogenic Target Implosions," to be published in Physics of Plasmas.

D. Zhao, R. Betti, and H. Aluie, "Scale Interactions and Anisotropy in Rayleigh–Taylor Turbulence," to be published in the Journal of Fluid Mechanics.

Conference Presentations

The following presentations were made at Advanced Solid-State Lasers, Ontario, Canada, 3–7 October 2021:

C. Dorrer, I. A. Begishev, S.-W. Bahk, and J. Bromage, "Spatially Resolved Characterization of Partially Deuterated KDP Crystals for Parametric Amplification."

G. W. Jenkins, C. Feng, and J. Bromage, "Simultaneous Spectral Broadening and Contrast Improvement Using Divided-Pulse Nonlinear Compression."

M. Spilatro and C. Dorrer, "Versatile Spectral Shaping of Spectrally Incoherent Pulses in the IR and UV."

A. K. Schwemmlein, C. Fagan, W. T. Shmayda, M. Sharpe, C. Stoeckl, C. J. Forrest, S. P. Regan, and W. U. Schröder, "First Demonstration of a Triton Beam Using Target Normal Sheath Acceleration," presented at the American Physical Society Division of Nuclear Physics, Boston, MA, 10–14 October 2021.

D. A. Chin, P. M. Nilson, D. T. Bishel, E. Smith, X. Gong, M. K. Ginnane, B. J. Henderson, D. N. Polsin, T. R. Boehly, J. R. Rygg, G. W. Collins, D. Trail, A. Amouretti, M. Harmand, O. Mathon, R. Torchio, J. J. Ruby, F. Coppari, A. Coleman, and Y. Ping, "XANES and EXAFS Progress Studying Compressed Iron Oxides on OMEGA," presented at Matter in Extreme Conditions from Material Science to Planetary Physics, virtual, 12–13 October 2021.

The following presentations were made at Laser Damage, virtual, 12–15 October 2021:

D. Broege, S. G. Demos, C. Dorrer, K. R. P. Kafka, and M. Spilatro, "The Impact of Intensity Fluctuations on Laser Damage."

R. Dent, B. N. Hoffman, A. A. Kozlov, N. Liu, A. L. Rigatti, S. G. Demos, and A. A. Shestopalov, "Embedded Contamination Induced by Etching in E-Beam-Deposited Silica: A Possible Precursor to Laser Damage."

S. Elhadj, C. Gavin, A. Bayramian, W. Clauson, M. Murachver, J. Jarboe, D. Kissinger, C. LeBlanc, N. Urban, J. Wallace, S. Demos, and K. L. Marshall, "Large-Area, Multi-Pulse Laser Lifetime of Purified Nematic Liquid Crystals at Near-Infrared Wavelengths."

R. Jia, B. N. Hoffman, A. A. Kozlov, S. G. Demos, and A. A. Shestopalov, "Monolayer Organic Thin Films as Contamination-Resistant Coatings in Optical Elements."

K. R. P. Kafka, T. Z. Kosc, and S. G. Demos, "Methods and Apparatus for Laser Damage and Functional Performance Characterization of Ultrafast Laser Optics."

T. Z. Kosc, S. G. Demos, T. J. Kessler, H. Huang, A. Maltsev, R. Negres, and J. C. Lambropoulos, "Minimizing Risk for Laser Damage Due to Transverse Stimulated Raman Scattering in Large-Aperture KDP/DKDP Plates for Polarization Control at 3ω."

K. L. Marshall, K. R. P. Kafka, N. D. Urban, J. U. Wallace, and S. G. Demos, "The Effect of Incident Polarization Handedness and Ellipticity on the Laser-Damage Resistance of Oriented Liquid Crystals in the Nanosecond Regime."

P. Tzeferacos, "Big Computers and Big Lasers: How Concerted Numerical Simulations and Laser-Driven Laboratory Experiments Can Shed Light on Fundamental Astrophysical Processes in Turbulent Magnetized Plasmas," presented at CIRC Symposium, Rochester, 15 October 2021.

The following presentations were made at the Industrial Associates Meeting, Rochester, NY, 20–22 October 2021:

G. Chen, R. Adam, D. E. Bürgler, J. Cheng, D. Chaktraborty, I. Komissarov, S. Heidtfeld, D. Cao, H. Hardtdegen, M. Mikulics, A. Alostaz, F. Wang, M. Büscher, C. M. Schneider, L. Gladczuk, P. Przysłupki, and R. Sobolewski, "Ultrabroadband Spintronic THz Emitters Excited by Femtosecond Laser Pulse."

G. W. Jenkins, C. Feng, and J. Bromage, "Simultaneous Spectral Broadening and Contrast Improvement Using Divided-Pulse Nonlinear Compression."

E. M. Campbell, "A Vision for the Future for High-Power Laser Research and Applications," presented at OPTICSMEET 2021, Nice, France, 1–3 November 2021.

The following presentations were made at the 42nd Tritium Focus Group, Los Alamos, NM, 2–3 November 2021:

M. Sharpe and W. T. Shmayda, "Measurement of Palladium Hydride Isotherms Using H_2, D_2, and H_2/D_2 Mixtures."

W. T. Shmayda, H. Mutha, and K. Ryan, "The SPARC Tritium Fuel Cycle."

The following presentations were made at the 63rd Annual Meeting of the American Physical Society Division of Plasma Physics, Pittsburgh, PA, 8–12 November 2021:

M. B. P. Adams, P.-A. Gourdain, P. Tzeferacos, S. Feister, J. J. Pilgram, C. G. Constantin, and C. Niemann, "Exploration of Magnetic-Field Generation via Biermann Battery Using the *FLASH* Code to Model Experiments Performed at UCLA's Phoenix Laboratory."

M. V. Ambat, R. Boni, J. L. Shaw, P. Franke, K. R. McMillen, M. VanDusen-Gross, H. G. Rinderknecht, D. Ramsey, T. T. Simpson, J. P. Palastro, S.-W. Bahk, J. Bromage, and D. H. Froula, "Effects of Chromatic Aberration in a Dephasingless Laser Wakefield Accelerator."

K. S. Anderson, E. C. Hansen, J. A. Marozas, T. J. B. Collins, V. N. Goncharov, M. M. Marinak, and S. Sepke, "Computational Modeling of the Target Mounting Stalk in Direct-Drive Implosions."

A. Armstrong, A. Reyes, M. B. P. Adams, P. Farmakis, E. C. Hansen, Y. Lu, D. Michta, K. Moczulski, D. Q. Lamb, and P. Tzeferacos, "Implementation and Verification of Braginskii Viscosity in the *FLASH* Code."

J. Baltazar, R. C. Shah, D. Cao, V. Gopalaswamy, R. Betti, D. Patel, C. Stoeckl, W. Theobald, K. M. Woo, and S. P. Regan, "Diagnosing Low-Mode ($\ell \leq 6$) and Mid-Mode ($6 < \ell \leq 40$) Asymmetries in the Explosion Phase of Laser-Direct-Drive DT Cryogenic Implosions on OMEGA."

D. H. Barnak, R. Betti, V. Gopalaswamy, A. Lees, and A. Shvydky, "Understanding Shock-Release Experiments Using a Numerical Simulation of VISAR."

D. T. Bishel, P. M. Nilson, D. A. Chin, J. J. Ruby, E. Smith, S. X. Hu, J. R. Rygg, G. W. Collins, and E. V. Marley, "Utilizing Implosions to Constrain Atomic Physics of Gbar Materials."

G. Bruhaug, H. G. Rinderknecht, M. S. Wei, D. T. Bishel, G. W. Collins, J. R. Rygg, Y. E, K. Garriga, X. C. Zhang, R. Smith, A. Necas, and K. Zhai, "High-Power, High-Energy THz Generation with Joule and Kilojoule-Class Lasers."

M. Burns, R. K. Follett, A. Bowman, S. Zhai, A. Poudel, S. Dwarkadas, S. Pai, and A. B. Sefkow, "Heterogeneous Plasma Physics Codes in TriForce: Progress and Next Steps."

D. Cao, R. C. Shah, C. A. Thomas, A. Lees, V. Gopalaswamy, R. Betti, D. Patel, W. Theobald, J. P. Knauer, P. B. Radha, C. Stoeckl, S. P. Regan, W. Scullin, T. J. B. Collins, and V. N. Goncharov, "Understanding Origins of Observed Fusion-Yield Dependencies for Direct-Drive Implosions on OMEGA."

S. H. Cao, R. Betti, V. Gopalaswamy, H. Huang, D. Patel, C. Ren, M. J. Rosenberg, A. Shvydky, C. Stoeckl, and H. Wen, "Predicting Hot-Electron Generation in Inertial Confinement Fusion with Particle-in-Cell Simulations."

A. Casner, V. Bouffetier, L. Ceurvorst, G. Perez Callejo, T. Goudal, H. W. Sio, J. L. Peebles, P. Tzeferacos, V. Smalyuk, and O. A. Hurricane, "Mitigation of the Kelvin–Helmholtz Instability in HED Conditions by a Strong External Magnetic Field."

L. Ceurvorst, L. Masse, S. Khan, D. A. Martinez, N. Izumi, V. A. Smalyuk, T. Goudal, V. Bouffetier, A. Casner, B. Canaud, V. N. Goncharov, and I. V. Igumenshchev, "Effects of Ablation and Mode Coupling on the Deeply Nonlinear Stages of the Rayleigh–Taylor Instability."

D. A. Chin, P. M. Nilson, D. T. Bishel, E. Smith, R. S. Craxton, J. R. Rygg, G. W. Collins, J. J. Ruby, F. Coppari, A. Coleman, and Y. Ping, "Characterization of X-Ray Emission from Spherical Shells for X-Ray Absorption Spectroscopy Experiments on OMEGA 60."

S. Chowdry, S. Zhang, S. X. Hu, and G. Kagan, "Incorporating Quantum Electronics in Classical Calculations for Dense Plasmas."

K. Churnetski, K. M. Woo, W. Theobald, P. B. Radha, R. Betti, V. Gopalaswamy, I. V. Igumenshchev, S. T. Ivancic, M. Michalko, R. C. Shah, C. Stoeckl, C. A. Thomas, and S. P. Regan, "Three-Dimensional Hot-Spot Reconstruction from Cryogenic DT Polar-Direct-Drive Implosions on OMEGA."

A. Colaïtis, D. H. Edgell, I. V. Igumenshchev, D. Turnbull, J. P. Palastro, R. K. Follett, V. N. Goncharov, and D. H. Froula, "Low-Mode Asymmetry Induced by Polarized Cross-Beam Energy Transfer Interaction in Laser-Direct-Drive Spherical Implosions on OMEGA."

T. J. B. Collins, P. M. Nilson, R. Epstein, D. T. Bishel, D. A. Chin, J. J. Ruby, J. Kendrick, D. Guy, S. T. Ivancic, F. J. Marshall, C. Stoeckl, V. N. Goncharov, and D. H. Froula, "Theory and Modeling of Blast-Wave–Driven Interfacial Hydrodynamic Instability in OMEGA Planar Experiments."

R. S. Craxton, W. Y. Wang, M. A. Marangola, and E. M. Campbell, "A Dual Laser-Beam Configuration Compatible with Both Symmetric Direct Drive and Spherical Hohlraums."

J. R. Davies, D. H. Barnak, E. C. Hansen, P. V. Heuer, L. S. Leal, J. L. Peebles, and A. Birkel, "Evaluation of Direct Inversion of Proton Radiographs in the Context of Cylindrical Implosions."

A. Diaw, N. M. Cook, S. Coleman, J. P. Edelen, E. C. Hansen, and P. Tzeferacos, "Resistivity and Heat Conduction Modeling in Capillary Discharges."

D. H. Edgell, A. Colaitis, R. S. Craxton, R. K. Follett, M. J. Guardalben, A. Kalb, J. Katz, J. Kwiatkowski, O. M. Mannion, P. B. Radha, A. Shvydky, C. Stoeckl, D. Turnbull, and D. H. Froula, "Nonuniformity in Direct-Drive Implosions Caused by Polarization Smoothing" (invited).

R. Ejaz, V. Gopalaswamy, and R. Betti, "A Deep Learning Approach to Design Inertial Confinement Fusion Experiments."

R. Epstein, V. N. Goncharov, S. X. Hu, D. Cao, A. Shvydky, P. W. McKenty, G. W. Collins, D. Haberberger, J. L. Kline, and S. M. Finnegan, "Assessment of Radiation Trapping in Inertial Confinement Fusion Implosion Experiments with High-*Z*–Lined, Single-Shell Targets."

P. Farmakis, M. McMullan, A. Reyes, J. Laune, M. B. P. Adams, A. Armstrong, E. C. Hansen, Y. Lu, D. Michta, K. Moczulski, D. Lamb, and P. Tzeferacos, "Expanding the Tabulated Equation-of-State Implementations in the *FLASH* Code for the *SESAME* Database."

R. K. Follett, H. Wen, J. G. Shaw, D. H. Froula, A. V. Maximov, A. A. Solodov, D. Turnbull, J. P. Palastro, J. F. Myatt, and J. W. Bates, "A Local-Field Approach to Understanding Multibeam Laser–Plasma Instabilities."

C. J. Forrest, D. Cao, V. N. Glebov, V. N. Goncharov, V. Gopalaswamy, J. P. Knauer, O. M. Mannion, Z. L. Mohamed, S. P. Regan, R. C. Shah, C. Stoeckl, and K. M. Woo, "Inference of Isotropic and Anisotropic Flow in Laser Direct-Drive Cryogenic DT Implosions on OMEGA."

P. Franke, D. Ramsey, T. T. Simpson, D. Turnbull, D. H. Froula, and J. P. Palastro, "Optical Shock-Enhanced Self-Photon Acceleration."

F. García-Rubio, R. Betti, J. Sanz, and H. Aluie, "Magneto-hydrodynamic Instabilities in Ablation Fronts and Coronal Plasmas" (invited).

M. Gatu Johnson, P. J. Adrian, J. A. Frenje, T. M. Johnson, N. Kabadi, B. G. Lahmann, R. Petrasso, W. J. Garbett, R. S. Craxton, M. Hohenberger, H. D. Whitley, C. B. Yeamans, and A. B. Zylstra, "Measurement of Hot-Electron-Driven Fast Ions in Polar-Direct-Drive Exploding-Pusher Implosions on the NIF."

M. K. Ginnane, D. N. Polsin, X. Gong, M. C. Marshall, T. R. Boehly, J. R. Rygg, G. W. Collins, A. Lazicki, R. Kraus, J. H. Eggert, D. E. Fratanduono, J. P. Davis, C. A. McCoy, C. Seagle, and S. Root, "X-Ray Diffraction Measurements of Shocked and Shock-Ramped Platinum."

V. N. Goncharov, I. V. Igumenshchev, W. Trickey, N. Shaffer, K. M. Woo, T. J. B. Collins, E. M. Campbell, and Y. Lawrence, "Mitigating Deceleration Rayleigh–Taylor Growth in Inertial Confinement Fusion Designs."

X. Gong, D. N. Polsin, R. Paul, M. C. Marshall, M. K. Ginnane, B. J. Henderson, J. R. Rygg, G. W. Collins, and J. H. Eggert, "X-Ray Diffraction of Ramp-Compressed Silicon."

V. Gopalaswamy, R. Betti, J. P. Knauer, D. Patel, A. Lees, K. M. Woo, C. A. Thomas, D. Cao, O. M. Mannion, R. C. Shah, C. J. Forrest, Z. L. Mohamed, C. Stoeckl, V. N. Glebov, S. P. Regan, D. H. Edgell, M. J. Rosenberg, I. V. Igumenshchev, P. B. Radha, K. S. Anderson, J. R. Davies, T. J. B. Collins, V. N. Goncharov, K. Churnetski, W. Theobald, E. M. Campbell, R. T. Janezic, D. R. Harding, M. J. Bonino, S. Sampat, K. A. Bauer, S. F. B. Morse, M. Gatu Johnson, R. D. Petrasso, C. K. Li, and J. A. Frenje, "Advances Toward Hydro-Equivalent Ignition in OMEGA Direct-Drive Implosions" (invited).

D. Haberberger, A. Shvydky, S. T. Ivancic, V. N. Goncharov, C. Stoeckl, and D. H. Froula, "Schlieren Refraction Measurements of Implosion Density Profiles."

E. C. Hansen, M. B. P. Adams, A. Armstrong, J. R. Davies, P. Farmakis, F. García-Rubio, Y. Lu, D. Michta, K. Moczulski, C. Ren, A. C. Reyes, A. Sefkow, H. Wen, P. Tzeferacos, S. Langendorf, P. Ney, H. Rahman, and E. Ruskov, "Extended Magnetohydrodynamics in the *FLASH* Code."

B. J. Henderson, M. C. Marshall, J. R. Rygg, D. N. Polsin, L. E. Hansen, M. K. Ginnane, and G. W. Collins, "Thermal Emission and Reflectivity of Shocked SiO_2 Aerogel for Broadband Optical Probing."

P. V. Heuer, L S. Leal, J. R. Davies, E. C. Hansen, D. H. Barnak, J. L. Peebles, and A. Birkel, "Proton Radiography of Self-Generated Magnetic Fields in Laser-Driven Cylindrical Implosions."

P. V. Heuer, Y. Zhang, C. Ren, J. R. Davies, D. B. Schaeffer, M. S. Weidl, C. Niemann, W. Fox, and D. Caprioli, "Studying Quasi-Parallel Collisionless Shocks in the Laboratory."

S. X. Hu, P. M. Nilson, D. T. Bishel, D. A. Chin, V. V. Karasiev, I. E. Golovkin, M. Gu, T. Walton, and S. B. Hansen, "Probing Extreme Atomic Physics at Petapascal Pressures."

M. Huff, J. R. Rygg, G. W. Collins, T. R. Boehly, D. N. Polsin, M. Nakajima, B. J. Henderson, M. C. Marshall, T. A. Suer, D. E. Fratanduono, M. Millot, R. F. Smith, C. A. McCoy, and L. E. Hansen, "Measurements of Sound Speed in Iron Shock-Compressed Iron to ~3000 GPa."

I. V. Igumenshchev, V. N. Goncharov, E. M. Campbell, T. J. B. Collins, M. J. Rosenberg, N. Shaffer, W. Theobald, W. Trickey, R. C. Shah, A. Shvydky, A. Colaïtis, S. Atzeni, and L. Savino, "Dynamic Shell Stability to Low-Mode Perturbations."

S. T. Ivancic, W. Theobald, K. Churnetski, M. Michalko, R. Spielman, S. P. Regan, A. Raymond, J. D. Kilkenny, A. Carpenter, C. Trosseille, D. K. Bradley, J. D. Hares, A. K. L. Dymoke Bradshaw, G. Rochau, M. Sanchez, and D. Garand, "Design of the Third X-Ray Line of Sight for OMEGA."

T. R. Joshi, R. C. Shah, W. Theobald, I. V. Igumenshchev, J. Baltazar, D. Cao, and S. P. Regan, "Analysis of Modulations Observed in X-Ray Self-Emission Images of OMEGA Direct-Drive Inertial Confinement Fusion Implosions."

V. V. Karasiev, D. I. Mihaylov, S. X. Hu, S. B. Trickey, and J. W. Dufty, "Advancing the Accuracy of DFT Simulations for High-Energy-Density Plasmas by Developing Temperature-Dependent Exchange-Correlation Functionals" (invited).

J. Katz, A. L. Milder, D. Turnbull, S. T. Ivancic, D. H. Froula, M. Sherlock, P. Michel, L. Divol, D. Strozzi, and W. Rozmus, "Direct Measurements of Laser Absorption in Undersense Plasmas on OMEGA."

A. Kish, J. G. Shaw, M. Lavell, A. Sexton, and A. B. Sefkow, "Software Architecture Design for Modular Multiphysics Simulations."

J. P. Knauer, C. J. Forrest, Z. L. Mohamed, K. M. Woo, O. M. Mannion, I. V. Igumenshchev, R. Betti, V. Gopalaswamy, P. B. Radha, S. P. Regan, W. Theobald, M. Gatu Johnson, J. A. Frenje, A. J. Crilly, and B. D. Appelbe, "Effect of Mode-1 Perturbations on OMEGA Areal-Density Measurements."

M. J. Lavell, J. G. Shaw, A. Kish, A. Sexton, A. Srinivasan, S. Sikorski, and A. B. Sefkow, "Coulomb Collision Models for PIC Simulations of Field Reversed Configurations and Beam-Plasma Interactions."

Y. Lawrence, V. N. Goncharov, W. Trickey, I. V. Igumenshchev, K. Woo, and J. Carroll-Nellenback, "Deceleration Phase Rayleigh–Taylor Growth in Dynamic Shell ICF Designs."

Y. Lawrence, R. D. McBride, and A. B. Sefkow, "Transport Coefficient Sensitivities in a Semi-Analytic Model for MagLIF."

L. S. Leal, J. L. Peebles, D. H. Barnak, J. R. Davies, A. V. Maximov, E. C. Hansen, P. V. Heuer, A. B. Sefkow, and R. Betti, "Simulations of Ti-Layered Magnetized Liner Inertial Fusion Implosions on OMEGA Investigating the Effect of Mix."

A. Lees, D. Barnak, R. Betti, V. Gopalaswamy, A. Shvydky, and Z. K. Sprowal, "Measurements of Shock-Release Dynamics in Polystyrene Foils."

Y. Lu, S. Feister, J. Meinecke, F. Miniati, G. Gregori, A. Bott, A. Reyes, E. C. Hansen, J. T. Laune, B. Reville, J. S. Ross, D. Q. Lamb, and P. Tzeferacos, "Numerical Modeling of Laser-Driven Plasma Experiments Aiming to Study Turbulent Dynamo and Thermal Conduction at the National Ignition Facility."

O. M. Mannion, C. J. Forrest, V. Yu. Glebov, J. P. Knauer, P. W. McKenty, Z. L. Mohamed, S. P. Regan, C. Stoeckl, B. D. Appelbe, A. J. Crilly, W. T. Taitano, B. Keenan, P. Adrian, J. A. Frenje, N. Kabadi, and M. Gatu Johnson, "Fusion Neutron Energy Spectrum Measurements in Kinetic Plasmas."

M. J.-E. Manuel, M. Ghosh, R. Jonnalagadda, F. N. Beg, M. B. Adams, P. Tzeferacos, C. M. Huntington, B. Remington, J. S. Ross, D. D. Ryutov, H. W. Sio, G. F. Swadling, S. Wilks, and H.-S. Park, "Experimental Evidence of Early-Time Linear-Saturation of the Ion-Weibel Instability in Counter-streaming Plasmas."

J. A. Marozas, P. W. McKenty, T. J. B. Collins, M. J. Rosenberg, H. G. Rinderknecht, S. P. Regan, E. M. Campbell, C. B. Yeamans, B. E. Blue, L. Divol, G. E. Kemp, and H. D. Whitley, "National Ignition Facility Polar-Direct-Drive Exploding-Pusher Experiments—Improving Performance via Imprint Mitigation."

A. V. Maximov, D. Turnbull, R. K. Follett, D. H. Edgell, J. G. Shaw, H. Wen, D. H. Froula, and J. P. Palastro, "Absorption of Laser Light by Coupling to Incoherent Plasma Waves at Quarter-Critical Density."

P. W. McKenty, J. A. Marozas, T. J. B. Collins, M. J. Rosenberg, G. E. Kemp, C. B. Yeamans, and L. Divol, "Examining the Role of Cross-Beam Energy Transfer in NIF Direct-Drive Exploding-Pusher Experiments."

B. McLellan, S. Zhang, and S. X. Hu, "Revealing the Atomic Motion Composing the B1–B2 Structural Transformation of MgO Under High Pressures."

K. R. McMillen, M. V. Ambat, Z. Barfield, J. Pigeon, D. Haberberger, D. H. Froula, and J. L. Shaw, "Plasma Characterization for Raman Amplification."

D. Michta, P. Tzeferacos, F. Graziani, and G. W. Hammett, "A Many-Body Extension to Madelung Quantum Hydrodynamics."

D. I. Mihaylov, V. V. Karasiev, S. X. Hu, J. R. Rygg, V. N. Goncharov, and G. W. Collins, "Improved First-Principles Equation-of-State Table of Deuterium for High-Energy-Density Science Applications."

A. L. Milder, J. Katz, J. P. Palastro, D. H. Edgell, A. M. Hansen, D. Turnbull, D. H. Froula, M. Sherlock, and W. Rozmus, "Measurements of the Return-Current Instability with Ion-Acoustic Thomson Scattering."

S. C. Miller, V. N. Goncharov, T. J. B. Collins, and A. Shvydky, "Internal Perturbation Evolution and Amplification During the Early Phase of Inertial Confinement Fusion Implosions."

K. Moczulski, A. Reyes, M. B. P. Adams, A. Armstrong, P. Farmakis, E. C. Hansen, Y. Lu, D. Michta, D. Lamb, and P. Tzeferacos, "Implementation and Verification of LC Circuit for Z-Pinch *FLASH* Simulations."

Z. L. Mohamed, J. P. Knauer, A. Sorce, R. B. Brannon, R. T. Janezic, W. T. Shmayda, Y. H. Kim, K. Meaney, H. Geppert-Kleinrath, N. M. Hoffman, M. S. Rubery, A. B. Zylstra, and J. Jeet, "S-Factor Measurements for Gamma-Channel Fusion Reactions."

K. L. Nguyen, L. Yin, B. J. Albright, A. M. Hansen, D. Turnbull, R. K. Follett, D. H. Froula, and J. P. Palastro, "Cross-Beam Energy Transfer Saturation by Ion-Trapping–Induced Detuning."

K. Nichols, A. J. White, L. A. Collins, and S. X. Hu, "Investigating the Stopping Power of Warm Dense Plasmas Using Time-Dependent Mixed Density-Functional Theory."

P. M. Nilson, F. J. Marshall, T. J. B. Collins, R. Epstein, D. T. Bishel, D. A. Chin, J. J. Ruby, J. Kendrick, D. Guy, S. T. Ivancic, C. Stoeckl, V. N. Goncharov, and D. H. Froula, "High-Resolution X-Ray Imaging of Shock-Driven Interface Instabilities."

R. W. Paddock, R. H. Scott, W. J. Garbett, B. M. Haines, A. B. Zylstra, T. J. B. Collins, R. S. Craxton, and P. A. Norreys, "A Pathway Toward Burning Plasmas Through Low-Convergence-Ratio Direct-Drive ICF Implosions."

J. P. Palastro, P. Franke, D. H. Froula, L. Nguyen, D. Ramsey, and T. T. Simpson, "High Harmonic Generation Driven by a Flying Focus."

H. Pantell, L. E. Hansen, G. Tabak, M. F. Huff, G. Bruhaug, J. R. Rygg, and G. W. Collins, "Isotope Effects on High-Pressure Water."

D. Patel, R. Betti, C. Stoeckl, M. J. Rosenberg, V. Gopalaswamy, J. P. Knauer, S. P. Regan, W. Theobald, V. Yu. Glebov, and A. R. Christopherson, "Analysis of Hot-Electron Preheat of High-Performing OMEGA Cryogenic Implosions."

J. L. Peebles, J. R. Davies, D. H. Barnak, P. V. Heuer, L. S. Leal, F. J. Marshall, V. Yu. Glebov, and R. Betti, "Measurements of Laser-Preheat–Induced Mix in Scaled Magnetized Liner Inertial Fusion (MagLIF) Implosions."

D. N. Polsin, X. Gong, M. F. Huff, L. E. Hansen, B. J. Henderson, R. Paul, S. Burns, G. W. Collins, J. R. Rygg, A. Lazicki, F. Coppari, R. Smith, M. Millot, J. H. Eggert, M. I. McMahon, X. Wang, K. Hilleke, and E. Zurek, "Probing a New Regime of Extreme Chemistry at High-Energy-Density Conditions: Na as a Prototypical Example" (invited).

H. Poole, D. Cao, R. Epstein, I. Golovkin, T. Walton, S. X. Hu, M. Kasim, S. Vinko, J. R. Rygg, V. N. Goncharov, G. Gregori, and S. P. Regan, "A Feasibility Study of Using X-Ray Thomson Scattering to Diagnose the In-Flight Plasma Conditions of DT Cryogenic Implosions."

P. B. Radha, C. Stoeckl, W. Theobald, M. J. Rosenberg, M. Porcelli, R. Betti, E. M. Campbell, D. H. Edgell, V. N. Goncharov, J. P. Knauer, S. P. Regan, A. Shvydky, and A. A. Solodov, "Validation of Energy Coupling Models from kJ to MJ Scale."

D. Ramsey, P. Franke, D. H. Froula, T. T. Simpson, K. Weichman, J. P. Palastro, B. Malaca, M. Pardal, J. Vieira, A. Di Piazza, and M. Formanek, "Nonlinear Thomson Scattering with Ponderomotive Control."

S. P. Regan, O. M. Mannion, C. J. Forrest, H. McClow, Z. L. Mohamed, A. Kalb, J. Kwiatkowski, J. P. Knauer, C. Stoeckl, R. C. Shah, V. Yu. Glebov, W. Theobald, K. Churnetski, R. Betti, V. Gopalaswamy, H. G. Rinderknecht, I. V. Igumenshchev, P. B. Radha, V. N. Goncharov, D. H. Edgell, J. Katz, D. Turnbull, D. H. Froula, M. J. Bonino, D. R. Harding, C. M. Shuldberg, R. W. Luo, M. Hoppe, A. Colaïtis, and E. M. Campbell, "Systematic Trends of Hot-Spot Flow Velocity in Laser-Direct-Drive Implosions on OMEGA."

C. Ren, H. Wen, E. C. Hansen, S. J. Langendorf, D. Michta, and P. Tzeferacos, "PIC Simulations of Colliding Plasma Jets in Plasma Liner Experiment."

A. Reyes, M. B. P. Adams, A. Armstrong, K. Moczulski, P. Farmakis, E. C. Hansen, Y. Lu, D. Michta, P. Tzeferacos, J. Grove, and D. Q. Lamb, "Implementation of a 2-D Unsplit Volume of Fluid Interface—Capturing Method for Multifluid Compressible Flows in the *FLASH* Code."

H. G. Rinderknecht, M. S. Wei, G. Bruhaug, K. Weichman, J. P. Palastro, J. D. Zuegel, A. Arefiev, T. Wang, T. Toncian, A. Laso Garcia, D. Doria, K. Spohr, H. J. Quevedo, T. Ditmire, J. Williams, A. Haid, and D. Stutman, "Relativistically Transparent Magnetic Filament: A Laser-Plasma Platform for Efficient Electron Acceleration and MeV Photon Radiation."

M. J. Rosenberg, A. A. Solodov, A. R. Christopherson, R. Betti, P. B. Radha, C. Stoeckl, C. J. Forrest, V. Yu. Glebov, F. J. Marshall, S. P. Regan, T. J. B. Collins, D. H. Froula, J. P. Palastro, V. N. Goncharov, M. Hohenberger, B. Bachmann, G. N. Hall, P. Michel, and C. Krauland "Hot-Electron Preheat in Hydrodynamically Scaled Direct-Drive Implosions at the National Ignition Facility and OMEGA."

J. R. Rygg, G. W. Collins, and P. M. Celliers, "Plasma Waves and the Compressibility of Warm Dense Hydrogen."

M. J. Schmitt, B. S. Scheiner, D. Schmidt, L. Kot, B. Keenan, M. J. Rosenberg, P. W. McKenty, and R. S. Craxton, "Ablative Energetics of Large-Capsule, Low-Intensity Direct-Drive Implosions at the National Ignition Facility."

A. K. Schwemmlein, C. E. Fagan, W. T. Shmayda, M. Sharpe, C. Stoeckl, C. J. Forrest, S. P. Regan, and W. U. Schröder, "First Demonstration of a Triton Beam Using Target Normal Sheath Acceleration."

A. B. Sefkow, J. G. Shaw, A. Kish, M. Lavell, R. Masti, A. Sexton, S. Borve, A. Bowman, M. Burns, J. Carroll-Nellenback, S. Cohen, J. R. Davies, S. Dwarkadas, E. Evans,

R. K. Follett, M. Haddad, K. Hemsley, A. Kokash, Y. Lawrence, B. G. Logan, R. L. McCrory, A. Nahar, J. H. Nuckolls, S. Pai, A. Poudel, T. Seabourne, W. Scullin, S. Sikorski, A. Srinivasan, H. Stojkovic, A. Velberg, K. Yanik, and S. Zhai, "Overview of TriForce: Projects, Progress, and Plans."

N. R. Shaffer, A. V. Maximov, V. N. Goncharov, and M. Sherlock, "Impact of Bandwidth on the Electron Distribution Functions of Laser-Produced Plasmas."

R. C. Shah, D. Cao, R. Epstein, M. J. Rosenberg, W. Theobald, V. Gopalaswamy, R. Betti, S. P. Regan, P. Volegov, and B. Bachmann, "Mix, Temperature, and Compression of Statistical Model Optimized Cryogenic Implosions."

J. L. Shaw, G. Bruhaug, M. Freeman, F. Merrill, V. Geppert-Kleinrath, and C. Wilde, "Electron Radiography Based on Electron Beams from Laser-Plasma Accelerators."

A. Shvydky, J. L. Peebles, M. J. Rosenberg, A. V. Maximov, K. S. Anderson, V. N. Goncharov, J. A. Marozas, P. W. McKenty, P. B. Radha, S. P. Regan, T. C. Sangster, M. Hohenberger, J. M. Di Nicola, J. M. Koning, M. M. Marinak, L. Masse, M. Karasik, and L. Antonelli, "National Ignition Facility Planar Imprint Experiments."

T. T. Simpson, D. Ramsey, P. Franke, M. V. Ambat, K. Weichman, D. Turnbull, D. H. Froula, and J. P. Palastro, "Spatiotemporal Control of Laser Intensity Through Cross-Phase Modulation."

A. A. Solodov, M. J. Rosenberg, M. Stoeckl, R. Betti, W. Seka, R. Epstein, C. Stoeckl, R. K. Follett, P. B. Radha, S. P. Regan, D. H. Froula, J. P. Palastro, V. N. Goncharov, A. R. Christopherson, B. Bachmann, M. Hohenberger, P. Michel, and J. F. Myatt, "Hot-Electron Preheat and Mitigation in Polar-Direct-Drive Experiments at the National Ignition Facility."

Z. K. Sprowal, L. E. Hansen, M. Zaghoo, J. R. Rygg, T. R. Boehly, D. N. Polsin, M. Huff, G. W. Collins, D. G. Hicks, and P. M. Celliers, "Accessing High Density States in D_2 Using Double Shock."

C. Stoeckl, W. Theobald, P. B. Radha, T. Filkins, and S. P. Regan, "Energy-Coupling Experiments Using Solid Spheres in the Polar-Direct-Drive Configuration on OMEGA."

G. Tabak, M. A. Millot, S. Hamel, T. Ogawa, P. M. Celliers, D. E. Fratanduono, A. Lazicki, D. Swift, S. Brygoo, P. Loubeyre, T. R. Boehly, N. Dasenbrock-Gammon, R. Dias, L. E. Hansen, B. J. Henderson, M. Zaghoo, S. Ali, R. Kodama, K. Miyanishi, N. Ozaki, T. Sano, R. Jeanloz, D. G. Hicks, G. W. Collins, J. H. Eggert, and J. R. Rygg, "Equation of State and Metallization of Methane Shock Compressed to 400 GPa."

W. Theobald, M. J. Rosenberg, P. B. Radha, S. P. Regan, C. Stoeckl, L. Ceurvorst, R. Betti, K. S. Anderson, J. A. Marozas, V. N. Goncharov, E. M. Campbell, C. M. Shuldberg, R. W. Luo, W. Sweet, D. N. Kaczala, B. Bachmann, T. Döppner, M. Hohenberger, R. Scott, and A. Colaïtis, "Laser-Direct-Drive Energy Coupling at 4×10^{14} W/cm^2 to 1.2×10^{15} W/cm^2 from Spherical Solid-Plastic Implosions at the National Ignition Facility."

C. A. Thomas, W. Theobald, J. P. Knauer, C. Stoeckl, T. J. B. Collins, V. N. Goncharov, R. Betti, E. M. Campbell, K. S. Anderson, K. A. Bauer, D. Cao, R. S. Craxton, D. H. Edgell, R. Epstein, C. J. Forrest, V. Yu. Glebov, V. Gopalaswamy, I. V. Igumenshchev, S. T. Ivancic, D. W. Jacobs-Perkins, R. T. Janezic, T. Joshi, J. Kwiatkowski, A. Lees, F. J. Marshall, M. Michalko, Z. L. Mohamed, D. Patel, J. L. Peebles, P. B. Radha, S. P. Regan, H. G. Rinderknecht, M. J. Rosenberg, S. Sampat, T. C. Sangster, R. C. Shah, K. L. Baker, A. L. Kritcher, M. Tabak, M. C. Herrmann, A. R. Christopherson, and O. M. Mannion, "Laser-Direct-Drive Cryogenic Implosion Performance on OMEGA Versus Target and Laser-Spot Radius."

W. Trickey, V. N. Goncharov, E. M. Campbell, T. J. B. Collins, M. J. Rosenberg, N. Shaffer, W. Theobald, R. C. Shah, A. Shvydky, I. V. Igumenshchev, A. Colaïtis, S. Atzeni, and L. Savino, "Optimization of Beam-Port Configurations to Minimize Low-Mode Perturbations in High-Yield Inertial Confinement Fusion Targets."

W. Trickey, R. H. H. Scott, and N. Woolsey, "Shock-Augmented Ignition Using Indirect Drive."

P. Tzeferacos, A. Reyes, Y. Lu, A. Armstrong, K. Moczulski, G. Gregori, J. Meinecke, H. Poole, L. Chen, T. Campbell, A. Bell, S. Sarkar, F. Miniati, A. Schekochihin, D. Lamb, D. H. Froula, J. Katz, D. Haberberger, D. Turnbull, S. Fess, H.-S. Park, J. S. Ross, T. Doeppner, J. Emig, C. Goyon, D. Ryutov, B. Remington, A. Zylstra, C.-K. Li, A. Birkel, R. D. Petrasso, H. Sio, F. H. Séguin, A. F. A. Bott, C. Palmer, B. Khiar, S. Feister, A. Casner, D. Ryu, B. Reville, C. J. Forrest, J. Foster, Y. Sakawa, F. Fiuza, E. Churazov, R. Bingham, T. White, and E. Zweibel, "Strong Suppression of Heat Conduction in Laser-Driven Magnetized Turbulent Plasmas."

M. VanDusen-Gross, K. Weichman, D. R. Harding, A. Arefiev, J. Williams, A. Haid, and H. G. Rinderknecht, "Design of Experiments to Study Relativistically Transparent Magnetic Filaments Using OMEGA EP."

K. Weichman, A. V. Arefiev, H. Mao, F. N. Beg, J. P. Palastro, A. P. L. Robinson, M. Murakami, S. Fujioka, J. J. Santos, T. Toncian, T. Ditmire, H. Quevedo, Y. Shi, and V. V. Ivanov, "Effects of Kilotesla-Level Applied Magnetic Fields on Relativistic Laser–Plasma Interactions" (invited).

H. Wen, R. K. Follett, A. V. Maximov, and J. P. Palastro, "Mitigation of Inflationary Stimulated Raman Scattering with Laser Bandwidth."

C. A. Williams, R. Betti, V. Gopalaswamy, A. Lees, J. P. Knauer, C. J. Forrest, D. Patel, S. Sampat, R. T. Janezic, D. Cao, O. M. Mannion, P. B. Radha, S. P. Regan, R. C. Shah, C. A. Thomas, W. Theobald, and K. M. Woo, "Improving Performance and Understanding of Direct-Drive Inertial Fusion Implosions Using Statistical Modeling of Experimental Data."

K. M. Woo, R. Betti, C. A. Thomas, C. Stoeckl, K. Churnetski, C. J. Forrest, Z. L. Mohamed, B. Zirps, S. P. Regan, T. J. B. Collins, W. Theobald, R. C. Shah, O. M. Mannion, D. Patel, D. Cao, J. P. Knauer, V. N. Goncharov, P. B. Radha, H. G. Rinderknecht, R. Epstein, V. Gopalaswamy, and F. J. Marshall, "Three-Dimensional Hot-Spot Reconstruction in Inertial Fusion Implosions."

S. Zhang, M. C. Marshall, J. R. Rygg, A. Shvydky, D. Haberberger, V. N. Goncharov, T. R. Boehly, G. W. Collins, S. X. Hu, D. E. Fratanduono, and A. Lazicki, "Species Separation in Polystyrene Shock Release Evidenced by Molecular-Dynamics Simulations and Laser-Drive Experiments."

Y. Zhang, P. V. Heuer, J. R. Davies, and C. Ren, "Magnetized Collisionless Shock Formation Mediated by the Modified-Two-Stream Instability."

D. E. Keller and V. V. Karasiev, "VASP 6.2.1 Runtime Comparison for Extreme Thermodynamic Condition Simulations Using Graphics-Processing Units," presented at the 12th IEEE Workshop on Performance Modeling, Benchmarking, and Simulation of High-Performamce Computer Systems, virtual, 14–19 November 2021.

C. Deeney, "The Laboratory for Laser Energetics: An Overview," presented at the L3Harris visit, Rochester, NY, 15 November 2021.

E. M. Campbell, "Inertial Fusion Energy: Opportunities and Challenges," presented at the Inertial Fusion Energy Workshop, Livermore, CA, 16 November 2021.

C. Deeney, "The Laboratory for Laser Energetics: An Overview," presented at the Danny Lowe visit, Rochester, NY, 16 November 2021.

The following presentations were made at the OES Annual Meeting, virtual, 17–18 November 2021:

E. M. Campbell, "ICF-Facility Operations LLE 10.7."

S. P. Regan, "ICF Diagnostics and Instrumentation: LLE."

T. C. Sangster, "MTE 10.8."

M. Wang and D. R. Harding, "Mechanical Properties of Micrometer-Size Foam-Like Auxetic Structures," presented at the MRS Fall Meeting, Boston, MA, 28 November–3 December 2021.

E. M. Campbell, "Principles of Inertial Confinement Fusion," presented at the NROTC visit, Rochester, NY, 1 December 2021.

The following presentations were made at the Cooperative Agreement Review Meeting, Rochester, NY, 6–7 December 2021:

E. M. Campbell, "The Laboratory for Laser Energetics: An Overview of the FY19–FY23 Cooperative Agreement."

G. W. Collins, "HEDS Curriculum and Mentoring at the University of Rochester."

G. W. Collins, S. X. Hu, and J. R. Rygg, "Laboratory for Laser Energetics Contributions to the Stockpile Stewardship Mission."

C. Deeney and E. M. Campbell, "The Laboratory for Laser Energetics: Our Cooperative Agreement Going Forward."

V. N. Goncharov, "Review of Ignition Science Campaigns."

V. Gopalaswamy, R. Betti, J. P. Knauer, D. Patel, A. Lees, K. M. Woo, C. A. Thomas, D. Cao, O. M. Mannion, R. C. Shah, C. J. Forrest, Z. L. Mohamed, C. Stoeckl, V. Yu. Glebov, S. P. Regan, D. H. Edgell, M. J. Rosenberg, I. V. Igumenshchev, P. B. Radha, K. S. Anderson, J. R. Davies, T. J. B. Collins, V. N. Goncharov, E. M. Campbell, R. T. Janezic, D. R. Harding, M. J. Bonino, S. Sampat, K. A. Bauer, S. F. B. Morse, M. Gatu Johnson, R. D. Petrasso, C. K. Li, and J. A. Frenje, "OMEGA DT Cryogenic Implosion Progress."

D. R. Harding, A. Behlok, M. J. Bonino, T. Cracium, S. Fess, J. Fooks, S. Karim, I. Knudsen, K. Lintz, N. Redden, D. Wasilewski, M. Wittman, Y. Lu, P. Fan, and X. Huang, "Target Production and Development at LLE."

S. X. Hu, "Highlights of Recent Progress in High-Energy-Density Physics Theory/Computation at LLE."

S. F. B. Morse, "Omega Facility Performance FY19–FY23."

S. P. Regan, "DOE Cooperative FY19–FY23 Agreement: Diagnostic Development (10.3)."

J. R. Rygg, D. N. Polsin, X. Gong, M. C. Marshall, G. W. Collins, J.-P. Davis, C. McCoy, C. Seagle, A. Lazicki, R. Kraus, J. H. Eggert, and D. E. Fratanduono, "High-Energy-Density Experiments: Case Studies."

C. Sorce, "Engineering, Information Technology and Cybersecurity, and Safety."

S. Stagnitto, "University of Rochester Support of the Laboratory for Laser Energetics' Research Portfolio."

D. Turnbull, "Laser–Plasma Instabilities: Deep Dive."

M. S. Wei, "Education and User Access."

J. D. Zuegel, "Laser and Materials Technology Division and Major Projects."

The following presentations were made at the National Diagnostic Workshop, virtual, 7–9 December 2021:

S. T. Ivancic, W. Theobald, K. Churnetski, M. Michalko, R. Spielman, S. P. Regan, A. Raymond, J. D. Kilkenny, A. Carpenter, C. Trosseille, D. K. Bradley, J. D. Hares, A. K. L. Dymoke-Bradshaw, G. Rochau, M. Sanchez, and D. Garand, "Design of the Third X-Ray Line of Sight for OMEGA."

A. L. Milder, J. Katz, R. Boni, D. Nelson, J. P. Palastro, P. Franke, J. L. Shaw, S. T. Ivancic, A. M. Hansen, D. Turnbull, I. A. Begishev, K. Daub, Z. Barfield, R. K. Follett, D. H. Froula, M. Sherlock, H. P. Le, T. Chapman, and W. Rozmus, "Measurements of Non-Maxwellian Electron Distribution Functions Using Angularly Resolved Thomson Scattering."

J. P. Palastro, P. Franke, M. Lim Pac Chong, K. L. Nguyen, J. Pigeon, D. Ramsey, H. G. Rinderknecht, J. L. Shaw, T. T. Simpson, D. Turnbull, K. Weichman, D. H. Froula, M. Formanek, A. Di Piazza, B. Malaca, M. Pardal, and J. Vieira, "Advanced Radiation Sources Enabled by Spatiotemporal Control of Laser Intensity."

J. L. Peebles, "Magnetized Target Capabilities and Diagnostic Needs at LLE."

H. G. Rinderknecht, J. P. Knauer, W. Theobald, R. Fairbanks, B. Brannon, V. Kobilansky, R. Peck, J. Armstrong, M. Weisbeck, J. Brown, P. B. Radha, S. P. Regan, J. Kunimune, P. Adrian, M. Gatu Johnson, J. A. Frenje, F. H. Séguin, and B. Bachmann, "An Introduction to Knock-on Deuteron Imaging for Diagnosing the Fuel and Hot Spot in Direct-Drive ICF Implosions."

The following presentations were made at the 2021 IEEE Pulsed Power Conference and Symposium on Fusion Engineering, Denver, CO, 12–16 December 2021:

M. Sharpe, W. T. Shmayda, and J. J. Ruby, "Influence of Heat Treatments on the Near-Surface Tritium Concentration Profiles."

W. T. Shmayda, H. Mutha, and K. Ryan, "Tritium Recovery from SPARC."

C. A. Thomas, E. M. Campbell, and M. Tabak, "Review of Inertial Confinement Fusion: Physics and Engineering Challenges" (invited).

The following presentations were made at the American Geophysical Union Fall Meeting, New Orleans, LA, 13–17 December 2021:

M. Ghosh, S. Zhang, and S. X. Hu, "Mechanism of Cooperative Diffusion in bcc Iron Under Earth and Super-Earth's Inner Core Conditions."

R. Paul, K. Nichols, S. Zhang, S. X. Hu, and V. V. Karasiev, "Melting, Acoustic Properties, and Thermal Conditions of FeO_2 Near Core–Mantle Boundary Conditions."

E. M. Campbell, "ICF Research at the University of Rochester's Laboratory for Laser Energetics," presented at the 42nd Annual Meeting of Fusion Power Associates, virtual, 15–16 December 2021.

E. M. Campbell, "University of Rochester and the Laboratory for Laser Energetics: An Overview," presented at the 3rd INFUSE Workshop, virtual, 16–17 December 2021.

R. Betti, "Thermonuclear Ignition in Laser-Driven Inertial Confinement Fusion," presented at the Centro Ricerche Frascati, Frascati, Italy, 17 December 2021.

UNIVERSITY OF ROCHESTER
LABORATORY FOR LASER ENERGETICS

Volume 170
January–March 2022
DOE/NA/3856-1736

LLE Review

Quarterly Report

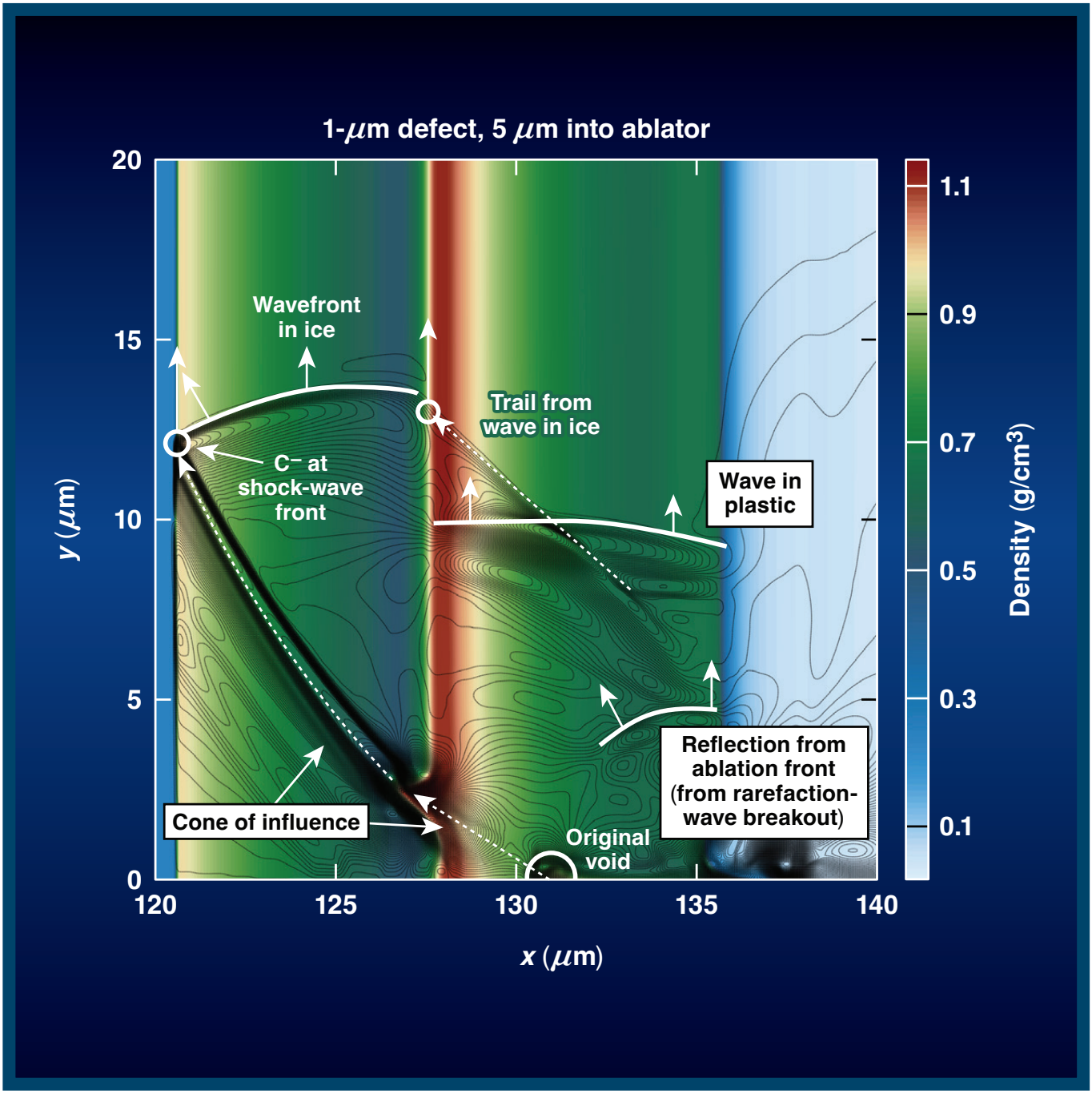

About the Cover:

The cover photo shows the density contour from a *Cygnus* simulation of a 2-D planar foil that contains a 1-μm defect located in the ablator (5 μm from the CH–DT interface). The color corresponds to density and the black lines correspond to y-velocity contours. The target accelerates from right to left, and the axis of symmetry is at $y = 0$. This shows the target after the first shock has passed through the CH–DT interface and into the ice. The shock front is located near $x = 121$ μm and the CH–DT interface is near $x = 128$ μm. The 1-D entropy wave that originates with the defect is labeled in the image just behind the CH–DT interface [near $(x, y) = (131, 0)$ μm]. In the image, perturbation information can be seen propagating along various ripples, after the shock has passed through the defect. When the shock interacts with the defect, the shock front becomes locally deformed. Since the perturbation wave has both x and y components, this deformation spreads laterally along the shock front, leaving a "trail" of vorticity in a cone-like manner, with its origin at the fluid trajectory of the original defect. The extent of this vorticity cone (labeled in the image by the dashed white line) is determined by the material sound speed, shock strength, and defect placement. As the original perturbation cone from the first shock front expands into the target, new waves (such as rarefaction waves) carry this updated information back to the ablation front. Additionally, the distortion laterally expands along the surface of the ablation front due to the 2-D nature of the flow.

Internal target defects create complex wave phenomena, yet simple single-mode (cosine) perturbations can provide clues as to how these complex wave dynamics evolve. In the image on the right, four different single-mode perturbations (λ = wavelength) are applied at different locations (x_p) relative to the interface within the ice or ablator material of a planar 2-D foil. This image shows that distortion growth is larger for large-wavelength modes that originate closer to the outer surface of the target due to shock transit time and the rarefaction wave created by the material interface.

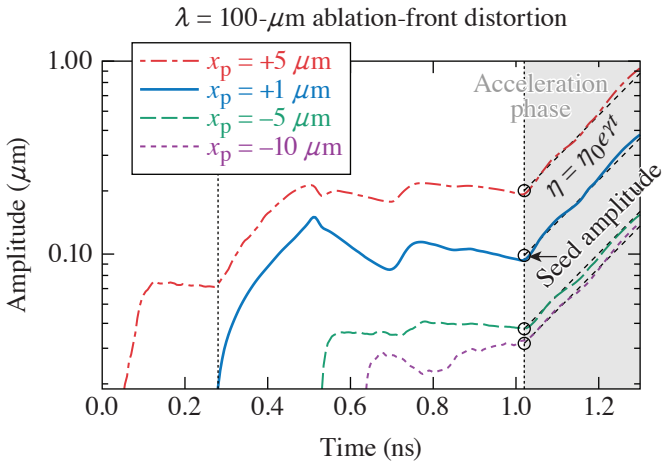

E30033JR

The work described in this volume includes current research at the Laboratory for Laser Energetics, which is supported by New York State Energy Research and Development Authority, the University of Rochester, the U.S. Department of Energy Office of Inertial Confinement Fusion under Cooperative Agreement No. DE-NA0003856, and other agencies.

Printed in the United States of America
Available from
National Technical Information Services
U.S. Department of Commerce
5285 Port Royal Road
Springfield, VA 22161
www.ntis.gov

For questions or comments, contact Milton J. Shoup III, Editor, Laboratory for Laser Energetics, 250 East River Road, Rochester, NY 14623-1299, (585) 275-9636.

www.lle.rochester.edu

UNIVERSITY OF ROCHESTER
LABORATORY FOR LASER ENERGETICS

Volume 170
January–March 2022
DOE/NA/3856-1736

LLE Review

Quarterly Report

UR LLE

Contents

In Brief

This volume of LLE Review 170 covers the period from January–March 2022. Articles appearing in this volume are the principal summarized results for long-form research articles. Readers seeking a more-detailed account of research activities are invited to seek out the primary materials appearing in print, detailed in the publications and presentations section at the end of this volume.

Highlights of research presented in this volume include:

- S. C. Miller and V. N. Goncharov model instability seeding mechanisms caused by internal defects in inertial confinement fusion targets (p. 1).
- A. Colaïtis *et al*. present detailed calculations that capture the persistent low-mode asymmetries evident in laser-direct-drive implosions on the OMEGA Laser System (p. 5).
- V. Gopalaswamy *et al.* present an analysis of limited coverage effects on areal-density measurements in inertial confinement fusion implosions on the OMEGA Laser System (p. 10).
- P. V. Heuer *et al.* report on diagnosing magnetic fields in cylindrical implosions with oblique proton radiography on the OMEGA Laser System (p. 16).
- L. S. Leal *et al.* model the effect of laser preheat in magnetized liner inertial fusion at the Omega Laser Facility (p. 19).
- K. M. Woo *et al.* present an analysis of core asymmetries in inertial confinement fusion implosions using 3-D hot-spot reconstruction of experimental data from the OMEGA Laser System (p. 21).
- J. R. Davies and P. V. Heuer conduct an evaluation of the direct inversion of proton radiographs in the context of cylindrical implosions (p. 24).
- H. Wen *et al.* report particle-in-cell modeling of plasma-jet merging in the large-Hall-parameter regime (p. 27).
- K. Weichman *et al.* present progress in modeling relativistic laser–plasma interaction with kilotesla-level applied magnetic fields (p. 30).
- G. Bruhaug *et al.* report the first single-shot electron radiography images using an electron beam from a 100-J-class laser-plasma accelerator (p. 35).
- G. Bruhaug *et al.* present on the development of a hardened THz energy meter for use on the kilojoule-scale, short-pulse OMEGA EP laser (p. 38).
- C. Dorrer and J. L Shaw demonstrate a single-shot cross-correlator based on the sum–frequency generation of counter-propagating beams in SBN61 ($Sr_xBa_{1-x}Nb_20_6$ with $x = 0.61$) using the Multi-Terawatt laser ($\lambda_A = 1053$ nm) and the idler of the MTW-OPAL laser ($\lambda_B = 1170$ nm) (p. 41).
- K. L. Marshall *et al.* report on the multiparameter laser performance characterization of liquid crystals for polarization control devices in the nanosecond regime (p. 44).
- M. Sharpe, W. T. Shmayda, and J. Ruby report on the experimentally determined influence of heat treatments on the near-surface tritium concentration profiles in 316 stainless steel (p. 47).
- G. Chen *et al.* experimentally determine the electron effective mass in highly resistive GaAs by exploiting the influence of a magnetic field on optically excited transient THz surface emissions (p. 50).

- J. L. Peebles *et al.* provide an assessment of generating quasi-static magnetic fields using laser-driven "capacitor" coils (p. 53).
- R. B. Spielman discusses pulsed-power innovations for next-generation, high-current drivers (p. 57).
- J. Puth *et al*. summarize operations of the Omega Laser Facility during the second quarter of FY22 (p. 60).

Milton Shoup III
Editor

Instability Seeding Mechanisms due to Internal Defects in Inertial Confinement Fusion Targets

S. C. Miller and V. N. Goncharov

Laboratory for Laser Energetics and Department of Mechanical Engineering, University of Rochester

Performance degradation in laser-driven inertial confinement fusion implosions is caused by several effects, one of which is Rayleigh–Taylor instability growth. Target imperfections from manufacturing processes create instability seeds in the form of roughness or isolated "dome" features on the outer surface, gaps or separation between material layers, ice-layer roughness, and internal defects such as voids and bubbles. Additionally, tritium decay from the DT fuel can deposit energy into the ablator and DT ice layers and cause localized swelling in the plastic ablator material.1 A comprehensive understanding of seeding mechanisms is essential to characterize the impact of target defects on in-flight shell integrity and mass injection into the central, lower-density vapor region. An analysis of early-time behavior of both single-mode shell mass modulations and isolated voids is performed by examining the evolution of the acoustic waves launched by these target imperfections. A systematic study of localized perturbation growth as a function of defect placement and size is presented. The use of low-density ablator materials (such as foams) is suggested as a potential mitigation strategy to improve target robustness against the impact of defect-initiated growth.

A new parallel high-order multiphysics code (*Cygnus*[2]) is used to simulate internal ("bulk") perturbations inside the solid-density DT ice and plastic ablator materials. Perturbations are applied to planar 2-D foils (driven by a laser-like heat flux up to the start the acceleration phase) to study hydrodynamic wave propagation and seeding mechanisms at the ablation front. Convergence effects are not significant in early-time evolution, and the use of planar foils simplifies the analysis.

The foils used in this work are defined by three fluid regions: a 100-μm-thick, low-density $\rho = 0.001$-g/cm^3 layer representing the vapor region; a 40-μm-thick, $\rho = 0.25$-g/cm^3 layer representing DT ice; and an 8-μm-thick, heavier-density $\rho = 1$-g/cm^3 layer to mimic the plastic (CH) ablator. Density perturbations are applied in two forms: single-mode sinusoidal (to study basic seeding mechanisms) and isolated Gaussian voids (to closer mimic a realistic defect).

Figure 1 shows the trajectories of the ablation front, CH–DT interface, DT gas–ice interface, and two shocks created by the single-picket laser pulse (plotted in the lower pane). When shocks pass through an internal perturbation, such as a defect, a void in the material, or an interfacial gap, perturbation waves are launched that travel along characteristic hypersurfaces. For small perturbations decomposed into Fourier harmonics, each wave harmonic travels along characteristics defined as $(\mathrm{d}x/\mathrm{d}t)_{C^+} = U + c_s$ (the C^+ characteristic), as $(\mathrm{d}x/\mathrm{d}t)_{C^-} = U - c_s$ (the C^- characteristic), and $(\mathrm{d}x/\mathrm{d}t)_e = U$ (the entropy wave that travels with the local fluid velocity), where U is local fluid velocity and c_s is local sound speed. These characteristic trajectories define how perturbations propagate throughout the target and deposit seeds for instability growth. In the event of a shock-perturbation interaction, the C^+ characteristic wave carries the information back to the ablation front, the C^- characteristic wave catches up to and perturbs the shock front, and the entropy wave travels with the original defect (and defines the trajectory of the shock-induced vorticity).

Figure 2 shows the results from single-mode sinusoidal perturbations applied at various depths in the ice and ablator material of the foil. These depths are reported as relative to the CH–DT interface (where a positive value denotes a position inside the ablator material). Figure 2 plots the evolution of the distortion amplitude (peak to valley) of the ablation front due to perturbations with a single-mode wavelength of 100 μm. The time history of the ablation-front distortion shows the arrival of particular hydrodynamics waves such as shocks, rarefaction waves, and other characteristic waves. The two perturbations that start in the

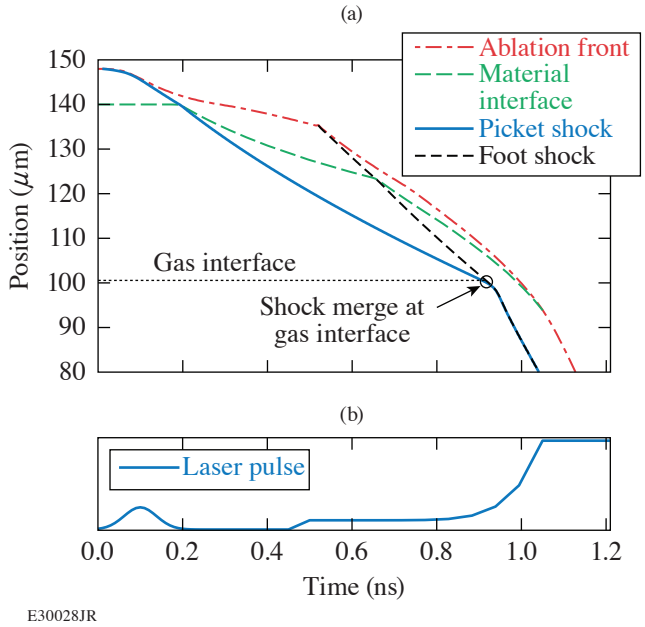

Figure 1
Interface and shock trajectories (position versus time) for the target and laser pulse.

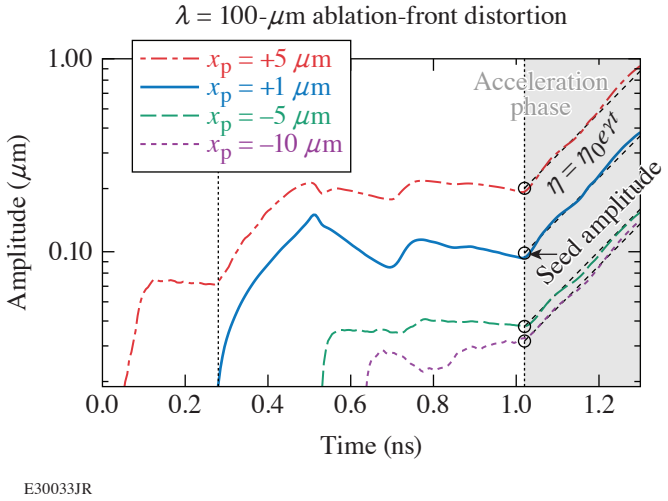

Figure 2
Ablation-front distortion history corresponding to perturbations at different locations in the ablator and DT ice. The acceleration phase is shaded in light gray. The dashed line is the exponential fit to $\eta = \eta_0 e^{\gamma t}$, and the seed amplitude is extracted from this curve. The initial perturbation depths (x_p) are +5, +1, –5, and –10 μm relative to the CH–DT interface for the red, blue, green, and purple lines, respectively. The vertical dotted black line near t = 0.3 ns indicae the arrival of the rarefaction wave at the ablation front.

ablator (red and blue curves) show significantly larger growth due to the rarefaction wave created by the interaction of the first shock (from the picket) and the CH-DT interface. This feedout growth process causes perturbations that start in the ablator to create larger seeds for instability growth when compared to those that originate in the ice. These seeds are defined as the amplitude of the distortion at the ablation front at the start of the acceleration phase (after which exponential RT growth occurs, or $\eta \sim \eta_0 e^{\gamma t}$, where γ is the growth rate and η is distortion). Figure 3 summarizes the seed amplitude (η_0) for perturbation wavelengths from 5 to 100 μm at different depths within the target material and shows the trend that perturbation seeds are largest when defects originate in the ablator and reduce as the initial position moves farther into the ice. As the wavelength reduces, however, interactions like destructive interference and phase change create wavelength-dependent behavior that complicates the position versus seed amplitude relationship. One region of particular interest [in Fig. 3(b)] is just inside of the CH–DT interface (near $x_p = -5$ μm). Here the interaction of the distorted CH–DT interface effectively cancels out or delays the onset of distortion growth at the ablation front (and reduces the acceleration-phase seed).

Simulations of isolated defects create complex wave interactions more likely to mimic target manufacturing defects, but much of the trends from single-mode perturbations apply. Figure 4(a) shows the density contour of the foil after the second shock has passed through a 1-μm defect (in the ablator). The black contour lines show velocity in the y direction and help to highlight

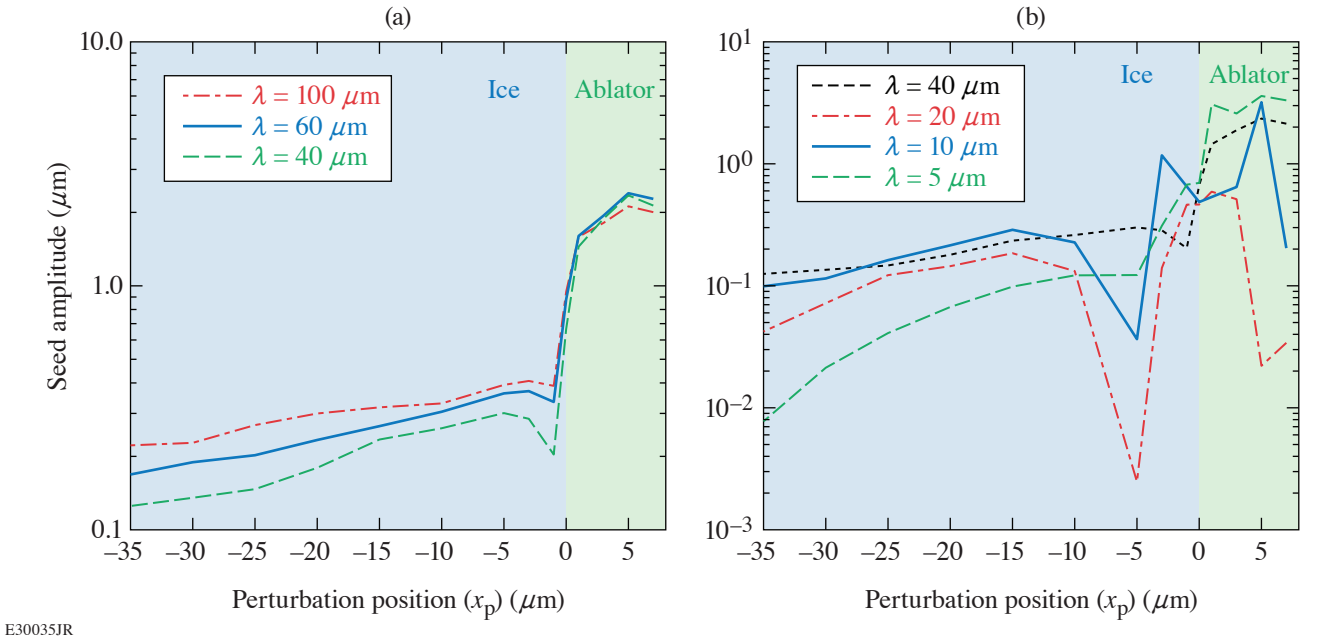

Figure 3
Scaled seed amplitudes as a function of perturbation position for (a) long-wavelength ($\lambda \geq 40$-mm) and (b) short wavelength ($\lambda < 40$-mm), single-mode perturbations.

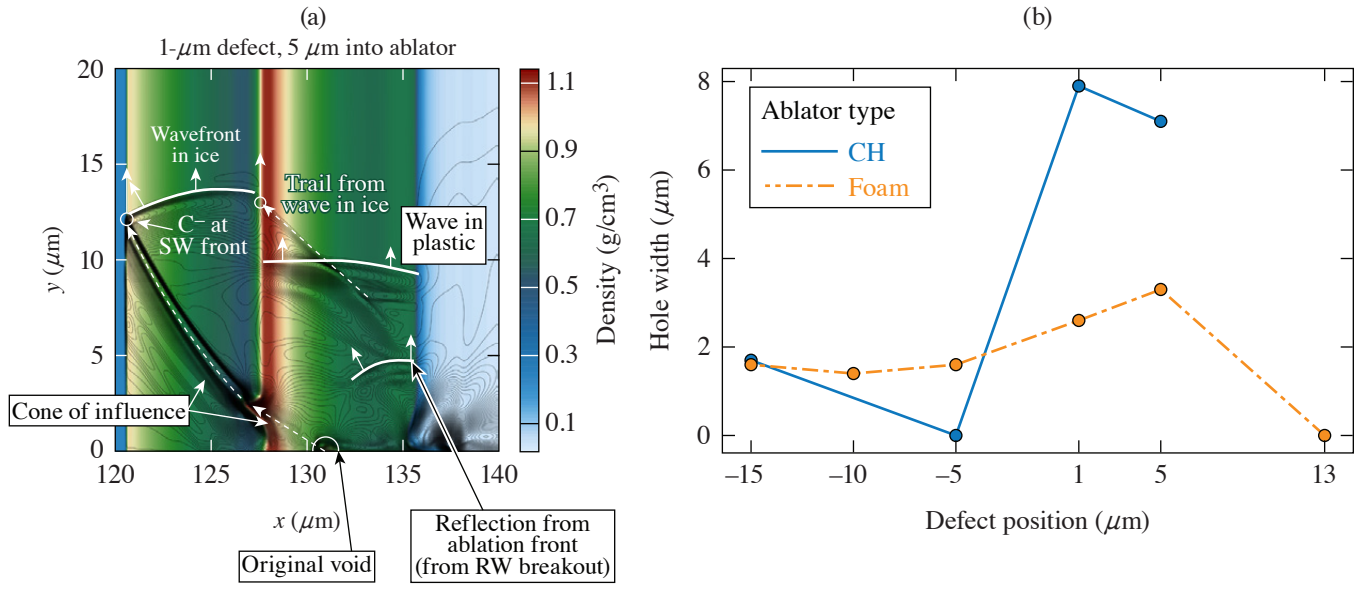

Figure 4
(a) Wave evolution for an isolated ablator defect (5 μm into the ablator from the CH–DT interface) at 0.5 ns after the first shock passage. Evolution in the y direction contributes to an extension of the maximum perturbation in y compared to the initial defect size. The contour colors show density and contour black lines show y velocity. (b) Hole sizes from shell punctures as a result of isolated defects in CH and wetted-foam targets approximately 300 ps after the start of the acceleration phase. RW: rarefaction wave; SW: shock wave.

particular wave features. These features include the wavefronts propagating through the different materials (ice and CH) and the lateral expansion of the defect perturbation. The lateral propagation is a unique feature of isolated defects (compared to sinusoidal perturbations). Isolated defect simulations show significant shell mass modulations and punctures at the start of the acceleration phase, depending on the position and size of the defect. Figure 4(b) shows the width of the hole due to a 1-μm defect located at various positions in the ice and ablator. Here, the degradation effects mimic the trend from short-wavelength, single-mode perturbations; ablator defects are more detrimental, and the effect is reduced just inward of the CH–DT interface.

A surrogate model that uses a wetted-foam ablator is proposed as a potential mitigation strategy to minimize the effects of manufacturing defects. In this design, the density is reduced from 1.0 (for CH) to 0.3 g/cm^3, and the shell thickness is increased to 26.7 μm (up from 8 μm) to conserve total shell mass compared to the CH ablator design. The smaller density reduces the strength of the rarefaction wave that travels from the ablator–ice interface (this rarefaction wave creates the large feedout growth shown in Fig. 1), and the increased thickness is beneficial because it isolates the defect perturbation (similar to how ice defects evolve). This effect can be seen in Fig. 4(b), where the foam ablator shows an overall reduction in hole width created by the defect.

Future work will examine internal defect evolution in 3-D and will include additional effects like convergent geometry along with and a more-detailed treatment of the materials (material-specific equations of state, radiation opacity, multiple materials, etc.). Additional work will seek to optimize shell thickness and continue to study alternative foam-like ablator designs.

This material is based upon work supported by the Department of Energy National Nuclear Security Administration under Award Number DE-NA0003856, the University of Rochester, and the New York State Energy Research and Development Authority.

1. D. R. Harding and W. T. Shmayda, Fusion Sci. Technol. **63**, 125 (2013).
2. S. C. Miller, "Hydrodynamic Instabilities in Inertial Confinement Fusion: Physics, Numerical Methods, and Implementation," Ph.D. Thesis, University of Rochester, 2022.

Three-Dimensional Simulations Capture the Persistent Low-Mode Asymmetries Evident in Laser-Direct-Drive Implosions on OMEGA

A. Colaïtis,[1] I. V. Igumenshchev,[2] D. H. Edgell,[2] D. Turnbull,[2] R. C. Shah,[2] O. M. Mannion,[2] C. Stoeckl,[2] D. W. Jacobs-Perkins,[2] A. Shvydky,[2] R. T. Janezic,[2] A. Kalb,[2] D. Cao,[2] C. J. Forrest,[2] J. Kwiatkowski,[2] S. P. Regan,[2] W. Theobald,[2] V. N. Goncharov,[2] and D. H. Froula[2]

[1]Université de Bordeaux, Centre Lasers Intenses et Applications, France
[2]Laboratory for Laser Energetics, University of Rochester

In this summary, detailed calculations are presented that include the first 3-D hydrodynamic simulations with sufficient physics models included to reproduce and quantify the anomalies observed in direct-drive implosions on OMEGA. When including all the known effects [polarized cross-beam energy transfer (CBET), mispointing, target offset], the simulations reproduce the measurements for bang time, yield, hot-spot flow velocity, and direction. To quantify these effects within the integrated experiments and describe the complex physical processes of polarized CBET and its interplay with multidimensional plasma hydrodynamics, an inline CBET model capable of accounting for polarization was implemented in a 3-D hydrodynamic code with a 3-D laser propagation solver. These integrated simulations were used to assess the effect of unpolarized and polarized CBET, explore the sensitivity of current direct-drive experiments to the various low-mode sources, and assess the predictive capabilities of such detailed 3-D modeling tools—an important component of the inertial confinement fusion program. Notably, current levels of beam mispointing, imbalance, target offset, and asymmetry from polarized CBET were found to degrade yields by more than 40%. Finally, mitigation strategies are explored: attempting to compensate the mode-1 asymmetry with a preimposed target offset and redesigning the double polarization rotators. These results were summarized in Ref. 1 and detailed in Refs. 2 and 3.

For the past few years, direct-drive implosion experiments conducted on the OMEGA Laser System[4] have reached a sufficient degree of control such that the errors induced by beam power imbalance, beam pointing inaccuracy, and target offset are relatively small. Despite these improvements, a large flow anomaly is still observed across many experiments, with a flow direction that appears systematic[5] (Fig. 1). Recently, it was proposed in Ref. 6 that a potential source of systematic low modes on the OMEGA laser[4] originates from polarized CBET. According to the authors of Ref. 6, the polarization dependency of CBET induces a significant low-mode anomaly in the laser drive, with its direction (in terms of spherical harmonics mode $\ell = 1$) being consistent with typical measured flow velocities from neutron diagnostics. Conclusions were reached, however, using post-processing of 1-D hydrodynamics simulations, which do not allow for a quantitative assessment of the final influence of polarized CBET on measured flow velocity and direction, for which inline modeling is required. Moreover, accounting for the compounded effect of beam balance, beam pointing error, and target offset in addition to polarized CBET requires a 3-D modeling of both the laser and hydrodynamics.

This lead to the development of the first inline-capable polarized CBET model, implemented within the inverse ray-tracing framework of the *IFRIIT*[7] code. Inline simulations were performed using a heterogeneous multiple-data, multiple-program framework coupling the *ASTER*[9,10] 3-D radiation-hydrodynamic code with the *IFRIIT*[7,10] 3-D laser propagation solver, running on 6000 cores of the French Commission for Atomic Energy and Alternative Energies' Très Grand Centre de Calcul (CEA TGCC) supercomputer, making it possible to describe the complex physical processes of polarized CBET and its interplay with plasma hydrodynamics. These integrated simulations were used to (1) quantify the sensitivity of current target designs to the best setup performances of the OMEGA Laser System, (2) assess if the source of the systematic flow can be identified, and (3) test various strategies for mitigation of the low-mode asymmetries.

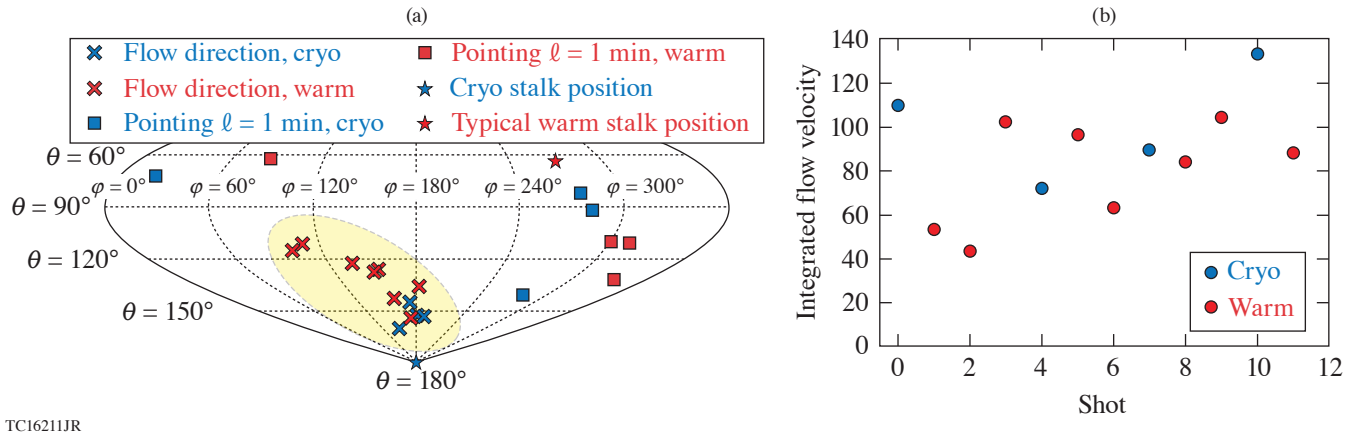

Figure 1
(a) Fusing DT flow direction shown in a sinusoidal projection of the OMEGA chamber and (b) associated flow magnitude in km/s in best-setup implosions (see also Refs. 5 and 11). The yellow region highlights the systematic anomaly.

The inline polarization model proposed here was developed within the field formulation of geometrical ray optics. The ray electric field is written $a = A\exp k_0\psi$, where k_0 is the vacuum wave number, A is the field swelling due to refraction, and ψ is a phase that includes the effects of absorption and energy exchange. The field at caustics is described using an etalon integral method,[12] which allows reconstruction of the Airy pattern without introducing free parameters. The ray field is then described onto the Frenet reference frame,[13] an orthogonal basis associated with the ray and defined at every point by a tangent $\mathbf{1} = \mathbf{k}/|\mathbf{k}|$, a normal $\boldsymbol{\nu}$ parallel to the permittivity gradient component transverse to the ray, and a binormal $\mathbf{b} = 1 \times \boldsymbol{\nu}$. The Frenet frame rotates with the ray, which allows for local accounting of polarization transport through refraction. The exchange of amplitude between the ray-field components in the Frenet frame, denoted $(A_n)^{\mathrm{T}} = (a_{n,\nu_n}, a_{n,b_n})$ for field n, can be written[13] as $\partial_{1_n} A_n = \underline{\underline{D_n}} A_n$ with $\underline{\underline{D_n}}$ a tensor that accounts for three polarization effects: polarization rotation due to refraction, polarization rotation of the probe beam toward the pump beam, and ellipticity induced in the initially linear polarizations due to CBET-induced plasma birefringence.

In the final model, the ray amplitude A is computed according to ray theory from a single inverse ray-tracing step,[14] while the ray phase is obtained by integrating the permittivity along the ray trajectory, $\psi = \int \varepsilon''[\mathbf{r}(\hat{\tau})\mathrm{d}\hat{\tau}/2]$, which includes ε'', the effect of polarized CBET from $\underline{\underline{D_n}}$, as well as collisional absorption and Langdon effect.[10,15] Pump depletion is obtained by iterating the ray phase computation until convergence. The final formulation of the laser propagation model has no free parameters, contrary to what is commonly used in inline CBET models to either limit caustic fields or tune the CBET interaction.[16–19] This polarized CBET model was validated against academic test cases and against the *BeamletCrosser* post-processor[2,6] and is now used in inline 3-D *ASTER/IFRIIT*[9,10] simulations. The full polarized CBET model and its validation are presented in Ref. 2.

The 12 shots reported in Fig. 1 span 19 months of operation and were obtained with good performance metrics for beam pointing, beam balance, offset error, target quality, and diagnostic quality. Out of these 12, three shots were modeled; 94343, 98755, and 98768. Among those, 94343 and 98768 are cryogenic shots, whereas 98755 is a warm plastic shot. Shot 98768 is a large-diameter shot with $D_t = 1012$ μm, while the others are smaller targets with $D_t \sim 980$ μm. To this set, we also add shot 94712 (Ref. 11), which was a cryogenic shot with poor pointing performances, contrary to the other three noted above. For these experiments, the beam pointing was measured at the beginning of the shot day. In addition, for shot 98755, pointing was also measured at the end of the shot day, providing two references. Finally, the ice-thickness uniformity was characterized using optical measurements prior to the shots. For the targets of interest, the ice layer nonuniformity was estimated to be less than the instrument resolution, i.e., <1% for the mode $\ell = 1$.

An extensive set of simulations was executed while varying the CBET model and/or the number of low-mode sources, which are included. The CBET model was toggled from off, to the commonly used unpolarized model[20] where the polarization effect for polarization-smoothed beams [e.g., distributed polarization rotation (DPR)] is modeled with fixed polarization and without any

rotation or ellipticity effects to the fully polarized model presented here. In all simulations, the Spitzer–Härm[21] heat conduction model was used at all times except in the first picket where the flux was limited with $f_{\text{lim}} = 0.1$ (Ref. 8).

The inline simulations are compared to various measurements: peak rise time of the neutron rate, yield, flow velocity magnitude, and direction. Several conclusions can be drawn from the simulations results for neutron data, some of which are reported in Fig. 2: (1) The CBET model alone gets nuclear bang time correctly, implying that the zero-order drive energetics are correct and well described by the model [Fig. 2(a)]. This also suggests that other effects not accounted for here, such as two-plasmon decay, do not significantly modify the total drive.[22] (2) Unpolarized and polarized CBET simulations with power balance and pointing variations get the neutron yield correct because both drive energetics and symmetry are important for the yield [Fig. 2(b)]. (3) Both CBET models with power balance and pointing variations match the flow velocity correctly for shot 94712 because the large pointing error dominates the low-mode sources. (4) Polarized CBET with power balance and pointing is needed to get the flow velocity correct for the more-accurately pointed shot 94343 (the low offset of 3.5 μm is seen to play a minor role). This indicates that the polarization effect becomes more important as other low-mode sources become smaller. The flow direction is reproduced correctly in all simulations as long as the effects of polarized CBET, beam imbalance, and beam pointing are accounted for. The full comparison to experiments is reported in Ref. 3.

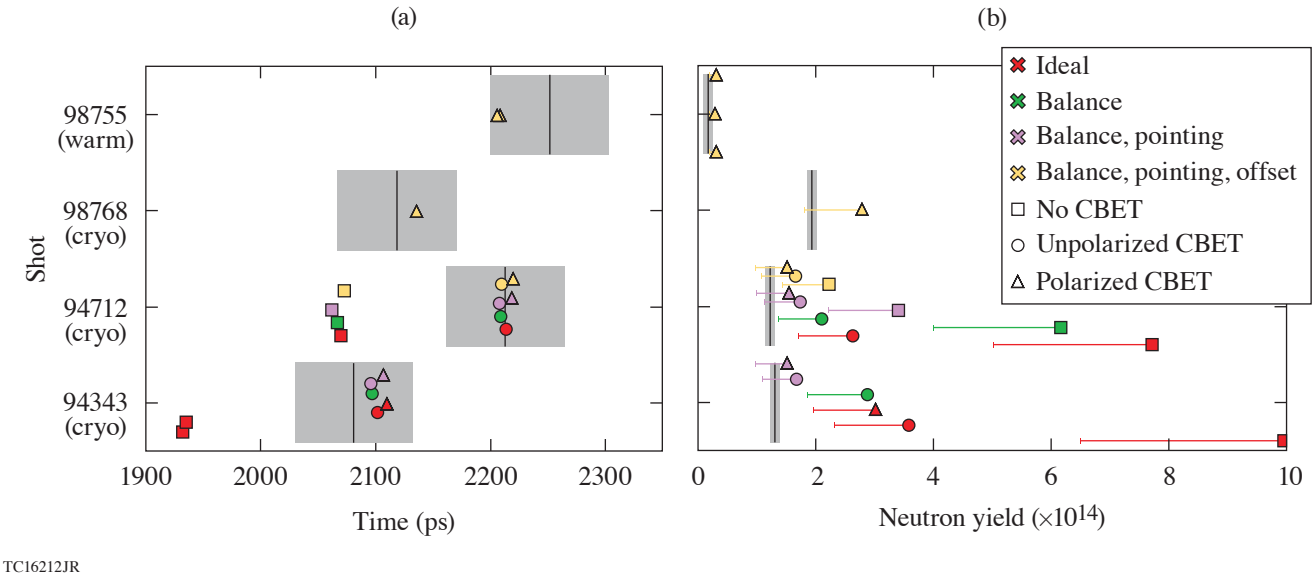

Figure 2
[(a),(b)] Comparison of the simulated (colored symbols) and measured (gray-shaded areas) (a) peak neutron rise time and (b) neutron yield. Simulations include a variety of low-mode sources and were conducted with and without CBET (see legends). Error bars on the simulated neutron yield account for the effect of small-scale mixing. Experimental yields are corrected for tritium aging.[23]

By examining the various simulations, it is observed that these best-setup OMEGA implosions lose ~40% in yield due to effects of balance, pointing, and offset alone [Fig. 3(a)]. In that framework, the polarization effect of CBET causes only a small drop in yield, by about 6%. However, in cases where there is no prior low-mode asymmetry from balance or pointing, the polarized CBET alone reduces the yield by 18% and induces an ~90-km/s flow anomaly compared to an unpolarized CBET case. In addition, the effect of unpolarized CBET alone reduces the yield by ~65% and amplifies the mode-10 anomaly by a factor of 2 to 3, leading to target perforation [Fig. 3(c)]. This is a strong argument for mitigation of the polarized CBET anomaly. It is observed, however, that the yield's dependency on low modes is more severe in cases without CBET because the latter was acting to mitigate drive asymmetries. These results highlight how CBET is a coupling loss mechanism that should be mitigated altogether in future driver designs.

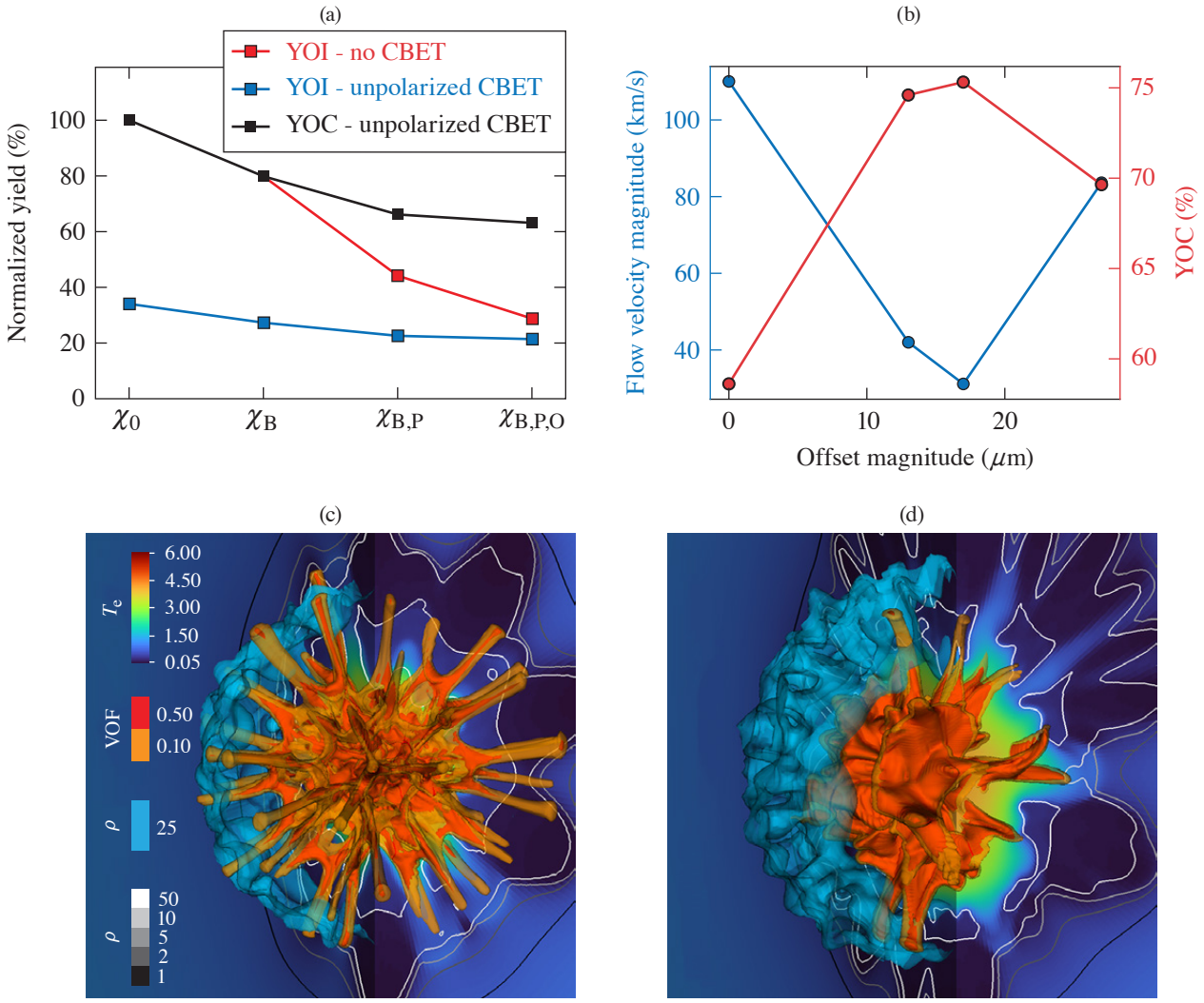

TC161213JR

Figure 3

(a) Scaling of the YOI (yield-over-ideal case in the absence of CBET) and YOC (yield-over-clean case in the presence of CBET) for simulations with and without unpolarized CBET, as a function of low-mode asymmetry sources (cases are labeled with a χ on the x axis; subscript 0 refers to the ideal case; B, P, and O indicate that beam balance, pointing, and offset were accounted for, respectively). (b) Flow anomaly (blue) and YOC (red) as functions of offset magnitude for a case with measured power balance and beam pointing ($\chi_{B,P}$). The target offset is in the opposite direction of the measured flow without offset. [(c),(d)] Target hot-spot electron temperature [colored background (keV)], 10% and 50% volume fraction of DT gas (orange and red volume contours, respectively), 25-g/cm^3 density isovalue (light blue volume contour), and 1-, 2-, 5-, 10-, and 50-g/cm^3 isocontours (black to white contour lines), for (c) an ideal case (χ_0) with unpolarized CBET. (d) A "real-setup" implosion accounting for power balance and beam pointing ($\chi_{B,P}$), with polarized CBET, is shown for comparison. All figures here relate to shot 94343.

Finally, two mitigation strategies are explored to compensate for the low-mode polarized CBET anomaly: offset compensation and DPR redesign. The offset compensation is able to increase the yield by ~15% [Fig. 3(b)] and reduce the modal $\ell = 1$ anomaly from the polarization effect by a factor of ~3. The offset compensation is not able to further improve the performances, however, due to the presence of other modes, notably from the polarized CBET anomaly but also from pointing and balance errors. Alternatively, considering a design of the DPR with only a 10-μm spot separation and half the smoothing by spectral dispersion (SSD) bandwidth, the simulations show that the flow direction and magnitude anomaly from the polarization effect disappear, and the unpolarized result is recovered. It is noted that halving the SSD bandwidth must be done in consideration of the potential effect on high mode-growth (not modeled here).

This work was granted access to the HPC resources of TGCC under the allocation 2020-A0070506129, 2021-A0090506129 made by GENCI, and PRACE grant number 2021240055. This work has been carried out within the framework of the EUROfusion Consortium, funded by the European Union via the Euratom Research and Training Programme (Grant Agreement No 101052200—EUROfusion). Views and opinions expressed are however those of the author(s) only and do not necessarily reflect those of the European Union or the European Commission. Neither the European Union nor the European Commission can be held responsible for them. The involved teams have operated within the framework of the Enabling Research Project: ENR-IFE.01.CEA "Advancing shock ignition for direct-drive inertial fusion." The software used in this work was developed in part at the University of Rochester's Laboratory for Laser Energetics. This material is based upon work supported by the Department of Energy National Nuclear Security Administration under Award No. DE-NA0003856, the University of Rochester, and the New York State Energy Research and Development Authority.

1. A. Colaïtis *et al.*, Phys. Rev. Lett. **129**, 095001 (2022).
2. A. Colaïtis *et al.*, "3-D Simulations of Implosions in Presence of Low Mode Asymmetries Part 1: Inline Polarized Cross Beam Energy Transfer Modeling," submitted to Plasma Physics and Controlled Fusion.
3. A. Colaïtis *et al.*, "3-D Simulations of Implosions in Presence of Low Mode Asymmetries Part 2: Systematic Flow Anomalies and Low Modes Impact on Performances on OMEGA," submitted to Plasma Physics and Controlled Fusion.
4. T. R. Boehly *et al.*, Opt. Commun. **133**, 495 (1997).
5. S. P. Regan *et al.*, Bull. Am. Phys. Soc. **66**, CO04.00011 (2021).
6. D. H. Edgell *et al.*, Phys. Rev. Lett. **127**, 075001 (2021).
7. A. Colaïtis *et al.*, Phys. Plasmas **26**, 072706 (2019).
8. I. V. Igumenshchev *et al.*, Phys. Plasmas **23**, 052702 (2016).
9. I. V. Igumenshchev *et al.*, Phys. Plasmas **24**, 056307 (2017).
10. A. Colaïtis *et al.*, J. Comput. Phys. **443**, 110537 (2021).
11. O. M. Mannion *et al.*, Phys. Plasmas **28**, 042701 (2021).
12. Yu. A. Kravtsov and Yu. I. Orlov, *Caustics, Catastrophes and Wave Fields*, 2nd ed., Springer Series on Wave Phenomena (Springer-Verlag, Berlin, 1993).
13. Yu. A. Kravtsov and N. Y. Zhu, *Theory of Diffraction: Heuristic Approaches*, Alpha Science Series on Wave Phenomena (Alpha Science International Ltd., Oxford, United Kingdom, 2010).
14. A. Colaïtis *et al.*, Phys. Plasmas **26**, 032301 (2019).
15. A. B. Langdon, Phys. Rev. Lett. **44**, 575 (1980).
16. I. V. Igumenshchev *et al.*, Phys. Plasmas **17**, 122708 (2010).
17. J. A. Marozas *et al.*, Phys. Plasmas **25**, 056314 (2018).
18. D. H. Edgell *et al.*, Phys. Plasmas **24**, 062706 (2017).
19. R. K. Follett *et al.*, Phys. Rev. E **98**, 043202 (2018).
20. P. Michel *et al.*, Phys. Plasmas **16**, 042702 (2009).
21. L. Spitzer, Jr. and R. Härm, Phys. Rev. **89**, 977 (1953).
22. D. Turnbull *et al.*, Phys. Rev. Lett. **124**, 185001 (2020).
23. A. Lees *et al.*, Phys. Rev. Lett. **127**, 105001 (2021).

Analysis of Limited Coverage Effects on Areal-Density Measurements in Inertial Confinement Fusion Implosions

V. Gopalaswamy,[1,2] R. Betti,[1,2,3] P. B. Radha,[1] A. J. Crilly,[4] K. M. Woo,[1] A. Lees,[1,2] C. A. Thomas,[1]
I. V. Igumenshchev,[1] S. C. Miller,[1,2] J. P. Knauer,[1] C. Stoeckl,[1] C. J. Forrest,[1] O. M. Mannion,[1,3,5] Z. L. Mohamed,[1,3]
H. G. Rinderknecht,[1] and P. V. Heuer[1]

[1]Laboratory for Laser Energetics, University of Rochester
[2]Department of Mechanical Engineering, University of Rochester
[3]Department of Physics and Astronomy, University of Rochester
[4]Imperial College London
[5]Sandia National Laboratories

To assess the quality of an inertial confinement fusion (ICF) experiment, various performance metrics based on the Lawson triple product[1–8] have been devised. These performance metrics must exceed a critical number to provide net energy gain. In direct-drive ICF implosions at the Omega Laser Facility,[9] the performance metric of interest is the so-called no-alpha normalized Lawson parameter χ

$$\chi = \rho R^{0.6} \left(0.12 \frac{Y_{16}}{M}\right)^{0.34}. \tag{1}$$

In an experiment, the areal density and yield can be diagnosed directly, while the stagnated DT mass can be estimated from simulations or from experimental data to infer χ. When χ is close to unity, alpha heating dominates the energetics of a hot spot, leading to ignition, which is a prerequisite for high-gain implosions. Due to the strong dependence of χ on the ρR, an accurate diagnosis is of critical importance. On OMEGA, an approach that synthesizes experiments and simulations[10–12] to create predictive models has led to dramatic increases in experimental performance, primarily through increases in neutron yield. References 10–12 present highly accurate predictive models for the neutron yield, but do not address the ρR—primarily because these models are not sufficiently accurate to drive experimental design. Achieving a comparable quality of predictive capability for ρR as exists for the yield is a necessary prerequisite for the predictive-model–driven campaign on OMEGA to optimize ρR since the effective "step-size" of an iterative scheme to improve the ρR is roughly bounded below by the prediction uncertainty.

One reason for the lack of predictive capability for ρR is that it is an inherently 3-D measurement with different diagnostics integrating over varying regions of the sphere relative to a fixed line of sight. A predictive model for the 1-D–equivalent ρR, which is what we are attempting to optimize in experiments, will have an uncertainty that is at least as large as this limited coverage error, which in turn sets the minimum step-size of the iterative scheme to improve the ρR in experiments.

To generate physically reasonable 3-D configurations for use in *IRIS*, the 3-D radiation-hydrodynamic simulation *ASTER*[13] is used. Three configurations are considered. In the first, the effect of illumination asymmetry arising from the beam geometry is considered. In the second and third configurations, the illumination resulting from a fixed beam size of $R_b = 330\ \mu$m is modulated with varying $\ell = 1$, $m = 0$ and $\ell = 2$, $m = 0$ perturbations, respectively, both aligned along the $+z$ axis. The detectors used are specified in Table I, and the detector permutations are specified in Table II. The MRS virtual detector simulates the action of the magnetic recoil spectrometer,[14] while the P7/H10 BS virtual detectors simulate the action of the neutron-time-of-flight (nTOF) backscatter measurement.[15] The P7/H10 FW virtual detectors simulate the action of a hypothetical forward scatter measurement

Table I: Detector configurations used in this work. See Table II for the permutations used. The P7 and H10 nTOF detectors are located at the center of P7 and H7 in the OMEGA target chamber, respectively. At the present time, the nTOF's are only capable of backscatter (BS) measurements. The forward scatter (FW) measurement on the nTOF's is under investigation.

Detector	θ_{det} (rad)	ϕ_{det} (rad)
P7 FW	2.03	2.83
P7 BS	2.03	2.83
H10 FW	1.35	2.83
H10 BS	1.35	5.27

Table II: Detector perumutations that are considered in this work. Note that the MRS + P7BS permutation is the one that is currently used in OMEGA experiments. Due to the unique details of each detector and experiment, it is possible that some measurements may be compromised on certain experiments.

Configuration	P7 FW	P7 BS	H10 FW	H10 BS	MRS FW
MRS Only					
MRS + P7BS					
MRS + H10BS					x
MRS + P7/H10BS		x			x
MRS + P7/H10BS + P7FW		x		x	x
MRS + P7/H10BS + H10FW	x	x		x	x
All	x	x	x	x	x

from the nTOF's that are under investigation on OMEGA. Note that the "MRS + P7BS" permutation represents the currently used permutation on OMEGA to assess the 1-D–equivalent ρR. For each simulation, each permutation of detectors is evaluated for each pair of (θ', ϕ'). The 1-D–equivalent ρR [that is, the areal density of a perturbed implosion that is appropriate to use in Eq. (1)], $\langle \rho R \rangle$, is calculated by a harmonic average over the observed ρL by virtual detectors that are distributed uniformly over the sphere, where the ρL of a particular virtual detector is the neutron-averaged path length integral of the density for all primary (i.e., not scattered) virtual particles binned in that virtual detector and is the best estimate of the "real" areal density that would be seen by that detector.

First, consider the highest ℓ-mode simulation case of the beam mode. At stagnation, the shell can be moderately to severely perturbed due to the driven mode.[12] However, ρR is inferred in experiments from integrals over the neutron spectrum, which corresponds (assuming a point source) to sampling over conical sections of the shell. Combined with the distributed source of a real hot spot, the inferred ρR from either the backscatter or forward-scatter measurement is found to be uniform over the sphere (although it may still be degraded with respect to 1-D), as seen in Fig. 1.

Next, consider the effect of the $\ell = 1$ mode. The strength of the mode is parametrized by the effective ion-temperature asymmetry $R_T = T_{\text{max}}/T_{\text{min}}$ it generates, and bin configurations belonging to similar R_T together to visualize the results. It is found that as the number of detectors used to infer an average ρR increases, the error in that inference decreases, although some detectors are more valuable than others (e.g., P10 backscatter is more valuable than P7 backscatter), as visualized in Fig. 2. This is due to the fixed positions of the diagnostics with respect to each other. With sufficient detectors, the error due to the mode 1 for high-performance–relevant implosions (i.e., $R_T \rightarrow 1$) approaches the acceptable limit of 5%.

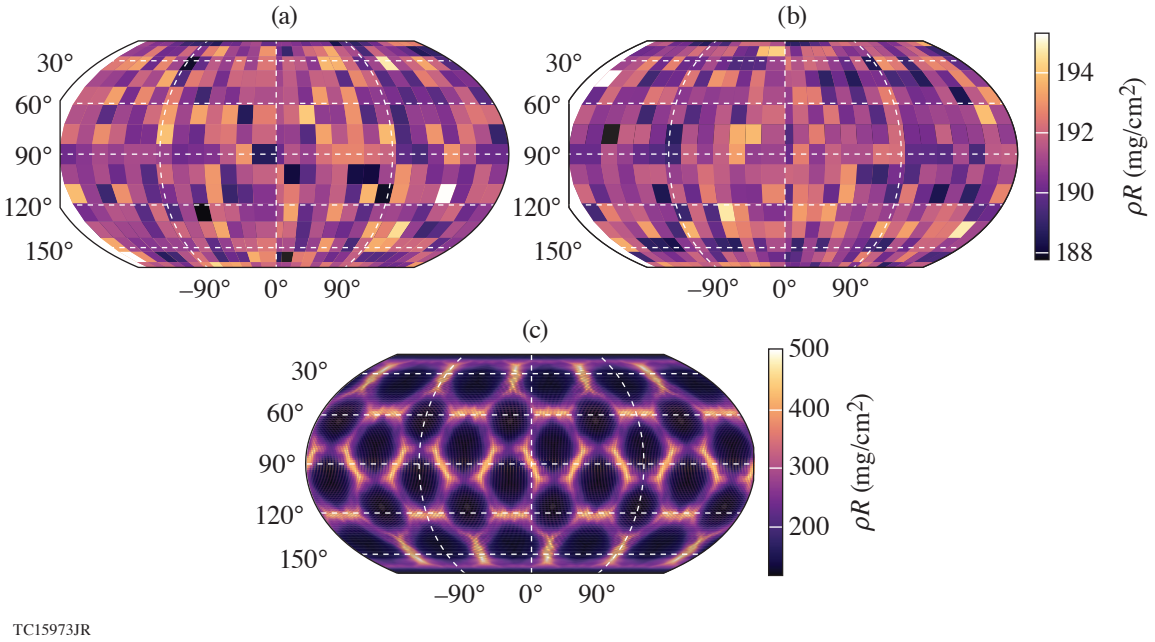

Figure 1
A projection of (a) the inferred ρR from the backscatter edge, (b) the inferred ρR from the forward-scatter edge for a simulation, and (c) $\int \rho \mathrm{d}r$ at bang time for a simulation with a target of radius 490 μm and a laser beam with radius 330 μm. Despite a rather large perturbation being driven, the effects of distributed source and integration over the edge result in no observable structured variation.

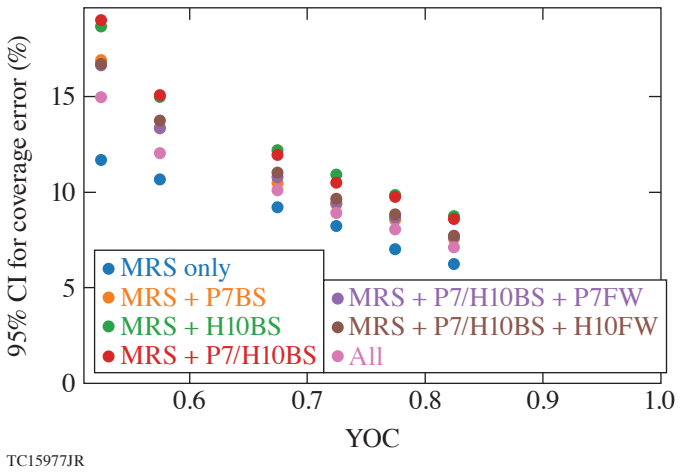

Figure 2
The 2σ upper bound on the coverage error for each detector permutation for simulations with similar yield over clean (YOC), over a range of YOC's. Unlike with the $\ell = 1$ case, there is no observable parameterizing the degradation due to $\ell = 2$, and so the YOC is used directly. Unlike the $\ell = 1$ case, adding any one backscatter detector increases the error rather than decreasing it. Although the addition of the forward-scatter measurements on the nTOF's does decrease the error relative in the case where only backscatter nTOF measurements are considered, they nevertheless are not reduced below the level when only the MRS is considered. Since this is a result of the relative orientations of the nTOF and MRS detectors on OMEGA, this is a result specific to the OMEGA setup, and not a general observation. CI: confidence interval.

In the $\ell = 2$ mode case, the strength of the mode is parametrized by its yield degradation YOC = $Y_{3\text{-D}}/Y_{1\text{-D}}$, and bin the various configurations accordingly, as before. The results are visualized in Fig. 3. First, using only the MRS forward-scatter measurement results in a lower error than combining the MRS with any backscatter measurement. This counterintuitive result can be understood when the relative orientations of various integration regions are considered. In the $\ell = 1$ case considered above, the orientations meant that the H10 backscatter measurement was strongly anticorrelated with the MRS (since the ρR varied with an $\ell = 1$ pattern), while the P7 backscatter measurement was only weakly correlated with the MRS. Since the $\langle \rho R \rangle$ lies in between the maxima and minima, an average (by whatever mechanism) of measurements best reproduces the $\langle \rho R \rangle$ if some measurements are greater than $\langle \rho R \rangle$, and some are less. In the $\ell = 2$ case, H10 and P7 backscatter measurements are, due to their specific orientations on the

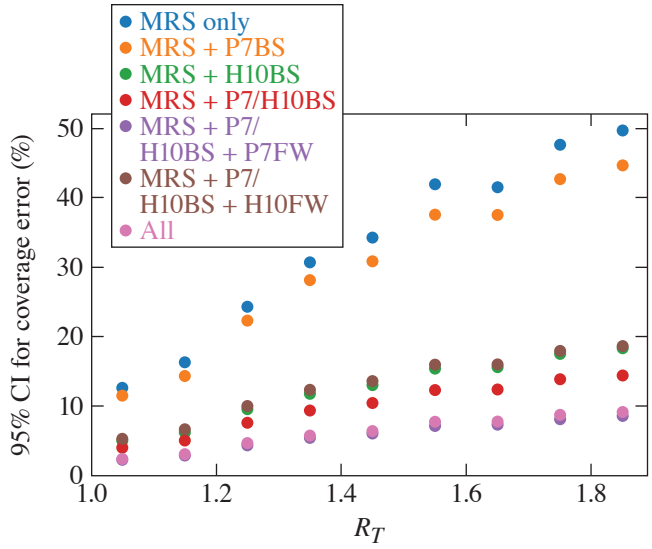

Figure 3
The 2σ upper bound on the coverage error for each detector permutation for all simulations with similar R_T over a range of R_T. First, note that having only the MRS (blue circles) has an extremely high error for even small values of R_T. Adding the P7 nTOF (orange circles) is not as valuable as adding the H10 nTOF (green circles) since the P7 backscatter and MRS forward-scatter regions are nearer to each other than the H10 backscatter and MRS forward scatter, and vice versa for the hypothetical P7 and H10 forward-scatter measurement. Nevertheless, adding all five detector configurations significantly reduces error from the currently used detector configuration.

OMEGA system, well correlated with the MRS (H10 more so than P7). In addition, the backscatter measurements sample a much smaller region of the shell than the forward scatter and, thus, have a higher probability of measuring an extremely different ρR from the MRS (again, H10 more than P7). Therefore, when including them in an average, it is possible to move the average further away from the $\langle \rho R \rangle$, and thereby increase the composite error. From there, including additional forward-scatter measurements either from P7 or H10 detectors reduces the error since a larger region of the shell is sampled. However, it is insufficient to correct for the bias induced by the backscatter measurement.

Finally, having established a measure of the likely values of how the measured ρR deviates from $\langle \rho R \rangle$ that can be expected under reasonable conditions, one considers whether it is possible to recover $\langle \rho R \rangle$, even if only in restricted cases. Here, the only case considered will be where the $\ell = 1$ mode dominates. The reason for choosing only this case is that the $\ell = 1$ case is the only one where the yield degradation due to the mode can be inferred on OMEGA at this time. Defining $R_{\rho R} = \rho R / \langle \rho R \rangle$ as the deviation of the measured ρR at some line of sight from the true 4π average $\langle \rho R \rangle$, it is noted that since the orientation of the mode with respect to each detector is known and deterministic, it is reasonable to presume that there ought to be a relationship between the $R_{\rho R}$ at the detector location and both a measure of the mode amplitude and the central angle y between the mode maximum and detector position. The mode amplitude can be parametrized either by the R_T, or by the ratio of the bulk flow to the implosion velocity $\tilde{v}$. A suggested ansatz for $R_{\rho R}$ is given by

$$R_{\rho R} \cdot (R_T, \psi) = R_T \alpha + A(R_T - 1)\beta \cos(\psi - \psi_0), \tag{2}$$

$$R_{\rho R} \cdot (\tilde{v}, \psi) = \exp(\alpha \tilde{v}) + A\tilde{v}\beta \cos(\psi - \psi_0), \tag{3}$$

where A, α, β, and ψ_0 are constants that differ for forward and backward scatter and will be determined by fitting to the data, and are summarized in Table III. A graphic presentation the quality of the fits is shown in Fig. 4 and indicates that Eqs. (2) and (3) accurately represent the modulation of ρR over the sphere.

Using the coefficients in Table I, it is also possible to calculate a final "prediction" of the ρR that would be used in experiments, assuming only the existing OMEGA detectors are used. This is shown in Fig. 5, where the arithmetic average of the detector predictions using the coefficients in Table III is shown for each simulation in the $\ell = 1$ dataset. If such a reconstruction could be performed on OMEGA, the uncertainty from the $\ell = 1$ modes can be made sufficiently low (<3.5%) for incremental iterative schemes to be successful on OMEGA. This suggests that generating such procedures for $\ell = 2$ should be a high priority since these modes are known to exist on OMEGA.

Table III: Fit parameters of Eqs. (2) and (3) for the forward and backscatter detectors.

Detector	α	β	ψ	A
Forward scatter (R_T)	0.34	0.62	–0.21	0.65
Backscatter (R_T)	0.46	0.64	–0.24	–0.78
Forward scatter ($\tilde{v}$)	0.32	1.09	–0.24	1.07
Backscatter ($\tilde{v}$)	0.44	1.05	0.37	–1.22

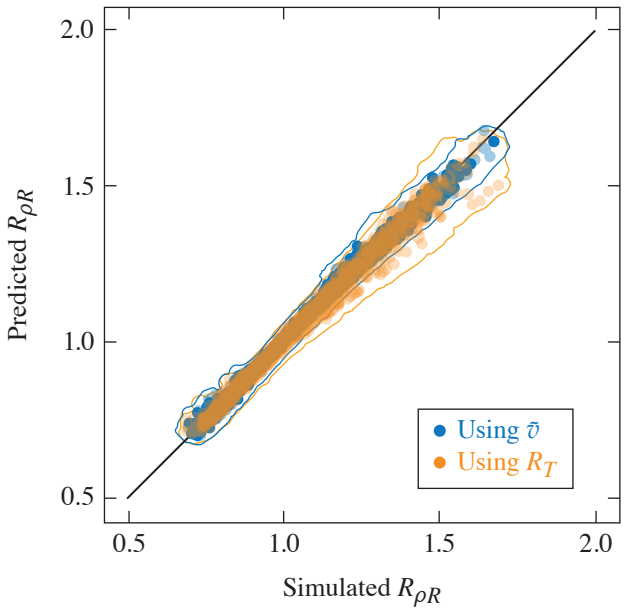

TC15980JR

Figure 4
The accuracy of Eq. (2) (orange circles) and Eq. (3) (blue circles) in reconstructing the $R_{\rho R}$ across the entire dataset for each detector separately, assuming the orientation and amplitude of the $\ell = 1$ mode is known. Due to the large number of points in the full dataset, 10% are selected randomly and plotted. The solid line shows the extent of the full dataset for both cases. The $R_{\rho R}$ calculated from the simulations is on the horizontal axis, while the prediction from Eqs. (2) and (3) is on the vertical axis.

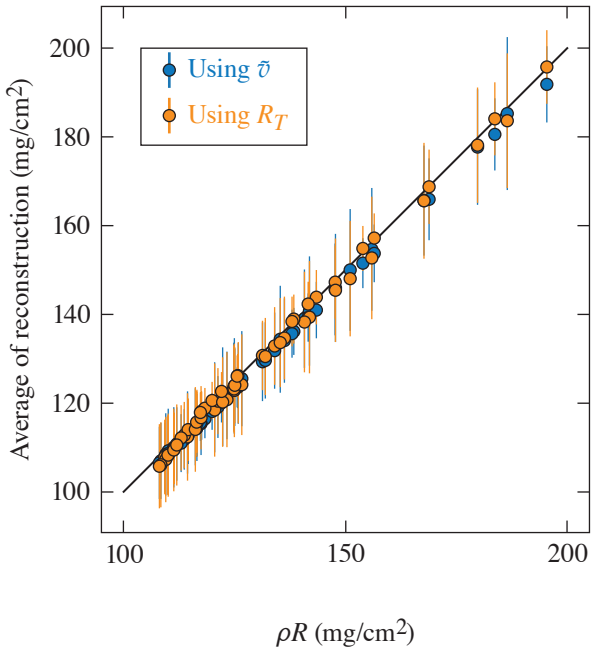

TC15981J1

Figure 5
The accuracy of harmonically averaging the reconstructed ρR inferred using Eq. (2) (blue circles) and Eq. (3) (orange circles) in predicting $\langle \rho R \rangle$ for all simulations in the dataset using only the MRS and P7/H10 backscatter detectors, assuming the orientation and amplitude of the $\ell = 1$ mode is known. Error bars represent the 2σ range of the reconstruction when varying mode orientations with respect to fixed detector locations. The method is clearly accurate across the full range of conditions, with an rms error of roughly 3.5% for both the R_T and ($\tilde{v}$) models.

Accurate measurements of the ρR are integral to an accurate understanding of the performance of cryogenic direct-drive ICF experiments on OMEGA. Quantifying and rectifying the errors that are incurred by incomplete coverage are a necessary step toward achieving the accuracy necessary to design OMEGA experiments that will scale to hydrodynamically equivalent ignition. Quantifying this error is also a step toward a quantification of the total uncertainty in the 1-D–equivalent ρR that arises as a combination of coverage and measurement uncertainty. Considered here are the effects of limited detector coverage over a range of core conditions using *ASTER* simulations, post-processed with *IRIS* with varying $\ell = 1$ and 2 modes, for a number of permutations of existing and hypothetical detectors used on OMEGA. The expected uncertainty is quantified due to the induced asymmetry over the credible range of expected perturbations on OMEGA. It is then found that the error due to limited detector coverage tends to decrease as additional detectors are added in the $\ell = 1$ case, but find that due to the specific detector geometry on OMEGA, the $\ell = 2$ coverage uncertainty can increase as additional backscatter measurements are made. The coverage error due to the $\ell = 1$ mode is robustly eliminated if the existing nTOF detectors on OMEGA were capable of forward-scattering measurements. After postulating that the orientation and yield degradation caused by a mode could be used to reconstruct the 1-D–equivalent ρR, it is shown that this is indeed possible in cases that are dominated by large $\ell = 1$ modes, and that the error in reconstructing the true 1-D–equivalent ρR can be made acceptably low with existing OMEGA diagnostics.

This material is based upon work supported by the Department of Energy National Nuclear Security Administration under Award Number DE-NA0003856, the University of Rochester, and the New York State Energy Research and Development Authority.

1. J. D. Lawson, Proc. Phys. Soc. Lond. B **70**, 6 (1957).
2. R. Betti and O. A. Hurricane, Nat. Phys. **12**, 435 (2016).
3. A. R. Christopherson *et al.*, Phys. Plasmas **25**, 012703 (2018).
4. R. Betti *et al.*, Phys. Plasmas **17**, 058102 (2010).
5. P. Y. Chang *et al.*, Phys. Rev. Lett. **104**, 135002 (2010).
6. B. K. Spears *et al.*, Phys. Plasmas **19**, 056316 (2012).
7. R. Betti *et al.*, Phys. Rev. Lett. **114**, 255003 (2015).
8. C. D. Zhou and R. Betti, Phys. Plasmas **14**, 072703 (2007).
9. T. R. Boehly *et al.*, Opt. Commun. **133**, 495 (1997).
10. V. Gopalaswamy *et al.*, Nature **565**, 581 (2019).
11. A. Lees *et al.*, Phys. Rev. Lett. **127**, 105001 (2021).
12. V. Gopalaswamy *et al.*, Phys. Plasmas **28**, 122705 (2021).
13. I. V. Igumenshchev *et al.*, Phys. Plasmas **23**, 052702 (2016).
14. M. Gatu Johnson *et al.*, Rev. Sci. Instrum. **89**, 10I129 (2018).
15. C. J. Forrest *et al.*, Rev. Sci. Instrum. **83**, 10D919 (2012).

Diagnosing Magnetic Fields in Cylindrical Implosions with Oblique Proton Radiography

P. V. Heuer,[1] L. S. Leal,[1] J. R. Davies,[1] E. C. Hansen,[1] D. H. Barnak,[1] J. L. Peebles,[1] F. García-Rubio,[1] B. Pollock,[2] J. Moody,[2] A. Birkel,[3] and F. H. Séguin[3]

[1]Laboratory for Laser Energetics, University of Rochester
[2]Lawrence Livermore National Laboratory
[3]Plasma Science and Fusion Center, Massachusetts Institute of Technology

Cylindrical implosions can be used to amplify an applied axial magnetic field via flux compression, which can be used to study fundamental plasma physics in high magnetic fields[1] and is a key feature of the magnetized liner inertial fusion (MagLIF) energy scheme.[2] Previous experiments on the OMEGA Laser System have measured flux compression in cylindrical implosions using proton radiography.[3,4] These experiments were followed by the development of the laser-driven MagLIF platform,[5] which uses smaller-diameter cylindrical targets with a higher maximum convergence that reach maximum convergence more quickly. However, attempts to use proton radiography with this platform to measure the compressed axial magnetic field in the same manner as previous work have so far been unsuccessful, primarily due to the impact on the radiographs of other strong electric and magnetic fields near the target. This summary analyzes the results of two recent experiments that attempted to measure the compressed magnetic field in a cylindrical implosion using the laser-driven MagLIF platform and demonstrate how the measurement is obscured by the presence of self-generated magnetic fields.

Two experiments were conducted [hereinafter Exp. 1 and Exp. 2 using the setup shown in Fig. 1(a)]. In both experiments, the target is a plastic (CH) cylinder imploded using 40 beams (1.5-ns square-shaped pulse, total energy 16 kJ) with an overlapped intensity of 10^{14} W/cm^2. In Exp. 1 the target is gas filled (14 atm H_2), which is preheated by an axial beam prior to compression as in MagLIF. In Exp. 2 the cylinder interior is initially vacuum but soon fills with CH plasma when the shock driven by the compression beam breaks out into the interior. A set of external coils driven by MIFEDS (magneto-inertial fusion electrical discharge system)[6] provides an axial magnetic field (9 T in Exp. 1, 5 T in Exp. 2). An unmagnetized shot (with the coils in place but not energized) was taken in Exp. 1. Experiment 2 was identical except for the thickness of the cylinder and the addition of a foil to block some of the protons [visible in Fig. 1(d)].

Proton radiography[7] is used to diagnose the fields. A D^{3}He backlighter capsule 11 mm from the cylinder is imploded by 16 beams to produce 3-MeV and 15-MeV protons. The protons pass through the target cylinder walls with negligible scattering (verified on the unmagnetized shot) but are deflected by electric and magnetic fields in the vicinity of the target. The protons are then recorded on two CR-39 plates (shielded by 7.5 μm of tantalum and separated by 200 μm of aluminum to differentiate between the two proton energies) at a distance of 270 mm. In both experiments, the timing of the proton source is chosen to match the peak convergence of the implosion (which is also the peak of neutron production, or "bang time") at $t = 1.5 \pm 0.1$ ns. Due to the target chamber geometry, in both experiments the proton radiography axis is tilted relative to the target normal by an angle θ_T, making this "oblique" proton radiography.

To directly compare simulations to experimental results, synthetic proton radiographs are generated using an open-source particle-tracing algorithm that was developed for the PlasmaPy project as part of this work.[8] Three-dimensional simulations of the experiment, including the coronal plasma produced by the compression beams, were performed using the multiphysics

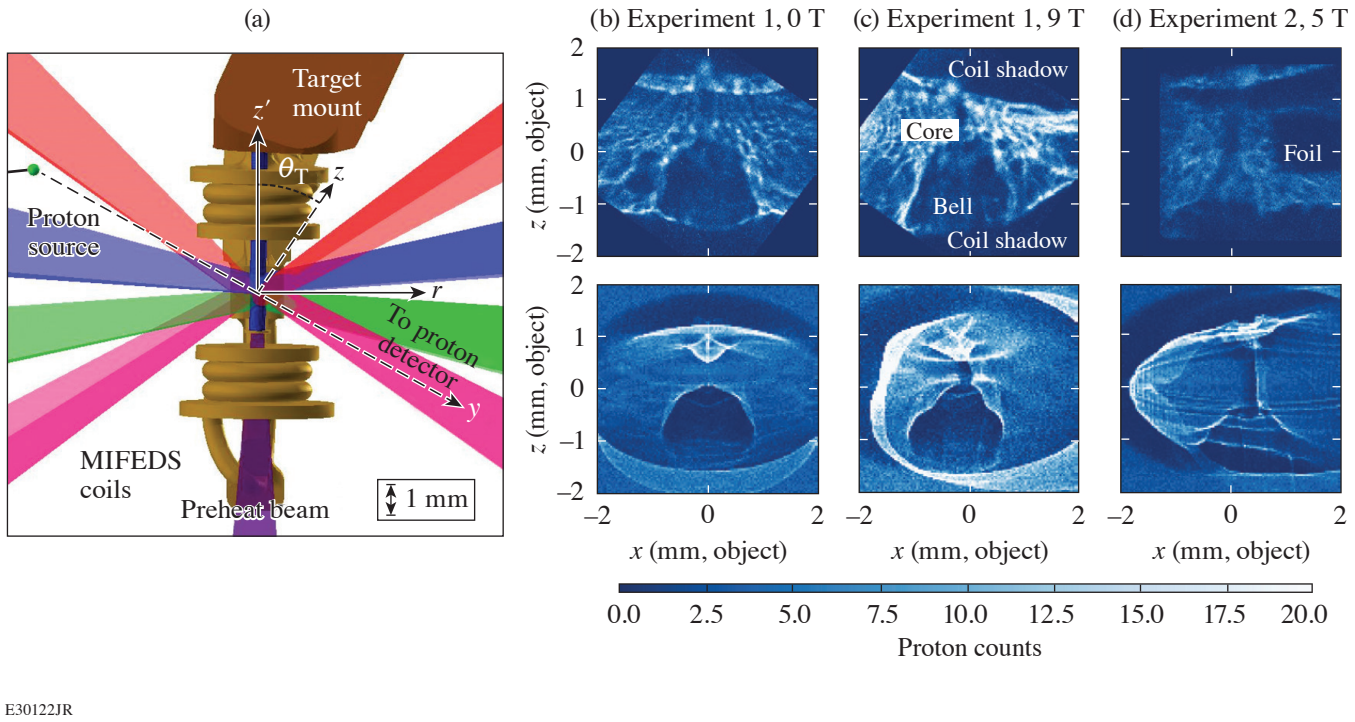

Figure 1
(a) A diagram of the setup for Exp. 1, with only a subset of the compression beams shown for clarity. (The setup for Exp. 2 is similar.) [(b)–(d)] Experimental proton radiographs (top row) for both experiments and the corresponding synthetic radiographs (bottom row) show good agreement.

radiation-hydrodynamic code *HYDRA*. A population of test protons was then traced through the simulated electric and magnetic fields and onto a detector to create synthetic radiographs. The resulting radiographs for Exp. 1 are shown in Figs. 1(b)–1(c) and Fig. 1(d) shows the radiograph for Exp. 2. All radiographs contain similar features. The "bell"-shaped feature is created by self-generated azimuthal magnetic fields in the coronal plasma produced by the drive beams, while the "core" feature visible on the magnetized radiographs is due to the compressed axial field. Small ripple features on the experimental data are not reproduced in the synthetic radiographs: this "small-scale structure" is likely due to kinetic effects such as instabilities or charge-separation fronts. Shadows are visible at the top and bottom of the experimental radiographs where protons are blocked by the MIFEDS coils.

Several approaches, including direct inversion algorithms, are applied to try and recover the line-integrated magnetic field from the experimental radiographs. However, while these techniques work reasonably well with the synthetic data, the loss of protons in the shadows of the MIFEDS fields and the presence of the small-scale structure prevent them from working with the experimental data. It is concluded that these experimental radiographs are consistent with the presence of a compressed axial field, but that a measurement of the compressed field is prevented by the self-generated azimuthal magnetic fields in the coronal plasma and the small-scale structure fields.

These results are compared to previous experiments on the OMEGA Laser System,[3,4] which successfully measured the compressed axial magnetic field in a similar cylindrical implosion. Comparing the design of this experiment to the current work provides guidance for the design of future work, suggesting that the radiography angle θ_T, target dimensions, laser pulse duration, and coil geometry are important parameters that determine the feasibility of this type of measurement. In many experiments, the ability to change these features is limited by other design considerations. However, future attempts to measure compressed axial magnetic fields in cylindrical implosions should include among these considerations the potential impact of self-generated fields on the measurement.

This material is based upon work supported by the Advanced Research Projects Agency-Energy (ARPA-E) under Award Number DE-AR0000568, the Department of Energy National Nuclear Security Administration under Award Numbers DE-NA0003856 and DE-SC0020431, the University of Rochester, and the New York State Energy Research and Development Authority.

1. C. A. Walsh *et al.*, Plasma Phys. Control. Fusion **64**, 025007 (2022).
2. S. A. Slutz *et al.*, Phys. Plasmas **17**, 056303 (2010).
3. O. V. Gotchev *et al.*, Phys. Rev. Lett. **103**, 215004 (2009).
4. J. P. Knauer *et al.*, Phys. Plasmas **17**, 056318 (2010).
5. J. R. Davies *et al.*, Phys. Plasmas **24**, 062701 (2017).
6. G. Fiksel *et al.*, Rev. Sci. Instrum. **86**, 016105 (2015).
7. N. L. Kugland *et al.*, Rev. Sci. Instrum. **83**, 101301 (2012).
8. PlasmaPy Community *et al.*, PlasmaPy (Version 0.8.1), Zenodo, Accessed 14 September 2022, https://doi.org/10.5281/zenodo.6774350.

The Effect of Laser Preheat in Magnetized Liner Inertial Fusion at the Omega Laser Facility

L. S. Leal,[1,2] A. V. Maximov,[1,3] E. C. Hansen,[1,2] J. R. Davies,[1] D. H. Barnak,[1] J. L. Peebles,[1] K. M. Woo,[1] P. V. Heuer,[1] A. B. Sefkow,[1,2,3] and R. Betti[1,2,3]

[1]Laboratory for Laser Energetics, University of Rochester
[2]Department of Physics and Astronomy, University of Rochester
[3]Department of Mechanical Engineering, University of Rochester

An important effect in magnetized transport is represented by the Nernst term in Ohm's law that advects magnetic fields down electron temperature gradients.[1–3] This term has been shown to be dominant over the fluid motion in plasmas below the critical density of the preheating laser. It is also possible that magnetic-flux transport in the hot spot is dominated by Nernst advection.[4] The preheat laser can also lead to material from the window or wall of the targets mixing with the fuel region.[5] This summary is focused on modeling the effect of preheat on the dynamics of the fuel in magnetic liner inertial fusion (MagLIF) experiments and the importance of certain terms in the magnetohydrodynamics model, specifically the Nernst effect, as well as the effect of wall material being mixed with the fuel within the capsule. Three-dimensional simulations are used to characterize the effects on yield and implosion characteristics when varying the preheat laser energy.

Three-dimensional radiation-hydrodynamic simulations show there is an optimal laser preheat energy for laser-driven MagLIF on OMEGA, with a 27-T initial magnetic field, resulting in a peak in neutron yield. A similar peak in neutron yield as a function of laser preheat energy was observed in experiments; however, the experimental yield and the optimal laser preheat energy were lower than predicted in simulations. By comparing simulations that do or do not include the Nernst effect, it was found that the Nernst effect is necessary to properly model how laser preheat affects the field dynamics in the fuel region of MagLIF. The drop from the peak in neutron yield with increasing laser preheat energy past the optimal value is larger with the Nernst effect. It is noted that with increasing preheat laser energy, there is less magnetic-field enhancement due to compression and the radial profile of the density becomes less dominated by edge effects.

A 2-D slice of the magnetic field was normalized to the initial seed magnetic field with and without Nernst effect at bang time where the fuel region is outlined. In the case without the Nernst effect, the magnetic field peaks at the radial edge of the fuel region in the center of the z axis. The magnetic field at the edges is convected with the blast wave during the preheat stage, remains at the edge throughout the implosion, and experiences flux compression. In Fig. 1(a) where the simulation includes the Nernst effect, flux compression occurs at the overdriven ends; however, the magnetic field at the center of the z axis has largely been advected out of the fuel region.

Simulations using a mix model show that including mix in implosions leads to yield degradation and can also shift the optimal laser preheat energy to a lower value. The use of premixed region limits the simulation's ability to exactly match the material penetrations occurring in experiments, but gives some insight to the effects of mix. Unlike MagLIF at Sandia National Laboratories, the primary-yield degradation mechanism from mix in MagLIF on OMEGA is not only from radiative losses (since neutron-averaged ion temperatures are not consistently lower between clean simulation and simulations with mix). The added mass from mix lowers the convergence ratios and the Hall parameter across the capsule fuel region, modifying plasma transport coefficients. Simulations also suggest that higher seed magnetic fields available from upcoming generations of MIFEDS (magneto-inertial fusion electrical discharge system) will further enhance yield in D–D cylindrical implosions. A future expanded study

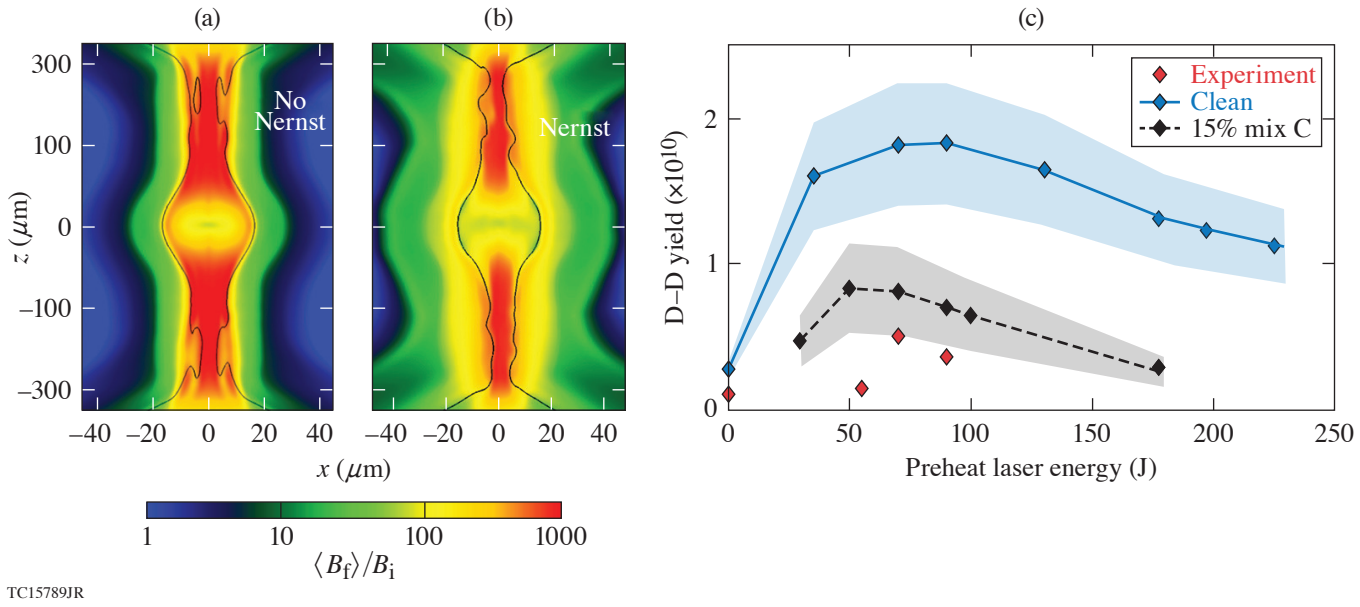

Figure 1
Two-dimensional slice of log scale magnetic-field enhancement (magnetic field over the initial seed field) at bang time for 90-J preheat laser energy and 27-T seed magnetic field from simulations (a) without the Nernst effect and (b) with the Nernst effect where the fuel region is outlined in black. (c) D–D neutron yield over varying preheat laser energies from experiments (red), clean simulations (blue), and simulations mixed with 15% C in the fuel region (black) with 27-T seed field including the Nernst effect.

of the mix effect will be needed to ascertain the degree to which mix products may penetrate the core, as well as its behavior at different preheat laser energies. Simulations can then attempt to model mix nonuniformly to study the impact on transport in the fuel region. As simulations with the mix model see a large drop in yield, they can lead to estimates on when yield degradation from increasing preheat laser energy could impact future experiments.

This material is based upon work supported by the Department of Energy National Nuclear Security Administration under Award Number DE-NA0003856, the University of Rochester, and the New York State Energy Research and Development Authority.

1. S. I. Braginskii, Sov. Phys. JETP **6**, 358 (1958).
2. E. M. Epperlein and M. G. Haines, Phys. Fluids **29**, 1029 (1986).
3. D. H. Froula *et al.*, Phys. Rev. Lett. **108**, 125003 (2012).
4. A. L. Velikovich, J. L. Giuliani, and S. T. Zalesak, Phys. Plasmas **26**, 112702 (2019).
5. A. J. Harvey-Thompson *et al.*, Phys. Plasmas **25**, 112705 (2018).

Analysis of Core Asymmetries in Inertial Confinement Fusion Implosions Using Three-Dimensional Hot-Spot Reconstruction

K. M. Woo,[1] R. Betti,[1] C. A. Thomas,[1] C. Stoeckl,[1] K. Churnetski,[1] C. J. Forrest,[1] Z. L. Mohamed,[1] B. Zirps,[2] S. P. Regan,[1] T. J. B. Collins,[1] W. Theobald,[1] R. C. Shah,[1] O. M. Mannion,[1] D. Patel,[1] D. Cao,[1] J. P. Knauer,[1] V. Yu. Glebov,[1] V. N. Goncharov,[1] P. B. Radha,[1] H. G. Rinderknecht,[1] R. Epstein,[1] V. Gopalaswamy,[1] F. J. Marshall,[1] S. T. Ivancic,[1] and E. M. Campbell[1]

[1]Laboratory for Laser Energetics, University of Rochester
[2]Department of Mechanical Engineering, University of Rochester

Three-dimensional effects play a crucial role during the hot-spot formation in inertial confinement fusion implosions. To characterize effects of low modes on hot-spot formations, a data-analysis technique for 3-D hot-spot reconstruction from experimental observables was developed. In summary, the effective flow direction, governed by the maximum eigenvalue in the velocity variance of apparent ion temperatures, was found to agree with the measured hot-spot flows for implosions dominated by mode $\ell = 1$. Asymmetries in areal-density (ρR) measurements were found to be characterized by a unique cosine variation along the hot-spot flow axis. A 3-D hot-spot x-ray emission tomography method was developed to reconstruct the 3-D hot-spot plasma emissivity using a generalized spherical-harmonic Gaussian function. The mapping between the projections from the 3-D hot-spot emission model and the measured x-ray images along multiple views is obtained by a gradient descent optimization algorithm.

Spherically symmetric flows,[1,2] turbulences,[3] and 3-D flows[4] are sources of velocity variances in neutron velocity spectra. Non-stagnating hot-spot flows kinematically boost the velocity of neutrons, produced from deuterium (D) and tritium (T) nuclear fusion reactions. The hot-spot residual fluid motion modifies the neutron velocity distribution so that the width of a neutron velocity spectrum is broadened according to a unique function of the velocity variance $\sigma = \mathrm{var}\left[v_{\mathrm{flow}} \cdot d_{\mathrm{LOS}}\right]$, where v_{flow} is the hot-spot flow velocity measured in the laboratory frame and d_{LOS} is the line of sight (LOS) unit vector, pointing from the target chamber center to the position of a detector. The velocity variance is a measurement for the hot-spot flow residual kinetic energy (RKE) since it measures the square of hot-spot flow velocity fluctuations. It contains six independent components $\sigma_{ij} = \left\langle\left(v_i - \bar{v}_i\right)\cdot\left(v_j - \bar{v}_j\right)\right\rangle$, including three directional variances with $i = j$ and three covariances with $i \neq j$. Indices i and j go from 1 to 3, representing x, y, and z Cartesian coordinates, respectively. Since covariances are unchanged upon exchanging i and j indices, the velocity variance matrix is Hermitian. This implies that σ is diagonalizable with real eigenvalues λ_i, which are the components of the hot-spot RKE along three orthonormal eigenvector directions e_i. This behavior is consistent with the fact that the trace of σ, the total hot-spot residual kinetic energy, is invariant under the special orthogonal SO(3) transformation in the 3-D Euclidean space. Hence, an apparent ion temperature measured at a given LOS is related to the hot-spot RKE's along the three eigenvector directions through the SO(3) transformation

$$T_{\mathrm{LOS}} = T_{\mathrm{thermal}} + M_{\mathrm{DT}} \sum_{i=1}^{3} \lambda_i \left\langle d_{\mathrm{LOS}} \middle| e_i \right\rangle^2, \tag{1}$$

where T_{thermal} is the ion thermal temperature in the center of mass frame of D–T nuclear reactions, and the bracket notation represents the inner product between the LOS unit vector and the ith eigenvector. Equation (1) is a generalized result to explain variations in apparent ion temperatures nonrelativistically. When implosions are dominated by mode 1, Eq. (1) implies a cosine-square variation along the eigenvector direction with the maximum eigenvalue, i.e., the hot-spot RKE of the jet. The extrapolation

for the cosine-square variation in OMEGA ion-temperature measurements using Eq. (1) is illustrated in Fig. 1(a). When implosions contain mode 2, the difference between eigenvalues parallel $\lambda_{\parallel}$ and perpendicular $\lambda_{\perp}$ to the rotational axis implies a nonvanishing ion-temperature asymmetry. Even the measured hot-spot flow velocity is zero since symmetric mode-2 hot-spot flows do not change the first moment of neutron velocity spectra. This phenomenon is illustrated by Fig. 1(b). A good agreement between the trend of experimental data and *DEC3D* simulations with a uniform 2% initial velocity perturbation of mode 2 on varying mode-1 perturbations is obtained. A semi-analytic model is derived to explain the mode-1 ρR degradation. Both 4π averaged and variations in ρR are found to be a function of the ion-temperature ratio $R_T = T_{\max}/T_{\min}$,

$$\frac{(\rho R)\mathrm{LOS}}{(\rho R)1\text{-D}} = R_T^{\alpha} + \sqrt{R_T^{2\alpha} - R_T^{2\beta}}\,\cos\theta_{\mathrm{LOS\text{-}flow}}\,, \tag{2}$$

where $\alpha = -0.3$ and $\beta = -0.47$ are parameters obtained from *DEC3D* mode-1 simulations, and $\theta_{\mathrm{LOS-flow}}$ is the inclination angle between the LOS and the measured hot-spot flow vectors. The extrapolation for the mode-1 angular-dependence in areal density measurements is illustrated by Fig. 1(c). The 3-D kernel as stated by Eq. (2) is shown to accurately fit the H10 ρR measurements. A 3-D x-ray emission tomography method was devised to reconstruct arbitrary hot-spot shapes using a generalized spherical harmonic Gaussian function,

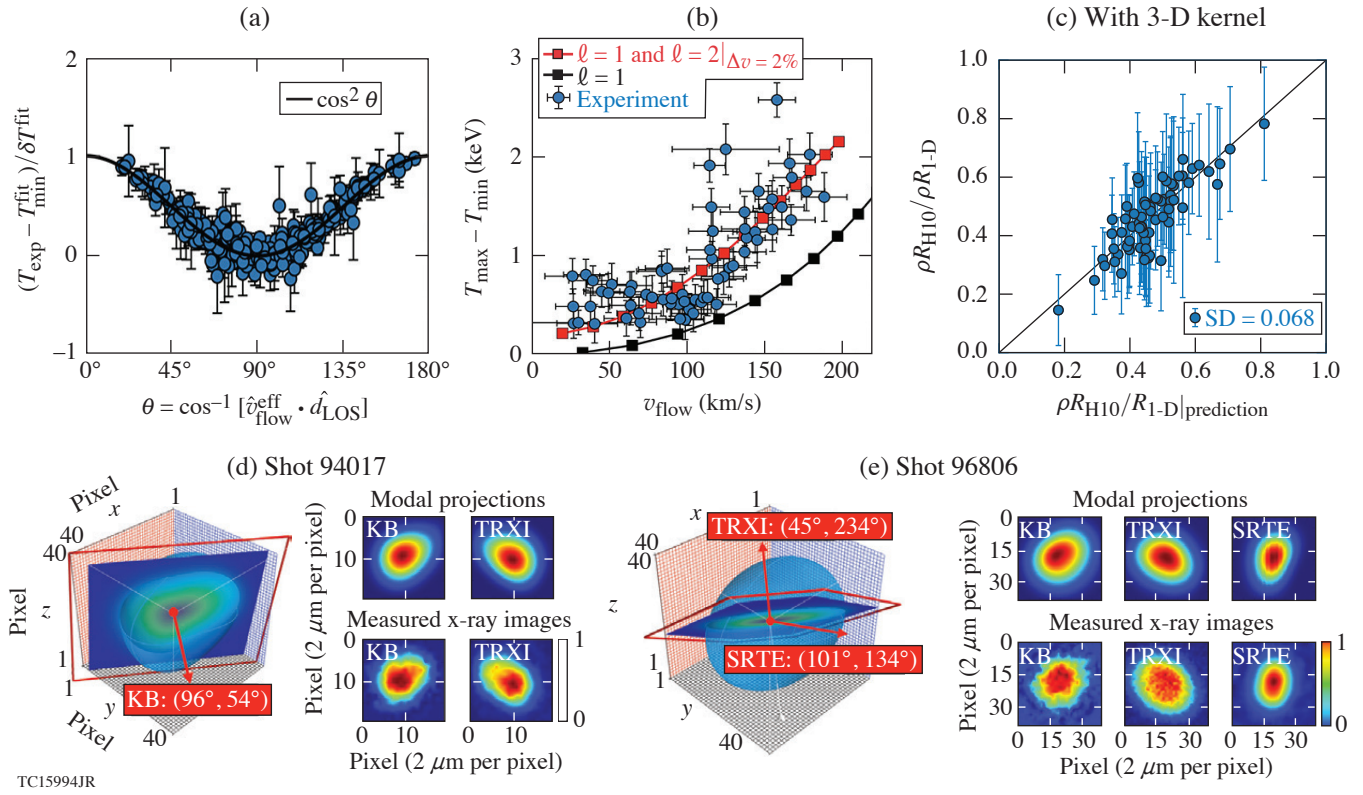

Figure 1
Analysis of core asymmetries in OMEGA implosion experiments. (a) The extrapolation for the cosine-square variation in ion-temperature measurements using Eq. (1). (b) The reconstruction for the trend of T_i and flow relation using *DEC3D* simulations. (c) The extrapolation for the mode-1 angular-dependence in areal density measurements using the 3-D kernel in Eq. (2). [(d),(e)] Three-dimensional hot-spot reconstructions for shots 94017 and 96806 using the generalized spherical-harmonic Gaussian model in Eq. (3). SD: standard deviation; KB: Kirkpatrick–Baez; TRXI: time-resolved x-ray imager; SRTE: spatially resolved x-ray imager.

$$\ln \varepsilon_{\nu} = \sum_{n=0}^{\infty} \sigma_n R^n \left[1 + \sum_{\ell=1}^{\infty} \sum_{m=-\ell}^{\ell} \sum_{k=0}^{\infty} A_{\ell mk} R^k Y_{\ell m}(\theta, \phi) \right]^n . \tag{3}$$

Expansion coefficients in Eq. (3) are determined by minimizing the root-mean-square deviations between modal projections and measured x-ray images measured at multiple views using the gradient descent optimization algorithm. Three-dimensional hot-spot reconstructions are illustrated in Fig. 1(d) and 1(e). The mode-1 skew signature and the mode-2 ellipticity are well reconstructed for shots 94017 and 96806, respectively.

This material is based upon work supported by the Department of Energy National Nuclear Security Administration under Award No. DE-NA0003856, the University of Rochester, and the New York State Energy Research and Development Authority and DOE grant DE-SC0022132.

1. R. E. Chrien, K. A. Klare and T. J. Murphy Rev. Sci. Instrum. **68**, 607 (1997).
2. T. J. Murphy, R. E. Chrien and K. A. Klare Rev. Sci. Instrum. **68**, 614 (1997).
3. T. J. Murphy, Phys. Plasmas **21**, 072701 (2014).
4. K. M. Woo *et al.*, Phys. Plasmas **25**, 102710 (2018).

Evaluation of Direct Inversion of Proton Radiographs in the Context of Cylindrical Implosions

J. R. Davies and P. V. Heuer

Laboratory for Laser Energetics, University of Rochester

Proton radiography is frequently used on OMEGA and OMEGA EP to infer electric and magnetic fields. If proton energy loss and scattering are negligible, proton deflection at the detector will be determined by the path-integrated transverse Lorentz force experienced by the protons. The most common technique used to infer fields from intensity modulations on the detector has been proton tracing in given fields, either assumed or obtained from simulations. Recently, a number of authors have used direct inversion to infer the fields,[1–6] and many of these direct inversion routines are publicly available on GitHub.[1–5] Direct inversion provides a solution independent of biases; particle tracing in specified forces is subject to user biases, and tracing in forces determined from simulations is limited by knowledge of the experimental conditions to be simulated and the physics included in the simulations. Publicly available direct inversion routines were applied to proton radiography data from cylindrical implosion experiments on OMEGA. As a first step, a series of test problems is generated using proton tracing to evaluate the routines.[7] These test problems are publicly available[8] as hdf5 files in pradformat.[9] The test results are summarized here.

Direct inversion determines deflections at the detector that map the source intensity (I_0) to the measured intensity (I). There is no unique solution to this problem, as demonstrated by the trivial case of simply swapping two particles on the detector. There is a unique solution, however, that minimizes total deflection and does not allow particles to be moved over one another. If proton trajectories to the detector do not cross, direct inversion will give the solution. If proton trajectories do cross, direct inversion will give one out of an infinite family of solutions, which is still useful information. In mathematics, direct inversion is known as the optimal transport problem, first described in a paper by Monge published in 1781 (Ref. 10), which derives what is now known as the Monge–Ampère equation. All but one of the publicly available direct inversion routines solve the Monge–Ampère equation.[1–4] The other routine[5] uses iterative methods to construct power diagrams (weighted Voronoi diagrams) of the source and measured intensities with equal flux in each cell, determining the deflections from the movement of cell centroids. Direct inversion can be applied to radiography with any charged particle, and to shadowgraphy where photons are deflected by gradients in refractive index.[5] In order to relate the deflections obtained at the detector to the forces in the object, one must assume a small angle deflection in the object ($\ll$1 rad or 57.3°) so that the deflections are proportional to the line-integrated force along the original trajectory. In practice, this is not a major restriction since the proton radiography and shadowgraphy setups used on OMEGA and OMEGA EP subtend a small angle at the target. If there are regions where large angle deflections occur, information on the forces in these regions will be lost.

Test radiographs or, equivalently, shadowgraphs, were generated by particle tracing through purely radial force profiles in cylinders and spheres for a range of force amplitudes with uniform source intensities. In cylinders a Gaussian potential [$F_r \propto r \exp(-r^2/R_2)$], a linear profile ($F_r \propto r$ for $r \leq R$)], and a top-hat profile (F_r = constant for $r \leq R$) were used. The linear profile was chosen to represent the electric field in an isothermal, cylindrical expansion,[11] ignoring the rapidly decaying field in the electron sheath beyond the ion front. The top-hat profile was chosen to represent the axial magnetic field in a cylindrical implosion, which is discontinuous at the inner surface of the shell. For spheres, a Gaussian potential was used. Force is expressed as a dimensionless parameter

$$\mu = \frac{2LF}{Mpv},$$

where L is object-to-detector distance, M is magnification, F is Lorentz force, p is particle momentum, and v is particle velocity, or

$$\mu = \frac{L}{\mathrm{M}} \frac{\mathrm{d}\left(n_\mathrm{e}/n_\mathrm{c}\right)/\mathrm{d}r}{\sqrt{1-n_\mathrm{e}/n_\mathrm{c}}}$$

for shadowgraphy, where n_e is electron density and n_c is the critical density of the probe. All distances are expressed in terms of the object size R. Trajectories cross in all cases for the linear and top-hat profiles and for both cylindrical and spherical Gaussian potentials when $\mu_{\max} \geq 1.08$ or $\mu_{\max} \leq -0.484$, negative values indicating a focusing force.

Five direct inversion routines were found on GitHub.[1–5] Two of the routines, both Monge–Ampère solvers, did not run.[1,2] The other two Monge–Ampère solvers were found to be essentially identical, which is not surprising considering they are implementations of the same algorithm by the same author.[3,4] Therefore, one Monge-Ampère routine and one power-diagram routine[5] was available to evaluate. The Monge–Ampère routine could not solve the cylindrical problems because it uses fixed deflection potential boundary conditions, which would also cause issues with any problem that has modulations near the boundary. The correct boundary conditions to obtain a minimum deflection from the Monge–Ampère equation are to set the deflections across the boundaries to zero.[2] The Monge-Ampère routine accurately inverted the spherical Gaussian tests when trajectories did not cross and did so roughly 1000× faster than the power-diagram routine, but failed when trajectories crossed. The failure was obvious from the poor reproduction of the measured intensity. The failure appears to be caused by the adaptive time step, which rapidly falls to the specified minimum value for tests where deflected trajectories cross. The power-diagram routine successfully inverted all but two of the test problems. The power diagram failed for the top-hat profile with $\mu_{\max} = 2$ and a smaller bin width (0.015R) than the final value we settled on (0.025R); however, for the coarser bin width an adequate solution was obtained. The power-diagram routine failed for a spherical Gaussian with $\mu_{\max} = -0.5$ and the issue was not resolved by coarser binning, the bin width of 0.052R already being too coarse to resolve the sharp peak. The power-diagram routine moves the sites closest to the corners into the corners in order to interpolate the deflections to all points on the original grid, which, for this strongly focusing test, leads to significant distortion of the entire region. Examples of the line-integrated forces obtained by the power-diagram routine for the cylindrical tests are given in Fig. 1. In all cases the measured intensity was accurately reproduced. The inversion underestimates the original line-integrated forces when trajectories cross because it gives a minimum deflection solution. It should be remembered that when trajectories cross, there exists an infinite family of solutions for the line-integrated force. As a result of these tests, only the power-diagram routine was used to analyze the proton radiographs of cylindrical implosions.[12]

This material is based upon work supported by the U. S. Department of Energy's Advanced Research Projects Agency-Energy under Award Number DE-AR0000568 and National Nuclear Security Administration under Award Number DE-NA0003856, the University of Rochester, and the New York State Energy Research and Development Authority.

1. C. Graziani *et al.*, Rev. Sci. Instrum. **88**, 123507 (2017).
2. A. F. A. Bott *et al.*, J. Plasma Phys. **83**, 905830614 (2017); PROBLEM Solver (PROton-imaged B-field nonLinear Extraction Module), Accessed 12 July 2021, https://github.com/flash-center/PROBLEM.
3. M. F. Kasim, Invert Shadowgraphy and Proton Radiography, Accessed 8 July 2021, https://github.com/mfkasim1/invert-shadowgraphy.
4. M. F. Kasim *et al.*, Phys. Rev. E **100**, 033208 (2019); M. F. Kasim, PRNS (Proton Radiography with No Source), Accessed 12 July 2021, https://github.com/OxfordHED/proton-radiography-no-source.
5. M. F. Kasim *et al.*, Phys. Rev. E **95**, 023306 (2017); M. F. Kasim, Invert Shadowgraphy and Proton Radiography, Accessed 8 July 2021, https://github.com/mfkasim1/invert-shadowgraphy.
6. N. F. Y. Chen *et al.*, Phys. Rev. E **95**, 043305 (2017).
7. J. R. Davies and P. V. Heuer, "Evaluation of Direct Inversion of Proton Radiographs in the Context of Cylindrical Implosions," Physics Archive: https://doi.org/10.48550/arXiv.2203.00495 (2022).
8. J. Davies and P. Heuer, Synthetic Proton Radiographs for Testing Direct Inversion Algorithms, Zenodo, Accessed 3 August 2022, https://doi.org/10.5281/zenodo.6632986.

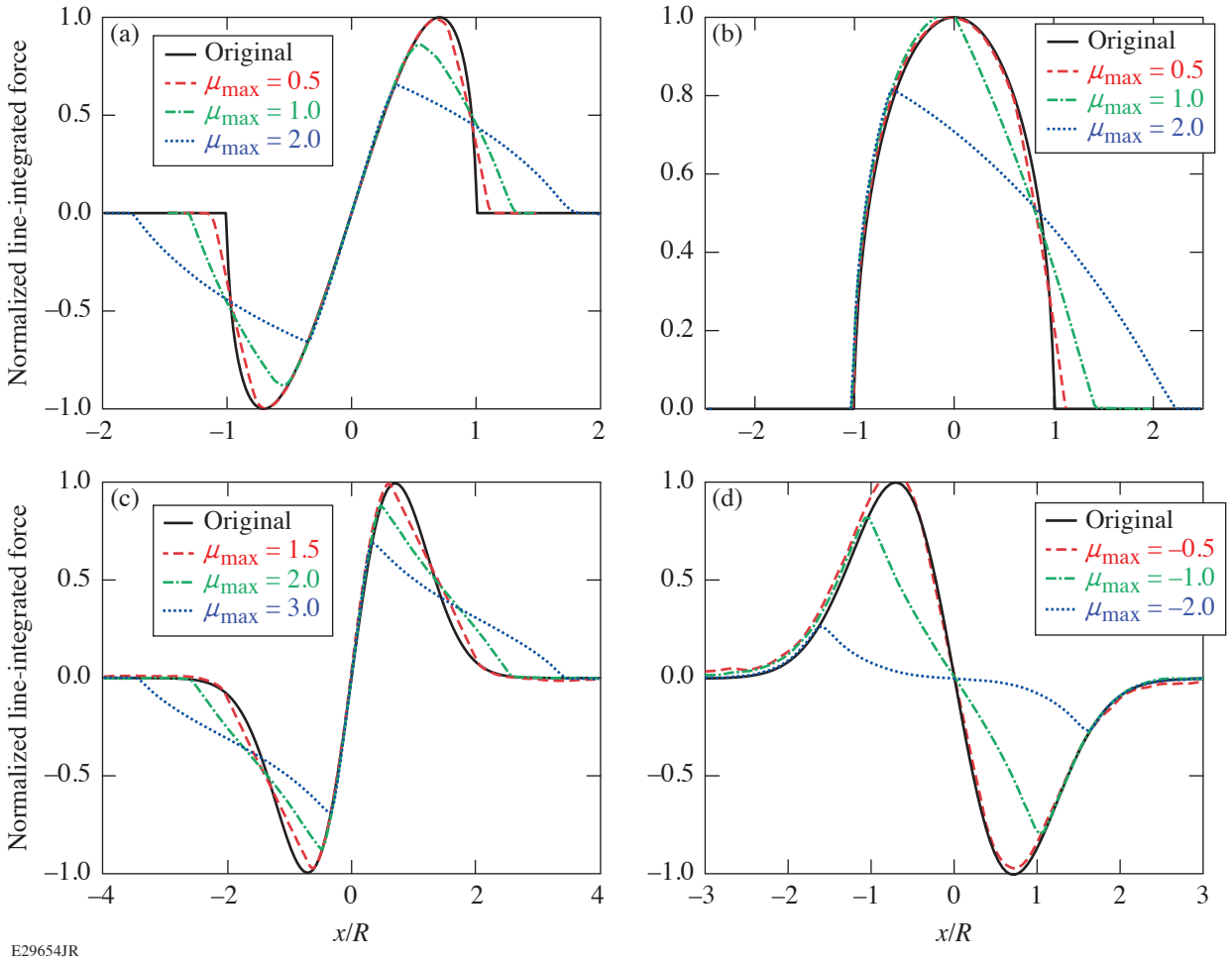

Figure 1

Line-integrated forces from the power-diagram routine for cylindrical test problems from (a) the linear profile, (b) the top-hat profile, and [(c),(d)] the Gaussian potential, normalized so that the maximum of the original is 1.

9. Pradformat (Proton Radiography File Format Tools), Accessed 12 July 2021, https://github.com/phyzicist/pradformat.
10. G. Monge, Mém. de l'Ac. R. des. Sc. An., 666 (1781).
11. M. Murakami and M. M. Basko, Phys. Plasmas **13**, 012105 (2006).
12. P. V. Heuer *et al.*, Phys. Plasmas **29**, 072708 (2022).

Particle-in-Cell Modeling of Plasma-Jet Merging in the Large-Hall-Parameter Regime

H. Wen,[1] C. Ren,[2,3] E. C. Hansen,[2] D. Michta,[2] Y. Zhang,[3] S. Langendorf,[4] and P. Tzeferacos[1,2]

[1]Laboratory for Laser Energetics, University of Rochester
[2]Department of Mechanical Engineering, University of Rochester
[3]Department of Physics and Astronomy, University of Rochester
[4]Physics Division, Los Alamos National Laboratory

Plasma-jet–driven magneto-inertial fusion (PJMIF) offers a novel "reactor-friendly" alternative approach to fusion energy that assembles targets by launching magnetized plasma jets from plasma guns at large standoff distances.[1] Fusion reactions take place in an all-gas/plasma architecture, avoiding repetitive hardware destruction. Furthermore, magnetic fields in the assembled target reduce thermal conduction and facilitate ignition. Most of the previous studies on this concept focused on the hydrodynamics,[2–5] while possible kinetic physics,[6] especially in target formation and compression, have not been well explored. Presented here are particle-in-cell (PIC) simulations with the code *OSIRIS* of two colliding counter-propagating magnetized jets to study the kinetic physics in the target formation process. The *OSIRIS* simulation results show that the fuel plasma jets can be stopped due to a microinstability—the modified two-stream instability (MTSI)[7,8]—rather than coulomb collisions. A comparison of 2-D simulations with *OSIRIS* and the single-fluid magnetohydrodynamic code *FLASH* shows that the codes predict similar macroscopic behaviors of the jets stopping and their subsequent expansion, despite the lack of kinetic physics in the *FLASH* simulations. The results provide validation for using *FLASH* to model target formation and beyond for plasma liner experiments (PLX's).

The total ion $v_x - x$ phase space and the spectrum of the longitudinal electric field E_x are shown in Fig. 1 to illustrate the two dominant MTSI modes identified in the simulation. One of the MTSI modes corresponded to the interaction between the incoming ions and the interpenetrated ions from the counter-propagating jet. This MTSI mode is localized in region 1 [locations between the two solid black vertical lines in the ion phase space as shown in Figs. 1(a)–1(c)]. The incoming and interpenetrating jets can be easily identified since the distribution within region 1 has two distinct peaks on the v_x axis. Using the parameters obtained in region 1, we found that the MTSI growth rate was $\gamma_{\mathrm{MTSI}} = 0.1\ \mathrm{ns}^{-1}$ for the fastest growing mode at $k = 0.65\omega_{\mathrm{pe}}/c$, where ω_{pe} is the local plasma frequency and c is the speed of light. The MTSI mode in region 1 initiated a shock that propagated to the left. A localized electrostatic field started to build up across the shock front as the MTSI grew. The interpenetrated ions were accelerated by this field to a longitudinal velocity of about 240 km/s (the sum of the plasma jet velocity and the shock velocity) and sustained that velocity afterward, as illustrated by the phase space features in region 1 in Figs. 1(b) and 1(c). The fastest-growing modes evaluated using parameters obtained from region 1 at different times are overlaid as the black solid line in Fig. 1(d), which agrees reasonably well with the dominant MTSI mode (the bright feature started around $k = 0.7\omega_{\mathrm{pe}}/c$ at $t \approx 70$ ns), including the shift to lower k at a later time. The other MTSI mode (first appeared around $t \approx 85$ ns with $k = 1.2\omega_{\mathrm{pe}}/c$) in Fig. 1(d) corresponded to the interaction between the incoming ions and the reflected ions. This MTSI mode was localized in region 2, locations between the two dashed vertical lines in Figs. 1(b) and 1(c), which tracked the shock-front propagation. Figure 1(d) plots the fastest-growing MTSI mode as a dashed black line that agreed well with the bright feature to the right of the initial MTSI mode corresponding to region 1. As evident in Fig. 1(d), this MTSI mode occurred later than the initial MTSI mode because the shock was generated by the initial MTSI mode. The wave number k_x of these two MTSI modes both shifted to smaller values over time, mainly due to the decreasing density and magnetic field in regions 1 and 2.

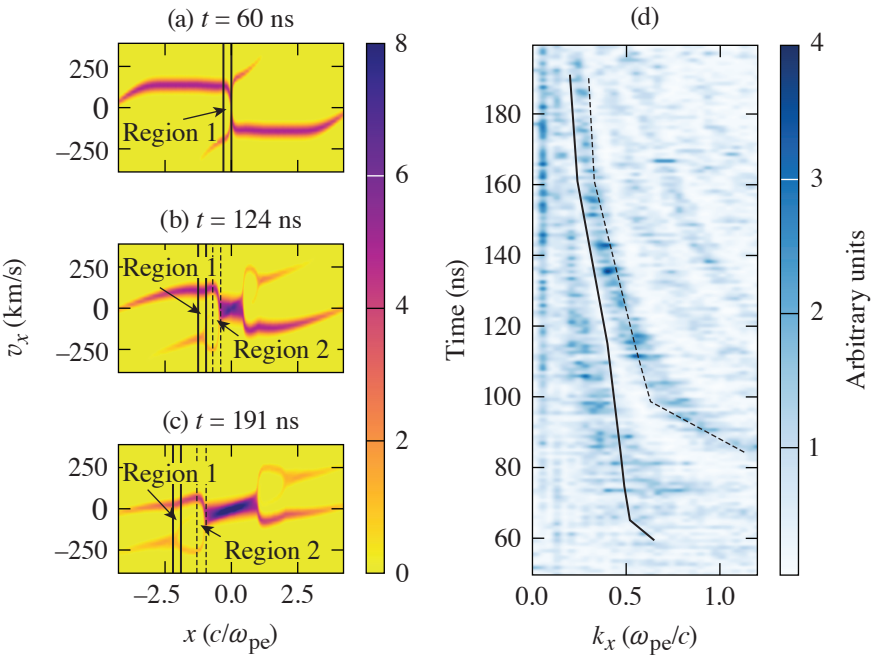

TC16003JR

Figure 1
Ion v_x–x phase space at (a) $t = 60$ ns, (b) $t = 124$ ns, and (c) $t = 191$ ns; (d) the spectrum of longitudinal electric field E_x. The solid and dashed black lines in the plot (d) correspond to the fastest-growing MTSI modes with parameters obtained from the regions 1 and 2 [plots (a)–(c)], respectively.

Figure 2 shows the time evolution of the plasma β, the electron Hall parameter χ_e, and the ion Hall parameter χ_i in the central merging region obtained from *OSIRIS* and *FLASH* simulations. The dimensionless parameters predicted by the two codes were on the same order of magnitude. During the jet-merging process and before the merged plasma expansion, i.e., between 50 and 200 ns, χ_e, and χ_i were greater than unity; the plasma β was close to unity. This is the desired characteristic of planned PLX. The same level of agreement between the two codes was achieved for the electron and ion Hall parameters. The plasma β differed more in the antiparallel-B case: β in *OSIRIS* was consistently larger than in *FLASH*. This is likely due to the interpenetrated species carrying magnetic fields to the other jet, leading to the enhanced magnetic-field cancellation.

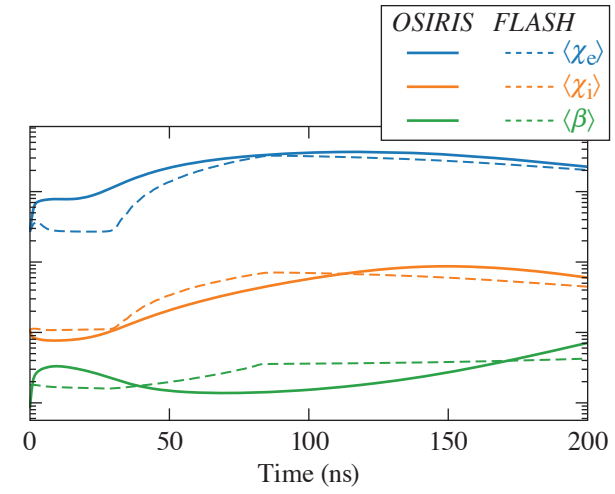

TC16011JR

Figure 2
The dimensionless parameters near the merging region obtained in *OSIRIS* (solid lines) and *FLASH* (dashed lines) simulations of a 5-eV plasma jet collision: electron Hall parameter $\langle\chi_e\rangle$ parameter (blue lines), ion Hall parameter $\langle\chi_i\rangle$ (orange lines), and plasma $\langle\beta\rangle$ (green lines). The angle bracket corresponds to spatial average.

In summary, the MTSI is identified to be the main mechanism responsible for stopping the plasma jets and preventing species interpenetration. The 2-D PIC simulations validate the results of the radiation magneto-hydrodynamics code *FLASH*, which will be the primary tool for modeling various stages of future PJMIF experiments.

This material was based upon the work supported, in part, by the Advanced Research Projects Agency-Energy (ARPA-E), U.S. Department of Energy (DOE), under Award Nos. DE-AR0001272and DE-SC0020431; by the U.S. DOE National Nuclear Security Administration (NNSA) under Award No. DE-NA0003856; the University of Rochester; and the New York State Energy Research and Development Authority. This manuscript has been authored in collaboration with Los Alamos National Laboratory/Triad National Security, LLC, Contract No. 89233218CNA000001, with the U.S. Department of Energy/National Nuclear Security Administration. This research used resources of the National Energy Research Scientific Computing Center (NERSC), a U.S. Department of Energy Office of Science User Facility located at the Lawrence Berkeley National Laboratory, operated under Contract No. DE-AC02-05CH11231 using NERSC Award No. FES-ERCAP0017949.

1. S. C. Hsu and S. J. Langendorf, J. Fusion Energy **38**, 182 (2019).
2. J. S. Davis *et al.*, Phys. Plasmas **19**, 102701 (2012).
3. J. T. Cassibry, M. Stanic, and S. C. Hsu, Phys. Plasmas **20**, 032706 (2013).
4. W. Shih *et al.*, Phys. Plasmas **26**, 032704 (2019).
5. K. Schillo and J. Cassibry, Phys. Plasmas **27**, 042707 (2020).
6. C. Thoma, D. R. Welch, and S. C. Hsu, Phys. Plasmas **20**, 082128 (2013).
7. J. B. McBride *et al.*, Phys. Fluids **15**, 2367 (1972).
8. S. P. Gary, *Theory of Space Plasma Microinstabilities*, Cambridge Atmospheric and Space Science Series (Cambridge University Press, Cambridge, 1993).

Progress in Relativistic Laser–Plasma Interaction with Kilotesla-Level Applied Magnetic Fields

K. Weichman,[1] A. P. L. Robinson,[2] M. Murakami,[3] J. J. Santos,[4] S. Fujioka,[3] T. Toncian,[5] J. P. Palastro,[1] and A. V. Arefiev[6,7]

[1]Laboratory for Laser Energetics, University of Rochester
[2]Central Laser Facility, STFC Rutherford Appleton Laboratory
[3]Institute of Laser Engineering, Osaka University, Japan
[4]University of Bordeaux, CNRS, CEA, CELIA, France
[5]Institute for Radiation Physics, Helmholtz-Zentrum Dresden-Rossendorf, Germany
[6]Department of Mechanical and Aerospace Engineering, University of California, San Diego
[7]Center for Energy Research, University of California, San Diego

Recent advances in vacuum magnetic-field–generation techniques[1–6] have renewed interest in the fundamentals of laser–plasma interaction in the presence of strong magnetic fields. In part, this interest has been motivated by the potential for applied magnetic fields to benefit applications of laser–plasma interaction at relativistic intensity ($I_0 \sim 10^{18}$ W/cm^2 for ~1-μm wavelength), including ion acceleration, inertial fusion energy, and the laboratory study of astrophysical phenomena. This summary builds on recent progress in understanding the basic physics of relativistic laser–plasma interaction with kilotesla-level applied magnetic fields: surface magnetic fields and the diamagnetic effect in laser–solid interaction, the effect of embedded magnetic fields on plasma expansion and ion acceleration, and magnetic-field–associated changes in the direct laser acceleration of electrons.

First, although plasma is conventionally considered diamagnetic and often acts to exclude magnetic fields, laser–plasma interactions have long been known to self-generate strong fields[7] and amplify applied magnetic fields.[8] The spatial localization of hot-electron production from an overdense target and the presence of a neutralizing cold return current offer additional opportunities for magnetic-field generation and amplification associated with kinetic electron dynamics, among which is surface magnetic-field generation arising from the inability of the hot-electron current to change the applied field in a conductive opaque target.[9] This surface magnetic field can influence later plasma dynamics including target expansion[9] and may reverse the sign of the magnetic field generated by laser-driven implosions when it is destabilized.[10] The latter case is of particular interest as a platform for extreme magnetic-field amplification. However, the process underlying the sign reversal phenomenon[10,11] has yet to be conclusively settled. This work introduces a computationally efficient model that is predictive of the sign of the magnetic field produced in implosions. This model demonstrates correlation between sign reversal in cylindrical implosions and instability of the surface magnetic field in a simplified planar configuration (Fig. 1).

Second, until recently, the effect of applied magnetic fields on laser-driven plasma expansion and ion acceleration has primarily been studied in the context of astrophysical jet dynamics[12] involving long time-scale (~nanosecond) evolution in sub-100-tesla magnetic fields, which necessitates magnetohydrodynamic modeling and eliminates the consideration of kinetic effects. The sheath-based ion-acceleration regime driven by short, relativistic intensity laser pules, on the other hand, is conducive to multidimensional kinetic modeling. Recent work in this regime has revealed the possibility of using an applied magnetic field to reverse the typical outward divergence associated with target normal sheath acceleration into focusing and improving the ion energy and number.[13,14] In this case, ion focusing, which is highly desirable and much studied under nonmagnetized conditions, is produced by eventual magnetization of the electron sheath as the plasma expands.[14] Observing ion focusing experimentally, however, will require the spatial scale of the applied magnetic field to be comparable to or greater than the focal length. This work introduces

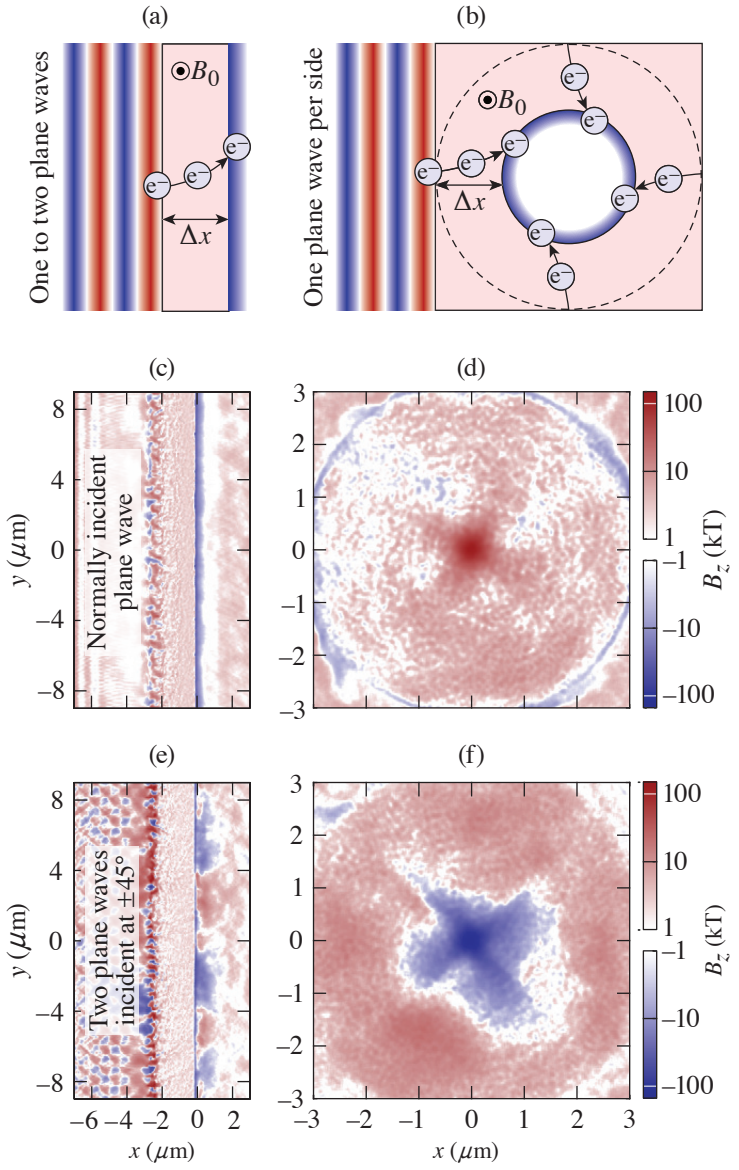

Figure 1
Planar model capturing surface magnetic-field stability and sign of the amplified field in implosions. [(a),(b)] Schematic of surface magnetic-field generation in (a) a planar target and (b) an implosion target with either square (solid line) or circular (dashed line) outer cross section. (c) Stable surface magnetic field in a planar target with normally incident plane wave pulse and (d) seed-aligned amplified magnetic field in a square implosion target. (e) Unstable surface magnetic field in a planar target with two obliquely incident pulses and (f) an amplified field in a circular implosion target.

a simple scaling model for sheath magnetization and subsequent ion focusing (Fig. 2). From this, realistic ion focal lengths are predicted that are likely compatible with the spatial extent of currently available applied magnetic fields.

Finally, while conventional electron acceleration mechanisms typically leave the majority of electrons cold either spectrally or spatially after the laser pulse has passed, direct laser acceleration (DLA) with an applied magnetic field is capable of volumetrically heating electrons to relativistic energy.[15–17] In the regime where the applied magnetic field affects the acceleration dynamics in a single accelerating laser half-cycle,[18] even modestly relativistic laser pulses can deliver significantly relativistic electron energy ($\gamma \sim 10$ or more). A configuration employing a secondary laser pulse prior to the main accelerating pulse (to provide the preheating necessary to enter this regime) was recently demonstrated to heat the majority of electrons in a large plasma volume to nonperturbatively relativistic energy.[18] The resulting optically diagnosable, relativistically thermal plasma is highly desirable for fundamental experimental studies in basic plasma physics, astrophysics and laboratory astrophysics, and laser-plasma physics. This work obtains an estimate for the average electron energy generated via magnetically assisted DLA (Fig. 3), which suggests plasma heating is most efficient for long, low (relativisitic)-intensity laser pulses.

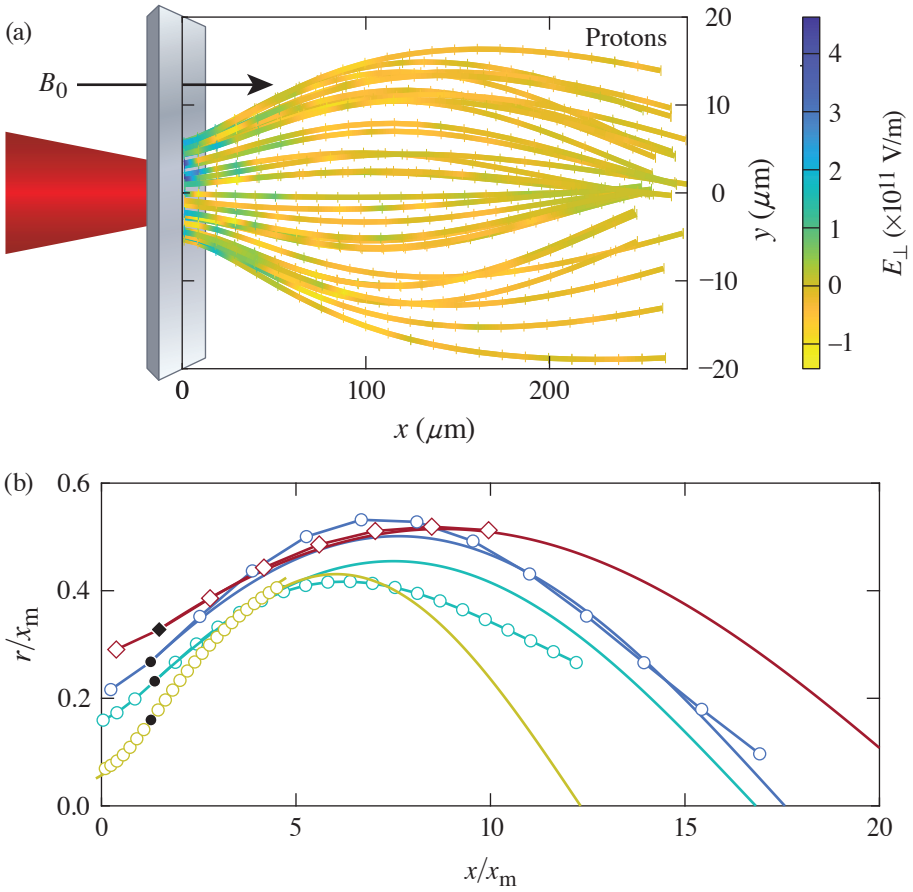

Figure 2
Model of ion focusing in magnetized electron sheath acceleration. (a) Schematic of ion acceleration with a target-normal applied magnetic field with proton trajectories. (b) Average high-energy proton trajectories from simulations keeping the laser waist divided by B_0 constant. $x_m \equiv (2\varepsilon_i T_e)^{1/2}/|e|B_0$.

Together, these results highlight the promise of applied magnetic fields in relativistic laser–plasma interactions. Current magnetic-field capabilities can already enable novel and highly desirable phenomena relevant to laser-plasma applications. The continual development of magnetic-field–generation techniques supports these efforts by opening new parameter regimes to exploration.

This material is based upon work supported by the Department of Energy National Nuclear Security Administration under Award Number DE-NA0003856, the University of Rochester, and the New York State Energy Research and Development Authority. A.V.A. was supported by NSF Grant No. 1903098. A.V.A. was supported by NSF Grant No. 1903098. The support of DOE does not constitute an endorsement by DOE of the views expressed in this paper. Particle-in-cell simulations were performed using *EPOCH*,[19] developed under UK EPSRC Grant Nos. EP/G054940, EP/G055165, and EP/G056803. This work used HPC resources of the National Energy Research Scientific Computing Center (NERSC), a U.S. Department of Energy Office of Science User Facility operated under Contract No. DE-AC02-05CH11231 using NERSC award FES-ERCAP-0021627, and the Extreme Science and Engineering Discovery Environment (XSEDE),[20] which is supported by National Science Foundation grant number ACI-1548562, under allocation TG-PHY210072 on the Texas Advanced Computing Center (TACC) at The University of Texas at Austin.

1. S. Fujioka *et al.*, Sci. Rep. **3**, 1170 (2013).
2. J. J. Santos *et al.*, New J. Phys. **17**, 083051 (2015).
3. L. Gao *et al.*, Phys. Plasmas **23**, 043106 (2016).
4. C. Goyon *et al.*, Phys. Rev. E **95**, 033208 (2017).
5. V. V. Ivanov *et al.*, Rev. Sci. Instrum. **89**, 033504 (2018).
6. G. Fiksel *et al.*, Rev. Sci. Instrum. **86**, 016105 (2015).
7. Z. M. Sheng and J. Meyer-ter Vehn, Phys. Rev. E **54**, 1833 (1996).

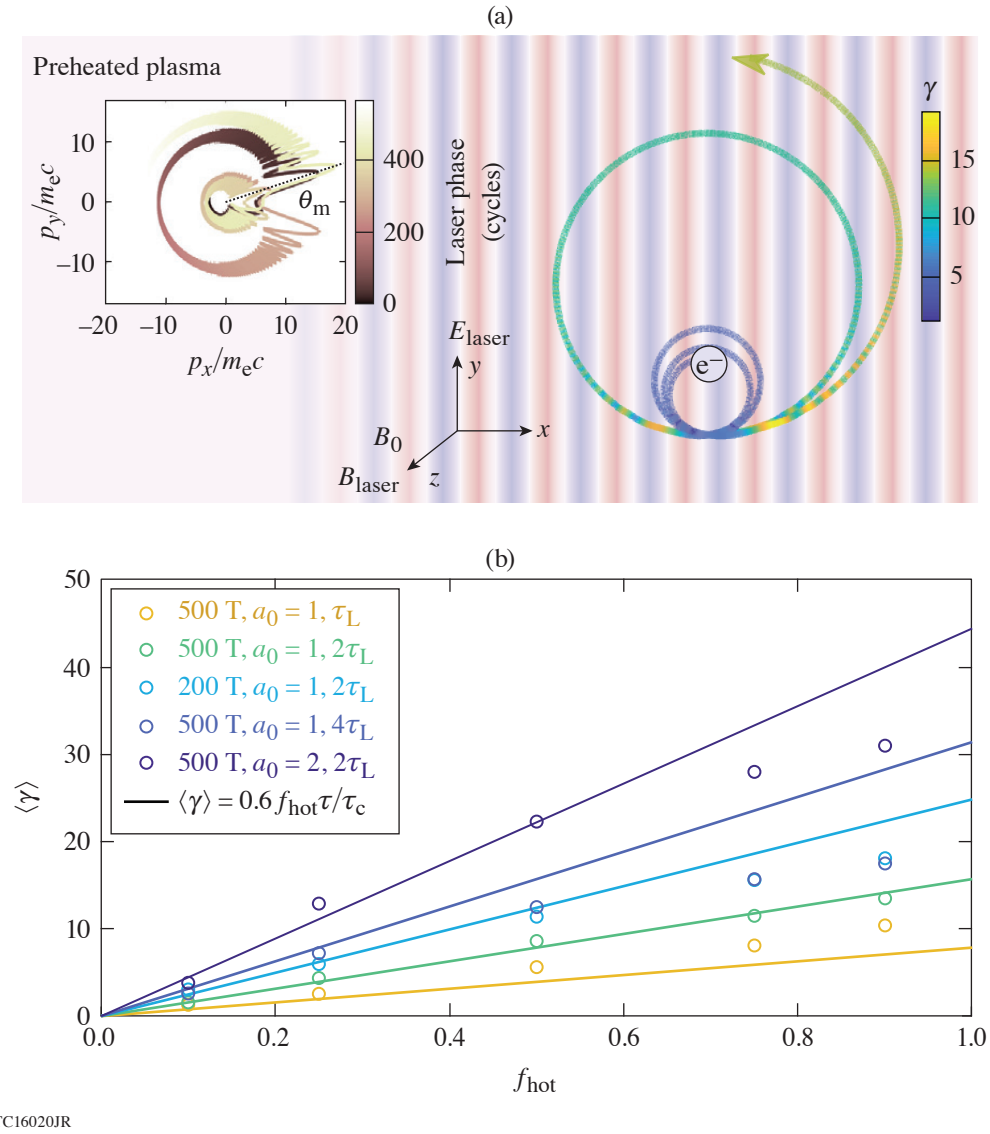

Figure 3
Half-cycle magnetically assisted direct laser acceleration in a preheated plasma. (a) Example of the many-kick electron acceleration process. (b) Average electron energy from particle-in-cell simulations varying the initial fraction of electrons above the the threshold for energy gain (f_{hot}). τ, τ_L, and τ_C are the pulse duration, the maximum Larmor period after a single kick, and the non-relativistic cyclotron period, respectively.

8. O. V. Gotchev *et al.*, Phys. Rev. Lett. **103**, 215004 (2009).
9. K. Weichman *et al.*, New J. Phys. **22**, 113009 (2020).
10. K. Weichman *et al.*, Appl. Phys. Lett. **117**, 244101 (2020).
11. Y.-J. Gu and M. Murakami, Sci. Rep. **11**, 23592 (2021).
12. B. Albertazzi *et al.*, Science **346**, 325 (2014).
13. A. Arefiev, T. Toncian, and G. Fiksel, New J. Phys. **18**, 105011 (2016).
14. K. Weichman *et al.*, Sci. Rep. **10**, 18966 (2020).
15. A. V. Arefiev, A. P. L. Robinson, and V. N. Khudik, J. Plasma Phys. **81**, 475810404 (2015).
16. A. P. L. Robinson and A. V. Arefiev, Phys. Plasmas **27**, 023110 (2020).

17. K. Weichman *et al.*, "Underdense Relativistically Thermal Plasma Produced by Magnetically Assisted Direct Laser Acceleration," Physics Archive: https://doi.org/10.48550/arXiv:2202.07015 (2022).
18. A. Arefiev, Z. Gong, and A. P. L. Robinson, Phys. Rev. E 101, 043201 (2020).
19. T. D. Arber *et al.*, Plasma Phys. Control. Fusion **57**, 113001 (2015).
20. J. Towns *et al.*, Comput. Sci. Eng. **16**, 62 (2014).

Single-Shot Electron Radiography Using a Laser-Plasma Accelerator

G. Bruhaug,[1,2] M. S. Freeman,[3] H. G. Rinderknecht,[1] L. P. Neukirch,[3] C. H. Wilde,[3] F. E. Merrill,[3] J. R. Rygg,[1,2,4] M. S. Wei,[1] G. W. Collins,[1,2,4] and J. L. Shaw[1]

[1]Laboratory for Laser Energetics, University of Rochester
[2]Department of Mechanical Engineering, University of Rochester
[3]Los Alamos National Laboratory
[4]Department of Physics and Astronomy, University of Rochester

To investigate the physical structure of compressed targets, laser-generated x-ray[1,2] or proton radiography[3–5] is typically used, with protons providing the extra feature of electromagnetic field sensitivity. Although x-ray and proton probes are the standard laser-generated diagnostic, there is another laser-generated probe that has seen little use: namely, relativistic electrons. Small-scale high-energy-density (HED) research facilities have performed electron radiography of ultrafast laser–plasma interactions,[6] but this capability has never before been extended to kJ- or MJ-class facilities. The work presented in this summary builds upon previous electron radiography (eRad) work using radio-frequency (rf) linear accelerators[7–9] and small-scale lasers[6–10] and extends it to kJ-class facilities via the already available picosecond lasers for electron-beam generation using a laser-plasma accelerator (LPA).[11,12]

Here, we report the first single-shot eRad images using an electron beam from a 100-J-class LPA. Both contact and projection radiography images of static targets were obtained in materials ranging from plastic to tungsten, and resolutions as good as 90-μm were achieved. This work lays the foundation for future electron radiography of laser-driven targets at kJ- and MJ-class facilities.

Radio-frequency–powered linear accelerators generate monochromatic, low-emittance electron beams suitable for high-quality electron radiography.[7–9] Such systems are rarely available, however, at the same facilities as large HED drivers and cannot easily be installed for experiments due to cost and space constraints. Nevertheless, these HED facilities often have ps lasers available, such as the OMEGA EP, NIF-ARC, PETAL, and Z-Petawatt lasers, which can be used to efficiently generate relativistic electron beams via LPA techniques.[11] This method could allow electron beams to be generated for radiography without needing to add a large and costly rf linear accelerator to an HED facility. A laser-driven eRad system also possesses the temporal characteristics that could make it an ideal diagnostic of other picosecond-scale processes for which linear accelerators do not provide sufficient instantaneous electron flux.

Electron radiography provides a complementary probe to existing x-ray and proton radiography techniques. Unlike laser-generated protons, laser-generated electrons are able to penetrate more material at a given energy. For example, a typical laser-generated 15-MeV proton will be fully stopped by ~2 mm of plastic at standard density and temperature, while a 15-MeV electron will require multiple centimeters of plastic to be fully stopped.[13] Relativistic electrons are also more sensitive to magnetic fields than protons for a given energy, but less sensitive to electric fields. This makes electrons an excellent complement to protons for radiography of electromagnetic fields.

The experiments were performed using the OMEGA EP LPA electron beam[11] and performed in both contact and projection radiography configurations (see Fig. 1).

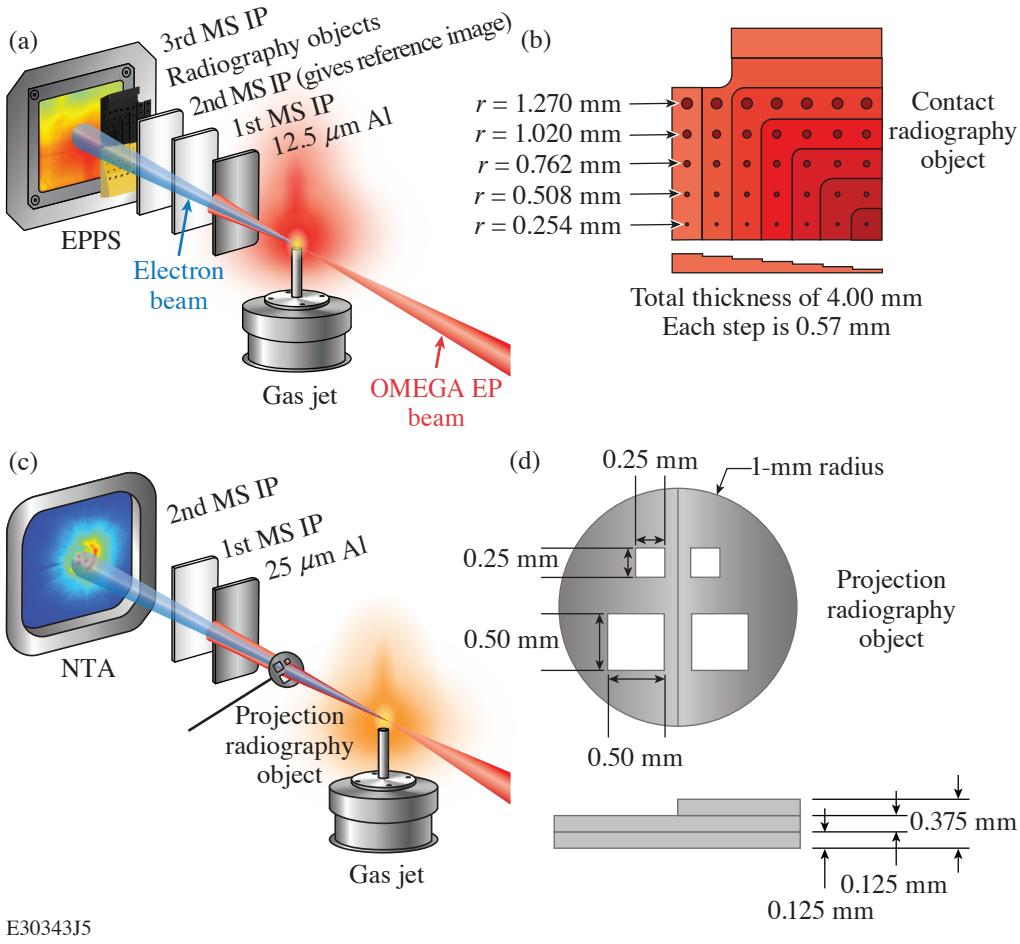

Figure 1
(a) Experimental setup for contact LPA eRad using radiography test objects (b) placed directly onto image plates and (c) projection LPA eRad using 2-mm-diam radiography test objects (d) offset from the image plates by distances ranging from 3.58 to 33.58 cm. MS IP: MS image plate; EPPS: electron–positron–proton spectrometer; NTA: near target arm.

Objects ranging from plastic to tungsten were radiographed at a wide variety of distances and thicknesses. This allowed testing the effect of target Z, density, thickness, and target magnification. The results of contact radiography can be seen in Fig. 2 and projection radiography in Fig. 3.

Resolutions nearing 90 μm were seen, but with little variation in magnification or target material. The resolution degraded with target thickness as expected, but nearly 4 mm of tungsten were able to be radiographed successfully. This shows the extreme penetrative capability of this new diagnostic platform. Laser-induced electric fields in projection radiography were also measured and found to be ~1 GV/m, which is in line with previous literature on the topic.[14]

This material is based upon work supported by the Department of Energy National Nuclear Security Administration under Award Number DE-NA0003856, the University of Rochester, and the New York State Energy Research and Development Authority.

1. E. L. Dewald *et al.*, Rev. Sci. Instrum. **89**, 10G108 (2018).
2. C. Courtois *et al.*, Phys. Plasmas **18**, 023101 (2011).
3. J. R. Rygg *et al.*, Science **319**, 1223 (2008).

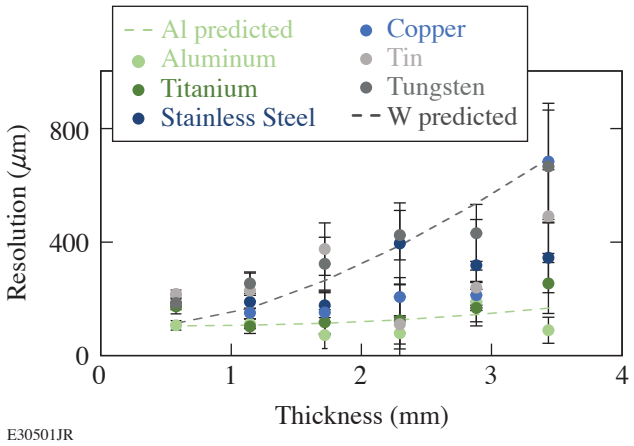

Figure 2
Average measured resolution of contact radiography test object versus target thickness. Theoretical predictions[15] for the tungsten and aluminum are included to guide the eye at the extremes of contact radiography test object *Z* numbers. The error bars are calculated using standard deviation between any repeat radiographs of the same target.

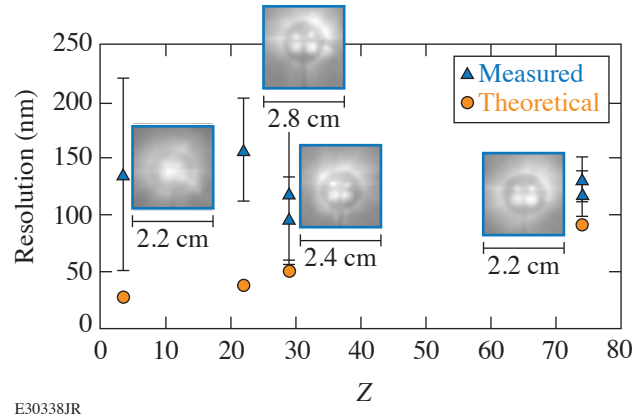

Figure 3
Resolution versus atomic number (*Z*) of the target material for the projection configuration when the image plate was 8 cm from the location of the best laser focus. Each data point has the radiograph recorded on the image plate next to it. Resolution is measured at the edges of each hole in the object as well as the outer edge. Error bars were calculated via the standard deviation between the resolution measurements on the same object.

4. A. B. Zylstra *et al.*, Rev. Sci. Instrum. **83**, 013511 (2012).
5. C. K. Li *et al.*, Phys. Plasmas **16**, 056304 (2009).
6. W. Schumaker *et al.*, Phys. Rev. Lett. **110**, 015003 (2013).
7. F. E. Merrill, Laser Part. Beams **33**, 425 (2015).
8. F. E. Merrill *et al.*, Appl. Phys. Lett. **112**, 144103 (2018).
9. F. Merrill *et al.*, Nucl. Instrum. Methods Phys. Res. B **261**, 382 (2007).
10. D. Hazra *et al.*, Phys. Rev. Accel. Beams **22**, 074701 (2019).
11. J. L. Shaw *et al.*, Sci. Rep. **11**, 7498 (2021).
12. F. Albert *et al.*, Nucl. Fusion **59**, 032003 (2018).
13. M. J. Berger *et al.*, (2017), *ESTAR*, *PSTAR*, and *ASTAR*: Computer Programs for Calculating Stopping-Power and Range Tables for Electrons, Protons, and Helium Ions (Ver. 2.0.1). [Online] Available: https://www.nist.gov/pml/stopping-power-range-tables-electrons-protons-and-helium-ions [17 August 2018].
14. J. L. Dubois *et al.*, Phys. Rev. E **89**, 013102 (2014).
15. A. Nassiri, Argonne National Laboratory, Urbana, IL, Report LA-165 (1991).

Development of a Hardened THz Energy Meter for Use on the Kilojoule-Scale, Short-Pulse OMEGA EP Laser

G. Bruhaug,[1,2] H. G. Rinderknecht,[1] Y. E,[3] M. S. Wei,[1] R. B. Brannon,[1] D. Guy,[1] R. G. Peck,[1] N. Landis,[1] G. Brent,[1] R. Fairbanks,[1] C. McAtee,[1] T. Walker,[1] T. Buczek,[1] M. Krieger,[1] M. H. Romanofsky,[1] C. Mileham,[1] K. G. Francis,[3] X. C. Zhang,[3] G. W. Collins,[1,2,4] and J. R. Rygg[1,2,4]

[1]Laboratory for Laser Energetics, University of Rochester
[2]Department of Mechanical Engineering, University of Rochester
[3]The Institute of Optics, University of Rochester
[4]Department of Physics and Astronomy, University of Rochester

Terahertz radiation occupies the frequency range between microwave and infrared radiation, making it a unique pump and probe of matter that interacts with matter in neither a purely photonic nor a bulk electronic fashion.[1–3] Because of the unique nature of THz radiation, there is a large interest in high-power sources for nonlinear time-domain spectroscopy and relativistic light–matter interactions at the extremes of low frequency;[1,3] however, the generation of such THz pulses is extremely difficult with traditional methods. Recent work with laser-plasma THz generation has shown great promise in scaling THz pulses to the terawatt and >100-mJ scale using ps, kJ-scale lasers to drive solid, liquid, or gaseous targets.[1] To maximize the THz power and pulse energy, lasers with both high energy (kJ) and high intensity (>10^{18} W/cm^2) must be used. These lasers are most commonly single shot and are well known for their immense electromagnetic pulse (EMP),[4] hard x-ray,[5] and charged-particle generation.[6] The OMEGA EP laser is especially challenging due to the peak EMP field measured being one of the highest seen on any laser (~500 kV/m) (Ref. 4). This adds to the already challenging task of THz detection due to the low efficiency (average of 0.1%) of laser THz generation in these systems. All available THz detection methods rely on electronics,[2] further compounding the EMP noise issue in these experiments.

This summary outlines the development of a ten-inch manipulator (TIM)–mounted THz energy meter, known as a THz background/energy meter (TBEM), for use on the kilojoule-class OMEGA EP laser and the associated challenges with the development of this detector. The TBEM is a broadband (0.3- to 10-THz or 1-mm to 30-μm) energy meter based on THz-sensitive pyrometers and capable of detecting broadband THz pulses as weak as ~50 μJ emitted in 4π or as strong as ~2 J emitted in 4π before suffering saturation of the detection element.

TBEM is a 112.5-cm-long, 20.9-cm-wide, TIM-mounted diagnostic weighing 33.1 kg primarily due to the inclusion of 19.8 kg of tungsten radiation shielding. As shown in Fig. 1, the diagnostic consists of a light-tight aluminum chassis with a front-mounted TPX[7] (THz and optical light transmissive) lens and filter pack extending 36.8 cm from the main body. This front lens allows for THz radiation to be collected 15 cm from target chamber center, maximizing the sensitivity of the detector. In front of the lens is a removable high-resistivity silicon wafer that acts as a THz-transmissive blast shield. The filter pack attached to the front lens can hold THz filters to alter the portion of the spectrum sampled and irises to reduce the amount of THz radiation sampled while operated in the forward position. This lens and filter assembly can also be removed and the detector operated while retracted from target chamber to further protect the electronics from EMP and radiation. A schematic of the detector and the THz transmission spectrum of the optical components can be seen in Fig. 2.

THz detection is accomplished by using commercially available nanojoule-sensitive pyrometers,[8] which are commonly used for commercial and scientific THz detection. A pyrometer is a broadband-sensitive energy meter that relies on the pyroelectric

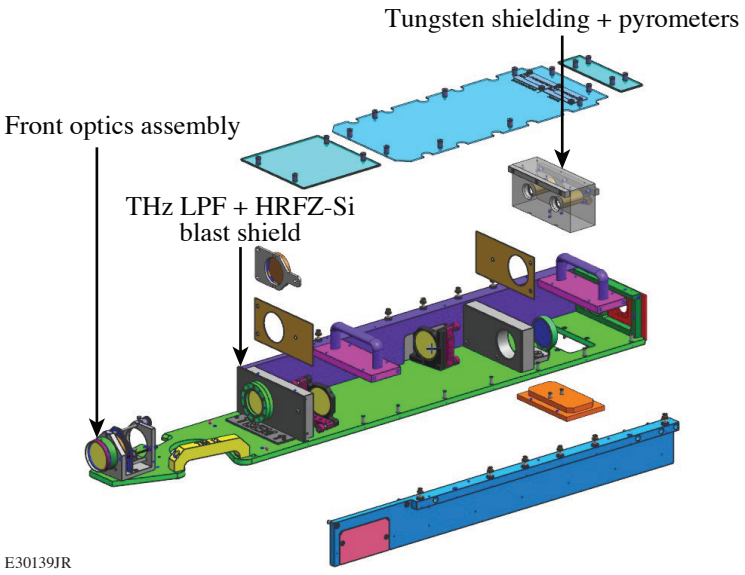

Figure 1
Expanded view of a TBEM detector assembly. LPF: low-pass filter; HRFZ: high-resistivity silicon.

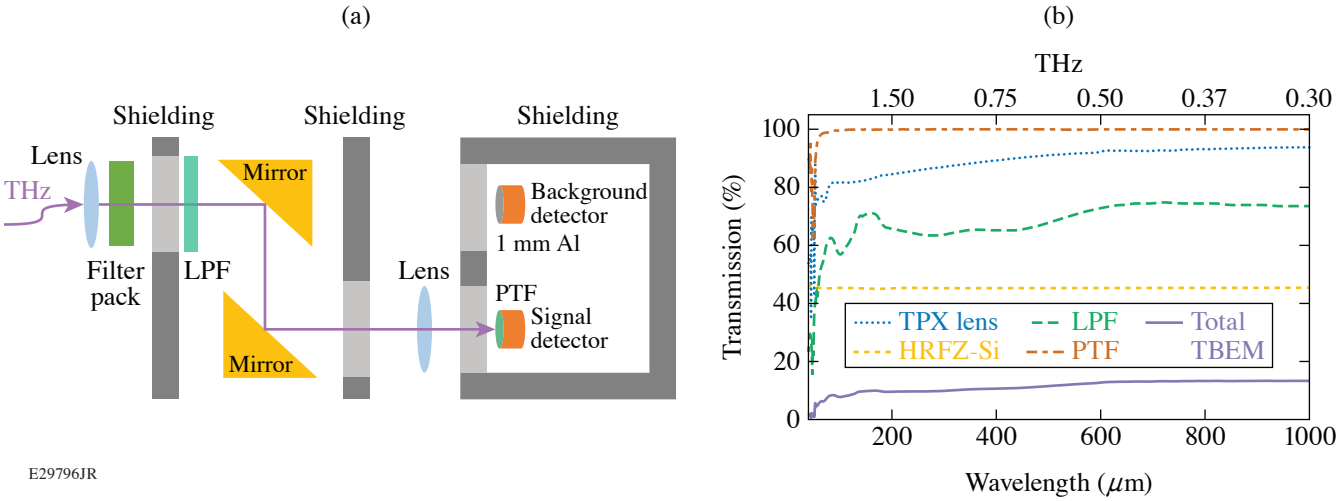

Figure 2
(a) Full optical path of the TBEM detector and (b) THz transmission of the optical components and full detector.[7,9] PTF: polytetrafluoroethylene.

effect to detect a change in energy deposition.[2,8] The sensor is built in a series of layers similar to a capacitor with two electrodes around an inner layer of pyroelectric material. One electrode is darkened to best absorb the wavelength range of interest. Upon pulsed irradiation, the pyrometer will heat up and the polarization direction in the pyroelectric material will change. A charge disparity then develops across the pyroelectric crystal, and a voltage pulse is generated that is proportional to the amount of energy deposited into the sensor.

The initial concept for TBEM was built and tested for use on the Multi-Terawatt (MTW) laser to support THz target design campaigns. The results have been extremely promising. Four campaigns were then undertaken on OMEGA EP to test the TBEM detectors with the final two campaigns showing repeatable THz detection. The first campaign did not have the full complement of radiation shielding in place and suffered from massive x-ray and EMP noise problems (Fig. 3.). The second campaign had the radiation and EMP shielding upgraded and showed more-promising results. As with MTW, it was found that using plastic target stalks reduced the noise, but in this case the reduction was not enough to observe THz signal above the background.

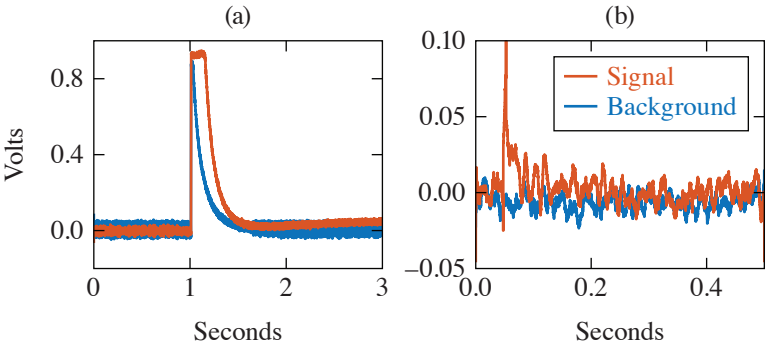

Figure 3
Example of data taken from one TBEM on the (a) first and (b) second OMEGA EP THz campaigns with ~100 J of laser energy used (July 2021 and March 2022, respectively). EMP and x rays, caused by extremely high background noise, can be seen in (a) when there was less shielding present on the detector.

For the third and fourth campaigns, the detectors were upgraded with the full complement of tungsten shielding described above, as well as improved cable EMP shielding. THz generation was reliably detected on both foil and microchannel targets with laser energies ranging from 100 to 500 J. Example THz detections from these experiments can be seen in Fig. 4.

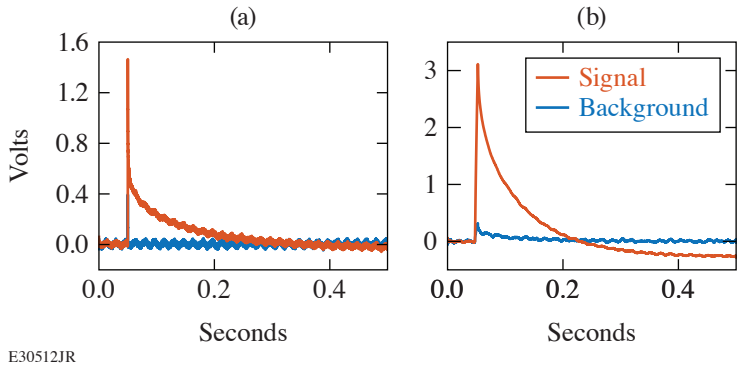

Figure 4
Example of data taken from one TBEM on third and fourth OMEGA EP campaign (June 2022): (a) from a foil irradiated with ~100 J of laser energy and (b) from a microchannel target irradiated with ~300 J of laser energy.

The THz yields were estimated to be ~130 mJ from the foil target and ~300 mJ from the microchannel target, which are in line with the estimated generation efficiencies of these target types for the given laser energy.[1,10] The additional EMP shielding on the pyrometer wiring was found to be crucial for the most energetic laser shots.

This material is based upon work supported by the Department of Energy National Nuclear Security Administration under Award Number DE-NA0003856, the University of Rochester, and the New York State Energy Research and Development Authority.

1. G. Liao *et al.*, Proc. Natl. Acad. Sci. **116**, 3994 (2019).
2. F. Sizov, Opto-Electronics Rev. **18**, 10 (2009); 223(E) (2010).
3. H. A. Hafez *et al.*, J. Opt. **18**, 093004 (2016).
4. S. Mondal *et al.*, J. Opt. Soc. Am. B **35**, A93 (2018).
5. C. Courtois *et al.*, Phys. Plasmas **18**, 023101 (2011).
6. J. L. Shaw *et al.*, Sci. Rep. **11**, 7498 (2021).
7. V. E. Rogalin, I. A. Kaplunov, and G. I. Kropotov, Opt. Spectrosc. **125**, 1053 (2018).
8. Gentec-EO, Accessed 23 March 2022, https://www.gentec-eo.com/products/qs5-thz-bl.
9. M. S. Kitai *et al.*, Radiophys. Quantum Electron. **57**, 881 (2015).
10. L. Yi and T. Fülöp, Phys. Rev. Lett. **123**, 094801 (2019).

Single-Shot Cross-Correlation of Counter-Propagating, Short Optical Pulses Using Random Quasi-Phase Matching

C. Dorrer and J. L. Shaw

Laboratory for Laser Energetics, University of Rochester

A single-shot cross-correlator based on the sum–frequency generation (SFG) of counter-propagating beams in SBN61 ($Sr_xBa_{1-x}Nb_2O_6$ with $x = 0.61$) has been demonstrated.[1] Random quasi-phase matching in disordered ferroelectric crystals such as SBN61 allows for nonlinear interactions in nonstandard geometries, e.g., the observation of a transverse second-harmonic–generation signal resulting from two co-propagating or counter-propagating pulses.[2,3] This diagnostic measures the cross-correlation between two laser facilities, leading to the relative delay between the pulses generated by each facility on every shot. It supports their precise co-timing and the study of their relative jitter with high precision over a time range larger than 150 ps.

The cross-correlation of optical pulses with instantaneous power profile $P_A(t)$ and $P_B(t)$ generated by the Multi-Terawatt (MTW) laser ($\lambda_A = 1053$ nm) and the idler of the MTW-OPAL laser ($\lambda_B = 1170$ nm) [Fig. 1(a)] were measured. The two beams are focused in a counter-propagating configuration in the underdense-plasma target chamber designed for Raman-amplification studies. Transverse SFG in an SBN61 maps out the cross-correlation signal $C_{AB}(\tau) = \int P_A(t)P_B(t-\tau)\mathrm{d}t$, where τ is the relative delay between the two pulses onto the longitudinal spatial coordinate. The generated transverse signal is re-imaged onto a camera, therefore allowing for single-shot cross-correlation acquisition over a range of relative delay set by the crystal length and group velocity of the two pulses, resulting in more than 150 ps for the 10-mm crystal used in these experiments. Both pulses generate a time-integrated transverse second-harmonic–generation signal at 526.5 nm and 585 nm, respectively, adding a background on the cross-correlation signal of interest [Fig. 1(b)]. Background-free acquisition with enhanced signal-to-noise ratio is obtained using a bandpass filter at the SFG wavelength (~550 nm). The cross-correlator has been used to co-time the two laser facilities at the common focal region where Raman-amplification in a gas jet are conducted. It has also provided valuable information on the relative jitter between the two laser facilities and for pulse-shape optimization.

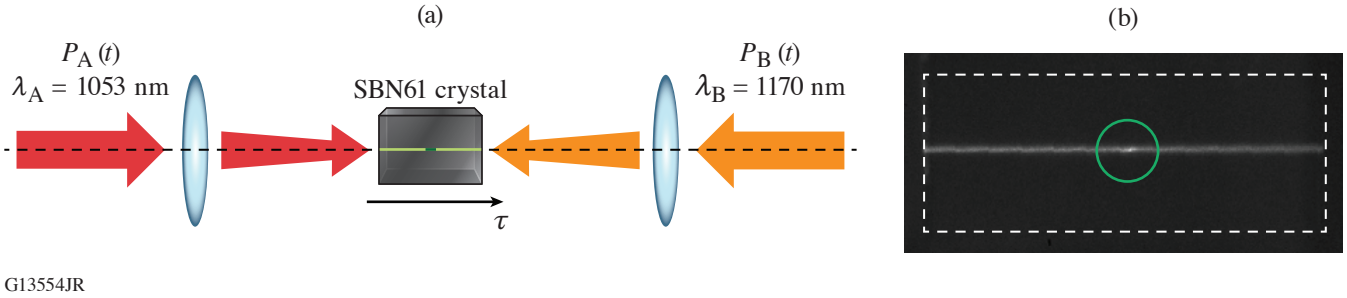

Figure 1
(a) Experimental setup. (b) Example of a signal acquired by the camera, without spectral filtering. The green circle identifies the cross-correlation signal, which is the only signal acquired by the camera when a bandpass filter at the SFG wavelength is used to remove the time-integrated SHG signals.

Fourier processing of the measured cross-correlation trace allows for extraction of its delay relative to reference and retiming for averaging purposes (Fig. 2). The collection of relative delays over a large number of shots represents the statistics of the jitter between the two laser facilities. As an example of application, Fig. 3(a) displays histograms of the relative delay between the two

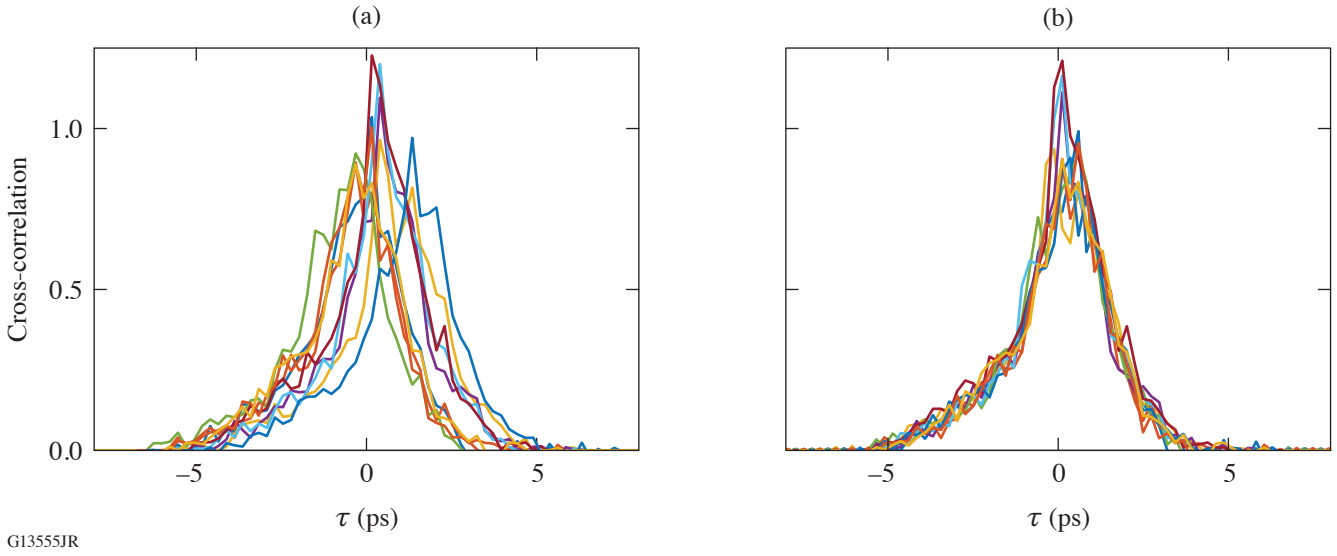

Figure 2
A set of ten measured single-shot cross-correlations (a) before and (b) after retiming.

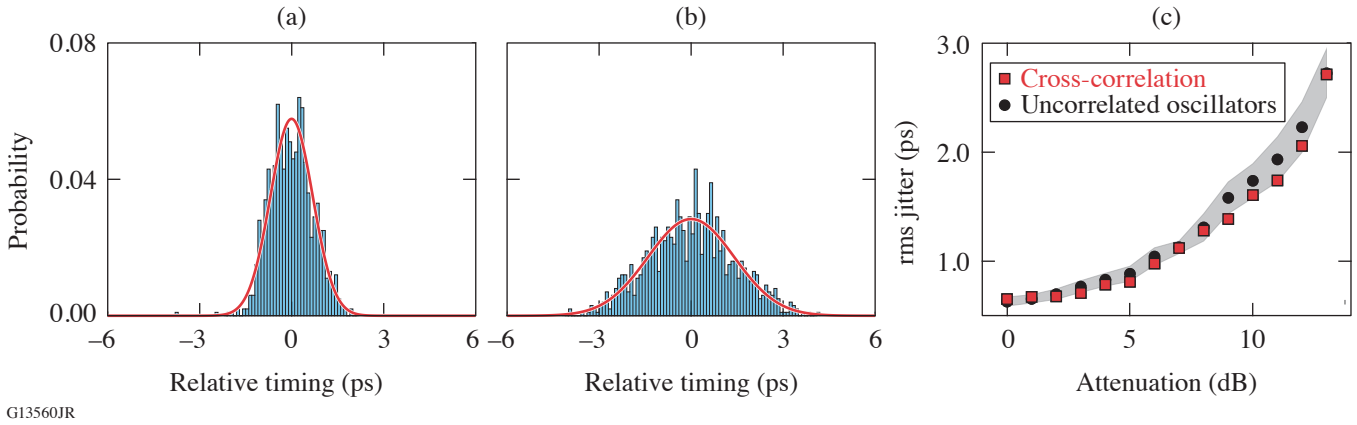

Figure 3
Probability histograms of the delay between the two laser sources measured (a) with a nominal synchronization-photodiode signal and (b) with a 9-dB attenuation. The bin size is 0.1 ps in all cases. A normal distribution with identical standard deviation has been added to (a) and (b) (red lines). On (c), the rms jitter determined from the measured cross-correlations (red squares) is compared to the rms jitter calculated from the jitter reported by the synchronization unit of the two mode-locked lasers (black circles, with confidence interval indicated by the shaded area).

facilities measured for three different synchronization configurations of the mode-locked laser seeding the MTW laser. Attenuation of its reference signal leads to poorer synchronization of that laser to the LLE reference frequency, thereby inducing a higher jitter for that particular laser and for the relative delay between the two facilities. The rms jitter calculated from the measured cross-correlations is in good agreement with the jitter calculated from the jitter of each mode-locked oscillator [Fig. 3(b)].

This simple approach supports the determination of the relative timing between two laser sources on a single shot, which is particularly important for low-repetition-rate sources. It also offers a direct approach to single-shot determination of the time-varying instantaneous power of an optical pulse by cross-correlation with a shorter ancillary pulse. Such determination is important for the development and optimization of chirped-pulse–amplification systems delivering pulses close to their Fourier transform–limited duration, but also for systems delivering pulses with a coherence time much shorter than their duration, e.g.,

incoherent pulses. Accurate single-shot temporal characterization with high resolution and long record length is paramount for safe operation and optimal interaction with the targets. SBN crystals as long as 20 mm are commercially available, leading to a 300-ps temporal window. Longer acquisition windows can be obtained by combining multiple crystals or implementing multiple passes in a single crystal with different relative delays between the two sources. Cross-correlations in disordered nonlinear crystals can also support the optimization of spatial overlap and timing in complex experiments involving multiple laser beams, such as the counter-propagating geometry used for Raman amplification and the crossing of beams at large angles used for Compton scattering.

This material is based upon work supported by the Department of Energy National Nuclear Security Administration under Award Number DE-NA0003856, the Department of Energy Office of Science under Award Number DE-SC0016253, the University of Rochester, and the New York State Energy Research and Development Authority. The authors thank I. A. Begishev, S. Bucht, R. Roides, M. V. Ambat, and K. McMillen for experimental assistance during this campaign.

1. C. Dorrer and J. L. Shaw, Opt. Express **30**, 16,677 (2022).
2. J. Trull *et al.*, Opt. Express **15**, 15,868 (2007).
3. R. Fischer *et al.*, Appl. Phys. Lett. **91**, 031104 (2007).

Multiparameter Laser Performance Characterization of Liquid Crystals for Polarization Control Devices in the Nanosecond Regime

K. L. Marshall,[1] K. R.P. Kafka,[1] N. D. Urban,[1] J. U. Wallace,[1,2] and S. G. Demos[1]

[1]Laboratory for Laser Energetics, University of Rochester
[2]Department of Chemistry, D'Youville College

The interactions of liquid crystals (LC's) with polarized light have been studied widely and have spawned numerous device applications, including the fabrication of optical elements for high-power and large-aperture laser systems. Such devices have numerous advantages that include scalability to large apertures, cost effectiveness, high optical quality and contrast, broad angular tolerance, and laser-induced–damage thresholds (LIDT's) for optimized materials at 1054 nm of >30 J/cm^2, 3 J/cm^2, and 1 J/cm^2 at 1-ns, 10-ps, and 600-fs pulse durations, respectively.[1,2] Evaluation of the LIDT of LC materials has been performed historically in long-path-length LC cells (50 to 100 μm) to gain an understanding of the LC material's behavior under exposure to high-energy laser pulses without competing physicochemical interactions with surface-anchoring layers and conditions (LC elastic constants, boundary molecular tilt angle, alignment materials chemistry and application methods[2,3]). Although useful for screening LC materials by chemical class to determine general laser survivability, such long-path-length testing gives very little insight on how the LC's LIDT may be affected in device applications where the LC molecules are constrained in a monodomain alignment state induced by contact with substrates bearing a polymer alignment layer (e.g., wave plates, mirrors, and beam shapers). In such cases, variations in optical behavior as a function of laser beam polarization due to molecular orientation, chemical interactions, or generation of electric-field enhancements in the LC material are a distinct possibility.[4–6] This summary reports on the first study of the nanosecond-pulsed LIDT's dependence on incident polarization for several optical devices employing nematic and chiral-nematic LC's oriented by surface alignment layers. Accelerated lifetime testing was also performed to characterize the ability of these materials and devices to maintain their performance under multi-pulse irradiation with increasing laser fluence at both 1053 nm and 351 nm (Ref. 7).

Figure 1 shows generic molecular structures of LC components with differing degrees of π-electron density (saturation) that were evaluated for their multipulse laser damage behavior in optical element configurations typically used in high-peak-power lasers (e.g., circular polarizers and wave plates), where the LC molecular director, which defines the average long-range orientation of the LC molecular axes in the bulk, is constrained to adopt a monodomain or nearly monodomain orientation.

A pulsed nanosecond laser system operated at either its fundamental wavelength (1053 nm) or the third harmonic (351 nm) was used along with a novel detection system employing a polarization-sensitive camera to detect both the onset of performance degradation and classical LIDT of several LC mixture compositions in both circular polarizers and wave-plate device geometries. These measurements were designed to explore a "laser-induced functional threshold" (LIFT), defined as a reduction in one or more system-defined, key device functional parameters (e.g., transmission, reflection, birefringence, polarization rotation, contrast) that may occur at fluences lower than those required to produce the visible and permanent evidence of material modification typically defined as laser-induced damage. The point at which the value of LIFT drops below a system-defined tolerance metric is taken as the LIFT "trigger point." For the purposes of this study, the LIFT trigger pointy was a reduction in transmission to <98% (Ref. 7).

Testing of these LC materials at 1053 nm and 351 nm showed that their LIDT behavior depends significantly on the incident polarization state for laser light encountering the input surface of the LC test device at near-normal incidence (7°). For LC circular polarizer devices, the LIDT varied as a function of incident circular-polarization handedness by a factor of 30% to 80% for a given sample (Fig. 2). It appears that an angular dependence of high-peak-power LIDT on incident polarization in LC materials

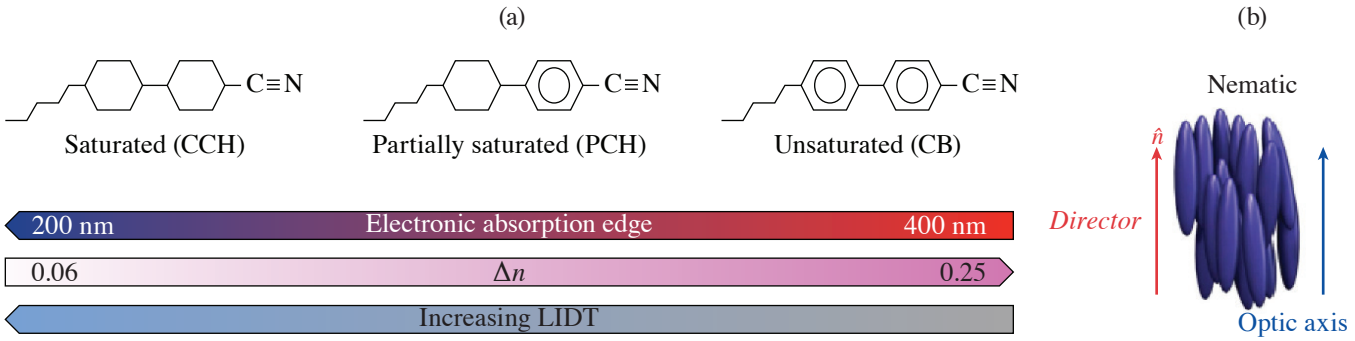

Figure 1
(a) Molecular structures for the three classes of LC compounds evaluated and a graphical representation of the dependence of optical absorbance, birefringence, and laser damage with respect to these classes. (b) Molecular ordering in the nematic LC phase. For this class of LC materials, both the LC director and the optic axis are parallell to the molecular axis.

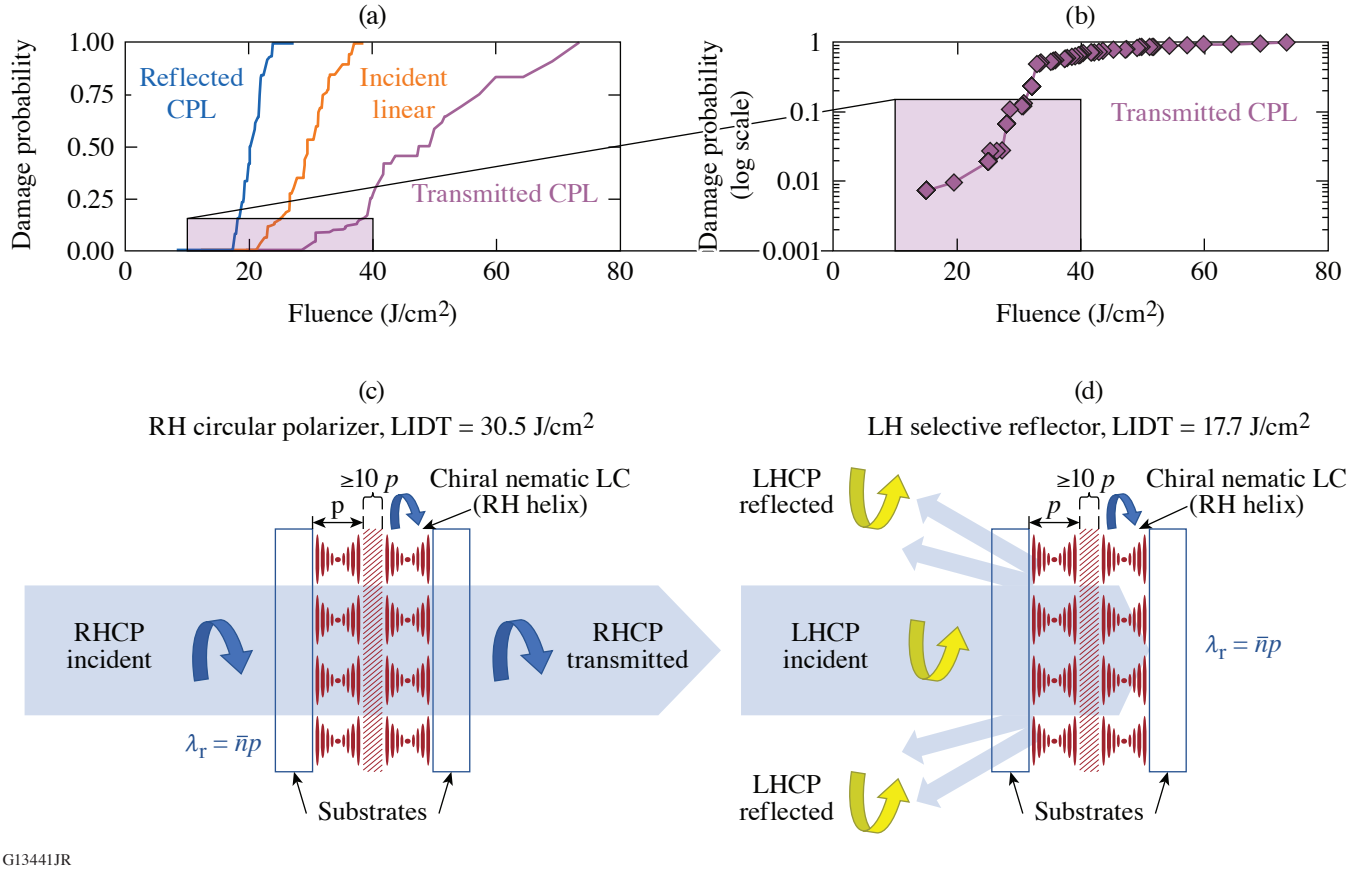

Figure 2
(a) Damage probabilities for the chiral-nematic LC circular polarizer/isolator device as a function of 1053-nm, 1.4-ns laser fluence and incident polarization; (b) damage probabilities for transmitted circularly polarized light pulses incident on the device at low fluence [corresponding to the inset in Fig. 2(a)]. The data, plotted on a logarithmic scale, represent an additional 250 sites of 1-on-1 damage data collected by line-scanning the sample; [(c),(d)] the interaction of circularly polarized light of opposite handedness on the LC structure, along with the representative LIDT thresholds. For (c), incident circular polarized light with the same twist sense as the LC helix (right-handed) is transmitted, whereas in (d) for the same device, incident circular polarization of the opposite handedness (left-handed) is selectively reflected due to Bragg scattering. A cell thickness of at least ten pitch lengths (p), indicated by the area filled with diagonal slashes near the center of the cell, is required to observe these effects with sufficient magnitude for device applications.

has not been reported previously. The results suggest that multipulse functionality was best preserved in LC devices having the highest degree of saturation.

Certain compositions of saturated, UV transparent nematic LC mixtures evaluated in a wave-plate geometry displayed remarkable robustness in LIFT testing at 351 nm, with one CCH-based LC mixture (LLE1202) being able to survive as many as 1000 1-ns pulses at 2 J/cm^2 (5-Hz repetition rate) before displaying any significant change in its functional performance (Fig. 3). The LIDT was seen to vary as a function of input polarization by 30% to 80% within the same device, while the multi-pulse LIFT depends on irradiation conditions such as laser fluence and wavelength.

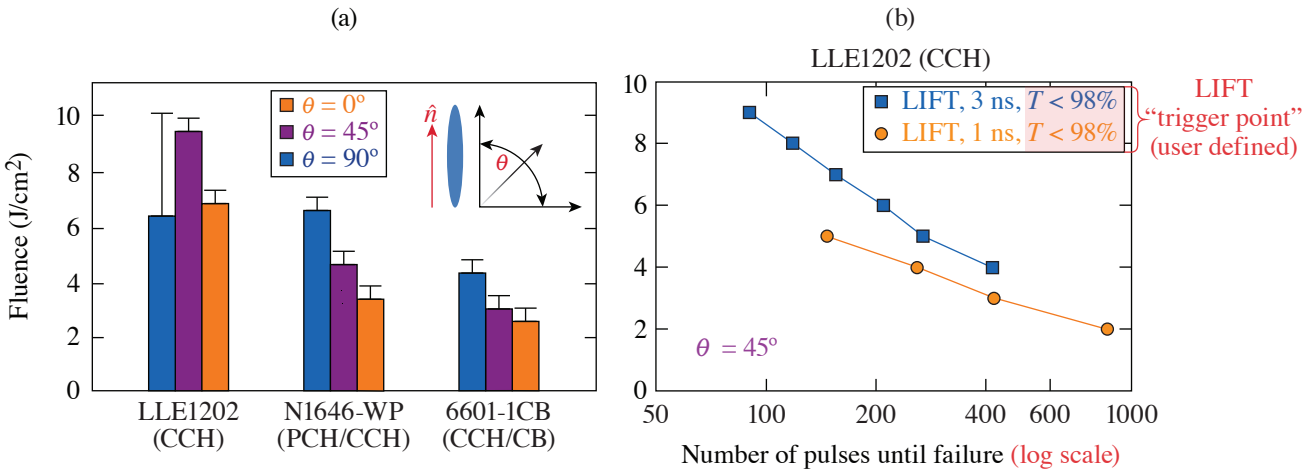

Figure 3
(a) LIDT at 351-nm, 1-ns pulse duration as a function of incident linear polarization angle with respect to the LC director. Uncertainty bars extend to the nominal 0% and 100% damage probability fluences. (b). LIFT results for LLE1210 at 351 nm for both 1-ns and 3-ns laser pulses delivered at a 5-Hz repetition rate. The high saturation of this CCH-based LC material allows it to withstand nearly 1000 pulses at 2 J/cm^2. The inset in (a) shows the orientation of the LC director with respect to the incident laser polarization.

These promising results highlight the potential of this class of LC materials in nanosecond-regime, high-peak-power lasers such as OMEGA for applications as polarization control and polarization-smoothing optics. Another distinct advantage of LC optics is that in the event they do sustain damage, they can be refurbished and reinstalled in a laser system with a relatively low cost of materials and effort. The results also illustrate the necessity of taking the molecular structure and electron delocalization of LC mesogens into account when designing new materials for such emerging applications.

This material is based upon work supported by the Department of Energy National Nuclear Security Administration under Award Number DE-NA0003856, the University of Rochester, and the New York State Energy Research and Development Authority.

1. S. D. Jacobs *et al.*, J. Opt. Soc. Am. B **5**, 1962 (1988).
2. T. Z. Kosc *et al.*, Sci. Rep. **9**, 16435 (2019).
3. A. Schmid *et al.*, Mol. Cryst. Liq. Cryst. **207**, 33 (1991).
4. J. Lu *et al.*, J. Appl. Phys. **80**, 5028 (1996).
5. C.-H. Wen, S. Gauza, and S.-T. Wu, J. Soc. Inf. Disp. **13**, 805 (2005).
6. Y. H. Wang *et al.*, IEICE Trans. Electron. **E-83-C**, 1553 (2000).
7. K. L. Marshall *et al.*, Sci. Rep. **12**, 10969 (2022).

Influence of Heat Treatments on Near-Surface Tritium Concentration Profiles

M. Sharpe, W. T. Shmayda, and J. J. Ruby

Laboratory for Laser Energetics, University of Rochester

At room temperature, tritium interacts with all metals (aluminum, copper, stainless steel, etc.) to some extent.[1] Such interactions can lead to a buildup of tritium on the metal's surface and just under the surface of the metal.[2–4] The presence of high tritium concentrations in these locations is a large concern for all tritium-handling facilities. These facilities contain a large quantity of metals that routinely come in contact with tritium gas. Over time, tritium buildup in these metals can lead to radiological hazards and high waste disposal costs. To mitigate tritium contamination in metals, it is common to heat the metal to high temperatures.[5,6] The details of this thermal desorption method (maximum temperature, dwell time, etc.) depend on the contaminated metal as well as the expected tritium dosing. To date, however, no systematic study has been performed showing how tritium migrates within the metal as a result of a chosen thermal desorption temperature and time. The current work addresses this gap in knowledge by showing how the tritium distribution within stainless steel, type 316 (SS316) responds to temperatures between 100°C and 300°C. The surface and near-surface concentrations were measured using a combination of a $ZnCl_2$ wash and sequential acid etching to reveal a high-resolution tritium concentration profile. Tritium deeper within the metal was measured using high-temperature thermal desorption to remove residual tritium from the bulk metal.

To measure the effect of heating on the tritium distribution within SS316, a series of samples were first exposed to tritium gas for 8 h at 25°C. Each sample was then heated to temperatures between 100°C and 300°C for 120 min under a stagnant, dry argon atmosphere. The tritium distribution was then measured by performing a $ZnCl_2$ wash first to remove surface tritium. Following this wash, the samples were then acid etched to reveal the tritium concentrations immediately under the surface (<100 μm). Finally, the residual tritium deeper in the samples was measured using high-temperature thermal desorption (550°C for 4 h). For comparison, several control samples were not heated prior to the $ZnCl_2$ wash, acid etching, and high temperature thermal desorption procedures.

The resulting concentration profiles (Fig. 1) show two notable deviations from the control samples. First, the surface activity decreases significantly with increasing preheating temperature as expected. Second, the near-surface (1 nm to 1 μm) tritium concentrations differ for only the 200°C and 300°C cases; the 100°C and 150°C preheating appears to have had no influence on the near-surface concentrations. Heating to temperatures greater than or equal to 200°C resulted in decreased concentrations in the near surface (~0.1 μm).

Integrating the concentration profiles shown in Fig. 1 reveals the total tritium remaining within each region of the SS316 sample. These integrals (Fig. 2) show that surface-bound tritium decreases with increasing preheating temperature, while tritium deeper in the metal (>1 μm) increases. Tritium quantities in the intermediate region (<1 μm) remain constant until the sample is heated to 200°C or greater. Above 200°C, the quantity of tritium decreases to a new, lower value.

These data indicate how tritium migrates within SS316 in response to moderate heating. Heating SS316 causes tritium to desorb from the surface and migrate deeper into the metal. Taking the median values of the data shown in Fig. 2, the quantity of tritium "lost" from the surface is greater than the tritium activity released from the surface. This indicates that tritium preferentially migrates into the metal as opposed to desorbing from the surface. Desorption from the surface is possibly not as favorable due to the gas conditions. The samples were kept under dry argon during the preheating phase. Past studies have shown that tritiated

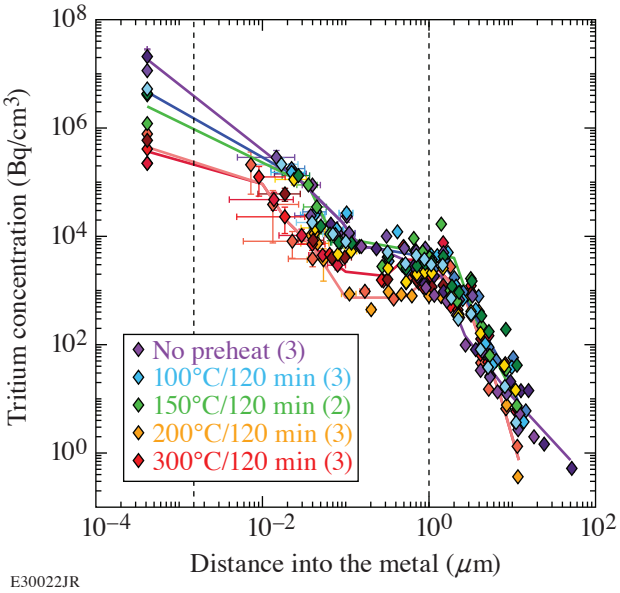

Figure 1
Tritium concentration profiles in the near surface of SS316 samples. Five preheating conditions are shown: no heating (purple), 100°C (blue), 150°C (green), 200°C (orange), and 300°C (red). Vertical dashed lines indicate different regions of the sample: surface (<1 nm), near-surface (<1 μm), and bulk (>1 μm). Each preheating condition was repeated with different SS316 samples that were exposed to tritium at the same time.

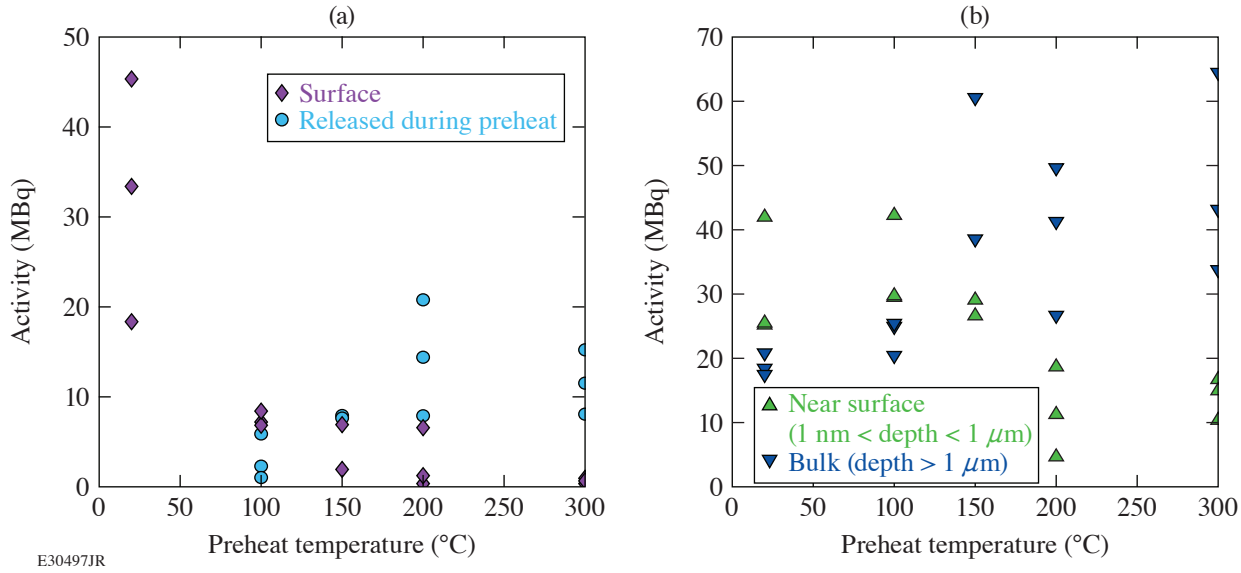

Figure 2
(a) Integrated tritium remaining on the surface and released during preheating and (b) tritium remaining in the near surface and bulk with respect to the preheating temperatures. Results from control samples are shown at 20°C.

water desorption is the primary release mechanism of tritium from SS316.[7–9] By limiting this mechanism for tritium desorption from the surface, tritium will preferentially migrate in the direction of the concentration gradient deeper into the metal.

Tritium quantities in the near surface do not appreciably change until the preheat temperature reaches 200°C (Fig. 1). These results indicate that a minimum temperature of 200°C is required to trigger near-surface tritium mobility for migration deeper into the substrate or desorption from the surface. Previous work has also demonstrated that heating SS316 to at least 200°C is required for the onset of desorption.[10,11] The increase in migration above 200°C indicates that tritium immediately below the surface is not bound at octahedral sites. The depletion of the near surface tritium and the increased desorbed tritium quantities by heating to 200°C suggests that tritium is bound in a hydrated iron (III) oxide: FeO(OH). Such binding explains three observations: First, hydrogen isotopes can be bound strongly to oxygen impurities in metals. Korzhavyi and Sandström used a density functional

theory calculation to simulate hydrogen interacting with an oxygen defect in copper.[12] Their results show a fourfold increase in the binding energy, as compared to a site without oxygen. Assuming oxygen in stainless steel has a similar effect, such deep trap states may explain the observed lack of tritium migration during the lengthy storage periods. Second, dehydration of hydrated iron (III) oxide occurs at 200°C (Ref. 13). Because tritium would be bound in the hydrate, dehydration would remove tritium from the near-surface region. Finally, dehydration may supply the oxygen and hydrogen/tritium necessary for tritiated water desorption from the surface. In this scenario, the primary pathway for tritium desorption is present even for dry inert gas atmospheres: the metal effectively supplies the water molecules for desorption.

The effect of heat treatments on the tritium distribution in SS316 samples was measured. It was found that the heating causes tritium to migrate both out of the sample and deeper into the bulk of the material. Tritium preferentially migrates deeper into the metal for temperatures less than 200°C, with very little desorbing from the surface. On reaching 200°C or above, dehydration of the hydrated iron (III) oxide occurs. The dehydration process reduces the tritium inventory in the near surface by allowing tritium to either desorb from the surface as tritiated water or diffuse deeper into the metal.

This material is based upon work supported by the Department of Energy National Nuclear Security Administration under Award Number DE-NA0003856, the University of Rochester, and the New York State Energy Research and Development Authority.

1. M. Nishikawa *et al.*, J. Nucl. Mater. **277**, 99 (2000).
2. A. Perevezentsev *et al.*, Fusion Sci. Technol. **41**, 746 (2002).
3. M. D. Sharpe *et al.*, Fusion Eng. Des. **130**, 76 (2018).
4. M. Sharpe, C. Fagan, and W. T. Shmayda, Fusion Sci. Technol. **75**, 1053 (2019).
5. A. N. Perevezentsev *et al.*, Fusion Sci. Technol. **52**, 84 (2007).
6. S. Rosanvallon *et al.*, Fusion Sci. Technol. **60**, 855 (2011).
7. K. Akaishi *et al.*, J. Vac. Sci. Technol. A **26**, 321 (2008).
8. M. J. Quinlan *et al.*, Fusion Sci. Technol. **54**, 519 (2008).
9. Y. Torikai *et al.*, Fusion Sci. Technol. **41**, 736 (2002).
10. W. T. Shmayda *et al.*, Fusion Sci. Technol. **68**, 766 (2015).
11. R.-D. Penzhorn *et al.*, Fusion Sci. Technol. **64**, 45 (2013).
12. P. A. Korzhavyi and R. Sandström, Comput. Mater. Sci. **84**, 122 (2014).
13. N. N. Greenwood and A. Earnshaw, eds. *Chemistry of the Elements*, 2nd ed. (Elsevier, New York, 1997).

Effective Mass Determination in Highly Resistive GaAs by Exploiting the Influence of a Magnetic Field on Optically Excited Transient THz Surface Emissions

G. Chen,[1,2] D. Chakraborty,[1,2] J. Cheng,[1,2] M. Mikulics,[3] C. Chimera,[4] I. Komissarov,[4] R. Adam,[5] D. E. Bürgler,[5] C. M. Schneider,[5,6] H. Hardtdegen,[3] and R. Sobolewski[1,2,4]

[1]Laboratory for Laser Energetics, University of Rochester
[2]Materials Science Graduate Program, University of Rochester
[3]Research Centre Jülich, Ernst Ruska Centre for Microscopy and Spectroscopy with Electrons, Germany
[4]Department of Electrical and Computer Engineering, University of Rochester
[5]Research Centre Jülich, Peter Grünberg Institute (PGI-6), Germany
[6]Department of Physics, University of California Davis

Generating broadband, free-space terahertz transients by pumping the surface of a semiconductor with femtosecond optical laser pulses is a well-established technique, generally called THz surface emission.[1] Several radiation models have been proposed to explain the THz surface emission such as surface depletion created by the internal electric field perpendicular to the sample surface,[2–5] nonlinear optical rectification,[6,7] and photocurrent generated by the photo-Dember effect.[8–10] It was also demonstrated that an external magnetic field applied in the plane of a semiconductor can tune the amplitude of the surface-emitted THz radiation. The enhancement of the THz amplitude was ascribed to the Lorentz force, induced by the applied magnetic field, which introduced an additional acceleration to the photocarriers.[11,12] Time-domain, nonequilibrium carrier relaxation dynamics can be characterized by an optical pump–probe spectroscopy technique,[13] which allows one to further analyze how the Lorentz force affects photocarriers and to determine the relationship between the THz transient amplitude enhancement and the semiconductor carrier mobility.

For these studies, five different, highly resistive (111)-oriented GaAs samples characterized by different mobilities and crystalline conditions were used. Namely, a standard semi-insulating GaAs wafer (SI GaAs), a semi-insulating GaAs wafer annealed at 300°C (annealed GaAs), and three nitrogen-ion–implanted GaAs specimens, implanted at an energy of 191 keV with a dose of $\sim 8 \times 10^{11}$ ions/cm^2 (Refs. 14 and 15), and, subsequently, annealed at 300°C, 350°C, and 400°C, denoted as N-GaAs 300, N-GaAs 350, and N-GaAs 400, respectively.

Experiments were performed using THz time-domain spectroscopy (THz-TDS) and optical femtosecond pump–probe spectroscopy (F-PPS). In both cases, a commercial Ti:sapphire laser that generated a train of nominal, 100-fs-wide laser pulses at 800-nm wavelength and 76-MHz repetition rate was used. In the THz-TDS setup,[16] the laser beam was split into two branches with a 90:10 power ratio. The high-power branch, after bouncing from a retroreflector mounted on a delay stage, was focused on our test GaAs sample to generate bursts of electromagnetic radiation, i.e., single-picosecond transients with the frequency spectrum extending into THz, while the low-power branch was used for the THz transient detection and focused on a commercial low-temperature–grown GaAs photoconductive (PC) THz detector with z-axis polarization sensitivity (perpendicular to the optical table).[17] A 5-mm-diam and ~10-mm-focal-length Teflon™ (polytetrafluoroethylene) lens, located between the test sample and the THz detector, collimated the transmitted THz radiation. In addition, an external magnetic field **B** was applied in the sample plane along the x axis, while the surface-emitted THz radiation was collected along the y direction, as indicated in Fig. 1. The F-PPS system was implemented to measure the nonequilibrium carrier dynamics in the samples. In this setup[18,19] optical pulses were split into two beams by a 60/40 beam splitter. Pump pulses had the higher power, and the beam was modulated with an acousto-optic modulator. The lower-power probe beam was delayed with respect to the pump by reflection from a retroreflector

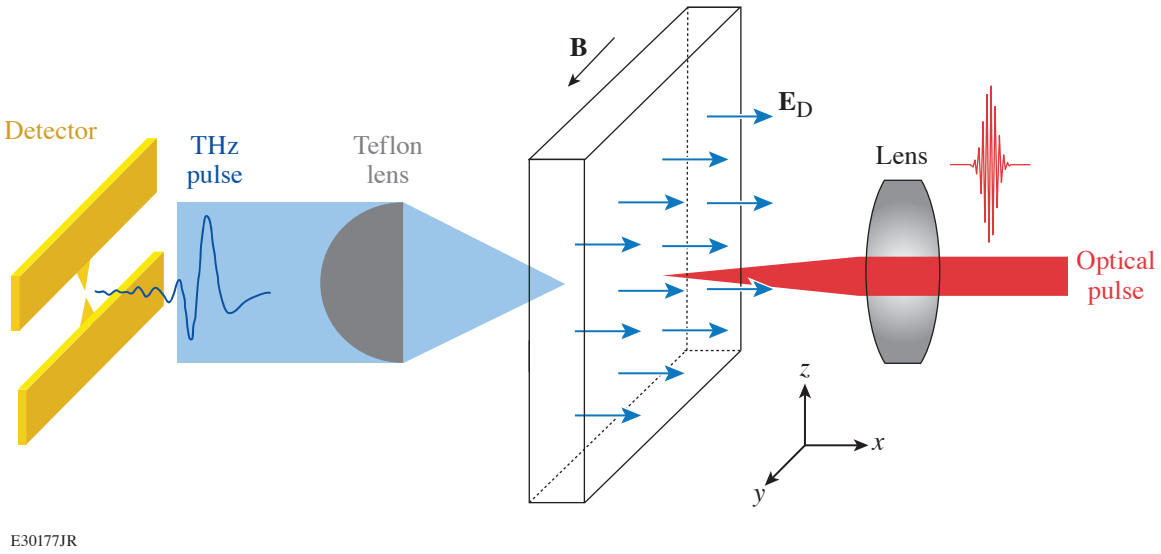

Figure 1
Schematics of the basic experimental geometry. The surface of the sample is parallel to the x–z plane. The built-in depletion electric field $\mathbf{E}_D$ is along the y axis and perpendicular to the sample surface. A lens is used to focus a laser beam at the surface of the sample, and a Teflon lens placed after the sample collimates the emitted THz radiation toward a PC THz detector aligned in such a way that it can only sense the z component of the THz transient. An external magnetic field applied along the x axis was used in the **B**-field enhancement experiments.

mounted on a delay stage. Both pump and probe beams were focused on the same spot of the sample; the beam size of the probe (~20 μm in diameter) was kept slightly smaller than that of the pump beam (~30 μm in diameter) to ensure probing only the optically excited area of the sample. To limit the probe-related electron heating to a minimum and to ensure a decent signal-to-noise ratio, the power ratio of the pump to probe beams was set to ~10:1. The probe beam was reflected at the sample surface and directed toward a photodetector connected to a lock-in amplifier to record the normalized reflectivity change ($\Delta R/R$) waveforms as a function of the time delay between the pump and probe pulses.

Figure 2 shows the dependence $k = (q/m^*)\tau_1$, where q is the elementary charge, m^* is the electron effective mass, and τ_1 is the relaxation time, for all five types of GaAs samples (black circles) and reveals a universal linear relationship (black solid line). This indicates that τ_1, derived based on the Drude model, is the trapping time for the samples. During this time, the Lorentz force accelerates electrons before they get trapped by defect states. Therefore, a high density of defects/traps in a semiconductor, e.g., in case of the N-GaAs samples, leads to a shorter carrier lifetime, which, in turn, limits the impact of the magnetic field on the THz transient.

The next important conclusion from Fig. 2 is that within the linear fit, the effective mass $m^* = q/(k/\tau_1)$ for all samples is exactly the same and the extracted value is $m^*/m_0 = 0.059$ (m_0 is the electron mass), which is close to the accepted value of 0.063 for GaAs single crystals,[20] and illustrated by the dashed line corresponding to the k dependence for $m^*/m_0 = 0.063$. The latter is an interesting result and shows that despite the large differences in the crystallinity of the test samples, the effective mass derived from our magnetic-field experiments remains constant and very close to the effective mass of electrons in GaAs with a perfect crystalline structure. The only deviation from the ideal m^* value observed was for the annealed GaAs sample. Contrary to the other samples, the clear distinction between trapping and recombination processes is somewhat difficult to establish.

In conclusion, we exhaustively analyzed the transient emission of THz signals, emitted from highly resistive GaAs samples with different crystallinity, excited by femtosecond optical pulses. The observed magnetic field impacted the THz transient generation, and the corresponding enhancement factor was directly proportional to the applied **B** field. Interestingly, the slope of the enhancement factor dependence was directly proportional to the samples' nonequilibrium trapping time measured using

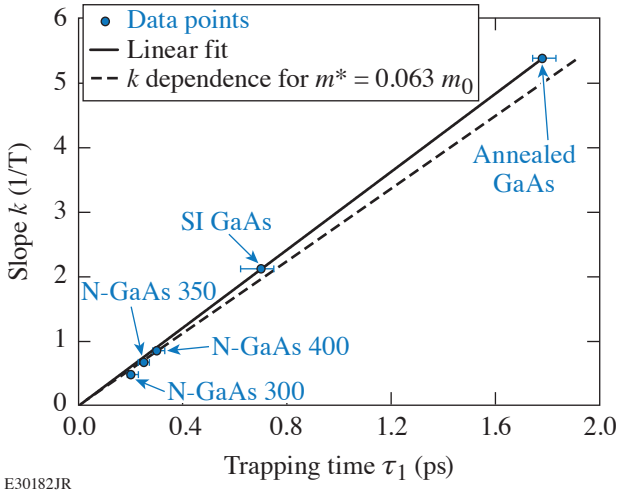

Figure 2
Dependence of the slope k on the trapping time τ_1. The circles are experimental data, and the black line is the best linear fit yielding $m^*/m_0 = 0.059$. The dashed line corresponds to the k dependence for the literature $m^*/m_0 = 0.063$.

femtosecond optical pump–probe spectroscopy. The latter enabled the determination of the electron effective mass $m^*/m_0 = 0.059$ that was very close to the literature m^* value for GaAs single crystals. The latter reveals that GaAs samples with very different crystallinity, including highly defected, N-implanted samples, all have an m^* value essentially equal to that of the ideal crystal.

This material is based upon work that was supported in Rochester in part by the National Science Foundation Grant Number 1842712. The work at the Research Center Jülich was performed within JuSPARC (Jülich Short-pulse Particle Acceleration and Radiation Center), a strategy project funded by the Federal Ministry of Education and Research (Bundesministerium für Bildung und Forschung).

1. X.-C. Zhang *et al.*, Appl. Phys. Lett. **56**, 1011 (1990).
2. X.-C. Zhang and D. H. Auston, J. Appl. Phys. **71**, 326 (1992).
3. R. Kersting *et al.*, Phys. Rev. B **58**, 4553 (1998).
4. J. N. Heyman *et al.*, Phys. Rev. B **64**, 085202 (2001).
5. J. S. Hwang *et al.*, Appl. Phys. Lett. **87**, 121107 (2005).
6. S. L. Chuang *et al.*, Phys. Rev. Lett. **68**, 102 (1992).
7. M. Reid, I. V. Cravetchi, and R. Fedosejevs, Phys. Rev. B **72**, 035201 (2005).
8. K. Liu *et al.*, Phys. Rev. B **73**, 155330 (2006).
9. R. Mendis *et al.*, J. Appl. Phys. **98**, 126104 (2005).
10. A. Reklaitis, J. Appl. Phys. **108**, 053102 (2010).
11. X.-C. Zhang *et al.*, Appl. Phys. Lett. **62**, 2003 (1993).
12. C. Weiss, R. Wallenstein, and R. Beigang, Appl. Phys. Lett. **77**, 4160 (2000).
13. A. Othonos, J. Appl. Phys. **83**, 1789 (1998); **84**, 1708(E) (1998).
14. M. Mikulics *et al.*, Appl. Phys. Lett. **87**, 041106 (2005).
15. M. Mikulics *et al.*, Appl. Phys. Lett. **88**, 041118 (2006).
16. R. Adam *et al.*, Appl. Phys. Lett. **114**, 212405 (2019).
17. A. Geižutis *et al.*, Opt. Mater. **30**, 786 (2008).
18. J. Zhang *et al.*, J. Appl. Phys. **110**, 113112 (2011).
19. J. Serafini *et al.*, Semicond. Sci. Technol. **31**, 045006 (2016).
20. G. Margaritondo, in *Encyclopedia of Condensed Matter Physics*, edited by F. Bassani, G. L. Liedl, and P. Wyder (Elsevier, Oxford, 2005), pp. 311–321.

An Assessment of Generating Quasi-Static Magnetic Fields Using Laser-Driven "Capacitor" Coils

J. L. Peebles, J. R. Davies, D. H. Barnak, F. Garcia-Rubio, P. V. Heuer, G. Brent, R. Spielman, and R. Betti

Laboratory for Laser Energetics, University of Rochester

Over the previous decade, numerous experiments have been performed using a laser to drive a strong, quasi-static magnetic field. Field strength and energy density measurements of these experiments have varied by many orders of magnitude, painting a confusing picture of the effectiveness of these laser-driven coils (LDC's) as tools for generating consistent fields. At the higher end of the field energy spectrum, kilotesla field measurements have been used to justify future experimental platforms, theoretical work, and inertial confinement fusion concepts. In this work we present the results from our own experiments designed to measure magnetic fields from LDC's as well as a review of the body of experiments that have been undertaken in this field. We demonstrate how problems with prior diagnostic analyses have led to overestimates of the magnetic fields generated from LDC's.

The first aspect of these experiments that must be addressed is conversion of laser energy to magnetic-field energy. While it is easy to claim results are feasible as long as energy in the magnetic field is less than the energy in the driving laser, the reality is that no laser experiment has a significant amount of free energy to generate a magnetic field. For certain experiments, the total laser absorption can be as high as 90%, but for the majority of experiments using drivers similar to those in most LDC experiments, it is much lower (50%). Hot-electron production is a potential source of free energy. Up to ~30% of the laser energy could be converted to hot electrons at the higher values of $I\lambda^2$ used.[1] For the parameters of most LDC experiments with lower $I\lambda^2$, however, a smaller percentage of the laser energy would be converted into hot electrons.[2] When considering that all the potential energy sinks for this conversion, at most half the energy put into hot electrons can be converted to current. Therefore, a physically reasonable upper limit on laser-energy conversion to magnetic energy would appear to be 15% and, in most cases, should be much less. Examining each LDC experiment's energy conversion by integrating the field energy density ($B^2/2\mu_0$) over a $10 \times 10 \times 10$-mm^3 volume produces the results in Fig. 1.[3–15]

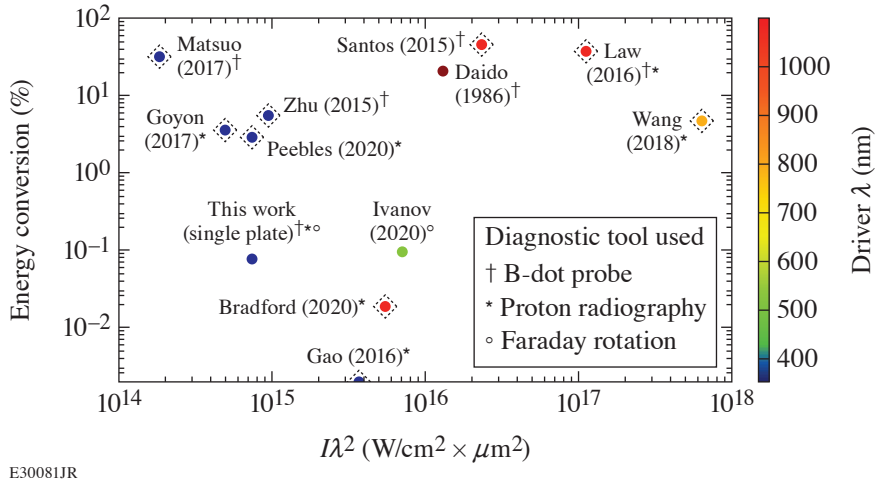

Figure 1
The calculated energy conversion from laser energy to field energy for the variety of LDC experiments.[3–15] Superscripts denote the diagnostic tool used to arrive at the result, while dotted diamonds around a shot indicate the presence of a short-pulse beam on the experiment. Experiments with conversion over 10% stand out because they have suspiciously high energy conversion.

Looking at the body of experiments, a trend emerges: several experiments measured fields that contained energy equal to 30%–40% of the energy of the driving laser. These experiments also coincidentally measured the primary result using the B-dot while a short-pulse, high-intensity laser was present. This is highly indicative that the B-dot probe responds differently to these experiments than other diagnostics. To address this, we performed our own experiments with LDC's using the entire battery of magnetic-field diagnostics: axial and transverse proton probing, Faraday rotation, and B-dot probes, as shown in Fig. 2. Two types of coils were tested to examine the effect of having the second plate on the target and were driven by a 1-ns, up-to-1.25-kJ, long-pulse UV beam.

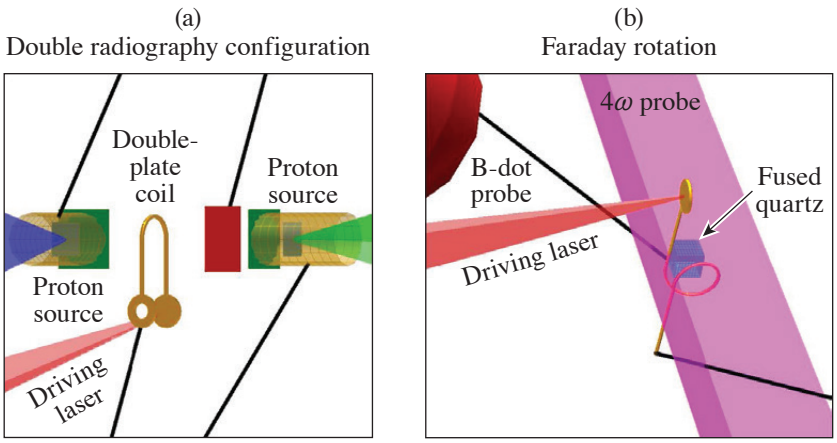

Figure 2
Experimental platform used to study the fields generated by LDC targets using a battery of diagnostics. (a) One campaign used both the sidelighter and backlighter beams to simultaneously probe the coil transverse and axially with protons. (b) A setup used the 4ω probe with a piece of fused quartz for Faraday rotation (polarimetry). All experiments had a B-dot probe placed roughly 2 cm from the loop attached to a 6-GHz-bandwidth balun and scope.

Several results from our experiments are shown in Fig. 3. A 40-T reference magnetic field was generated by MIFEDS (magneto-inertial fusion electrical discharge system) and probed by the axial proton probe [Fig. 3(a)]. As protons travel through the magnetic field, a secondary deflection from the radial magnetic field induces a rotation of the reference mesh. This rotation increases with field strength and decreases with proton energy. The same proton probe was applied to our LDC's and produced no measurable rotation. This indicates that the magnetic field in the LDC is below the measurement threshold (20 kA in the coil) for the axial probe. Using the more-sensitive transverse proton probe on the LDC produces a bulge near the top of the LDC, indicative of a small current of 2.5 kA. This current is far below that measured by most of the experiments shown in Fig. 1 and indicates a much poorer laser-to-field-energy conversion ratio.

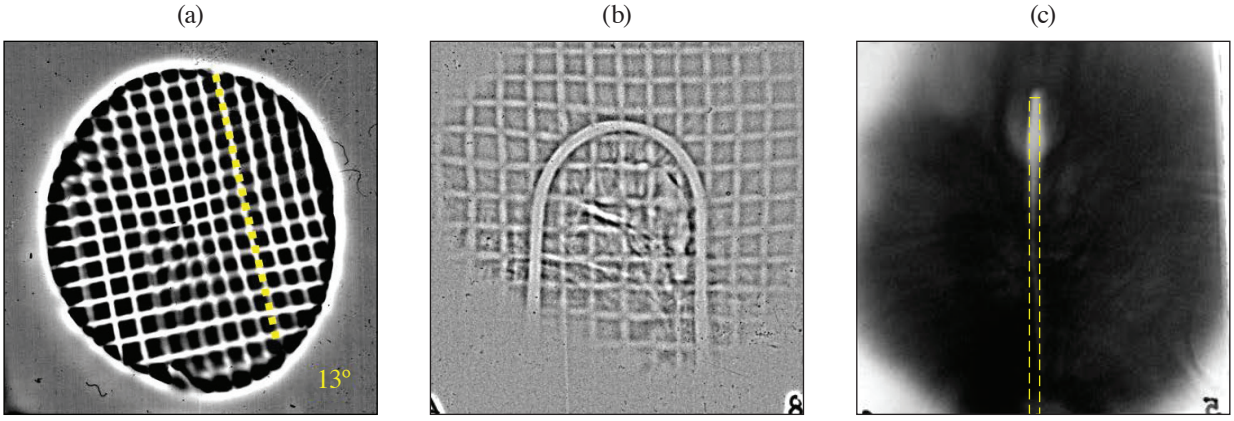

Figure 3
Axial proton probes of a known magnetic field generated by (a) MIFEDS and (b) a double-plate LDC. In (a) MIFEDS generated a 40-T field that induced an apparent rotation of the mesh fiducial dependent on the proton energy. This diagnostic technique is sensitive to fields generated by currents greater than 20 kA. In (b) no such rotation is measured, indicating that any current must be less than 20 kA. (c) A transverse proton probe of the same LDC shows a slight bulge near the top of the coil, indicating a current of ~2.5 kA.

Supplementing the proton radiography measurements were the Faraday rotation and B-dot probe diagnostics. Faraday rotation measures the magnetic field in a medium by comparing the rotation difference between orthogonal polarizations as they pass through the medium in the presence of a magnetic field. In the case of our LDC experiment, no significant rotation was measured in the two polarizations of the 4ω probe. The error in the measurement between the two polarizations is ±2%, which corresponds to a measurement limit of a 7.5-kA current in our coil, consistent with a 2.5-kA measurement of the proton probe. The B-dot probe acquired measurements in all experimental configurations, both with and without the short-pulse beams. When comparing the data in Fig. 4 it is clear that the B-dot probe is heavily influenced by the presence of the short-pulse beam. Since the short pulse-beams were timed 1 ns after the long-pulse drive beam in order to probe the interaction after the drive, the signal contributions between the two types of beams can be differentiated on the scope. When we account for the scope and cable attenuation based on assumed signal frequency, the signal from the long-pulse beam implies a current of 62.5 kA, much higher than all other diagnostics. The signal from the short pulse is roughly an order of magnitude higher than that of the long pulse, implying a very unrealistic current of over 600 kA.

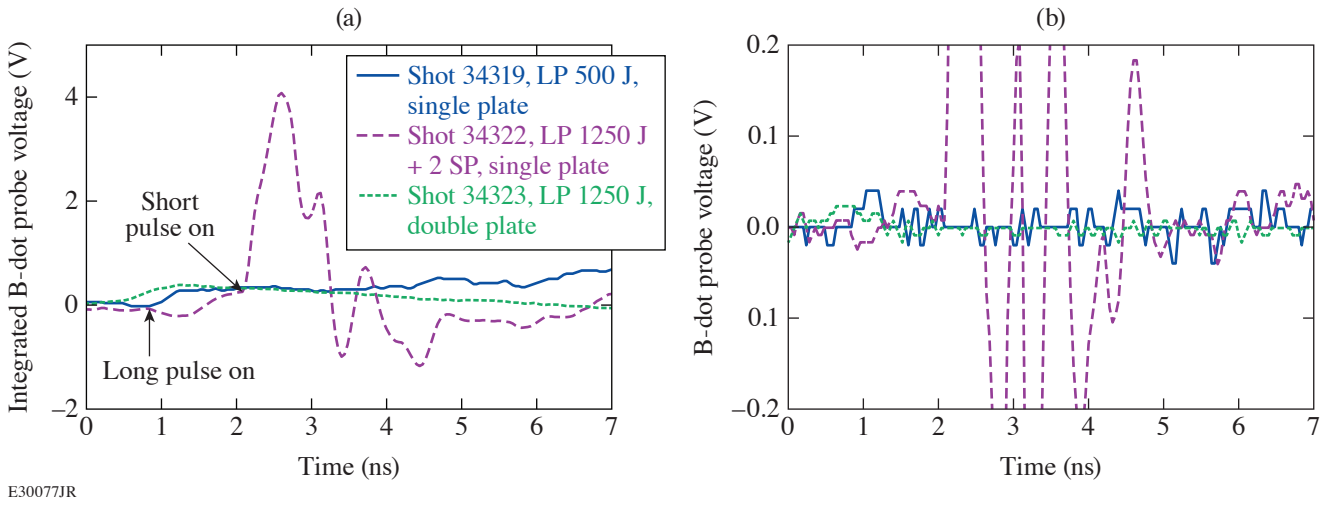

Figure 4

(a) Integrated B-dot probe signals for three different shots: two without short-pulse beams with different coil types and one with the short-pulse beams. The signal with the short-pulse beams is over 10× higher (4 V compared to 0.34 V) than that of the long-pulse beam drive only. The spike in signal from the short pulse is delayed compared to the long pulse due to the beam timings used on the experiment and time of flight from target to B-dot probe. (b) Raw data for the same shots, demonstrating the poor signal-to-noise ratio on the experiments without the short pulse. The signal is varying as quickly as the diagnostic can measure, indicating that the majority of signal is oscillating faster than 6 GHz.

While a B-dot probe (with differentiation) is designed in theory to measure only a changing magnetic field, in reality the entire probe and cabling is subject to effects that are not completely neutralized, such as capacitive coupling, where electric fields can induce significant voltage. The signal generated on the B-dot probe by the short-pulse beam clearly indicates current that is unphysical from a conservation of energy perspective; however, this effect explains the conclusions of many previous LDC experiments shown in Fig. 1. The "highest performing" experiments also utilized a B-dot probe in conjunction with proton radiography using a short-pulse, high-intensity beam. Similar to our experiment, other diagnostics (proton radiography or Faraday rotation) typically indicated field values far lower than the B-dot probe; however, in most of these experiments the B-dot probe result is given preference because of its larger value, despite the poorer accuracy of the method. When we account for this short-pulse interference of the B-dot probe, the majority of results fall into more-reasonable energy conversion ratios of, at most, a few percent.

We began experiments on laser-driven coils to develop a consistent platform for applying and measuring external magnetization of an experiment. In some regards we were successful: a field was measured that was relatively consistent across all diagnostics; however, the field values we measured departed severely from those in other publications. These experiments comprehensively demonstrated that laser-driven coils are not well described by a circuit or capacitor model nor do they produce

uniform consistent fields. Our experiments at best could convert less than a percent of driving laser energy into the magnetic field at the coil, far less than the optimistic conclusions of other experiments. B-dot probes and Faraday rotation were found to be ineffective at measuring magnetic fields in our higher-power LDC experiments because they were subject to the extreme radiation and electric-field environment. Proton radiography produced a precise and detailed picture of electrostatic and magnetic fields around the LDC, but a higher degree of confidence in our conclusions drawn from radiographs was obtained only by probing in two directions simultaneously.

This material is based upon work supported by the Department of Energy National Nuclear Security Administration under Award Numbers DE-NA0003856 and DE-NA0003868, the Office of Fusion Energy Sciences Award Number DE-SC0021072, the University of Rochester, and the New York State Energy Research and Development Authority.

1. J. R. Davies, Plasma Phys. Control. Fusion **51**, 014006 (2009).
2. C. Garban-Labaune *et al.*, Phys. Rev. Lett. **48**, 1018 (1982).
3. H. Daido *et al.*, Phys. Rev. Lett. **56**, 846 (1986).
4. J. J. Santos *et al.*, New J. Phys. **17**, 083051 (2015).
5. K. F. F. Law *et al.*, Appl. Phys. Lett. **108**, 091104 (2016).
6. C. Courtois *et al.*, J. Appl. Phys. **98**, 054913 (2005).
7. A. Tarifeño, C. Pavez, and L. Soto, J. Phys.: Conf. Ser. **134**, 012048 (2008).
8. L. Gao *et al.*, Phys. Plasmas **23**, 043106 (2016).
9. C. Goyon *et al.*, Phys. Rev. E **95**, 033208 (2017).
10. W. Wang *et al.*, Phys. Plasmas **25**, 083111 (2018).
11. B. J. Zhu *et al.*, Appl. Phys. Lett. **107**, 261903 (2015).
12. K. Matsuo *et al.*, Phys. Rev. E **95**, 053204 (2017).
13. V. V. Ivanov *et al.*, Phys. Plasmas **27**, 033102 (2020).
14. P. Bradford *et al.*, High Power Laser Sci. Eng. **8**, e11 (2020).
15. J. L. Peebles *et al.*, Phys. Plasmas **27**, 063109 (2020).

Pulsed-Power Innovations for Next-Generation, High-Current Drivers

R. B. Spielman

Laboratory for Laser Energetics, University of Rochester

Recent proposals to build larger high-current drivers to be used for high-energy-density physics, inertial confinement fusion, radiation effects testing, and basic science will present challenges.[1] Drivers significantly larger than the Z Machine at Sandia National Laboratories encounter increasing difficulties in water power flow, insulator performance, and vacuum power flow. The physics requirements of imploding loads limit a designer's flexibility in choosing machine parameters such as current rise time, driving impedance, and total inductance. This summary enumerates these physics constraints and shows how they impact driver design. This leads to the conclusion that advances in pulsed-power understanding and pulsed-power capabilities are needed to control risk and to build a cost-effective driver at peak currents of ~60 MA.

The Z machine, driving an imploding load, requires a peak insulator voltage of ~4 MV while delivering up to 25 MA to the load.[2] The current rise time is ~100 to 110 ns and the overall implosion times are 100 ns to 120 ns (Refs. 3–5). Scaling Z today at 25 MA to a new next-generation pulsed-power facility (NGPPF) at 60 MA requires that the driving voltage scale proportionally with the increased peak current (other parameters held constant). This results in a driver with a peak voltage at least ~2.4× larger than Z.[6,7] These scaled voltages will exist at all locations in the driver for all times during the pulse. This summary describes the physics constraints on driver parameters, discusses the pulsed-power impact on the pulsed-power design, and finally asks if advances in pulsed-power physics understanding and pulsed-power engineering can reduce the risk and cost of an NGPP driver.

Magneto-Rayleigh–Taylor (MRT) physics drives *Z*-pinch drivers to implosions times of 100 ns or less.[2,8,9] In the case of an NGPPF driver, implosion quality is paramount. It becomes difficult to justify a significant increase in the implosion time (current rise time) to reduce the voltage (and power) risk beyond 100 ns unless MRT can be stabilized to some extent.

Electrical coupling efficiency to the load is a huge part of driver optimization. Simplistically, the electrical coupling (to stored magnetic energy) is optimized when $L/Zt \sim 1$, where L is the total inductance of the load, Z is the impedance of the driver, and t is the rise time of the current. Given from MRT consideration that the current rise time t is constrained, we see that increases in the load inductance L must be accompanied by an increase in driver impedance Z. However, the coupling efficiency to the load is $\sim\Delta L/L$, where ΔL is the change in inductance due to the dynamic load and L here is the total final inductance. For a convergence ratio of ~10:1, the change in inductance of a 2-cm-long load is ~9.4 nH. We see that coupling to the load is optimized for lower total inductances. As a result, the overall coupling efficiency from available driver energy drives us to a lower inductance and lower impedance driver. The driver inductance and impedance are not free parameters.

Higher-voltage NGPP drivers force larger gaps in the water section of any driver because, for a voltage rise time of ~100 ns, the threshold for electrical discharges in water is 300 kV/cm. The only ways to increase the gap in the water section near the load are to increase the radius of the insulator stack (height scales with radius at constant impedance) and increase the impedance of the water lines. Both of these approaches will be required.

The largest-diameter parts that can be built and shipped across the country are roughly 6 m in diameter. With this assumption, the only additional way to increase the driver voltage is by using multiple levels of insulators and magnetically insulated

transmission lines (MITL's). (See Fig. 1 for a four-level example.) The key advantage of increasing the number of MITL levels is an increase in the water transmission-line gap for a given insulator stack radius because the levels are driven in parallel. A secondary impact is the paralleling of the MITL inductances at the post-hole convolute. Inductance is a secondary impact because the reduced current per MITL level forces an increase in MITL inductance to hold the electron vacuum flow nearly constant. The number of MITL levels and the insulator stack radius effectively determine the maximum current for a given design.

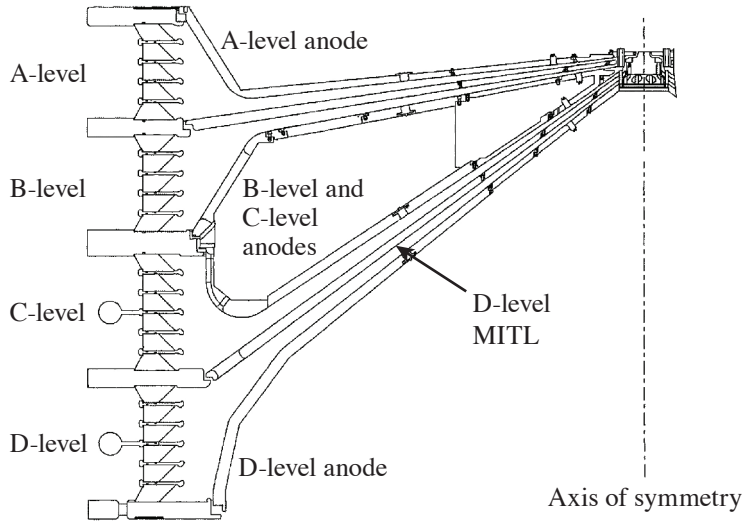

Figure 1
Schematic of a double-disk MITL that shows the insulator stack, the vacuum flare region, the MITL's, the post-hole convolute, the inner disk MITL, and the load region.

An impedance of $Z = 6.67\ h/r\ \Omega$ per level for a four-level MITL is used to estimate the peak current of a Z machine–like design. One potential design impedance is 0.180 Ω, so the individual level impedance is now increased to 0.72 Ω. This results in a water-transmission line gap of 32.4 cm at a radius of 3 m. Following the arguments of maximum electric field above, the peak allowed voltage is ~4.8 MV and the peak current is ~50 MA. Higher-current drivers will require a larger-radius insulator stack, a higher driving impedance, and/or more MITL levels.

The increased voltage on NGPPF (everywhere and at all times) will create difficulties in pulsed-power design and result in increased current losses and reduced coupling efficiency to dynamic loads. Mitigating losses by increasing physical gap results in an increase in inductance that reduces peak current and decreases coupling efficiency. Further increases in driving voltage are required to obtain the design load current. This is a strong feedback effect that can limit the overall magnitude of a potential NGPP driver. Kinetic energy delivered to a relevant load becomes the key metric for comparing various driver designs. It is possible to design a pulsed-power driver that achieves 60 MA at the load that couples insufficient energy to a dynamic load.

It is likely that there is an effective limit to the peak current and kinetic energy of a pulsed-power driver that is based on cost, shot rate, and programmatic impact. A 60-MA-class driver can be built but such a driver, based on today's pulsed-power understanding, will be costly and inefficient.

This material is based upon work supported by the Department of Energy National Nuclear Security Administration under Award Number DE-NA0003856, the University of Rochester, the New York State Energy Research and Development Authority.

1. D. B. Sinars *et al.*, Phys. Plasmas **27**, 070501 (2020).
2. T. W. Hussey and N. F. Roderick, Phys. Fluids **24**, 1384 (1981).
3. E. A. Weinbrecht *et al.*, in *2005 IEEE Pulsed Power Conference*, edited by J. Maenchen and E. Schamiloglu (IEEE, Monterey, CA, 2005), pp. 170–173.

4. M. E. Savage *et al.*, in *16th IEEE International Pulsed Power Conference*, edited by E. Schamiloglu and F. Peterkin (IEEE, New York, 2007), Vol. 2, pp. 979–984.
5. M. E. Savage *et al.*, in 2011 IEEE Pulsed Power Conference, edited by R. P. Joshi (IEEE, Piscataway, NJ, 2011), pp. 983–990.
6. W. A. Stygar *et al.*, Phys. Rev. Spec. Top., Accel. Beams **10**, 030401 (2007).
7. W. A. Stygar *et al.*, Phys. Rev. ST Accel. Beams **18**, 110401 (2015).
8. N. F. Roderick and T. W. Hussey, J. Appl. Phys. **56**, 1387 (1984).
9. T. W. Hussey *et al.*, Phys. Plasmas **2**, 2055 (1995).

FY22 Q2 Laser Facility Report

J. Puth, M. Labuzeta, D. Canning, and R. T. Janezic

Laboratory for Laser Energetics, University of Rochester

During the second quarter of FY22, the Omega Facility conducted 322 target shots on OMEGA and 238 target shots on OMEGA EP for a total of 570 target shots (see Tables I and II). OMEGA averaged 9.9 target shots per operating day, averaging 90.8% Availability and 95.6% Experimental Effectiveness. OMEGA EP averaged 8.8 target shots per operating day, averaging 94.8% Availability and 96.9% Experimental Effectiveness.

Table I: OMEGA Laser System target shot summary for Q2 FY22.

Program	Laboratory	Planned Number of Target Shots	Actual Number of Target Shots
ICF	LLE	110	111
	LANL	11	12
	SNL	11	8
ICF Subtotal		132	131
HED	LLE	33	25
	LANL	22	27
	LLNL	55	43
	SNL	11	11
HED Subtotal		121	106
LBS	LLE	22	18
	LLNL	27.5	29
LBS Subtotal		49.5	47
NLUF		22	23
Calibration		0	25
Grand Total		324.5	332

NLUF: National Laser Users Facility

Table II: OMEGA EP Laser System target shot summary for Q2 FY22.

Program	Laboratory	Planned Number of Target Shots	Actual Number of Target Shots
ICF	LLE	24.5	38
	LLNL	14	11
ICF Subtotal		38.5	49
HED	LLE	7	7
	LANL	14	16
	LLNL	28	29
HED Subtotal		49	52
LBS	LLE	14	22
	LLNL	14	23
LBS Subtotal		28	45
CMAP		14	16
LaserNetUS		14	18
NLUF		28	38
Calibration	LLE	0	20
Grand Total		171.5	238

CMAP: Center for Matter at Atomic Pressures

Publications and Conference Presentations

Publications

C. H. Allen, M. Oliver, L. Divol, O. L. Landen, Y. Ping, M. Scholmerich, R. Wallace, R. Earley, W. Theobald, T. G. White, and T. Döppner, "Toward an Integrated Platform for Characterizing Laser-Driven, Isochorically Heated Plasmas with 1 mm Spatial Resolution," Appl. Opt. **61**, 1987 (2022).

P. T. Campbell, C. A. Walsh, B. K. Russell, J. P. Chittenden, A. Crilly, G. Fiksel, L. Gao, I. V. Igumenshchev, P. M. Nilson, A. G. R. Thomas, K. Krushelnick, and L. Willingale, "Measuring Magnetic Flux Suppression in High-Power Laser-Plasma Interactions," Phys. Plasmas **29**, 012701 (2022).

T. J. B. Collins, C. Stoeckl, R. Epstein, W. A. Bittle, C. J. Forrest, V. Yu. Glebov, V. N. Goncharov, D. R. Harding, S. X. Hu, D. W. Jacobs-Perkins, T. Z. Kosc, J. A. Marozas, C. Mileham, F. J. Marshall, S. F. B. Morse, P. B. Radha, S. P. Regan, B. Rice, T. C. Sangster, M. J. Shoup III, W. T. Shmayda, C. Sorce, W. Theobald, and M. D. Wittman, "Causes of Fuel–Ablator Mix Inferred from Modeling of Monochromatic Time-Gated Radiography of OMEGA Cryogenic Implosions," Phys. Plasmas **29**, 012702 (2022).

C. Dorrer and M. Spilatro, "Spectral and Temporal Shaping of Spectrally Incoherent Pulses in the Infrared and Ultraviolet," Opt. Express **30**, 4942 (2022).

M. Formanek, D. Ramsey, J. P. Palastro, and A. Di Piazza, "Radiation Reaction Enhancement in Flying Focus Pulses," Phys. Rev. A **105**, L020203 (2022).

A. M. Hansen, K. L. Nguyen, D. Turnbull, B. J. Albright, R. K. Follett, R. Huff, J. Katz, D. Mastrosimone, A. L. Milder, L. Yin, J. P. Palastro, and D. H. Froula, "Cross-Beam Energy Transfer Saturation: Ion Heating and Pump Depletion," Plasma Phys. Control. Fusion **64**, 034003 (2022).

G. W. Jenkins, C. Feng, and J. Bromage, "Energy Scaling Beyond the Gas Ionization Threshold with Divided-Pulse Nonlinear Compression," Opt. Lett. **47**, 1450 (2022).

V. V. Karasiev, D. I. Mihaylov, and S. X. Hu, "Meta-GGA Exchange-Correlation Free Energy Density Functional to Increase the Accuracy of Warm Dense Matter Simulations," Phys. Rev. B **105**, L081109 (2022).

M. F. Kasim, D. Watson-Parris, L. Deaconu, S. Oliver, P. Hatfield, D. H. Froula, G. Gregori, M. Jarvis, S. Khatiwala, J. Korenaga, J. Topp-Mugglestone, E. Viezzer, and S. M. Vinko, "Building High Accuracy Emulators for Scientific Simulations with Deep Neural Architecture Search," Mach. Learn.: Sci. Technol. **3**, 015013 (2022).

R. G. Kraus, R. J. Hemley, S. J. Ali, J. L. Belof, L. X. Benedict, J. Bernier, D. Braun, R. E. Cohen, G. W. Collins, F. Coppari, M. P. Desjarlais, D. Fratanduono, S. Hamel, A. Krygier, A. Lazicki, J. Mcnaney, M. Millot, P. C. Myint, M. G. Newman, J. R. Rygg, D. M. Sterbentz, S. T. Stewart, L. Stixrude, D. C. Swift, C. Wehrenberg, and J. H. Eggert, "Measuring the Melting Curve of Iron at Super-Earth Core Conditions," Science **375**, 202 (2022).

M. C. Marshall, M. G. Gorman, D. N. Polsin, J. H. Eggert, M. K. Ginnane, J. R. Rygg, G. W. Collins, and L. D. Leininger, "Diamond Formation in Double-Shocked Epoxy to 150 GPa," J. Appl. Phys. **131**, 085904 (2022).

J. Meinecke, P. Tzeferacos, J. S. Ross, A. F. A. Bott, S. Feister, H.-S. Park, A. R. Bell, R. Blandford, R. L. Berger, R. Bingham, A. Casner, L. E. Chen, J. Foster, D. H. Froula, C. Goyon, D. Kalantar, M. Koenig, B. Lahmann, C.-K. Li, Y. Lu, C. A. J. Palmer, R. D. Petrasso, H. Poole, B. Remington, B. Reville, A. Reyes, A. Rigby, D. Ryu, G. Swadling, A. Zylstra, F. Miniati, S. Sarkar, A. A. Schekochihin, D. Q. Lamb, and G. Gregori, "Strong Suppression of Heat Conduction in a Laboratory Replica of Galaxy-Cluster Turbulent Plasmas," Sci. Adv. **8**, eabj6799 (2022).

S. F. Nwabunwanne and W. R. Donaldson, "Interdigitated Electrode Geometry Variation and External Quantum Effi-

ciency of GaN/AlGaN–Based Metal–Semiconductor–Metal UV Photodetectors," Proc. SPIE **12001**, 120010F (2022).

J. J. Pilgram, M. B. P. Adams, C. G. Constantin, P. V. Heuer, S. Ghazaryan, M. Kaloyan, R. S. Dorst, D. B. Schaeffer, P. Tzeferacos, and C. Niemann, "High Repetition Rate Exploration of the Bierman Battery Effect in Laser Produced Plasmas Over Large Spatial Regions," High Power Laser Sci. Eng. **10**, e13 (2022).

N. R. Shaffer and C. E. Starrett, "Dense Plasma Opacity via the Multiple-Scattering Method," Phys. Rev. E **105**, 015203 (2022).

T. T. Simpson, D. Ramsey, P. Franke, K. Weichman, M. V. Ambat, D. Turnbull, D. H. Froula, and J. P. Palastro, "Spatiotemporal Control of Laser Intensity Through Cross-Phase Modulation," Opt. Express **30**, 9878 (2022).

G. F. Swadling and J. Katz, "Novel Design for a Polarizing DUV Spectrometer Using a Wollaston Prism and Its Application as a Diagnostic for Measuring Thomson Scattering Data in the Presence of Strong Self-Emission Backgrounds," Rev. Sci. Instrum. **93**, 013501 (2022).

W. Theobald, D. Cao, R. C. Shah, C. A. Thomas, I. V. Igumenshchev, K. A. Bauer, R. Betti, M. J. Bonino, E. M. Campbell, A. R. Christopherson, K. Churnetski, D. H. Edgell, C. J. Forrest, J. A. Frenje, M. Gatu Johnson, V. Yu. Glebov, V. N. Goncharov, V. Gopalswamy, D. R. Harding, S. X. Hu, S. T. Ivancic, D. W. Jacobs-Perkins, R. T. Janezic, T. Joshi, J. P. Knauer, A. Lees, R. W. Luo, O. M. Mannion, F. J. Marshall, Z. L. Mohamed, S. F. B. Morse, D. Patel, J. L. Peebles, R. D. Petrasso, P. B. Radha, H. G. Rinderknecht, M. J. Rosenberg, S. Sampat, T. C. Sangster, W. T. Shmayda, C. M. Shuldberg, A. Shvydky, C. Sorce, C. Stoeckl, M. D. Wittman, and S. P. Regan, "Enhanced Laser-Energy Coupling with Small-Spot Distributed Phase Plates (SG5-650) in OMEGA DT Cryogenic Target Implosions," Phys. Plasmas **29**, 012705 (2022).

A. J. White, L. A. Collins, K. Nichols, and S. X. Hu, "Mixed Stochastic-Deterministic Time-Dependent Density Functional Theory: Application to Stopping Power of Warm Dense Carbon," J. Phys.: Condens. Matter **34**, 174001 (2022).

S. Zhang, D. E. Fratanduono, M. C. Marshall, J. R. Rygg, A. E. Lazicki, A. Shvydky, D. Haberberger, V. N. Goncharov, T. R. Boehly, G. W. Collins, and S. X. Hu, "Species Separation in Polystyrene Shock Release Evidenced by Molecular-Dynamics Simulations and Laser-Drive Experiments," Phys. Rev. Research **4**, 013126 (2022).

S. Zhang, M. A. Morales, R. Jeanloz, M. Millot, S. X. Hu, and E. Zurek, "Nature of the Bonded-to-Atomic Transition in Liquid Silica to TPa Pressures," J. Appl. Phys. **131**, 071101 (2022).

D. Zhao, R. Betti, and H. Aluie, "Scale Interactions and Anisotropy in Rayleigh–Taylor Turbulence," J. Fluid Mech. **930**, A29 (2022).

Forthcoming Publications

S.-W. Bahk, I. A. Begishev, R. Roides, C. Mileham, R. Cuffney, C. Feng, B. M. Webb, C. Jeon, M. Spilatro, S. Bucht, C. Dorrer, and J. Bromage, "Effect of the Pump Beam Profile and Wavefront on the Amplified Signal Wavefront in Optical Parametric Amplifiers," to be published in Optics Express.

A. Bose, J. Peebles, C. A. Walsh, J. A. Frenje, N. V. Kabadi, P. J. Adrian, G. D. Sutcliffe, M. Gatu Johnson, C. A. Frank, J. R. Davies, R. Betti, V. Yu. Glebov, F. J. Marshall, S. P. Regan, C. Stoeckl, E. M. Campbell, H. Sio, J. Moody, A. Crilly, B. D. Appelbe, J. P. Chittenden, S. Atzeni, F. Barbato, A. Forte, C. K. Li, F. H. Séguin, and R. D. Petrasso, "Effect of Strongly Magnetized Electrons and Ions on Heat Flow and Symmetry of Inertial Fusion Implosions," to be published in Physical Review Letters.

G. W. Jenkins, C. Feng, and J. Bromage, "Simultaneous Contrast Improvement and Temporal Compression Using Divided-Pulse Nonlinear Compression," to be published in Optics Express.

D. Kim, R. F. Smith, I. K. Ocampo, F. Coppari, M. C. Marshall, M. K. Ginnane, J. K. Wicks, S. J. Tracy, M. Millot, A. Lazicki, J. R. Rygg, J. H. Eggert, and T. S. Duffy, "Structure and Density of Silicon Carbide to 1.5 TPa and Implications for Extrasolar Planets," to be published in Nature Communications.

T. Z. Kosc, H. Huang, T. J. Kessler, and S. G. Demos, "Angular Dependence of the Transverse Raman Scattering in KDP and DKDP in Geometries Suitable for Beam Polarization Control," to be published in Optics Express.

L. S. Leal, A. V. Maximov, E. C. Hansen, J. R. Davies, D. H. Barnak, J. L. Peebles, K. M. Woo, P. V. Heuer, A. B. Sefkow, and R. Betti, "The Effect of Laser Preheat in Magnetized Liner Inertial Fusion at OMEGA," to be published in Physics of Plasmas.

R. W. Paddock, H. Martin, R. T. Ruskov, R. H. H. Scott, W. Garbett, B. M. Haines, A. B. Zylstra, E. M. Campbell, T. J. B. Collins, R. S. Craxton, C. A. Thomas, V. N. Goncharov, R. Aboushelbaya, Q. S. Feng, M. W. von der Leyen, I. Ouatu, B. T. Spiers, R. Timmis, R. H. W. Wang, and P. A. Norreys, "Pathways Towards Break Even for Low Convergence Ratio Direct-Drive Inertial Confinement Fusion," to be published in the Journal of Plasma Physics.

D. N. Polsin, A. Lazicki, X. Gong, S. J. Burns, F. Coppari, L. E. Hansen, B. J. Henderson, M. F. Huff, M. I. McMahon, M. Millot, R. Paul, R. F. Smith, J. H. Eggert, G. W. Collins, and J. R. Rygg, "Structural Complexity in Ramp-Compressed Sodium to 480 GPa," to be published in Nature Communications.

G. F. Swadling, C. Bruulsema, W. Rozmus, and J. Katz, "Quantitative Assessment of Fitting Errors Associated with Streak Camera Noise in Thomson Scattering Data Analysis," to be published in Review of Scientific Instruments.

Conference Presentations

E. M. Campbell, "Perspectives on Inertial Fusion Energy," presented at LLE Research and Review, 14 January 2022.

S. F. Nwabunwanne and W. R. Donaldson, "Interdigitated Electrode Geometry Variation and External Quantum Efficiency of GaN/AlGaN-Based Metal–Semiconductor–Metal UV Photodetectors," presented at Photonics West 2022, San Francisco, CA, 22–27 January 2022.

P. V. Heuer, S. Feister, N. A. Murphy, and J. R. Davies, "Open Source Software and Data Formats for High-Energy-Density Physics," presented at Laser-Plasma–Accelerator Control Systems and Machine Learning, virtual, 24–28 January 2022.

R. B. Spielman, E. M. Campbell, C. Deeney, P. Tzeferacos, and J. D. Zuegel, "Short-Pulse Lasers for Directed-Energy Hypersonic Defense, Swarms, and More," presented at the Visit of J. Stiles, Rochester, NY, 26 January 2022.

The following presentations were made at the National Ignition Facility and Jupiter Laser Facility User Meeting, Livermore, CA, 7–9 February 2022:

A. Armstrong, A. Reyes, M. B. P. Adams, P. Farmakis, E. C. Hansen, Y. Lu, D. Michta, K. Moczulski, D. Q. Lamb, and P. Tzeferacos, "Implementation and Verification of Braginskii Viscosity in the *FLASH* Code."

L. Ceurvorst, L. Masse, S. F. Khan, D. Martinez, N. Izumi, V. Smalyuk, T. Goudal, V. Bouffetier, A. Casner, B. Canaud, V. N. Goncharov, and I. V. Igumenshchev, "Observing the Effects of Ablation and Perforation on the Deeply Nonlinear Rayleigh–Taylor Instability."

G. W. Collins, "Extreme Matters: Pressure to Explore New Worlds and Revolutionary States of Matter."

P. Farmakis, M. McMullan, A. Reyes, J. Laune, M. B. P. Adams, A. Armstrong, E. C. Hansen, Y. Lu, D. Michta, K. Moczulski, D. Q. Lamb, and P. Tzeferacos, "Expanding the Tabulated Equation-of-State Implementations in the *FLASH* Code of the *SESAME* Database."

Y. Lu, S. Feister, J. Meinecke, F. Miniati, G. Gregori, A. Bott, A. Reyes, E. C. Hansen, J. T. Laune, B. Reville, J. S. Ross, D. Q. Lamb, and P. Tzeferacos, "Numerical Modeling of Laser-Driven Plasma Experiments Aiming to Study Turbulent Dynamo and Thermal Conduction at the National Ignition Facility."

K. Moczulski, A. Reyes, M. B. P. Adams, A. Armstrong, P. Farmakis, E. Hansen, Y. Lu., D. Michta, D. Q. Lamb, and P. Tzeferacos, "Implementation and Verification of LC Circuit for *Z*-Pinch *FLASH* Simulations."

D. N. Polsin, G. W. Collins, J. R. Rygg, X. Gong, M. Huff, M. K. Ginnane, M. McMahon, E. Zurek, A. Lazicki, S. Bonev, M. Gorman, R. Briggs, J. H. Eggert, and J. Wark,

"Transforming Simple Metals to Topological Insulators: Sodium to 18 Mbar."

V. Gopalaswamy, R. Betti, J. P. Knauer, D. Patel, A. Lees, A. R. Christopherson, K. M. Woo, C. A. Thomas, D. Cao, O. M. Mannion, R. C. Shah, C. J. Forrest, Z. L. Mohamed, C. Stoeckl, V. Yu. Glebov, S. P. Regan, D. H. Edgell, M. J. Rosenberg, I. V. Igumenshchev, P. B. Radha, K. S. Anderson, J. R. Davies, T. J. B. Collins, V. N. Goncharov, E. M. Campbell, R. Janezic, D. R. Harding, M. J. Bonino, S. Sampat, S. F. B. Morse, M. Gatu Johnson, R. D. Petrasso, C. K. Li, and J. A. Frenje, "Fusion Energy via Laser-Driven Inertial Confinement," presented at Reed College Physics Seminar, virtual, 9 February 2022.

E. M. Campbell, "Perspectives on Inertial Fusion Energy," presented at the Rochester Institute of Technology Spring Seminar, Rochester, NY, 10 February 2022.

W. Theobald, "LLE is Leading Innovative ICF/IFR Diagnostic Development, which is Amplified Through Participation in the National Diagnostics Working Group," presented at the Workshop on New Inertial Fusion Energy/ High-Energy-Density Physics Laser Facility, virtual, 10 February 2022.

V. V. Karasiev, D. I. Mihaylov, S. X. Hu, S. B. Trickey, and J. W. Dufty, "Meta-GGA Exchange-Correlation Free-Energy Density Functional: Achieving Unprecedented Accuracy for Warm-Dense-Matter Simulations," presented at the 61st Sanibel Symposium, St. Simons Island GA, 13–18 February 2022.

J. D. Zuegel, "High-Energy Lasers for Driving Dynamic Materials Experiments," presented at the NNSA Advanced Photon Sources Sector Opportunities Workshop, virtual, 15–17 February 2022.

E. M. Campbell, "Perspectives on Inertial Fusion Energy," presented at the PB11 Science Seminar, virtual, 17 February 2022.

C. Deeney, "National Nuclear Security: 21st Century Science and Technology Perspectives," presented at the World Affairs Council, West Palm Beach, FL, 21 February 2022.

D. H. Froula, "Thomson Scattering from a Different Perspective," presented at the Oxford Seminar, Oxford, UK, 21 February 2022.

J. D. Zuegel, "Kilojoule Lasers for Dynamic Compression Studies," presented at Science with High-Power Lasers, PETRA IV Workshop, virtual, 22–23 February 2022.

The following presentations were made at the Inertial Fusion Energy Science and Technology Workshop, virtual, 22–24 February 2022:

V. N. Goncharov, "Inertial Fusion Energy Target Designs with Advanced Laser Technologies."

J. D. Zuegel, "A Broad View of Solid-State Laser Drivers for Inertial Fusion Energy."

E. M. Campbell, "LLE Perspective," presented at the Office of Experimental Sciences Executives Meeting, virtual, 24 February 2022.

J. P. Palastro, "Research at the Laboratory for Laser Energetics," presented at the Physical Sciences and Astronomy Recruitment Event, Rochester, NY, 25 February 2022.

E. M. Campbell, "Perspectives on Inertial Fusion Energy," presented at the Plasma Science and Fusion Center Seminar, virtual, 7 March 2022.

The following presentations were made at the Ecosystem for Collaborative Leadership and Inclusive Innovation in Plasma Science and Engineering, Alexandria, VA, 9–11 March 2022:

G. W. Collins, "Extreme Matters: Pressures to Explore New Worlds and Revolutionary States of Matter."

P. Tzeferacos, "Laser-Driven Experiments Shed New Light on Magnetized Turbulence and Fluctuation Dynamo in Astrophysical Plasmas."

J. D. Zuegel, "Multi-Petawatt Physics Prioritization (MP3) Workshop."

The following presentations were made at Matter in Extreme Conditions from Material Science to Planetary Physics, Montgenevre, France, 12–19 March 2022:

D. A. Chin, P. M. Nilson, D. T. Bishel, R. Paul, E. Smith, X. Gong, M. K. Ginnane, B. J. Henderson, D. N. Polsin, S. X. Hu, J. R. Rygg, G. W. Collins, D. Trail, A. Amouretti, M. Harmand, O. Mathon, R. Torchio, J. J. Ruby, F. Coppari, A. Coleman, and Y. Ping, "X-Ray Absorption Spectroscopy Temperature Measurements at High-Energy-Density Conditions."

D. H. Froula, "Thomson Scattering from a Different Perspective."

S. X. Hu, V. V. Karasiev, P. M. Nilson, D. T. Bishel, D. A. Chin, K. Nichols, R. Paul, R. Goshadze, M. Ghosh, J. Hinz, S. Zhang, D. I. Mihaylov, G. W. Collins, N. Shaffer, L. A. Collins, A. J. White, V. Recoules, N. Brouwer, M. Torrent, I. E. Golovkin, M. Gu, T. Walton, and S. B. Hansen, "Understanding Matter in Extreme Conditions with *ab initio* Calculations."

Z. K. Sprowal, L. E. Hansen, M. F. Huff, D. N. Polsin, D. G. Hicks, T. R. Boehly, J. R. Rygg, and G. W. Collins, "Accessing High Density States in D_2 Using Double Shock."

The following presentations were made at the APS March Meeting, Chicago, IL, 14–18 March 2022:

M. Ghosh, S. Zhang, and S. X. Hu, "*Ab Initio* Investigation of the Cooperative Diffusion in Body-Centered-Cubic Iron Under Inner-Core Conditions of Earth and Super-Earth Exoplanets."

R. M. N. Goshadze, V. V. Karasiev, D. I. Mihaylov, and S. X. Hu, "Equation of State of Metallization of CH Along the Principal Hugoniot."

B. J. Henderson, M. C. Marshall, J. R. Rygg, D. N. Polsin, L. E. Hansen, M. K. Ginnane, and G. W. Collins, "Silica Aerogel as a Bright Optical Source for High-Energy-Density Experiments."

M. Huff, J. R. Rygg, G. W. Collins, T. R. Boehly, D. N. Polsin, M. Nakajima, B. J. Henderson, M. C. Marshall, T. A. Suer, D. E. Fratanduono, M. Millot, R. F. Smith, C. A. McCoy, and L. E. Hansen, "Measurements of Sound Speed in Iron Shock Compressed to ~3000 GPa."

R. Paul, S. Zhang, V. V. Karasiev, and S. X. Hu, "Thermal-Induced Evolution of Magnetic Properties of FeO_2 Under High Pressures."

S. Zhang, M. A. Morales, R. Jeanloz, M. Millot, S. X. Hu, and E. Zurek, "Nature of the Bonded-to-Atomic Transition in Liquid Silica at Extreme Conditions."

M. Ghosh, S. Zhang, and S. X. Hu, "An Exotic Phase of Iron in Earth's Inner Core: A First-Principles–Based Study on the Mechanism of Cooperative Diffusion in Body-Centered-Cubic Iron," presented at the University of Rochester Graduate Education and Postdoctoral Affairs Research Symposium, Rochester, NY, 23 March 2022.

C. Deeney, "The Laboratory for Laser Energetics: Progress in Science and Technology," presented at the Plasma Science and Fusion Center Seminar, virtual, 28 March 2022.

UNIVERSITY OF ROCHESTER
LABORATORY FOR LASER ENERGETICS

Volume 171
April–June 2022
DOE/NA/3856-1752

LLE Review

Quarterly Report

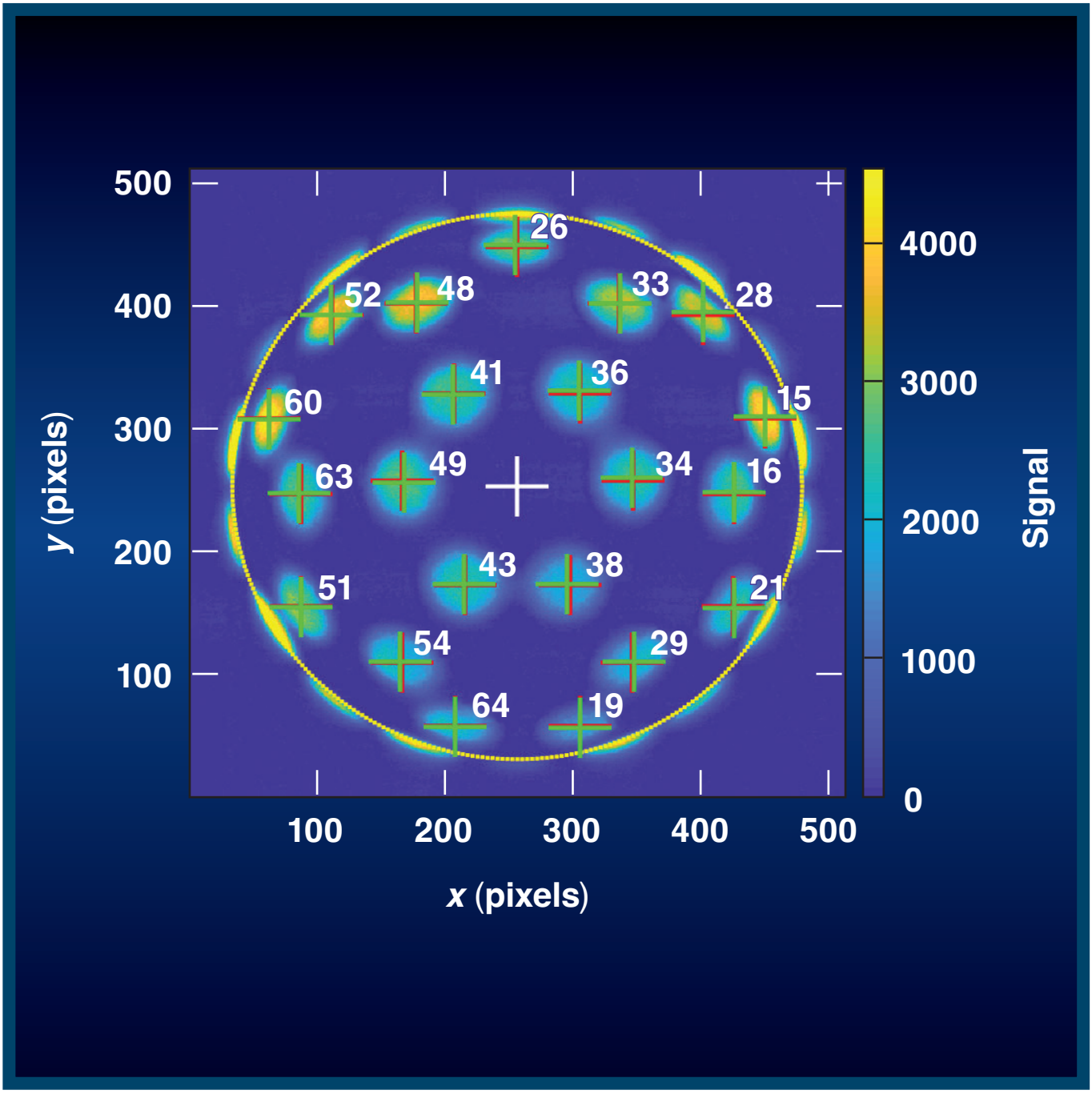

About the Cover:

The cover picture shows an x-ray image recorded on a charge-injection–device electronic sensor by one of the ten x-ray pinhole cameras located in TIM-5 in during a pointing shot. Beam-pointing accuracy is verified on the OMEGA Laser System by irradiating a 4-mm-diam Au-coated spherical target with ~23 kJ of laser energy. The large target diameter is used to separate the individual ~850-μm-diam laser spots that are typically overlapped on the ~1-mm-diam implosion targets. The spatial intensity distribution of the individual laser beams is carefully shaped and smoothed using distributed phase plates (DPP's), polarization wedges, and smoothing by spectral dispersion. A well-defined edge of the target can also be observed from the shadow of the beams behind the horizon of the sphere (yellow circle), which can be used to evaluate the location of the center of the sphere (white cross). The position of up to 21 beams can be evaluated from this image (red crosses) and compared to the desired locations (green crosses).

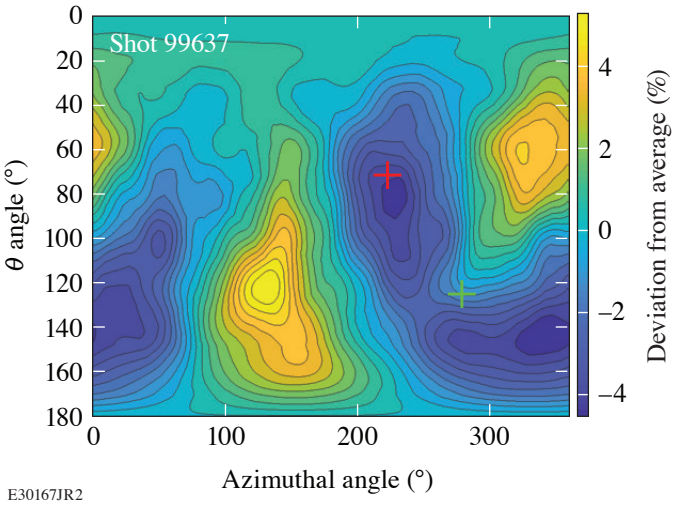

E30167JR2

To assess the impact of the pointing errors on the illumination uniformity, the on-target intensity distribution is calculated by overlapping all 60 beams onto a sphere of the typical diameter of an implosion target of ~870 μm. The pointing of the beams is set according to the evaluation of the data from the pointing shots. Identical beam profiles are assumed for all 60 beams, with a super-Gaussian intensity profile as set by the DPP. The resulting intensity map is shown in the figure on the right. Additionally, a modal decomposition into ℓ modes is performed, with the inferred direction of the $\ell = 1$ mode (red cross) and $\ell = 2$ mode (green cross) indicated in the above image.

The work described in this volume includes current research at the Laboratory for Laser Energetics, which is supported by New York State Energy Research and Development Authority, the University of Rochester, the U.S. Department of Energy Office of Inertial Confinement Fusion under Cooperative Agreement No. DE-NA0003856, and other agencies.

Printed in the United States of America
Available from
National Technical Information Services
U.S. Department of Commerce
5285 Port Royal Road
Springfield, VA 22161
www.ntis.gov

For questions or comments, contact Milton J. Shoup III, Editor, Laboratory for Laser Energetics, 250 East River Road, Rochester, NY 14623-1299, (585) 275-9636.

www.lle.rochester.edu

UNIVERSITY OF ROCHESTER
LABORATORY FOR LASER ENERGETICS

Volume 171
April–June 2022
DOE/NA/3856-1752

LLE Review

Quarterly Report

Contents

In Brief

This volume of LLE Review 171 covers the period from April–June 2022. Articles appearing in this volume are the principal summarized results for long-form research articles. Readers seeking a more-detailed account of research activities are invited to seek out the primary materials appearing in print, detailed in the publications and presentations section at the end of this volume.

Highlights of research presented in this volume include:

- C. Stoeckl *et al.* present beam-pointing verification using x-ray pinhole cameras on the 60-beam OMEGA Laser (p. 1).
- C. J. Forrest *et al.* describe measurements of low-mode asymmetries in the areal density of laser-direct-drive DT cryogenic implosions on OMEGA using neutron spectroscopy (p. 3).
- F. García-Rubio *et al.* discuss the theory of the magnetothermal instability in coronal plasma flows (p. 6).
- N. Acharya, H. Aluie, and J. K. Shang discuss a numerical investigation of a laser-driven shock interaction with a deformable particle (p. 9).
- S. X. Hu *et al.* describe probing extreme atomic physics at Gbar pressures (p. 11).
- H. Yin *et al.* report on the effective drift velocity from turbulent transport by vorticity (p. 13).
- L. Ceurvorst *et al.* report on the development of an x-ray radiography platform to study laser-direct-drive energy coupling at the National Ignition Facility (p. 15).
- D. H. Edgell *et al.* present on the use of a scattered-light uniformity imager for diagnosing laser-absorption asymmetries on OMEGA (p. 18).
- K. Churnetski *et al.* present three-dimensional hot-spot x-ray emission tomography results from cryogenic deuterium–tritium direct-drive implosions on OMEGA (p. 20).
- V. Yu. Glebov *et al.* demonstrate a new neutron time-of-flight detector for deuterium–deuterium yield and ion-temperature measurements on OMEGA (p. 24).
- H. G. Rinderknecht *et al.* report on a knock-on deuteron imager used for measurements of fuel and hot-spot asymmetry in direct-drive inertial confinement fusion implosions (p. 26).
- D. Weiner *et al.* discuss the design and implementation of a digital optical microscope for measuring submicron defects on cryogenic DT targets (p. 29).
- S. F. Nwabunwanne and W. R. Donaldson discuss the performance of a new class of tunable picosecond AlGaN UV photodiodes (p. 32).
- J. Katz *et al.* report on the measurement of laser absorption in underdense plasmas using near-field imaging of the incident and transmitted beams (p. 35).
- S. T. Ivancic *et al.* discuss the design of the high-yield time-gated x-ray hot-spot imager for OMEGA (p. 38).
- C. Dorrer *et al.* demonstrate high-resolution mapping of phase-matching conditions in second-order nonlinear crystals (p. 40).

- S. Bucht *et al.* report on achieving 100-GW idler pulses from an existing petawatt optical parametric chirped-pulse amplifier (p. 43).
- J. Zhang, W. R. Donaldson, and G. P. Agrawal discuss the impact of Raman scattering on the temporal reflection from a short soliton (p. 46).
- S. Zhang *et al.* report on a the first-principles equation of state of CHON resin for inertial confinement fusion applications (p. 49).
- B. J. Henderson *et al.* present measurements of the shocked-silica aerogel radiance transition (p. 52).
- R. M. N. Goshadze *et al.* present an analysis of shock-induced metallization of polystyrene along the principal Hugoniot investigated by advanced thermal density functionals (p. 54).
- J. A Frenje *et al.* report on the 13th Omega Laser Facility Users Group Workshop, held in person and virtually from 27–29 April 2022 (p. 57).
- J. Puth *et al.* summarize operations of the Omega Laser Facility during the third quarter of FY22 (p. 66).

Milton Shoup III
Editor

Beam-Pointing Verification Using X-Ray Pinhole Cameras on the 60-Beam OMEGA Laser

C. Stoeckl, D. Cao, L. Ceurvorst, A. Kalb, J. Kwiatkowski, A. Shvydky, and W. Theobald

Laboratory for Laser Energetics, University of Rochester

On the OMEGA Laser System, the beam-pointing accuracy is verified by irradiating a 4-mm-diam Au-coated spherical target with ~23 kJ of laser energy.[1] Up to ten x-ray pinhole cameras record the emission from all 60 beam spots [see Fig. 1(a)]. A new set of algorithms has been developed to improve the accuracy of the pointing evaluation. An updated edge-finding procedure allows one to infer the center of the sphere with subpixel accuracy. A new approach was introduced to back-propagate the pixel locations on the 2-D image to the 3-D surface of the sphere. A fast Fourier transform-based noise reduction method significantly improves the signal-to-noise ratio of the data. Based on the beam-pointing analysis, hard-sphere calculations of the laser-drive illumination uniformity on the target surface and the decomposition of the illumination distribution into lower order modes (1 to 10) are evaluated.

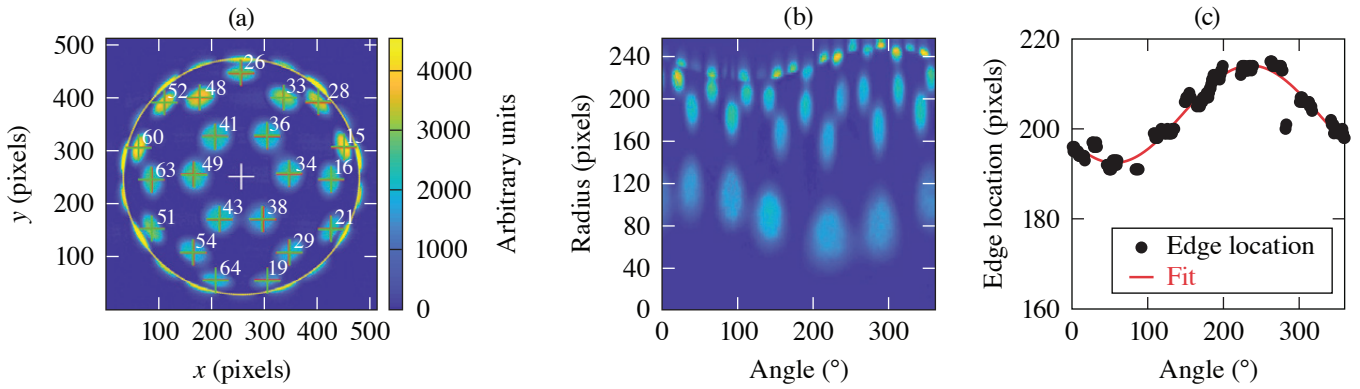

Figure 1
(a) X-ray image from one of the ten x-ray pinhole cameras acquired during a pointing shot. The position of up to 21 beams can be evaluated (red crosses) and compared to the desired locations (green crosses). The white cross shows the evaluated center of the sphere and the yellow circle is the outside radius. (b) Angular lineouts from a first guess of the center of the image of the sphere. (c) Evaluated location of the edge of the sphere compared to a cosine fit.

To infer the location of the center of the sphere, radial lineouts starting from a first estimate of the center (x_e, y_e) of the image are taken in 1° angular increments. Figure 1(b) shows a composite of these lineouts in the form of a 2-D image. The edge feature from the self-shadowing of the beams behind the horizon can be clearly seen at the top of the image. The location of the edge is determined as the position of the maximum of the gradient of each lineout and plotted in Fig. 2(c). Lines with low signal or high noise are discarded. A cosine function of the form $r = r_0 + a * \cos(t + b)$ is fitted to the data, with t as the angle, b as the phase offset, and a as the amplitude of the radial variation. From simple geometry, two offsets (dx, dy) can be computed that correct the estimated center to provide a better fit of the center $x_f = x_e + dx$; $y_f = y_e + dy$. Depending on the magnitude of the radial variation, this process can be repeated to get the best fit of the center.

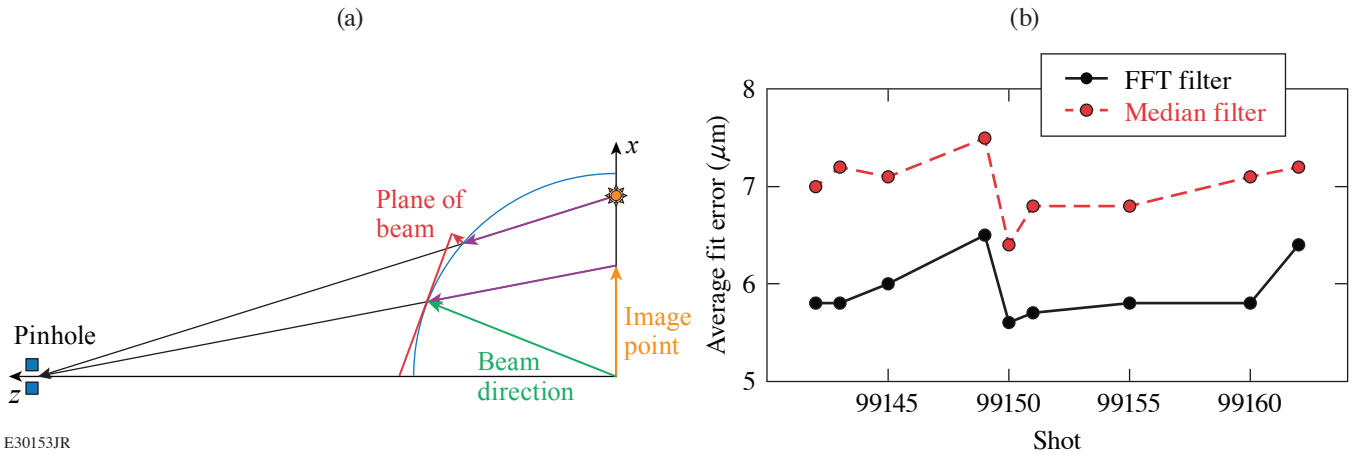

Figure 2
(a) Sketch of the geometry used to project the emission recorded from the individual beams into the planes perpendicular to the beam propagation direction. (b) Average pointing error evaluated from a median filtered image compared to a fast Fourier transform (FFT)-filtered image.

The x-ray pinhole camera image is a 2-D projection of the emission from a 3-D sphere. To infer the intensity distribution on the sphere, the image from the sensor is mapped to the object plane through the pinhole, and then each pixel location is projected onto the sphere [see purple arrow in Fig. 2(a)]. Since the intensity distribution of the laser focus is defined in a plane perpendicular to the laser propagation direction, the pixel locations on the sphere for a single beam are further projected onto the plane perpendicular to the laser direction tangent to the surface of the sphere [red arrow in Fig. 2(a)]. This procedure corrects all geometric effects of the imaging and compensates the ellipticity of the beams close to the edge of the image very well.

Simple median filters are typically used to clean up the raw charge-injection–device (CID) images under the assumption that the noise seen is purely statistical and uncorrelated. Upon more-detailed inspection of the images, it became obvious that there are medium- and large-scale correlations in the noise mostly caused by imperfections in the readout system. To clean up these correlated features a 2-D FFT is generated from the image and the regions in the FFT corresponding to high spatial frequencies or clearly identifiable background features are set to zero. A cleaned-up image is then reconstructed using the inverse FFT. The evaluation of the pointing with the FFT filtered images show a significant improvement in fit error [see Fig. 2(b)].

The limiting factors on the accuracy of the pointing evaluation, which are currently of the order of 5 μm, are most likely the quality of the pointing targets, noise (especially correlated features) in the CID readout, and imperfections in the intensity distribution of the laser beam focus. A more-uniform coating for of targets would reduce the artifacts in the image, like the “holes” [as seen in Fig. 1(a)], and lead to better fits. It is also likely that the FFT filter can be further improved by using an evolutionary algorithm or a machine learning approach.

This material is based upon work supported by the Department of Energy National Nuclear Security Administration under Award Number DE-NA0003856, the University of Rochester, and the New York State Energy Research and Development Authority.

1. R. A. Forties and F. J. Marshall, Rev. Sci. Instrum. **76**, 073505 (2005).

Measurements of Low-Mode Asymmetries in the Areal Density of Laser-Direct-Drive Deuterium–Tritium Cryogenic Implosions on OMEGA Using Neutron Spectroscopy

C. J. Forrest,[1] A. Crilly,[2] A. Schwemmlein,[1] M. Gatu Johnson,[3] O. M. Mannion,[4] B. Appelbe,[2] R. Betti,[1] V. Yu. Glebov,[1] V. Gopalaswamy,[1] J. P. Knauer,[1] Z. L. Mohamed,[1] P. B. Radha,[1] S. P. Regan,[1] C. Stoeckl,[1] and W. Theobald[1]

[1]Laboratory for Laser Energetics, University of Rochester
[2]Centre for Inertial Fusion Studies, the Blackett Laboratory, Imperial College London
[3]Plasma Science and Fusion Center, Massachusetts Institute of Technology
[4]Sandia National Laboratories

The OMEGA laser is used to study direct-drive inertial confinement fusion (ICF) by symmetrically irradiating a thin shell target with nominally identical laser beams. The shell is comprised of an outer plastic ablator (<10 μm) and a layer of cryogenic deuterium–tritium (DT) ice (~50 μm) encapsulating a vapor region DT gas. In these target designs, the incident laser ablates the thin shell, which then launches one or multiple shocks through the remaining converging shell and into the vapor region. The shock-transit stage of the implosion is followed by a deceleration phase, where the kinetic energy of the converging shell is converted to the internal energy of the hot spot. To achieve conditions relevant for ignition implosion designs, the hot-spot size must exceed the mean free path of the fusing ions and alpha particles in order to remain confined in the dense plasma. This requirement is essential to maximize the energy deposition of the alpha particle in the hot spot and surrounding dense fuel. Targets that are not compressed symmetrically will be unable to fully convert their shell kinetic energy to hot-spot thermal energy.

Areal density is one of the key parameters that determines the confinement time in ICF experiments, and low-mode asymmetries in the compressed fuel are detrimental to the implosion performance. The energy spectra from scattering of the primary DT neutrons off the compressed cold fuel assembly are used to investigate low-mode nonuniformities in direct-drive cryogenic DT implosions. For spherically symmetric implosions, the shape of the energy spectrum is primarily determined by the elastic and inelastic scattering cross sections for both neutron–deuterium (nD) and neutron–tritium (nT) kinematic interactions given by

$$\frac{\mathrm{d}N}{\mathrm{d}E} = Y_\mathrm{n}\left\{\left[\mathrm{DT} + \frac{1}{2}\frac{f_\mathrm{d}}{f_\mathrm{t}}\frac{\langle\sigma\nu_\mathrm{dd}\rangle}{\langle\sigma\nu_\mathrm{dt}\rangle}\,\mathrm{DD} + \frac{f_\mathrm{t}}{f_\mathrm{d}}\frac{\langle\sigma\nu_\mathrm{tt}\rangle}{\langle\sigma\nu_\mathrm{dt}\rangle}\,\mathrm{TT}\right]\right.$$

$$\left. + \rho L N_\mathrm{a}\left[\frac{\left(\mathrm{d}\sigma_\mathrm{nD}/\mathrm{d}E\right)f_\mathrm{d} + \left(\mathrm{d}\sigma_\mathrm{nT}/\mathrm{d}E\right)f_\mathrm{t}}{f_\mathrm{d}m_\mathrm{d} + f_\mathrm{t}m_\mathrm{t}} + \frac{\left(\mathrm{d}\sigma^\mathrm{d}_{\sigma_\mathrm{n2n}}/\mathrm{d}E\right)f_\mathrm{d}}{f_\mathrm{d}m_\mathrm{d} + f_\mathrm{t}m_\mathrm{t}} + \frac{\left(\mathrm{d}\sigma^\mathrm{t}_{\sigma_\mathrm{n2n}}/\mathrm{d}E\right)f_\mathrm{t}}{f_\mathrm{d}m_\mathrm{d} + f_\mathrm{t}m_\mathrm{t}}\right]\right\},$$

where Y_n is the primary DT yield, f_d and f_t are the fuel fraction of the fuel, and $\langle\sigma\nu\rangle$ is the reactivity rate with the associated fusing pair of ions. In the above expression DT, DD, and TT represent the shape of the primary neutron energy spectra for each reaction. The differential and double-differential cross-sections require a term to better describe this variation in the cold fuel, assuming a low-mode ($\ell = 1$) distribution as given by

$$\frac{\mathrm{d}\sigma}{\mathrm{d}E} = \int \left(\frac{\mathrm{d}\sigma}{\mathrm{d}\Omega}\right)\left(1 + \frac{\Delta\rho L}{\rho L} * \cos\theta\right)\mathrm{d}E,$$

$$\frac{\mathrm{d}\sigma_{\mathrm{n,2n}}}{\mathrm{d}E} = \int 2\pi\left(\frac{\mathrm{d}^2\sigma}{\mathrm{d}E\mathrm{d}\Omega}\right)\left(1 + \frac{\Delta\rho L}{\rho L} * \cos\theta\right)\mathrm{d}\cos\theta.$$

Experimental observations shown in Fig. 1 of the low-mode variations cold fuel assembly ($\rho L_0 + \rho L_1$) show good agreement with this recently developed model, indicating a departure from a spherical symmetry of the compressed DT fuel assembly.

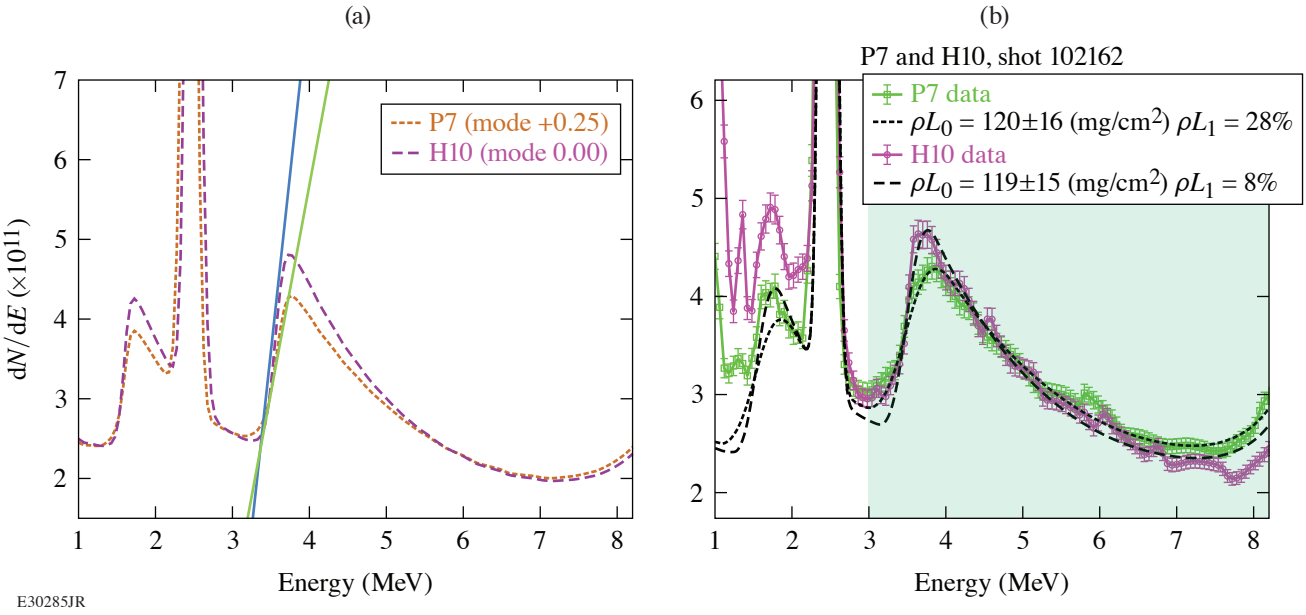

Figure 1
(a) An example of a cryogenic implosion with a significant mode 1 that shows qualitative agreement with the broadening of the kinematic edge due to the anisotropy of the cold fuel depending on the spectrometer's line of sight as predicted by the model. (b) A model illustrates the broadening of the kinematic edge due to the anisotropy of the cold fuel depending on the spectrometer's line of sight. Straight lines tangent to the nT edges are included to emphasize the difference in slopes. An example of a cryogenic implosion with a significant mode 1 shows qualitative agreement with the broadening of the kinematic edge due to the anisotropy of the cold fuel depending on the spectrometers line of sight as predicted by the model.

Another key signature in the presence of a low-mode variation is the broadening of the kinematic end point due to anisotropy of the dense fuel conditions has been observed. Recent theoretical[1] and experimental[2] studies have showed that the neutron-backscatter edge presents a novel measurement of the hydrodynamic conditions at stagnation. The spectral shape of the edge is determined by the velocity distribution of the scattering ions. When there is a large mode-1 variation in areal density, hydrodynamic models predict that the higher areal density side will decelerate slower than the lower areal density side.[3] The lower areal density side will therefore exhibit a larger variation in scattering ion velocities and consequently will produce a broader backscatter edge; the opposite is true for the higher areal density side.

More-recent hydrodynamics simulations of OMEGA implosions perturbed by a mode 1 were post-processed with a neutron transport code to obtain synthetic spectra on the P7 and H10 OMEGA lines of sight showing the anisotropic edge broadening. This anisotropy has been predicted in simulation to appear (Fig. 1) in the backscatter edge shape along different lines of sight. Measurements on the broadening of the kinematic edges show qualitative agreement with the anisotropy of the dense fuel conditions from separate lines of sight given by the model prediction. The anisotropy is also correlated with the observed mode-1

areal-density asymmetry. The P7 line of sight observes a positive mode-1 areal-density asymmetry and therefore backscatter occurs in a lower areal-density region for this line of sight.

This material is based upon work supported by the Department of Energy National Nuclear Security Administration under Award Number DE-NA0003856, the University of Rochester, and the New York State Energy Research and Development Authority.

1. A. J. Crilly *et al.*, Phys. Plasmas **27**, 012701 (2020).
2. O. M. Mannion *et al.*, Phys. Rev. E **105**, 055205 (2022).
3. B. K. Spears *et al.*, Phys. Plasmas **21**, 042702 (2014).

The Theory of Magnetothermal Instability in Coronal Plasma Flows

F. García-Rubio,[1,2] R. Betti,[1,2,3] J. Sanz,[4] and H. Aluie[1,2]

[1]Laboratory for Laser Energetics, University of Rochester
[2]Department of Mechanical Engineering, University of Rochester
[3]Department of Physics and Astronomy, University of Rochester
[4]Escuela Técnica Superior de Ingeniería Aeronáutica y del Espacio, Universidad Politécnica de Madrid, Spain

In this summary, the theory of the magnetothermal instability (MTI) is revisited through the lens of the stability of uniform systems, and its implication in the corona dynamics of direct-drive implosions is discussed. The underlying mechanism of this instability corresponds exclusively to the interplay between the Biermann battery generating magnetic (B) fields and the Righi–Leduc term bending the heat flux lines, as shown in Fig. 1. In its most simple configuration, a temperature perturbation δT results in B-field generation $\delta\vec{B}$ via the Biermann battery. This allows the Righi–Leduc heat flux, $\vec{q}_{\mathrm{RL}} \propto \left(T_0^4/n_0\right)\nabla T_0 \times \delta\vec{B}$, to pump heat into the hotter regions of the fluid, thereby driving the MTI by amplifying the δT perturbation.

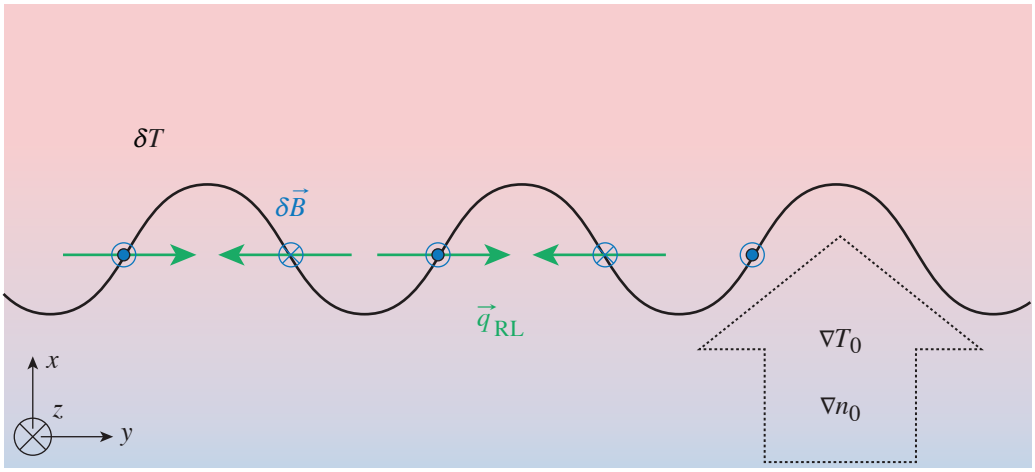

Figure 1
Schematic of the magnetothermal instability as first explained in Ref. 1. It relied on the background ∇T_0 and ∇n_0 being aligned.

The main novelty in the linear stability analysis performed in this summary corresponds to the distinction between the convective and the absolute nature of the perturbation growth. Previous analyses[1–3] identified the MTI as a convective instability and observed significant suppression of its growth rate caused by Nernst convection.[3] In the present linear analysis, we have applied the instability criteria derived by Briggs[4] to prove that, in the region where the Nernst and plasma blowoff velocities cancel, the MTI can be absolute and wave-packet perturbations grow *in situ*. The growth rate thereby derived becomes

$$\gamma \mathrm{MTI}_{\mathrm{ns}^{-1}} = 0.19 i\overline{\omega}_{M_2} \frac{10}{\log \Lambda} \frac{\gamma_0''}{\gamma_0 \delta_0 Z} \frac{T_{\mathrm{keV}}^{5/2}}{n_{10^{22}\mathrm{cm}^{-3}}} \left(\frac{\mathrm{d} \log T}{\mathrm{d}x_{100\,\mu\mathrm{m}}} \right)^2,$$

where γ_0'', γ_0, and δ_0 are coefficients that depend on the atomic number Z given in Braginskii,[5] and the dimensionless frequency $i\overline{\omega}_{M_2}$ depends on the isothermal Mach number (Ma) of the section in the corona in consideration and the pressure-to-temperature gradient ration (δ), Fig. 2.

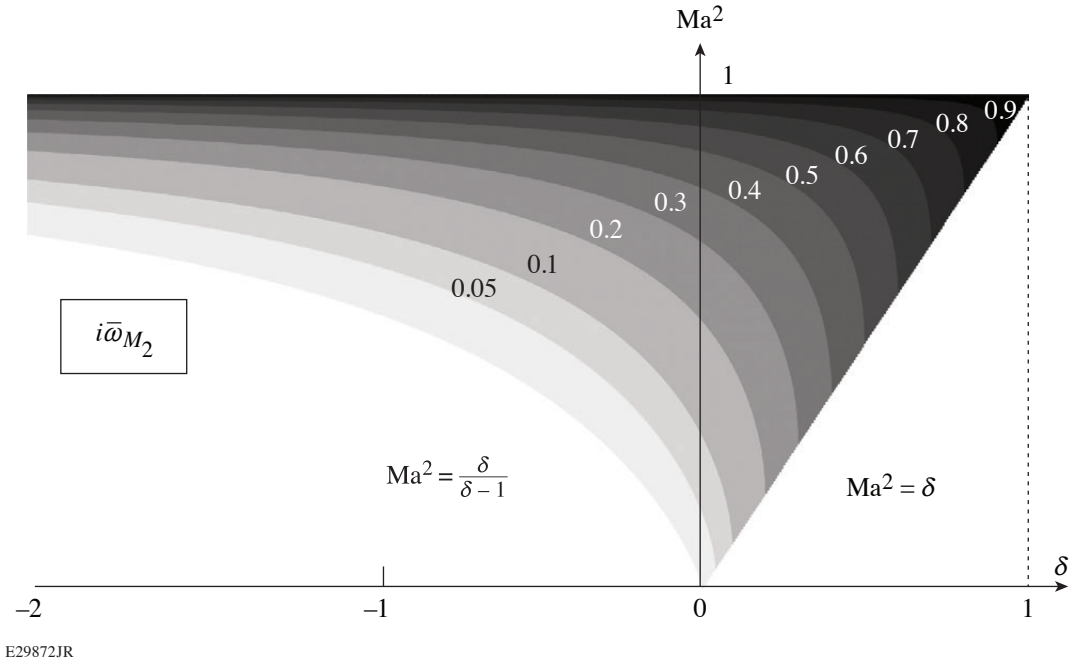

Figure 2
Isocontours of the temporal growth rate $i\overline{\omega}_{M_2}$ in the phase space isothermal Mach number Ma and pressure-to-temperature gradient ratio δ.

The analysis has been extended to derive the dispersion relation for short-wavelength perturbations developing in nonuniform profiles with application to coronal plasmas. It is found that the condition for MTI requires the net B-field convection velocity to be small at the isothermal sonic section, and the plasma conditions in this section govern the dynamics of the instability. This theory reveals a picture of the MTI where the conduction layer is the dynamically active region of the corona. Here is found the spatial resonance that causes perturbations to grow *in situ*, hence traveling with the imploding shell and potentially altering its dynamics. The structure of the unstable perturbations tends to elongate filaments in the azimuthal direction, in agreement with the observations made in Ref. 6. They can spread out to regions of outflowing convection velocity, being subsequently stretched radially and filling the outer corona. This picture is in qualitative agreement with the proton radiographs of imploding fast-ignition capsules performed by Rygg *et al.*,[7] who observed striated fields that originate close to the capsule surface, and conjectured that the vast spatial extent of these fields reflects an outward convection of filamentary structures originally produced inside the critical surface.

Applying this theory to direct-drive inertial confinement fusion implosions provides an MTI growth rate in the range of a fraction to few gigahertz (see Fig. 3), which is milder than the ones discussed by Manuel *et al.*[8] and Bissell *et al.*[9] (several to tens of gigahertz). This is mainly due to authors employing growth rate expressions derived from a convective instability analysis, which favors lower-density, higher-temperature regions (outer corona) as more-unstable regions. The outer corona indeed supports unstable waves, but we deem we must impose the requirement for absolute instability to account how the MTI affects the dynamics of the implosion. This holds the plasma state at the conduction layer responsible for the growth rate of the MTI. Finally, analysis of hydro-equivalent implosions suggests that unstable perturbations undergo more *e* foldings of growth in larger-size targets.

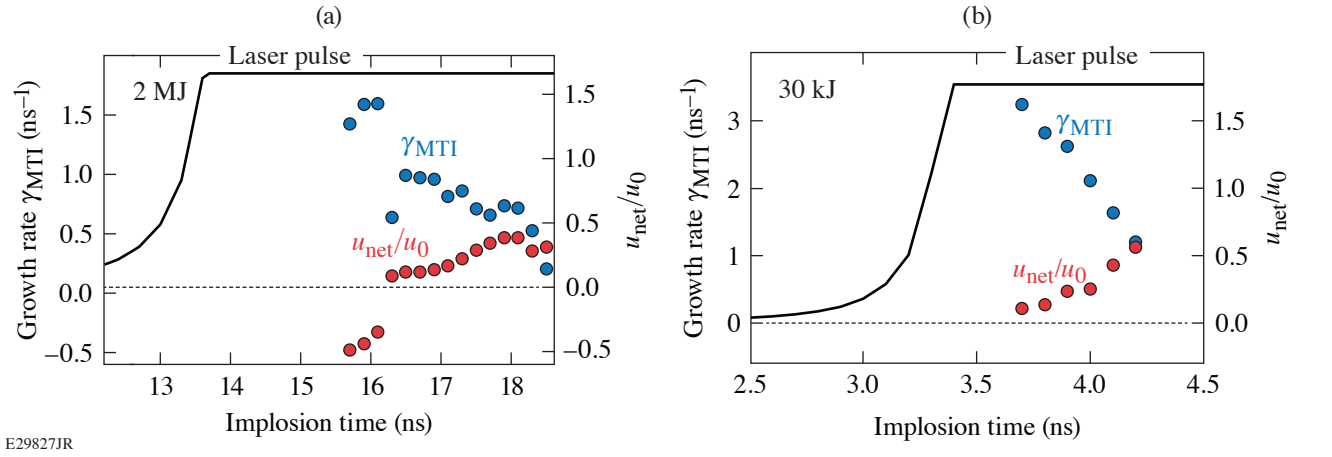

Figure 3
Maximum growth rate γ and velocity ratio u_{net}/u_0 at the isothermal sonic point for(a) 2-MJ and (b) 30-kJ direct-drive implosions. The laser power pulse shape is plotted for reference.

This work is supported by the Department of Energy Office of Science, Fusion Energy Sciences program grants DE-SC0016258, DE-SC0014318 and DE-SC0021072. F. García-Rubio was also supported by the Advanced Research Projects Agency-Energy (ARPA-E), U.S. Department of Energy, under Award No. DE-AR0001272. J. Sanz was also supported by the Spanish Ministerio de Economía y Competitividad, Project No. RTI2018-098801-B-I00. H. Aluie was also supported by U.S. DOE grants DE-SC0020229 and DE-SC0019329, U.S. NASA grant 80NSSC18K0772, U.S. NSF grants OCE-2123496 and PHY-2020249, and U.S. NNSA grants DE-NA0003856 and DE-NA0003914. This material is based upon work supported by the University of Rochester and the New York State Energy Research and Development Authority.

1. D. A. Tidman and R. A. Shanny, Phys. Fluids **17**, 1207 (1974).
2. J. J. Bissell, C. P. Ridgers, and R. J. Kingham, Phys. Rev. Lett. **105**, 175001 (2010).
3. M. Sherlock and J. J. Bissell, Phys. Rev. Lett. **124**, 055001 (2020).
4. R. J. Briggs, *Electron-Stream Interaction with Plasmas* (MIT Press, Cambridge, MA, 1964).
5. S. I. Braginskii, in *Reviews of Plasma Physics*, edited by M. A. Leontovich (Consultants Bureau, New York, 1965), Vol. 1, pp. 205–311.
6. I. V. Igumenshchev *et al.*, Phys. Plasmas **21**, 062707 (2014).
7. J. R. Rygg *et al.*, Science **319**, 1223 (2008).
8. M. J.-E. Manuel *et al.*, Phys. Plasmas **20**, 056301 (2013).
9. J. J. Bissell, R. J. Kingham, and C. P. Ridgers, Phys. Plasmas **19**, 052107 (2012).

Numerical Investigation of Laser-Driven Shock Interaction with a Deformable Particle

N. Acharya,[1,2] H. Aluie,[1,2] and J. K. Shang[1,2]

[1]Department of Mechanical Engineering, University of Rochester
[2]Laboratory for Laser Energetics, University of Rochester

To accurately simulate material behavior at relatively low temperatures, i.e., in the sub-eV range, we require models with strength properties in the solid/liquid regime. Such models are not often included in most radiation-hydrodynamics simulation codes including *FLASH*,[1] which are used as tools to design high-energy-density (HED) experiments. In addition, high-temperature equation-of-state (EOS) models used for simulations become less predictive of the thermodynamic material properties necessary for describing the hydrodynamic processes taking place at low temperatures. For instance, in *FLASH*, only thermal pressure contributes to the computation of the local sound speed. This entirely neglects the existence of nonthermal pressure, which is a property that determines the behavior of shock-compressed solids. Theoretically, this leads to higher material compressibility even at low shock pressures. Veification was carried out in 2-D *FLASH* simulations of an ~50-GPa ablation-driven shock propagating over an Al particle embedded in epoxy (CH) and observed ~3.5× compression and significant deformation of the particle in Fig. 1(a). The predicted evolution of the particle modeled with *IONMIX* EOS did not reproduce the experimental shock Hugoniot.[2] Hence, a technique was developed to implement a modified form of ideal gas EOS to model the materials (including Al, Ti, and W) and study the dynamics of the embedded particle. The simulated shock Hugoniots of multiple materials modeled using this technique compared well with experimental data. Examination of the flow field [see Fig. 1(b)] demonstrated that the unsteady drag coefficient for the particle featured a peak drag due to an unsteady interaction with the transmitted shock and a drag minimum due to shock focusing on the rear end of the particle. However, unlike previous studies performed without laser drives, the particle drag coefficient featured a second minimum due to rarefaction stretching associated with laser shutoff.

Numerous simulations were conducted that investigated the particle response for a range of particle densities, sizes, and acoustic impedances. These results revealed that lighter particles, such as Al, gained significant momentum up to 96% from the shocked CH compared to 29% in the case of heavier W. Finally, the effect of particle acoustic impedance on the bulk particle response was studied. Despite differences observed in the early stage of shock interaction, the acoustic impedance did not influence the peak particle velocity. This identified particle-to-host density ratio as a dominant factor in determining the inviscid terminal velocity of the particle. Time-scale analysis in previous works has pointed out that the shock–particle interaction time scale could be of the same order as the viscous time scale, particularly for condensed-matter systems.[3] Therefore, viscous effects coupled with rarefaction stretching effect could be important for particle drag calculation in the intermediate to later stages of shock interaction.

Finally, the simplified approach of modeling materials for hydrodynamic simulations presented in this work could be useful in studying propagation of shock waves through condensed media, in particular, dispersal of particles in multiphase explosives. The method could also be applied to understand the particle dynamics of tracers for their potential applications to x-ray particle image velocimetry in HED flows.

This work was performed under the auspices of the U.S. Department of Energy under Grant No. DE-SC0019329 within the joint HEDLP program and was supported by the Laboratory Basic Sciences program administered by UR/LLE for DOE/NNSA. H. Aluie was also supported by U.S. DOE Grant Nos. DE-SC0014318 and DE-SC0020229, NSF Grant Nos. PHY-2020249 and OCE-2123496, U.S. NASA Grant No. 80NSSC18K0772, and U.S. NNSA Grant Nos. DE-NA0003856 and DE-NA0003914. J. K.

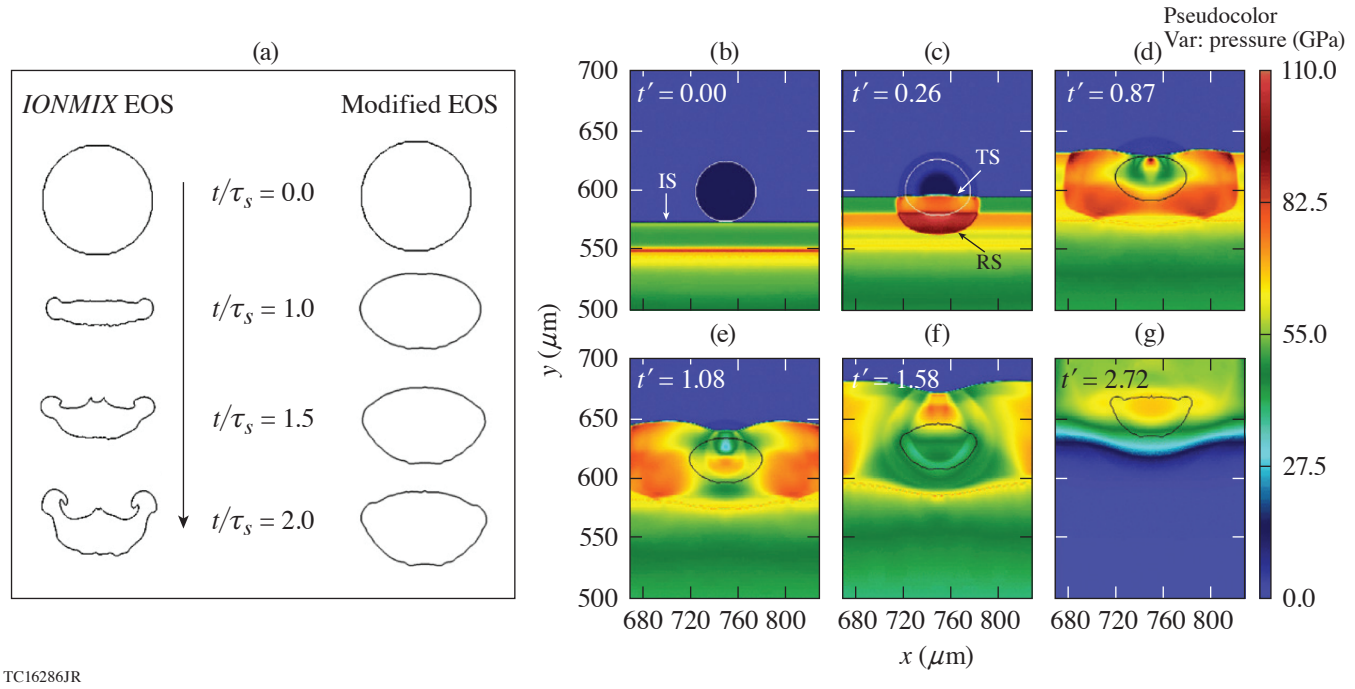

Figure 1
(a) Deformation of an Al particle in CH subjected to a 55-GPa shock with materials modeled using *IONMIX* EOS and a modified ideal gas EOS. τ_s is the shock–particle interaction time based on the particle diameter d_p and shock speed u_s. (b) Contour plots of pressure at increasing times for the post-shock pressure of 55 GPa in CH. Computational domain near the Al particle (modeled using modified EOS) is shown. The white curve [in (b) and (c)] or black curve [in (d)–(g)] is a particle interface constructed using cells around the particle with 25% mass-fraction cutoff. IS, TS, and RS denote incident, transmitted and reflected shock, respectively.

Shang was also supported by NSF Grant No. PHY2020249 and NNSA Grant No. DE-NA0003914. The software used in this work was developed in part by the DOE NNSA- and DOE Office of Science-supported Flash Center for Computational Science at the University of Chicago and the University of Rochester.

1. B. Fryxell *et al.*, Astrophys. J. Suppl. Ser. **131**, 273 (2000).
2. S. P. Marsh, ed. *LASL Shock Hugoniot Data*, Los Alamos Series on Dynamic Material Properties (University of California, Berkeley, CA, 1980).
3. F. Zhang, P. A. Thibault, and R. Link, Proc. Roy. Soc. A **459**, 705 (2003).

Understanding Extreme Atomic Physics at Gbar Pressure

S. X. Hu,[1,2] D. T. Bishel,[1,3] D. A. Chin,[1,3] P. M. Nilson,[1] V. V. Karasiev,[1] I. E. Golovkin,[4] M. Gu,[4] S. B. Hansen,[5] D. I. Mihaylov,[1] N. R. Shaffer,[1] S. Zhang,[1] and T. Walton[4]

[1]Laboratory for Laser Energetics, University of Rochester
[2]Department of Mechanical Engineering, University of Rochester
[3]Department of Physics and Astronomy, University of Rochester
[4]Prism Computational Sciences
[5]Sandia National Laboratories

Spectroscopic measurements of dense plasmas at billions of atmospheres (i.e., Gbar = billions of times the pressure at the Earth's surface) provide tests of the fundamental understanding of how matter behaves at extreme conditions, and by extension, the interpretation of dense astrophysical objects such as white dwarf stars. Developing reliable atomic physics models at these conditions, benchmarked by experimental data, is crucial to an improved understanding of radiation transport in both stars and inertial fusion targets. However, detailed spectroscopic measurements at these conditions are rare, and traditional collisional-radiative-equilibrium (CRE) models,[1] based on isolated-atom calculations and *ad hoc* continuum lowering models, have proved questionable at and beyond solid density, leaving open the possibility for more-accurate methods.

Reported here are x-ray spectroscopy measurements at gigabar pressures using laser-driven implosions. These measurements are used to test a density functional theory (DFT)-based multiband kinetic model (*VERITAS*), which was developed in this work. The *VERITAS* model uses DFT-derived band (atomic level) information to compute the radiative transition rates that can be coupled to the radiation transfer equation to describe the radiation generation and transport processes in a dense plasma. With Cu (as a witness element) doped inside a 30-μm-thick plastic shell implosion, time-integrated and time-resolved Cu K_α emission and 1*s*–2*p* absorption measurements during shell stagnation were performed. These observations are directly connected to the time-dependent atomic ionization balance in the assembled dense plasma. The system is further constrained by integrated measurements of the compressed areal density (ρR), neutron yield, bang time, and ion temperature, allowing the spectroscopic data to differentiate the DFT-based kinetic model from traditional treatments based on isolated-atom calculations and *ad hoc* continuum-lowering models.

DRACO-simulated dynamic plasma conditions was used to investigate x-ray generation and transport through the target using two CRE models (*ATBASE* and *FAC*) and the DFT-based kinetic code *VERITAS*. The predicted time-integrated spectra are compared with the experimental measurements in Fig. 1, in which the x-ray signal is plotted as a function of photon energy (all normalized to the continuum signal level at 7800 eV). The experimental spectra [Fig. 1(b); target is shown as inset in Fig. 1(b)] show both the pronounced K_α emission peaked at ~8042 eV and the 1*s*–2*p* absorption of Cu in the higher-photon energy range of 8100 to 8250 eV. Both the location and amplitude of the emission and absorption features are appropriately captured by *VERITAS* [Fig. 1(a)].

Figures 1(c) and 1(d) show the *Spect3D* simulation results in which either the atomic database (*ATBASE*) or the flexible atomic code (*FAC*) calculations are combined with the Ecker–Kroll and Stewart–Pyatt continuum-lowering models. When these CRE results are compared to experiments, they give a conflicting conclusion about the continuum-lowering model. Namely, the experimental emission and absorption features are qualitatively reproduced by the two CRE simulations of "*ATBASE* + Stewart–Pyatt" and "*FAC* + Ecker–Kroll" in Figs. 1(d) and 1(e) (although the emission peaks are too high), while the other two combinations

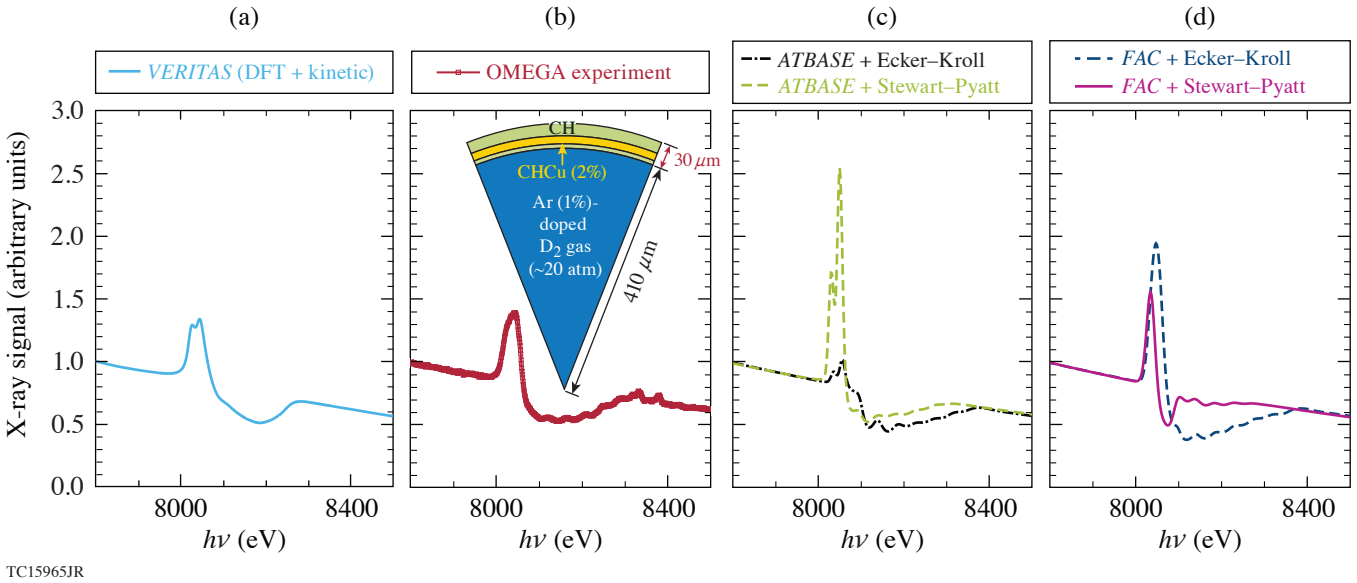

Figure 1
Comparisons of time-integrated x-ray spectra: (a) *VERITAS* DFT model prediction for the time-integrated K_α emission and 1*s*–2*p* absorption signals from a laser-driven implosion with a Cu-doped plastic layer. The model prediction is compared to (b) OMEGA experimental data, (c) CRE model predictions using the atomic database *ATBASE* in combination with Stewart–Pyatt and Ecker–Kroll continuum-lowering models, and (d) CRE model predictions using the *FAC* code with two different continuum-lowering models.

drastically disagree with experiments. This illustrates again the dilemma of the traditional spectroscopic treatment for warm dense plasmas: which *ad hoc* continuum-lowering model works better depends on the atomic physics model that is invoked. The resemblance between the *FAC* + Ecker–Kroll model [Fig. 1(d)] and experiments is likely coincidental since other recent measurements of ionization-potential depression have defied the Ecker–Kroll model. Overall, the DFT-based *VERITAS* model,[2] without invocation of an *ad hoc* continuum lowering model, better resembles the observed x-ray signal in the experiments. Nonetheless, one can see that the *VERITAS*-predicted continuum slope, the K_α-emission amplitude, and the 1*s*–2*p* absorption width are still slightly mismatched with respect to the experiment.

To summarize, a theoretical and experimental study of atomic physics in Cu-doped plastic at several billion atmospheres of pressure has been performed. Overall, a DFT-based approach reproduces many of the emission and absorption features that are observed in the experiment, while traditional plasma spectroscopy treatments show sensitivity to the combination of atomic physics and continuum-lowering models that are implemented. This sensitivity contributes to the present open questions on the validity of *ad hoc* continuum-lowering models. This work indicates the necessity for a self-consistent treatment of dense plasma effects on altering atomic energy levels/bands and their populations at ultrahigh pressures. The DFT-based *VERITAS* approach, with potential future benchmarks using other buried metal and metal-alloy layers, could provide a reliable way for simulating radiation generation and transport in dense plasmas encountered in stars and inertial fusion targets. The experimental scheme reported here, based on a laser-driven implosion, can be readily extended to a wide range of materials in single- and multishell geometries, opening the way for far-reaching investigations of extreme atomic physics and DFT models at tremendous pressures.

This material is based upon work supported by the Department of Energy National Nuclear Security Administration under Award Number DE-NA0003856, the University of Rochester, and the New York State Energy Research and Development Authority.

1. J. J. MacFarlane *et al.*, High Energy Density Phys. **3**, 181 (2007).
2. S. X. Hu *et al.*, Nat. Commun. **13**, 6780 (2022).

Effective Drift Velocity from Turbulent Transport by Vorticity

H. Yin,[1] H. Aluie,[1,2] S. Rai,[1] A. Lees,[1,2] D. Zhao,[1] S. M. Griffies,[3] A. Adcroft,[3] and J. K. Shang[1,2]

[1]Department of Mechanical Engineering, University of Rochester
[2]Laboratory for Laser Energetics, University of Rochester
[3]NOAA/Geophysical Fluid Dynamics Laboratory and Princeton University Program in Atmospheric and Oceanic Sciences

Highlighted here are the differing roles of vorticity and strain in the transport of coarse-grained scalars at length-scales larger than l by smaller-scale (subscale or subgrid or unresolved) turbulence. We use the first term in a multiscale gradient expansion due to Eyink,[1] which exhibits excellent correlation with the exact subscale physics when the partitioning length l is any scale smaller than that of the spectral peak. We show that unlike subscale strain, which acts as an anisotropic diffusion/anti-diffusion tensor, subscale vorticity's contribution is solely a conservative advection of coarse-grained quantities by an eddy-induced non-divergent velocity, $\mathbf{v}_*$, that is proportional to the curl of vorticity. Therefore, material (Lagrangian) advection of coarse-grained quantities is accomplished not by the coarse-grained flow velocity, $\bar{\mathbf{u}}_l$, but by the effective velocity, $\bar{\mathbf{u}}_l + \mathbf{v}_*$, the physics of which may improve hydrodynamic modeling.

Basic considerations from fluid dynamics indicate that the distance between particles in a laminar flow is determined by the strain.[2] Vorticity merely imparts a rotation on their separation vector $\mathbf{r}$ without affecting its magnitude. This behavior can be seen by considering the velocity, $\mathbf{u}$, difference between particles P and Q at positions $\mathbf{x}$ and $\mathbf{x} + \mathbf{r}$, respectively,

$$\mathbf{u}_Q - \mathbf{u}_P = \delta\mathbf{u} = \mathbf{u}(\mathbf{x}+\mathbf{r}) - \mathbf{u}(\mathbf{x}) = \mathbf{r}\cdot\nabla\mathbf{u}\,\big|_{\mathrm{x}} + ..., \tag{1}$$

where a Taylor-series expansion is justified for short distances $|\mathbf{r}|$ over which the flow is sufficiently smooth. In the Lagrangian frame of P at $\mathbf{x}$, the separation from Q evolves as

$$\frac{D\mathbf{r}}{Dt} = \delta\mathbf{u} = \mathbf{r}\cdot\mathbf{S} + \underbrace{\mathbf{r}\cdot\boldsymbol{\Omega}}_{\frac{1}{2}\boldsymbol{\omega}\times\mathbf{r}}, \tag{2}$$

where the velocity gradient tensor, $\nabla\mathbf{u} = \mathbf{S} + \boldsymbol{\Omega}$, has been decomposed into the symmetric strain rate tensor $\mathbf{S} = \left[\nabla\mathbf{u} - (\nabla\mathbf{u})^T\right]/2$ and the antisymmetric vorticity tensor $\boldsymbol{\Omega} = \left[\nabla\mathbf{u} - (\nabla\mathbf{u})^T\right]/2 = -1/2\epsilon_{ijk}\omega_k$. Here, $\boldsymbol{\omega} = \nabla \times \mathbf{u}$ is vorticity and ϵ_{ijk} is the Levi–Civita symbol. Taking an inner product of Eq. (2) with $\mathbf{r}$,

$$\frac{1}{2}\frac{D|\mathbf{r}|^2}{\mathrm{d}t} = \mathbf{r}\cdot\mathbf{S}\cdot\mathbf{r}, \tag{3}$$

shows that the distance is determined by the strain. Vorticity in Eq. (2) only acts to rotate $\mathbf{r}$ without changing its magnitude.

These considerations hinge on the critical assumption that the flow is sufficiently smooth over separation $\mathbf{r}$, which is patently invalid in a turbulent flow for $\mathbf{r}$ at inertial scales.[3] However, a version of this story survives due to the property of scale locality,[4] which justifies an expansion in scale. The main result of this research is Eq. (4),

$$\partial_t \overline{C}_l + \nabla \cdot \left[\left(\overline{\mathbf{u}}_l + \mathbf{v}_* \right) \overline{C}_l \right] = -\nabla \cdot \left[\mathbf{J}(C) \right], \tag{4a}$$

$$\mathbf{v}_* = \frac{1}{2} A l^2 \nabla \times \left(\nabla \times \overline{\mathbf{u}}_l \right), \tag{4b}$$

where Eq. (4a) shows us that coarse-grained simulations in general, including those from radiation-hydrodynamics inertial confinement fusion codes, may need to solve this equation to represent the unresolved (subgrid) vorticity physics self-consistently. Equation (4b) is an expression for the eddy-induced advection velocity $\mathbf{v}_*$ affecting length scales larger than l, which may be the grid cell size in a simulation. In Eq. (4a), $\mathbf{J}(C)$ can represent traditional subgrid models such as turbulent diffusion,[5] $\mathbf{J}(C) = -\alpha_{\text{turb}} \nabla \overline{C}_l$.

In summary, it is shown that unlike subscale strain, which acts as an anisotropic diffusion/anti-diffusion tensor, subscale vorticity's contribution at leading order is solely a conservative advection of coarse-grained scalars by an eddy-induced velocity $\mathbf{v}_*$ proportional to the curl of vorticity. Evidence of excellent agreement between the leading order terms and the exact ones from a 3-D compressible turbulence simulation are shown in Fig. 1. While the focus of this summary was on the transport of scalars, a similar analysis may also apply to the transport of momentum. Since the convergence of Eyink's expansion and, therefore, the dominance of the leading order term relies on ultraviolet scale locality,[4] these results and conclusions may not hold at length scales larger than those of the spectral peak. In other words, for coarse-grained simulations to use this modeling framework, they need to directly resolve the most energetic scales. Otherwise, some of the assumptions may not be valid. Note that the unresolved (subgrid) scales can still have the dominant vorticity contribution since energy and vorticity can occupy different scale ranges.

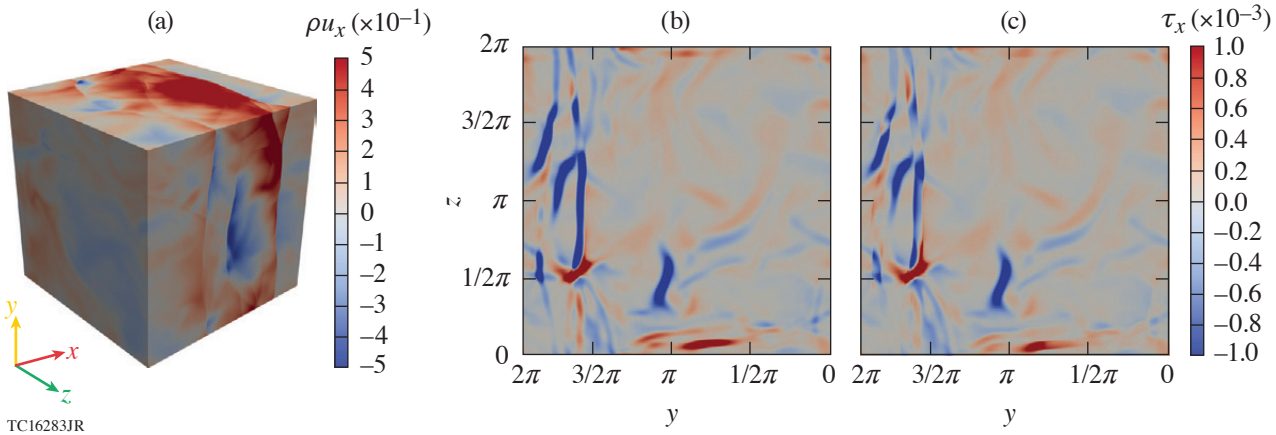

Figure 1
(a) Visualization of x component of momentum, ρu_x, in physical space from the 1024^3 compressible turbulence direct numerical simulation (DNS). The image is shown at an instant of time after the flow has reached steady state. Shocks can be seen as discontinuities. [(b),(c)] A 2-D slice at $x = 0$ from a snapshot of the 3-D compressible turbulence DNS, comparing the (b) exact $\overline{\tau}_l(u_x, \rho)$ at $l = 0.19635$ with (c) its approximation $\tau_m = 1/3 M_2 l^2 \partial_k \overline{\rho} \partial_k \overline{u}_x$.

This research was funded by U.S. DOE grant DE-SC0020229. Partial support from U.S. NSF grants PHY-2020249, OCE-2123496, U.S. NASA grant 80NSSC18K0772, and U.S. NNSA grant DE-NA0003856 is acknowledged.

1. G. L. Eyink, J. Fluid Mech. **549**, 159 (2006).
2. P. K. Kundu, I. M. Cohen, and D. R. Dowling, *Fluid Mechanics*, 6th ed. (Elsevier, 2016).
3. S. B. Pope, *Turbulent Flows* (Cambridge University Press, Cambridge, 2000).
4. H. Aluie, Phys. Rev. Lett. **106**, 174502 (2011).
5. J. Smagorinsky, Mon. Weather Rev. **91**, 99 (1963).

Development of an X-Ray Radiography Platform to Study Laser-Direct-Drive Energy Coupling at the National Ignition Facility

L. Ceurvorst,[1] W. Theobald,[1,2] M. J. Rosenberg,[1] P. B. Radha,[1] C. Stoeckl,[1] R. Betti,[1,2] K. S. Anderson,[1] J. A. Marozas,[1] V. N. Goncharov,[1,2] E. M. Campbell,[1] C. M. Shuldberg,[3] R. W. Luo,[3] W. Sweet,[3] L. Aghaian,[3] L. Carlson,[3] B. Bachmann,[4] T. Döppner,[4] M. Hohenberger,[4] K. Glize,[5] R. H. H. Scott,[5] A. Colaïtis,[6] and S. P. Regan[1,2]

[1]Laboratory for Laser Energetics, University of Rochester
[2]Department of Mechanical Engineering, University of Rochester
[3]General Atomics
[4]Lawrence Livermore National Laboratory
[5]Central Laser Facility, STFC Rutherford Appleton Laboratory
[6]Centre Lasers Intenses et Applications, Université de Bordeaux-CNRS-CEA

The coupling of laser energy to an imploding target in direct-drive inertial confinement fusion (ICF) is a key parameter that determines the ablation pressure and the implosion velocity of the shell. According to current models, cross-beam energy transfer (CBET) is a major factor that limits the ablation pressure on National Ignition Facility (NIF)-scale targets, reducing implosion velocity and shell kinetic energy. Hence, accurate measurements of the laser coupling efficiency for NIF-scale implosions are an important aspect of direct-drive ICF research. To obtain these measurements, a platform was developed on the NIF using x-ray radiography and self-emission imaging to diagnose the evolution of a directly driven solid spherical target. This plastic (CH) sphere was driven by 184 NIF beams in polar direct drive at three different intensities using a 7-ns ramp pulse. The remaining eight NIF beams were focused onto a copper backlighting foil to generate x rays that probed the target before being collected by a pinhole array coupled to a gated x-ray detector. This summary details the analysis technique used to reconstruct the target's density profile from these radiographs.

In the paraxial approximation, where the x rays are roughly parallel to the optical axis, the transmission T of x rays passing through a plasma is given by:

$$T(x,y) = e^{-\tau(x,y)}$$
$$\tau(x,y) = \int \mu(x,y,z)\rho(x,y,z)\mathrm{d}z, \tag{1}$$

where τ is the optical depth, μ is the opacity, and ρ is the density. The implosions performed in these experiments are expected to remain roughly spherically symmetric, meaning that both the opacity and density should primarily be radial functions. In this limit, Eq. (1) shows that the optical depth is simply the Abel transformation of the attenuation, equal to the opacity times the density. Therefore, the radiographs can be converted to optical depth images, azimuthally averaged, and Abel inverted to yield the attenuation profiles.

To convert radiographs to optical depth images, the transmission of the target must first be inferred by dividing the raw signal by a fitted backlighter profile. Typically, this is done by fitting the unobstructed portions of the backlighter emission with an appropriate function, in this case, the superposition of two super-Gaussians. As can be seen in Fig. 1(a), however, the backlighter was largely eclipsed by the target itself, leaving little unobstructed data with which to perform the fit. Instead, the entire image was used in the calculations by multiplying the backlighter emission profile by a simplified transmission function, resulting in fits such as the one shown in Fig. 1(b). The transmission images were then obtained by dividing the raw image by the fitted backlighter emission as displayed in Fig. 1(d).

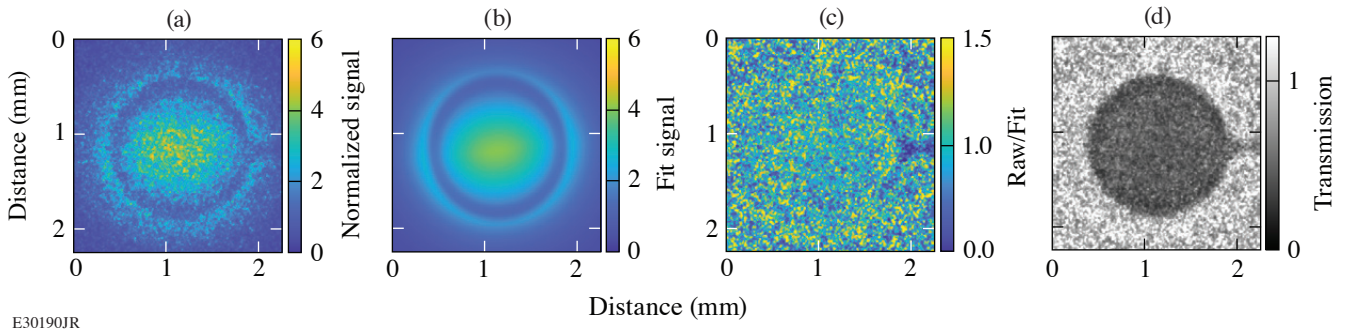

Figure 1
Converting radiographs into transmission images. (a) A single radiographic sub-image is taken from shot N210519-001 7.1 ns after the start of the drive. (b) This image is then fit with a simplified backlighter and transmission profile. (c) Dividing the raw radiograph by its fitted profile produces a flat image composed primarily of noise, confirming the quality of the fit. Note the stalk is not included in the fit and thus appears on the right side of this image. (d) The raw image is divided by the fitted backlighter profile to produce the final transmission image.

The resulting transmission was then converted to optical depth using Eq. (1), and the azimuthally averaged optical depth profiles were Abel inverted to obtain the system's radial attenuation. The final step of analysis was to separate the density and opacity profiles. Ahead of the shock, the target should not be significantly heated, maintaining its cold opacity value. After the shock, however, the material can be heated and ionized enough to reduce its overall opacity. A crude approximation was made that the opacity should be roughly constant in this shocked region, and its value was determined by matching the calculated target mass in the experiment to the accompanying *DRACO*[1] simulations. This yielded a hot opacity of 2.5±0.2 cm^2/g, similar to the 2.7 cm^2/g calculated by post-processing the simulations with *Spect3D*.[2]

Using this step function for the opacity, the final density profiles were inferred and compared to the simulations as shown in Fig. 2. The shock trajectories were in rough agreement, indicated by the rise in density. However, the subsequent fall in density corresponding to the ablation front occurred at a larger radius in the experiment compared to the simulations. This is similar to the trends seen previously with thin-shell targets.[3] At the time, the thicker observed shocked region was suspected to be caused by hydrodynamic instabilities. However, the ablation front is not accelerating here, largely eliminating this possibility.

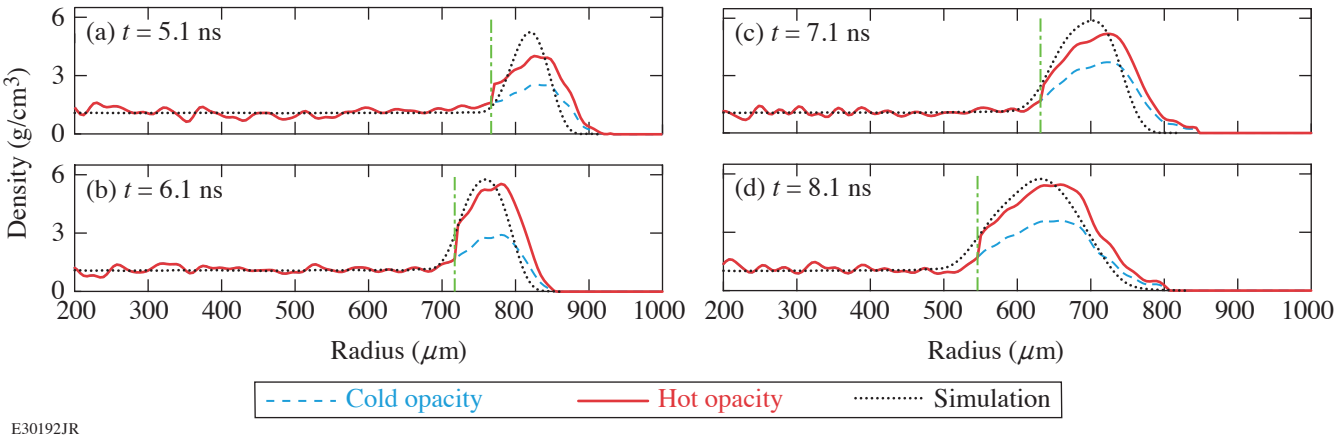

Figure 2
Inferred azimuthally averaged density profiles. The initial density calculation using only cold opacity (dashed blue curve) and mass conserving calculation using a stepped opacity profile (solid red curve) are compared to the simulated density profile convolved with the instrument response function of the system (dotted black curve) (a) 5.1 ns, (b) 6.1 ns, (c) 7.1 ns, and (d) 8.1 ns after the start of the drive. Vertical (dashed–dotted green) lines indicate the shock position beyond which the calculated hot opacity was applied.

To confirm that this discrepancy was not caused by the analysis technique, the same algorithm was applied to artificial radiographs calculated using *Spect3D*. The results of this analysis showed a 0.06 g/cm^3 rms error caused largely by the Abel inversion algorithm. As shown in Fig. 3, no shift to the reconstructed shock and ablation fronts was detected. The analysis also investigated the role of noise, which showed no systematic shift to these trajectories. The discrepancy in ablation front trajectory, therefore, appears to be physical. A comparison to simulations at all explored intensities and pulse shapes is now underway to distinguish between various effects such as preheat, CBET, and nonlocal heat-transport models. The results of this ongoing investigation will be published in a future manuscript.

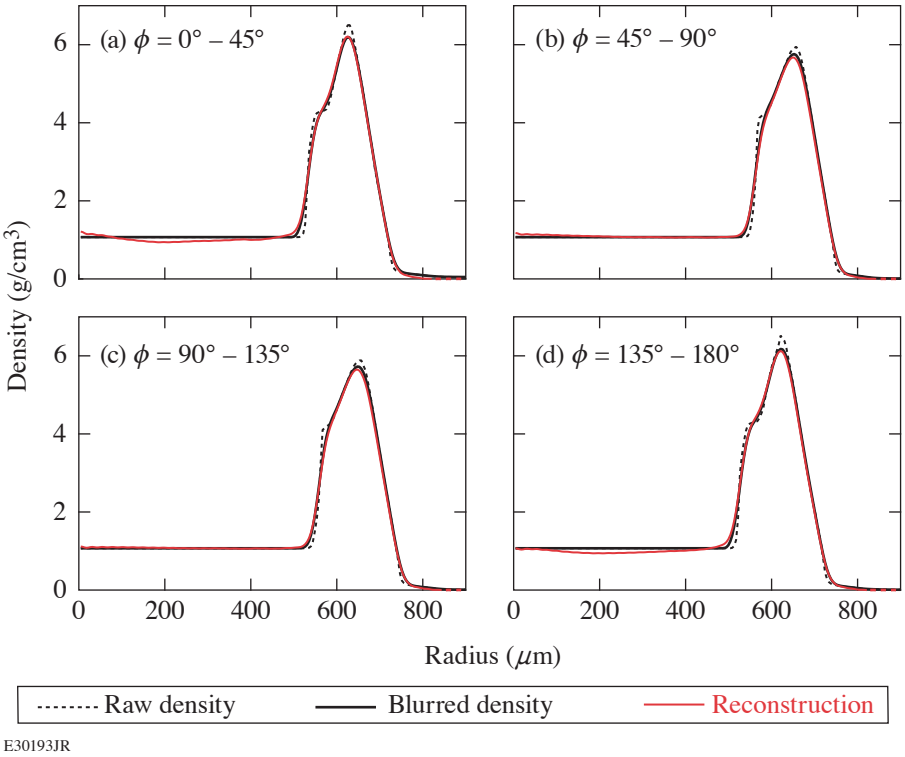

Figure 3
Validation of technique. Transmission images are calculated using *Spect3D*, and azimuthally dependent density profiles are reconstructed using this analysis technique. The data were calculated using azimuthal bins of (a) 0° to 45°, (b) 45° to 90°, (c) 90° to 135°, and (d) 135° to 180°. The reconstructed profiles (solid red curves) closely align with the original density profiles after accounting for the instrument response (solid black curves). The rms error between these two curves is 0.06 g/cm^3. Compared to the original density profile (dashed black curve), more features are lost because of imaging resolution than because of the reconstruction technique.

This material is based upon work supported by the Department of Energy National Nuclear Security Administration under Award Number DE-NA0003856, the University of Rochester, and the New York State Energy Research and Development Authority.

1. P. B. Radha *et al.*, Phys. Plasmas **23**, 056305 (2016).
2. J. MacFarlane *et al.*, High Energy Density Phys. **3**, 181 (2007).
3. M. Hohenberger *et al.*, Phys. Plasmas **22**, 056308 (2015).

A Scattered-Light Uniformity Imager for Diagnosing Laser-Absorption Asymmetries on OMEGA

D. H. Edgell, J. Katz, R. Raimondi, D. Turnbull, and D. H. Froula

Laboratory for Laser Energetics, University of Rochester

Successful implosions require efficient and highly uniform deposition of laser energy. Simulations suggest that the nonuniformity must be below the 1% rms level to achieve ignition.[1] Accurate measurement of the laser absorption is essential to evaluate implosion performance, including various schemes to mitigate laser–plasma instability losses. Laser light scattered from a target is the most direct measurement for diagnosing laser absorption in a direct-drive implosion. Observations from OMEGA implosions have shown much larger scattered-light asymmetries than standard predictions.[2,3] To address the insufficiencies of the existing scattered-light instruments, a new diagnostic, the scattered-light uniformity imager (SLUI), has been designed and deployed on OMEGA to absolutely measure the scattered-light intensity and nonuniformity for the purpose of diagnosing the asymmetry and determining its effect on laser drive uniformity. SLUI's collect a much larger portion of the scattered light around the target than other diagnostics.

SLUI measures the angularly discriminated scattered-light intensity distribution over a collection cone area by imaging a translucent transmission diffuser plate using a charge-coupled–device (CCD)/lens assembly There are two major assemblies in each SLUI: the diffuser plate front-end ten-inch manipulator (TIM)-based payload and a rear-end imaging assembly [Fig. 1(a)]. The main component of the front end is the 0.5-mm-thick translucent white spectralon diffuser plate. A stray light baffle, debris shield, and antireflection absorbing filter are also incorporated into the diagnostic payload inserted into the target chamber. The imaging part of the diagnostic (light baffle, vacuum window, filters, lens, and CCD camera) is located outside the target chamber. A sample diffuser image is shown in Fig. 1(b). Fine-scale structures, such as highlighted by the inset, are believed to be caused by structure in the diffuser plate. Some large-scale variances over the image may also be caused by the diffuser plate nonuniformity. The fine- and large-scale diffuser effects will be clarified by upcoming flat-fielding measurements. Each SLUI instrument sensitivity is absolutely calibrated offline using a National Institute of Standards and Technology traceable photodiode.

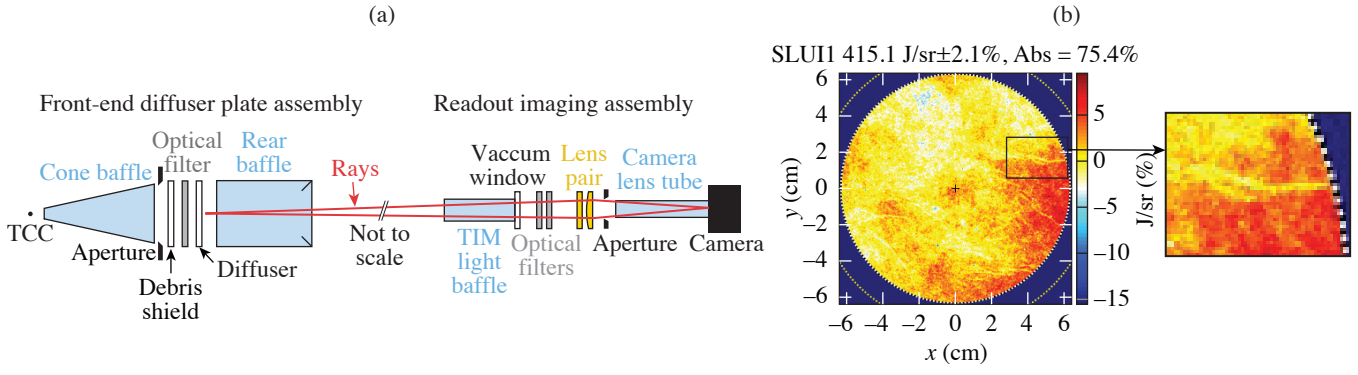

Figure 1
(a) The SLUI diagnostic. (b) Sample SLUI image of the diffuser plate for an OMEGA implosion. The inset highlights one of the small-scale features that are caused by the interior structure of the diffuser plate. TCC: target chamber center.

The standard operating position of the SLUI's places the diffuser plate standoff distance (SOD) at 31.5 cm from target chamber center (TCC) to avoid any chance of beam interference and helps reduce sputtering of baffle material on high-power shots. At this SOD, a SLUI has an effective *f* number of 2.5 and records the scattered light over a cone angle of 11.3° or ~0.97% of the total 4π emission area. Based on the measured point spread function, this effective area provides over 20K independent intensity measurements, enabling the study of the intensity and distribution of the scattered light over this area. Five SLUI's have been built and deployed in OMEGA's TIM diagnostic ports, covering almost 5% of the emission surface, enabling an absolute scattered-light measurement that according to modeling should be within a few percent of the global average. Five SLUI positions allowed resolution of the lowest modes (ℓ = 1,2) in the distribution. The large solid-angle image from each SLUI records the large local slopes in the distribution due to higher modes. Work is underway using these measured variations to evaluate the accuracy of the predicted scattered-light distributions and identify whether additional physics or other considerations need to be included.

The accuracy of the SLUI's measurements are sufficient to distinguish the effects of a 12-μm offset in target position. The green squares in Fig. 2 show the laser absorption inferred from each SLUI for an implosion that was centered at TCC within a couple of microns. The variation between the SLUI's is indicative of the scattered-light variation over the target chamber. The mean absorption for this shot is shown by the dotted black line. The blue diamonds are the laser absorptions inferred from SLUI from a similar implosion except that the target was intentionally offset 12 μm toward one of the SLUI's. The difference between the two implosions is illustrated by the red line. A consistent trend is found with a delta of about 5% absorption difference between the SLUI toward the offset and the SLUI away from the offset.

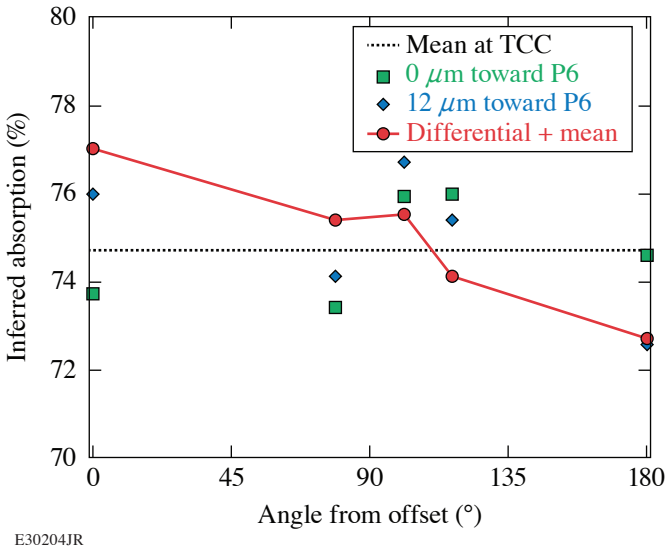

Figure 2
SLUI experimental measurements show the effect of a target offset. Shown is the laser absorption inferred for individual SLUI's for two similar implosions, one well centered at TCC (green squares) and the other intentionally offset ~12 μm toward one of the SLUI's (blue diamonds). The red line shows the difference between the two measurements centered on the mean overall absorption for the case at TCC (dotted black line).

The SLUI diagnostic is now available for deployment on OMEGA implosions, providing an absolutely calibrated platform to study the global laser absorption and sources of scattered-light and absorption asymmetries such as beam pointing, target offset, power balance, and polarization effects on cross-beam energy transfer.

This material is based upon work supported by the Department of Energy National Nuclear Security Administration under Award Number DE-NA0003856, the University of Rochester, and the New York State Energy Research and Development Authority.

1. V. N. Goncharov *et al.*, Plasma Phys. Control. Fusion **59**, 014008 (2017).
2. D. H. Edgell *et al.*, Phys. Rev. Lett. **127**, 075001 (2021).
3. O. M. Mannion *et al.*, Phys. Plasmas **28**, 042701 (2021).

Three-Dimensional Hot-Spot X-Ray Emission Tomography from Cryogenic Deuterium–Tritium Direct-Drive Implosions on OMEGA

K. Churnetski,[1,2] K. M. Woo,[1] W. Theobald,[1,2] P. B. Radha,[1] R. Betti,[1,2,3] V. Gopalaswamy,[1] I. V. Igumenshchev,[1] S. T. Ivancic,[1] M. Michalko,[1] R. C. Shah,[1] C. Stoeckl,[1] C. A. Thomas,[1] and S. P. Regan[1,2]

[1]Laboratory for Laser Energetics, University of Rochester
[2]Department of Mechanical Engineering, University of Rochester
[3]Department of Physics and Astronomy, University of Rochester

In direct-drive inertial confinement fusion (ICF),[1] laser beams are focused onto a spherical target to implode a thin shell composed of an outer ablation layer (typically plastic) and an inner layer of solid cryogenic deuterium–tritium (DT) fuel. The laser-direct-drive ICF concept is studied on the 60-beam, 30-kJ, 351-nm OMEGA laser,[2] which has produced high-performing implosions with hot-spot pressures exceeding 50 Gbar, described in Ref. 3. The recent application of statistical modeling significantly improved the implosion performance and the neutron yield.[4] Low-mode drive variations in the driver illumination and from target perturbations can significantly impact implosions.[5–7] The goal over the next several years is to further optimize OMEGA implosions and to demonstrate ignition-relevant implosions that when scaled to 2 MJ of laser energy, would enter the burning-plasma regime.[8,9] Three-dimensional hot-spot x-ray emission tomography is a powerful tool to diagnose low-mode asymmetries, which will help to mitigate low-mode perturbations and improve implosion performance. This work is embedded in a long-term project that aims to understand the physics and multidimensional effects that currently limit the hot-spot pressure in ICF implosions on OMEGA and to help to develop strategies to increase the hot-spot pressure.

OMEGA currently has a combination of time-gated and time-integrated x-ray diagnostics for hot-spot imaging along four lines of sight (LOS), which enable a 3-D interpretation of the hot-spot shape. These diagnostics include KBframed,[10] the single line-of-sight, time-resolved x-ray imager (SLOS-TRXI),[11] KB (formerly GMXI),[12] and a spatially resolved electron temperature diagnostic (SR-TE).[13] The diagnostics have different spatial and temporal resolutions, as well as slightly different spectral sensitivities. These four diagnostics are quasi-orthogonal from each other, allowing for a 3-D view of the imploding ICF core. Figure 1 shows the locations of the detectors on the OMEGA target chamber and example data from each detector.

A 3-D hot-spot emission model was developed to reconstruct the hot-spot emission profile of direct-drive implosions on OMEGA by combining the measured x-ray emission data from multiple LOS.[14] The radiation transfer equation along a single LOS is considered for a steady-state plasma in which the temperature and density distributions and the radiation field are independent of time.[15] The hot-spot plasma of cryogenic DT target implosions on OMEGA is optically thin for photon energies >2.5 keV. All of the x-ray imagers considered here satisfy this condition and absorption can be neglected.[13] Neither the absolute signal nor the temporal evolution of the hot-spot emission are taken into account in this simplified model. The spectral response is assumed to be the same for all the x-ray imagers. Using those simplifications and dropping the frequency dependence on the plasma emissivity ε, the projected x-ray image $I_{\hat{s}}$ along an observation direction $\hat{s}$ over a path length s is given by $I_{\hat{s}} \sim \int_{\hat{s}} \varepsilon \mathrm{d}s$.

A method described in Woo *et al.*[14] has been developed to reconstruct ε through a complete expansion set using both non-orthogonal polynomial and orthogonal polynomial expansions. The complex shape of the hot-spot emission can be described in terms of a model of generalized spherical-harmonic Gaussian functions,

$$\ln \varepsilon(r,\theta,\varphi) = \sum_{n=0}^{\infty} \sigma_n R^n \left[1 + \sum_{\ell=1}^{\infty} \sum_{m=-\ell}^{\ell} \sum_{k=0}^{\infty} A_{\ell m k} R^k Y_{\ell m}(\theta,\varphi)\right]^n. \quad (1)$$

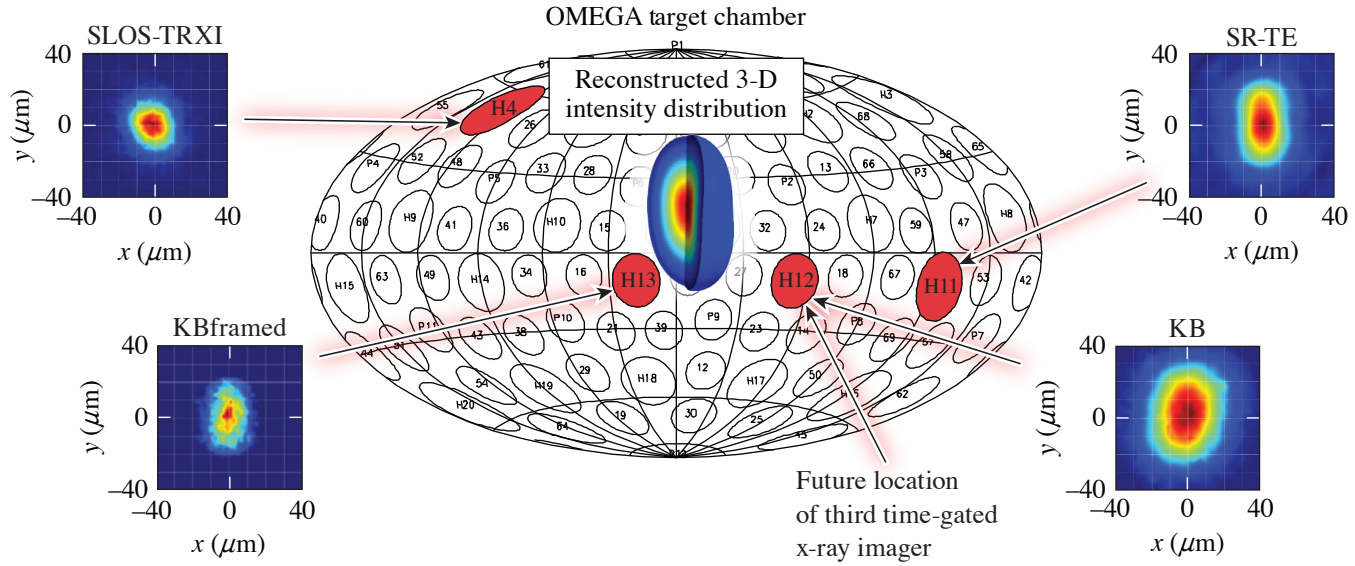

Figure 1
The locations of the existing four hot-spot x-ray imaging detectors on the OMEGA target chamber are indicated by the red circles. SLOS-TRXI is located in port H4 (45°, 234°), KBframed in port H13 (105°, 342°), KB in port H12 (96°, 54°), and SR-TE in port H11 (101°, 134°). The future third time-gated x-ray imager will also be located in port H12 (96°, 54°). Example data are shown for each diagnostic and the reconstructed 3-D hot-spot emission is displayed in the target chamber center. The polar and azimuthal angles for each detector are denoted in parenthesis.

The emissivity is described in spherical coordinates (r, θ, φ), where the origin of the coordinate system coincides with the peak of ε. In Eq. (1), R is the radius and $Y_{\ell,m}$ are the real spherical harmonic functions. The expansion coefficients, φ_n and $A_{\ell,m}$, are determined by a gradient-descent, machine-learning algorithm that minimizes a loss function, which is the fit error between the model and the normalized measured x-ray images.

To reconstruct the emission profile, an initial estimate is made for the solution of of ε, which is a 1-D Gaussian profile. This model is projected into the LOS of the x-ray detectors using a ray-tracing routine and the projections are compared with the experimental x-ray images from each diagnostic. The error between the model and the experimental images is calculated as the sum of the root-mean-square (rms) difference over the multiple lines of sight. The coefficients of the model are slightly perturbed, and this process is repeated for several iterations until the rms error is minimized.

Proof-of-principle simulations with the hydrodynamic code *DEC3D*[16] assuming a mode-2 perturbation were used to validate the 3-D reconstruction procedure. The result of the simulation was post-processed with the detector resolutions and spectral sensitivities using *Spect3D*[17] to create simulated x-ray images along the four lines of sight. Normally distributed random noise was added to the simulated x-ray images, and the hot-spot emission was reconstructed multiple times in a Monte Carlo simulation by varying the noise. The resulting 3-D reconstructions were projected along the detector lines of sight and the major and minor radii were calculated at the 1/e contour level for the reconstruction projections and simulated x-ray images. The radii agreed within the error bars, which gives confidence in the viability of this technique.

A direct-drive ICF campaign on OMEGA was conducted with deliberate laser-drive asymmetries to study the effect of hot-spot shape asymmetries on implosion performance. The polar-direct drive (PDD)[18] beam illumination geometry was applied by using 40 of the 60 OMEGA beams, switching off 20 beams around the equator. The 40 beams are grouped in three beam rings in the upper and lower hemisphere according to their polar angles.[18] The partition of beam energies in rings 1 and 3 was varied while keeping the total laser energy constant. The magnitude of the laser-drive asymmetry was varied to produce hot spots that

ranged from oblate to prolate in shape. Figure 2 shows data from three shots at stagnation from KBframed, which has an equatorial view of the capsule. Reconstructions were done for each shot during this campaign and compared to the experimental inputs.

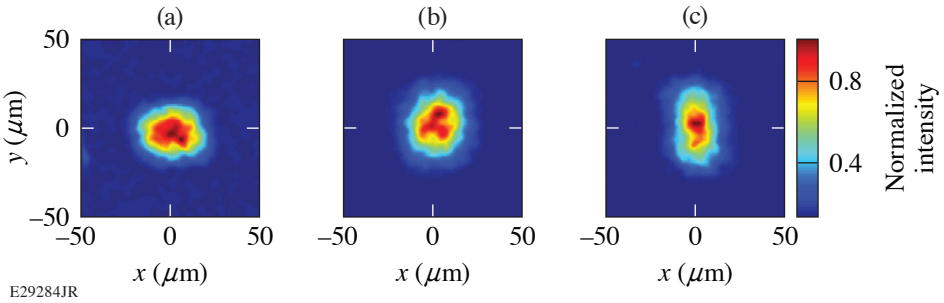

Figure 2
Experimental x-ray images from the KBframed diagnostic at stagnation of cryogenic DT target implosions performed with the PDD illumination geometry. The beam-energy balance was varied from a stronger drive on (a) the poles (shot 96578), to (b) a balanced drive (shot 96575), to (c) a stronger drive on the equator (shot 96581), while keeping the total laser energy conserved.

The reconstruction of shot 96581 is shown in Fig. 1. Data from SLOS-TRXI and KBframed are chosen to be from the time of peak emission, and data from KB channel 3 and SRTE channel 1 are used due to the similar energy ranges to those of SLOS-TRXI and KBframed. The differences in hot-spot size between the different diagnostics can be attributed to differences in time resolution. With a higher intensity of laser energy incident at the equator of the capsule, a prolate shape is expected in the hot-spot emission with the major axis aligned with the z axis of the target chamber. Spherical harmonic modes up to $\ell = 3$ were used in the reconstruction. The large $A_{2,0} = -0.47 \pm 0.03$ expansion coefficient indicates a strong mode $\ell = 2$ in the reconstruction, which can be seen in the experimental x-ray images. The $A_{2,0}$ coefficient is negative, which indicates a prolate shape and is consistent with what we expect from the laser-drive asymmetry. Reconstructions of other shots from this campaign also show the expected overall shape and orientation of the hot spot based on the laser-drive asymmetry and will be further discussed in a future publication.

This material is based upon work supported by the Department of Energy National Nuclear Security Administration under Award Number DE-NA0003856, the University of Rochester, and the New York State Energy Research and Development Authority.

1. R. S. Craxton *et al.*, Phys. Plasmas **22**, 110501 (2015).
2. T. R. Boehly *et al.*, Opt. Commun. **133**, 495 (1997).
3. S. P. Regan *et al.*, Phys. Rev. Lett. **117**, 025001 (2016); 059903(E) (2016).
4. V. Gopalaswamy *et al.*, Nature **565**, 581 (2019).
5. B. K. Spears *et al.*, Phys. Plasmas **21**, 042702 (2014).
6. O. M. Mannion *et al.*, Phys. Plasmas **28**, 042701 (2021).
7. H. G. Rinderknecht *et al.*, Phys. Rev. Lett. **124**, 145002 (2020).
8. O. A. Hurricane *et al.*, Phys. Plasmas **26**, 052704 (2019).
9. A. B. Zylstra *et al.*, Nature **601**, 542 (2022).
10. F. J. Marshall *et al.*, Rev. Sci. Instrum. **88**, 093702 (2017).)
11. W. Theobald *et al.*, Rev. Sci. Instrum. **89**, 10G117 (2018).
12. F. J. Marshall and J. A. Oertel, Rev. Sci. Instrum. **68**, 735 (1997).
13. D. Cao *et al.*, Phys. Plasmas **26**, 082709 (2019).
14. K. M. Woo *et al.*, Phys. Plasmas **29**, 082705 (2022).
15. Ya. B. Zel'dovich and Yu. P. Raizer, *Physics of Shock Waves and High-Temperature Hydrodynamic Phenomena*, edited by W. D. Hayes and R. F. Probstein (Dover, Mineola, NY, 2002).

16. K. M. Woo *et al.*, Phys. Plasmas **25**, 102710 (2018).
17. J. J. MacFarlane *et al.*, High Energy Density Phys. **3**, 181 (2007).
18. P. B. Radha *et al.*, Phys. Plasmas **19**, 082704 (2012).

A New Neutron Time-of-Flight Detector for Yield and Ion-Temperature Measurements at the Omega Laser Facility

V. Yu. Glebov,[1] C. J. Forrest,[1] J. Kendrick,[1] J. P. Knauer,[1] O. M. Mannion,[2] H. McClow,[1] S. P. Regan,[1] C. Stoeckl,[1] B. Stanley,[1] and W. Theobald[1]

[1]Laboratory for Laser Energetics, University of Rochester
[2]Sandia National Laboratories

A new neutron time-of-flight (nTOF) detector for deuterium–deuterium (D–D) fusion yield and ion-temperature measurements was designed, installed, and calibrated for the OMEGA Laser System. This detector provides an additional line of sight for D–D neutron yield and ion-temperature measurements for yields exceeding 1×10^{10} with higher precision than existing detectors. The nTOF detector consists of a 90-mm-diam, 20-mm-thick BC-422 scintillator and a gated Photek[1] photomultiplier tube (PMT240). This PMT has a 40-mm-diam photocathode, two microchannel plates, and provides a gain of up to 1×10^6. For DD measurements the PMT240 is operated at a bias voltage of –4.4 kV, corresponding to a PMT gain of 2×10^5. The PMT collects scintillating light through the 20-mm side of the scintillator without the use of a light guide. There is no lead shielding from hard x rays in order to allow the x-ray instrument response function of the detector to be easily measured. Instead, hard x-ray signals generated in implosion experiments are gated out by the PMT. The design provides a place for glass neutral-density (ND) filters between the scintillator and the PMT to avoid PMT saturation at high yields. The nTOF detector is installed in the OMEGA Target Bay along the P8A sub-port line of sight (LOS) with $\theta = 109.57°$ and $\phi = 90.00°$ (where θ and ϕ are the polar and azimuthal angles of the port in the target chamber coordinate system) at a distance of 5.3 m from the target chamber center. This detector is named P8A 5.3-m nTOF.

Until recently only two nTOF detectors on OMEGA [5.4-m nTOF (Ref. 2) located at 5.4 m from target chamber center (TCC) in sub-port H10G LOS with $\theta = 84.98°$ and $\phi = 311.76°$ and 12-m nTOFL (Ref. 3) located at 12.4 m from TCC in sub-port H8A LOS with $\theta = 87.86°$ and $\phi = 161.24°$] measured the D–D yield and ion temperature above the 2×10^{10} yield. The P8A 5.3-m nTOF detector provided an additional line of sight and increased the yield range of DD measurements on OMEGA. The P8A nTOF has a larger scintillator volume and records more neutron interactions than the other two detectors. The DD yield calibration of the P8A nTOF against the 12-m nTOFL detector is shown in Fig. 1. Only shots with yields exceeding 1×10^{10} were selected for the calibration. Figure 1(a) shows the charge of the neutron signal from P8A nTOF plotted versus the DD yield from the 12-m nTOF. The line in Fig. 1(a) is the linear fit of the data that is forced to go through the point (0,0). Figure 1(a) demonstrates a good linearity of the P8A nTOF detector signal for D–D yields up to 4×10^{11}. The data in Fig. 1 were recorded without an ND filter. When an ND filter is used there is practically no upper limit in D–D yield measurement for the P8A nTOF detector. Figure 1(b) shows the ratio of the yields from the two detectors as a function of the shot number.

Most of the LLE implosion campaigns are designed for DT yields in the range from 1×10^{13} to 1×10^{14} and recently for yields above 3×10^{14}. Therefore, the DT nTOF detectors on OMEGA were designed for such high yields. External OMEGA users, however, sometimes require DT yield measurements from 5×10^{10} to 1×10^{12}. The PMT high-voltage setting of P8A nTOF is adjusted from –4.4 kV for DD operation to –3.6 kV, corresponding to a PMT gain of 6×10^3 for the DT operation. The P8A nTOF was calibrated in DT yield against Cu activation. Figure 2(a) shows the charge of the neutron signal from P8A nTOF plotted versus the DT yield from Cu activation. The straight line in Fig. 2(a) is the linear fit of the data that is forced to go through the point (0,0). Figure 2(a) demonstrated that P8A nTOF is linear in desired DT yield range from 5×10^{10} to 1×10^{12}. Figure 2(b) shows the ratio of the yields from the two detectors as a function of shot number.

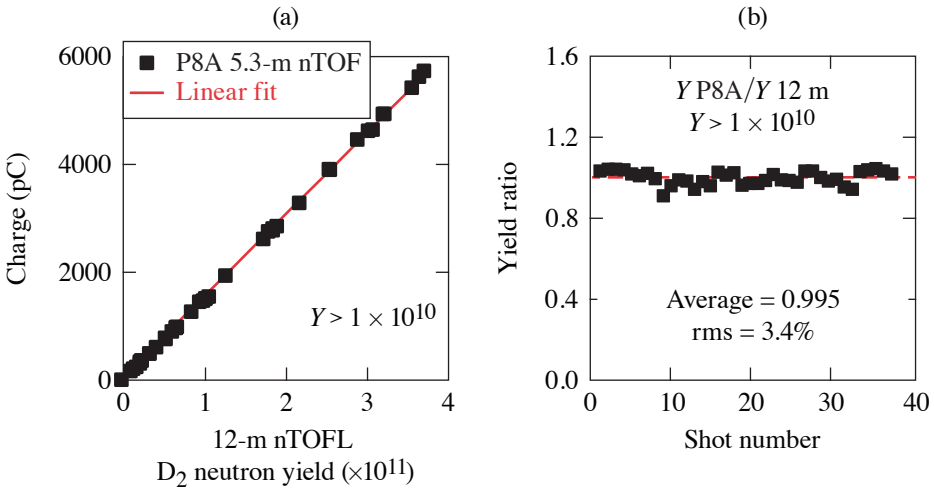

TC16083JR

Figure 1
(a) DD neutron calibration of P8A 5.3-m nTOF against 12-m nTOFL detector and (b) the ratio of DD yield measured by P8A 5.3-m nTOF and 12-m nTOFL detectors.

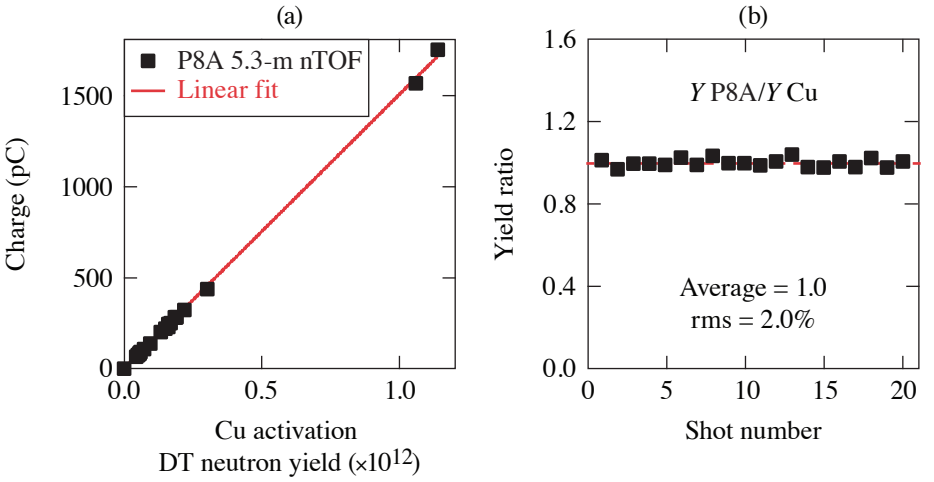

TC16085JR

Figure 2
(a) DT neutron calibration of P8A 5.3-m nTOF against copper activation and (b) the ratio of DT yield measured by P8A 5.3-m nTOF and copper activation.

A new nTOF detector was installed and calibrated on the OMEGA Laser System. This detector is now a standard OMEGA diagnostic for D–D yields above 1×10^{10} and DT yields from 5×10^{10} to 2×10^{12}.

This material is based upon work supported by the Department of Energy National Nuclear Security Administration under Award Number DE-NA0003856, the University of Rochester, and the New York State Energy Research and Development Authority. Sandia National Laboratories is a multimission laboratory managed and operated by National Technology & Engineering Solutions of Sandia, LLC, a wholly owned subsidiary of Honeywell International Inc., for the U.S. Department of Energy's National Nuclear Security Administration under contract DE-NA0003525. This paper describes objective technical results and analysis.

1. Photek Ltd., St. Leonards on Sea, East Sussex, TN38 9NS, United Kingdom, Accessed 9 September 2020, http://www.photek.com/.
2. M. A. Russotto and R. L. Kremens, Rev. Sci. Instrum. **61**, 3125 (1990).
3. V. Yu. Glebov *et al.*, Rev. Sci. Instrum. **75**, 3559 (2004).

A Knock-On Deuteron Imager for Measurements of Fuel and Hot-Spot Asymmetry in Direct-Drive Inertial Confinement Fusion Implosions

H. G. Rinderknecht,[1] P. V. Heuer,[1] J. Kunimune,[2] P. J. Adrian,[2] J. P. Knauer,[1] W. Theobald,[1] R. Fairbanks,[1] B. Brannon,[1] L. Ceurvorst,[1] V. Gopalaswamy,[1] C. A. Williams,[1] P. B. Radha,[1] S. P. Regan,[1] M. Gatu Johnson,[2] F. H. Séguin,[2] and J. A. Frenje[2]

[1]Laboratory for Laser Energetics, University of Rochester
[2]Plasma Science and Fusion Center, Massachusetts Institute of Technology

A knock-on deuteron imager (KoDI) has been implemented to measure the hot spot and fuel asymmetry of cryogenic inertial confinement fusion implosions on OMEGA. Energetic neutrons produced by D–T fusion elastically scatter ("knock-on") deuterons from the fuel layer with a probability that depends on ρR. Deuterons above 10 MeV are produced by near-forward scattering, and imaging them is equivalent to time-integrated neutron imaging of the hot spot. Deuterons below 6 MeV are produced by a combination of sidescattering and ranging in the fuel, and encode information about the spatial distribution of the dense fuel.

The KoDI instrument consists of a multi-penumbral aperture positioned 10 to 20 cm from the implosion using a ten-inch manipulator (TIM) and a detector pack at 350 cm from the implosion to record penumbral images with magnification of up to 35×. Range filters and the intrinsic properties of CR-39 (Ref. 1) are used to distinguish different charged-particle images by energy along the same line of sight. Image plates fielded behind the CR-39 record a 10-keV x-ray image using the same aperture.

Differential filtering is used to distinguish between high- and low-energy deuteron populations. The left half of the CR-39 is filtered by 135 μm tantalum, transmitting only deuterons initially above 10 MeV. The right half is filtered by 10 μm tantalum, transmitting deuterons initially above 2 MeV. The diameter of tracks is used to further discriminate the data into rough energy bins to interpret the images. While the exact diameter–energy relationship varies from sample to sample, the energy order and approximate energy range can be inferred. The analysis of the x-ray data is described in Ref. 2.

Penumbral imaging maximizes the statistics of the recorded signal. Each penumbral aperture is made by laser drilling a 200-μm-thick tantalum or 175-μm-thick tungsten substrate, producing a conical hole with an opening angle of 10°. Two effects cause the point-spread function (PSF) of the penumbral apertures to differ from the ideal knife edge: charged-particle scattering in the substrate and electrical charging of the array. Because of the high magnification of the camera, even a small amount of straggle is sufficient to produce a uniform background and the effect of scattering on the PSF blur is negligible. Electrical charging of the aperture array is more significant. A semi-analytic form of the charged-aperture PSF was derived using a numerically integrated electric field inside the array, $E(r)$:

$$\mathrm{PSF} = \left[\frac{\mathrm{d}r_\mathrm{i}'}{\mathrm{d}r_\mathrm{a}'}\right]^{-1}, r_\mathrm{i}' = r_\mathrm{a}' + \frac{e\Delta z}{4\pi\varepsilon_0}\left[\frac{Q}{K}\frac{D}{R_\mathrm{a}}\frac{M-1}{M^2}\right]E'\left(r_\mathrm{a}'\right), \tag{1}$$

where r_a and r_i are radial position in the aperture and image plane, R_a is the aperture radius, D the detector distance to target chamber center (TCC), Δz is the aperture thickness, M is the camera magnification, Q is the aperture charge density, K is the deuteron kinetic energy, and primes indicate normalized quantities $\left\{r_\mathrm{a}' = r_\mathrm{a}/R_\mathrm{a},\ r_\mathrm{i}' = r_\mathrm{i}/R_\mathrm{a}M,\ E' = E'/\left[Q/2\pi\varepsilon_0\right]\right\}$. The charged-aperture PSF is a family of curves that depends only on the value of the coefficient in square brackets, which we call V. [We select

$\Delta z = 200\ \mu$m and V has units of (coulomb/cm^2)/MeV.] Charging effects are negligible for values $V \lesssim 10^{-7}$, but become dominant for $V \gtrsim 3 \times 10^{-5}$. For accurate reconstructions using a charged aperture, the amount of charging must be known and the blurring caused by charging effects must not dominate the structure caused by the object. The PSF radius at 50% of maximum increases monotonically with the charging coefficient. The amount of charging from the data is inferred by comparing the projected radius of the deuteron aperture images with x-ray measurements of the camera magnification. Since V depends on particle energy, low-energy deuterons are more susceptible to the effects of charging than high-energy deuterons.

The images of the source are encoded in the recorded penumbral images and are recovered using the iterative reconstruction algorithm described by Gelfgat *et al.* in the limit of Poisson statistics.[3] We include a uniform background and begin with a uniform prior. Numerical testing shows that for N total tracks, the required number of iterations to converge grows as roughly $N^{0.33}$ for a fixed image size. The asymptotic reconstructions are overfit, concentrating numerical noise into high variations between neighboring pixels. To avoid overfitting, a condition for when to terminate the reconstruction is desirable and is under investigation.

The KoDI system was fielded on a series of direct-drive cryogenic implosions on OMEGA during 2021 and 2022. In the majority of the experiments, the diagnostic was fielded in TIM-1 with a magnification of 25 or 35. In one shot series (102560–102571), multiple KoDI instruments were fielded at different magnifications on each shot. Figure 1 shows the (a) deuteron and (b) x-ray data recorded on shot 102568. Analysis of the raw x-ray data indicated a magnification of 35.70±0.10. The deuteron data were analyzed to infer a charge-induced magnification increase of 5.4±0.3%. These values were used to calculate the point-spread function for reconstructing the data. A reconstruction of a high-energy deuteron image is shown in Fig. 1(c), and the corresponding reconstructed x-ray image in Fig. 1(d). The inferred shape and size of the hot spot is comparable between the x rays and deuterons. The 50% radius (P0) of the deuteron image was fit as 30 μm, with a significant mode-2 (P_2/P_0) of 30%. The axis of the mode-2 matches that seen in the reconstructed x-ray image. The camera was fielded in TIM-5, observing the implosion nearly perpendicularly to the stalk axis, and the observed mode-2 is elongated in the stalk direction.

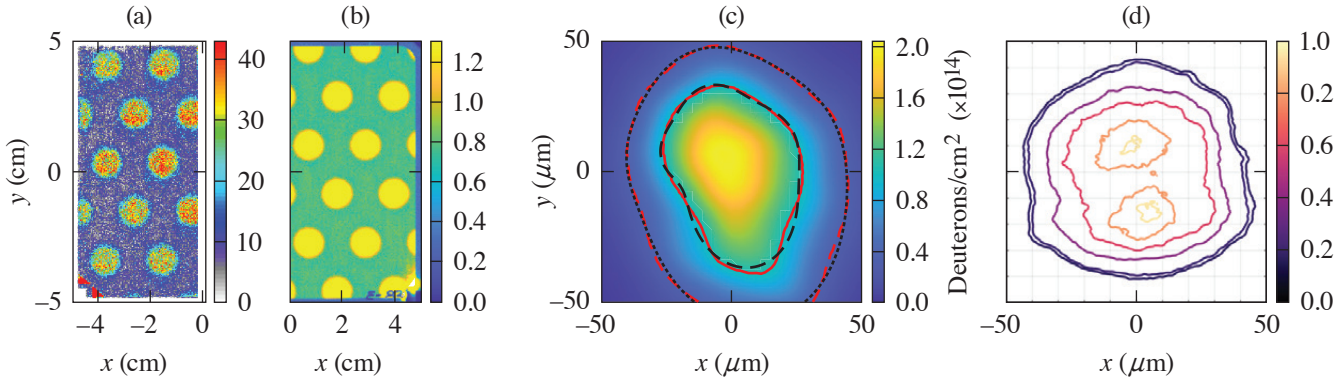

Figure 1
KoDI data recorded on OMEGA cryogenic implosion 102568. (a) High-energy deuteron image (>10 MeV, tracks per 400-μm square pixel); (b) 10-keV x-ray image (PSL per 100-μm square pixel); (c) reconstructed deuteron source with 50% and 17% intensity contours (red curves) and Legendre polynomial fits to $n = 4$ (black curves); and (d) reconstructed x-ray source.

Aperture charging was observed on the majority of the experiments and appears to show increased charging with aperture distance from TCC. The observed trend is not consistent with a prompt charging source that originates at TCC, which should fall off as R^2. The data are roughly consistent with a model in which the electromagnetic pulse (EMP) radiation produced by the laser–target interaction drives currents in the TIM body, for which farther distance from TCC allows a greater amount of time for the aperture to charge before being sampled by the deuterons.

While the charged-aperture PSF is, in principle, sufficient to interpret the diagnostic data, in practice, the reduction or elimination of aperture charging will significantly benefit the experiments by reducing analysis error and maximizing camera resolution,

and is necessary for low-energy deuteron images that are more severely distorted. Several approaches to controlling the aperture charging are being investigated, including replacing the front 30 cm of the diagnostic with a nonconductive material; fabricating the aperture from a nonconductive material such as silicon dioxide; and reducing the EMP source by changing the target mounting stalk.[4] These solutions will be tested in upcoming campaigns to assess their effects on the recorded data.

The data recorded by the KoDI diagnostic will enable detailed studies of the hot spot and assembled cold fuel on OMEGA. Comparisons of the high-energy deuteron and x-ray images will be used to infer the profiles of temperature and density to localize mix in the hot spot. Up to six lines of sight will be used to reconstruct the 3-D profiles of neutron emission and cold dense fuel. These data will provide unprecedented constraints on fuel assembly in direct-drive implosions, which will assist in the goals of reaching improved symmetry and hydro-equivalent ignition conditions on OMEGA.

This material is based upon work supported by the Department of Energy National Nuclear Security Administration under Award Number DE-NA0003856, the University of Rochester, and the New York State Energy Research and Development Authority.

1. N. Sinenian *et al.*, Rev. Sci. Instrum. **82**, 103303 (2011); **85**, 119901(E) (2014).
2. P. J. Adrian *et al.*, Rev. Sci. Instrum. **94**, 043548 (2021).
3. V. I. Gelfgat, E. L. Kosarev, and E. R. Podolyak, Comp. Phys. Commun. **74**, 335 (1993).
4. P. Bradford *et al.*, High Power Laser Sci. Eng. **6**, e21 (2018).

Design and Implementation of a Digital Optical Microscope for Measurement of Submicron Defects on Cryogenic DT Targets

D. Weiner, D. Bredesen, J. Bender, D. H. Edgell, C. Fella, V. N. Goncharov, D. W. Jacobs-Perkins, R. T. Janezic, M. W. Koch, S. F. B. Morse, S. P. Regan, S. Scarantino, M. J. Shoup III, M. D. Wittman, and J. Zou

Laboratory for Laser Energetics, University of Rochester

Submicron particles on the exterior surface of cryogenic deuterium–tritium (DT) target shells may contribute to hydrodynamic instability during target implosions that reduce predicted performance. Particles that originate from pre-existing shell defects or foreign material present within the target Fill/Transfer Station and are observed to exist on the surface after filling with a DT gas. Currently available imaging tools are limited to resolution of the order of 3 μm (Ref. 1). A digital optical microscope system has been developed that provides *in-situ* capability to image 0.5- to 1.0-μm features that are within a critical size range identified by physics considerations. The system design is described and initial results are presented.[2] Initial results indicate that the fill cycle process results in a statistically minor increase in defect count (+10%) and affected area (+4%), and that the pre-to-post fill particle distribution is unchanged.

The Fill/Transfer Station (FTS) is an existing system that houses a target during its fill cycle. Current target evaluation is done at a separate characterization station that is incompatible with cryogenic temperatures. Close examination of a target requires removal of the thermal shroud, which requires that the imaging system exist in a cryogenic environment. The target is held at a temperature of 40 to 50 K during observation.

A commercially available 40×, 0.60 N.A. long-working-distance microscope objective meets the 0.5-μm resolution goal. The projected 20-μm feature size implies that a camera sensor with pixel size less than 10 μm is required to avoid aliasing. A room-temperature test bed was designed and built to verify proof-of-concept using identical optics and illumination to enable comparison of pre- and post-fill images. A quasi-collimated illuminator was designed to reduce the formation hot spots in the target region that originate from LED source points and provide uniform irradiance in the target plane.

The prototype system is shown in Fig. 1. The mechanical design is comprised of three sections: an illuminator, the microscope holder and motion stage, and the charge-coupled–device camera. The microscope and illuminator assemblies are compatible with cryogenic temperatures while the camera is housed within a vacuum bubble to provide isolation from the cold environment. Heat sinks were included to provide for dissipation of thermal sources (LED and camera power supply). With the microscope located outside of the thermal shroud, the microscope translation stage is motorized with a range sufficient to move the objective to the target. Limit switches connected to the controls interface prevent inadvertent collisions between components. A prototype system was installed on the FTS.

The control system provides the ability to remotely power and adjust the LED illumination level, regulate the camera vacuum bubble temperature, and deliver motion control to the microscope and camera stages. To reduce the impact of target vibration and thermal load, the illumination is pulsed and synchronized with the camera's electronic shutter setting. The acquisition pulse width is adjusted to provide optimal integration time on the sensor. Interlocks prevent interference between the microscope, the FTS shroud puller, and the moving cryostat. A software interface is included for image acquisition, display, analysis, and storage. All major component controls are deliverable over an Ethernet connection.

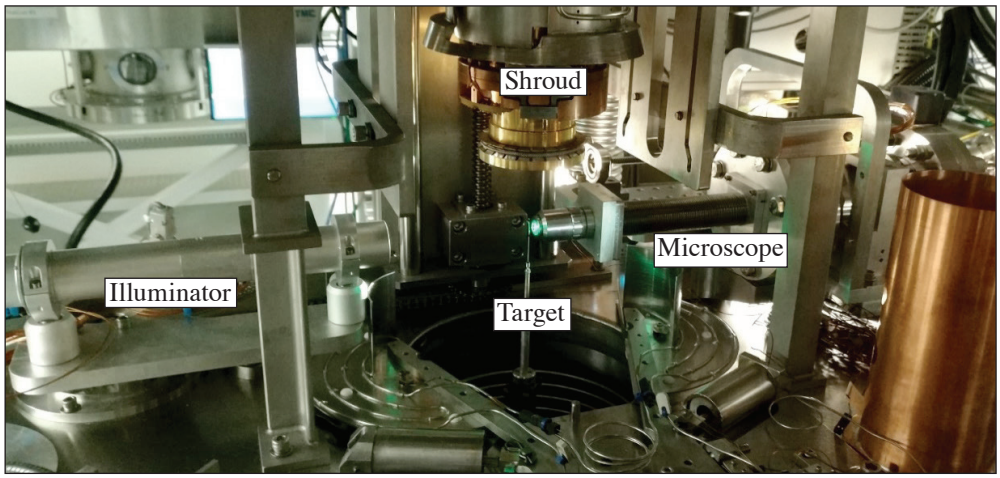

G13604JR

Figure 1
Installed FTS system showing key components.

A set of 12, 178 × 210-μm locations using pre-existing fiducial markers were established about the equator of the target shell, each of which was characterized under pre- and post-fill conditions. The warm temperature pre-fill and cryogenic post-fill optical systems used the same design with similar performance but separate systems. Each area was analyzed using all-in-focus (AIF)[3,4] and maximally stable extremal region (MSER)[5] image-processing techniques to detect and characterize micron-scale shell features. Images were pre-processed to normalize the bright-field background and optimize contrast. The AIF images were generated from a stack of eight to ten through-focus positions, which were then subject to an MSER algorithm for defect detection and statistical computation. A single target was used with a shell made from a glow-discharge polymer (GDP) process. Approximately 1% of the total shell area was analyzed and the results extrapolated. Figure 2 shows a side-by-side image comparison of one location for pre- and post-fill conditions.

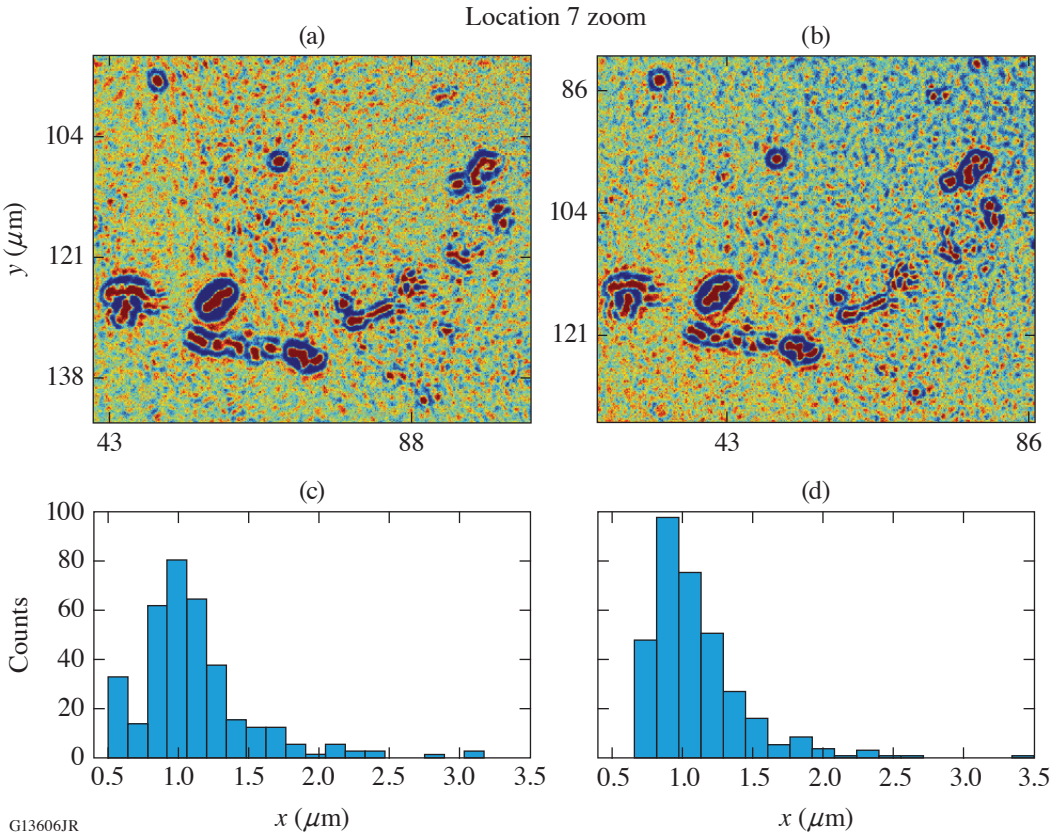

G13606JR

Figure 2
Image comparison for one of the 12 analyzed target areas.

The AIF/MSER techniques used found a 10% increase in feature counts and a 4% increase in feature area upon completion of the fill process (Fig. 3). While the plots suggest good agreement between the pre-fill and post-fill analysis, at present there is no assignment of error or degree of confidence assigned to the measurements.

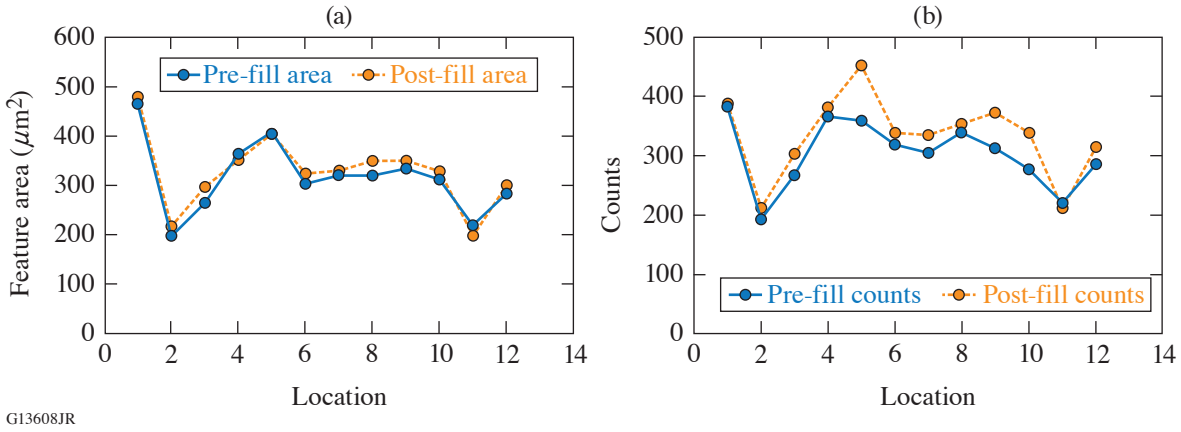

Figure 3
AIF/MSER analysis summary.

No new defects were identified between pre- and post-fill observations with the prototype system. Equivalent diameter size distribution for observed particles was between 0.5 to 2 μm (identified most significant for seeding hydrodynamic instabilities). Initial results indicate that the fill process does not significantly add to defect contribution, and that pre- and post-observation defect distributions are unchanged.

Future work is anticipated to include the testing of target shells made from materials other than GDP (e.g., polystyrene) containing fewer pre-existing defects and the collection of larger data sets to strengthen the statistical significance of results that are obtained. Periodic recharacterization of the platform using a surrogate target is also planned to monitor possible long time-scale system drift.

This material is based upon work supported by the Department of Energy National Nuclear Security Administration under Award Number DE-NA0003856, the University of Rochester, and the New York State Energy Research and Development Authority.

1. *LLE Review Quarterly Report* **104**, 169, Laboratory for Laser Energetics, University of Rochester, Rochester, NY, NTIS Order No. PB2006-108481 (2005).
2. D. R. Harding *et al.*, Matter Radiat. Extremes **3**, 312 (2018).
3. S. Pertuz *et al.*, IEEE Trans. Image Process. **22**, 1242 (2013).
4. F. Pérez Nava and J. P. Luke, in *2009 3DTV Conference: The True Vision - Capture, Transmission and Display of 3D Video* (IEEE, New York, 2009), pp. 1–4.
5. P. P. Ramya and J. Ajay, in *2019 1st International Conference on Innovations in Information and Communication Technology (ICIICT)* (IEEE, Chennai, India, 2019), pp. 1–4.

Tunable Picosecond AlGaN UV Photodiodes

S. F. Nwabunwanne and W. R. Donaldson

Laboratory for Laser Energetics and Department of Electrical and Computer Engineering, University of Rochester

Efficient and ultrafast UV photodetection is needed when characterizing high-temperature plasmas and ultrashort UV laser pulses. Semiconductor-based photodetectors (PD's) have not been widely used for these applications because of their reduced absorption depths in the UV spectrum, making streak cameras the dominant choice in the industry. A new category of photosensors built on $Al_xGa_{(1-x)}N$ (where x varies from 0 to 1) alloy provide tunable band gaps in the entire UV spectrum. Changing x varies from 0 to 1 and adjusts the band gap from 361 nm to 200 nm. Consequently, one can select the spectral window of interest for photosensing.

Laterally oriented AlGaN thin films were used to fabricate photodetectors with interdigitated electrodes.[1] These detectors recorded <30-ps response times, making them suitable for diagnosing ultrafast UV laser pulses and laser–plasma interactions.

This summary reports the outcomes of the spectral studies of detectors fabricated on different $Al_xGa_{(1-x)}N$ thin films where x is 0 to 0.3 (Ref. 1). Measured spectral responsivities are in the range of 0.43 A/W, which is comparable to other semiconductor-based detectors in the visible and infrared regions like silicon and InGaAs. High-quality semiconductors are critical for achieving these results, hence material characterization with x-ray diffraction is recommended prior to fabrication. The University of Rochester is in collaboration with Sydor Technologies to make these detectors available to the public. Some of the AlGaN PD's reported in Refs. 1 and 2, as well as newly fabricated GaN ($x = 0$) PD's with the same design parameters given in Ref. 1, were investigated for a comparison of their spectral selectivity profiles. The objective of this investigation was to determine the spectral responsivity and the ultrafast characteristics of our $Al_xGa_{(1-x)}N$ detectors with x ranging from 0 to 0.3

Figure 1 portrays the temporal response of a Au intrinsic $Al_{0.1}Ga_{0.9}N$ circular asymmetric (CA) device under study and a silicon reference PD at 260 nm under 20-V bias voltage. The voltage response of the AlGaN detector was 1.4 V with a 33-ps rise time

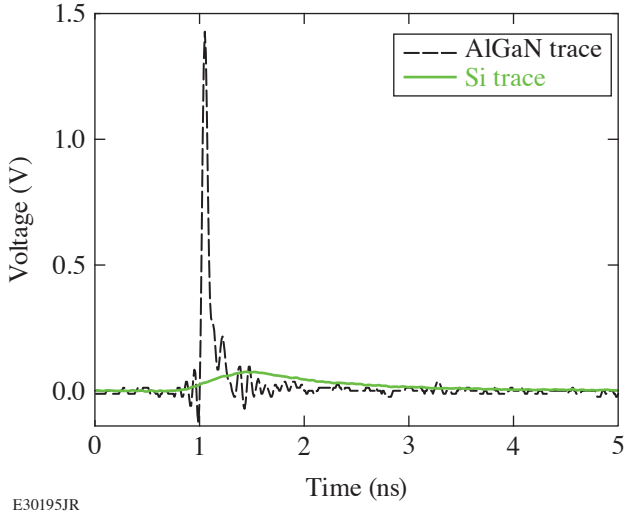

Figure 1
Au intrinsic $Al_{0.1}Ga_{0.9}N$ CA device response (black curve) under 20-V bias and Si reference detector (green curve) at 260 nm with rise times of 33 ps and 430 ps, and FWHM of 60 ps and 1.2 ns for AlGaN and Si PD's, respectively.

and a 60-ps full width half maximum. The pulse width of the device's temporal response increased from 26 ps (the resolution of the 12.5-GHz Tektronix oscilloscope) to 60 ps because of the delays introduced by the measurement system.[3]

The spectral responsivity of another AlGaN device that had 10% Al and rectangular asymmetric (RA) Pt (Ref. 1) metal contacts is depicted in Fig. 2. This detector's responsivity peaked at 315 nm with 0.43 A/W and a rapid cut off at 360 nm. The high responsivity supports the recorded external quantum efficiency of these photodiodes reported in Ref. 1. The responsivity dropped at shorter wavelengths because the absorption depth of photons within the AlGaN thin film reduced from 77 nm at 280 nm to 48 nm at 240 nm.

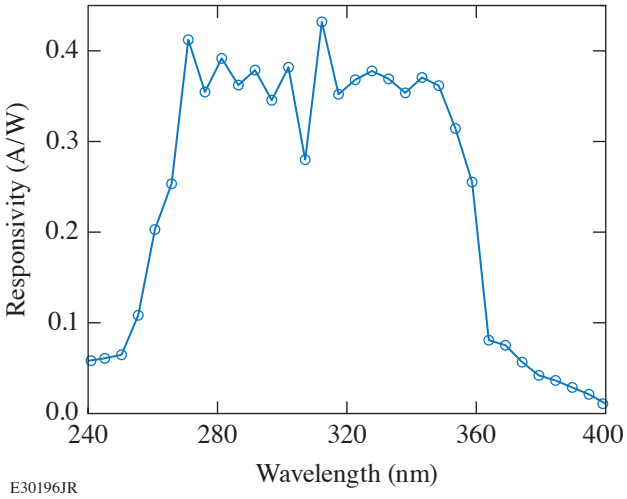

Figure 2
Pt intrinsic $Al_{0.1}Ga_{0.9}N$ RA device with spectral responsivity at 10-V bias voltage with peak responsivity of 0.43 A/W at 315 nm.

The spectral responsivity properties of another AlGaN UV PD that has 20% Al with CA Au metal is presented in Fig. 3. The data were measured under a 10-V bias voltage. This detector exhibited a maximum spectral responsivity of 0.033 A/W at 280 nm and a rapid cut off at 300 nm. The rising Al content implies that this diode will sense only deep UV wavelengths but a factor of 10 decrease in responsivity is recorded at 280 nm.

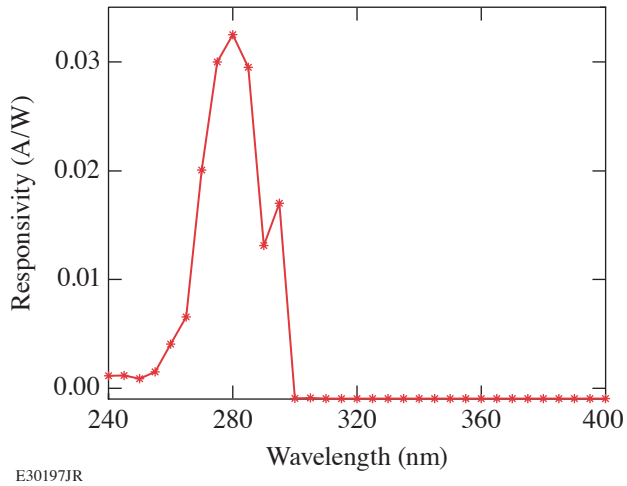

Figure 3
Au intrinsic $Al_{0.2}Ga_{0.8}N$ CA device with spectral responsivity at 10-V bias voltage with maximum responsivity of 0.033 A/W at 280 nm.

Summing up, the spectral responsivity of our AlGaN UV detectors in a metal–semiconductor–metal configuration was discussed. The results demonstrated that the applicability of AlGaN-based UV detectors in high-energy investigations of laser–plasma interactions, which have multiple sources of light in close proximity, require ultrafast and efficient UV photodetection. Finally,

it is necessary to carefully select the Al composition that meets the spectral window that needs to be sensed as this determines if the realized PD will meet the application requirements.

This material is based upon work supported by the Department of Energy National Nuclear Security Administration under Award Number DE-NA0003856, the University of Rochester, and the New York State Energy Research and Development Authority.

1. S. F. Nwabunwanne and W. R. Donaldson, IEEE J. Quantum Electron. **57**, 4000608 (2021).
2. S. Nwabunwanne and W. Donaldson, Proc. SPIE **12001**, 120010F (2022).
3. Y. Zhao and W. R. Donaldson, J. Mater. Res. **33**, 2627 (2018).

Measurement of Laser Absorption in Underdense Plasmas Using Near-Field Imaging of the Incident and Transmitted Beams

J. Katz,[1] D. Turnbull,[1] S. T. Ivancic,[1] A. L. Milder,[1] and D. H. Froula[1,2]

[1]Laboratory for Laser Energetics, University of Rochester
[2]Department of Physics and Astronomy, University of Rochester

Measurements of laser absorption in high-temperature, underdense plasmas produced at the Omega Laser Facility are made using two near-field imaging detectors that diagnose the spatial profile and energy of the port P9 beam before and after it transmits through the plasma. By comparing the signal ratios of these detectors for shots with and without plasma, absorption is measured without the need for absolute energy calibration of either detector. Complementary diagnostics monitor laser backscatter and spatially resolve key plasma parameters,[1] including ion and electron temperature and electron density, along the beam propagation length. Simultaneous measurements of the plasma conditions and total beam absorption provide means to experimentally validate physics models used to predict absorption in plasmas relevant to inertial confinement fusion.

The experimental platform, shown in Fig. 1, utilizes a set of 351-nm heater beams to ionize a 2-mm-diam, cylindrical column of neutral gas that is injected into target chamber center (TCC) using a gas-jet delivery system. The 527-nm P9 probe beam is then fired into the plasma. Experimental conditions can be varied by adjusting the 351-nm heater-beam energies and timings or by changing the gas type and initial neutral gas density. Total absorption in these high-temperature (>100-eV), millimeter-scale-length plasmas are often a few percent or less. As such, high-precision measurements of the input and transmitted beam energies are required. It is also important to confirm that any potential energy loss to the transmitted beam from mechanisms other than absorption remain energetically insignificant.

The input beam is sampled using a partial reflection from a full-aperture, 30-cm-diam uncoated-wedge pickoff located before the target chamber vacuum window and final-focus lens assembly. An uncoated, concave mirror focuses the reflected beam at *f*/10, allowing it to be recorded directly with a 13 × 13-mm sensor. The P9 transmitted-beam diagnostic (P9TBD)[2] characterizes the transmitted light by terminating the expanded beam on a semi-transparent diffuser and imaging the illuminated surface using a lens and charge-coupled–device (CCD) camera. The near-field image measures both the transmitted beam energy and the degree of any potential beam filamentation or whole beam refraction. The nominal diameter of the expanded beam at the diffuser plane is 28 cm. The 45-cm (*f*/4) acceptance aperture of the P9TBD allows energy of the beam to be measured even in the presence of moderate levels of beam refraction or filamentation.[3]

For an ideal detector, the total signal recorded on the CCD images is proportional to the amount of energy present at TCC. The proportionality constant, K, given in analog-to-digital units (ADU) per joule of photon energy, is influenced by a number of factors including the optical throughput between the sample point and TCC, the sensor quantum efficiency, the camera digitizer gain, and the throughput of any optical filtration used to adjust signal levels. It is difficult to accurately quantify all of these components individually. If the energy loss in the transmitted beam is limited to absorption alone, however, knowledge of the individual instrument sensitivities is not required to determine absorption since the measurement depends only on the ratio of the instrument sensitives K and the total signals.

$$\mathrm{ABS} = 1 - \frac{c_{\mathrm{Trans}}}{\underbrace{c_0}_{K}} \frac{\sum \mathrm{CCD}e^{-}_{\mathrm{Trans}}}{\sum \mathrm{CCD}e^{-}_{0}},$$

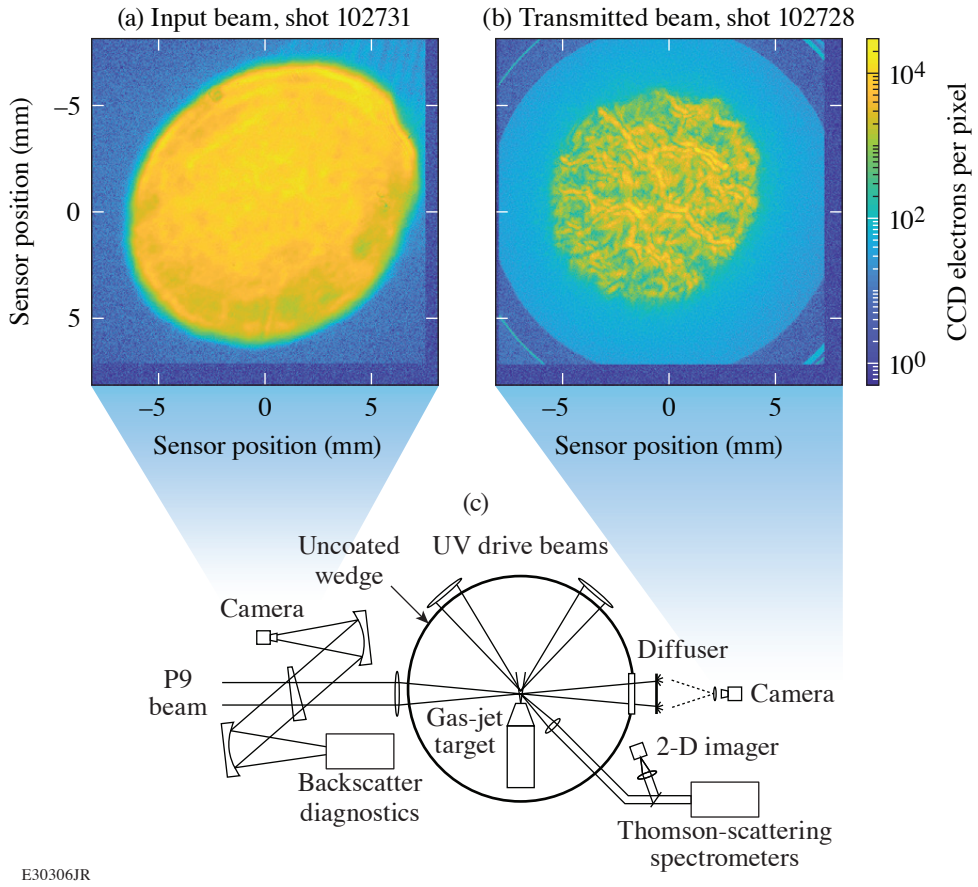

Figure 1
The amount of laser energy deposited in the plasma from a single beam is inferred by comparing input and output energies. Two CCD cameras measure the incident and transmitted beam spatial profiles and energies with high precision. Back and sidescatter diagnostics are used to verify that energy losses from laser–plasma instabilities are energetically insignificant.

where K is measured experimentally by taking a calibration shot with no plasma present. In this case, there is no absorption, $E_0 = E_{\text{Trans}}$, and K is given by the ratio of the input to transmitted signals. To the extent that c_0 and c_{Trans} remain stable over time, the accuracy of the absorption measurement is driven by the measurement precision of the two detectors. Two calibration shots are normally taken during a shot day to confirm the measurement stability and typically agree to within ±0.01%. Additionally, the measurement stability and precision of the two detectors was benchmarked using a full-aperture, Q-switched laser propagated along the P9 beamline through TCC. Synchronized images were recorded at 5-min intervals over a period of 8 h and the ratio of the detector sensitivities was measured. The measurement variation followed a normal distribution with a standard deviation of ±0.014% and showed no noticeable drifts as a function of time.

The amount of stray 2ω light from the other OMEGA drive beams that scatters into the P9 energy detectors is also measured. For these calibration shots, the plasma is heated by the drive beams but the P9 probe beam is turned off and the background level is measured directly. If a variety of beam energies are fielded during the shot day, the magnitude of the background subtraction is scaled by the total 2ω light present in the experiment, as measured by the harmonic energy diagnostic.[4] Baffling and optical filtration help limit the background signal levels to less than 0.05% of the primary signal.

Propagating the expected errors present in the calibrations and the statistical noise in the signal summations, the overall uncertainty of a typical absorption measurement is estimated to be ±0.07%. With these capabilities, the mechanics of inverse bremsstrahlung heating can be explored experimentally with exceptional quantitative detail.

This material is based upon work supported by the Department of Energy National Nuclear Security Administration under Award Number DE-NA0003856, the University of Rochester, and the New York State Energy Research and Development Authority.

1. J. Katz *et al.*, J. Instrum. **8**, C12009 (2013).
2. J. Katz *et al.*, Rev. Sci. Instrum. **92**, 033526 (2021).
3. D. Turnbull *et al.*, Phys. Rev. Lett. **129**, 025001 (2022).
4. *LLE Review Quarterly Report* **63**, 110, Laboratory for Laser Energetics, Rochester, NY, NTIS Order No. DE96000767 (1995).

Design of the High-Yield, Time-Gated X-Ray Hot-Spot Imager for OMEGA

S. T. Ivancic,[1] W. Theobald,[1] K. Churnetski,[1] M. Michalko,[1] D. Willistein,[1] W. A. Bittle,[1] S. P. Regan,[1] A. Carpenter,[2] C. Trosseille,[2] J. D. Kilkenny,[3] A. Raymond,[3] J. D. Hares,[4] A. K. L. Dymoke Bradshaw,[4] G. Rochau,[5] and D. Garand[6]

[1]Laboratory for Laser Energetics, University of Rochester
[2]Lawrence Livermore National Laboratory
[3]General Atomics
[4]Kentech Instruments Ltd., UK
[5]Sandia National Laboratories
[6]Sydor Technologies

Low-mode 3-D nonuniformities of the compressed core in inertial confinement fusion (ICF) implosions are important to diagnose because they represent inefficiency in the conversion of kinetic to internal energy of the core.[1] X-ray projection to infer 3-D shape is incisive for understanding drive nonuniformities and their potential mitigations.[2] Demonstration of using time-integrated x-ray imaging has been developed,[3,4] which is transferrable to time-resolved analysis with a suite of time-synchronized detectors with sufficient signal. Drift-tube imagers[5,6] coupled to high-speed hybrid complementary metal-oxide semiconductor (hCMOS) detectors[7] have a number of advantages over framing cameras[8] especially for being fieldable in a harsh neutron environment such as those found near the target chamber during high-yield implosions. Radiation-hardened electronic readout is essential to provide real-time data. A third, time-gated x-ray line of sight is proposed for OMEGA to provide an additional view to allow for time-resolved 3-D tomographic reconstruction of the hot-spot shape. The simultaneous operation of this new imager with the existing time-gated x-ray imaging lines of sight on OMEGA[9,10] will enable a time-resolved reconstruction of the low-mode shape of the ICF hot spot.

The x-ray hot-spot imager consists of three distinct subassemblies illustrated schematically in Fig. 1: A 22.5× magnification pinhole-array imager provides a multitude of images at an intermediate plane located outside of the OMEGA tank wall on a large-format photocathode. The x rays are converted to photoelectrons, which are imaged by a demagnifying, dilation drift tube that reduces the photoelectron image by 2× on a detector plane while providing temporal magnification of 100 to 350×. The demagnification serves two purposes, first it allows the imager to operate at a larger magnification that serves to lower the current at the photocathode. Demagnification is required in order to form the image to a suitable size to be detected by available solid-state detectors. In this case the photoelectron images are recorded by two side-by-side hCMOS[10] sensors, which are capable of recording eight sequential frames with an adjustable integration time in the range of 1 to 10 ns. The temporal magnification maps eight 20-ps sequential frames onto the hCMOS with a varying duration from 2 to 7 ns. This magnification allows the entire x-ray emission history of the hot spot to be captured.

The photoelectrons are constrained by a homogeneous axial magnetic field to move helical orbits along the axis of the drift tube, providing an upright photoelectron image onto the hCMOS detector. The design of the tube is segmented with the magnetic-field strength increasing in the latter two segments to provide the 2:1 demagnification of the drifting photoelectron signal as it traverses the tube. Simulations using magnetostatic modeling using the field solver *COMSOL* have been performed to measure the effect of segmentation of the solenoidal field into four separate tube parts working together. The overall effect is negligible relative to the sizes of the imager point-spread function and blurring caused by the drift tube.

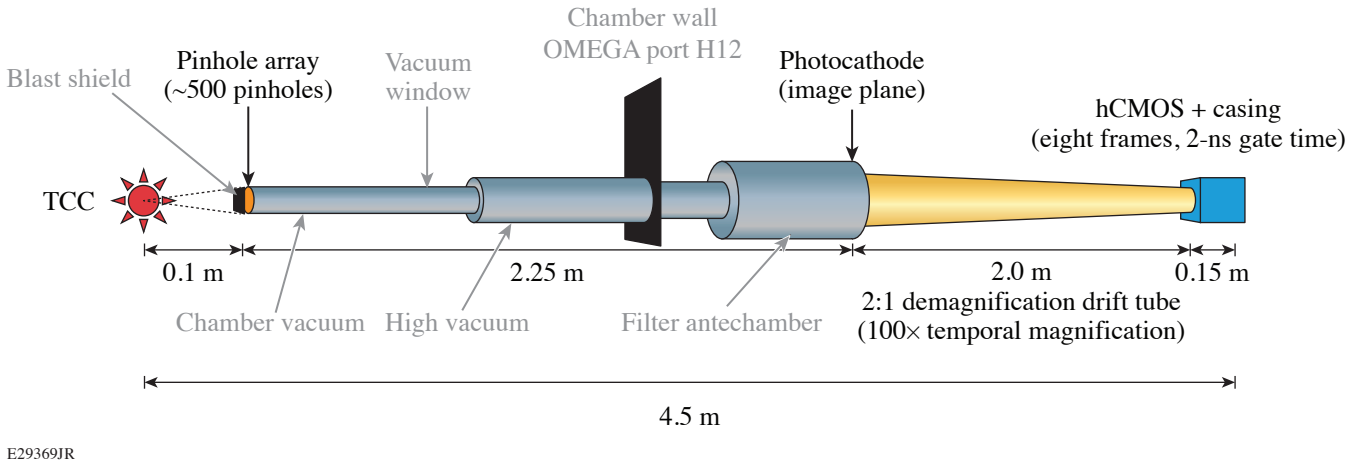

Figure 1
Schematic of the overall x-ray imaging system. A pinhole array is situated 100 mm from the target chamber center (TCC). The x-ray images pass through a beryllium vacuum window located in a re-entrant tube inside the tank that separates the tritium-contaminated tank vacuum from a separate clean vacuum volume that includes the instrument inclusive of the drift tube. The x-ray image emerges from the target chamber out of OMEGA port H12 to an intermediate image plane located 2.25 m from the pinhole array. An access hatch forward of the image plane allows for x-ray filters to be introduced over some or all of the x-ray images. The x-ray imager casts >500 images onto a 50-mm × 50-mm intermediate image plane.

This material is based upon work supported by the Department of Energy National Nuclear Security Administration under Award Number DE-NA0003856, the University of Rochester, and the New York State Energy Research and Development Authority.

1. K. M. Woo *et al.*, Phys. Plasmas **25**, 102710 (2018).
2. O. M. Mannion *et al.*, Phys. Plasmas **28**, 042701 (2021).
3. K. Churnetski *et al.*, Rev. Sci. Instrum. **93**, 093530 (2022).
4. S. M. Glenn *et al.*,, Rev. Sci. Instrum. **83**, 10E519 (2012).
5. T. J. Hilsabeck *et al.*, Rev. Sci. Instrum. **81**, 10E317 (2010).
6. K. Engelhorn *et al.*, Rev. Sci. Instrum. **89**, 10G123 (2018).
7. L. Claus *et al.*, Proc. SPIE **10390**, 103900A (2017).
8. D. K. Bradley *et al.*, Rev. Sci. Instrum. **66**, 716 (1995).
9. W. Theobald *et al.*, Rev. Sci. Instrum. **89**, 10G117 (2018).
10. F. J. Marshall *et al.*, Rev. Sci. Instrum. **88**, 093702 (2017).

High-Resolution Mapping of Phase-Matching Conditions in Second-Order Nonlinear Crystals

C. Dorrer, I. A. Begishev, S.-W. Bahk, and J. Bromage

Laboratory for Laser Energetics, University of Rochester

Nonlinear crystals are widely used for frequency conversion of lasers and optical parametric amplification. Phase matching between the interacting waves is required for efficient operation.[1] This can generally be achieved by temperature or angle tuning, which both allow precise control the optical index. Such global tuning is sufficient when the interacting beams and the crystal have spatially uniform properties. This is a reasonable assumption for relatively small nonlinear crystals. However, the local crystals properties are impacted by environmental stability during growth, stress within the boule, and impurities in the growth solution. These issues are particularly important for the large-aperture ($\sim 40 \times 40$-cm^2) KDP and partially deuterated KDP (DKDP) that are required to support doubling and tripling of inertial confinement fusion laser systems.[2,3] Variations in axis angle θ and deuteration level X can decrease the frequency-conversion efficiency and uniformity. Large-aperture deuterated KDP crystals will be required for optical parametric chirped-pulse–amplification systems delivering ultrashort optical pulses with peak power well beyond 1 PW (Ref. 4).

While x-ray techniques, optical interferometry, and spectroscopy can be used to spatially resolve the physical characteristics of nonlinear crystals, mapping the local phase-matching conditions is a more-direct approach to performance quantification for an actual laser system. This work demonstrates the high-resolution characterization of local phase-matching conditions for second-harmonic generation of a beam at 1053 nm in several laser crystals, including partially deuterated KDP crystals used for broadband optical parametric amplification of pulses at 920 nm by a pump pulse at 526.5 nm (Ref. 5).

A test bed capable of characterizing crystals over apertures as large as 50×50 mm^2 has been developed [Fig. 1(a)]. A Nd:YLF regenerative amplifier seeded by a fiber front end delivers 1053-nm (λ_1) 350-ps pulses collimated to an ~1-mm diameter. The crystal under test (length L) is mounted on two translation stages that provide transverse scanning in front of the static laser beam. The phase-mismatch $\Delta k_{SHG}L$ for second-harmonic generation (SHG) is proportional to the normalized energy variation $S(x,y) = [\eta(x,y)/(1/2)]-1$, where η is measured at 526.5 nm (λ_2) for the crystal angularly detuned from ideal phase matching [(θ_+) and (θ_-) in Fig. 1(b)]. The nonideal translation stages induce small position-dependent angular rotations of the crystal that can impact phase matching. To alleviate this, the 1053-nm beam is stabilized by a piezo-actuated mirror using the feedback signal from a four-quadrant photodetector on which the beam reflected by the crystal's input face is incident.

As an example of application, the normalized energy variation S is shown in Fig. 2 for a crystal with a deuteration level equal to 98%. For the first two measurements, the input face is the same [labeled as (A) on the figure], whereas the input face is the opposite face for the third measurement [labeled as (B) on the figure]. This crystal has variations in normalized energy up to 25%. Anticorrelated variations of S are obtained when operating at θ_- and θ_+ [Figs. 2(a) and 2(b)]. The high-frequency variations, e.g., in the upper-right corner on Fig. 2(a), are not measurement artifacts. They consistently correspond to a sign change between Figs. 2(a) and 2(b), indicating that they are caused by a local change in phase matching instead of another effect such as low local transmission. This is confirmed by the measured energy variations after a 180° rotation along the vertical axis [Fig. 2(c)]. The low-frequency variations in S are symmetric along the x axis for the two crystal orientations differing by the 180° crystal rotation [Figs. 2(a) and 2(c)]. This indicates that they are caused by bulk variations and do not depend on the propagation direction within the crystal. The observed 25% variations in S are consistent with 20-μrad angular variations and 0.025% deuteration variations.

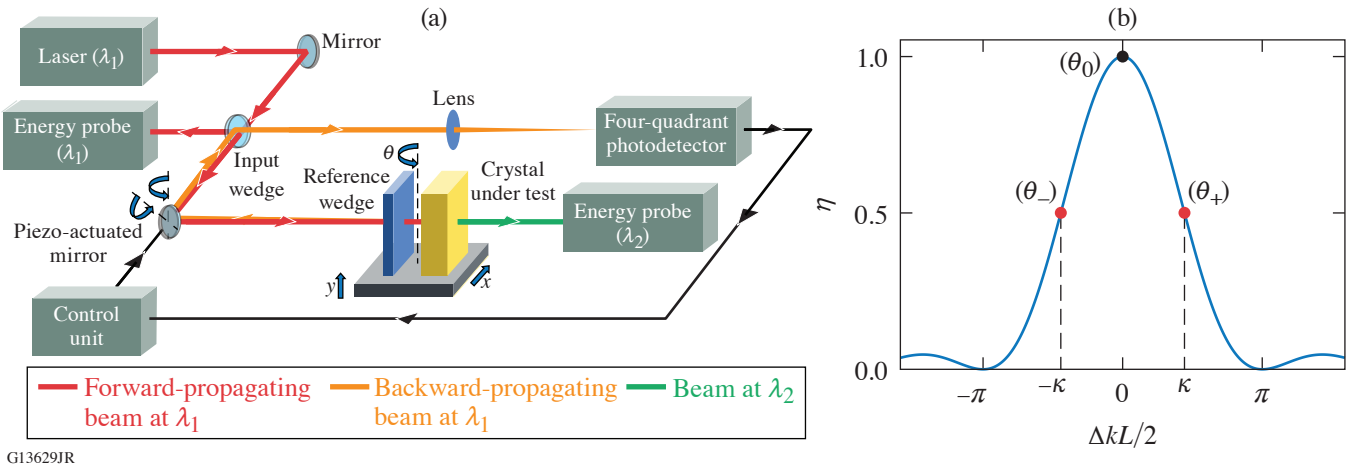

Figure 1
(a) Setup for spatially resolved measurement of the SHG energy, indicating the forward-propagating beam at λ_1 (red line), the backward-propagating beam at λ_1 (orange line), and the beam at λ_2 (green line). (b) Relative SHG efficiency η as a function of the phase mismatch ΔkL.

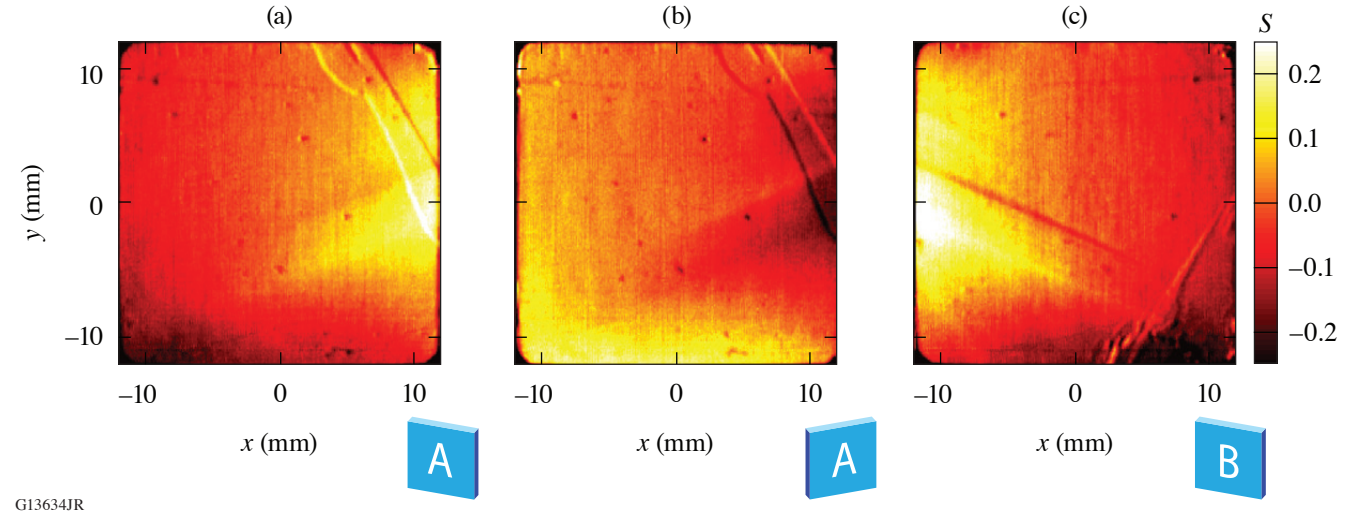

Figure 2
Normalized energy variation S for a crystal with a deuteration level equal to 98%. (a) and (b) correspond to characterization with the same face (A) at the input, and different phase-matching angles θ_- and θ_+, respectively. (c) corresponds to a 180° rotation of the crystal, i.e., characterization with the other face (B) at the input, and phase matching angle θ_-.

The high-frequency variations in S observed in the upper right corner of Fig. 2(a) are, however, not observed in the upper left corner of Fig. 2(c), indicating that these variations are caused by disruptions in phase matching occurring at or close to the input surface. Analytical derivations and experimental results obtained on other crystals confirm that surface variations, such as those introduced by irregularities in sol-gel antireflection coatings, can impact the phase-matching conditions.

A novel approach to the characterization of transverse variations in phase-matching conditions in nonlinear crystals has been demonstrated. SHG in the detuned crystal under test unambiguously converts the local phase mismatch onto energy at the upconverted frequency. Transverse scanning of the crystal combined with beam stabilization maps out phase-matching variations over an aperture only limited by the scanning range of the translation stages. The characterization of partially deuterated

KDP crystals with submillimeter resolution over a 50×50-mm^2 aperture has revealed the impact of spatially nonuniform crystal properties and high-frequency surface variations due to coating imperfections.

The authors thank A. Bolognesi, M. Barczys, T. McKean, and M. Spilatro for experimental assistance with the 1053-nm source. This material is based upon work supported by the Department of Energy National Nuclear Security Administration under Award Number DE-NA0003856, the University of Rochester, and the New York State Energy Research and Development Authority.

1. R. Boyd, *Nonlinear Optics*, 3rd ed. (Academic Press, Amsterdam, 2008), pp. 217–221.
2. J. J. De Yoreo, A. K. Burnham, and P. K. Whitman, Int. Mater. Rev. **47**, 113 (2002).
3. J. M. Auerbach *et al.*, Appl. Opt. **40**, 1404 (2001).
4. C. N. Danson *et al.*, High Power Laser Sci. Eng. **7**, e54 (2019).
5. C. Dorrer *et al.*, Opt. Mater. Express **12**, 3679 (2022).

Utilizing the MTW-OPAL Idler to Seed a Raman Plasma Amplifier

S. Bucht, R. G. Roides, B. Webb, D. Haberberger, C. Feng, D. H. Froula, and J. Bromage

Laboratory for Laser Energetics, University of Rochester

A Raman plasma amplifier (RPA) promises to overcome the damage limitations of chirped-pulse–amplification (CPA)[1] compression gratings by using a "damage-free" plasma to transfer energy from a multipicosecond high-energy pulse to a longer-wavelength femtosecond seed pulse.[2] This technology promises to achieve focused intensities exceeding 10^{23} W/cm^2 if pumped with the output of an Nd:glass-based CPA system laser[3] but requires a 1100- to 1250-nm seed pulse. Simulations show that to achieve an efficient amplifier, a high-intensity (10^{15} W/cm^2), sub-200-fs duration seed pulse is required.[4,5]

One technique for creating such a laser is by using the idler of an optical parametric chirped-pulse–amplification (OPCPA) system.[6] OPCPA systems produce two broadband pulses: a signal, which is seeded, and an idler, which has a wavelength that is red shifted. The Multi-Terawatt optical parametric amplifier line (MTW-OPAL) Laser System,[7,8] which produces 7-J, 20-fs pulses at 910 nm, consists of an ultrabroadband front end (UFE), a cylindrical Offner stretcher (COS), a power amplifier (N4), and a final DKDP amplifier (N5) as shown in Fig. 1(b). The idler that exits the N4 power amplifier has a bandwidth that ranges from 1100 to 1500 nm and 70 mJ of energy; if compressed and focused it would provide an ideal laser to seed an efficient RPA.

Using this idler requires overcoming two disadvantages that are a result of phase matching and energy conservation. First, phase matching in N4 produces an idler that is angularly dispersed, which hampers pulse focusing and compression.[9] Second, energy conservation inverts the spectral phase of the idler relative to the signal,[10] significantly changing the typical stretch–amplify–compress process of CPA.[1] Here we address both the phase reversal and angular dispersion of the MTW-OPAL idler with the addition of several optical subsystems to achieve 100-GW pulses at 1170 nm with 120-fs durations.

For ease of switching between the conventional MTW-OPAL configuration [Fig. 1(b)] and an idler OPAL configuration [Fig. 1(a)], many of the subsystems were left unchanged between the two modes of operation. No changes were made to the UFE or the N4 pump laser. The differences include switching from the COS to an alternate grism stretcher (GrS), operating at a reduced bandwidth, and bypassing the final amplifier (N5). This GrS accounts for the inversion of the idler spectral phase and allows for a standard grating compressor to be used to compress the idler (IGC). Angular dispersion was compensated with an angular dispersion compensator (ADC) prior to compression.

The design of the GrS is the result of compromise between a full compression of the pulse and optic manufacturing limitations.[11] Each grism is made from a 45°, N-SF57 prism mounted 1 mm away from a 1480-lp/mm gold grating. This design fully compensates for the two lowest orders of spectral phase (group-delay dispersion and third-order dispersion) but has some residual fourth-order dispersion. The stretcher also reduces bandwidth of OPAL to wavelengths that correspond those of interest for an RPA and a roof mirror double passes the pulse to a duration of 1 ns.

The idler exiting N4 is imaged with a 3× achromatic image relay onto two custom prisms to reduce angular dispersion from 123 μrad/nm to <0.5 μrad/nm. The idler is then compressed with a pair of parallel 1285-lp/mm gratings (PGL) and a roof mirror. Slant distance and input angle are selected to maximize peak power as measured with a custom IR-SPIDER (APE).[12] The compressed pulse was measured to have a full-width-half-maximum (FWHM) pulse duration of 120±10 fs (Fig. 2).

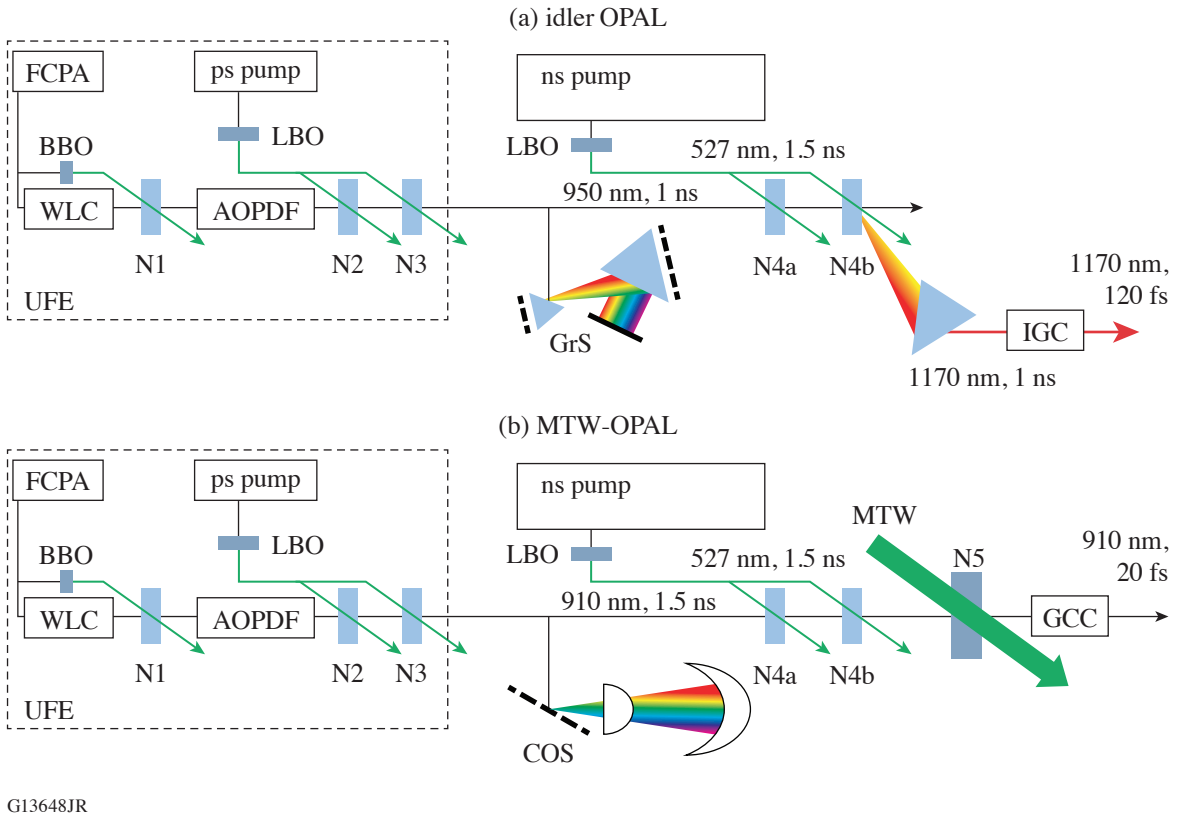

Figure 1

(a) A schematic of the idler OPAL and (b) standard MTW-OPAL configurations shows that they share many components including the UFE, the pre- and power amplifiers (N4a and N4b), and a nanosecond pump laser. (a) Systems added to operate the OPAL idler include an alternate grism stretcher (GrS), ADC, and an IGC. (b) The components of MTW-OPAL that are unused are the final amplifier, which is pumped by the MTW laser (N5), a COS, and grating compressor chamber (GCC). FCPA: fiber chirped pulse amplifier; WLC: white-light continuum; AOPDF: acoustic-optic-programable dispersive filter.

The focused and compressed idler had an average peak intensity of 5×10^{15} W/cm^2, which is about an order of magnitude lower than the transform-limited and diffraction-limited (TL-DL) intensity. The diffraction- and transform-limited intensity is based on the measured near-field beam profile and spectrum (row 1 in Table I). Reduction of this peak intensity is calculated from a subset of spatiotemporal effects: linear angular dispersion (AD), residual spectral phase, and monochromatic wavefront. Residual spectral phase was measured with the IR-SPIDER described above, while monochromatic wavefront was measured with a focal-spot diagnostic. This diagnostic was also used to measure residual angular dispersion by blocking all but two wavelengths in the GrS. How each of these spatiotemporal effects individually impact the achievable peak intensity is calculated in rows 2–4 in Table I. In the fifth row of Table I, all three spatiotemporal effects are applied.

Table I: Contributions to peak intensity.

	FWHM Pulse duration	Spot radii (μm)	AD$_x$,AD$_y$ (μrad/nm)	Intensity (W/cm^2)
TL-DL	50.2	19.6	0,0	56×10^{15}
Spectral phase	120	–		$14.1 \pm 0.8 \times 10^{15}$
Monochromatic wavefront	–	21.5 to 70		$18 \pm 3.7 \times 10^{15}$
Linear angular dispersion	–	–	<0.5, 0.5	35 to 56×10^{15}
Combined	120	21.5 to 70	<0.5, 0.5	$4.7 \pm 1 \times 10^{15}$

TL-DL: transform-limited; AD: angular dispersion

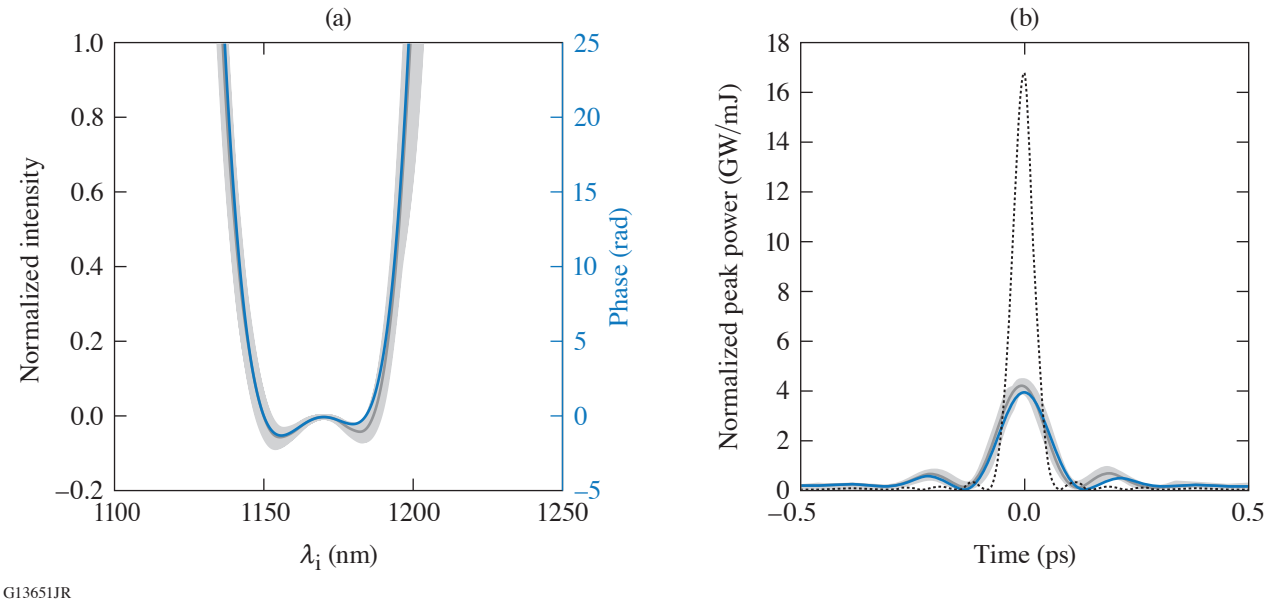

Figure 2
(a) The idler phase is measured over 100 shots by the IR-SPIDER and is denoted by the shaded area. The average phase and spectrum are shown by the solid gray and dotted curves, respectively, and closely matches the expected phase (blue curve). (b) The measured peak power is 4× lower than transform limited (black dotted curve), but matches the temporal pulse predicted by the design of the grism stretcher/grating compressor pair.

In conclusion, the compression of the idler to 100-GW peak powers from an existing OPCPA system has been demonstrated. While operating at a reduced peak intensity from the transform and diffraction limit, the idler from high-peak-power OPCPA systems achieves 100-GW pulses and provides a unique opportunity to further study the limits of laser technology.

This material is based upon the work supported by the Department of Energy Office of Science under Award No. DE-SC0016253, the Department of Energy National Nuclear Security Administration under Award No. DE-NA0003856, the University of Rochester, and the New York State Energy Research and Development Authority.

1. D. Strickland and G. Mourou, Opt. Commun. **56**, 219 (1985).
2. V. M. Malkin, G. Shvets, and N. J. Fisch, Phys. Rev. Lett. **82**, 4448 (1999).
3. J. H. Kelly *et al.*, J. Phys. IV France **133**, 75 (2006).
4. J. D. Sadler, "Optimisation and Applications of Raman Plasma Amplifiers," Ph.D. thesis, University of Oxford, 2017.
5. D. Haberberger *et al.*, Phys. Plasmas **28**, 062311 (2021).
6. A. Dubietis, G. Jonusauskas, and A. Piskarskas, Opt. Commun. **88**, 437 (1992).
7. J. Bromage *et al.*, High Power Laser Sci. Eng. **7**, e4 (2019).
8. J. Bromage *et al.*, High Power Laser Sci. Eng. **9**, e63 (2021).
9. T. Wilhelm, J. Piel, and E. Riedle, Opt. Lett. **22**, 1494 (1997).
10. I. N. Ross *et al.*, J. Opt. Soc. Am. B **19**, 2945 (2002).
11. S. Bucht *et al.*, J. Opt. Soc. Am. B **36**, 2325 (2019).
12. "APE Angewandte Physik & Elektronik GmbH," Ultrafast Laser Diagnostics & Tuneable Laser Solutions, Berlin, Germany.

Impact of Raman Scattering on Temporal Reflection from a Short Soliton

J. Zhang,[1] W. R. Donaldson,[2] and G. P. Agrawal[1]

[1]The Institute of Optics, University of Rochester
[2]Laborotary for Laser Energetics, University of Rochester

An optical pulse can be reflected at a temporal boundary across which the refractive index changes with time.[1] The reflected pulse is frequency shifted by an amount set by the law of momentum conservation. While a temporal boundary where the refractive index changes everywhere at the same time is hard to create in practice, reflection can also happen at a moving boundary. Such a boundary can be created through the optical Kerr effect by injecting an intense pump pulse into a dispersive nonlinear medium. This configuration has been studied in optical fibers when a weak pulse collides with an optical soliton.[2–4]

When a femtosecond soliton is formed inside an optical fiber, intrapulse Raman scattering between its different spectral components leads to a continuous red shift that decelerates the soliton as it propagates. This work considers the situation where a weak pulse reflects from such a decelerating soliton. It is shown that the reflected pulse can be much shorter than the input pulse, involving a new type of temporal focusing. The effect is explained using space–time duality and derive an approximate transformation law for Gaussian-shape input pulses.

Using the generalized nonlinear Schrödinger equation, the temporal reflection of a probe pulse from a soliton (called the pump pulse) is numerically simulated. Results are shown in Fig. 1 for a realistic set of parameters for silica fibers. In the time domain,

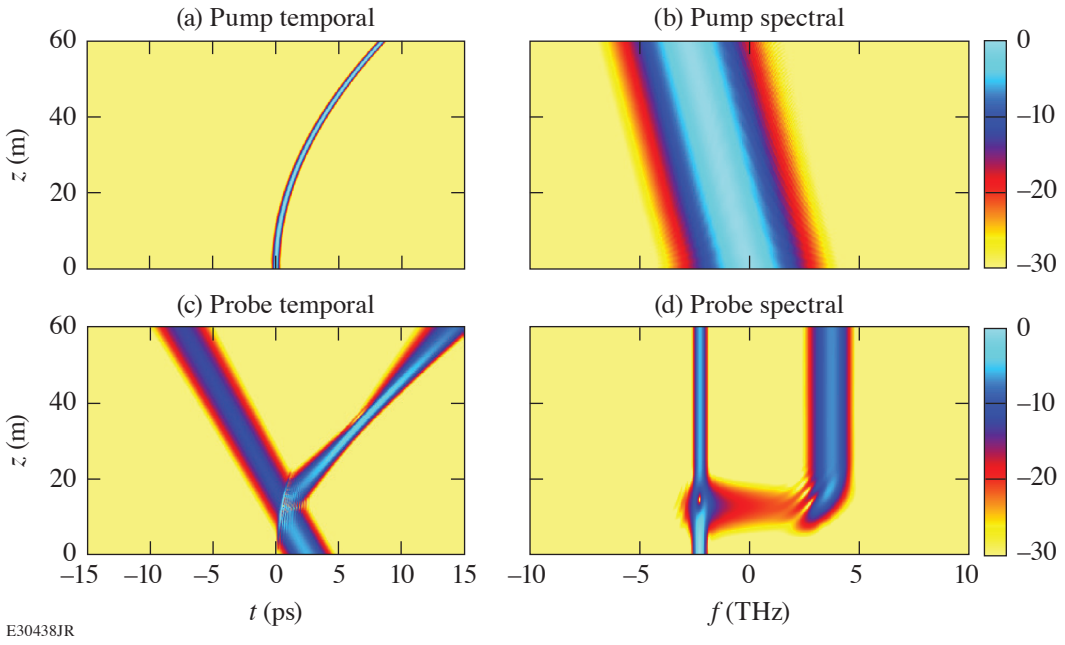

Figure 1
Simulation of temporal reflection of a probe pulse on a pump soliton. The pump soliton continuously red shifts because of Raman scattering.

the trajectory of the soliton has a parabolic shape because of its Raman-induced deceleration. When the probe pulse hits the pump pulse, it splits into a reflected pulse and a transmitted pulse.

The reflected pulse undergoes a frequency shift and its spectrum becomes broader than the incident spectrum. The reflected pulse also becomes narrower before it broadens again. This is an example of temporal focusing induced by the decelerating soliton. This effect can be explained using the concept of space–time duality.[5] The decelerating soliton forms a temporal boundary with a parabolic trajectory. A probe pulse reflected from this boundary is analogous to an optical beam being reflected by a parabolic-shaped mirror. It has been found that temporal focusing is more significant for longer incident pulses.

An approximate analytic theory has been developed that describes how the spectrum of an incident Gaussian pulse is modified when the pulse is reflected by a decelerating soliton. Figure 2 compares the analytical prediction with the numerical results. Both the reflected pulse spectrum and the rms pulse width of the reflected pulse agree well with the numerical simulations. The analytical approximation can be used to understand the temporal focusing effect.

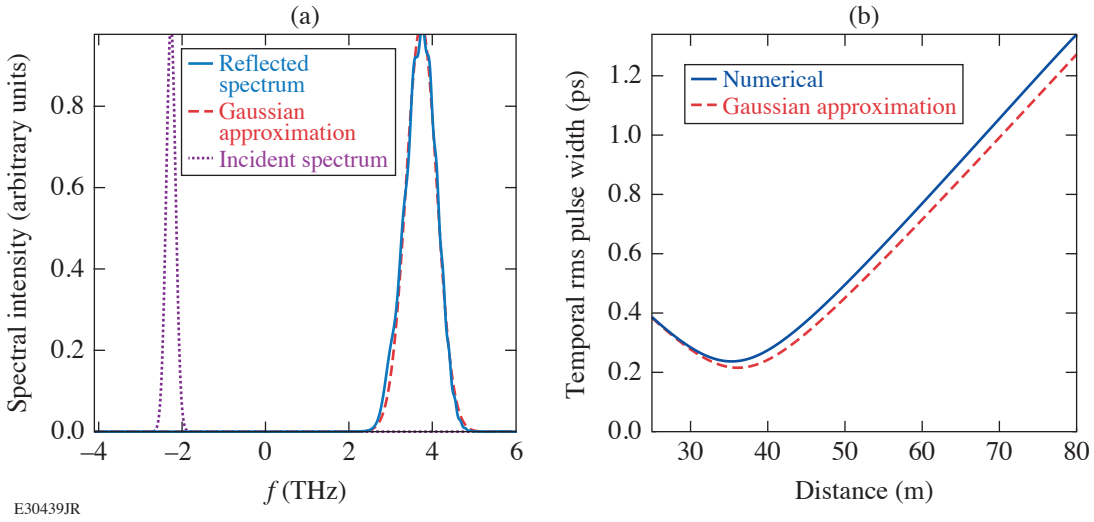

Figure 2
Comparison of analytical formula with numerical result. (a) Reflected pulse spectrum; (b) rms pulse width of a reflected pulse as it propagates.

This work is supported by National Science Foundation (ECCS-1933328). This material is based upon work supported by the Department of Energy National Nuclear Security Administration under Award Number DE-NA0003856, the University of Rochester, and the New York State Energy Research and Development Authority.

1. B. W. Plansinis, W. R. Donaldson, and G. P. Agrawal, Phys. Rev. Lett. **115**, 183901 (2015).
2. T. G. Philbin *et al.*, Science **319**, 1367 (2008).
3. K. E. Webb *et al.*, Nat. Commun. **5**, 4969 (2014).
4. L. Tartara, IEEE J. Quantum Electron. **48**, 1439 (2012).
5. B. H. Kolner, IEEE J. Quantum Electron. **30**, 1951 (1994).

A First-Principles Equation of State of CHON for Inertial Confinement Fusion Applications

S. Zhang,[1] V. V. Karasiev,[1] N. R Shaffer,[1] S. X. Hu,[1] D. Mihaylov,[1] K. Nichols,[1] R. Paul,[1] R. M. N. Goshadze,[1] M. Ghosh,[1] J. Hinz,[1] R. Epstein,[1] and S. Goedecker[2]

[1]Laboratory for Laser Energetics, University of Rochester
[2]Department of Physics, University of Basel, Switzerland

In laser-direct-drive (LDD) inertial confinement fusion (ICF) targets, a foam layer or ablator materials with radial density gradients can mitigate laser imprint and reduce hydrodynamic instabilities during ablation.[1,2] This can be realized by taking advantage of the two-photon polymerization (TPP) technique, which can precisely fabricate CHON polyacrylate resin into shell structures with superb lateral structure uniformity (to the level of 1 μm) (Ref. 3). To test the new ideas and optimize designs to improve target performance in relevant ICF and high-energy-density experiments, high-quality equations of state (EOS) of the target materials are required. In contrast to CH, however, which has been a widely used ablator material with relatively well understood EOS,[4–7] an EOS for CHON is still missing.

For this study, a wide-range (0 to 1044 g/cm^3 and 0 to 10^9 K) EOS table was constructed for a C-H-O-N quaternary compound ($C_{16}H_{27}O_6N_1$, stoichiometry that matches the resin material used in the laboratory for TPP printing) from first-principles simulations. The calculations combine two state-of-the-art approaches: Kohn–Sham density functional theory molecular dynamics (KS-DFT-MD) with an accurate meta-generalized gradient approximation (GGA)-level thermal exchange-correlation functional (T-SCAN-L) and orbital-free (OF) DFT-MD with lately developed Luo–Karasiev–Trickey γ Thomas–Fermi (LKTγTF) tunable noninteracting free-energy functionals. The thermal functional LKTγTF is constructed through a convex combination of LKT GGA[8] and Thomas–Fermi (TF)[9] functionals, where γ is determined for each density by matching the pressure from our OF-DFT-MD calculations at a high temperature (1 to 3×10^5 K) to the corresponding value from the KS-DFT-MD calculations; energies from OF-DFT-MD are uniformly shifted along each isochore to align with the KS-DFT-MD values at the matching temperature. This approach is similar but superior to previous EOS studies that stitch KS and OF but use TF functional in the OF calculations.[5,10,11] The first-principles EOS calculations are performed along 27 isochores (between 0.05 and 1044 g/cm^3) at 24 different temperatures (between 1000 and 10^9 K). The data have been extrapolated to lower densities and temperatures to produce a wide-range EOS table.

The EOS results show smooth bridging of KS and OF data at the matching condition. Figure 1 shows the EOS data approach the fully ionized ideal gas values in the limit of high temperatures (10^6 to 10^7 K, higher at higher densities). At lower temperatures, the energies and pressures for isochores of up to 4 to 7.5 g/cm^3 are below the ideal gas values because of the weaker ion and electron thermal contributions; for higher densities, the EOS increasingly exceeds the ideal gas values because of the increased degeneracy of electrons. The slope variations in the energy plots between different densities reflect changes in heat capacity; the differences between energy and pressure plots define the profile of the Grüneisen parameter. Both are caused by the joint effects of ion thermal vibration and electron thermal excitation.

Based on the calculated EOS, the predicted Hugoniot of CHON resin [Fig. 2(a)] shows a sharper profile and larger compression maximum by ~2% than that of pure CH polystyrene because of the coexistence of nitrogen and oxygen. Calculations of thermodynamic properties show overall consistency with that of CH along their respective Hugoniots [Figs. 2(b) and 2(c)]. Both exhibit a local minimum in heat capacity and maximum in the Grüneisen parameter at 2 to 3×10^4 K, which corresponds to

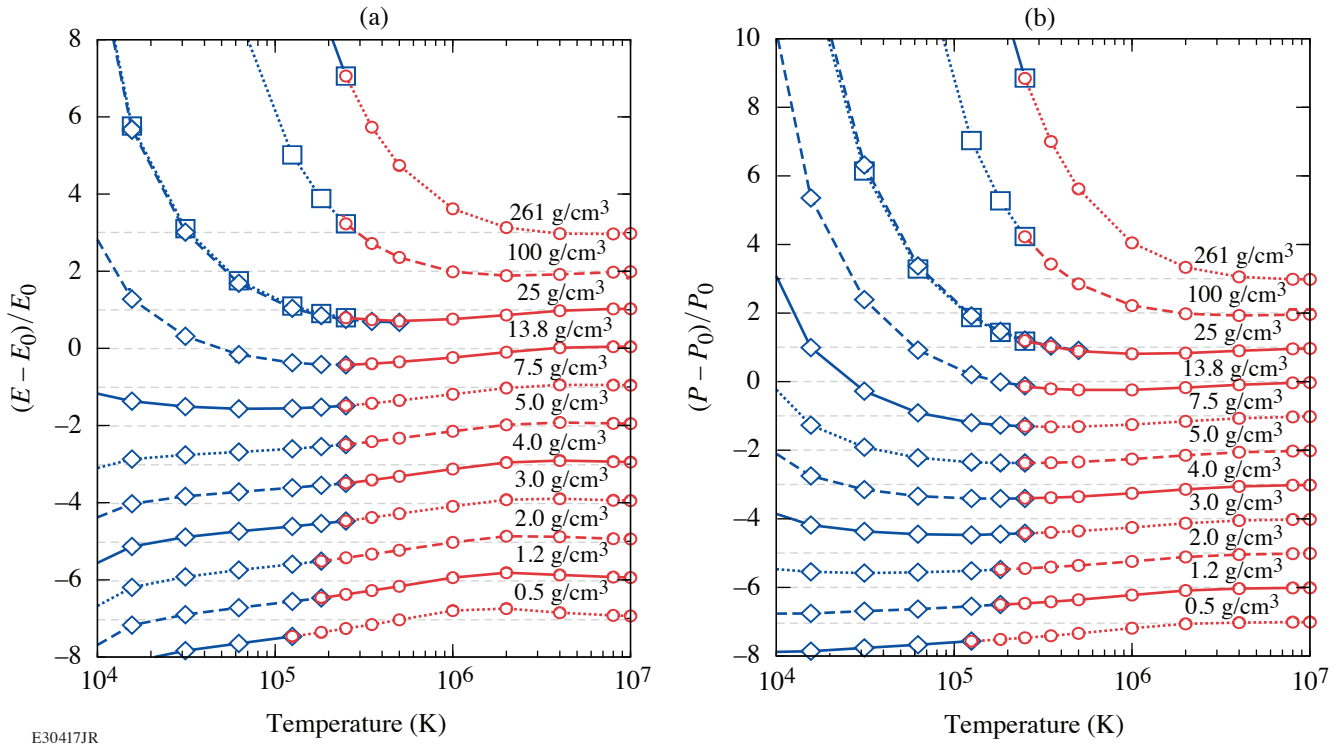

Figure 1
Matching KS (blue) and OF (red) (a) energies and (b) pressures along selected isochores. Data shown are relative to values of fully ionized ideal gas (denoted by E_0 and P_0 and shown with dashed gray horizontal lines). Blue diamonds and squares denote calculations using projector-augmented-wave and bare-coulomb potentials, respectively, which agree well with each other. Different isochores have been shifted apart for clarity.

bonded-to-atomic transition,[12] and a peak in heat capacity and a basin in the Grüneisen parameter at 10^6 K, corresponding to ionization of the K shell. The heat capacity and the Grüneisen parameters are found to reach the fully ionized ideal gas limit at 10^7 K. It is also found that the thermal expansion coefficient and the bulk sound velocity show independence of the isochore once the temperature exceeds 10^6 K.

To test the laser absorption and hydrodynamic efficiency of CHON resin as a potential ablator material for LDD targets, radiation-hydrodynamic simulations were performed of cryogenic DT implosion targets by using the 1-D radiation-hydrodynamics code *LILAC*.[13] The CHON results are compared with the conventional CH ablator. Results from the simulations show CHON outperforms CH as the ablator for LDD target designs (Fig. 3) due to a slight increase in the laser absorption fraction, which should further prompt the fabrication of the CHON shell with a foam layer for laser-imprint mitigation.

This material is based upon work supported by the Department of Energy National Nuclear Security Administration under Award Number DE-NA0003856, the University of Rochester, and the New York State Energy Research and Development Authority. V. V. Karasiev, D. I. Mihaylov, R. M. N. Goshadze, and S. X. Hu also acknowledge support by the U.S. NSF PHY Grant No. 1802964.

1. N. Metzler, A. L. Velikovich, and J. H. Gardner, Phys. Plasmas **6**, 3283 (1999).
2. S. X. Hu *et al.*, Phys. Plasmas **25**, 082710 (2018).
3. O. Stein *et al.*, Fusion Sci. Technol. **73**, 153 (2018)
4. M. A. Barrios *et al.*, Phys. Plasmas **17**, 056307 (2010).
5. S. X. Hu *et al.*, Phys. Rev. E **92**, 043104 (2015).
6. S. Zhang *et al.*, Phys. Rev. E **96**, 013204 (2017); S. Zhang *et al.*, J. Chem. Phys. **148**, 102318 (2018).

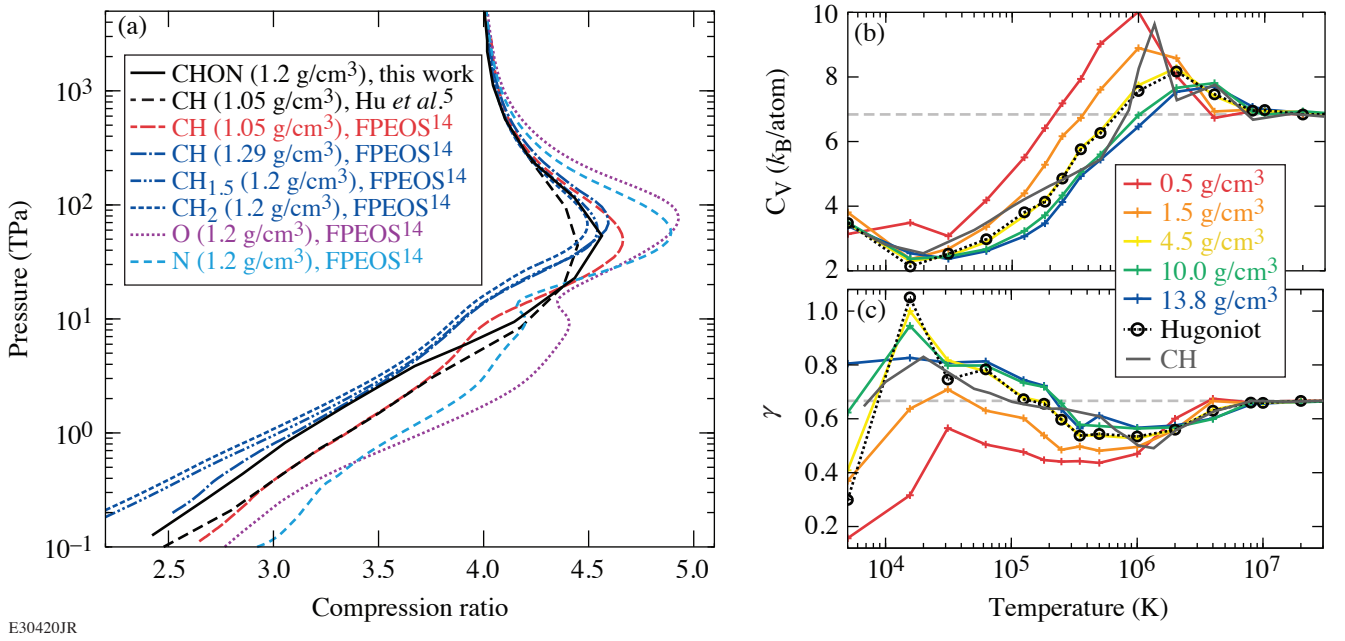

Figure 2
(a) Pressure-compression ratio Hugoniot, (b) heat capacity, and (c) Grüneisen parameter of CHON compared with that of CH. In (a), results of C–H compounds[5,6] and of O and N from first-principles EOS[14] are shown for comparison. In (b) and (c), the horizontal gray dashed lines denote the corresponding values of a fully ionized ideal gas.

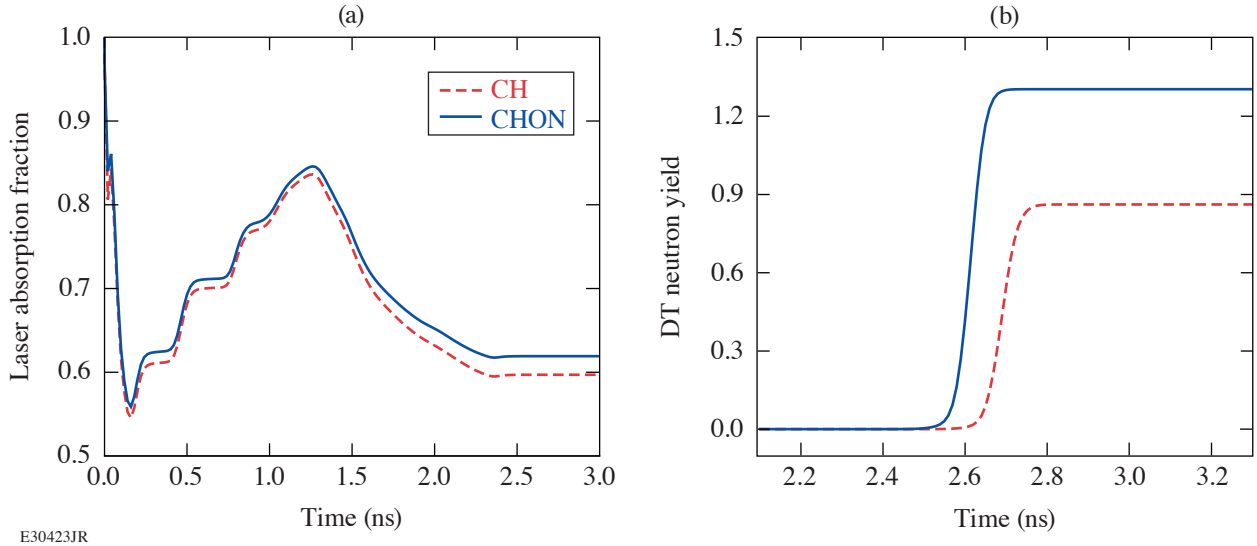

Figure 3
Comparison in (a) the time evolution of laser absorption fraction and (b) neutron yield at later time of the implosion when using targets with CH or CHON ablators. The simulations are based on a typical OMEGA-scale cryo-DT target with a 50-μm-thick DT-ice layer covered by 8-μm-thick CH ablator (ρ_0 = 1.05 g/cm^3) or 7-μm-thick CHON ablator (ρ_0 = 1.2 g/cm^3) to have equivalent target mass. The simulations employ the same laser pulse (total UV laser energy of ~27 kJ, shape optimized for the CH target assembly on OMEGA).

7. A. L. Kritcher *et al.*, Nature **584**, 51 (2020).
8. K. Luo, V. V. Karasiev, and S. B. Trickey, Phys. Rev. B **101**, 075116 (2020).
9. R. P. Feynman, N. Metropolis, and E. Teller, Phys. Rev. **75**, 1561 (1949).
10. S. X. Hu *et al.*, Phys. Rev. B **94**, 094109 (2016); Phys. Rev. E **95**, 043210 (2017).
11. Y. H. Ding and S. X. Hu, Phys. Plasmas **24**, 062702 (2017).
12. S. Zhang *et al.*, J. Appl. Phys. **131**, 071101 (2022).
13. J. Delettrez *et al.*, Phys. Rev. A **36**, 3926 (1987).
14. B. Militzer *et al.*, Phys. Rev. E **103**, 013203 (2021).

Shocked-Silica Aerogel Radiance Transition

B. J. Henderson,[1,2] J. R. Rygg,[1,2,3] M. C. Marshall,[1] M. K. Ginnane,[1] L. E. Hansen,[4] E. Davies,[5] P. M. Celliers,[5] and G. W. Collins[1,2,3]

[1]Laboratory for Laser Energetics, University of Rochester
[2]Department of Physics and Astronomy, University of Rochester
[3]Department of Mechanical Engineering, University of Rochester
[4]Sandia National Laboratories
[5]Lawrence Livermore National Laboratory

The objective of this work was to measure the radiance of shock fronts in SiO_2 aerogel at various initial densities. The optical properties of shock-compressed fused silica, quartz,[1] and stishovite[2] have been characterized and used as standards for temperature and reflectance measurements.[3] This work measures the optical radiant behavior of shock-compressed SiO_2 aerogel, which is expected to be significantly hotter, and thus brighter, at comparable shock pressures, than shock-compressed SiO_2 starting at solid density.[4,5] These measurements can be used to constrain radiative-hydrodynamics in inertial confinement fusion simulations of implosions using aerogel liners and to generate an optimally bright broadband source for high-energy-density–physics experiments.

Experiments were performed on the OMEGA EP Laser System. Targets were irradiated by one to four laser beams (λ = 351 nm) on a polystyrene (CH) ablator, producing strong shock waves that compress the planar samples. These experiments used laser irradiance between 10 and 200 TW/cm^2 produced by 2-, 2.5-, and 4-ns temporally square and ramp-top laser pulses with spatially uniform spot diameters of approximately 1100 or 1800 μm through the use of distributed phase plates. The targets were composed of a 40-μm CH ablator (refractive index n = 1.59 at λ = 532 nm, ρ_0 = 1.05 g/cm^3), a 50-μm quartz pusher (n = 1.547, ρ_0 = 2.65 g/cm^3), and a 250-μm SiO_2 aerogel sample (n = 1.02 to 1.06, ρ_0 = 0.1 to 0.3 g/cm^3). Shock velocity, reflectivity, and radiance were measured using a velocity interferometer for any reflector (VISAR) and a streaked optical pyrometer (SOP).

Brightness temperature of the shocked aerogel was determined by measuring the radiance of the shock front using the SOP. The SOP collects time- and spatially resolved thermal emission from the shock front integrated over wavelengths between 590 and 850 nm, with a peak efficiency at 600 nm. The SOP signal is converted to brightness temperature using an absolute calibration of the OMEGA EP SOP, which follows the procedure described in Ref. 6.

SiO_2 aerogel exhibits behavior that is starkly different from its higher-density counterparts (Fig. 1). Specifically, the exponent of the power law fit a is ~2 with no observed slope change for fused silica, quartz, and stishovite. For SiO_2 aerogel, a is 2 below the change in slope and ~1 above the change in slope. Below the change in slope observed in aerogel, the six T_{bright}–P curves for SiO_2 form a set of parallel lines. Some possible causes for this behavior include: (a) radiative precursor ahead of the shock, (b) a conductive precursor, and (c) shock propagation in aerogel microstructure.

This material was based upon work supported by the Department of Energy National Nuclear Security Administration under Award No. DE-NA0003856, the University of Rochester, and the New York State Energy Re-search and Development Authority. A portion of this work was performed under the auspices of NSF Physics Frontier Center Award No. PHY-2020249, and under the auspices of the U.S. Department of Energy by Lawrence Livermore National Laboratory under Contract No. DE-AC52-07NA27344.

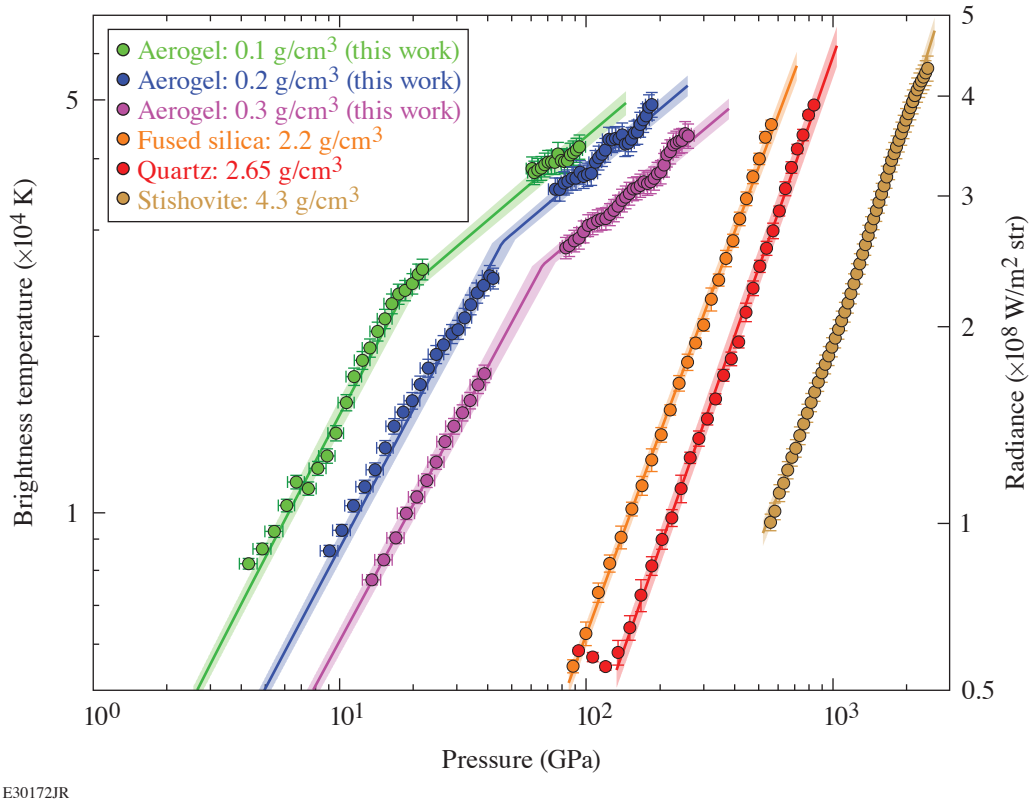

Figure 1
Brightness temperature (and integrated radiance in the 590- to 850-nm band) versus inferred pressure for shock compressed SiO_2 aerogel (green, blue, and pink circles) and their two-part power-law fits (green, blue, and pink curves). Shaded regions represent 1σ confidence intervals. Measurements of fused silica (orange circles),[1] quartz (red circles),[1] and stishovite (brown circles)[2] are fit with a single power-law function (orange, red, and brown curves).

1. D. G. Hicks *et al.*, Phys. Rev. Lett. **97**, 025502 (2006).
2. M. Millot *et al.*, Science **347**, 418 (2015).
3. S. Brygoo *et al.*, J. Appl. Phys. **118**, 195901 (2015).
4. J. C. Boettger, Los Alamos National Laboratory NM, New Mexico, Report LA-11488-MS (1989).
5. Ya. B. Zel'dovich and Yu. P. Raĭzer, in *Physics of Shock Waves and High-Temperature Hydrodynamic Phenomena*, edited by W. D. Hayes and R. F. Probstein (Academic Press, New York, 1966), Vol. I, Chap. II, pp. 107–175.
6. M. C. Gregor *et al.*, Rev. Sci. Instrum. **87**, 114903 (2016).

Shock-Induced Metallization of Polystyrene Along the Principal Hugoniot Investigated by Advanced Thermal Density Functionals

R. M. N. Goshadze, V. V. Karasiev, D. I. Mihaylov, and S. X. Hu

Laboratory for Laser Energetics, University of Rochester

Use of a recently developed thermal strongly constrained and appropriately normed Laplacian (T-SCAN-L)-dependent meta-generalized gradient approximation exchange correlation (XC) density functional[1] and thermal hybrid XC density functional (KDT0)[2] within the framework of density functional theory as implemented in Vienna *ab-initio* simulation package (VASP) to show that the inclusion of thermal and inhomogeneity effects is crucial for accurate prediction of structural evolution and corresponding insulator–metal transition (IMT) during shock compression. Optical reflectivity calculated as an indicator of IMT is in perfect accord with experimental data.[3] The discrepancy between experiment and *ab-initio* simulation results was reported several times during last decade.[4–6]

The equation of state (EOS) of shocked material just behind the shock front satisfies the Rankine–Hugoniot equation

$$E_1 - E_0 + \frac{1}{2}(P_1 + P_0)\left(\frac{1}{\rho_1} - \frac{1}{\rho_0}\right) = 0,$$

where the subscripts "0" and "1" stand for unshocked and shocked sides, respectively. The unshocked side of the ablator (CH) is in ambient conditions. At ambient conditions (T = 300 K and ρ = 1.055 g/cm^3), the pressure P_0 can be approximated by zero since it is orders of magnitude lower than the pressure at ~10^3 K. Based on the results from the *ab-initio* molecular dynamics (AIMD) calculations, E_0 is set to be –93 kJ/g.

Figure 1 shows the comparison between various experimental and theoretical studies of principal Hugoniot on the pressure–density plane. Both Perdew–Burke–Ernzerhof (PBE)[5] and T-SCAN-L AIMD calculations overestimate shock pressure compared

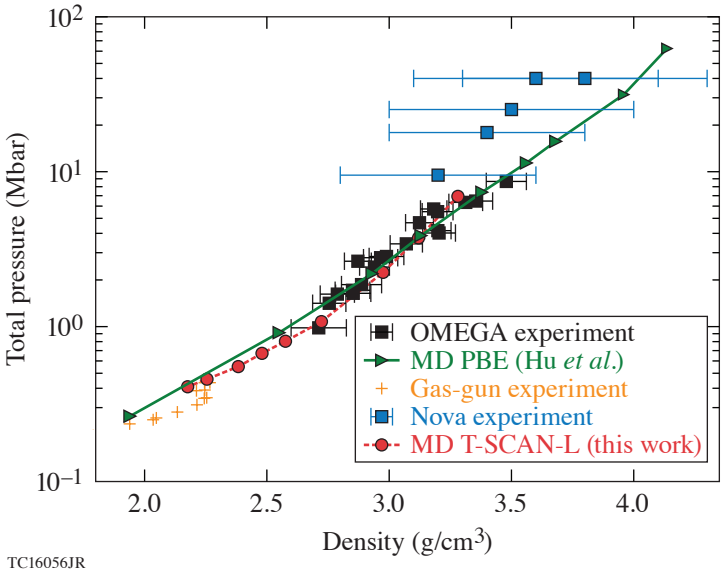

Figure 1
CH pressure as a function of density along the principal Hugoniot. The T-SCAN-L results are compared with PBE calculations by Hu *et al.*,[5] the Nova experiment,[7] gas-gun experiment,[8] and the OMEGA experiment[3] based on latest quartz EOS (black rectangles).

to a gas-gun[8] experiment below 1 Mbar. In the mid-pressure range (1 to 10 Mbar), T-SCAN-L shows concave behavior opposing more-linear PBE results. Apart from using a higher-rung XC functional with explicit temperature dependence, this change might also be associated with the proper treatment of structural characteristics of shocked CH. We carefully run structural relaxation until no structure remains, observing melting/dissociation exactly at these mid-range pressures.

Optical calculations are performed within the Kubo–Greenwood formalism, obtaining CH reflectivity by averaging the uncorrelated snapshots of ionic configurations from the AIMD simulations. The details of the process can be found in Ref. 5. A comparison of the results from the calculations with the OMEGA experiment and PBE-based AIMD study[5] is shown in Fig. 2. Note that the reflectivity turn-on point is shifted to higher pressures and the jump is much sharper, making it in perfect agreement with the OMEGA experiment. By separately plotting the results obtained by T-SCAN-L and KDT0 on top of the T-SCAN-L–generated ionic configurations in Fig. 2, we demonstrate that the improved results are the consequence of not only accurate ionic configurations, but also accurate electronic structure calculations. There are several factors that contribute to this enhancement. Foremost, our PBE calculations show that it underestimates the drop in density of states (DOS) as compared to T-SCAN-L at exactly the same conditions as shown in Fig. 3, which shows a comparison of DOS in the temperature range from 3500 to 5000 K along the principal Hugoniot. The second aspect is the shift in Hugoniot data. At lower densities, T-SCAN-L gives lower Hugoniot pressures compared to PBE calculations. As a result, the Hugoniot points at a fixed density predicted by T-SCAN-L have much less molecular dissociation and consequently exhibit a deeper drop in DOS, leading to smaller reflectivity.

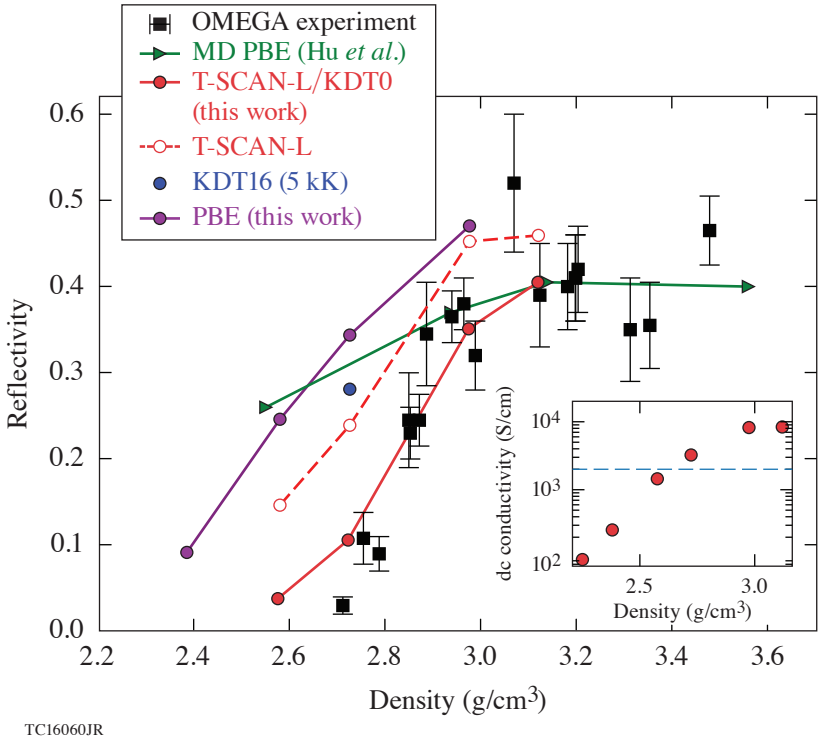

Figure 2
Reflectivity of shocked CH along the principal Hugoniot at 532-nm VISAR (velocity interferometer system for any reflection) light.

This material is based upon work supported by the Department of Energy National Nuclear Security Administration under Award Number DE-NA0003856 and US National Science Foundation PHY Grant No. 1802964.

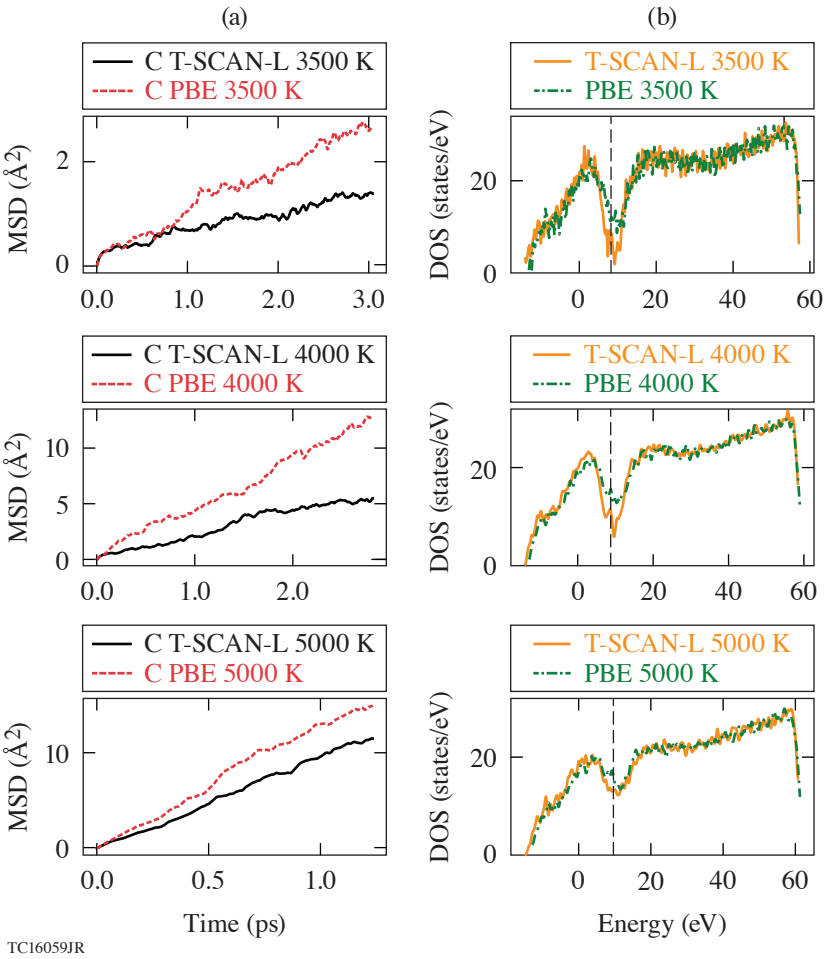

Figure 3
(a) Comparison of mean square displacement predicted by PBE versus TSCAN-L XC functionals and (b) comparison of corresponding DOS in the temperature range of 3500 to 5000 K. MSD: mean squared displacement.

1. V. V. Karasiev, D. I. Mihaylov, and S. X. Hu, Phys. Rev. Lett. **105**, L081109 (2022).
2. D. I. Mihaylov, V. V. Karasiev, and S. X. Hu, Phys. Rev. B **101**, 245141 (2020).
3. M. A. Barrios *et al.*, Phys. Plasmas **17**, 056307 (2010).
4. C. Wang, X.-T. He, and P. Zhang, Phys. Plasmas **18**, 082707 (2011).
5. S. X. Hu, T. R. Boehly, and L. A. Collins, Phys. Rev. E **89**, 063104 (2014).
6. N. J. Hartley *et al.*, Matter Radiat. Extremes **5**, 028401 (2020).
7. R. Cauble *et al.*, Phys. Plasmas **4**, 1857 (1997).
8. S. P. Marsh, ed. LASL Shock Hugoniot Data, Los Alamos Series on Dynamic Material Properties (University of California, Berkeley, CA, 1980).

The 13th Omega Laser Facility Users Group Hybrid Workshop

J. A. Frenje,[1] S. Ali,[2] E. Merritt,[3] K. Falk,[4] S. Finnegan,[3] M. Gatu Johnson,[1] J. P. Knauer,[5] M. P. Valdivia,[6] and L. Willingale

[1]Massachusetts Institute of Technology
[2]Lawrence Livermore National Laboratory
[3]Los Alamos National Laboratory
[4]Helmholtz-Zentrum Dresden-Rossendorf, Germany
[5]Laboratory for Laser Energetics, University of Rochester
[6]University of California, San Diego
[7]University of Michigan

Overview

On 27–29 April 2022, 158 researchers from more than 40 universities and laboratories and 13 countries gathered at LLE for the 13th Omega Laser Facility Users Group (OLUG) Hybrid Workshop (Fig. 1). Of these researchers, 103 had registered to attend the workshop in person and 55 had registered to attend the workshop virtually. The main goal of the three-day workshop was to facilitate a continuing dialog among the Omega users, the users and LLE management, and the users and the broader scientific community along with providing an opportunity for students and postdoctoral fellows to present their research at LLE in an interactive and informal atmosphere. What makes the annual OLUG Workshop unique is that it brings users together from all over the world, facilitating a vibrant dialog among them about their experiences running experiments at Omega, as can be seen in photographs shown in this summary.

U2877JR

Figure 1
In-person attendees at the 13th OLUG Hybrid Workshop.

A major part of OLUG's responsibility is to enhance the Omega Laser Facility and its capabilities by defining a set of Findings and Recommendations (F&R's) each year. In this year's workshop, the F&R discussions were stimulating and lively. As shown at the end of this report, 25 F&R's were defined and grouped into several categories. LLE management use these F&R's as a guide for making decisions about the Omega Laser Facility operations, priorities, and future changes.

The workshop included five science talks given by leading world authorities that described the breadth and excitement of high-energy-density (HED) science undertaken at Omega and other facilities in U.S. Two facility talks about the future of Omega proved especially enlightening to the OLUG participants. The workshop attendees also had a chance to hear the National Nuclear Security Administration's (NNSA's) and National Science Foundation's (NSF's) perspectives on the research conducted at Omega and how it fits into their national programs. A summary of this year's OLUG Executive Committee (ExCom) election was also presented. Another workshop highlight was the evening tutorial session given by LLE, in which the gas-jet platform, the MIFEDS (magneto-inertial fusion electrical discharge system) experimental platform, and as the *PlasmaPy* and *Fiducia* open-source codes were presented.

A student/postdoctoral-panel discussion was held to focus on their experiences at Omega and present their thoughts and recommendations on facility improvements. Several discussions were sparked by this forum, which resulted in the student/postdoctoral report summarized at the end of this summary. Another important event was the discussion on careers in HED science, which brought students together with potential future employers.

A total of 51 students and postdoctoral fellows (Fig. 2), 36 of whom were supported by travel grants from NNSA, attended the workshop and presented three sessions of posters. The presentations involved a large range of topics including target fabrication, inertial confinement fusion (ICF) experiments and simulations, and laboratory astrophysics, all of which generated spirited discussions, probing questions, and many suggestions. An award ceremony for the best student and postdoc posters was also held.

U2878JR

Figure 2
A total of 51 students and postdoctoral fellows attended the workshop and made engaging poster presentations.

The Workshop Presentations

A wide-ranging series of presentations and posters were presented during the workshop. The invited presentations covered facility, government, and science. The science talks focused on several interesting topics, including high-energy-density plasmas, laboratory astrophysics, and burning plasmas in ICF. Two facility talks—"The Renewal of the Five-Year LLE Cooperative Agreement" by Acting LLE Director Dr. Chris Deeney and "The LLE Sustainment Plan" by Omega Laser Facility Division Director Mr. Samuel Morse—presented important details on the status, performance, and path forward of the Omega Laser Facility. Mr. Morse also gave an enlightening talk on the "OMEGA Facility Update and Progress on OLUG Recommendations." Dr. Sarah Nelson, Acting Director of the NNSA Office of Experimental Sciences, presented an excellent perspective on the importance of the Omega facility within her program, and Dr. Slava Lukin, the Director for Plasma Physics at NSF, provided an informative overview of his program and the importance of training and educating the next-generation scientist in the area of plasma physics. In addition to the invited presentations, 63 contributed posters, presented in three sessions, covered a wide spectrum of work at Omega including target fabrication, ICF experiments, diagnostics, HED-plasma theory and simulations, laboratory astrophysics, material science, and laser–plasma interactions along with diversity, equity, and inclusion. Out of these posters, 51 were presented by graduate students, postdocs, and undergraduate students. These poster sessions offered ample opportunities for informal discussions about Omega experiments and their connections to work at other facilities. A set of four exciting facility talks were also given by LLE in an evening tutorial session. Figures 3–8 provide a representative sampling of the workshop's presentations and ambience.

Figure 3
In the plenary sessions, authorities spoke about science opportunities, government perspectives, and the evolving capabilities of the Omega Laser Facility to enable new science frontiers. (a) Dr. Chris Deeney, the Acting LLE Director, kicked off the workshop with a perspective on the renewal of the five-year LLE Cooperative Agreement; (b) Prof. Petros Tzeferacos of the University of Rochester (UR) gave an inspiring presentation on the Flash Center for Computational Science at the UR, and (c) Dr. Sarah Nelson, the Acting Director of the NNSA Office of Experimental Sciences, provided a bigger-picture perspective on the importance of the Omega Laser Facility within her program.

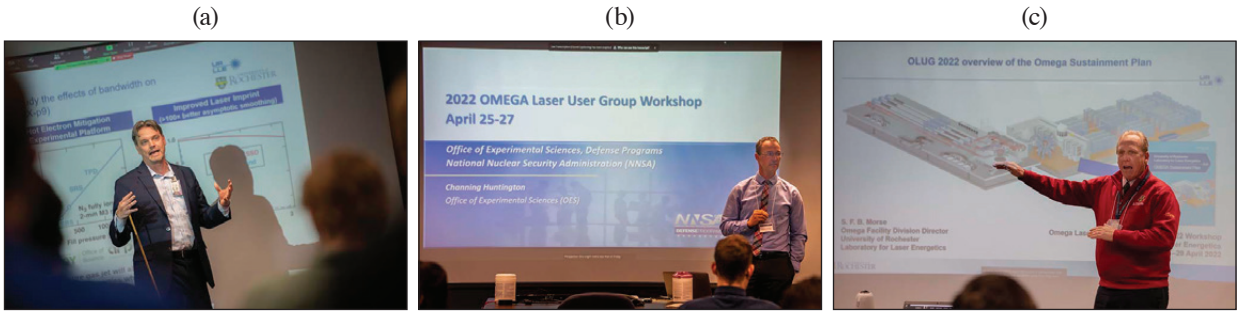

Figure 4
(a) UR Prof. Dustin Froula gave an exciting talk on the science that can be done on the Fourth-Generation Laser for Ultra-broadband eXperiments (FLUX); (b) Dr. Channing Huntington provided a wonderful personal account on his journey from a graduate student at University of Michigan (UM), conducting experiments at Omega, to working at the NNSA Office of Experimental Sciences; and (c) Samuel Morse (LLE) discussed the Omega sustainment plan, which is critical to the future of the laboratory and to the OLUG community. Mr. Morse's extensive knowledge of the facility is invaluable to those planning Omega experiments.

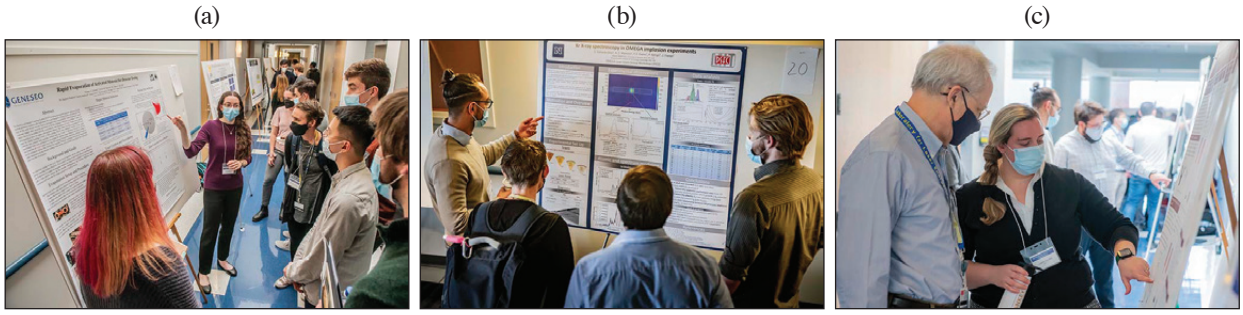

Figure 5
Sixty-three posters were presented in three sessions on a wide spectrum of work at Omega. Out of these posters, 51 were presented by graduate students, postdocs, and undergraduate students. In an interactive yet informal setting, these poster sessions provided opportunities for students and young researchers to present their research from Omega experiments and their connections to work at other facilities. (a) Undergraduate students Vizma Leimanis and Jessica Dawson [State University of New York (SUNY) Geneseo] discussed their work on "Rapid Evaporation of Activated Material for Detector Testing" with OLUG ExCom member Dr. Maria Gatu Johnson (MIT) and other students; (b) graduate student Enac Gallardo-Villaseca (University of Nevada, Reno) presented his work on "Krypton X-Ray Spectroscopy in OMEGA Implosion Experiments;" and (c) graduate student Camille Samulski (Virginia Tech) discusses her poster with LLE Senior Scientist Dr. Reuben Epstein on "Single-Feature Perturbation Seeded Rayleigh–Taylor Instability Studied in Planar Geometry."

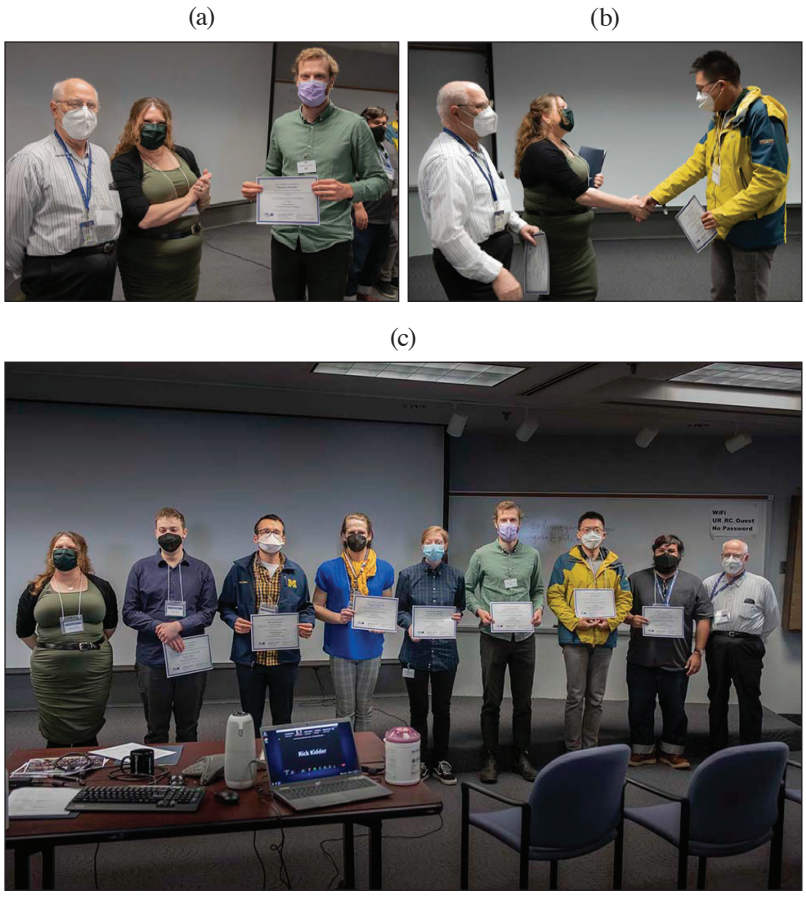

Figure 6
An award ceremony chaired by Drs. Liz Merritt and Jim Knauer was held for the best student and postdoctoral posters. (a) Graeme Sutcliffe (MIT) won the graduate student category; (b) Shu Zhang (Princeton) won the postdoctoral category. (c) Dr. Liz Merritt, Cameron Frank (graduate student at the University of Delaware), Michael Wadas [graduate student at UM (University of Michigan)], Abigail Armstrong (graduate student at UR), Skylar Dannhoff (graduate student at MIT), Graeme Sutcliffe (graduate student at MIT), Shu Zhang (postdoc at Princeton), Neel Kabadi (postdoc at MIT), and Dr. Jim Knauer. Not shown in the picture are Justin Kunimune (graduate student at MIT), Adam Brown (Houghton College) who won the undergraduate student category, and Jovahn Roumell (undergraduate student at SUNY Geneseo).

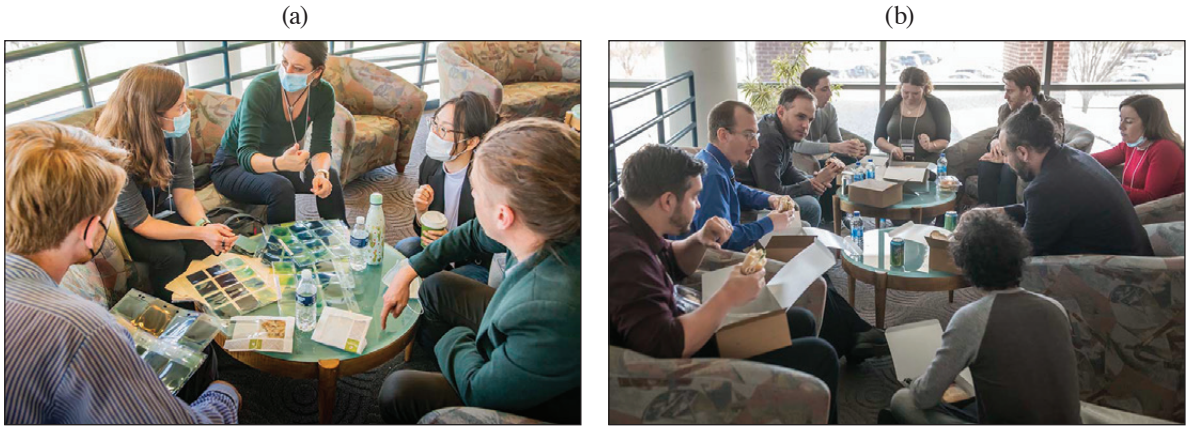

U2883JR

Figure 7
Productive discussions among researchers from around the world occurred in several informal settings.

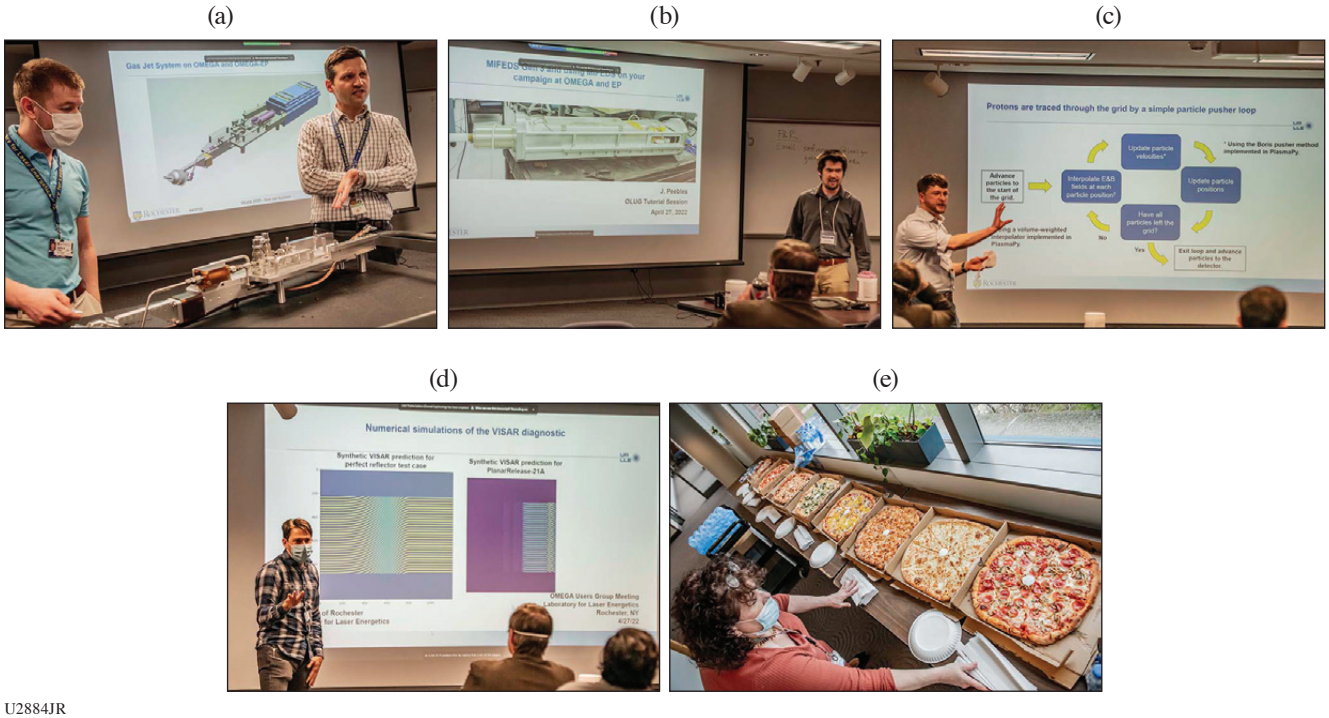

U2884JR

Figure 8
An evening tutorial session given by LLE highly regarded by the OLUG workshop participants. (a) Dr. Steven Ivancic and Tim Filkins discussed the "Gas-Jet System on OMEGA and OMEGA EP," which helped the external users get a better idea of what can be done with the system; (b) Dr. Jonathan Peebles gave an informative presentation on the "MIFEDS Generation-3 and Using It on Users' Experimental Campaign on OMEGA and OMEGA EP;" (c) Dr. Peter Heuer gave an inspiring talk on the "*PlasmaPy* Open-Source Code," which truly engaged the younger audience; (d) Dr. Daniel Barnak presented "*Fiducia* Open-Source Code and Analysis Software for the Dante-Diagnostic Data;" and (e) Mrs. Kim Truebger arranged for pizza to be served during the evening's tutorial session.

U2885JR

Figure 9
The student/postdoctoral panel presented important insights from young researchers working at the Omega facility. (a) Suzanne Ali (LLNL), not shown, Heath LeFevre (UM), Ellie Tubman (LLNL), Gabriel Perez-Callejo (University of Valladolid, Spain), and Brandon Russel (UM) led the discussion. (b) Graduate student Hongmei Tang (UM) brought her thoughts and recommendations.

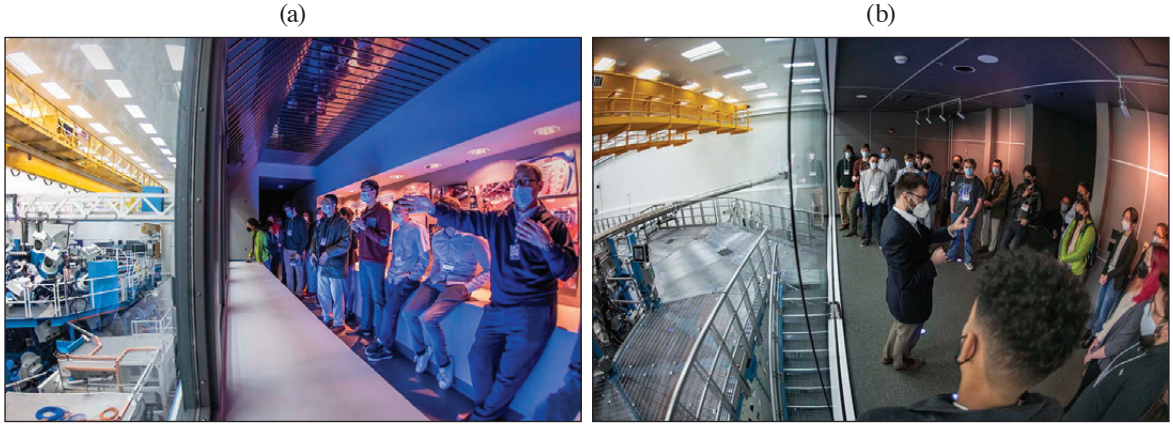

U2886JR

Figure 10
Mark Labuzeta and David Canning led tours of OMEGA and OMEGA EP, respectively. For many of the younger researchers, this was a great opportunity to learn about the facilities.

Summary of Findings and Recommendations

A big part of OLUG's responsibility is to enhance the Omega facility and its capabilities by defining a set of F&R's each year. Drs. Maria Gatu Johnson (MIT) and Sean Finnegan [Los Alamos National Laboratory (LANL)] led this year's F&R session, As shown below, 25 F&R's were defined and grouped into several categories at this workshop, i.e., general (1), documentation (2), calibration (3), diagnostics (4–15), target capability (16–18), laser systems (19–22), and data management (23–25). The LLE management is using these F&R's as a guide for making decisions about the operations of the Omega Laser Facility, priorities, and future changes. An update on the implementation of these F&R's will be presented by the LLE management at the OLUG satellite meeting on 18 October 2022 at the American Physical Society Division of Plasma Physics (APS-DPP) Conference in Spokane, WA.

1. Add equipment for improved hybrid workshop execution.
2. Ensure that users have access to detailed up-to-date documentation on diagnostics.
3. Make calibration data readily available on the PI portal.

4. Add a third VISAR (velocity interferometer system for any reflector) leg on the active shock breakout (ASBO) diagnostic on OMEGA EP and/or OMEGA.
5. Increase VISAR etalon support thickness for improved ASBO resolution.
6. Add a timing fiducial to Dante, noted in the Sustainment Plan (requires modern digitizers).
7. Add an optical Thomson-scattering diagnostic to OMEGA EP (multiple submissions).
8. Add the capability to infer directional flow vector on D_2 gas-filled or low-DT yield implosions.
9. Add the capability for neutron time-of-flight detectors to measure secondary DT-neutron spectra.
10. Reduce min/max camera timing jitter.
11. Improve Dante maintenance and documentation.
12. Create the ability to run streaked x-ray diagnostics with a gas jet.
13. Add gated spatially resolved x-ray spectroscopy.
14. Provide an additional Target Positioning System, more (mini) ten-inch manipulators (TIM's) and/or nuclear diagnostic inserters for OMEGA.
15. Add a diagnostic for forward-scattered light on OMEGA EP.
16. Characterize gas-jet nozzles (a TIM lab nozzle characterization test bench is now available to users).
17. Provide planar cryo on OMEGA EP.
18. Enable the ability to change MIFEDS leads on shot day
19. Increase UV power on OMEGA EP.
20. Enable 20-ns pulse duration on OMEGA EP.
21. Increase the quantity of tight-focus circular super-Gaussian distributed phase plates.
22. Extend backlighter beam delay.
23. Update HDF5 and utilize standard meta-data formats (multiple submissions).
24. Enable instant analysis of data on shot day.
25. Develop more open-source analysis software.

Findings and Recommendations from the Student/Postdoctoral Panel

Every year at the OLUG Workshop, a group of early career scientists, mainly students and postdocs, lead a discussion with the community on topics relevant to young researchers, including issues specific to the pandemic effects on early career scientists, the organization of the OLUG Workshop, and recommendations for the facility. Suzanne Ali [Lawrence Livermore National Laboratory (LLNL)] and Heath LeFevre (UM) led the discussion together with Ellie Tubman (LLNL), Gabriel Perez-Callejo (University of Valladolid, Spain), and Brandon Russel (UM). From these discussions, the following F&R were identified:

1. Develop a better framework for mentorship and guidance for early career scientists.
2. Facilitate cross-institution mentorship, matching up new researchers doing work at Omega with more-experienced mentors.
3. Form something like a journal club for topics related to experimental planning and analysis (monthly or biweekly, with a pre-meeting poll on the discussion topic).
4. Improve and modernize the web-based resources available to users.
5. Continue to improve documentation for diagnostic systems and targets.
6. Better advertise the existing online forum. A Microsoft Teams channel (or similar) is recommended specifically for users to ask questions to other users.
7. Record tutorials for some of the online resources for data access.
8. Enable access to calibration information for diagnostics via an online database.

Nominations and Election of Members for the OLUG ExCom

An OLUG ExCom election was held this year to elect three new members. A nominating committee was formed in November 2021 to request January nominations for the February 2022 election. Pia Valdivia [Chair, University of California, San Diego (UCSD), Hui Chen (LLNL), and Lan Gao (Princeton Plasma Physics Laboratory) formed the election committee. From a three-candidate ballot, Derek Schaeffer (Princeton) was elected as university representative to replace Maria Gatu Johnson (MIT); Verena Geppert-Kleinrath (LANL) was elected as national lab representative to replace Liz Merritt (LANL); and Heath LeFevre

(UM) was elected as the junior representative to replace Suzanne Ali (LLNL). In addition, Jim Knauer stepped down as the LLE ex-officio after 13 years of service. Jessica Shaw is the new LLE ex-officio.

For the May 2022–April 2023 period, the OLUG ExCom members are (a) four from U.S. university/small business: Johan Frenje (MIT, Chair), Maria-Pia Valdivia (UCSD, Vice Chair), Derek Schaeffer (Princeton), and Louise Willingale (UM); (b) three from national laboratory/major business: Verena Geppert-Kleinrath (LANL), Sean Finnegan (LANL), and Alison Saunders (LLNL); (c) one non-U.S. researcher: Katerina Falk [Helmholtz-Zentrum Dresden-Rossendorf (HZDM), Germany); (d) one from the junior researcher list: Heath LeFevre (UM); and (e) LLE ex-officio: Jessica Shaw. The OLUG ExCom thanks Maria Gatu Johnson, Liz Merritt, Suzanne Ali, and Jim Knauer for their service and excellent work making OLUG such a vibrant community.

U2887JR

Figure 11
Dr. Pia Valdivia (UCSD) presented the results from the 2022 OLUG ExCom elections.

(a)

(b)

(c)

(d)

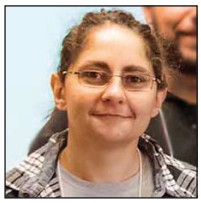

U2888JR

Figure 12
Members of the 2022 OLUG ExCom. (a) Back row (left to right): Jim Knauer (LLE), Liz Merrit (LANL), Katerina Falk (HZDR), Sean Finnegan (LANL), and Pia Valdivia (UCSD). Front row (left to right): Johan Frenje (MIT) and Maria Gatu Johnson (MIT); (b) Alison Saunders (LLNL); (c) Louise Willingale (UM); and (d) Suzanne Ali (LLNL) attended the workshop virtually.

Conclusions and Future Workshops

This OLUG Workshop, with 158 attendees, was part of a process that will keep members of the community involved in conversations and collaborations with each other and with the Omega Laser Facility. In addition, OLUG ExCom members and LLE management have an ongoing dialog to assess progress, compatibility with facility resources, and impact toward the implementation of the F&R's. An update on the implementation of these F&R's will be presented by the LLE management at the OLUG satellite meeting on 18 October 2022 at the APS-DPP Conference in Spokane, WA, and in depth at the 2023 OLUG Workshop.

Acknowledgment

This OLUG workshop was made possible in part by LLE at the University of Rochester for the use and availability of critical resources and support. In addition, OLUG thanks the LLE management for their exceptional responsiveness to our F&R's. For capturing the ambience and spirit of the workshop through his camera lens, we thank Eugene Kowaluk. To NNSA, we gratefully acknowledge the financial assistance for student/postdoctoral travel expenses. We also thank Kim Truebger for her incredible work setting up and executing the workshop.

FY22 Q3 Laser Facility Report

J. Puth, M. Labuzeta, D. Canning, and R. T. Janezic

Laboratory for Laser Energetics, University of Rochester

During the third quarter of FY22, the Omega Facility conducted 337 target shots on OMEGA and 242 target shots on OMEGA EP for a total of 579 target shots (see Tables I and II). OMEGA averaged 10.5 target shots per operating day, averaging 94.9% Availability and 94.7% Experimental Effectiveness. OMEGA EP averaged 8.3 target shots per operating day, averaging 95.4% Availability and 98.8% Experimental Effectiveness.

Table I: OMEGA Laser System target shot summary for Q3 FY22.

Program	Laboratory	Planned Number of Target Shots	Actual Number of Target Shots
ICF	LLE	66	61
	LANL	11	11
	LLNL	16.5	17
	SNL	5.5	6
ICF Subtotal		99	95
HED	LLE	33	38
	LANL	22	22
	LLNL	27.5	31
	SNL	11	12
HED Subtotal		93.5	103
LBS	LLNL	22	24
LBS Subtotal		22	24
NLUF		60.5	67
CEA		5.5	6
APL		11	12
CMAP		11	8
Calibration	LLE	0	22
Grand Total		302.5	337

APL: Applied Physics Labs (Johns Hopkins University)
CEA: Commissariat à l'énergie atomique aux énergies alternatives
CMAP: Center for Matter at Atomic Pressures
NLUF: National Laser Users Facility

Table II: OMEGA EP Laser System target shot summary for Q3 FY22.

Program	Laboratory	Planned Number of Target Shots	Actual Number of Target Shots
ICF	LLE	35	49
	LLNL	7	7
	SNL	7	6
ICF Subtotal		49	62
HED	LLE	14	17
	LANL	14	22
	LLNL	49	68
	SNL	7	10
HED Subtotal		84	117
CMAP		7	11
LaserNetUS		7	9
NLUF		28	25
Calibration	LLE	0	18
Grand Total		175	242

Publications and Conference Presentations

Publications

N. Acharya, H. Aluie, and J. K. Shang, "Numerical Investigation of Laser-Driven Shock Interaction with a Deformable Particle," Phys. Plasmas **29**, 052302 (2022).

S.-W. Bahk, I. A. Begishev, R. Roides, C. Mileham, R. Cuffney, C. Feng, B. M. Webb, C. Jeon, M. Spilatro, S. Bucht, C. Dorrer, and J. Bromage, "Effect of the Pump Beam Profile and Wavefront on the Amplified Signal Wavefront in Optical Parametric Amplifiers," Opt. Express **30**, 12,995 (2022).

A. Bose, J. Peebles, C. A. Walsh, J. A. Frenje, N. V. Kabadi, P. J. Adrian, G. D. Sutcliffe, M. Gatu Johnson, C. A. Frank, J. R. Davies, R. Betti, V. Yu. Glebov, F. J. Marshall, S. P. Regan, C. Stoeckl, E. M. Campbell, H. Sio, J. Moody, A. Crilly, B. D. Appelbe, J. P. Chittenden, S. Atzeni, F. Barbato, A. Forte, C. K. Li, F. H. Séguin, and R. D. Petrasso, "Effect of Strongly Magnetized Electrons and Ions on Heat Flow and Symmetry of Inertial Fusion Implosions," Phys. Rev. Lett. **128**, 195002 (2022).

A. F. A. Bott, L. Chen, P. Tzeferacos, C. A. J. Palmer, A. R. Bell, R. Bingham, A. Birkel, D. H. Froula, J. Katz, M. W. Kunz, C.-K. Li, H.-S. Park, R. Petrasso, J. S. Ross, B. Reville, D. Ryu, F. H. Séguin, T. G. White, A. A. Schekochihin, D. Q. Lamb, and G. Gregori, "Insensitivity of a Turbulent Laser-Plasma Dynamo to Initial Conditions," Matter Radiat. Extremes **7**, 046901 (2022).

S. J. Burns, J. R. Rygg, D. Polsin, B. Henderson, M. Marshall, S. Zhang, S. X. Hu, and G. Collins, "Planar, Longitudinal, Compressive Waves in Solids: Thermodynamics and Uniaxial Strain Restrictions," J. Appl. Phys. **131**, 215904 (2022).

D. A. Chin, J. J. Ruby, P. M. Nilson, D. T. Bishel, F. Coppari, Y. Ping, A. L. Coleman, R. S. Craxton, J. R. Rygg, and G. W. Collins, "Emission Phases of Implosion Sources for X-Ray Absorption Fine Structure Spectroscopy," Phys. Plasmas **29**, 052702 (2022).

A. Diaw, S. J. Coleman, N. M. Cook, J. P. Edelen, E. C. Hansen, and P. Tzeferacos, "Impact of Electron Transport Models on Capillary Discharge Plasmas," Phys. Plasmas **29**, 063101 (2022).

C. Dorrer and J. L. Shaw, "Single-Shot Cross-Correlation of Counter-Propagating, Short Optical Pulses Using Random Quasi-Phase-Matching," Opt. Express **30**, 16,677 (2022).

R. K. Follett, H. Wen, D. H. Froula, D. Turnbull, and J. P. Palastro, "Independent-Hot-Spot Approach to Multibeam Laser-Plasma Instabilities," Phys. Rev. E **105**, L063201 (2022).

G. W. Jenkins, C. Feng, and J. Bromage, "Simultaneous Contrast Improvement and Temporal Compression Using Divided-Pulse Nonlinear Compression," Opt. Express **30**, 13,968 (2022).

D. Kim, R. F. Smith, I. K. Ocampo, F. Coppari, M. C. Marshall, M. K. Ginnane, J. K. Wicks, S. J. Tracy, M. Millot, A. Lazicki, J. R. Rygg, J. H. Eggert, and T. S. Duffy, "Structure and Density of Silicon Carbide to 1.5 TPa and Implications for Extrasolar Planets," Nat. Commun. **13**, 2260 (2022).

Y.-J. Kim, B. Militzer, B. Boates, S. Bonev, P. M. Celliers, G. W. Collins, K. P. Driver, D. E. Fratanduono, S. Hamel, R. Jeanloz, J. R. Rygg, D. C. Swift, J. H. Eggert, and M. Millot, "Evidence for Dissociation and Ionization in Shock Compressed Nitrogen to 800 GPa," Phys. Rev. Lett. **129**, 015701(2022).

R. K. Kirkwood, P. L. Poole, D. H. Kalantar, T. D. Chapman, S. C. Wilks, M. R. Edwards, D. P. Turnbull, P. Michel, L. Divol, N. J. Fisch, P. Norreys, W. Rozmus, J. Bude, B. E. Blue, K. B. Fournier, B. M. Van Wonterghem, and A. MacKinnon, "Production of High Fluence Laser Beams Using Ion Wave Plasma Optics," Appl. Phys. Lett. **120**, 200501 (2022).

T. Z. Kosc, H. Huang, T. J. Kessler, and S. G. Demos, "Angular Dependence of the Transverse Raman Scattering in KDP and DKDP in Geometries Suitable for Beam Polarization Control," Opt. Express **30**, 12,918 (2022).

L. S. Leal, A. V. Maximov, E. C. Hansen, J. R. Davies, D. H. Barnak, J. L. Peebles, K. M. Woo, P. V. Heuer, A. B. Sefkow, and R. Betti, "Effect of Laser Preheat in Magnetized Liner Inertial Fusion at OMEGA," Phys. Plasmas **29**, 042703 (2022).

S. Malko, W. Cayzac, V. Ospina-Bohórquez, K. Bhutwala, M. Bailly-Grandvaux, C. McGuffey, R. Fedosejevs, X. Vaisseau, An. Tauschwitz, J. I. Apiñaniz, D. De Luis, G. Gatti, M. Huault, J. A. Perez Hernandez, S. X. Hu, A. J. White, L. A. Collins, K. Nichols, P. Neumayer, G. Faussurier, J. Vorberger, G. Prestopino, C. Verona, J. J. Santos, D. Batani, F. N. Beg, L. Roso, and L. Volpe, "Proton Stopping Measurements at Low Velocity in Warm Dense Carbon," Nat. Commun. **13**, 2893 (2022).

O. M. Mannion, A. J. Crilly, C. J. Forrest, B. D. Appelbe, R. Betti, V. Yu. Glebov, V. Gopalaswamy, J. P. Knauer, Z. L. Mohamed, C. Stoeckl, J. P. Chittenden, and S. P. Regan, "Measurements of the Temperature and Velocity of the Dense Fuel Layer in Inertial Confinement Fusion Experiments," Phys. Rev. E **105**, 055205 (2022).

K. L. Marshall, K. R. P. Kafka, N. D. Urban, J. U. Wallace, and S. G. Demos, "Multiparameter Laser Performance Characterization of Liquid Crystals for Polarization Control Devices in the Nanosecond Regime," Sci. Rep. **12**, 10969 (2022).

J. Musgrave and J. Bromage, "Impact of the Optical Parametric Amplification Phase on Laser Pulse Compression," Appl. Opt. **61**, 3838 (2022).

R. W. Paddock, H. Martin, R. T. Ruskov, R. H. H. Scott, W. Garbett, B. M. Haines, A. B. Zylstra, E. M. Campbell, T. J. B. Collins, R. S. Craxton, C. A. Thomas, V. N. Goncharov, R. Aboushelbaya, Q. S. Feng, M. W. von der Leyen, I. Ouatu, B. T. Spiers, R. Timmis, R. H. W. Wang, and P. A. Norreys, "Pathways Towards Break Even for Low Convergence Ratio Direct-Drive Inertial Confinement Fusion," J. Plasma Phys. **88**, 905880314 (2022).

D. N. Polsin, A. Lazicki, X. Gong, S. J. Burns, F. Coppari, L. E. Hansen, B. J. Henderson, M. F. Huff, M. I. McMahon, M. Millot, R. Paul, R. F. Smith, J. H. Eggert, G. W. Collins, and J. R. Rygg, "Structural Complexity in Ramp-Compressed Sodium to 480 GPa," Nat. Commun. **13**, 2534 (2022).

D. Ramsey, B. Malaca, A. Di Piazza, M. Formanek, P. Franke, D. H. Froula, M. Pardal, T. T. Simpson, J. Vieira, K. Weichman, and J. P. Palastro, "Nonlinear Thomson Scattering with Ponderomotive Control," Phys. Rev. E **105**, 065201 (2022).

G. F. Swadling, C. Bruulsema, W. Rozmus, and J. Katz, "Quantitative Assessment of Fitting Errors Associated with Streak Camera Noise in Thomson Scattering Data Analysis," Rev. Sci. Instrum. **93**, 043503 (2022).

K. Weichman, A. P. L. Robinson, M. Murakami, J. J. Santos, S. Fujioka, T. Toncian, J. P. Palastro, and A. V. Arefiev, "Progress in Relativistic Laser–Plasma Interaction with Kilotesla-Level Applied Magnetic Fields," Phys. Plasmas **29**, 053104 (2022) (invited).

H. Wen, C. Ren, E. C. Hansen, D. Michta, Y. Zhang, S. Langendorf, and P. Tzeferacos, "Particle-in-Cell Modeling of Plasma Jet Merging in the Large-Hall-Parameter Regime," Phys. Plasmas **29**, 062706 (2022).

J. Zhang, W. R. Donaldson, and G. P. Agrawal, "Temporal Reflection of an Optical Pulse from a Short Soliton: Impact of Raman Scattering," J. Opt. Soc. Am. B **39**, 1950 (2022).

Forthcoming Publications

A. F. Antoniadis, D. Drikakis, P. S. Farmakis, L. Fu, I. Kokkinakis, X. Nogueira, P. A. S. F. Silva, M. Skote, V. Titarev, and P. Tsoutsanis, "UCNS3D: An Open-Source High-Order Finite-Volume Unstructured CFD Solver," to be published in Computer Physics Communications.

Z. Chen, S. X. Hu, and N. P. Bigelow, "Imprinting a Three-Dimensional Skyrmion in a Bose–Einstein Condensate Via a Raman Process," to be published in the Journal of Low Temperature Physics.

V. Gopalaswamy, R. Betti, P. B. Radha, A. J. Crilly, K. M. Woo, A. Lees, C. Thomas, I. V. Igumenshchev, S. C. Miller, J. P. Knauer, C. Stoeckl, C. J. Forrest, O. M. Mannion, Z. L. Mohamed, H. G. Rinderknecht, and P. V. Heuer, "Analysis of Limited Coverage Effects on Areal Density Measurements in Inertial Confinement Fusion Implosions," to be published in Physics of Plasmas.

S. S. Harilal, M. C. Phillips, D. H. Froula, K. K. Anoop, R. C. Issac, and F. N. Beg, "Optical Diagnostics of Laser-Produced Plasmas," to be published in the Reviews of Modern Physics.

P. V. Heuer, L. S. Leal, J. R. Davies, E. C. Hansen, D. H. Barnak, J. L. Peebles, F. García-Rubio, B. Pollock, J. Moody, A. Birkel, and F. H. Séguin, "Diagnosing Magnetic Fields in

Cylindrical Implosions with Oblique Proton Radiography," to be published in Physics of Plasmas.

M. P. Jeske, W. Zhang, and M. Anthamatten "Two-Photon Printing of Shape-Memory Microstructures and Metasurfaces via Radical-Mediated Thiol-Vinyl Hydrothiolation," to be published in Advanced Materials Technologies.

K. R. P. Kafka, T. Z. Kosc, and S. G. Demos, "Methods and Apparatus for Comprehensive Characterization of Performance Attributes and Damage Thresholds of Ultrafast Laser Optics," to be published in Optical Engineering.

H. Poole, D. Cao, R. Epstein, I. Golovkin, T. Walton, S. X. Hu, M. Kasim, S. M. Vinko, J. R. Rygg, V. N. Goncharov, G. Gregori, and S. P. Regan, "A Case Study of Using X-Ray Thomson Scattering to Diagnose the In-Flight Plasma Condition of DT Cryogenic Implosions," to be published in Physics of Plasmas.

A. K. Schwemmlein, C. Stoeckl, C. J. Forrest, W. T. Shmayda, S. P. Regan, W. U. Schröder, "First Demonstration of a Triton Beam Using Target Normal Sheath Acceleration," to be published in Nuclear Instruments and Methods in Physics Research B.

R. C. Shah, D. Cao, L. Aghaian, B. Bachmann, R. Betti, E. M. Campbell, R. Epstein, C. J. Forrest, A. Forsman, V. Yu. Glebov, V. N. Goncharov, V. Gopalaswamy, D. R. Harding, S. X. Hu, I. V. Igumenshchev, R. T. Janezic, L. Keaty, J. P. Knauer, D. Kobs, A. Lees, O. M. Mannion, Z. L. Mohamed, D. Patel, M. J. Rosenberg, W. T. Shmayda, C. Stoeckl, W. Theobald, C. A. Thomas, P. Volegov, K. M. Woo, and S. P. Regan, "Bound on Hot-Spot Mix in High-Velocity, High-Adiabat Direct-Drive Cryogenic Implosions Based on Comparison of Absolute X-Ray and Neutron Yields," to be published in Physical Review E.

S. Singh, A. L. Coleman, S. Zhang, F. Coppari, M. G. Gorman, R. F. Smith, J. H. Briggs, and D. E. Fratanduono, "Quantitative Analysis of Diffraction by Liquids Using a Pink-Spectrum X-Ray Source," to be published in the Journal of Synchrotron Radiation.

R. Sobolewski, "Optical Detectors and Sensors," to be published in the Handbook of Superconducting Materials.

D. Turnbull, J. Katz, D. E. Hinkel, P. Michel, T. Chapman, L. Divol, E. Kur, S. MacLaren, A. L. Milder, M. Rosen, A. Shvydky, G. B. Zimmerman, and D. H. Froula, "Beam Spray Thresholds in ICF-Relevant Plasmas," to be published in Physical Review Letters.

N. D. Urban, K. R. P. Kafka, K. L. Marshall, and S. G. Demos, "Laser-Induced Damage Characteristics of Fused Silica Surfaces Polished to Different Depths Using Fluid Jet Polishing," to be published in Optical Engineering.

K. M. Woo, R. Betti, C. A. Thomas, C. Stoeckl, K. Churnetski, C. J. Forrest, Z. L. Mohamed, B. Zirps, S. P. Regan, T. J. B. Collins, W. Theobald, R. C. Shah, O. M. Mannion, D. Patel, D. Cao, J. P. Knauer, V. Yu. Glebov, V. N. Goncharov, P. B. Radha, H. G. Rinderknecht, R. Epstein, V. Gopalaswamy, F. J. Marshall, S. T. Ivancic, and E. M. Campbell, "Analysis of Core Asymmetries in Inertial Confinement Fusion Implosions Using Three-Dimensional Hot-Spot Reconstruction," to be published in Physics of Plasmas.

D. Zhang, J. Li, J. Xin, R. Yan, Z. Wan, H. Zhang, and J. Zheng, "Self-Generated Magnetic Field in Ablative Rayleigh–Taylor Instability," to be published in Physics of Plasmas.

Conference Presentations

The following presentations were made at the 2022 Panchanatan Visit, Rochester, NY, 11 April 2022:

C. Deeney, "An Overview of the Laboratory for Laser Energetics: Always 'Reaching for the Brightest Light.' "

V. Gopalaswamy, "Data-Driven Experimental Design at LLE."

E. M. Hill, "LLE is a Word Leader for Designing, Innovating, and Constructing State-of-the-Art Lasers for a Wide Range of Scientific Applications for Ourselves and the Broader Scientific Community."

M. F. Huff, "Measuring Sound Speed in Shocked Iron."

J. Katz, "Diagnostic Development and Advanced Instrumentation for Fundamental Physics."

Z. K. Sprowal, L. E. Hansen, M. F. Huff, D. N. Polsin, T. R. Boehly, J. R. Rygg, G. W. Collins, and D. G. Hicks, "Accessing High-Density States in D_2 Using Double Shocks."

M. S. Wei, "User Community."

C. A. Williams, "Convergence Research in Inertial Confinement Fusion."

J. D. Zuegel, "Laser Materials Technology Division and Major Projects," presented at the NNSA–OES Visit, virtual, 12 April 2022.

R. B. Spielman, "The Design of Self-Magnetically Insulated Transmission Lines for a 10-MA Intermediate-Scale Facility," presented at the Cornell University Seminar, Cornell, NY, 13 April 2022.

J. Bromage, S.-W. Bahk, M. Bedzyk, I. A. Begishev, S. Bucht, C. Dorrer, C. Feng, B. N. Hoffman, C. Jeon, C. Mileham, J. B. Oliver, R. G. Roides, E. M. Schiesser, K. Shaughnessy, M. J. Shoup III, M. Spilatro, B. Webb, D. Weiner, and J. D. Zuegel, "Development of Ultra-Intense OPCPA Technologies on the MTW-OPAL System," presented at the 11th Advanced Lasers and Photon Sources, Yokohama, Japan, 18–21 April 2022 (invited).

S. X. Hu, P. M. Nilson, D. T. Bishel, D. A. Chin, V. V. Karasiev, D. I. Mihaylov, N. R. Shaffer, S. Zhang, V. Recoules, N. Brouwer, M. Torrent, I. E. Golovkin, M. Gu, T. Walton, and S. B. Hansen, "Probing Atomic Physics at Extreme Conditions," presented at the International Conference on High-Energy-Density Sciences, Yokohama, Japan, 18–22 April 2022 (invited).

J. D. Zuegel, J. Bromage, D. H. Froula, E. M. Hill, J. P. Palastro, J. C. Puth, H. G. Rinderknecht, J. L. Shaw, C. J. Forrest, and L. J. Waxer, "Proposed EP-OPAL Laser Facility," presented at the MP3 Workshop, Paris, France, 20–22 April 2022.

C. Deeney, "Pulsed-Power Research at LLE," presented at the ZNetUS Workshop, virtual, 21–22 April 2022.

The following presentations were made at the 2022 ARPA-E Fusion Programs Annual Meeting, San Francisco, CA, 26–27 April 2022:

J. R. Davies, H. Berger, C. J. Forrest, V. Yu. Glebov, H. McClow, M. Sharpe, and W. T. Shmayda, "The LLE Diagnostic Resource Team for Innovative Fusion Concepts."

V. N. Goncharov, I. V. Igumenshchev, W. Trickey, R. K. Follett, N. Shaffer, A. Pineau, Y. Lawrence, M. Tobin, W. Meier, S. Woodruff, C. Dorrer, and J. D. Zuegel, "Advanced Inertial Fusion Energy Target Designs with Next-Generation Laser Technologies."

P. Tzeferacos, A. Sefkow, C. Ren, R. Betti, J. R. Davies, H. Wen, J. G. Shaw, E. C. Hansen, D. Michta, F. García-Rubio, and K. M. Woo, "A Simulation Resource Team for Innovative Fusion Concepts in the BETHE Program."

The following presentations were made at the 2022 Omega Laser Facility Users Group, Rochester, NY, 27–29 April 2022:

A. Armstrong, A. Reyes, M. B. P. Adams, P. Farmakis, E. C. Hansen, Y. Lu, D. Michta, K. Moczulski, D. Q Lamb, and P. Tzeferacos, "Implementation and Verification of Spitzer Viscosity in the *FLASH* Code."

D. H. Barnak, "Self-Optimizing Savitzky–Golay Filter for Generalized Signal Denoising."

D. H. Barnak, R. Betti, V. Gopalaswamy, A. Lees, and A. Shvydky, "Numerical Simulations of the VISAR Diagnostic."

D. H. Barnak, J. R. Davies, J. P. Knauer, and P. M. Kozlowski, "*FIDUCIA*: A New User's Course into the Wonderful World of Cubic Spline Unfolding."

G. Bruhaug, H. G. Rinderknecht, M. S. Wei, B. Brannon, D. Guy, R. Peck, N. Landis, G. Brent, R. Fairbanks, C. McAtee, T. Walker, T. Buczek, M. Krieger, M. Romanofsky, Y. E, K. Garriga, X. C. Zhang, G. W. Collins, and J. R. Rygg, "High-Power, High-Energy THz Generation Using Joule- and Kilojoule-Class Lasers."

C. Deeney, "The Next Cooperative Agreement: FY24–FY28."

P. Farmakis, M. McMullan, A. Reyes, J. Laune, M. B. P. Adams, A. Armstrong, E. C. Hansen, Y. Lu, D. Michta,

K. Moczulski, D. Lamb, and P. Tzeferacos, "Expanding the Tabulated Equationof-State Implementations in the *FLASH* Code for the *SESAME* Database."

D. H. Froula, "Fourth-Generation Laser for Ultra-Broadband Experiments."

E. C. Hansen, P. Farmakis, D. Michta, C. Ren, A. C. Reyes, H. Wen, S. Langendorf, and P. Tzeferacos, "Simulating the Plasma Liner Experiment (PLX) with the *FLASH* Code."

P. V. Heuer, J. R. Davies, D. Stanczak, E. Everson, and N. Murphy, "Synthetic Diagnostics for High-Energy-Density Physics in *PlasmaPy*."

S. T. Ivancic, "Gas-Jet System on OMEGA and OMEGA EP."

T. J. Kessler and M. Romo-Gonzalez, "Inclusion, Diversity, and Equity at the Laboratory for Laser Energetics."

Y. Lu, S. Feister, J. Meinecke, F. Miniati, G. Gregori, A. Bott, A. Reyes, E. C. Hansen, J. T. Laune, B. Reville, J. S. Ross, D. Q. Lamb, and P. Tzeferacos, "Numerical Modeling of Laser-Driven Plasma Experiments Aiming to Study Turbulent Dynamo and Thermal Conduction at the National Ignition Facility."

D. Michta, P. Tzeferacos, S. Bolanos, and M. Manuel, "*FLASH* Simulations of the Magnetized Quasi-Parallel Collisionless Shock Experiments on OMEGA EP."

K. Moczulski, A. Reyes, M. B. P. Adams, A. Armstrong, P. Farmakis, E. C. Hansen, Y. Lu, D. Michta, D. Q. Lamb, and P. Tzeferacos, "Implementation and Verification of LC Circuit for *Z*-Pinch *FLASH* Simulations."

S. F. B. Morse, "Omega Facility OLUG 2022 Update: Progress on Recommendations and Items of General Interest."

S. F. B. Morse, "The Sustainment Plan for the Omega Laser Facility."

J. L. Peebles, "Generating Magnetic Fields Using MIFEDS on Your Campaign at OMEGA/OMEGA EP."

A. Reyes, M. B. P. Adams, A. Armstrong, K. Moczulski, P. Farmakis, E. C. Hansen, Y. Lu, D. Michta, J. Grove, and P. Tzeferacos, "Volume-of-Fluid Representation of Multifluid Compressible Hydrodynamics in the *FLASH* Code."

P. Tzeferacos, "Big Lasers and Big Computers: The Flash Center for Computational Science and the *FLASH* Code at UR."

A. Bowman, M. Burns, A. Poudel, S. Zhai, S. Dwarkadas, A. B. Sefkow, and S. Pai, "Cross-Beam Energy Transfer on Graphics Processing Units," presented at Senior Design Day, Rochester, NY, 29 April 2022.

D. Mihaylov, "Improving the Accuracy of Density Functional Theory Simulations of Warm Dense Matter by Including Exchange-Correlation Thermal Effects," presented at the Center for Advanced Systems Understanding Seminar, virtual, 3 May 2022.

The following presentations were made at the 17th Direct Drive and Fast Ignition Workshop, Madrid, Spain, 3–5 May 2022:

E. M. Campbell, "Perspective on Inertial Fusion Energy."

L. Ceurvorst, W. Theobald, M. J. Rosenberg, P. B. Radha, S. P. Regan, C. Stoeckl, R. Betti, K. S. Anderson, J. A. Marozas, V. N. Goncharov, E. M. Campbell, C. M. Shuldberg, R. W. Luo, W. Sweet, L. Aghaiain, D. N. Kaczala, B. Bachmann, T. Döppner, M. Hohenberger, K. Glize, R. H. H. Scott, and A. Colaïtis, "Laser-Direct-Drive Energy-Coupling Experiments Using Solid Spheres at the National Ignition Facility."

V. N. Goncharov, W. Trickey, I. V. Igumenshchev, N. Shaffer, Y. Lawrence, S. Atzeni, and L. Savino, "Advanced Target Designs for Laser-Direct-Drive Inertial Confinement Fusion."

S. X. Hu, L. Ceurvorst, J. L. Peebles, V. N. Goncharov, Y.-F. Lu, A. Pineau, G. Duchateau, K. R. P. Kafka, S. G. Demos, W. Theobald, S. P. Regan, A. Shvydky, T. J. B. Collins, V. V. Karasiev, S. Zhang, D. R. Harding, R. C. Shah, E. M. Campbell, and C. Deeney, "Review on Laser Imprint for Direct-Drive Inertial Confinement Fusion Implosions."

S. P. Regan, V. N. Goncharov, E. M. Campbell, R. Betti, P. Adrian, K. S. Anderson, B. Appelbe, J. Baltazar, D. H. Barnak, J. Bates, K. A. Bauer, R. Boni, M. J. Bonino, D. Cao, A. Colaïtis, D. Canning, K. Churnetski, T. J. B. Collins, G. W.

Collins, A. J. Crilly, J. R. Davies, S. G. Demos, C. Dorrer, R. F. Earley, R. Epstein, M. Farrell, R. K. Follett, C. J. Forrest, J. A. Frenje, D. H. Froula, M. Gatu-Johnson, V. Yu. Glebov, V. Gopalaswamy, A. M. Hansen, D. R. Harding, P. V. Heuer, E. M. Hill, S. X. Hu, H. Huang, J. Hund, I. V. Igumenshchev, S. T. Ivancic, D. W. Jacobs-Perkins, R. T. Janezic, M. Karasik, J. Katz, J. P. Knauer, B. Kruschwitz, J. Kunimune, M. Labuzeta, A. Lees, O. M. Mannion, J. A. Marozas, P. W. McKenty, S. F. B. Morse, P. M. Nilson, J. P. Palastro, D. Patel, J. L. Peebles, P. B. Radha, H. G. Rinderknecht, M. J. Rosenberg, J. R. Rygg, S. Sampat, T. C. Sangster, R. C. Shah, M. Sharpe, W. T. Shmayda, M. J. Shoup III, C. Shuldberg, A. Shvydky, A. A. Solodov, Z. K. Sprowal, C. Sorce, A. Sorce, C. Stoeckl, C. A. Thomas, W. Theobald, D. Turnbull, L. J. Waxer, M. D. Wittman, K. M. Woo, and J. D. Zuegel, "Accomplishments of the 100-Gbar Campaign on OMEGA."

R. C. Shah, S. X. Hu, I. V. Igumenshchev, J. Baltazar, D. Cao, C. J. Forrest, V. N. Goncharov, V. Gopalaswamy, D. Patel, W. Theobald, S. P. Regan, and F. Philippe, "Anomalous X-Ray Emission at Early Stages of Hot-Spot Formation in Deuterium–Tritium Cryogenic Implosions."

W. Trickey, V. N. Goncharov, E. M. Campbell, Y. Lawrence, M. J. Rosenberg, N. Shaffer, W. Theobald, R. C. Shah, A. Shvydky, I. V. Igumenshchev, A. Colaïtis, S. Atzeni, and L. Savino, "Multidimensional Modeling of Low-Mode Perturbations in the Dynamic-Shell Inertial Confinement Fusion Design."

The following presentations were made at the 2022 Center for Matter at Atomic Pressures, Rochester, NY, 5–6 May 2022:

D. Bishel, P. M. Nilson, D. A. Chin, E. Smith, S. X. Hu, V. V. Karasiev, J. R. Rygg, G. W. Collins, J. J. Ruby, and E. V. Marley, "Interrogating the Atomic Structure of Dense Plasmas by X-Ray Absorption Spectroscopy of Implosion Shells."

D. A. Chin, P. M. Nilson, D. T. Bishel, R. Paul, E. Smith, X. Gong, M. K. Ginnane, B. J. Henderson, D. N. Polsin, S. X. Hu, J. R. Rygg, G. W. Collins, D. Trail, A. Amouretti, M. Harmand, O. Mathon, R. Torchio, J. J. Ruby, F. Coppari, A. Coleman, and Y. Ping, "X-Ray Fine Absorption Fine Structure Spectroscopy Measurements of High-Energy-Density Matter."

Z. K. Sprowal, L. E. Hansen, M. F. Huff, D. N. Polsin, D. G. Hicks, T. R. Boehly, J. R. Rygg, and G. W. Collins, "Accessing High-Density States in D_2 Using Double Shock."

S. Zhang, "Isentrope and Equation of State of Solid Hydrogen."

C. Jeon, "Smart Cities and Lasers: Connecting the Dots," presented at the Han Yang University Seminar, virtual, 6 May 2022.

The following presentations were made at the 2022 Materials Research Society Spring Meeting, Honolulu, HI, 8–25 May 2022:

S. M. Fess, D. R. Harding, M. J. Bonino, R. F. Earley, P. Fan, X. Huang, Y.-F. Lu, S. P. Regan, and E. M. Campbell, "Fabrication of Shells and Foams via Two-Photon Polymerization for Laser-Fusion Experiments."

D. R. Harding, S. M. Fess, M. Bonino, R. F. Earley, Y.-F. Lu, X. Huang, P. Fan, S. P. Regan, and E. M. Campbell, "Multiphoton Applications in Laser Fusion Research: From Printing Fusion-Fuel Targets with Sub-150-nm Features to Acquiring Three-Dimensional Structural and Elemental Information of the Target."

M. P. Jeske and M. Anthamatten, "Thermally Responsive Resins for Free-Radical and Base-Catalyzed Two-Photon Polymerization."

P. Tzeferacos, "*FLASH* for *Z*-Pinch Experiments and Extended MHD," presented at the 2022 Center for Matter Under Extreme Conditions Review, San Diego, CA, 10–11 May 2022.

The following presentations were made at the 24th High-Temperature Plasma Diagnostic Conference, Rochester, NY, 15–19 May 2022:

J. Baltazar, R. Betti, K. Churnetski, V. Gopalaswamy, J. P. Knauer, D. Patel, H. G. Rinderknecht, R. C. Shah, C. Stoeckl, C. A. Willliams, and S. P. Regan, "Diagnosing Low-Mode ($\ell < 6$) and Mid-Mode ($6 \leq \ell \leq 20$) Asymmetries in the

Explosion Phase of Laser-Direct-Drive Deuterium–Tritium Cryogenic Implosions on OMEGA."

G. Bruhaug, H. G. Rinderknecht, M. S. Wei, B. Brannon, D. Guy, R. G. Peck, N. Landis, G. Brent, R. Fairbanks, C. McAtee, T. Walker, T. Buczek, M. Krieger, M. Romanofsky, Y. E, K. Garriga, X. C. Zhang, G. W. Collins, and J. R. Rygg, "Development of a Hardened THz Energy Meter for Use on the Kilojoule-Scale, Short-Pulse OMEGA EP Laser."

L. Ceurvorst, W. Theobald, M. J. Rosenberg, P. B. Radha, S. P. Regan, C. Stoeckl, R. Betti, K. S. Anderson, J. A. Marozas, V. N. Goncharov, E. M. Campbell, C. M. Shuldberg, R. W. Luo, W. Sweet, L. Aghaian, D. N. Kaczala, B. Bachmann, T. Döppner, M. Hohenberger, K. Glize, R. H. H. Scott, and A. Colaïtis, "Development of an X-Ray Radiography Platform to Study Laser-Direct-Drive Energy Coupling at the National Ignition Facility."

J. Cheng, G. Chen, D. Chakraborty, S. Kutcher, J. Wen, H. Chen, S. Trivedi, and R. Sobolewski, "(Cd,Mg)Te for Picosecond Response Optical to X-Ray Radiation Detectors."

K. Churnetski, K. M. Woo, W. Theobald, P. B. Radha, R. Betti, V. Gopalaswamy, I. V. Igumenshchev, S. T. Ivancic, M. Michalko, R. C. Shah, C. Stoeckl, C. A. Thomas, and S. P. Regan, "Three-Dimensional Hot-Spot X-Ray Emission Tomography from Cryogenic Deuterium–Tritium Direct-Drive Implosions on OMEGA."

R. Cuffney, J. Shamlian, M. Sharpe, T. Lewis, M. J. Shoup III, J. Bromage, B. Golick, N. Palmer, A. Golod, B. Hatch, and M. Miller, "4ω Fiducial Generator: Provides Optical Timing Reference Marks for Streak Cameras."

D. H. Edgell, J. Katz, R. Raimondi, D. Turnbull, and D. H. Froula, "Scattered-Light Uniformity Imager for Diagnosing Laser Absorption Asymmetries on OMEGA."

T. Filkins, M. J. Rosenberg, R. Bahr, J. Katz, and S. T. Ivancic, "Calibration of the Sub-Aperture Backscatter System on OMEGA EP."

C. J. Forrest, R. Betti, J. P. Knauer, V. Yu. Glebov, V. Gopalaswamy, O. M. Mannion, Z. L. Mohamed, P. B. Radha, S. P. Regan, A. Schwemmlein, C. Stoeckl, W. Theobald, J. A. Frenje, M. Gatu Johnson, B. Appelbe, and A. J. Crilly, "Measurements of Low-Mode Asymmetries in Areal Density of Laser-Direct-Drive DT Cryogenic Implosions on OMEGA Using Neutron Spectroscopy" (invited).

V. Yu. Glebov, C. J. Forrest, J. Kendrick, J. P. Knauer, H. McClow, S. P. Regan, C. Stoeckl, B. Stanley, W. Theobald, and O. M. Mannion, "A New Neutron Time-of-Flight Detector for D_2 Yield and Ion-Temperature Measurements on OMEGA."

D. Haberberger, A. Shvydky, and D. H. Froula, "Fresnel Zone Plate Calculations for the Application to Laser-Plasma Experiments."

P. V. Heuer, D. Stanczak, E. T. Everson, N. A. Murphy, and J. R. Davies, "Open-Source Analysis Software for High-Temperature Plasma Diagnostics."

S. T. Ivancic, W. Theobald, K. Churnetski, M. Michalko, D. Willistein, W. Bittle, S. P. Regan, A. Carpenter, C. Trosseille, J. D. Kilkenny, A. Raymond, J. D. Hares, A. K. L. Dymoke-Bradshaw, G. Rochau, and D. Garand "Design of the High-Yield Time-Gated X-Ray Hot-Spot Imager (XRHSI) for OMEGA."

T. R. Joshi, R. C. Shah, W. Theobald, K. Churnetski, P. B. Radha, D. Cao, C. A. Thomas, J. Baltazar, and S. P. Regan, "Diagnosis of the Imploding Shell Asymmetry in Polar-Direct-Drive DT Cryogenic Target Implosions on OMEGA."

J. Katz, D. Turnbull, S. T. Ivancic, A. L. Milder, and D. H. Froula, "Measurement of Laser Absorption in Underdense Plasmas Using Near-Field Imaging of the Incident and Transmitted Beams."

J. P. Knauer, C. J. Forrest, V. Gopalaswamy, and Z. L. Mohamed, "Normalized Time Axis for Neutron Time-of-Flight Analysis."

S. Kostick, M. J. Rosenberg, W. Theobald, J. Katz, N. Lemos, E. Tubman, J. S. Ross, N. Butler, G. Swadling, R. Sommers, J. D. Moody, R. S. Craxton, A. Sharma, and S. P. Regan, "Assessment of the Calibration of the Scattered-Light Time-History Diagnostic at the National Ignition Facility."

H. McClow, H. Berger, J. R. Davies, C. J. Forrest, G. Gates, S. T. Ivancic, J. Katz, J. Ruby, A. Sorce, and W. Theobald, "First Measurements with a Single-Hit Neutron Spectrometer."

S. F. Nwabunwanne and W. R. Donaldson, "Tunable, Picosecond AlGaN UV Photodiodes."

H. Poole, M. K. Ginnane, J. Topp-Mugglestone, R. Saha, D. N. Polsin, G. W. Collins, S. X. Hu, T. White, S. P. Regan,

G. Gregori, and J. R. Rygg, "Measurements of Warm-Dense-Matter Silicon Based on Angularly and Spectrally Dispersed X-Ray Scattering."

H. G. Rinderknecht, P. V. Heuer, V. Gopalaswamy, J. P. Knauer, C. A. Williams, W. Theobald, R. Fairbanks, B. Brannon, V. Kobilansky, R. Peck, J. Armstrong, M. Weisbeck, J. Brown, L. Ceurvorst, P. B. Radha, S. P. Regan, J. Kunimune, P. Adrian, M. Gatu Johnson, J. A. Frenje, F. Séguin, A. J. Crilly, B. Appelbe, and B. Bachmann, "A Knock-On Deuteron Imager for Measurements of Fuel and Hot-Spot Asymmetry in Direct-Drive Inertial Confinement Fusion Implosions" (invited).

M. Romo-Gonzalez and R. Boni, "Free-Standing Thin Membrane Zero *B*-Integral Beam Splitters."

B. Stanley, C. J. Forrest, and S. T. Ivancic, "Nuclear Activation Analysis of Zirconium-90 Isomeric and Ground-State Reactions at the Omega Laser Facility."

C. Stoeckl, D. Cao, L. Ceurvorst, A. Kalb, J. Kwiatkowski, A. Shvydky, and W. Theobald, "Beam Pointing Verification Using X-Ray Pinhole Cameras on the 60-Beam OMEGA Laser."

The following presentations were made at CLEO 2022, San Jose, CA, 15–20 May 2022:

C. Dorrer and J. L. Shaw, "Single-Shot Cross-Correlation of Counter-Propagating Pulses in a Disordered Nonlinear Crystal."

C. Dorrer and M. A. Spilatro, "Spectral and Temporal Shaping of Spectrally Incoherent UV Pulses by Sum-Frequency Generation."

G. W. Jenkins, C. Feng, and J. Bromage, "Energy Scaling Beyond Gas-Ionization Thresholds with Divided-Pulse Nonlinear Compression."

J. P. Palastro, "Laser–Plasma Interactions Driven by Flying Focus Pulses."

J. Zhang, W. R. Donaldson, and G. P. Agrawal, "Theory and Applications of Temporal Reflection in a Dispersive Medium."

The following presentations were made at the 49th International Conference on Plasma Science, Seattle, WA, 22–26 May 2022:

C. Deeney, E. M. Campbell, V. N. Goncharov, R. Betti, J. D. Zuegel, S. P. Regan, G. W. Collins, S. F. B. Morse, C. Sorce, D. H. Froula, and M. S. Wei, "Laboratory for Laser Energetics: Progress in Science and Technology."

J. Katz, R. Boni, A. L. Milder, D. Nelson, K. Daub, and D. H. Froula, "A High-Numerical-Aperture, Angularly Resolved Thomson-Scattering Spectrometer" (invited).

V. N. Goncharov, W. Trickey, N. Shaffer, A. Peneau, I. V. Igumenshchev, R. K. Follett, T. J. B. Collins, C. Dorrer, J. D. Zuegel, M. Tobin, W. Meier, and Y. Lawrence, "Advanced Inertial Fusion Energy Target Designs with Next-Generation Laser Technologies," presented at the ARPA-E Summit, Denver, CO, 23–25 May 2022.

V. N. Goncharov, W. Trickey, I. V. Igumenshchev, N. Shaffer, T. J. B. Collins, R. K. Follett, C. Stoeckl, R. C. Shah, C. Dorrer, J. D. Zuegel, D. R. Harding, S. Fess, E. M. Campbell, C. Deeney, S. Atzeni, L. Savino, F. Barbato, and A. Colaïtis, "Direct-Drive Designs and Experiments on OMEGA," presented at the EUROfusion Science Meeting, virtual, 27 May 2022.

The following presentations were made at the 50th Anomalous Absorption Conference, Skytop, PA, 5–10 June 2022:

Z. Barfield, J. L. Peebles, P. Tzeferacos, D. Mastrosimone, J. Katz, P. V. Heuer, and D. H. Froula, "Measurements of Anisotropic Temperatures in Magnetized Gas-Jet Plasmas."

S. H. Cao, D. Patel, A. Lees, V. Gopalaswamy, C. Stoeckl, M. J. Rosenberg, H. Wen, H. Huang, A. Shvydky, R. Betti, and C. Ren, "Predicting Hot-Electron Generation in Inertial Confinement Fusion with Particle-in-Cell Simulations."

D. H. Edgell, A. Colaïtis, M. J. Guardalben, A. Kalb, J. Katz, J. Kwiatkowski, O. M. Mannion, A. Shvydky, C. Stoeckl, D. Turnbull, and D. H. Froula, "Cross-Beam Energy Transfer-Induced Nonuniformity in Direct-Drive Implosions on OMEGA."

R. Epstein, V. N. Goncharov, S. X. Hu, D. Cao, A. Shvydky, P. W. McKenty, G. W. Collins, and D. Haberberger, "Assessment of Radiation Trapping in Inertial Confinement Fusion Implosion Experiments with High-*Z*-Lined, Single-Shell Targets."

V. N. Goncharov, W. Trickey, I. V. Igumenshchev, N. Shaffer, T. J. B. Collins, R. K. Follett, W. Theobald, C. Stoeckl, R. C. Shah, C. Dorrer, J. D. Zuegel, D. R. Harding, S. Fess, E. M. Campbell, C. Deeney, S. Atzeni, L. Savino, F. Barbato, and A. Colaïtis, "Physics Requirements for High-Gain Inertial Confinement Fusion Target Designs."

D. Haberberger, A. Shvydky, C. Stoeckl, V. N. Goncharov, and D. H. Froula, "Schlieren Refraction Imaging for Cryo Implosions."

L. S. Leal, A. V. Maximov, F. García-Rubio, R. Betti, and V. V. Ivanov, "Modeling of Laser-Driven Ablative Magneto-thermal Instability."

A. V. Maximov, D. Turnbull, D. H. Edgell, R. K. Follett, H. Wen, J. P. Palastro, and D. H. Froula, "Nonlinear Laser–Plasma Coupling Caused by Two-Plasmon Decay and Cross-Beam Energy Transfer."

K. L. Nguyen, A. M. Hansen, D. Turnbull, R. K. Follett, D. H. Edgell, D. H. Froula, J. P. Palastro, L. Yin, and B. J. Albright, "Cross-Beam Energy Transfer Saturation by Ion-Trapping-Induced Detuning."

J. P. Palastro, D. Ramsey, M. Ambat, P. Franke, D. H. Froula, J. Pigeon, J. L. Shaw, T. T. Simpson, K. Weichman, B. Barbosa, B. Malaca, M. Pardal, J. Vieira, M. Vranic, M. Formanek, A. Di Piazza, J. Pierce, and W. Mori, "Nonlinear Thomson Scattering with Ponderomotive Control."

D. Ramsey, A. Di Piazza, M. Formanek, P. Franke, D. H. Froula, W. Mori, J. Pierce, T. T. Simpson, K. Weichman, and J. P. Palastro, "Exact Analytic Solutions Yielding Flying Focus Pulses (EASYFFP)."

H. G. Rinderknecht, G. Bruhaug, K. Weichman, M. Van Dusen-Gross, J. P. Palastro, M. S. Wei, A. Arefiev, T. Wang, T. Toncian, A. Laso Garcia, D. Doria, K. Spohr, H. J. Quevedo, T. Ditmire, J. Williams, A. Haid, and D. Stutman, "Relativistically Transparent Magnetic Filaments: a Short-Pulse Path to MegaTesla Fields and Efficient Gamma Radiation."

N. R. Shaffer, V. N. Goncharov, A. V. Maximov, and M. Sherlock, "An Extended Vlasov–Foller–Planck Approach to Laser Absorption and Ponderomotive Effects."

T. T. Simpson, J. Pigeon, M. Lim Pac Chong, D. Ramsey, K. Weichman, D. H. Froula, and J. P. Palastro, "High-Energy Two-Color Terahertz Generation."

A. A. Solodov, M. J. Rosenberg, M. Stoeckl, R. Betti, W. Seka, R. Epstein, C. Stoeckl, R. K. Follett, P. B. Radha, S. P. Regan, D. H. Froula, J. P. Palastro, E. M. Campbell, V. N. Goncharov, A. R. Christopherson, B. Bachman, M. Hohenberger, P. Michel, and J. F. Myatt, "Hot-Electron Preheat and Mitigation in Polar-Direct-Drive Experiments at the National Ignition Facility."

D. Turnbull, J. Katz, A. L. Milder, A. Shvydky, D. H. Froula, D. E. Hinkel, P. Michel, T. Chapman, L. Divol, E. Kur, S. MacLaren, M. Rosen, and G. B. Zimmerman, "Beam Spray Thresholds in ICF-Relevant Plasmas."

K. Weichman, J. P. Palastro, A. P. L. Robinson, and A. V. Arefiev, "Relativistically Thermal Plasma Generation by Magnetically Assisted Direct Laser Acceleration."

H. Wen, R. K. Follett, A. V. Maximov, and J. P. Palastro, "Mitigation of Inflationary Stimulated Raman Scattering with Laser Bandwidth."

The following presentations were made at the 24th Target Fabrication Specialist meeting, virtual, 6–9 June 2022:

J. M. García-Figueroa and D. R. Harding, "Observations on Smooth Diamond-Like Composition Films Deposited at Low Temperature via an Electron Cyclotron Resonance-Microwave-Chemical Vapor Deposition One-Step Process."

M. Wang and D. R. Harding, "Mechanical Properties of Micrometer-Size Foam Structures."

C. Deeney, "LLE Strategy," presented at the Office of Experimental Sciences Executives Meeting, Washington, DC, 8–9 June 2022.

The following presentations were made at Technology of Fusion Energy, Anaheim, CA, 12–16 June 2022:

M. Sharpe, C. Fagan, and W. T. Shmayda, "Influence of Microstructure on the Absorption of Tritium into Gold-Plated 316 Stainless Steel."

W. T. Shmayda, E. Dombrowski, and H. K. Mutha, "Pumping and Purifying the SPARC Tokamak Exhaust."

D. A. Chin, P. M. Nilson, J. J. Ruby, D. T. Bishel, R. Paul, M. Signor, A. Amouretti, A. Coleman, F. Coppari, M. K. Ginnane, X. Gong, M. Harmand, B. J. Henderson, S. X. Hu, O. Mathon, D. N. Polsin, E. Smith, R. Torchio, D. Trail, Y. Ping, J. R. Rygg, and G. W. Collins, "X-Ray Absorption Fine Structure Spectroscopy of Iron Compounds at High-Energy-Density Conditions," presented at the DOE NNSA Stewardship Science Graduate Fellowship, Santa Fe, NM, 20–23 June 2022.

E. M. Campbell, "Overview of Inertial Confinement Fusion History, Challenges, and Prospects for Driver-Target Concepts," presented at the Basic Research Needs Workshop, virtual, 21–23 June 2022.

R. B. Spielman and T. Joshi, "Annual Technical Review," presented at the Materials Science in Extreme Environments Annual Technical Review Meeting, Baltimore, MD, 22–24 June 2022.

C. Deeney, "The Laboratory for Laser Energetics: Progress in Science and Technology," presented at the Washington State University Institute for Shock Physics, Pullman, WA, 27 June 2022 (invited).

R Betti, A. Casner, X. Ribeyre, and W. Theobald, "Progress in Laser Direct Drive: Conventional and Shock Ignition," presented at the 48th European Physical Society Conference on Plasma Physics, virtual, 27 June–1 July 2022.

UNIVERSITY OF ROCHESTER
LABORATORY FOR LASER ENERGETICS

Volume 172
July–September 2022
DOE/NA/3856-1775

LLE Review

Quarterly Report

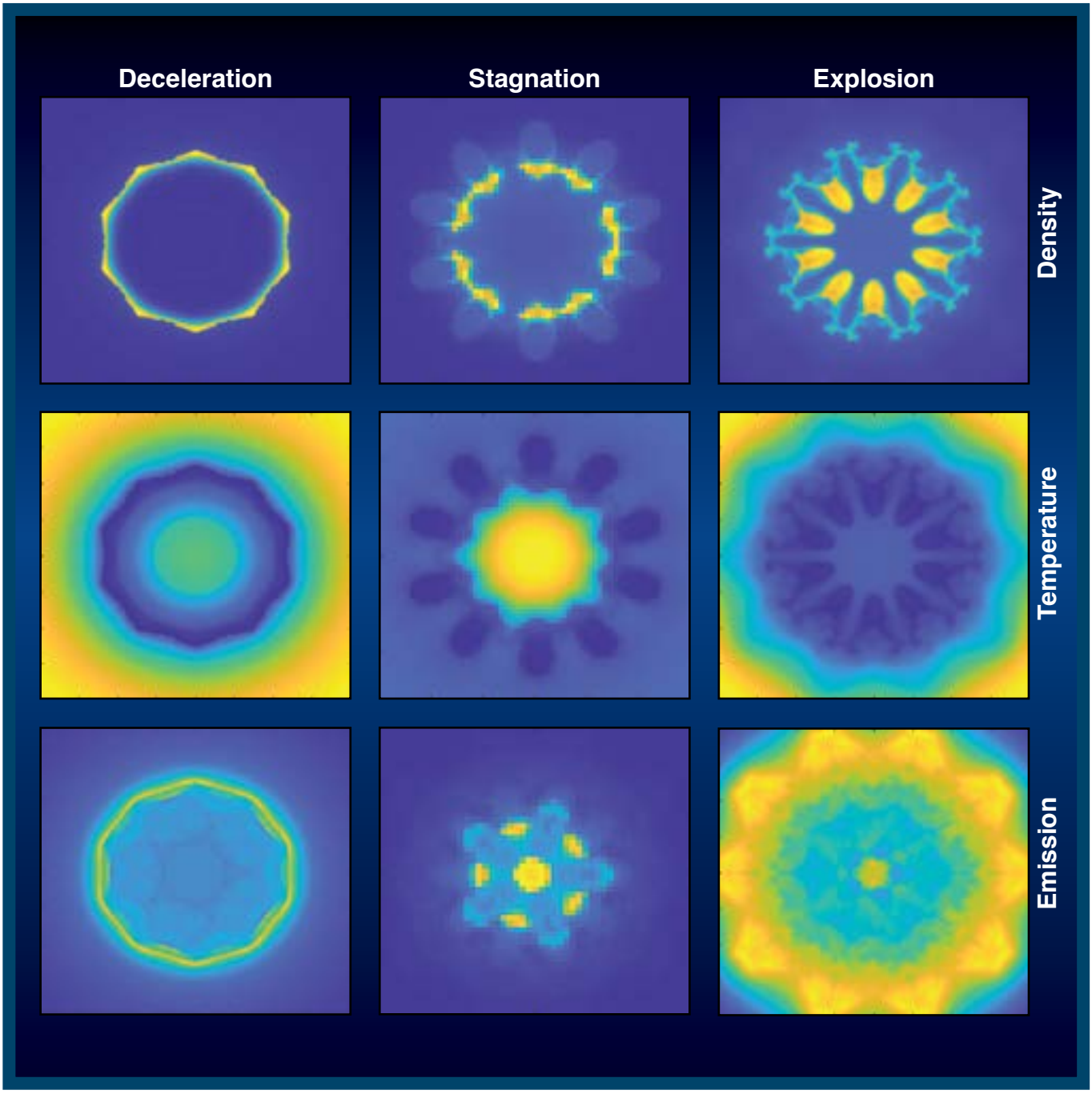

About the Cover:

The cover picture shows density (top row) and temperature (middle row) maps from 3-D *ASTER* simulations of a DT cryogenic implosion with a beam-to-target ratio of $R_b/R_t = 0.75$, and post-processed synthetic x-ray images (bottom row) for three different phases of the implosion: deceleration (left column), stagnation (middle column), and post-stagnation (explosion) (right column). These maps cover an area of 400 μm × 400 μm. The low-density regions in the shell in the deceleration phase correspond to the regions of the shell that are broken during the stagnation and post-stagnation phases. The post-stagnation x-ray image correlates well with the density profile, where the brightest regions in the image correspond to the shell locations where material is being ejected. Compared to the deceleration and stagnation phases, the structures in the post-stagnation x-ray image are spatially larger and are easier to analyze.

Simulations predict that the coupling of the laser energy to the target can be increased by lowering R_b/R_t. This change, however, also increases beam-overlap perturbations that cause distortions in the dense shell and lead to shell breakup at stagnation. To diagnose the shell breakup, the x-ray self-emission from the implosions was recorded during the post-stagnation phase with a filtered 16-pinhole array imager and x-ray framing camera using an exposure time of ~40 ps. The figure below shows experimental images obtained in implosions with different R_b/R_t. A Fourier decomposition is applied to the outer peak signal of the images to diagnose the low- and mid-mode asymmetries in the implosion. The images and modal analysis show higher low- and mid-mode amplitudes for the implosion with $R_b/R_t \sim 0.77$ compared with the implosion with $R_b/R_t \sim 0.95$, which indicates a better hydrodynamic instability for the implosion with higher R_b/R_t.

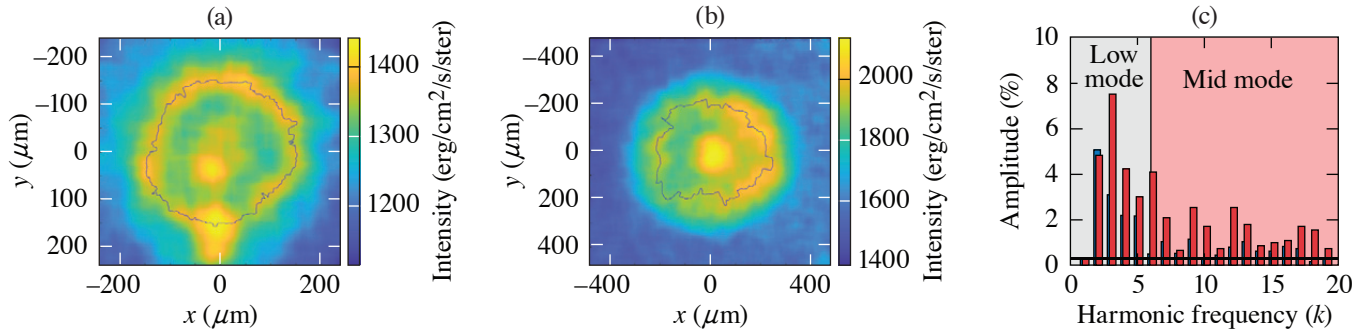

E30231JR

The work described in this volume includes current research at the Laboratory for Laser Energetics, which is supported by New York State Energy Research and Development Authority, the University of Rochester, the U.S. Department of Energy Office of Inertial Confinement Fusion under Cooperative Agreement No. DE-NA0003856, and other agencies.

Printed in the United States of America
Available from
National Technical Information Services
U.S. Department of Commerce
5285 Port Royal Road
Springfield, VA 22161
www.ntis.gov

For questions or comments, contact Nickolaos Savidis, Editor, Laboratory for Laser Energetics, 250 East River Road, Rochester, NY 14623-1299, (585) 275-3413.

www.lle.rochester.edu

UNIVERSITY OF ROCHESTER
LABORATORY FOR LASER ENERGETICS

Volume 172
July–September 2022
DOE/NA/3856-1775

LLE Review

Quarterly Report

UR LLE

Contents

Director's Remarks

C. Deeney

Director, Laboratory for Laser Energetics

The Laboratory for Laser Energetics (LLE) is funded primarily by the U.S. Department of Energy (DOE) National Nuclear Security Administration's (NNSA's) Office of Experimental Sciences Inertial Confinement Fusion (ICF) Program through a five-year Cooperative Agreement. The fiscal year ending September 2022 (FY22) comprised the fourth year of work under DOE/NNSA Cooperative Agreement No. DE-NA0003856. The Laboratory is also sponsored by the New York State Energy Research Development Authority and other federal agencies such as the DOE Office of Science and the National Science Foundation. I was honored to become the fifth Director of LLE, succeeding Dr. E. Michael Campbell who retired in March 2022.

The year 2022 was exciting for the National ICF Program and LLE. Ignition was achieved at the National Ignition Facility for the first time, producing more energy out of the implosion than the input laser energy to the target. LLE has made many contributions to the pursuit of ignition, including laser technologies, diagnostics, simulation capabilities, physics understanding, and student education. Groundbreaking for the construction of a new $42M addition to the LLE Complex (funded by the University of Rochester) occurred in August 2022. LLE submitted a proposal to renew the Cooperative Agreement with DOE/NNSA for FY24–FY28.

This report summarizes work conducted at LLE during FY22 that includes research on the ICF and High-Energy-Density (HED) science campaigns; laser, optical materials and advanced technology development; operation of the Omega Laser Facility for the ICF and HED campaigns, the National Laser Users' Facility, Laboratory Basic Science Program, and other external users, including the newly established LaserNetUS supported by the DOE Office of Fusion Energy Sciences; and programs focusing on the education of high school, undergraduate, and graduate students.

- The Omega Laser Facility conducted 2110 target shots in FY22, close to the average annual number of shots since FY14 with nearly 60% of the shots performed for external users. These experiments are critical to LLE and the national community achieving progress in the ICF/HED Physics mission, in advancing science, and in training students.

- Mission Impact: All of the completion criteria for the 15 NNSA Level II milestones were achieved.

- Scientific Output: One hundred and one technical manuscripts were published in peer-reviewed scientific journals during FY22.

- Sixteen Ph.D. degrees were conferred on graduate students during 2022 whose primary research was performed at the Laboratory either as students of the University of Rochester or as students of other collaborating user institutions who performed experiments or worked with scientists at the Omega Laser Facility.

- One University of Rochester Ph.D. graduate (Alison Christopherson) won the American Physical Society Division of Plasma Physics Marshall N. Rosenbluth Outstanding Doctoral Thesis Award.

- Radha Bahukutumbi, a Distinguished Scientist in the Theory Division, received the Leadership Award at the annual meeting of the Fusion Power Associates.

- Steve Ivancic, head of the Diagnostic Development and Integration Group, received a Defense Programs Award of Excellence from Lawrence Livermore National Laboratory.

Key technical highlights included:

- A series of high in-flight aspect ratio and high-velocity implosions on OMEGA produced yields between 2.6×10^{14} and 3.1×10^{14}, all above the previous yield record. The highest yield implosion, when corrected for ^{3}He buildup using statistical modeling, would have produced a yield of nearly 1 kJ, roughly the same as the shell kinetic energy. These direct-drive implosions enable Ph.D. research on ICF and open opportunities for future ICF optimization.

- Layered DT implosions with silicon dopants performed significantly better (higher yields) than comparable targets without dopants, confirming that the dopant suppresses imprint while only modestly increasing the shell adiabat via x-ray preheat.

- The Lawrence Livermore National Laboratory (LLNL)/LLE Neutron Sources collaboration conducted a polar-direct-drive exploding-pusher experiment at the National Ignition Facility that produced a record laser-direct-drive (LDD) yield of 1.6×10^{16} with a laser pulse of 1.6 MJ.

- The proof-of-concept for the LLE dynamic-shell ignition design, where pulse shaping dynamically creates a high-density shell with a DT wetted-foam target, was demonstrated using 3-D–printed foam capsules.

- Constrained by integrated implosion measurements, spectroscopic observables revealed that a density functional theory (DFT)-based kinetic model developed by LLE scientists (*VERITAS*) reproduces a majority of the emission and absorption features observed in experiments, while the traditional collisional-radiative-equilibrium treatment with *ad hoc* continuum lowering does not, suggesting that self-consistent treatment of dense plasma effects is needed at very high pressures.

- In collaboration with LLNL, LLE scientists showed that diamond can precipitate from twice-shocked CH polymers (e.g., ICF ablators) in the presence of oxygen, nitrogen, and chlorine.

- An LLE–LLNL team conclusively demonstrated species separation in the release of strongly shocked CH, finding that the hydrogen ions carry 10 to 100× more mass than the carbon ions to large distances, confirming a hypothesis developed to understand the seeds of instability growth in plastic ICF ablators.

- Based on x-ray diffraction measurements of sevenfold compressed sodium, a team from LLE and LLNL observed the *hP4* electride phase at a pressure of 480 GPa and a temperature of 3000 K (a regime where core electron overlap was thought to stabilize against this phase), indicating that electride formation is possible on nanosecond time scales at high temperatures.

- A decades-old discrepancy between theory and measurement on the shock-induced metallization of polystyrene was resolved using a new exchange correlation functional that properly captures the shock-induced dissociation of carbon and correctly predicts the band-gap closing behavior at 1 to 2 Mbar.

- New DFT calculations of Fe and Cr opacity at stellar interior densities and temperatures did not resolve the iron opacity "mystery" identified some time ago at Sandia National Laboratories' Z Pulsed Power Facility. The new calculations showed good agreement with the measured Cr opacity but did not agree with Z's measurements of the Fe opacity.

- Recent experiments showed that micron-scale x-ray radiography is possible for a wide range of flow visualizations at ultrahigh pressures using a new LLE-developed Fresnel zone plate imaging diagnostic.

- The first electron radiographs of a test object were acquired (in collaboration with Los Alamos National Laboratory) using a laser-plasma accelerator platform on OMEGA EP.

- The 13th Omega Laser Facility Users Group (OLUG) Workshop, held 27–29 April 2022 at LLE, attracted nearly 200 researchers from around the world.

- The 24th Topical Conference on High-Temperature Plasma Diagnostics (HTPD), hosted by LLE in Rochester, NY, attracted 370 registered participants. The HTPD conference showcased the latest in advanced instrumentation in the fields of magnetic confinement fusion, inertial confinement fusion, high-energy-density plasmas, space plasmas, astrophysics, and industrial applications.

- The 50th Anomalous Absorption Conference 2022 hosted and organized by LLE was held 5–10 June in Skytop, PA. Conference topics included theoretical and experimental studies in parametric instabilities, radiation hydrodynamics, particle acceleration, HED physics, short-pulse laser–matter interactions, and ICF.

- A classified report on the scope of applications within the Stockpile Stewardship Program for platforms that rely on LDD was submitted to the NNSA Office of Experimental Science, completing one of the milestones in the ICF five-year plan.

As the fifth Director working with the senior leadership team, we have set our vision to be "the leading academic institution advancing laser technologies, inertial confinement fusion, and high-energy-density science at scale." I hope you agree that FY22 met this vision.

In Brief

This volume of LLE Review 172 covers the period from July–September 2022. Articles appearing in this volume are the principal summarized results for long-form research articles. Readers seeking a more-detailed account of research activities are invited to seek out the primary materials appearing in print, detailed in the publications and presentations section at the end of this volume.

Highlights of research presented in this volume include:

- J. Baltazar *et al.* develop a technique to diagnose the low- and mid-mode asymmetries in the post-stagnation phase of a deuterium–tritium (DT) cryogenic implosion with the aim of relating the post-stagnation phase measurement to the shell breakup caused by an increase in beam overlap perturbations due to a lower R_b/R_t (p. 1).

- M. J. Rosenberg *et al.* analyze laser–plasma instability mitigation techniques for direct-drive inertial confinement fusion (ICF) by examining stimulated Raman scattering and two-plasmon–decay instabilities, assessing their dependence on density scale length and overlapping laser beam geometry critical to ICF ignition/fusion gain (p. 4).

- A. Shvydky *et al.* propose a new approach in producing uniform beam intensity distributions applied on a sphere for laser-direct-drive ICF system configurations based on mathematical spherical *t* designs to find optimal beam configurations, targeting a reduction of spherical harmonics and nonuniformity modes (p. 7).

- R. K. Follett *et al.* develop a series of test cases for validation of ray-based cross-beam energy transfer (CBET) models against wave-based calculations. Comparisons between various ray-based models show that an etalon integral field reconstruction with a coherent caustic correction and caustic gain truncation is the preferred ray-based CBET model, with equal to improved performance without increasing compuational cost (p. 10).

- T. R. Joshi *et al.* extend the application of the x-ray self-emission imaging technique to polar-direct-drive ICF implosions with cryogenically layered DT targets on OMEGA, diagnosing in-flight asymmetries (p. 13).

- J. R. Davies, P. V. Heuer, and A. F. A. Bott develop an electrostatic particle-in-cell (PIC) algorithm that was compared to algorithms for charged-particle radiography and shadowgraphy used in laser-plasma experiments, deducing a Monge–Ampère code applied as first order, and a PIC code if the Monge–Ampère code fails or requires a subsequent, more-accurate inversion (p. 18).

- A. L. Milder *et al.* present first measurements of the threshold and linear growth rate of the return-current instability driven by electron heat flux, where characterization of the plasma conditions show that the return-current instability occurs concurrently with nonlocal transport (p. 22).

- G. Bruhaug *et al.* present a method to determine the resolution for laser-plasma acceleration electron radiography that include accounting for drive laser image distortions, quantifying plasma-generated electric fields in laser-ablated targets by measuring electron radiography image feature sizes, and estimating field strength needed to produce those features (p. 25).

- V. V. Karasiev *et al.* apply first-principles density functional theory to calculate optical properties (mass-absorption coefficient and opacity) of Cr and Fe at stellar interior temperatures to explore whether *ab initio* calculations can resolve the disagreement between previous atomic physics calculations and measured data (p. 28).

- D. A. Chin *et al.* designed and built two extended x-ray absorption fine structure (EXAFS) flat crystal x-ray spectrometers (EFX's) for high-resolution x-ray spectroscopy over a large energy range with flexible, on-shot energy dispersion calibration capabilities, enabling x-ray absorption near-edge spectroscopy measurements to be made on OMEGA (p. 31).

- J. Cheng *et al.* demonstrate a promising candidate for ultrafast optical/near-infrared to x-ray radiation detector applications with a photodetector sensitive to both optical and x-ray picosecond pulses based on in-house grown cadmium magnesium telluride (Cd,Mg) Te single crystal (p. 34).
- D. Ramsey *et al.* derive exact solutions to Maxwell's equations for the electromagnetic fields of a constant-velocity flying-focus pulse and identified small differences to the paraxial solutions for a wide range of parameters, justifying paraxial solutions for many applications in many regimes, such as a spatiotemporal pulse-shaping technique (p. 38).
- K. R. P. Kafka, T. Z. Kosc, and S. G. Demos assess operational performance limits of optics and aspects required for the development of improved optic designs/reliable operational fluence limits for ultrashort optical performance characterization beyond the standard laser-induced–damage threshold testing system specifications that only characterize the damage-initiation threshold (p. 41).
- E. P. Power *et al*. design, simulate, fabricate, and test a prototype flow-cell, integrated-cooling substrate built using cordierite ceramic and demonstrate average power handling up to 3.88-W/cm^2 absorbed power density with 54-nm peak-to-valley deformation in a sub-aperture test, with a <30 s observed mechanical stabilization time scale (p. 44).
- M. Romo-Gonzalez and R. Boni test a zero *B*-integral pellicle beam splitter composed of uncoated nitrocellulose, having a maximum reflectivity of ∼30% with negligible absorption in the near-infrared (p. 48).
- L. J. Waxer, J. Bromage, and B. E. Kruschwitz provide an overview of the various topics they wrote in the SPIE Spotlight series e-book on petawatt laser systems, introducing the reader to the laser science and technology underpinning petawatt laser systems and technological advances required for state-of-the-art high-intensity laser performance (p. 51).
- R. S. Craxton summarizes the 33rd LLE Summer High School Research Program (p. 54). Sixteen students were invited from Rochester-area high schools to participate in the lab's state-of-the art research environment.
- T. J. Kessler, M. Romo-Gonzalez, and R. Ghosh report on the Broad Exposure to Science and Technology (BEST) Program, a research program designed to engage teachers and students from historically marginalized experiences in various aspects of science and technology that support LLE's laser science and applications research (p. 57).
- J. Puth *et al.* summarize operations of the Omega Laser Facility during the fourth quarter of FY22 (p. 62).
- M. J. Shoup III highlights the groundbreaking and early days of the LLE building expansion (p. 64).
- This volume concludes with the FY22 Laser Facility Report, the FY22 Education Summary, and overviews of the National Laser Users' Facility, Laboratory Basic Science, and LaserNetUS Programs.

Nickolaos Savidis
Editor

Diagnosing Low-Mode ($\ell < 6$) and Mid-Mode ($6 \leq \ell \leq 60$) Asymmetries in the Post-Stagnation Phase of Cryogenic Implosions on OMEGA

J. Baltazar,[1,2] R. Betti,[1,2] K. Churnetski,[1,2] V. Gopalaswamy,[1] J. P. Knauer,[1] D. Patel,[1] H. G. Rinderknecht,[1] R. C. Shah,[1] C. Stoeckl,[1] C. A. Williams,[1] and S. P. Regan[1,2]

[1]Laboratory for Laser Energetics, University of Rochester
[2]Department of Mechanical Engineering, University of Rochester

In order to achieve ignition-relevant conditions in direct-drive inertial confinement fusion (ICF) implosions, the hot spot must reach pressures exceeding ~100 Gbar (Ref. 1). Simulations of 1-D implosions predict that these pressures can be achieved by driving low- ($\alpha < 3$) to mid-adiabat ($\alpha > 4$) implosions, where mid-adiabat implosions require mitigation of cross-beam energy transfer (CBET) losses.[2] The performance of low-adiabat implosions is sensitive to ablation-surface modulations caused by target features and laser nonuniformity imprint, which becomes the seed for the Rayleigh–Taylor instability.[3] On some high-performance implosions[4] with $\alpha > 4$, CBET losses are mitigated by reducing the laser beam size, which reduces the ratio of the beam radius (R_b) to the initial target radius (R_t) below one and increases the laser coupling. Simulations predict that by increasing the on-target laser coupling, the hydrodynamic efficiency increases. However, this change also increases beam-overlap perturbations that causes distortions in the dense shell and leads to shell breakup at stagnation.[2] An interesting approach to diagnose the shell breakup was inspired by previous work at Lawrence Livermore National Laboratory,[5] where low modes were diagnosed by self-emission imaging in the explosion phase of DT cryogenic indirectly driven ICF implosions that were not diagnosed in the stagnation phase.

In this study, x-ray self-emission from the implosions is recorded with a filtered 16-pinhole array imager and an x-ray framing camera (XRFC) to produce gated-images of x-ray emission.[3,6] A 0.3-μm aluminum and 1-μm polypropylene filter is employed to record x rays with energies >800 eV. The framing camera is timed to record images in the explosion phase. A 3-D *ASTER*[2] simulation of a DT cryogenic implosion has been post-processed through *Spect3D*[7] to produce synthetic x-ray images that are analyzed to investigate x-ray signatures of the shell breakup. The synthetic images are integrated over 40 ps and blurred with 20-μm FWHM to match the instrument response function of the XRFC. The 3-D *ASTER* simulation was run with phase plates to produce a smaller beam radius compared to the radius of the target ($R_b/R_t \sim 0.75$) The evolution of the density, temperature, and emission from the deceleration phase to the post-stagnation (explosion) phase is shown in Fig. 1. The reduced R_b/R_t leads to an increase in beam-mode perturbations that evolve throughout the deceleration, stagnation, and explosion phase, where in the explosion phase the perturbed features are more apparent compared to the previous stages.

Figure 2 shows experimental images obtained in implosion using setups with different R_b/R_t. A Fourier decomposition is applied to the outer peak signal of the images to diagnose the low- and mid-mode asymmetries in the implosion. The images are first mapped onto a radius and angle coordinate system, where the radius is the distance from the center and the angle corresponds with the angle with respect to the x axis. The modal analysis for two implosions with different R_b/R_t is shown in Fig. 2(c). The implosion with $R_b/R_t \sim 0.77$ shows higher low- and mid-mode amplitudes compared with the implosion with $R_b/R_t \sim 0.95$. At a larger R_b/R_t, more beams overlap at the target surface, which leads to a more-uniform laser-intensity profile, less hydro instability seeds in the low/mid spatial modes, and lower measured mode amplitudes.

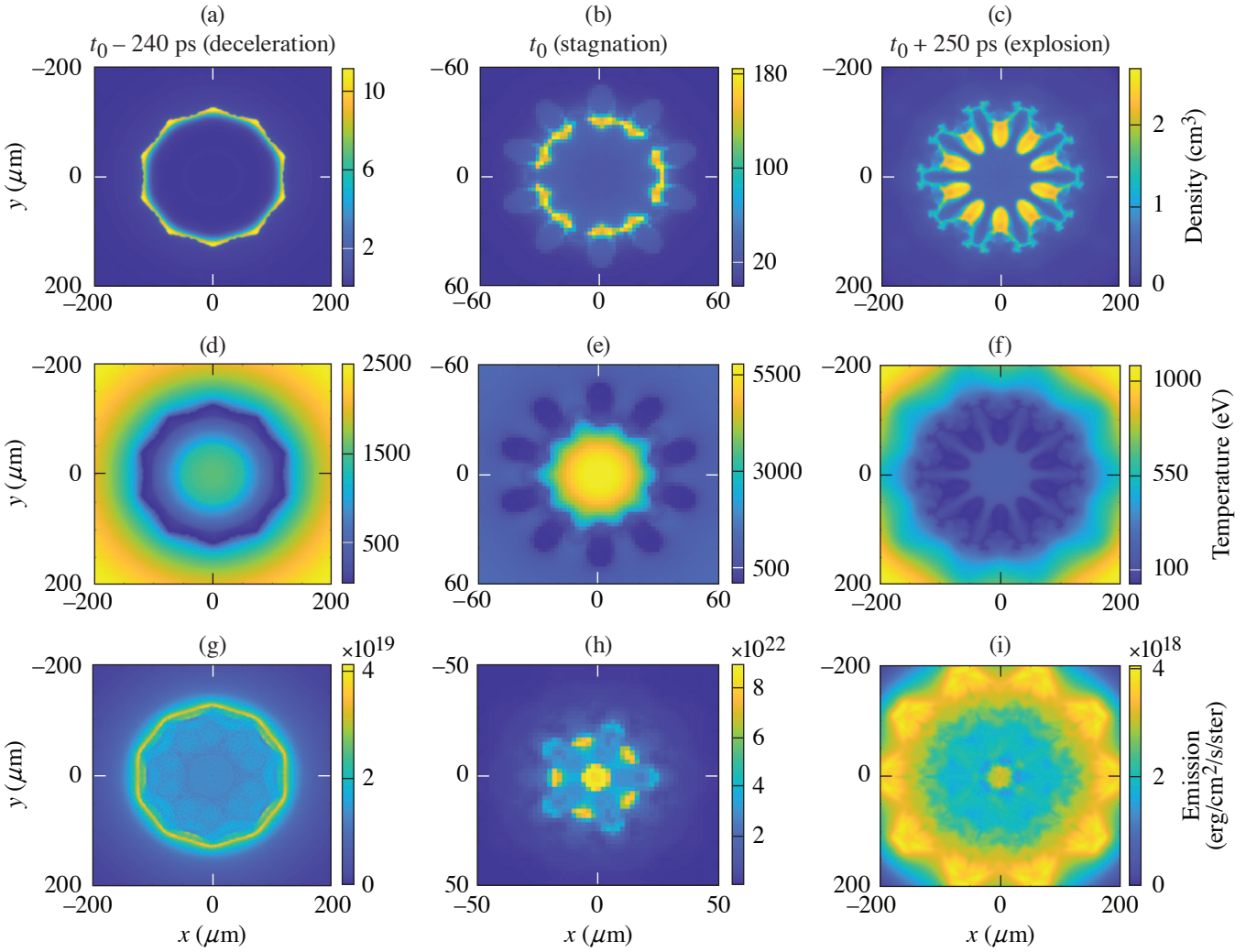

Figure 1
Evolution of the [(a)–(c)] density, [(d)–(f)] temperature, and [(g)–(i)] x-ray emission during the deceleration, stagnation, and explosion phases of a cryogenic DT implosion with a $R_b/R_t \sim 0.75$ (3-D *ASTER* simulation). The low-density regions in the shell in the deceleration phase correspond to the regions of the shell that are broken during the stagnation and post-stagnation phases. Therefore, the shell nonuniformity is seeded by the beam perturbation and leads to the breakup of the shell. The post-stagnation phase x-ray image resembles the density profile and the brightest regions in the image correspond to the broken shell locations where material is being ejected. Compared to the deceleration and stagnation phase, the signature in the post-stagnation phase x-ray measurement is spatially larger and is easier to analyze.

In conclusion, a technique was developed to diagnose the low- and mid-mode asymmetries in the explosion phase of a DT cryogenic implosion. This technique is developed with the aim of relating the explosion phase measurement to the shell breakup caused by an increase in beam overlap perturbations due to a lower R_b/R_t. An R_b/R_t sensitivity analysis from explosion phase measurements on OMEGA shows that the mid-mode rms value increases as the R_b/R_t value decreases, which is expected due to an increase in nonuniformity from the reduced beam overlap. A Monte Carlo simulation is underway to determine the error in the measurements and to guide the necessary changes in experimental setup to obtain better measurements.

This material is based upon work supported by the Department of Energy National Nuclear Security Administration under Award Number DE-NA0003856, the University of Rochester, and the New York State Energy Research and Development Authority.

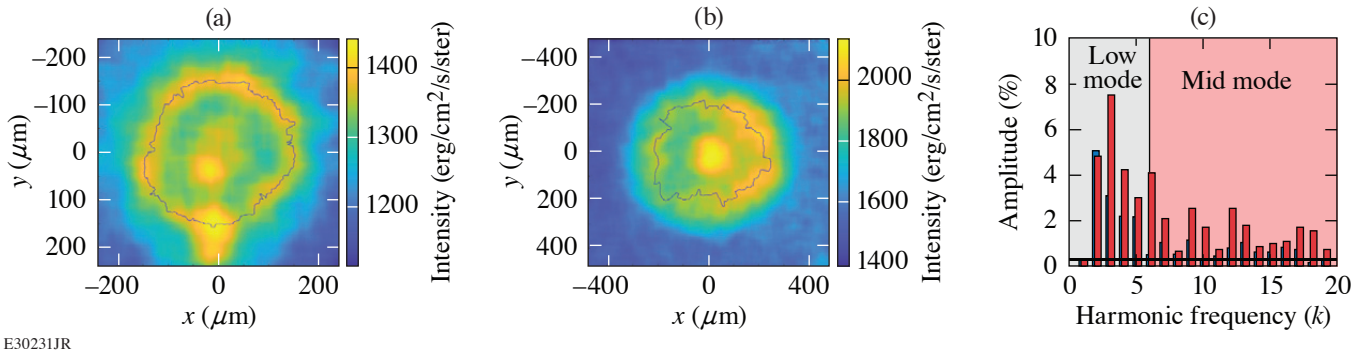

Figure 2
Experimental measurements for implosions with an R_b/R_t of (a) 0.95 and (b) 0.77. (c) The mode spectrum is plotted for both implosions [red is the analysis for the image shown in (a) and blue is the analysis for the image shown in (b)] and shows higher low- and mid-modes for the implosion with a lower R_b/R_t.

1. V. N. Goncharov *et al.*, Phys. Plasmas **21**, 056315 (2014).
2. I. V. Igumenshchev *et al.*, Phys. Plasmas **23**, 052702 (2016).
3. S. X. Hu *et al.*, Phys. Plasmas **23**, 102701 (2016).
4. V. Gopalaswamy *et al.*, Nature **565**, 581 (2019); A. Lees *et al.*, Phys. Rev. Lett. **127**, 105001 (2021).
5. A. Pak *et al.*, Phys. Plasmas **20**, 056315 (2013).
6. D. T. Michel *et al.*, Rev. Sci. Instrum. **83**, 10E530 (2012).
7. Prism Computational Sciences, Inc., Madison, WI 53711.

Effect of Overlapping Laser Beams and Density Scale Length in Laser–Plasma Instability Experiments on OMEGA EP

M. J. Rosenberg,[1] A. A. Solodov,[1] J. F. Myatt,[2] S. Hironaka,[2] J. Sivajeyan,[2] R. K. Follett,[1] T. Filkins,[1] A. V. Maximov,[1] C. Ren,[1,3,4] S. Cao,[1,3] P. Michel,[5] M. S. Wei,[1] J. P. Palastro,[1] R. H. H. Scott,[6] K. Glize,[6] and S. P. Regan[1]

[1]Laboratory for Laser Energetics, University of Rochester
[2]Department of Electrical and Computer Engineering, University of Alberta
3Department of Mechanical Engineering, University of Rochester
[4]Department of Physics and Astronomy, University of Rochester
[5]Lawrence Livermore National Laboratory
[6]Central Laser Facility, STFC Rutherford Appleton Laboratory

Laser–plasma instabilities (LPI's) are a concern in inertial confinement fusion (ICF) experiments because of the reduction in laser energy and potential generation of hot electrons, which can limit compression of the imploding capsule. Stimulated Raman scattering (SRS) and two-plasmon decay (TPD) can occur at densities at and below the quarter-critical density of the laser [$n_e = n_c/4$, where n_e is the electron density and n_c is the critical density for the laser wavelength λ_0 (in μm) (with $n_c \approx 1.1 \times 10^{21}\ \lambda_0^{-2}$ cm^{-3}), and have been observed at ICF-relevant intensities. Understanding these instabilities and their dependence on density scale length and overlapping laser beam geometry is critical to the pursuit of ICF ignition and fusion gain.

Planar- and spherical-geometry experiments were conducted on OMEGA EP to systematically explore SRS and TPD at scale lengths intermediate between previous experiments, at shorter scale length on OMEGA and longer scale length at the National Ignition Facility (NIF), and with different overlapped laser geometry. Solid 700-μm-diam CH spheres and 250-μm-thick CH slabs were irradiated with one or four beams and 750-μm spot size or with one beam and a 400-μm spot in a 2-ns square pulse or 4-ns ramp pulse with total laser energy of 8.2 to 9.3 kJ.

Figure 1 shows the 2-D *DRACO*-simulated quarter-critical density scale length, temperature, intensity, and threshold parameters for SRS and TPD for four-beam planar [Figs. 1(a)–1(d)] and spherical experiments [Figs. 1(e)–1(h)] with 750-μm phase plates and a 2-ns square pulse. Planar four-beam experiments were predicted to reach density scale lengths on axis of around 300 μm, electron temperatures of 2.8 keV, and overlapped laser intensities of 8×10^{14} W/cm^2. In contrast, four-beam spherical experiments were predicted to reach scale lengths of only 150 μm and similar electron temperatures (2.7 keV) and overlapped laser intensities (8.5×10^{14} W/cm^2). Planar one-beam experiments with the 750-μm spot had reduced intensity, temperature, and scale length, while one-beam experiments with the 400-μm spot size had a 190-μm scale length and laser intensity (4×10^{14} W/cm^2) between the 750-μm one-beam and four-beam experiments.

Time-resolved scattered-light spectra between wavelengths of 400 and 750 nm were measured for a variety of experiments driven by the 2-ns square pulse, as shown in Fig. 2. TPD is evident in a doublet feature corresponding to half-harmonic ($\omega/2$) emission around 702 nm, while SRS appears as a singlet red-shifted $\omega/2$ feature from absolute backscatter at quarter-critical density or as a broad-wavelength feature <680 nm generated in the underdense region. TPD is most prominent in the four-beam planar and spherical experiments, while SRS is generally favored in one-beam experiments, especially at high intensity with the small distributed phase plates (DPP's).

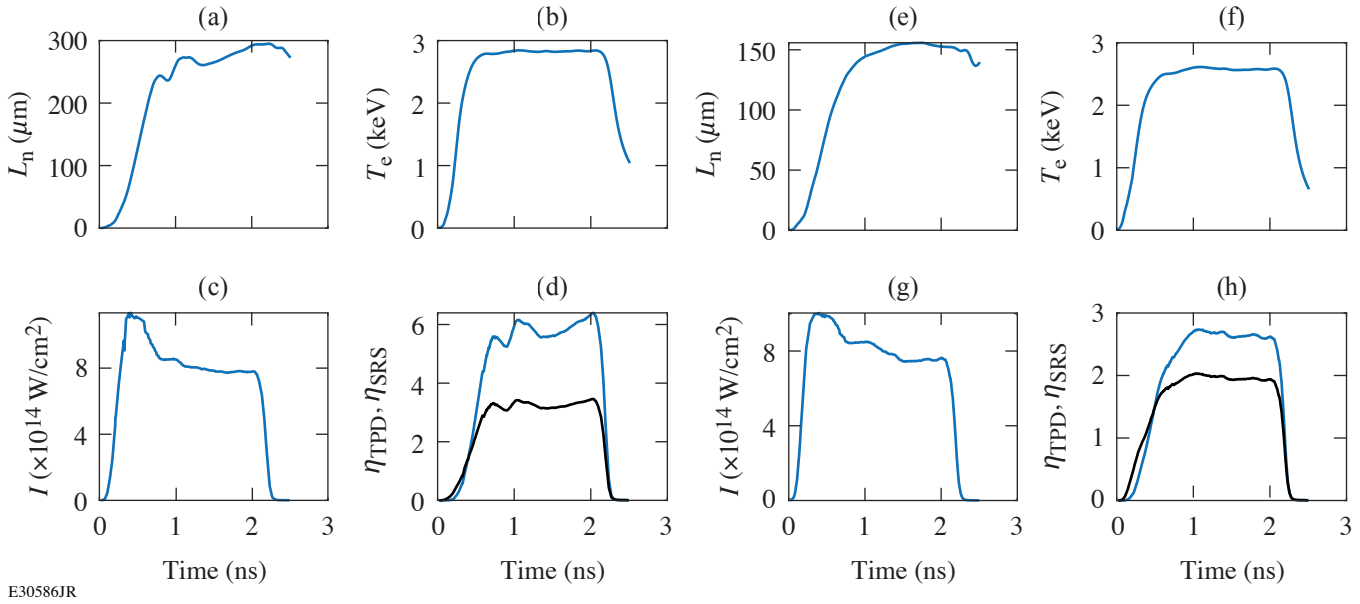

Figure 1
Two-dimensional *DRACO*-simulated plasma conditions at the quarter-critical density along the axis of symmetry for [(a)–(d)] a planar experiment and [(e)–(i)] a spherical experiment, driven by four beams in a 2-ns square pulse. The [(a),(e)] density scale length, [(b),(f)] electron temperature, [(c),(g)] overlapped laser intensity, and [(d),(h)] SRS (blue curves) and TPD (black curves) threshold parameters η are shown.

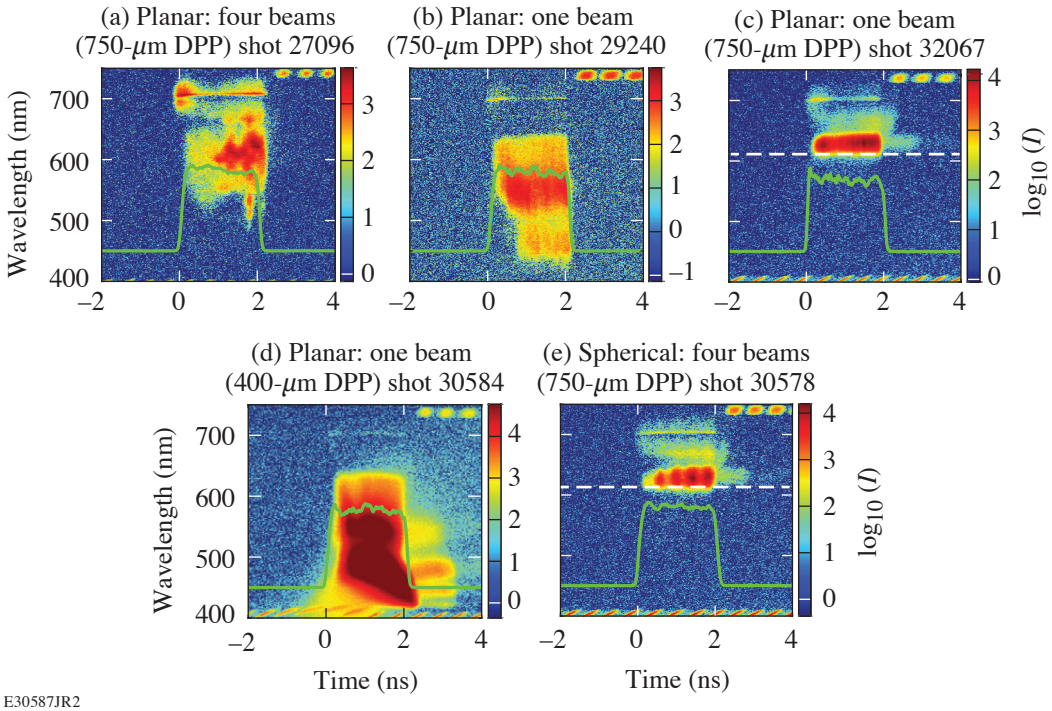

Figure 2
Measured time-resolved scattered-light spectra for experiments with a 2-ns square pulse (green line) and (a) a planar target irradiated by four beams, [(b),(c)] a planar target irradiated with one beam with a 750-μm spot size, (d) a planar target irradiated by one beam with a 400-μm spot size, and (e) a 700-μm-diam spherical target irradiated by four beams. [(c),(e)] The dashed white line represents the 630-nm cutoff of a long-pass filter, with (b) showing data from a nominally identical experiment as (c), but without the long-pass filter. The green line represents the laser pulse. The signal is strongly saturated in the 450- to 550-nm range in (d). Different neutral density filters and sub-aperture backscatter diagnostic throughput for each shot limits comparison of absolute signal levels.

Comparison to previous experiments on OMEGA[1] and the NIF[2] elucidate the effect of scale length and single-beam versus overlapped laser intensity on the prevalence of SRS and TPD. Typical OMEGA 60-beam spherical experiments at ∼150-mm scale length and low ($<10^{14}$ W/cm^2) single-beam intensity show evidence only of TPD and not SRS. Planar and spherical experiments at ∼400- to 600-μm scale length on the NIF are dominated by SRS and show negligible TPD. In combination with these experiments on OMEGA EP, it is evident that shorter density scale lengths and lower single-beam intensities (at sufficient overlapped intensity) are relatively favorable for TPD, while longer density scale lengths and higher single-beam intensities are relatively more favorable for SRS. These results are generally consistent with absolute TPD and SRS threshold considerations and the prevailing theory that TPD is more of a multibeam instability than SRS. This work will contribute to LPI mitigation techniques for direct-drive ICF.

This material is based upon work supported by the Department of Energy National Nuclear Security Administration under Award Number DE-NA0003856, the University of Rochester, and the New York State Energy Research and Development Authority.

1. W. Seka *et al*., Phys. Plasmas **16**, 052701 (2009)
2. M. J. Rosenberg *et al*., Phys. Rev. Lett. **120**, 055001 (2018); M. J. Rosenberg *et al*., Phys. Plasmas **27**, 042705 (2020).

Optimization of Irradiation Configuration Using Spherical *t* Designs for Laser-Direct-Drive Inertial Confinement Fusion

A. Shvydky, W. Trickey, A. V. Maximov, I. V. Igumenshchev, P. W. McKenty, and V. N. Goncharov

Laboratory for Laser Energetics, University of Rochester

In laser-direct-drive inertial confinement fusion (ICF), a cryogenically cooled spherical shell of deuterium–tritium (DT) fuel covered with a plastic layer on the outside is irradiated by a number of laser beams. The laser irradiation ablates the outer plastic (ablator) layer, compressing the fuel to reach ignition conditions.[1–3] Because of the finite number of beams (e.g., 60 on the OMEGA Laser System[4]) the laser irradiation nonuniformity on the target surface leads to a nonuniform shell compression and reduction in the implosion performance.

The beam-overlap uniformity improves with increasing the number of beams N. Optimization of beam port locations to minimize drive asymmetries for a given number of beams is an important consideration in designing an ICF implosion facility. There have been two basic methodologies of obtaining beam configurations presented in literature. One is based on either augmenting or composing together regular polyhedrons.[4,5] Advantages of this method include a symmetric intensity distribution with minimized nonuniformity for a few select values of N. A disadvantage is the lack of a systematic extension to an arbitrary N. The other method is the charged-particle method, which uses a system of N particles constrained to a sphere that repel each other with a coulomb force (or another distance-dependent force). The beam configurations are chosen to correspond to particle configurations that minimize the potential energy.[6–8] The advantage of the method is its simplicity in obtaining beam configurations for arbitrary N. The disadvantage is a slow decay of nonuniformity with the number of beams as, e.g., $1\sqrt{N}$ in Ref. 8. Neither of the above methods offer a way of finding beam configurations that simultaneously eliminate spherical harmonic modes below a certain number, which has been recognized as an important strategy in designing the irradiation system.[5]

In this summary, we propose new beam configurations based on spherical t designs, which are studied in the area of mathematics known as spherical designs.[9] New configurations have the advantage of combining the following properties: all of the nonuniformity modes with $\ell \leq t$ are zero, nonuniformity amplitudes decrease strongly with the number of beams, and intensity distribution on spherical targets exhibit symmetric patterns. Computational methods developed in the field of spherical designs (see, e.g., Refs. 10 and 11) offer a systematic approach of obtaining such configurations for any number of beams[10] feasible for a direct-drive ICF facility.

The beam configuration of the OMEGA Laser System[4] is practically a 60-beam 9-design (a spherical t design with $t = 9$). It has all $\ell \leq 9$ exactly equal to zero, except for mode 6, which is close to zero. OMEGA is not a regular truncated icosahedron "soccer ball," which is only a 5-design, but rather a "stretched soccer ball" whose hexagonal faces have unequal sides A and B with the stretch factor $A/B = 1.2$ [see Fig. 1(a)]. The ratio $A/B = 1.21$ is quoted in Ref. 5 to eliminate mode $\ell = 6$ in the stretched soccer ball configuration. Values of the stretch factor in both OMEGA and Ref. 5 are within 0.5% from the exact value $A/B = 1.205285...$ that can be calculated following the method from Ref. 12, where it was recognized that the stretched soccer ball with the optimal stretch factor is a better approximation for a sphere than the regular soccer ball.

Remarkably, a 10-design exists for a set of 60 points,[13] which we will call $T60$. The $T60$ configuration eliminates ℓ modes up to and including mode 10 and is shown in Fig. 1(b) along with the $M60$ configuration [Fig. 1(c)] obtained in Ref. 6 using the charged-particle method. Although $T60$ has [3,3]+ symmetry group and is the union of five snub tetrahedrons,[13] there are no

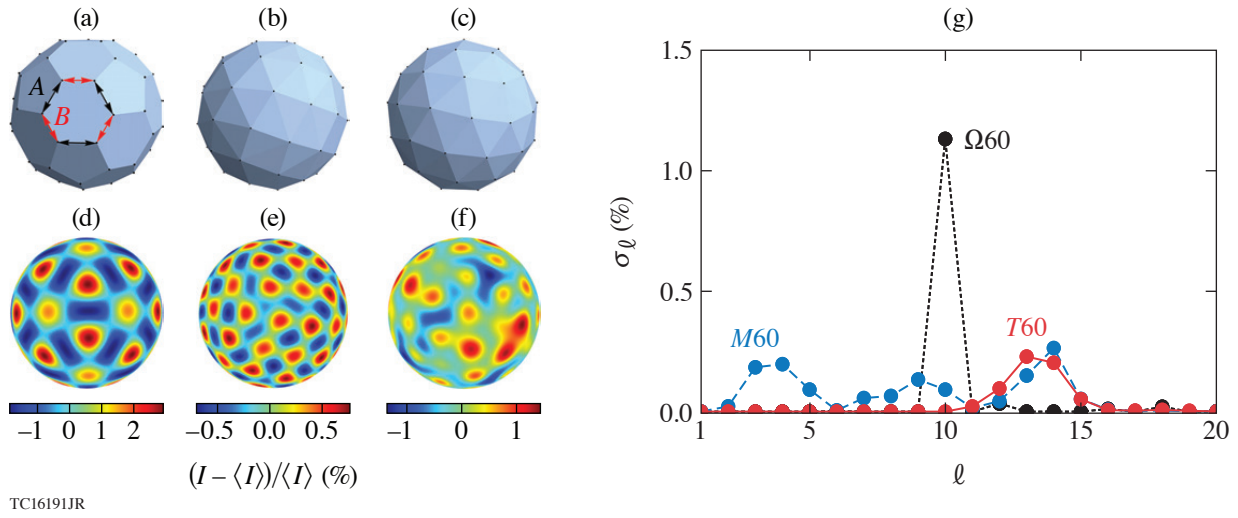

Figure 1
Beam configurations of (a) OMEGA, (b) *T*60, and (c) *M*60. Absorbed intensity distributions for (d) OMEGA, (e) *T*60, and (f) *M*60 configurations. (g) Plot of rms nonuniformity σ_ℓ as a function of mode number ℓ for OMEGA (black curve), *T*60, (red curve), and *M*60 (blue curve) configurations.

visually discernible symmetries in *T*60 point locations (much like in *M*60) in comparison to the aesthetically pleasing OMEGA laser. Figures 1(d)–1(f) show the intensity distributions produced by 60 laser beams from the OMEGA, *T*60, and *M*60 configurations, respectively. As an example, for Fig. 1, the beams were chosen to have the following profiles,

$$I_a(\theta) = I_0 \exp\left[-(\sin\theta/0.635)^{4.19}\right] \cdot \max(\cos\theta, 0), \tag{1}$$

which correspond to profiles produced by SG5-650 phase plates[14] on 450-μm-diam targets on the OMEGA Laser System. Similar to OMEGA, *T*60 produces a symmetric illumination pattern [compare Figs. 1(d) and 1(e)], while *M*60 produces less-regular illumination pattern [see Fig. 1(f)]. Out of the three configurations, the 10-design configuration produces the lowest intensity variation amplitude. Figure 1(g) shows the ℓ-mode spectra, σ_ℓ versus ℓ, corresponding to configurations in Figs. 1(a)–1(c). One can see dominant mode 10 and zero modes $\ell < 10$ for OMEGA. *M*60 has significant amplitude in a broad range of modes from $\ell = 2$ to $\ell = 14$. *T*60 has modes $\ell =$ (11 to 15) with amplitudes that are similar to that of *M*60 but, as expected, has zero modes $\ell < 11$.

Future direct-drive ICF laser systems will look to improve uniformity, which means increasing t in t-design configurations using the least number of beams N. Finding t designs with the smallest N for a given t happens to be one of the main problems in spherical design theory. It was conjectured that the spherical t designs exist for any t and require at least number of points $N \approx (1/2)t^2$ (see Ref. 13), where t designs are listed for every $N \leq 100$. The authors' website in Ref. 13 also contains point coordinates for t designs when $N = 12m$, $m = 1,2,3...$ with the number of points up to $N = 240$ and $t = 21$. Below, we will use these designs as an example. It is worth noting that numerical methods have been developed that make it possible to calculate t designs with $t \leq 1000$ and corresponding $N \leq 10^6$ (see, e.g., Ref. 10).

Figures 2(a)–2(d) show the intensity distribution for four $N = 12m$ spherical t designs with $t = 11$, 13, 16, and 21 and $N = 72$, 96, 144, and 240, which we call *T*72, *T*96, *T*144, and *T*240, respectively. Similar to *T*60, the $N = 12m$ configurations with a higher number of beams have intrinsic symmetry groups and show symmetric intensity distribution patterns. Note a dramatic reduction of the nonuniformity amplitude with t. Figure 2(e) shows ℓ-mode spectra σ_ℓ for the five $N = 12m$ t designs, four designs from Figs. 2(a)–2(d), and *T*60 from Fig. 1(b). One can see zero amplitude of modes $\ell \leq t$ and a sharp decrease of the σ_ℓ for large ℓ for all t designs.

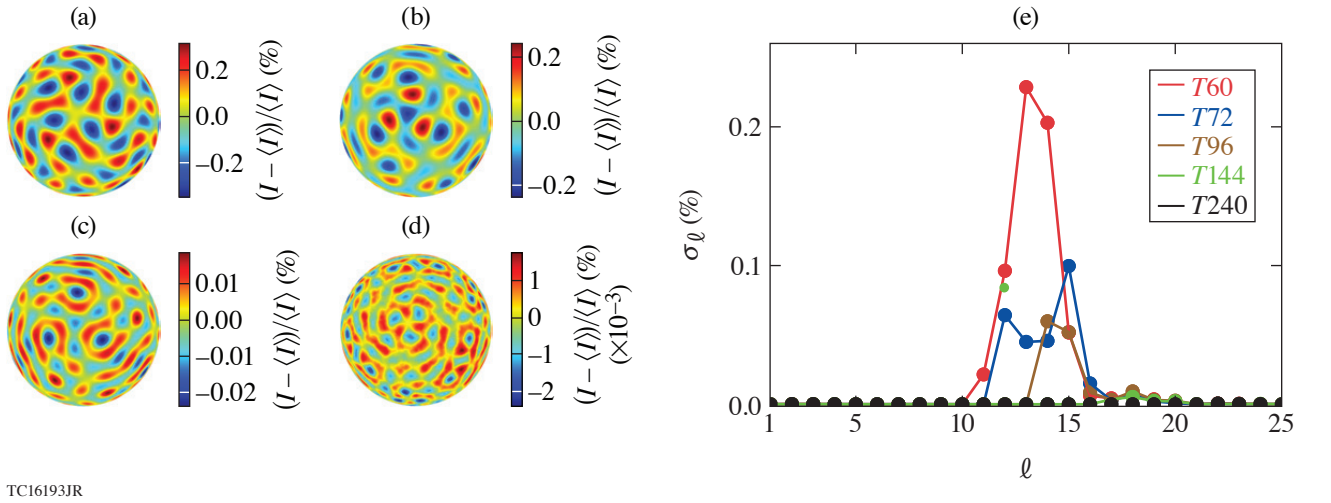

Figure 2
Intensity distributions for (a) $T72$, (b) $T96$, (c) $T144$, and (d) $T240$ configurations. (e) Plot of rms nonuniformity σ_ℓ as a function of mode number ℓ for $T60$ (red), $T72$ (blue), $T96$ (brown), $T144$ (green), and $T240$ (black) configurations.

In this summary, we have proposed a new approach to systematically obtain beam configurations for laser-direct-drive ICF systems that are based on t designs from the area of mathematics known as spherical designs. The t-design beam configurations offer the following advantages: (a) they eliminate all nonuniformity modes $\ell \leq t$, where t increases with the number of beams as $\sim\sqrt{2N}$; (b) the rms nonuniformity drops rapidly with the number of beams as a high power of N or close to exponentially with N; and (c) t designs with intrinsic symmetries show symmetric intensity-distribution patterns (although, it may have only aesthetic benefits). We envision that future laser-direct-drive ICF facilities will use t-design beam configurations with a number of beams that will be determined by the nonuniformity requirements. As a final note, spherical t designs can be used, more generally, in applications where a uniformity of an action on a sphere applied at discrete points is required, e.g., a uniformity of pressure applied with a system of identical actuators.

Funding was provided by the ARPA-E BETHE Grant No. DEFOA-0002212. This material is based upon work supported by the Department of Energy National Nuclear Security Administration under Award No. DE-NA0003856, the University of Rochester, and the New York State Energy Research and Development Authority.

1. J. Nuckolls *et al.*, Nature **239**, 139 (1972).
2. J. D. Lindl, Phys. Plasmas **2**, 3933 (1995).
3. R. S. Craxton *et al.*, Phys. Plasmas **22**, 110501 (2015).
4. *LLE Review Quarterly Report* **39**, 113 (1989).
5. M. Murakami, Appl. Phys. Lett. **66**, 1587 (1995).
6. M. Murakami *et al.*, Phys. Plasmas **17**, 082702 (2010).
7. M. Murakami and D. Nishi, Matter Radiat. Extremes **2**, 55 (2017).
8. W. Trickey *et al.*, Front. Phys. **9**, 784258 (2021).
9. P. Delsarte, J. M. Goethals, and J. J. Seidel, Geom. Dedicata **6**, 363 (1977).
10. M. Gräf and D. Potts, Numer. Math. **119**, 699 (2011).
11. R. S. Womersley, in *Contemporary Computational Mathematics–A Celebration of the 80th Birthday of Ian Sloan*, edited by J. Dick, F. Y. Kuo, and H. Woźniakowski (Springer, Cham, 2018), pp. 1243–1285.
12. J. M. Goethals and J. J. Seidel, Nieuw Archief voor Wiskunde **XXIX**, 50 (1981).
13. R. H. Hardin and N. J. A. Sloane, Discrete Comput. Geom. **15**, 429 (1996).
14. W. Theobald *et al.*, Phys. Plasmas **29**, 012705 (2022).

Validation of Ray-Based Cross-Beam Energy Transfer Models

R. K. Follett,[1] A. Colaïtis,[2] D. Turnbull,[1] D. H. Froula,[1] and J. P. Palastro[1]

[1]Laboratory for Laser Energetics, University of Rochester
[2]Centre Lasers Intenses et Applications

This summary presents a series of comparisons between ray- and wave-based CBET calculations that highlight the essential physics that must be included in a ray-based CBET model. The comparison cases are designed to aid in the validation of ray-based CBET models by including precise input parameters and quantitative comparison metrics and/or wave-based field data.[1] The cases vary in complexity from simple 2-D two-beam interactions in a linear density gradient to 60 beams interacting in a 3-D spherical plasma profile. We have found that in all cases the most sophisticated algorithm (etalon integral field reconstruction[2] with a coherent caustic correction and caustic gain truncation[3]) performed at least as well as its more-simplistic counterparts without increasing the overall computational cost and should be the preferred algorithm for use in ray-based CBET codes. A particular emphasis is placed on energy conservation because ray-based CBET models typically do not conserve energy explicitly and require artificial correction. We show that the intrinsic lack of energy conservation inherent to ray-based algorithms significantly affects the accuracy and that artificially correcting energy-conservation errors can have a large impact on results.

In direct-drive inertial confinement fusion (ICF), a millimeter-scale spherical capsule is illuminated by symmetrically oriented laser beams.[4–6] The lasers ablate the outer layer of the capsule, which generates pressure to implode the fuel. In addition to depositing thermal energy in the ablator, the lasers can resonantly drive various laser–plasma instabilities (LPI's) that can degrade the quality of the implosion. One of the predominant LPI's that impacts ICF implosions is cross-beam energy transfer (CBET), where laser beams exchange energy through a ponderomotively driven ion-acoustic wave.[7,8] CBET reduces the overall laser absorption in direct-drive ICF because it tends to transfer energy from the incoming lasers to outgoing reflected/refracted light.

Many of the radiation-hydrodynamics codes used to design ICF implosions include CBET models, but implementation details vary significantly between codes and artificial multipliers are often required to reproduce experimental results.[2,3,8–16] One of the underlying reasons for the prevalence of artificial multipliers is that it is not clear what level of accuracy is even possible with ray-based codes because there are very few analytic results available for use as test cases. An excellent way to validate ray-based CBET models, however, is with wave-based calculations. Wave-based CBET models naturally include all of the physics that can only be approximately included in ray-based models. Due to the much higher computational cost, it is not currently possible to run 3-D wave-based CBET calculations at the scale of ICF experiments, but all of physics required for ray-based CBET models can be studied in subscale simulations.

The *LPSE* results are compared to ray-based results from two different codes. The first is a relatively simple test-oriented code that was developed in conjunction with *LPSE* for the specific purpose of making comparisons between ray-based CBET algorithms and *LPSE* results.[3] We also include results from the *IFRIIT*[2,13] laser deposition code implemented in 3-D *ASTER* (Ref. 17). *IFRIIT* provides an interesting comparison point because it implements some of the algorithms detailed in this summary for the electromagnetic-field calculation, while it differs significantly on other points—most notably on the use of inverse ray tracing versus forward ray tracing. Finally, it is an inline model, implying that contrary to the test-oriented ray-based code, it was formulated for speed while still being able to reproduce the *LPSE* results.

Figure 1 shows the laser absorption as a function of grid resolution for 2-D 16-beam simulations in an azimuthally symmetric plasma profile that is based on fits to a *LILAC* simulation of an OMEGA implosion. The various subfigures correspond to scaled versions of the original hydro profile ranging from 1/64th scale to full scale (S = 1/64 to S = 1). The various ray-based CBET models that were used are as follows: (1) "FL, no CGT" corresponds to field-limiter treatment of the caustic without caustic gain truncation (which leads to slow convergence); (2) "FL, no CC" corresponds to a field-limiter treatment of the caustic without using a coherent treatment of the fields in the caustic region (which leads to poor energy conservation); (3) "FL" corresponds to a field-limiter treatment with both CGT and a coherent caustic treatment; (4) "EI" corresponds to an etalon integral field reconstruction with both CGT and a coherent caustic treatment; (5) "*IFRIIT*" corresponds to results from the *IFRIIT* code that uses the same physical model as "EI" but with a different numerical implementation.

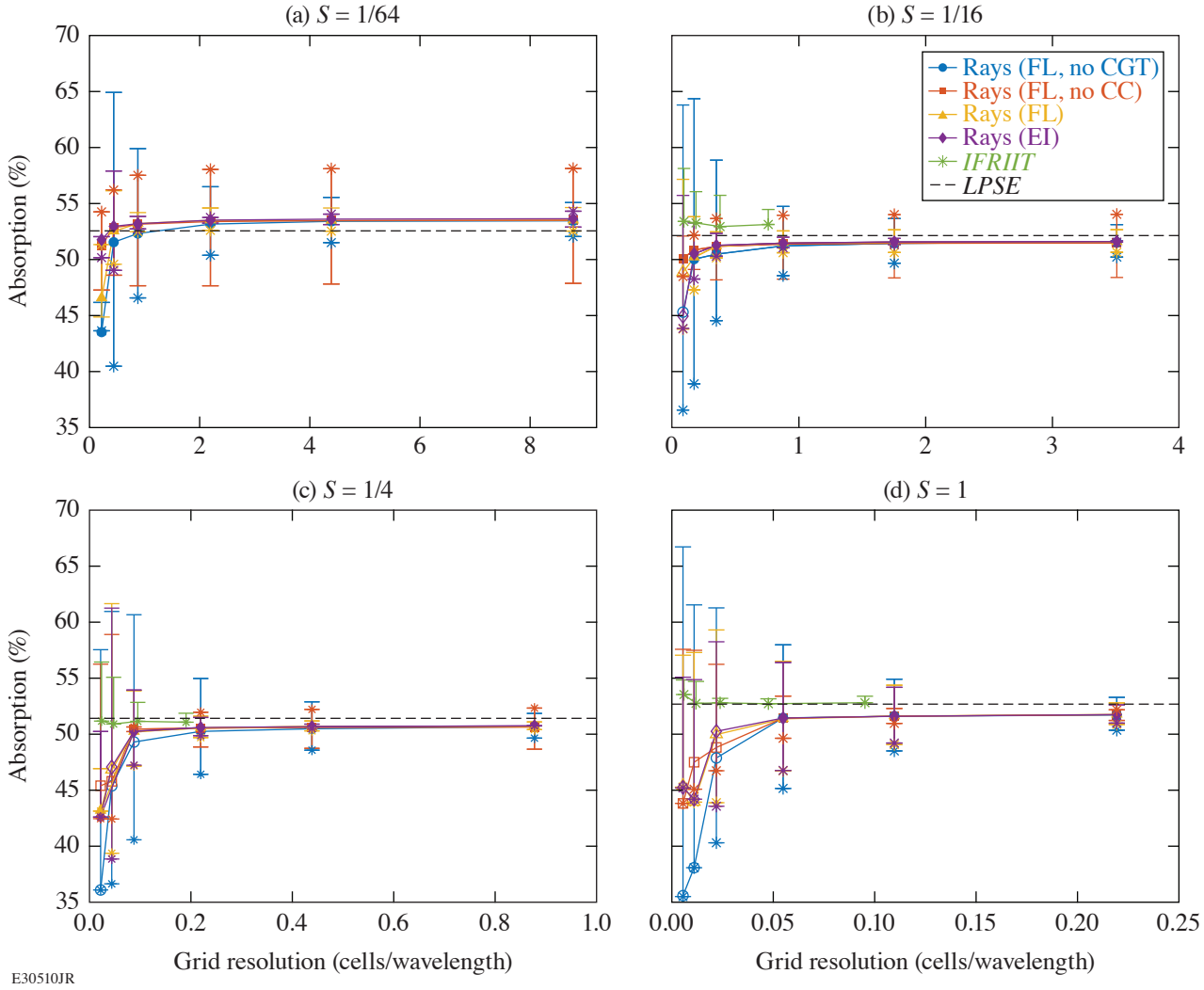

Figure 1
Laser absorption as a function of grid resolution for 16-beam 2-D simulations at (a) 1/64 scale, (b) 1/16 scale, (c) 1/4 scale, and (d) full scale. *LPSE* results are shown with horizontal black dashed lines. The stars represent the ray-based results without enforcing energy conservation, and the solid markers represent the energy-conserving results (open markers correspond to cases where energy conservation could not be achieved). The error bars show the size of the uncorrected energy-conservation error. The various ray-based approaches are FL without CGT (blue circles), FL without the coherent caustic correction (red squares), FL (yellow triangles), and EI (purple diamonds). The *IFRIIT* results are shown with green stars.

In all cases the converged ray-based results are in good agreement with the *LPSE* simulations ($\lesssim$1% difference in absorption). The ray-based results are plotted in a way that displays the absorption results and the energy-conservation properties on the same axes. Specifically, stars show the uncorrected absorption (energy conservation not enforced), and the solid markers show the absorption after enforcing energy conservation (open markers are used in cases where energy conservation could not be achieved). The range of the error bars corresponds to the range of absorption that could be achieved if all of the missing (extra) energy is added to (subtracted from) absorption or scattered (unabsorbed) light. Accordingly, any reasonable approach to enforcing energy conservation will result in an absorption within the error bar. Alternatively, a reasonable approach exists to enforcing energy conservation that would lead to any result between the error bars. An ideal algorithm would have the star on top of the solid marker (and vanishing error bounds), meaning that energy was conserved without any artificial correction. The results are plotted in this way because it is critically important to consider the impact of the somewhat arbitrary approach that is used to enforce energy-conservation ray-based CBET codes.

The "FL, no CC" model with $S = 1/64$ [Fig. 1(a)] provides a good example of why it is important to consider the uncorrected energy-conservation error. By simply comparing the converged solutions after correcting for energy conservation, the "FL, no CC" model gives the same result as the more-sophisticated models. However, the uncorrected energy-conservation error is greater than 10%, suggesting that the somewhat arbitrary choice of algorithm for enforcing energy conservation was a huge lever on the final result (the star being at the top of the error bar implies that extra energy was created). Conversely, the error bars using the EI method are much smaller ($\sim$1%), meaning that artificially enforcing energy conservation does not have a significant impact on those results. Note that the energy-conservation error (in the converged solution) tends to improve with increasing scale because a smaller fraction of the CBET is occurring in the caustic region. Achieving convergence at large scales can, however, be difficult because it becomes harder to resolve the caustics.

This material is based upon work supported by the Department of Energy National Nuclear Security Administration under Award Number DE-NA0003856, ARPA-E BETHE grant number DE-FOA-0002212, the University of Rochester, and the New York State Energy Research and Development Authority.

1. R. K. Follett, *LPSE* Data for Ray-Based CBET Test Cases (1.0.0) [Data set]. Zenodo (2022), Accessed 7 March 2023, http://dx.doi.org/10.5281/zenodo.6962934.
2. A. Colaïtis *et al.*, Phys. Plasmas **26**, 032301 (2019).
3. R. K. Follett *et al.*, Phys. Rev. E **98**, 043202 (2018).
4. J. Nuckolls *et al.*, Nature **239**, 139 (1972).
5. R. S. Craxton *et al.*, Phys. Plasmas **22**, 110501 (2015).
6. S. Atzeni and J. Meyer-ter-Vehn, *The Physics of Inertial Fusion: Beam Plasma Interaction, Hydrodynamics, Hot Dense Matter*, 1st ed., International Series of Monographs on Physics, Vol. 125 (Oxford University Press, Oxford, 2004).
7. C. J. Randall, J. R. Albritton, and J. J. Thomson, Phys. Fluids **24**, 1474 (1981).
8. P. Michel *et al.*, Phys. Plasmas **20**, 056308 (2013).
9. I. V. Igumenshchev *et al.*, Phys. Plasmas **19**, 056314 (2012).
10. A. Colaïtis *et al.*, Phys. Plasmas **23**, 032118 (2016).
11. J. A. Marozas *et al.*, Phys. Plasmas **25**, 056314 (2018).
12. A. Colaïtis *et al.*, Phys. Plasmas **25**, 033114 (2018).
13. A. Colaïtis *et al.*, J. Comput. Phys. **443**, 110537 (2021).
14. D. H. Edgell *et al.*, Phys. Plasmas **24**, 062706 (2017).
15. A. K. Davis *et al.*, Phys. Plasmas **23**, 056306 (2016).
16. D. J. Strozzi *et al.*, Phys. Rev. Lett. **118**, 025002 (2017).
17. I. V. Igumenshchev *et al.*, Phys. Plasmas **23**, 052702 (2016).

Diagnosis of the Imploding Shell Asymmetry in Polar-Direct-Drive Deuterium–Tritium Cryogenic Target Implosions on OMEGA

T. R. Joshi, R. C. Shah, W. Theobald, K. Churnetski, P. B. Radha, D. Cao, C. A. Thomas, J. Baltazar, and S. P. Regan

Laboratory for Laser Energetics, University of Rochester

The polar-direct-drive (PDD)[1–6] approach has been developed for performing laser-direct-drive inertial confinement fusion (ICF) experiments at the National Ignition Facility (NIF)[7] using the current configuration of laser beams customized for indirect-drive implosions. The NIF lacks beams near the equator for a symmetric illumination; therefore, the beams must be repointed to adequately irradiate the equator for direct-drive experiments.[8,9] The repointed beams have decreased energy coupling with the target, thereby requiring higher drive energies and unique pulse shapes to prevent reduced drive uniformity.[4] The irradiation nonuniformity caused by the PDD geometry reduces the implosion performance of OMEGA[10] ambient target implosions,[3,6] but it has never been evaluated in cryogenic target implosions. There is an ongoing effort on OMEGA to understand the hydrodynamic scaling of the best-performing symmetrically irradiated cryogenic target implosions,[11] as well as to study the impact of a PDD illumination geometry in order to improve our understanding of scaling from OMEGA to future NIF direct-drive cryogenic target implosions. The 40-beam PDD configuration on OMEGA provides a good approximation to the NIF PDD conditions.[1] However, differences remain in terms of the beams' angle of incidence, number of beams, number of rings, flexibility in laser pulse shaping, and laser smoothing.[4]

X-ray[2–4] radiography and self-emission imaging[12–14] techniques have been widely used to measure shell asymmetries and trajectories of imploded shells on OMEGA and the NIF. In this summary, we have extended the application of the x-ray self-emission imaging technique to PDD ICF implosions with cryogenically layered deuterium–tritium (DT) targets on OMEGA. The in-flight shell asymmetries were diagnosed at various times during the implosion, which were caused by the beam-pointing geometry and pre-imposed variations in the energy partition between the different groups of laser beams.

PDD ICF experiments with cryogenically layered DT targets were performed for the first time on OMEGA. The PDD illumination was achieved by using 40 of the 60 OMEGA[10] UV beams by switching off 20 beams around the equator. Figure 1(a) shows a schematic map of the OMEGA target chamber with the blue circles indicating the used beam ports. The 40 beams are grouped in three beam rings in the upper and lower hemisphere according to their polar angles. The beams were repointed to achieve the best possible illumination uniformity.[6] In each group of six rings, there were five, five, and ten laser beams, respectively. Figure 1(b) shows the beam pointing scheme, which was fixed during the experiment. The dashed lines indicate the repointing locations for the beams from the upper hemisphere. The beams from rings 1, 2, and 3 were repointed by 123 μm, 157 μm, and 219 μm, respectively. The displacement represents the distance from the target center along the direction perpendicular to the beam axis. The pointing condition was optimized with pre-shot *DRACO*[15] simulations.

All targets contained a DT ice shell overcoated by a thin plastic (CD) ablator layer, and the core of the shell was filled with DT vapor. The outer diameter of the CD shell was 767 μm and the thicknesses of the CD ablator and the DT ice layer were 6.2 μm and 33.5 μm, respectively. The laser pulse consisted of a picket that launched a shock controlling the shell adiabat ($\alpha \approx 4$, ratio of plasma pressure to the Thomas–Fermi pressure at peak density) and then gradually rose to a 1.4-ns dual-step main drive pulse [see Fig. 1(c)]. The total UV laser energy on target was 12.7$\pm$0.2 kJ, where the average was calculated for a set of five shots (three shots are discussed here) and the error represents the standard deviation. All 40 beams were outfitted with small-spot distributed phase plates (SG5-650),[16–18] polarization smoothing,[19] and 2-D smoothing by spectral dispersion[20] at 0.3-THz bandwidth and

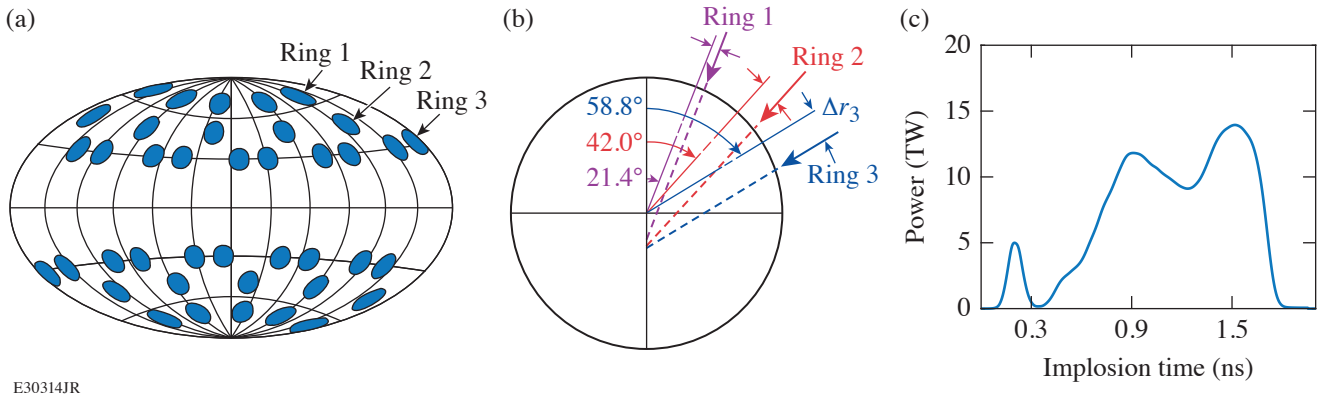

Figure 1
(a) Beam-port configuration for a PDD implosion on OMEGA. (b) Beam-pointing schemes and target geometry. The dashed lines show the shifted beams for OMEGA PDD geometry. (c) Pulse shape used for the implosions.

three-color cycles.[21,22] The partition of beam energies in rings 1 and 3 was varied while keeping the total laser energy constant. By denoting with ΔE_3 the change in energy of ring 3 (irradiating closer to the equator) and with ΔE_1 the change in energy of ring 1 (irradiating closer to the pole), the change in ring energy ratio is defined as $\Delta D = (\Delta E_3 - \Delta E_1)/E_{\text{tot}}$, where E_{tot} is the total energy on target. The nominal ring energy partition for a balanced drive ($\Delta D = 0$) is $E_1/E_{\text{tot}} = 0.25$, $E_2/E_{\text{tot}} = 0.25$, and $E_3 E_{\text{tot}} = 0.5$. Table I shows a summary of the discussed shots with drive imbalance condition, parameter ΔD, total laser energy on target, energy in each ring, and the measured neutron yield.

Table I: Summary of the shot number, drive imbalance condition, drive imbalance parameter, total laser energy on target, energy in each ring, and the measured neutron yield from DT fusion reactions.

Shot number	Drive	ΔD	E_{tot}(kJ)	E_1 (J)	E_2 (J)	E_3 (J)	Neutron yield (10^{13})
96575	Balanced	1.0%	12.7	3132	3155	6433	1.32±0.09
96578	Strong on poles	−4.6%	12.9	3522	3203	6173	1.93±0.07
96581	Stronger on equator	−10.6%	12.9	2560	3190	7158	1.34±0.09

The x-ray emission from the shell was recorded temporally and spatially resolved during the acceleration phase of the implosion with two pinhole cameras coupled to x-ray framing cameras in TIM-1 ($\theta = 63.44°$, $\varphi = 126°$ and in TIM-5 ($\theta = 101.81°$, $\varphi = 270°$), where TIM stands for ten-inch manipulator and θ and φ, respectively, are the polar angle and azimuthal angle coordinates of the OMEGA target chamber ports. An array of sixteen 15-μm-diam pinholes were used to produce 16 temporally resolved x-ray self-emission images[12,13,23] of the target on a four-strip x-ray framing camera.[24,25] Figure 2 shows x-ray self-emission images from the TIM-1 camera after the laser burned through the outer CD layer. The outer and inner rings in the images come from the emission at the CD–DT interface and the DT ice layer ablation front, respectively.[13] Here only the DT ablation front is analyzed because of its close proximity to the dense DT shell. The emission from the outer CD–DT interface layer is quickly diminishing in time due to the evaporation and rarefaction of the material in the plasma corona. Images in Figs. 2(a)–2(c) were acquired from shots 96578, 96575, and 96581, respectively, and at roughly the similar times relative to the start of their laser pulses. In shot 96578, the target is driven stronger on the poles with $\Delta D = -4.6\%$ and the shape of the DT ablation front in the measured image in Fig. 2(a) is oblate. In shot 96581, the target is driven stronger on the equator with $\Delta D = 10.6\%$ and the shape of the DT ablation front becomes prolate as shown in Fig. 2(c). In shot 96575, the drive was more balanced, and consequently a rounder shape can be seen in Fig. 2(b). Similar images were obtained from the TIM-5 camera. The shape of the DT ablation front was determined by tracking the peak x-ray emission in the inner ring with respect to the polar angle in the image plane.

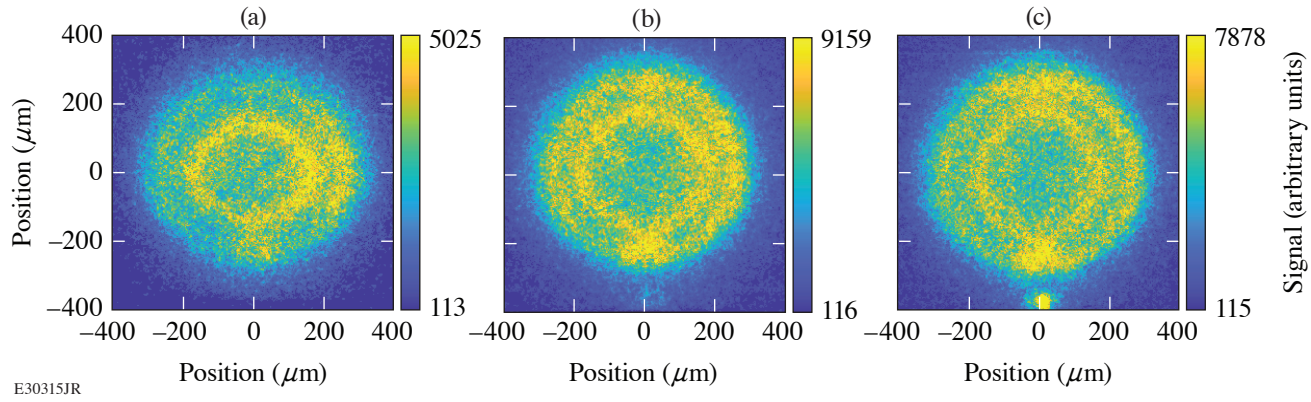

Figure 2
Measured x-ray self-emission images from three shots with different laser drive balance. Images from shots (a) 96578 ($\Delta D = -4.6\%$), (b) 96575 ($\Delta D = 1.0\%$), and (c) 96581 ($\Delta D = 10.6\%$). The camera was positioned in TIM-1 ($\theta = 63.44°$, $\varphi = 126°$). The x-ray self-emission images in (a)–(c) were recorded at 1.67±0.1 ns, 1.62±0.1 ns, and 1.58±0.1 ns, respectively, relative to the start of the laser pulse in their implosions.

Figure 3 shows the temporal evolution of P_2 from the three shots with different drive imbalance from the two different lines of sight (TIM-1 and TIM-5). The normalized mode amplitude is plotted along the ordinate versus the ablation-front radius on the abscissa. Since the ablation-front radius decreased with time during the compression phase, the corresponding time axis progresses from right to left. The P_2 amplitude magnitude at a large radius of ~350 μm (early time) is similarly small (<2%) for all the shots. The P_2 amplitude of the targets before the shots was measured to be <0.3% (Ref. 26). Both views show similar trends, although there are slight differences in the P_2 amplitude, which might indicate a systematic error in the data analysis. The temporal evolution of modes 4 and 6 from the three shots with different drive imbalance remain similar within the measurement uncertainty, and modes higher than 6 are negligible. The sign of the P_2 amplitude indicates whether the shell is oblate (negative) or prolate (positive).[3,14] In Fig. 3, the P_2 amplitude of two different shots (96578 and 96581) have opposite signs, particularly in the later phase of the implosions. The P_2 amplitudes in shot 96575 are close to zero (slightly negative) and always lie in between the amplitudes from shots 96578 and 96581. Errors for each mode are estimated by the difference in extracted mode amplitude when fitting to the left and right halves of the ablation surface in the self-emission images separately. We recall here that the energy of each beam in ring 1 (close to pole) in shot 96578 was increased ($\Delta D = -4.6\%$) and that the energy of each beam in ring 3 (close to equator) in shot 96581 was increased ($\Delta D = 10.6\%$).

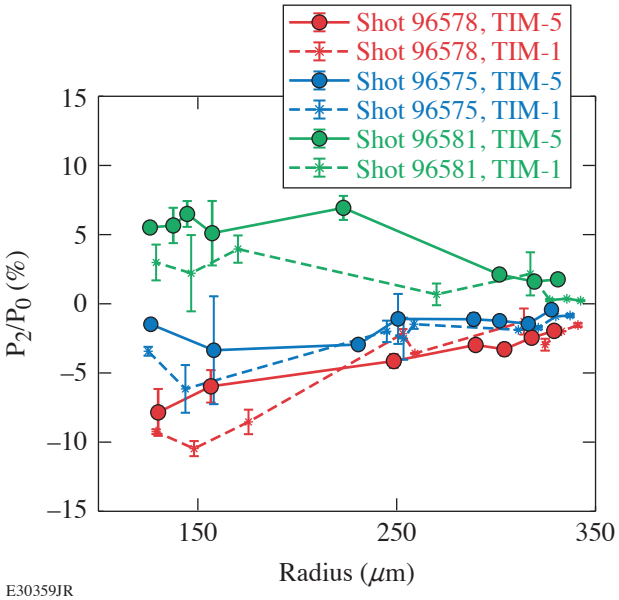

Figure 3
Comparisons of the temporal evolution of ℓ-mode 2 inferred from the shots 96578, 96575, and 96581 from the TIM-1 camera (star symbols, dashed lines) and the TIM-5 camera (circle symbols, solid lines).

Figure 4 shows that the extremum P_2 amplitude inferred from the TIM-1 and TIM-5 cameras varies linearly with the drive imbalance parameter ΔD. The dashed line represents a linear fit through all the data points. The slight vertical offset between the TIM-1 and the TIM-5 data set might indicate a systematic error in the data analysis. The P_2 amplitude is minimized for $\Delta D \sim 5\%$ and not as expected for $\Delta D = 0$. This might indicate that the energy coupling of non-normal laser rays in the equatorial region is over predicted in the current models. This trend also correlates with a 30% reduction in neutron yield (see Table I) for the shot with the largest ℓ-mode 2 amplitude. Future experiments will test the hypothesis of a minimal P_2 amplitude for a drive imbalance parameter of $\Delta D \sim 5\%$ for the current design and will perform similar experiments for designs with different shell adiabats. The observations of higher P_2 amplitudes in shot 96578 suggest that the shell asymmetry is higher when we increase the energies of the beams closer to the poles compared to the increase of the energies of the beams closer to the equator. This work will help to improve the understanding of the degradation mechanisms from the PDD beam geometry.

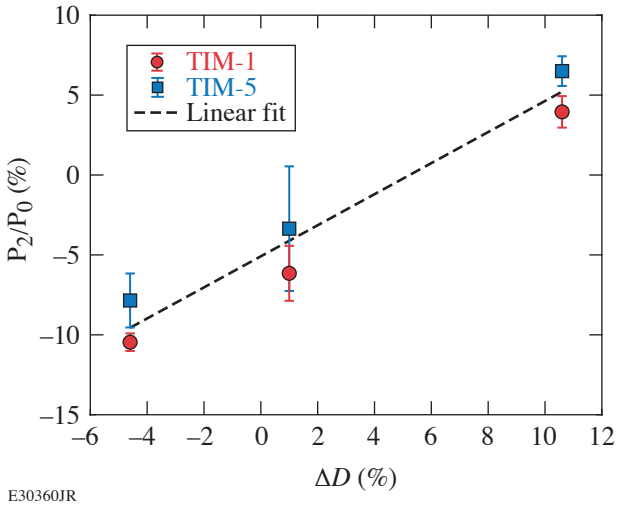

Figure 4
Inferred extremum P_2 amplitude versus drive imbalance parameter ΔD.

This material is based upon work supported by the Department of Energy National Nuclear Security Administration under Award Number DE-NA0003856, the University of Rochester, and the New York State Energy Research and Development Authority.

1. S. Skupsky *et al.*, Phys. Plasmas **11**, 2763 (2004).
2. R. S. Craxton *et al.*, Phys. Plasmas **12**, 056304 (2005).
3. F. Marshall *et al.*, J. Phys. IV France **133**, 153 (2006).
4. J. A. Marozas *et al.*, Phys. Plasmas **13**, 056311 (2006).
5. T. J. B. Collins *et al.*, Phys. Plasmas **19**, 056308 (2012).
6. P. B. Radha *et al.*, Phys. Plasmas **19**, 082704 (2012).
7. E. I. Moses, IEEE Trans. Plasma Sci. **38**, 684 (2010).
8. M. Hohenberger *et al.*, Phys. Plasmas **22**, 056308 (2015).
9. P. B. Radha *et al.*, Phys. Plasmas **23**, 056305 (2016).
10. T. R. Boehly *et al.*, Opt. Commun. **133**, 495 (1997).
11. V. Gopalaswamy *et al.*, Nature **565**, 581 (2019).
12. D. T. Michel *et al.*, Rev. Sci. Instrum. **83**, 10E530 (2012).
13. D. T. Michel *et al.*, Phys. Rev. Lett. **114**, 155002 (2015).
14. Y. Dong *et al.*, Plasma Sci. Technol. **22**, 084003 (2020).
15. P. B. Radha *et al.*, Phys. Plasmas **12**, 032702 (2005).
16. Y. Kato *et al.*, Phys. Rev. Lett. **53**, 1057 (1984).
17. T. J. Kessler *et al.*, Proc. SPIE **1870**, 95 (1993).
18. W. Theobald *et al.*, Phys. Plasmas **29**, 012705 (2022).

19. J. E. Rothenberg, J. Appl. Phys. **87**, 3654 (2000).
20. S. Skupsky *et al*., J. Appl. Phys. **66**, 3456 (1989).
21. *LLE Review Quarterly Report* **80**, 197 (1999).
22. S. P. Regan *et al*., J. Opt. Soc. Am. B **22**, 998 (2005).
23. A. K. Davis *et al*., Rev. Sci. Instrum. **87**, 11E340 (2016).
24. D. K. Bradley *et al*., Rev. Sci. Instrum. **63**, 4813 (1992).
25. D. K. Bradley *et al*., Rev. Sci. Instrum. **72**, 694 (2001).
26. D. H. Edgell *et al*., Fusion Science and Technology **49**, 616 (2006).

Quantitative Proton Radiography and Shadowgraphy for Arbitrary Intensities

J. R. Davies,[1] P. V. Heuer,[1] and A. F. A. Bott[2]

[1]Laboratory for Laser Energetics, University of Rochester
[2]Clarendon Laboratory, University of Oxford

Charged-particle radiography, most commonly with protons, and shadowgraphy are widely used in laser-plasma experiments to infer electric and magnetic fields and electron density, respectively. For many experiments of interest, intensity modulations due to absorption and scattering of the charged particles or photons can be neglected; therefore, intensity modulations are caused by deflections in the plasma. Deflection at the detector can then be expressed in terms of a path-integrated transverse Lorentz force for charged-particle radiography and a path-integrated transverse refractive index gradient for shadowgraphy. We will adopt the generic term deflectometry to describe both charged-particle radiography and shadowgraphy in the regime where intensity modulations are due principally to deflection.

A number of papers in plasma physics have used direct inversion of deflectometry data to obtain a path-integrated Lorentz force or refractive index gradient. These direct inversion algorithms find a minimum deflection solution where trajectories do not cross. Therefore, if trajectories did cross, the direct inversion may not reproduce the actual profiles. Direct inversion, however, does provide one possible solution to what is then a degenerate problem, subject to known constraints, which can be useful information. Most of these direct-inversion codes are publicly available.[1–5] These papers concentrate on proton radiography, with only one explicitly considering shadowgraphy,[1] and none considering the possibility of radiography with a relativistic particle, which is possible in laser-plasma experiments using electrons from a laser-plasma accelerator.

From a mathematical point of view, the direct-inversion problem was first formulated in a paper by Monge published in 1781,[6] and then in a modern mathematical manner by Kantorovich in 1942,[7] leading to the name Monge–Kantorovich problem or, more descriptively, the optimal transport problem. Monge and Kantorovich both considered finding the minimum cost for leveling a land area as an application of the theory. Kantorovich added "location of consumption stations with respect to production stations" as a second application of the theory. Since then, numerous applications have been found, of which direct inversion of deflectometry data by minimizing total deflection is perhaps the most recent.

The majority of the publicly available direct-inversion codes[3–5] solve the Monge–Ampère equation first derived by Monge and then stated in a more-general form by Ampère in 1819, although the numerical algorithm used in these codes was only published in 2011.[8] The Poisson equations considered by some authors,[1,2] and frequently mentioned in texts discussing shadowgraphy, can be considered special cases of the Monge–Ampère equation, valid in the limit of very small deflections.

If we consider the problem in terms of the data, then direct inversion comes down to determining the movement of counts in detector bins that map the source intensity I_0 (the signal on the detector in the absence of an object) to the measured intensity I, or vice versa. From this point of view, and from the perspective of a plasma physicist, it occurred to us that an algorithm based on an electrostatic plasma model should always be able to obtain a solution. The source or measured intensity can be treated as an initial electron distribution and the other intensity as a fixed ion distribution. Electrostatic forces will then cause the electron distribution to evolve to the ion distribution. The displacement of the electrons from their initial to their equilibrium positions will give the deflections at the detector. Oscillations about the desired equilibrium positions can be damped by applying drag to

the electrons. Electrostatic plus kinetic energy will decay steadily and go to zero in equilibrium since drag removes energy from the system, providing a simple convergence criterion.

The first scheme that occurred to us was an electrostatic particle-in-cell (PIC) code with the addition of electron drag; because this is a common type of code in plasma physics, efficient, robust algorithms exist, and it could make use of existing codes. We then considered a fluid code as a potentially faster, less memory-intensive alternative. A Lagrangian scheme, where the numerical grid moves with the fluid, provides the most direct method of determining the deflections. A Eulerian scheme, where the numerical grid is fixed, would require tracking the center of mass of the initial fluid elements in every cell, and so could require more calculations than a PIC code. Therefore, we also implemented a Lagrangian fluid scheme. We started with 1-D codes as a quick method to test the algorithms before writing 2-D codes.

To make a fair comparison of the electrostatic algorithm to the Sulman, Williams, and Russell algorithm for solving the Monge–Ampère equation,[3–5,8] we returned to the original *MATLAB* script of *PROBLEM*, which is not provided on GitHub, and added an inbuilt convergence criterion and an adaptive time step. We also compared our codes to the power-diagram algorithm,[1] which uses weighted Voronoi, or power diagrams of the intensities to determine the deflections at the detector.

Our codes output what we refer to as a dimensionless line-integrated transverse force. For charged-particle radiography,

$$\mathcal{F}_x = \frac{L}{Mw_x}\frac{q}{p\overline{v}}\int E_x - vB_y \mathrm{d}z, \quad \mathcal{F}_y = \frac{L}{Mw_y}\frac{q}{p\overline{v}}\int E_y - vB_x \mathrm{d}z,$$

which is valid for a relativistic particle. For shadowgraphy,

$$\mathcal{F}_x = \frac{L}{Mw_x}\frac{1}{2}\int \frac{\partial n'_\mathrm{e}/\partial x}{1-n'_\mathrm{e}}\mathrm{d}z, \quad \mathcal{F}_y = \frac{L}{Mw_\mathrm{y}}\frac{1}{2}\int \frac{\partial n'_\mathrm{e}/\partial y}{1-n'_\mathrm{e}}\mathrm{d}z,$$

where L is the object-to-detector distance, M is magnification, w is the detector pixel width in the object plane, q is the charge, p is momentum, v is velocity, z is the probing axis, and $n'_\mathrm{e} = n_\mathrm{e}/n_\mathrm{c}$, where n_e is electron density and n_c is critical density for the shadowgraphy probe.

Our codes are written in *MATLAB* and are publicly available.[9] Python versions of the 2-D PIC code and the Monge–Ampère code are under development.[10]

To test the codes, we used synthetic radiographs that we had generated previously by proton tracing in specified radial forces in cylindrical and spherical geometry for a range of profiles and amplitudes,[11] which are publicly available as hdf5 files in prad-format.[12] The force is expressed as a dimensionless parameter μ

$$\mu = \frac{2LF}{Mpv}, \quad \mu = -\frac{L}{M}\frac{\mathrm{d}n'_\mathrm{e}/\mathrm{d}r}{1-n'_\mathrm{e}}$$

for charged-particle radiography and shadowgraphy, respectively. Results for cylindrical Gaussian potentials with $\mu_\mathrm{max} = 0.5$ (defocusing) and –0.25 (focusing), values where trajectories do not cross, are shown in Fig. 1. All of our codes accurately reproduced the measured intensity and the line-integrated transverse force to within the noise level of the original intensity. We carried out an extensive range of tests intended to push the limits of the codes.

Only the PIC code obtained a solution for every case. The 2-D Lagrangian code failed for large-intensity modulations, but was faster than the 2-D PIC code without massively parallel processing, which would be possible with a PIC code. The Monge–Ampère code was considerably faster than the electrostatic codes in 2-D without massively parallel processing, but failed for intensities with extensive regions of zero signal, high contrast ratios, or large deflections across the boundaries, and could not obtain the

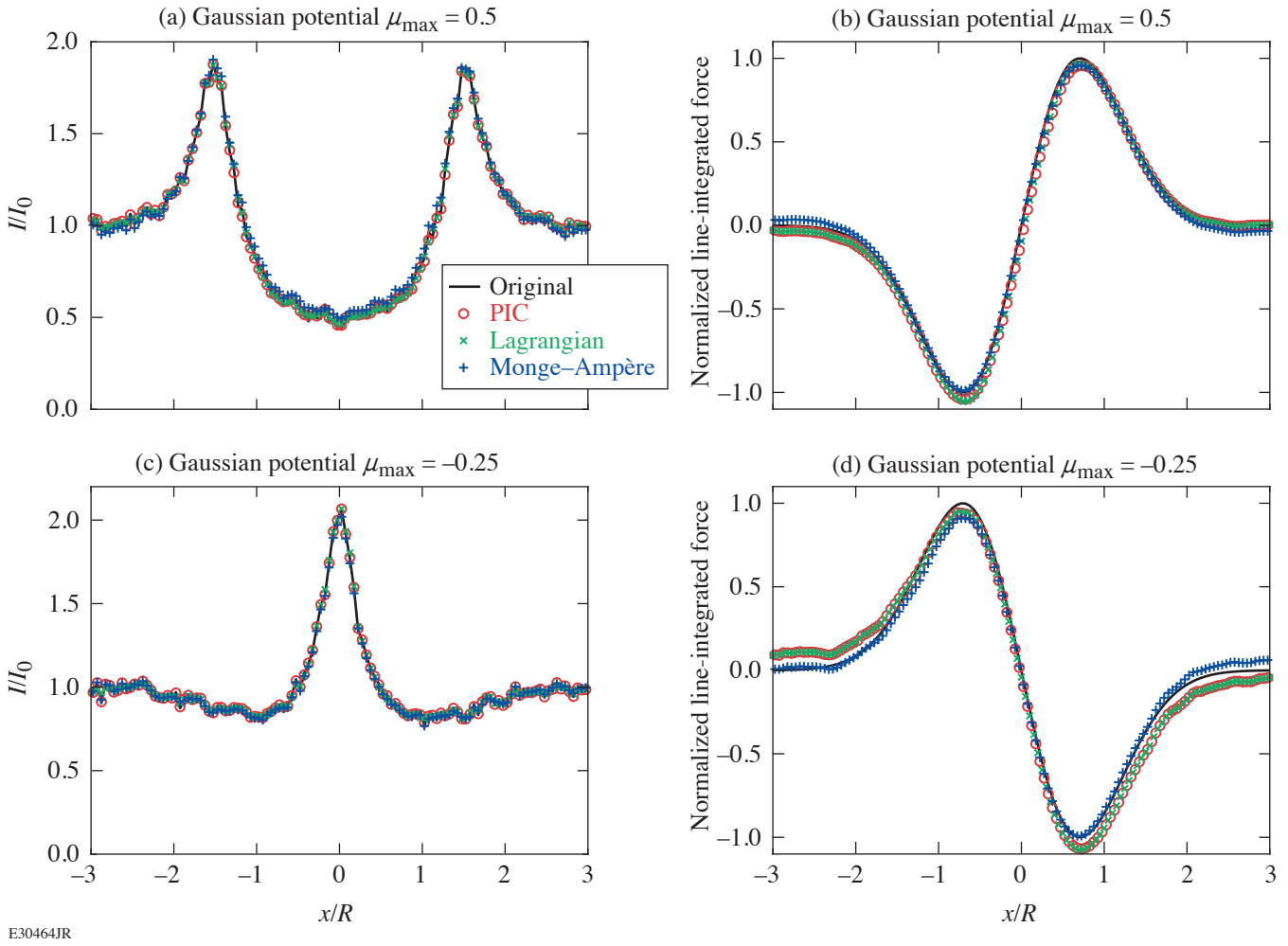

Figure 1
Results for a cylindrical Gaussian potential [(a),(c)] intensity profiles and [(b),(d)] line-integrated transverse force normalized so that the maximum of the original is 1 for μ_{max} = 0.5 and –0.25, respectively.

same degree of convergence to the measured intensity as the electrostatic codes. The power-diagram code was by far the slowest and failed for large peaks in the intensity. In 1-D, however, the Lagrangian code was the fastest and always obtained a solution.

Our final recommendations are to use the Monge–Ampère code to take a quick first look at data, and to use the PIC code if the Monge–Ampère code fails or a more-accurate inversion is desired. In the rare case of 1-D problems, the Lagrangian code is the best option.

This material is based upon work supported by the Department of Energy, under Award Number DE-SC0020431, by the Department of Energy National Nuclear Security Administration under Award Number DE-NA0003856, the University of Rochester, and the New York State Energy Research and Development Authority.

1. M. F. Kasim *et al.*, Phys. Rev. E **95**, 023306 (2017).
2. C. Graziani *et al.*, Rev. Sci. Instrum. **88**, 123507 (2017); PRaLine Code (Proton Radiography Linear Reconstruction, the "reconstruction" is silent), Accessed 03 March 2023, https://github.com/flash-center/PRaLine.

3. M. F. Kasim, Invert Shadowgraphy and Proton Radiography, Accessed 03 March 2023, https://github.com/mfkasim1/invert-shadowgraphy.
4. A. F. A. Bott *et al.*, J. Plasma Phys. **83**, 905830614 (2017); PROBLEM Solver (PROton-imaged B-field nonLinear Extraction Module), Accessed 03 March 2023, https://github.com/flash-center/PROBLEM.
5. M. F. Kasim *et al.*, Phys. Rev. E **100**, 033208 (2019); M. F. Kasim, PRNS (Proton Radiography with No Source), Accessed 03 March 2023, https://github.com/OxfordHED/proton-radiography-no-source.
6. G. Monge, Mém. de l'Ac. R. des. Sc. An. **1**, 666 (1781).
7. L. Kantorovitch, Manage. Sci. **5**, 1 (1958).
8. M. M. Sulman, J. F. Williams, and R. D. Russell, Appl. Numer. Math. **61**, 298 (2011).
9. J. R. Davies, A 1-D Electrostatic PIC Code for Direct Inversion of Deflectometry Data (Version 2), Zenodo, Accessed 7 March 2023, http://doi.org/10.5281/zenodo.6638904; J. R. Davies, A 2-D Electrostatic PIC Code for Direct Inversion of Deflectometry Data (Version 1), Zenodo, Accessed 7 March 2023, http://doi.org/10.5281/zenodo.6638812; J. R. Davies, A 1-D Electrostatic, Lagrangian Two-Fluid Code for the Direct Inversion of Deflectometry Data (Version 1), Zenodo, Accessed 7 March 2023, http://doi.org/10.5281/zenodo.6638911; J. R. Davies, A 2-D Electrostatic Lagrangian Two-Fluid Code for the Direct Inversion of Deflectometry Data (Version 1), Zenodo, Accessed 7 March 2023, https://doi.org/10.5281/zenodo.6638929; J. R. Davies and A. F. A. Bott, A Matlab Function to Solve the Monge–Ampere Equation Using the Sulman, Williams and Russell Algorithm (Version 1), Zenodo, Accessed 7 March 2023, (https://doi.org/10.5281/zenodo.6685314.
10. P. Heuer, InvertDeflectPy: A Collection of Algorithms for Inverting Deflectometry Data, Accessed 7 March 2023, https://github.com/pheuer/InvertDeflectPy.
11. J. Davies and P. Heuer, Synthetic Proton Radiographs for Testing Direct Inversion Algorithms, Zenodo, Accessed 7 March 2023, https://doi.org/10.5281/zenodo.6632986.
12. P. Feister, Pradformat (Particle Radiography File Format Tools)-MATLAB Package, Accessed 7 March 2023, https://github.com/sfeister/pradformat/blob/f9b95d1d87f26d01e59ab7f145d414e7043fe488/MATLAB/README.md.

Direct Measurement of the Return-Current Instability

A. L. Milder,[1,2,3] J. Zielinski,[3] J. Katz,[1] W. Rozmus,[3] D. H. Edgell,[1] A. M. Hansen,[1] M. Sherlock,[4] C. Bruulsema,[3] J. P. Palastro,[1] D. Turnbull,[1] and D. H. Frolua[1,2]

[1]Laboratory for Laser Energetics, University of Rochester
[2]Department of Physics and Astronomy, University of Rochester
[3]Department of Physics, University of Alberta
[4]Lawrence Livermore National Laboratory

Measurements were made of the return-current instability growth rate, demonstrating its concurrence with nonlocal transport. Thomson scattering was used to measure a maximum growth rate of 5.1×10^9 Hz, which was 3× less than classical Spitzer–Härm theory predicts. The measured plasma conditions indicate the heat flux was nonlocal and Vlasov–Fokker–Planck (VFP) simulations that account for nonlocality reproduce the measured growth rates. Furthermore, the threshold for the return-current instability was measured ($\delta_T = 0.017 \pm 0.002$) to be in good agreement with previous theoretical models.

Significant progress has been made in understanding laboratory and astrophysical plasmas through the use of fluid approximations,[1] but recently an increasing amount of work has been dedicated to understanding the kinetic effects and how the microscale physics impacts the larger macroscopic systems. In particular, kinetic effects associated with nonlocal transport have impacted the interpretation of inertial confinement fusion implosions, laboratory astrophysics, and high-energy-density experiments. Understanding transport and transport-driven instabilities often starts with the classical theories of Spitzer and Härm[2] or Braginskii.[3] Historically, challenges in accounting for kinetic effects, particularly in heat transport, have been addressed with *ad hoc* corrections to the Spitzer–Härm theory in order to match experimental observables.

In a plasma, heat-carrying electrons travel down the temperature gradient (q_{flux}), generating a neutralizing return current (j_{return}) consisting of slower counter-propagating electrons. When the return current is large enough to shift the peak of the electron distribution function beyond the phase velocity of the ion-acoustic waves, the slope of the distribution function becomes inverted and the electrons transfer energy to the waves (inverse Landau damping). These transport-driven waves become absolutely unstable when the inverse Landau damping rate exceeds the ion damping rate.[1] This return-current instability (RCI) is predicted to drive a broad turbulent spectrum of ion-acoustic waves that limit the return current, inhibit heat transport,[4,5] modify laser absorption,[6,7] and alter the fluctuation spectrum from which other ion instabilities grow.[8–10] Previous experimental work has shown anomalous absorption linked to ion turbulence[6] and evidence of reduced heat flux.[5]

In this summary, we present the first measurements of the threshold and linear growth rate of the return-current instability driven by electron heat flux. The thorough characterization of the plasma conditions show that the return-current instability occurs concurrently with nonlocal transport. Thomson scattering was used to measure a maximum RCI growth rate of 5.1×10^9 Hz, which was 3× less than classical Spitzer–Härm theory predicts, but the RCI threshold was measured ($\delta_T = 0.017 \pm 0.002$) to be in good agreement with previous theoretical models.[4,9] Measured plasma conditions indicate that the heat flux was nonlocal and electron velocity distribution functions from VFP simulations, which treat this nonlocality kinetically, reproduce the measured growth rates. These experiments provide a thorough description of the plasma conditions and the associated return-current instability, which enabled detailed comparison with theory and simulations and can now be used to better understand the impact of return-current instability in laboratory and astrophysical plasmas.

A supersonic Mach-3 gas jet with an exit diameter of 2 mm produced an argon gas plume. Eleven 351-nm ultraviolet beams of the OMEGA Laser System were focused 2 mm above the nozzle to heat the plasma. Each beam delivered 200 J in a 1-ns duration full-width at half-maximum (FWHM) flattop pulse. The beams used distributed phase plates, polarization smoothing, and smoothing by spectral dispersion and achieved a peak overlapped intensity of $I_{\text{total}} = 1.1 \times 10^{15}$ W/cm^2.

The overlapped beams produced a hot region of plasma surrounded by a colder region. The overlapped intensity profile created an electron temperature gradient that drove "fast" electrons from the hot region to the cold region. The Thomson-scattered light was collected from various radial locations in the plasma by moving the heater beams and gas jet. The configuration maintained the probed ion-acoustic wave vector parallel to the direction of the heat flux. A distributed phase plate was used on the Thomson-scattering probe beam ($\lambda_0 = 526.5$ nm) to produce a 200-μm FWHM flattop focal spot. This beam was used with ~4 J in a 300-ps FWHM flattop pulse ($I_{2\omega} = 4.2 \times 10^{13}$ W/cm^2) delayed 700 ps from the start of the heater beams to measure spatially resolved Thomson scattering or with ~5 J in a 2-ns FWHM flattop pulse, co-timed with the beginning of the heating beams, and a 100-μm phase plate ($I_{2\omega} = 3.2 \times 10^{13}$ W/cm^2) to measure temporally resolved Thomson scattering. The Thomson-scattering diagnostic, both temporally and spatially resolved, collects light with a 60° scattering angle.

Figure 1 shows the measured temporally resolved ion-acoustic wave amplitudes while the plasma conditions were quasi-stationary (500 to 1000 ps). At 475 μm [Fig. 1(a)], the ion-acoustic wave grows as a function of time consistent with the return-current instability. This is further supported by comparison with growth-rate calculations from the Spitzer–Härm theory and from VFP simulations. The growth rate in the Spitzer–Härm theory was found to be significantly larger than observed in the plasma, which is attributed to the nonlocality of the heat transport. VFP simulations, which include these effects kinetically, show excellent agreement with the data. At a radius of 200 μm [Fig. 1(b)], the ion-acoustic wave decays as a function of time, indicating that the plasma was stable to the return-current instability. The ion-acoustic wave was driven above the thermal fluctuation level at early time, likely by transient RCI or ponderomotive and thermal effects as the plasma was being formed.

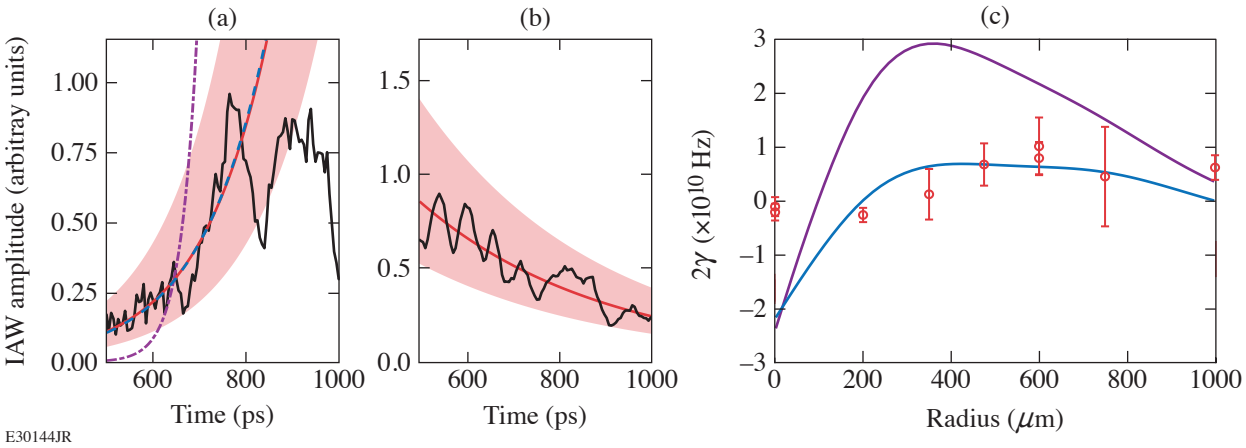

Figure 1
The ion-acoustic wave amplitude (black curves) at a radius of (a) 475 μm and (b) 200 μm are matched with an exponential model (red curves) with a shaded 90% confidence interval. (a) Exponential models with growth rates from the Spitzer–Härm theory (purple curve) and VFP simulations (blue curve) are compared to the data. (c) Measured growth rates (red) are compared to growth rates from the Spitzer–Härm theory (purple curve) and VFP simulations (blue curve) as a function of the radius.

Figure 1(c) compares the ion-acoustic growth rates from simulation and experiment as a function of space. As with the case at 475 μm, the Spitzer–Härm theory overpredicts the growth rate at all spatial locations. Nonlocal transport, included in VFP, was needed to match the measured growth rates. Experiment and simulation showed the return-current instability occurred over a large spatial extent from ~300 to 1000 μm but is maximized around 600 μm where the temperature gradient is large. This association with the temperature gradient helps identify this instability as a transport-driven instability. Simulations predicted the instability

threshold was crossed around 200 μm, while experimental data show the threshold between 200 μm and 350 μm. VFP simulations were performed with the code K2 (Ref. 11) and the resulting distribution functions were used to determine the growth rate.

Calculating the Knudsen number as a function of radius indicates that the return-current instability has a threshold of $\delta_T = 0.017 \pm 0.002$. The Knudsen number is within this range between $r = 200$ μm and $r = 350$ μm where the threshold was noted in Fig. 1(c). The Knudsen number (δ_T) is the scale parameter for the heat-flux distribution function perturbation, and therefore the return-current instability. An analytical threshold for the instability from Tikhonchuk *et al.*[5] is a reliable estimate for the return-current instability threshold. The threshold for the instability is also very close to the threshold for thermal transport nonlocality given by $\delta_T > 0.06/\sqrt{Z}$ (Ref. 12), i.e., RCI will occur where the transport relations are nonlocal.

Heat transport is a ubiquitous process in plasma physics that is impacted by nonlocality and the instabilities it causes. This work has demonstrated the need to account for this nonlocality in the calculation of growth rates for instabilities involving ion-acoustic waves, such as the return-current instability, and to account for the return-current instability under conditions of nonlocal transport. Large spatial extents have been found for both the nonlocal transport and the return-current instability. This can result in changes to instabilities and plasma conditions at a significant distance from the most unstable region. The threshold for the return-current instability was found and is in good agreement with a simple temperature- and density-based model that can be used predictively in future work.

This material is based upon work supported by the Department of Energy National Nuclear Security Administration under Award Number DE-NA0003856, the Office of Fusion Energy Sciences under Award Number DE-SC0016253, the University of Rochester, and the New York State Energy Research and Development Authority. The work of M. Sherlock was performed under the auspices of the U.S. Department of Energy by Lawrence Livermore National Laboratory under Contract DE-AC52-07NA27344.

1. D. W. Forslund, J. Geophys. Res., Space Phys. **75**, 17 (1970).
2. L. Spitzer, Jr. and R. Härm, Phys. Rev. **89**, 977 (1953).
3. S. I. Braginskii, in *Reviews of Plasma Physics*, edited by M. A. Leontovich (Consultants Bureau, New York, 1965), Vol. 1, pp. 205–311.
4. V. T. Tikhonchuk *et al.*, Phys. Plasmas **2**, 4169 (1995).
5. D. R. Gray and J. D. Kilkenny, Plasma Phys. **22**, 81 (1980).
6. S. H. Glenzer *et al.*, Phys. Rev. Lett. **88**, 235002 (2002).
7. W. M. Manheimer, D. G. Colombant, and B. H. Ripin, Phys. Rev. Lett. **38**, 1135 (1977).
8. W. Rozmus *et al.*, Plasma Phys. Control. Fusion **60**, 014004 (2018).
9. A. V. Brantov, V. Yu. Bychenkov, and W. Rozmus, Phys. Plasmas **8**, 3558 (2001).
10. J. D. Moody *et al.*, Phys. Plasmas **7**, 2114 (2000).
11. M. Sherlock, J. P. Brodrick, and C. P. Ridgers, Phys. Plasmas **24**, 082706 (2017).
12. V. Yu. Bychenkov *et al.*, Phys. Rev. Lett. **75**, 4405 (1995).

Analysis Methods for Electron Radiography Based on Laser-Plasma Accelerators

G. Bruhaug,[1,2] M. S. Freeman,[3] H. G. Rinderknecht,[1] L. P. Neukirch,[3] C. H. Wilde,[3] F. E Merrill,[3] J. R. Rygg,[1,2,4] M. S. Wei,[1] G. W. Collins,[1,2,4] and J. L. Shaw[1]

[1]Laboratory for Laser Energetics, University of Rochester
[2]Department of Mechanical Engineering, University of Rochester
[3]Los Alamos National Laboratory
[4]Department of Physics and Astronomy, University of Rochester

Electron radiography (eRad) is a proven, highly penetrative radiography technique that has typically been performed with traditional linear accelerators (LINAC's).[1,2] Recent work has extended electron radiography techniques into the laser-plasma acceleration (LPA) regime[3,4] with an emphasis on the radiography of laser-driven dynamics systems.

To compare LPA eRad to traditional LINAC eRad and other radiography methods, the resolution and transmission of said source must be determined. In addition, LPA-based eRad can modify the properties of the object being radiographed via a laser-generated plasma if the drive laser is not dumped.[4] Here we present analysis methods to determine the resolution for LPA eRad that include accounting for image distortion caused by the drive laser.

A polychromatic electron beam generated via LPA with an average energy of ~20 MeV and a bunch charge of up to 700 nC was used to radiograph various test objects in both contact and projection radiography.[4,5] All radiographs were taken using MS (multipurpose standard) image plates with 12.5 μm of aluminium in front to dump the laser. MeV-scale electrons have been found to have a relatively flat energy response in image plates and are detected at high efficiency.[6] All images were then analyzed via the software ImageJ[7] and the final scans were gray-scale balanced to make the clearest images.

It should be noted that the majority of the LPA drive laser is transmitted through the LPA plasma source. In the projected configuration the laser impacts the front face of the projection radiography object with ~10^{15} W/cm^2 intensity and ~20 to 100 J of laser energy depending on drive specifics. This excess laser energy will impact the target ~100 fs before the electron beam arrives and will generate plasma on the front surface of the object.[4] Consequently, even these supposedly "static" radiography objects were, in reality, laser-ablated dynamic radiography objects.

Contact radiography provided the ability to remove the transverse structure of the electron beam using the image plate placed in front of the radiography object to record the beam transverse structure before the beam passes through the radiography object. Transverse structure from the beam adds additional blurring to the radiograph that can be eliminated via image division using the software ImageJ.[7] Using these adjusted images, image resolution was determined by creating a box lineout tens of pixels wide across the edges generated by the thickness steps in the radiography object [see Fig. 1(a)] and across the edges of the holes in each thickness step. An error function of the form shown in Eq. (1) was then fitted to the lineout as shown in Fig. 1(b).

$$y = a + b\,\mathrm{erf}\left(\frac{x-c}{d}\right). \tag{1}$$

Variables a, b, c, and d are fitting parameters for the error function with d giving the resolution. This procedure was repeated across all edges of holes, all edges of the object, and all thickness steps on the object. The results were then averaged for each thickness of material to produce a final resolution at each thickness of material.

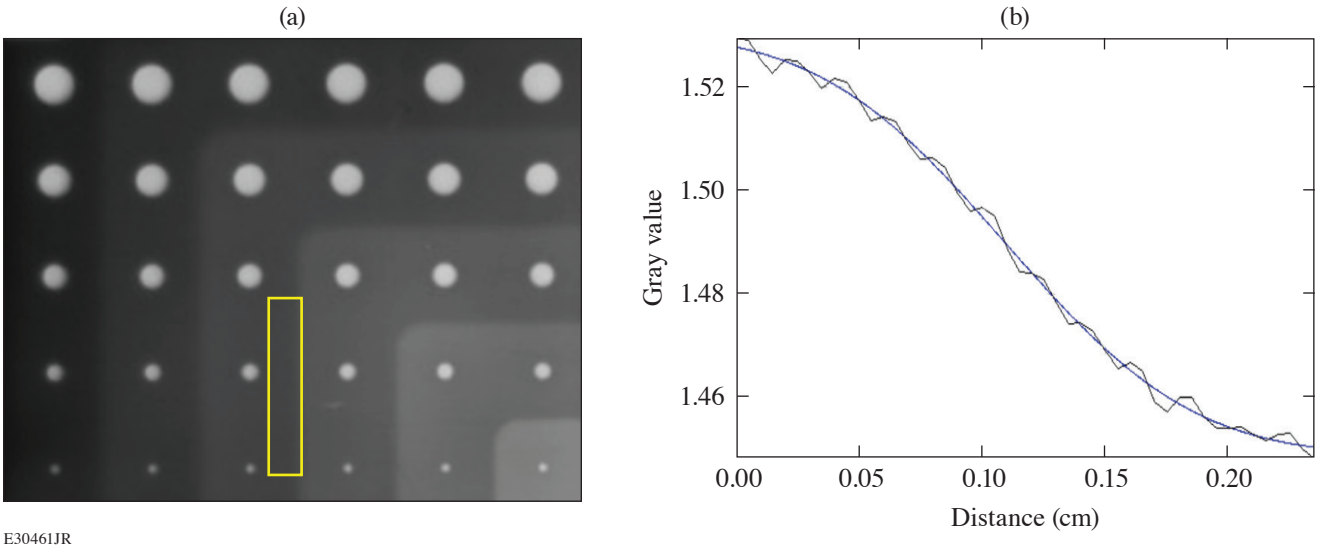

Figure 1
(a) Example of a resolution measurement across thickness step edge for tungsten contact radiography object. The yellow box across the thickness step edge shows the outline of the data used to make the measurement. (b) Lineout of boxed region from (a) (black curve) and error function fit (blue curve).

To determine the resolution in projection radiography, the final image plate scan is taken and gray scale is balanced for maximum clarity. Box lineouts tens of pixels wide are then taken across the central step in object thickness as well as the object outer edges and hole edges. An error function is fitted to the lineouts and the resolution taken from that function is shown in Fig. 2. These measurements are performed multiple times around the resolution measurement point of interest (i.e., an edge or a step-in material thickness) and then averaged to determine a final value.

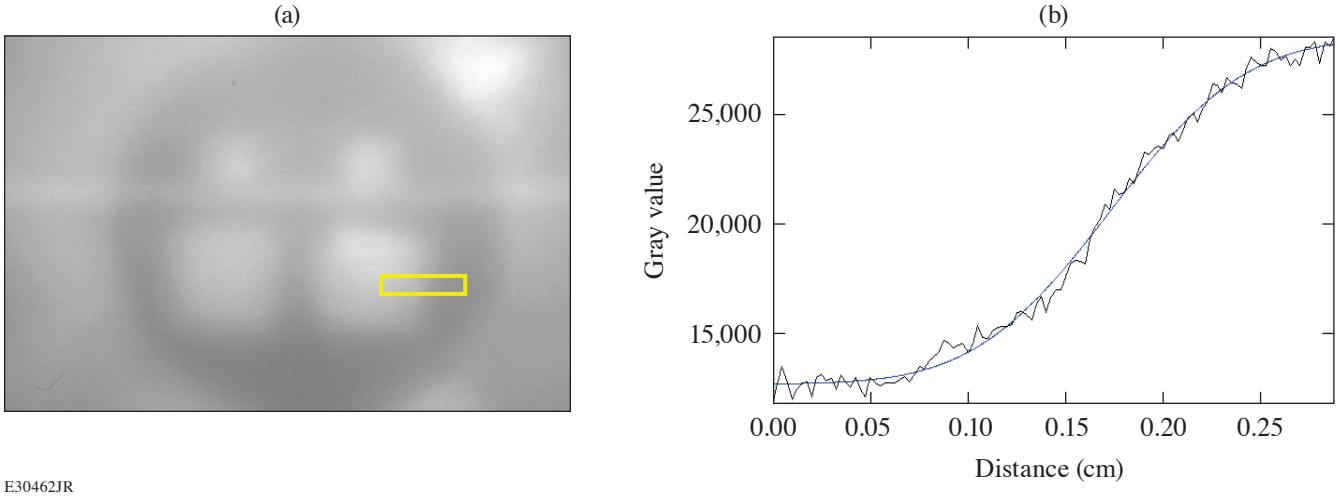

Figure 2
(a) Example of a resolution measurement across a hole for tungsten projection radiography object. The yellow box across the thickness step edge shows the outline of the data used to make the measurement. (b) Lineout of boxed region from (a) (black curve) and error function fit (blue curve).

Plasma-generated electric fields in laser-ablated targets can be roughly measured by measuring the size of features in the eRad image and estimating the field strength needed to produce those features. When measuring the sizes of the static projection radiography objects, it was noticed that the resulting radiographs were ∼1.5× smaller than expected, as illustrated in Fig. 3. Previous data suggest that this size discrepancy was caused by plasma-generated electric fields acting like an electrostatic lens on the electron beam.[8] Using the average electron beam energy of ∼20 MeV (Ref. 5), it was determined that the electric field that corresponded to ∼1 GV/m (Ref. 4) would generate the magnification discrepancies seen. This is well in line with previous laser-plasma electric-field strengths at this laser intensity.[8]

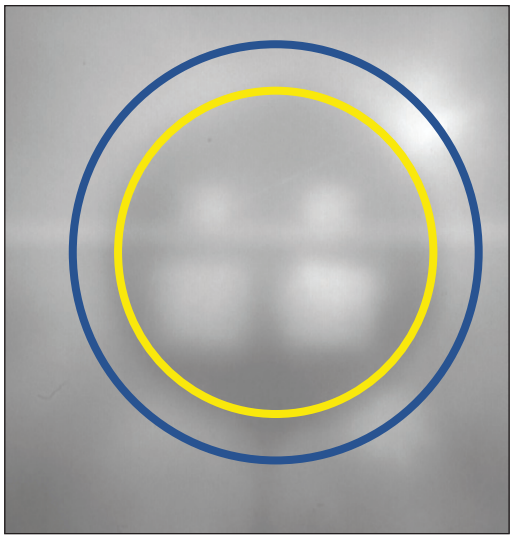

E30463JR

Figure 3
Projected radiograph of tungsten radiography object showing the size discrepancy caused by the plasma electric field focusing of the electron beam. The blue outline shows the expected image size of ∼1.8 cm if there was no plasma focusing, and the yellow circle shows the measured diameter of ∼1.2 cm.

This material is based upon work supported by the Department of Energy National Nuclear Security Administration under Award Number DE-NA0003856, the U.S. Department of Energy under Awards DE-SC00215057, the University of Rochester, and the New York State Energy Research and Development Authority.

1. F. Merrill *et al.*, Nucl. Instrum. Methods Phys. Res. B **261**, 382 (2007).
2. F. E. Merrill *et al.*, Appl. Phys. Lett. **112**, 144103 (2018).
3. W. Schumaker *et al.*, Phys. Rev. Lett. **110**, 015003 (2013).
4. G. Bruhaug *et al.*, Sci. Rep. **13**, 2227 (2023).
5. J. L. Shaw *et al.*, Sci. Rep. **11**, 7498 (2021).
6. G. Boutoux *et al.*, Rev. Sci. Instrum. **86**, 113304 (2015).
7. C. A. Schneider, W. S. Rasband, and K.W. Eliceiri, Nat. Methods **9**, 671 (2012).
8. J. L. Dubois *et al.*, Phys. Rev. E **89**, 013102 (2014).

A First-Principles Study of L-Shell Iron and Chromium Opacity at Stellar Interior Temperatures

V. V. Karasiev,[1] S. X. Hu,[1] N. R. Shaffer,[1] and G. Miloshevsky[2]

[1]Laboratory for Laser Energetics, University of Rochester
[2]Department of Mechanical and Nuclear Engineering, Virginia Commonwealth University

Accurate prediction of optical properties of matter across a wide range of material densities and temperatures is of great importance in planetary science, astrophysics, and inertial confinement fusion.[1–4] Building a reliable opacity model for materials under extreme conditions is one of the grand challenges in high-energy-density physics, especially across the most complicated warm-dense-matter (WDM) domain of thermodynamic conditions when both the coulomb coupling parameter and the electron degeneracy are close to unity. The traditional opacity models based on physics of isolated atoms when the important plasma density and temperature effects such as Stark broadening, ionization potential depression (IPD), and continuum lowering are incorporated via corrections often become unreliable beyond the ideal plasma conditions.

In this work we use a first-principles density functional theory (DFT)-based methodology to calculate optical properties (mass-absorption coefficient and opacity) of Cr and Fe at stellar interior temperatures corresponding to recent experiments.[5,6] The purpose is to explore whether or not such *ab initio* calculations can resolve the reported disagreement between previous atomic physics calculations and measured data.[5,6] Our DFT results are compared to the real-space Green's function (RSGF) method[7–9] and to the radiative emissivity and opacity of dense plasmas (REODP) atomistic model.[10]

A free-energy DFT-based methodology for optical property calculations in the WDM domain presented in Ref. 11 handles deeply bounded core electrons on an equal footing with free electrons in the system and self-consistently takes into account effects such as quasistatic pressure broadening due to interaction with neighboring ions [in case of calculations on molecular dynamics (MD) multi-ion supercell snapshots], the IPD, continuum lowering, and Fermi surface rising. The methodology incorporates a combination of the Kubo–Greenwood (KG) optical data, evaluated on a set of the *ab initio* molecular dynamics (AIMD) snapshots, with a periodic single-atom-in-a-cell calculation at the same thermodynamic conditions. KG calculations on snapshots account for the influence of the local plasma environment, which is important for photon energies near the L and K edges. Kubo–Greenwood data from periodic calculations with single atom cover the tail regions beyond the L and K edges.

The Kubo–Greenwood formulation implemented in the post-processing code *KGEC* (Kubo–Greenwood electronic conductivity) for use with the *Quantum-Espresso* large-scale DFT-based simulation package, *KGEC@Quantum-Espresso*,[12,13] calculates the frequency-dependent real and imaginary parts of electric conductivity, $\sigma_1(\omega)$ and $\sigma_2(\omega)$; the real part of the index of refraction, $n(\omega)$; the absorption coefficient, $\alpha(\omega) = \sigma_1(\omega)\,[4\pi/n(\omega)c]$; and the mass-absorption coefficient $\alpha m(\omega) = \alpha(\omega)/\rho$ (where c is the speed of light, ρ is the material density, and the photon energy is $\hbar\omega = h\nu$). The optical properties were calculated for a single-atom-in-a-cell and as an average over a selected set of uncorrelated two-atom MD snapshots. Eventually the grouped Rosseland mean opacities for a narrow 4-eV group of photon energies are calculated.

In this study we are focused on the L-shell absorption and opacity calculations at temperatures when the deep 1*s* bands remain fully populated. Therefore, 1*s* frozen-core projector augmented wave (PAW) data sets for Fe and Cr are generated using the *ATOMPAW* code.[14] A small augmentation sphere radius $r_{\mathrm{PAW}} = 0.35$ bohr requires a relatively high cutoff energy of $E_{\mathrm{cut}} = 800$ Ry to converge electronic pressure. The optical properties are calculated using the Kubo–Greenwood formulation implemented within

the PAW formalism in *KGEC@Quantum-Espresso*[12,13,15] packages. The Gaussian broadening was done with relatively large δ = 15 eV due to the sparsity of states in the case of the single-atom-in-a-cell calculations.

Table I shows free-electron densities of chromium and iron calculated at T = 182 eV and ρ = 0.161 g/cm^3 and 0.165 g/cm^3, respectively. Theoretical predictions by all three methods are in very good agreement; relative differences of the REODP and RSGF values with respect to the DFT data do not exceed 2% and 4%, respectively, matching the experimental value of 3 × 10^{22} cm^{-3} from measurements for Cr and Fe.

Table I: Free-electron density (in cm^{-3} units) for chromium and iron at T = 182 eV and ρ_{Cr} = 0.161 g/cm^3, ρ_{Fe} = 0.165, respectively, as predicted by the DFT, REODP, and RSGF methods.

System	DFT	REODPe	RSGF
Cr	3.00 × 10^{22}	2.95 × 10^{22}	3.12 × 10^{22}
Fe	3.00 × 10^{22}	2.95 × 10^{22}	3.12 × 10^{22}

Figure 1 shows our main results for opacity of chromium and iron calculated at T = 182 eV and material density of 0.161 g/cm^3 and 0.165 g/cm^3, respectively, alongside with experimental measurements. At short wavelengths below ~9.5 A [the L-shell bound-continuum region for photon energies above ~1.2 keV], the agreement between all three theoretical data and experiments is very good for chromium: the REODP curve goes straight through the experimental data, while the DFT and RSGF data are located slightly below, touching the yellow-shaded experimental error bars. The situation for iron is different; opacity predicted by theoretical methods in the L-shell bound-continuum region is underestimated by about 50% as compared to the experimental data. The REODP curve is slightly closer to the experimental data as compared to the DFT single-atom-in-a-cell and RSGF simulations.

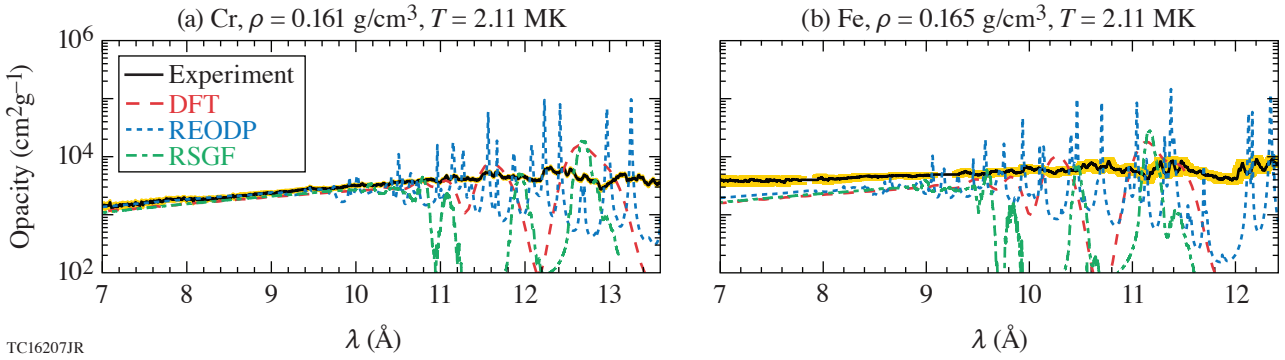

Figure 1
Opacity of iron and chromium at 0.165 g/cm^3 and 0.165 g/cm^3, respectively. A comparison is made between the experimental measurements (solid black curve, the yellow-shaded area corresponds to the experimental measurements error) and three theoretical predictions at T = 182 eV.

In the wavelength range above 9.5 A, opacity is dominated mostly by the bound–bound absorption lines. The DFT and RSGF calculations predict a small set of smooth and strong discrete lines separated by deep windows. The REODP method predicts a richer spectrum of sharp peaks. The REODP-calculated opacities represent the detailed all-line spectra without any kind of averaging into spectral groups. The peaks and wings of the lines are resolved with a high accuracy. The spectral lines are roughly centered on the experimental opacity curves. However, none of our theoretical predictions is close to the measured bound–bound opacity in that range. The DFT predictions for the bound–bound absorption can be improved by performing the Kubo–Greenwood optical calculations on top of the AIMD snapshots for larger supercells including more than two atoms by considering more-realistic charge-state distributions. However, such demanded calculations, on both memory and time, are currently out of reach.

This material is based upon work supported by the Department of Energy National Nuclear Security Administration under Award Number DE-NA0003856, U.S. National Science Foundation PHY Grants No. 1802964 and No. 2205521, Defense Threat

Reduction Agency under Grants No. HDTRA1-19-1-0019 and HDTRA1-20-2-0001, the University of Rochester, and the New York State Energy Research and Development Authority. This research used resources of the National Energy Research Scientific Computing Center, a DOE Office of Science User Facility supported by the Office of Science of the U.S. Department of Energy under Contract No. DE-AC02-05CH11231 using NERSC award FES-ERCAP0021234.

1. J. J. Fortney and N. Nettelmann, Space Sci. Rev. **152**, 423 (2010).
2. C. A. Iglesias, F. J. Rogers, and D. Saumon, Astrophys. J. Lett. **569**, L111 (2002).
3. S. X. Hu *et al.*, Phys. Rev. E **90**, 033111 (2014).
4. S. X. Hu *et al.*, Phys. Plasmas **22**, 056304 (2015).
5. J. E. Bailey *et al.*, Nature **517**, 56 (2015).
6. T. Nagayama *et al.*, Phys. Rev. Lett. **122**, 235001 (2019).
7. J. J. Rehr and R. C. Albers, Rev. Mod. Phys. **72**, 621 (2000).
8. Y. Wang *et al.*, Phys. Rev. Lett. **75**, 2867 (1995).
9. N. Shaffer and C. E. Starrett, Phys. Rev. E **150**, 015203 (2022).
10. G. Miloshevsky and A. Hassanein, Phys. Rev. E **92**, 033109 (2015).
11. V. V Karasiev and S. X. Hu, Phys. Rev. E **103**, 033202 (2021).
12. L. Calderín, V. V. Karasiev, and S. B. Trickey, Comput. Phys. Commun. **221**, 118 (2017).
13. P. Giannozzi *et al.*, J. Phys.: Condens. Matter **21**, 395502 (2009).
14. N. A. W. Holzwarth, A. R. Tackett, and G. E. Matthews, Comp. Phys. Commun. **135**, 329 (2001).
15. V. V. Karasiev, T. Sjostrom, and S. B. Trickey, Comput. Phys. Commun. **185**, 3240 (2014).

High-Resolution X-Ray Spectrometer for X-Ray Absorption Fine Structure Spectroscopy

D. A. Chin,[1,2] P. M. Nilson,[2] D. Mastrosimone,[2] D. Guy,[2] J. J. Ruby,[3] D. T. Bishel,[1,2] J. F. Seely,[4] F. Coppari,[3] Y. Ping,[3] J. R. Rygg,[1,2,5] and G. W. Collins[1,2,5]

[1]Department of Physics and Astronomy, University of Rochester
[2]Laboratory for Laser Energetics, University of Rochester
[3]Lawrence Livermore National Laboratory
[4]Syntek Technologies
[5]Department of Mechanical Engineering, University of Rochester

Two extended x-ray absorption fine structure (EXAFS) flat crystal x-ray spectrometers (EFX's) were designed and built for high-resolution x-ray spectroscopy over a large energy range with flexible, on-shot energy dispersion calibration capabilities. EFX uses a flat silicon [111] crystal in the reflection geometry as the energy dispersive optic covering the energy range of 6.3 to 11.4 keV and achieving a spectral resolution of 4.5 eV with a source size of 50 μm at 7.2 keV. A shot-to-shot configurable calibration filter pack and Bayesian inference routine were used to constrain the energy dispersion relation to within $\pm$3 eV. EFX was primarily designed for x-ray absorption fine structure (XAFS) spectroscopy and provides significant improvement to the OMEGA XAFS experimental platform at the Laboratory for Laser Energetics. EFX is capable of performing EXAFS measurements of multiple absorption edges simultaneously on metal alloys and x-ray absorption near-edge spectroscopy to measure the electron structure of compressed 3*d* transition metals.

Two EFX spectrometers were designed and built for OMEGA. Diagrams of the physical housing of EFX are shown in Fig. 1, where Fig. 1(a) highlights the different components of EFX and Fig. 1(b) shows a photograph of EFX. The primary components of the spectrometer are a flat silicon [111] crystal and flat image-plate detector, which is loaded into EFX through the back of the housing, opposite the x-ray source. The crystal and detector are held in an aluminum housing with an entrance port for the x rays on one side, as shown in Fig. 1(a). Four crystals were built for EFX: three 170-mm-long Si [111] crystals and one 110-mm-long Si [111] crystal. A blast shield to protect the crystal and a filter pack to characterize the energy dispersion are held in the front of EFX. To reduce noise, EFX has a 3.175-mm-thick, external tungsten shell and a 12.7-mm-thick, tungsten line-of-sight block that protects the detector from the x-ray source.

The performance of EFX was tested on OMEGA by simultaneously measuring EXAFS from multiple K edges of an alloy material. Invar ($Fe_{64}Ni_{36}$) foil was placed in the front-end filter pack of the EFX and the EXAFS spectrum from the Fe and Ni K edges was measured. The resulting spectra are shown in Fig. 2(a). By measuring two edges simultaneously, we are able to analyze both the iron and nickel K edges, allowing for more information to be extracted from a single shot.

The improved spectral resolution of EFX allows for x-ray absorption near-edge spectrometry (XANES) measurements to be made on OMEGA. Figure 2(b) shows the XANES from an iron foil in the front end of the EFX. A spectrum measured by an x-ray spectrometer (XRS) on the same shot is also shown for reference. XRS has been previously used to measure EXAFS on OMEGA[1] but was not able to perform XANES measurements. To highlight the key XANES features, the spectrum from iron measured at a synchrotron[2] is shown in the inset. The improved resolution of EFX is shown in the spectrum's steeper slope and ability to begin to capture the white line (point A) and central modulation (point B), which can be used to distinguish structural changes and melting in iron.[3] XANES pre-edge features have also been shown to increase with increasing compression,[4] meaning

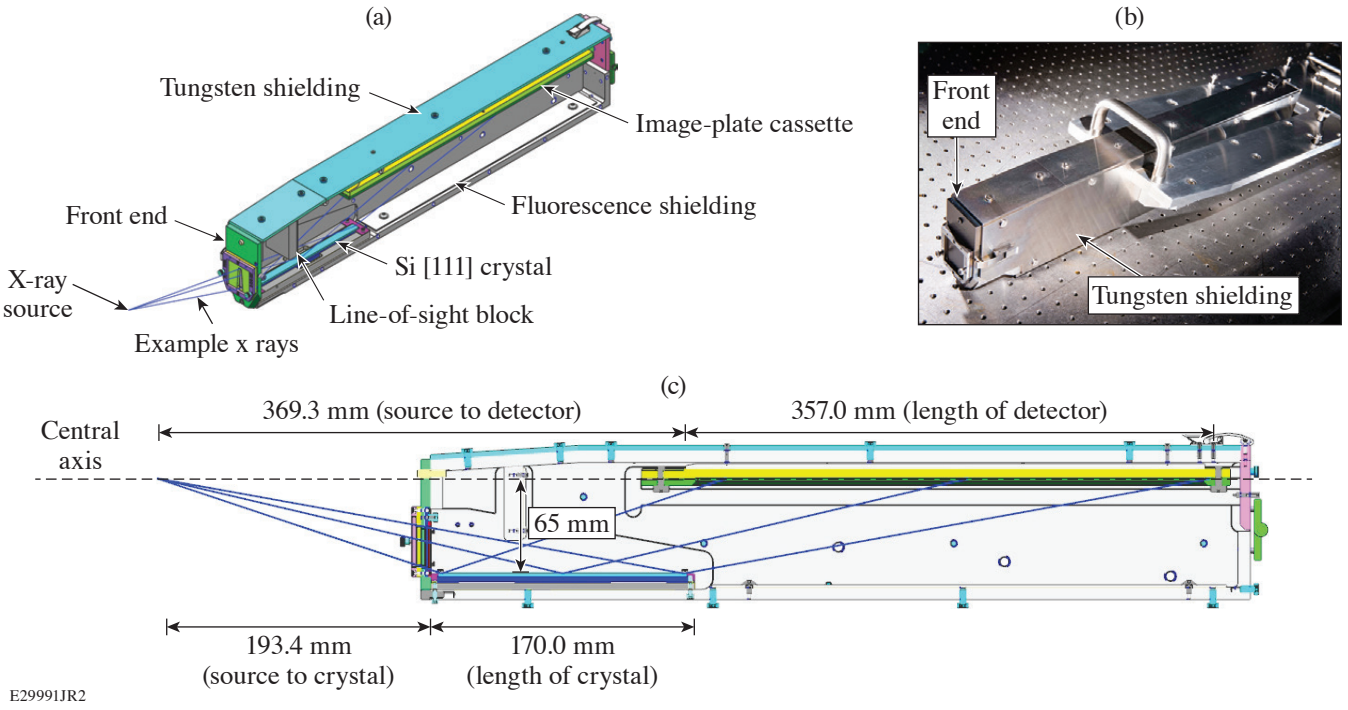

Figure 1
(a) Schematic of EFX showing the positions of the Si [111] crystal, the front end, and image-plate detector. (b) Photograph of EFX. (c) Cross section of EFX, highlighting the relevant distances for energy-dispersion calculations.

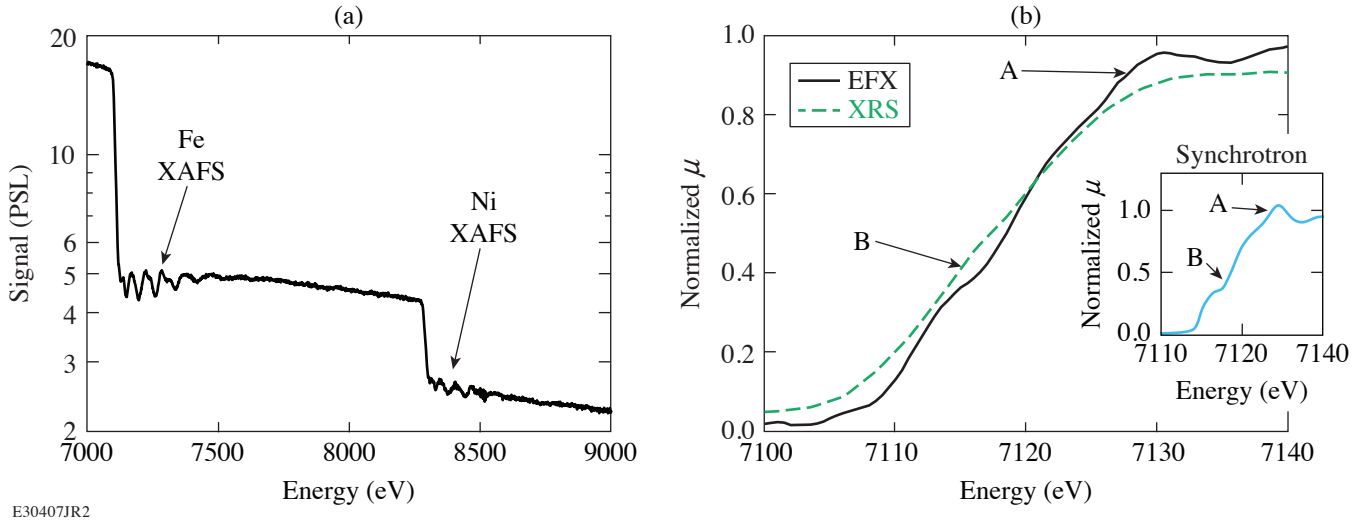

Figure 2
(a) Measured EXAFS spectra from Invar ($Fe_{64}Ni_{36}$) showing the Fe and Ni K edges from shot 100646. The figure demonstrates the capability of EFX to perform EXAFS on multiple edges of the same alloy simultaneously. (b) Comparison of iron XANES data between an EFX spectrum (black solid line) and an XRS spectrum (green dashed line), both taken on shot 97178. The higher resolution of EFX allows it to capture more detail in the white line (point A) and the central modulation (point B). Inset: An iron synchrotron spectrum,[2] where the same A and B points are highlighted similar to (b).

that these features may become more apparent during laser-driven experiments. This improved resolution in the XANES region of the spectrum will allow for future electron structure measurements of compressed materials.[4]

This material is based upon work supported by the Department of Energy National Nuclear Security Administration under Award Number DE-NA0003856. D. A. Chin acknowledges DOE NNSA SSGF support, which is provided under Cooperative Agreement No. DE-NA0003960. This collaborative work was partially supported under the auspices of the U.S. Department of Energy by Lawrence Livermore National Laboratory under Contracts No. DE-AC52-07NA27344.

1. Y. Ping *et al.*, Rev. Sci. Instrum. **84**, 123105 (2013).
2. International X-Ray Absorption Society: Fe Data, IXAS X-Ray Absorption Data Library, Accessed 10 May 2021, https://xaslib.xrayabsorption.org/elem/.
3. M. Harmand *et al.*, Phys. Rev. B **92**, 024108 (2015).
4. A. Sanson *et al.*, Phys. Rev. B **94**, 014112 (2016).

(Cd,Mg)Te Crystals for Picosecond-Response Optical-to-X-Ray Radiation Detectors

J. Cheng,[1,2] G. Chen,[1,2] D. Chakraborty,[1,2] S. Kutcher,[3] J. Wen,[3] H. Chen,[3] S. Trivedi,[3] and Roman Sobolewski,[1,2,4]

[1]Materials Science Graduate Program, University of Rochester
[2]Laboratory for Laser Energetics, University of Rochester
[3]Brimrose Technology
[4]Departments of Electrical and Computer Engineering and Physics and Astronomy, University of Rochester

We demonstrate a photodetector sensitive to both optical and x-ray picosecond pulses based on our in-house grown cadmium magnesium telluride (Cd,Mg)Te single crystal. Specifically, we developed In-doped $Cd_{0.96}Mg_{0.04}Te$ material and discuss its femtosecond optical photoresponse, as well as the detector performance, like <100-pA dark current and up to 0.22-mA/W responsivity for 780-nm-wavelength optical radiation. The detector exposed to Ti fluorescence (K_α) x-ray pulses at 4.5 keV, generated by a free-electron laser beam with a central energy of 9.8 keV and <100-fs pulse width, exhibited readout-electronics–limited 200-ps full-width-at-half-maximum photoresponse, demonstrating that it is suitable for coarse timing in free-electron laser x-ray/optical femtosecond pump–probe spectroscopy applications.

Ultrafast, solid-state detectors covering the optical/near-infrared to x-ray radiation spectrum are in high demand due to their versatile applications, including optical/x-ray subpicosecond pump–probe spectroscopy. Only a few available photodetectors can adequately do this job. Si-based photodetectors cover a wide range of wavelengths and can operate in the x-ray range; however, they degrade due to environmental effects as well as radiation damage.[1] Photodetectors based on metal–semiconductor–metal (MSM) structures with interdigitated electrodes, fabricated on low-temperature–grown GaAs (LT-GaAs), such as, e.g., a HAMAMATSU G4176-03 photodetector, are typically designed for picosecond temporal response for optical signals.[2]

We demonstrate that (Cd,Mg)Te (CMT) is a very promising candidate as a dual-optical/x-ray ultrafast detector. CMT is a ternary compound with a tunable direct energy gap from ~1.5 eV to 3.1 eV by changing the Mg content.[3] At the same time, due to the presence of a high-stopping-power Te element, crystals very effectively absorb high-energy x-ray photons [for a 1-mm-thick (Cd,Mn)Te crystal, the 1/*e* absorption drop occurs at 94.2 keV; Ref. 4]. The carrier lifetime of doped CMT can be comparable to that of LT-GaAs, which is critical in ultrafast temporal resolution. Ultralow device leakage current is another essential criterion, and CMT can have a lower leakage current than GaAs in the same MSM arrangement because of its larger band gap.

The $Cd_{1-x}Mg_xTe$ (x is between 0 to 0.45) crystal exhibits the zinc blende structure and it is the latest member of ternary alloys that include (Cd,Zn)Te and (Cd,Mn)Te, both well known for x-ray detection applications.[4,5] (Cd,Mg)Te possesses all the necessary qualities for an optimal radiation detector, like high material density (5.83 g/cm^3), high effective mass (49.5), ultrahigh resistivity (~10^{10} Ωcm), and good electron mobility lifetime ($\mu\tau$) product (>10^{-4} cm^{2}V^{-1}) (Ref. 6). In addition, the CMT "parent" crystals, CdTe and MgTe, exhibit very close lattice constants, 6.48 Å and 6.42 Å, respectively,[7] leading to a high-quality growth of CMT single crystals. At room temperature, the band gap of $Cd_{1-x}Mg_xTe$ is a linear function of x, increasing at a rate of around 15 meV per Mg atomic percent.[3] At $x = 0$, the CdTe band gap is 1.503 eV (Ref. 3).

Brimrose developed an innovative in-house procedure to purify magnesium to the highest achievable level. This proprietary technique involves sublimation under dynamic vacuum. The process uses two ampoules—the inner pyrolytic boron nitride (PBN)

ampoule is placed inside the graphitized fused-silica ampoule of a length a little longer than the PBN ampoule. Thus Mg (in molten or vapor phase) is prevented from reacting with the outer fused-silica ampoule, which is connected to the high-vacuum system.

The vertical Bridgman method was used to grow high-purity CMT single crystals.[8] Approximately 1-in.-diam ingots are grown, sliced into 1-mm-thick wafers (Fig. 1), and, finally, cut into suitably sized samples (from 4 × 4 mm^2 to 10 × 10 mm^2). During the growth process, the content of Mg can be modified and selective dopants can be added. Additionally, post-growth annealing can be optimized in order to engineer a material that will exhibit characteristics required for a given application. We determined that 3% to 8% Mg and 2% to 5% In doping led to CMT crystals with a suitable band gap and acceptable electron mobility times lifetime ($\mu\tau$) product (>10^{-4} cm^{2}V^{-1}), as well as a large enough resistivity (>10^{10} W-cm) for detector applications.[9]

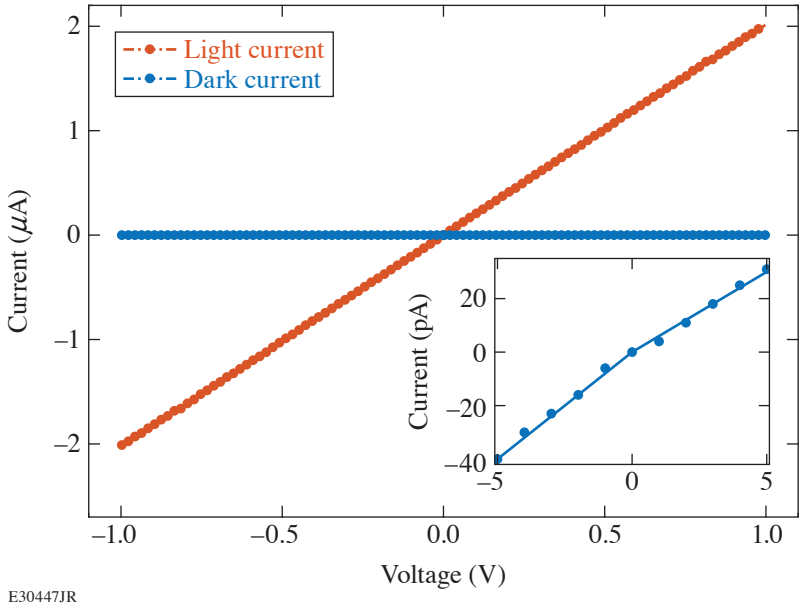

Figure 1
Current–voltage (I–V) characteristics under light (orange) and dark (blue) conditions for a tested CMT device. The inset shows the dark current I–V in detail (bulk measurement across a CMT sample).

We selected the Mg concentration in (Cd,Mg)Te the way that the crystal should have the band gap compatible for an optical photodetector operation within the tunability of a Ti:sapphire femtosecond pulsed laser. For this purpose, we performed optical reflection and transmission spectra measurements using a PerkinElmer Lambda 900 spectrometer with samples placed at normal incidence. The Tauc plot for direct-band-gap material[10] combines the collected experimental spectra and presents the crystal absorption spectrum. We observed a sharp optical transition edge and the band gap E_G = 1.57 eV, with a small absorption tail below E_G that is typically related to shallow sub-gap trap states. For photons with energies above E_G we see the full absorption. In-doped, $Cd_{0.96}Mg_{0.04}Te$ crystals were used in the subsequent detector fabrication.

Photoresponse measurements were carried out in the surface-mode configuration with an optical beam, generated by a Ti:sapphire laser (780-nm wavelength) focused between the electrodes. A bank of neutral-density filters was used to control the laser intensity and the current–voltage (I–V) characteristics were collected using a digital sourcemeter. Figure 1 demonstrates a strong photoconductive effect of our CMT MSM diode. Under optical excitation (orange curve; 20-mW laser power) a photocurrent reaches ~2 μA at a 1-V bias. The I–V dependence is linear, indicating an absence of Schottky barriers. At the same time, the dark current (blue curve) is completely negligible. In the measurements above, we used the bias voltage only up to 1 V in order to avoid a possible breakdown between the electrodes separated by just 25 μm.

Further systematic photoresponse characterization was carried out on our CMT diodes, including the photocurrent and responsivity dependencies on voltage for a wide range of incident optical powers. Figure 2 shows a family of the responsivity traces as a function of detector bias voltage for incident power in the 20-μW to 20-mW range. We note that for our device, the responsivity increases as the decrease of incident power. This phenomenon is related to the intrinsic gain mechanism in semiconductors characterized by a substantial disparity in electron and hole mobilities. The greatest responsivity obtained is 0.22 mA/W, but we

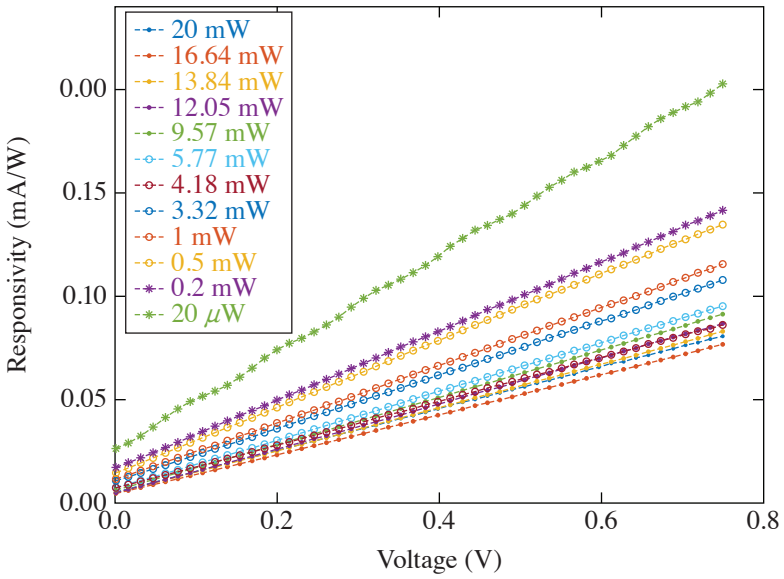

Figure 2
CMT diode responsivity versus bias voltage for several incident power levels of the 780-nm-wavelength radiation (bulk measurement across a CMT sample).

expect to increase it very substantially when the surface detector structure is fabricated in a form of a large-area interdigitated-electrode configuration to increase the collection of carriers generated by the light/x-ray radiation.

The CMT diode was also a subject of preliminary tests at the SLAC National Accelerator Laboratory. Figure 3 presents an actual oscilloscope image of the diode response to an x-ray pulse. To prevent damage to the detector, a <100-fs-wide, 9.8-keV central energy, and 120-Hz repetition rate train of x-ray pulses from a free-electron laser were directed onto a titanium target, so the signal shown in Fig. 3 is actually the x-ray fluorescence at the Ti K_α edge (4.5 keV). The observed signal has an ~0.2-ns FWHM and a <100-ps rise time, limited by the detection electronics. The above parameters make our device suitable for course timing of optical/x-ray subpicosecond pump–probe spectroscopy experiments.

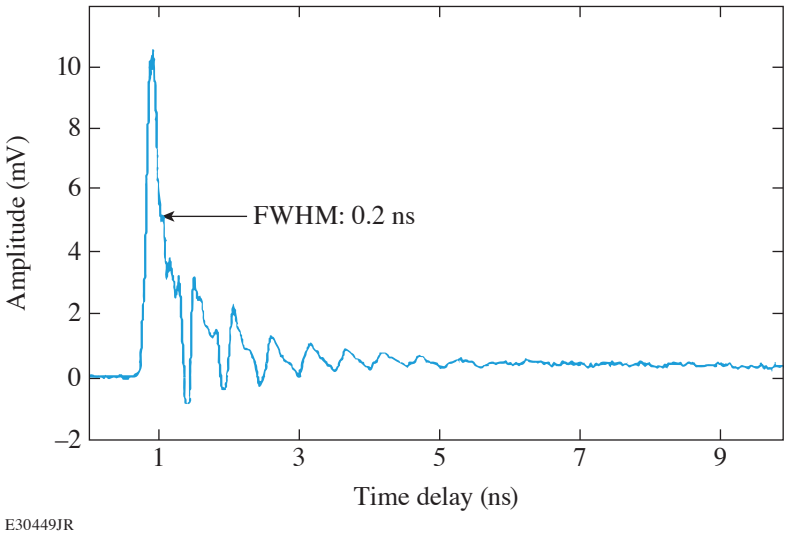

Figure 3
Oscilloscope plot of the time-resolved CMT detector response to a pulsed x-ray signal generated at the SLAC National Accelerator Laboratory. After-pulse oscillations are due to the impedance mismatch in the electronics detection channel.

We demonstrate that (Cd,Mg)Te is a very promising candidate for ultrafast optical/near-infrared to x-ray radiation detector applications. We selected the In-doped $Cd_{0.96}Mg_{0.04}Te$ crystal for our detectors, so its optical bandwidth made it sensitive to the Ti:sapphire light, while In doping resulted in an ultrahighly resistive material characterized by a <100-pA leakage dark current and 2.4-ps electron relaxation time. The detector was tested at the SLAC National Accelerator Laboratory and exhibited a

response signal of 200-ps FWHM (electronics limited) when exposed to Ti fluorescence (K_α) x-ray pulses at 4.5 keV, generated by a free-electron laser beam with the central energy of 9.8 keV and <100-fs pulse width. The latter confirms CMT suitability for the free-electron laser pump–probe spectroscopy timing applications.

The authors thank Drs. Takahiro Sato and David Fritz from the SLAC National Accelerator Laboratory for providing Fig. 3. This work was supported in part by the Department of Energy Phase I SBIR program under Award: DE-SC0021468 and monitored by Dr. Eliane S. Lessner and Dr. Yiping Feng (DOE/SLAC).

1. M. Shanmugam *et al.*, J. Instrum. **10** (2015).
2. Hamamatsu Preliminary Data, Ultrafast Response of Several Tens Picosecond; G4176-03, Accessed 27 February 2023, https://www.datasheet.cloud/pdfviewer?url=https%3A%2F%2Fpdf.datasheet.cloud%2Fdatasheets-1%2Fhamamatsu_photonics_k.k.%2FG4176-03.pdf.
3. E. G. LeBlanc *et al.*, J. Electron. Mater. **46**, 5379 (2017).
4. A. S. Cross *et al.*, Nucl. Instrum. Methods Phys. Res. A **624**, 649 (2010).
5. Y. Eisen, A. Shor, and I. Mardor, IEEE Trans. Nucl. Sci. **51**, 1191 (2004).
6. S. B. Trivedi *et al.*, *Next Generation Semiconductor-Based Radiation Detectors Using Cadmium Magnesium Telluride (Phase I Grant—DE-SC0011328)*, U.S. Department of Energy, Washington, DC, Report DOE/11172015-Final (2017).
7. J.-H. Yang *et al.*, Phys. Rev. B **79**, 245202 (2009).
8. S. B. Trivedi *et al.*, J. Cryst. Growth **310**, 1099 (2008).
9. J. Serafini *et al.*, Semicond. Sci. Technol. **34**, 035021 (2019).
10. J. Tauc, R. Grigorovici, and A. Vancu, Phys. Stat. Sol. (B) **15**, 627 (1966).

Exact Solutions for the Electromagnetic Fields of a Flying Focus

D. Ramsey,[1] A. Di Piazza,[2] M. Formanek,[3] P. Franke,[1] D. H. Froula,[1] B. Malaca,[4] W. B. Mori,[5] J. R. Pierce,[5] T. T Simpson,[1] J. Vieira,[4] M. Vranic,[4] K. Weichman,[1] and J. P. Palastro[1]

[1]Laboratory for Laser Energetics, University of Rochester
[2]Max-Planck-Institut für Kernphysik
[3]ELI-Beamlines, Institute of Physics of Czech Academy of Sciences
[4]GoLP/Instituto de Plasmas e Fusão Nuclear, Instituto Superior Técnico, Universidade de Lisboa
[5]University of California Los Angeles

All focused laser fields exhibit a moving focus in some frame of reference. In the laboratory frame, an ideal lens focuses every frequency, temporal slice, and annulus of a laser pulse to the same location. The pulse moves through the focus at its group velocity and diffracts over a Rayleigh range. In any other Lorentz frame, the focus moves. "Flying-focus" techniques recreate these moving foci in the laboratory frame by modifying the focal time and location of each frequency, temporal slice, or annulus of a pulse. The intensity peak formed by the moving focus can travel at any arbitrary velocity while maintaining a near-constant profile over many Rayleigh ranges. All of these features make the flying focus an ideal spatiotemporal pulse-shaping technique to enhance a vast array of laser-based applications.

Assessing the extent to which a flying focus can enable or enhance these applications requires an accurate description of the electromagnetic fields. With the exception of the special case $v_I = -c$, all of the aforementioned applications were modeled using approximate solutions for the electromagnetic fields of flying-focus pulses. In the case of conventional pulses with stationary foci, improving the accuracy of approximate solutions has been found to impact models of phenomena ranging from direct laser acceleration to optical trapping. Methods for obtaining accurate solutions to Maxwell's equations for conventional laser pulses come in three forms: a "Lax"-like series expansion in which corrections to paraxial fields can be calculated recursively; a series expansions of exact spectral integrals for each field component; and the complex source-point method (CSPM), which exploits the invariance of Maxwell's equations under a translation in the complex plane to transform multipole solutions into beam-like solutions. Of these three, the CSPM is unique in its ability to provide closed-form solutions that exactly satisfy Maxwell's equations.[1] As a result, the solutions can be Lorentz transformed without introducing additional error.

In this summary, we derive exact solutions to Maxwell's equations for the electromagnetic fields of a constant-velocity flying-focus pulse. Figure 1 illustrates a schematic of the theoretical approach. The approach combines the CSPM with a Lorentz transformation from a frame in which the focus is stationary to a frame in which the focus is moving. The vector solutions are inherently non-paraxial, can have arbitrary polarization, and are generalized to higher-order radial and orbital angular momentum modes. Subluminal ($|v_I < c|$) and superluminal ($|v_I > c|$) solutions are constructed from multipole spherical and hyperbolic wave solutions, respectively. Propagating the fields backward in space reveals that each solution corresponds to a pulse that was focused by a lens with a time-dependent focal length. Thus, these solutions can be experimentally realized using the flying-focus X (Ref. 2). For a wide range of parameters, the differences between the exact solutions and simpler paraxial solutions are small, justifying the use of paraxial solutions for theoretical or computational studies of flying-focus applications in many regimes.

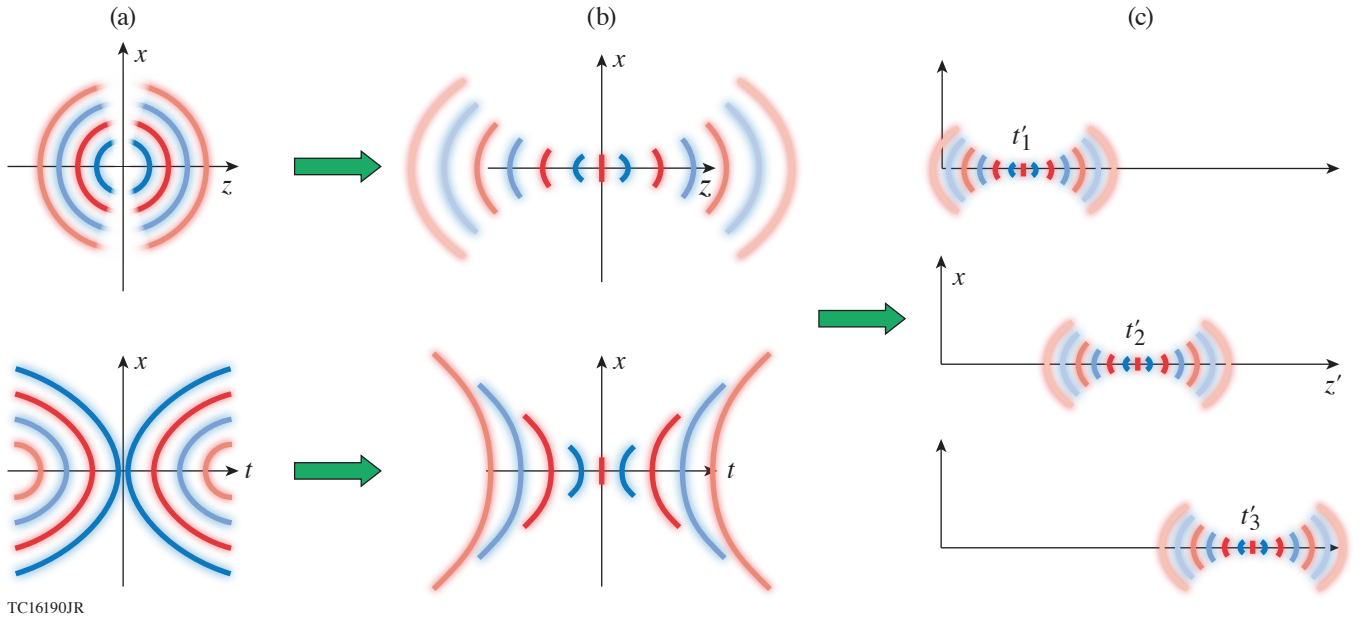

Figure 1
A schematic of the theoretical approach. (a) The approach starts with a multipole spherical (top) or hyperbolic (bottom) solution. (b) A displacement of the coordinate z (top) or t (bottom) into its complex plane transforms the multipole solution into a beam-like solution with a stationary focus in space (top) or time (bottom). (c) A Lorentz transformation of either beam-like solution from a frame of reference in which the foci appear stationary to the laboratory frame produces the exact electromagnetic fields of a flying focus.

As an example, the lowest-order mode electromagnetic fields with polarization vector $\hat{\mathbf{x}}$ are generated by the electric Hertz vector

$$\mathbf{\Pi}_e(\mathbf{x},t) = \frac{1}{2}\alpha_{00} j_0(\omega R/c) e^{i\omega t}\hat{\mathbf{x}} + \text{c.c.} \tag{1}$$

and magnetic Hertz $\mathbf{\Pi}_m = \hat{\mathbf{z}} \times \mathbf{\Pi}_e$ [Fig. 1(a)], where ω is the angular frequency and α_{00} is an arbitrary constant. After computing the corresponding four potential, the coordinate R is translated into the complex domain as $R \rightarrow \sqrt{x^2 + y^2 + (z - iZ_R)^2}$, where Z_R is the Rayleigh range of the resulting beam-like solution [Fig. 1(b)]. Finally, a Lorentz boost in the axial direction results in a flying focus [Fig. 1(c)]. All of these operations preserve the resulting electromagnetic fields as solutions to Maxwell's equations.

Figures 2(a)–2(f) display cross sections of the resulting electric and magnetic fields at the location of the moving focus $z' = v_I t'$ for $v_I = 0.5c$ and $\omega w_0/c = 20$, where the primed terms are as observed in the laboratory frame and w_0 is the spot size at focus. The predominant electric and magnetic fields, E'_x and B'_y have equal amplitudes and Gaussian-like transverse profiles. The remaining vector components exhibit more-complex spatial structure, but are much smaller in amplitude. Figure 2(g) illustrates the motion of the focus in the laboratory frame. The cycle-averaged longitudinal component of the Poynting vector $S'_z = c\hat{\mathbf{z}} \cdot \mathbf{E}' \times \mathbf{B}'/4\pi$ is plotted as a function of z' and t' at $x = y = 0$. For comparison, the dashed black line demarcates the speed of light trajectory $z' = ct'$.

This material is based upon work supported by the Office of Fusion Energy Sciences under Award Number DE-SC0019135 and DE-SC00215057, the Department of Energy National Nuclear Security Administration under Award Number DE-NA0003856, the University of Rochester, and the New York State Energy Research and Development Authority.

1. A. L. Cullen and P. K. Yu, Proc. Roy. Soc. A **366**, 155 (1979).
2. T. T. Simpson *et al.*, Opt. Express **30**, 9878 (2022).

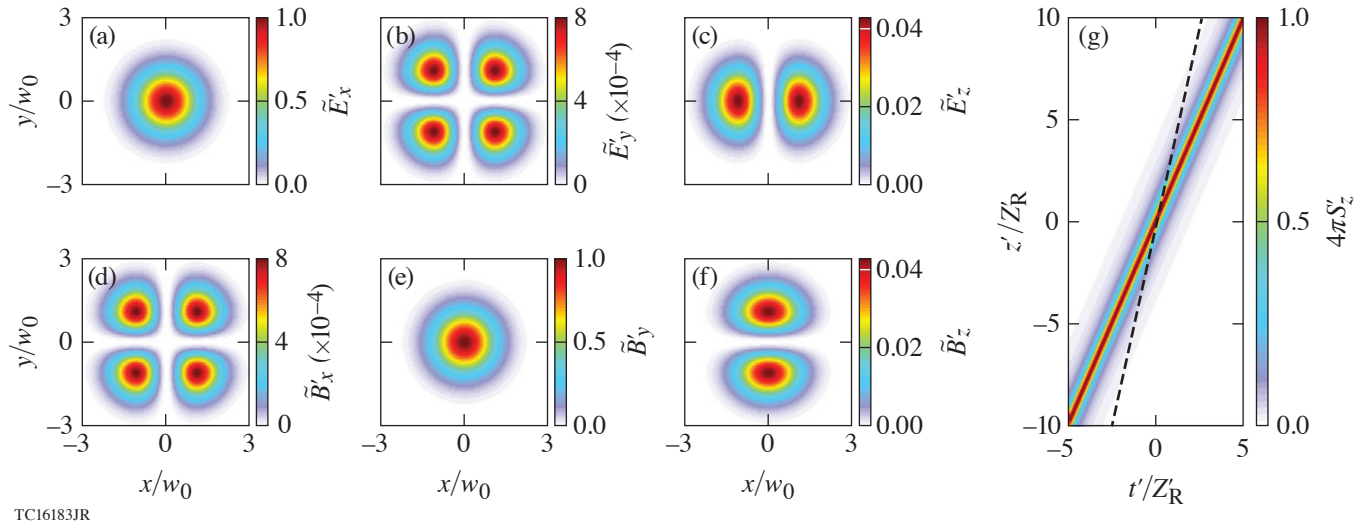

Figure 2

The lowest mode subluminal focus with $v_f = 0.5c$ and $\kappa' w_0 = 20$. [(a)–(f)] Cross sections of the electromagnetic-field amplitudes at the location of the moving focus $z' = v_f t'$. Here $\widehat{E}' = \langle E'^2 \rangle^{1/2}$, where $\langle\ \rangle$ denotes a cycle average. The amplitudes are normalized to the $(\widetilde{E}'_x)$. (g) The longitudinal component of the cycle-averaged Poynting vector S'_z at $x = y = 0$, showing the motion of the focus. The dashed black line demarcates the trajectory $z' = ct'$ for reference.

Methods and Apparatus for Comprehensive Characterization of Performance Attributes and Limits of Ultrafast Laser Optics

K. R. P. Kafka, T. Z. Kosc, and S. G. Demos

Laboratory for Laser Energetics, University of Rochester

The output power of ultrashort-pulse laser systems can be affected by the ability of the constituent optical components to withstand the generated laser intensity, typically defined by the laser-induced–damage threshold (LIDT). However, large-aperture optics employed in the most powerful laser systems can operate using optics that have sustained some damage with limited performance degradation. In this regime, the operational lifetime of an optic then begins to be governed by the rate of damage growth (increase in size of the damaged area) under subsequent exposure to system laser pulses. Furthermore, recent reports have shown that the optical properties of materials exposed to ultrashort laser pulses can be transiently modified by the high electric-field intensities that can still be below the LIDT fluences. This in turn may cause the modification of the functionality of a device without the initiation of damage.[1] The vast majority of literature to date has focused primarily on measuring the LIDT under single- and multipulse excitation. There is clearly a need to expand the characterization protocols for such optics to include evaluation for the laser-induced–damage growth and functional failure thresholds. The present work describes a system that was developed to provide comprehensive performance characterization, including damage initiation, damage growth, and laser-induced functional degradation for near-infrared, femtosecond-pulsed applications.

A schematic of the testing apparatus developed as part of this work is shown in Fig. 1, with the main components consisting of an ultrafast laser and the experimental damage-testing platform located inside a vacuum chamber. It employs a custom-built optical parametric chirped-pulse–amplification laser system ("Ultraflux," EKSPLA) with 20-fs pulse duration, 820-nm to 970-nm tunable central wavelength, 5-Hz repetition rate, and up to 2-mJ output pulse energy. An *in-situ* dark-field microscope monitors the sample surface to detect damage initiation and/or growth. The reflected beam from the surface of the sample is imaged onto a camera located outside the chamber (L and M7, respectively, in Fig. 1) for laser-induced functional threshold (LIFT) characterization.

Since accurate measurements of damage-growth parameters require the test beam to be significantly larger than the initial and subsequently growing damage site, this system is designed to provide beam area variation of more than one order of magnitude. This was achieved by mounting the beam-focusing optic [off-axis parabolic mirror (OAP) in Fig. 1] on a translation stage together with folding mirror M4 to control the distance from the sample. As these two optics move in tandem, the beam size on the sample changes without disturbing the beam alignment. To facilitate utilization of near-LIDT fluences across a wide range of beam sizes, many of the necessary system features required considerations for management of B-integral (nonlinear phase) that is introduced at high energies in the large-beam configuration. These considerations impacted the design of pulse energy control, polarization control, vacuum window, and beam sampling for diagnostics after all resulting in a calculated total of about $B \approx 1$ at maximum pulse energy.

The operation of the system is demonstrated by the testing of a low-group-delay-dispersion metal-dielectric mirror coating that is designed for broadband enhanced reflection in the near-infrared. This sample was tested at 890-nm central wavelength using 22-fs pulses at a 45°angle of incidence under vacuum environment. The damage-growth measurements were carried out by first initiating damage sites using the smallest beam with a single pulse at a fluence 10% to 15% above the LIDT. This formed a damage site with a diameter of approximately 20 to 30 μm, a precursor from which to measure damage growth. Then the beam size was increased to a 350-μm Gaussian diameter, and each precursor was irradiated by 50 pulses at a fixed fluence. Figure 2(a)

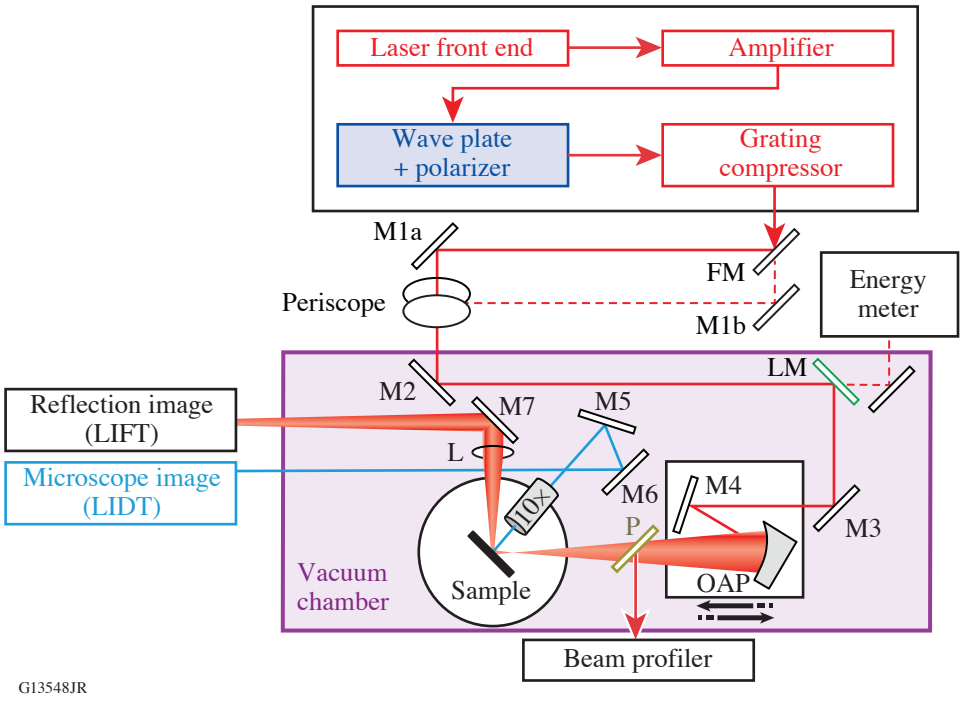

Figure 1
Schematic of performance characterization apparatus. FM: flip mirror; M#: mirror; LM: leaky mirror; OAP: off-axis parabolic mirror; P: pickoff; 10×: 10× microscope objective lens; L: lens.

depicts the size of the single-pulse damage initiation site with respect to the enlarged test beam. The remainder of Fig. 2 shows examples of non-growing and growing sites with each test polarization, imaged off-line using differential interference contrast microscopy. By comparing images of the sample before and after multipulse irradiation, the presence or absence of damage growth was determined for each site, making it possible to calculate the fluence thresholds.

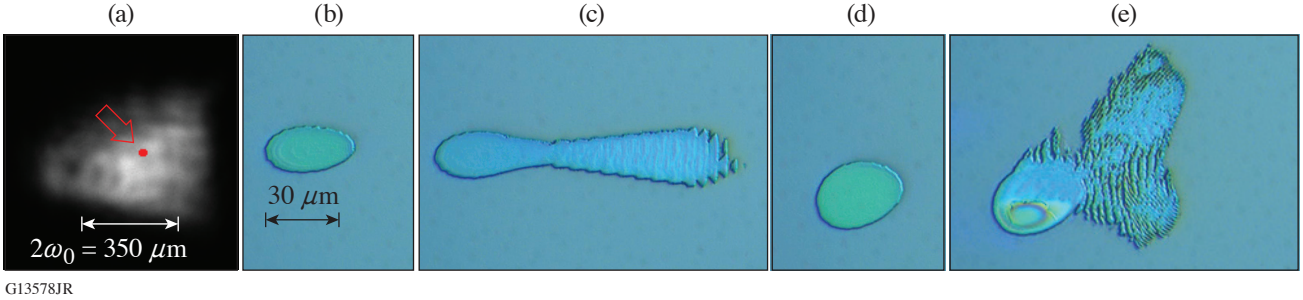

Figure 2
Example morphologies of a damage-growth experiment in optical microscopy. (a) The 30-μm damage initiation site (purposely generated to become the "seed" site for damage-growth experiments) is shown in red overlaid on an example beam profile. For *s* polarization: (b) non-growing site, (c) growing site at 0.34 J/cm^2. For *p* polarization: (d) non-growing site, and (e) growing site at 0.43 J/cm^2. The laser is incident from the left.

The functional performance (a change of the reflection) can be observed by calculating the ratio of reflected beam images from different pulses after first normalizing those images to the total energy. Specifically, reflected beam images represent the ratio between (1) a given test pulse and (2) a previous pulse that did not initiate damage. An example sequence of ratio images showing a detected functional change is depicted in Fig. 3, alongside the concurrent images from *in-situ* dark-field microscopy that show damage has formed. The lineouts across the respective interaction regions are shown in Fig. 3(f). Starting with the

pulse in Fig. 3(a), no damage is initiated, and the lineout shows a constant value. In Fig. 3(b), there is clearly a measurable drop of reflectance in the center of the laser beam (indicating functional modification), consistent with energy loss and the onset of damage. The dark-field images shown before and after damage initiation [Figs. 3(d) and 3(e), respectively]. Because in this example the LIFT occurred concurrently to the initiation of damage, the ratio image from the next pulse [Fig. 3(c)] has severely reduced central reflectance (from 1.0 to 0.3) due to low reflectivity of the ablation site. This suggests that a system designed to measure LIFT could simultaneously be a sensitive *in-situ* diagnostic for LIDT measurement with *S*-on-1 or *R*-on-1 protocols.

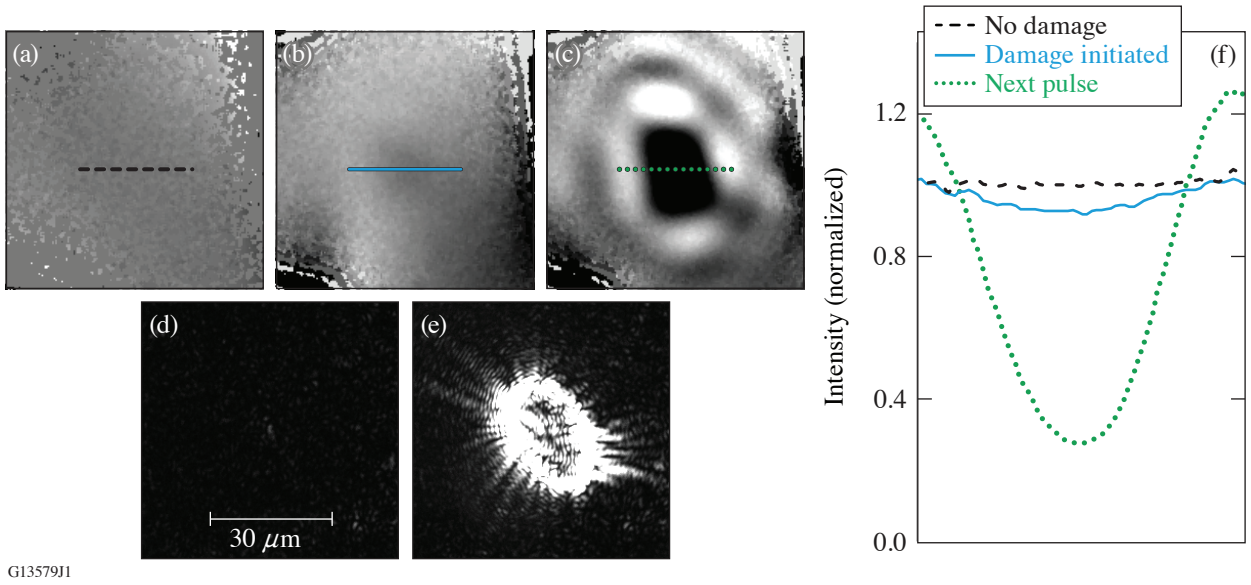

Figure 3
In-situ microscopy of damage formation using [(a)–(c),(f)] functional performance characterization and [(d),(e)] dark-field microscopy. Reflected beam images of (a) a pulse that did not damage, (b) the pulse that initiated damage, (c) the next pulse after damage initiation. Each image in (a)–(c) was normalized by a reflected beam image of a previous pulse that did not initiate damage. (f) The lineouts of the respective reflection images. Dark-field microscope image of the sample, collected (d) before damage initiation, (e) after damage initiation but before the next pulse.

The system and methodology for the characterization of optical components for large-aperture, ultrashort pulse laser systems aims to address current and future needs to support the development of next-generation 100-PW-class laser systems. Achieving the technical objectives required novel implementation of the testing system to avoid problematic nonlinear beam-propagation effects. Initial results underscore that precise damage-testing measurements of optical elements using ultrashort pulses with an expanded and multifaceted definition of damage is important to provide a wide range of information regarding the processes involved that can aid development of improved optic designs and reliable operational fluence limits.

This material is based upon work supported by the Department of Energy National Nuclear Security Administration under Award Number DE-NA0003856, the University of Rochester, and the New York State Energy Research and Development Authority.

1. O. Razskazovskaya *et al.*, Proc. SPIE **9237**, 92370L (2014).

Design and Demonstration of the "Flow-Cell" Integrated-Flow, Active-Cooling Substrate for High-Average-Power Substrates

E. P. Power, S. Bucht, K. R. P. Kafka, J. Bromage, and J. D. Zuegel

Laboratory for Laser Energetics, University of Rochester

We designed, fabricated, and tested a prototype flow-cell integrated-cooling substrate built using cordierite ceramic and demonstrated average power handling up to 3.88-W/cm^2 absorbed power density with 54-nm peak-to-valley deformation in a subaperture test.[1,2] Mechanical stabilization was observed to occur on a time scale <30 s. Model predictions indicate a full-aperture performance limit of 2.6-W/cm^2 absorbed power density with <λ/10 deformation and <90-s stabilization time, equivalent to 100-mJ/cm^2 fluence per pulse with a 1-kHz repetition rate on an optic with 2.6% absorption. Chirped-pulse–amplification lasers commonly use gold-coated compressor gratings operating with beam-normal fluences of ~100 mJ/cm^2 to stay below the short-pulse damage-fluence limit. Existing multiterawatt and petawatt femtosecond lasers operate at relatively low repetition rate (Hz and slower); thermal effects are not experienced by gratings located in vacuum chambers at these low-average powers. Thermal expansion of gratings under high-average-power conditions will cause wavefront deformation (focusing errors) and modify the frequency-dependent path lengths through the system (compression errors), leading to unacceptable spatial and temporal degradation of the focused laser spot and compressed pulse, respectively. Joule-class lasers operating at kilowatt average powers would require large beam sizes (~300 cm^2 or ~20 cm diam) with current gratings given their ~10-W/cm^2 average power (~10 mJ/cm^2 at 1 kHz) handling capacity. Simulations show that new gratings fabricated on thermally stable and actively cooled substrates can reduce pulse width, improve temporal contrast, and decrease focal-spot degradation,[3] but significantly better thermal management of diffraction gratings is needed for future high-average-power lasers for accelerator and beam-combining applications.

The flow-cell integrated active-cooling design is built around a hexagonal unit cell. The close-packed structure of cells is similar to lightweighted optics for aerospace applications, the primary differences being a closed back and integrated fluid input/output channels. The final prototype design uses a hexagon inscribed in a 13-mm diameter with 8-mm pocket depth and cell-to-cell wall thickness of 2 mm. Exterior dimensions for the prototype are 130.18 × 63.5 × 47.29 mm^3, with a defined clear aperture of 101.6 × 50.8 mm^2 centered on the front surface. The front boundary of each cell is located 5 mm behind the optical surface. Figure 1 shows the interior structure of the fabricated prototype.

COMSOL modeling was performed using unidirectional coupling between pressure in the fluid domain and deformation in the solid domain. That is, it was assumed that the small nanometer-scale motion of the fluid–solid boundaries would not impact fluid flow, which is defined by millimeter-scale geometric features. Therefore, as discussed in more detail in Ref. 1, steady-state isothermal turbulent flow was computed once, and the resulting fluid velocities and pressures were used as static input to the follow-up thermomechanical computation. The predicted temperature rise of <1° C in the fluid is assumed insufficient to require a fully coupled model including non-isothermal flow. Input and output coolant baths were computed only in the fluid domain; we are uninterested in the response of the steel plenum pieces fabricated as dual-purpose optic mount/fluid baths.

Figure 2 shows the heater beam delivery and metrology for testing thermally loaded samples. The device under test was held under vacuum in a custom-built cylindrical vacuum chamber. The heater beam entrance and exit ports were arranged 90° apart, allowing 45° incidence on the test optic. The heater source available in our setup was a 976-nm cw source with a maximum on-target power of ~100 W. A commercial Fizeau interferometer (Zygo Dynafiz) was used at normal incidence using a 632.8-nm

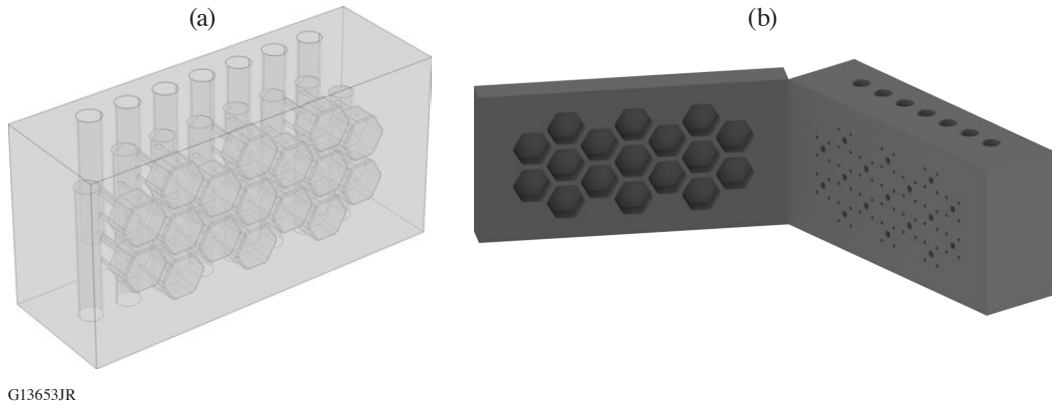

Figure 1
(a) Transparent rendering of the prototype optic used in modeling. The optical surface is toward the front, fluid input is through the top columns, and coolant drainage is through the bottom (obscured). (b) Opaque rendering of the prototype optic cut open at the back plane of the flow cells to aid visualizing input and output channels for individual unit cells.

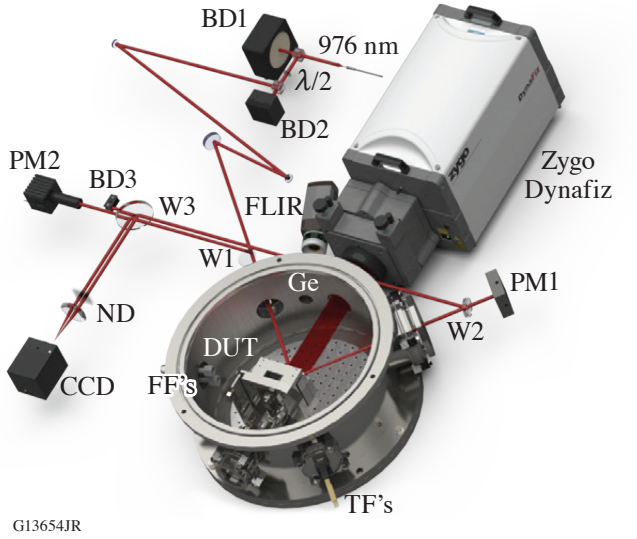

Figure 2
Thermal loading test stand layout using the 976-nm heater source. BD1: water-cooled beam dump; BD2, BD3: air-cooled beam dumps; W1, W2, W3: uncoated wedges; PM1: water-cooled thermopile; PM2: air-cooled Si diode + integrating sphere; FF: fluid feedthrough; TF: thermocouple feedthrough; ND: neutral-density filter; CCD: charge-coupled device; DUT: device under test. A Ge window for the FLIR thermal imaging camera is shown; all other windows are V-coated for the appropriate wavelength (976-nm heater or 632.8-nm Fizeau).

stabilized HeNe laser. A small Ge window placed near the interferometer window allows a thermal imaging camera (FLIR) to view the heated area. Eight type-K thermocouple feedthroughs allowed for spot measurement of temperature in a variety of locations on the sample, mount, or chamber. Two fluid feedthroughs allowed coolant flow for in vacuum liquid-cooled components.

Cordierite ceramic was selected as the material for the flow-cell prototype due to its superior thermomechanical properties: 4.0 W/m-K thermal conductivity and $<0.02 \times 10^{-6}$ K^{-1} thermal expansion coefficient. Steady-state and time-dependent testing of a flow-cell prototype was performed using 97.1 W of optical power, corresponding to 3.88 W/cm^2 absorbed power density. The incidence angle in the COMSOL model was set to 45° to match laboratory conditions. Unfortunately, the 976-nm laser source does not have additional power available; therefore, the beam size could not be increased to cover a larger portion of the clear aperture. Results measured when heating the flow-cell with 3.88 W/cm^2 absorbed power density are shown in Figs. 3(a) and 3(c), with COMSOL model results in Fig. 3(b). Agreement between the modeled and measured steady-state response in Figs. 3(b) and 3(c) is excellent, differing by 0.2 nm peak-to-valley (p–v). Also in excellent agreement is the time-dependent response in Fig. 3(a); stabilization dynamics measured in the laboratory are well matched by model predictions, and the observed mechanical stabilization time is <30 s to reach >99% of the steady-state deformation.

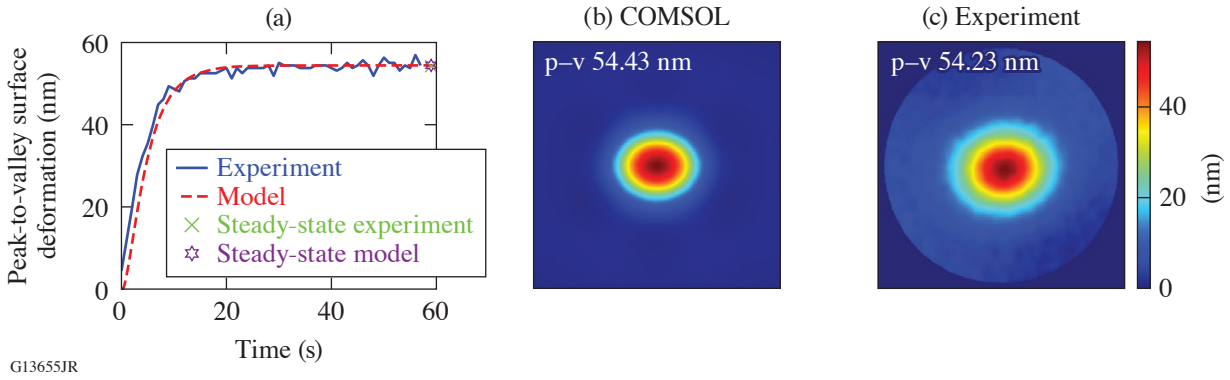

Figure 3
(a) Stabilization dynamics of the flow-cell prototype as indicated by the measured p–v surface deformation (blue curve): the sample was heated with a 1.3-cm-diam beam with absorbed power density of 3.88 W/cm^2. Surface maps were acquired in fast Fizeau mode at 1 Hz; $t = 0$ marks the initiation of the heater beam. Model results for the same conditions (red curve) are an excellent match; the dynamics and stabilization time scales are well reproduced. Mechanical stabilization was observed to occur in <30 s. (b) COMSOL steady-state model prediction for surface deformation, and (c) measured surface deformation after 5 min of continuous heating.

We used the same COMSOL model that successfully predicted sub-aperture behavior to predict full-aperture performance. The only model parameters changed were beam diameter (increased to 5 cm) and optical power (increased to 1 kW). The resulting absorbed power density was 2.6 W/cm^2, slightly above our 2.5-W/cm^2 design target. Figure 4 shows the results from this modeling effort: (a) shows that the thermal profile is qualitatively similar to the sub-aperture case we tested in the laboratory, with peak temperature on the surface slightly lower in this scenario due to the lower absorbed power density, and (b) shows the surface deformation dynamics: surface deformation reaches >99% of the steady-state value in <90 s. The steady-state model predicts 80-nm deformation for 2.6-W/cm^2 absorbed power density, meeting the $\lambda/10$ limit at 800 nm.

We simulated the dynamic response of a passively cooled cordierite brick with identical outer dimensions and beam geometry as the flow-cell prototype and found an upper limit of ~0.1 W/cm^2 absorbed power density to maintain p–v deformation $<\lambda/10$. As expected, stabilization was orders of magnitude slower, reaching the >99% threshold for p–v deformation required 4.75 h, as shown in the inset of Fig. 4(b).

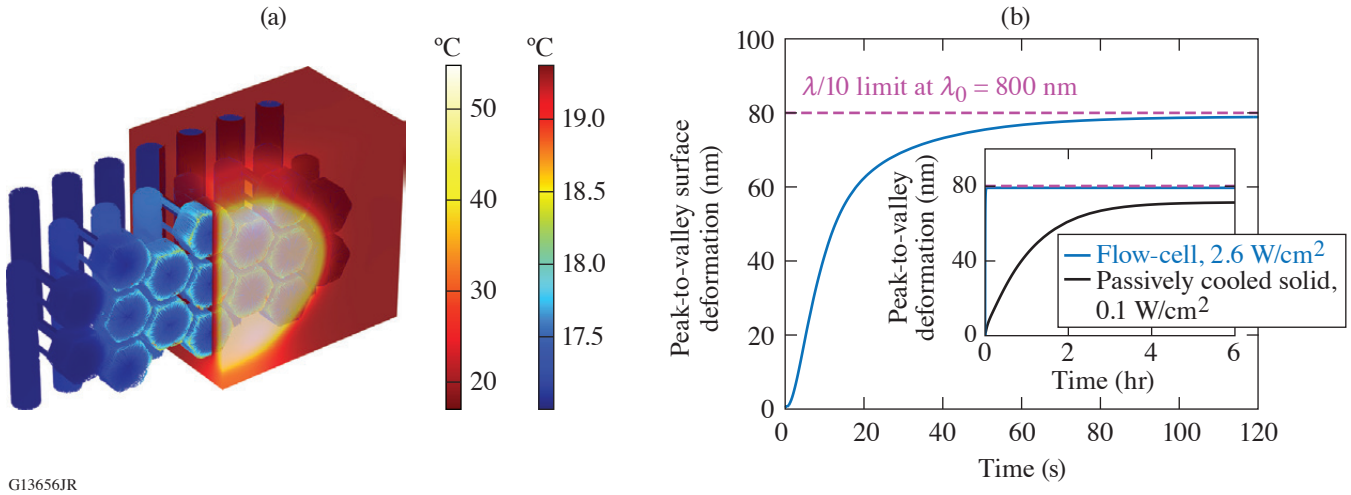

Figure 4
COMSOL results for the flow-cell prototype heated with a 5-cm-diam beam. (a) Temperature profile using 2.6-W/cm^2 absorbed power density; the solid domain is semi-transparent. (b) Predicted heating dynamics: the mechanical stabilization time was <90 s. Inset: dynamic response of a passively cooled cordierite brick heated with 0.1 W/cm^2.

In separate testing, Plymouth Grating Labs fabricated four Au-coated gratings on cordierite coupons, as well as two reference gratings on fused silica. Diffraction efficiency and laser-damage–threshold measurements for test gratings fabricated on cordierite coupons reveal no red flags, with average efficiencies of 88.4%, 89.9%, 91.5%, and 91.7%; all measurements were made at 799 nm. Despite higher-amplitude content in polished cordierite 1-D power spectral densities, diffraction efficiency measurements of the best two gratings on cordierite are within 1% of witness gratings on glass, and 50-on-1 laser-damage threshold is identical at 250 mJ/cm^2 for both glass and cordierite gratings.

This material is based upon work supported by the Department of Energy Office of Science under Award Number DE-SC0019496, the University of Rochester, and the New York State Energy Research and Development Authority.

1. E. P. Power *et al.*, Opt. Express **30**, 42,525 (2022).
2. E. P. Power *et al.*, "Demonstration of the "Flow-Cell" Integrated-Flow Active Cooling Substrate for High-Average-Power," submitted to Optics Letters.
3. D. A. Alessi *et al.*, Opt. Express **24**, 30,015 (2016).

Free-Standing Thin-Membrane, Zero *B*-Integral Beam Splitters

M. Romo-Gonzalez and R. Boni

Laboratory for Laser Energetics, University of Rochester

Uncoated nitrocellulose pellicles have a maximum reflectivity of ~30% with negligible absorption in the near-infrared (NIR). Our application used nitrocellulose pellicle beam splitters with a pulse of 30 ps and 135 fs for 1053-nm and 1170-nm beams, at a damage threshold of 1.3 J/cm^2 for 500 fs, λ = 1053-nm pulses[1] for nitrocellulose; our requirements were not limited by the material. Typical pellicle thickness of 2 μm to 5 μm effectively eliminates the *B*-integral, whose minimization is critical for propagating high-power laser pulses through an optical medium. Alternatively, a typical uncoated glass beam splitter can be made thin to control *B*-integral contribution while maintaining optical flatness imaging in reflection for these applications. These glass beam-splitter substrates are limited by ratios greater than the ~4% yielded from the uncoated surface of the glass and as a result, require at least one thin-film dielectric coating to be applied. The application of dielectric coatings introduces mechanical stress, which can significantly warp the substrate, rendering it unsuitable for imaging in reflection.

Pellicles (125-mm-diam, 2.2-μm- and 1.56-μm-thick λ/4 flat nitrocellulose membranes) were used to replace the 3-mm-thick dielectric coated NBK-7 glass plates used as λ = 1053-nm and λ = 1170-nm beam splitters that became warped upon coating.

A generalized multilayer thin-film modeling program was written to determine the thickness of the pellicle film that yields the desired reflectivity at the wavelength, angle of incidence, and polarization of interest following the matrix method described by Thelen.[2] The solution used by Thelen expresses a system of equations that solve Maxwell's equation for *s* and *p* polarization at the interface boundaries Z_1 and Z_2 in Fig. 1 into a matrix form in Eqs. (1) and (2).

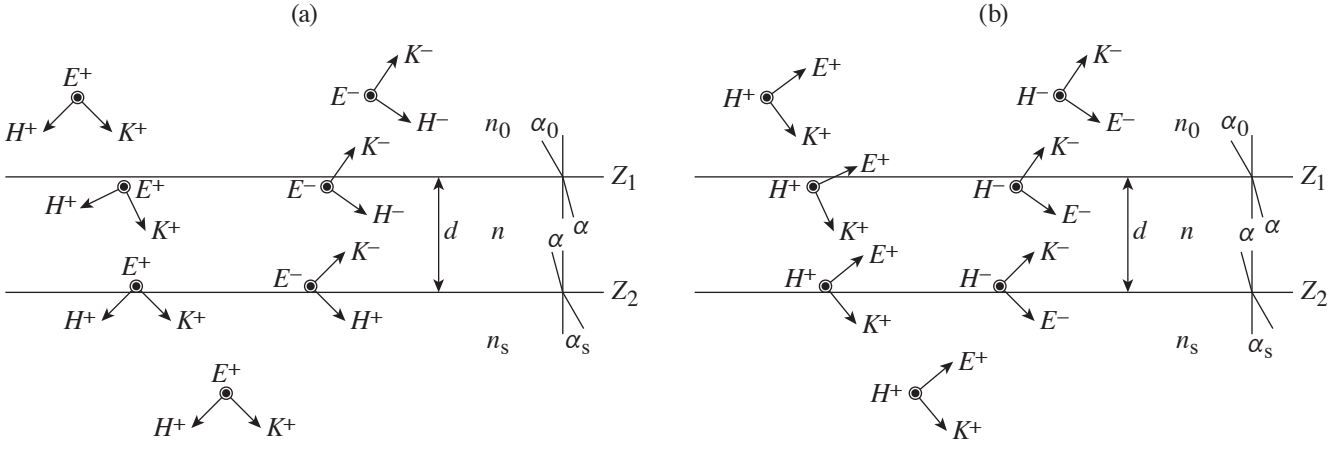

Figure 1
The electromagnetic fields at the boundaries of a thin film: (a) *s* polarization, where $\vec{E}$ is perpendicular to the plane of incidence and (b) *p* polarization, where $\vec{E}$ is parallel to the plane of incidence.

$$\begin{bmatrix} E(Z_1) \\ Z_0 H(Z_1) \end{bmatrix} = \begin{bmatrix} \cos\phi & \frac{i\sin\phi}{n} \\ in\sin\phi & \cos\phi \end{bmatrix} \begin{bmatrix} E(Z_2) \\ Z_0 H(Z_2) \end{bmatrix}, \tag{1}$$

$$\begin{bmatrix} E \\ ZH \end{bmatrix} = \begin{bmatrix} 1 & 1 \\ n & -n \end{bmatrix} \begin{bmatrix} E^+ \\ E^- \end{bmatrix}. \tag{2}$$

Equations (1) and (2) provide the matrix transfer function [Eq. (3)] of the electric fields across the layer, where δ is an infinitesimal distance from the boundary layer and M_{11} through M_{22} are the elements of the 2×2 matrix in Eq. (1). A compact matrix transfer can be written as seen in Eq. (4) for a multilayer of thin films.

$$\begin{bmatrix} E^+(z_1-\delta) \\ E^-(z_1-\delta) \end{bmatrix} = \begin{bmatrix} 1 & 1 \\ n & -n \end{bmatrix}^{-1} \begin{bmatrix} M_{11} & M_{12} \\ M_{21} & M_{22} \end{bmatrix} \begin{bmatrix} 1 & 1 \\ n & -n \end{bmatrix} \begin{bmatrix} E^+(z_2-\delta) \\ E^-(z_2-\delta) \end{bmatrix}, \tag{3}$$

$$\begin{bmatrix} E^+(z_1-\delta) \\ E^-(z_1-\delta) \end{bmatrix} = \begin{bmatrix} Q_{11} & Q_{12} \\ Q_{21} & Q_{22} \end{bmatrix} \begin{bmatrix} E^+(z_2-\delta) \\ E^-(z_2-\delta) \end{bmatrix}. \tag{4}$$

Since there is no reflected wave in the exit medium, $E^-(z_2 + \delta) = 0$, the amplitude of the reflectance $\vec{R}$ is shown in Eq. (5) and the reflected and transmitted energy coefficients **R** and **T** in Eq. (7) are yielded by Eqs. (5) and (6) in the absence of absorption, where $\vec{R}^*$ is the complex conjugate

$$\vec{R} = \frac{E^-(z_1-\delta)}{E^+(z_1-\delta)} = \frac{Q_{21}}{Q_{11}}, \tag{5}$$

$$\mathbf{R} = \vec{R}\vec{R}^*, \tag{6}$$

$$\mathbf{T} = 1 - \boldsymbol{R}. \tag{7}$$

In our implementation of Thelen's matrix equations, we found solutions that correctly solve for the reflected and transmitted energy coefficients **R** and **T** while considering absorption as a factor in the thin-film layers.

Spectrophotometer measurements of various pellicles and illumination configurations agree well with the model predictions. Figure 2(a) shows agreement between the predicted and measured transmission of a 2.2-μm-thick pellicle at a 45° angle of incidence with unpolarized light. Figure 2(b) results led to the replacement of one of the coated BK7 substrate beam splitters.

The imaginary component of the index for nitrocellulose was included in the model so the effect of absorption on reflectivity and transmission at shorter wavelengths could be investigated. The transmission measurement of a 2.5-μm-thick nitrocellulose pellicle was used in conjunction with modeling to estimate the absorption coefficient, κ. These results are shown in Fig. 3.

A thin-film model was used in conjunction with transmission and reflection measurements of pellicles at UV and visible wavelengths to determine the absorption coefficient for nitrocellulose from 220 nm to 1.2 μm. When exploring the experimental setup of propagating high-power laser pulses through optical mediums, such as a pellicle beam splitter, understanding the absorption is crucial to understanding the properties in the UV to NIR. Future applications and explorations include a more-accurate determination of the complex index of refraction and its performance.

This material is based upon work supported by the Department of Energy National Nuclear Security Administration under Award Number DE-NA0003856, the Department of Energy Office of Science under Award Numbers DE-SC0016253 and DE-SC0021057, the University of Rochester, and the New York State Energy Research and Development Authority.

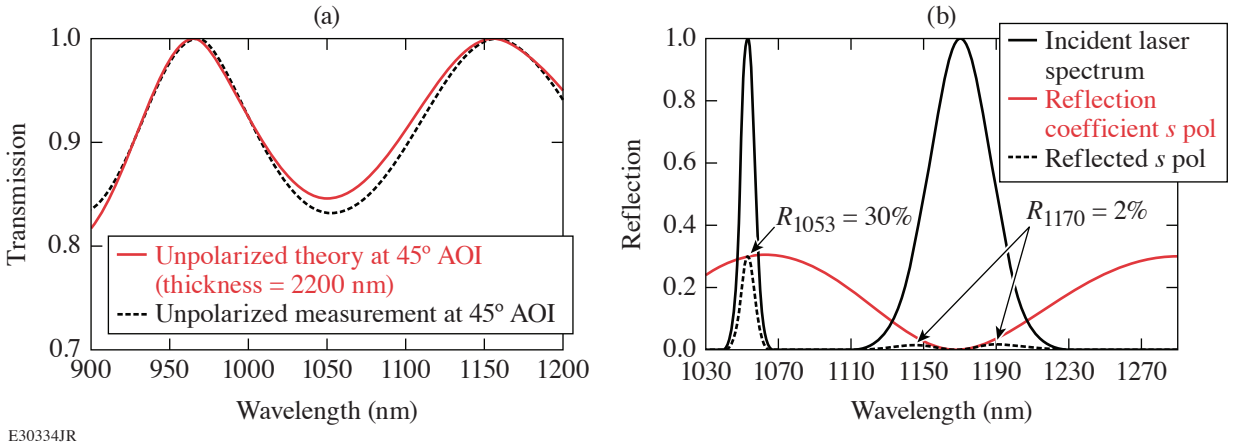

Figure 2
(a) Model prediction and measurement. Transmission of unpolarized light at a 45° angle of incidence (AOI) through a 2.2-μm-thick nitrocellulose pellicle. (b) Pellicle beam-splitter replacement. Reflection of *s*-polarized light at a 45° AOI through a 2.2-μm-thick nitrocellulose pellicle.

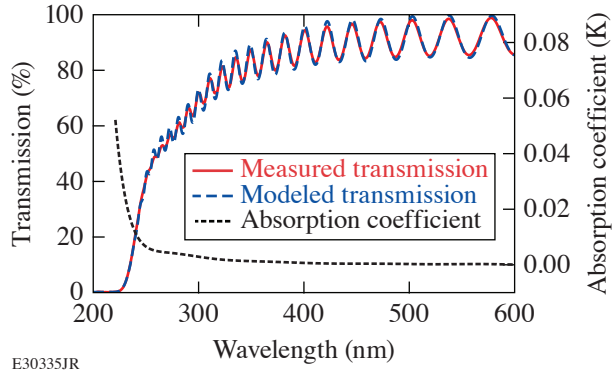

Figure 3
Measured and modeled pellicle transmission with absorption. Transmission of unpolarized light at normal incidence through a 2.2-μm-thick nitrocellulose pellicle and the absorption coefficient κ used in the modeling.

1. M. Kimmel *et al.*, Proc. SPIE **7132**, 71321O (2008).
2. A. Thelen, *Design of Optical Interference Coatings*, McGraw-Hill Optical and Electro-Optical Engineering Series (McGraw-Hill, New York, 1989).

Petawatt Laser Systems

L. J. Waxer, J. Bromage, B. E. Kruschwitz

Laboratory for Laser Energetics, University of Rochester

Since lasers were first demonstrated,[1] researchers have endeavored to increase their focused intensity (power/unit area). Within a few years, the demonstration of Q-switching[2] and then mode locking[3–7] significantly increased the peak power of lasers. However, the following two decades saw little progress in achieving substantially higher peak powers. Then, in 1985, the first demonstration of chirped-pulse amplification (CPA)[8] paved the way for dramatic increases in the peak power of lasers and their accompanying focused intensity. Today, peak powers as high as 10^{16} W or 10 PW (Ref. 9) and focused intensities of 10^{23} W/cm^2 (Ref. 10) have been demonstrated in the laboratory.

The ability to achieve these intensities in the laboratory creates extreme conditions that make possible, for example, the study of high-density laser–plasma interactions, the generation of beams of particles (electrons, positrons, neutrons, protons) and radiation (x ray, gamma ray), particle acceleration, the study of quantum vacuum interactions, and science on an attosecond time scale.[11] These opportunities have spurred an enormous international effort to build high-intensity laser facilities that support a large variety of scientific endeavors.[12] The authors have written an e-book for the SPIE Spotlight Series that introduces the reader to the laser science and technology underpinning petawatt laser systems, hopefully providing an appreciation of the substantial technological advances required to achieve today's state-of-the-art high-intensity laser system performance. This summary provides an overview of the various topics covered by the Spotlight e-book.

An overview of the building blocks of a petawatt laser system is shown in Fig. 1. CPA-based petawatt laser systems begin with seed pulses that are generated from mode-locked laser cavities employing broadband gain media such as titanium-doped sapphire or neodymium-doped glass. Depending on the performance requirements and the specific architecture of the petawatt laser system, conditioning that improves pulse contrast, shapes the spectrum to overcome gain narrowing, or uses the pulse itself to generate ultrabroadband light via nonlinear processes that serve as the seed for the system are employed prior to amplification. This work reviews broadband materials, common mode-locking methods, and various pulse-conditioning techniques utilized in petawatt laser systems.

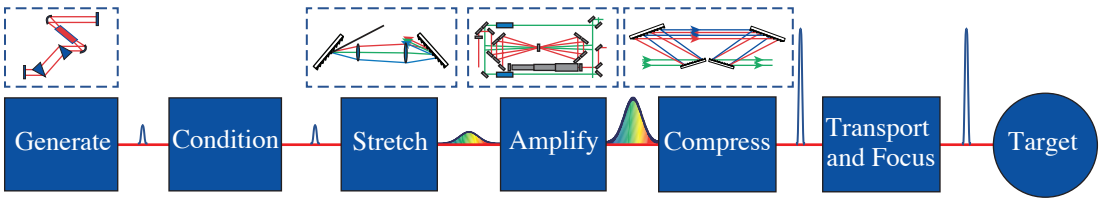

Figure 1
Building blocks of a petawatt laser system incorporating the CPA architecture.

To reach petawatt-level peak powers, these seed pulses require eight to nine orders of magnitude of amplification. Nonlinear optical effects and optical damage, however, significantly limit the ability to directly amplify ultrashort laser pulses. CPA first stretches a broadband pulse in time so that the peak power inside the amplifier is significantly reduced, thus avoiding destructive

nonlinear effects. Then after amplification, the pulse is recompressed back to near its original duration, generating a high-energy ultrashort pulse. We introduce the reader to the effects of dispersion on ultrashort pulses and how dispersion is used to stretch and compress the duration of these pulses. Nonlinear effects relevant to high-power laser systems are described along with a discussion of how one determines the minimum stretched pulse width required to safely achieve a particular output energy. Finally, we review the design of pulse stretchers, compressors, and considerations necessary to minimize the final output pulse width.

There are currently two approaches that have been demonstrated for generating petawatt laser pulses. One produces 150- to 1000-J pulses with durations between 150 and 1000 fs (10^{-15} s). The other generates much shorter pulses (~20 to 30 fs) with tens to hundreds of joules of energy. In either case, broadband amplifiers are required to safely generate the required energy while simultaneously maintaining sufficient bandwidth of the pulse. Two basic types of amplifiers have been developed; one uses energy-storage laser media that are optically energized or "pumped," and the other uses nonlinear crystals to mediate the exchange of energy from a high-energy narrowband pump pulse to a weaker broadband seed. We describe the principles of both types, how they can be combined using the relative strengths of each to form "hybrid" systems, and considerations for scaling to higher *average* powers (e.g., increased repetition rates) and future approaches.

Delivering petawatt laser peak powers to a target would not have been possible without large-aperture optics that have both broadband reflectivity (or diffraction efficiency) and high damage thresholds. This necessitated significant technological development to produce compressor diffraction gratings and transport mirrors that met these requirements while maintaining high wavefront quality for tight focusing. Even with high damage thresholds, the highest-energy petawatt laser systems motivated the development of fabrication techniques that could deliver the above qualities at meter-scale apertures. Since they are critical components of these laser systems, gold and broadband multi-dielectric coating development, large-aperture manufacturing, and issues of damage are reviewed.

Equally important is the ability to control and diagnose the performance of the laser system. Optimal recompression of the amplified pulse requires accurate *characterization* of the output pulse and fine *control* of the relative phase of the spectral components based on these measurements. Realizing the maximum intensity on target requires near-diffraction-limited focusing. Achieving this entails accurate focal-spot characterization, preferably at the target location, and the ability to manipulate the wavefront of the on-target beam. We review techniques for phase measurement and control in both the spectral and spatial domains, and introduce the reader to spatiotemporal couplings, which span both domains.

For most of the science enabled by petawatt laser systems, it is the peak *intensity* on target that is the critical parameter, not the peak power. This makes the final focusing of the laser a key consideration in the system design. Although minimizing wavefront aberrations and spatiotemporal couplings in the front end, amplifiers, and pulse compressor is critical to preserve the focusability of the laser beam, ultimately the focal spot size is defined by the parameters and performance of the final focusing optics. We discuss large-aperture, low-*f*-number off-axis parabolas that are used to achieve small focal areas, schema to protect high-value final optics from target debris, methods for improving on-target pulse contrast at the back end of the system, techniques to characterize the *in-situ f*ocal spot size at the target location, and future prospects for increasing on-target intensity.

The journey from the first demonstration of lasing action to the realization of 10-PW laser pulses took 60 years and significant technological development. Today, there are petawatt-class laser facilities all over the world (see ICUIL website[13]) with many more in the design and construction phase. These facilities make possible scientific explorations that were previously unachievable in the laboratory. This work introduces the reader to the laser science, engineering, and technology required to successfully deliver the highest focused intensities on Earth.

This material is based upon work supported by the Department of Energy National Nuclear Security Administration under Award Number DE-NA0003856, the University of Rochester, and the New York State Energy Research and Development Authority.

1. T. H. Maiman, Nature **187**, 493 (1960).
2. F. J. McClung and R. W. Hellwarth, J. Appl. Phys. **33**, 828 (1962).

3. A. Yariv, J. Appl. Phys. **36**, 388 (1965).
4. A. J. DeMaria, D. A. Stetser, and H. Heynau, Appl. Phys. Lett. **8**, 174 (1966).
5. M. DiDomenico, Jr., J. Appl. Phys. **35**, 2870 (1964).
6. L. E. Hargrove, R. L. Fork, and M. A. Pollack, Appl. Phys. Lett. **5**, 4 (1964).
7. H. W. Mocker and R. J. Collins, Appl. Phys. Lett. **7**, 270 (1965).
8. D. Strickland and G. Mourou, Opt. Commun. **56**, 219 (1985).
9. C. Radier *et al*., High Power Laser Sci. Eng. **10**, e21 (2022).
10. J. W. Yoon *et al*., Optica **8**, 630 (2021).
11. The National Academies of Sciences, Engineering, and Medicine, *Opportunities in Intense Ultrafast Laser: Reaching for the Brightest Light* (The National Academies Press, Washington, DC, 2018), p. 346.
12. C. N. Danson *et al*., High Power Laser Sci. Eng. **7**, e54 (2019).
13. Intense Laser Labs World Wide, Accessed 27 March 2023, https://www.icuil.org/activities/laser-labs.html.

LLE's Summer High School Research Program

R. S. Craxton

Laboratory for Laser Energetics, University of Rochester

During the summer of 2022, 16 students from Rochester-area high schools participated in the Laboratory for Laser Energetics' Summer High School Research Program (Fig. 1). This was the 33rd year of the program, which started in 1989. The 2020 program was unfortunately canceled because of the pandemic. In 2021, LLE held a fully virtual program for students who had applied and been interviewed for the 2020 program, and in 2022 LLE was able to return to a normal, in-person program.

I3194JR

Figure 1
Front Row: Cameron Ryan, Alisha Upal, Dr. Stephen Craxton, Grace Wu, Rick Zhou; Middle Row: Jackson McCarten, John Giess, Elizabeth Norris, Jenny Zhao, Samuel Gray, David Villani, Jayden Roberts, Olivia Fietkiewicz; Back Row: Arjun Patel, Sara Davies, Vinay Pendri, and Micah Kim.

The goal of LLE's program is to excite a group of highly motivated high school students about careers in the areas of science and technology by exposing them to research in a state-of-the-art environment. Too often, students are exposed to "research" only through classroom laboratories, which have prescribed procedures and predictable results. In LLE's summer program, the students experience many of the trials, tribulations, and rewards of scientific research. By participating in research in a real environment, the students often become more excited about careers in science and technology. In addition, LLE gains from the contributions of the many highly talented students who are attracted to the program.

The students spent most of their time working on their individual research projects with members of LLE's technical staff. The projects were related to current research activities at LLE and covered a broad range of areas of interest including experimental

diagnostic development, computer modeling of implosion physics, physical and computational chemistry, laser physics, optical engineering, terahertz radiation, future laser system design, and scientific data management (see Table I).

The students attended weekly seminars on technical topics associated with LLE's research. Topics this year included laser physics, fusion, nonlinear optics, fission energy, pulsed power, fiber optics, and LLE's cryogenic target program. The students also received safety training, learned how to give scientific presentations, and were introduced to LLE's computational resources.

Table I: High School Students and Projects—Summer 2022.

Name	High School	Supervisor	Project Title
Sara Davies	Pittsford Sutherland	R. S. Craxton	Direct-Drive Uniformity Calculations for a Future High-Gain Laser Facility
Olivia Fietkiewicz	Mercy	S. Bucht	Measuring the Mode Field Diameter of Single-Mode Fibers Using the Knife-Edge Technique
John Giess	McQuaid	V. N. Goncharov and K. M. Woo	Mitigating Hydrodynamic Instabilities in the Deceleration Phase of Inertial Confinement Fusion
Samuel Gray	Brighton	W. T. Shmayda and E. Dombrowski	Characterizing a Cryosorption Pump for Collecting Tokamak Exhausts
Michah Kim	Home School	D. W. Jacobs-Perkins	Design, Fabrication, and Testing of a 3-D–Printed Optomechanical Assembly for the MIFEDS Coil Characterization Station
Jackson McCarten	Webster Schroeder	B. N. Hoffman and K. R. P. Kafka	Viability Testing of Polymer Coating for Optical Cleaning Applications
Elizabeth Norris	Brighton	M. D. Wittman	Determining the Absorption Efficiency of a Flow-Through Pd-Bed as a Function of Initial $^4He:D_2$ Ratio and Flow Rate
Arjun Patel	Brighton	D. Chakraborty and R. Sobolewski	Terahertz Time-Domain Characterization of Biological Tissues Modeled Using COMSOL Multiphysics
Vinay Pendri	Pittsford Mendon	K. L. Marshall	Computational Modeling of Electron Density Polarization in Liquid Crystals Using Time-Dependent Density Functional Theory
Jayden Roberts	Brockport	S. T. Ivancic	Investigation of Microwave-Induced Chemical Etching
Cameron Ryan	McQuaid	R. W. Kidder	Containerized Application Management for Cloud-Based Scientific Analysis
Alisha Upal	Pittsford Sutherland	R. S. Craxton	Development of a National Ignition Facility Laser Configuration with X-Ray Backlighting of a Foam Ball Target
David Villani	Harley School	M. J. Guardalben	Energy Prediction on the OMEGA EP Laser System Using Neural Networks
Grace Wu	Pittsford Mendon	I. A. Begishev	Measurement of the Refractive Index of KDP and ADP Crystals at Low Temperatures
Jenny Zhao	Pittsford Mendon	K. L. Marshall and N. D. Urban	Chiroptical Properties and Mesophase Stability of Saturated Chiral Dopants for High-Peak-Power Liquid Crystal Device Applications
Rick Zhou	Brighton	W. T. Shmayda and M. Sharpe	Measuring the Performance of Molecular Sieve Driers

The program culminated on 24 August with the "High School Student Summer Research Symposium," at which the students presented the results of their research to an audience including parents, teachers, and LLE staff. The students' written reports will be made available on the LLE Website and bound into a permanent record of their work that can be cited in scientific publications.

Four hundred and fifteen high school students have now participated in the program. This year's students were selected from just under 40 applicants.

At the symposium, LLE presented its 24th annual William D. Ryan Inspirational Teacher Award to Mrs. Dawn Knapp, a mathematics teacher at Victor High School. This award is presented to a teacher who motivated one of the participants in LLE's Summer High School Research Program to study science, mathematics, or technology and includes a $1000 cash prize. Teachers are nominated by alumni of the summer program. Mrs. Knapp was nominated by Semma Alfatlawi, a participant in the 2021 program. In her nomination letter, Semma recalled her first encounter with Mrs. Knapp: "As I enter her room for the first time, I am immediately greeted with elation and a smile. I look around at all the perseverance posters and math jokes... her voice echoing through the room as she excitedly welcomes her new students... and immediately conclude that this is going to be a life-changing class. I have never seen another teacher like Mrs. Knapp." She observed that Mrs. Knapp noticed her yearning for math knowledge and "broadened it like no one had before." She found that "the combination of her devotion to teaching and fascination with math makes her an immediate role model to all her students." She cited open discussions in class about math problems that "brought laughter and human connections along with it, and showed me how community and education go hand in hand to reward people through cooperation as well as increasing intelligence and the ability to problem solve." In conclusion, Semma stated: "Thinking about my experiences with Mrs. Knapp never ceases to brighten my day… I will carry the life lessons that Mrs. Knapp has taught me as I continue to grow, and will never forget how much a warm smile and excitement for education can brighten the future."

This material is based upon work supported by the Department of Energy National Nuclear Security Administration under Award Number DE-NA0003856, the University of Rochester, and the New York State Energy Research and Development Authority.

2022 BEST Student and Teacher Research Program

T. J. Kessler, M. Romo-Gonzalez, and R. Ghosh

Laboratory for Laser Energetics, University of Rochester

The primary goal of the Broad Exposure to Science and Technology (BEST) Research Program is to engage teachers and students from historically marginalized experiences in various aspects of science and technology that support LLE's laser science and applications research.[1] This broad exposure helps guide students in their pursuit of science, technology, engineering, and math (STEM) fields and encourages them to explore the next generation of related jobs and careers. The BEST Program was carried out at East High School within the Rochester City School District (RCSD) during the summer of 2022. Five students and two teachers participated in this research experience over a six-week period during the months of July and August. Students were also given credit toward high school graduation through the Work-Based Learning Program sponsored by the RCSD.

I3187JR

Figure 1
The students and teachers who participated in the 2022 BEST program included (left to right); Terry Kessler [LLE DEI (Diversity, Equity, and Inclusion) Manager], Nigel Copeland (East High), Tiketa Thomas (Rochester Early College), Isis Wearing (Johanna Perrin Middle School), Olivia Galloway [YWCP (Young Women's College Prep)], Chavon Phelps (YWCP, teacher), Bre'Ay'zha White (YWCP), Trent Russell (East High teacher), and Marco Romo-Gonzalez (LLE DEI Deputy Manager).

Multi-faceted scientific institutions, such as UR/LLE, employ a wide variety of professionals to carry out a diverse set of research and development activities. Each of these research activities requires support teams consisting of professionals who

contribute their expertise to ensure a thriving research program. Exposure to the members of the LLE community provides the students and teachers with an understanding of the broad range of research activities as well as the rich diversity of individual professionals that enable successful research programs.

A team of LLE volunteers worked with the BEST students and teachers in a variety of science, technology, skilled trade, and technical communication fields. Twenty volunteers spent between one and two days at East High school over the six-week period. These volunteers, experts in their field, were able to bring detailed information, coupled with hands-on opportunities, into the high school laboratory environment.

The teachers and students were exposed to many different areas of science and technology research including laboratory safety, optical microscopy, spectroscopy, magnetic technology, illustrations and graphic design, light polarization and liquid crystal applications, high-energy-density physics (HEDP), diffraction grating applications, electrical technology, building operations and maintenance, optical system alignment, database applications, acoustics, code development, and laser holography. The importance of engineering support for research, including chemical, electrical, mechanical, optical, and computer engineering, together with support from facilities groups and graphics experts, were emphasized to highlight the extensive teamwork required to make scientific advancements and be able to communicate the results (see Fig. 2).

I3191JR

Figure 2
Members of the Publications and Illustrations department at LLE, Heather Palmer (near monitor), Mike Franchot (near board at right), and Jenny Hamson (far right) are shown instructing the BEST students and teachers on the principles of technical communication through graphical illustrations.

One of the areas of science that is central to fusion science is electricity and magnetism, especially electromagnetic waves or light. Both laser fusion and magnetic fusion are studied around the world to eventually harness the vast resource of nuclear energy. In addition, many technological applications involve electromagnetic systems and the electromagnetic spectrum. Bob Boni, research engineer, taught the BEST group to use the magnetic compasses in their cell phones to locate magnets hidden around the classroom and to build and test electric motors (Fig. 3).

(a) (b)

I3188JR

Figure 3
(a) Deputy Diversity Manager, Marco Romo-Gonzalez and research engineer, Bob Boni are shown working with students Isis Wearing and Bre'Ay'zha White to construct electric motors. (b) Bre'Ay'zha is shown examining the operation of a completed motor.

Spectrometers are used to study of the absorption and emission of light and other radiation by matter. There are numerous applications of spectroscopy at LLE, including optical material composition analysis, light-scattering investigations, and the study of laser–matter interaction. Jeremy Pigeon, scientist in the Plasma and Ultrafast Laser Science and Engineering Group, worked with students and teachers to construct a cell-phone spectrometer. Stavros Demos, Group Leader of Optical Materials Technology, activated a spectrometer for the students to measure the wavelength transmission of optical filter glass. Spectroscopy reliably engages the curious mind into the many wonders of light (Fig. 4).

(a) (b)

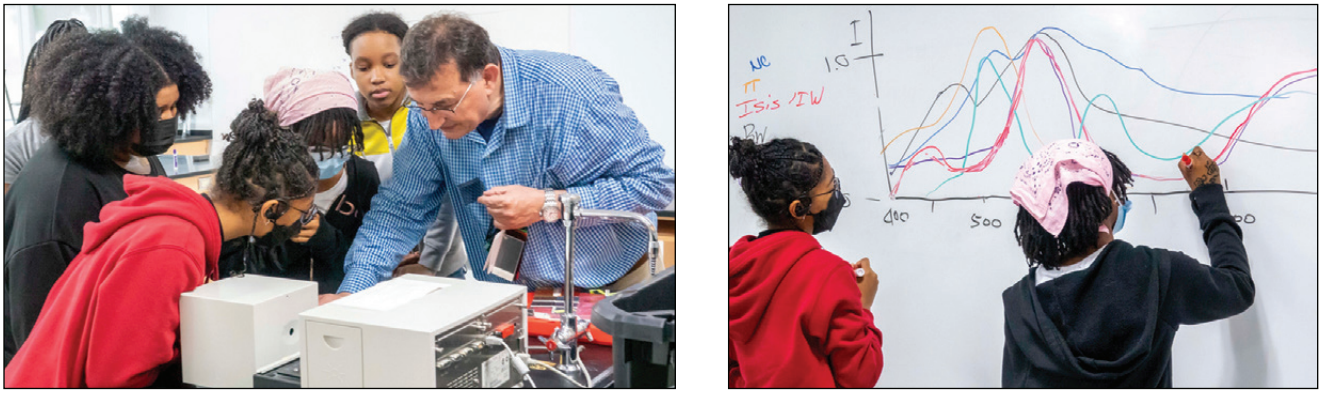

I3189JR

Figure 4
(a) Senior scientist, Stavros Demos, is shown demonstrating use of a spectrometer to measure the wavelength-dependent transmission of glass filters. (b) BEST students Tiketa Thomas and Isis Wearing are shown plotting the observed transmitted spectra for one of the color filters.

In this second year of LLE's BEST Program, aspects of theoretical physics and computation were introduced in ways that engaged the students and teachers. Theoretical physicist, Duc Cao, provided instructive examples of computer code development while Suxing Hu, Group Leader of HEDP Theory, shared his personal career path from grade school to graduate school and his professional experiences. In addition, graduate students from the University of Rochester's physics department developed a series of demonstrations to simulate superconductivity and compressed matter without the danger associated with very cold and very hot conditions (Fig. 5).

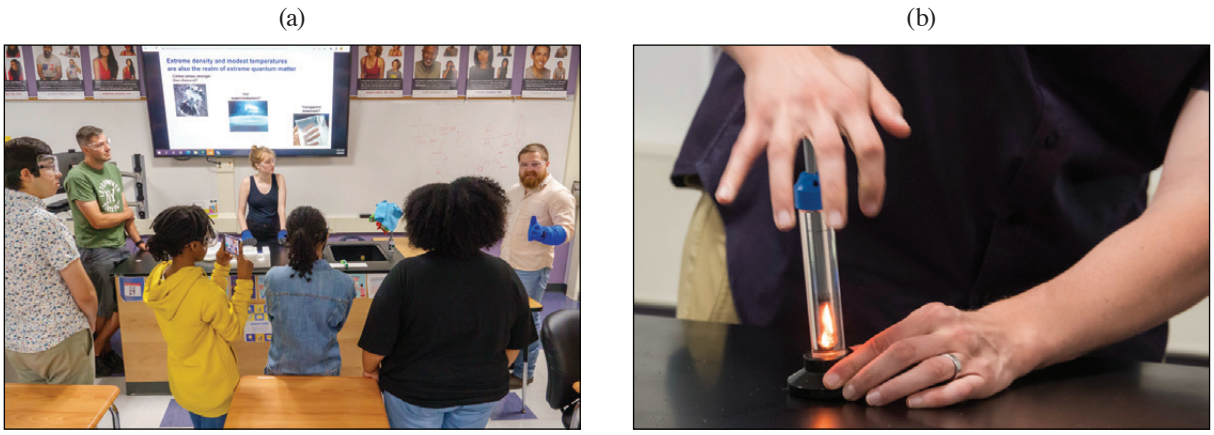

Figure 5
(a) Graduate students Maggie Huff and Gerrit Bruhaug (wearing blue gloves) demonstrate magnetic effects under extremely cold temperatures. (b) Graduate student David Bishel is shown igniting cotton strands by compressing the air with a plunger in a sealed glass cylinder.

The BEST participants visited LLE three times during the summer program to tour the OMEGA lasers, optical manufacturing facilities, and other support laboratories (Fig. 6). Together, the students and teachers were exposed to elements of science and technology that underscored the importance of their STEM high school curricula. Laboratory Director, Chris Deeney, emphasized the importance of STEM education and the numerous areas of employment in the DOE/NNSA complex. In addition, the BEST group participated in tours of optics and imaging related departments at Monroe Community College, the Rochester Institute of Technology, and the University of Rochester.

Figure 6
(a) During one of the visits to LLE, the BEST program participants met with the LLE Director, Chris Deeney (left), to learn about the scientific mission of the laboratory and the variety of staff careers that form a successful research team. (b) During another visit to LLE, the students and teachers were exposed to many of the trades needed to build and maintain a large laboratory complex. Nate Heckman (Facilities Group) is shown bending an electrical conduit with student Olivia Galloway.

Throughout the following school year, the students and teachers of the BEST Program serve as ambassadors for outreach to other students enrolled at RCSD high schools. They created a PowerPoint presentation showing the broad range of science and technology topics included in the program. In addition, a photomontage video was created to show the relationship between the BEST Program experiences and the wide variety of work activities carried out at LLE. The images for the photomontage were generated by LLE photographer, Eugene Kowaluk, and by several of the program participants.

On the last day of the six-week schedule, LLE mentors joined the students and teachers to celebrate completion of the 2022 BEST research program and to share their broad exposure to science and technology with family members (Fig. 7). The attendees had the opportunity to describe their roles in the program and to highlight their area of interest. In planning for the 2023 BEST program, students from several additional RCSD high schools are being invited to participate in this unique learning experience.

I3193JR

Figure 7
Members of the LLE staff, students, teachers, and parents assembled in front of the teaching monitor and "Google Board" on which questions are posted each day for further investigation.

1. T. J. Kessler, LLE Review Quarterly Report **169** (2021).

FY22 Q4 Laser Facility Report

J. Puth, M. Labuzeta, D. Canning, and R. T. Janezic

Laboratory for Laser Energetics, University of Rochester

During the fourth quarter of FY22, the Omega Facility conducted 331 target shots on OMEGA and 202 target shots on OMEGA EP for a total of 533 target shots (see Tables I and II). OMEGA averaged 10.3 target shots per operating day, averaging 91.1% Availability and 94.1% Experimental Effectiveness. OMEGA EP averaged 7.7 target shots per operating day, averaging 92.8% Availability and 93.1% Experimental Effectiveness.

Table I: OMEGA Laser System target shot summary for Q4 FY22.

Program	Laboratory	Planned Number of Target Shots	Actual Number of Target Shots
ICF	LLE	88	70
	LLNL	22	23
ICF Subtotal		110	93
HED	LLE	22	20
	LANL	44	48
	LLNL	27.5	20
HED Subtotal		93.5	88
LBS	LLE	22	16
	PPPL	11	10
	SLAC	11	7
LBS Subtotal		44	33
APL		11	10
CEA		27.5	29
NLUF		44	44
OFES		11	14
Calibration	LLE	0	20
Grand Total		341	331

APL: Applied Physics Labs (Johns Hopkins University)
CEA: Commissariat à l'énergie atomique aux énergies alternatives
NLUF: National Laser Users Facility
OFES: Office of Fusion Energy Sciences

Table II: OMEGA EP Laser System target shot summary for Q4 FY22.

Program	Laboratory	Planned Number of Target Shots	Actual Number of Target Shots
ICF	LLE	17.5	19
	LLNL	21	23
	NRL	7	8
ICF Subtotal		45.5	50
HED	LLE	21	27
	LANL	7	7
	LLNL	31.5	33
HED Subtotal		59.5	67
LBS	LLE	3.5	3
	LLNL	7	13
LBS Subtotal		10.5	16
CMAP		7	10
LaserNetUS		7	7
NLUF		35	42
Calibration	LLE	21	10
Grand Total		185.5	202

CMAP: Center for Matter at Atomic Pressures

Groundbreaking for the LLE Building Expansion

M. J. Shoup III

Laboratory for Laser Energetics, University of Rochester

Groundbreaking to celebrate the construction of the new addition to the LLE Complex occurred on 17 August with representatives from federal, state, and local offices; University senior leadership; and LLE (Fig. 1).

Figure 1
(a) Artist rendering of LLE building expansion. (b) Groundbreaking ceremony. Shown from left to right: Senior Associate Vice President for Facilities and Services, Michael Chihoski; Provost, David Figlio; Brighton Town Supervisor, Bill Moehle; New York State Senator, Jeremy Cooney; Executive Vice President of Administration and Finance and CFO, Elizabeth Milavec; University Trustee, Larry Kessler; University Trustee, Wayne LeChase; New York State Representative, Sarah Clark; LLE Director, Chris Deeney; University of Rochester President, Sarah Mangelsdorf; U.S. Congressman, Joe Morelle; Deputy State Director for U.S. Senator Kirsten Gillibrand, Jarred Jones; Director of Economic Development, New York State Energy Research and Development Authority (NYSERDA), Kevin Hale; and University of Rochester Interim Vice President for Research, Stephen Dewhurst.

Initial planning work for the project began in 2019. In January 2020, the Board of Trustees Committee on Facilities approved entering into a contract for the design of the addition at a cost of $3,538,700. Design work kicked off in November 2020 and was completed in March 2022. For construction, four bids were solicited and two competitive bids were received, with LeChase Construction being the lowest bidder. The University entered into a Guaranteed Maximum Price contract with LeChase Construction for the addition. The total cost of this project will not exceed $42,265,736, inclusive of previously approved design costs.

Achieving permitting approval for the project with the Town of Brighton was an unexpectedly difficult and drawn out process. A primary sticking point was a conservation easement to accommodate a vernal pond on the LLE site. Diligent efforts by LLE

staff, Nixon Peabody, and the Office of Government and Community Relations were ultimately successful in finding a mutually agreeable solution; however, the start of construction was slightly delayed. The final approval for this project also accounts for a potential future EP-OPAL expansion.

The new 66,600-sq.-ft, three-floor building will house laboratory and office space for approximately 110 scientists and LLE personnel and includes a class-1000 target fabrication laboratory and thin-film coating laboratory, a laser computing facility, and several other wet laboratory and general laboratory spaces. The largest laboratory space will house the AMICA Laser System—a state-of-the-art, high-energy, long-pulse laser that scientists at LLE are assembling for Stanford University's SLAC National Accelerator Laboratory Matter at Extreme Condition Upgrade (MEC-U).

A team consisting of 23 local companies was contracted and mobilized to start the building construction project. Site clearing began on 5 July 2023 and progressed into foundation work through September 2023 (see Figs. 2–4). Over that three-month period the site was cleared and graded, and foundation work was started. Exceptional weather allowed the team to perform better than originally scheduled. Although it is early in the construction project, the team is still on track for a March 2024 completion.

Figure 2
The second day of site clearing on 6 July 2023.

Figure 3
Foundation work in full swing at the end of September 2023.

Figure 4
Footers being poured for the perimeter of the new building.

FY22 Laser Facility Report

J. Puth, M. Labuzeta, D. Canning, R. T. Janezic, G. Pien, and S. T. Ivancic

Laboratory for Laser Energetics, University of Rochester

Under the facility governance plan, experimental time at the Omega Laser Facility is allocated to four NNSA-supported programs: Inertial Confinement Fusion (ICF), High-Energy Density (HED), National Laser Users' Facility (NLUF), and Laboratory Basic Science (LBS). FY22 will be the final year under these programs; beginning in FY23 the allocation will be determined by the combined HED Council per guidance from the NNSA Office of Experimental Science.

During FY22, the Omega Laser Facility conducted 1233 target shots on OMEGA and 889 target shots on OMEGA EP, with a total of 2122 target shots (see the shot summaries for OMEGA and OMEGA EP in Tables I and II, respectively). The ICF and HED Programs conducted 60% of the NNSA-supported facility shots in FY22. More than half of these experiments were conducted by scientists from Lawrence Livermore National Laboratory (LLNL), Los Alamos National Laboratory (LANL), Sandia National Laboratories (SNL), and the Naval Research Laboratory (NRL). About 6% of the facility shots were used to maintain operational effectiveness. The NLUF and LBS programs described below conducted 15% of the NNSA target shots. The facility also delivered 199 shots ($\sim$9% of the total) for external users who purchased the shot time. Overall, externally led investigators used 59% of the facility time. (See Figs. 1 and 2 for the fractional use by the various programs, including shot time that was purchased by outside users for OMEGA and OMEGA EP, respectively).

OMEGA investigators rated the overall experimental effectiveness of the facility at 93.4%, while OMEGA EP was rated at 94.2%. OMEGA averaged 11 target shots per day, averaging 91.9% Availability. OMEGA EP averaged nine target shots per day, averaging 92.5% Availability.

During Q4, construction of the new laboratory and office space at LLE required additional effort to mitigate the effects of construction vibrations that will continue in FY23. The Shot Director was able to contact the construction manager to halt problematic vibrations for the final preparations and shot cycle. Construction can occasionally impact availability but has been effectively minimized by planning and procedure.

In FY22, the facility continued to evolve to meet the needs of the scientific community.

To achieve higher uniformity in the pulse power balance, LLE built a laser diagnostic to passively measure the transmission of each beamline. This diagnostic has helped to identify degraded optics and will be systematically employed in the future to decrease the effort required to balance beamline energetics.

The magneto-inertial fusion electrical discharge system (MIFEDS) was significantly redesigned to improve the high-voltage safety and increase reliability and efficiency of operations.

Table I: OMEGA Laser System target shot summary for FY22.

Program	Laboratory	Number of Campaigns	Planned Number of Target Shots	Actual Number of Target Shots
ICF	LLE	33.5	368.5	346
	LANL	3	33	35
	LLNL	4.5	49.5	46
	SNL	1.5	16.5	14
ICF Subtotal		42.5	467.5	441
HED	LLE	9	99	91
	LANL	9	99	106
	LLNL	12	132	117
	SNL	2	22	23
HED Subtotal		32	352	337
LBS	LLE	4	44	34
	LLNL	6.5	71.5	74
	PPPL	1	11	10
	SLAC	1	11	7
LBS Subtotal		12.5	137.5	125
NLUF		13.5	148.5	153
AIBS		2	22	17
CEA		3	33	35
APL		3	33	36
CMAP		1	11	8
OFES		1	11	14
Calibration		0	0	67
Grand Total		110.5	1215.5	1233

AIBS: Academic and Industrial Basic Science
APL: Applied Physics Labs (Johns Hopkins University)
CEA: Commissariat à l'énergie atomique aux énergies alternatives
CMAP: Center for Matter at Atomic Pressures
NLUF: National Laser Users Facility
OFES: Office of Fusion Energy Sciences
PPPL: Princeton Plasma Physics Laboratory

New diagnostics and upgrades to diagnostics in the LLE inventory continue to increase the breadth of measurements that can be achieved. Many of these projects are conceived and led by external laboratory researchers. Ten diagnostic upgrade projects were completed in FY22 including:

- Talbot–Lau x-ray deflectometer upgrade [led by Johns Hopkins University (JHU)]
- Applied Physics Lab fast accumulating radiometer diagnostic suite upgrades (led by JHU)
- gas Cherenkov detector modified with Ti puck (led by LANL)
- copper activation sampling (led by LLNL)
- scattered-light diode (led by LLNL)
- vacuum Cherenkov detector (led by LLNL)
- MiniDMX upgrade (data acquisition system and detector array) (led by CEA)

Table II: OMEGA EP Laser System target shot summary for FY22.

Program	Laboratory	Number of Campaigns	Planned Number of Target Shots	Actual Number of Target Shots
ICF	LLE	13	91	119
	LLNL	9	63	67
	NRL	2	14	17
	SNL	1	7	6
ICF Subtotal		25	175	209
HED	LLE	8	56	67
	LANL	6	42	53
	LLNL	18.5	129.5	157
	SNL	1	7	10
HED Subtotal		33.5	234.5	287
LBS		3.5	24.5	39
		4.5	31.5	54
		1	7	6
LBS Subtotal		9	63	99
NLUF		17.5	122.5	144
CEA		1	7	8
LaserNetUS		4	28	34
CMAP		5	35	47
Calibration	LLE	3	21	61
Grand Total		98	686	889

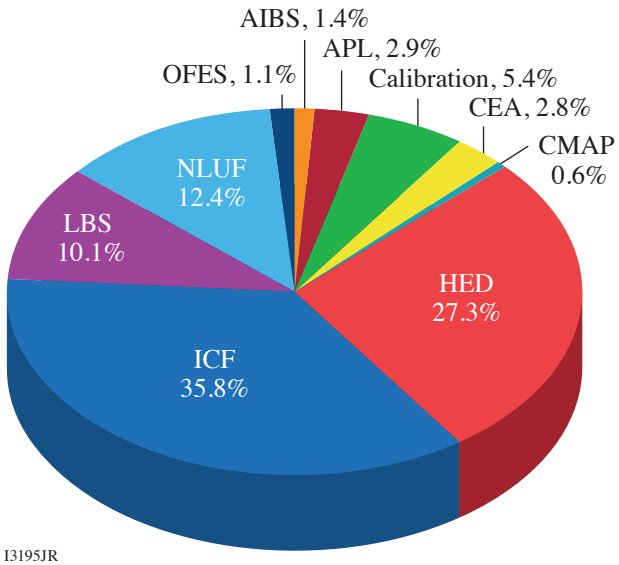

Figure 1
Fractional breakdown of FY22 shots on OMEGA by NNSA-supported programs.

- transmission grating spectrometer image-plate modification (led by NRL)
- scattered-light uniformity instrument (led by LLE)
- THz background energy measurement diagnostic (led by LLE)

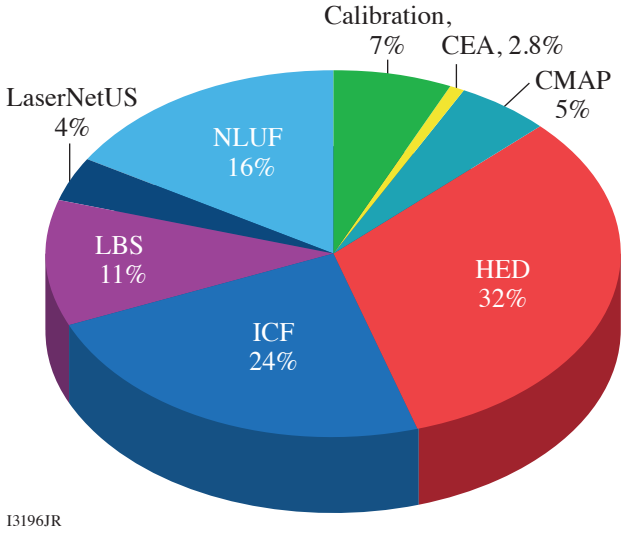

Figure 2
Fractional breakdown of FY21 shots on OMEGA EP by NNSA-supported programs.

Education Summary

M. S. Wei

Laboratory for Laser Energetics, University of Rochester

Education/training is a primary technical mission for LLE. LLE is the only place where students can be trained at scale for careers in national security related to the science of Stockpile Stewardship. The education programs at LLE include a high school research program that exposes students to a professional environment where they work alongside scientists and engineers for a summer; undergraduate programs where students conduct research or work part-time with scientists and engineers often in the summer with some throughout an academic year (or longer) to understand how classroom education is applied to real world problems; graduate education where students are immersed in the science of high energy density (HED) physics and lasers to earn MS and Ph.D. degrees; and a new high school program for underrepresented minority students and their teachers in the local Rochester area. This report provides a summary of these activities in FY22.

Summer High School Research Program

Since 1989, LLE has held the annual Summer High School Research Program for Rochester-area high school students who have just completed their junior year. The eight-week program provides an exceptional opportunity for highly motivated students to experience scientific research in a professional environment. Sixteen students participated in the 2022 program (see p. 54). Four hundred and fifteen students from 55 high schools have participated in the program to date including 143 students who identify as female. Thirty-nine students have become Scholars in the prestigious Regeneron Science Talent Search based on the research projects they carried out at LLE. Many of the students progress to major in science-related disciplines at nationally recognized universities, and more than 100 have now received their doctoral degrees, which was a featured news article by the University of Rochester.[1]

Broad Exposure to Science and Technology Student and Teacher Research Program

Started during FY20 by T. J. Kessler, the LLE Diversity Manager, the goal of the Broad Exposure to Science and Technology (BEST) initiative is to engage underrepresented high school students and their teachers from the Rochester City School District (RCSD) in various aspects of science and technology that support laser science and applications research at LLE. Two RCSD high school science and technology teachers and five high school students participated in this second year of LLE's BEST Program carried out at the RCSD's East High School over the six-week period during the summer of 2022 (see p. 57). A team of 20 LLE volunteers worked with the BEST students and teachers in a greater number of fields, including HED physics, magnetics, acoustics, theoretical physics, database management, graphic design, and the technology trades that support all research activities at LLE. The BEST participants visited LLE three times during the summer program to tour the OMEGA lasers, optical manufacturing facilities, and other support laboratories. The teachers and students of the BEST Program serve as ambassadors for outreach to other students at RCSD high schools, assisting in expanding the number of BEST candidates for the following year. Both an RCSD teacher and student from the 2021 BEST program participated in a visit by the director of the National Science Foundation to UR/LLE during the spring of 2022.

Undergraduate Student Program

Although LLE does not have a formal undergraduate student program, it has provided unique work-study opportunities for undergraduate research and co-op internships by involving undergraduate and community college students in its research activi-

ties. These students come from the University of Rochester, the Rochester Institute of Technology (RIT), the State University of New York (SUNY) at Geneseo, Cornell University, Monroe Community College, and other institutions. LLE scientists also host and mentor students participating in the Research Experience for Undergraduate Program funded by the National Science Foundation, and from 2022 the new Plasma and Fusion Undergraduate Research Opportunity (PFURO) Program funded by the Office of Fusion Energy Sciences. During FY22, 49 undergraduates including 17 co-op students and three PFURO students conducted research and work-study at LLE. To meet increased needs, LLE's undergraduate student program will be expanded into a formal program from FY23 and coordinated by a dedicated new program director.

Graduate Student Program

Graduate students use the Omega Laser Facility as well as other LLE facilities to conduct inertial confinement fusion (ICF) and high-energy-density–physics research to earn advanced degrees. These students make significant contributions to the LLE research output (e.g., they write a large fraction of the manuscripts published annually by LLE). Thirty-five UR faculty members across eight academic departments hold secondary appointments with LLE, increasing the breadth of leadership in science and technology. Sixteen scientists and research engineers at LLE hold secondary faculty appointments with the University in five different academic departments. The large number of faculty and LLE staff enable the Laboratory to pull together a new high-energy-density science (HEDS) curriculum and educate a large number of graduate students. More than 80 UR graduate students were involved in research at LLE in FY22 (see Table I), among which 67 students were directly funded by LLE via the NNSA-supported University of Rochester Frank Horton Fellowship Program. Their research includes theoretical and experimental plasma physics and fusion science, HED physics, x-ray and atomic physics, nuclear physics, material properties under extreme pressure, astrophysics, ultrafast optoelectronics, high-power laser development and applications, nonlinear optics, optical materials and optical fabrication technology, and target fabrication.

In FY22, LLE directly funded graduate/undergraduate research with twelve external academic partners including SUNY Geneseo, RIT, the University of Delaware, Massachusetts Institute of Technology's Plasma Science and Fusion Center, the University of Michigan, the University of Nebraska-Lincoln, the University of Nevada at Reno, Stony Brook University, the University of California at Los Angeles, the University of Alberta, Imperial College London, and Oxford University. These programs involved 22 undergraduate students including 20 from SUNY Geneseo, 19 graduate students, six postdoctoral researchers, eight scientists and research staff, and 17 faculty members.

In addition, LLE has significantly facilitated the education and training of several hundred students and postdoctoral researchers in the HEDP and ICF science areas from other universities through their participation in the National Laser Users' Facility, Laboratory Basic Science, LaserNetUS, and collaborations with LLE and DOE national laboratories. More than 70 graduate students (including 16 mentioned above) from 28 universities (see Table I in the **External Users' Program**, p. 80) and over 40 postdoctoral researchers were involved in these external user-led research projects with experiments conducted at the Omega Laser Facility in FY22.

Sixteen graduate students, including nine from the University of Rochester and seven from other academic institutions have successfully completed their thesis research and obtained Ph.D. degrees in calendar year 2022. Table II lists their name, university, and current employer. Seven of them (44% of the total), including three from UR, joined the NNSA laboratories, five stayed within academia, and four work in the private sector.

1. L. Valich, University of Rochester, Laser Lab Springboards 100-Plus High Schoolers to Doctoral Degrees, Accessed 3 July 2023, https://www.rochester.edu/newscenter/laser-lab-springboards-100-plus-high-schoolers-to-doctoral-degrees-517662/.

Table I: More than 80 graduate students, including 67 LLE-funded UR Frank Horton Fellows (marked by *), conducted research at LLE during FY22.

Student Name	Department	Faculty Advisor	LLE Advisor (if different)	Research Area	Notes
N. Acharya*	ME	J. Shang	D. N. Polsin	Viscosity Measurements in High-Energy-Density Fluids	New Horton Fellow
M. Adams	PA	P.-A. Gourdain/ P. Tzeferacos		Elucidation of Magnetic-Field Generation via Laser-Target Illumination in the Magnetohydrodynamic Framework	Former Horton Fellow; graduated in 2022
M. V. Ambat*	ME	D. H. Froula	J. L. Shaw	First-Light Laser Wakefield Acceleration Experiments on MTW-OPAL	
A. Anand*	PA	J. Carroll-Nellenback		The Role of Exoplanetary Magnetic Fields in Atmospheric Evolution and Habitability	
A. Armstrong*	PA	P. Tzeferacos		Radiative, High-Energy-Density Magnetized Turbulence: Charting the Uncharted Plasma Regimes of Fluctuation Dynamo	
B. Arnold*	PA	S. X. Hu		Developing a Finite-Element Discrete-Variable-Representation–Based Real-Space Density-Function-Theory Code for High-Energy-Density Physics	New Horton Fellow
J. Baltazar*	ME	S. P. Regan	R. C. Shah	Inertial Confinement Fusion Implosion Physics	
Z. Barfield*	PA	D. H. Froula		Heat Transport in High Magnetic Fields	
D. T. Bishel*	PA	G. W. Collins/ J. R. Rygg	P. M. Nilson	X-Ray Spectroscopy of Hot Dense Matter: Plasma Screening of Atomic Orbitals at Atomic Pressures	
G. Bruhaug*	ME	G. W. Collins/ J. R. Rygg	H. G. Rinderknecht/ M. S. Wei	Short-Pulse Laser-Generated Probes for High-Energy-Density Experiments	
S. Cao*	ME	C. Ren	R. Betti	Predicting Hot Electrons for Inertial Confinement Fusion	
D. Chakraborty	ECE	R. Sobolewski		Optics and Imaging	
G. Chen	ECE	R. Sobolewski		Novel Terahertz Sources and Terahertz Time-Domain Spectroscopy: Characterization of Novel Materials	
J. Cheng	MS	R. Sobolewski		Terahertz and Optical Pump–Probe Spectroscopy	
D. A. Chin	PA	G. W. Collins/ J. R. Rygg	P. M. Nilson	X-Ray Absorption Spectroscopy for the Study of Materials Under Extreme Conditions	NNSA Stockpile Stewardship Graduate Fellow (a former Horton Fellow)

Table I: More than 80 graduate students, including 67 LLE-funded UR Frank Horton Fellows (marked by *), conducted research at LLE during FY22 (continued).

Student Name	Department	Faculty Advisor	LLE Advisor (if different)	Research Area	Notes
K. Churnetski*	ME	S. P. Regan	W. Theobald	Three-Dimensional Hot-Spot X-Ray Emission Reconstruction for Mitigation of Low-Mode Asymmetries on OMEGA	
C. Danly	ME	R. Betti		Spatial Measurements of Ion Temperatures of Inertial Confinement Fusion Hot Spots	Technical Advisor: V. Geppert-Kleinrath (LANL)
R. Dent*	CHE	A. Shestopalov	S. G. Demos	Next-Generation Gratings for High-Power Lasers	
J. D'Souza*	PA	P.-A. Gourdain	S. Zhang	Large-Scale High-Energy-Density Simulations with *ab initio* Quality	New Horton Fellow
R. Ejaz*	ME	R. Betti		Understanding the Physics of Areal-Density Degradation in Direct-Drive OMEGA Implosions Through Dedicated Experiments and Statistical Modeling	
I. N. Erez*	PA	P.-A. Gourdain		Achieving High Magnetization with Cylindrically Converging Plasma Flows	New Horton Fellow
M. Evans*	PA	P.-A. Gourdain		The Study of Warm Dense Matter Generated by Pulsed-Power Generators	
P. Farmakis*	ME	R. Betti	R. Betti/ P. Tzeferacos	Three-Dimensional Reconstruction of the Compressed Core in OMEGA Direct-Drive Implosions	
P. Franke*	PA	D. H. Froula		Measuring the Dynamics of Electron Plasma Waves with Thomson Scattering	Graduated in 2022
J. García-Figueroa	CHE	D. R. Harding		Electron Cyclotron Resonance Microwave Chemical Vapor Deposition Method and Its Influence over the Properties of Vapor-Deposited Hydrocarbon Films	Former Horton, graduated in 2022
K. Garriga	OPT	X. C. Zhang		Terahertz Research	
M. Ghosh*	CHE	D. McCamant	S. Zhang	Chemistry of Planetary Materials Under Extreme Pressure and Temperature Conditions	
M. K. Ginnane*	ME	G. W. Collins/ J. R. Rygg		Compressibility, Structure, and Melting of Platinum to 500 GPa	
X. Gong*	ME	G. W. Collins/ J. R. Rygg		Structure and Electronic Properties of Sodium and Potassium at High Pressure	

Table I: More than 80 graduate students, including 67 LLE-funded UR Frank Horton Fellows (marked by *), conducted research at LLE during FY22 (continued).

Student Name	Department	Faculty Advisor	LLE Advisor (if different)	Research Area	Notes
R. Goshadze*	ME	Y. Gao	V. V. Karasiev	Deep Neural Network for Learning Noninteractive Free-Energy Density Functional to Enhance Density Functional Theory-Based Simulations Relevant to High-Energy-Density Physics	New Horton Fellow
S. Gupta*	OPT	P. S. Carney/ J. M. Zavislan	M. D. Wittman	Quantitative Confocal Phase Imaging for the Inspection of Target Capsules	
H. Hasson*	PA	P.-A. Gourdain		Understanding the Transition from Accretion Flows to Magnetized Turbulent Jets Using Pulsed-Power Drivers	New Horton Fellow
S. K. Harter	EES	M. Nakajima	D. N. Polsin	Planetary Science	
B. J. Henderson*	PA	G. W. Collins/ J. R. Rygg		Hugoniot Measurements of Silicon and Radiance Transition in Shocked Silica Aerogel	
J. Hinz*	PA	S. Rajeev	V. V. Karasiev	Developing Accurate Free-Energy Density Functionals via Machine Learning for Warm-Dense-Matter Simulations	
R. Holcomb*	OPT	J. Bromage		Machine-Learning Control of High-Average-Power Lasers for Ultrafast Applications	
M. F. Huff*	PA	G. W. Collins/ J. R. Rygg		The Equation of State of Shocked Iron and Bridgmanite	
G. W. Jenkins*	OPT	J. Bromage		Divided-Pulse Coherent Combination for Scaling High-Power Nonlinear Processes	Graduated in 2022
M. Jeske*	CHE	D. R. Harding		Engineering Resins for Two-Photon Polymerization	
R. Jia*	CHE	A. Shestopalov	S. G. Demos	Effects of Organic Monolayer Coatings on Optical Substrates	
A. Kish*	PA	A. B. Sefkow		Algorithms for Long-Time-Scale Plasma Simulation	
S. Kostick*	ME	W. Theobald	M. J. Rosenberg	Laser–Energy Coupling in Direct-Drive Experiments at the National Ignition Facility and Omega	New Horton Fellow
K. Kotorashvili*	PA	E. G. Blackman		Magnetic-Field Generation, Mass Transport, and Spin Evolution in Hydrogen Burning Stars and White Dwarfs	
A. LaPierre	CH	G. W. Collins/ J. R. Rygg		Development of Raman Spectroscopy for Dynamic Compression Experiments on OMEGA	

Table I: More than 80 graduate students, including 67 LLE-funded UR Frank Horton Fellows (marked by *), conducted research at LLE during FY22 (continued).

Student Name	Department	Faculty Advisor	LLE Advisor (if different)	Research Area	Notes
M. Lavell*	ME	A. B. Sefkow		The Development of Hybrid Fluid-Kinetic Numerical Models for Simulating Fusion-Relevant Plasmas	
L. S. Leal*	PA	R. Betti	A. V. Maximov	Simulations and Studies of Inertial Confinement Fusion Relevant Laser-Generated Plasmas in External Magnetic Fields	Graduated in 2022
A. Lees*	ME	R. Betti		Understanding the Fusion Yield Dependencies in OMEGA Implosions Using Statistical Modeling	
Y. Liu*	OPT	B. E. Kruschwitz		Development of an Electro-Optical–Based Ultraviolet Pulse Measurement System	
R. Markwick*	PA	A. Frank		Laboratory Astrophysics Studies of Colliding Radiative Magnetized Flows	New Horton Fellow
J. Martinez	ME	S. P. Regan	C. J. Forrest	Measurements of the Scattered Neutron Energy Spectrum from OMEGA Cryogenic Implosions	
T. Mason	CHE	R. B. Spielman		Pulsed-Power Technology	
M. M. McKie*	PA	D. H. Froula	J. L. Shaw	Wave Breaking of Electron Plasma Waves as it Applies to Hot-Electron Generation and Laser-Plasma Amplifiers	
B. McLellan*	PA	P. Tzeferacos	S. X. Hu/ S. Zhang	A Theoretical Study of Structural Transformations, Hydrodynamic Motion, and Optical Properties of Crystals and Amorphous High-Energy-Density Materials	
K. R. McMillen*	PA	D. H. Froula	J. L. Shaw	Filamentation of Picosecond Pulses Through Underdense Plasmas	
S. C. Miller*	ME	V. N. Goncharov		Hydrodynamic Instabilities of Inertial Confinement Fusion Implosions	Graduated in 2022
K. Moczulski*	ME	P. Tzeferacos		Characterization of Magnetized Turbulence and Fluctuation Dynamo Through *FLASH* Simulations and OMEGA Experiments	
K. L. Nguyen*	PA	J. P. Palastro		Nonlinear Saturation of Cross-Beam Energy Transfer	
K. A. Nichols*	PA	S. X. Hu		*Ab initio* Investigations of Nonlocal Electron and Ion Transport in High-Energy-Density Plasmas	
S. F. Nwabunwanne*	ECE	W. R. Donaldson		Design, Fabrication, and Characterization of AlGaN-Based Ultrafast Metal–Semiconductor–Metal Photodiodes	

Table I: More than 80 graduate students, including 67 LLE-funded UR Frank Horton Fellows (marked by *), conducted research at LLE during FY22 (continued).

Student Name	Department	Faculty Advisor	LLE Advisor (if different)	Research Area	Notes
H. Pantell*	PA	G. W. Collins/ J. R. Rygg		Thermodynamic and Mass Transport Properties of Planetary Materials at Extreme Conditions	
S. Paramanick*	PA	E. G. Blackman		Multiscale Study of Supersonic Plasma Wind Interacting with a Magnetized Earth-Like Planet	New Horton Fellow
H. Pasan*	PA	R. Dias	G. W. Collins	Novel Hydrogen Rich Materials at High-Energy-Density Conditions: Route to "Hot" Superconductivity	
D. Patel*	ME	R. Betti		High- and Mid-Mode Number Stability of OMEGA Cryogenic Implosions	
R. Paul*	ME	S. X. Hu		High-Pressure Phase Diagram of Ramp-Compressed Materials	Graduated in 2022
D. Ramsey*	PA	J. P. Palastro		Electron Dynamics and Radiation Generation in a Flying Focus	
J. Ruby*	CH	W. U. Schroeder	W. T. Shmayda	Effects of Surfaces on Superpermeation	
A. Sexton*	ME.	A. B. Sefkow		Advanced Graphics Processing Units Algorithms for Simulations of Inertial Confinement Fusion and High-Energy-Density Physics	New Horton Fellow
M. Signor*	PA	G. W. Collins/ J. R. Rygg		Using X-Ray Spectroscopy to Study Material Properties at High Energy Densities	New Horton Fellow
T. T. Simpson*	PA	J. P. Palastro		A Flying Focus Driven by Self Focusing	
E. Smith*	PA	G. W. Collins/ J. R. Rygg		Understanding Materials Assembled to Extreme States via Laser-Driven Implosions Using Bayesian Inference	
Z. K. Sprowal*	PA	G. W. Collins/ J. R. Rygg		Off-Hugoniot Studies in Hydrogen and Hydrocarbons	
R. Swertfeger*	OPT	J. Bromage		High-Power Ultrafast Amplifiers Using Cryogenically Cooled, Diode-Pumped Fluoride Crystals	New Horton Fellow
A. Syeda	ME	J. Shang/ H. Aluie		Particle Tracking with X-Ray Radiography in Shock-Driven Flows and Viscometry Using Shocked Particles	
G. Tabak*	PA	G. W. Collins/ J. R. Rygg		Experimental Investigation of Warm Dense Matter	
M. VanDusen-Gross*	PA	H. G. Rinderknecht		Electron and Gamma Signatures of Relativistically Transparent Magnetic Filament Experiments	

Table I: More than 80 graduate students including 67 LLE-funded UR Frank Horton Fellows (marked by *) conducted research at LLE during FY22 (continued).

Student Name	Department	Faculty Advisor	LLE Advisor (if different)	Research Area	Notes
M. Wang*	CHE	D. R. Harding		Using Two-Photon Polymerization to "Write" Millimeter-Size Structures with Micron Resolution	
C. A. Williams*	PA	R. Betti		High-Yield Cryogenic Implosions on OMEGA	
J. Young*	PA	P.-A. Gourdain		Laser-Triggered X Pinches	
J. Zhang	OPT	G. Agrawal	W. R. Donaldson	Slow Light in Photonic Crystal Fiber	
Y. Zhang*	ME	J. R. Davies		Kinetic Study of Magnetized Collisionless Shock Formation and Particle Acceleration	

ME: Mechanical Engineering
PA: Physics and Astronomy
CH: Chemistry
CHE: Chemical Engineering
OPT: Institute of Optics
ECE: Electrical and Computer Engineering
EES: Earth and Environmental Sciences
MS: Material Science

Table II: Sixteen students successfully defended their Ph.D. theses in calendar year 2022.

Name	Ph.D. Institution	Current Position, Employer
M. Adams	University of Rochester	Postdoc, Sandia National Laboratories
G. Chen	University of Rochester	System Engineer, KLA
P. Franke	University of Rochester	Scientist, Tau Systems Inc.
J. García-Figueroa	University of Rochester	Postdoc, Johns Hopkins University
B. J. Henderson	University of Rochester	Specialist in Optical Design, L3Harris Technologies
G. Jenkins	University of Rochester	Senior Optical Design Engineer, ASML
L. S. Leal	University of Rochester	Postdoc, Lawrence Livermore National Laboratory (LLNL)
S. Miller	University of Rochester	Assistant Scientist, LLE
R. Paul	University of Rochester	Postdoc, LLNL
M. Khan	University of York	Postdoc, University of York
D. Kim	Princeton University	Postdoc, Carnegie Institute of Science
G. Righi	University of California, San Diego	Postdoc, LLNL
B. Russell	University of Michigan	Postdoc, University of Michigan
R. Simpson	Massachusetts Institute of Technology (MIT)	Lawrence Fellow, LLNL
G. Sutcliffe	MIT	Postdoc at MIT, to join LLNL (HEDS Center Postdoc Fellow)
R. Vandervort	University of Michigan	Postdoc, Los Alamos National Laboratory

External Users' Program

M. S. Wei

Laboratory for Laser Energetics, University of Rochester

Under the facility governance plan implemented in FY08 to formalize the scheduling of the Omega Laser Facility as a National Nuclear Security Administration (NNSA) User Facility, Omega Facility shots are allocated by programs following NNSA guidance. NNSA funds about 190 shot days each year on the OMEGA and OMEGA EP Laser Systems for experiments. The principal uses of Omega are for NNSA-supported research and development in high-energy-density physics recommended by the HED Council and basic science through peer-reviewed proposals. The majority (~68%) of these shot days are committed to the national Inertial Confinement Fusion (ICF) Program and the High-Energy-Density Program with shots conducted by scientists from Lawrence Livermore National Laboratory (LLNL), Los Alamos National Laboratory (LANL), Sandia National Laboratories (SNL), the Naval Research Laboratory (NRL), and LLE. In FY22, the Omega Laser Facility delivered a total of 2110 shots over 207 days, among which 1390 target shots (including 128 calibration shots) were conducted for the ICF and HED campaigns, which are ~65.9% of the overall facility shots. The successful completion of the large number of experiments at the Omega Laser Facility during the COVID-19 global pandemic is attributed to the "RemotePI" operation protocol that enabled experimental principal investigators (PI's) and collaborators to safely and effectively conduct experiments via remote access.

The Basic Science Program at the Omega Laser Facility, with projects selected through open-call and peer-reviewed processes, is typically allotted between 25% to 29% of the total NNSA-funded Omega Facility shot days. The program has two distinct components: (1) the National Laser Users' Facility (NLUF) experiments (~18% of the NNSA-funded shot time) led by researchers from U.S. academia and business; and (2) the Laboratory Basic Science (LBS) experiments (with ~11% of the NNSA-funded shot time) that are led by the NNSA HED laboratories including LLNL, LANL, SNL, NRL, and LLE and the Office of Science laboratories such as SLAC National Accelerator Laboratory, and Princeton Plasma Physics Laboratory (PPPL). In FY22, the NLUF and LBS programs obtained 314 and 224 target shots, respectively, and together accounted for ~25.5% of the overall facility shots.

Since FY20, LLE has provided a few additional shot days each year on OMEGA EP to the users of the newly established LaserNetUS network funded by the DOE Office of Fusion Sciences (FES) with user experimental proposals annually solicitated and selected by a fully independent proposal review panel process. The LaserNetUS program obtained 34 target shots on OMEGA EP in FY22.

Since FY21, a few additional shot days each year at the Omega Laser Facility have also been made available to the University of Rochester (UR)-hosted Center for Matter at Atomic Pressure (CMAP), a new Physics Frontier Center funded by the National Science Foundation (NSF). CMAP is a collaboration among faculty, scientists, researchers, and students at UR, Massachusetts Institute of Technology (MIT), Princeton University, the University of California at Berkeley and Davis, the University of Buffalo, and LLNL. CMAP researchers conduct laboratory-based exploration of planets and stars throughout the universe and obtained 55 target shots in FY22.

During FY22, the Omega Laser Facility was also used to support research grants led by LLE scientists and funded by FES (14 target shots on OMEGA) and for other externally funded programs led by teams from the Johns Hopkins University's (JHU's) Applied Physics Laboratory (APL) (36 target shots on OMEGA) and the French le Commissariat à l'énergie atomique et aux énergies alternatives (CEA) (43 target shots on OMEGA and OMEGA EP). These externally funded experiments are conducted at the facility on the basis of special agreements put in place by UR/LLE and participating institutions with the endorsement of NNSA.

The facility users who conducted experiments during this year included 23 collaborative teams participating in the NLUF Program, 20 teams led by scientists from LLNL, LANL, LLE, SLAC, and PPPL participating in the LBS Program; three project teams participating in the LaserNetUS Program; six project teams from CMAP; many collaborative teams from the national laboratories (LLNL, LANL, SNL, NRL) and LLE conducting ICF experiments; investigators from LLNL, LANL, SNL, and LLE conducting experiments for HED campaigns; and researchers from APL and CEA.

A critical part of the Omega external users' programs is the training of graduate students and postdoctoral researchers in HED and plasma physics. In total, over 70 graduate students (see Table I) from 28 other universities,18 undergraduate students, and more than 40 postdoctoral researchers participated in these external user-led research projects with experiments at the Omega Laser Facility during FY22, among which seven students successfully defended their Ph.D. theses in calendar year 2022 (see the highlighted names in Table I). It is worth noting that 25 of these graduate students are new to the Omega Laser Facility.

Table I: More than 70 graduate students from 28 universities have conducted research utilizing the Omega Laser Facility through NLUF, LBS, and LaserNetUS, and/or via collaborations with national labs and LLE during FY22. Seven students successfully defended their Ph.D. theses in calendar year 2022 (see shaded cells).

Name	Institution	Advisor(s)	Notes
A. Aghedo	Florida A&M University	Albert (LLNL)	LLNL collaboration including LBS projects
E. Grace	Georgia Tech (GT)	Trebino (GT)/ Ma (LLNL)	LLNL collaboration (PI: Swadling)
J. Gonzalez Quiles	JHU	Wicks	
Y. Li	JHU	Wicks	
T. Perez	JHU	Wicks	
Z. Ye	JHU	Wicks	
P. J. Adrian	MIT	Frenje	
C. Chang	MIT	Li/Frenje	
S. Danhoff	MIT	Frenje	
T. Evans	MIT	Frenje	
T. M. Johnson	MIT	Li	
J. Kunimune	MIT	Frenje	NNSA Laboratory Residency Graduate Fellow
J. Pearcy	MIT	Li	
B. Reichelt	MIT	Li	NNSA Laboratory Residency Graduate Fellow
R. Simpson	MIT	Winslow (MIT)/ Ma (LLNL)	LLNL collaboration; graduated in 2022; joined LLNL as Lawrence Postdoc Fellow
G. Sutcliffe	MIT	Li	Defended Ph.D. thesis in October 2022; to join LLNL as the High-Energy-Density Science Center Postdoc Fellow
J. Copley	Princeton University	Duffy	New
S. Han	Princeton University	Duffy	
C. Johnson	Princeton University	–	LBS (PI: Malko); new
D. Kim	Princeton University	Duffy	Graduated in March 2022; Postdoc at Carnegie Science
I. Ocampo	Princeton University	Duffy	

Table I: More than 70 graduate students from 28 universities have conducted research utilizing the Omega Laser Facility through NLUF, LBS, and LaserNetUS, and/or via collaborations with national labs and LLE during FY22. Seven students successfully defended their Ph.D. theses in calendar year 2022 (see shaded cells) (continued).

Name	Institution	Advisor(s)	Notes
B. Cage	Rice University	Liang	New
W. Riedel	Stanford University	Cappelli	
S. You	Stanford University	Edwards	LLNL collaboration–LBS; new
W. Gammel	University of Arizona	–	LANL collaboration (PI: Palaniyappan); new
D. Lioce	University of California, Berkeley	–	LANL collaboration (PI: Kozlowski); new
M. Harwell	University of California, Davis (UC Davis)	Stewart	CMAP
A. Postema	UC Davis	Stewart	CMAP; new
R. Lee	University of California, Los Angeles (UCLA)	Mori	
M. Sinclair	UCLA	Joshi	LLNL collaboration including LBS (PI: Albert)
K. Bhutwala	University of Califonia, San Diego (UC San Diego)	Beg	
A. Bogale	UC San Diego	Beg	
T. Cordova	UC San Diego	Beg	LLNL collaboration
A. Li	UC San Diego	Meyers	
M. Postornik	UC San Diego	Arefiev	LLNL collaboration (PI: Smith); new
G. Righi	UC San Diego	Meyers	LaserNetUS and LLNL collaboration; graduated in July 2022; postdoc at LLNL
J. Saret	UC San Diego	Beg	NLUF (PI: McGuffey, General Atomics); new
I-L. Yeh	UC San Diego	Arefiev	NLUF (PI: Willingale, UM); new
C. Frank	University of Delaware	Bose	Princeton Plasma Physics Laboratory-LBS (PI: Malko); new
K. Bolduc	University of Massachusetts, Amherst	–	LLNL collaboration (PI: Smith); new
A. Angulo	University of Michigan (UM)	Kuranz	
K. Bryant	UM	Kuranz	
S. Coffing	UM	Drake	LANL collaboration (PI: Kozlowski)
C. Fiedler-Kawaguchi	UM	Kuranz	LANL collaboration (PI: Rasmus)
K. Kelso	UM	Kuranz	
J. Kinney	UM	Kuranz	New
J. Latham	UM	Krushelnick	New

Table I: More than 70 graduate students from 28 universities have conducted research utilizing the Omega Laser Facility through NLUF, LBS, and LaserNetUS, and/or via collaborations with national labs and LLE during FY22. Seven students successfully defended their Ph.D. theses in calendar year 2022 (see shaded cells) (continued).

Name	Institution	Advisor(s)	Notes
S. Miller	UM	McBride	SNL collaboration (PI: Gomez); new
B. Russell	UM	Willingale	Graduated in Sept. 2022; postdoc at UM
M. Springstead	UM	Kuranz	NLUF and LLNL collaboration (PI: Swadling)
H. Tang	UM	Willingale	
R. Vandervort	UM	Drake/Kuranz	Graduated in July 2022; postdoc at LANL
M. Wadas	UM	Johnsen	LaserNetUS and LLNL collaboration
C. Allen	University of Nevada (UNR)	White	
J. Clapp	UNR	Mancini	new
E. Gallardo-Diaz	UNR	Mancini	
T. Griffin	UNR	White	new
J. Rowland	UNR	Mancini	
J. King	University of New Mexico	–	SNL collaboration (PI: Aguirre); new
E. Smith	University of Notre Dame	–	LANL collaboration (PI: Kozlowski); new
C. Danley	UR/LANL	–	LANL collaboration
I. Pagano	University of Texas, Austin	Downer	LLNL collaboration including LBS (PI: Albert)
C. Samulski	Virginia Tech	Srinivasan	
M. Vescovi	Helmholtz-Zentrum Dresden-Rossendorf	–	NLUF collaboration (PI: Valdivia); new
V. Valenzuela	Imperial Collage	–	LLNL collaboration including LBS (PI: Swadling); new
F. Barbato	Sapienza Università di Roma	Atzeni	LLE collaboration–LBS (PI: Igumenshchev); new
L. Savino	Sapienza Università di Roma	Atzeni	LLE collaboration–LBS (PI: Igumenshchev); new
C. Bruulsema	University of Alberta	Rozmus	LLE and LLNL collaborations
R. Loitard	University of Bordeaux	–	LLE collaboration–LBS (PI: Igumenshchev); new
S. Iaquinta	University of Oxford	Gregori	NLUF and LLE collaboration
H. Poole	University of Oxford	Gregori	NLUF and LLE collaboration
M. Khan	University of York	Woolsey	Rutherford Appleton Laboratory/York (PI: Scott) and LLE collaboration (PI: Theobald); graduated in May 2022; postdoc at York

FY22 National Laser Users' Facility Program

M. S. Wei

Laboratory for Laser Energetics, University of Rochester

The Office of Experimental Sciences of the National Nuclear Security Administration within the U.S. Department of Energy funds the operations of LLE and specifically, of the National Laser Users' Facility (NLUF), thus making it possible for users from universities and industry in the United States to conduct basic science experiments without a direct facility charge. To better serve a growing, diverse user community and streamline the process, the NLUF Program has evolved into a facility-access-only program starting from FY22. During FY21, LLE completed a call for proposals, review, and selection process for the NLUF experiments to be conducted at the Omega Laser Facility during FY22 and FY23. After peer review by an independent proposal review panel for scientific merit and broad impact and the feasibility and executability review by the Omega facility and experimental support team, LLE selected 27 proposals for Omega shot allocation with a total of 25.5 and 34 shot days for experiments in FY22 (Q2–Q4) and FY23, respectively.

FY22 was the first of a two-year period of performance for these 27 NLUF projects (Table I). In addition, a few FY21 NLUF projects as carryover also completed experiments during FY22. In total, 314 target shots were conducted for NLUF projects during FY22. The NLUF experiments conducted during FY22 are summarized in this section.

Table I: Four FY21 carryover projects (in gray) conducted shots during FY22. Twenty-one (in blue) of the 27 new NLUF projects approved for the FY22–FY23 Omega Laser shot allocation conducted shots during FY22. The remaining six (in yellow) are scheduled for FY23.

Principal Investigator	Institution	NLUF Project Title/Article Title
F. N. Beg	University of California, San Diego	Charged-Particle Transport and Energy Deposition in Warm Dense Matter with and without an External Magnetic Field/ Measurements of Temperature Evolution in Copper from Intense Proton Beam Energy Deposition
W. Fox	Princeton University	Magnetic Reconnection in High-Energy-Density Plasmas
H. Ji/L. Gao	Princeton University/Princeton Plasma Physics Laboratory	Study of Particle Acceleration from Magnetically Driven Collisionless Reconnection at Low Plasma Beta Using Laser-Powered Capacitor Coils/Electron Exhaust Jets and Current-Driven Kinetic Instabilities in Laser-Powered Magnetic Reconnection
C. K. Li	Massachusetts Institute of Technology	Inertial Confinement Fusion Interface
M. Bailly-Grandvaux	University of California, San Diego	Effects of an External Magnetic Field on Laser–Plasma Instabilities
T. Duffy	Princeton University	Dynamic Compression of Exoplanetary Materials: Pressure-Induced B1–B2 Phase Transition in ZnO Under Laser-Driven Ramp Compression

Table I: Four FY21 carryover projects (in gray) conducted shots during FY22. Twenty-one (in blue) of the 27 new NLUF projects approved for the FY22–FY23 Omega Laser shot allocation conducted shots during FY22. The remaining six (in yellow) are scheduled for FY23 (continued).

Principal Investigator	Institution	Title
J. A. Frenje	Massachusetts Institute of Technology	Advanced Studies of Kinetic and Multi-Ion-Fluid Effects, Electron-Heat Conduction, Ion–Electron Equilibration, and Ion-Stopping Power in High-Energy-Density Plasmas/Multi-Ion Campaign: Studies of Multi-Ion and Kinetic Effcts in Shock and Ablatively Driven Implosions
M. Gatu Johnson	Massachusetts Institute of Technology	Study of Diffusion, Interpenetration, Instability, and Dynamics at the Ablator–Gas Interface in Inertial Confinement Fusion-Relevant Conditions/Ablator–Gas Interface Dynamics and Mix in Confinement Fusion-Relevant Conditions
R. Jeanloz/G. Tabak	University of California, Berkeley/LLE	Search for Immiscibility in Hydrogen–Neon Mixtures at Jupiter-Interior Conditions/Report for DACPlanet-22A/B
K. Krushelnick	University of Michigan	The Dynamics and Reconnection of Strong Magnetic Fields Using OMEGA EP/Plasmoid Magnetic Reconnection Between Long-Pulse Laser-Driven Plasmas Perturbed by a Short-Pulse Laser
C. C. Kuranz/ H. LeFevre	University of Michigan	Radiation Transport in Strongly Coupled Plasmas/Achieving Neutron Star Envelope Relevant Conditions Through a Radiative Shock in Strongly Coupled Plasmas
C. C. Kuranz/ H. LeFevre	University of Michigan	Photoionization Fronts on the OMEGA Laser/Observation of a Radiative Heat Front in Ar Using the Omega Gas-Jet System
D. Lamb/P. Tzeferacos	University of Chicago/ LLE	Onset, Subsistence, and Decay of Magnetized Turbulence and Fluctuation Dynamo
E. Liang	Rice University	Collision of Magnetized Jets Created by Hollow-Ring Lasers Irradiating High-*Z*–Doped CH Targets
R. C. Mancini	University of Nevada, Reno	X-Ray Heating and Ionization of Photoionized Plasmas in a Steady State
W. L. Mao	Stanford University	Low-Entropy Diamond Formation Pathways for Reactive H Chemistry/Shock-Induced Hydrogen Chemistry for Hydride Formation
C. McGuffey	General Atomics	Opacity of Ionized Iron Under Broad Pressure and Temperature Conditions/Driving Iron to Dense, Hot Conditions Using the Long- and Short-Pulse Beams of OMEGA EP
J. Shang	University of Rochester	Tracking Rarefaction with Particle Image Velocimetry
B. Srinivasan	Virginia Tech	Rayleigh–Taylor Evolution of Isoloated-Feature Perturbations in a Background Magnetic Field
S. Tochitsky/N. Lemos	University of California, Los Angeles/LLNL	Control of Laser–Plasma Interactions in Three-Dimensional–Printed Foam Structures with Graded Density
S. J. Tracy	Carnegie Institute for Science	Dynamic Compression of Iron Carbide at Exoplanetary Core Conditions

Table I: Four FY21 carryover projects (in gray) conducted shots during FY22. Twenty-one (in blue) of the 27 new NLUF projects approved for the FY22–FY23 Omega Laser shot allocation conducted shots during FY22. The remaining six (in yellow) are scheduled for FY23 (continued).

Principal Investigator	Institution	Title
P. Valdivia	University of California, San Diego/Johns Hopkins University	Phase-Contrast Imaging of Inner Shell Release Through Talbot–Lau X-Ray Interferometry/Monochromatic Talbot–Lau X-Ray Deflectometer for the OMEGA EP and Multi-Terawatt Lasers
T. White	University of Nevada, Reno	Experimental Measurement of Thermal Conductivity in Warm Dense Matter
J. Wicks	Johns Hopkins University	Exploration of Decomposition Kinetics in the Warm-Dense-Matter Regime: Orientation and Melting Effects
L. Willingale	University of Michigan	Direct Laser Acceleration of Electrons for Bright, Directional Radiation Sources/Relativistic Intensity Laser Channeling and Direct Laser Acceleration of Electrons from an Underdense Plasma
G. Fiksel	University of Michigan	Study of a Self-Generated Magnetic Field in Imploding D^3He Backlighter Capsules and Its Effect on the Properties of the Diagnostic Proton Beams
H. Ji	Princeton University	Thomson-Scattering Measurement of Non-Maxwellian Electrons and Current-Driven Instabilities During Low-Beta Magnetically Driven Reconnection
J. Kim	University of California, San Diego	Efficient Ion Acceleration by Continuous Fields in the Target Transparency Regime
D. Schaeffer	Princeton University (now at University of California, Los Angeles)	Detailed Measurements of Electric and Magnetic Fields in Laser-Driven, Ion-Scale Magnetospheres
D. Schaeffer	Princeton University (now at University of California, Los Angeles)	Particle Heating by High-Mach-Number Collisionless Shocks in Magnetized HED Plasmas
F. H. Séguin	Massachusetts Institute of Technology	Study of Magnetized Plasmas in Shock-Driven Inertial Confinement Fusion Implosions and in Laser-Driven Hohlraums

Measurements of Temperature Evolution in Copper from Intense Proton Beam Energy Deposition

M. Bailly-Grandvaux,[1] C. McGuffey,[2] J. Kim,[1] K. Bhutwala,[1] J. Saret,[1] D. Mariscal,[3] T. Ma,[3] P. M. Nilson,[4] T. Filkins,[4] W. Theobald,[4] A. Haid,[2] S. T. Ivancic,[4] and F. N. Beg[1*]

[1]Center for Energy Research, University of California, San Diego

[2]General Atomics

[3]Lawrence Livermore National Laboratory

[4]Laboratory for Laser Energetics, University of Rochester

[*]Principal Investigator

OMEGA EP can deliver intense proton and ion beams with tens of joules that can then rapidly deposit their energy in bulk samples, leading to isochoric heating of materials into the warm-dense-matter regime. Our group previously studied proton beam transport in thick plastic foams on OMEGA EP, a work that was published recently.[1] Following results from our previous shot day,[2] the FY22 NLUF shot day examined the bulk heating resulting from laser-generated proton beams focused onto solid Cu disks (10- or 25-μm thick $\times$ 200-μm diameter). To quantify the heating, the K_α fluorescence emitted by the Cu was measured with a high-resolution streaked spectrometer (HiResSpec). This diagnostic was used successfully for the first time with proton-heated samples. The Cu temperature was obtained with a few picoseconds resolution and it reached ~50 eV in ~35 ps (Ref. 3).

In the recent FY22 shot day, a steep-walled hollow plastic cone with 100-μm openings at its tip was added where the Cu sample was attached. These cones were used to focus the proton beam into a small spot.[4] The target and diagnostic lines of sight for these shots are shown in Figs. 1(a) and 1(b).

On the primary target configurations discussed above and shown in Figs. 1(a) and 1(b), we collected time-resolved spectra of the K_{α_1} and K_{α_2} and line emissions using the HiResSpec diagnostic in the range of 7.97 to 8.11 keV with a spectral resolution of $E/\Delta E \sim 5000$ and time resolution of ~2 ps. Experimental spectra are compared with spectra calculated using the collisional-radiative spectral analysis code *PrismSPECT*, which together describe the evolution of temperature in the sample and are shown in Fig. 2(a). These spectra are complemented with time-dependent simulations performed with the 1-D radiation-hydrodynamics code *HELIOS*, shown in Fig. 2(b), using as an input the proton beam characteristics inferred from the Thompson parabola ion energy (TPIE) analyzer, radiochromic film diagnostics (RCF), and results from previous work.[4]

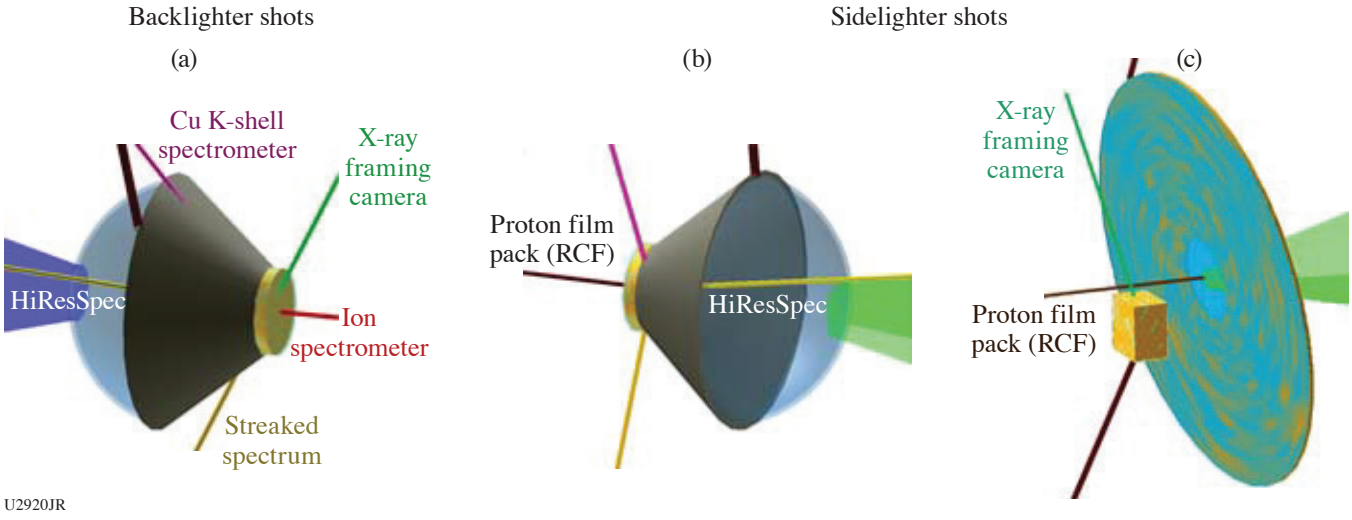

Figure 1
[(a),(b)] Experimental configurations for the Cu disk proton heating experiment. Configurations (a) and (b) used the same laser and target conditions but had complementary diagnostics for the proton beam characterization, an ion spectrometer, or a film pack. Configuration (c) provided a measurement of energy deposition as well as time-resolved images of the top Cu face, giving a cross-sectional view of the emission profile.

The temperature evolution inferred from the *PrismSPECT* analysis and simulated in *HELIOS* are shown in Fig. 2(c). A good agreement was obtained once the sample was heated above 20 eV, into the regime where K_α lines shifts start to be measured.

Remaining analysis includes continued construction of synthetic K_α spectra with more-advanced atomic models to improve comparison with the measured spectra, especially at late times (>50 ps) where the K_α spectra are significantly broadened by spatial gradients and a possible hydrodynamic expansion. Hybrid particle-in-cell simulations using the *LSP* code are also being performed to model the proton and electron transport through the cone and energy deposition into the sample.

We also performed a shot where the proton beam was generated by a thin foil, directed unfocused onto a Cu half block, as shown in Fig. 1(c). Due to the absence of a focusing structure, the measured temperatures were low (<20 eV). With the Cu block intersecting only part of the beam, radiochromic films provided the unblocked and transmitted beam's energy distribution, hence potentially extracting energy deposition. However, significant charging of the Cu block was observed, affecting the measurement.

The experiment was conducted on the OMEGA EP Laser System at the University of Rochester's Laboratory for Laser Energetics with the beam time through the National Laser Users' Facility (NLUF) program. This material is based upon work supported by the Department of Energy, National Nuclear Security Administration under Award Number DE-NA0003943, the University of Rochester, and the New York State Energy Research and Development Authority.

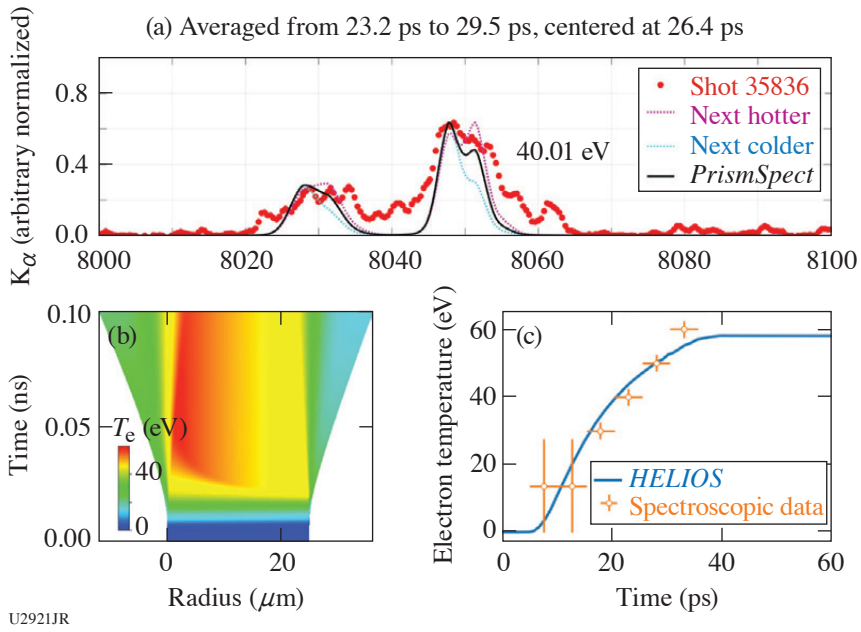

Figure 2
Experimental and simulation results collectively describing temperature evolution in Cu disks. Sample time-integrated spectrum with corresponding iterated time-dependent (a) *PrismSPECT* simulations describe measured temperature evolution and (b) *HELIOS* simulates 1-D temperature evolution. (c) A good agreement in the evolution of sample temperature is obtained once $T > 20$ eV, where K_α line shifts occur.

Magnetic Reconnection in High-Energy-Density Plasmas

W. Fox,[1,2*] D. B. Schaeffer,[2] S. Malko,[1] G. Fiksel,[3] and M. J. Rosenberg[4]
[1]Princeton Plasma Physics Laboratory
[2]Princeton University, Department of Astrophysical Sciences
[3]University of Michigan
[4]Laboratory for Laser Energetics, University of Rochester
[*]Principal Investigator

Magnetic reconnection[5] is a fundamental process in astrophysical plasmas that can convert magnetic energy to plasma kinetic energy, and it underlies processes in cosmic plasmas such as solar flares and substorms in the Eartth's magnetotail. In this project, we conducted laboratory experiments using OMEGA to study how magnetic reconnection proceeds under the conditions of laser-produced plasmas.[5] In these plasmas, magnetic fields are self-generated in the plasma by the Biermann battery effect. Creating two neighboring plumes produces a collision of two magnetized plasmas, driving together the oppositely directed magnetic-field lines and driving magnetic reconnection, which can be observed using the OMEGA suite of plasma diagnostics including x-ray imaging, Thomson scattering, and proton radiography. Laser-produced plasmas are an exciting platform for magnetic reconnection experiments because they can reach a large normalized system size regime, where the plasma is much larger than intrinsic plasma scales such as the electron and ion gyro radius, while simultaneously maintaining low particle collisionality due to high temperature (see Fig. 3). Our recent campaign has conducted experiments at National Ignition Facility and OMEGA, where the range of experiments allows scanning parameters such as the size, temperature, and density of the plasma.[6]

For these particular experiments on OMEGA, we determined that an important and necessary milestone for the project was to improve and validate techniques for analyzing proton radiography data to infer experimental magnetic fields. We therefore devoted several shots to conducting proton radiography measurements of a single expanding plasma plume, which is the simplest possible system to analyze, but which has several pitfalls uncovered in other recent experiments. In particular, our recent work has identified the importance of obtaining and applying boundary conditions on the magnetic field, and second that it is important to deal with intrinsic nonuniformities in the probing proton beam.[6] These new data will allow us to validate techniques for dealing with both issues. Over the rest of the experimental day we obtained additional experimental data on reconnecting plasmas, including Thomson scattering, x-ray images, and proton radiographs. The single-plume experiments, however, are particularly interesting and we present them here in this report.

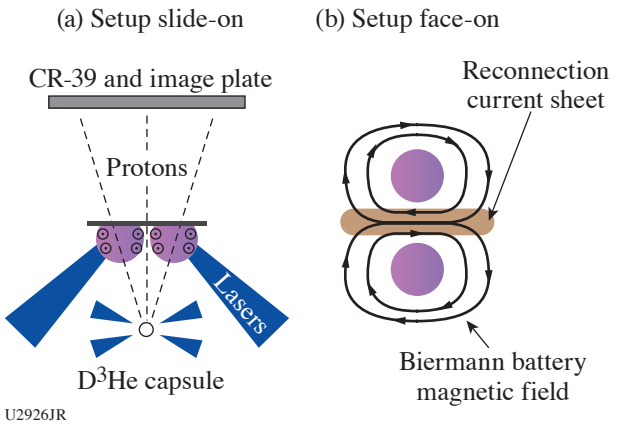

Figure 3
The general setup of laser-driven magnetic reconnection experiments. (a) Side-on view, showing self-generated Biermann-battery magnetic fields in expanding plasmas, and probing of fields by monoenergetic protons from a driven D–^{3}He fusion implosion. (b) Face-on view, showing self-generated Biermann battery fields and formation of a magnetic reconnection current sheet where the two plasmas collide.

For this shot sequence, shown in Fig. 4, we radiographed the evolution of a single plasma plume, driven by two overlapped beams with near-normal incidence, with an on-target energy near 900 J in 1 ns, using standard OMEGA phase plates. The plumes were radiographed after 1.5 ns of evolution, using 15-MeV protons from a imploding D^{3}He capsule. We conducted experiments with three different probing techniques. First, we used a full mesh behind the target [Fig. 4(a)], which breaks the proton beam into multiple beamlets. The magnetic-field strength and direction can be directly inferred from the deflection of the beamlets, albeit at reduced spatial resolution (one data point per beamlet). In addition to the proton data shown here, we additionally obtained an x-ray shadow of the mesh using an image-plate detector at the back of the proton detector stack.[7] The x-ray mesh image provides a direct location of the "undeflected" location of each beamlet.

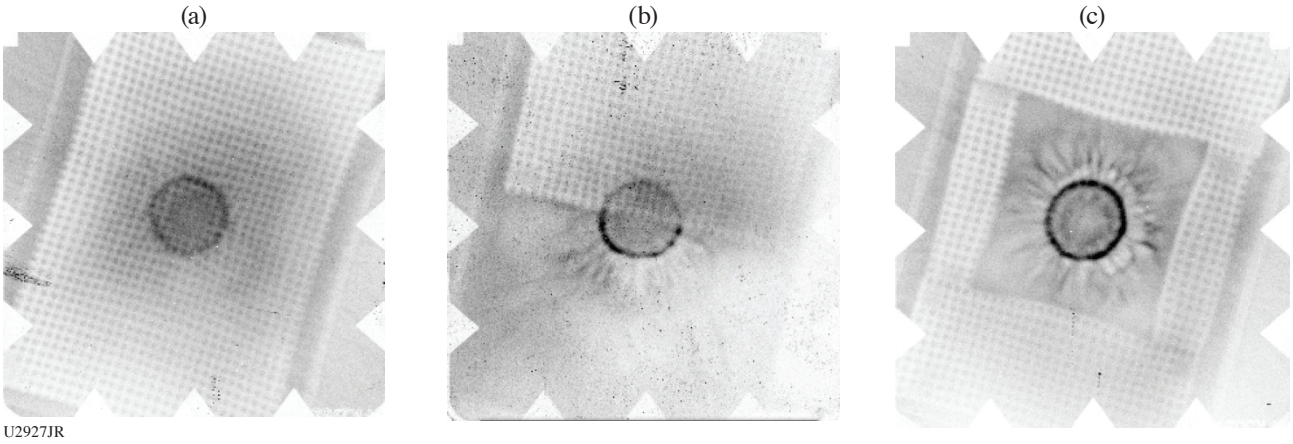

Figure 4
Shown are 15-MeV proton radiographs of expanding plasma plumes. The different experiments show the identical point of evolution of an isolated expanding plume, with three different probing techniques: (a) full mesh behind the foil, (b) half-mesh, and (c) boundary mesh.

We additionally obtained data using a half-mesh [Fig. 4(b)], or boundary mesh [Fig. 4(c)]. In the half-mesh, half of the plume is covered with a mesh, while the other half is a pure-proton-fluence image. In the pure-fluence image, we can observe several features that we commonly see in these plasmas, namely dark circular ring, which is produced by the proton focusing by the global Biermann battery magnetic field wrapping around the plume. Second, we now also observe fine-scale magnetic structures in the plume, which are obscured in the mesh image due to the sacrificed resolution. The pure-fluence data will be analyzed using reconstruction techniques.[6,8] In the half-mesh image, the results can be directly validated against the mesh data, assuming symmetry. Finally, in the boundary mesh case, we will conduct a fluence reconstruction of the central plume, using "help" from outer boundary conditions on the magnetic field, as inferred from the boundary mesh data.

We thank the support of the facility scientists. Experimental time at OMEGA was provided through the LLE Academic and Industrial Basic Science Program. Funding support was provided through Joint FES-NNSA Program in HEDP.

Electron Exhaust Jets and Current-Driven Kinetic Instabilities in Laser-Powered Magnetic Reconnection

S. Zhang,[1] A. Chien,[1] L. Gao,[2] H. Ji,[1,2*] E. G. Blackman,[3] R. K. Follett,[4] D. H. Froula,[4] J. Katz,[4] W. Daughton,[5] C. K. Li,[6] A. Birkel,[6] R. D. Petrasso,[6] J. D. Moody,[7] and H. Chen[7]
[1]Princeton University
[2]Princeton Plasma Physics Laboratory
[3]Department of Physics and Astronomy, University of Rochester
[4]Laboratory for Laser Energetics, University of Rochester
[5]Los Alamos National Laboratory
[6]Massachusetts Institute of Technology
[7]Lawrence Livermore National Laboratory
[*]Principal Investigator

Magnetic reconnection is a ubiquitous phenomenon in space and astrophysical plasmas that rapidly converts magnetic energy into particles and flows. Current-driven instabilities may play an important role in facilitating magnetic energy dissipation. Using two Academic and Industrial Basic Science (AIBS) campaigns on OMEGA, we combined the laser-driven capacitor-coil experiments with time-resolved collective Thomson scattering to study the kinetic physics in the collisionless reconnection, including the evolution of the non-Maxwellian velocity distribution function, electron jets, and kinetic instabilities. Thomson scattering reveals electron-acoustic waves (EAW's) with phase velocities near the electron thermal speed, indicating a non-Maxwellian distribution overcoming Landau damping. We also observed bursty and asymmetric ion-acoustic waves (IAW's), confirming the existence of the electron jet and the current-driven ion-acoustic instabilities (IAI's). The IAW bursts are followed by EAW bursts and electron heating. One- and two-dimensional particle-in-cell (PIC) simulations show that current-driven IAI can form double layers, which induce an electron two-stream instability generating EAW bursts in accordance with the measurements. Our experiments and simulations demonstrate that the electron outflow jet is unstable and can dissipate energy via the nonlinear development of the current-driven instabilities involving electron–ion coupling. We have submitted our findings to Nature Physics and the manuscript is now under review.[9]

The experimental platform is shown in Fig. 5. The capacitor-coil target is made of a 50-μm-thick Cu foil. The coils have a 600-μm diameter and 500-μm-length legs and are separated by 600 μm. The magnetic field generated by the capacitor-coil targets

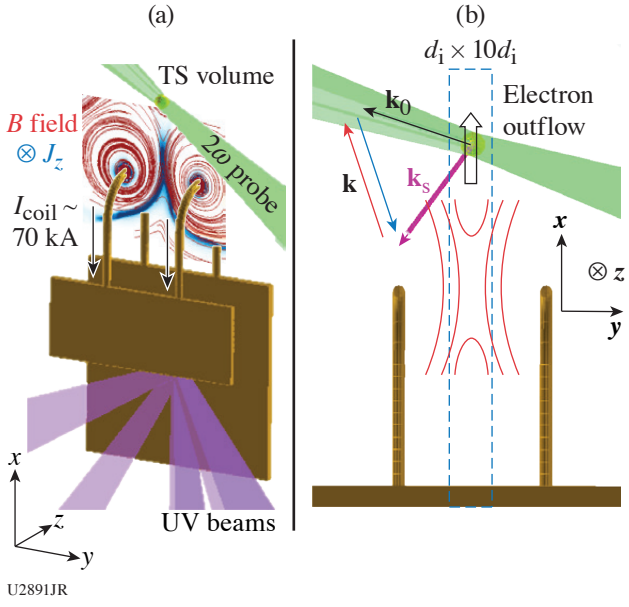

Figure 5
Experimental setup. Six beams of 500-J, 1-ns UV lasers are used to irradiate the back plate of the capacitor, driving current in the coils with $I_{coil} \sim 70$ kA. (a) *FLASH* magnetohydrodynamic (MHD) simulation results are overlapped to show the structure of the magnetic field (red lines) and the out-of-plane current density (blue) in the z direction. A 2ω (527-nm) Thomson-scattering (TS) beam (green) probes the reconnection exhaust region, 600 μm above the center point between the top of the coils. (b) $\mathbf{k}_0$ and $\mathbf{k}_s$ are the wave vectors of the probe beam and the collected scattered light. The red and blue arrows indicate wave vectors ($\mathbf{k}$) of waves in plasma that scatter the probe light to the collector. These $\mathbf{k}$'s are in the x–y plane and 17° off the outflow direction.

is profiled by proton radiography.[10–12] The upstream magnetic field strength is ~40 T at 6 ns after the lasers' onset. The proton radiography also shows the center feature, indicating the reconnection current sheet.

The non-Maxwellian distribution and the kinetic instabilities of the reconnection exhaust are shown in the Thomson-scattering spectrogram . As shown in Fig. 6(a), the IAW-resonant scattering is bursty and asymmetric. The asymmetric IAW spectrum before the bursts can be reproduced in the synthetic TS spectrum with relative drift between electrons and ions as shown in Fig. 6(c). The bursts confirm the existence of the current-driven IAI's. Figure 6(b) shows that the asymmetric IAW peaks are accompanied by an electron-acoustic wave resonant peak, which needs a two-stream distribution as shown in Fig. 6(d) to reproduce.

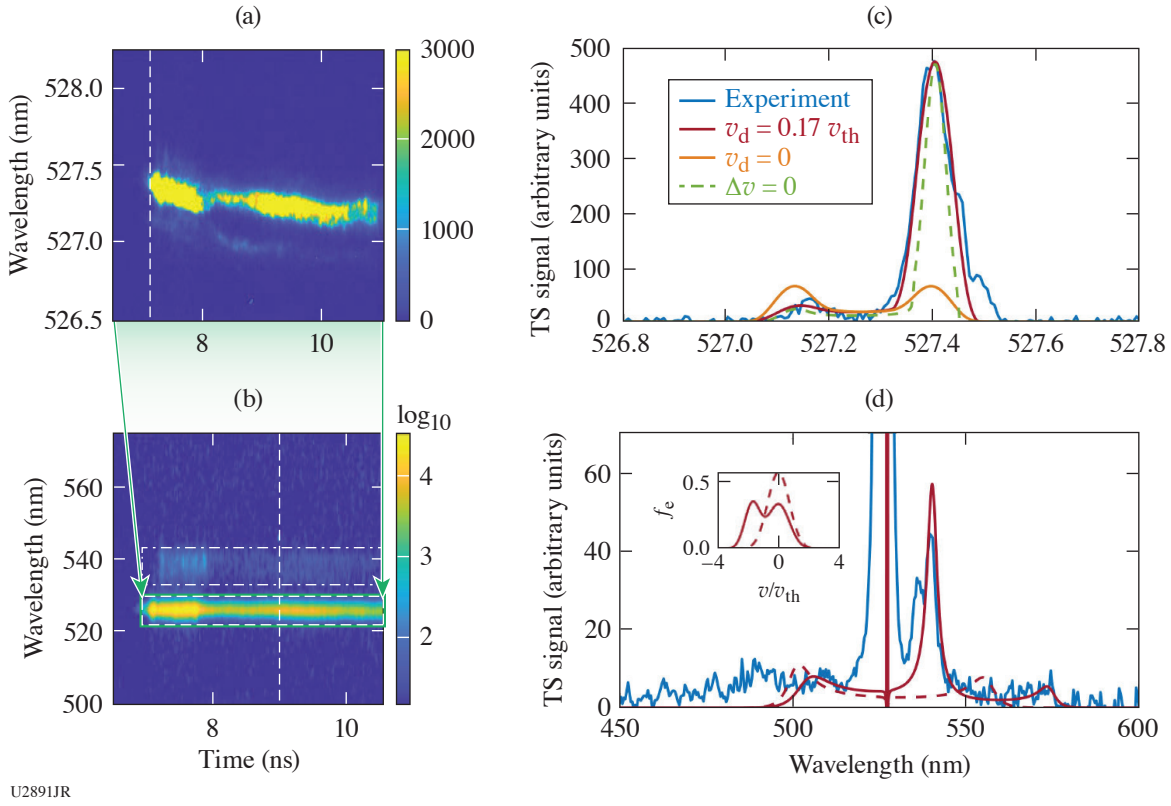

Figure 6
[(a),(b)] Time-resolved Thomson scattering (TS) at $t = 7$ to 10 ns. The IAW resonant peaks in (a) are highly asymmetric (10:1 to 100:1). (c) The spectrum along the vertical dashed line of (a) before the IAW bursts and the comparison with the synthetic TS spectra. The highly asymmetric IAW's can be reproduced with electrons streaming relative to ions with $v_d \sim 0.17\ v_{th}$. (b) The EAW peak along with the IAW feature. (d) The spectrum at 9 ns [along vertical dashed line of (b)] with a fitted synthetic spectrum (red solid line). A two-stream electron distribution is needed to reproduce the strong EAW signal. The distribution is shown as the solid line in the inserted plot. For reference, the synthetic TS spectrum from a Maxwellian distribution is shown as the dashed line.

We acknowledge the Omega Laser Facility staff at the Laboratory for Laser Energetics. This work was performed under the auspices of U.S. DOE NNSA under the AIBS program, and the DOE Office of Science under the HEDLP program with award number DE-SC0020103.

Inertial Confinement Fusion Interface 22A

B. Reichelt and C. K. Li*
Massachusetts Institute of Technology
*Principal Investigator

Inertial Confinement Fusion (ICF) Interface 22A was a makeup shot day for ICF Interface 21A, a separated reactant type shot day from 2021 that had a target assembly issue with out-of-spec glue spots. Like the original experiment, this day aimed to study the issue of interface mix for an 8-μm-thick target using a CD ablator separated from a ^{3}He gas fill by an inert CH layer of varying thickness. Thus, D^{3}He protons and D_2 protons/neutrons provide information about mix since their ratio is proportional to $n_{^3\mathrm{He}}/n_{\mathrm{D}}$. Further, the use of reactions that produce charged particles enables the use of the nuclear-imaging diagnostic proton core imaging spectrometer, which sheds further insight into the region that is producing reactions and how localized the mix is.

This shot day utilized targets that were significantly thinner than previous campaigns in the hopes of probing a regime more dominated by kinetic effects. Of particular interest is determining the accuracy of various mixing models in systems where strong shocks exist, which has become more programmatically relevant as OMEGA cryo shots have worked to increase implosion velocity. Both hydrodynamic and fully kinetic models are being interrogated using the LANL codes *xRAGE* and *iFP*, respectively.

Early analysis of nuclear data has been done to determine the charged-particle spectra emitted from the implosion shown in Fig. 7. As shown, the relationship between the CH buffer layer thickness and the spectral peak/width is not immediately apparent, but might be possible to relate to implosion ρR through stopping power and straggling formulas. There are interesting trends seen in the yields, however, which show an inversion effect as a function of offset thickness similar to past experiments for thicker capsules with lower temperatures.[13] Work is ongoing to analyze the time and spatially resolved nuclear diagnostic data collected by this experiment and to compare to predictions from hydrodynamic and kinetic simulations.

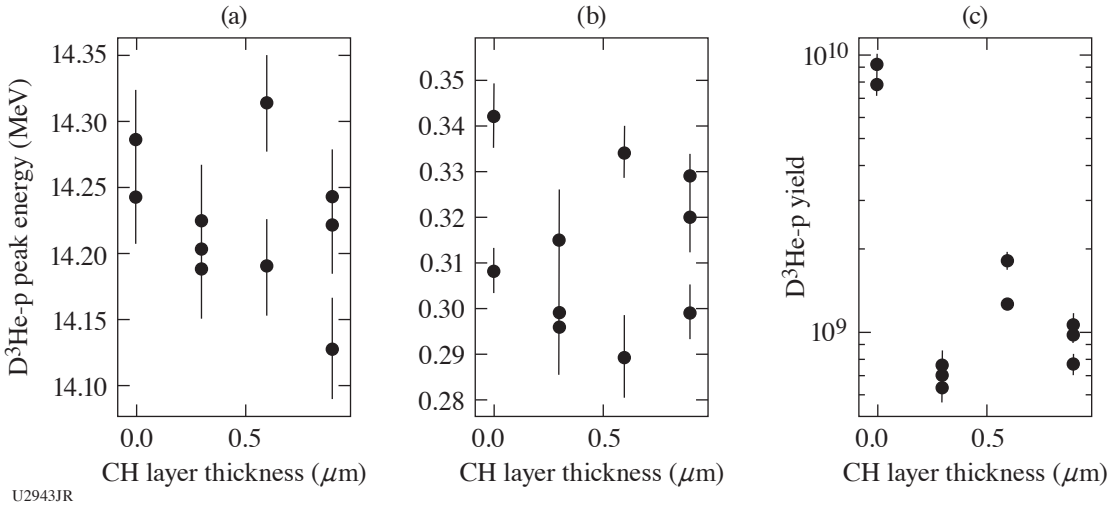

Figure 7
Analysis of D^{3}He proton spectra data from ICF Interface 22A using the wedge-range-filter array diagnostic.

This work is funded by DOE/NNSA Center of Excellence Contract DE-NA0003868. B. Reichelt is supported by NNSA Stewardship Science Graduate Fellowship Contract DE-NA0003960.

Effects of an External Magnetic Field on Laser–Plasma Instabilities

M. Bailly-Grandvaux,[1*] S. Bolaños,[1] R. Lee,[2] M. J.-E Manuel,[3] W. B. Mori,[2] F. Tsung,[2] B. Winjum,[4] and F. N. Beg[1]
[1]Center for Energy Research, University of California, San Diego
[2]Physics and Astronomy Department, University of California, Los Angeles
[3]General Atomics
[4]Office of Advanced Research Computing, University of California, Los Angeles
[*]Principal Investigator

Laser–plasma instabilities (LPI's) play a detrimental role in energy coupling to the target in inertial confinement fusion (ICF). This fundamental constraint of energy coupling of high-power lasers to plasma has been studied extensively over the last couple of decades under a wide variety of laser and plasma parameters. The recent development of applied strong magnetic fields for use in ICF and laboratory astrophysics experiments, however, has opened opportunities to investigate the role of external magnetic fields on LPI's. Recent numerical studies have shown that stimulated Raman scattering (SRS)[14] can be mitigated by external magnetic fields in the kinetic regime of the instability and warrant systematic experimental studies to validate modeling.

With this aim, we developed a platform for OMEGA EP to investigate the effect of an external magnetic field on SRS. A first shot day experiment was carried out in FY20, where we successfully demonstrated the feasibility to investigate backward-SRS (BSRS) in the kinetic regime and in a magnetized environment.[15] The experiment relied on the ability to measure the BSRS light when a laser pulse propagated through a magnetized gas-jet target, as sketched in Fig. 8(a). To measure the backscattered light, we used the sub-aperture backscatter (SABS) diagnostic, which provided a temporal and spectral resolution. The dual magneto-inertial fusion electrical discharge system (MIFEDS) ten-inch manipulator (TIM)-based pulsed-power device was fielded to embed the gas jet in a quasi-perpendicular and uniform magnetic field of ~22 T. The Rowland x-ray spectrometer and the 4ω-probe diagnostics suite were fielded in order to estimate the plasma conditions by comparing them with radiation-magnetohydrodynamic simulations (using *FLASH* and *GORGON* codes). We modified the platform in light of the first shot day experience: the MIFEDS axis was oriented in the same direction as the gas flow [Fig. 8(a)]. We also modified the laser profile of the interaction beam [orange curve in Fig. 8(b)] and added a heater beam. The main benefit of the heater beam is to prepare the plasma prior to the excitation beam interaction with improved uniformity. Its larger size reduces gradients within the smaller excitation beam spot size and lowers the intensity on target to avoid filamentation during heating. The SRS driver (Beam 4) utilized a special laser shape (a train of short pulses) to aid the interpretation of the BSRS signal by drastically reducing temporal variations of plasma conditions within the interaction of a 100-ps pulse.

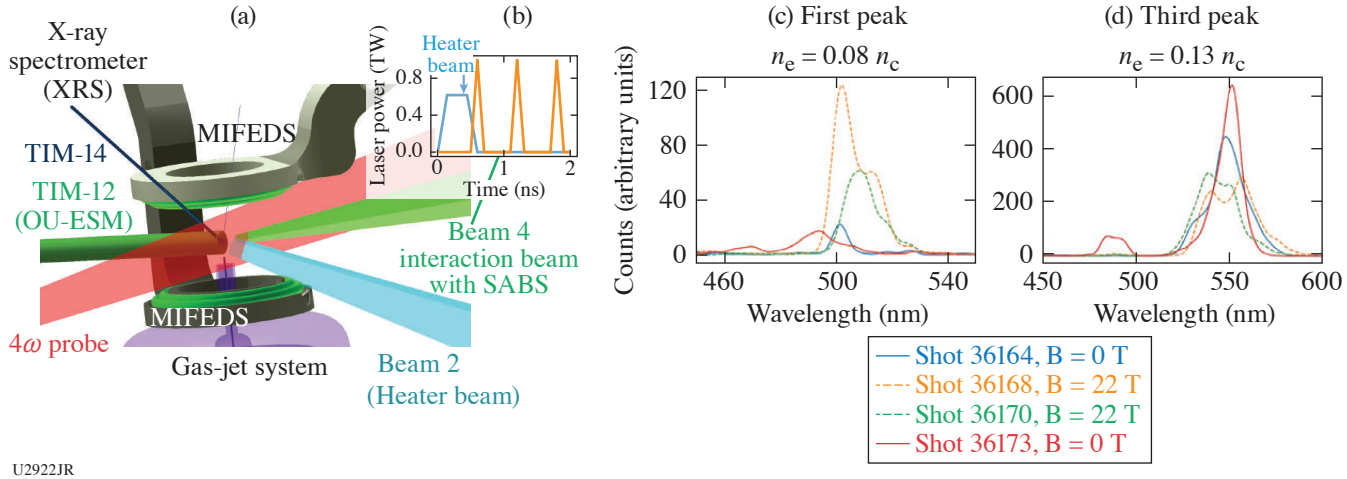

Figure 8
(a) *VISRAD* schematic of the experimental platform. (b) Temporal profiles of the laser power at target chamber center. [(c),(d)] Spectra of the backscattered light measured with SABS. Solid lines are shots without an external B field, and dashed lines are shots with an applied B field of 22 T. Spectra of the (c) first peak (d) the third peak. Note that the density is estimated according to the wavelength shift. OU-ESM: Osaka University electron spectrometer.

In the latest MagSRS-22A campaign, seven shots were performed. The first two shots of the day were performed with an argon pressure of 550 psi. The following shots were performed with a pressure of 880 psi in order to reach a higher density and thus reach the desired kinetic regime ($k\lambda_D \sim 0.2$ to 0.35). Three out of the five 880-psi shots were magnetized shots. We note that in one magnetized shot, MIFEDS failed, likely due to an arcing effect.

The SRS emission excited by a train of short 100-ps pulses is separated in the streaked spectral measurements, making it possible to correlate the spectra to specific plasma conditions for each pulse, as illustrated in Figs. 8(c) and 8(d). Since the time between pulses (~600 ps) is larger than the hydrodynamic time scale, the SRS excitation occurs in different conditions, meaning we diagnose the magnetic effect in various regimes. Figures 8(c) and 8(d) show the spectra measured with the SABS diagnostic for the first and third pulses where we observe contradictory behavior in the presence of the applied B field. For the third peak [$n_e \sim 13\%\ n_c$, see Fig. 8(d)], we observe mitigation of SRS reflectivity in the presence of the external B field, as expected. This is the first experimental evidence of SRS mitigation with B field. On the other hand, for the first peak [$n_e \sim 8\%\ n_c$, see Fig. 8(c)], we observe an apparent enhancement of the SRS reflectivity when applying an external magnetic field. We suspect that this enhancement is due to a rescattering mechanism. For the second peak (not shown) the backscattered light spectra are shifted to a wavelength corresponding to lower densities of $n_e \sim 5\%\ n_c$, although the data were not reproducible for repeated shots. As seen by the shift of the BSRS wavelength, shot-to-shot variations are related to hydrodynamic fluctuations that seem to be significant ~1 ns after the laser–plasma interaction (heater beam) and averaged out later in time.

We estimate the electron density from the backscatter wavelength. Indeed, the backscatter wavelength is strongly dependent on electron density. The electron temperature also induces a small shift. We fielded the Rowland x-ray spectrometer to estimate an average temperature of ~800 eV. Figure 9(a) shows the time-integrated K-shell emissions from the Ar gas jet and the synthetic spectra calculated by the collisional-radiative spectral analysis code *PrismSPECT*. With this measurement, we were able to correct the estimation of the electron density from the wavelength shifts in the backscatter spectra.

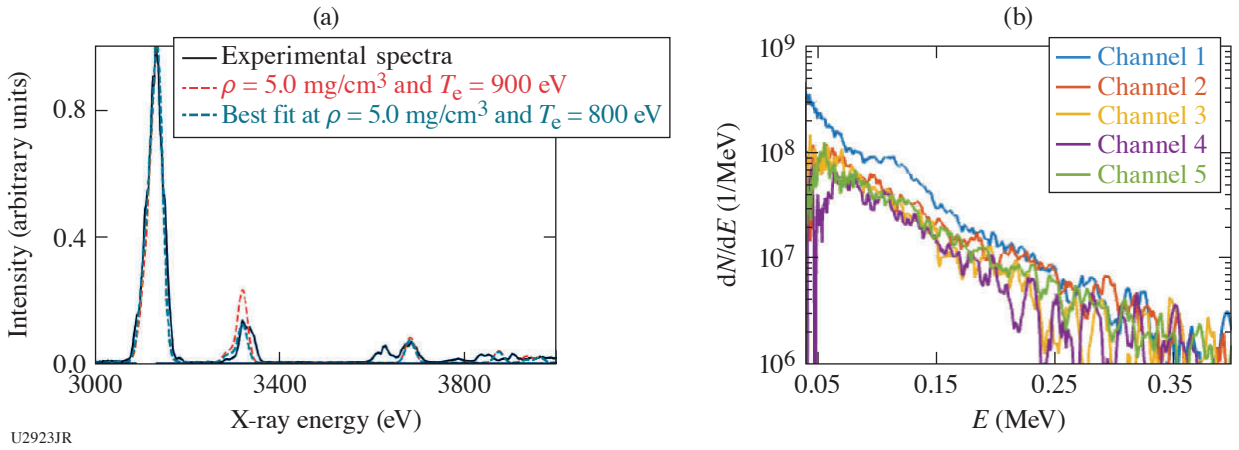

Figure 9
(a) XRS signal with a fit using *PrismSPECT*, giving an average electron temperature of ~800 eV. (b) Electron spectra measured at various angles via the OU-ESM.

In the studied regime, the wave-particle interaction plays a crucial role. A part of the electrons become trapped in the electron plasma wave and are accelerated at the phase velocity of the electron plasma wave in the direction of the laser. We fielded the OU-ESM electron spectrometer to measure the energy distribution of hot electrons. When unmagnetized, these hot electrons reduce the Landau damping and enable the growth of the SRS at $k\lambda_D \sim 0.3$. Figure 9 shows the electron spectra measured on one of the unmagnetized shots with a pressure of 880 psi. It reveals the presence of hot electrons with a temperature reaching ~300 keV, while no electrons were detected at the lower pressure of 550 psi. The OU-ESM is angularly resolved, such that each of the channels collects a sample of the electron beam at a different angle. Here, channel 1 is the channel the most aligned with the SRS driver

beam (Beam 4). We note an increase in the number of electrons (×2) for $E < 150$ keV, suggesting they were probably accelerated by the electron plasma wave induced by the SRS driver. Yet, the measured temperature is above our expectation and suggests that other LPI's occurred.[16] More particle-in-cell simulations will be run to understand the origin of such hot electrons. We did not detect any electrons in magnetized shots due to the deflections by the large-volume B field generated by the MIFEDS coils.

The experiment was conducted on the OMEGAG EP Laser System at the University of Rochester's Laboratory for Laser Energetics with the beam time through the NLUF Program. This material is based upon work supported by the Department of Energy, National Nuclear Security Administration under Award Numbers DE-NA0003842 and DE-NA0003856, the University of Rochester, and the New York State Energy Research and Development Authority.

Pressure Induced B1–B2 Phase Transition in ZnO Under Laser-Driven Ramp Compression

I. K. Ocampo,[1] D. Kim,[1] F. Coppari,[2] R. F. Smith,[2] and T. S. Duffy[1*]
[1]Department of Geosciences, Princeton University
[2]Lawrence Livermore National Laboratory
[*]Principal Investigator

ZnO is a wide-band-gap semiconductor (3.37 eV) well suited for use in electronic and optoelectronic devices (UV emission lasers and detectors, chemical sensors, and solar cells).[17] At ambient conditions, ZnO crystallizes in the wurtzite-type structure (B4, $P6_3mc$). Under quasi-hydrostatic loading, ZnO undergoes a phase transition from a B4-type to a B1-type structure (*Fm-3m*) at ~10 GPa (Ref. 18). Although no further phase transitions have been observed in ZnO experimentally up to ~209 GPa, density functional theory calculations predict that the B2 phase (*Pm-3m*) will become stable at high pressures. The calculated B1–B2 transition pressure varies by approximately 25% between two existing computational studies.[19,20] A tetragonal phase (B10, *P4/nmm*) has also been predicated to become thermodynamically stable over a narrow pressure region (236 to 316 GPa). In this study, we utilized the pulse-shaping capabilities of the OMEGA laser to ramp compress ZnO up to ~800 GPa and probe the atomic level structure of highly compressed ZnO using the powder x-ray diffraction image-plate (PXRDIP) diagnostic. These experiments allow us to directly test theoretical predictions of phase stability and equations of state.

Polycrystalline ZnO foils were synthesized by cold-pressing ZnO powders at 1.7 GPa in a diamond-anvil cell with 800-μm culets. Scanning electron microscope images of the foils were used to estimate the porosity of the foils (~3%). The ZnO foils were sandwiched between an ablator and a single-crystal diamond (SCD) tamper. The ablator for these experiments consisted of two SCD plates with a thin gold coating deposited in between, which acts to shield heat generated at the ablation surface. The ablator–ZnO–tamper target package was then centered over a Ta foil with a 300-μm pinhole and mounted onto the front of the PXRDIP diagnostic box. A 7- to 10-ns ramp shaped pulse was used to ablate the surface of the target package and quasi-isentropically compress the sample. When the target was expected to be at peak stress according to pre-shot hydrocode simulations, a 1-ns laser pulse was used to irradiate a Cu backlighter foil, generating quasi-monochromatic x rays (8.37 keV) that were diffracted from the target and recorded using the PXRDIP diagnostic. A line-VISAR (velocity interferometer system for any reflector) was used to monitor the planarity of the laser drive as well as the particle velocity at the SCD tamper-free surface. We used a Monte Carlo backward-propagating characteristics algorithm to infer the stress history in the sample and estimate the uncertainty in the achieved stress during the x-ray flash.

We have previously reported a series of laser-driven, ramp-compression experiments on ZnO with peak stresses from 260 to 620 GPa where we observed the onset of the B1–B2 phase transition between 299 and 332 GPa. This result is in very good agreement with theoretical predictions. Preliminary analyses of these data also suggest that the B1 and B2 phases remain in coexistence from 330 to 620 GPa. This shows that ramp compression can produce a remarkably large mixed-phase region. In our recent campaign, XRDEOS-22A-NLUF, we conducted four new experiments on OMEGA, extending the pressure–density data for this material up to 800 GPa. At 650 GPa, only the B2 phase was observed. To test the repeatability of this result, another experiment was conducted at 651 GPa and again, only the B2 phase was observed. This provides a high accuracy constraint on the extent of the B1–B2 mixed-phase region under ramp compression (300 to 650 GPa). The extreme metastability of the B1-type structure under the nanosecond time scales of our experiments suggests a kinetic limitation to the B1–B2 transition, yet further experi-

ments are required to evaluate the role of non-hydrostaticity and material strength on this fundamental phase transformation. The diffraction results from our experiment at 800 GPa are shown in Fig. 10. Two sample diffraction peaks could be indexed as corresponding to the (010) and (011) reflections of the B2-type structure. At this stress, ZnO has experienced a more than 2.6-fold increase in its ambient density. This work is ongoing and further experiments will be conducted to develop a pressure–density equation of state of the high-pressure B2 phase.

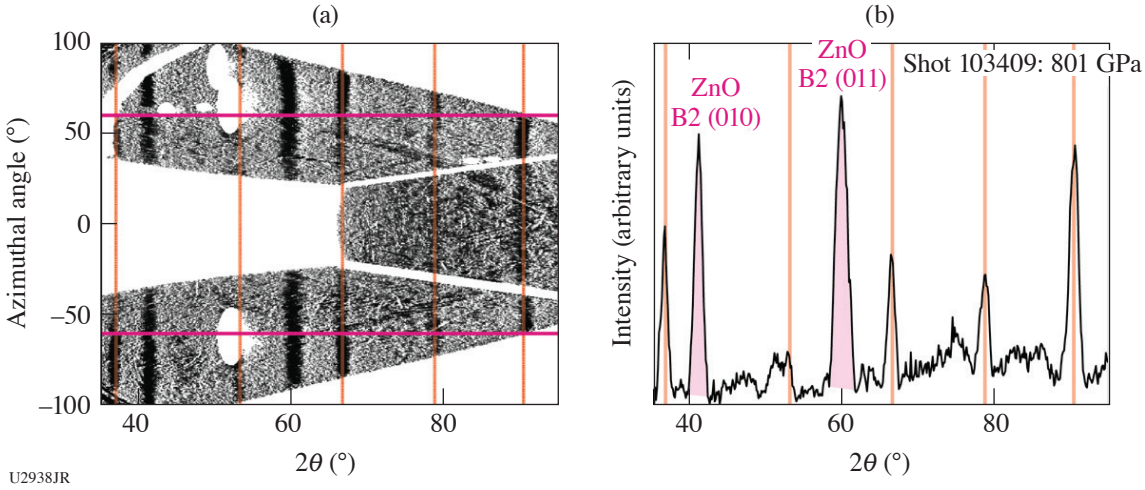

Figure 10
Diffraction results from shot 103409, our highest stress experiments (801 GPa). (a) The dewarped image plates projected into 2θ–ϕ space. Orange vertical lines highlight diffraction from the Ta pinhole. (b) The 1-D diffraction pattern integrated over the azimuthal angles specified by the horizontal magenta lines.

This work was supported by DOE Office of Science, Fusion Energy Sciences under Contract No. DE-SC0020005, the LaserNetUS initiative at the Omega Laser Facility, NNSA Contract No. DE-NA0003957, and National Science Foundation (NSF) EAR-1644614.

MultiIon Campaign: Studies of Multi-Ion and Kinetic Effects in Shock and Ablatively Driven Implosions

T. Evans,[1] N. V. Kabadi,[2] P. Adrian,[1] J. Kunimune,[1] E. Gallardo-Diaz,[3] R. C. Mancini,[3] C. Stoeckl,[2] V. N. Glebov,[2] and J. A. Frenje[1*]
[1]Plasma Science and Fusion Center, Massachusetts Institute of Technology
[2]Laboratory for Laser Energetics, University of Rochester
[3]University of Nevada, Reno
*Principal Investigator

MultiIon-22A and MultiIon-22B focused on studying the impact of multi-ion and kinetic effects on several observables during the shock-burn phase and subsequent compression phase in both shock- and ablatively driven implosions. Previous work demonstrated the presence of thermal decoupling and a significant deviation from hydrodynamic behavior of implosions with low initial gas-fill density (or pressure).[21,22] Yield, ion temperature, emission histories of x rays, neutrons, and protons were measured simultaneously in each implosion experiment. The measured data set is being compared to both hydrodynamic and kinetic simulations to understand the influence of multi-ion and kinetic effects at different stages of an ICF implosion.

As shown in Fig. 11, the MultiIon-22A experiment featured 2.8-μm Hoppe-glass capsules with four different initial gas-fill densities, ranging from 0.5 mg/cm^3 to 3.5 mg/cm^3. The variation in initial gas-fill density was selected to obtain a range of Knudsen numbers (K_n) spanning the transition from kinetic to hydro-like behavior. K_n is defined as the ratio of the ion–ion mean free path to the system size (radius of the shell), and is proportional to the square of the temperature over density:

$$K_n = \frac{\lambda_{ii}}{R_{\text{shell}}} \propto \frac{T^2}{n}.$$

Data demonstrate a large discrepancy between the yield in the lower-density cases and that predicted by hydrodynamic theory alone, even where hydrodynamic simulations effectively match other key implosion parameters, including bang time and ion temperature (see Fig. 12). Further analysis of data from this shot day will include comparison to fully kinetic simulations, which are expected to recreate the observed discrepancy.

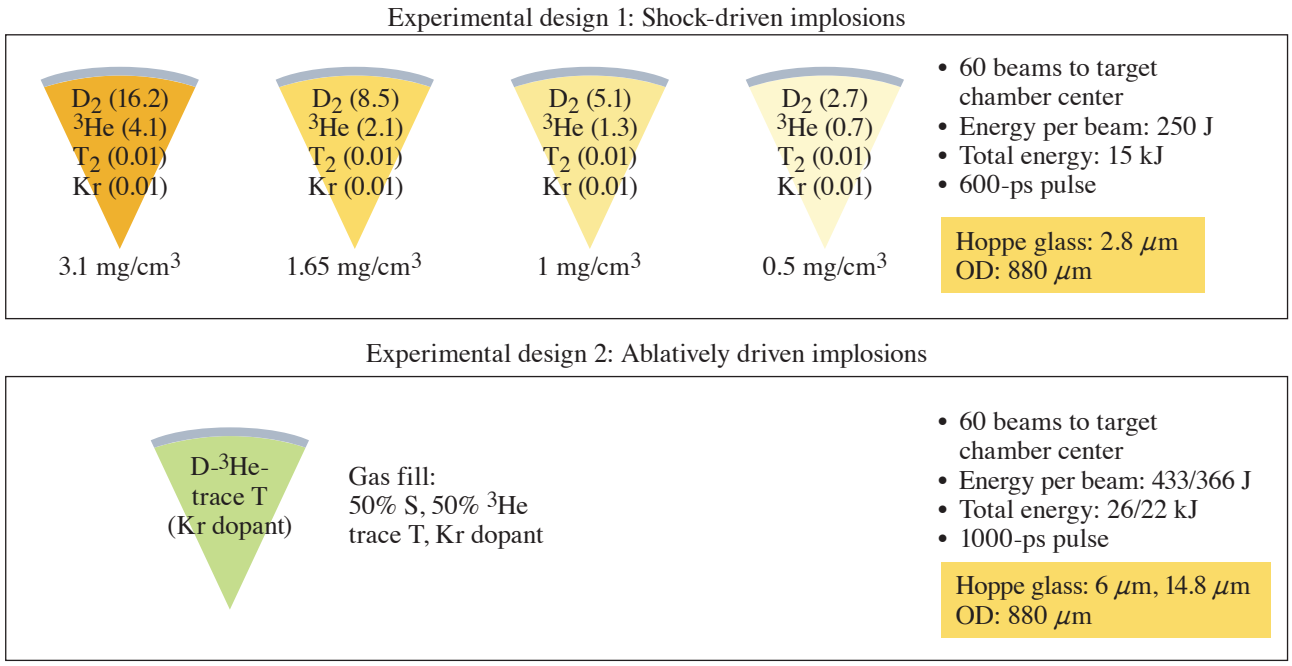

Figure 11
Capsule and laser specifications for both MultiIon-22A and MultiIon-22B experiments.

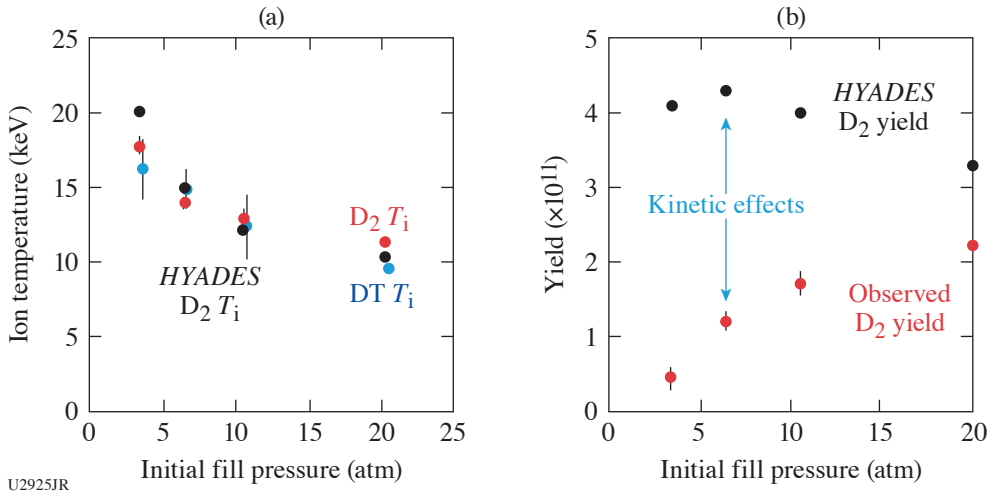

Figure 12
(a) Measured and hydro-simulated D_2 and DT ion temperature versus initial gas-fill pressure. A preliminary evaluation suggests a good agreement between data and simulation is observed. (b) Measured and hydro-simulated D_2 yield versus initial gas-fill pressure. The yield shows a large discrepancy at lower fill pressures, clearly indicating the impact kinetic effects, which will be further analyzed.

The MultiIon-22B experiment featured 6-μm and 15-μm-thick Hoppe-glass capsules that were illuminated by two different laser driver energies. The purpose with these capsule and laser configurations was to generate compression-driven implosions and study how kinetic effects persist from the shock-burn phase to the subsequent compression phase. In addition, the different shell thicknesses and laser energies provide different shock strengths. The analysis of the resulting data is ongoing and will involve both hydrodynamic and kinetic simulations with the intention of linking key implosion parameters to those observed in MultiIon-22A.

In summary, excellent data were obtained with the primary particle x-ray temporal diagnostic[23] and neutron temporal diagnostic in both the MultiIon-22A and MultiIon-22B experiments. The analysis of the resulting data is underway. Continued analysis will link the results of the two shot days and inform a dynamic model of the impact of shock-burn phase kinetic effects on the subsequent compression phase.

This work was supported by DOE/NNSA contracts DE-NA0003868, DE-NA0003856, and DE-NA0003938. Thank you to collaborators at MIT and LLE for support and guidance.

Ablator–Gas Interface Dynamics and Mix in Inertial Confinement Fusion-Relevant Conditions

J. Kunimune,[1] B. Reichelt,[1] P. Adrian,[1] S. Anderson,[2] B. Appelbe,[3] A. Crilly,[3] T. Evans,[1] C. J. Forrest,[4] J. A. Frenje,[1] V. Yu. Glebov,[4] B. M. Haines,[2] T. M. Johnson,[1] C. K. Li,[1] H. G. Rinderknecht,[4] G. D. Sutcliffe,[1] W. Taitano,[2] and M. Gatu Johnson[1*]
[1]Massachusetts Institute of Technology
[2]Los Alamos National Laboratory
[3]Imperial College, London
[4]Laboratory for Laser Energetics, University of Rochester
[*]Principal Investigator

The main goal of this NLUF campaign is to validate and confirm the impact of "kinetic mix,"[24] where fast streaming ions generated during the shock phase of an ICF implosion impact core plasma conditions. Reaching this goal also requires quantifying the relative impact of other mix effects (hydro-instabilities, diffusion, and localized mix) as a function of implosion conditions (to isolate the kinetic mix effect, these other effects must be mitigated or understood). During FY22, two initial experiments were executed as part of this project: LocMix-22A (0.5 shot days, PI MIT Ph.D. student Justin Kunimune) and KinMix-22A (one shot day, PI MIT Ph.D. student B. Reichelt).

Targets for LocMix-22A and KinMix-22A are shown in Fig. 13. All were filled to the same number density and had the same outer diameter, and both campaigns used both 6-μm and 15-μm-thick plastic shells to vary implosion conditions from more kinetic (6 μm) to more hydro-like (15 μm), with the anticipation that kinetic and diffusion mix will dominate at 6 μm with hydro (instability) mix starting to play more of a role at 15 μm.

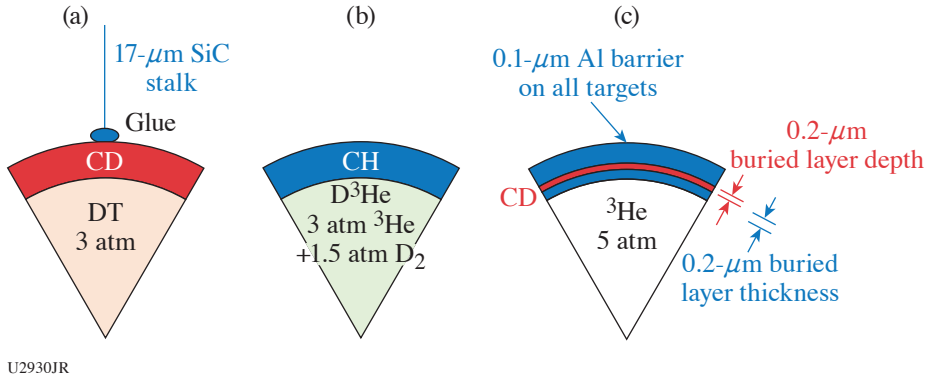

Figure 13
Pie diagrams for targets used for (a) LocMix-22A and [(b),(c)] KinMix-22A. For each experiment, total shell thickness of 6 μm and 15 μm were used to vary implosion conditions from strongly shock driven and thus highly kinetic (6-μm shell) to more compressively driven and hence more hydro-like (15-μm shell). The goal of LocMix-22A was to quantify localized mix due to stalk impact by using imaging diagnostics and one to two stalks, while the goal of KinMix-22A was to study the balance of diffusion/kinetic/hydro mix as a function of implosion conditions using nuclear observables with time-resolved nuclear burn-history measurements as the primary diagnostic.

The specific goal of LocMix-22A was to measure impact of localized mix due to the capsule stalk mount. To this end, half of the implosions used a single stalk, while half used two stalks in opposing geometry. The primary diagnostics were three-axis x-ray and knock-on deuteron (KOd) imaging (Fig. 14). Three x-ray images in different energy bands were obtained in each of three near-orthogonal viewing directions; these data will be used to reconstruct spatial electron temperature profiles. *xRAGE* simulations predict that the effect of the stalk mix will be a region of less x-ray emission due to injection of material that is ~2 keV colder than the surrounding fuel;[25] if correct, this should be clearly visible in the x-ray data. The KOd come from DT neutrons scattering off of D in the fuel or CD shell. By imaging deuterons in different energy bands, differences in morphology of the fuel (high-energy, forward-scattered deuterons) and shell (lower-energy, side-scattered deuterons) should be discernible. Analysis of both x-ray and KOd images are still in the early stages; preliminary images from the TIM-4 viewing angle are also shown in Fig. 14.

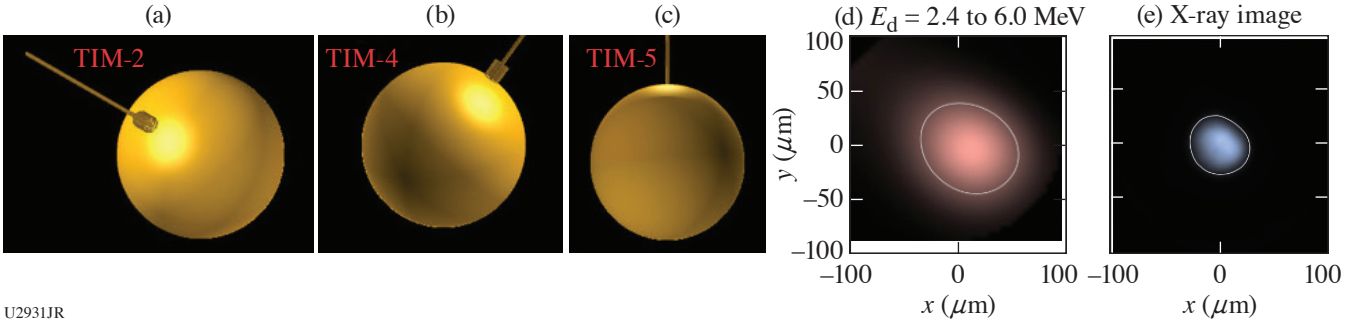

Figure 14
[(a)–(c)] LocMix-22A used three near-orthogonal penumbral imaging detectors in OMEGA TIM-2, -4, and -5 set up to measure (d) knock-on deuterons and (e) x rays in three different energy bands. (d) The TIM-4 deuteron image in the 2.4- to 6.0-MeV energy band, and (e) the x-ray image recorded in the same location. Analysis is in progress to infer stalk impact through reconstruction of the spatial electron temperature distribution from the x-ray images in different energy bands, and through the study of asymmetries in the knock-on deuteron emission.

KinMix-22A used directly comparable buried-layer targets, with a CD tracer layer and pure ^{3}He gas fill, and reference targets, with CH shells and 50:50 D^{3}He fill, to study the level (through integrated nuclear signatures) and timing (through nuclear burn history measurements) of mix. Detailed analysis of the data is in progress; preliminary D^{3}He yields show substantially more mixing for the thin shell (6 μm) than thick shell (15 μm) targets (Table II). The particle x-ray temporal diagnostic (PXTD) also recorded good data on this experiment, which will be used to address the relative timing of proton emission versus peak convergence for the two shell thicknesses, thus helping constrain the mix mechanisms responsible for injecting deuterium into the fuel as a function of implosion conditions.

Table II: Highly preliminary results from KinMix-22A suggest substantially more shell mixing (D^{3}He signal) for the 6-μm shells than for the 15-μm shells (10% of the control versus 2% of the control D^{3}He yield, respectively). CR-39 etching and scanning is still in progress to finalize these numbers. nTOF: neutron time of flight.

Total shell thickness (μm)	Capsule fill	Laser pulse	YDD$_n$ estimated (nTOF)	YD^{3}He$_P$ estimated (nTOF)	DD$_n$ temperature (nTOF)
14.3	4.5 atm D^{3}He	SG010	1×10^{10}	6×10^9	6 keV
14.6	5 atm ^{3}He	SG010	2.5×10^8	1×10^8	2.5 keV
6.3	5 atm ^{3}He	SG006	4×10^7	1×10^9	Uncertain (5 to 15 keV)
5.8	4.5 atm D^{3}He	SG006	1.5×10^{10}	1×10^{10}	15 keV

The KinMix-22A and LocMix-22A datasets will be completed with further buried-layer data from KinMix-23A, and with measurements of the ion release from 6-μm and 15-μm flat foils in opposing geometry with a gas jet in between, using Thomson scattering and x-ray imaging, on FoilGasDist-23A.

This material is based upon work supported by the National Nuclear Security Administration, Stewardship Science Academic Alliances, under Award Number DE-NA0003868. The experiments were conducted at the Omega Laser Facility with the beam time through the NLUF under the auspices of the U.S. DOE/NNSA by the University of Rochester's Laboratory for Laser Energetics under Contract DE-NA0003856. B. Reichelt is supported by NNSA SSGF Contract DE-NA0003960.

Report for DACPlanet-22A/B

G. Tabak,[1,2*] G. W. Collins,[1,2,3] J. R. Rygg,[1,2,3] R. Dias,[2,3] N. Dasenbrock-Gammon,[2] T.-A. Suer,[1,3] S. Brygoo,[4] P. Loubeyre,[4] and R. Jeanloz[5*]
[1]Laboratory for Laser Energetics, University of Rochester
[2]Department of Physics and Astronomy, University of Rochester
[3]Department of Mechanical Engineering, University of Rochester
[4]Commissariat à l'énergie atomique et aux energies alternatives
[5]University of California, Berkeley
[*]Principal Investigators

The purpose of this campaign was to study a hydrogen–neon gas mixture with planetary science applications in mind. Hydrogen and neon are present in gas giants such as Saturn and the two are predicted to be immiscible at certain pressure–temperature conditions inside these planets. Documenting the exact location of the demixing boundary has implications for planetary modeling. This study is a follow-up on similar experiments performed on hydrogen–helium mixtures.[26]

The experimental approach was to precompress H_2–Ne mixtures (20% Ne by mole) in diamond-anvil cells (DAC's) to 4 GPa and shock compress them using the high-power lasers at LLE. At the 4-GPa precompression, hydrogen and neon are liquid and miscible, making it possible to prepare a homogeneous sample at liquid initial densities. The resulting Hugoniot curve is predicted to span pressure–temperature conditions relevant to planets and cross the demixing boundary, beyond which (i.e., at the most extreme conditions) the hydrogen and neon are miscible. A quartz layer was inserted into the DAC chamber to serve as a material standard. The filled DAC's were characterized to measure the sample pressure and chamber thickness. The targets were then driven with a 1-ns square pulse drive on the OMEGA 60-beam laser, driving a shock wave through the samples. VISAR and SOP (streaked optical pyrometry) were used to measure the shock velocity, reflectivity, and self-emission.

Excellent velocimetry and pyrometry data were obtained using VISAR and SOP (see Fig. 15). Impedance matching with quartz will be used to infer the pressure and density of the gas mixture. The self-emission and VISAR fringe amplitude will be referenced to quartz to measure the reflectivity and temperature of the shocked gas mixture. The expected signature of the demixing boundary is a discontinuity in the reflectivity along the Hugoniot. Such a signature has been observed for hydrogen–helium mixtures.[26]

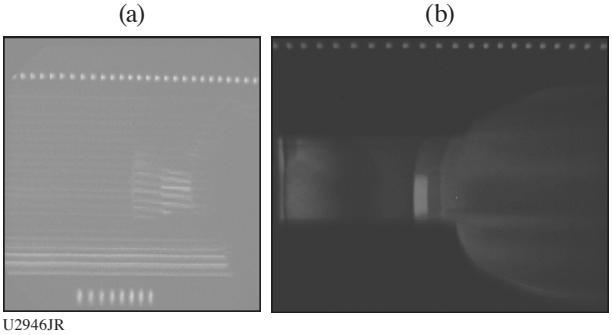

U2946JR

Figure 15
(a) VISAR and (b) SOP data for shot 103818. The two fringe events at the spatial center of the streak camera image indicate shock breakout into quartz and then into the gas mixture. The self-emission of the quartz standard is clearly seen as the small rectangular region on the SOP image, after which the gas mixture self-emission is recorded.

Several data points on the hydrogen–neon mixture have been obtained, providing the first step to understanding the mixture. Additional data will be obtained in FY23 that should provide definitive evidence of the expected reflectivity discontinuity in order to demarcate the demixing threshold. In particular, more shots at lower pressures (<150 GPa) are needed to study the region of interest. The resulting impedance match with quartz would entail a quartz sample that is either absorbing or transparent at the

VISAR probe frequency (532 nm), so some targets will be prepared instead with a fused-silica window. The fused silica becomes reflective at lower pressures than quartz, so this will facilitate lower shock pressure experiments with a reflective material standard.

Plasmoid Magnetic Reconnection Between Long-Pulse, Laser-Driven Plasmas Perturbed by a Short-Pulse Laser

J. L. Latham,[1] B. K. Russell,[1] L. Willingale,[1] P. T. Campbell,[1] G. Fiksel,[1] P. M. Nilson,[2] and K. M. Krushelnick[1*]
[1]Center for Ultrafast Optical Science, University of Michigan
[2]Laboratory for Laser Energetics, University of Rochester
[*]Principal Investigator

To understand magnetic reconnection in high-energy-density plasmas,[27] this campaign studied the magnetic fields of a three-pulse geometry, where a short-pulse laser illuminated the interaction region between two expanding plasma plumes, each driven by a long-pulse laser. Pre-shot studies anticipated that the reconnection rate would increase with the temperature of the interaction region, à la plasmoid reconnection theory,[28] but that the outflowing plasma from the short-pulse laser would inhibit reconnection.

In the experiment, plastic targets were irradiated by two UV beams with an intensity of 1.1×10^{14} W/cm^2 for 2.5 ns ("long-pulse lasers"). Some of the targets were also irradiated by an IR beam with an intensity of 2×10^{19} W/cm^2 for 10 ps ("short-pulse laser"). The resulting magnetic (and electric) fields were recorded in radiochromic film (RCF), using a proton beam created by a second short-pulse laser incident at a copper foil located 8 mm away from the target. The data show dark rings around each of the laser spots, and in several cases a highly complicated structure (Fig. 16).

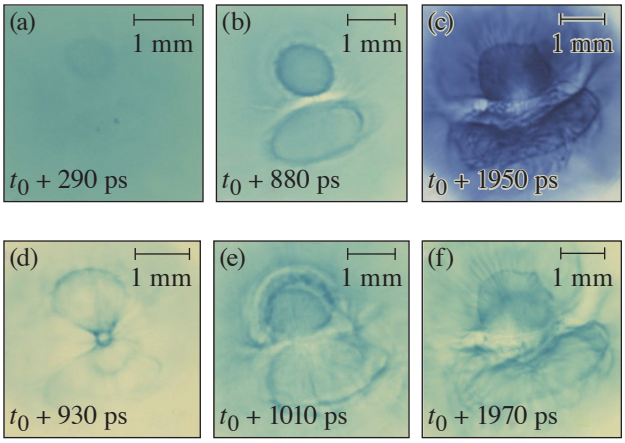

Figure 16
Scans of RCF irradiated by 24-MeV protons that passed through the main laser target. The time that the proton beam passed through the target is indicated on each film where t_0 is the onset of the UV beams. For shots (a)–(c) there was no short-pulse laser on the main target. For films (d)–(f), the short-pulse laser arrived at times t_0 + 360 ps, t_0 + 940 ps, and t_0 + 950 ps, respectively.

Plasmoid reconnection theory alone is not sufficient to explain the dynamics of the magnetic fields in this experiment. The discontinuities in the dark regions of the film indicate that reconnection may have been inhibited rather than enhanced. A future experiment is required to capture the dynamics in between the time windows captured in this experiment. The laser–plasma interaction is also being investigated using computer simulations.

The experiment was conducted at the Omega Laser Facility with the beam time through NLUF under the auspices of the U.S. DOE/NNSA by the University of Rochester's Laboratory for Laser Energetics under Contract DE-NA0003856.

Achieving Neutron Star Envelope-Relevant Conditions Through a Radiative Shock in a Strongly Coupled Plasma

C. C. Kuranz,* H. J. LeFevre,* S. D. Baalrud, and J. Kinney
Nuclear Engineering and Radiological Sciences, University of Michigan
*Principal Investigators

Compact objects are some of the most extreme environments in the universe. The temperatures and densities inside a neutron star can reach truly extraordinary values of 10^9 K and 10^{14} g/cm^3, respectively, at masses of around one solar mass. This makes these objects extremely small (tens of kilometers diameter), which make them difficult to directly observe.[29] In the envelope of a neutron star, in the more-outer portions, radiation dominates the heat transport, and the plasma is not fully stripped, which makes the opacities difficult to model.[30] The strong ion coupling (with the coupling parameter ~10) is a challenging regime for theory and radiation is not typically considered in these systems.[31] Additionally, the strongly coupled nature of this plasma will affect the contributions of bremsstrahlung to the emissivity and opacity, which is not currently adequately modeled. The dimensionless parameter to determine if a shock is radiative is

$$R_F = \frac{2\sigma T^4}{\rho u_s^3},$$

where σ is the Stefan–Boltzmann coefficient, T is the immediate post-shock temperature, ρ is the mass density, and u_s is the shock velocity. If R_F is greater than or about one, then the radiative energy fluxes are significant in the system and the shock is radiative. The coupling parameter determines if the microphysics or bulk physics drives the evolution of the system and one writes it as

$$\Gamma_{ii} = \frac{q^2 Z^2}{4\pi\varepsilon_0 \bar{d} T},$$

where q is the fundamental charge, Z is the ionization, ε_0 is the permittivity of free space, d is the Wigner–Seitz radius, and T is the plasma ion temperature. If Γ_{ii} is greater than one, then the plasma is strongly coupled.

The SCRaP Campaign addresses these problems with a novel capsule implosion experiment. It uses an 860-μm-outer-diam capsule with a 7-μm outer plastic layer and a mid-Z metal layer on the interior surface. The experiments described here used three capsule designs with three different material layers: 0.2 μm of nickel, 0.4 μm of titanium, or 0.7 μm of aluminum. The different layer thicknesses provide capsules of equal mass, so the drive energy can remain unchanged between the different capsule designs. The drive consisted of 60 beams with SG5-650 phase plates and 1-ns square pulses using about 120 J per beam. This resulted in an average irradiance of 3×10^{14} W/cm^2 over the surface of the capsule. The primary diagnostics used to measure the conditions in these experiments were x-ray framing cameras and a time-integrated spectrometer. The framing cameras used 8× magnification and a 50-ps pulse forming module. The Henway spectrometer uses four convex crystals with image-plate detectors covering a spectral range of about 3 to 13 keV.

Figure 17(a) shows contrast-enhanced framing camera data of a nickel-lined capsule implosion. These images have a pair of 20-μm-thick copper and 12.5-μm-thick nickel foils at the rear filter to act as an imager of K-shell emission from nickel. This makes the images show where only the nickel is during the implosion. The regions labeled 1, 2, and 3 in Fig. 17(a) show the imploding shell, the accretion of matter at the center of the shell, forming a shock, and the shock reaching the plastic resulting in rapid cooling, respectively. Figure 17(b) shows the measured velocity of the rebounding shock as about 180 km/s. Figure 17(c) shows the line emission from the highly ionized Ni and an absorption feature at lower energies due to the absorption of bremsstrahlung produced in the hot, dense core of the capsule implosion along the radial gradient in conditions.

This shock velocity is lower than what 1-D radiation hydrodynamics predict, and 2-D simulations are in progress to determine if structure in the imploding material leads to these effects. Further analysis of the spectra will provide the ionization of the pre-shock material and the volume-averaged density, which will be useful for constraining the dimensionless parameters described above.

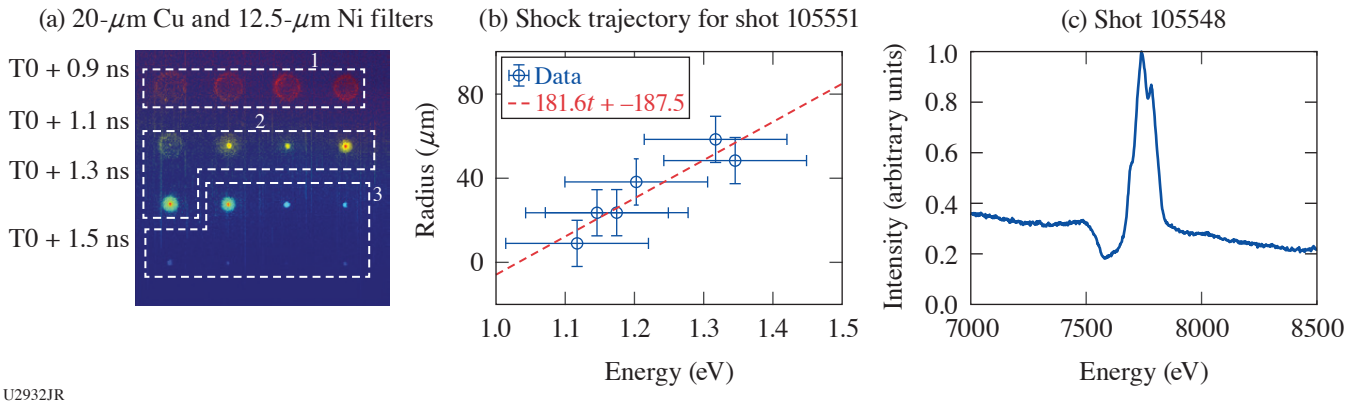

Figure 17
(a) Contrast enhanced framing camera data of a Ni-lined capsule implosion showing region 1 where the Ni shell is imploding and decreasing in radius, region 2 where mass begins accreting at the center of the capsule and forms a rebounding shock, and region 3 where the shock reaches the plastic then expands and cools. (b) The trajectory of the rebounding shock from (a). The linear fit to the data shows a shock velocity of about 180 μm/ns. (c) Spectroscopic data showing the 2 ≥ 1 emission features of Li, Be, and B-like emission features of Ni with an absorption feature to the red of the emission lines due to gradients in the plasma.

This material is based upon work supported by the National Science Foundation MPS-Ascend Postdoctoral Research Fellowship under Grant No. 2138109. This work is supported by SSAA Grant 13432116, and the NLUF Program, grant number DE-NA0002719, and through LLE/NNSA Cooperative Agreement No. DE-NA0003856.

Observation of a Radiative Heat Front in Ar Using the OMEGA Gas-Jet System

C. C. Kuranz,[1*] H. J. LeFevre,[1*] and K. V. Kelso[2]
[1]Department of Nuclear Engineering and Radiological Sciences, University of Michigan
[2]Department of Applied Physics, University of Michigan
[*]Principal Investigators

Radiation from hot, massive stars in star-forming regions can heat the surrounding nebula, heating it and producing an HII region, which consists of ionized hydrogen.[32] This heating propagates as a radiation-driven heat front and this may influence the development of clumps in the nebula, which is an open question in astrophysics.[33,34] The PIonFront Campaign on OMEGA creates a radiative heat front to study the radiation hydrodynamics of this system and understand the ionizing radiation–matter interactions that drive its evolution. The goal of this work is to produce a radiative heat front where photoionization dominates the energy deposition. To determine if that is the case and the front is in the desired physics regime, the dimensionless parameters α and β define the physics regime. The parameter α is the ratio of recombination to photoionization

$$\alpha = \frac{^{n}(\mathrm{i}+1)^{n_\mathrm{e}} R_{\mathrm{i}+1,\mathrm{i}}}{n_\mathrm{i}\Gamma_{\mathrm{i},\mathrm{i}+1}},$$

where n_i is the number density of the ith ionization state, n_e is the electron number density, $R_{\mathrm{i}+1,\mathrm{i}}$ is the recombination rate coefficient, and $\Gamma_{\mathrm{i}+1,\mathrm{i}}$ is the photoionization rate. If α is less than one, then photoionization dominates over recombination. The parameter β is one plus the ratio of electron collisional ionization to recombination

$$\beta = 1 + \frac{n_\mathrm{i}\langle\sigma v\rangle_{\mathrm{i},\mathrm{i}+1}}{n_{\mathrm{i}+1}R_{\mathrm{i}+1,\mathrm{i}}},$$

where $\langle\sigma v\rangle_{\mathrm{i},\mathrm{i}+1}$ is the electron collisional ionization rate coefficient, and all the other values are the same as for α.

To conduct these experiments, it is necessary to have a driving x-ray source and a propagation medium. These experiments use a 500-nm-thick gold foil, irradiated with a 5-ns laser pulse with an irradiance of 10^{14} W/cm^2 to create a bright, quasi-blackbody source. The OMEGA gas-jet system using argon gas with a 2-mm-diam, Mach 5 nozzle and a backing pressure of 750 psi acts as the propagating medium.[35] Figure 18(a) demonstrates the experimental geometry. A capsule implosion using 17 beams with 1-ns square pulses creates a bright, short-lived (~200-ps) probe source for absorption spectroscopy of the argon K shell. The spectroscopic measurement uses a flat, pentaerithritol crystal using an MS image plate as a detector with the backlighter duration self-gating the signal. Figure 18(b) shows the time series of the absorption spectroscopy measurements, indicating a cold plasma with minimal changes to the spectrum until after 2.5 ns after the drive turns on when $n = 1 \rightarrow 3$ and $n = 1 \rightarrow 2$ transitions in argon appear. Additionally, the argon K edge shifts to higher energy due to ionization from the heat front. This indicates a delay in the arrival of the heating at the probe location in the center of the gas jet, 3 mm from the initial driving source position, relative to the speed of light. The appearance of $n = 1 \rightarrow 2$ transitions also indicates that the source ionizes the argon the neon-like state and likely stops at the chlorine-like state. Figure 18(b) shows the time series of spectra over several shots that demonstrates the increase in ionization as the radiative heat front passes the measurement volume.

Currently, the radiation-hydrodynamics simulations of these experiments overpredict the velocity of the heat front. This makes it difficult to compare synthetic spectra to the measured results. Efforts are underway to improve the model of the driving source used in the experiment to address this discrepancy between simulation and experiment. These combined efforts will result in a determination of α and β using the measured and simulated results with models for the atomic rate coefficients.

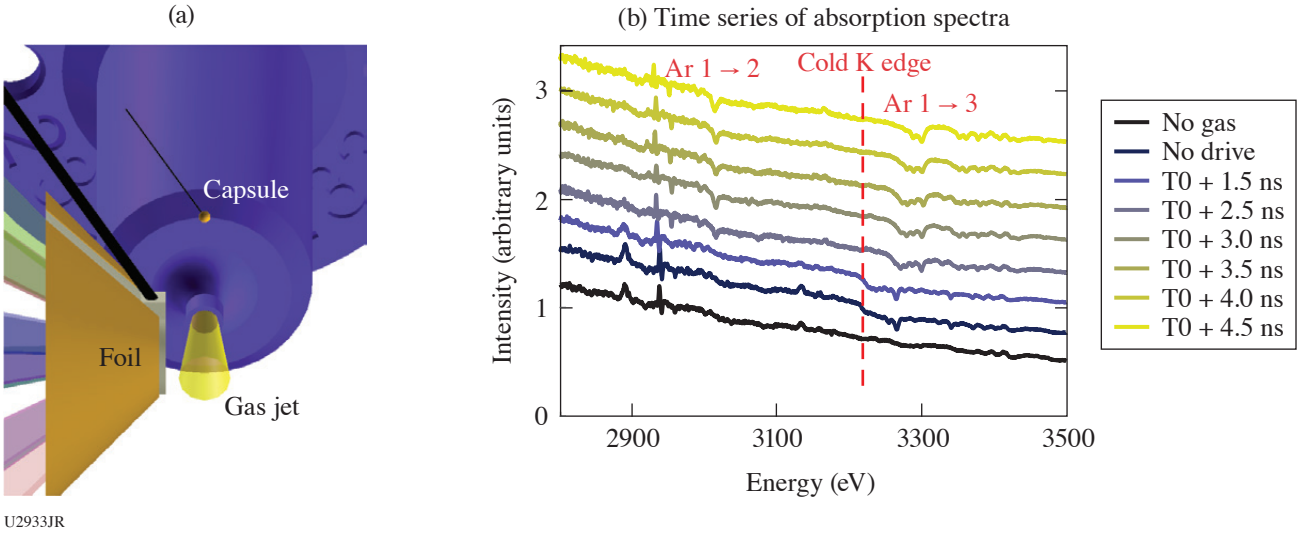

Figure 18
(a) A *VISRAD* model of the gold foil target, the capsule backlighter, and the gas jet. (b) A series of spectra with one spectrum collected during a single shot progressing upward from the bottom. The first (bluest) spectrum is from a capsule backlighter only and the next spectrum has a capsule backlighter with undriven Ar gas. The following spectra moving upward show a delayed onset of a blue shifting of the K edge, which indicates ionization. This is indicative of a heat front propagating through the gas column.

This material is based upon work supported by the National Science Foundation MPS-Ascend Postdoctoral Research Fellowship under Grant 2138109. This work is funded by the U.S. Department of Energy NNSA Center of Excellence under cooperative agreement number DE-NA0003869, and through the LLE/NNSA Cooperative Agreement No. DE-NA0003856.

Onset, Subsistence, and Decay of Magnetized Turbulence and Fluctuation Dynamo

H. Poole,[1] A. F. A. Bott,[1,2] C. A. J. Palmer,[3] Y. Lu,[4] S. Iaquinta,[1] S. Zhang,[1] K. Moczulski,[4,5] P. Farmakis,[4,5] A. Reyes,[4] A. Armstrong,[4,5] D. H. Froula,[5] J. Katz,[5] T. Johnson,[6] C. K. Li,[6] R. D. Petrasso,[6] J. S. Ross,[7] H.-S. Park,[7] P. Tzeferacos,[1,4,5*] G. Gregori,[1] and D. Lamb[8*]
[1]Department of Physics, University of Oxford
[2]Department of Astrophysical Sciences, Princeton University
[3]Centre for Plasma Physics, School of Mathematics and Physics, Queen's University Belfast
[4]Flash Center for Computational Science, Department of Physics and Astronomy, University of Rochester
[5]Laboratory for Laser Energetics, University of Rochester
[6]Plasma Science and Fusion Center, Massachusetts Institute of Technology
[7]Lawrence Livermore National Laboratory
[8]Department of Astronomy and Astrophysics, University of Chicago
[*]Principal Investigators

Magnetic fields are ubiquitous in the universe and are salient agents in numerous astrophysical processes;[36] their origin, however, is not fully understood. Guided by high-fidelity *FLASH*[37,38] simulations, the TDYNO collaboration has conceived, designed,[39] and successfully executed experimental campaigns at the Omega Laser Facility through the NLUF Program that demonstrated turbulent dynamo in the laboratory for the first time,[40] establishing laboratory experiments as a component in the study of turbulent magnetized plasmas.[41] Our more-recent experimental results on OMEGA were able to realize a time-resolved characterization of the evolution of magnetized turbulence in the magnetic Prandtl number (*Pm*) order-unity regime,[42] which is directly relevant to that of idealized fluctuation dynamo simulations and demonstrated the insensitivity of the dynamo achieved in the experiments to initial conditions.[43] The TDYNO platform was also successfully deployed to create an experimental analogue for transport of ultrahigh energy cosmic rays in stochastic magnetic fields.[44] The success of past OMEGA campaigns enabled the launch of a concerted effort to study and characterize turbulent dynamo in various plasma regimes and for different astrophysical environments, springboarding sister experimental campaigns at world-class laser facilities. Using large-scale *FLASH* simulations, we ported the TDYNO platform to the National Ignition Facility at Lawrence Livermore National Laboratory, where the hundredfold increase in available energy enabled us to demonstrate turbulent dynamo in a regime relevant for magnetized turbulence in galaxy clusters. The strong magnetization of the turbulent plasma resulted in prominent reduction of local heat transport and highly structured temperature distributions[45] seen in intracluster medium plasmas and explaining hot galaxy cluster cores. In experiments at the French Laser Mégajoule Facility (the first academic experiment there) we demonstrated, for the first time, magnetic-field amplification in supersonic turbulence[46] relevant to the star-forming interstellar medium. As a result, we can now critically assess dynamo theory and numerical predictions through dedicated experiments with the TDYNO platform. Under the auspices of the NLUF Program, we are building on our recent work and achievements, and are executing an experimental campaign on OMEGA to answer key fundamental questions pertinent to the onset, subsistence, and decay of magnetized turbulence and turbulent dynamo: (1) What is the range of critical magnetic Reynolds numbers for the onset of subsonic fluctuation dynamo in the *Pm* order-unity regime, where most resistive-MHD driven-turbulence simulations in the literature lie? (2) How does the magnetic energy of the saturated dynamo state depend on *Pm*? Can we reach larger magnetic fields if high plasma temperatures are sustained? (3) How, why, and at what rate do magnetized turbulence and its magnetic energy decay?

The first shot day of our ongoing OMEGA campaign was carried out 3 June 2022 and was geared toward measuring the decay rate of magnetized turbulence and characterizing the dissipation of magnetic energy at late times, i.e., question 3 above. To date, our OMEGA experimental campaigns have focused on the onset and saturation of the fluctuation dynamo mechanism but have not studied how the magnetic energy and plasma turbulence eventually decay. While the hydrodynamic case of how the kinetic energy decays was solved by Kolmogorov[47] in 1941, theories for the decay of nonhelical stochastic magnetic fields have only recently been proposed, predicting specific decay power laws ($\propto t^{-10/9}$ and $\propto t^{-20/17}$ in the fast- and slow-reconnection regimes, respectively). The platform deployed is shown in Fig. 19(a) and is similar to the one we fielded on OMEGA for our previous successful TDYNO campaigns[42] with diagnostics trained at late times of the plasma evolution. The assembly is comprised of two composite targets and two grids that are connected by a pair of cylindrical shields. The composite targets are 3 mm in diameter and consist of a 50-μm-thick polystyrene foil (CH) and a 230-μm-thick polystyrene washer. The polystyrene

washers were machined to have a 400-μm-diam cylindrical "well" in their centers. The two targets are mounted 8 mm apart and the pair of grids is placed between them. The two grids are made of polyimide and are mounted 4 mm apart—each of them 2 mm away from the respective proximate face of the foil target. The grids have a diameter of 3 mm, a thickness of 250 μm, and consist of 300-μm-wide holes and 100-μm wires, offset with respect to each other to break the mirror symmetry of the assembly: grid A (red) has a hole in the center, while grid B (blue) does not. Rectangular cones on each target shield the diagnostics from the intense x-ray emission produced when a sequence of ten 1-ns-duration laser beams coming from different angles illuminate each target. The two targets are driven for 10 ns, delivering a total of 5 kJ per target on an area defined by the laser SG5 phase plates. The temporal profile of the drive is a flattop profile. As shown in the *FLASH* simulation we performed for the platform design, the beams drive a pair of counter-propagating, high-magnetic Reynolds number *Rm*, plasma flows that carry the seed magnetic fields generated by Biermann battery. The flows propagate through a pair of grids [Fig. 19(b)] that destabilize the flow and define the driving scale of the turbulence (*L*). The flows then meet at the center of the chamber to form a hot, turbulent interaction region where the magnetic fields are amplified to saturation values [Fig. 19(c)].

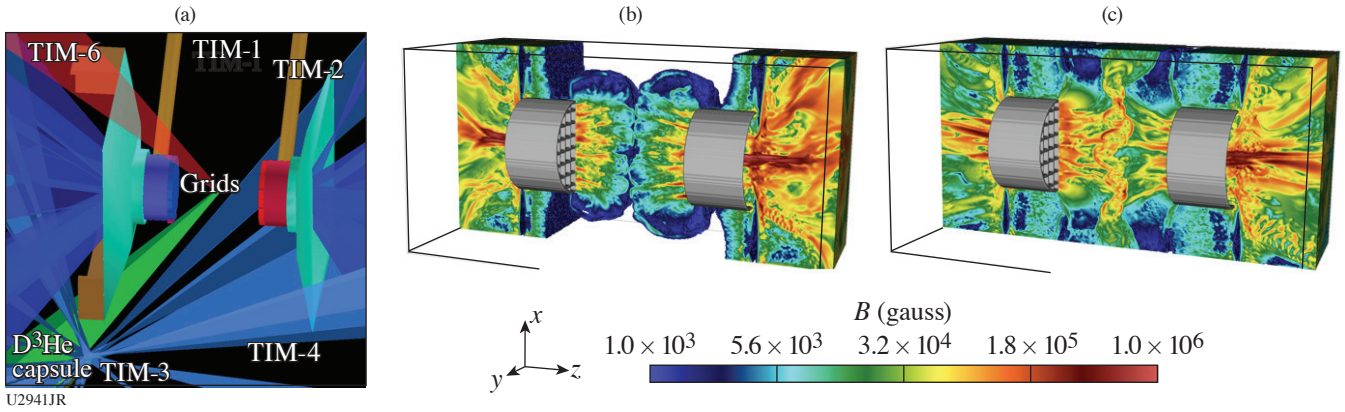

Figure 19
Turbulent dynamo experiments on OMEGA. (a) *VISRAD* schematic of the TDYNO platform for OMEGA to study the decay of the turbulence and its kinetic and magnetic energy. (b) *FLASH* simulation of experiment showing the flows carrying seed magnetic fields to the center where the turbulent interaction is established. (c) Same as (b) but after the establishment of the turbulent interaction region. There, fluctuation dynamo action amplifies the magnetic fields to saturation values prior to their subsequent decay at $t > 30$ ns.

To fully characterize the properties of the magnetized turbulent plasma at late times (>28 ns after the laser drive), we fielded our mature suite of experimental diagnostics [Fig. 19(a)] that consists of (1) an x-ray framing camera (TIM-1: XRFC3) to measure the x-ray fluctuations [Fig. 20(a)] associated with the turbulent spectrum; (2) the 4ω optical Thomson-scattering diagnostic (TIM-4: alignment cart and TIM-6: collection cone) to characterize plasma temperatures, density, and velocities by measuring the ion-acoustic wave (IAW) signal and the electron plasma wave (EPW) signal; and (3) proton radiography (TIM-3: target positioner for the D^3He capsule and TIM-2: CR-39 film pack) to record the 3-MeV and the 15-MeV [Fig. 20(b)] protons generated by the implosion of a D^3He MIT capsule, which are subsequently deflected by the stochastic magnetic field of the turbulent plasma. The proton radiographs are being post-processed to recover the path-integrated magnetic-field maps using the inversion techniques we developed.[8]

The shots yielded a wealth of experimental data and preliminary analysis indicates that we were in fact able to capture the decay rates of the turbulence. The temporal decay of the x-ray intensity fluctuations, and therefore in the turbulent kinetic energy, is clearly visible in the x-ray images we recorded [Fig. 20(a)]. Moreover, the 4ω Thomson-scattering diagnostic (not shown) yielded detailed information on the plasma state (ion and electron temperatures, bulk flow velocity, turbulent velocity, and electron density). Finally, the proton-radiography diagnostic performed perfectly, and the magnetic-field decay was captured in a sequence of proton radiographs [Fig. 20(b)]. We are grateful to the MIT team for their careful etching and development. In the radiographs, we see the gradual reduction in time of the stochastic features but also a reduction in their sharpness, both indica-

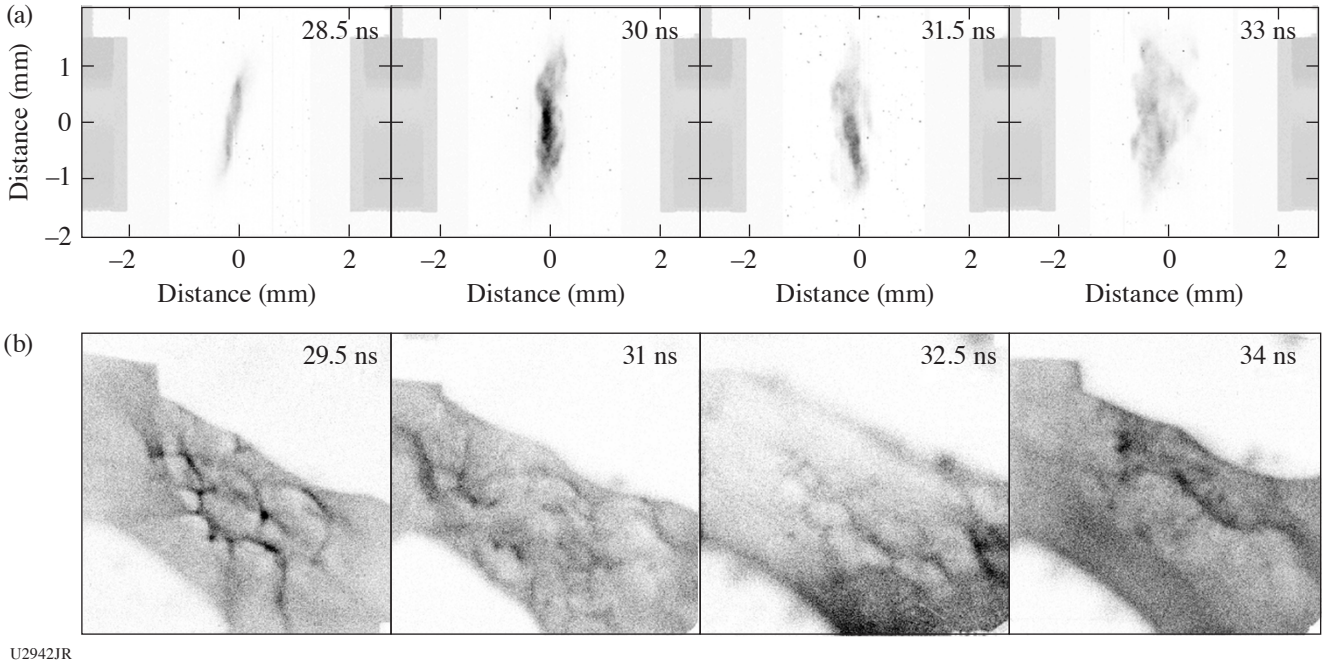

Figure 20

Experimental results. (a) Self-emission x-ray images of the turbulent interaction region from the 2× magnification framing camera at 28.5 ns, 30 ns, 31.5 ns, and 33 ns. The images were taken using a mylar-vanadium filter and can also be used to recover electron temperature information using the method we developed for our National Ignition Facility campaign.[45] Both emission and stochastic features decay in time, which can furnish the decay rate for the kinetic energy. (b) Late-time 15.0-MeV proton images of interaction-region plasma. The D^3He capsule is imploded using 17 270-J beams, each with a 600-ps pulse length and 1.82-mm defocus. This results in the generation of ~109 3.3- and 15.0-MeV protons via nuclear fusion reactions. These protons pass through the stochastic magnetic field and are deflected before reaching the CR-39 detector. The proton images are now being post-processed to recover path-integrated magnetic-field measurements[8] that will quantify the decay rate of the magnetic energy. The gradual reduction in time of the stochastic features and their sharpness is visible, indicative of magnetic energy decay.

tive of a measurable reduction in magnetic energy values. The quantitative analysis of these results will furnish the decay rates that we sought to characterize in this shot day. Despite the complexity of the experimental platform, with the help of personnel from the Laboratory for Laser Energetics, we were able to perform 12 shots during our first shot day. The experimental data are currently being analyzed and promise to further our understanding of how astrophysical magnetized turbulence decays.

The research leading to these results received funding from the U.K. EPSRC (grant numbers EP/M022331/1 and EP/N014472/1); the European Research Council under the European Community's Seventh Framework Programme (FP7/2007-2013)/ERC grant agreements nos. 256973 and 247039; the U.S. DOE under Contract No. B591485 to LLNL; Field Work Proposal No. 57789 to ANL and Awards DE-SC0016566, DE-NA0003605, and DE-NA0003934 to the University of Chicago; DE-NA0003868 to the Massachusetts Institute of Technology; DE-NA0001808, 89233118CNA000010, and 89233119CNA000063 to General Atomics; subcontract nos. 536203 and 630138 (LANL) and B632670 (LLNL) and Award DE-SC0021990 to the Flash Center for Computational Science, University of Rochester; and Cooperative Agreement DE-NA0003856 to the Laboratory for Laser Energetics (LLE), University of Rochester. LLNL work was performed under the auspices of the U.S. Department of Energy by Lawrence Livermore National Laboratory under Contract DE-AC52-07NA27344. We acknowledge support from the NSF under grants PHY-1619573 and PHY-2033925. Awards of compute time were provided by the U.S. DOE ALCC program. Compute time was provided by the U.S. DOE ALCC and ERCAP programs, and the LLE High-Performance Computing group. We acknowledge funding from grants 2016R1A5A1013277 and 2020R1A2C2102800 of the NRF of Korea. Support from AWE plc. and the STFC of the UK is also acknowledged. The Omega shots were allocated through the U.S. DOE NNSA NLUF Program at LLE. The software used in this work was developed in part by the DOE NNSA- and DOE Office of Science-supported Flash Center for Computational Science at the University of Chicago and the University of Rochester.

Collision of Magnetized Jets Created by Hollow Ring Lasers Irradiating High-Z-Doped CH Targets

E. P. Liang,[1*] L. Gao,[2,3] and H. Ji[2,3]
[1]Rice University
[2]Princeton University
[3]Princeton Plasma Physics Laboratory
[*]Principal Investigator

In our 2022 NLUF experiment we investigated the effects of radiative cooling on magnetized, high-beta shocks by colliding head-on two supersonic magnetized jets created by irradiating Fe-doped flat CH targets using a hollow ring of laser beams.[48,49] In earlier OMEGA experiments we successfully demonstrated the creation of such shocks with two opposing jets by using 19 beams from each hemisphere of OMEGA to irradiate flat pure CH targets in a hollow ring pattern. We have characterized the properties of these magnetized jets and shocks and investigated the role of electron thermal conductivity. In the 2022 experiment we explored the effects of radiative cooling by adding 1% to 2% (atomic) Fe dopants to the CH targets to increase the radiative cooling and systematically compare the results with those from pure CH targets. This project is in progress since we only received the first half of proton radiography (Prad) data from MIT at the writing of this report. The preliminary data from all diagnostics appear excellent. We are confident of achieving our original scientific objectives. Our next experiment of this NLUF project, currently scheduled for May 2023, will use Sn-doped CH targets to further increase the effects of radiative cooling. The final results of both experiments will have broad applications to magnetized radiative shocks in both astrophysics and magnetized high-energy-density science, including magnetized ICF.

Experiment Setup and Diagnostics

In the 27 April 2022 experiment, 19 beams from each hemisphere of OMEGA were configured to form an 800-μm-radius hollow ring pattern, irradiating a 1% to 2%-Fe-doped flat CH disk. Two such disks face each other at a separation of 6.4 mm. MG magnetized jets launched from each target collide head-on at mid-plane centered near target chamber cebter (TCC). Strongly magnetized shocks were created and propagated upstream into the jet body. Radiative cooling from the Fe dopants is expected to affect the magnetic-field strength, electron transport, and shock strength, structure, and evolution. We plan to systematically compare the results of Fe-doped CH targets with those of pure-CH targets to quantify the effects of high-Z dopants and compare with 3-D *FLASH* simulation results. The primary diagnostics are the same as those used in our earlier experiments: Thomson scattering (TS) at both TCC and off-TCC locations, x-ray framing camera time-lapse x-ray imaging, and proton radiography using D^{3}He protons for OMEGA shots. Figure 21 is a sketch of the experimental setup and diagnostics.

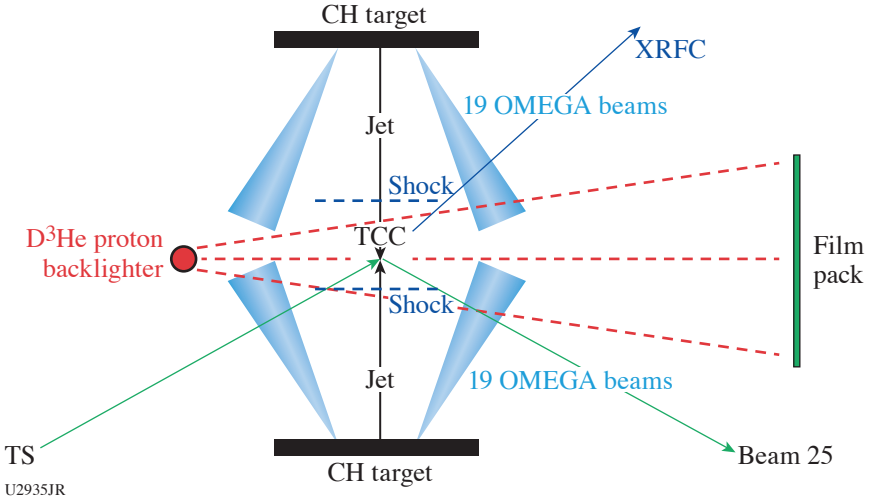

Figure 21
Sketch of experimental setup of colliding MG jets experiment using 38 OMEGA beams to irradiate two opposite flat CH disks separated by 6.4 mm. Locations of the main diagnostics are also indicated. In the 2022 experiment the CH disks were doped with 1% to 2% (atomic number) Fe.

Preliminary Results of the 220427 Experiment

We successfully completed nine shots on 27 April 2022 and obtained excellent data from all three diagnostics. Sample data are shown below even though we have not had the time to complete the detailed analysis, modeling, and comparison with earlier experiments. These tasks are in progress.

Figure 22 shows Prad images that are consistent with the conceptual picture of strong poloidal fields parallel to the jet axis, while strong transverse fields are created and amplified near the contact surface by the collision. Even though these images resemble those of earlier experiments with pure-CH targets, we expect the detailed field configurations and evolution will vary with radiative cooling. This will be investigated after the fields are fully deconvolved from the Prad images and compared with 3-D *FLASH* simulations, which are ongoing. The magnetic fields will strongly impact electron thermal conduction.

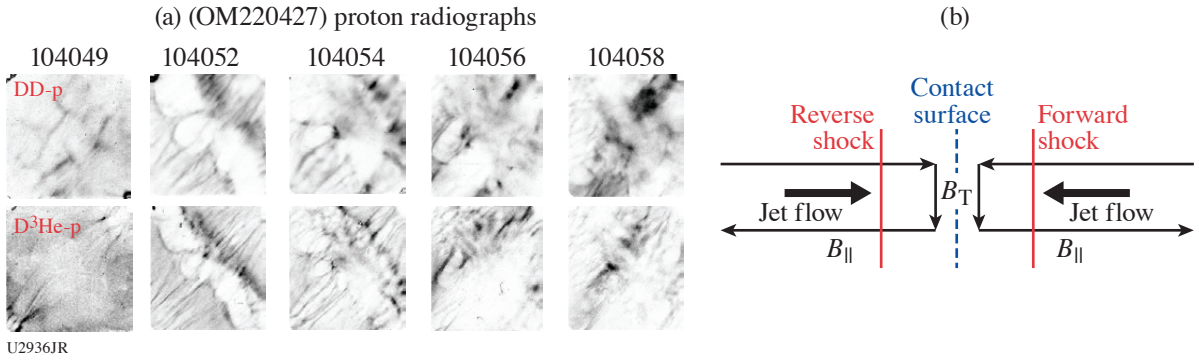

Figure 22
(a) Prad images of the 220427 experiment showing the evolution of ordered poloidal fields along jet axis and transverse fields along the contact surface, consistent with the conceptual picture below. Jet axis lies at 45° from lower left to upper right.

Figure 23 compares the TS data at TCC from 2021 (pure-CH) and 2022 (Fe-doped) experiments. They suggest that the electron temperature and density are lower, but the ion temperature and flow velocity are higher in the Fe-doped cases. These results will be compared with 3-D *FLASH* results before we can provide physical interpretations because the effects of radiative cooling are complex and highly nonlinear. All these results will be used to design and optimize our next NLUF experiment scheduled for May 2023.

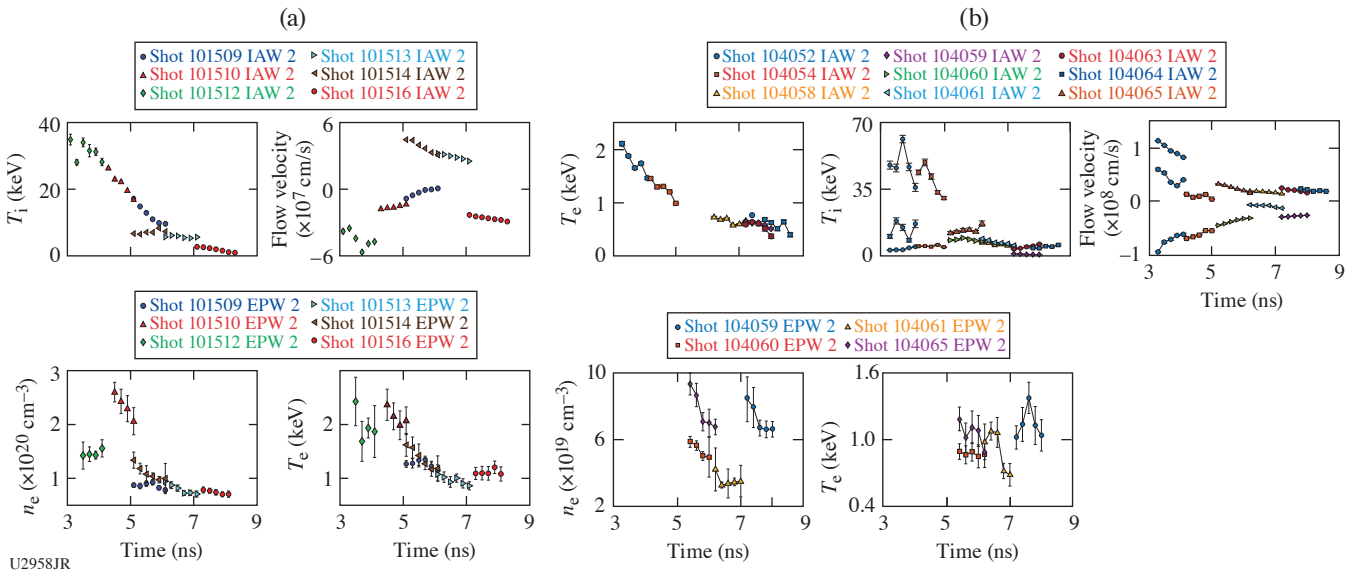

Figure 23
Comparison of TS data at TCC from (a) 210811 (pure CH) and (b) 220427 (Fe-doped CH) show that T_e and n_e are lower, while T_i and flow velocity are higher, for the Fe-doped targets.

Rice University graduate students Yingchao Lu (Ph.D., 2021, current University of Rochester postdoc) and Brandon Cage (second year) and undergraduate student Jackson White (BS, 2021), Princeton University graduate student Abe Chen and postdoc Sue Zhang, contributed to these experiments.

This work was supported by DOE DE-NA0003942.

X-Ray Heating and Ionization of Photoionized Plasmas in Steady State

R. C. Mancini,[1*] R. F. Heeter,[2] D. Liedahl,[2] and S. P. Regan[3]
[1]University of Nevada, Reno
[2]Lawrence Livermore National Laboratory
[3]Laboratory for Laser Energetics, University of Rochester
[*]Principal Investigator

The goal of this project is to study the x-ray heating, temperature, and ionization properties of plasmas produced and sustained by a broadband intense x-ray flux, i.e., photoionized plasmas, with experiments on OMEGA EP. Most laboratory work performed to date on high-energy-density laboratory physics pertains to collisional plasmas, i.e., plasmas where electron collisional processes play a dominant role in the plasma ionization and atomic physics. Relatively little attention has been paid, however, to studying and understanding the basic properties of laboratory photoionized plasmas where both photoionization and photoexcitation, driven by an external broadband x-ray flux, become dominant. These relatively low-density plasmas are important for understanding a myriad of astrophysical phenomena including x-ray binaries, warm absorbers in active galactic nuclei, and the accretion disks formed in the vicinity of compact objects. The quantitative information that we obtain from these systems is mainly based on the analysis of x-ray astronomy observations made by orbiting telescopes such as Chandra and XMM-Newton.

Given the time scales of astrophysics phenomena, the models implemented in astrophysical codes assume that the plasma is in steady state. In the case of photoionized plasmas, the type of steady state is photoionization equilibrium (PIE), where photon-driven photoionization is counterbalanced by electron-driven radiative and dielectronic recombination. Achieving PIE in the laboratory is challenging since it requires large driver energy and long times. We have established a new experimental platform on OMEGA EP that uses a plastic-tamped silicon sample driven by the 30-ns-duration, broadband x-ray flux produced by the "Gatling-gun" radiation source. This source is comprised of three copper hohlraums that are sequentially driven by three OMEGA EP beams, each one delivering 4 kJ of UV energy in a 10-ns square pulse shape. Each copper hohlraum has a length of 2.8 mm and an inner diameter of 1.4 mm, and is filled with TPX foam. The laser beams sequentially illuminate one hohlraum at a time, thus producing an x-ray flux characteristic of 90-eV radiation temperature for a time of 30 ns. The relatively long duration of the Gatling-gun radiation source is critical to produce a photoionized in steady state. The experiment setup is schematically illustrated in Fig. 24.

The experiment employs the four OMEGA EP beams and has three target components. Beams B3, B2, and B4 sequentially drive the "Gatling-gun" (GG) x-ray source. Each of these beams lasts for 10 ns. The 30-ns-duration x-ray flux of GG irradiates the photoionization sample, i.e., a plastic-tamped SiFe or SiO foil, to produce a photoionized plasma that undergoes a controlled expansion. Beam B1 is independently fired to drive a Ti laser-produced plasma source of backlit photons to probe the photoionized plasma at different times in nominally identical shots via transmission spectroscopy. This laser beam is 1 ns long and delivers 1 kJ of UV energy onto a Ti slab target in a 1-ns square pulse shape. The radiative recombination continuum emission photons of the Ti laser-produced plasmas backlight and probe the photoionized plasma via K-shell absorption spectroscopy. From this measurement, the charged-state distribution and electron temperature of the plasma can be extracted.

The combination of a 30-ns-long x-ray flux to produce and sustain the photoionized plasma and the possibility of performing transmission spectroscopy with a relatively short duration (i.e., 1-ns) source of backlit photons is key to demonstrating that the plasma is in steady state. In addition, gated imaging measurements of the plasma self-emission provide the density of the plasma. The GG performance is monitored with a VISAR package located on the back end of GG and the active shock breakout (ASBO) and SOP diagnostics, as well as a grating spectrometer to record the broadband spectral distribution GG x-ray flux. The GG x-ray source has a characteristic radiation temperature T_R = 90 eV and lasts for 30 ns.

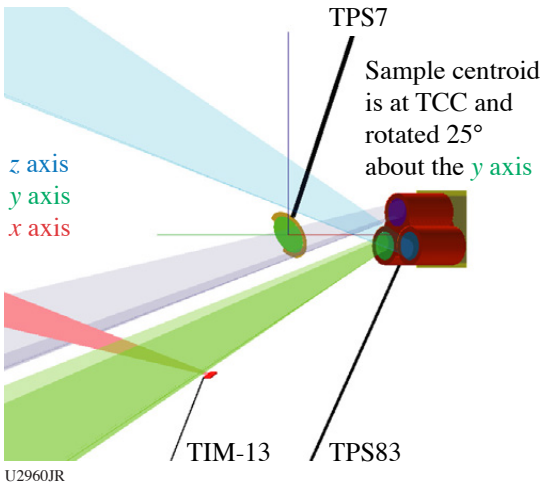

Figure 24
Schematic of the experiment setup. OMEGA EP beams B3, B2, and B4 fire sequentially in time to drive the three-hohlraum Cu Gatling-gun x-ray source, producing a 30-ns x-ray flux, while beam B1 is independently fired to drive the Ti backlight source. Details of Target Positioning Systems (TPS), TIM's, and diagnostics used in the experiment: TIM-10: SSCA/SXS streaked spectrometer for K-shell transmission spectrum of Si plasma; TIM-11: XRFC5/VSG_1 (variable speed grating) gated spectrometer for Cu x-ray flux; TIM-12: ASBO and SOP diagnostics for VISAR hohlraum radiation temperature; TIM-13: Ti backlighter (BL); TIM-14: SFC1 (Sydor framing camera 1)/VSG_2 gated spectrometer for imaging Si L-shell emission spectroscopy.

The spatial extension of the blowoff TPX/copper plasma from the copper hohlraums is monitored with the 4ω probe laser to make sure that it does not reach the silicon sample. The silicon photoionized plasma is probed with self-emission spectra recorded with a grating spectrometer, and K-shell line absorption spectra are recorded with a KAP crystal streaked spectrometer.

Figure 25 displays measurements recorded in three nominally identical OMEGA EP shots, i.e., 32980, 32981 and 32982, where the Ti backlighter was fired at three different times to monitor the evolution of the plasma-charged distribution via transmission spectroscopy. Everything else in the experiments remained the same. The earliest observation at t = 8 ns shows weak n = 1 to 2 line absorption in F- and O-like Si ions and n = 1 to 3 in Ne-like Si; this indicates that the Si ionization is just breaking into the L-shell range of ions. Later in time, at t = 18 ns and t = 25 ns, the transmission spectrum is dominated by n = 1 to 2 in Ne transitions in F-, O-, N-, and C-like Si ions and it is very similar at both times. This is an indication that the charge-state distribution is the same and thus in steady state. These observations are the first experimental evidence of having achieved a steady-state charged-state distribution in a laboratory photoionized plasma, i.e., PIE.

Shock-Induced Hydrogen Chemistry for Hydride Formation

S. Pandolfi,[1] C. Mcguire,[2] R. Smith,[2] M. C. Marshall,[3] D. Kraus,[4] W. Mao,[5*] A. Gleason,[1] and J. H. Eggert[2]
[1]SLAC National Accelerator Laboratory
[2]Lawrence Livermore National Laboratory
[3]Laboratory for Laser Energetics, University of Rochester
[4]University of Rostock
[5]Stanford University
[*]Principal Investigator

Recent work showing diamond formation in nonreactive polymers under laser-driven compression[50–52] has demonstrated that it is possible to initiate and characterize controlled reactive chemistry over ultrafast (i.e., nanosecond) time scales. Here, we use a novel approach that builds on previous work to: (a) extend previous studies to low-entropy pathways at multi-Mbar pressures; and (b) use shock-induced polymer dissociation and diamond formation as a source of reactive hydrogen (H) atoms to initiate reactive chemistry and hydrides formation.

In this experiment, we used a new sample fabrication procedure that has been recently developed by part of the group, and that allows us to embed particles of selected heteroatoms, in this case iron (Fe), in a polymer matrix, specifically Stycast epoxy.[53] This sample design ensures that, as the dissociation of the polymer takes place under dynamic compression, the heteroatoms are

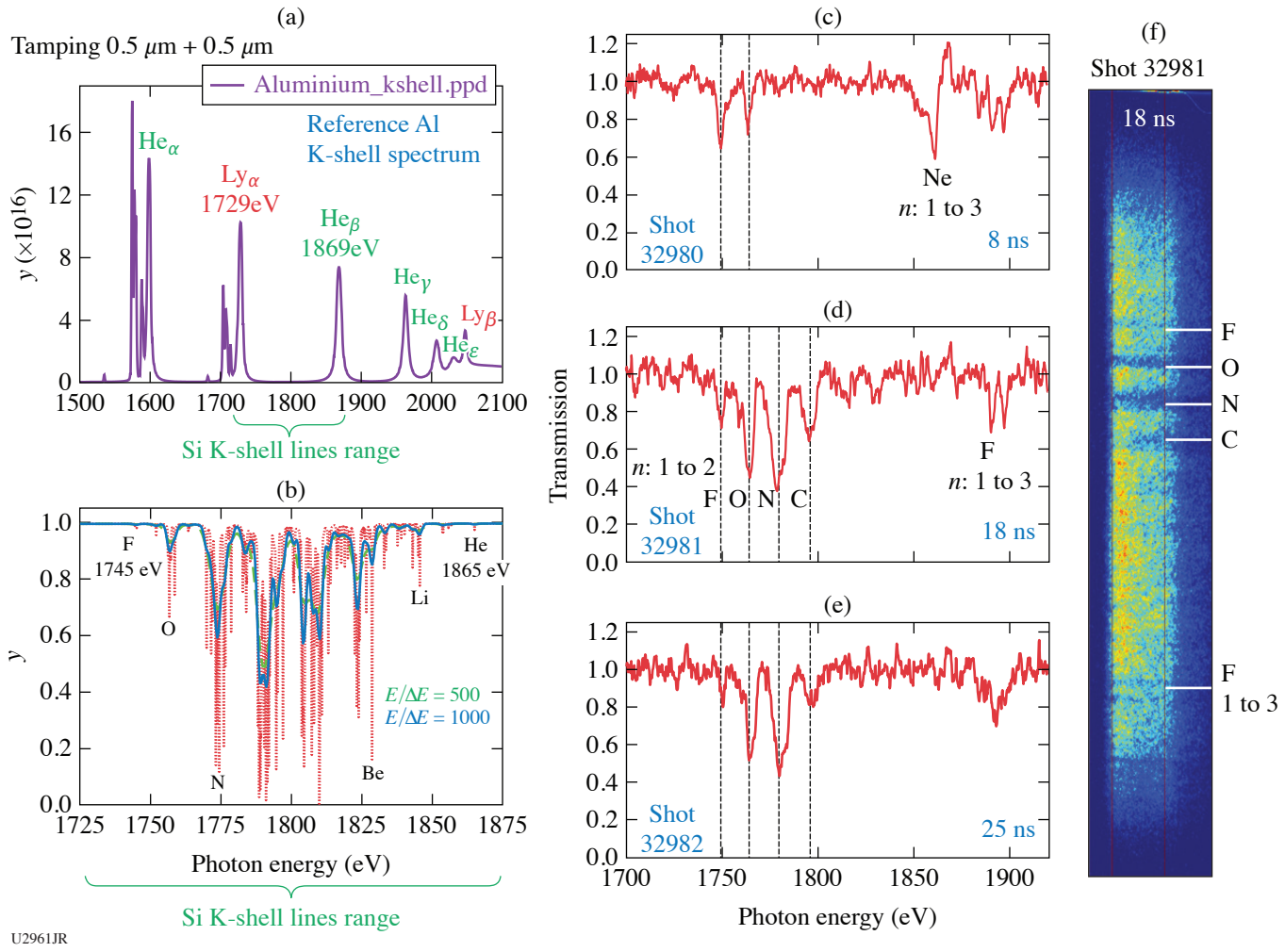

Figure 25

(a) Reference Al K-shell line emission spectrum used to calibrate the photon energy axis, (b) range of Si K-shell line absorption spectrum bounded by the Al Ly_α and He_β lines, and [(c)–(e)] experimental transmission from three nominally identical experiments using 0.5-μm plastic-tamped samples that show steady-state charged distribution in the Si photoionized plasma at t = 18 ns and t = 25 ns (right). (f) The image data is the streaked spectrum recorded with TIM-10/streaked x-ray camera A/streaked x-ray spectrometer (see Fig. 24) from which the transmission is extracted.

surrounded by a carbon- and H-rich environment, promoting eventual chemical reaction. We used the PXRDIP diagnostic and a Fe backlighter to collect x-ray diffraction (XRD) data to characterize the structural evolution of the sample as it undergoes compression; changes in the structure and eventual chemical reaction leading to hydride (or carbide) formation can be readily detected by studying the arrangement of the Fe atoms. Results from our first day of experiments are reported in Fig. 26.

Data analysis shows that single-shock compression yields to polymer dissociation and crystallization of the FeH hydride with double hexagonal close-packed (dhcp) structure [Fig. 26(b)]. This structure differs from the stable one for pure Fe, i.e., a hcp (hexagonal close-packed) structure, demonstrating that the mobility and energy of the H atoms released by polymer dissociation is sufficient to extensively react with the embedded Fe particles. Data collected under ramp compression (i.e., isentropic, low-entropy compression pathways) show a markedly different pattern, compatible with pure hcp Fe, and no signature of diamond formation. This result and other runs performed on pure epoxy show that the low-energy pathways achievable under ramp compression do not lead to diamond crystallization, most likely due to energetic barriers. During FY23, our efforts will focus on exploiting the pulse-shaping capabilities on OMEGA EP to realize a combined shock + ramp compression profile. The initial shock-compression will provide the necessary energy to initiate polymer decomposition, while the following ramp compression will allow us to characterize the hydrides forming at multi-Mbar pressure.

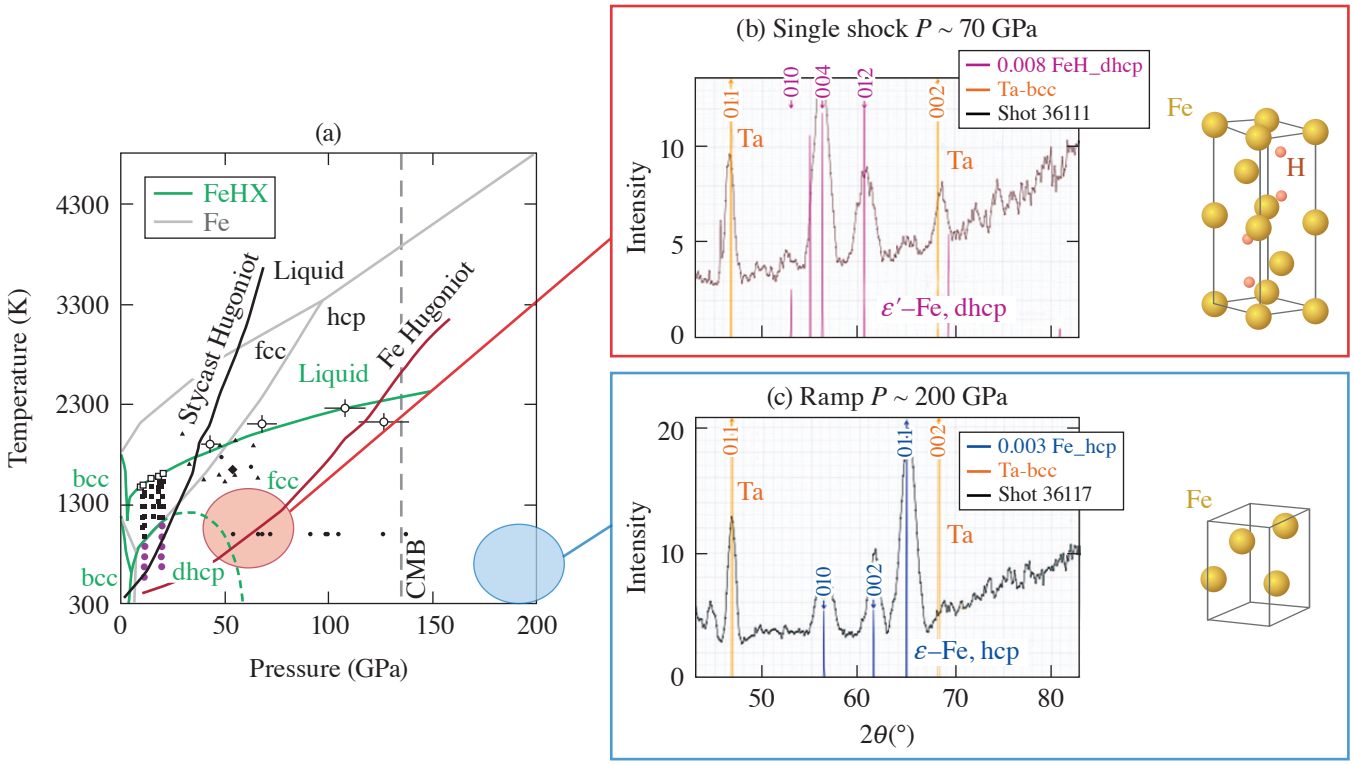

Figure 26
XRD diffraction data collected using different compression profiles. (a) Phase diagram of Fe and iron hydrides, shown in gray and green, respectively, are overlaid with the Hugoniot curve for both pure Fe (red) and pure Stycast. Data obtained using (b) single-shock compression up to 70 GPa and (c) low-entropy ramp compression up to 200 GPa. bcc: body-centered cubic; fcc: face-centered cubic; CMB: core mantle boundary.

Furthermore, part of the experimental time has been dedicated to velocimetry studies to better characterize the samples' equation of state. With a specific target design, we have been able to simultaneously measure our samples and a known material used as reference, quartz in this case, as shown in Fig. 27. The results will be used to further refine the equation of state of the epoxy–Fe mixture and to inform theoretical models investigating epoxy–metal mixtures.

This work is funded through the NLUF Program at LLE. Parts of this work was performed under the auspices of the U.S. Department of Energy by Lawrence Livermore National Laboratory under Contract DE-AC52-07NA27344 and was supported by the LLNL-LDRD Program under Project No. 21-ERD-032. Travel was partially funded by the 2019 DOEFES ECA.

Driving Iron to Dense, Hot Conditions Using Long- and Short-Pulse Beams of OMEGA EP

C. McGuffey,[1*] M. A. Meyers,[2] F. N. Beg,[2] G. Righi,[2] A. Li,[2] M. Bailly-Grandvaux,[2] and J. Kim[2]
[1]General Atomics
[2]University of California, San Diego
[*]Principal Investigator

Iron is an abundant constituent of all burning stars. The opacity of iron is a critical parameter to the inner workings of sun-like stars, constraining the radiative flux leaving the interior, and thus the temperature and nuclear reaction rates. A material's opacity, κ_ν, at a certain frequency, ν, is defined such that

$$I(x) = I_0 e^{-i\kappa_\nu \rho x},$$

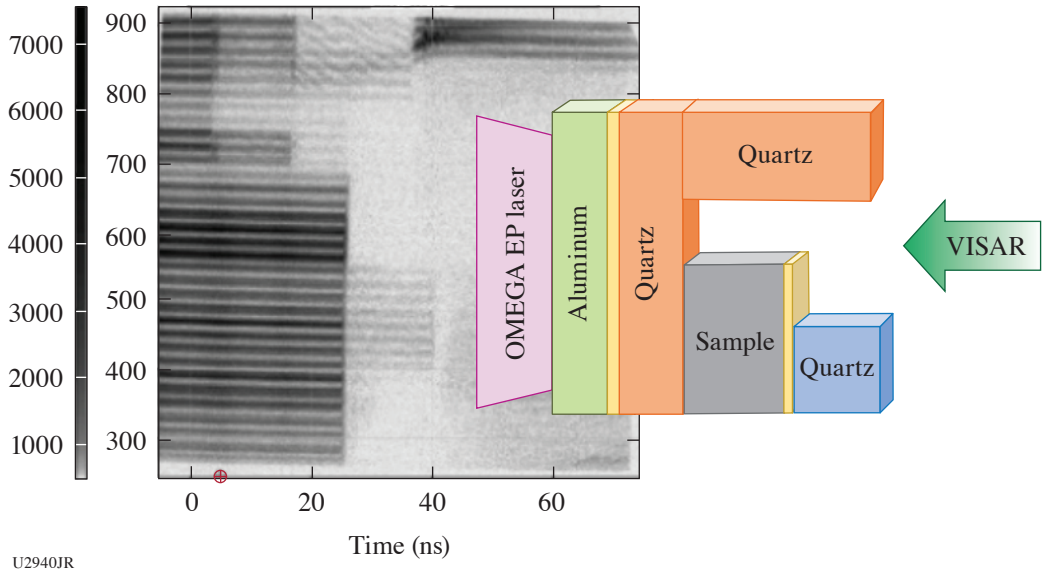

Figure 27
Velocimetry data obtained using the active shock breakout diagnostic and schematic view of the target assembly designed for equation-of-state measurements.

where $I(x)$ is the intensity, lower than the incident intensity I_0, after traveling a distance x through the material with mass density ρ. Opacity is cumulative of multiple contributions. For the materials present in high-energy-density (HED) systems, which are hot and partially or highly ionized, photoelectronic absorption develops multiplicity for all the ionic states present; Doppler broadening and continuum-lowering effects may be present, for example. High-atomic-number, opacity calculations can become intractable, even with large computational resources. This is to say that HED opacity is highly situationally dependent and challenging to model. That is why experimental opacity measurements are important, and in highly radiative HED systems including stars, hohlraums, and ICF capsules, opacity measurements are needed in a variety of conditions.

The FeHotCompress experiment, allocated through the NLUF Program, seeks a methodology for creating dense, hot Fe samples and measuring their opacity on the OMEGA EP Laser System. The methodology combines two common uses of large laser facilities: laser compression[54] and isochoric heating from a laser-driven proton beam.[1,4,55] Laser-direct-drive compression of planar materials has been used to apply well-controlled, high pressure on materials for decades, pushing beyond what diamond-anvil cells can do to study material properties at high pressure. When compressed by an appropriate ramp pulse shape, high density can be attained with minimal temperature increase. Separately, short-pulse laser drivers or the charged-particle beams they create can heat samples quickly enough for the material to retain its initial density ("isochorically"). This dual-drive approach provides flexibility in the conditions that can be attained and could offer a high data collection rate compared to other major iron opacity campaigns using flagship x-ray drivers.

In the FeHotCompress configuration, long-pulse beams irradiate an iron sample package using distributed phase plates for broad, quasi-1-D drive. Short-pulse Beam 1 irradiates a curved plastic foil to direct protons into the sample. Short-pulse Beam 2 serves as an x-ray continuum backlighter with a bare Ti wire target. The objective of the campaign is to collect absorption spectra of Fe in a hot, compressed condition. On the first shot day, x-ray signatures of the three beam types were collected, one by one, using two x-ray spectrometers, which presented challenges. The proton spectrum was recorded for future use in simulations of the target heating. Streaked, spectrally resolved x-ray emission measurements were also taken with the PJ-X streak camera + streaked x-ray spectrometer diagnostic. Figure 28 shows these data for a two-beam shot.

We acknowledge travel support to participate in this shot day provided by the National Nuclear Security Administration. Three students participated in the shot day.

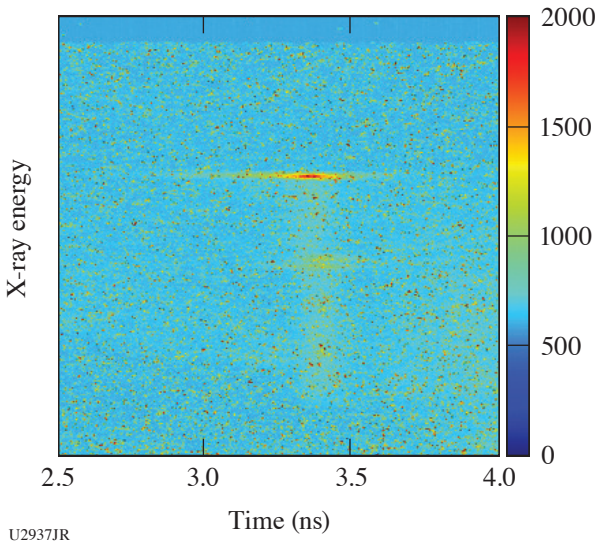

Figure 28
Streaked and spectrally resolved x-ray emission above 5.5 keV from Fe driven by a long-pulse beam and Ti irradiated by a short-pulse beam. Cold and hot Fe lines are seen late in the drive, as is a continuum from the short pulse arrival at 3.4 ns.

Tracking Rarefaction with Particle Image Velocimetry

J. Shang,[1,2*] H. Aluie,[1,2] D. N. Polsin,[1,2] and R. Betti[1,2]
[1]Department of Mechanical Engineering, University of Rochester
[2]Laboratory for Laser Energetics, University of Rochester
[*]Principal Investigator

Prior OMEGA experiments of a plasma releasing into a vacuum suggested that the released material travels more than twice the distance and spreads over 4× the range predicted by radiation-hydrodynamic codes, which could account for a reduction in target performance by a factor of 2 (Ref. 56). In this campaign, we sought to measure the evolution of the rarefaction wave from the leading to the trailing edge by imaging the position of particles embedded in the rear surface of an irradiated CH foil. At shock breakout, the particles would become entrained and move with the fluid.

In the experiment, we used titanium microspheres as the tracer particles and a framing camera to capture the backlit samples over time. A representative sequence of radiographs from the same shot is shown in Fig. 29, where the three particles can be seen in most frames as dark ellipsoids. After release, the particles appear to compress and then expand. Due to this expansion, it is not evident from the images whether the particles have moved appreciably.

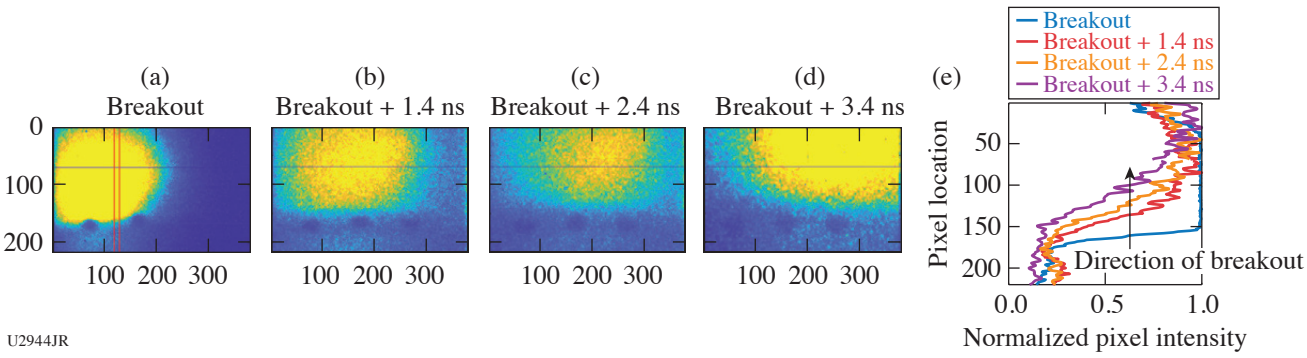

Figure 29
(a–d) Radiographs of the apex of a thin hemispherical plastic shell embedded with three titanium spherical particles (45-μm diameter, dark bodies) during and after shock breakout. The rarefaction wave travels from the bottom to the top of the image. The particles initially compress, and after 2.4 ns, appear to expand with the rarefaction wave. (e) Lineouts of normal pixel intensity in the area between two of the particles, outlined in the breakout image in red.

A qualitative analysis of the radiographs appears to show that the density gradient of the plasma decreases over time as the trailing edge of the rarefaction wave propagates into the vacuum. Further analysis is needed to determine if this is consistent with the angular filter refractometry data.

The experiment was conducted at the Omega Laser Facility at the University of Rochester's Laboratory for Laser Energetics with beam time through NLUF Program. This work was supported by the Department of Energy National Nuclear Security Administration under awards DE-SC0019329 and DE-NA0003914. Partial support from grants NSF PHY-2020249 and DE-SC0020229 and DE-NA0003914 is also acknowledged.

Rayleigh–Taylor Evolution of Isolated-Feature Perturbations in a Background Magnetic Field

B. Srinivasan,[1*] C. Samulski,[1] M. J.-E. Manuel,[2] and P. M. Nilson[3]
[1]Kevin T. Crofton Department of Aerospace and Ocean Engineering, Virginia Tech
[2]General Atomics
[3]Laboratory for Laser Energetics, University of Rochester
[*]Principal Investigator

The project aims to study magnetic-field effects on the Rayleigh–Taylor (RT) evolution of single-feature perturbations, such as those that exist in fill tubes, and to validate modeling which predicts reduced mix-width growth in the presence of magnetic fields. To achieve this, we developed a magnetized, shock-tube platform to study blast-wave–driven RT growth using the Fresnel zone plate (FZP) diagnostic.

On the first shot day, we tested the newly developed platform to explore whether the unmagnetized RT growth is detectable using the FZP diagnostic for two targets with different single-feature perturbations that were predicted to have significantly different evolution from simulations. We executed seven shots for the two targets by varying the timing of the diagnostic (0 ns, 3.5 ns, 5 ns, and 8 ns) to capture different stages of the RT evolution for each of the targets. Some raw FZP data from the shots are included to show a comparison between the two targets with different single-feature perturbations, where Fig. 30(a) is at 3.5 ns and Fig. 30(b) is at 5 ns.

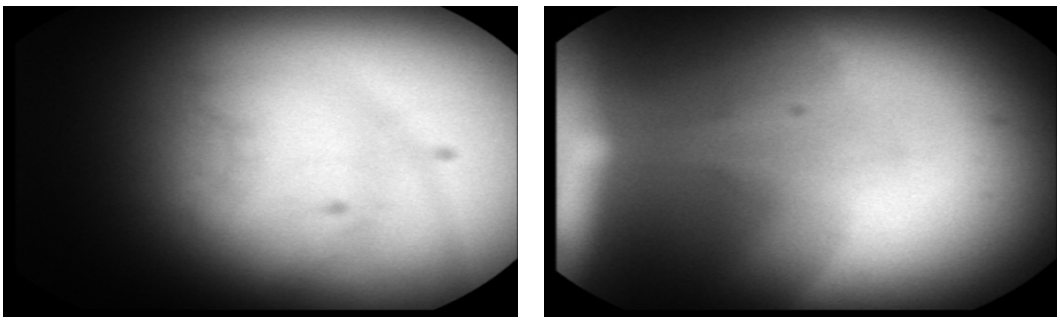

U2945JR

Figure 30
A quick analysis of the FZP images shows that (a) has multiple forks occurring with RT growth, whereas (b) has a more-uniform bubble growth, which is consistent with predictions from simulation.

Early analysis shows that our timing prediction from simulations needs a little refinement but there is generally good agreement of RT features between simulations and experiments. The features, however, were not captured with sufficient contrast to be clear and easily diagnosable for early and late times. These lessons are being applied toward the second shot day where further analysis is in progress to refine the timing in the simulations to improve the predictive capability. Additionally, the target is being redesigned due to the need for better contrast when using the FZP diagnostic. This was a successful shot day because it tested a new platform and provided very useful and relevant information to prepare for upcoming magnetized shots.

This work was supported by the DOE Office of Science under award number DE-SC0022319 and the NLUF Program for awarding and supporting the targets and the shot days.

Control of Laser–Plasma Interactions in Three-Dimensional–Printed Foam Structures with Graded Density

S. Tochitsky,[1*] N. Lemos,[2*] R. Simpson,[2] F. Fiuza,[3] A. Haid,[4] A. Pak,[2] D. Haberberger,[5] and C. Joshi[1]
[1]University of California, Los Angeles
[2]Lawrence Livermore National Laboratory
[3]Stanford Linear Accelerator Center
[4]General Atomics
[5]Laboratory for Laser Energetics, University of Rochester
[*]Principal Investigators

This work aimed to explore, through experiments and simulations, how laser-driven ion acceleration in a near-critical-density 3-D–printed target can be controlled by tailoring its density profile. We measured an enhancement up to 30%±20% of the maximum proton energy supported by a hotter electron distribution using a 3-D–printed target when compared with a simple 2-μm CH foil.

Intense research is being conducted into sources of laser-accelerated ions around the world (see e.g., a review by Macchi *et al*.[57] and the references therein). It is known that interactions of high-intensity lasers with solid-density targets can accelerate ion beams to tens of MeV/u by a well-studied target normal sheath acceleration (TNSA) mechanism or TNSA enhanced via radiation-induced transparency,[58,59] so-called breakout afterburner mechanisms.[60] Efforts to increase the maximum ion energy have largely focused on the development of novel acceleration mechanisms relying on ultrathin ($\leq$100-nm) targets that require utilization of single or double plasma mirrors to mitigate the effect of the laser prepulse to provide target survival. In this study we used special 3-D–printed targets in order to optimize the plasma density profile to maximize the laser absorption and proton/ion acceleration and minimize the sensitivity to laser prepulse. With the new 3-D printing technology, it is possible to fabricate complex structures with unprecedented geometric detail. Figure 31 shows an example of the targets that were fabricated by the General Atomics team who collaborated with us on the project and used this work as an opportunity to advance resolution of 3-D printing technology and metrology. We tested targets with different density gradients and maximum densities on the front and back surfaces, as well as targets with log-pile and stochastic low-density structures with densities in the range of 10^{20} to 10^{22} cm^{-3}.

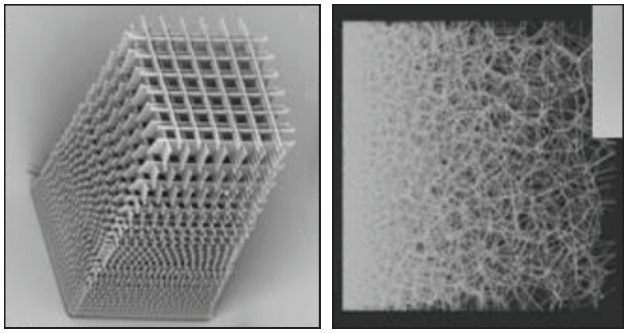

U2948JR

Figure 31
Examples of (a) a 3-D–printed log pile and (b) stochastic foam structure with graded density.

These targets were irradiated by the OMEGA EP laser with a pulse duration of 1 ps and maximum energy of 500 J. The spectrum of accelerated protons was measured using a Thomson parabola and a radiochromic film stack developed at LLNL (PROBIES). As a baseline, we used a 2-μm CH target that accelerated protons up to ~60 MeV from TNSA. Preliminary results show that an optimized 3-D–printed density profile target can accelerate protons up to at least 80-MeV energies. There targets showed good reproducibility that was relatively independent of the laser prepulse. Moreover, the log-pile targets seem to produce higher-energy protons than the stochastic targets.

Support by DOE Office of Science Early Career Research Program (Fusion Energy Sciences) under DOE-SC FWP 1651 and NNSA grant DE-NA0003842.

Dynamic Compression of Iron Carbide at Exoplanetary Core Conditions

S. J. Tracy,[1*] D. Kim,[1] S. Takagi,[1] I. I. Oleynik,[2] R. F. Smith,[3] F. Coppari,[3] M. Millot,[3] S. M. Clarke,[3] and J. H. Eggert[3]
[1]Carnegie Institution for Science
[2]University of South Florida
[3]Lawrence Livermore National Laboratory
[*]Principal Investigator

Our major scientific goal was to investigate the stable crystal structure of iron carbide (Fe_3C) at the pressure–temperature conditions of planetary cores. These results are highly sought after to establish improved models of structure, formation, and evolution of the cores of Earth and carbon-rich exoplanets. During our first shot day in September 2022, we utilized the unique capabilities of OMEGA EP to load Fe_3C samples along the principal isentrope to pressures between 250 and 600 GPa using a 10-ns ramped pulse. The compressed samples were probed with x-ray diffraction using the PXRDIP diagnostic [Fig. 32(d)][61] and pressures were determined using the ASBO diagnostic [Fig. 32(a)].[62] Figure 32 shows preliminary results for shot 37643 with a probe stress of 380 GPa. Early analysis of our results reveals that the orthorhombic Fe_3C structure is stable up to 600 GPa, placing new constraints on the Fe_3C phase diagram and equation of state.

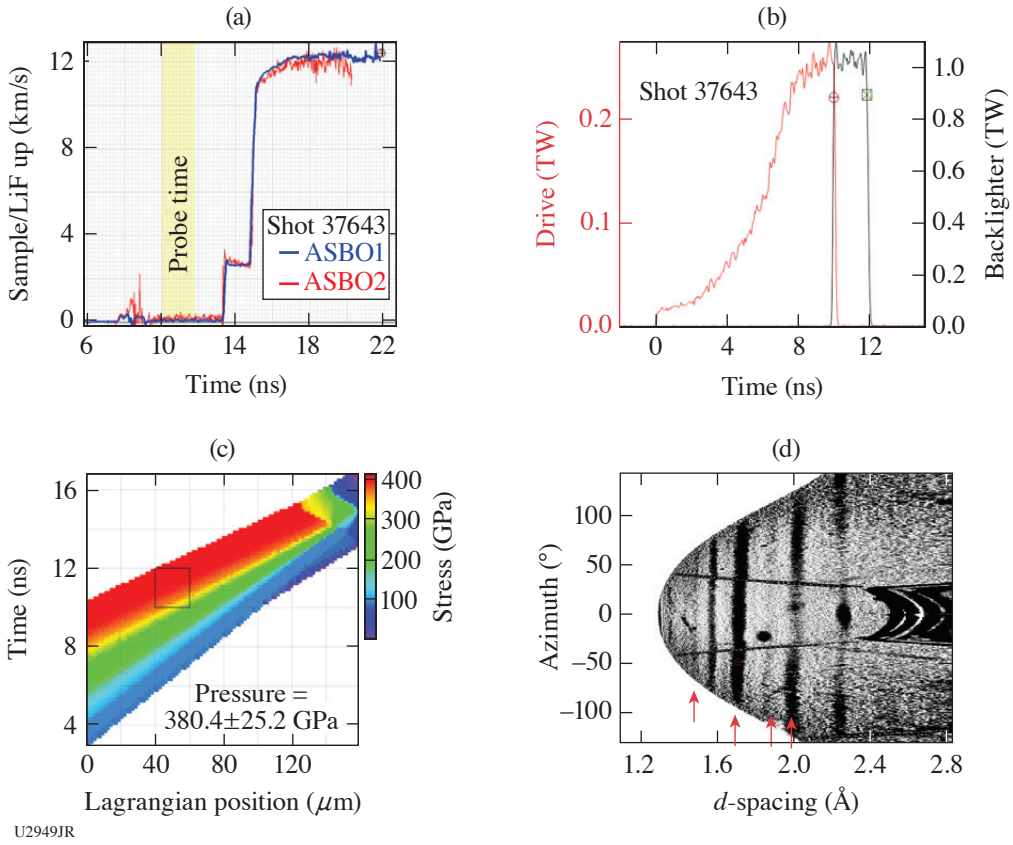

Figure 32
Preliminary analysis of results from shot 37643 for Fe_3C ramp compressed to a peak stress of 380 GPa. (a) VISAR data, Fe_3C–LiF interface velocity with 2-ns x-ray probe time in the yellow band. (b) Drive laser pulse (red trace). X rays are generated using a 2-ns square pulse (black trace). (c) Preliminary analysis of VISAR data showing a calculated map of stress distribution within the target assembly as a function of time. (d) De-warped x-ray diffraction data image plates with red arrows indicating compressed Fe_3C peaks.

The research is supported by the Department of Energy National Nuclear Security Administration under Award No. NA0004089.

Monochromatic Talbot–Lau X-Ray Deflectometer for the OMEGA EP and Multi-Terawatt Lasers

M. P. Valdivia[1,2*] C. Stoeckl,[3] T. Filkins,[3] C. Mileham,[3] M. Romanofsky,[3] I. A. Begishev,[3] V. Bouffetier,[4] G. Perez-Callejo,[5] A. Casner,[6] and D. Stutman[2,7]
[1]Center for Energy Research, University of California, San Diego
[2]Department of Physics and Astronomy, The Johns Hopkins University
[3]Laboratory for Laser Energetics, University of Rochester
[4]European XFEL GmbH, Germany
[5]Departamento de Física Teórica, Atómica y Óptica, Universidad de Valladolid, Spain
[6]CEA-CESTA, France
[7]ELI-NP, Institute for Physics and Nuclear Engineering, Romania
[*]Principal Investigator

The accurate diagnostic of density profiles in high-energy-density physics (HEDP) is an important but challenging task due to the high densities, small spatial scales, and short time scales encountered. In FY22, monochromatic 8-keV Talbot–Lau x-ray interferometry diagnostic capabilities were established for the OMEGA EP and Multi-Terawatt (MTW) lasers to increase HEDP phase-contrast diagnostic accuracy. Laterally graded multilayer mirrors were integrated to the design and the Talbot–Lau x-ray deflectometry (TXD) technique was improved based on previous results.[63] A new on-site x-ray calibration station reproduced vacuum chamber geometry, allowing for reliable instrument alignment. Preliminary experiments on MTW determined laser and target conditions, leading to optimal x-ray backlighter production for the 8-keV TXD (Table III). Additionally, a dedicated interferometry analysis code with a post-processing module was developed, delivering x-ray transmission, phase, and dark-field maps from moiré images.[64] Electron density retrieval methods were further enhanced by integrating phase-stepping capabilities to the analysis tool, making it possible to record *ex-situ* reference images on-site using the x-ray station in combination with x-ray backlighting from a copper x-ray tube.[65]

Monochromatic TXD (M-TXD) achieves high contrast (21% to 30%) close to the theoretical value (35%) for this configuration. Even with lower relative x-ray charge-coupled–device (CCD) counts, the signal-to-noise ratio (SNR) nearly doubles that of standard TXD, proving that monochromatic TXD successfully selects 8-keV contribution from Cu K_α emission, improving diagnostic performance by increasing electron density retrieval accuracy. Previously, alternative backlighter target configurations enhanced spatial resolution, albeit at the cost of reduced moiré fringe contrast due to increased high-energy emission (>8 keV) from hot-electron recirculation.[66] Therefore, x-ray backlighter quality from Cu wire targets and planar foils irradiated normal to the surface [i.e., edge-on from the TXD diagnostic line of sight (LOS)] and at standard 50° was evaluated for M-TXD.

Table III: Monochromatic TXD parameters for three MTW laser pulse lengths and standard TXD parameters for a matching laser pulse length.

Laser pulse length (ps)	Laser Intensity ($\times 10^{14}$ W/cm^2)	SNR	Contrast (%)	Relative CCD counts
25 (at 27 J)	7.3	6.0 to 7.9	24 to 25	1.00
60 (at 36 J)	4.1	6.9 to 7.2	21 to 24	1.30
80 (at 29 J)	2.5	6.0 to 8.6	27 to 30	0.71
Standard TXD				
24 (at 27 J)	4.4	3.5	19	1.85

Figure 33 shows M-TXD moiré images recorded using x-ray backlighting from Cu foil and wire targets irradiated at $I \sim 4 \times 10^{14}$ W/cm^2. Foils irradiated at 50° delivered a moiré fringe contrast of 24% and 6.9 SNR compared to a Cu wire contrast of 11% and 1.9 SNR for similar detector counts. Considering a Cu K_α conversion efficiency (CE) of $\sim 3 \times 10^{-5}$ for foils and $\sim 9 \times 10^{-6}$ for wires, it can be concluded that an overall photon count increase (higher laser intensity) could improve performance of wire x-ray backlighters, although additional data are needed to better determine their suitability for M-TXD diagnostics. Meanwhile, foils irradiated at 90° delivered 7% contrast and 1.2 SNR with reduced detector counts (~20%), which are inconsistent with CE measure-

ments. Lower photon counts can be attributed to diagnostic LOS and target misalignment, as observed on selected 50° foil shots. In the M-TXD configuration, a mirror alignment precision of ∼0.015° is required, which translates to extremely sensitive backlighter target and diagnostic LOS alignment. While x-ray emission from foils irradiated at 50° propagate toward the mirror unobstructed at 90°, x rays are obstructed by the foil itself. Since MTW's laser intensity was varied by displacing the target away from the laser focal spot, foils irradiated at 90° (edge-on to diagnostic) are most sensitive to alignment since the foil is displaced away from the mirror surface. Moreover, if the emission is highly directional, the total x rays reflected by the mirror would be further reduced. In turn, wire targets are less affected since the laser spot size is larger than their diameter and total x-ray emission is limited by the amount of material irradiated along the wire length. Consistent with the results shown, high moiré fringe contrast was measured (27% to 30%) for laser incidence angles of 50°, 70°, and 80° with similar detector photon counts. Respective spatial resolutions of ∼10.1 μm, ∼7.6 μm, and ∼5.6 μm, were measured with a 5.5-μm effective detector pixel size. Thus, 80° irradiation is an adequate compromise between spatial resolution and x-ray flux optimization, as is supported by previous results obtained in FY21.

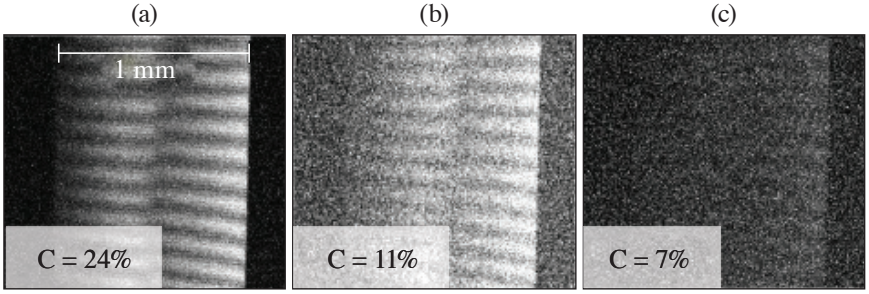

Figure 33
M-TXD moiré from Cu targets irradiated at $I \sim 4 \times 10^{14}$ W/cm^2: (a) foil at 50° from surface, (b) wire, and (c) foil at 90°. *The field of view is restricted due to mirror length. Contrast was enhanced to better showcase fringes. "Broken fringes" (middle of image) are due to grating imperfections.[67]

A 500-μm-diam CH rod was probed with M-TXD by laser irradiating ($I \sim 3 \times 10^{14}$ W/cm^2) foils at 50° (Fig. 34). The moiré images were analyzed with the newly developed Talbot numerical tool (TNT). Matching reference images were not available through experimental acquisition or *ex-situ* phase-stepping methods, hence, a reference was selected from images recorded with different laser parameters through correlation. Phase retrieval was enabled by the backlighter background removal feature included in TNT, included in consideration of data acquisition limitations encountered in most HEDP experiments. The feature allows for postprocessing using reference images recorded with different x-ray sources, which is a powerful resource for TXD diagnostics. Figure 34(d) shows the x-ray refraction angle profile retrieved with TNT (yellow). The G0 source grating background refraction profile (purple curve), obtained from the reference image and a flat field background reveals the grating structure imperfections that contribute to the overall x-ray refraction profile retrieved with TNT. In this case, grating imperfections are significant enough to prevent accurate phase retrieval in the "broken" fringe section. Nevertheless, outside this area, the x-ray refraction angle profile matches simulations within experimental error. Note that *IDEA*, a standard phase-retrieval code, could not deliver a phase map using this input, which proves TNT is a valuable advancement for TXD diagnostic techniques.

An NLUF OMEGA EP campaign was performed in FY22Q4. Multiple factors contributed to a total lack of M-TXD data. Ground vibrations due to building construction and imprecise source grating target fabrication/mounting affected M-TXD rail alignment. Laser beam source failure delayed shots and persistent x-ray CCD data acquisition failures, along with incorrect mounting of a collimator plate, caused further delays and data loss. Improvements and procedure changes have been made in response to these issues where appropriate. Note that x-ray backlighter spectral data were successfully acquired and will be used to complement data from previous campaigns, which will be the subject of a future publication. Further, in preparation for a second NLUF shot (FY23Q2), additional measures have been taken to ensure proper diagnostic performance. The previous OMEGA EP campaign goals to determine laser parameters for optimal x-ray backlighter considering moiré fringe contrast and spatial resolution will be pursued.

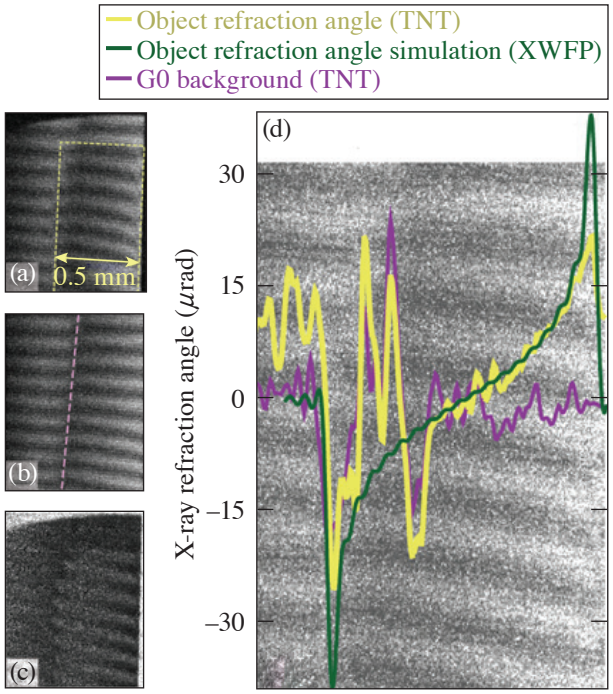

Figure 34
(a) CH rod moiré (yellow line) recorded with an ~36-J, 70-ps laser pulse. (b) Reference moiré from a 36-J, 60-ps laser pulse. The pink line marks grating imperfections. (c) Differential object/reference image. (d) X-ray refraction angle profile from TNT, simulations, and reference "background." XWFP: X-ray wavefront propagation.

This work was supported by NNSA Grant HEDLP DE-NA0003882. OMEGA EP laser beam time was awarded through NLUF by the University of Rochester's Laboratory for Laser Energetics under the auspices of the U.S. DOE/NNSA Contract DE-NA0003856.

Experimental Measurement of Thermal Conductivity in Warm Dense Matter

T. G. White,[1*] T. Doeppner,[2] C. H. Allen,[1] M. Oliver,[3] L. Divol,[2] A. Kemp,[2] E. Kemp,[2] O. Landen,[2] Y. Ping,[2] M. Schölmerich,[2] and W. Theobald[4]
[1]University of Nevada, Reno
[2]Lawrence Livermore National Laboratory
[3]Central Laser Facility, UK
[4]Laboratory for Laser Energetics, University of Rochester
[*]Principal Investigator

The thermal conductivity for materials at warm-dense-matter (WDM) conditions plays a vital role in planetary physics and ICF efforts. In the former, predictions of the power supplied by the geodynamo are utilized to constrain the Earth's evolution, while in the latter, heat transport between the layers plays an essential role in capsule implosions. As is typical for transport properties in the warm-dense-matter regime, however, a dearth of experimental measurements has led to a considerable body of theoretical and computational work that exhibit significant differences.

At the interface between two materials, initially at different temperatures, slow thermal conduction combined with rapid pressure equilibration produces gradients in the density profile on either side of the interface. On a nanosecond time scale, these density gradients typically have scale lengths of the order of 1 μm. We have developed a radiography platform for OMEGA that uses thin slits cut with a focused ion beam to perform micron-scale radiography—the highest spatial resolution achieved to date. Furthermore, due to the partially spatially coherent source, we observe significant diffractive and refractive effects in the radiograph; therefore, the technique is termed Fresnel diffractive radiography.

Initial data taken using plastic-coated tungsten wires are shown in Fig. 35. The data taken at 0 ns (i.e., no drive lasers) provided a measurement of the platform resolution,[68,69] which is less than 2 μm. A time sequence of the wire evolution after the drive was obtained, where we clearly see the outgoing shock wave launched from the expanding tungsten and the rarefaction wave traveling inward from the outside of the cylinder, both of which can be used to constrain the material equation of state and deposited energy. Most importantly, the high-resolution radiography captured information at the interface, with a well-characterized diffraction pattern observed in the 4-ns data at ~12 μm.

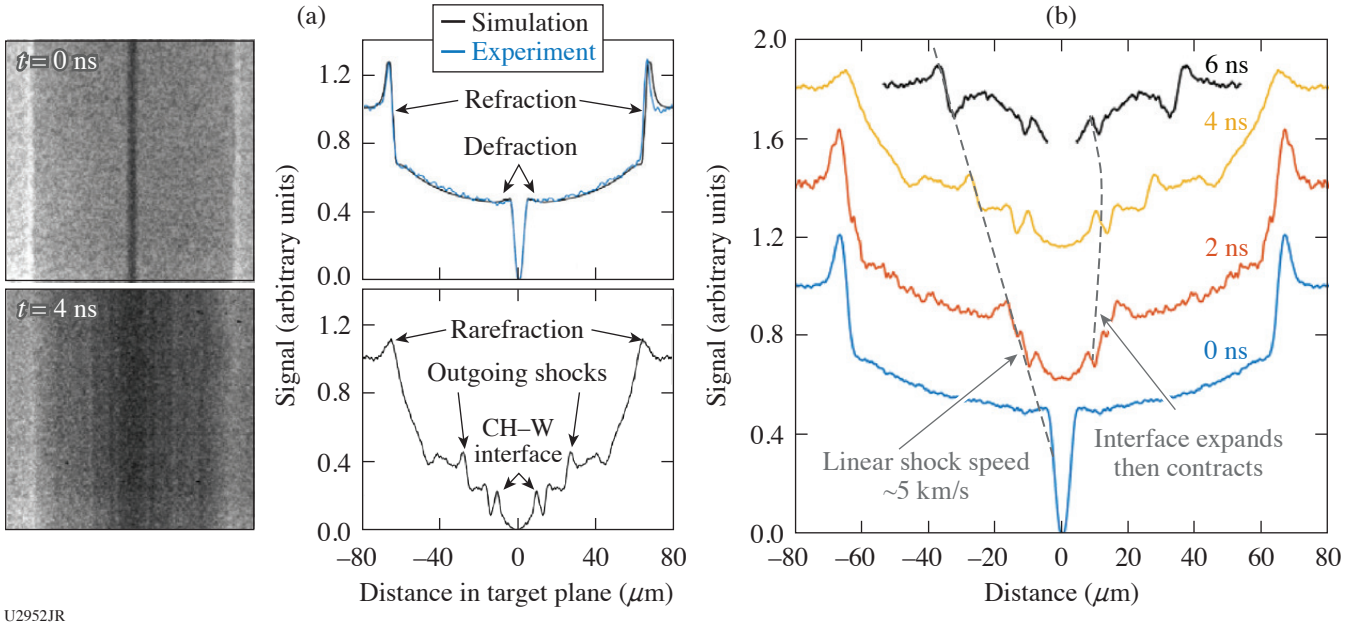

Figure 35
(a) Radiographs and lineouts of a cold target (top) and a driven target (bottom). A clear change in the features is evident in the lineouts, showing the expanded W–CH interface, as well as shock waves launched into the CH. (b) A plot showing the time evolution of our data over the course of the experiment. The signal lineouts are spread out vertically to better see the changes. The shock trajectory and interface evolution are highlighted by the dashed lines.

To analyze the driven data, we solve the Fresnel–Kirchoff integral[70] for a synthetic density profile, incorporating a parameterized material interface to resolve the features we see in the data. Specifically, we expect to see a discontinuity at the interface with a density slope on either side. As seen in Fig. 36, our simulated density profile reproduces the experimental diffraction pattern exceptionally well. We note, however, that the shock is additionally blurred in the experimental data due to its high velocity and the 250-ps gate time of the framing camera. We use Bayesian inference to sample parameter space to better constrain our results and provide error estimates. From this we have extracted the density scale lengths in each material, approximately 0.9±0.15 μm for the tungsten and 1.6±0.3 μm for the plastic.

In these initial experiments, we used tungsten wires due it the high opacity. However, we have now changed from plastic-coated tungsten to plastic-coated nickel and copper wires since as these materials are of broader interest. We are still in the process of analyzing the results and are simultaneously working to improve the platform for our next shot day. Thus far, this work has resulted in two publications (see Refs. 68 and 69). In addition, we are currently working toward a publication on our thermal conductivity measurement.

This work has been supported by the National Science Foundation under Grant No. PHY-2045718. The work of T. Doeppner, L. Divol, A. Kemp, E. Kemp, O. Landen, Y. Ping, and M. Schölmerich was performed under the auspices of the U.S. Department of Energy by Lawrence Livermore National Laboratory under Contract DE-AC52-07NA27344 and supported by Laboratory Directed Research and Development (LDRD) Grant No. 21-ERD-029.

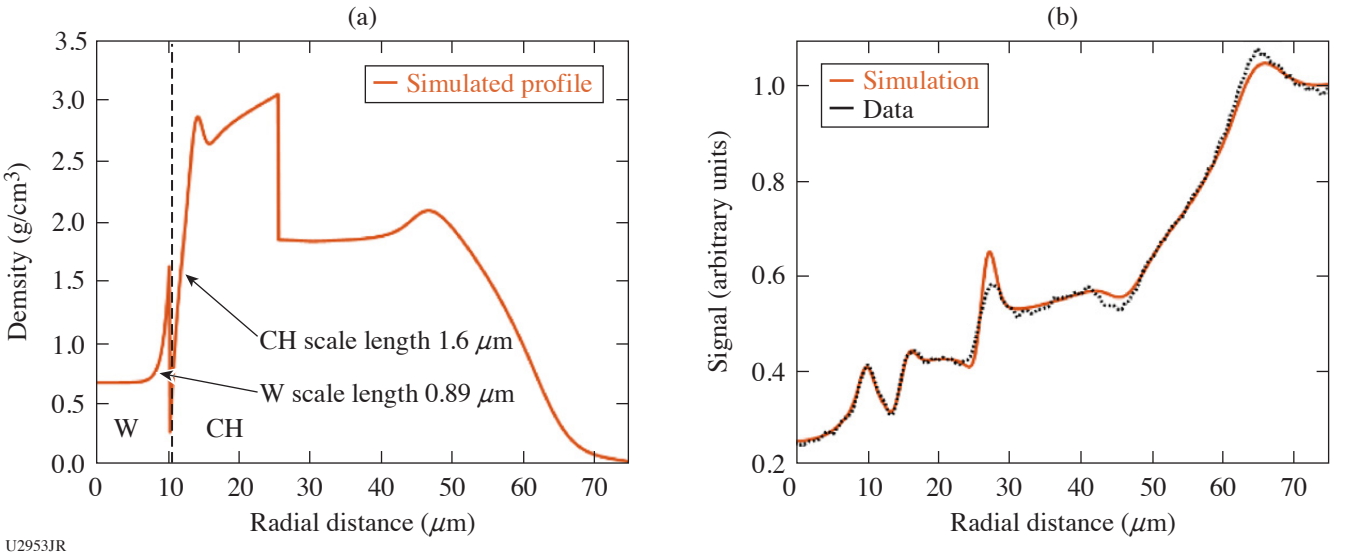

Figure 36
(a) Simulated radial density profiles that we have created to match our data, with a discontinuity at the interface, the outward-traveling shock wave, and the rarefaction of the outer plastic edge. The material interface is located at a radius of around 10 μm. The measured scale lengths of each material's density profile are given. (b) The simulated diffraction pattern from the density profile given in (a) is compared with the data at 4 ns from above. We see excellent fitting, especially in the region near the material interface at 10 μm. The shock wave at 27 μm has not considered any motion blurring, and as such diverges from the data.

Relativistic Intensity Laser Channeling and Direct Laser Acceleration of Electrons from an Underdense Plasma

H. Tang,[1] I.-L. Yeh,[2] P. T. Campbell,[1] F. Albert,[3] H. Chen,[3] Y. Ma,[1] A. McKelvey,[1] P. M. Nilson,[4] B. K. Russell,[1] J. L. Shaw,[4] A. G. R. Thomas,[1] A. V. Arefiev,[2] and L. Willingale[1*]
[1]University of Michigan
[2]University of California, San Diego
[3]Lawrence Livermore National Laboratory
[4]Laboratory for Laser Energetics, University of Rochester
[*]Principal Investigator

Laser–plasma interactions generate high-energy electrons, which have a number of potential applications, including generating secondary sources like bright x-ray radiation, electron–positron pairs, ion acceleration, or neutron generation. The direct laser acceleration (DLA) mechanism uses the laser's electric field, in the presence of an external field such as the channel fields, to produce a relativistic electron beam. Our experiments aim to understand the DLA dynamics and optimize the high-energy electron beam production. The experimental variables are plasma density, laser pulse duration, focusing geometry, and laser energy. For the FY22 shots, expanded the parameter space was explored, building on previous data; the secondary x-ray emission using a Ross pair filter was also investigated.

The apodized backlighter laser pulse was focused onto the edge of a 2-mm-diam helium gas-jet target with a plasma density of either $0.01n_c$ or $0.004n_c$, where n_c is the critical density. An *f*/5 apodizer was utilized for most shots. The laser energy was decreased from 110 J to 12 J to observe the acceleration mechanism in low a_0 regime. We also performed one shot using an *f*/8 apodizer to study the effect of a large beam. In order to study the effect of laser pulse duration on laser channeling, we used a 3-ps pulse for our final shot. The main diagnostics were EPPS3 Rad (electron–positron–proton spectrometer) and proton radiography, which employed the sidelighter beam, and a 50-μm Cu foil to generate the proton beam. Additionally, the 4ω probe was turned on, taking shadowgraphy and angular filter refractometry data to observe the channel.

As shown in Fig. 37(a), the proton radiography imaged the laser channel structure after a 3-ps laser pulse propagation through the gas column from left to right. The channel walls generate a bump in the center of the picture, implying the formation of

new laser modes when the laser travels through the plasma. The dark line segment inside the channel (shown by orange arrow) indicates the field reversal, which is due to the ion motion. Figure 37(b) shows the electron spectra. Electrons with energy up to 170 MeV were observed. The effective temperature decreases with the laser energy for a fixed laser focal spot size. Figure 37(c) shows the Ross pair filters and a raw image of the x ray on an image plate. The x-ray diagnostic was installed behind the EPPS. The Ross pair filters contain eight sections, which are made by different metal materials with varying thicknesses. A hole was on the back of the filter; therefore, eight small sections blocked the x ray with different cutoff energies, forming a round disk with eight sections of different brightnesses. A rough analysis estimated the x-ray energy to be in the 10- to 100-KeV range. Further calculation and calibration need to be performed for x-ray measurement.

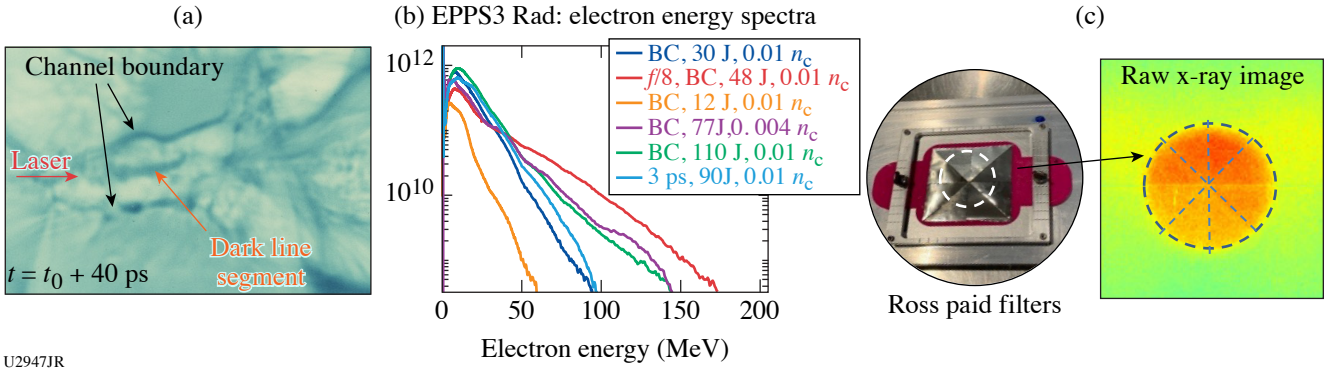

Figure 37
(a) Raw proton radiography image from shot 37147. The red arrow represents the laser propagation direction, the black arrows point at the channel walls, and the orange arrow points at the dark line segment inside the channel. The image was taken 40 ps after the interaction. (b) Electron spectra from the 16 June 2022 shot day. (c) Ross pair filters and raw x-ray image from shot 37147.

This material is based upon work supported by the Department of Energy/NNSA under Award Number DE-NA0004030.

1. K. Bhutwala *et al.*, Phys. Rev. E **105**, 055206 (2022).
2. C. McGuffey *et al.*, Bull. Am. Phys. Soc. **65**, VO05.00005 (2020).
3. J. Saret *et al.*, "Measurements of Temperature Evolution in Copper from Intense Proton Beam Energy Deposition," in preparation.
4. C. McGuffey *et al.*, Sci. Rep. **10**, 9415 (2020).
5. W. Fox, A. Bhattacharjee, and K. Germaschewski, Phys. Rev. Lett. **106**, 215003 (2011).
6. W. Fox *et al.*, submitted to Physical Review Letters, available arXiv:2003.06351 (2020).
7. C. L. Johnson *et al.*, Rev. Sci. Instrum. **93**, 023502 (2022).
8. A. F. A. Bott *et al.*, J. Plasma Phys. **83**, 905830614 (2017).
9. S. Zhang *et al.*, "Ion and Electron Acoustic Bursts During Anti-Parallel Reconnection Driven by Lasers," to be published in Nature Physics.
10. L. Gao *et al.*, Phys. Plasmas **23**, 043106 (2016).
11. A. Chien *et al.*, Phys. Plasmas **26**, 062113 (2019).
12. A. Chien *et al.*, Phys. Plasmas **28**, 052105 (2021).
13. K. D. Meaney, presented at the 64th Annual Meeting of the APS Division of Plasma Physics, Spokane, WA, 17–21 October 2022 (YI01.00002).
14. B. J. Winjum, F. S. Tsung, and W. B. Mori, Phys. Rev. E **98**, 043208 (2018).
15. M. Bailly-Grandvaux *et al.*, J. Plasma Phys. **89**, 175890201 (2023).
16. B. J. Winjum *et al.*, Phys. Rev. Lett. **110**, 165001 (2013).
17. X. Sha *et al.*, Sci. Rep. **5**, 11003 (2015).
18. H. Liu, J. S. Tse, and H. Mao, J. Appl. Phys. **100**, 093509 (2006).

19. J. E. Jaffe *et al.*, Phys. Rev. B **62**, 1660 (2000).
20. Z. Li *et al.*, Phys. Rev. B **79**, 193201 (2009).
21 N. V. Kabadi *et al.*, Phys. Rev. E **104**, L013201 (2021).
22. M. J. Rosenberg *et al.*, Phys. Rev. Lett. **112**, 185001 (2014).
23. H. Sio *et al.*, Rev. Sci. Instrum. **87**, 11D701 (2016).
24. B. Reichelt *et al.*, Bull. Am. Phys. Soc. **66**, UO04.00006 (2021).
25. M. Gatu Johnson *et al.*, Phys. Plasmas **27**, 032704 (2020).
26. S. Brygoo *et al.*, Nature **593**, 517 (2021).
27. P. M. Nilson *et al.*, Phys. Rev. Lett. **97**, 255001 (2006).
28. R. Samtaney *et al.*, Phys. Rev. Lett. **103**, 105004 (2009).
29. E. Greco *et al.*, Astrophys. J. Lett. **908**, L45 (2021).
30. J. E. Gudmundsson, C. J. Pethick, and R. I. Epstein, Astrophys. J. **272**, 286 (1983).
31. S. D. Bergeson *et al.*, Phys. Plasmas **26**, 100501 (2019).
32. B. Strömgren, Astrophys. J. **89**, 526 (1939).
33. R. P. Drake *et al.*, Astrophys. J. **833**, 249 (2016).
34. A. Mizuta *et al.*, Astrophys. J. **621**, 803 (2005).
35. A. M. Hansen *et al.*, Rev. Sci. Instrum. **89**, 10C103 (2018).
36. E. N. Parker, *Cosmical Magnetic Fields: Their Origin and Their Activity*, The International Series of Monographs on Physics (Clarendon Press, Oxford, 1979).
37. B. Fryxell *et al.*, Astrophys. J. Suppl. Ser. **131**, 273 (2000).
38. P. Tzeferacos *et al.*, High Energy Density Phys. **17**, 24 (2015).
39. P. Tzeferacos *et al.*, Phys. Plasmas **24**, 041404 (2017).
40. P. Tzeferacos *et al.*, Nat. Commun. **9**, 591 (2018).
41. *2019 John Dawson Award for Excellence in Plasma Physics Research Recipient*, Petros Tzeferacos, University of Chicago, (2019).
42. A. F. A. Bott *et al.*, Proc. Natl. Acad. Sci. **118**, e2015729118 (2021).
43. A. F. A. Bott *et al.*, Matter Radiat. Extremes **7**, 046901 (2022).
44. L. E. Chen *et al.*, Astrophys. J. **892**, 114 (2020).
45. J. Meinecke *et al.*, Sci. Adv. **8**, eabj6799 (2022).
46. A.F. A. Bott *et al.*, Phys. Rev. Lett. **127**, 175002 (2021).
47. A. Kolmogorov, Dokl. Akad. Nauk SSSR **30**, 301 (1941).
48. L. Gao *et al.*, Astrophys. J. Lett. **873**, L11 (2019).
49. Y. Lu *et al.*, Phys. Plasmas **26**, 022902 (2019).
50. Z. He *et al.*, Sci. Adv. **8**, eabo0617 (2022).
51. D. Kraus *et al.*, Nat. Astron. **1**, 606 (2017).
52. M. C. Marshall *et al.*, J. Appl. Phys. **131**, 085904 (2022).
53. R. F. Smith *et al.*, J. Appl. Phys. **131**, 245901 (2022).
54. R. F. Smith *et al.*, Nature **511**, 330 (2014).
55. P. K. Patel *et al.*, Phys. Rev. Lett. **91**, 125004 (2003).
56. D. Haberberger *et al.*, Phys. Rev. Lett. **123**, 235001 (2019).
57. A. Macchi, M. Borghesi, and M. Passoni, Rev. Mod. Phys. **85**, 751 (2013).
58. S. Palaniyappan *et al.*, Nat. Commun. **6**, 10170 (2015).
59. A. Higginson *et al.*, Nat. Commun. **9**, 724 (2018).
60. L. Yin *et al.*, Phys. Rev. Lett. **107**, 045003 (2011).
61. J. R. Rygg *et al.*, Rev. Sci. Instrum. **83**, 113904 (2012).
62. P. M. Celliers *et al.*, Rev. Sci. Instrum. **75**, 4916 (2004).
63. M. P. Valdivia *et al.*, Rev. Sci. Instrum. **92**, 065110 (2021).
64. G. Pérez-Callejo *et al.*, Phys. Plasmas **29**, 043901 (2022).

65. G. Pérez-Callejo *et al.*, "Phase Imaging of Irradiated Foils at the OMEGA EP Facility Using Phase-Stepping X-Ray Talbot–Lau Interferometry," in preparation.
66. M. P. Valdivia *et al.*, Rev. Sci. Instrum. **89**, 10G127 (2018).
67. M. P. Valdivia, D. Stutman, and M. Finkenthal, Rev. Sci. Instrum. **85**, 073702 (2014).
68. C. H. Allen *et al.*, Appl. Opt. **61**, 1987 (2022).
69. M. Oliver *et al.*, Rev. Sci. Instrum. **93**, 093502 (2022).
70. A. Pogany, D. Gao, and S. W. Wilkins, Rev. Sci. Instrum. **68**, 2774 (1997).

FY22 Laboratory Basic Science Program

M. S. Wei

Laboratory for Laser Energetics, University of Rochester

The Laboratory Basic Science (LBS) Program awarded 21 projects with a total allocation of 22 shot days for a full-year schedule at the Omega Laser Facility in FY22 including six carryover FY21 LBS projects with shots in Q1FY22. A total of 224 target shots were conducted for the LBS Program in FY22. These experiments were led by scientists from Lawrence Livermore National Laboratory (LLNL), SLAC, Princeton Plasma Physics Laboratory (PPPL), and LLE (see Table I). The LBS experiments conducted in FY22 are summarized in this section.

During FY22, LLE issued a solicitation for LBS proposals for beam time in FY23. A total of 20 proposals were submitted, requesting a total of 30 Omega shot days, which was about 150% of the notional allocation for the LBS Program. The reduced number of proposals compared to prior years was attributed to several factors including an early deadline (by a month due to the change of the annual Omega Scheduling meeting from June 2022 to May 2022) and many overlapping activities such as proposals to the High-Energy-Density (HED) Council for shots at the National Ignition Facility and white papers for the Laboratory Directed Research and Development (LDRD) Program at LLNL, among others. An independent LBS Proposal Review Panel (PRP) consisting of eight subject-matter experts from universities, national laboratories, and industry reviewed and ranked the proposals. Based on the LBS PRP's recommendation, 19 proposals were selected and allocated a total of 21.5 shot days for experiments at the Omega Laser Facility in FY23, as shown in Table II.

Table I: LBS Projets with experiments conducted at the Omega Laser Facility in FY22, including six carryovers from the FY21 LBS Program (gray shaded cells).

Principal Investigator	Lead Institution	Title
H. Chen/M. R. Edwards	LLNL/Stanford Univeristy	Developing a Magnetic Mirror Trap for Laser-Produced Relativistic Electron–Positron Pairs/Exploring Electron and Electron–Positron Plasma Dynamics
H. Chen/G. Gregori	LLNL/University of Oxford	Measuring Particle Transport in Turbulent Plasmas/Laboratory Model of Particle Acceleration in Supernova Shocks
F. Coppari/Y. Kim	LLNL	Measurements of Shock Equation of State and Melting Temperature of H:N:O and H:C:N:O Mixtures
L. Gao	PPPL	Particle Acceleration from Magnetically Driven Collisionless Reconnection Using Short-Pulse, Laser-Powered Capacitor Coils
H. G. Rinderknecht	LLE	Initial Relativistically Transparent Microchannel Experiments on OMEGA EP
A. Zylstra/J. Jeet	LLNL	Inertial Confinement Fusion Plasma-Based Measurements of the T + ^{4}He Cross Section
F. Albert	LLNL	High-Precision X-Ray Radiography Driven by Laser Wakefield Acceleration/X-Ray Sources from Laser Wakefield Acceleration on OMEGA EP

Table I: LBS Projets with experiments conducted at the Omega Laser Facility in FY22, including six carryovers from the FY21 LBS Program (gray shaded cells) (continued).

Principal Investigator	Lead Institution	Title
G. Bruhaug	LLE	Relativistic THz-Matter Interactions/Extreme THz Generation and Detection
G. W. Collins/ A. Schwemmlein	LLE	Quantum States of Hydrogen: Toward a Superconducting Superfluid
A. Gleason	SLAC	Viscosity Measurements Using Tracer Particles
I. V. Igumenshchev/ V. N. Goncharov	LLE	Formation of Dynamic Shells Using Foam Ball Targets
J. Jeet	LLNL	Cross-Calibration of the D–T γ-to-Neutron and D–^{3}He γ-to-Protron Branching Ratios Against the ^{12}C(n,n$'$)γ Reaction/Inertial Confinement Fusion Plasma-Based Measurements of the D–T γ-to-Neutron and D–^{3}He γ-to-Protron Branching Ratios
S. Malko	PPPL	Detailed Benchmarking of the Nernst Effect in a Magnetized High-Energy-Density Plasma
J. L. Peebles	LLE	Probing In-Flight Vacuum Magnetic-Field Compression on OMEGA
M. J. Rosenberg	LLE	Electron Energization in Colliding and Reconnecting Magnetized Plasmas
M. Schneider	LLNL	Using Isoelectronic Line Ratios to Measure Density in Nonlocal Thermodynamic Equilibrium Plasmas/Measuring Electron Densities in Nonlocal Thermodynamic Equilibrium Plasmas Using Isoelectronic Line Ratios
S. Singh/S. Clarke	LLNL	The Effect of Ni Concentration on Phase Transformation Dynamics in the Fe-Ni Binary System/Probing the Fe–Ni Phase Space Using Powder X-Ray Diffraction Image Plates
R. F. Smith	LLNL	Measuring the Viscosity of MgO at Lower-Mantle Conditions
C. Stoeckl/A. Schwemmlein	LLE	Development of a New Experimental Platform LIANS on OMEGA EP for Deuteron and Triton-Induced Nuclear Reactions—Studying the T–T Reaction at Energies Exceeding 2 MeV on OMEGA
G. Swadling	LLNL	Angular Momentum Transport in Disk-Jet Transitions

Table II: Nineteen projects from the FY23 LBS Program approved for target shots at the Omega Laser Facility in FY23.

Principal Investigator	Lead Institution	Title
F. Albert	LLNL	X-Ray Radiography of Laser-Driven Shocks Using Laser Wakefield Acceleration
L. Ceurvorst	LLE	Amplification of Laser Imprint with Strong Magnetic Fields
K. Churnetski	LLE	Evaluating Shock-Augmented Ignition and Late-Time Laser–Capsule Coupling in Laser Inertial Fusion
G. W. Collins	LLE	Quantum States of Hydrogen: Toward a Superconducing Superfluid
J. R. Davies	LLE	Measurement of a Self-Generated Magnetic Field in Laser–Foil Interactions with Oblique Proton Probing
C. J. Forrest	LLE	Multiple Reactant Implosions to Improve Cross-Section Measurements of Reactions Relevant to Nuclear Astrophysics
L. Gao	PPPL	Multi-Scale Reconnection and Particle Acceleration in Long Current Sheets During Magnetically Driven Collisionless Reconnection at Low Plasma β

Table II: Nineteen projects from the FY23 LBS Program approved for target shots at the Omega Laser Facility in FY23 (continued).

Principal Investigator	Institution	Title
F. García-Rubio	LLE	Driving Magnetized Collisionless Shocks with Solid Pistons on OMEGA EP
A. Gleason	SLAC	Particle Tracking in High-Energy-Density Flows
D. Haberberger	LLE	Raman Pump Propagation
P. V. Heuer	LLE	Benchmarking Nernst Advection in Local and Nonlocal Regimes
M. Holec	LLNL	Nonlocal Electron Transport in Collisional Magnetized Plasma Jets
Y. Kim	LANL	Development of an Ion Stopping-Power Platform at Low Projectile-to-Thermal Velocity Ratio
S. Malko	PPPL	Proton Radiography of a Bounded, Magnetized Plasma Relevant to MagLIF
J. L. Peebles	LLE	Measurement and Application of Short-Pulse Compressed Magnetic Field
M. Sherlock	LLNL	Study of Magnetization Effects in Cylindrically Imploded Hot Dense Plasmas Using Dopant Spectroscopy Techniques
R. Smith	LLNL	Novel Experiments to Measure Viscosity of Minerals at the Conditions of Planetary Interiors
C. Stoeckl	LLE	Investigating the Dynamics and Stability of Astrophysical-Relevant Plasma Jets
G. Swadling	LLNL	Effects of Collisionality in Angular Momentum Transport in Disk-Jet Transitions

Exploring Electron and Electron–Positron Plasma Dynamics

M. R. Edwards,[1*] S. You,[2] J. von der Linden,[3] J. L. Peebles,[4] L. Willingale,[5] G. Fiksel,[5] and H. Chen[2*]
[1]Stanford University
[2]Lawrence Livermore National Laboratory
[3]Max Planck Institute for Plasma Physics
[4]Laboratory for Laser Energetics, University of Rochester
[5]University of Michigan
[*]Principal Investigators

To explore instabilities of relativistic electron and electron–positron beams, this experiment aimed to collide a relativistic electron–positron jet with a low-density hydrocarbon plasma and examine the interaction region for the development of magnetic-field filaments. This work aims both to understand the fundamental properties of electron and electron–positron plasmas and to explore possible scaled experiments with astrophysical relevance.

In the experiment, electron–positron jets were produced by focusing the backlighter beam on specially designed large-diameter gold-copper targets that controlled the positron acceleration. A background plasma was generated using Beam 3 on a hydrocarbon disk target. The interaction zone was imaged with sidelighter-driven proton radiography and the properties of the jet were characterized with an electron–proton–positron spectrometer (EPPS). We used the magneto-inertial fusion electrical discharge system (MIFEDS) to control the focusing of low-energy electrons and positrons into the interaction zone.

Particle spectrometer measurements confirmed control over positron energy using large-diameter targets and control over low-energy electron and positron focusing using MIFEDS. We observed the development of large-scale instabilities (Fig. 1), suggesting the presence of an electron-driven instability. These results suggest progress toward a platform for studying relativistic electron jet instabilities using kilojoule-class lasers.

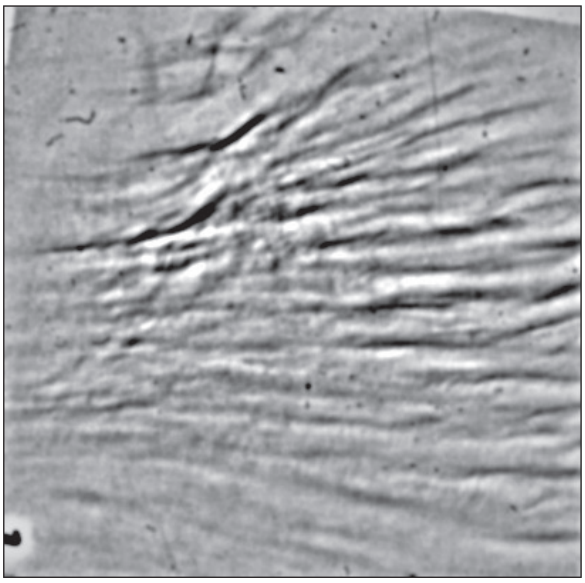

U2900JR

Figure 1
Filtered proton radiography image-plate data showing evidence of instability development in an electron beam crossing a background plasma.

Laboratory Model of Particle Acceleration in Supernova Shocks

H. Chen,[1*] C. A. J. Palmer,[2] H. Poole,[3] A. R. Bell,[3] A. Bott,[4] G. Gregori,[3*] O. Karnbach,[3] J. Matthews,[3] D. Lamb,[5] R. D. Petrasso,[6] P. Tzeferacos,[7] A. Birkel,[6] C. K. Li,[6] and H.-S. Park[1]
[1]Lawrence Livermore National Laboratory
[2]Queen's University, Belfast, UK
[3]University of Oxford, UK
[4]Princeton University
[5]University of Chicago
[6]Massachusetts Institute of Technology
[7]Laboratory for Laser Energetics, University of Rochester
[*]Principal Investigator

Magneto-collisional instabilities (MCI's) have been proposed as an explanation for the observation of acceleration of cosmic rays (CR's) to energies higher than those predicted by simple models in the turbulent magnetized plasmas surrounding supernova remnants. The instabilities, driven by high-intensity currents of CR's, can lead to amplification of the plasma magnetic fields, which results in prolonged trapping of the energetic CR in the turbulent plasma and, consequently, higher maximum energies. This is particularly true for a subset of these instabilities, the "nonresonant hybrid instability," which drives the growth of fields at the scale of the Larmor radius of the CR current. Due to the nature of this instability, covering a high dynamic range of spatial and temporal scales and requiring the inclusion of kinetic processes, computational simulations struggle to accurately model the process.

A joint shot day at LLE in 2019 aimed to explore this field amplification in the laboratory using the well-established turbulent dynamo target platform (TDYNO) to create a turbulent plasma embedded with stochastic magnetic fields, and a high-energy (2-kJ), short-pulse (100-ps) OMEGA EP laser beam to produce a high-intensity proton current that would drive the instability (Fig. 2). The results of this shot day indicated the generation of a >1-kA proton beam with a cutoff energy of approximately 3 MeV, which was only detected when the turbulent plasma was not present.

This may indicate MCI's inhibition of the proton propagation or disruption to the proton-generation mechanism due to the close proximity of the proton source to the turbulent plasmas. Follow-up experiments in 2021 aimed to directly compare the density and magnetic-field structure of the plasma turbulence with and without a high-current drive beam, as well as test for confirmation signatures of proton production using a modified target design. As in 2019, the main diagnostics included an x-ray framing camera to measure self-emission from the turbulent plasma, proton radiography using a D^3He capsule irradiated with 17 OMEGA beams

(450 J/beam, 1 ns) to probe the magnetic-field structure of the plasma, the EPPS to measure the energy spectrum of the target normal sheath acceleration (TNSA) proton beam, and the Zinc von Hamos spectrometer to measure protons induced x-ray emission from a tracer foil on the proton-generation target.

Data were obtained for a direct comparison on the proton radiography and x-ray self-emission with and without the high-current instability drive beam. This confirmed that a change in structure of the x-ray self-emission from the standard TDYNO plasma, observed in 2019, was not due to the presence of the proton beam, but likely due to a small change in ordering and therefore orientation of the TDYNO drive beam (Fig. 3). This is being investigated further using the radiation hydrocode *FLASH*.

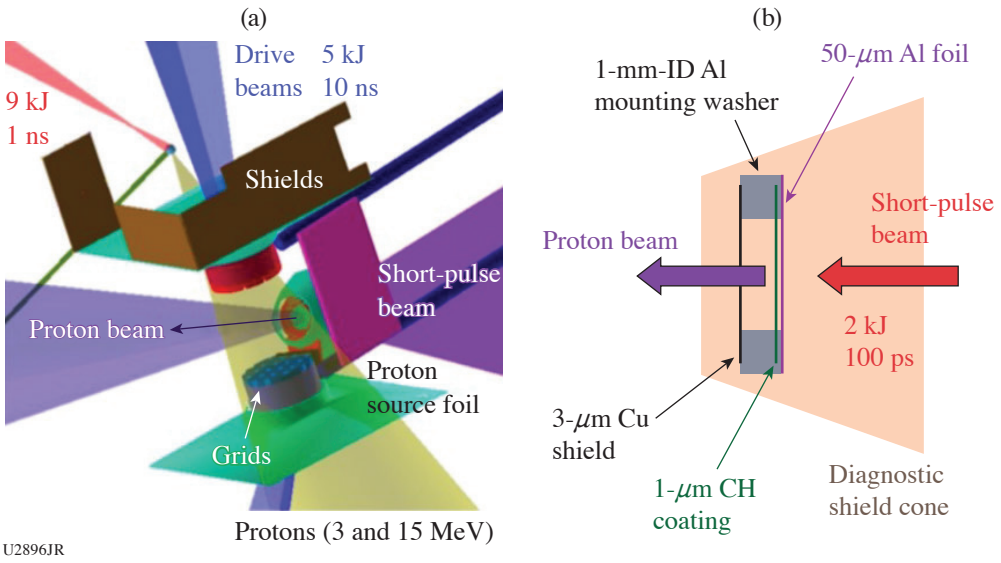

Figure 2
(a) Experimental configuration and (b) a TNSA target. The EPPS diagnostic sits along the axis of the marked proton beam.

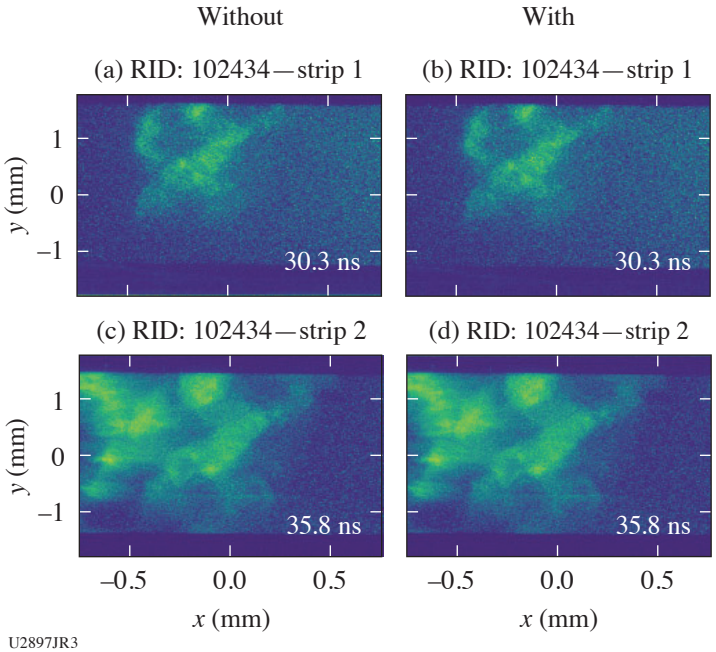

Figure 3
Comparison of the evolution of the plasma density structure via the x-ray self-emission measured at two times, 30.3 ns and 35.8 ns, respectively, for shots [(a) and (c)] without or [(b) and (d)] with the high-energy OMEGA EP interaction. While the structure is qualitatively different from typical TDYNO data, with a central hole, the two shots here do not indicate that structural changes are due to the propagation of a high-current proton beam.

The zinc von Hamos spectrometer suffered from strong continuum background due to the capsule drive, but the spectra indicated the presence of several lines consistent with copper emission, which is most clearly visible on shots without the D^3He backlighter capsule or turbulent plasma (Fig. 4). Analysis is ongoing to determine whether this diagnostic can confirm that proton-beam acceleration is not prevented by the presence of the turbulent plasma.

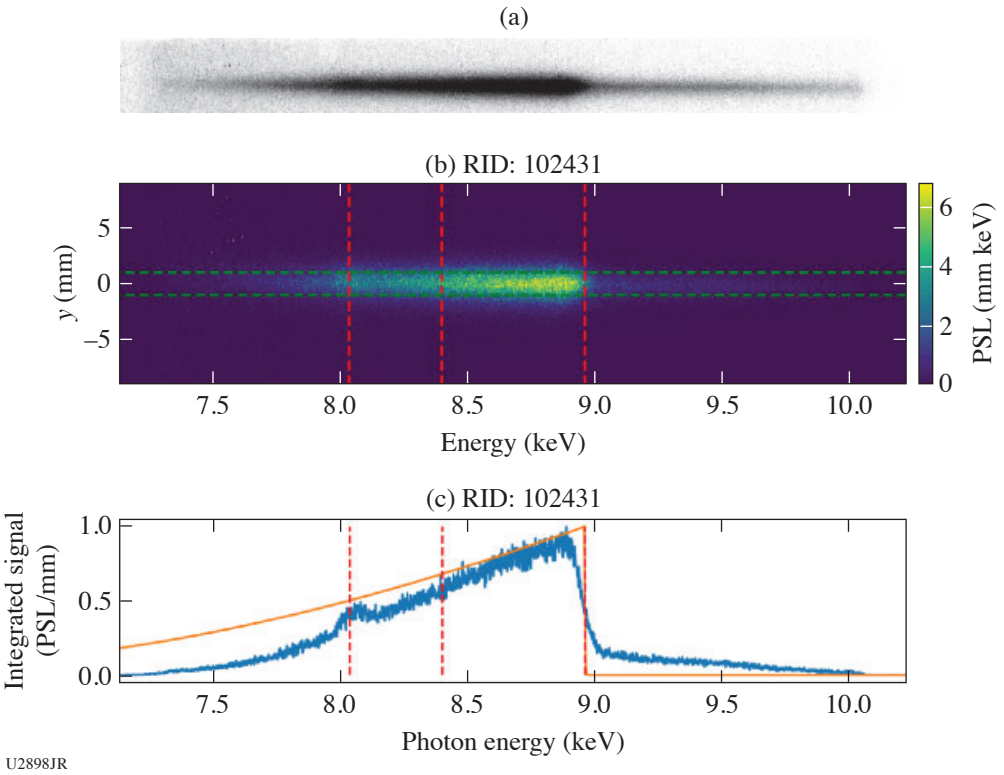

Figure 4
Zinc von Hamos spectra from an OMEGA EP shot showing (a) the raw data, (b) processed image, and (c) an integrated signal lineout, which indicates excess emission consistent with copper K_α emission with only the copper in the target included in the tracer layer of the OMEGA EP target.

Measurements of Shock Equation of State and Melting Temperature of H:N:O and H:C:N:O Mixtures

Y.-J. Kim,[1] M. Bethkenhagen,[2] S. Hamel,[1] M. Wadas,[3] S. Stanley,[4] M. Millot,[1] and F. Coppari[1*]
[1]Lawrence Livermore National Laboratory
[2]Rostock University, Germany
[3]University of Michigan
[4]Johns Hopkins University
[*]Principal Investigator

This ExtChmDAC-21 campaign under the support of the LBS Program aims at investigating the optical and thermodynamic properties of ammonia-rich H:N:O and synthetic Uranus (SU) H:C:N:O mixtures at the extreme pressure–temperature conditions that we expect in the deep interior of icy giant planets such as Uranus and Neptune. This work expands on our recent discovery of superionic water ice (or ice XVIII)[1–3] to reveal the possible existence of the superionic phase in the icy planet constituents as well as its melting temperature.

We prepared ammonia monohydrate (AMH, $NH_3{\cdot}H_2O$), ammonia hemihydrate (AHH, $2NH_3{\cdot}H_2O$), and SU mixtures, and documented their optical properties at the ambient condition.[4] These liquid mixtures were precompressed to 1 to 2 GPa in diamond anvil cells (DAC's) to increase their initial density at room temperature, achieve lower temperatures but higher compression under dynamic loading, and finally reach planetary interior conditions. With excellent laser performance and support, we collected 14 system shots in the one-day allocation. Doppler velocimetry (VISAR) and streaked optical pyrometry (SOP) were used to track the shock-wave propagation through the precompressed sample and to document the pressure–density–temperature shock equation of state as well as the evolution of the optical properties (reflectivity, absorption coefficient) along the shock Hugoniot curves using a quartz reference (see Fig. 5) (Refs. 5,6). The ongoing data analysis will be used to improve our understanding of chemical bonding changes in this regime and benchmark future improved equation-of-state and planetary models.

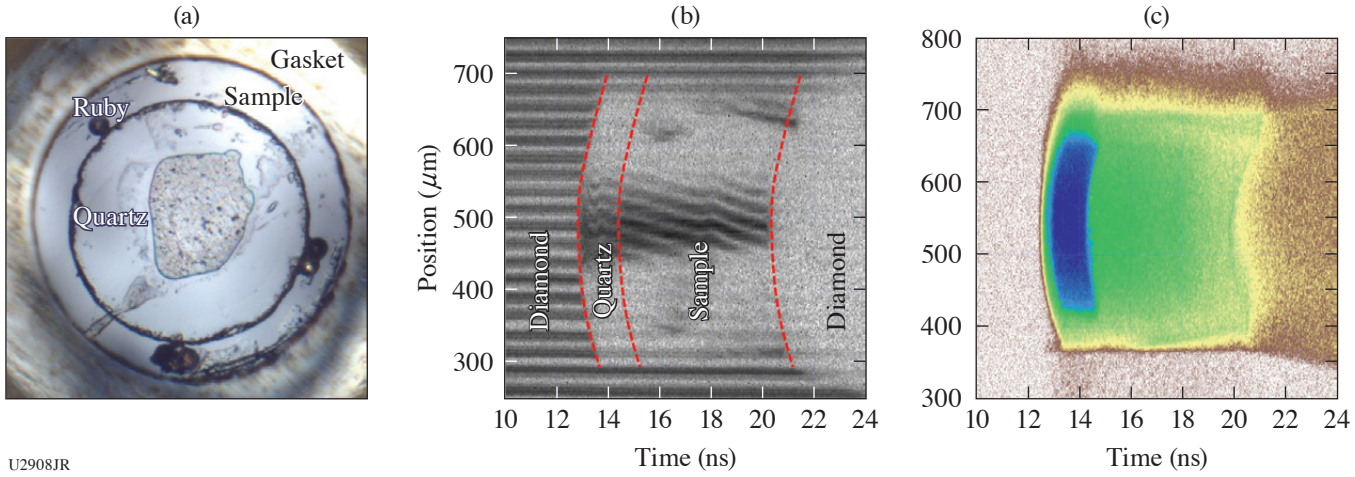

Figure 5
(a) Sample image. Example of (b) VISAR and (c) SOP data showing the decaying shock along the 100-mm-thick SU mixture on OMEGA.

This work was prepared by LLNL under Contract Number DE-AC52-07NA27344 and was supported by LLNL LDRD Program No. 19-ERD-031.

Particle Acceleration from Magnetically Driven Collisionless Reconnection Using Short-Pulse, Laser-Powered Capacitor Coils

L. Gao,[1*] S. Zhang,[2] A. Chien,[2] H. Ji,[1,2] E. G. Blackman,[3] and P. M. Nilson[4]
[1]Princeton Plasma Physics Laboratory
[2]Princeton University
[3]Department of Physics and Astronomy, University of Rochester
[4]Laboratory for Laser Energetics, University of Rochester
[*]Principal Investigator

Magnetic reconnection is a ubiquitous astrophysical process whereby magnetic energy is rapidly converted into plasma kinetic energy in the form of bulk flow, thermal energy, and nonthermal particles. The latter is often regarded as an observational signature of reconnection, which can be a more-efficient particle accelerator than other processes such as collisionless shocks. In the past ∼six years, our team has developed a platform to study acceleration of nonthermal electrons from magnetic reconnection at low plasma beta using UV laser-powered capacitor coils.[7] For the first time, nonthermal electrons accelerated by the reconnection electric field have been measured.[8] In our previous LBS campaigns, we have measured ultrastrong magnetic fields using short-pulse, laser-powered capacitor coils. The measured magnetic fields driven by the short-pulse lasers are ∼2 to 3× larger than those with UV lasers. In this new FY22 LBS shot day, we extended our platform to study particle acceleration by magnetically driven axisymmetric reconnection using short-pulse, laser-powered capacitor coils.

The experimental platform is shown in Fig. 6. The main target was composed of two Cu plates with an extended wing in the back plate, connected by a pair of parallel U-shaped coils. The OMEGA EP sidelighter (SL) was focused onto the wing section of the backplate, positively charging it up. The resulting voltage difference between the back and front plate drives currents in both coils for reconnection. Ultrafast protons generated by the backlighter (BL) probed through the coils to measure the magnetic-field distributions around the coils. The primary advantages of this target design were to (1) perform face-on proton radiography of the reconnection region, and (2) position multiple particle spectrometers around the coils to capture particles at various angles with respect to the reconnection region. The proton data, however, show very small magnetic-field generation for the new target. As a reference, our single-coil experiment used a capacitor coil target without the tiny wing and the SL was directly focused onto the back plate.

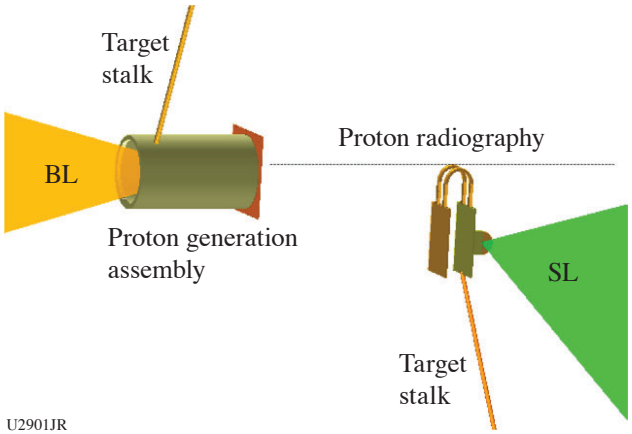

Figure 6
Experimental setup. The OMEGA EP SL was focused onto the wing section of the back plate, positively charging it up. The resulting voltage difference between the back and front plate drives currents in both coils, creating reconnection. Ultrafast protons generated by the BL probed through the coils and were collected by the proton film pack.

Two shots were dedicated to exploring magnetic-field evolution using the old single-coil target, where the SL was focused onto the back Cu plate. Figure 7 shows the proton images collected at 1 ns and 25 ps after the SL drive was turned off. Large and well-defined voids are observed for both cases, indicating a slow decay time of the coil current.

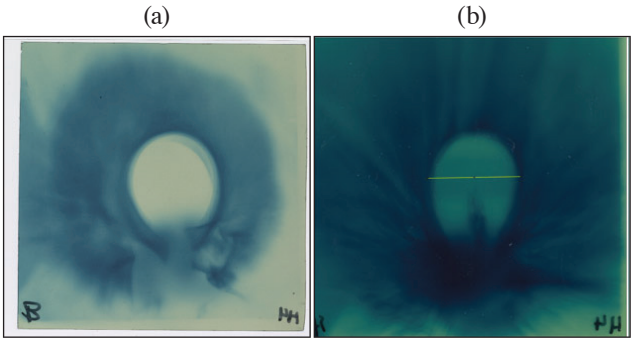

Figure 7
Proton radiographs of the single wire case at (a) 1 ns and (b) 25 ps, respectively, after the SL was turned off. The slight bubble is caused by magnetic fields around the wire deflecting incident protons.

In parallel to the LBS shot day, we conducted two LaserNetUS campaigns using the short-pulse, laser-powered coils for reconnection. Although the new target design with the tiny wing on the back plate did not work out, the data collected on this LBS day helped us with experiment designs for the two LaserNetUS campaigns where successful particle spectra were measured.

We acknowledge the Omega Laser Facility staff at the Laboratory for Laser Energetics. This work was performed under the auspices of U.S. DOE NNSA under the LBS Program, and the DOE Office of Science under the HEDLP Program No. DE-SC0020103.

Initial Relativistically Transparent Microchannel Experiments on OMEGA EP

H. G. Rinderknecht,* G. Bruhaug, M. VanDusen-Gross, and K. Weichman
Laboratory for Laser Energetics, University of Rochester
*Principal Investigator

In relativistically transparent interactions of high-intensity lasers with an overdense plasma, the ponderomotive force of the laser pulse is predicted to drive relativistic current filaments, which in turn produce an azimuthal magnetic filament strong enough to trap electrons.[9] The trapped electrons are predicted to be rapidly accelerated by direct laser acceleration (DLA) to high energies. In this campaign we studied magnetic filament acceleration using the OMEGA EP laser interacting with microchannel targets. The targets were arrays of 6-μm-ID microchannels filled with low-density CH foam, as shown in Figs. 8(a) and 8(b). From prior experiments and scaling laws,[10] we predicted that targets with lower density (3 mg/cm^3) would accelerate electrons more efficiently than targets with higher density (5 mg/cm^3); empty channel targets were also shot as a control.

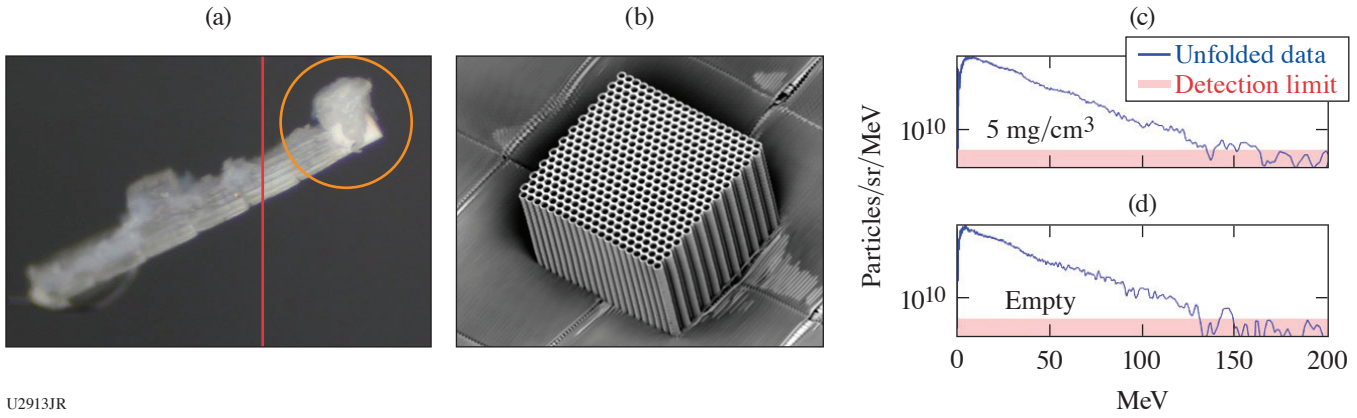

Figure 8
(a) Targets used in the experiment. The active component (orange) is an array of 6-μm-ID, 200-μm-long microchannels, either empty or filled with 3 mg/cm^3 or 5 mg/cm^3 CH foam. (b) Electron microscope image of an empty microchannel array. (c) Recorded electron spectrum from channels with 5-mg/cm^3 fill; (d) no fill. Recorded electron spectra were comparable for all target types.

The EPPS spectrometer recorded electron acceleration from all target types [Figs. 8(c) and 8(d)]. While both the fluence of electrons F and the average electron energy $\langle E\rangle$ increased significantly with higher peak laser amplitude $a_0\left(F \propto a_0^3,\ \langle E\rangle \propto a_0\right)$, no clear difference was observed between the three types of targets used. X-ray data recorded with the bremsstrahlung MeV x-ray spectrometer (BMXS) also did not show a significant difference in radiation between target types.

Post-shot 3-D particle-in-cell (PIC) simulations indicate that, for laser–channel interactions on the time scale of OMEGA EP, the initial channel fill is blown out of the channel within the first 300 fs of the interaction. Subsequently, plasma pulled from the channel wall fills the channels to a density of roughly 7× the plasma critical density in all cases, resulting in identical magnetic filament formation and electron acceleration in all cases. This supports the data interpretation that, on the time scale of OMEGA EP interactions, the magnetic filament acceleration is observed; however, initial plasma density does not determine the acceleration performance.

This material is based upon work supported by the DOE NNSA under Award Number DE-NA0003856, the University of Rochester, and the New York State Energy Research and Development Authority.

Inertial Confinement Fusion Plasma-Based Measurements of the T + ^{4}He Cross Section

J. Jeet,[1*] A. B. Zylstra,[1*] M. Rubery,[1] Y. Kim,[2] Z. L. Mohamed,[2] M. Gatu Johnson,[3] C. J. Forrest,[4] and V. Yu. Glebov[4]
[1]Lawrence Livermore National Laboratory
[2]Los Alamos National Laboratory
[3]Plasma Science and Fusion Center, Massachusetts Institute of Technology
[4]Laboratory for Laser Energetics, University of Rochester
[*]Principal Investigators

Inertial confinement fusion (ICF) implosions provide a relatively new platform for studying nuclear astrophysics. Unlike beam-target accelerator measurements, nuclear reactions occurring in these implosion experiments are a direct surrogate for astrophysical systems since the reactions occur at comparable plasma conditions. The tritium (T) + ^{4}He reaction is important for big-bang nucleosynthesis (BBN) production of ^{7}Li, which has a notable abundance anomaly. Observations of metal-poor halo stars[11] show approximately one-third of the ^{7}Li abundance from predictions that match the abundance inferred from the cosmic microwave background.[12] The important energy range for BBN is a center of mass energy (E_{CM}) between 60 and 160 keV (Ref. 13), corresponding to a range in temperature of 13 to 50 keV. The lower end of this range can be easily studied with implosions conducted at ICF facilities. The T + ^{4}He reaction produces ^{7}Li and a 2.4-MeV gamma, the latter of which can be measured using gamma detectors based on the Cherenkov mechanism. The gas Cherenkov detector (GCD-1) with a fused-silica radiator as well as the vacuum Cherenkov detector (VCD) are used to measure the gammas from this reaction. The implosions use all 60 of the OMEGA beams at 500 J per beam and a 1-ns square

pulse width. The capsules are 1-mm-diam, ~3-μm-thick Hoppe glass. The target fills consist of T + ^{4}He, as well as T_2 for a baseline comparison. Additionally, DT implosions are conducted along with a carbon puck attached to GCD-1 to calibrate both GCD-1 as well as the VCD.[14] Figure 9(a) shows the results of the calibration of the detector response, for both the GCD-1 and the VCD, to 4.4-MeV carbon gammas resulting from inelastic scattering of DT neutrons with the carbon puck. Figure 9(b) shows the gamma measurements made by GCD-1. These are average signals from multiple shots for each fuel type normalized to both the DT and TT neutron yields. The DT and TT yield-normalized signals measured for the T^{4}He fills (black solid and blue solid curves, respectively) are consistent and within 10%. These are significantly larger than the background measurements provided by the T_2 gas fills (dashed curves).

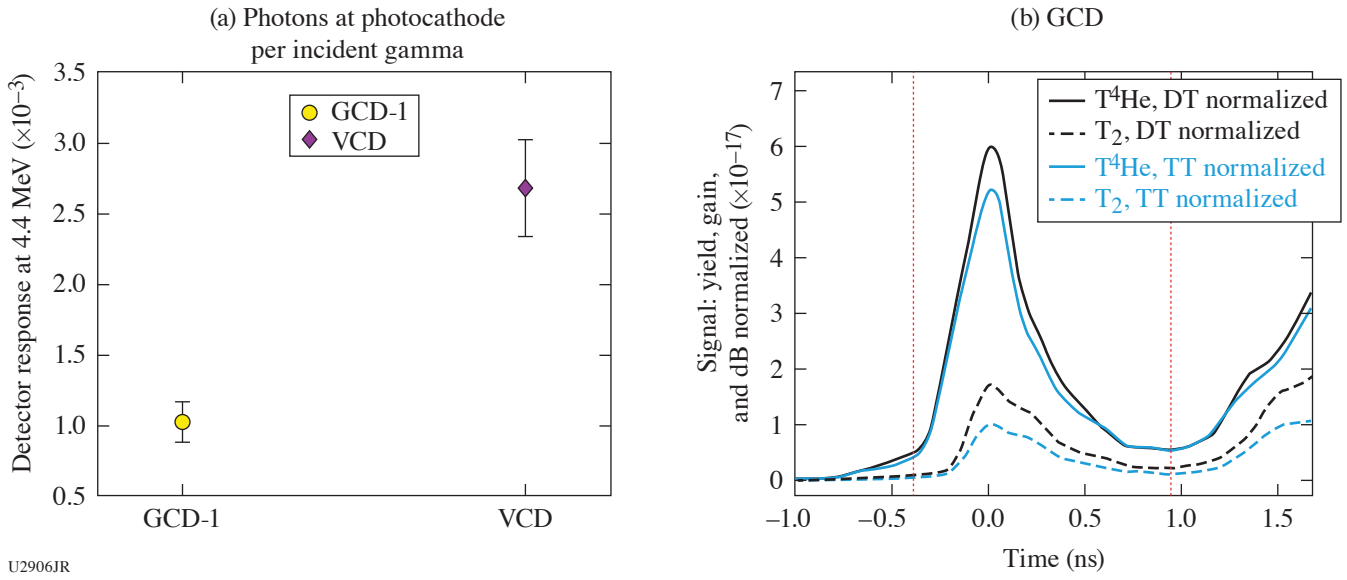

Figure 9
(a) The detector response, for both the GCD-1 with a fused-silica radiator as well as the VCD, is measured to 4.4-MeV gammas, resulting from inelastic scattering of DT neutrons with a carbon puck attached to the GCD-1. (b) Average gamma signals as measured by GCD-1 are shown for each fuel type, T^{4}He (solid) and T_2 (dashed), and normalized to the DT (black) and TT (blue) neutron yields. The excess gamma signal in the T + ^{4}He reaction relative to the T_2 gas fills, for each type of yield normalization, agree with one another within a factor of 10%.

The excess gamma signal, along with the detector calibrations, will be used to determine *S* factor for the T + ^{4}He reaction. The results of these experiments can potentially impact the BBN modeling community by improving confidence in the reaction rate at relevant energies.

We thank the operations crews and engineering staff at Omega for supporting these experiments. This work was performed under the auspices of the U.S. Department of Energy by Lawrence Livermore National Laboratory in part under Contract No. DE-AC52-07NA27344 and supported by the U.S. DOE Early Career Research Program (Fusion Energy Sciences) under FWP SCW1658.

X-Ray Sources from Laser Wakefield Acceleration on OMEGA EP

F. Albert,[1*] I. Pagano,[1,2] N. Lemos,[1] J. Williams,[1] H. Chen,[1] J. L. Shaw,[3] D. H. Froula,[3] C. Arrowsmith,[4] A. Aghedo,[5] M. Sinclair,[6] and C. Joshi[6]
[1]Lawrence Livermore National Laboratory
[2]University of Texas, Austin
[3]Laboratory for Laser Energetics, University of Rochester
[4]University of Oxford, UK
[5]Florida A&M University
[6]University of California, Los Angeles
*Principal Investigator

X-ray backlighting is one of the most used methods to look into the extreme temperatures, pressures, and densities created during laser-driven high-energy-density science (HEDS) experiments. Over the years, much effort has gone into developing backlighting techniques to look into these states of matter, with new sources and diagnostics. The properties of an x-ray backlighter (flux, source size, spectrum, duration) required for an experiment depend on the application being studied and on the quantity being measured. The goal of the Wakefield-EP shot series is to develop a new type of x-ray backlighter, which could be advantageous for applications requiring broadband spectra, small source sizes (sub-50 μm), short duration (less than 10 ps), and x rays extending beyond 100 keV. Our proposed x-ray sources are based on laser wakefield acceleration (LWFA) of electrons in the self-modulated regime (SMLWFA). Specifically, we aim to develop three different x-ray sources based on betatron radiation, Compton scattering, and bremsstrahlung emission.

The WakefieldLBS-EP-22A shot day was a continuation of our previous work, aimed at producing and detecting x-ray radiation produced by SMLWFA using a modified version of the EPPS diagnostic. We enlarged apertures to 5 mm (instead of 1 mm) and included a hole at the back of the magnet box, as well as a stack of nine image plates at the back of the ten-inch manipulator (TIM) boat to detect betatron radiation. In addition to betatron radiation, this year we also measured x rays produced by inverse Compton scattering, where the OMEGA EP laser pulse was reflected by a foil onto the accelerated electrons to produce high-energy x rays. We also implemented a new crosshair on the front end of the EPPS diagnostic to be able to measure the x-ray source size. The wakefield platform continued to produce robust electron beam data, recording a >100-nC charge electron beam at each shot, as well as two temperature spectra extending up to about 200 MeV (see Fig. 10).

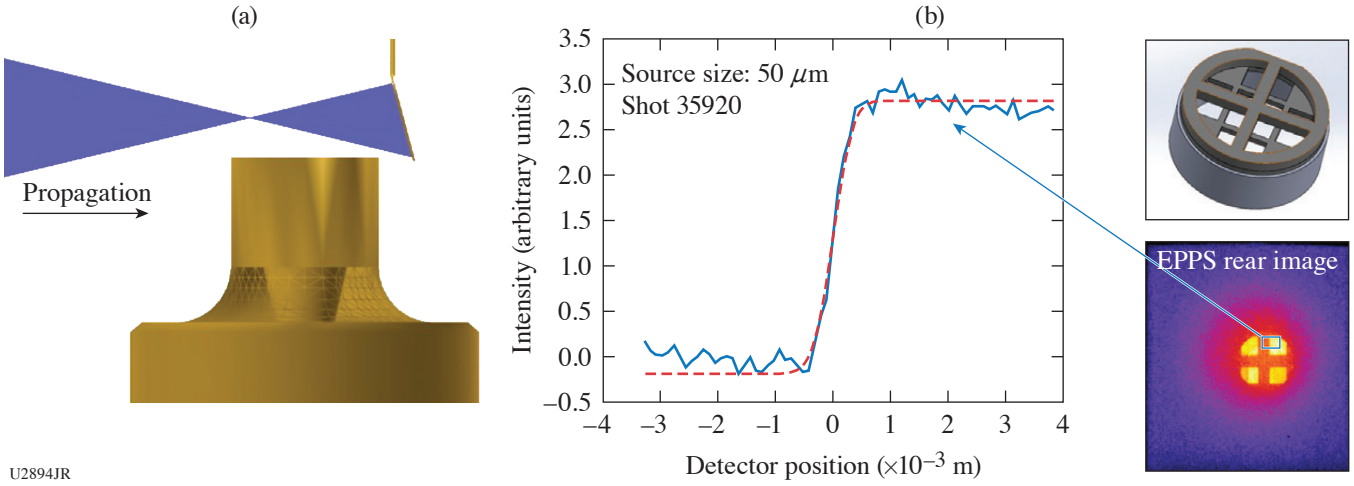

Figure 10
Results obtained during the WakefieldLBS-EP-22A shot day using the modified EPPS diagnostic. (a) Setup for an inverse Compton scattering x-ray source; (b) x-ray source size measurement and analysis.

Extreme THz Generation and Detection

G. Bruhaug,[1*] H. G. Rinderknecht,[1] Y. E,[2] M. S. Wei,[1] K. G. Francis,[2] X. C. Zhang,[2] G. W. Collins,[1] and J. R. Rygg[1]
[1]Laboratory for Laser Energetics, University of Rochester
[2]The Institute of Optics, University of Rochester
[*]Principal Investigator

For several decades, the creation of THz radiation was considered extremely challenging due to the frequency in question being too fast for classic electronic switching techniques and not efficiently generated via classic optical sources.[15] The first usable THz sources were based on large particle accelerators and were created via either synchrotron radiation or as free-electron lasers.[15,16] Later source development led to the creation of laser-based sources utilizing nonlinear crystals for frequency conversion.[15–18] Commercial laser-based sources of THz radiation are now widely available and utilized for homeland security applications, medical imaging, and traditional materials science research. However, these laser-based sources are limited in average and

peak THz power by the damage limits of nonlinear crystals.[15–18] This limits their applications in noisy environments and as drivers for pump–probe experiments. Newer laser-plasma–based THz sources have been developed using high-intensity lasers (>10^{18} W/cm^2) and have shown great promise as both experimental pumps and probes.[15,18] These THz generation methods involve irradiating foils, wires, and gas jets with high-intensity lasers.[15–20]

We performed the first laser-plasma THz generation experiments on OMEGA EP that tested our new THz background/energy meter (TBEM) detectors and showed extremely high THz yield from foil targets, similar to previous experiments on smaller lasers.[15] Analysis is still ongoing, but we estimate hundreds of mJ of THz were made from laser energies ranging up to 200 J. In addition, we performed the first ever attempts at THz/proton interferometry using TNSA protons. This measurement utilized OMEGA EP's unique dual-axis short-pulse capability and performed the first ever proton measurements of extreme THz fields, but not at the same time as the TBEM detectors due to background noise issues that have now been resolved in the detector design. A typical TNSA "proton tube" target was driven with a 10-ps, 900-J laser pulse and then ~90 ps later a THz generating foil was driven with a 0.7-fs, 500-J laser [Fig. 11(a)]. Both targets were positioned 5 mm from target chamber center, keeping each target out of the sheath field region of the resulting plasmas.

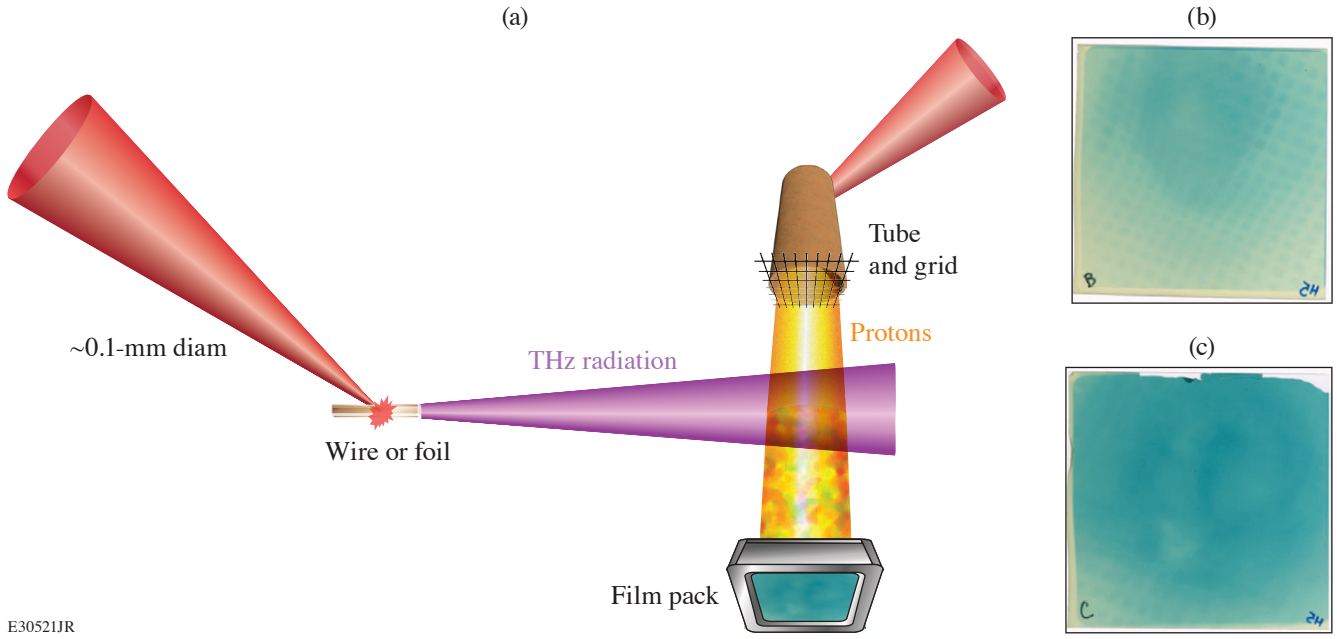

Figure 11
(a) Outline of the THz/proton interferometry experimental setup; (b) 15-MeV proton radiograph without any THz radiation present; and (c) 15-MeV proton radiograph with a THz pulse incident on the protons.

The THz pulse is believed to be single or even half-cycle, which allows the large (GV/m) electric fields in the pulse to provide net momentum to the protons. A test shot was taken [Fig. 11(b)] without a THz foil and a typical TNSA proton source is seen. The addition of a THz pulse altered the proton radiographs [Fig. 11(c)] in energies ranging from 10 to 28 MeV. These phenomena were repeatable between shots and became weaker with a lower-energy laser driver, as would be expected. Analysis is still ongoing but we believe GV/m electric fields generated this effect, requiring >100-mJ THz pulses. We anticipate that further analysis will allow exact discernment of the THz pulse energy and field strength, as well as provide a rough estimate as to the spectral distribution. The TBEM research and development performed during these experiments were also crucial for finalizing detector design and allowing for the detection of even higher THz yields on later OMEGA EP experiments.

This material is based upon work supported by the Department of Energy National Nuclear Security Administration under Award Number DE-NA0003856, the University of Rochester, and the New York State Energy Research and Development Authority.

Quantum States of Hydrogen: Toward a Superconducting Superfluid

A. Schwemmlein,[1*] G. W. Collins,[1*] R. Jeanloz,[2] S. Brygoo,[3] P. M. Celliers,[4] J. H. Eggert,[4] D. E. Fratanduono,[4] R. Hemley,[5] P. Loubeyre,[3] M. Millot,[4] J. R. Rygg,[1] Y. Kim,[4] J. Sater,[4] L. E. Hansen,[1] Z. K. Sprowal,[1] and R. Earley[1]
[1]Laboratory for Laser Energetics, University of Rochester
[2]University of California, Berkeley
[3]Commissariat à l'énergie atomique et aux énergies alternatives, France
[4]Lawrence Livermore National Laboratory
[5]University of Illinois, Chicago
[*]Principal Investigators

Crystalline metallic hydrogen has attracted significant theoretical interest since the 1930s (Ref. 21). Recent theoretical work suggests that its quantum nature gives rise to remarkable properties like high-temperature superconductivity.[22] In addition, metallic hydrogen is the predominant constituent of giant planets and stars; it is thus the most abundant form of condensed matter in the universe. Experimental studies of crystalline metallic hydrogen, however, have only recently become possible using dynamic-compression experiments at high-intensity laser facilities like Omega.

To reach the necessary low temperatures (<1000 K) and high pressures (>500 GPa), a low-temperature and entropy initial state is compressed using a custom OMEGA pulse shape approximating an isentropic drive. To reduce the entropy of the targets, only hydrogen molecules in the low-entropy solid and parastate, where the proton spins not aligned, are used. This special state of hydrogen was successfully produced in a newly developed target fill and diagnostic station, which confirmed >95% purity and stability of this state over hours in the standard planar cryo targets. These targets were cooled down in the target chamber to 10 K while observing the formation of a uniform solid using the VISAR field of view.

Raw data with a preliminary analysis of a representative shot is shown in Fig. 12. The VISAR fringes (background) were converted into the pusher velocity (green) that was subsequently matched using a hydrocode, which finally revealed a maximum

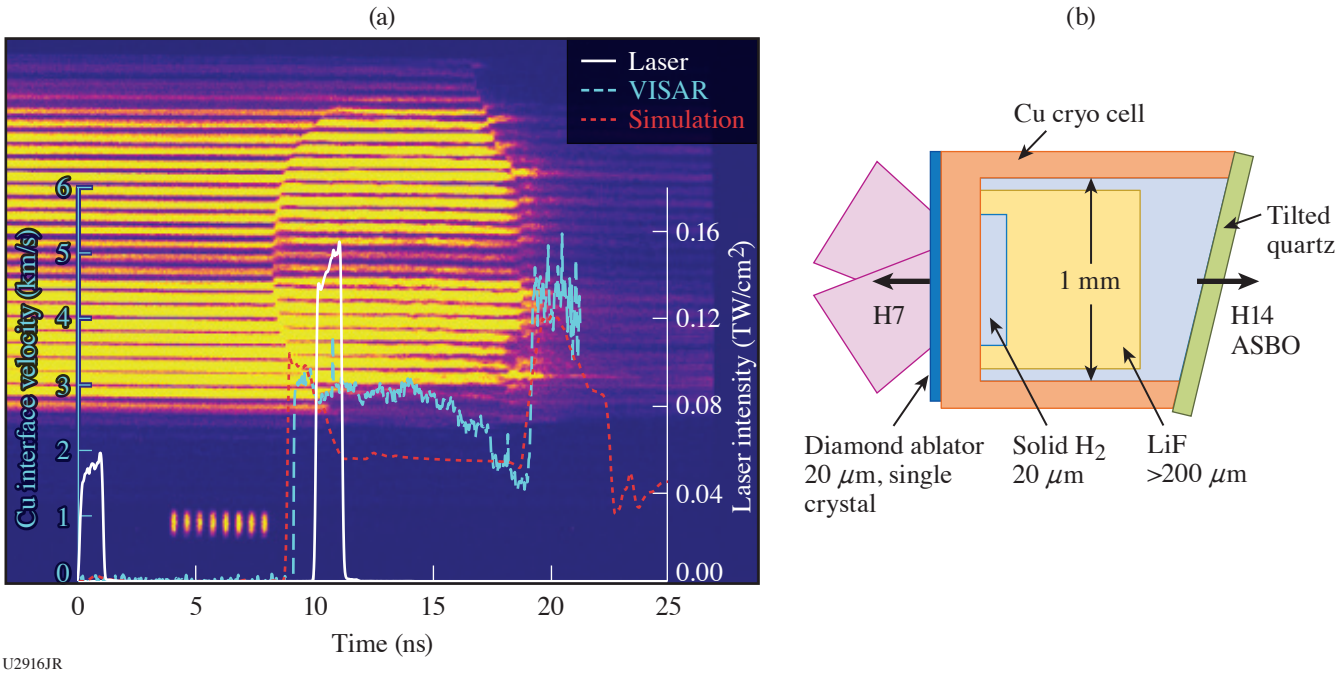

Figure 12
(a) VISAR raw data and analysis of (b) a 10-K parahydrogen target shot by a two pulse sequence. The VISAR sees the copper pusher in front of the 20-μm-thick hydrogen payload. The simulation revealed that a maximum pressure of 40 GPa was reached. Future experiments will use these two pulses in combination with a 12-ns ramp.

pressure of 40 GPa inside the 20-μm hydrogen payload. For this experiment, the first two pulses of a six-pulse sequence that was optimized using a hydrocode were tested. These two 1-ns square pulses initiate the ablation and reverberate inside the hydrogen to increase the pressure to several tens of GPa. A subsequent 12-ns ramp will be added in future experiments to increase the pressure to 700 GPa at a temperature around 1000 K. Simulations using the standard code *HYADES* indicate that these conditions can be met.

This experiment was conducted at the Omega Laser Facility at the University of Rochester's Laboratory for Laser Energetics with the beam time through the Laboratory Basic Science program.

Viscosity Measurements Using Tracer Particles

A. Gleason,[1*] J. Shang,[2,3] D. N. Polsin,[2,3] H. Aluie,[2,3] and J. R. Rygg[2,3]
[1]SLAC National Accelerator Laboratory, Stanford University
[2]Department of Mechanical Engineering, University of Rochester
[3]Laboratory for Laser Energetics, University of Rochester
[*]Principal Investigator

Any study of hydrodynamic flows in HED environments requires knowledge of material properties such as dynamic viscosity, and its inclusion in simulations can dramatically alter flows such as in inertial confinement fusion implosions.[23] Measurements of viscosity under HED conditions are sparse. In this campaign, we collected additional data to quantify the viscosity of epoxy, a surrogate for polystyrene and other commonly used ablator materials, to corroborate against a previous campaign. The method relies on measuring the acceleration of bluff bodies embedded in the material of interest since the hydrodynamic forces include viscous contributions; the viscosity can be estimated from the trajectory.[24]

In the experiment, the epoxy was embedded with titanium microspheres. The target was then shock compressed to ~215 GPa and we imaged the backlit target at different times after the shock had traversed the spheres. Figure 13 shows images of the instantaneous particle position and compression of two Ti spheres entrained in the flow behind the shock, and their displacement from their pre-shock location. Due to the lower mass of the spheres compared to the last experiment, we expect that our analysis will show they accelerate faster than the spheres in our last campaign.

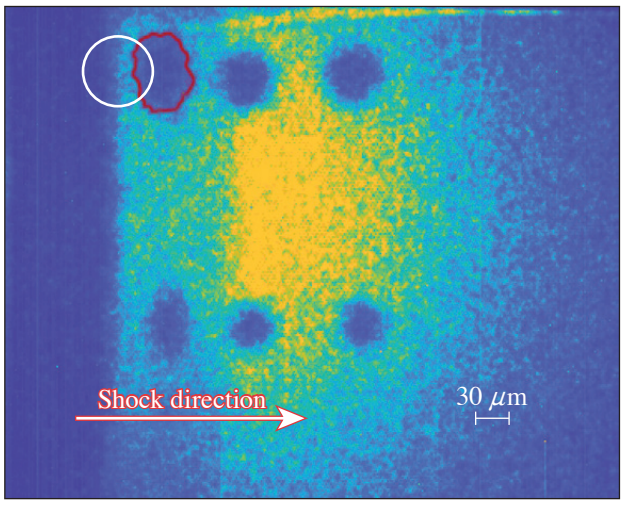

U2903JR

Figure 13
Radiograph of shocked and unshocked titanium particles for shot 105537 at t = 19.7 ns after the drive. The initial location of the larger sphere is outlined in white; the instantaneous particle position is shown in red, showing a displacement of about 40 μm after acceleration. Spheres are compressed behind the shock.

The experiment was conducted at the Omega Laser Facility at the University of Rochester's Laboratory for Laser Energetics with the beam time through the LBS Program. This work was supported by the DOE Office of Fusion Energy Sciences under the Early Career Award for A. Gleason. This work was also supported by US Department of Energy and NNSA under awards DE-SC0019329 and DE-NA0003914. Partial support from grants NSF PHY-2020249, DE-SC0020229 and DE-NA0003914 is also acknowledged.

Formation of Dynamic Shells Using Foam Ball Targets

I. V. Igumenshchev,[1*] W. Theobald,[1] C. Stoeckl,[1] R. C. Shah,[1] D. T. Bishel,[1] V. N. Goncharov,[1*] P. Adrian,[1] M. J. Bonino,[1] E. M. Campbell,[1] D. A. Chin,[1] T. J. B. Collins,[1] S. Fess,[1] D. R. Harding,[1] S. Sampat,[1] N. R. Shaffer,[1] A. Shvydky,[1] W. T. Trickey,[1] L. J. Waxer,[1] A. Colaïtis,[2] R. Loitard,[2] S. Atzeni,[3] F. Barbato,[3] and L. Savino[3]
[1]Laboratory for Laser Energetics, University of Rochester
[2]Centre Lasers Intenses et Applications, France
[3]University of Rome, Italy
[*]Principal Investigators

A dynamic-shell (DS) concept in direct-drive ICF utilizes the conventional hot-spot–ignition scheme and uses about 3-mm-diam sphere targets of liquid deuterium–tritium (DT) as a fuel.[25] Implosion shells of DT, which are required for hot-spot ignition, are developed dynamically from such sphere targets. This development and ignition are accomplished in four distinct evolution stages. In the first stage, a liquid DT sphere target is compressed by a few-Mbar convergent shock wave, which is launched by intense laser beams symmetrically irradiating the target. The second stage starts when this shock reaches the target center, reflects, and is transformed into a blast wave, causing the shock-compressed fuel, now becoming a plasma cloud, to expand. The third stage begins with launching convergent shocks at the outer edge of the expanding cloud. These shocks decelerate and reverse the expansion, resulting in a dynamic formation of a dense shell. In the fourth stage, this shell is imploded using a megajoule laser pulse similar to that in the conventional hot-spot–ignition scheme.

Proof-of-principle experiments on the OMEGA laser[26] have demonstrated, for the first time, the feasibility of DS formation and stability of DS's to low-mode perturbations (for Legendre modes less than about 10) using a scaled-down experimental setup to accommodate limitations in the available laser energy (<20 kJ) and pulse duration (<4 ns). The experiments used room-temperature surrogate sphere targets consisting of a CH foam and having an outer diameter of about 600 μm [see Fig. 14(a)]. Foam targets in the OMEGA experiments undergo the same evolution stages (compression, expansion, and shell formation) as in the ignition design, excluding the final implosion/ignition stage. Figure 14(b) illustrates these stages, showing a simulated shock diagram in gray scales for OMEGA shot 105251. The laser pulse is shown by a red line and has 11.2-kJ energy. The square pulse in the beginning of the pulse (see the red line) launches a shock that initially compresses the target. This shock reflects from the center at t = 1.4 ns, forming a blast wave and resulting in expansion of the compressed target mass. The second square pulse, which

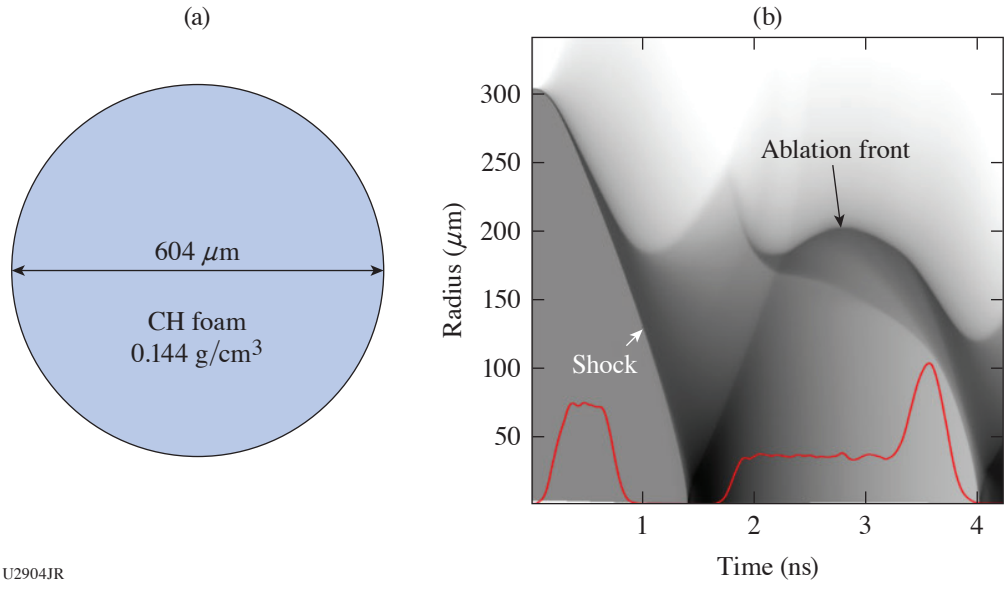

Figure 14
(a) Foam-ball target and (b) simulated log-density evolution, or "shock diagram," for OMEGA shot 105251. The red line in (b) shows the laser pulse in relative units.

starts at $t = 1.8$ ns, decelerates the expanding mass by sending convergent shocks and forms a dense shell. The outer shell radius, which is defined as the radius of the ablation front and seen as a density-contrast interface in Fig. 14(b), is initially reduced to about 180 μm at 2.15 ns, then increased, reaching about 200 μm at 2.8 ns, and then decreased again, approaching the minimum of about 120 μm at 4.0 ns [see Fig. 14(b)]. The power spike at the end of the pulse helps to additionally compress the shell mass, increasing the contrast in density at about 3.7 to 4 ns. This time interval is the most favorable for probing the formation of DS.

The experiments employed three x-ray diagnostics to evidence the DS formation. These include a streaked self-emission radiography,[27] backlighting radiography,[28] and framed shadowgraphy.[29] Figure 15(a) shows the streak data (the color map) aligned with the laser pulse (the white line) that were obtained in shot 105251. Two bright spots at $t \approx 1.4$ and 3.9 ns near $y = 0$ correspond to shock bounce events that were predicted in simulations [see Fig. 14(b)]. The bright region between $t \approx 1.9$ and 3.9 ns represents the emission at the ablation-front during the formation of DS. The rims bounding this region in the top and bottom show the ablation front trajectory. These data, while not directly indicating the formation of DS, make it possible to verify the simulations in Fig. 14(b), which show good quantitative agreements with inferred shock timing and ablation-front trajectory.

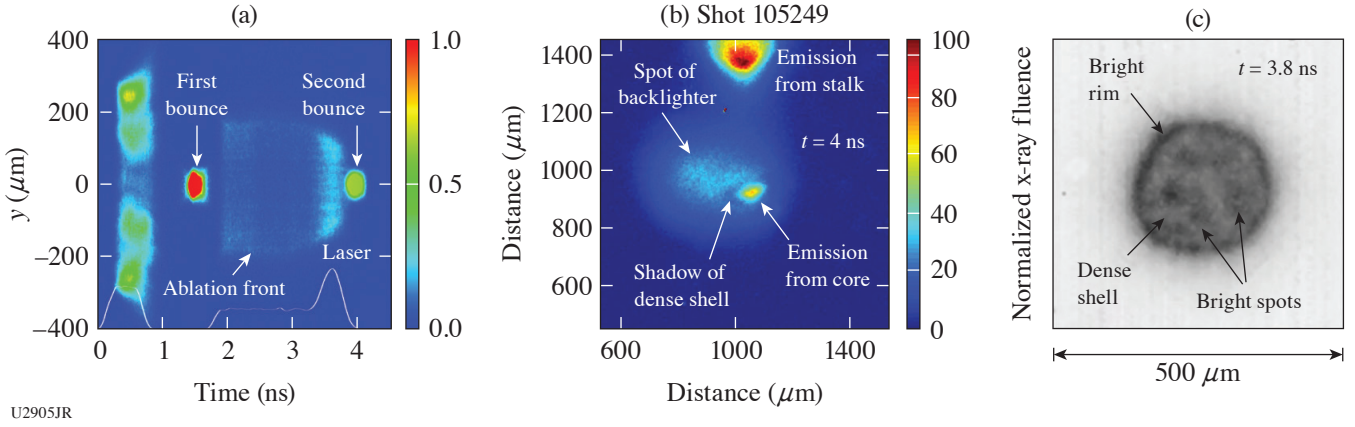

Figure 15
(a) X-ray streaked self-emission radiograph from shot 105251, (b) backlighting radiograph from shot 105249, and (c) framed shadowgraph from shot 105251.

Figure 15(b) illustrates results of backlighting radiography performed using joint OMEGA and OMEGA EP shot 105249. A 25-ps x-ray backlighter pulse (1.865 keV) was fired at $t \approx 4.0$ ns using the high-intensity OMEGA EP beam illuminating a Si foil target. This moment corresponds to the maximum convergence of DS, causing bright emission of the hot shell interior, or the core. The shadow on the background of backlighter and core emission is clearly visible in Fig. 15(b) and directly evidences the formation of a DS. Note the emission from remnants of a plastic (CH) stalk in the upper part of this figure. This stalk had a diameter of 50 μm and was used to mount the target. Its emission is observed far from the shell and without apparent influence of the formation of DS. This agrees with results of 3-D radiation-hydrodynamic simulations using the code *ASTER*,[30] which predict that the stalk is completely ablated off during earlier evolution (up to $t \approx 2$ ns) and does not significantly affect the shell dynamics.

The shadowgraph in Fig. 15(c) shows the DS at the late stage of its formation, $t \approx 3.8$ ns. The bright (dark in the image) circular rim in this figure corresponds to x-ray emission just outside the ablation front. The less-bright regions inside the rim represent the developed DS, which shadows x rays coming from the ablation front on the opposite side of the shell with respect to the viewing direction and from the hot shell interior. The five almost symmetric bright spots (again, darker in the image) inside the rim appear from perturbations in the shell coming from the OMEGA 60-beam illumination pattern. There are five of them because the viewing direction is projected through the center of a pentagon formed by the OMEGA beam ports. Three-dimensional *ASTER* simulations suggest that OMEGA beam overlapping can result in dips in the dense shell in the locations of maximum on-target intensity. This causes the emission from the shell interior to escape more efficiently through these dips resulting in imaging symmetric bright spots.

This material is based upon work supported by the Department of Energy National Nuclear Security Administration under Award Number DE-NA0003856 and ARPA-E BETHE Grant No. DE-FOA-0002212. The experiment was conducted at the Omega Laser Facility at the University of Rochester's Laboratory for Laser Energetics with the beam time through the Laboratory Basic Science program.

Inertial Confinement Fusion Plasma-Based Measurements of the D–T γ-to-Neutron and the D–^{3}He γ-to-Proton Branching Ratios

J. Jeet,[1*] A. B. Zylstra,[1] M. Rubery,[1] M. Eckart,[1] Y. Kim,[2] Z. L. Mohamed,[2] K. Meaney,[2] M. Gatu Johnson,[3] C. J. Forrest,[4] and V. Yu. Glebov[4]
[1]Lawrence Livermore National Laboratory
[2]Los Alamos National Laboratory
[3]Plasma Science and Fusion Center, Massachusetts Institute of Technology
[4]Laboratory for Laser Energetics, University of Rochester
[*]Principal Investigator

The D–T γ-to-neutron branching ratio [^{3}H(d,γ)^{5}He/^{3}H(d,n)^{4}He] has been previously determined in beam–target-based experiments as well as in ICF experiments.[31,32] In the latter case, neutron-induced backgrounds are significantly reduced compared to the former due to the short-pulse nature of ICF implosions and the use of gas Cherenkov γ-ray detectors. A benefit of ICF-based measurements is the ability to achieve lower center-of-mass energies as compared to accelerators. Previous ICF-based experiments, however, report a large uncertainty in the D–T γ-to-neutron branching ratio of ≈48%. A more-precise value for the branching ratio based on data taken at OMEGA has been determined. This relies on a cross-calibration against the better known ^{12}C neutron inelastic scattering cross section [^{12}C(n,n′)γ] in a puck-based experiment involving the gas Cherenkov detector (GCD-3). A D–T branching ratio value of $(4.6\pm0.6) \times 10^{-5}$ is determined by this method;[33] the results are shown in Fig. 16 and compared to values obtained in previous experiments. This campaign will improve this experiment to further reduce the uncertainty in the measurement. We will also provide a measurement of the D–^{3}He γ-to-proton branching ratio to significantly better precision than reported by previous experiments, which are limited to ≈33%. This is made possible due to an absolute detector calibration that relies on the inelastic scattering of DT neutrons in a carbon puck attached to the GCD-3 (Ref. 14). The resulting 4.4-MeV gammas are temporally separated from the primary gamma signal resulting from the D–T fusion and can be isolated by performing a yield-normalized subtraction of a background signal that does not field the carbon puck. Signals as measured by the VCD are shown in Fig. 17 for the D–T implosions.

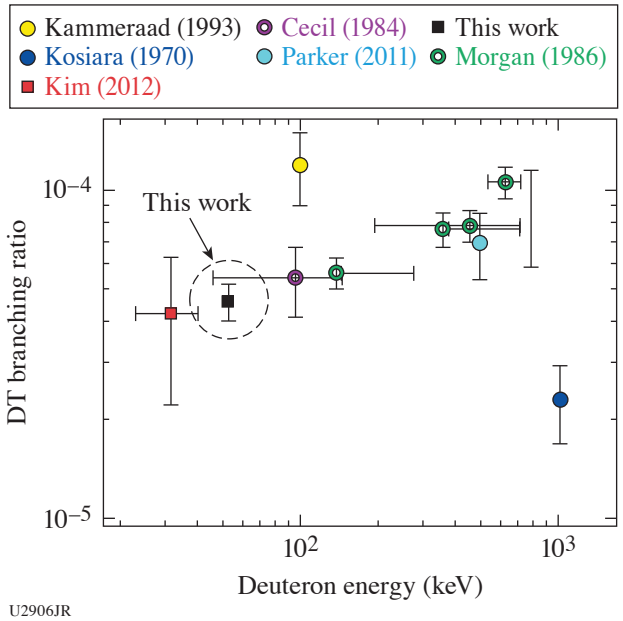

Figure 16
The D–T branching ratio measurement resulting from the work of Ref. 33 is shown (black square) along with other recent experiments (Refs. 31 and 32), which include both beam–target-based measurements (dark blue circle) as well as an ICF-based result (red square).

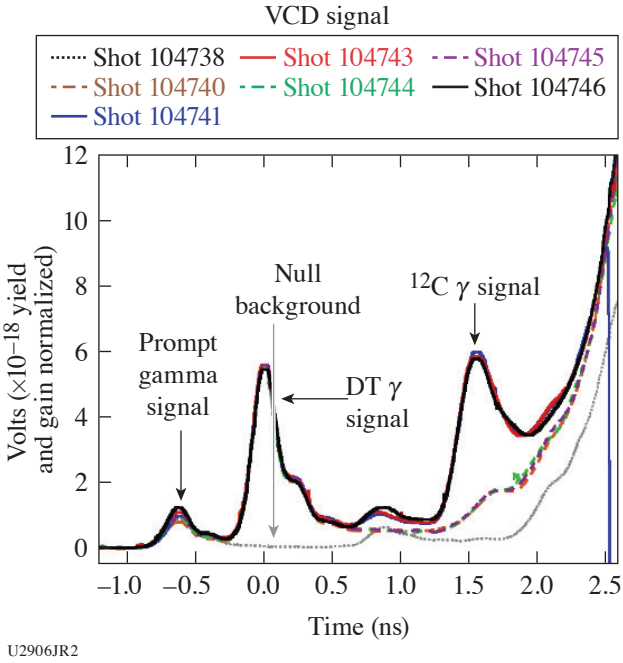

Figure 17
D–T implosion signals as measured by the VCD. Each signal is comprised of different features. The prompt gamma signal results from direct interaction of gammas with the photomultiplier tube inside the VCD. The DT gamma signal results from the fusion and is delayed with respect to the prompt gamma signal. The ^{12}C gamma signal results from the inelastic scattering of DT neutrons with a carbon puck attached to the GCD-3. The resulting 4.4-MeV gammas are temporally separated from the primary D–T fusion gammas.

Relative to the experimental data analyzed in Ref. 33, these experiments were optimized to improve the precision in the measurement. The TIM diagnostic loadout is kept minimal to reduce the extraneous neutron-induced noise that can coincide with the ^{12}C gamma signal. A thinner capsule shell is used to minimize shell areal-density contributions to the primary D–T fusion gamma signal. Measurements were taken with multiple gamma detectors, GCD-3 as well as the VCD, at different threshold energies. The ratio of the ^{12}C gamma signal to that of the DT gamma signal allows for extraction of the D–T branching ratio while eliminating the need for absolute detector calibrations and systematic yield uncertainties for the measured DT neutrons. D^{3}He shots were also conducted in this campaign to determine the gamma-to-proton branching ratio, which is measured to higher precision using the absolute detector calibration provided by the ^{12}C gamma measurement.

With improved measurements of the ^{12}C(n,n′)γ scattering cross section or the D–T γ spectrum, the data taken in this campaign can be revisited and systematic uncertainties in the D–T γ-to-neutron and D–^{3}He γ-to-proton branching ratios can be further reduced.

We thank the operations crews and engineering staff at Omega for supporting these experiments. This work was performed under the auspices of the U.S. Department of Energy by Lawrence Livermore National Laboratory in part under Contract No. DE-AC52-07NA27344 and supported by the U.S. DOE Early Career Research Program (Fusion Energy Sciences) under FWP SCW1658.

Detailed Benchmarking of the Nernst Effect in a Magnetized High-Energy-Density Plasma

S. Malko,[1*] W. Fox,[1,2] D. B. Schaeffer,[2] C. Walsh,[3] G. Fiksel,[4] A. J. Harvey-Thompson,[5] M. Weiss,[5] A. Hansen,[5] D. Ruiz,[5] A. Bose,[6] C. Frank,[6] P. Heuer,[7] and J. Davies[7]

[1]Princeton Plasma Physics Laboratory
[2]Princeton University
[3]Lawrence Livermore National Laboratory
[4]Center for Ultrafast Optical Science, University of Michigan
[5]Sandia National Laboratories
[6]University of Delaware
[7]Laboratory for Laser Energetics, U. Rochester
[*]Principal Investigator

Magnetic fields are known to affect and suppress heat flux through thermomagnetic effects in HED laser-produced plasmas.[34] In the high-beta and moderate collisionality regimes on HED plasmas, however, the heat flux can also feedback and drive advection of the magnetic field via the Nernst effect. This can be important for several applications of magnetized HED plasmas, including magnetized liner inertial fusion (MagLIF).[35] The heating laser creates a radial temperature and density gradient in the D_2 fuel perpendicular to the axial magnetic field. Simulations show that the Nernst effect significantly reduces the performance of the MagLIF preheat phase by advecting the applied axial magnetic field out of the fuel, thereby increasing energy losses due to thermal conduction.[36] Nernst transport can also strongly affect the dynamics of both externally applied and self-generated magnetic fields in hohlraums and ablation fronts in directly driven capsules in ICF and ICF hot spots. The detailed experimental benchmarking of numerical models that include the Nernst effect are crucial and required to further understand how to control such magnetized plasma systems. To identify the importance of this effect, one can introduce the "Nernst number" N_e, which gives the ratio of the characteristic velocity of the Nernst field advection v_N to the sonic plasma expansion v_s, $N_e = v_N/v_s$.

Here we report on novel experimental platform NerntEffect22A at the Omega Laser Facility for benchmark Nernst effect in the regime where the Nernst advection dominates the frozen-in plasma flow $0.1 < N_e < 1$. The platform is based on laser heating of a gas jet in a magnetic field and simultaneous direct measurement of the Nernst velocity and plasma conditions (density and temperature). In order to design this experiment and find the regime of interest, we performed a pre-shot parametric study with 1-D *GORGON*[37] by varying gas densities, gas type, laser energy, and magnetic field. In addition, *FLUKA*[38] Monte Carlo simulations were used to obtain expected proton signal level and design proton radiography diagnostics.

The setup of experiment is presented at Fig. 18. One OMEGA beam (heater) with 500-J energy is used to heat a H_2 gas jet in a cylindrically symmetric volume aligned parallel to an external magnetic field of approximately 5 T produced by MIFEDS. Proton radiography with 3- and 15-MeV monoenergetic protons produced from a D–^{3}He implosion was used to measure the magnetic fields at several expansion times. The plasma parameters (n_e, T_e) and radial bulk flow speed of plasma at different positions across cavity (0, +250 μm, +500 μm) were measured by time-resolved 2ω optical Thompson scattering (OTS).

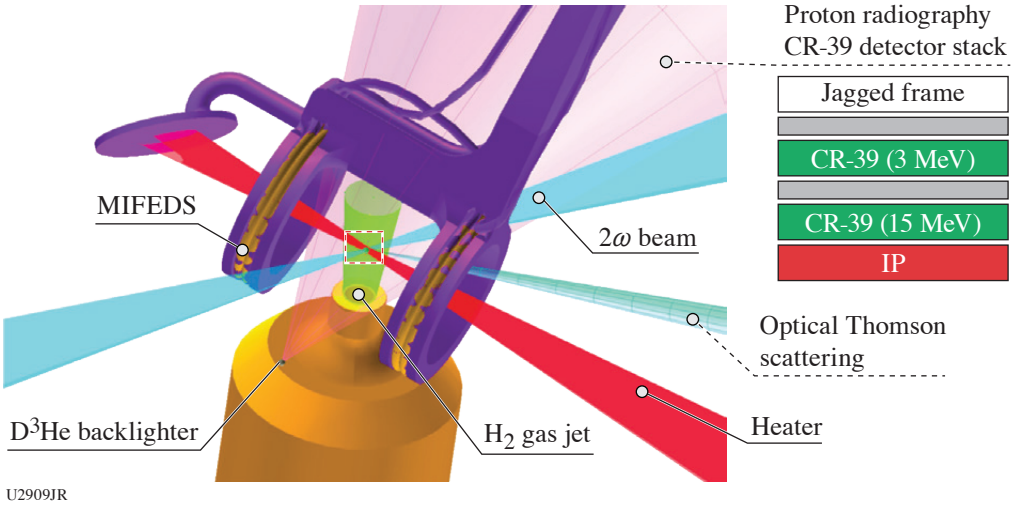

Figure 18
The experimental setup at the Omega Laser Facility. IP: image plate.

The example of obtained proton radiography data at 0.5- and 1-ns expansion time is shown in Fig. 19. We have observed a clear magnetic-field cavitation and pileup on the edges of the cavity as predicted by 1-D *GORGON* simulations. The measured time evolution of the cavity will allow us to calculate the cavitation rate and thus the Nernst velocity. The preliminary analysis of OTS electron plasmon wave (EPW) and ion-acoustic wave (IAW) spectra at the center of cavity provided electron temperature of $T_e \sim 400$ eV and electron density of 1×10^{20} cm^{-3} at 700-ps expansion time. Based on these measurements we have estimated $N_e \sim 0.28$ compared to 0.12 for the MagLIF preheat phase.[39] These experimental results will be compared with *GORGON*, *HYDRA*, and *LILAC* simulations.

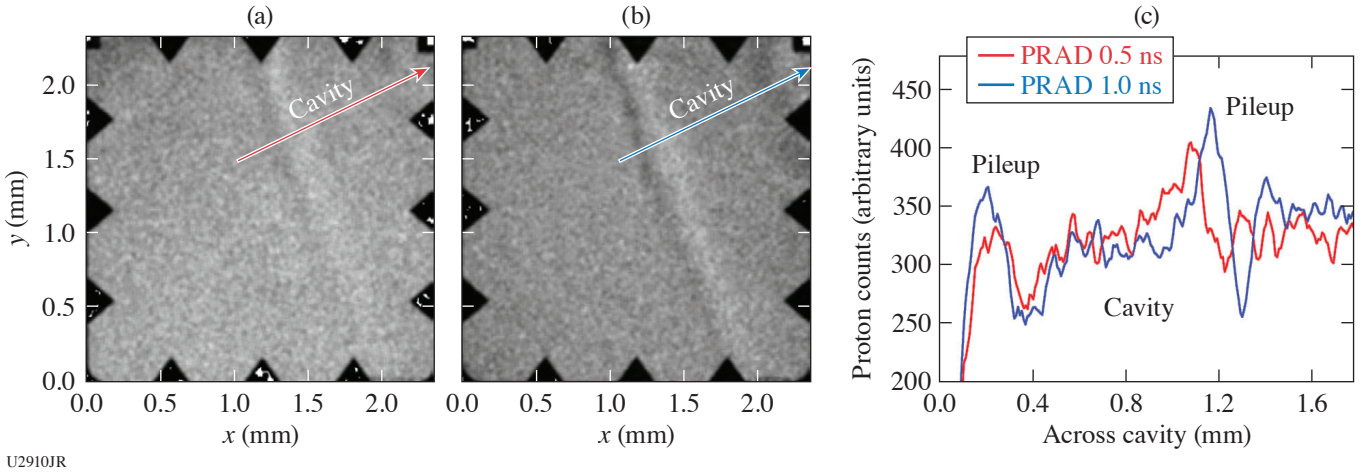

Figure 19
The raw proton radiography CR-39 images obtained with 15-MeV protons. PRAD acquired at (a) 0.5-ns and (b) 1-ns expansion time. (c) The lineout across the cavity obtained from at 0.5 ns (red curve) and 1 ns (blue curve). PRAD: proton radiography.

In summary, we have developed a novel experimental platform for benchmarking of Nernst effect in an open-geometry configuration at the Omega Laser Facility. We have successfully measured cavitation of magnetic fields by proton radiography and electron temperature and density, as well as bulk flow velocity at different positions across cavity by 2ω optical Thomson scattering. The preliminary analysis of proton radiography results indicates magnetic-field advection in time and pileup at the edges of the cavity. These results will be used for benchmarking extended magnetohydrodynamic codes. This platform can be also used to benchmark the Nernst effect in low- (high Nernst number $5 < N_e < 10$) and high-magnetization regimes ($0.1 < N_e$) by tuning magnetic field and gas-jet parameters.

Probing In-Flight Vacuum Magnetic-Field Compression on OMEGA

J. L. Peebles,* F. García-Rubio, J. R. Davies, D. H. Barnak, P. V. Heuer, and R. Betti
Laboratory for Laser Energetics, University of Rochester
*Principal Investigator

Measurements of the compression of a magnetic field have remained elusive in laser-driven magnetohydrodynamic (MHD) experiments. These measurements are required to validate simulations for field conservation and loss mechanisms. The primary goal of this campaign was to measure the magnetic field at different stages of compression in a cylindrical target, which would provide experimental feedback for MHD codes. To do this, an experiment was carried out where a strong magnetic field (>65 T) was applied to a cylindrical implosion with a large radius. This large radius (twice the size of a typical cylindrical implosion on OMEGA) was chosen to provide enough of a window for proton probing to be used. Prior issues with using proton probing to measure magnetic fields transverse to the primary field axis was that deflection was too large; to address this we probed down the axis of the cylinder, which has been proven to be a more-accurate measurement for fields of this magnitude. Ideally this probing could be done while the shell is in-flight, providing many data points on field strength and compression.

The experimental setup is shown in Fig. 20. The well-benchmarked cylindrical implosion setup used for MagLIF experiments was modified to drive a narrower portion of the cylinder. Since the cylinder was twice the radius of typical cylindrical experiments, intensity on target had to be maintained by doubling beams on a portion half the length of the typical MagLIF implosion. The tube was left empty of gas for ease of construction since field compression should occur regardless of fill. A D^3He exploding-pusher proton source was used to probe the interaction; since the drive for the exploding pusher and the cylinder needed to be the same pulse shape and the proton source benefits from shorter, higher-intensity pulses, there was a long coasting period for the compressing cylinder. An image plate placed on the wedge range filter module (WRFM) allowed for a simultaneous x-ray measurement of the mesh fiducial, which indicated the initial angle of the mesh without field deflections.

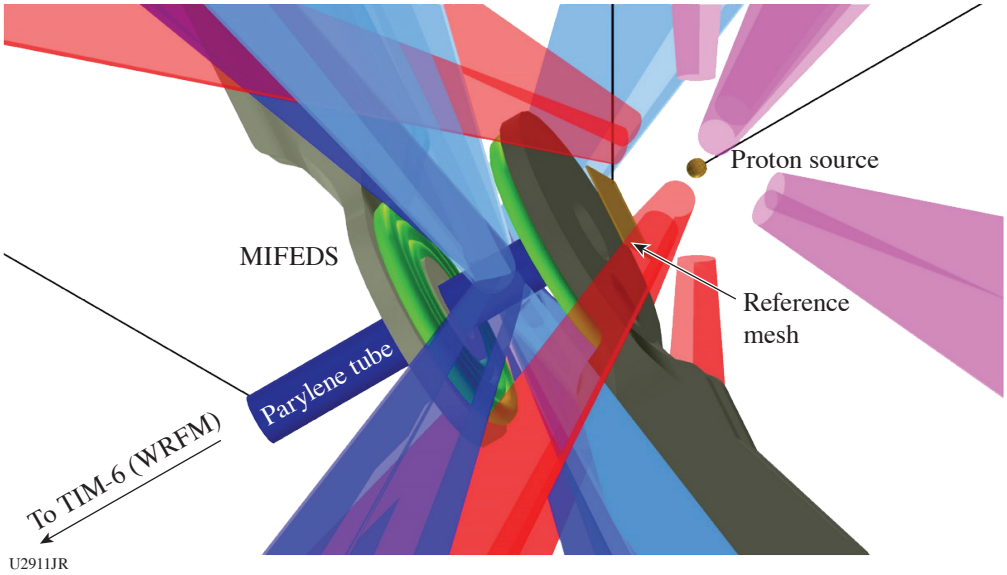

Figure 20
Schematic of the experimental setup. A large-radius cylindrical implosion is radiographed axially by protons, measuring the field applied by the MIFEDS coils.

Six shots were carried out in the campaign: three without the magnetic field and three shots with the magnetic field. The reference shots without the magnetic field were able to image the reference mesh at two different stages of compression. Since there was no field, the mesh appeared to be stable regardless of probe time, with the compressing shell scattering the protons later in time. As shown in Fig. 21, the mesh can be distinguished at nearly any stage of compression. X-ray framing camera data indicated that the shell coasts to full compression by 4.5 ns, where the probe at 3.5 ns can probe a region roughly 350 μm in diameter. Proton attenuation from scattering removes most of the signal from the regions where the shell has been in flight, although the proton signal appeared to decrease throughout the shot day (despite neutronics indicating otherwise).

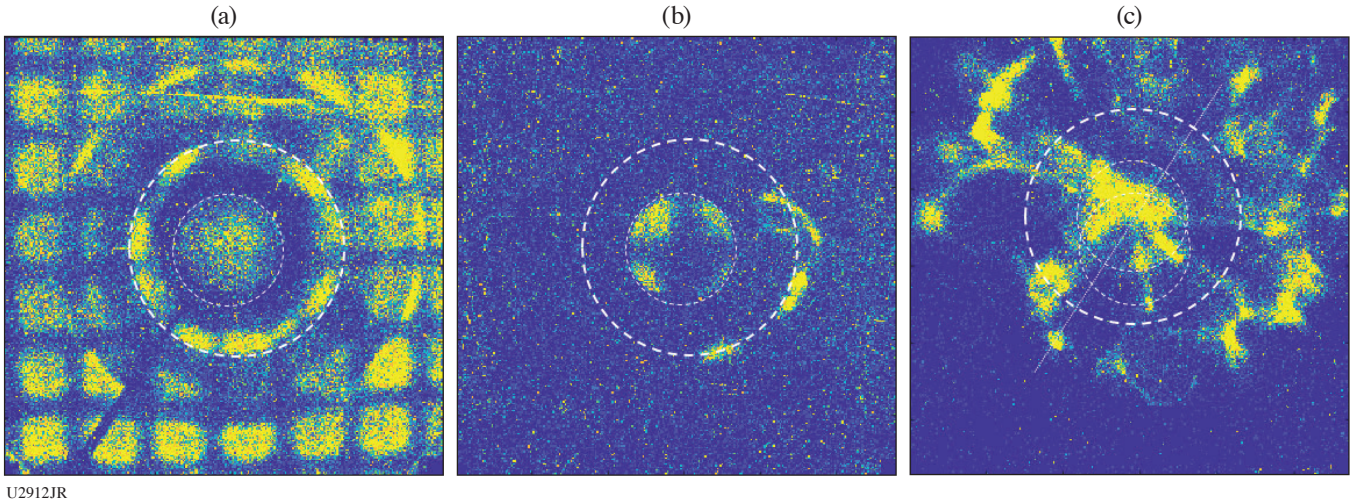

Figure 21
Proton probes of three different shots. The probes are timed at 1.0, 3.5, and 3.5 ns with the field off, off and on, and left to right, respectively. The grid is clearly distinguishable in the first two images, although at 3.5 ns the cylinder is nearly fully compressed. When the field is added, however, the mesh distorted beyond identifiability, even though the compression is at the same stage as the second image.

Difficulties with the MIFEDS led the diagnostic to be disqualified for use after the shot day since the unit entered a self-charge state when getting ready for the seventh shot and destroyed the target. For one of the magnetized shots, the reference mesh was apparently lost close to shot time (after the Target Viewing System was shuttered). Late timing of the proton probe for another magnetized shot led to missing the compressed field. This led to only one shot with usable magnetized data. Due to a mistiming of one of the MIFEDS units, the field was lower and asymmetric. Upon adding the external magnetic field, the very clear mesh was heavily distorted such that the angle of the mesh could not be identified. Fourier analysis indicated that some features may be aligned with a 37° rotation of the mesh; however, this appears unlikely since this would indicate much higher field compression than the shell at this stage could accomplish. While the field for this shot was not ideal, it alone does not explain the complete distortion of the radiograph. More likely, the ends of the field compression region are significantly more complex than an ideal compression.

For future shot days exploring field compression it would be of great benefit to have additional data points earlier in the compression. Presumably, field-distortion effects would not be so strong early into compression. By probing earlier in time, more of the mesh is visible on the probe, making the process of identifying mesh lines and angles much more likely. Other improvements would include shortening the length of the tube; the length of tube combined with the proximity to the proton source meant that two of the rings seen on the early time radiographs are the uncompressed regions of the tube close to and far away from the source. Shortening the tube to 1 to 2 mm (rather than 10+ mm) would shrink this feature substantially. Improvements made to the MIFEDS diagnostic since this shot day have also made its usage much more reliable.

This experiment was conducted at the Omega Laser Facility at the University of Rochester's Laboratory for Laser Energetics with the beam time through the Laboratory Basic Science program.

Electron Energization in Colliding and Reconnecting Magnetized Plasmas

M. J. Rosenberg,[1*] G. Fiksel,[2] W. Fox,[3] D. Schaeffer,[4] and C. K. Li[5]
[1]Laboratory for Laser Energetics, University of Rochester
[2]University of Michigan
[3]Princeton Plasma Physics Laboratory
[4]Princeton University
[5]Massachusetts Institute of Technology
[*]Principal Investigator

The MagRecon-22A shot day on OMEGA (17 February 2022) through the LBS Program successfully demonstrated an enhancement in the suprathermal electron population in laser-plasma experiments that drove the collision or reconnection of plasma plumes carrying self-generated magnetic fields. The energization of particles during the annihilation of magnetic fields is a common process in astrophysical plasmas, but is poorly understood and has rarely been investigated in the laboratory. The experiments use the interaction of 200-J, 0.5-ns laser pulses with 5-μm-thick CH foils to produce Biermann-battery magnetic fields that azimuthally encircle the expanding plasma created by each beam. While previous experiments[40] [illustrated schematically in Fig. 22(a)] showed that the interaction of two adjacent plasma plumes containing antiparallel magnetic fields, which undergo magnetic reconnection, enhanced the energetic electron population in the direction of the reconnection current sheet, it was not proven whether this was due to the collision or due to reconnection itself. To address this question, this shot day employed the configuration shown in Fig. 22(b), in which the experimental geometry is altered so that the magnetic fields are parallel in the collision region and do not reconnect.

The energized electron spectra are shown in Fig. 23. Preliminary analysis shows that experiments with colliding parallel fields produce significantly more than twice the energized electron population than experiments with only a single laser–foil interaction (and therefore no collision), indicating that the plasma plume collision contributes partially to the acceleration of electrons regardless of the magnetic-field orientation or any reconnection. In addition, the magnetic reconnection experiments show more electron energization than in experiments driving the collision of parallel magnetic fields, although there is significant shot-to-shot variation. These results suggest that the magnetized plasma plume collision causes some acceleration of electrons, possibly through a Fermi-like mechanism, but that magnetic reconnection is a significant contributor to electron energization. This platform can therefore be used in further experiments to study the dependence of magnetic reconnection-induced particle energization on reconnection parameters like collisionality.

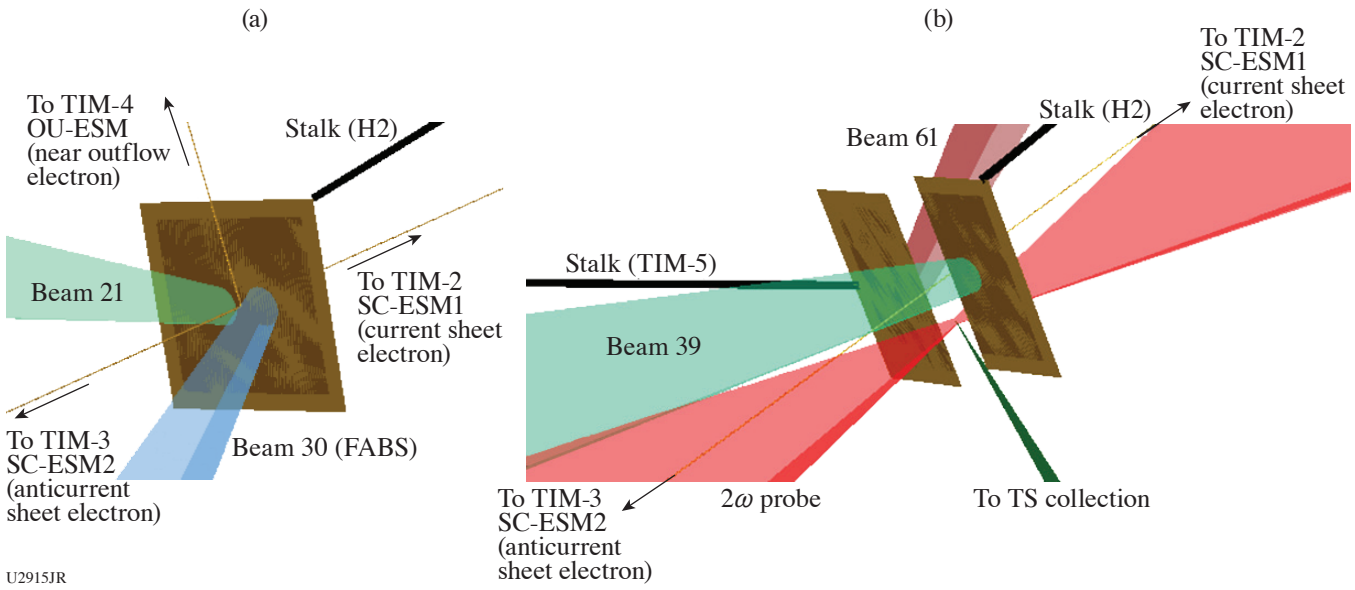

Figure 22
Experimental setup for (a) reconnection of anti-parallel magnetic fields and (b) collision (but no reconnection) of parallel magnetic fields. OU-ESM: Osaka University electron spectrometer; SC-ESM: single channel spectrometer; FABS: full-aperture backscatter station; TS: Thomson scattering.

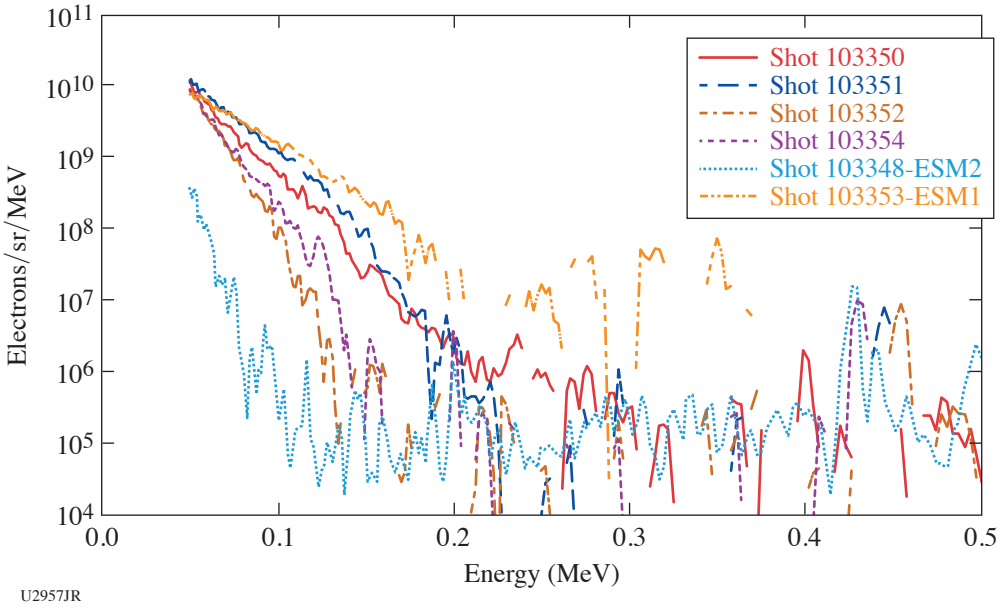

Figure 23
Measured energetic electron spectra for: one-beam experiments (no collision nor reconnection) (dashed curve), colliding parallel magnetic-field experiments (collision, but no reconnection) (thin solid curves), and reconnection (thick solid curves) experiments. The data have been background subtracted. The reconnection spectrum shows more energization than the parallel magnetic-field experiments (with significant variation).

These experiments were conducted at the Omega Laser Facility at the University of Rochester's Laboratory for Laser Energetics with the beam time through the Laboratory Basic Science Program.

Measuring Electron Densities in Nonlocal Thermodynamic Equilibrium Plasmas Using Isoelectronic Line Ratios

G. Pérez-Callejo,[1] E. V. Marley,[2] D. A. Liedahl,[2] J. A. Emig,[2] and M. B. Schneider[2*]
[1]Universidad de Valladolid, Spain
[2]Lawrence Livermore National Laboratory
[*]Principal Investigator

Measuring electron temperatures and densities in HED plasmas is no easy task. To that end, several different diagnostics have been designed, each exploiting one or several characteristics of these extreme plasmas, in order to extract information about their conditions. In particular, x-ray spectroscopy has proved to be a reliable diagnostic that can provide valuable information about the atomic structure of the elements in the plasma. A particularly bright component of the x-ray emission of HED plasmas is the He-like emission since He-like ions are present over a wide range of temperatures and densities. The brightest emission from these ions is, in most cases, the He_α complex, which comprises two He-like transitions and a significant contribution from Li-like ions. However, this complex is also heavily affected by optical depth effects, sensitive to gradients in the plasma, which makes it difficult to extract useful information (and usually other simpler lines are used).

In this experiment, we generated a uniform two-element plasma using a similar platform that was used in the past to characterize optical depth effects.[41] By placing a thin disk of CaS buried in a CH tamper, an axially expanding cylindrical plasma at 1 to 2 keV with $n_\mathrm{e} \sim 10^{21}$ cm^{-3} was generated. We recorded the x-ray emission spectra from both Ca and S, as well as the target size as a function of time. Since Ca and S are in the same proportion in the plasma, and at the same temperature and density conditions, the optical depth effects on their He_α emission are very similar and can be canceled out. This makes it possible to extract the electron density from the ratio $\left(w_\mathrm{s}/y_\mathrm{s}\right)/\left(w_{\mathrm{c}_\alpha}/y_{\mathrm{c}_\alpha}\right)$, where w and y are the two He-like transitions that make up the He_α emmission and the subindices are used to denote the element. All of the instruments obtained good data, which are currently being post-processed. Preliminary analysis of the data hints to the possibility that S dissolved into the target rather than staying confined to the buried layer (Fig. 24). This was a possibility since it was the first time that a salt-like component was used in this configuration, and target development was necessary. Careful post-processing of the spectral data is required to verify this possibility.

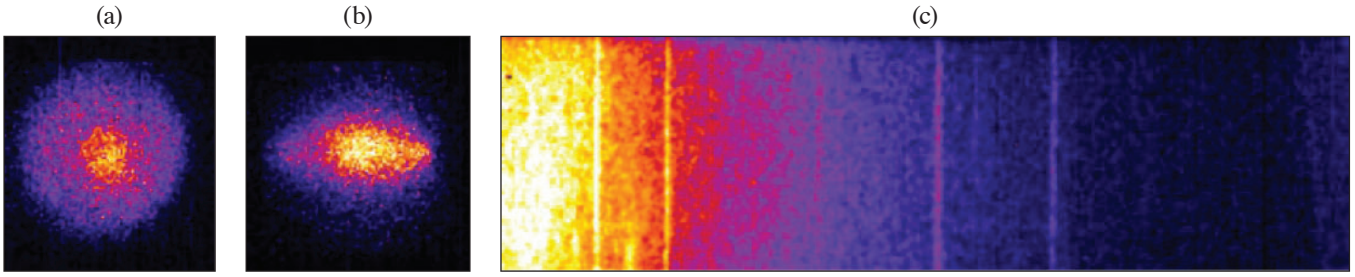

Figure 24
Example set of data from the experiment. (a) Top and (b) side view of the cylindrical plasma(c) S x-ray emission spectrum. The Ca spectrum was only obtained on film, which is currently being digitized.

This work was performed under the auspices of the U.S. Department of Energy by Lawrence Livermore National Laboratory under Contract DE-AC52-07NA27344. This document was prepared as an account of work sponsored by an agency of the United States government. Neither the United States government nor Lawrence Livermore National Security, LLC, nor any of their employees makes any warranty, expressed or implied, or assumes any legal liability or responsibility for the accuracy, completeness, or usefulness of any information, apparatus, product, or process disclosed, or represents that its use would not infringe privately owned rights. Reference herein to any specific commercial product, process, or service by trade name, trademark, manufacturer, or otherwise does not necessarily constitute or imply its endorsement, recommendation, or favoring by the United States government or Lawrence Livermore National Security, LLC. The views and opinions of authors expressed herein do not necessarily state or reflect those of the United States government or Lawrence Livermore National Security, LLC, and shall not be used for advertising or product endorsement purposes. The work has also been supported by the Research Grant No. PID2019-108764RB-I00 from the Spanish Ministry of Science and Innovation.

Probing the Fe–Ni Phase Space Using Powder X-Ray Diffraction Image Plates

S. M. Clarke,[1*] S. Singh,[1*] K. Bolduc,[2] and R. F. Smith[1]
[1]Lawrence Livermore National Laboratory
[2]University of Massachusetts, Amherst
[*]Principal Investigators

In this campaign we studied Fe–Ni, an alloyed material with geophysical relevance, under dynamic compression. The three goals to this experiment were to (1) determine the effect of Ni composition on the onset of melting on the Hugoniot, (2) understand the stability field of the γ [face-centered cubic (fcc)] phase within the alloy, and (3) develop a general methodology for investigating alloy materials under dynamic compression. Previous static compression experiments have shown that the incorporation of nickel expands the stability field of the fcc phase relative to the hexagonal close-packed (hcp) phase, thus changing the slope of the phase boundary.[42]

We successfully performed 13 shots: eight probing a shocked state and five probing a ramped state. For each shot we used one beam as a 2-ns x-ray backlighter and one beam to drive a shock- or ramp-compression wave in the sample. From the ramp-compression experiments, we found that alloying did not change the structure along the ramp quasi-isentrope. The Fe–Ni alloy maintained the hcp structure like the behavior of pure Fe. Preliminary analysis suggests we reached alloy densities over 15 g/cm^3. For the shock-compression samples, we targeted pressures near the melt line (see Fig. 25). Preliminary analysis suggests a diffraction signal consistent with melt in some shots, and a mixture of melt and high-pressure hcp phase in other shots. Pressure determination for these shots is ongoing, and when the analysis is complete, we will compare the onset of melt for the alloy to that of Fe to better understand the effect of alloying on the melt line. We do not observe the existence of a high-pressure bcc phase on the Hugoniot, in contrast to previous findings from other groups and theoretical predictions.[43] We hope to include all the data in a publication about the behavior of Fe–Ni alloys under dynamic compression.

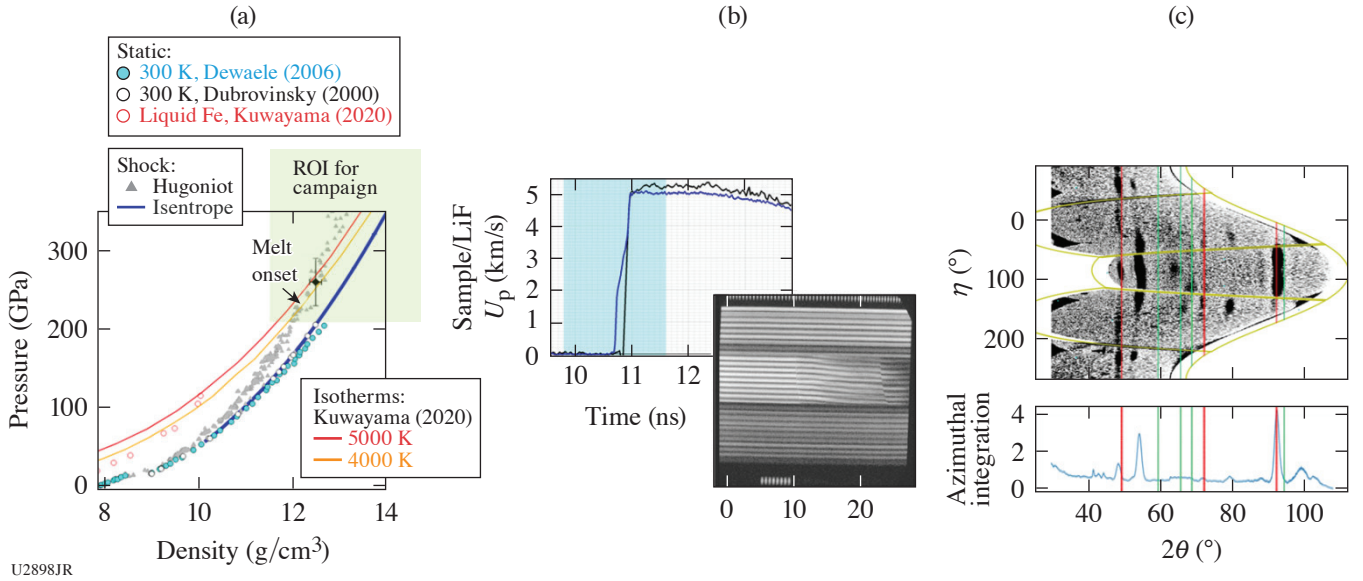

Figure 25
(a) Density versus pressure plot for Fe with the region of interest for this campaign highlighted in green. (b) Example of raw VISAR data and analyzed data showing the particle velocity at the sample/LiF interface, which can be used to determine the pressure in the sample. The blue highlighted region shows where the 2-ns x-ray pulse probed in time. (c) An example of analyzed data from the powder x-ray diffraction image-plate (PXRDIP) diagnostic. This diagnostic will provide information about the density and phase of the alloy on compression. ROI: region of interest.

This work was performed under the auspices of the U.S. Department of Energy by Lawrence Livermore National Laboratory under Contract DE-AC52-07NA27344.

Measuring the Viscosity of MgO at Lower-Mantle Conditions

R. F. Smith,[1*] T. Perez,[2] S. Ali,[1] P. M. Celliers,[1] F. Coppari,[1] J. H. Eggert,[1] and J. K. Wicks[2]
[1]Lawrence Livermore National Laboratory
[2]Department of Earth and Planetary Sciences, Johns Hopkins University
[*]Principal Investigator

The viscosity of MgO under high pressures and temperatures strongly influences a terrestrial planet's mantle dynamics, which impacts the planet's chemical and thermal evolution. Characterizing mantle dynamics is crucial in our understanding of the geologic history of planets in our solar system, as well as establishing habitability of exoplanetary systems. Despite the importance of MgO viscosity, there is currently no consensus from either theory or experiment on its value at mantle conditions. Here we use new experimental techniques to constrain the rheological properties of MgO at pressures and temperatures relevant to the Earth's mantle. The results of these experiments will constrain mantle dynamics models, aiding our understanding of planetary interior evolution and surface habitability.

The OMEGA EP laser ramp drive allows us to reach lower-mantle pressures over a wide range of strain rates while providing direct constraints of viscosity with the OMEGA EP active shock breakout (ASBO–VISAR) diagnostic. The target design for this experimental campaign is shown schematically in Fig. 26. Perturbed interfaces between ablation layer and sample create perturbed shock waves and Rayleigh–Taylor (RT) instabilities that can be tracked with VISAR to constrain rheological properties. An example of the data obtained is shown in Fig. 27. Our shot day was very successful and data analysis is ongoing.

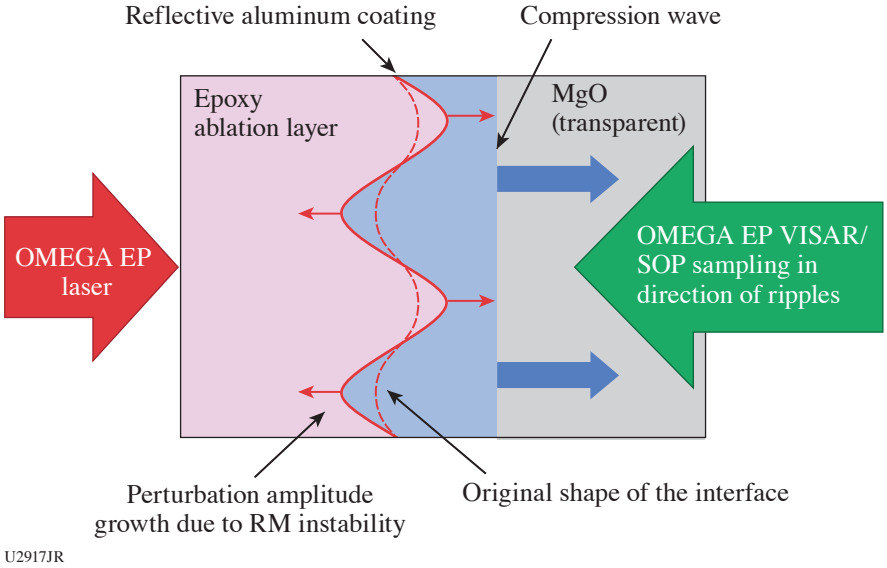

Figure 26
Conceptual design of viscosity measurements on OMEGA EP. The laser-ablated shock wave takes on sinusoidal shape after passing through rippled epoxy–MgO interface and undergoes damped oscillation controlled by viscosity. VISAR/SOP can track continuous breakout of ripple anti-node on wedged interface and therefore can constrain viscosity. RM: Richtmyer–Meskov.

This experiment was conducted at the Omega Laser Facility at the University of Rochester's Laboratory for Laser Energetics with the beam time through the Laboratory Basic Science program.

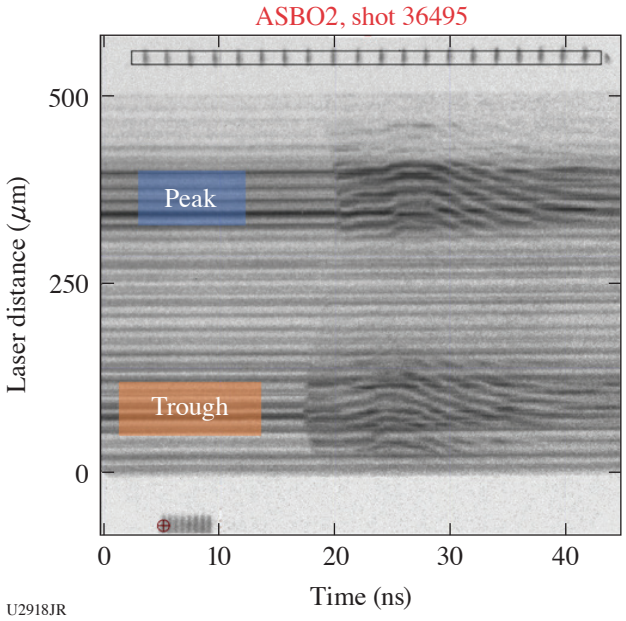

Figure 27
Example VISAR/ASBO data using the design from Fig. 26.

Studying the T–T Reaction at Energies Exceeding 2 MeV on OMEGA

A. Schwemmlein,[1*] C. Stoeckl,[1*] W. U. Schröder,[2] and W. T. Shmayda[1]
[1]Laboratory for Laser Energetics, University of Rochester
[2]Department of Chemistry, University of Rochester
[*]Principal Investigator

TNSA provides a unique opportunity to generate rare-isotope particle beams for nuclear-reaction experiments. Such experiments can be done at short-pulse laser facilities. In this technique, the surface of a small ($500 \times 500 \times 20$-μm^3) metallic converter foil is doped with the particle specie to be accelerated. When the foil is hit from the back with a high-power ($>10^{18}$ W/cm^2) laser pulse, particles from the foil surface layers are ejected and accelerated by the strong electric fields generated in the process. This approach is especially interesting for the generation of a beam of energetic tritons ($^3H^+$), which is presently not available anywhere. TNSA pilot studies on OMEGA EP[44,45] have generated beams of tritons capable of inducing nuclear reactions, for example, D–T fusion in a secondary, deuterated physics target. Utilizing this beam to study the tritium–tritium (T–T) reaction in a similar fashion can answer open questions about the predominant T–T reaction channel, as well as the structure of the compound nucleus ^{6}He. It is noteworthy that the tritium used in viable TNSA experiments is confined within small volumes of metal lattice and in amounts that are orders-of-magnitude smaller than in comparable accelerator experiments.

A follow-up experiment utilized improved converter and physics targets, each consisting of a stainless-steel substrate and an unpassivated 500-nm titanium layer. A radio-chemical analysis of the targets revealed a tritium content about 5× higher (670 μCi versus 130 μCi) compared to the pilot study. A control experiment with this type of converter foil and a secondary deuterated physics target produced the expected D–T fusion neutrons (see Fig. 28). However, the total neutron yield did not improve appreciably compared to the pilot study, suggesting that the additional tritium in the improved converter foil did not participate in the TNSA process.

A new experiment was conducted to study the triton-on-tritium (t–T) reaction. Here, the deuterated physics target was replaced with a tritiated physics target. The resulting spectrum of TT neutrons is compared in Fig. 28 with those of the D–T control reaction. The absence of neutrons above the background in the former spectrum is consistent with the much-lower T–T reaction cross section that was previously reported,[46] up to about $E_t \approx 1$ MeV. This new result is a first indication that the T–T reaction does not proceed via the third excited state of ^{6}He at 2.3 MeV above the T–T reaction threshold—an energy that could not be reached in past experiments. Like in the D–T reaction, which proceeds via ^{5}He, population of this ^{6}He state would noticeably increase the reaction cross section.

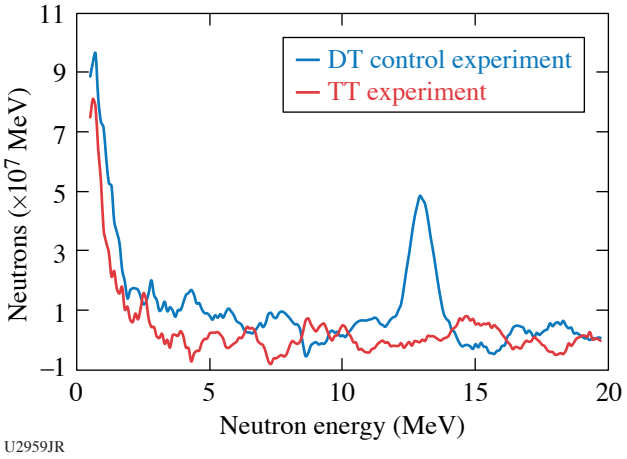

Figure 28
Neutron time-of-flight spectrum from the "8 × 4 nTOF" detector in energy space. While the TNSA triton beam generated a DT peak with a secondary deuterated target in the control experiment, no neutrons above the background were observed in the experiment with a secondary tritiated target.

These experiments were conducted at the Omega Laser Facility at the University of Rochester's Laboratory for Laser Energetics with the beam time through the Laboratory Basic Science Program.

Angular Momentum Transport in Disk-Jet Transitions

G. Swadling,[1*] F. Suzuki-Vidal,[2] V. Valenzuela-Villaseca,[2] M. Bailly-Grandvaux,[3] and C. Walsh[1]
[1]Lawrence Livermore National Laboratory
[2]Imperial College London, UK
[3]University of California, San Diego
[*]Principal Investigator

First experiments were performed on OMEGA looking at the formation of supersonic rotating plasmas as a platform to study fundamental HED hydrodynamics and laboratory astrophysics.[47] These experiments were part of the AngMomentumDisk-22A Campaign and were performed on 9 February 2022.

The experiments consisted of a target package made of six V-shaped apertures in a circular array with a diameter of ~12 mm [Fig. 29(a)], 3-D printed in CH. Each V-shaped target has a 5° tilt respect to the axis of the array, with each target "face" illuminated by a 3ω 500-ns, 1-ns square beam. This drives simultaneous radial plasma flows off-axis, injecting initial angular momentum and thus driving a rotating plasma.

The main diagnostic was optical Thomson scattering in spatially resolved mode, using 120 J with a duration of 3.7 ns. Scattered light was collected at 63° from the input **k** vector. Data consisted of IAW and EPW spectra. Example results are shown in Figs. 29(b) and 29(c) from 5 to 8.7 ns at a position −500 μm from the axis of the array. The results were very consistent for all shots. Analysis of the IAW spectra at 8 ns is shown in Fig. 29(d), which results in plasma parameters of the rotating plasma constrained by analysis of the EPW spectra at the same time. Plasma parameters are in line with 3-D numerical simulations with the *GORGON* code.[48]

The experiment was conducted at the Omega Laser Facility at the University of Rochester's Laboratory for Laser Energetics with the beam time through the Laboratory Basic Science (LBS) Program. Work was performed under the auspices of the U.S. DOE by LLNL under Contract DE-AC52-07NA27344. Research supported by The Royal Society through a University Research Fellowship.

1. M. Millot *et al.*, Nature **569**, 251 (2019).
2. M. Millot *et al.*, Nat. Phys. **14**, 297 (2018).
3. B. Cheng *et al.*, Nat. Phys. **17**, 1228 (2021).
4. Y.-J. Kim *et al.*, Sci. Rep. **11**, 5610 (2021).
5. S. Brygoo *et al.*, J. Appl. Phys. **118**, 195901 (2015).

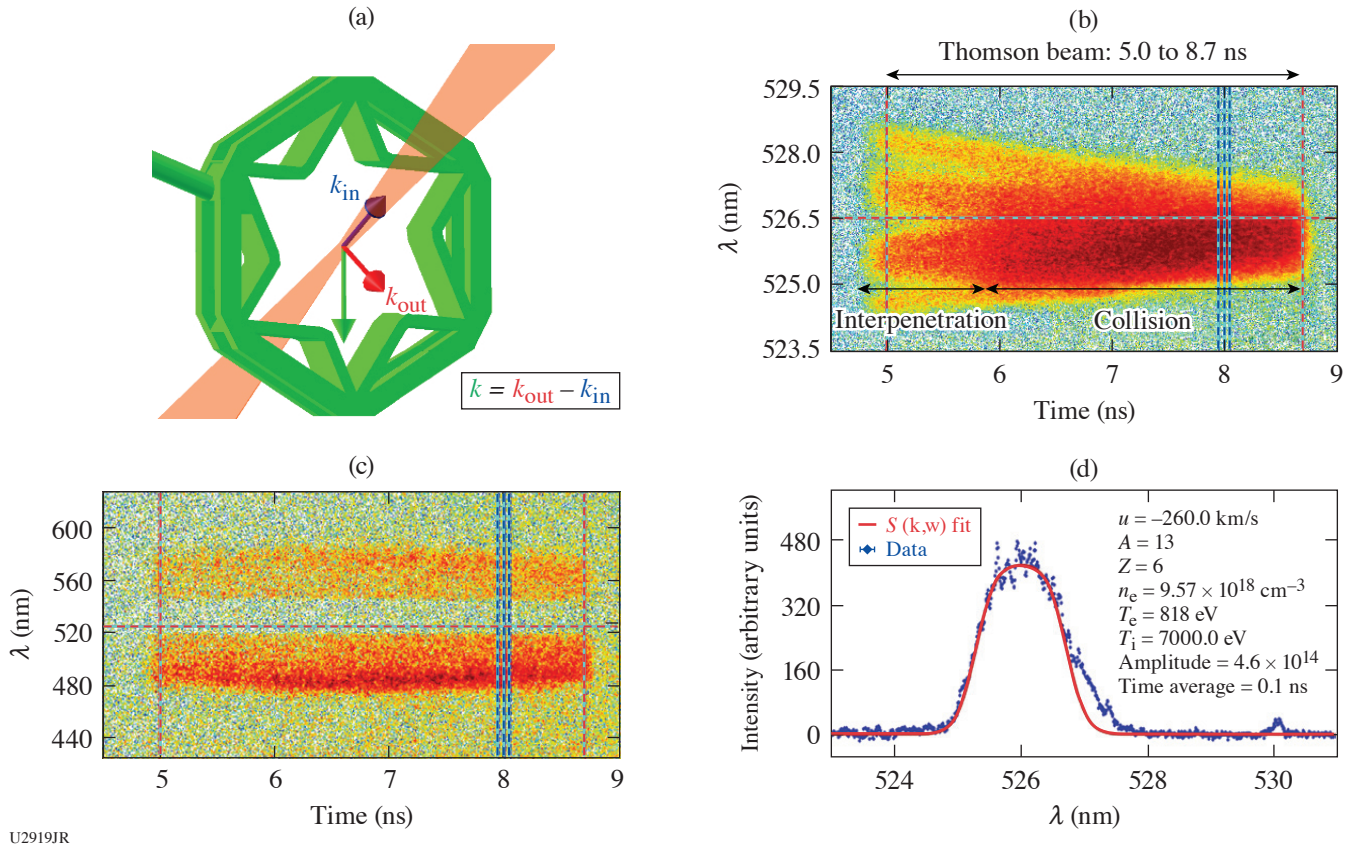

Figure 29
Overview of AngMomentumDisk-22A shot day. (a) *VISRAD* view of sixfold target with Thomson scattering geometry. [(b),(c)] Example results from Thomson scattering (shot 103212), EPW and IAW, respectively. Data were obtained from 5 to 8.7 ns after the beams illuminated the targets. (d) Lineout from IAW data at 8 ns, integrated over 100 ps together with a fit of the theoretical spectral density function $S(k,w)$, which allows measuring plasma parameters in the rotating plasma.

6. Y.-J. Kim *et al.*, Phys. Rev. Lett. **129**, 015701 (2022).
7. L. Gao *et al.*, Phys. Plasmas **23**, 043106 (2016).
8. A. Chien *et al.*, Nat. Phys. **19**, 254 (2023).
9. D. J. Stark, T. Toncian, and A. V. Arefiev, Phys. Rev. Lett. **116**, 185003 (2016).
10. H. G. Rinderknecht *et al.*, New J. Phys. **23**, 095009 (2021).
11. F. Spite and M. Spite, Astron. Astrophys. **115**, 357 (1982).
12. M. Tegmark *et al.*, Phys. Rev. D **69**, 103501 (2004).
13. S. Burles *et al.*, Phys. Rev. Lett. **82**, 4176 (1999).
14. A. B. Zylstra *et al.*, Rev. Sci. Instrum. **90**, 123504 (2019).
15. G. Q. Liao and Y. T. Li, IEEE Trans. Plasma Sci. **47**, 3002 (2019).
16. G. Liao *et al.*, Proc. Natl. Acad. Sci. **116**, 3994 (2019).
17. S. Herzer *et al.*, New J. Phys. **20**, 063019 (2018).
18. K. Y. Kim, University of Maryland, College Park, MD, Technical Report DOE-UMCP-3891 (5 May 2016).
19. G.-Q. Liao *et al.*, Phys. Rev. X **10**, 031062 (2020).
20. Y. Zeng *et al.*, Opt. Express **28**, 15258 (2020).
21. E. Wigner and H. B. Huntington, J. Chem. Phys. **3**, 764 (1935).
22. J. M. McMahon and D. M. Ceperley, Phys. Rev. B **84** (14), 144515 (2011); **85** (21), 219902(E) (2011).)
23. B. M. Haines *et al.*, Phys. Plasmas **21**, 092306 (2014).
24. L. V. Al'tshuler, S. E. Brusnikin, and E. A. Kuz'menkov, J. Appl. Mech. Tech. Phys. **28**, 129 (1987).

25. V. N. Goncharov *et al.*, Phys. Rev. Lett. **125**, 065001 (2020).
26. T. R. Boehly *et al.*, Opt. Commun. **133**, 495 (1997).
27. S. Ressel *et al.*, Phys. Plasmas **29**, 072713 (2022).
28. C. Stoeckl *et al.*, Rev. Sci. Instrum. **87**, 11E323 (2016).
29. D. T. Michel *et al.*, Rev. Sci. Instrum. **83**, 10E530 (2012).
30. I. V. Igumenshchev *et al.*, Phys. Plasmas **23**, 052702 (2016); A. Colaïtis *et al.*, J. Comput. Phys. **443**, 110537 (2021).
31. C. E. Parker, "The ^{3}H(d, γ) Reaction and the ^{3}H(d, γ)/^{3}H(d, n) Branching Ratio for $E_{\text{c.m.}} \leq 300$ keV," Ph.D. Thesis, Ohio University, 2016.
32. Y. Kim *et al.*, Phys. Rev. C **85**, 061601 (2012).
33. J. Jeet *et al.*, Phys. Rev. C **104**, 054611 (2021).
34. A. Nishiguchi *et al.*, Phys. Rev. Lett. **53**, 262 (1984).
35. S. A. Slutz *et al.*, Phys. Plasmas **17**, 056303 (2010).
36. M. R. Gomez *et al.*, Phys. Rev. Lett. **125**, 155002 (2020).
37. C. A. Walsh *et al.*, Phys. Rev. Lett. **118**, 155001 (2017).
38. C. Ahdida *et al.*, Front. Phys. **9**, 788253 (2022).
39. M. R. Weis *et al.*, Phys. Plasmas **28**, 012705 (2021).
40. G. Fiksel *et al.*, J. Plasma Phys. **87**, 905870411 (2021).
41. G. Pérez-Callejo *et al.*, Phys. Rev. Lett. **126**, 085001 (2021).
42. T. Komabayashi, K. Hirose, and Y. Ohishi, Phys. Chem. Miner. **39**, 329 (2012).
43. L. Dubrovinsky *et al.*, Science **316**, 1880 (2007).
44. A. K. Schwemmlein *et al.*, Nucl. Instrum. Methods Phys. Res. B **522**, 27 (2022).
45. C. Stoeckl *et al.*, Nucl. Instrum. Methods Phys. Res. B **453**, 41 (2019).
46. C. Wong, J. D. Anderson, and J. W. McClure, Nucl. Phys. **71**, 106 (1965).
47. D. D. Ryutov, Astrophys. Space Sci. **336**, 21 (2011).
48. A. Ciardi *et al.*, Phys. Plasmas **14**, 056501 (2007).

FY22 LaserNetUS Program

M. S. Wei

Laboratory for Laser Energetics, University of Rochester

UR/LLE is part of the LaserNetUS Collaborative Network established in 2018 and funded by the Department of Energy Fusion Energy Sciences within the Office of Science. The mission of LaserNetUS is to reestablish U.S. scientific competitiveness in high-energy-density physics and high-field optical science by advancing the frontiers of laser-science research, providing students and scientists with broad access to unique facilities and enabling technologies, and fostering collaboration among researchers and networks from around the world. During FY22, LaserNetUS facility nodes consisted of ten institutions including Colorado State University, Lawrence Berkeley National Laboratory, Lawrence Livermore National Laboratory (LLNL), SLAC, The Ohio State University, the University of Central Florida, the University of Nebraska-Lincoln, Institut National de la Recherche Scientifique, the University of Rochester, and the University of Texas at Austin. Through a coordinated annual call for proposals and an independent proposal review panel process, the LaserNetUS network makes available a variety of ultrafast, high-peak-power and high-energy, petawatt-class lasers including LLE's four-beam, high-energy and high-intensity OMEGA EP laser to users who do not have regular access to ultrahigh-intensity lasers.

UR/LLE provides an average of four shot days each year on OMEGA EP to LaserNetUS users. Since 2019, 18 projects have been awarded a total of 20 shot days on OMEGA EP, including 13 projects from the first three solicitations for shots in Cycle-1 (2019–2020), Cycle-2 (2020–2021), and Cycle-3 (2021–2022), and five new projects from the fourth solicitation completed during FY22 for experiments in Cycle-4 (2022–2023). During FY22, a total of 34 target shots were successfully conducted over four shot days for three LaserNetUS projects led by scientists from Princeton University, the University of California, San Diego (UCSD), and Lawrence Livermore National Laboratory (see Table I below). These three experiments involved three graduate students and four postdoctoral researchers. FY22 LaserNetUS user experiments are summarized below.

Table I: During FY22, three LaserNetUS Cycle-3 projects (blue-shaded cells) completed 34 target shots over four shot days and five new LaserNetUS projects selected from the Cycle-4 solicitation were approved with a total of five shot days for experiments on OMEGA EP in FY23.

Principal Investigator	Institution	Title	LaserNetUS beam-time cycle
M. R. Edwards	LLNL	Reaching an Electron–Positron Plasma with OMEGA EP	3
G. Righi	UCSD (now at LLNL)	Understanding Temperature Dependence of Iron Strength at High Pressure with Ramped Compression on OMEGA EP	3
S. Zhang	Princeton University	Study of Particle Acceleration in Magnetic Reconnection Using Laser-Powered Coils	3
M. Manuel	General Atomics	Characterization of Early-Stage, Quasi-Parallel, Collisionless-Shock Formation	4

Table I: During FY22, three LaserNetUS Cycle-3 projects (shaded cells) completed 34 target shots over four shot days and five new LaserNetUS projects selected from the Cycle-4 solicitation were approved with a total of five shot days for experiments on OMEGA EP in FY23 (continued).

Principal Investigator	Institution	Title	LaserNetUS beam-time cycle
I. Oleynik	University of South Florida	Exploring Metastability and Phase Transitions in Dynamically Compressed Amorphous Carbon	4
D. Schaeffer	Princeton University (now at University of California, Los Angeles)	Dependence of Particle Acceleration on Shock Structure in Magnetized Collisionless Shocks on OMEGA EP	4
M. Wadas	University of Michigan	Observation and Scaling of Vortex Rings Ejected from Shock-Accelerated Interfaces	4
J. Wicks	Johns Hopkins University	*In Situ* X-Ray Diffraction Study of Shock-Compressed Diamond: Improving Equation-of-State Models Through Data-Driven Experimental Designs	4

Controlling the Energy of Relativistic Positron Jets

M. R. Edwards,[1*] J. von der Linden,[2] J. L. Peebles,[3] L. Willingale,[4] G. Fiksel,[4] A. Link,[1] and H. Chen[1]
[1]Lawrence Livermore National Laboratory
[2]Max Planck Institute for Plasma Physics
[3]Laboratory for Laser Energetics, University of Rochester
[4]University of Michigan
[*]Principal Investigator

Creating a platform to study the physics of relativistic electron–positron plasmas requires control over the key parameters of laser-driven positron jets. Specifically, the positron beams produced by kilojoule-scale, 10-ps laser pulses focused on gold targets are too high in energy for efficient interactions at the electron and positron densities that we are currently able to achieve. The energy of generated positrons is dominated by their acceleration in the sheath field on the back surface of gold-disk targets. Here we examined two approaches for controlling the energy of these positron jets: (1) we increased the target diameter and (2) we generated a plasma using a long-pulse beam on the back surface of our primary target. Both approaches were designed to reduce the accelerating sheath field. Initial results indicate successful reduction in the average measured positron energy using both approaches. Figure 1 shows how the distribution of positron energies decreased for larger target diameters, following model expectations.

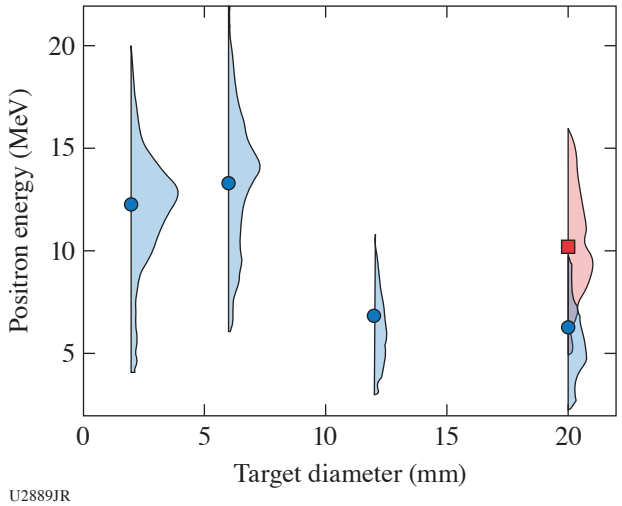

Figure 1
Measured positron energy distributions as a function of target diameter. Blue points are taken for targets under the same conditions. The red square corresponds to data taken with a microwire-coated target, producing enhanced yield and less energy reduction.

Initial analysis suggests scaling behavior follows expectations and that both mechanisms can, in principle, be used for energy control. The addition of microwires at the target front surface enhanced yield and reduced the effectiveness of the sheath field reduction.

Understanding Temperature Dependence of Iron Strength at High Pressure with Ramped Compression on OMEGA EP

G. Righi,[1*] Y.-J. Kim,[1] C. Stan,[1] M. Hill,[1] T. Lockard,[1] R. Rudd,[1] H.-S. Park,[1] and M. Meyers[2]
[1]Lawrence Livermore National Laboratory
[2]University of California, San Diego
[*]Principal Investigator

A fundamental material property—strength—is studied under high-stress and -temperature loading conditions (150 GPa, thousands of K) relevant to the interior of rocky planetary bodies. Experiments on OMEGA EP are well suited to probe this region of plastic deformation to better understand iron strength under these extreme conditions and to test physics-based constitutive models. Hydrodynamic simulations were used to design unique laser pulse shapes to probe iron samples at constant, high pressure, and different temperatures.

In the experiment, the Rayleigh–Taylor instability was used to infer the material's strength by analyzing the amount of growth of preimposed ripples and comparing to growth simulations. The VISAR (velocity interferometer system for any reflector) diagnostic was used to measure the pressure incident on the iron after laser irradiation of the custom 30-ns laser pulse. Radiography was used to image ripple iron samples at specific times (Fig. 2).

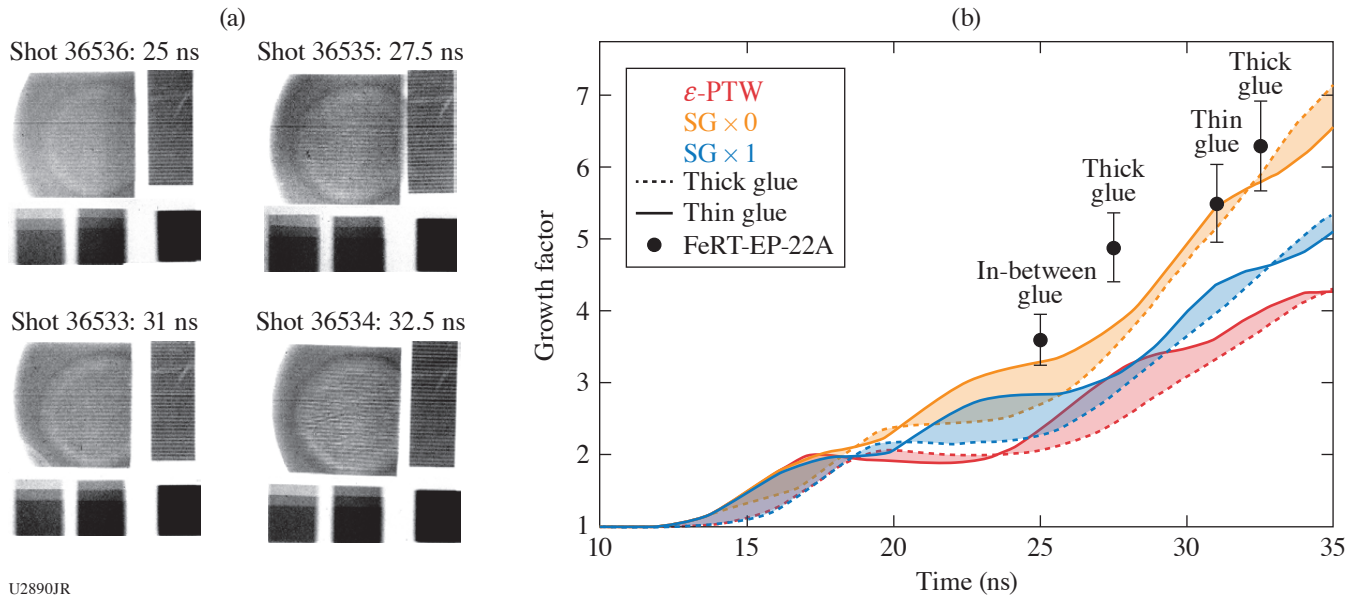

Figure 2
(a) High-quality radiographs taken at different delay times. The large, rippled sample shows clear evidence of laser spot size. Ripple material on the right side of each image is undriven material used for growth factor calculation. Steps and knife-edge on the bottom of each image are calibration metrics. (b) Growth factor predicted from hydrodynamic simulations compared to experimental data. Curves represent varying glue thicknesses according to target metrology. Data are consistent with low strength. PTW: Preston–Tonks–Wallace;[1] SG: Steinberg–Guinan.[2]

High-pressure, high-temperature shots (200 GPa, ~4000 K) were taken during one OMEGA EP shot day and preliminary results found that growth is larger than is predicted by the Preston–Tonks–Wallace[1] and Steinberg–Guinan[2] strength models. This suggests that iron is weaker than expected, contradictory to recent ultrahigh-pressure iron experiments at the National Ignition Facility. The differences between the experimental and simulated growth could be attributed to: (1) the high temperature allows

for easier deformation that the models and simulations are not accurately predicting or (2) the iron is unexpectedly melting. Further post-shot analysis and post-shot simulations will confirm results. An additional shot day is needed to probe the high-pressure, low-temperature regime of iron strength not discussed here.

The material is based upon work supported by the LLNL Academic Collaboration Team University Program (ACT-UP) award (subcontract B639114) and the Department of Energy, National nuclear Security Administration under Award Number DE-NA0003842. Part of this work was performed under the auspices of the U.S. Department of Energy by Lawrence Livermore National Laboratory under Contract DE-AC52-07NA27344.

Particle Acceleration Mechanisms in Magnetically Driven Reconnection Using Laser-Powered Capacitor Coils

S. Zhang,[1] A. Chien,[1] L. Gao,[2*] H. Ji,[1,2*] E. G. Blackman,[3] D. H. Froula,[4] D. Haberberger,[4] W. Daughton,[5] J. Moody,[6] and H. Chen[6]
[1]Princeton University
[2]Princeton Plasma Physics Laboratory
[3]Department of Physics and Astronomy, University of Rochester
[4]Laboratory for Laser Energetics, University of Rochester
[5]Los Alamos National Laboratory
[6]Lawrence Livermore National Laboratory
[*]Principal Investigators

Magnetic reconnection is a ubiquitous astrophysical process, whereby magnetic energy is rapidly converted into plasma kinetic energy in the form of bulk flow, thermal energy, and nonthermal particles. The latter is often regarded as an observational signature of reconnection, which can be a more-efficient particle accelerator than other processes such as collisionless shocks. In the past ~six years, our team has developed a platform to study acceleration of nonthermal electrons from magnetic reconnection at low plasma beta using UV laser-powered capacitor coils.[3] For the first time, nonthermal electrons accelerated by the reconnection electric field have been measured.[4] Using the short-pulse laser-powered capacitor coils newly developed by our group, we extended our platform to a new regime with tripled magnetic-field strength to achieve particle acceleration by magnetically driven axisymmetric reconnection with one order of magnitude higher energy. In FY22, under the LaserNetUS program, we successfully performed two shot days on OMEGA EP. The proton data show a clear signature of current sheet formation and evolution. Particle acceleration was also observed. Detailed analyses and particle-in-cell (PIC) simulations are underway.

The experimental setup shown in Fig. 3 built on our previous experiments using the short-pulse IR lasers. The main target is composed of two Cu plates with a laser entrance hole in the front plate, connected by a pair of parallel U-shaped coils. OMEGA EP backlighter Beam 2 was used to irradiate the back plate center at a 45° incidence angle, thereby positively charging up the back Cu

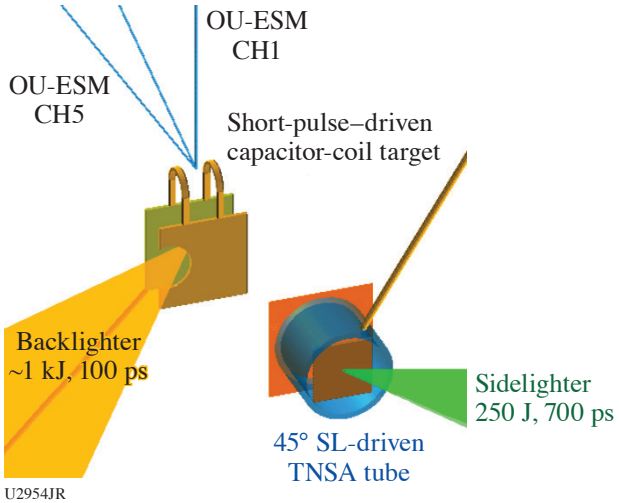

Figure 3
Experimental setup. The OMEGA EP BL was focused onto the back plate, positively charging it up. The resulting voltage difference between the back and front plate drives currents in both coils, creating reconnection. Ultrafast protons generated by the SL probed through the coils and was collected by a proton film back held by TIM-14. For shots aiming for particle acceleration, proton radiography was turned off, and OU-ESM, EPPS, and SC-ESM's were fielded at TIM-11, TIM-12, TIM-10, and TIM-13 to monitor particles at various angles.

plate. The voltage difference between the back and front plate drove the currents in both coils, creating reconnection in between. Face-on proton radiography was used to probe through the coils, capturing the magnetic-field topology change and associated fine structures. We positioned multiple particle spectrometers such as the Osaka University Electron Spectrometer (OU-ESM), single-channel electron spectrometer (SC-ESM), and electron–positron–proton spectrometer (EPPS) in TIM-10 to TIM-13 (ten-inch manipulators) to capture the energetic particles accelerated tangentially along the X-line, and compare the particle spectra at various distances and angles with respect to the reconnection region.

Figure 4 presents two examples of the proton images taken at 1 ns and 3 ns, with respect to the beginning of the sidelighter (SL) drive. Compared to the proton images obtained with UV lasers, these proton images see almost no plasma effects around the coils. Two prolate voids corresponding to magnetic-field generation around the coils are observed. In addition, at 3 ns a center feature developed between the voids corresponding to current sheet formation.

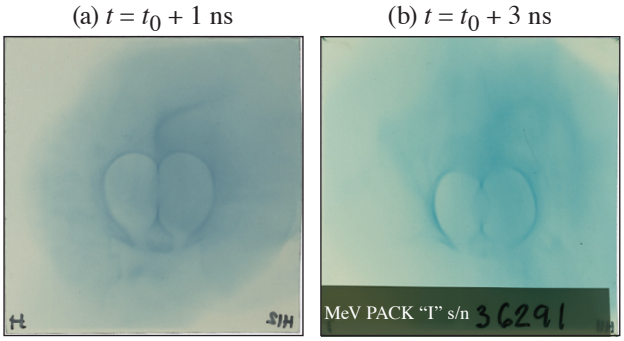

Figure 4
Photon radiographs taken at (a) 1 ns and (b) 3 ns with respect to the beginning of the SL.

Figure 5(a) presents the OU-ESM data for the reconnection case and Figs. 5(b) and 5(c) present two no-reconnection cases. The no-reconnection case had only one coil (either left or right), thereby no reconnection occurred. Compared to the data from the no-reconnection cases, the electron spectra for the reconnection case had much higher signals and a significant bump at ~80 keV is clearly seen. These data will be compared with in-depth PIC simulations as well as our previous observations using the UV drivers.

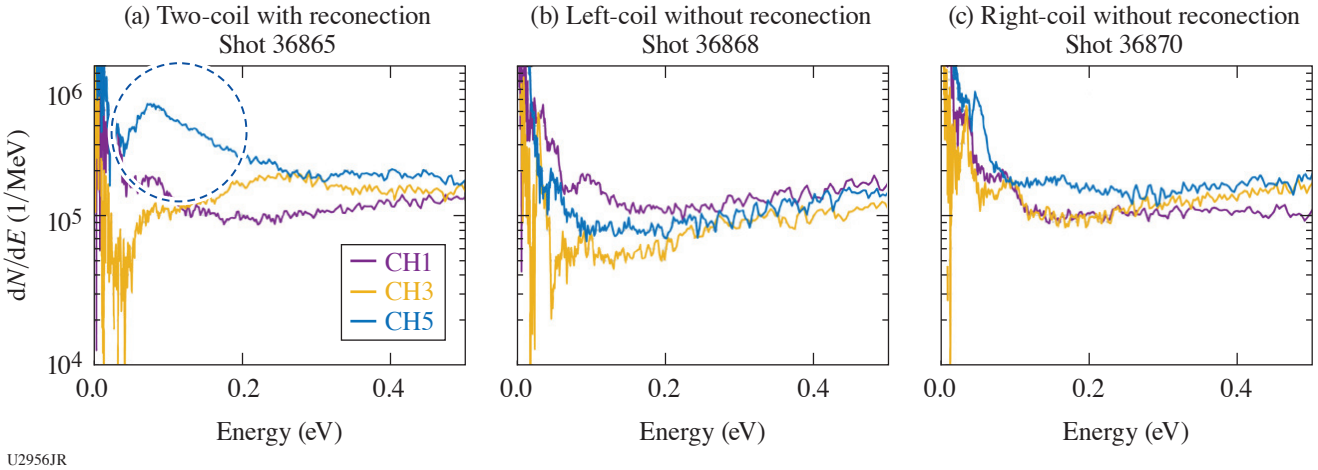

Figure 5
(a) OU-ESM data for the reconnection case and [(b),(c)] two no-reconnection cases.

We acknowledge the Omega Laser Facility staff at the Laboratory for Laser Energetics. This work was performed under the auspices of U.S. DOE Office of Science under the HEDLP program with award number DE-SC0020103 with beam time through LaserNetUS.

1. D. L. Preston, D. L. Tonks, and D. C. Wallace, J. Appl. Phys. **93**, 211 (2003).
2. D. J. Steinberg, S. G. Cochran, and M. W. Guinan, J. Appl. Phys. **51**, 1498 (1980).
3. L. Gao *et al.*, Phys. Plasmas **23**, 043106 (2016).
4. A. Chien *et al.*, Nat. Phys. **19**, 254 (2023).

Publications and Conference Presentations

Publications

H. Abu-Shawareb *et al.*, "Lawson Criterion for Ignition Exceeded in an Inertial Fusion Experiment," Phys. Rev. Lett. **129**, 075001 (2022).

D. Barlow, T. Goffrey, K. Bennett, R. H. H. Scott, K. Glize, W. Theobald, K. Anderson, A. A. Solodov, M. J. Rosenberg, M. Hohenberger, N. C. Woolsey, P. Bradford, M. Khan, and T. D. Arber, "Role of Hot Electrons in Shock Ignition Constrained by Experiment at the National Ignition Facility," Phys. Plasmas **29**, 082704 (2022).

G. Bruhaug, G. W. Collins, H. G. Rinderknecht, J. R. Rygg, J. L. Shaw, M. S. Wei, M. S. Freeman, F. E. Merrill, L. P. Neukirch, and C. H. Wilde, "Analysis Methods for Electron Radiography Based on Laser-Plasma Accelerators," in Proc. NAPAC2022 (JACoW Publishing, Geneva, Switzerland, 2022), pp. 274–277.

Z. Chen, S. X. Hu, and N. P. Bigelow, "Imprinting a Three-Dimensional Skyrmion in a Bose–Einstein Condensate Via a Raman Process," J. Low Temp. Phys. **208**, 172 (2022).

K. Churnetski, K. M. Woo, W. Theobald, P. B. Radha, R. Betti, V. Gopalaswamy, I. V. Igumenshchev, S. T. Ivancic, M. Michalko, R. C. Shah, C. Stoeckl, C. A. Thomas, and S. P. Regan, "Three-Dimensional Hot-Spot X-Ray Emission Tomography from Cryogenic Deuterium–Tritium Direct-Drive Implosions on OMEGA," Rev. Sci. Instrum. **93**, 093530 (2022).

S. X. Coffing, C. L. Fryer, H. F. Robey, C. J. Fontes, S. R. Wood, P. M. Kozlowski, H. M. Johns, D. D. Meyerhofer, T. Byvank, A. Liao, and T. J. Urbatsch, "Inferring the Temperature Profile of the Radiative Shock in the COAX Experiment with Shock Radiography, Dante, and Spectral Temperature Diagnostics," Phys. Plasmas **29**, 083302 (2022).

A. Colaïtis, D. P. Turnbull, I. V. Igumenshchev, D. Edgell, R. C. Shah, O. M. Mannion, C. Stoeckl, D. Jacobs-Perkins, A. Shvydky, R. Janezic, A. Kalb, D. Cao, C. J. Forrest, J. Kwiatkowski, S. Regan, W. Theobald, V. N. Goncharov, and D. H. Froula, "3D Simulations Capture the Persistent Low-Mode Asymmetries Evident in Laser-Direct-Drive Implosions on OMEGA," Phys. Rev. Lett. **129**, 095001 (2022).

T. Cordova, M. J. MacDonald, T. Döppner, F. N. Beg, M. Dozieres, B. Kozioziemski, N. A. Pablant, C. M. Sorce, and N. G. Whiting, "Absolute Calibration of the Conical Crystal Configuration of the Zinc Spectrometer (ZSPEC) at the OMEGA Laser Facility," Rev. Sci. Instrum. **93**, 083509 (2022).

C. Dorrer, I. A. Begishev, S.-W. Bahk, and J. Bromage, "High-Resolution Mapping of Phase-Matching Conditions in Second-Order Nonlinear Crystals," Opt. Mater. Express **12**, 3679 (2022).

F. García-Rubio, R. Betti, J. Sanz, and H. Aluie, "Theory of the Magnetothermal Instability in Coronal Plasma Flows," Phys. Plasmas **29**, 092106 (2022).

V. Yu. Glebov, C. J. Forrest, J. Kendrick, J. P. Knauer, O. M. Mannion, H. McClow, S. P. Regan, C. Stoeckl, B. Stanley, and W. Theobald, "A New Neutron Time-of-Flight Detector for Yield and Ion-Temperature Measurements on OMEGA Laser Facility," Rev. Sci. Instrum. **93**, 093522 (2022).

V. Gopalaswamy, R. Betti, P. B. Radha, A. J. Crilly, K. M. Woo, A. Lees, C. Thomas, I. V. Igumenshchev, S. C. Miller, J. P. Knauer, C. Stoeckl, C. J. Forrest, O. M. Mannion, Z. L. Mohamed, H. G. Rinderknecht, and P. V. Heuer, "Analysis of Limited Coverage Effects on Areal Density Measurements in Inertial Confinement Fusion Implosions," Phys. Plasmas **29**, 072706 (2022).

B. M. Haines, D. E. Keller, K. P. Long, M. D. McKay, Jr., Z. J. Medin, H. Park, R. M. Rauenzahn, H. A. Scott, K. S. Anderson, T. J. B. Collins, L. M. Green, J. A. Marozas, P. W. McKenty, J. H. Peterson, E. L. Vold, C. Di Stefano, R. S. Lester, J. P. Sauppe, D. J. Stark, and J. Velechovsky, "The Development of a High-Resolution Eulerian Radiation-Hydrodynamics Simulation Capability for Laser-Driven Hohlraums," Phys. Plasmas **29**, 083901 (2022).

S. S. Harilal, M. C. Phillips, D. H. Froula, K. K. Anoop, R. C. Issac, and F. N. Beg, "Optical Diagnostics of Laser-Produced Plasmas," Rev. Mod. Phys. **94**, 035002 (2022).

B. J. Henderson, J. R. Rygg, M. C. Marshall, M. K. Ginnane, L. E. Hansen, E. Davies, P. M. Celliers, and G. W. Collins, "Shocked Silica Aerogel Radiance Transition," J. Appl. Phys. **132**, 095902 (2022).

P. V. Heuer, L. S. Leal, J. R. Davies, E. C. Hansen, D. H. Barnak, J. L. Peebles, F. García-Rubio, B. Pollock, J. Moody, A. Birkel, and F. Séguin, "Diagnosing Magnetic Fields in Cylindrical Implosions with Oblique Proton Radiography," Phys. Plasmas **29**, 072708 (2022).

M. P. Jeske, W. Zhang, and M. Anthamatten, "Two-Photon Printing of Shape-Memory Microstructures and Metasurfaces via Radical-Mediated Thiol-Vinyl Hydrothiolation," Adv. Mater. Technol. **7**, 2101725 (2022).

T. R. Joshi, R. C. Shah, W. Theobald, K. Churnetski, P. B. Radha, D. Cao, C. A. Thomas, J. Baltazar, and S. P. Regan, "Diagnosis of the Imploding Shell Asymmetry in Polar-Direct-Drive Deuterium–Tritium Cryogenic Target Implosions on OMEGA," Rev. Sci. Instrum. **93**, 093524 (2022).

K. R. P. Kafka, T. Z. Kosc, and S. G. Demos, "Methods and Apparatus for Comprehensive Characterization of Performance Attributes and Damage Thresholds of Ultrafast Laser Optics," Opt. Eng. **61**, 071605 (2022).

J. H. Kunimune, H. G. Rinderknecht, P. J. Adrian, P. V. Heuer, S. P. Regan, F. H. Séguin, M. Gatu Johnson, R. P. Bahukutumbi, J. P. Knauer, B. L. Bachmann, and J. A. Frenje, "Knock-On Deuteron Imaging for Diagnosing the Morphology of an ICF Implosion at OMEGA," Phys. Plasmas **29**, 072711 (2022).

A. L. Milder, J. Zielinski, J. Katz, W. Rozmus, D. Edgell, A. Hansen, M. Sherlock, C. Bruulsema, J. P. Palastro, D. Turnbull, and D. H. Froula, "Direct Measurement of the Return Current Instability in a Laser-Produced Plasma," Phys. Rev. Lett. **129**, 115002 (2022).

S. C. Miller and V. N. Goncharov, "Instability Seeding Mechanisms Due to Internal Defects in Inertial Confinement Fusion Targets," Phys. Plasmas **29**, 082701 (2022).

M. Oliver, C. H. Allen, L. Divol, Z. Karmiol, O. L. Landen, Y. Ping, R. Wallace, M. Schölmerich, W. Theobald, T. Döppner, and T. G. White, "Diffraction Enhanced Imaging Utilizing a Laser Produced X-Ray Source," Rev. Sci. Instrum. **93**, 093502 (2022).

J. L. Peebles, J. R. Davies, D. H. Barnak, F. García-Rubio, P. V. Heuer, G. Brent, R. Spielman, and R. Betti, "An Assessment of Generating Quasi-Static Magnetic Fields Using Laser-Driven 'Capacitor' Coils," Phys. Plasmas **29**, 080501 (2022).

A. Pineau, K. R. P. Kafka, S. G. Demos, T. Z. Kosc, V. N. Goncharov, S. X. Hu, and G. Duchateau, "Benchmarking Solid-to-Plasma Transition Modeling for Inertial Confinement Fusion Laser-Imprint with a Pump-Probe Experiment," Phys. Rev. Research **4**, 033178 (2022).

H. Poole, D. Cao, R. Epstein, I. Golovkin, T. Walton, S. X. Hu, M. Kasim, S. M. Vinko, J. R. Rygg, V. N. Goncharov, G. Gregori, and S. P. Regan, "A Case Study of Using X-Ray Thomson Scattering to Diagnose the In-Flight Plasma Conditions of DT Cryogenic Implosions," Phys. Plasmas **29**, 072703 (2022).

S. Ressel, J. J. Ruby, G. W. Collins, and J. R. Rygg, "Density Reconstruction in Convergent High-Energy-Density Systems Using X-Ray Radiography and Bayesian Inference," Phys. Plasmas **29**, 072713 (2022).

H. G. Rinderknecht, P. V. Heuer, J. Kunimune, P. J. Adrian, J. P. Knauer, W. Theobald, R. Fairbanks, B. Brannon, L. Ceurvorst, V. Gopalaswamy, C. A. Williams, P. B. Radha, S. P. Regan, M. Gatu Johnson, F. H. Séguin, and J. A. Frenje, "A Knock-On Deuteron Imager for Measurements of Fuel and Hotspot Asymmetry in Direct-Drive Inertial Confinement Fusion Implosions," Rev. Sci. Instrum. **93**, 093507 (2022) (invited).

A. K. Schwemmlein, C. Stoeckl, C. J. Forrest, W. T. Shmayda, S. P. Regan, and W. U. Schröder, "First Demonstration of a Triton Beam Using Target Normal Sheath Acceleration," Nucl. Instrum. Methods Phys. Res. B **522**, 27 (2022).

R. C. Shah, D. Cao, L. Alghaian, B. Bachmann, R. Betti, E. M. Campbell, R. Epstein, C. J. Forrest, A. Forsman, V. Yu. Glebov, V. N. Goncharov, V. Gopalaswamy, D. R. Harding, S. X. Hu, I. V. Igumenshchev, R. T. Janezic, L. Keaty, J. P. Knauer, D. Kobs, A. Lees, O. M. Mannion, Z. L. Mohamed, D. Patel, M. J. Rosenberg, W. T. Shmayda, C. Stoeckl, W. Theobald, C. A. Thomas, P. Volegov, K. M. Woo, and S. P. Regan, "Bound on Hot-Spot Mix in High-Velocity, HighAdiabat Direct-Drive Cryogenic Implosions Based on Comparison of Absolute X-Ray and Neutron Yields," Phys. Rev. E **106**, L013201 (2022).

S. Singh, A. L. Coleman, S. Zhang, F. Coppari, M. G. Gorman, R. F. Smith, J. H. Eggert, R. Briggs, and D. E. Fratanduono, "Quantitative Analysis of Diffraction by Liquids Using a Pink-Spectrum X-Ray Source," J. Synchrotron Radiat. **29**, 1033 (2022).

H. Sio, O. Larroche, A. Bose, S. Atzeni, J. A. Frenje, N. V. Kabadi, M. Gatu Johnson, C. K. Li, V. Glebov, C. Stoeckl, B. Lahmann, P. J. Adrian, S. P. Regan, A. Birkel, F. H. Séguin, and R. D. Petrasso, "Fuel–Shell Mix and Yield Degradation in Kinetic Shock-Driven Inertial Confinement Fusion Implosions," Phys. Plasmas **29**, 072710 (2022).

R. Sobolewski, "Optical Detectors and Sensors," in *Handbook of Superconductivity: Characterization and Applications*, 2nd ed., edited by D. A. Cardwell, D. C. Larbalestier, and A. I. Braginski (Taylor & Francis, New York, 2022), Vol. III, Chap. H4.5, pp. 780–796.

R. B. Spielman, "Pulsed-Power Innovations for Next-Generation, High-Current Drivers," IEEE Trans. Plasma Sci. **50**, 2621 (2022).

B. A. Storer, M. Buzzicotti, H. Khatri, S. M. Griffies, and H. Aluie, "Global Energy Spectrum of the General Oceanic Circulation," Nat. Commun. **13**, 5314 (2022).

D. Turnbull, J. Katz, D. E. Hinkel, P. Michel, T. Chapman, L. Divol, E. Kur, S. MacLaren, A. L. Milder, M. Rosen, A. Shvydky, G. B. Zimmerman, and D. H. Froula, "Beam Spray Thresholds in ICF-Relevant Plasmas," Phys. Rev. Lett. **129**, 025001 (2022).

N. D. Urban, K. R. P. Kafka, K. L. Marshall, and S. G. Demos, "Laser-Induced Damage Characteristics of Fused Silica Surfaces Polished to Different Depths Using Fluid Jet Polishing," Opt. Eng. **61**, 071604 (2022).

K. M. Woo, R. Betti, C. A. Thomas, C. Stoeckl, K. Churnetski, C. J. Forrest, Z. L. Mohamed, B. Zirps, S. P. Regan, T. J. B. Collins, W. Theobald, R. C. Shah, O. M. Mannion, D. Patel, D. Cao, J. P. Knauer, V. Yu. Glebov, V. N. Goncharov, P. B. Radha, H. G. Rinderknecht, R. Epstein, V. Gopalaswamy, F. J. Marshall, S. T. Ivancic, and E. M. Campbell, "Analysis of Core Asymmetries in Inertial Confinement Fusion Implosions Using Three-Dimensional Hot-Spot Reconstruction," Phys. Plasmas **29**, 082705 (2022).

Y. Zou, L. Chamandy, J. Carroll-Nellenback, E. G. Blackman, and A. Frank, "Jets from Main Sequence and White Dwarf Companions During Common Envelope Evolution," Mon. Not. R. Astron. Soc. **514**, 3041 (2022).

Forthcoming Publications

H. Aluie, S. Rai, H. Yin, A. Lees, D. Zhao, S. M. Griffies, A. Adcroft, and J. K. Shang, "Effective Drift Velocity from Turbulent Transport by Vorticity," to be published in Physical Review Fluids.

A. F. Antoniadis, D. Drikakis, P. S. Farmakis, L. Fu, I. Kokkinakis, X. Nogueira, P. A. S. F. Silva, M. Skote, V. Titarev, P. Tsoutsanis, "UCNS3D: An Open-Source High-Order Finite-Volume Unstructured CFD Solver," to be published in Computer Physics Communications.

N. Birge, V. Geppert-Kleinrath, C. Danly, B. Haines, S. T. Ivancic, J. Jorgenson, J. Katz, E. Mendoza, A. T. Sorce, L. Tafoya, C. Wilde, and P. Volegov, "Instrument Design for an Inertial Confinement Fusion Ion Temperature Imager," to be published in Review of Scientific Instruments.

E. G. Blackman and S. V. Lebedev, "Persistent Mysteries of Jet Engines, Formation, Propagation, and Particle Acceleration: Have They Been Addressed Experimentally?" to be published in New Astronomy Reviews.

L. Ceurvorst, W. Theobald, M. J. Rosenberg, P. B. Radha, C. Stoeckl, R. Betti, K. S. Anderson, J. A. Marozas, V. N. Goncharov, E. M. Campbell, C. M. Shuldberg, R. W. Luo, W. Sweet, L. Aghaian, L. Carlson, B. Bachmann, T. Döppner, M. Hohenberger, K. Glize, R. H. H. Scott, A. Colaïtis, and S. P. Regan, "Development of an X-Ray Radiography Platform to Study Laser-Direct-Drive Energy Coupling at the National Ignition Facility," to be published in Review of Scientific Instruments.

F. Coppari, D. E. Fratanduono, M. Millot, R. G. Kraus, A. Lazicki, J. R. Rygg, R. F. Smith, and J. H. Eggert, "X-Ray Diffraction Measurements and Pressure Determination in Nanosecond Compression of Solids up to 600 GPa," to be published in Physical Review B.

D. H. Edgell, J. Katz, R. Raimondi, D. Turnbull, and D. H. Froula, "Scattered-Light Uniformity Imager for Diagnosing Laser Absorption Asymmetries on OMEGA," to be published in Review of Scientific Instruments.

C. J. Forrest, A. Crilly, A. Schwemmlein, M. Gatu-Johnson, O. M. Mannion, B. Appelbe, R. Betti, V. Yu. Glebov, V. Gopalaswamy, J. P. Knauer, Z. L. Mohamed, P. B. Radha, S. P. Regan, C. Stoeckl, and W. Theobald, "Measurements of Low-Mode Asymmetries in Areal Density of Laser-Direct-Drive Deuterium–Tritium Cryogenic Implosions on OMEGA Using Neutron Spectroscopy," to be published in Review of Scientific Instruments (invited).

H. Geppert-Kleinrath, Y. Kim, K. Meany, M. Rubery, J. Carrera, and E. Mariscal, "Gas Scintillation Mitigation in Gas Cherenkov Detectors for Inertial Confinement Fusion," to be published in Review of Scientific Instruments (invited).

R. Ghosh, X. Liu, and M. Z. Yates, "Flexible Copper Metal Circuits via Desktop Laser Printed Masks," to be published in Advanced Materials Technologies.

M. G. Gorman, S. Elatresh, A. Lazicki, M. M. E. Cormier, S. A. Bonev, D. McGonegle, R. Briggs, A. L. Coleman, S. D. Rothman, L. Peacock, J. V. Bernier, F. Coppari, D. G. Braun, J. R. Rygg, D. E. Fratanduono, R. Hoffmann, G. W. Collins, J. S. Wark, R. F. Smith, J. H. Eggert, and M. I. McMahon, "Experimental Observation of Open Structures in Elemental Magnesium at Terapascal Pressures," to be published in Nature Physics.

D. S. Hodge, A. F. T. Leong, S. Pandolfi, K. Kurzer-Ogul, D. S. Montgomery, H. Aluie, C. Bolme, T. Carver, E. Cunningham, C. B. Curry, M. Dayton, F.-J. Decker, E. Galtier, P. Hart, D. Khaghani, H. J. Lee, K. Li, Y. Liu, K. Ramos, J. Shang, S. Vetter, B. Nagler, R. L. Sandberg, and A. E. Gleason, "Multi-Frame, Ultrafast, X-Ray Microscope for Imaging Shockwave Dynamics," to be published in Optics Express.

N. Kabadi, P. Adrian, C. Stoeckl, A. Sorce, H. W. Sio, M. Bedzyk, T. Evans, S. Ivancic, J. Katz, J. Knauer, J. Pearcy, D. Weiner, R. Betti, A. Birkel, D. Cao, M. Gatu Johnson, S. P. Regan, R. D. Petrasso, and J. Frenje, "The Phase-2 Particle X-Ray Temporal Diagnostic for Simultaneous Measurement of Multiple X-Ray and Nuclear Emission Histories from OMEGA Implosions," to be published in Review of Scientific Instruments (invited).

A. Krygier, C. E. Wehrenberg, J. V. Bernier, S. Clarke, A. L. Coleman, F. Coppari, T. S. Duffy, M. G. Gorman, M. Hohenberger, D. Kalantar, G. E. Kemp, S. F. Khan, C. Krauland, R. G. Kraus, A. Lazicki, M. J. MacDonald, A. G. MacPhee, E. Marley, M. C. Marshall, M. May, J. M. McNaney, M. Millot, Y. Ping, P. L. Poole, J. R. Rygg, M. Schneider, H. Sio, S. Stoupin, D. Swift, C. Yeamans, T. Zobrist, R. F. Smith, and J. H. Eggert, "X-Ray Source Characterization and Sample Heating on X-Ray Diffraction Experiments at the National Ignition Facility," to be published in Physics of Plasmas.

R. N. Markwick, A. Frank, J. Carroll-Nellenback, E. G. Blackman, P. M. Hartigan, S. V. Lebedev, D. R. Russell, J. W. D. Halliday, and L. G. Suttle, "Morphology of Shocked Lateral Outflows in Colliding Hydrodynamic Flows," to be published in Physics of Plasmas.

S. Pandolfi, T. Carver, D. Hodge, A. F. T. Leong, K. Kurzer-Ogul, P. Hart, E. Galtier, D. Khaghani, E. Cunningham, B. Nagler, H. J. Lee, C. Bolme, K. Ramos, K. Li, Y. Liu, A. Sakdinawat, S. Marchesini, P. M. Kozlowski, C. B. Curry, F.-J. Decker, S. Vetter, J. Shang, H. Aluie, M. Dayton, D. S. Montgomery, R. L. Sandberg, and A. E. Gleason, "Novel Fabrication Tools for Dynamic Compression Targets with Engineered Voids Using Photolithography Methods," to be published in Review of Scientific Instruments.

J. J. Pigeon, S. Ya. Tochitsky, D. Tovey, G. J. Louwrens, I. Ben-Zvi, and C. Joshi, "Interferometric Measurements of the Resonant Nonlinearity of IR-Active Minor Air Constituents," to be published in the Journal of the Optical Society of America B.

L. Savino, V. N. Goncharov, I. V. Igumenshchev, and S. Atzeni, "Studies on Dynamical Shell Formation for Direct-Drive Laser Fusion," to be published in Il Nuovo Cimento.

M. Sharpe, W. T. Shmayda, and J. J. Ruby, "Influence of Heat Treatments on the Near-Surface Tritium Concentration Profiles," to be published in IEEE Transactions on Plasma Science.

C. Stoeckl, D. Cao, L. Ceurvorst, A. Kalb, J. Kwiatkowski, A. Shvydky, and W. Theobald, "Beam-Pointing Verification Using X-Ray Pinhole Cameras on the 60-Beam OMEGA Laser," to be published in Review of Scientific Instruments.

M. P. Valdivia, G. Perez-Callejo, V. Bouffetier, G. W. Collins IV, C. Stoeckl, T. Filkins, C. Mileham, M. Romanofsky, I. A. Begishev, W. Theobald, S. R. Klein, M. K. Schneider, F. N. Beg, A. Casner, and D. Stutman, "Current Advances on Talbot–Lau X-Ray Imaging Diagnostics for High-Energy-Density Experiments," to be published in Review of Scientific Instruments (invited).

K. Weichman, J. P. Palastro, A. P. L. Robinson, R. Bingham, and A. V. Arefiev, "Underdense Relativistically Thermal

Plasma Produced by Magnetically Assisted Direct Laser Acceleration," to be published in Physical Review Research.

S. Zhang, V. V. Karasiev, N. Shaffer, D. I. Mihaylov, K. Nichols, R. Paul, R. M. N. Goshadze, M. Ghosh, J. Hinz, R. Epstein, S. Goedecker, and S. X. Hu, "First-Principles Equation of State of CHON Resin for Inertial Confinement Fusion Applications," to be published in Physical Review E.

Conference Presentations

K. Churnetski, K. M. Woo, W. Theobald, P. B. Radha, R. Betti, V. Gopalaswamy, I. V. Igumenshchev, S. T. Ivancic, M. Michalko, R. C. Shah, C. Stoeckl, C. A. Thomas, and S. P. Regan, "Three-Dimensional Hot-Spot X-Ray Emission Tomography from Cryogenic Deuterium–Tritium Direct-Drive Implosions on OMEGA," presented at the 9th Plasmas in Super-Intense Laser Fields, Erice, Italy, 1–11 July 2022.

F. García-Rubio, R. Betti, J. Sanz, and H. Aluie, "Magneto-hydrodynamic Instabilities in Ablation Fronts and Coronal Plasmas," presented at the Plasma Science and Technology Seminar, Princeton, NJ, 5 July 2022.

W. T. Shmayda, "Fusion-Related Tritium Research and Development at the Laboratory for Laser Energetics," presented at the 20th Tritium Users Group, Culham, UK, 5–6 July 2022.

C. Deeney, "The Laboratory for Laser Energetics: An Overview," presented at the Jill Hruby Visit, Rochester, NY, 6 July 2022.

The following presentations were made at the 22nd Biennial Conference of the APS Topical Group on Shock Comprehension of Condensed Matter, Anaheim, CA, 10–15 July 2022:

M. K. Ginnane, D. N. Polsin, X. Gong, M. C. Marshall, T. R. Boehly, J. R. Rygg, G. W. Collins, A. Lazicki, R. Kraus, J. H. Eggert, D. E. Fratanduono, J.-P. Davis, C. A. McCoy, C. Seagle, and S. Root, "X-Ray Diffraction of Shocked Platinum."

X. Gong, M. C. Marshall, M. K. Ginnane, R. Boni, J. R. Rygg, and G. W. Collins, "Extending Optical Pyrometry for Temperature Measurements Below 5000 K."

E. Smith, D. T. Bishel, D. A. Chin, J. R. Rygg, G. W. Collins, and J. J. Ruby, "Shock-Wave Properties in High-Energy-Density Environments."

S. Zhang, S. X. Hu, M. C. Marshall, J. R. Rygg, A. Shvydky, D. Haberberger, V. N. Goncharov, T. R. Boehly, G. W. Collins, D. E. Fratanduono, and A. E. Lazicki, "Molecular-Dynamics Simulations and Laser-Drive Shock-Release Experiments on Polystyrene Under Inertial Confinement Fusion Conditions."

S. Zhang, R. Paul, M. Ghosh, T.-A. Suer, M. Millot, M. A. Morales, F. Malone, R. Jeanloz, E. Zurek, S. X. Hu, J. R. Rygg, and G. W. Collins, "Equations of State and Phase Transformations in Rocky Materials to TPa Pressures."

T. R. Joshi, R. B. Spielman, E. N. Hahn, M. Bailly-Grandvaux, T. Cordova, R. E. Turner, J. E. Garay, and F. N. Beg, "Investigation of Laser Ablation as a Function of Pulse Length in Silicon at 10^{15} W/cm^2 Intensities," presented at the Association of Nepali Physicists in America, virtual, 15–17 July 2022.

The following presentations were made at the Research at High Pressure, Holderness, NH, 17–22 July 2022:

D. A. Chin, P. M. Nilson, D. T. Bishel, B. J. Henderson, R. Paul, D. N. Polsin, M. Signor, S. X. Hu, M. K. Ginnane, X. Gong, E. A. Smith, A. Coleman, F. Coppari, Y. Ping, J. J. Ruby, D. Trail, A. Amouretti, M. Harmand, R. Torchio, J. R. Rygg, and G. W. Collins, "X-Ray Absorption Fine Structure Spectroscopy of Iron Compounds at High-Energy-Density Conditions."

H. Pantell, G. W. Collins, and J. R. Rygg, "The Rosenfeld Viscosity and Phase Changes in Silicates."

Z. K. Sprowal, L. E. Hansen, M. F. Huff, D. N. Polsin, D. G. Hicks, T. R. Boehly, J. R. Rygg, and G. W. Collins, "Accessing High-Density States in D_2 Using Double Shock."

T.-A. Suer, X. Gong, M. C. Marshall, S. Zhang, M. K. Ginnane, M. Huff, A. LaPierre, D. A. Chin, J. R. Rygg, and G. W. Collins, "A New Phase of Aluminum Oxide Observed at ~450 GPa."

T. J. B. Collins and P. Tzeferacos, "Computational Modeling at the University of Rochester's Laboratory for Laser Energetics and Flash Center: Advanced Simulation Tools for High-Energy-Density Physics," presented at Materials Science in Extreme Environments, virtual, 2 August 2022.

The following presentations were made at the J. Stiles Visit, Rochester, NY, 3 August 2022:

R. B. Spielman, P. Tzeferacos, S. G. Demos, S. P. Regan, and C. Deeney, "Pulsed Laser Lethality."

J. D. Zuegel, "The Laboratory for Laser Energetics: An Overview."

P. M. Nilson, F. J. Marshall, T. J. B. Collins, R. Epstein, D. T. Bishel, D. A. Chin, J. Kendrick, D. Guy, M. Krieger, W. J. Armstrong, D. Haberberger, S. M. Fess, D. Wasilewski, T. Cracium, M. J. Bonino, J. Katz, S. T. Ivancic, C. Stoeckl, V. N. Goncharov, D. H. Froula, J. J. Ruby, and R. Peters, "Flow Visualization at Ultrahigh Pressure," presented at the University of Michigan Talk, Ann Arbor, MI, 5 August 2022.

G. Bruhaug, J. L. Shaw, H. Rinderknecht, M. S. Wei, J. R. Rygg, G. W. Collins, M. Freeman, F. Merrill, L. P. Neukirch, C. Wilde, C. A. Walsh, and E. Tubman, "Laser-Plasma-Acceleration–Driven Electron Radiography on the OMEGA EP Laser," presented at the North American Particle Accelerator Conference, Albuquerque, NM, 7–12 August 2022.

The following presentations were made at the LaserNetUS User Group Meeting, Fort Collins, CO, 16–18 August 2022:

A. E. Raymond, S.-W. Bahk, I. A. Begishev, S. Bucht, C. Dorrer, C. Feng, C. Jeon, C. Mileham, R. G. Roides, M. Spilatro, B. Webb, and J. Bromage, "Status of the MTW-OPAL Laser System, a Prototype All-OPCPA System for Ultra-Intense Science."

H. G. Rinderknecht, G. Bruhaug, K. Weichman, M. VanDusen-Gross, J. P. Palastro, M. S. Wei, A. Arefiev, T. Wang, T. Toncian, A. Laso Garcia, D. Doria, K. Spohr, H. J. Quevedo, T. Ditmire, J. Williams, A. Haid, and D. Stutman, "Initial Experimental Results from Relativistically Transparent Magnetic Filament Experiments."

P. Tzeferacos, "*FLASH*—An Open Computational Tool for Laser-Driven High-Energy-Density Physics."

M. VanDusen-Gross, K. Weichman, D. R. Harding, A. Arefiev, A. G. MacPhee, A. Haid, and H. G. Rinderknecht, "Designing and Testing Optical Concentrator Targets for High-Intensity Lasers."

K. L. Marshall, J. U. Wallace, N. Urban, K. R. P. Kafka, and S. G. Demos, "The Impact of π-Electron Delocalization on the Chiroptical Properties, Mesophase Stability, and Laser-Damage Resistance of Chiral Dopants and Liquid Crystal Host Mixtures in High-Peak-Power Laser Applications," presented at Liquid Crystals XXVI, San Diego, CA, 21–25 August 2022 (invited).

D. Chakraborty, B. N. Mills, J. Cheng, S. A. Gerber, and R. Sobolewski, "Maximum A-Posteriori Probability THz Parameter Extraction for Pancreatic Ductal Adenocarcinoma," presented at the 47th International Conference on Infrared, Millimeter and Terahertz Waves, Delft, Netherlands, 28 August–2 September 2022.

The following presentations were made at the 13th International Laser Operations Workshop, Livermore, CA, 30 August–1 September 2022:

M. Barczys, D. Canning, M. J. Guardalben, B. E. Kruschwitz, T. McKean, J. O'Sullivan, N. Savidis, and L. J. Waxer, "OMEGA EP Updates from 2021–2022."

D. Canning, "Omega Facility Update."

A. Consentino, G. Pien, S. Householder, M. Labuzeta, D. Canning, J. Puth, and S. F. B. Morse, "LLE's Experience with Mix of Remote and In-Person PI."

M. Heimbueger, W. R. Donaldson, S. Sampat, and L. J. Waxer, "New Temporal Diagnostic Scheme Based on Semiconductor Technology."

E. M. Hill, C. Dorrer, J. D. Zuegel, S. Herman, A. Bolognesi, N. Ekanayake, K. Gibney, and M. Spilatro, "Overview of the Fourth-Generation Laser for Ultrabroadband eXperiments (FLUX) at the Laboratory for Laser Energetics."

S. T. Ivancic, R. B. Brannon, T. Filkins, J. Katz, A. Sorce, D. Mastrosimone, N. Pelepchan, M. Michalko, J. Tellinghuisen, B. Stanley, and J. Frelier, "Experimental Diagnostic Development and Integration at OMEGA."

M. Labuzeta, S. F. B. Morse, J. Puth, D. Canning, A. Consentino, and S. Householder, "The Role of Availability and Effectiveness Performance Metrics in the Omega Sustainment Plan."

C. Mileham, S.-W. Bahk, I. A. Begishev, S. Bucht, R. Cuffney, C. Dorrer, C. Feng, T. Filkins, C. Jeon, R. Roides, J. L. Shaw, M. Spilatro, C. Stoeckl, B. Webb, J. D. Zuegel, and J. Bromage, "An Overview of the Multi-Terawatt Facility Operational Paradigm."

S. Sampat, B. Ehrich, M. Heimbueger, S.-W. Bahk, J. Kwiatkowski, L. J. Waxer, B. E. Kruschwitz, and S. F. B. Morse, "Current Status of On-Target Uniformity Improvements on the OMEGA 60 Laser."

A. Sorce, G. Bogan, E. Power, R. Raimondi, D. Guy, M. Romanofsky, S. Ali, and P. M. Celliers, "OMEGA High-Resolution Velocimeter Laser Replacement Project: Considerations and Design Challenges for Integration at OMEGA."

S. Zhang, "Isentropes and Equations of State of Solid Hydrogen—Perspectives from Theory and Calculations," presented at the Center for Matter at Atomic Pressures Seminar, virtual, 2 September 2022.

The following presentations were made at the Laser-Induced Damage in Optical Materials 2022, Rochester, NY, 18–21 September 2022:

Z. S. Davidson, J. Wallace, Y. Sargol, N. Urban, S. G. Demos, K. L. Marshall, and S. Elhadj, "Laser Damage to Liquid Crystal Alignment Materials in Ordinary and Extraordinary Modes."

B. N. Hoffman, N. Savidis, S. Abbey, A. Kalb, A. L. Rigatti, and S. G. Demos, "Characterization of Particulate Contamination Inside the OMEGA EP Grating Compressor Chamber."

H. Huang, T. Z. Kosc, T. J. Kessler, and S. G. Demos, "Modeling of Transverse Stimulated Raman Scattering in KDP/DKDP Polarization Control Plates."

K. R. P. Kafka, "Cumulative Damage Probability Algorithm: Advantages and Limitations."

J. B. Oliver, A. A. Kozlov, J. Spaulding, C. Smith, S. MacNally, D. Coates, K. R. P. Kafka, A. L. Rigatti, and S. G. Demos, "Striated Composite Layers for High-Fluence Applications."

Y. Sargolzaeiaval, J. U. Wallace, N. D. Urban, S. G. Demos, K. L. Marshall, and S. Elhadj, "Optimized Liquid Crystals for High-Power Laser Beam Manipulation: An Evaluation and Feasibility Study."

N. D. Urban, K. R. P. Kafka, J.-M. Jang, K. L. Marshall, S. G. Demos, R. Emms, and D. Walker, "Laser-Damage Performance of Fused Silica and Potassium Dihydrogen Phosphate Surfaces Finished by Fluid Jet Polishing."

The following presentations were made at The International Committee on Ultrahigh-Intensity Lasers, Jeju, South Korea, 18–23 September 2022:

S.-W. Bahk, I. A. Begishev, R. Roides, C. Mileham, R. Cuffney, C. Feng, B. Webb, C. Jeon, M. Spilatro, S. Bucht, C. Dorrer, and J. Bromage, "Experimental Verification of Pump Wavefront Transfer in an Optical Parametric Amplifier."

S.-W. Bahk, S. Sampat, M. Heimbueger, J. Kwiatkowski, K. A. Bauer, and L. J. Waxer, "Single-Shot Wavefront Characterization of High-Energy Focal Spots in the OMEGA Target Chamber Using a Phase Diversity Grating."

J. Bromage, S.-W. Bahk, M. Bedzyk, I. A. Begishev, S. Bucht, C. Dorrer, C. Feng, B. N. Hoffman, C. Jeon, C. Mileham, J. B. Oliver, A. Raymond, R. G. Roides, E. M. Schiesser, K. Shaughnessy, M. J. Shoup III, M. Spilatro, B. Webb, D. Weiner, and J. D. Zuegel, "Commissioning and Performance of MTW-OPAL, an All-OPCPA System."

W. T. Shmayda, H. Mutha, E. Dombrowski, and K. Ryan, "SPARC Tokamak Tritium Processing Systems," presented at the 32nd Symposium on Fusion Technology, Dubrovnik, Croatia, 18–23 September 2022.

The following presentations were made at the 36th European Conference on Laser Interaction with Matter, Frascati, Italy, 19–23 September 2022:

R. Betti, V. Gopalaswamy, J. P. Knauer, D. Patel, A. Lees, K. M. Woo, C. A. Thomas, D. Cao, O. M. Mannion, R. C. Shah, C. J. Forrest, Z. L. Mohamed, C. Stoeckl, V. Yu. Glebov, S. P. Regan, D. H. Edgell, M. J. Rosenberg, I. V. Igumenshchev, P. B. Radha, K. S. Anderson, J. R. Davies, T. J. B. Collins, V. N. Goncharov, K. Churnetski, W. Theobald, A. A. Solodov, D. Turnbull, D. H. Froula, E. M. Campbell, R. T. Janezic, D. R. Harding, M. J. Bonino, S. Sampat, K. A. Bauer, S. F. B. Morse, M. Gatu Johnson, R. D. Petrasso, C. K. Li, and J. A. Frenje, "High-Performance Implosions on OMEGA and Prospects for Direct-Drive Ignition with Multimegajoule Lasers."

C. Dorrer, "The Fourth-Generation Laser for Ultrabroadband eXperiments (FLUX)."

D. Turnbull, C. Dorrer, D. H. Edgell, R. K. Follett, V. N. Goncharov, A. M. Hansen, A. L. Milder, K. L. Nguyen, J. P. Palastro, R. C. Shah, J. D. Zuegel, D. H. Froula, A. Colaïtis, and P. Michel, "Broadband Lasers will be a Game Changer for Inertial Confinement Fusion—Foundation for this Belief, Plans for Further Validation" (invited).

D. Haberberger, "Overview of Plasma Experiments and Diagnostics on Laser Facilities," presented at the HRMT-62 Collaboration Meeting at the European Council for Nuclear Research, Geneva, Switzerland, 26–27 September 2022.

The following presentations were made at the 8th Target Fabrication Workshop, Oxford, UK, 26-28 September 2022:

M. J. Bonino, D. R. Harding, A. Behlok, T. Cracium, S. Fess, S. Karim, I. Knudson, K. Lintz, N. Redden, D. Wasilewski, M. D. Wittman, J. Fooks, and K. Knolker, "Target Fabrication Capabilities at LLE."

D. R. Harding, S. M. Fess, M. J. Bonino, Y. Lu, and P. Fang, "3-D Printing Foam Targets."

D. R. Harding, J. D. Zuegel, T. B. Jones, R. Gram, M. Bobeica, Z. Bei, and W. Wang, "Technologies for Mass Producing IFE Targets and Determining Their Survival in an IFE Chamber."

UNIVERSITY OF ROCHESTER
LABORATORY FOR LASER ENERGETICS

Volume 169
October–December 2021
DOE/NA/3856-1700

LLE Review

Quarterly Report

About the Cover:

The high school students and teachers who participated in the 2021 Broad Exposure to Science and Technology (BEST) Research Program are shown engaging in various aspects of science and technology that support LLE's laser research program. They explored microscopy, spectroscopy, electronic technology, lasers, optical design, liquid crystals, and holography. The importance of continued STEM education in research, was emphasized by former LLE director, Mike Campbell, to highlight the extensive teamwork required to make advancements in laser development and scientific applications.

The BEST program was carried out at East High School within the Rochester City School District during the summer of 2021. The participants of the BEST program (shown left to right) include East High teachers Trent Russell and Gavin Jenkins, East High students Yusuf Gazali, Reganae Walters, Taiasia Gibson, and Ramir Wearen, and program coordinator Terry Kessler, LLE Diversity Manager.

LLE mentors exposed the BEST students and teachers to the key technologies that are central to the construction and operation of the OMEGA Laser System. Electronic circuits were explored by dissecting computer systems and practicing the microsoldering techniques. Lasers were brought into the classroom for demonstration and exhibition. Both interferometry and holography were experimentally explored to manufacture diffraction gratings and holographic 3-D images. In addition, liquid crystal materials were used to manufacture polarization optics and color-tuned paints. The philosophy that underpins the BEST program is that multiple early exposures help guide students in their pursuits of STEM fields and encourages them to explore the next generation of related jobs and careers.

I3113JR

The work described in this volume includes current research at the Laboratory for Laser Energetics, which is supported by New York State Energy Research and Development Authority, the University of Rochester, the U.S. Department of Energy Office of Inertial Confinement Fusion under Cooperative Agreement No. DE-NA0003856, and other agencies.

For questions or comments, contact Nickolaos Savidis, Editor, Laboratory for Laser Energetics, 250 East River Road, Rochester, NY 14623-1299, (585) 275-3413.

www.lle.rochester.edu

Printed in the United States of America
Available from
National Technical Information Services
U.S. Department of Commerce
5285 Port Royal Road
Springfield, VA 22161
www.ntis.gov

UNIVERSITY OF ROCHESTER
LABORATORY FOR LASER ENERGETICS

Volume 169
October–December 2021
DOE/NA/3856-1700

LLE Review

Quarterly Report

Contents

In Brief

This volume of LLE Review 169 covers the period from October–December 2021. Articles appearing in this volume are the principal summarized results for long-form research articles. Readers seeking a more-detailed account of research activities are invited to seek out the primary materials appearing in print, detailed in the publications and presentations section at the end of this volume.

Highlights of research presented in this volume include:

- R. C. Shah *et al.* report on a new continuum x-ray measurement to characterize hot-spot x-ray yield and hot-spot electron temperature of a series of implosions typical of current best cryogenic designs, comparing x-ray production relative to neutron production and assessing the ratio of hot-spot mix (p. 1).
- Y. Lawrence *et al.* show lowering the central density by a factor of 5 or more compared to the vapor density of deuterium–tritium (DT) at triple point can aid in achieving small hot-spot size without excessive amplification of deceleration-phase Rayleigh–Taylor instability, possibly enabling ignition and high gains in laser-direct-drive designs using lower energies (p. 5).
- D. A. Chin *et al.* experimentally identify three x-ray phases consisting of the corona, core stagnation, and afterflow using temporal, spatial, and spectral x-ray emission of implosion glow-discharge polymerization shells on OMEGA EP (p. 9).
- K. Weichman *et al.* demonstrate that the generation of underdense, relativisitically thermal plasma can be realized with currently available laser and magnetic-field–generation capabilities by leveraging two regimes of magnetically assisted direct laser acceleration (p. 12).
- R. K. Follett *et al.* create an independent-hot-spot model to predict multibeam instability behavior (p. 16). The model is applied to the absolute two-plasmon–decay instability and is shown to provide an improved description of laser–plasma instability behavior over the common-wave approach.
- S. Ressel *et al.* present the full uncertainty distributions inferred from radiography analysis in high-energy-density systems (p. 20). They demonstrate the importance of a full treatment of uncertainties, done here through Bayesian analysis, which is critical to avoid overconfidence in parameter estimates in this system due to the correlations between parameters and multiple maxima in the likelihood function introduced by typical experimantal noise sources.
- M. C. Marshall *et al.* use data from two OMEGA EP experiments to demonstrate that the chemical and thermodynamic conditions inside ice giant planets, which have inner ice layers dominated by CH_4, NH_3, and H_2O, are suitable for diamond formation (p. 23).
- V. V. Karasiev, D. I. Mihaylov, and S. X. Hu address exchange-correlation (XC) dependence thermal modeling in density-functional-theory simulations of warm dense matter and high-energy-density plasma effects by developing a thermalization framework for XC functionals and XC additive correction at the GGA level, improving simulation accuracy and agreement to experimental results (p. 26).
- S. Zhang *et al.* perform simulations from first principles and analyzed the structure, electron density, and thermodynamic properties of liquid SiO_2 at high-energy conditions to gain insights into the nature of the bonded-to-atomic transition (p. 29).
- H. Poole *et al.* conduct a feasibility study of using spatially integrated, spectrally resolved, x-ray Thomson-scattering measurements to diagnose the temperature, density, and ionization of the compressed DT shell of a cryogenic DT implosion at two-thirds convergence for both low- and high-adiabat implosions (p. 31).

- S. F. Nwabunwanne and W. R. Donaldson discuss the design and fabrication of $Al_xGa_{1-x}N$-based photodetectors with rectangular and circular asymmetric, interdigitated electrode geometries GaN/AlGaN semiconductors with an interest in high-efficiency detectors targeting semiconductor-driven ultrafast laser pulse characterization and plasma diagnostics (p. 34).
- J. Musgrave and J. Bromage investigate signal phase accumulation from pump wavefront errors and the potential impact on signal pulse compression, offering an approach to determine the suitability of a given pump laser to ensure there are no spatiotemporal pulse-broadening effects that degrade the laser's peak intensity (p. 37).
- G. W. Jenkins, C. Feng, and J. Bromage demonstrate a new method of contrast improvement that allows both contrast improvement and temporal compression in a single step—divided-pulse nonlinear compression (p. 40).
- C. Feng *et al*. develop a simple and cost-effective tool to reduce pump-induced temporal contrast degradation up to 15 dB by applying a pump-seed delay optimization and pump-to-signal noise transfer of a two-stage ultra-broadband optical parametric chirped-pulse amplifier (p. 43).
- C. Dorrer and M. Spilatro demonstrate broadband, spectrally incoherent nanosecond pulses with closed-loop pulse shaping, inspired by laser–plasma instability mitigation and improving target to high-energy laser pulse interactions (p. 46).
- S.-W. Bahk *et al*. analyze the effect of the pump beam wavefront phase and amplitude transferred to the idler and signal beam phase and amplitude using the analytic optical parametric amplifier (OPA) phase solution, wave-vector picture, and experimentally measured OPA phase using the MTW-OPAL laser (p. 50).
- T. Z. Kosc *et al*. develop and experimentally validate a modeling capability to evaluate large-aperture optics, applicable for minimizing transverse stimulated Raman scattering gain during crystal-cut optimization, predicting maximum operational fluence, and helping to develop novel designs with complex polarization control (p. 56).
- T. J. Kessler reports on the BEST Program, designed to engage underrepresented high school students and their teachers in various aspects of science and technology that support LLE's laser science and applications research (p. 58).
- J. Puth *et al*. summarize operations of the Omega Laser Facility during the first quarter of FY22 (p. 63).

Nickolaos Savidis
Editor

Bound on Hot-Spot Mix in High-Velocity, High-Adiabat Direct-Drive Cryogenic Implosions Based on Comparison of Absolute X-Ray and Neutron Yields

R. C. Shah,[1] D. Cao,[1] L. Aghaian,[2] B. Bachmann,[2] R. Betti,[1] E. M. Campbell,[1] R. Epstein,[1] C. J. Forrest,[1] A. Forsman,[2] V. Yu. Glebov,[1] V. N. Goncharov,[1] V. Gopalaswamy,[1] D. R. Harding,[1] S. X. Hu,[1] I. V. Igumenshchev,[1] R. T. Janezic,[1] L. Keaty,[2] J. P. Knauer,[1] D. Kobs,[2] A. Lees,[1] O. M. Mannion,[1] Z. L. Mohamed,[1] D. Patel,[1] M. J. Rosenberg,[1] C. Stoeckl,[1] W. Theobald,[1] C. A. Thomas,[1] P. Volegov,[3] K. M. Woo,[1] and S. P. Regan[1]

[1]Laboratory for Laser Energetics, University of Rochester
[2]Lawrence Livermore National Laboratory
[3]Los Alamos National Laboratory

Here we report on new continuum x-ray measurements to characterize hot-spot x-ray yield and hot-spot electron temperature of a series of implosions typical of current best cryogenic designs.[1] The objective of these measurements is to consider the consistency of x-ray production relative to neutron production and assess if this ratio implies hot-spot mix. Because of the insufficient time for equilibration given plasma parameters in these high-velocity implosions, there are significant differences between the hot-spot electron and ion temperature, which can influence the comparison of the x-ray and neutron yields. Based on the measured neutron yield and both hot-spot temperatures, the expected x-ray yield (assuming a pure-DT hot spot) is determined for each implosion and then compared to the measured x-ray yield. The x-ray and neutron yields are found to be consistent without invoking hot-spot mix within an estimated sensitivity corresponding to ~2% by atom, fully ionized carbon–deuterium plastic.

The x-ray yield and electron-temperature measurements were newly developed for this experiment. Approximately 30 images of each implosion were generated using an array of differentially filtered circular apertures and recorded on an absolutely calibrated image plate (IP).[2] The imaging apertures make it possible to distinguish the hot-spot x rays from a background of neutrons and coronal x rays (the spatial identification of hot spot as compared to coronal x rays was corroborated with simulation data). The x rays were filtered with Al foils in order to have four data channels. After accounting for IP response, the mean recorded energies of the channels ranged from 10 to 18 keV. In this range, the dense fuel was optically thin, and the signal level was within the dynamic range of a single scan read of the IP (consistent with the calibration). The channel measurements were used to constrain an isobaric hot-spot model, and the hot spot (assumed static) was used to calculate the volume integrated bremsstrahlung x-ray continuum using the free–free emissivity for hydrogen. [Figures 1(a)–1(c) show examples of the data, measured and modeled channel signals, and inferred spectrum for shot 96806.] Finally, a neutron-weighted electron temperature (T_e) was calculated to parameterize the hot-spot electron temperature on similar footing as the ion temperature. For the simulations, post-processed x rays were spatially and temporally selected to isolate the hot-spot contribution. The hot-spot x rays from the simulations were then filtered by the experimentally used channel responses and analyzed using the same procedure as for the data.

The measured hot-spot electron and ion temperatures for five cryogenic implosions of 25 February 2020 that are typical of current best performing designs, as well as the values from 1-D simulation, are shown in the bar plot of Fig. 2. In contrast to the x-ray yield and electron temperature, neutron yield and ion temperature are routinely measured in inertial confinement fusion experiments on OMEGA. The hot-spot ion temperature (T_i) is inferred based on the temporal width of the neutron time of flight (nTOF), which, under ideal circumstances, characterizes a neutron-weighted ion temperature. This inferred T_i will be inflated by flows, which, if anisotropic, will result in variations of the inferred value as observed from different lines of sight.[3] In our experiments, there were five independent nTOF's and shown are the maximum and minimum values of T_i for each shot. The range between the extremes was large for only the first shot, for which a target defect was observed and believed to cause a large

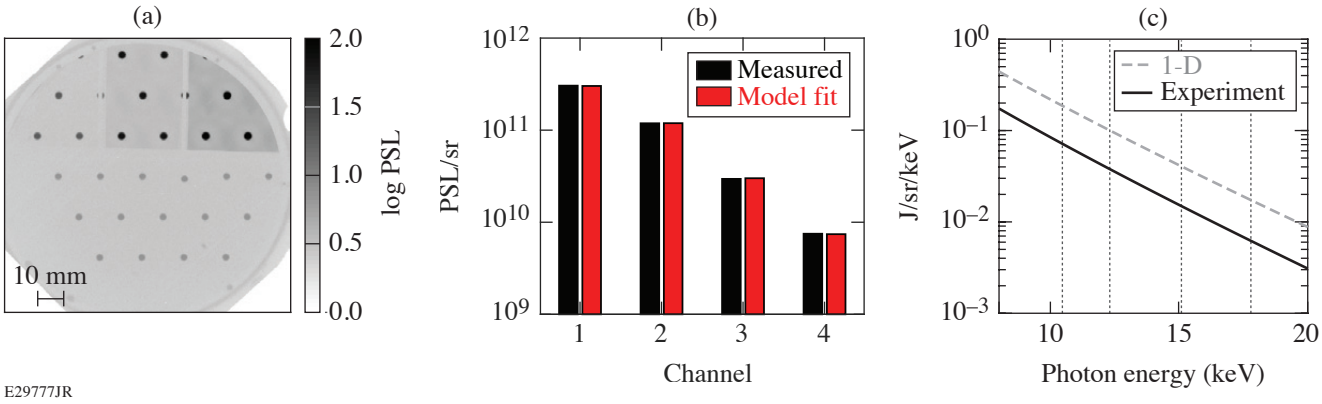

Figure 1
(a) Image-plate data for shot 96806 with image intensity reported in units of photostimulated luminescence (PSL). (b) Measured and fit channel signals. (c) The hot-spot model x-ray spectrum determined from the channel data. Dotted vertical lines indicate the mean recorded energy of each of the four imaging channels. For reference, the hot-spot model x-ray spectrum obtained from the identical analysis of the 1-D simulation is also plotted.

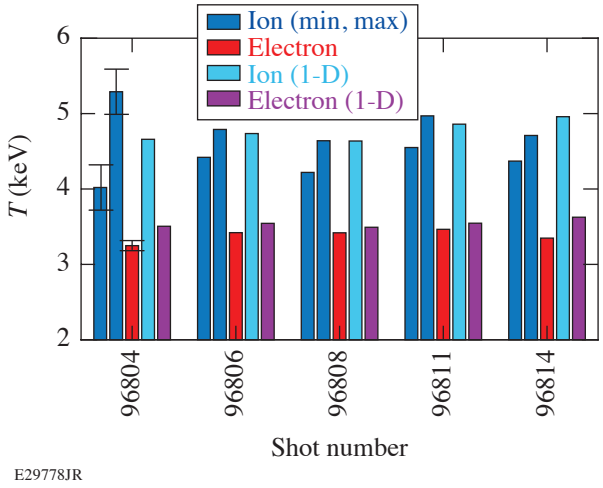

Figure 2
The measured hot-spot T_e is typically ~75% of the minimum T_i obtained from five independent lines of sight. The result is similar to what is obtained from 1-D simulations.

flow. In that case, the minimum T_i takes its lowest value. We have used the minimum nTOF T_i as the value best representative of the ion thermal conditions. Note that for the x-ray and neutron yield ratio comparison, an inflated value of T_i will increase the estimated hot-spot mix; therefore, in this sense the inferred mix quantification will be an upper bound estimate. Figure 2 also shows that the measured T_e value is typically ~75% of the minimum T_i. This degree of equilibration is similar to what is obtained in the 1-D simulation.

The predicted x-ray yield (Y_x) for a hot spot in the absence of mix is calculated using these temperatures as well as the measured neutron yield (Y_n). This result, along with the measured Y_x, is plotted in Fig. 3(a). There is a generally positive correlation of the measured x-ray and neutron yields contrasting what was reported by Ma *et al.*[4] in indirect-drive implosions of the National Ignition Campaign and for which mix was identified as a prominent issue. Additionally, since the measured and mapped values of Y_x do not significantly deviate, there is no measurable indication that mix is consistently present across these implosions. This is more explicitly shown in Fig. 3(b) as the ratio of the measured to mapped values, or x-ray enhancement. In this plot, the variability observed in the application of the model to a set of test simulations is indicated by the shaded region, and we interpret it as an estimate of the sensitivity by which we can measure an enhancement due to mix. The dashed lines in Fig. 3(b) indicate the value of the x-ray enhancement estimated for specified fractions of mix in the hot spot, accounting for the increase in both bremsstrahlung and recombination emission due to the carbon atoms. The measurement sensitivity is compromised by both the

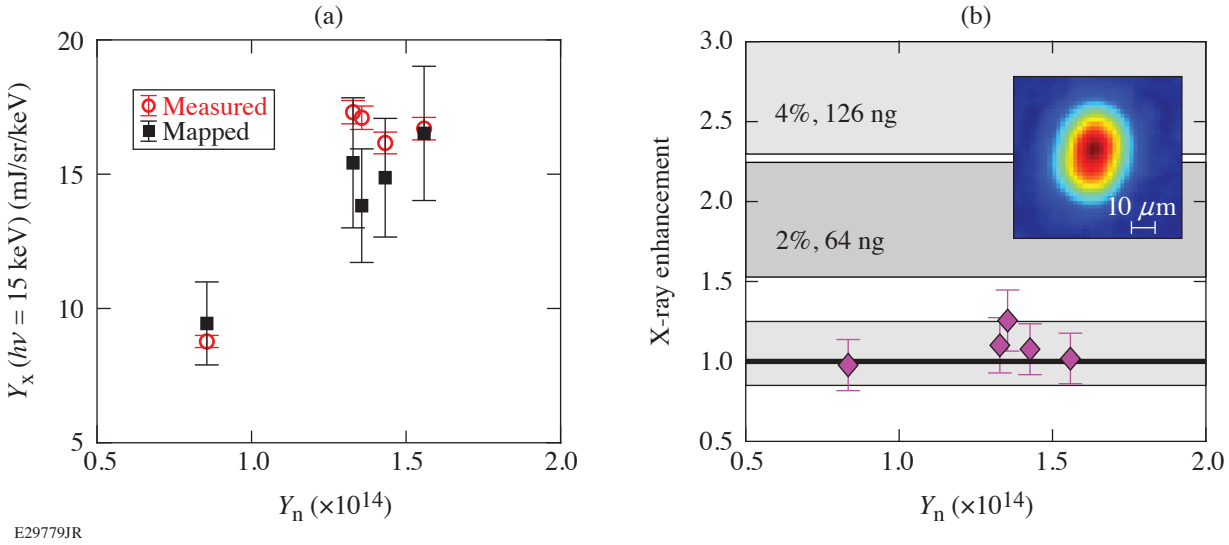

Figure 3
For each implosion, the measured Y_n, T_i, and T_e are used to calculate a mapped x-ray yield that is compared to the measured x-ray yield. (b) The x-ray enhancements fall within the systematic errors observed for the mapping (as determined by tests on a simulation database) indicated by the shaded gray region of the plot. The percentage values refer to percent-by-atom levels of CD mix required to cause the indicated level of x-ray enhancement. The inset shows the recovered hot-spot image from channel 1 for shot 96806.

error propagation (dominated by the hot-spot temperatures and indicated with error bars) as well as the model errors (indicated by the shaded region). We find no indication of hot-spot mix within the combined effect of these errors or an approximate sensitivity limited to ~2% by atom carbon–deuterium (64 ng, assuming a typical 1.2-μg hot spot). We have also extracted the hot-spot images from image-plate data using an established approximation to tomographic analysis,[5,6] applicable to the precisely machined circular apertures (General Atomics, San Diego). The inset of Fig. 3(b) shows the image with an estimated 8-μm resolution obtained from channel 1 for shot 96806. Typical of all the implosion and other channels, we do not identify the sorts of bright features which have been associated with mix in other experiments[7] in hot-spot images of these and similar implosions. It is plausible that decompression, peripheral bubbles, and residual motions, observed in multidimensional simulations[8] and also previously proposed based on experimental signatures,[9] dominate the hydrodynamic degradations without creating hot-spot mix.

In summary, measurements were presented of the x-ray yield and hot-spot electron temperature for direct-drive cryogenic implosion experiments. The comparison of the electron temperature with the ion temperature routinely characterized in the experiments was consistent with the prediction that ions and electrons remain substantially unequilibrated in the high-velocity, high-adiabat designs of present interest. The independently measured electron and ion temperatures of the hot spot with the D–T fusion neutron yield were used to estimate a corresponding x-ray yield expected from the nonequilibrium DT hot spot, assuming the absence of mix. The comparison of the measured and expected x-ray yields is consistent within the estimated sensitivity of the technique and therefore indicates that hot-spot mix, if present in these implosions, is at levels less than what the yield comparison can detect.

This material is based upon work supported by the Department of Energy National Nuclear Security Administration under Award Number DE-NA0003856, the University of Rochester, and the New York State Energy Research and Development Authority.

1. V. Gopalaswamy *et al.*, Nature **565**, 581 (2019).
2. M. J. Rosenberg *et al.*, Rev. Sci. Instrum. **90**, 013506 (2019); 029902(E) (2019).
3. T. J. Murphy, R. E. Chrien, and K. A. Klare, Rev. Sci. Instrum. **68**, 610 (1997).
4. T. Ma *et al.*, Phys. Rev. Lett. **111**, 085004 (2013).
5. B. Bachmann *et al.*, Rev. Sci. Instrum. **87**, 11E201 (2016).
6. G. Di Domenico *et al.*, Med. Phys. **43**, 294 (2016).

7. A. Pak *et al.*, Phys. Rev. Lett. **124**, 145001 (2020).
8. D. Cao *et al.*, "Understanding Origins of Observed Fusion Yield Dependencies," to be submitted to Physical Review Letters.
9. A. Bose *et al.*, Phys. Rev. E **94**, 011201(R) (2016).

Mitigation of Deceleration-Phase Rayleigh–Taylor Growth in Inertial Confinement Fusion Implosions

Y. Lawrence,[1,2] V. N. Goncharov,[2] K. M. Woo,[2] W. Trickey,[2] and I. V. Igumenshchev[2]

[1]University of Chicago
[2]Laboratory for Laser Energetics, University of Rochester

In inertial confinement fusion (ICF), small hot spots are desirable because they lower the threshold hot-spot energy required for ignition, $E_{\rm hs} > 16$ kJ $(R_{\rm hs}/50\ \mu{\rm m})^2$ (Refs. 1–4). However, they generally lead to greater implosion asymmetry due to the growth of the Rayleigh–Taylor (RT) instability on the inner shell surface during the deceleration phase. A challenge then arises of how to attain a high convergence ratio (CR, defined as the ratio of the initial inner shell radius to the hot-spot radius at peak compression), without excessively high RT growth. In this study we show that lowering the central density [by a factor of 5 or more compared to the vapor density of deuterium–tritium (DT) at triple point] has the greatest leverage in achieving small hot-spot sizes without excessive amplification of deceleration-phase RT.

First, we review some basic aspects of deceleration-phase RT growth. During the deceleration phase, initial perturbations on the inner shell surface grow exponentially because the less-dense hot spot pushes against the denser shell. Neglecting convergence effects and including only the instability drive term, $\Gamma_{\rm drive} = \int \sqrt{A_T k g}\, {\rm d}t$, where A_T is the Atwood number, g is the inner surface acceleration, and $k \cong \ell / R_{\rm hs}$ is the effective wave number ℓ [the inner surface perturbations are decomposed in spherical harmonics with the mode number ℓ (see also Ref. 5)] and $R_{\rm hs}$ is the position of the shell's inner surface. We postpone defining A_T until later in this summary and assume for now that $A_T \cong 1$. Evaluating this integral from the start of the deceleration phase until peak compression (when the hot-spot radius reaches its minimum value $R_{\rm hs,m}$), it can be shown that $\Gamma_{\rm drive} = \sqrt{2\ell}\,{\rm arcsinh}\left(\sqrt{{\rm CR_d} - 1}\right)$, where ${\rm CR_d} \equiv R_{\rm hs0} / R_{\rm hs,m}$ is the maximum hot-spot convergence ratio during shell deceleration and $R_{\rm hs0}$ is the hot-spot radius at the beginning of deceleration. So, to decrease the instability drive term, ${\rm CR_d}$ should be decreased, but to reduce the ignition threshold, $R_{\rm hs,m}$ must also be reduced. This means that the deceleration phase should start later (i.e., at a smaller radius); therefore, $R_{\rm hs0}$ needs to be reduced as well as ${\rm CR_d}$.

Now we turn to scaling laws for ${\rm CR_d}$ and $R_{\rm hs0}$ to identify the target design parameters that can achieve these desired reductions. It can be shown (following from Ref. 3) that

$$ {\rm CR_d} \sim \frac{v_{\rm imp}^{2/3}}{\alpha_{\rm inf}^{1/5} p_{\rm sh0}^{2/15}}, \tag{1} $$

where $v_{\rm imp}$ is the peak implosion velocity, $\alpha_{\rm inf}$ is the in-flight shell adiabat, and $p_{\rm sh0}$ is shell pressure at the onset of deceleration. Also,

$$ R_{\rm hs,m} = \frac{R_{\rm hs0}}{{\rm CR_d}} \sim R_0 \frac{p_0^{1/5} \alpha_{\rm inf}^{1/5}}{p_{\rm sh0}^{1/5} v_{\rm inf}^{2/3}}, \tag{2} $$

where R_0 is the initial inner surface radius and p_0 is the initial vapor (central) pressure of the target. Equations (1) and (2) show that CR_d and R_{hs0} can be reduced by lowering the initial vapor pressure p_0 and/or increasing the shell pressure at the start of deceleration p_{sh0}. The remaining reduction in RT growth for the lower-central-density design comes from the increase in the ablative stabilization and reduction in the Atwood number.

Mass ablation from the inner shell surface, characterized by an ablation velocity v_a, reduces RT growth since the hot spot preferentially ablates the RT spikes that contact the hot spot at higher temperature gradients. It can be shown (following from Refs. 6 and 7) that

$$v_a \sim \frac{\alpha_{inf}^{0.5} v_{imp}^{2.2}}{R_0 p_0^{0.2} p_{sh0}^{0.13}}, \quad \frac{v_a}{R_{hs,m}} \sim \frac{\alpha_{inf}^{0.3} v_{imp}^{2.85}}{R_0^2 p_0^{0.4} p_{sh0}^{0.07}}. \tag{3}$$

As with the deceleration-phase convergence ratio and hot-spot radius at the onset of deceleration, the mass ablation velocity v_a increases with a lower initial vapor pressure. Meanwhile, density scale lengths L_m that are higher correspond to lower Atwood numbers A_T. Following from the previously written scaling laws and Ref. 6, it can be shown that

$$L_m \sim R_0 p_0^{0.2} p_{sh0}^{0.27} \alpha_{inf}^{0.8} v_{imp}^{0.54}, \quad \frac{L_m}{R_{hs,m}} \sim v_{imp}^{1.2} p_{sh0}^{0.33}. \tag{4}$$

Equation (4) shows that L_m is larger in designs with increased shell pressure at the onset of deceleration, p_{sh0}. Taken together, the scaling laws in Eqs. (1)–(4) for CR_d, R_{hs0}, v_a, and L_m show the beneficial stabilizing effects of reducing the initial vapor density and increasing the shell pressure at the start of the deceleration phase. This is accomplished most efficiently by reducing the initial vapor pressure p_0. A lower initial vapor pressure leads to extra convergence of the central region necessary to build up its pressure and begin shell deceleration; then, because of the convergence effects, the shell pressure p_{sh0} at the beginning of deceleration increases as well. Furthermore, as will be shown in an upcoming paper, 1-D simulations in *LILAC*[8] show that low-central-density designs experience reduced CR_d and R_{hs0}, as well as increased v_a and L_m. However, the fairly weak dependence of the hot-spot convergence ratio and stabilizing terms on the initial vapor density requires that it must be significantly reduced (factor of 5 or more). While this is not feasible with nominal cryogenic targets, the new dynamic shell formation concept can achieve this reduction by controlling the strength of the blast wave and the duration of the target expansion phase.[9]

To validate these predictions, we use 2-D hydrodynamic simulations in *DEC2D*[10] to study perturbation amplification during shell deceleration for two dynamic shell designs driven by shorter and longer laser pulses. In Ref. 11, one can find details of the target dimensions and pulse shapes that produce central densities of 0.6 mg/cm^3 and 0.12 mg/cm^3, respectively. Figure 1 shows density maps for the two dynamic shell designs taken at times when the neutron production reaches $\dot{N} \cong 5 \times 10^{26}\,s^{-1}$. The perturbation amplification is significantly reduced in the lower-central-density design [Fig. 1(b)] compared to the high-central-density design [Fig. 1(a)], despite the smaller hot-spot size, in agreement with the scaling arguments described earlier. Similarly, Fig. 2(a), which shows the mode $\ell = 20$ growth for the two dynamic shell designs, again confirms larger stabilization effects in the lower-density design. Figure 2(b) compares even-mode spectra for the two designs. The greatest RT growth suppression for the lower-density design occurs at mid- and higher-mode numbers, while the improvement for the low-mode numbers is slightly more modest.

Motivated by various scaling laws, we have demonstrated with 2-D simulations that reducing the initial central density in ICF targets leads to smaller hot spots (reducing hot-spot energies required for ignition) and, at the same time, suppresses deceleration RT growth. The required central-density reduction can be achieved using the new dynamic shell-formation concept. These results show a promising path to achieving ignition and high gains in laser-direct-drive designs at moderate laser energies $E_{laser} \sim 1$ MJ.

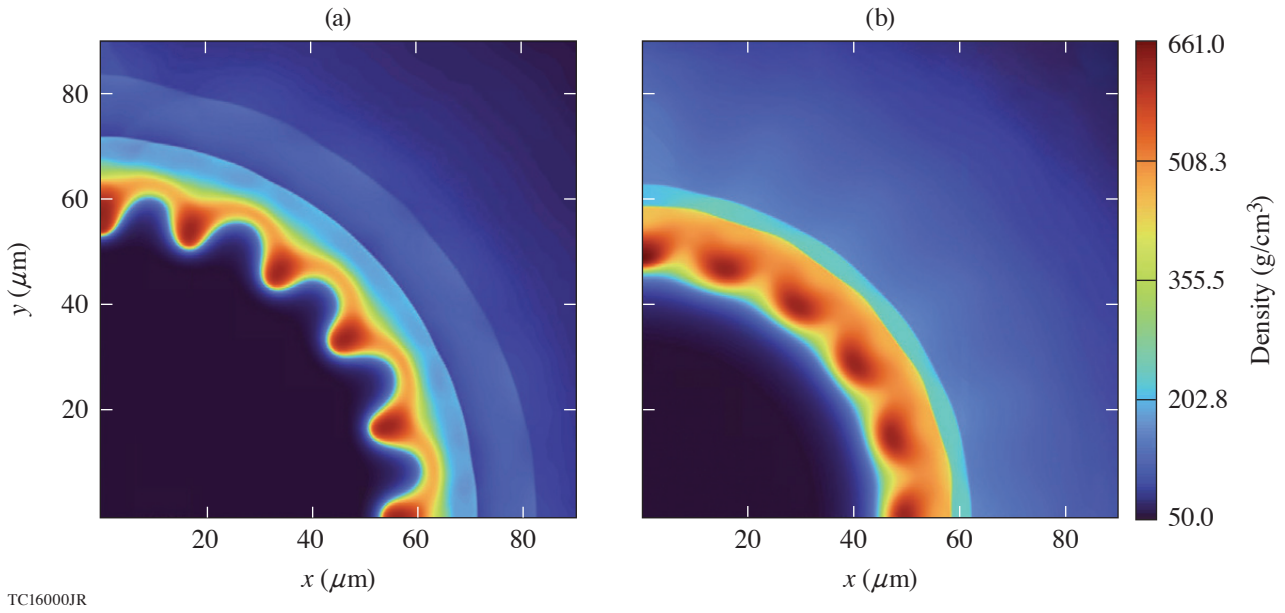

Figure 1
Two-dimensional density maps from mode $\ell = 20$ *DEC2D* simulations for the dynamic shell designs with (a) higher and (b) lower central densities (as described in Ref. 11), near stagnation at times of an equal neutron-production rate of $\dot{N} \cong 5 \times 10^{26}$ s^{-1}.

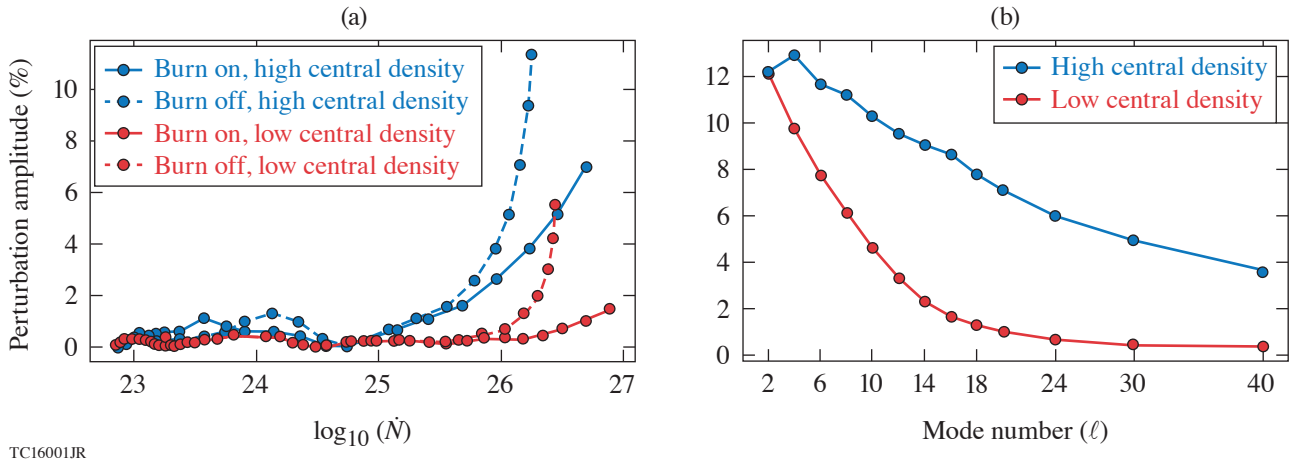

Figure 2
(a) Deceleration RT mode $\ell = 20$ evolution for dynamic shell designs with high/low central densities and alpha heating turned on or off. (b) Deceleration RT mode spectra with alpha heating turned on, taken at a neutron-production rate of $\dot{N} \cong 5 \times 10^{26}$ s^{-1} for the dynamic shell designs with high/low central densities. (Lines are used to guide the eye and do not represent fits.)

Funding was provided by the ARPA-E BETHE Grants No. DEFOA-0002212 and DE-AR0001272 and DOE OFES Award No. DE-SC0017951. This material is based upon work supported by the Department of Energy National Nuclear Security Administration under Award Number DE-NA0003856, the University of Rochester, and the New York State Energy Research and Development Authority.

1. J. D. Lindl, *Inertial Confinement Fusion: The Quest for Ignition and Energy Gain Using Indirect Drive* (Springer, New York, NY, 1998).
2. S. Atzeni and J. Meyer-ter-Vehn, *The Physics of Inertial Fusion: Beam Plasma Interaction, Hydrodynamics, Hot Dense Matter*, 1st ed., International Series of Monographs on Physics, Vol. **125** (Oxford University Press, Oxford, 2004).
3. V. N. Goncharov *et al.*, Phys. Plasmas **21**, 056315 (2014).
4. V. N. Goncharov *et al.*, Plasma Phys. Control. Fusion **59**, 014008 (2017).
5. V. N. Goncharov *et al.*, Phys. Plasmas **7**, 5118 (2000).
6. R. Betti *et al.*, Phys. Plasmas **8**, 5257 (2001).
7. C. D. Zhou and R. Betti, Phys. Plasmas **14**, 072703 (2007).
8. J. Delettrez *et al.*, Phys. Rev. A **36**, 3926 (1987).
9. V. N. Goncharov *et al.*, Phys. Rev. Lett. **125**, 065001 (2020).
10. K. M. Woo *et al.*, Phys. Plasmas **25**, 052704 (2018).
11. W. Trickey *et al.*, Front. Phys. **9**, 784258 (2021).

Emission Phases of Implosion X-Ray Sources for Absorption Spectroscopy

D. A. Chin,[1,2] J. J. Ruby,[1,2] P. M. Nilson,[1] D. T. Bishel,[1,2] F. Coppari,[3] Y. Ping,[3] A. L. Coleman,[3] R S. Craxton,[1] J. R. Rygg,[1,2,4] and G. W. Collins[1,2,4]

[1]Laboratory for Laser Energetics, University of Rochester
[2]Department of Physics and Astronomy, University of Rochester
[3]Lawrence Livermore National Laboratory
[4]Department of Mechanical Engineering, University of Rochester

At LLE's Omega Laser Facility, thin plastic shells were directly driven with ~20 kJ, resulting in a time-integrated x-ray yield of ~10^{12} ph/eV/sr at 7 keV. Using temporally, spatially, and spectrally discriminating diagnostics, three x-ray emission phases were identified: corona emission produced by the laser ablation of the shell, core stagnation, and afterglow emission due to the expanding hot material after stagnation. The newly measured corona and afterglow emission phases account for ~25% of the total x-ray signal and produce x-ray emission at a different time or larger radius than previously considered. The resulting implications of this additional emission for x-ray absorption fine structure (XAFS) spectroscopy are discussed.

This work presents a comprehensive measurement of the temporal, spatial, and spectral x-ray emission of implosion GDP (glow-discharge polymerization) shells on the OMEGA Laser System and identifies three experimental x-ray emission phases consisting of the corona, core stagnation, and afterglow. During the corona phase, the laser illuminates the shell, producing x-ray emission and driving a shock through the shell, causing the material to release inward. When the remaining material reaches the center, it stagnates, reaching Gbar pressures and producing a bright x-ray flash. After stagnating, the remaining material decompresses at Gbar pressures, remaining hot enough to emit x rays for a brief period of time. A schematic of each x-ray emission phase is shown in Fig. 1. To characterize the different emission phases, x-ray emission models were verified using a hydrodynamic simulation and fit to experimental data. The details of each emission phase are shown in Table I.

Table I: Fraction of the total emission in each phase obtained by fitting the streaked spectrum. The fractions are shown along with the 68% credible interval, which was calculated from uncertainty in the fit along with the variability between shots. The time duration was also calculated from the fit and represents the time interval that contains 95% of the signal. Lastly, the diameter was estimated from the time-integrated and time-resolved imaging.

	Corona	Core	Afterglow
Signal fraction	12^{+2}_{-2}	76^{+7}_{-6}	12^{+7}_{-6}
Time duration (ns)	0.2 to 1.1	1.0 to 1.1	1.1 to 1.4
Diameter (μm)	~850	~50	~300

The different spatial profiles of the x-ray sources directly impact the spectral resolution of the XAFS measurement. Using the Rowland (Yaakobi) x-ray spectrometer (XRS) as an example XAFS spectrometer, the impact of these three phases on the XAFS measurements can be estimated. An iron synchrotron absorption spectrum[1] was assumed to be the spectrum for a point source. To simulate the XAFS spectrum for the different source sizes, the point-source absorption spectrum was convolved with a Gaussian

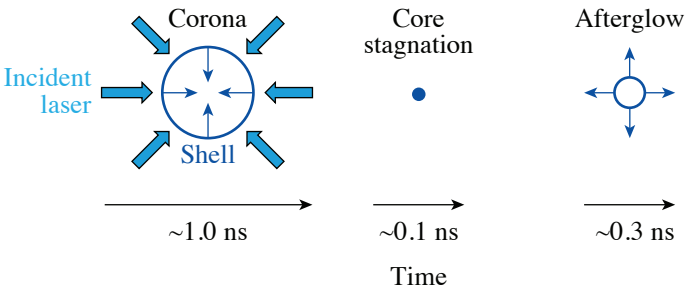

Figure 1
The x-ray emission occurs in three different phases: First, the incident laser causes the shell to emit x rays as the shell is ablated. Second, when the shell material stagnates in the center, there is a bright flash of x-ray emission. Finally, the remaining shell material expands and continues to emit x rays. The estimated time scale corresponds to an 865-μm-outer-diam, 9-μm-thick GDP shell.

function[2] whose full width at half maximum corresponded to the spectral resolution of each emission phase. The total signal was estimated by adding the signals from all three sources in transmission space while including the fractional weights from Table I.

The x-ray absorption near-edge spectroscopy (XANES) spectrum for each of the three phases along with the total signal is shown in Fig. 2(a). While the core spectrum is able to capture the majority of the features of the XANES spectrum, the corona and afterglow phases cannot. This is reflected in the total signal, which is not able to duplicate all of the features in the XANES spectrum. For example, the total spectrum loses the modulation, highlighted with the red arrow (in the inset plot), which can be used to distinguish structural changes and melting in iron.[3] Furthermore, the slope of the total spectrum is decreased, which must be accounted for when extracting the electron temperature.[4] Figure 2(b) shows the degraded extended x-ray absorption fine structure (EXAFS) spectra with each of the three phases and the total spectrum. Temperature can be extracted from the damping in the EXAFS modulations, and, under the harmonic approximation, this damping is given by $e^{-2k^2\mathrm{DWF}}$, where DWF represents the Debye–Waller factor.[5] Fitting[6] the point source and total signal spectra with this harmonic EXAFS approximation, the total signal spectrum has a DWF that is 16±6% larger. It should be noted that other spectrometers will have different spectral resolutions for each emission phase and will be impacted differently. Finally, these spectra represent a sample in a single thermodynamic state for the duration of the backlighter emission. If the material was not in a uniform thermodynamic state, each emission phase could potentially probe the material at a different density, temperature, or crystallographic structure resulting in shifting, amplifying, or decreasing XAFS modulations in unexpected ways.

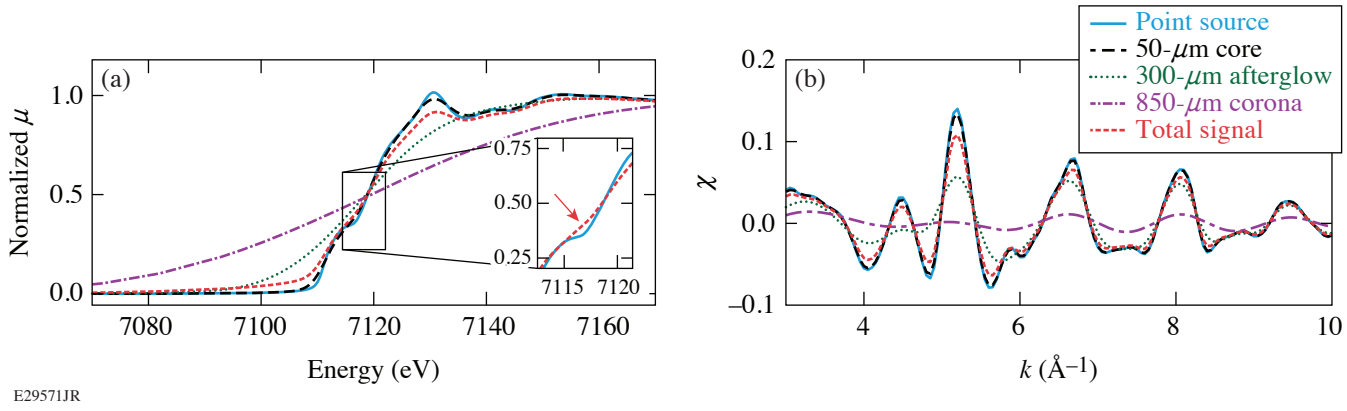

Figure 2
Iron XAFS spectra degraded with the three source sizes, assuming the XRS spectral resolutions. Iron synchrotron data[1] are assumed to give the point-source spectra. (a) XANES spectra as the normalized absorption coefficient (μ). The inset plot compares the point source and total signal with the other lines removed for visibility. The red arrow highlights a modulation that can be used to distinguish structural changes or melting in iron.[3] (b) The EXAFS data as $\chi(k)$ with E_0 = 7118 eV (Ref. 2).

This material is based upon work supported by the Department of Energy National Nuclear Security Administration under Award Number DE-NA0003856, the University of Rochester, and the New York State Energy Research and Development Authority. The support of DOE does not constitute an endorsement by DOE of the views expressed in this paper. D. Chin acknowledges

DOE NNSA SSGF support, which is provided under Cooperative Agreement No. DE-NA0003960. This collaborative work was partially supported under the auspices of the U.S. Department of Energy by Lawrence Livermore National Laboratory under Contract No. DE-AC52-07NA27344.

1. International X-Ray Absorption Society: Fe Data, IXAS X-Ray Absorption Data Library, Accessed 10 May 2021, https://xaslib.xrayabsorption.org/elem/.
2. B. Ravel and M. Newville, J. Synchrotron Rad. **12**, 537 (2005).
3. M. Harmand *et al.*, Phys. Rev. B **92**, 024108 (2015).
4. B. Kettle *et al.*, Phys. Rev. Lett. **123**, 254801 (2019).
5. E. Sevillano, H. Meuth, and J. J. Rehr, Phys. Rev. B **20**, 4908 (1979).
6. B. Ravel and M. Newville, J. Synchrotron Rad. **12**, 537 (2005).

Underdense Relativistically Thermal Plasma Produced by Magnetically Assisted Direct Laser Acceleration

K. Weichman,[1,2] J. P. Palastro,[1] A. P. L. Robinson,[3] and A. V. Arefiev[2,4]

[1]Laboratory for Laser Energetics, University of Rochester
[2]Department of Mechanical and Aerospace Engineering, University of California, San Diego
[3]Central Laser Facility, STFC Rutherford Appleton Laboratory
[4]Center for Energy Research, University of California, San Diego

The discovery of special relativity in 1905 transformed the fields of electromagnetism and charged-particle kinetics that, some 20 years later, would coalesce into the field of plasma physics. Predictions have continually emphasized the importance of special relativity in plasmas where the majority of electrons are relativistic regardless of reference frame, but, even today, experimental verifications of these predictions remain relatively rare. The laboratory generation of these relativistically thermal plasmas is needed to address open questions in astrophysics regarding shock acceleration and the origin of cosmic rays,[1] fast radio bursts,[2,3] and γ-ray bursts.[4] Relativistically thermal plasmas also feature a substantially modified response to electromagnetic radiation relative to the nonrelativistic or nonthermal cases, which is of significant interest in basic plasma physics,[5] laboratory astrophysics,[6,7] and laser-plasma physics.[8–11]

It is challenging, however, to produce relativistically thermal plasma in the laboratory with sufficient volume and duration for subsequent probing. Pulsed-power and microwave sources, while capable of igniting thermal plasma over large volumes, are incapable of reaching relativistic electron temperatures. Laser pulses with relativistic intensity ($I_0 \gtrsim 10^{18}$ W/cm^2 for $\lambda_0 = 1$-μm wavelength) are capable of imparting substantial energy to electrons, but they are conventionally unable to create persistent, large-volume plasma where the majority of electrons are relativistic. Configurations involving opaque plasma ($n_e > n_c$, where $n_c \approx 10^{21}$ cm^{-3} is the critical density for $\lambda_0 = 1$ μm),[12,13] near-critical density plasma,[14] or acceleration by the plasma (wakefield) electric field[15,16] typically leave the majority of electrons cold in either momentum or configuration space. In the underdense regime ($n_e < n_c$), laser pulses can volumetrically accelerate electrons to high energy,[17,18] but the plasma does not remain hot after the laser pulse passes due to the reversibility of the acceleration process. This reversibility is disrupted, however, by the addition of a uniform static magnetic field, enabling dramatic plasma heating.

We propose the first method to volumetrically generate relativistically thermal, underdense plasma. Our approach leverages two regimes of magnetically assisted direct laser acceleration, as illustrated in Figs. 1(a)–1(c). First, a $+x$-propagating, y-polarized relativistic short (20-fs) laser pulse interacts with electrons in an underdense (10^{-3} n_c) plasma with an embedded transverse magnetic field $B_0\hat{z} = 500$ T, imparting net energy as electrons slip through the full pulse duration [Fig. 1(b)]. Second, a longer (0.8-ps) laser pulse with the same propagation and polarization directions interacts with these preheated electrons, delivering half-laser-cycle energy kicks that promote the electron to higher-energy cyclotron orbits [Fig. 1(c)]. The short (subscript "s") and long (subscript "ℓ") laser pulses have peak normalized electric-field amplitude ($a_0 = \left| e \right| E_0 / mc\omega_0$, where ω_0 is the laser frequency) of $a_s = 5$ and $a_\ell = 1$. Simulations were conducted in 2-D using the particle-in-cell code *EPOCH*.[19]

The interaction of the two laser pulses with the target creates multi-MeV average electron energy over a large volume (e.g., $r < w/2 = 25$ μm, where w is the HWHM laser spot size), which persists for picoseconds following the interaction [Fig. 1(d)]. The corresponding momentum spectrum is 2-D isotropic (in p_x and p_y) with a flat energy spectrum. While the plasma can be heated somewhat by the short laser pulse and magnetic field alone, significant relativistic heating requires all three elements of

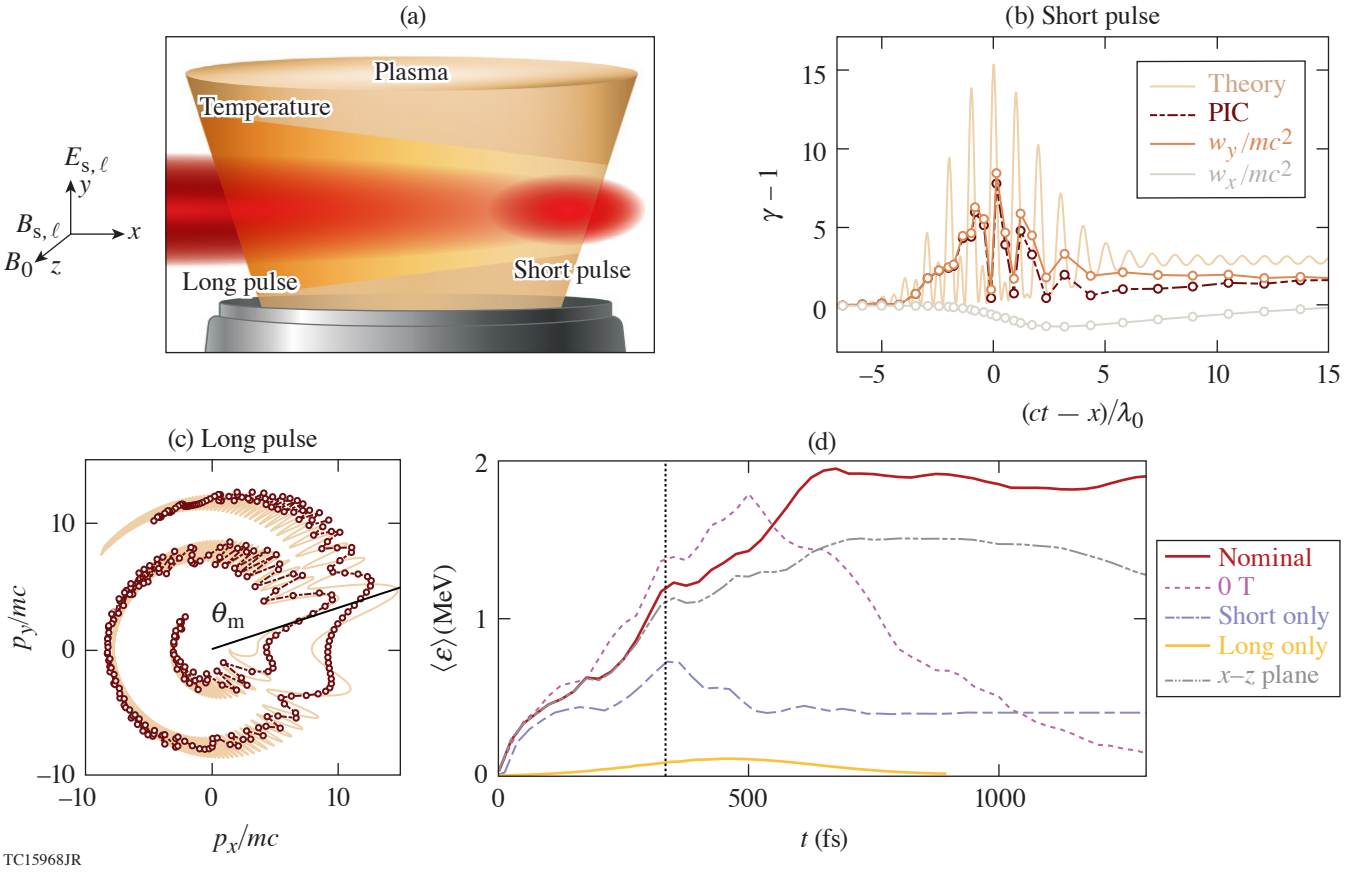

Figure 1
Generation of relativistic underdense plasma via magnetically assisted direct laser acceleration. (a) Illustration of laser and magnetic-field configuration. [(b),(c)] Example of the energy-gain process for a representative electron interacting with (b) the short pulse, and (c) the long pulse. w_y (w_x) is the work done by the transverse (longitudinal) electric field. (d) Average energy of all electrons in $r < 25$ μm. Vertical black dotted line: the time the peak of the short pulse leaves the plasma slab. The long-pulse intensity has dropped to a_ℓ/e at the right edge of the slab at the final time shown. The nominal case corresponds to both laser pulses and $B_{z0} = 500$ T, simulated in the x–y plane.

the short laser pulse, long laser pulse, and applied magnetic field [c.f., cases in Fig. 1(d)]. Unlike conventional laser-based heating methods, more than half of the electron population is heated to $\gamma \geqslant 2$, i.e., the plasma is relativistically thermal.

These observations are explainable as volumetric heating by magnetically assisted direct laser acceleration in the two distinct regimes covered by the short pulse and the long pulse. The energy retained following electron interaction with the short laser pulse through multicycle magnetically assisted direct laser acceleration[20] is used to catalyze subsequent heating by a long (picosecond) laser pulse via half-cycle magnetically assisted direct laser acceleration.[21] The latter process is capable of imparting higher net energy than the former; however it requires preheating of electrons, which in our case is provided by the short pulse.

The generation of relativistically thermal plasma is robust to increased electron density (up to $10^{-2}\,n_c$), finite laser spot size in the magnetic-field direction, and lower applied magnetic-field strength (e.g., 200 T). The average electron energy can additionally be increased by increasing the plasma size and the laser pulse duration, as shown in Fig. 2.

Our results demonstrate that the generation of underdense, relativisitically thermal plasma can be realized with currently available laser and magnetic-field–generation capabilities. With a 200-T magnetic field, we anticipate multi-MeV average electron energy under gas-jet–relevant conditions ($n_e \sim 10^{18}$ cm^{-3}, few-millimeter plasma size) using kilojoule-class laser pulses with a

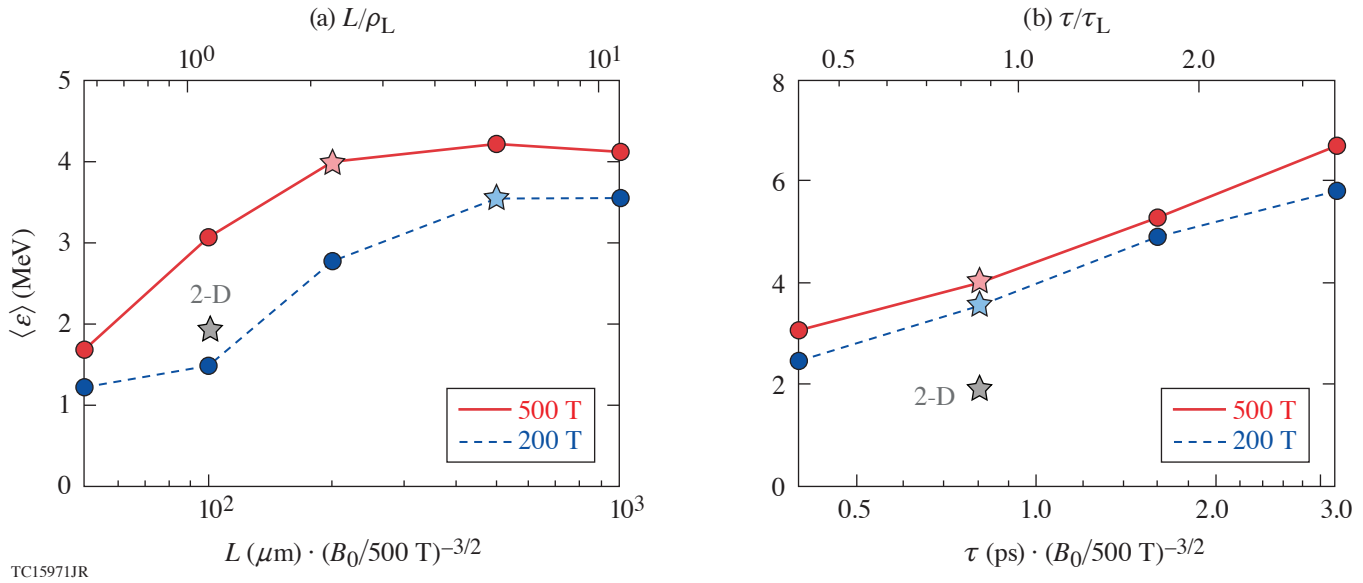

Figure 2
Strategies for improving average electron energy in 1-D particle-in-cell simulations. (a) Scan over plasma size near $L/\rho_L \sim 1$ with fixed duration. (b) Scan over long-pulse duration near $\tau_\ell/\tau_L \sim 1$ with fixed plasma size. ρ_L and τ_L are the Larmor radius and cyclotron period associated with the maximum energy that can be delivered in a half-cycle energy kick $\Delta\gamma \sim 2^{3/2}a^{3/2}_\ell\,(\omega_0/\omega_{c0})^{1/2}$. The starred points are shared between (a) and (b). The peak of the short pulse is kept coincident with a_ℓ/e on the rising edge of the long pulse. $\tau_s = 50$ fs for the 200-T cases.

few-hundred-micron spot size and 50-fs/multipicosecond duration. Our approach is thereby anticipated to offer the first practical access to the relativistically thermal plasma regime, enabling experimental verification of longstanding, foundational predictions in basic plasma physics, laboratory astrophysics, and laser-plasma physics.

We thank R. Bingham (STFC Rutherford-Appleton Laboratory) for useful discussions. This material is based upon work supported by the Department of Energy National Nuclear Security Administration under Award Number DE-NA0003856, the University of Rochester, and the New York State Energy Research and Development Authority, and the DOE Office of Science under Grant No. DESC0018312. A. V. Arefiev was supported by NSF Grant No. 1903098. The support of DOE does not constitute an endorsement by DOE of the views expressed in this paper. Particle-in-cell simulations were performed using *EPOCH*,[19] developed under UK EPSRC Grant Nos. EP/G054940, EP/G055165, and EP/G056803. This work used HPC resources of the National Energy Research Scientific Computing Center (NERSC), a U.S. Department of Energy Office of Science User Facility operated under Contract No. DE-AC02-05CH11231, and the Extreme Science and Engineering Discovery Environment (XSEDE),[22] which is supported by National Science Foundation grant number ACI-1548562, under allocation TG-PHY190034 on the Texas Advanced Computing Center (TACC) at The University of Texas at Austin.

1. R. Blandford and D. Eichler, Phys. Rep. **154**, 1 (1987).
2. R. Bingham *et al.*, Astrophys. J. **595**, 279 (2003).
3. B. D. Metzger, B. Margalit, and L. Sironi, Mon. Not. R. Astron. Soc. **485**, 4091 (2019).
4. P. Kumar and B. Zhang, Phys. Rep. **561**, 1 (2015).
5. J. Bergman and B. Eliasson, Phys. Plasmas **8**, 1482 (2001).
6. M. Lontano, S. Bulanov, and J. Koga, Phys. Plasmas **8**, 5113 (2001).
7. T.-Y. B. Yang, J. Arons, and A. B. Langdon, Phys. Plasmas **1**, 3059 (1994).
8. D. J. Stark *et al.*, Phys. Rev. Lett. **115**, 025002 (2015).
9. G. Li, W. B. Mori, and C. Ren, Phys. Rev. Lett. **110**, 155002 (2013).
10. Y. Zhao *et al.*, Phys. Plasmas **21**, 112114 (2014).
11. J. S. Ross *et al.*, Phys. Rev. Lett. **104**, 105001 (2010).

12. M. A. Purvis *et al*., Nat. Photonics **7**, 796 (2013).
13. S. M. Weng *et al*., Sci. Rep. **6**, 22150 (2016).
14. G. Li *et al*., Phys. Rev. Lett. **100**, 125002 (2008).
15. T. Tajima and J. M. Dawson, Phys. Rev. Lett. **43**, 267 (1979).
16. E. Esarey, C. B. Schroeder, and W. P. Leemans, Rev. Mod. Phys. **81**, 1229 (2009).
17. J. Krüger and M. Bovyn, J. Phys. A **9**, 1841 (1976).
18. F. V. Hartemann *et al*., Phys. Rev. E **51**, 4833 (1995).
19. T. D. Arber *et al*., Plasma Phys. Control. Fusion **57**, 113001 (2015).
20. A. P. L. Robinson and A. V. Arefiev, Phys. Plasmas **27**, 023110 (2020).
21. A. Arefiev, Z. Gong, and A. P. L. Robinson, Phys. Rev. E **101**, 043201 (2020).
22. J. Towns *et al*., Comput. Sci. Eng. **16**, 62 (2014).

An Independent-Hot-Spot Approach to Multibeam Laser–Plasma Instabilities

R. K. Follett, H. Wen, D. H. Froula, D. Turnbull, and J. P. Palastro

Laboratory for Laser Energetics, University of Rochester

In laser-driven inertial confinement fusion (ICF), a millimeter-scale cryogenic capsule of deuterium–tritium fuel with a thin outer ablator is imploded by either direct laser illumination (direct drive) or focusing the lasers onto the interior walls of a hohlraum to generate an x-ray bath (indirect drive).[1] In both cases, the many high-intensity laser beams overlapping in underdense plasma can drive various laser–plasma instabilities (LPI's) that can severely inhibit implosion performance.[2,3]

Analytic results for instability behavior are typically limited to the case of a single plane-wave laser driving instability in the linear regime. ICF experiments, however, involve multiple overlapping laser beams, each using a phase plate that generates a complex speckle pattern in the plasma,[4] and accurate predictions of instability behavior require a description that accounts for their combined interaction.[5] Analytic theories for instability behavior in a single speckled beam have been developed using the independent-hot-spot model, where a statistical description of the speckle intensity is combined with the single-speckle instability behavior to predict the global instability behavior.[6,7] Multibeam interactions have historically been described using the common-wave model, where wave-vector matching considerations are used to show that overlapping laser beams can couple to a shared daughter wave propagating along the drive-beam axis of symmetry.[8–13] However, recent experiments and simulations of multibeam LPI's have shown that the common-wave description often fails to predict instability behavior. In particular, laser beams that do not satisfy the geometric requirements imposed by the common-wave matching conditions can still contribute to instability growth.[14–16]

Here we develop a multibeam hot-spot model that provides a more-predictive description of LPI behavior than the widely used common-wave approach. The model is extended to include absolute instability in an inhomogeneous plasma and applied to the two-plasmon–decay (TPD) instability. The excellent agreement with multibeam *LPSE* simulations demonstrates its utility and shows that there is an important qualitative difference between 2-D and 3-D single-speckle instability thresholds that is not present in the plane-wave case and results in lower instability thresholds in 2-D. This approach leads to a new understanding of multibeam instability behavior that can be used to make better quantitative predictions for improving the design of experiments and future laser facilities.

Given a collection of N speckles, the absolute instability threshold occurs when the peak speckle intensity is equal to the single-speckle threshold, $I_M = I_{\text{thr,speckle}}$. Introducing the average laser intensity I_0 and ensemble averaging over speckle realizations, this can be written as

$$I_{\text{thr}} = \frac{1}{\left\langle I_M / I_0 \right\rangle} I_{\text{thr,speckle}}, \tag{1}$$

where we have defined the expected average intensity at threshold $I_{\text{thr}} \equiv \left\langle I_0 \right\rangle$. Accordingly, evaluation of the expected threshold in the independent-hot-spot model is reduced to the evaluation of $\left\langle I_M / I_0 \right\rangle$ and $I_{\text{thr,speckle}}$. The expected peak speckle intensity can be written in terms of the probability that every speckle intensity is less than u:[17]

$$\left\langle I_M / I_0 \right\rangle = \int_0^\infty \left[1 - P\left(I / I_0 < u\right)^N\right] \mathrm{d}u. \tag{2}$$

Reference 18 derives speckle distributions that are valid for high-intensity speckles but behave badly at low intensities. Accordingly, we use exponential distributions at low intensities to generate probability distributions that behave well at all intensities:

$$P\left(I/I_0 > u\right)_{2\text{-D}} = \begin{cases} e^{-u/\mu_2}, & u < u_{s2} \\ A_2\left[\left(\frac{1}{2}+\frac{\pi}{4}\right)u+\frac{1}{2}\right]e^{-u}, & u > u_{s2} \end{cases}, \tag{3}$$

$$P\left(I/I_0 > u\right)_{3\text{-D}} = \begin{cases} e^{-u/\mu_3}, & u < u_{s3} \\ A_3\left[u^{3/2}-\frac{3}{10}u^{1/2}\right]e^{-u}, & u > u_{s3} \end{cases}, \tag{4}$$

where the μ_i are parameters and the A_i and u_{si} are chosen to make the distributions and their first derivatives continuous. Here $\mu_2 = \mu_3 = 4$ was chosen on the basis of comparison to simulations, which gives $A_2 = 1.185$, $u_{s2} = 0.944$, $A_3 = 1.848$, and $u_{s3} = 2.210$.

Incorporating Eqs. (3) and (4) into Eq. (2), using the binomial theorem, and integrating gives

$$\left\langle I_M/I_0\right\rangle_{2\text{-D}} = \sum_{a=1}^{N}\binom{N}{a}(-1)^a\left[\frac{\mu_2}{a}\left(e^{-au_{s2}/\mu_2}-1\right)-A_2^a a^{-1-a}e^{2a/2+\pi}\left(\frac{2+\pi}{4}\right)^a\Gamma\left(1+a,\frac{2a}{2+\pi}+au_{s2}\right)\right], \tag{5}$$

$$\left\langle I_M/I_0\right\rangle_{3\text{-D}} = \sum_{a=1}^{N}\binom{N}{a}(-1)^a\left[\frac{\mu_3}{a}\left(e^{-au_{s3}/\mu_3}-1\right)-A_3^a\sum_{k=0}^{a}\binom{a}{k}\left(-\frac{3}{10}\right)^k a^{k-1-3a/2}\Gamma\left(1-k+3a/2,au_{s3}\right)\right], \tag{6}$$

where $\Gamma(s,x)$ is the incomplete gamma function.

To determine N, we restrict our discussion to instabilities that are spatially localized by plasma inhomogeneity such that N is the number of speckles in a cross section of the laser field (i.e., the interaction region is not significantly longer than the speckle length). Accordingly, N is approximately the laser power divided by the mean power in a speckle, $N = P_L/\langle P_s\rangle$. The laser power is the average intensity times the cross-sectional area ($P_L = I_0\sigma_b$). To determine the mean power in a speckle, we first average over the probability density of speckle intensities to obtain the mean speckle intensity $\left\langle I/I_0\right\rangle = \int_0^\infty uP(u)\mathrm{d}u$, where $P(u) = -\partial P\left(I/I_0 > u\right)/\partial u$. Equations (3) and (4) give

$$\left\langle I/I_0\right\rangle_{2\text{-D}} = \mu_2 - (\mu_2+u_{s2})e^{-u_{s2}/\mu_2} + A_2e^{-u_{s2}}\left[4+\pi+(4+\pi)u_{s2}+(2+\pi)u_{s2}^2\right]/4, \tag{7}$$

$$\left\langle I/I_0\right\rangle_{3\text{-D}} = \mu_3 - (\mu_3+u_{s3})e^{-u_{s3}/\mu_3} + A_3\left[\frac{3\sqrt{\pi}}{5}\operatorname{erfc}\left(\sqrt{u_{s3}}\right)+e^{-u_{s3}}\sqrt{u_{s3}}\left(u_{s3}^2+\frac{7}{10}u_{s3}+\frac{6}{5}\right)\right], \tag{8}$$

where $\operatorname{erfc}(x)$ is the complementary error function. For speckles with a Gaussian transverse profile $\left[I(r) = Ie^{-\left(2\sqrt{\log 2}\,r/w_s\right)^2}\right]$ and full width at half maximum (FWHM) w_s, integration over r gives the mean power in a speckle, $\langle P_s\rangle_{2\text{-D}} = \left\langle I/I_0\right\rangle_{2\text{-D}} I_0 w_s\sqrt{\pi/\log 2}$ and $\langle P_s\rangle_{3\text{-D}} = \left\langle I/I_0\right\rangle_{3\text{-D}} I_0 w_s^2\pi/(4\log 2)$. Finally, the expected number of speckles in 2-D and 3-D, respectively, is

$$N = \frac{\sigma_b}{w_s\left\langle I/I_0\right\rangle_{2\text{-D}}}\sqrt{\frac{\log 2}{\pi}}, \tag{9}$$

$$N = \frac{\sigma_b}{w_s^2 \langle I/I_0 \rangle_{3\text{-D}}} \frac{4\log 2}{\pi}. \tag{10}$$

The single-speckle threshold ($I_{\text{thr,speckle}}$) generally depends on the speckle size, plasma conditions, and the instability under consideration. An analytic approximation can be obtained by constructing a spatially localized solution out of the linear eigenmodes for a plane-wave drive laser,[19] but it is not sufficiently accurate for quantitative applications. Here we take a semi-analytic approach where the speckle statistics are given by Eqs. (5) and (6), while $I_{\text{thr,speckle}}$ is taken from single-speckle *LPSE* simulations.

Figure 1 compares Eq. (1) to various speckled-beam *LPSE* calculations. The thresholds are normalized to the threshold for a single plane-wave drive beam, $I_{\text{thr,TPD}}$ (Ref. 19). Figure 1(a) shows 2-D calculations using a single beam with a varying *f* number at $L_n = 200\ \mu$m, $T_e = 2$ keV, and $L_n = 400\ \mu$m, $T_e = 4$ keV, which are similar to the conditions in direct-drive ICF experiments on the OMEGA[20] and National Ignition Facility[15] lasers, respectively. The thresholds are higher in the longer-scale-length calculations because, for a given speckle width, the single-speckle threshold increases with increasing temperature and scale length. The non-monotonic nature of the thresholds is a result of the competition between the increasing thresholds with decreasing speckle size and the increased number of speckles with decreasing *f* number.

Figures 1(b) and 1(c) show 3-D instability thresholds for $L_n = 200\ \mu$m, $T_e = 2$ keV and $L_n = 400\ \mu$m, $T_e = 4$ keV, respectively, for three different beam configurations: (1) a single beam with varying *f* number; (2) six *f*/6.7 beams uniformly distributed on a cone relative to the *x* axis with polar angle θ and azimuthal angle for the *m*th beam $\varphi_m = 2\pi m/6$; and (3) eight *f*/6.7 beams organized into two four-beam cones with polar angles θ and $\theta/2$ and azimuthal angles $\varphi_m = 2\pi m/4$ and $\varphi_m = 2\pi m/4 + \pi/4$, respectively. For the multibeam cases, the horizontal axis corresponds to an effective *f* number given by the cone angle, $f_{\#} = 1/(2\tan\theta)$ and the beam polarizations were aligned. All three beam configurations give the same threshold to within statistical variations and are in good agreement with the semi-analytic model. This shows that the instability behavior is predominantly determined by the smallest (and highest intensity) speckles and justifies the treatment of the cones of beams as a single beam with a small effective *f* number.

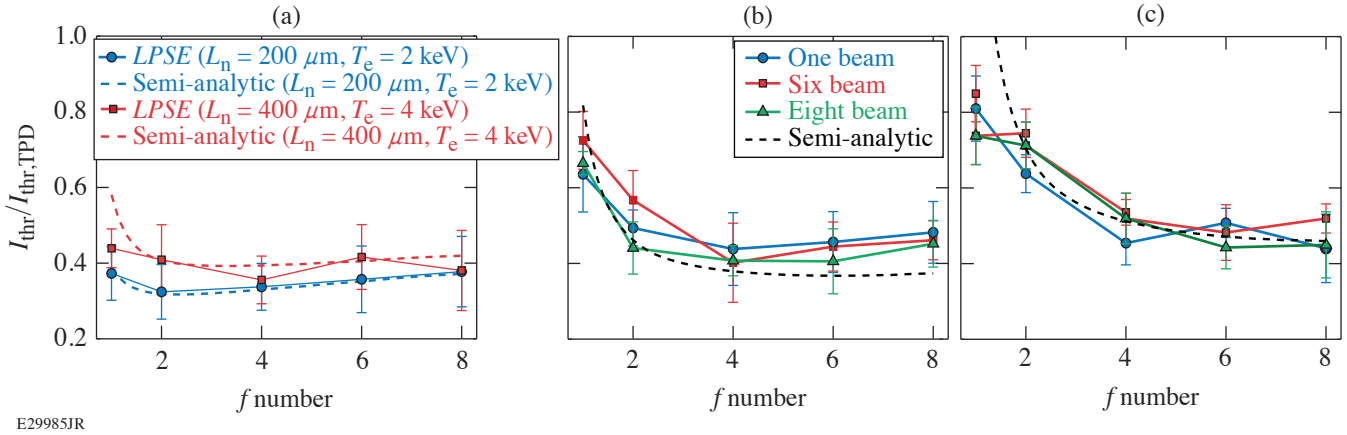

Figure 1
Absolute TPD instability thresholds for speckled beams (normalized to the plane-wave threshold). (a) Two-dimensional *LPSE* calculations at $L_n = 200\ \mu$m, $T_e = 2$ keV (blue circles), and $L_n = 400\ \mu$m, $T_e = 4$ keV (red squares). [(b),(c)] Three-dimensional *LPSE* calculations show $L_n = 200\ \mu$m, $T_e = 2$ keV and $L_n = 400\ \mu$m, $T_e = 4$ keV, respectively, for one beam (blue circles), six beams (red squares), and eight beams (green triangles). The dashed curves show the corresponding semi-analytic results. The error bars correspond to the standard deviation from an ensemble of 20 (5) speckle realizations in 2-D (3-D).

This material is based upon work supported by the Department of Energy National Nuclear Security Administration under Award Number DE-NA0003856, ARPA-E BETHE grant number DE-FOA-0002212, the University of Rochester, and the New York State Energy Research and Development Authority.

1. S. Atzeni and J. Meyer-ter-Vehn, *The Physics of Inertial Fusion: Beam Plasma Interaction, Hydrodynamics, Hot Dense Matter*, 1st ed., International Series of Monographs on Physics, Vol. 125 (Oxford University Press, Oxford, 2004).
2. W. L. Kruer, *The Physics of Laser Plasma Interactions, Frontiers in Physics*, Vol. 73, edited by D. Pines (Addison-Wesley, Redwood City, CA, 1988).
3. R. S. Craxton *et al*., Phys. Plasmas **22**, 110501 (2015).
4. Y. Kato *et al*., Phys. Rev. Lett. **53**, 1057 (1984).
5. C. Stoeckl *et al*., Phys. Rev. Lett. **90**, 235002 (2003).
6. H. A. Rose and D. F. DuBois, Phys. Rev. Lett. **72**, 2883 (1994).
7. V. T. Tikhonchuk, C. Labaune, and H. A. Baldis, Phys. Plasmas **3**, 3777 (1996).
8. D. F. DuBois, B. Bezzerides, and H. A. Rose, Phys. Fluids B **4**, 241 (1992).
9. D. T. Michel *et al*., Phys. Rev. Lett. **109**, 155007 (2012).
10. P. Michel *et al*., Phys. Rev. Lett. **115**, 055003 (2015).
11. J. Zhang *et al*., Phys. Rev. Lett. **113**, 105001 (2014).
12. D. T. Michel *et al*., Phys. Plasmas **20**, 055703 (2013).
13. J. F. Myatt *et al*., Phys. Plasmas **21**, 055501 (2014).
14. R. K. Follett *et al*., Phys. Plasmas **24**, 102134 (2017).
15. M. J. Rosenberg *et al*., Phys. Rev. Lett. **120**, 055001 (2018).
16. R. K. Follett *et al*., Phys. Rev. E **101**, 043214 (2020).
17. B. Eisenberg, Stat. Probab. Lett. **78**, 135 (2008).
18. J. Garnier, Phys. Plasmas **6**, 1601 (1999).
19. A. Simon *et al*., Phys. Fluids **26**, 3107 (1983).
20. T. R. Boehly *et al*., J. Appl. Phys. **85**, 3444 (1999).

Density Reconstruction in Convergent High-Energy-Density Systems Using X-Ray Radiography and Bayesian Inference

S. Ressel,[1,*] J. J. Ruby,[1,2,†] G. W. Collins,[1,2,3] and J. R. Rygg[1,2,3]

[1]Laboratory for Laser Energetics, University of Rochester
[2]Department of Physics and Astronomy, University of Rochester
[3]Department of Mechanical Engineering, University of Rochester
[*]Currently at Department of Atmospheric Sciences, University of Washington
[†]Currently at Lawrence Livermore National Laboratory

X-ray radiography is a technique frequently used to diagnose convergent high-energy-density (HED) systems, such as inertial confinement fusion (ICF) implosions, and to provide unique information that is not available through self-emission measurements. We investigate the scope and limits of that information using a radiography simulation combined with Bayesian inference workflow. The accuracy of density reconstruction from simulated radiographs of spherical implosions driven with 20 kJ of laser energy is assessed, including the increase or decrease in accuracy due to the addition of Lagrangian marker layers, Poisson noise, and improved prior information. This work is the first to present the full uncertainty distributions inferred from radiography analysis in HED systems and demonstrates the importance of constructing the full posterior probability density, as opposed to a point estimate, due to the modal structure of the likelihood surface introduced by typical experimental noise sources. This general methodology can be used for both robust analysis of radiographic data and improved design of radiography experiments by modeling the full experimental system.

The inference workflow was tested on realistic data generated from the 1-D radiation-hydrodynamic code *LILAC*, where a single spherically converging shock wave was simulated in a solid hydrocarbon sphere (CH) driven by 27 kJ of UV light using the *SESAME* 7592 EOS table and Los Alamos's astrophysical opacity tables. The resulting radial density profiles are used to generate a simulated radiograph, using a straight-line ray trace to simulate the optical system of an x-ray streak camera with a slit imager, to determine how much density-profile information is encoded in the lineout and to what extent the density profile can be reconstructed from lineout data.

The parameterization used to represent the *LILAC* density profile is similar in form to previous work[1] and is given by

$$\rho(r) = \rho_0; r < r_s,$$

$$\rho(r) = \rho_s + (\rho_p - \rho_s)(r - r_s)/(r_p - r_s); r_s < r < r_p,$$

$$\rho(r) = \rho_p \cdot \exp\left[-(r - r_p)^2/(2\sigma^2)\right]; r_p < r < r_e,$$

$$\rho(r) = \rho_e \cdot \exp\left[-a(r - r_e)\right]; r_e < r,$$

$$\text{and } \sigma = \sqrt{-(r_p - r_e)^2/2\ln(\rho_e - \rho_p)}. \quad (1)$$

where r_s, r_p, and r_e are the radial locations of the shock, peak density, and tail, respectively; ρ_0, ρ_s, ρ_p, and ρ_e are the densities of the material in ambient conditions, immediately after being shocked, at its maximum due to converging flows, and at the tail of the density profile, respectively; and α is a scale parameter that determines how quickly the density reduces to zero in the tail.

The results of using Bayesian inference to construct the posterior probability densities for the parameters in the density profile (shown in Fig. 1) demonstrate that some additional information is needed to constrain the inferred shock compression. Figure 2(a) shows the uniform prior distribution (green) for the shock compression, alongside the posteriors from inference including an additional constraint and including noise. A defining feature of the inference from these cases is the upper limit placed on the shock compression, which can be used in combination with outside information to further constrain the posterior.

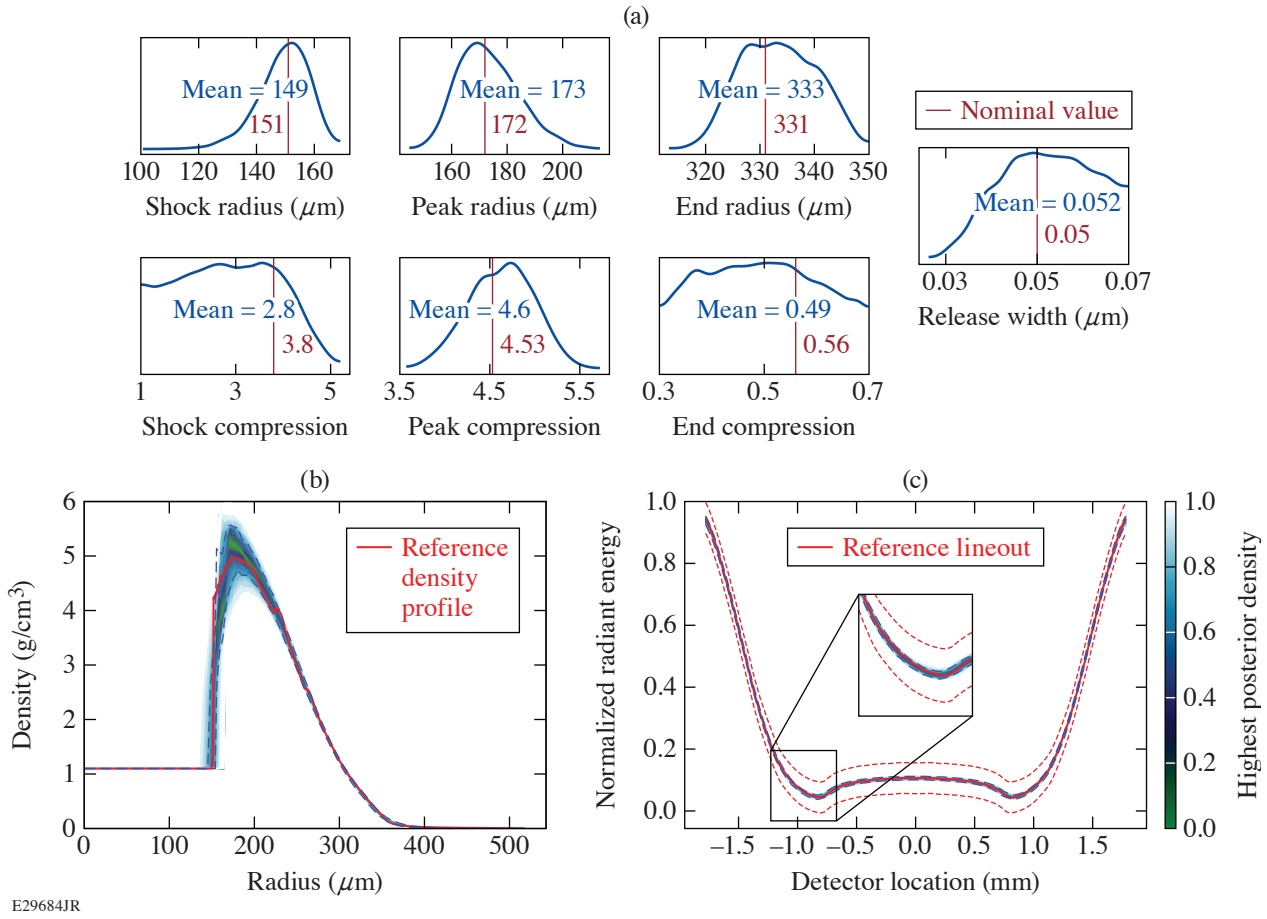

Figure 1

(a) Posterior distributions for each of the seven parameters of the model given in Eq. (1), as well as (b) posterior predictive distributions (PPD's) of the density profiles and (c) lineouts generated from said posterior distributions. A number of the parameters are well constrained, as shown by a single narrow peak in their posterior distributions, including the location of the shock, the location of the peak density, and the peak compression, and they all recover the underlying nominal value, given by the vertical red line, which is the least-squares best fit value recovered by fitting the simulated density profile with the assumed model. Notably, the posterior distribution for the shock compression (ρ_s/ρ_0) is not well constrained, presenting an upper bound of about 4, but roughly equal probability density across all values below 4. This can also be seen in (b), which is well matched to the reference density profile outside the region of the shock. Despite this, the PPD's of the lineouts in (c) are converged from the inference and well matched to the reference information, even around the feature due to the shock limb highlighted in the inset.

The simplest way to introduce this outside information is by using a more-informed prior distribution—for example, one that introduces a lower limit on the shock compression. A naive implementation is shown in Fig. 2(b) where the data-informed prior (orange) is simply a uniform distribution with a lower bound set by the maximum compression measurement of 3.39 (Ref. 2)

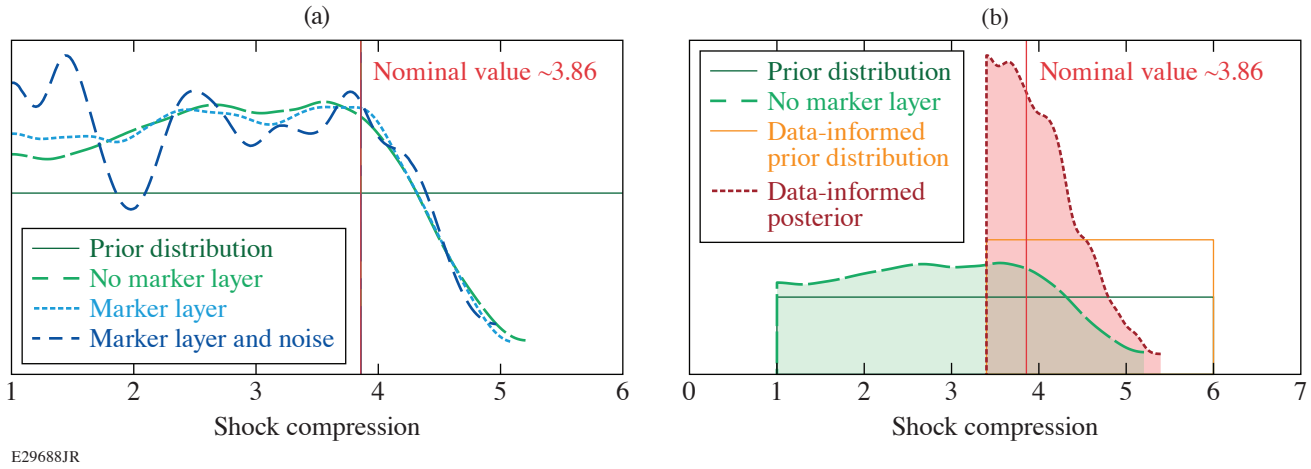

Figure 2

(a) Posterior distributions of the shock compression (ρ_s/ρ_0) for the cases with no noise and no Lagrangian marker layer (dashed green curve), no noise with a Lagrangian marker layer (dotted light blue curve), and with noise and a Lagrangian marker layer (dashed dark blue curve). Also shown are the prior used for each case (solid green, horizontal line) and the nominal value from the *LILAC* density profile (solid red, vertical line), given as ~3.86. All of the distributions show the same general trend that above a compression of 4 the probability density drops sharply, due to the peak compression behind the shock being well constrained and the shock jump necessarily being smaller, effectively giving an upper bound on the shock jump. There is little constraint on the lower end of the compression where the probability density is effectively flat between 1 and 4. The case with noise shows modal structure that, if point estimates are used, can give the impression of constraint while being only a local maximum in probability density. (b) The posterior for shock compression (dashed green curve) for the case with a broad uniform prior (solid green line) and posterior (dotted red curve) for the case with a narrow uniform prior (solid orange line) truncated at the low end at the location of previous measurements.[2] This demonstrates how Bayesian inference allows additional information to be leveraged to constrain a quantity that is otherwise unconstrained. The combination of the prior informing a lower limit of compression and the radiograph constraining upper limits of compression results in a nicely peaked posterior probability density that captures the proper underlying value (solid red line). The axes are expanded to demonstrate how the priors enforce that there is zero probability density outside of their bounds. Note that the data-informed posterior is largely asymmetric, although it presents a strongly peaked result that recovers the nominal value.

from previous data along the Hugoniot of CH up to 8.74 Mbar performed in planar geometry using a different methodology. Figure 2(b) also shows the posterior for shock compression given the new prior (red), which is now significantly more peaked than the previous results (green), meaning that there is a well-defined region of high probability density.

Although the shock compression is not strongly constrained by the radiograph alone, the density profile is well constrained by the radiograph measurement. In particular, the areal density (ρR) is very well constrained and is a quantity of particular interest within the ICF community. The findings here are in excellent agreement with previous radiography measurements taken on shells for the purpose of diagnosing metrics relevant to ICF modeling.[3] This work can be seen as an extension of those efforts with additional insight into the uncertainties associated with such reconstructions. Additionally, the peak density achieved within the bulk of the material behind the shock, which has a great effect on the propagation of the outgoing shock wave, is well constrained. Radiography measurements of this kind contain a great deal of information that can be used in combination with other measurements to develop a full picture of implosion experiments, including how materials respond to strong converging shock waves. This work can be used as a foundation to develop further investigations about the information contained in measurements of this type.

This material is based upon work supported by the Department of Energy National Nuclear Security Administration under Award Number DE-NA0003856, the U.S. Department of Energy, Office of Science, Office of Fusion Energy Sciences under Award No. DE-SC001926, the University of Rochester, and the New York State Energy Research and Development Authority.

1. D. C. Swift *et al.*, Rev. Sci. Instrum. **89**, 053505 (2018).
2. M. A. Barrios *et al.*, Phys. Plasmas **17**, 056307 (2010).
3. D. G. Hicks *et al.*, Phys. Plasmas **17**, 102703 (2010).

Diamond Formation in Double-Shocked Epoxy to 150 GPa

M. C. Marshall,[1] M. G. Gorman,[2] D. N. Polsin,[1,3] J. H. Eggert,[2] M. K. Ginnane,[1,3] J. R. Rygg,[1,3,4] G. W. Collins,[1,3,4] and L. D. Leininger[2]

[1]Laboratory for Laser Energetics, University of Rochester
[2]Lawrence Livermore National Laboratory
[3]Department of Mechanical Engineering, University of Rochester
[4]Department of Physics and Astronomy, University of Rochester

The formation of diamond from carbon-based polymers, compounds, or other carbon polymorphs (i.e., graphite) under extreme pressures has been actively researched for many decades.[1–12] Diamond can form by extreme heating and compression of some plastics,[1] methane,[2,3] and explosive materials.[10,12] For example, cubic diamond was detected from double-shocked polystyrene (CH) at 139 to 159 GPa using *in-situ* x-ray diffraction in experiments at the Linac Coherent Light Source (LCLS), indicating that breaking of the carbon and hydrogen bonds and restructuring of the carbon into diamond can occur over only nanosecond time scales.[1] The results presented here indicate that cubic diamond also forms from Stycast 1266 epoxy (C:H:Cl:N:O ≈ 27:38:1:1:5) (Ref. 13) doubly shocked to 80 and 148 GPa. These results demonstrate that the chemical and thermodynamic conditions inside ice giant planets, which have inner ice layers dominated by CH_4, NH_3, and H_2O, are suitable for diamond formation.

Two experiments were conducted on the OMEGA EP Laser System,[14] where laser beams were used to shock compress the target comprising an epoxy sample and a LiF window with a reflective Ti coating between them to measure the interface velocity using a velocity interferometer system for any reflector (VISAR).[15] When the shock wave is incident on the higher-impedance LiF interface, a return shock (reshock) is launched back through the epoxy, which approximately doubles the pressure. The target was probed with x rays, and the resulting diffraction pattern was measured using the powder x-ray diffraction image-plate diagnostic[16] when the epoxy was in the reshocked state. Diffraction consistent with cubic diamond was observed for both shots (Fig. 1). The pressure and temperature state during the x-ray exposure time were determined using hydrodynamic simulations matched to the measured epoxy/LiF interface velocity.

The results are compared to previous works in Fig. 1(a), where CH (Ref. 1), polyethylene (CH_2) (Ref. 5), methane (CH_4), (Refs. 2 and 3), and methane hydrate (MH) (Ref. 4) were also probed *in situ* at high pressures and temperatures to study diamond formation. Diamond formation from methane and methane hydrate is observed over ~10 to 80 GPa and ~2000 to 4000 K in laser-heated diamond-anvil cell experiments, where the samples are compressed and heated over seconds to hours.[2–4] At these conditions and compression rates, diamond formation is largely temperature dependent and the temperature threshold at which it occurs is lowered by the addition of oxygen as suggested by the methane hydrate experiments.[4] Diamond formation is not observed in singly shocked CH (Ref. 1) and CH_2 (Ref. 5) when they are compressed over nanoseconds at similar temperatures and pressures. While diamond still does not form in doubly shocked CH_2, it does form from doubly shocked CH and epoxy at ~80 to 200 GPa pressures and ~2000 to 6000 K temperatures. Diamond formation at these fast nanosecond times scales is not purely pressure or temperature dependent and is affected by the initial material composition and thermodynamic compression path (e.g., single versus double shock). These differences in behavior among all the experiments collectively suggest that the kinetics associated with the vastly different time scales, the thermodynamic path, and the chemical composition of the initial material play an important role in diamond formation at extreme conditions.

(a)

Diamond	No diamond	Initial material	Experiment type, time scale	
◆		Epoxy (C,H,O,N,Cl)	Laser shock, ~1 to 15 ns	Marshall (this work)
◆	+	CH	Laser shock, ~1 to 10 ns	Kraus[1]
	+ +	CH_2	Laser shock, ~1 to 10 ns	Hartley[5]
◆	+	MH (C,H,O)	LHDAC, ~10 to 120 min	Kadobayashi[4]
▭		CH_4	LHDAC, ~1 to 15 min	Benedetti[2]
▭		CH_4	LHDAC, ~10 s to 15 min	Hirai[3]

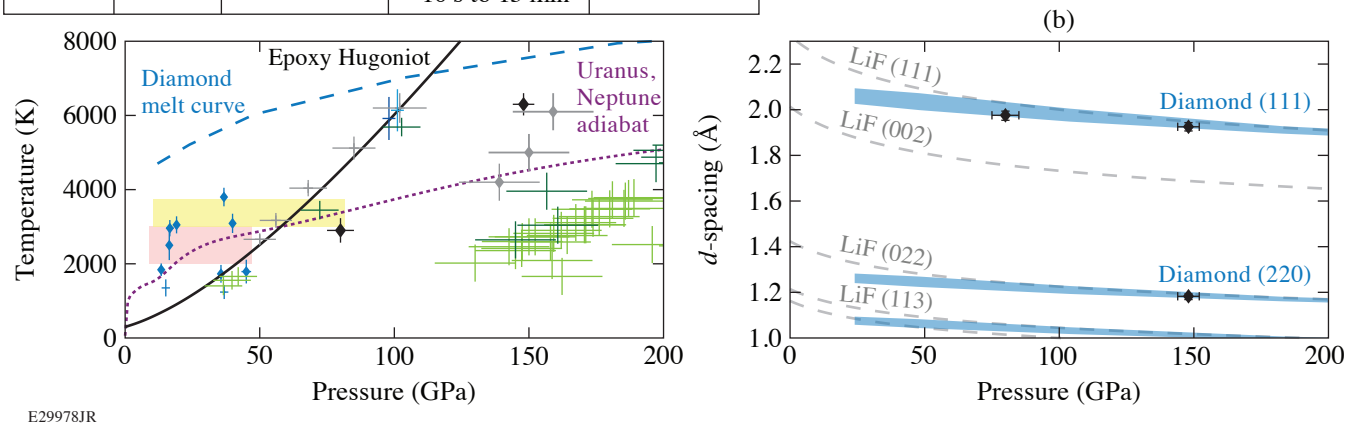

Figure 1
(a) Phase diagram showing diamond-formation results from compressed and heated epoxy, polystyrene (CH), polyethylene (CH_2), methane hydrate (MH), and methane (CH_4). Data points on singly shocked CH and CH_2 lie close to the epoxy Hugoniot (*SESAME* 7602). Data points from this work and all points above 120 GPa on CH and CH_2 are on doubly shocked samples. (b) Lattice *d*-spacing results from this work compared to predictions for compressed diamond (spanning the cold curve[17] to the melt curve[18] to encompass all possible temperature effects) and shocked LiF.

This material is based upon work supported by the Department of Energy National Nuclear Security Administration under Award Number DE-NA0003856, the University of Rochester, and the New York State Energy Research and Development Authority. This work was performed under the auspices of the U.S. Department of Energy by Lawrence Livermore National Laboratory (LLNL) under LLNL's Laboratory Directed Research and Development (LDRD) Program under Grant No. 18-SI-004. Lawrence Livermore National Laboratory is operated by Lawrence Livermore National Security, LLC, for the U.S. Department of Energy, National Nuclear Security Administration under Contract DE-AC52-07NA27344.

1. D. Kraus *et al.*, Nat. Astron. **1**, 606 (2017).
2. L. R. Benedetti *et al.*, Science **286**, 100 (1999).
3. H. Hirai *et al.*, Phys. Earth Planet. Inter. **174**, 242 (2009).
4. H. Kadobayashi *et al.*, Sci. Rep. **11**, 8165 (2021).
5. N. J. Hartley *et al.*, Sci. Rep. **9**, 4196 (2019).
6. D. Kraus *et al.*, Nat. Commun. **7**, 10970 (2016).
7. E. B. Watkins *et al.*, Sci. Rep. **12**, 631 (2022).
8. D. G. Morris, J. Appl. Phys. **51**, 2059 (1980).

9. F. H. Ree, J. Chem. Phys. **70**, 974 (1979).
10. M. van Thiel and F. H. Ree, J. Appl. Phys. **62**, 1761 (1987).
11. W. J. Nellis *et al.*, J. Chem. Phys. **75**, 3055 (1981).
12. J. B. Donnet *et al.*, Diam. Relat. Mater. **9**, 887 (2000).
13. We provide only an estimated C:H:Cl:N:O ratio for the final cured Stycast 1266 mixture, obtained by combining the listed components in the safety data sheets for Parts A and B by the quoted mix ratios and assuming a closed system. The exact composition of the Stycast 1266 Part A and B may vary from the quoted percentages or are trade secrets.
14. D. D. Meyerhofer *et al.*, J. Phys.: Conf. Ser. **244**, 032010 (2010).
15. P. M. Celliers *et al.*, Rev. Sci. Instrum. **75**, 4916 (2004).
16. J. R. Rygg *et al.*, Rev. Sci. Instrum. **83**, 113904 (2012).
17. A. Dewaele *et al.*, Phys. Rev. B **77**, 094106 (2008).
18. X. Wang, S. Scandolo, and R. Car, Phys. Rev. Lett. **95**, 185701 (2005).

Meta-GGA Exchange-Correlation Free Energy Density Functional to Increase the Accuracy of Warm-Dense-Matter Simulations

V. V. Karasiev, D. I. Mihaylov, and S. X. Hu

Laboratory for Laser Energetics, University of Rochester

High-energy-density physics includes a complicated warm-dense-matter (WDM) domain of state conditions that is characterized by elevated temperatures (from few to hundreds of eV) and pressures to 1 Mbar or greater. Accurate knowledge of equation of state, transport, and optical properties describing possible phase transitions (e.g., insulator-to-metal transition) across a warm dense regime plays an important role in planetary science, astrophysics, and inertial confinement fusion.[1–6] Currently, the vast majority of density-functional-theory (DFT) simulations of WDM and high-energy-density plasmas use the zero-temperature (ground-state) exchange-correlation (XC) functionals without explicit temperature dependence, which were developed by the condensed-matter physics and quantum chemistry communities, leading to neglect of thermal XC effects and degraded accuracy of predictions. The use of a ground-state XC functional is justified only at low electronic temperatures not exceeding a few tenths of the Fermi temperature or in the high-temperature limit when the XC contribution to the total free energy is negligible.[7–10] Recent development of the temperature-dependent Karasiev–Sjostrom–Dufty–Trickey (KSDT)[11] local-density approximation (LDA) (see Ref. 12 for the corrected set of parameters corrKSDT), the generalized gradient approximation (GGA)–type XC functional "KDT16" (Ref. 12), and the thermal hybrid KDT0[13] have shown that thermal XC effects are very important to increasing the accuracy of simulations at extreme conditions and improving agreement with experimental measurements as compared to the standard zero-temperature Perdew–Burke–Ernzerhof (PBE)[14] calculations. The way to improve overall accuracy of the thermal GGA XC functional is to use the next rung approximation at zero temperature and construct thermally extended meta-GGA XC.

In this work, we address this problem by developing a thermalization framework for XC functionals at the meta-GGA level of refinement and realization of a simple scheme via universal thermal XC additive correction at the GGA level of theory, which is applied to an accurate at low-T, ground-state meta-GGA XC. Thermal correction is applied to the ground-state deorbitalized, strongly constrained, and appropriately normed semilocal density functional (SCANL)[15–18]—to date, one of the most-accurate meta-GGA XC functionals, which, for example, is capable of accurately describing the liquid–liquid insulator-to-metal transition of warm dense hydrogen.[3] The resulting thermal meta-GGA XC functional, referred to here as T-SCAN-L, inherits the precision of the ground-state meta-GGA SCAN-L at low T, and most of the thermal XC effects are captured at the GGA level of theory, providing overall a much higher accuracy across the temperature regimes spanned by the WDM domain.

With increasing temperature, the electron density approaches the slowly varying regime. The KDT16 GGA functional, by construction, recovers the finite-T gradient expansion. Thermal XC corrections beyond the GGA level are expected to be small; therefore, in the following we propose a simple perturbative-like self-consistent approach via a universal thermal additive correction treated self-consistently, similar to the idea used in Ref. 19 to construct GGA XC with additive thermal LDA correction. The KDT16 XC free energy in the zero-T limit reduces to the ground-state PBE by construction:

$$\lim_{T\to 0} \mathcal{F}_{\mathrm{xc}}^{\mathrm{KDT16}}\left[n,T\right] \approx E_{\mathrm{xc}}^{\mathrm{PBE}}\left[n\right], \tag{1}$$

a choice driven by popularity of the PBE functional and by availability of pseudo-potentials and projector augmented wave (PAW) data sets generated by using the PBE XC. Given the quality of SCAN-L functional at zero temperature, we propose a simple temperature-dependent meta-GGA

$$\mathcal{F}_{\mathrm{xc}}^{\text{meta-GGA}}[n,T] = E_{\mathrm{xc}}^{\text{meta-GGA}}[n] + \Delta\mathcal{F}_{\mathrm{xc}}^{\mathrm{GGA}}[n,T], \tag{2}$$

with the additive thermal correction defined as follows:

$$\Delta\mathcal{F}_{\mathrm{xc}}^{\mathrm{GGA}}[n,T] := \mathcal{F}_{\mathrm{xc}}^{\mathrm{KDT16}}[n,T] - E_{\mathrm{xc}}^{\mathrm{PBE}}[n] \tag{3}$$

and meta-GGA = SCAN-L. An explicit functional form defined by Eqs. (2) and (3) is used in standard fully self-consistent DFT calculations with local XC potential calculated as a functional derivative of $\mathcal{F}_{\mathrm{xc}}^{\text{meta-GGA}}[n,T]$ with respect to electron density n.

Ab initio molecular dynamics (AIMD) simulations that demonstrate the superior accuracy of the new T-SCAN-L meta-GGA functional are for dense helium. Figure 1 compares relative errors for total pressures obtained from DFT simulations with four XC functionals and high-quality path-integral Monte Carlo (PIMC). PIMC is an efficient *first-principles* simulation technique for quantum systems at finite temperature that accurately takes into account the Coulombic interaction between electrons using pair-density matrices, so it therefore can be used to benchmark approximate XC density functionals at elevated temperatures.[7] Both ground-state functionals (PBE and SCAN-L) systematically overestimate the total pressure: the relative error with respect to the reference PIMC data is between 4.2% and 5.8% at T = 10.77 eV. In contrast, the T-SCAN-L total pressures are in excellent agreement with the PIMC values, demonstrating unprecedented accuracy between 0.05% and 0.35% for this range of densities. Relative differences between the KDT16 and PIMC values are larger as compared to the T-SCAN-L values and range from 0.4% to 1.4%. These comparisons show that T-SCAN-L calculations can improve the DFT simulation accuracy for He at these warm dense conditions by a factor of ~3 to 10 over the widely used XC functionals (PBE, SCANL, and KDT16). This clearly demonstrates that the T-SCAN-L meta-GGA functional can accurately capture combined XC thermal and nonhomogeneity effects. When temperature increases to 21.54 eV, the relative error of the ground-state functionals reduces to the range between 1.3% and 3.6% (because the XC contribution becomes less important as compared to the noninteracting free-energy term at high T), while the relative difference between T-SCAN-L and PIMC values is still less than ~1%.

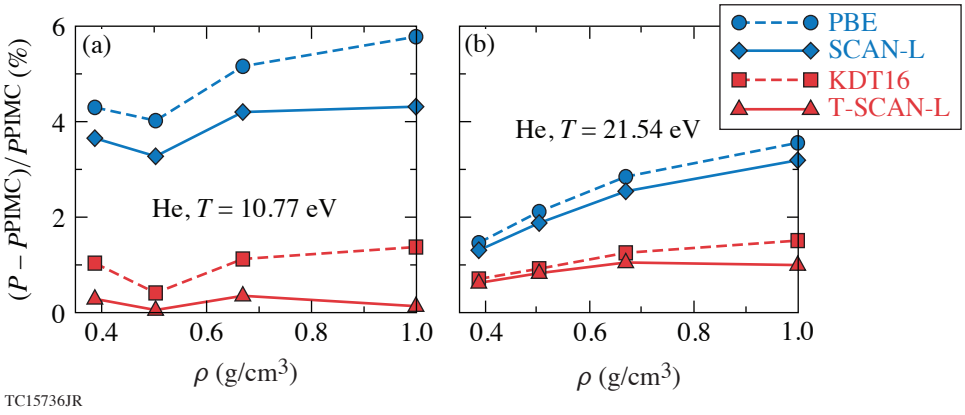

Figure 1
The relative error of total pressure from AIMD simulations of warm dense He using PBE, SCAL-L, KDT16, and T-SCAN-L XC functionals calculated with respect to the reference PIMC results and shown as a function of material density for two temperatures.

The simplest thermalization scheme, which uses a universal additive thermal correction and a perturbative-like self-consistent approach, has been implemented, leading to thermal T-SCAN-L functional. The nonempirical T-SCAN-L meta-GGA density functional takes into account combined thermal and nonhomogeneity effects at the meta-GGA level, providing a significantly higher accuracy for DFT to better predict material properties in the WDM regime, as compared to the thermal KDT16, and to the ground-state PBE and SCAN-L XC functionals. In the zero-temperature limit, T-SCAN-L reduces to its ground-state counterpart, therefore preserving the SCAN-L meta-GGA level of accuracy at low T.

This material is based upon work supported by the Department of Energy National Nuclear Security Administration under Award Number DE-NA0003856 and U.S. National Science Foundation PHY Grant No. 1802964. This research used resources of the National Energy Research Scientific Computing Center, a DOE Office of Science User Facility supported by the Office of Science of the U.S. Department of Energy under Contract No. DE-AC02-05CH11231.

1. J. J. Fortney and N. Nettelmann, Space Sci. Rev. **152**, 423 (2010).
2. W. Lorenzen, B. Holst, and R. Redmer, Phys. Rev. B **84**, 235109 (2011).
3. J. Hinz *et al*., Phys. Rev. Research **2**, 032065(R) (2020).
4. C. A. Iglesias, F. J. Rogers, and D. Saumon, Astrophys. J. Lett. **569**, L111 (2002).
5. S. X. Hu *et al*., Phys. Plasmas **22**, 056304 (2015).
6. V. V Karasiev and S. X. Hu, Phys. Rev. E **103**, 033202 (2021).
7. V. V. Karasiev, L. Calderín, and S. B. Trickey, Phys. Rev. E **93**, 063207 (2016).
8. V. V. Karasiev, S. B. Trickey, and J. W. Dufty, Phys. Rev. B **99**, 195134 (2019).
9. K. Ramakrishna, T. Dornheim, and J. Vorberger, Phys. Rev. B **101**, 195129 (2020).
10. M. Bonitz *et al*., Phys. Plasmas **27**, 042710 (2020).
11. V. V. Karasiev *et al*., Phys. Rev. Lett. **112**, 076403 (2014).
12. V. V. Karasiev, J. W. Dufty, and S. B. Trickey, Phys. Rev. Lett. **120**, 076401 (2018).
13. D. I. Mihaylov, V. V. Karasiev, and S. X. Hu, Phys. Rev. B **101**, 245141 (2020).
14. J. P. Perdew, K. Burke, and M. Ernzerhof, Phys. Rev. Lett. **77**, 3865 (1996); **78**, 1396(E) (1997).
15. J. Sun, A. Ruzsinszky, and J. P. Perdew, Phys. Rev. Lett. **115**, 036402 (2015).
16. H. Peng *et al*., Phys. Rev. X **6**, 041005 (2016).
17. D. Mejia-Rodriguez and S. B. Trickey, Phys. Rev. A **96**, 052512 (2017).
18. D. Mejia-Rodriguez and S. B. Trickey, Phys. Rev. B **98**, 115161 (2018).
19. T. Sjostrom and J. Daligault, Phys. Rev. B **90**, 155109 (2014).

Unveiling the Nature of the Bonded-to-Atomic Transition in Liquid SiO_2 to TPa Pressures

S. Zhang,[1] M. A. Morales,[2,3] R. Jeanloz,[4] M. Millot,[3] S. X. Hu,[1] and E. Zurek[5]

[1]Laboratory for Laser Energetics, University of Rochester
[2]Center for Computational Quantum Physics, Flatiron Institute
[3]Lawrence Livermore National Laboratory
[4]Departments of Earth and Planetary Science and Astronomy, University of California, Berkeley
[5]Department of Chemistry, State University of New York at Buffalo

SiO_2 is an important compound for theory, basic science, and technology, including as a laboratory standard for high-energy-density experiments. As a key constituent of Earth, terrestrial, and even giant planets, the response of SiO_2 to dynamic compression helps to determine (1) how planets form through giant impacts and (2) the high pressure–temperature material properties that control, for example, how the deep interiors of planets evolve.

Laser and magnetically driven experiments and first-principles calculations over the past two decades[1–12] have provided important constraints on the high-temperature phase diagram and properties of SiO_2 and established it as a standard for impedance matching at up to 1.2 TPa. Questions remain, however, about the liquid structure of SiO_2 at extreme conditions,[8,13–15] the understanding of which not only helps to clarify phase transitions and metallization that generally occurs in materials under significant compression but can also shed light on material transport properties (e.g., electrical and thermal conductivity) critical to modeling the dynamics of the magma ocean and magnetic-field generation in early Earth and super-Earth exoplanets, as well as for numerical simulations of giant impacts.

We have performed extensive simulations from first principles and in-depth analysis of the structure, electron density, and thermodynamic properties of liquid SiO_2 to gain insights into the nature of the bonded-to-atomic transition. Our results show that a heat capacity anomaly happens at 2 to 3×10^4 K (1.5 to 2.5 eV) over the pressure range of 0.1 to 1 TPa, coinciding with conditions where the lifetime of Si–O bonds equals 50 fs. This corresponds to bonded-to-atomic liquid transition temperatures that are lower and more sensitive to pressure than previous estimates based on laser-driven Hugoniot measurements (black line with diamonds versus gray dashed curve in Fig. 1). These results render a new bonded-to-atomic boundary of liquid SiO_2 that overlaps with the conditions of interest to giant-impact simulations, which indicates more-complex variations (i.e., a decrease and then an increase with temperatures) in heat capacity than that considered previously. This can rebalance the dissipation of irreversible work into temperature and entropy in events of giant impact, necessitating reconsideration of predictions by simulations that are based on empirical equation-of-state (EOS) models.

Furthermore, our calculated Hugoniots show overall agreement with experimental ones (see Fig. 1) and are similar to previous calculations using similar methods.[4,8,9,14] The discrepancies between theory and experiment in the stishovite temperature–pressure Hugoniot near melting, together with the previously shown inconsistencies at 1.0 to 2.5 TPa, emphasize the need for further development in both numerical simulations and dynamic compression experiments to improve constraints on the phase diagram, EOS, and properties of SiO_2 in regions off the Hugoniots of α-quartz and fused silica and elucidate the exotic behaviors affecting matter at extreme conditions. These include simulations that overcome the increased limitations of pseudopotentials and computational cost for reaching convergence at the high density/temperature conditions or go beyond LDA/GGA (local density approximation/generalized gradient approximation) for the exchange-correlation functional, as well as more in-depth experimental

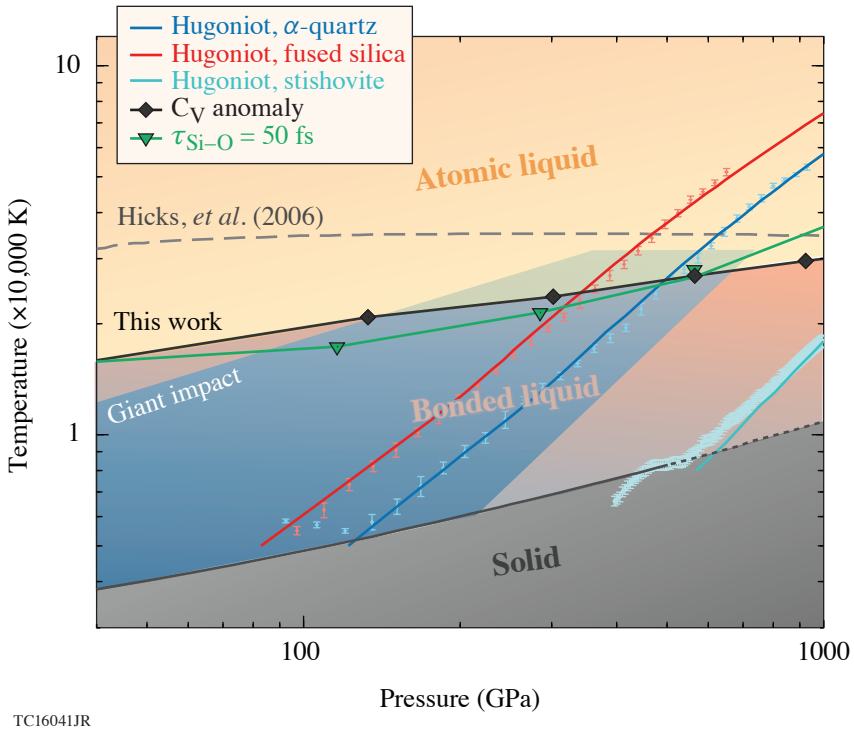

Figure 1
Phase diagram of SiO_2 featuring the bonded-to-atomic liquid transition determined in this work (black curve with diamond symbols) as compared to a previous estimation (Hicks *et al.*,[1] gray dashed curve). Also shown are the conditions for Si–O bond lifetime equaling 50 fs (green line with triangles), Hugoniots from this work (solid curves in red, blue, and turquoise for fused silica, α-quartz, and stishovite, respectively) in comparison to experiments[1,2] (lighter-colored symbols), the melting curve (solid dark-gray curve: measured; dashed dark-gray curve: extrapolated) from Millot *et al.*,[2] and the conditions of interest (blue shaded area) to giant impacts.[16]

studies, currently lacking benchmarking u_s–u_p data for stishovite between 0.2 and 1.2 TPa and relying on pyrometry and a gray-body approximation for temperature estimation.

This material is based upon work supported by the Department of Energy National Nuclear Security Administration under Award Number DE-NA0003856, the University of Rochester, and the New York State Energy Research and Development Authority.

1. D. G. Hicks *et al.*, Phys. Rev. Lett. **97**, 025502 (2006).
2. M. Millot *et al.*, Science **347**, 418 (2015).
3. M. D. Knudson and M. P. Desjarlais, Phys. Rev. B **88**, 184107 (2013).
4. T. Qi *et al.*, Phys. Plasmas **22**, 062706 (2015).
5. M. D. Knudson and R. W. Lemke, J. Appl. Phys. **114**, 053510 (2013).
6. C. A. McCoy *et al.*, J. Appl. Phys. **119**, 215901 (2016); **120**, 235901 (2016).
7. M. C. Marshall *et al.*, Phys. Rev. B **99**, 174101 (2019).
8. S. Root, J. P. Townsend, and M. D. Knudson, J. Appl. Phys. **126**, 165901 (2019).
9. T. Sjostrom and S. Crockett, AIP Conf. Proc. **1793**, 050010 (2017).
10. M. Li *et al.*, Phys. Rev. Lett. **120**, 215703 (2018).
11. M. Guarguaglini *et al.*, Nat. Commun. **12**, 840 (2021).
12. F. Soubiran and B. Militzer, Nat. Commun. **9**, 3883 (2018).
13. R. G. Kraus *et al.*, J. Geophys. Res. Planets **117**, E09009 (2012).
14. R. Scipioni, L. Stixrude, and M. P. Desjarlais, Proc. Nat. Acad. Sci. **114**, 9009 (2017).
15. E. C. R. Green, E. Artacho, and J. A. D. Connolly, Earth Planet. Sci. Lett. **491**, 11 (2018).
16. R. M. Canup, Icarus **168**, 433 (2004).

A Case Study of Using X-Ray Thomson Scattering to Diagnose the In-Flight Plasma Conditions of DT Cryogenic Implosions

H. Poole,[1] D. Cao,[2] R. Epstein,[2] I. Golovkin,[3] T. Walton,[3] S. X. Hu,[2] M. Kasim,[1] S. M. Vinko,[1] J. R. Rygg,[2] V. N. Goncharov,[2] G. Gregori,[1] and S. P. Regan[2]

[1]Department of Physics, University of Oxford
[2]Laboratory Laboratory for Laser Energetics, University of Rochester
[3]Prism Computational Sciences

The design of inertial confinement fusion ignition targets requires radiation-hydrodynamic simulations with accurate models of the fundamental material properties (i.e., equation of state, opacity, and conductivity). Validation of these models are required via experimentation. A feasibility study of using spatially integrated, spectrally resolved, x-ray Thomson-scattering (XRTS) measurements to diagnose the temperature, density, and ionization of the compressed DT shell of a cryogenic DT implosion at two-thirds convergence was conducted. This study involved analyzing the x-ray scattering data produced by targets with very different adiabats, specifically 2.8 and 8.0, to determine if their conditions were distinguishable.

Synthetic scattering spectra were generated using 1-D implosion simulations from the *LILAC* code[1] that were post-processed with the x-ray scattering model, which is incorporated within *Spect3D*.[2] To model the x-ray emissivity, a 1-kJ laser with a 10-ps pulse length and a source diameter of 50 μm was used to produce a Gaussian x-ray source, with a FWHM of 10 eV (Ref. 3). The scattering geometry is shown in Fig. 1. The detectors captured scattering data at $\theta_F = 40°$ and $\theta_B = 120°$. Two x-ray photon energies, 2 keV and 3.5 keV, were considered.

Using the output spectra from *Spect3D*, synthetic experimental data were produced by assuming a detector efficiency of $\Gamma_{det} \sim 10^{-5}$ and a spectral resolution of 3 eV/bin, which gives ~300 inelastically scattered photons resolved by the detector. Synthetic experimental noise was added by removing the uniform background signal and using the Poisson statistic, which estimates the noise as $\sim 1/N_t$, where N_t is the number of photons per spectral resolution element.

Before extracting the plasma parameters from the spatially integrated simulated spectra, the inverse problem instability must first be addressed, which implies that the same measured spectra could be fitted equally well by very different plasma parameters. Bayesian inference, using Markov–Chain Monte Carlo (MCMC) to sample the multidimensional space, is a more-robust approach to exploring the behavior of the complex multiparameter simulations.[4]

The MCMC exploration fit the entire spectra, assuming two weighted uniform plasma regions, one containing DT and the other CH. The cost function used to determine the appropriateness of each MCMC spectrum calculates the maximum percentage error to allow equal weighting of the fitting to the elastic and inelastic peaks between the MCMC spectrum I_{fit}, and the synthetic experimental spectra I_{raw},

$$\beta_{cost} = \max\left(\frac{I_{fit} - I_{raw}}{I_{raw}} \frac{1}{\sqrt{2}\,\sigma}\right)^2,$$

where σ is the standard deviation representative of the noise of the synthetic scattering spectra. The σ is selected such that the noise of the scattering signal falls comfortably within the spread of the accepted fits. A value of 0.075 was chosen. The forward-

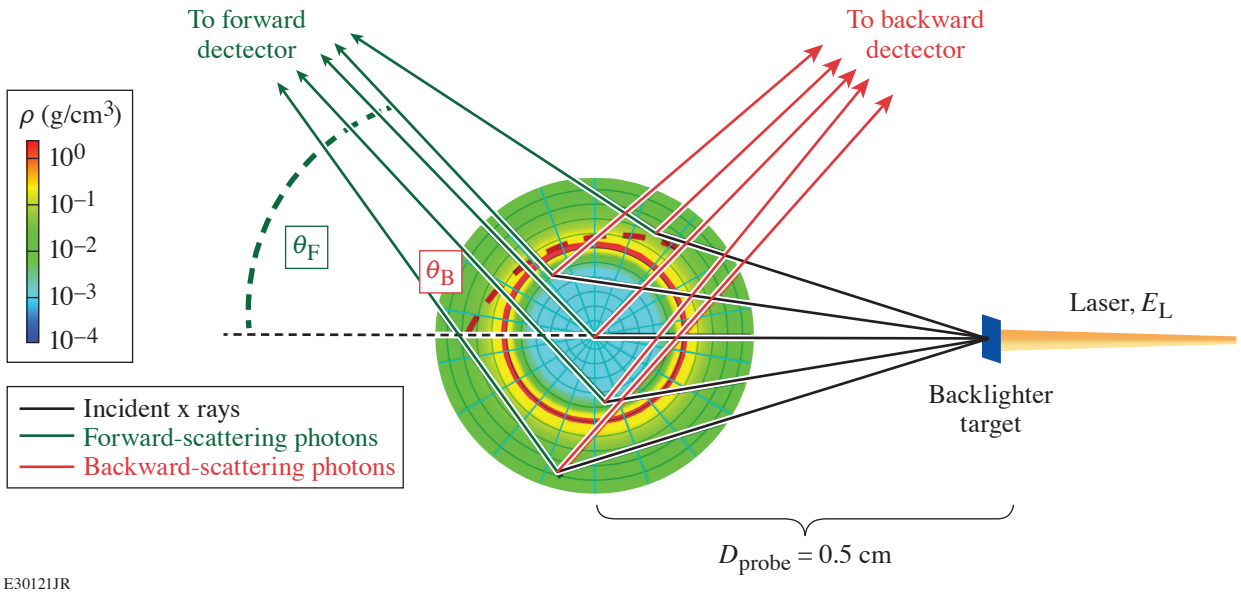

Figure 1
A sketch of the proposed experimental setup, with a laser of energy E_L incident on a backlighter target, producing x rays with a conversion efficiency of η_x. The scattering x rays are shown incident on the 3-D inferred density profile from *Spect3D* using the 1-D simulation data produced by the *LILAC* code. A schematic of the scattering events, recorded on the detector by *Spect3D*, from different zones throughout the implosion, is shown. The scattering geometry is demonstrated and not drawn to scale.

and backward-scattering spectra were analyzed separately, and their parameter distributions were combined to produce an overall distribution for each plasma parameter. The distributions for each adiabat and x-ray photon energy are shown in Table I.

Good agreement was found between the mass-averaged simulation parameter values and the MCMC distributions. There is, predictably, very little information regarding the CH plasma. This is due to its lower density compared to the DT compressed shell, meaning it does not contribute to the overall shape of the scattering. Overall, the optimum analysis presented in this summary to resolve the plasma conditions in the compressed shell, using a realistic laser probe from OMEGA EP, is performing MCMC analysis from spectra produced using a backward fielding detector. Since the collective forward-scattering detector is not required for sufficient convergence on the DT compressed shell parameters, either a 2-keV or 3.5-keV x-ray photon energy probe could be used. Better agreement may be achieved between the MCMC parameters and the simulations if a narrower bandwidth probe beam could be used.

Table I: The full spectral analysis of MCMC DT fitting parameters compared to the mass-weighted parameters from the *LILAC* 1-D simulations, focused on the compressed DT shell, for each adiabat and each probe.

DT parameter	T_e	n_e (cm^{-3})	Z
Adiabat = 2.8			
Simulation	25	5.5×10^{23}	0.97
MCMC 2 keV	33±8	$(5.2\pm0.6) \times 10^{23}$	0.94±0.03
MCMC 3.5 keV	25±3	$(5.0\pm0.3) \times 10^{23}$	0.95±0.03
Adiabat = 8.0			
Simulation	38	3.7×10^{23}	0.97
MCMC 2 keV	50±6	$(2.6\pm0.4) \times 10^{23}$	0.88±0.07
MCMC 3.5 keV	56±6	$(3.2\pm0.5) \times 10^{23}$	0.87±0.05

In summary, spatially integrated XRTS spectra for 1-D *LILAC*-simulated conditions of low- and high-adiabat, DT cryogenic implosions have been calculated at two-thirds convergence. Markov–Chain Monte Carlo analysis was performed for two different scattering setups. Information on the compressed shell conditions was obtained since it has been shown to be possible to use the spectral resolution in a spatially integrated measurement to discriminate between different regions in the plasma. Fielding just one detector in the noncollective scattering regime produces good agreement with the compressed shell mass-averaged parameters from the simulation. This technique can be used to resolve both the low- and high-adiabat implosions. In the future, similar analysis will be performed on the conditions at stagnation, the effect of mixing in the implosion, as well as investigations into 2-D and 3-D simulations using *DRACO* and *ASTER*.

This material is based upon work supported by the Department of Energy National Nuclear Security Administration under Award Number DE-NA0003856, the University of Rochester, and the New York State Energy Research and Development Authority.

1. J. Delettrez *et al.*, Phys. Rev. A **36**, 3926 (1987).
2. I. Golovkin *et al.*, High Energy Density Phys. **9**, 510 (2013).
3. C. Stoeckl *et al.*, Rev. Sci. Instrum. **85**, 11E501 (2014).
4. M. F. Kasim *et al.*, Phys. Plasmas **26**, 112706 (2019).

Interdigitated Electrode Geometry Variation and External Quantum Efficiency of GaN/AlGaN-Based Metal–Semiconductor–Metal Ultraviolet Photodetectors

S. F. Nwabunwanne and W. R. Donaldson

Laboratory for Laser Energetics
Department of Electrical and Computer Engineering, University of Rochester

Efficient and ultrafast $Al_xGa_{1-x}N$-based ultraviolet (UV) photodiodes are suitable candidates for UV photodetection because of their highly mobile carriers. The characteristics of $Al_xGa_{1-x}N$, a group III–V compound that has endeared it to the optoelectronics community, consist of a tunable direct band gap, superior electrical stability, elevated thermal resistivity, and robust performance in hazardous environments like inertial confinement chambers and space environments. $Al_xGa_{1-x}N$-based photodiodes (PD's) offer an important feature that permits the selection of a desired spectral window by simply altering the percentage composition of Al in the $Al_xGa_{1-x}N$ compound.[1,2]

AlGaN-based PD's produce the best response speed in the metal–semiconductor–metal (MSM) configuration because in this design, the response time is limited by the carrier transit time between the interdigitated fingers. Furthermore, in the MSM setup, the capacitance due to the interdigitated fingers is extremely small, of the order of 20×10^{-15} F, which leads to an ~1-ps resistor capacitor time constant for a 50-Ω external coupling circuit.[3]

Here, we discuss the successful design and fabrication of $Al_xGa_{1-x}N$-based photodetectors with rectangular and circular asymmetric, interdigitated electrode geometries GaN/AlGaN semiconductors. The thin films were grown on commercially available sapphire substrates via metal-organic chemical vapor deposition by KYMA Technologies.[4] The best-performing devices yielded a scope-limited pulse duration of 62 ps with a 29-ps rise time. The bias-independent external quantum efficiency of the devices was >70% for intrinsic devices at 60 V and >400% at 10 V. The main goal of this investigation was to establish the bias voltage that saturates the external quantum efficiency (EQE) of these devices.

Figure 1 depicts the device's epitaxial structure for both metals that were employed in the detectors. The experimental setup is shown in Fig. 2. UV light was produced by Astrella and an optical parametric amplifier (OPA) by a fourth-harmonic–generation technique. Astrella is an 800-nm Coherent laser operating at 1 kHz and possessing a 30-fs pulse duration. The 800-nm visible

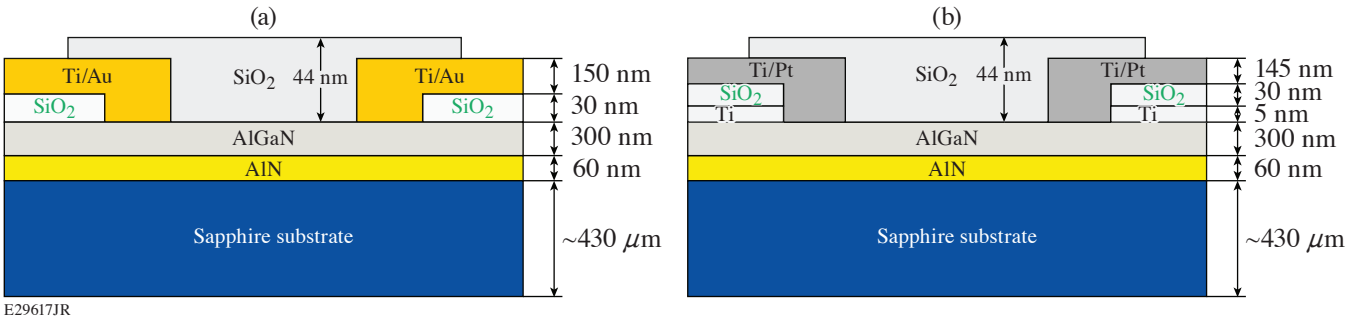

Figure 1
Epitaxial stack of the fabricated (a) Au and (b) Pt AlGaN-based MSM UV PD's for efficient and ultrafast UV detection.

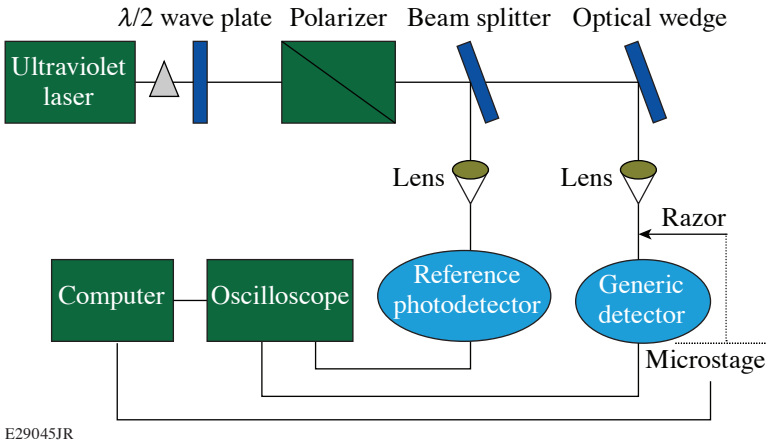

Figure 2
Experimental setup for ultrafast testing of AlGaN PD's at 262 nm (Ref. 1).

light output of Astrella served as the input pump laser to the OPA, which changes it to 262 nm of UV light using fourth-harmonic generation. The output energy per pulse from the OPA at 262 nm is 40×10^{-6} J, but only 0.749×10^{-9} J reached the detector under test. The reference detector was a 200- to 1100-nm Thorlab Det10 Si-biased detector.

Figure 3(a) posits the photocurrent of Pt intrinsic $Al_{0.2}Ga_{0.8}N$ with the circular asymmetric contact device as a function of bias voltage. The Schottky contact blocks current from –3.5 V to +3.5 V.

Figure 3(b) depicts the ultrafast impulse response function of Au $Al_{0.1}Ga_{0.9}N$ and Pt $Al_{0.2}Ga_{0.8}N$ intrinsic MSM UV photodiodes at 20-V bias voltage. The Au PD recorded a 29-ps rise time with 62-ps pulse duration, while the Pt PD showed a 34-ps rise time and 72-ps pulse width. The Au device exhibited the best response characteristics with a 29-ps rise time with 62-ps full width at half maximum; this response is not the intrinsic response time of the device due to the bandwidth limitation of the oscilloscope.

$$\mathrm{QE}(\eta) = \frac{I_{\mathrm{ph}}/e}{P/hv}. \tag{1}$$

The efficiency of the devices was computed using Eq. (1) and the results for Pt $Al_{0.1}Ga_{0.9}N$ *n*-doped circular asymmetric (CA) and Pt $Al_{0.2}Ga_{0.8}N$ intrinsic rectangular asymmetric (RA) detectors are plotted in Figs. 3(c) and 3(d), respectively.

The interdigitated electrode geometries of $Al_xGa_{1-x}N$ MSM UV photodiodes were redesigned as rectangular asymmetric and circular asymmetric fingers. These were successfully implemented and tested to establish their UV response profiles. Investigations were done to obtain the bias voltage that saturates these devices to find the detector's bias-independent EQE. The alterations of electrode geometry in addition to fewer electrodes on the devices reduced the effects of electrode shadowing and allowed about 34% more UV light to be absorbed. A combination of these factors resulted in the recorded bias-voltage–independent EQE of our devices. Establishment of the efficiency of these detectors will improve the quest for semiconductor-driven ultrafast laser pulse characterization and plasma diagnostics.

This material is based upon work supported by the Department of Energy National Nuclear Security Administration under Award Number DE-NA0003856, the University of Rochester, and the New York State Energy Research and Development Authority.

1. S. Nwabunwanne and W. Donaldson, Proc. SPIE **12001**, 120010F (2022).
2. E. Monroy *et al.*, Appl. Phys. Lett. **74**, 3401 (1999).
3. Y. Zhao and W. R. Donaldson, IEEE J. Quantum Electron. **56**, 4000607 (2020).
4. AlGaN Templates, Kyma Technologies Inc., Raleigh, NC 27617, accessed 10 June 2022, https://kymatech.com/products-services/materials/gan-related-iii-n-materials/499-algan-templates.

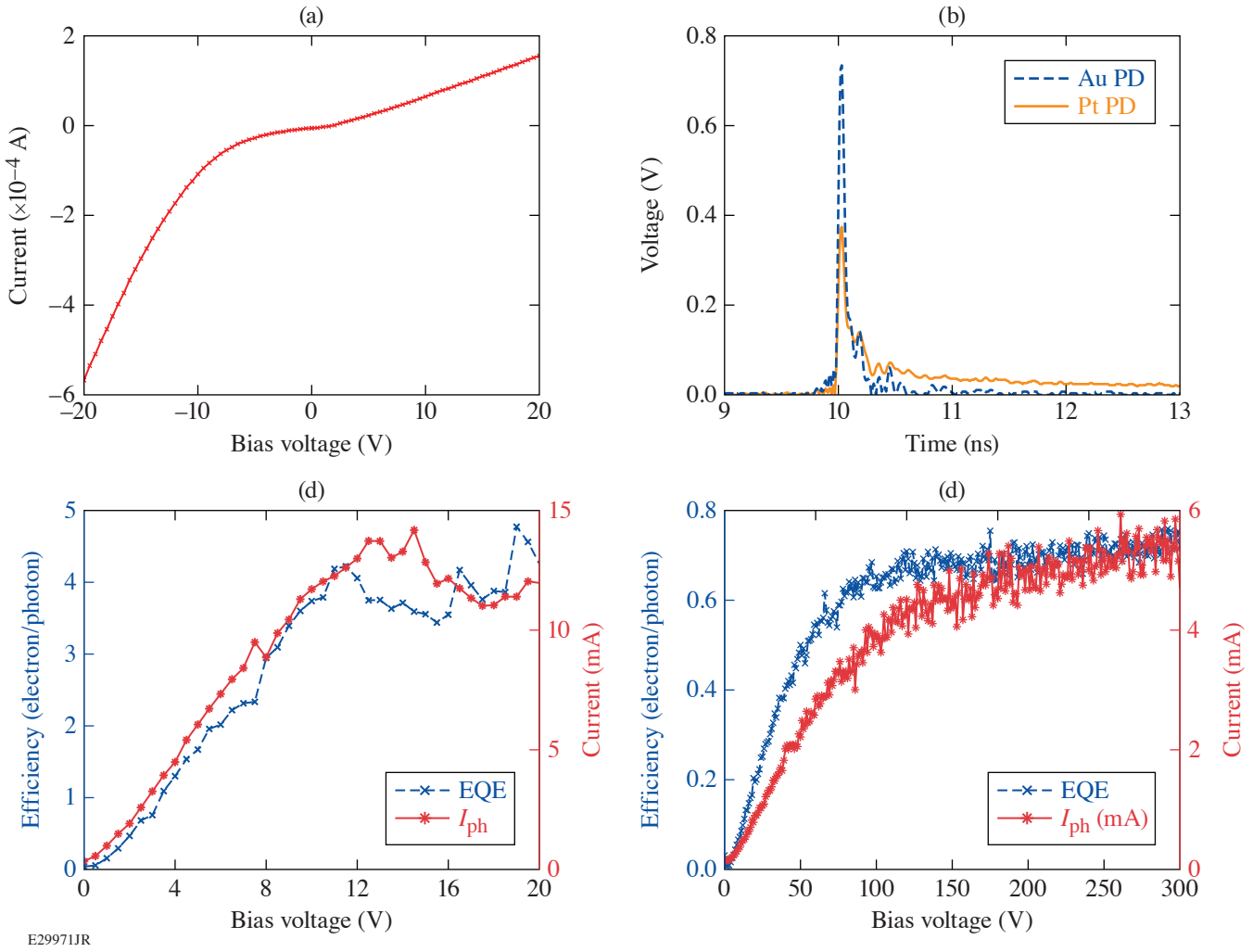

Figure 3
(a) Pt intrinsic $Al_{0.2}Ga_{0.8}N$ MSM UV photodiode I–V curve under dark conditions. (b) Au $Al_{0.1}Ga_{0.9}N$ and Pt $Al_{0.2}Ga_{0.8}N$ intrinsic MSM UV photodiodes' impulse response function at 20-V bias voltage. The Au PD yielded a 29-ps rise time with 62-ps pulse duration, while the Pt PD produced a 34-ps rise time and 72-ps pulse width. External quantum efficiency and photocurrent as a function of bias voltage. (c) Pt $Al_{0.1}Ga_{0.9}N$ *n*-doped CA device (saturation began at 10 V). (d) Pt $Al_{0.2}Ga_{0.8}N$ intrinsic RA device (saturation began at 60 V).

Impact of the Optical Parametric Amplification Phase on Laser Pulse Compression

J. Musgrave[1] and J. Bromage[2]

[1]Institute of Optics, University of Rochester
[2]Laboratory for Laser Energetics, University of Rochester

Optical parametric chirped-pulse amplification (OPCPA) has been widely used to provide high gain over broad bandwidths suitable for sub-20-fs pulses with multijoule energies, corresponding to petawatt peak powers.[1–3] Precise control and measurement of a system's spectral and spatial phases are required for Fourier transform–limited pulse compression and diffraction-limited focusing, respectively. Phase accumulated during optical parametric amplification (OPA) can degrade the compressibility and focusability of the pulse, reducing peak intensity. OPA is a three-wave mixing process where energy is transferred from a strong pump wave to a weak signal wave with the production of a third wave, called the "idler," to conserve energy and momentum. For efficient energy transfer, this process must be phase matched. Significant phase mismatch leads to reduction in gain and, as shown by Bahk,[4] can lead to signal phase accumulation. In this summary, we investigate signal phase accumulation from pump wavefront errors and evaluate the potential impact on signal pulse compression.

Broadband phase matching can be achieved by matching the group velocity of the signal and idler pulses using the amplifier material's birefringence and a noncollinear angle between the pump and signal.[5,6] Figure 1 shows relative orientation of the pump, signal, and idler k vectors to the crystal axis (O), with a noncollinear angle α.

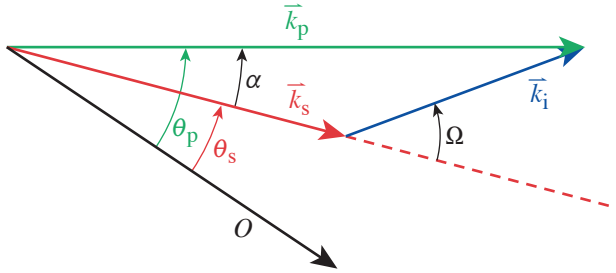

Figure 1
Phase matching between the wave vectors of the three beams: pump, signal, and idler. O is the optical axis of the nonlinear crystal.

The phase mismatch in the z direction is given by Eq. (1):

$$\Delta k = k_p \cos(\alpha) - k_s - \sqrt{k_p^2 \cos^2(\alpha) - k_p^2 + k_i^2}\,. \tag{1}$$

The sensitivity to pointing, caused either by global angular errors or local from wavefront aberrations, is given by the derivatives with respect to θ_p or θ_s for the pump and signal, respectively.[7] The resulting signal phase errors can be expressed analytically for the small-signal case or calculated numerically for higher-efficiency amplifiers.[7] In particular, modification of the signal spectral phase $\phi_s(\omega)$, an important parameter for determining pulse compression, can be evaluated for a range of pump and signal angular deviations from the optimum phase-matched condition.

As a test case, we chose the final amplifier of the Multi-Terawatt optical parametric amplifier line (MTW-OPAL), all-OPCPA system.[3] This amplifier uses 70% deuterated potassium dihydrogen phosphate (DKDP) crystals pumped by the second harmonic

of MTW to amplify 1.5-ns pulses centered at 920 nm with 140-nm bandwidths up to 11 J before recompression to sub-20 fs. For amplification, the pulse is chirped before the amplifier to 100,000× the Fourier transform limit; therefore, the interaction between the pump and the 140-nm-wide signal at a given time is essentially monochromatic. The sensitivity of the signal phase for this amplifier for a given angular error of the signal or pump is shown in Figs. 2(a) and 2(b), respectively. Curves for deuteration levels ranging from 70% to 100% are shown—the maximum range suitable for this system; they can be adjusted during the crystal growth with the relative amounts of hydrogen and deuterium. Changing the deuteration level requires changing the noncollinear angle α for optimum phase matching.[8] This, in turn, affects the phase-mismatch sensitivity and therefore the sensitivity of the signal phase to angular deviation. In the case of pump deviation [Fig. 2(a)], reducing the deuteration level causes an increase in pump-deviation sensitivity; for signal deviation [Fig. 2(b)], the opposite holds.

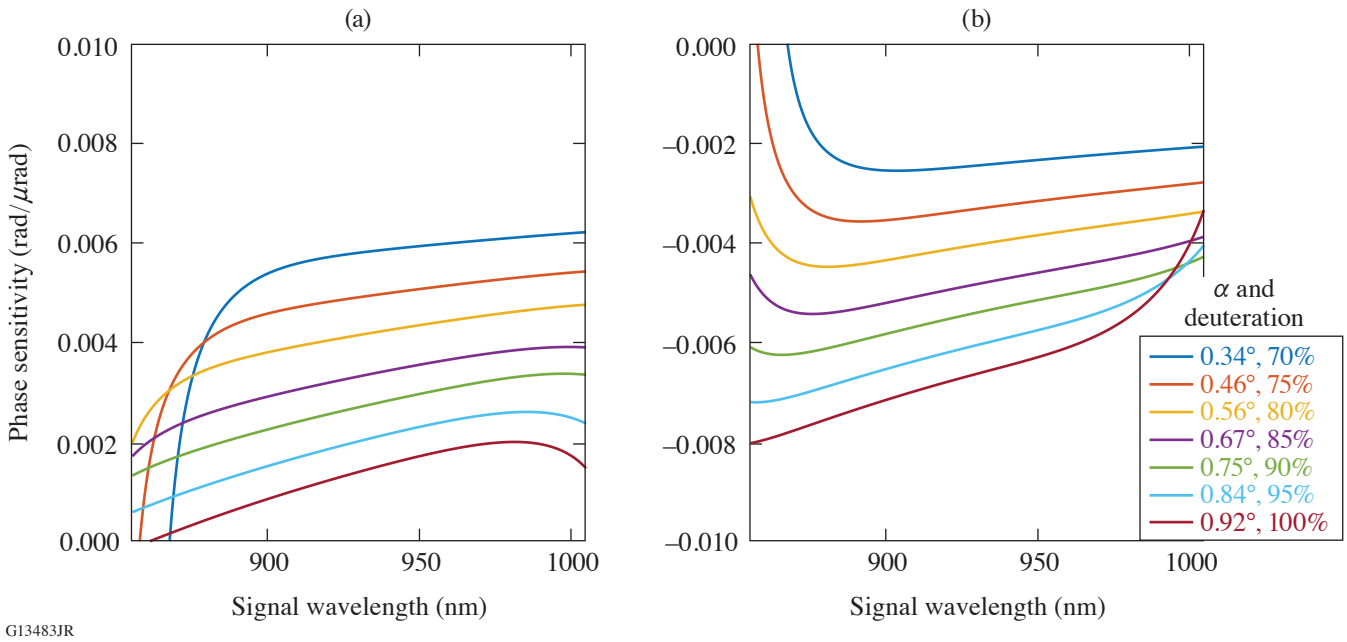

Figure 2
(a) Pump and (b) signal phase sensitivity across the signal wavelength for different deuteration levels and corresponding noncollinearity.

One point to note is that the phase sensitivity (in units of radians per microradian) is small but not zero and, in particular, can vary significantly across the signal bandwidth from 830 to 1010 nm. This variation in phase—a spectral phase error—can be problematic when it also has a spatially varying component, as would happen if the pump or signal angles vary locally. A number of cases were evaluated,[7] one of which is shown in Fig. 3, where the pump wavefront produces a local angular error of 500 μrad. This would produce a reduction in gain by ~50%, leading to local beam profile distortion. It would also change the local pulse (as shown in Fig. 3) with a shift of ~5 fs that, averaged over the beam profile, could cause a pulse broadening in the focal plane. Thankfully, in the case of the MTW-OPAL Laser System, wavefront slopes of this magnitude are not present and phase plates must be added to produce these effects.[9] Nonetheless, this analysis is valuable in determining the suitability of a given pump laser to ensure there are no spatiotemporal pulse-broadening effects that degrade the peak intensity achieved by the laser.

This material is based upon work supported by the Department of Energy National Nuclear Security Administration under Award Number DE-NA0003856, the University of Rochester, and the New York State Energy Research and Development Authority.

1. A. Dubietis, G. Jonusauskas, and A. Piskarskas, Opt. Commun. **88**, 437 (1992).
2. V. V. Lozhkarev *et al.*, Laser Phys. Lett. **4**, 421 (2007).
3. J. Bromage *et al.*, High Power Laser Sci. Eng. **9**, e63 (2021).
4. S. W. Bahk, Opt. Lett. **46**, 5368 (2021).

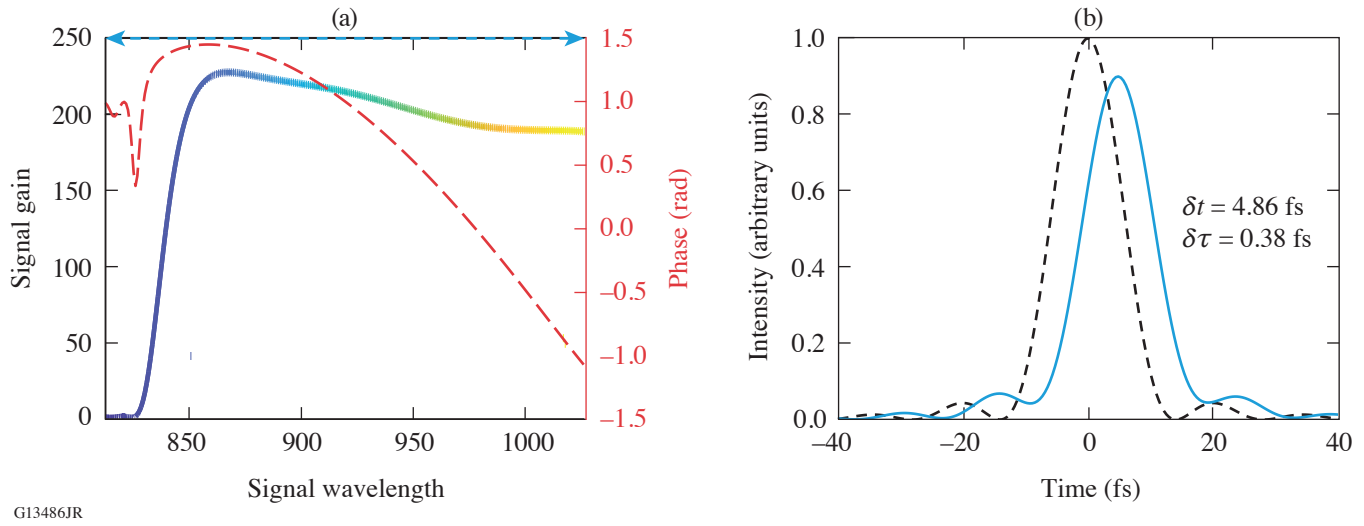

Figure 3
(a) Impact of angular error on signal gain and spectral phase. (b) Impact on the compressed pulse assuming equivalent gain across the spectrum (to show spectral phase effects). δt is the temporal shift of the peak, and $\delta\tau$ is the change in pulse full width at half maximum from the nominal 13 fs.

5. G. M. Gale *et al.*, Opt. Lett. **20**, 1562 (1995).
6. G. Cerullo and S. De Silvestri, Rev. Sci. Instrum. **74**, 1 (2003).
7. J. Musgrave and J. Bromage, Appl. Opt. **61**, 3838 (2022).
8. K. Fujioka *et al.*, J. Appl. Phys. **117** (9), 093103 (2015); **119**, 249902(E) (2016).
9. S. W. Bahk *et al.*, Opt. Express **30**, 12,995 (2022).

Simultaneous Contrast Improvement and Temporal Compression Using Divided-Pulse Nonlinear Compression

G. W. Jenkins,[1,2] C. Feng,[1] and J. Bromage[1]

[1]Laboratory for Laser Energetics, University of Rochester
[2]Institute of Optics, University of Rochester

Temporal contrast is an increasingly important specification for high-energy, ultrafast lasers because prepulses with only a fraction of a percent of the main pulse's energy can ionize the laser's target and modify experimental conditions before the main pulse arrives. To remove the prepulses, many temporal contrast improvement methods have been developed. We are particularly interested in methods such as nonlinear ellipse rotation (NER)[1] that allow simultaneous contrast improvement and spectral broadening.[2,3] Yb laser technology suffers from relatively long pulses (of the order of hundreds of femtoseconds to picoseconds) and requires temporal compression to efficiently pump many applications of interest. With NER, both contrast improvement and temporal compression can be accomplished in a single step.

In this summary, we demonstrate a new method of contrast improvement that allows both contrast improvement and temporal compression in a single step—divided-pulse nonlinear compression (DPNLC). In DPNLC, a high-energy pulse is divided into multiple low-energy pulses that are spectrally broadened through self-phase modulation (SPM) in gas, as illustrated in Fig. 1. After spectral broadening, the low-energy pulses are coherently recombined back into a high-energy pulse and the recombined pulse is compressed to its new transform limit. We have been developing DPNLC to overcome gas-ionization problems encountered at high energies but have found that the ability to apply an unequal nonlinear phase to the low-energy divided pulses allows us to use the method for contrast improvement as well.

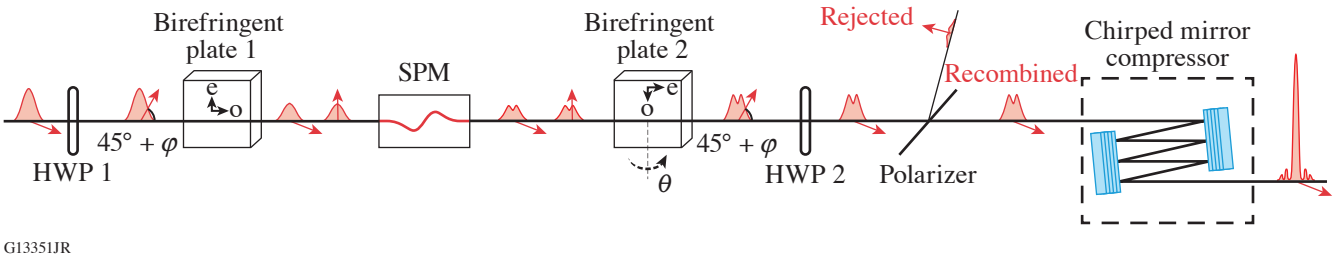

Figure 1
Apparatus for DPNLC. Birefringent plates with extraordinary axis "e" and ordinary axis "o" are used to divide one pulse into two low-energy, orthogonally polarized pulses. Red arrows indicate the pulse's polarization, and the distorted pulse shape after the SPM stage indicates an arbitrary reshaping by nonlinear processes in the SPM stage. After recombination, the polarization is cleaned with a polarizer and the pulse is compressed to a shorter duration with chirped mirrors. The angles φ and θ represent angular alignment errors in polarization and crystal angle of incidence, respectively. HWP: half-wave plate.

In our previous work,[4] we analyzed the alignment tolerances for DPNLC. The final result of our analysis was an expression for the pulse power in each polarization after the recombination step. The output is written as a Jones vector, where the top row is the power in the $\hat{p} = 45° + \varphi$ polarization and the bottom row is the power in the $\hat{m} = 45° + \varphi$ polarization:

$$\bar{P}_{\text{out}} = \frac{e^{-T^2}}{2\sqrt{\pi}} \begin{bmatrix} 1 + \sin^2(2\varphi) + \cos^2(2\varphi)\cos\left[2\phi_{\text{NL}}\sin(2\varphi)e^{-T^2} + \Delta\phi(\theta)\right] \\ \cos^2(2\varphi)\left\{1 - \cos\left[2\phi_{\text{NL}}\sin(2\varphi)e^{-T^2} + \Delta\phi(\theta)\right]\right\} \end{bmatrix}, \tag{1}$$

where we have normalized the expression so integrating over time gives a total energy of 1. In Eq. (1), the two most important alignment angles are the incoming polarization error (φ) and the angle of incidence (AOI, θ) on the second birefringent plate. The nonlinear phase accumulated in the SPM stage is represented by ϕ_{NL}, and $\Delta\phi(\theta) = \phi_2(\theta) - \phi_1$ is the difference in retardance between the two calcite plates. We developed a similar equation that describes a typical prepulse after recombination:

$$\bar{P}_{\text{pre}} = \frac{e^{-T^2}}{2\sqrt{\pi}} \begin{bmatrix} 1 + \sin^2(2\varphi) + \cos^2(2\varphi)\cos\left[\Delta\phi(\theta)\right] \\ \cos^2(2\varphi)\left\{1 - \cos\left[\Delta\phi(\theta)\right]\right\} \end{bmatrix}. \tag{2}$$

These equations indicate a simple method to improve the temporal contrast of the pulse train. Equation (2) shows that if the retardance difference $[\Delta\phi(\theta)]$ is set to zero, the entire prepulse will be found in the $\hat{p}$ polarization. Then we can apply a polarization alignment error (φ) to rotate the main pulse into the $\hat{m}$ polarization. Finally, we use a polarizer to pass the $\hat{m}$ polarization and reject the $\hat{p}$ polarization, thereby rejecting all of the prepulses.

We successfully demonstrated and quantified contrast improvement using these steps. Our laser system is a homebuilt Yb-doped, thin-disk regenerative amplifier that emits 1.2-ps pulses at a wavelength of 1030 nm, a repetition rate of 1 kHz, and an average power of 10 W. The pulses are coupled into a 1.8-m-long, 500-μm-inner-diam, hollow-core fiber (HCF) filled with 1.7 bar of argon for spectral broadening. The pulses accumulate 8.4 rad of nonlinear phase in the HCF. A 12-mm-thick, x-cut calcite plate divides the pulses in two before the HCF, and an identical plate recombines the pulses after the HCF, as previously illustrated in Fig. 1. A half-wave plate (HWP1) is placed before the first birefringent plate to carefully control the incoming polarization error φ, and a second HWP (HWP2) is placed after the last birefringent plate to select either the $\hat{p}$ or $\hat{m}$ polarization for transmission through the recombination polarizer.

First, we measured the original contrast of the laser system. The apparatus in Fig. 1 was aligned with zero alignment errors and measured near-perfect recombination into the $\hat{p}$ polarization (97.3% limited by a 2.5% p-polarization reflection on the polarizer). With this alignment, both the main pulse and prepulses are transmitted by the polarizer with maximum efficiency. The original contrast of the laser was measured by attenuating the beam with a set of neutral-density (ND) filters and then focusing it onto a photodiode. On the photodiode, both the main pulse and prepulses could clearly be seen, as shown in Fig. 2. The maximum prepulse height is 1.9 mV, while the main pulse is 2.3 V; therefore, the initial contrast of the laser is $\sim 10^{-3}$.

Next, we applied a polarization angle error to improve the contrast. We rotated HWP1 until the energy of the main pulse in the $\hat{m}$ was maximized (found at a HWP angle of 3°). Then we rotated HWP2 to transmit the $\hat{m}$ polarization and reject the $\hat{p}$ on the polarizer. We made the same photodiode measurement and found that the prepulses were rejected to below our measurement sensitivity, as shown in Fig. 2. The main pulse was transmitted with high efficiency and measured at 1.7 V.

To quantify the contrast improvement, we removed the ND filters until the prepulses became visible again. We removed 3.5 optical density of the ND filters; we then made fine adjustments to the AOI of calcite plate 2 and the angle of HWP2 to minimize the prepulses and measured a prepulse signal of 0.7 mV. This puts the new contrast of the pulse train at $\sim 10^{-7}$—an improvement of four orders of magnitude.

Finally, we compressed the contrast-improved pulse using a series of chirped mirrors (–43,000-fs group-delay dispersion) and measured the compressed pulse in a second-harmonic frequency-resolved optical gating system. The measured pulse was excellent, compressed with a FWHM pulse duration of 187 fs, close to its transform limit of 180 fs. The compressed pulse with-

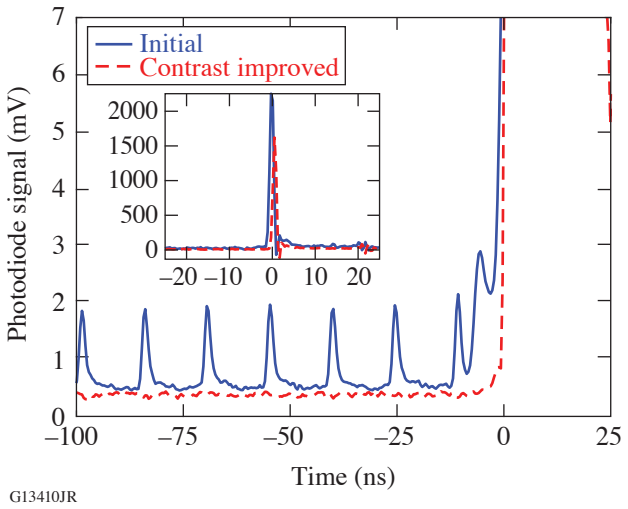

Figure 2
Captured photodiode signals from the pulse train. A train of prepulses with a maximum signal of 1.9 mV is clearly seen before the main pulse, which starts at time = 0. After the HWP's are rotated to improve the contrast, the prepulses are rejected and completely unmeasurable. At the same time, the height of the main pulse is reduced only from 2.3 V to 1.7 V, as shown in the inset.

out contrast improvement was compressible to a similar duration (186 fs with a transform limit of 185 fs) with the same chirped mirrors. Therefore, the contrast improvement method enables temporal compression equivalent to standard HCF operation.

In conclusion, we demonstrated a new method for temporal contrast improvement—divided-pulse nonlinear compression. By slightly misaligning the calcite plates used for pulse division and recombination, we rotated the polarization of the main pulse and rejected problematic prepulses on a polarizer. We measured four-orders-of-magnitude temporal contrast improvement and 72% efficiency for the main pulse, values comparable with other state-of-the-art temporal contrast improvement methods. Simultaneously, we compressed the pulse from 1.2 ps to 187 fs.

This material is based upon work supported by the Department of Energy National Nuclear Security Administration under Award Number DE-NA0003856, the University of Rochester, and the New York State Energy Research and Development Authority.

1. D. Homoelle *et al.*, Opt. Lett. **27**, 1646 (2002).
2. N. Smijesh *et al.*, Opt. Lett. **44**, 4028 (2019).
3. N. G. Khodakovskiy *et al.*, Laser Phys. Lett. **16**, 095001 (2019).
4. G. W. Jenkins, C. Feng, and J. Bromage, J. Opt. Soc. Am. B **38**, 3199 (2021).

Analysis of Pump-to-Signal Noise Transfer in Two-Stage Ultra-Broadband Optical Parametric Chirped-Pulse Amplification

C. Feng, C. Dorrer, C. Jeon, R. G. Roides, B. Webb, and J. Bromage

Laboratory for Laser Energetics, University of Rochester

Optical parametric chirped-pulse amplification (OPCPA) provides the most viable route for the development of tens to hundreds of petawatt peak-power laser systems.[1] In OPCPA, different mechanisms introduce either isolated pulses or a slowly varying pedestal before the main pulse, therefore degrading its temporal contrast, which is defined as the ratio of the peak power of the main pulse to the power of the light in some predetermined temporal range. When the laser beam is focused to interact with the target, the intensity of the light present before the main pulse can exceed a threshold for irreversible modification of the target (e.g., ~10^{12} W/cm^2) and have a detrimental effect on laser–matter interaction. Therefore, understanding the origins of contrast degradation and maximizing the temporal contrast are essential for the development of ultrahigh-peak-power laser facilities.

Pump temporal modulation is one mechanism that can degrade the temporal contrast of the recompressed signal because it induces high-frequency spectral modulation on the chirped signal spectrum during parametric amplification.[2] Pump modulation is commonly introduced by the interference between the main pump pulse and the amplified spontaneous emission (ASE). This modulation is broadband with its bandwidth proportional to the spectral bandwidth of the ASE. Spectrally filtering the ASE of the pump pulse using a narrowband filter is an effective way to reduce the high-frequency pump noise and, therefore, the pump-induced contrast degradation.[3]

In this work, we have investigated, for the first time to our knowledge, the pump-to-signal noise transfer in a two-stage ultra-broadband OPCPA and demonstrated a novel mechanism based on pump-seed delay optimization to reduce the pump-induced temporal contrast degradation by as much as 15 dB (Ref. 4). The results are widely applicable to support the design and development of OPCPA-based ultrahigh-peak-power systems, for which maximizing the temporal contrast is a high priority.

The experimental demonstration was performed in a two-stage ultra-broadband OPCPA system (Fig. 1), which is a subsystem of the Multi-Terawatt–pumped optical parametric amplifier line (MTW-OPAL), i.e., a 0.5-PW, 20-fs, all-OPCPA system.[5] The subsystem consists of an ultra-broadband front end (UFE), two noncollinear optical parametric amplifiers (NOPA4a and NOPA4b), a single pump laser for pumping both NOPA stages, and a grating compressor. In high-power OPCPA systems, it is common to use a single laser to pump several optical parametric amplification stages to reduce experimental complexity and cost. In such a system, the signal amplified in the first stage carries the pump modulations, and amplification in the second stage occurs with a pump pulse having the same modulations. The temporal modulations of the amplified chirped signal and the temporal contrast of the compressed signal pulse, therefore, depend on the difference in pump-seed delay t in different stages, as illustrated in Fig. 1.

We investigated pump pulses with two types of dominating noise, either a 30-GHz sinusoidal modulation or a broadband ASE modulation with ~40-GHz-bandwidth full width at half-maximum (FWHM). Figure 2 plots the experimental and simulation results obtained when NOPA4a and NOPA4b were in the linear amplification regime. The sinusoidally modulated pump pulse represents the case of a multilongitudinal-mode pump laser and was used to facilitate the identification and analysis of the pump-induced contrast degradation. As shown in Fig. 2(a), when the pump-seed delay τ at NOPA4b was equal to zero or to the sinusoidal modulation period T (i.e., T = 33.3 ps), and therefore the pump and seed modulations were in phase, the pump sinusoidal modulation introduced an isolated prepulse (postpulse) at –(+)0.64 ps in the cross-correlation signals of the NOPA4b

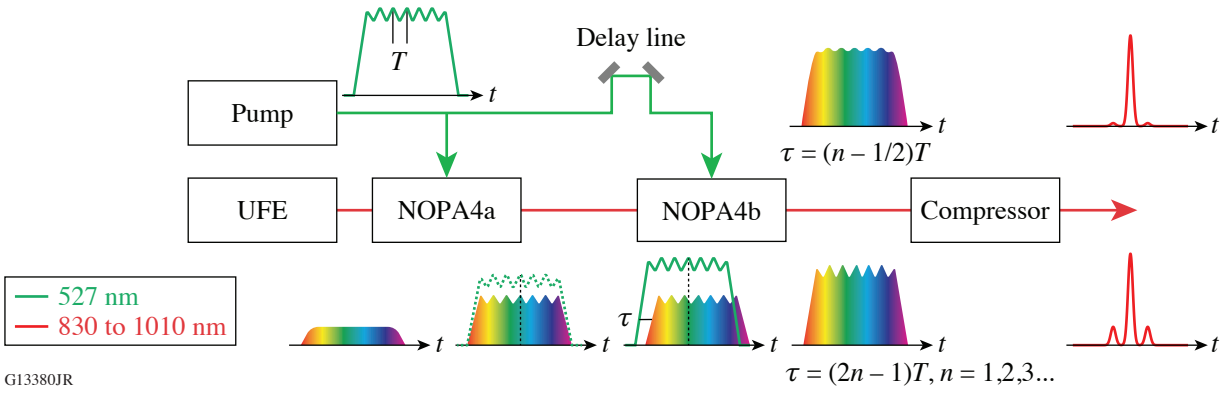

Figure 1
Experimental layout of the two-stage ultra-broadband OPCPA together with the illustrative pump and signal pulses propagating through the system. The delay line controls the pump-seed delay τ with <50-fs temporal resolution.

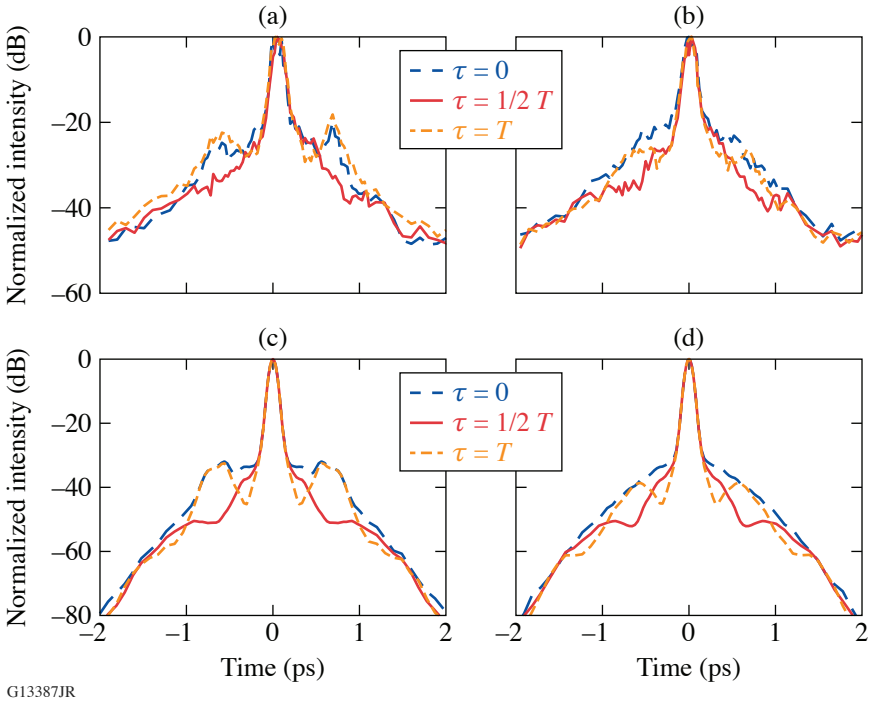

Figure 2
The [(a),(b)] measured and [(c),(d)] simulated cross-correlation signals of the compressed NOPA4b pulses at different pump-seed delays, when both NOPA4a and NOPA4b were operated in the linear regime. T = 33.3 ps corresponds to a modulation frequency equal to 30 GHz. [(a),(c)] The case of a pump pulse with both ASE and 30-GHz sinusoidal modulations; [(b),(d)] the case of a pump pulse with ASE modulation only.

compressed pulses. When the pump-seed delay was set to half the modulation period (i.e., 1/2 T = 16.7 ps) such that the pump and seed modulations had a π phase shift, the pre- and postpulse were strongly suppressed, resulting in the reduction of contrast degradation up to 15 dB. In the more-general case of a pump with broadband ASE modulation, a slowly varying broad pedestal was observed in the compressed pulse and a 10-dB reduction of the contrast degradation at τ = 1/2 T [Fig. 2(b)] was obtained. The simulated cross-correlation signals [Figs. 2(c) and 2(d)] well reproduced the pump-seed-delay–dependent effect.

When NOPA4a and NOPA4b were operated closer to saturation, the measured cross-correlation signals [Fig. 3(a)] showed negligible dependence on the pump-seed delay, which was reproduced by the simulations [Fig. 3(b)] where the limitations in spectral acceptance of the second- and third-harmonic generations in the high-dynamic-range scanning third-order cross-correlator (SEQUOIA®, Amplitude Technologies) were taken into account. These simulations also confirmed, however, that the negligible dependence on pump-seed delay is due to the limited spectral acceptance of the cross-correlator. In the absence of spectral band-

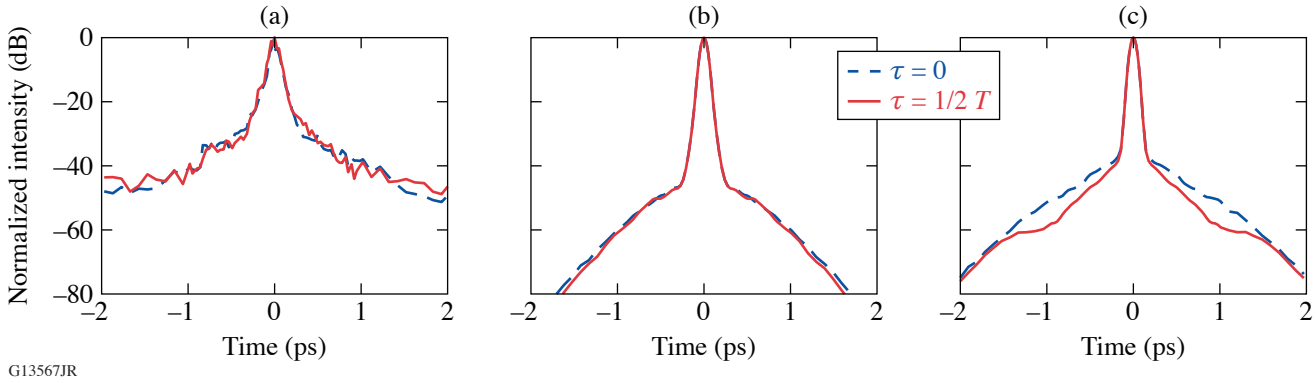

Figure 3
The (a) measured and [(b),(c)] simulated cross-correlation signals of the compressed NOPA4b pulses, when both NOPA4a and NOPA4b were operated closer to saturation and with pump ASE modulation. The spectral acceptance of the third-order harmonic generation in the cross-correlator was limited to 90-nm FWHM using a tenth-order super-Gaussian spectral filter to obtain the results in (b) or kept at >180 nm for the full signal bandwidth for getting the results in (c). Results obtained with only two, instead of three, pump-seed delays are presented for easier visualization of the delay-dependent contrast effect.

width limitation, both cross-correlation signals [Fig. 3(c)] and compressed pulses (simulation not shown) from simulations revealed the delay-dependent contrast effect. Therefore, the pump-seed delay can serve as a simple and cost-effective tool to minimize the pump-induced contrast degradation in a multi-stage OPCPA, even when parametric amplifiers are operated in saturation.

This material is based upon work supported by the Department of Energy National Nuclear Security Administration under Award Number DE-NA0003856, the University of Rochester, and the New York State Energy Research and Development Authority.

1. C. N. Danson *et al.*, High Power Laser Sci. Eng. **7**, e54 (2019).
2. N. Forget *et al.*, Opt. Lett. **30**, 2921 (2005).
3. C. Dorrer *et al.*, Opt. Lett. **32**, 2378 (2007).
4. C. Feng *et al.*, Opt. Express **29**, 40,240 (2021).
5. J. Bromage *et al.*, High Power Laser Sci. Eng. **7**, e4 (2019).

Spectral and Temporal Shaping of Spectrally Incoherent Pulses in the Infrared and Ultraviolet

C. Dorrer and M. Spilatro

Laboratory for Laser Energetics, University of Rochester

Laser–plasma instabilities (LPI's) hinder the interaction of high-energy laser pulses with targets. Simulations show that broadband, spectrally incoherent pulses can mitigate these instabilities. Optimizing laser operation and target interaction requires controlling the properties of these optical pulses. We demonstrate closed-loop control of the spectral density and pulse shape of nanosecond, spectrally incoherent pulses after optical parametric amplification in the infrared (~1053 nm) and sum–frequency generation to the ultraviolet (~351 nm) using spectral and temporal modulation in the fiber front end.[1] The high versatility of the demonstrated approaches can support the generation of high-energy, spectrally incoherent pulses by future laser facilities for improved LPI mitigation.

Temporal and spectral shaping are demonstrated on the fourth-generation laser for ultrabroadband experiments (FLUX) test bed, which is composed of a fiber front end, an optical parametric amplification (OPA) stage, a sum–frequency generation (SFG) stage, and a frequency-doubled Nd:YLF laser system generating the pump pulse for the OPA and SFG stage (Fig. 1). The fiber front end generates the broadband spectrally incoherent OPA seed and the coherent seed for the pump laser using a single high-bandwidth arbitrary waveform generator. The pump laser generates a sequence of two pulses to pump the OPA stage (second pulse) and the SFG stage (first pulse), with a relative delay set to compensate for the optical path difference at 1ω and 2ω between these two stages. Spectral shaping is implemented using a programmable filter (WaveShaper, II-VI). Temporal shaping is implemented using a Mach–Zehnder modulator (MZM) driven by a programmable arbitrary waveform generator (AWG70001, Tektronix).

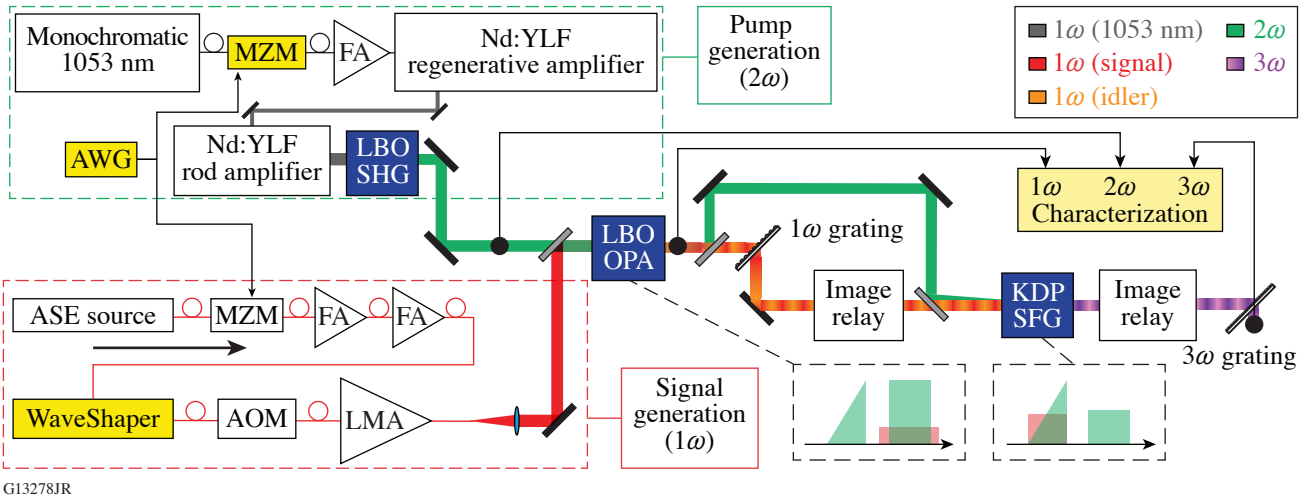

Figure 1

Experimental setup showing the signal generation at 1ω, pump generation at 2ω, amplification in the LBO OPA stage, and frequency conversion in the KDP SFG stage. The properties of the 1ω, 2ω, and 3ω pulses are measured after the OPA, SHG, and SFG stages, respectively. The insets represent the timing configuration for the 1ω pulse (in red) and the 2ω pulses (in green) within the OPA and SFG stages. SFG: sum frequency generation; SHG: sum-harmonic generation; ASE: amplified spontaneous emission; FA: fiber amplifier; AOM: acousto-optic modulator; LMA: large mode area.

The spectrum of the amplified signal measured after the OPA is shaped by controlling the spectrum of the input seed using the programmable spectral filter in the front end. Such shaping can precompensate the wavelength-dependent gain variations in the Yb-doped fiber amplifiers and OPA, although the latter are not expected to be significant, considering that a lithium triborate (LBO) OPA with that length has a bandwidth larger than 100 nm. Without spectral shaping, the OPA output spectrum peaks at ~1032 nm and has a full width at half maximum equal to 7 nm. The wavelength-dependent filter transmission is iteratively modified to decrease the error between the measured spectrum and target spectrum S_{target} (both peak-normalized to 1) using closed-loop control following

$$T_{n+1}(\lambda) = T_n(\lambda) + \eta\left[S_n(\lambda) - S_{\text{target}}(\lambda)\right], \tag{1}$$

where T_n and S_n are the transmission and spectrum as a function of wavelength λ at iteration n, respectively. For stability, the feedback is implemented with η typically equal to –0.1. Initial conditions correspond to a fully transmissive spectral filter [$T_0(\lambda) = 1$] and the resulting spectrum $S_0(\lambda)$. The wavelength axes of the spectral filter and spectrometer are precisely mapped by generating and measuring narrow Gaussian spectra. Figure 2 presents spectral-shaping examples for which S_{target} has been set to a 10-nm flattop profile with a central wavelength ranging from 1032 to 1044 nm [Figs. 2(a)–2(d)] and to the same flattop profiles modulated by a parabolic term [Figs. 2(e)–2(h)]. This simulates spectral shaping for operation at different central wavelengths with precompensation of spectral gain narrowing in subsequent amplifiers.

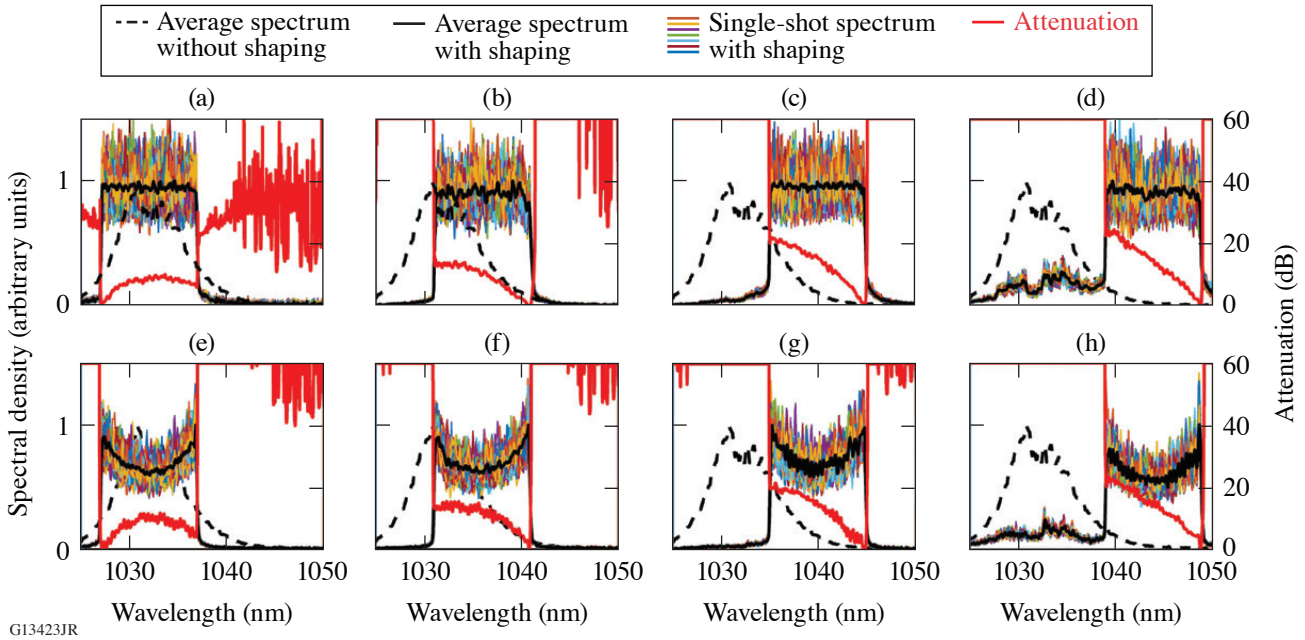

Figure 2
Spectral shaping of the OPA output signal. In the first row, S_{target} is a 10-nm flattop spectrum centered at (a) 1032, (b) 1036, (c) 1040, and (d) 1044 nm. In the second row [(e)–(h)], S_{target} is set to a 10-nm flattop spectrum with parabolic modulation centered at the same wavelengths. In all plots, the spectra averaged over 100 acquisitions without and with shaping are plotted using a dashed black line and solid black line, respectively. The spectra acquired over 100 successive shots are plotted with thin colored lines. The transmission of the spectral filter, in dB, is plotted with a thick red line.

The spectrally shaped 1ω pulses from the OPA are converted to spectrally shaped 3ω pulses using SFG with a narrowband 2ω pulse in a noncollinear angularly dispersed geometry.[2] SFG with a monochromatic field translates the input field along the frequency axis; i.e., it leads to identical spectral features for the input 1ω wave and output 3ω waves if the spectral acceptance is large enough. Figure 3 compares the 1ω and 3ω spectra, where the two wavelength ranges have been set to cover the same frequency range. For Fig. 3(a), the spectral-filter transmission is constant, whereas closed-loop control with various target spectra

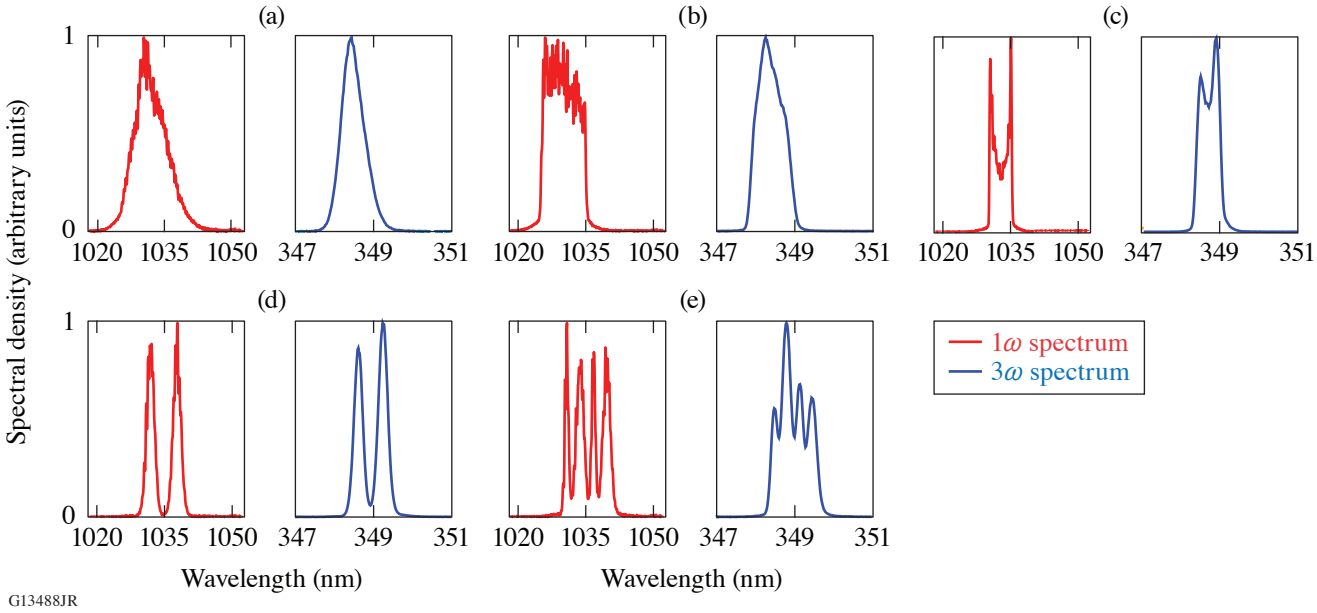

Figure 3
Spectral shaping of the SFG output signal corresponding to a shaped OPA output signal. Plots (a)–(e) show the 1ω spectrum (red line) and the 3ω spectrum (blue line), which are plotted over wavelength ranges that correspond to the same frequency span (10 THz).

was used for the results shown in Figs. 3(b)–3(e). There is generally good agreement between the measured spectral shapes at 1ω and 3ω, although the latter have broader features because of the lower resolution of the UV spectrometer compared to the IR spectrometer (0.25 THz versus 0.05 THz).

Closed-loop pulse shaping has been implemented between the AWG-driven MZM in the fiber front end and the 2ω pulse shape after SHG. A preliminary calibration based on the generation of short Gaussian pulses at different times within the injection window of the regenerative amplifier maps out the linear relation between the time base of the AWG and oscilloscope. Saturation in the fiber amplifiers and Nd:YLF amplifiers leads to significant square-pulse distortion; i.e., the gain at earlier times is significantly higher than at later times within the pump pulse, while the gain observed at a given time depends on the energy that has been extracted at earlier times. Square-pulse distortion in the laser amplifiers, the nonlinear transfer function of the MZM relative to its drive voltage, and the nonlinear second-harmonic generation makes the temporal shaping of the output pulse a complex task. Closed-loop control to generate the pulse shape P_{target} is implemented as follows:

$$W_{n+1}(t) = W_n(t) + \eta\left[P_n(t) - P_{\text{target}}(t)\right], \tag{2}$$

where W_n and P_n are the time-dependent waveform and power at iteration n, respectively. The AWG and MZM are set to implement a monotonic relation between voltage and transmission, while operation at a reference voltage corresponds to the null transmission of the MZM. The shaped pulses, composed of the high-order super-Gaussian OPA pump pulse and the user-defined SFG pump pulse, are routed after convergence to the OPA and SFG stage. Figure 4 displays the shaped 2ω pulse and the resulting 3ω pulse for various user-defined profiles. A super-Gaussian OPA pump pulse (second pulse) is consistently obtained, allowing for temporally uniform OPA saturation. This leads to a flat-in-time amplified 1ω signal, and transfer of the SFG pump pulse shape (first pulse) from 2ω to 3ω via SFG.

This material is based upon work supported by the Department of Energy National Nuclear Security Administration under Award Number DE-NA0003856, the University of Rochester, and the New York State Energy Research and Development Authority.

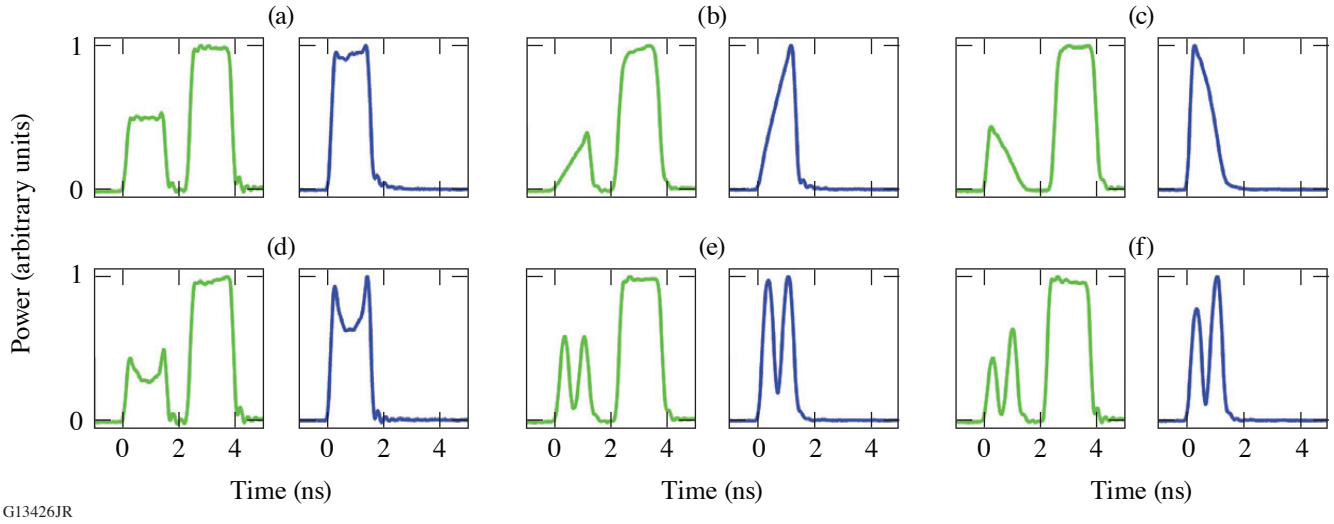

Figure 4
Temporal shaping of the 2ω pump pulse (solid green line) and resulting 3ω pulse shape (solid blue line) for target profiles equal to (a) a super-Gaussian pulse, (b) a positive ramp, (c) a negative ramp, (d) a modulated super-Gaussian pulse, (e) a pair of short pulses with identical amplitudes, and (f) a pair of short pulses with unequal amplitudes. The 2ω pulse is composed of the SFG pump pulse (first pulse) and the OPA pump pulse (second pulse).

1. C. Dorrer and M. Spilatro, Opt. Express **30**, 4942 (2022).
2. C. Dorrer *et al.*, Opt. Express **29**, 16,135 (2021).

Effect of the Pump-Beam Profile and Wavefront on the Amplified Signal Wavefront in Optical Parametric Amplifiers

S.-W. Bahk, I. A. Begishev, R. G. Roides, C. Mileham, R. Cuffney, C. Feng, B. M. Webb, C. Jeon, M. Spilatro, S. Bucht, C. Dorrer, and J. Bromage

Laboratory for Laser Energetics, University of Rochester

Optical parametric chirped-pulse amplification (OPCPA) is known to have advantages over conventional chirped-pulse amplification based on population inversion gain medium.[1] The bandwidth can be extended more than 100 nm without being limited by gain narrowing. The angle between pump and signal beams can be adjusted to provide an even-broader gain bandwidth than collinear geometry. The thermal effect is minimal due to instantaneous energy transfer from pump to signal. The temporal contrast is, in general, better because fewer amplifiers are required and the parametric fluorescence is confined within the pump pulse duration. The OPCPA scheme is a practical way to amplify ultra-broadband pulses to kilojoule energies using commercially available large potassium dihydrogen phosphate (KDP) crystals and existing high-energy nanosecond driver lasers in laser fusion facilities.[2] Deuterated potassium dihydrogen phosphate (DKDP)-based OPCPA systems have been demonstrated on the PEARL laser at the Institute of Applied Physics in Russia[3] and LLE's Multi-Terawatt optical parametric amplifier line (MTW-OPAL).[4] OPCPA lasers based on lithium triborate (LBO)[5,6] or yttrium calcium oxyborate (YCOB)[7] crystals show promising performance at the 800-nm central wavelength seeded by a Ti:sapphire oscillator.

The amplified signal intensity in an optical parametric amplifier (OPA) is a nonlinear function of pump intensity. In general, a flattop pump profile at a fixed intensity is optimal for good conversion efficiency from the pump to signal. In this regime, the amplified signal-beam profile and spectrum are saturated following the pump-beam profile and the pulse shape. The amplification-induced signal phase or "OPA phase" exhibits a phase shift similar to the one observed in a population inversion system.[8] Several authors have investigated the effect of pump on the OPA phase. Ross *et al*. concluded that the OPA phase is a function of pump intensity. They have formally shown that the pump-beam phase impacts the idler phase but does not affect the signal phase.[9] Li *et al*. have experimentally shown that astigmatism in the pump beam is transferred to the idler beam.[10]

Others, however, found that the OPA phase is affected by the pump phase as well. Wei *et al*. have numerically shown that the pump-beam walk-off introduces phase transfer from pump to signal and suggested a walk-off–compensated geometry to mitigate this effect.[11] The same group later experimentally demonstrated the mitigation effect.[12] Chen *et al.* gave a qualitative description of the pump-to-signal phase transfer effect being proportional to the pump wavefront derivative.[13]

Authors in Refs. 10–13 studied the effect of input beam wavefronts on the OPA phase using wave equations and numerical simulations. We analyze this effect using the analytic OPA phase solution and the wave-vector picture. The phase solutions of the three waves in an OPA process have been studied by several researchers[9,14] and were recently presented in closed form in Ref. 15. The main results for the case of zero idler input are summarized here for convenience:

$$\phi_s(L) = \phi_s(0) + \psi_s\left[\Delta k, I_s(0), I_p(0), L\right], \tag{1}$$

$$\phi_i(L) = \pi/2 - \phi_s(0) + \phi_p(0) - \Delta kL/2. \tag{2}$$

The function ψ_s is an additional phase introduced in the signal beam by the OPA process and will be equivalently called the "OPA phase." The ψ_s is a function determined by four independent parameters and has a term made of the incomplete elliptic integral of the third kind [for the detailed expression of ψ_s, refer to Eq. (17) of Ref. 15]. I and ϕ denote intensity and phase with the subscripts "s, i, p" indicating signal, idler, and pump, respectively; L is the crystal thickness. The OPA phase is determined by the input signal and pump intensities, the wave-vector mismatch (Δk), and the crystal thickness (L). The dependence on the input signal's intensity is weak for the normal OPA regime, where $I_s(0) \ll I_p(0)$.

Equation (2) shows that the phases of the input signal [$\phi_s(0)$] and input pump [$\phi_p(0)$] are all directly transferred to the output idler phase. Although this is mostly true, the OPA phase ψ_s is not entirely immune to input phase aberrations. The subtlety lies in the fact that the wave vector is normal to the input phase front in a spatially coherent beam; therefore, the spatial phase variation is accompanied by variation in Δk, which in turn impacts ψ_s. (We assume here a regime where diffraction is negligible over the length of the crystal.) The OPA phase also depends on the input pump intensity independently from the input phase.

The OPA phase is linear with respect to Δk within amplification bandwidth. The OPA phase in the linear regime can be approximated as

$$\psi_s \sim -\frac{\Delta k}{2} L\left\{1 - \frac{1}{a\sqrt{I_p(0)L}} \tanh\left[a\sqrt{I_p(0)L}\right]\right\}, \tag{3}$$

where $a\left(d_{\text{eff}}/c\right)\sqrt{2\eta_0\omega_s\omega_i/n_s n_i n_p}$ (Ref. 15). One can numerically show that $a\sqrt{I_p(0)}L \sim 1.16\log_{10}(\text{gain}) + 1.36$ in the depletion regime with perfect phase matching, where gain is defined as the ratio of output to input signal intensities [$I_s(L)/I_s(0)$]. For a 20-dB gain, $a\sqrt{I_p(0)}L \sim 3.68$, and Eq. (3) in terms of relative phase can be further approximated to

$$\Delta\psi_s \sim -0.36\Delta(\Delta k)L. \tag{4}$$

The local wave vectors of pump and signal waves are normal to their phase front. The wave-vector mismatch is a function of pump and signal phase slopes or derivatives. $\Delta(\Delta k)$ can be written as

$$\Delta(\Delta k) = \left(-\rho_{p,x} + \frac{k_{s,0}}{n_i k_{i,0}} a_{x,0}\right)\frac{\partial\phi_{p,0}}{\partial x} + \left(-\frac{k_{p,0}}{n_i k_{i,0}} a_{x,0}\right)\frac{\partial\phi_{s,0}}{\partial x} + \left(\frac{k_{s,0}}{n_i k_{i,0}} a_{y,0}\right)\frac{\partial\phi_{p,0}}{\partial y} + \left(-\frac{k_{p,0}}{n_i k_{i,0}} a_{y,0}\right)\frac{\partial\phi_{s,0}}{\partial y}. \tag{5}$$

The Δ notation in the above equations denotes relative change across two points in space. The incident pump and signal phase terms here are residual phases that do not include tilt terms corresponding to the incidence angles. Equation (5) shows that the noncollinear interaction angle allows both seed and pump-beam wavefront gradients to be transferred to the OPA phase. On the other hand, the birefringence term ($\rho_{p,x}$) always enables the pump wavefront transfer-to-OPA phase even with the collinear geometry. It is possible to mitigate the birefringence-induced OPA phase by choosing the sign of the noncollinear angle in order to cancel the coefficient of the pump phase gradient, which is the first term in Eq. (5). This was attempted by Wei and Yuan,[11,12] but the cancellation of the pump gradient term increases the signal gradient term, only shifting the problem from the pump to the signal side. Such cancellation is also a trade-off with other considerations that typically constrain the relative angle between pump and signal, e.g., bandwidth requirements and mitigation of parasitic second-harmonic generation.

Equations (4) and (5) show good agreement with the wave-equation approach of Refs. 10–13 in the absence of diffraction except that the small spatial positions shift in the beams coming from birefringence and the noncollinear angle does not appear in the wave-vector approach.

The spatial variation of the pump-beam amplitude can also affect the OPA phase. Figure 1 shows the OPA phase variation with respect to pump intensity using the more-accurate OPA phase expression in Eq. (17) of Ref. 15. Equation (4) is not accurate enough at pump intensities below what is required for depletion or at comparable signal and pump intensities. These plots were

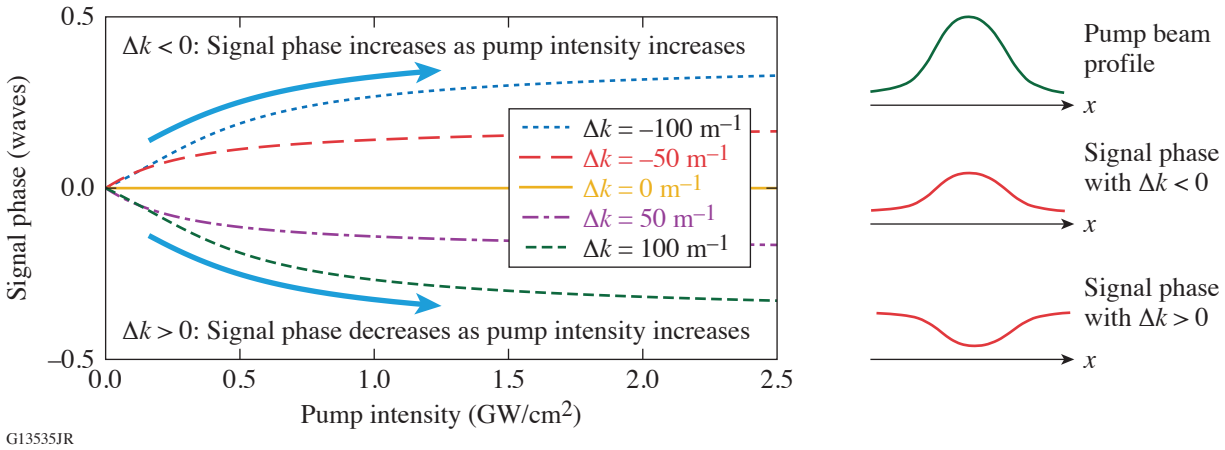

Figure 1
Effect of pump-beam intensity on the signal phase at different wave-vector mismatches.

generated using a 1-MW/cm^2 signal at 920 nm and a pump intensity at 527 nm from 0 GW/cm^2 to its depletion intensity, which is 2.5 GW/cm^2 for a 52-mm-long crystal. Unlike the phase effect, the amplitude effect depends on the sign of Δk. With positive Δk, the signal phase decreases with increasing pump intensity, whereas the trend is the opposite for negative Δk. When the phase mismatch is not equal to 0, the pump-beam shape is imprinted onto the signal phase. This qualitative behavior is illustrated on the right-hand side of Fig. 1 for a Gaussian-like pump beam.

It is interesting to note that this is similar to the intensity-dependent nonlinear effect with a sign dependency on phase matching as in cascaded nonlinearity.[15,16] The sign and amplitude change for spectral variations in Δk implies chromatic aberrations depend on the way Δk varies across the spectrum. Wang *et al*. described the chromatic effects in more detail.[17] With the linear dependence of Δk on frequency and a Gaussian-profile pump beam, this results in a radial group delay. The relative strength of the dispersion terms of Δk can easily change, depending on the phase-matching conditions and may exhibit more-complicated spatiotemporal coupling. On the other hand, chromatic effects induced by the pump phase are not significant because the signal phase's response is linear with the same slope wherever Δk is within the amplification bandwidth.

We conducted experiments to verify the prediction of pump wavefront and amplitude effect on the OPA phase in the final amplifier of the MTW-OPAL laser. Details about the MTW-OPAL system and the final pump laser are provided in Refs. 4 and 18. We specifically study the pump phase's effect in a collinear amplification geometry and the pump amplitude's effect. The amplifier, called NOPA5 being the fifth noncollinear OPA in the system, is based on a 52-mm-long, 70%-deuterated KDP crystal. The pump-signal angle for an optimum amplification bandwidth depends on the deuteration level.[19] The amplifier is currently configured in a collinear geometry because this configuration is optimal for the 70% DKDP crystal. The seed beam is a 100-mJ, 42-mm square beam. The seed pulse has a 150-nm bandwidth stretched to 1.2 ns. The pump beam is a 50-J, 40-mm square beam with a 1.7-ns pulse width. Beam size, pulse width, and bandwidth are estimated at 20% of the peak. The pump and signal are combined with a broadband dichroic mirror. The input pump wavefront and the output signal wavefront were sampled through leaky mirrors and measured with wavefront sensors after down-collimation and imaging. The signal wavefront was measured with a 930-nm bandpass filter. The inherent aberrations in the signal beam imaging system are estimated to be 0.16 waves peak to valley (p–v) based on a double-pass retro measurement. The design aberrations in the pump beam's imaging system are 0.2 waves p–v but no special effort was taken to measure the pump beam's diagnostic aberrations. The spectra of the input and output pulses are sampled by fiber-coupled diffusers and transported to a multichannel spectrometer. The energies of the pump and signal pulses are either measured directly with calorimeters or indirectly in the diagnostics beam path with calibration factors. The crystal is angle tuned using a precision rotation stage. We induce specific phase modulations on the pump beam using a phase plate after the main pump amplifiers or specific amplitude modulation upstream before the amplifiers using a programmable beam-shaping system.[20]

A high-order phase plate with ~2.5 waves (p–v) transmitted wavefront at 526 nm was inserted in the pump-beam path to introduce a more-complex phase profile, as shown in Fig. 2(a). The resulting signal intensity and wavefront, with bandpass filtration at 930 nm, are shown in Fig. 2(b); the calculated counterparts are shown in Fig. 2(c). The measured wavefront is a relative wavefront referenced against the amplified signal wavefront without the phase plate. The amplitude and overall shape of the measured and calculated wavefronts, in particular local extrema, are in excellent agreement.

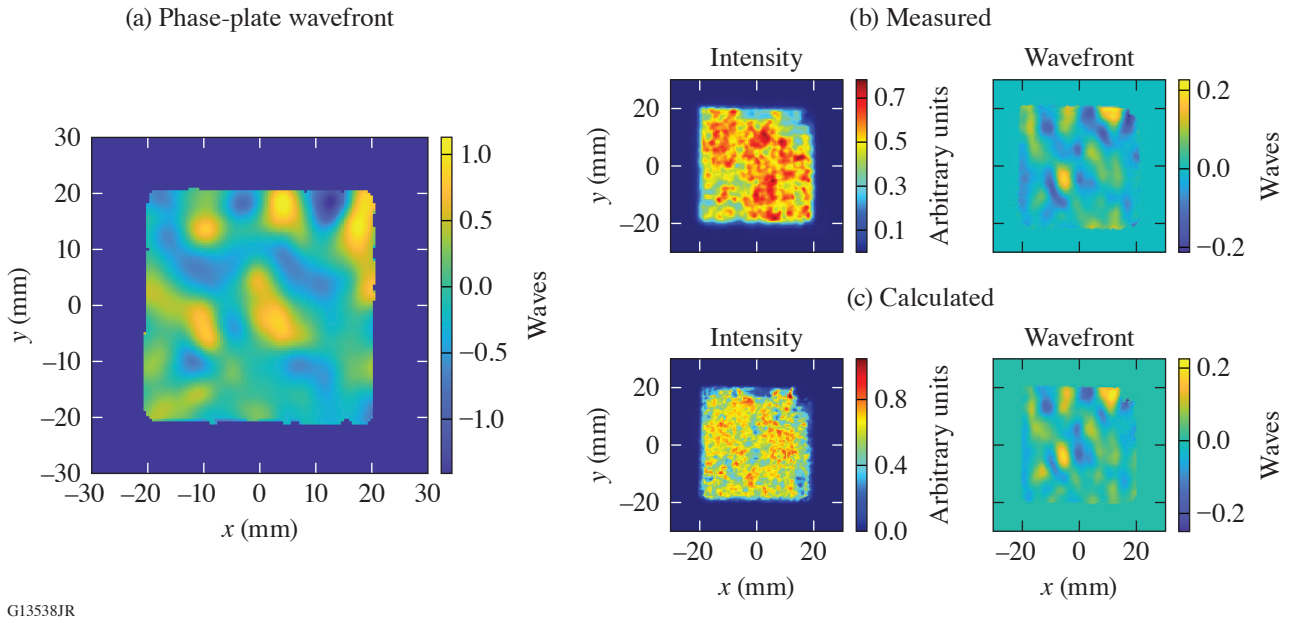

Figure 2
(a) Transmitted wavefront of the phase plate, (b) measured intensity and wavefront, and (c) calculated intensity and wavefront at 930 nm.

To investigate the amplitude effect, the beam-shaping system[20] for the pump beam was used to produce a cylindrical Gaussian-like beam as shown in Fig. 3(a). The crystal angle was detuned ±0.017° to change the sign of Δk and demonstrate its sign sensitivity on the induced wavefront. The lineouts of the measured and calculated wavefronts at 930 nm are shown in Fig. 3(b) as solid and dashed lines, as shown in the legend. The lineouts are averaged over 80% of the central region of the beam in the y direction. This comparison shows a good agreement in the overall quadratic shape following from the pump-beam profile. We also measured the wavefronts at three wavelengths (890 nm, 930 nm, and 990 nm) using bandpass filters installed in front of three separate wavefront sensors as shown in Fig. 3(c), which directly show chromatic effect.

We presented a detailed theory of the OPA phase produced by the pump and signal wavefronts and measured the OPA phase from the pump wavefront. The main theoretical result is that the OPA phase is proportional to the derivative of the pump and signal wavefronts in the phase-matching direction. The birefringent walk-off and noncollinear interaction geometry couple the phase derivative terms to phase mismatch and therefore to the OPA phase. The effect of the pump-beam profile has also been investigated. Our expressions showed the OPA phase depends on the pump intensity and the sign of the phase mismatch. The signal wavefront modulation caused by the pump-intensity modulation is more sensitive at a lower pump intensity. A small amount of chromatic aberrations following the shape of the pump profile is expected.

We performed experiments demonstrating both the phase and amplitude effect of the pump beam on the OPA phase using a broadband OPA amplifier in a collinear geometry. The pump wavefront effect was investigated by adding a high-order phase plate in the pump beam. The experiment confirmed that the induced signal phase is related to the pump phase gradient in the phase-matching direction. The OPA phase due to the pump beam profile was measured for different phase-matching conditions

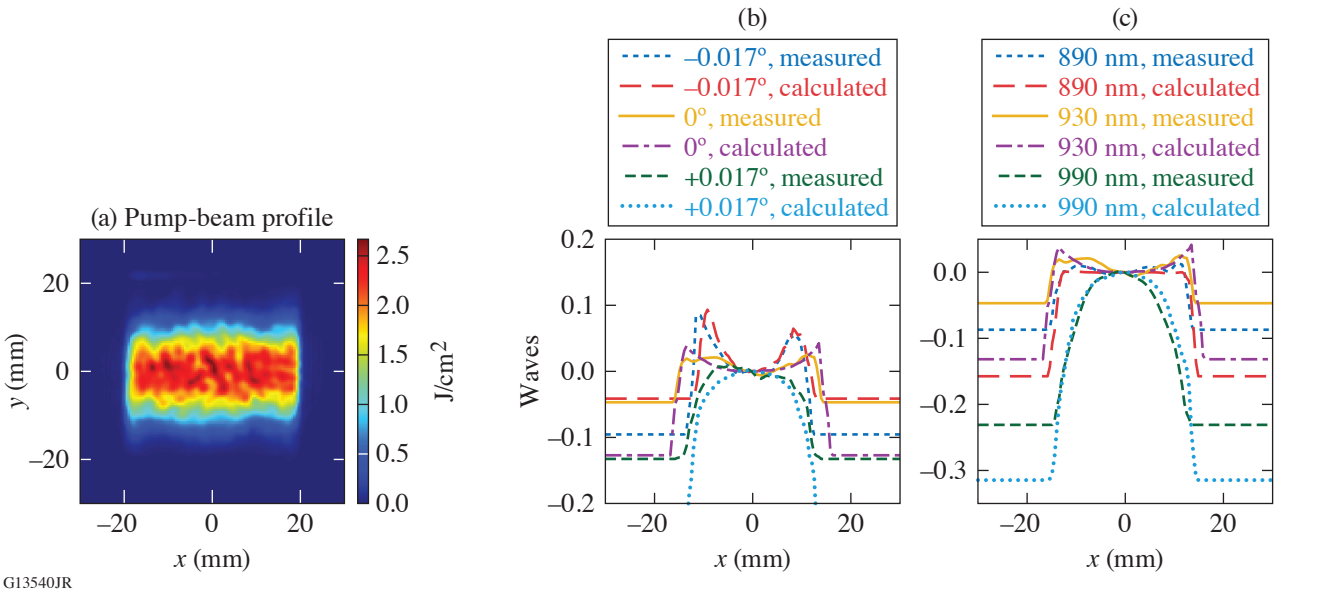

Figure 3
(a) Vertically nonuniform pump-beam profile; (b) measured and calculated wavefront-averaged vertical lineouts at different crystal tuning angles; (c) measured and calculated wavefront averaged lineouts at three wavelengths at 0°.

obtained by slightly detuning the crystal. The measurements confirmed that the amplitude-induced OPA phase depends on the sign of the phase mismatch and the pump-beam profile.

The traditional understanding of the general behavior of the pump-beam wavefront being transferred to the idler beam is, in general, correct in the sense that the OPA phase introduced by the pump-beam wavefront is generally an order of magnitude smaller than the pump wavefront directly transferred to the idler beam. The transfer to the signal beam can be non-negligible, however, for a larger system with large wavefront errors. The experimental verification of the pump and signal phase effect for noncollinear geometry will be discussed in subsequent publications. We expect the considerations presented in this summary will play an important role for future construction of a scaled-up high-energy broadband OPCPA system, where the wavefront becomes difficult to control as the beam size increases.

This material is based upon work supported by the Department of Energy National Nuclear Security Administration under Award Number DE-NA0003856, the University of Rochester, and the New York State Energy Research and Development Authority.

1. G. A. Mourou, T. Tajima, and S. V. Bulanov, Rev. Mod. Phys. **78**, 309 (2006).
2. C. N. Danson *et al.*, High Power Laser Sci. Eng. **7**, e54 (2019).
3. V. V. Lozhkarev *et al.*, Opt. Express **14**, 446 (2006).
4. J. Bromage *et al.*, High Power Laser Sci. Eng. **9**, e63 (2021).
5. L. Xu *et al.*, Opt. Lett. **38**, 4837 (2013).
6. M. Galletti *et al.*, High Power Laser Sci. Eng. **8**, e31 (2020).
7. S. Yang *et al.*, Opt. Express **28**, 11,645 (2020).
8. R. S. Nagymihaly *et al.*, Opt. Express **27**, 1226 (2019).
9. I. N. Ross *et al.*, J. Opt. Soc. Am. B **19**, 2945 (2002).
10. W. Li *et al.*, Appl. Phys. B **123**, 37 (2016).
11. X. Wei *et al.*, Opt. Express **16**, 8904 (2008).
12. P. Yuan *et al.*, High Power Laser Sci. Eng. **2**, e30 (2014).
13. Y. Chen *et al.*, Adv. Condens. Matter Phys. **2018**, 5731938 (2018).

14. H. J. Bakker *et al.*, Phys. Rev. A **42**, 4085 (1990).
15. S. W. Bahk, Opt. Lett. **46**, 5368 (2021).
16. R. DeSalvo *et al.*, Opt. Lett. **17**, 28 (1992).
17. Y. Wang *et al.*, Opt. Lett. **46**, 5743 (2021).
18. I. A. Begishev *et al.*, Appl. Opt. **60**, 11,104 (2021).
19. K. Ogawa *et al.*, Opt. Express **17**, 7744 (2009).
20. S.-W. Bahk, I. A. Begishev, and J. D. Zuegel, Opt. Commun. **333**, 45 (2014).

Evaluation of Transverse Raman Scattering in KDP and DKDP in Geometries Suitable for Beam Polarization Control

T. Z. Kosc, H. Huang, T. J. Kessler, and S. G. Demos

Laboratory for Laser Energetics, University of Rochester

KDP and DKDP are particularly suitable materials for polarization control due to their ability to grow in large sizes and their inherent birefringence. However, their performance in large-aperture, high-fluence systems at 351 nm is hindered by the generation of transverse stimulated Raman scattering (TSRS)[1,2] seeded by the strong symmetric A_1 Raman mode. This process transfers energy to parasitic transverse beams and thereby limits the maximum power output in order to avoid damage to the optic and its mount. The intensity of the TSRS signal is governed by the propagation length (optic size) L; the laser intensity I_{pump}; and the Raman-gain coefficient g, where the latter is directly proportional to the spontaneous Raman-scattering cross section, $d\sigma/d\Omega$:

$$I_{\text{TSRS}} \sim \exp\left(gI_{\text{pump}}L\right), \text{ where } g = \left(8\pi cM \big/ \hbar\omega_s^3 n^2 \Delta\bar{\nu}\right) \cdot \left(d\sigma \big/ d\Omega\right).$$

The strength of the Raman-scattering cross section in a given orientation is related to the mode's Raman polarizability tensor which was only recently ascertained with high accuracy (due to the presence of numerous measurement artifacts mainly arising from depolarization of the pump beam and Raman signal during propagation in these birefringent materials) for both KDP and 70% DKDP.[3]

The goal of this work is to develop a modeling capability to evaluate the TSRS risk and its directional dependence in geometries relevant to polarization control. This ability, in turn, will enable optimization of the design (such as the crystal-cut orientation) of KDP or DKDP polarization control optics and guide the design of future laser systems. To support this modeling effort, a detailed experimental study of the transverse Raman scattering was conducted to validate the model accuracy. Experiments were performed using a novel setup detailed in Ref. 4 that utilized spherical samples to enable accurate measurements at relevant excitation geometries. A complete set of data was acquired by varying three parameters: (1) the angular position θ of the optic axis (OA) with respect to the vertical pump beam between 0° and 90°, (2) the angular alignment α of the pump-laser polarization relative to the vertical plane containing the OA, and (3) the transmission axis of the signal analyzer (parallel and orthogonal with respect to the beam-propagation direction). The data shown in Fig. 1 were obtained for an excitation and signal collection geometry suitable for polarization control (angle between OA projection on transverse plane and laser polarization $\alpha = 45°$). The signal intensity is normalized to the signal corresponding to the orientation that produces the maximum spontaneous Raman-scattering cross section in each material. The signal detected using the parallel analyzer arises mainly from polarization artifacts, which also cause the complex peak and valley features detected when using the orthogonal analyzer. As Fig. 1(c) demonstrates, the model is capable of reproducing the experimental results fairly accurately when considering the experimental conditions (a 32-mm-diam sphere, an ~0.5° incident half-angle, and a 5.7° collection half-angle).

The ray-tracing model tracks the spontaneous Raman emission using geometrical optics. Rays are generated from each point source (with initial intensity determined according to the relevant tensor products) and propagate in all directions as either ordinary (o) or extraordinary (e) components acquiring different phases. In the cross-section simulations, the source volume contains a large number of such source points and the collected Raman o and e photons are considered mutually incoherent. The corresponding experimental results (with the analyzer parallel and perpendicular to the pump laser) are estimated as the sums of the projections of the o and e components.

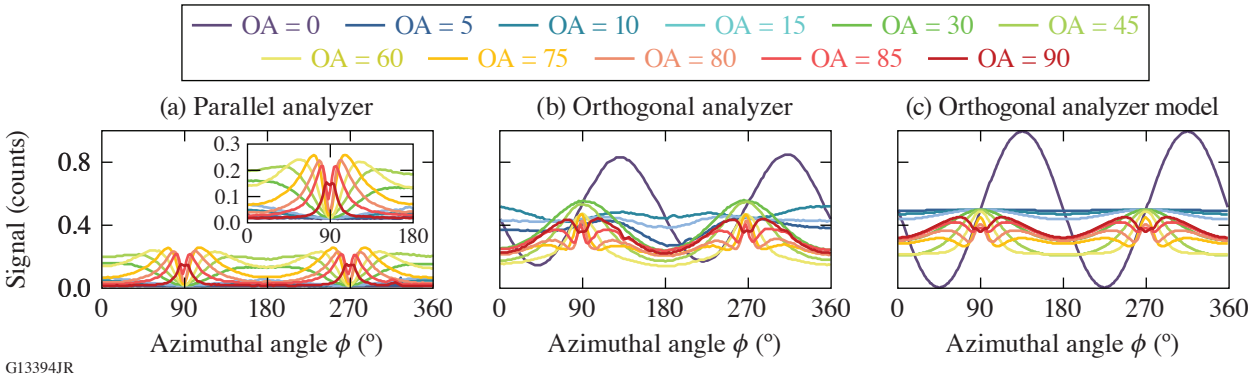

Figure 1
Data acquired using the KDP spherical sample with the Raman signal analyzer aligned (a) parallel and (b) perpendicular to the pump laser. (c) Ray-trace modeling reproduced experimental data, including polarization rotation artifacts. The pump polarization was set at $\alpha = 45°$ with respect to the vertical plane containing the crystal OA, whose position is varied between 0° and 90° with respect to the beam-propagation direction.

The ray-trace modeling also confirmed that the polarization rotation artifacts decrease as the collection aperture size is reduced. If we assume a collimated beam propagating though the crystal and the Raman scattering detected over an infinitely small collection angle, the signal with the analyzer perpendicular to the pump beam will converge the shape of the total signal (sum of the two analyzer positions). This behavior is shown in Fig. 2, which includes the (a) experimental and (b) modeling results.

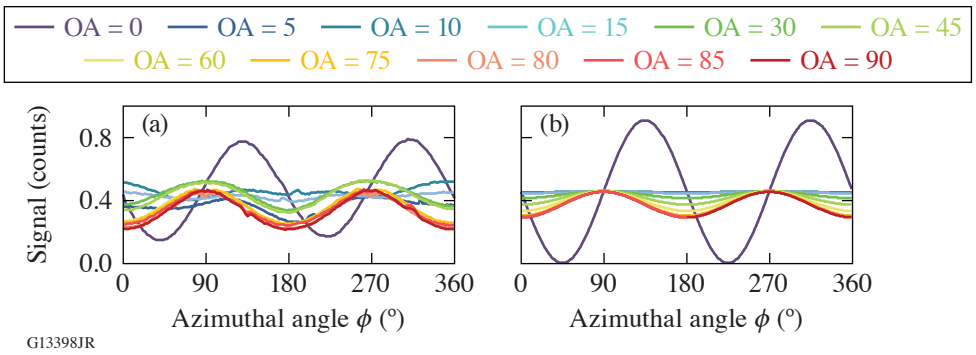

Figure 2
The sum of the parallel and perpendicular polarizations is shown as the total Raman signal for (a) experimental data and (b) the model. The polar angle varied between 0° and 90°, and the profile color coding is the same as in Fig. 1.

The results discussed above can be directly applied for the assessment of the TSRS risk in large-aperture laser systems. The validation of the model and methodology by the experimental results provides confidence on its use to guide crystal-cut optimization needed to minimize TSRS gain, to predict maximum operational fluence, or to help develop novel designs with complex polarization control properties in large-aperture optics. Future work will consider the design of specialized optics and include the ray paths contained by total internal reflection or retroreflected conditions that introduce longer gain paths.

This material is based upon work supported by the Department of Energy National Nuclear Security Administration under Award Number DE-NA0003856, the University of Rochester, and the New York State Energy Research and Development Authority.

1. C. E. Barker *et al.*, Proc. SPIE **2633**, 501 (1995).
2. S. N. Dixit *et al.*, J. Phys. IV France **133**, 717 (2005).
3. T. Z. Kosc *et al.*, Sci. Rep. **10**, 16283 (2020).
4. T. Z. Kosc *et al.*, Rev. Sci. Instrum. **91**, 015101 (2020).

LLE BEST Student and Teacher Research Program: Broad Exposure to Science and Technology

T. J. Kessler

Laboratory for Laser Energetics, University of Rochester

The primary goal of the Broad Exposure to Science and Technology (BEST) Research Program is to engage underrepresented high school students and their teachers in various aspects of science and technology that support LLE's laser science and applications research. This broad exposure helps guide students in their pursuit of STEM fields and encourages them to explore the next generation of related jobs and careers. Teacher participation equips educators with knowledge and experience that can be brought back to their schools to enhance science and technology curricula during the school year. The BEST program was carried out at East High School within the Rochester City School District (RCSD) during the summer of 2021. Four high school students and two teachers participated in the pilot program (Fig. 1). This research experience occurred over a six-week period during the months of July and August.

I3044JR

Figure 1
The participants of the BEST program in 2021 included (from left to right) East High teachers Trent Russell and Gavin Jenkins, East High students Yusuf Gazali, Reganae Walters, Taiasia Gibson, and Ramir Wearen, and program coordinator Terry Kessler, LLE Diversity Manager.

The teachers and students were exposed to different areas of science and technology research such as optical microscopy, optical testing and design, holography, liquid crystals, the Omega Laser Facility, and technical communications. The importance of engineering support for research, including chemical, electrical, mechanical, optical, computer, and workspace engineering, were emphasized to highlight the extensive teamwork required to make advancements in these fields. Students and teachers were given tours of LLE's laser science and technology laboratories during the program period.

The BEST team attended LLE Zoom presentations and discussions each week. They carried out science and technology research at East High School using temporarily relocated LLE equipment including microscopy, interferometry, and holography systems. Some examples of the many experimental activities are shown on the screen located in the middle of the white board (Fig. 1). The white board or "Google Board" displays each day's goals and the many questions generated by the students and teachers during lectures, demonstrations, and laboratory investigations.

Large scientific institutions, such as UR/LLE, employ many different types of professionals to carry out their research activities. Each of the many research and support activities requires teams consisting of these professionals. This matrix relationship shown in Fig. 2 is what allows LLE to maintain a successful research program. Exposure to this science and technology matrix provided the students and teachers with an understanding of the broad diversity of research activities as well as the rich diversity of individual professionals that enable the research to flourish.

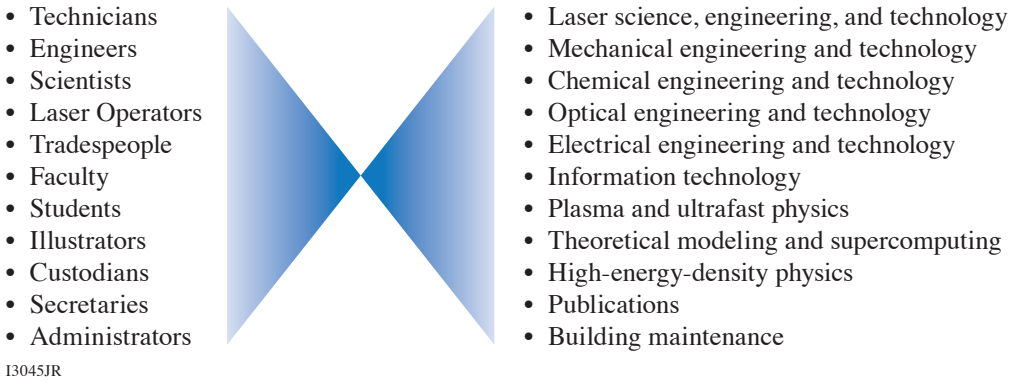

Figure 2
The BEST students and teachers were introduced to the many employment positions (left) that constitute the workforce at LLE. These positions support the wide variety of activities (right) needed to maintain the thriving science and technology research at LLE. Exposure to the LLE workforce provides guidance for students to choose their education and training experiences.

A team of LLE volunteers worked with the BEST students and teachers in a variety of science and technology fields (see Fig. 3). Each volunteer spent between one and four days at East High school over a six-week period. The program coordinator provided backup in order for the team members to maintain a flexible schedule during the summer months. Each volunteer, being an expert in their research field, was able to bring detailed information, coupled with hands-on opportunities, into the high school laboratory environment. For future summer programs, it is envisioned that the students and teachers will be exposed to additional fields of science and technology including laboratory operations, light–matter interaction, publications, and the technology trades that support all research activities at LLE.

LLE mentors exposed the students and teachers in the BEST Program to various technologies that are critical to the design and operation of the OMEGA 60 and OMEGA EP Laser Systems (see Fig. 4). Circuit board technologies were explored by dissecting computer systems, studying hardware design, and practicing the microsoldering techniques used to assemble electronic components. Laser hardware, such as alignment lasers and laser amplifier materials, were brought into the classroom for demonstration and exhibition. In addition, the phase transitions of liquid crystal materials were investigated, while optical components used to control the polarization and color of light were manufactured. This broad exposure highlighted the technologies that connect electronics, optics, and chemistry to laser systems.

I3046JR1

Figure 3
A team of nine LLE participants [(shown left to right) Terry Kessler, lasers/holography; Karen Cera, laboratory safety; Stavros Demos, spectroscopy/microscopy; Tanya Kosc, light polarization; Mike Krowl, electronics technology; Ken Marshall and Nate Urban, liquid crystals; Brian Kruschwitz, grating applications; and Nickolaos Savidis, optical design] worked with the BEST students and teachers in a variety of science and technology fields including laboratory safety, holography, spectroscopy, microscopy, light polarization, mechanical systems, electronics technology, liquid crystals, chemistry, diffraction gratings, and optical system design and prototyping.

(a)

(b)

(c)

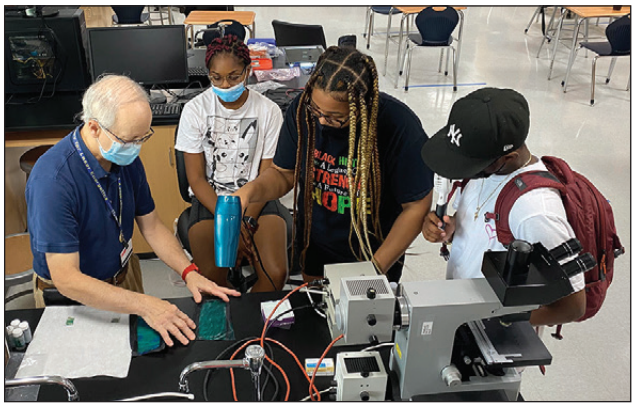

I3047JR

Figure 4
(a) Tanya Kosc, Optical Materials Technology Group Scientist, is shown exhibiting a neodymium-doped laser amplifier rod. (b) Mike Krowl, Electronics Group Technician, is shown instructing the students and teachers in circuit board technology including computer components and microsoldering techniques. (c) Ken Marshall, Optical Materials Technology Senior Research Engineer, is shown working with students on techniques to apply layers of liquid crystal to flexible fabrics.

A holographic interferometer was constructed at East High to record array-generating diffraction gratings. The number of reconstructed spots (orders) was plotted as a function of the development time in seconds (Fig. 5). Students view the multicolor orders by looking through the diffraction grating at a white-light source. The array of multicolor spots was photographed showing the characteristic blue to red angular shift for each order. This activity provided the hands-on experience to understand how gratings and grating spectrometers work. LLE mentors built on this experience to instruct the students and teachers on the basic concepts of chirped-pulse amplification and smoothing by spectral dispersion, two important laser schemes to produce high-intensity short pulses and uniform focal spots, respectively.

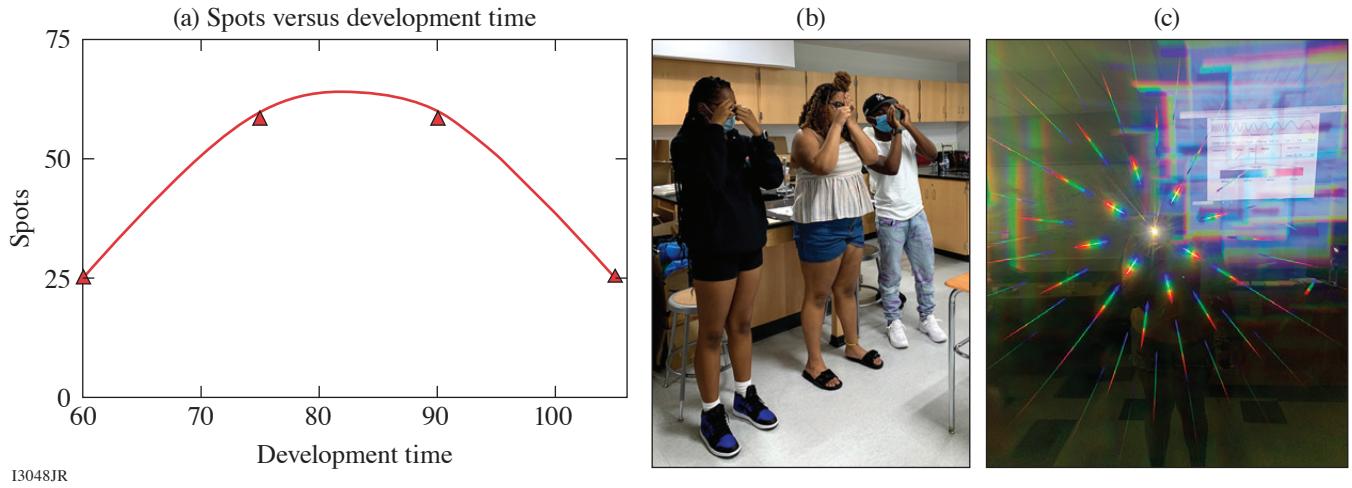

Figure 5
(a) The number of reconstructed spots from a multi-order diffraction grating was plotted as a function of the development time in seconds. (b) Students view the multicolor orders by looking through the diffraction grating at a white-light source. (c) The array of multicolor spots shows the characteristic blue to red angular shift for each order.

Spectroscopy is the study of the absorption and emission of light and other radiation by matter. There are numerous applications of spectroscopy at LLE including optical material composition analysis, light-scattering investigations, and the study of laser–matter interaction. Brian Kruschwitz, Group Leader of OMEGA System Science, worked with students to construct a grating spectrometer in a chemistry classroom at East High School. Stavros Demos, Group Leader of Optical Materials Technology, brought a spectrometer into the classroom to measure the wavelength transmission of optical filter glass. Using a color scale on a large classroom monitor, the students were able to make visual assessments of the filters' transmissions in order to compare objective and subjective spectral analyses (Fig. 6).

Due to COVID 19, the BEST participants visited LLE for only one day during the last week of the summer program to tour the OMEGA and OMEGA EP lasers, optical manufacturing facilities, and other support laboratories (Fig. 7). Together, the students and teachers were exposed to elements of science and technology that underscored the importance of their normal high school curricula. In addition, this group participated in tours of optics and imaging-related departments at Monroe Community College, the Rochester Institute of Technology, and the University of Rochester.

An important aspect of the BEST program involves the students' roles as ambassadors for outreach to other students enrolled at East High and other RCSD high schools. Two projects were completed for this purpose. First, the students and teachers created a PowerPoint presentation showing the broad range of science and technology topics included in the program. Second, a photomontage video was created to show the relationship between the BEST program and the work carried out at LLE. This video was accepted as an Innovative Spotlight in the 2022 University of Rochester Equity, Diversity, and Inclusion Leadership Summit. In planning for the 2022 BEST program, students from several RCSD high schools including East High, Young Women's College Prep, Monroe Upper High, and Rochester Early College others are being invited to participate.

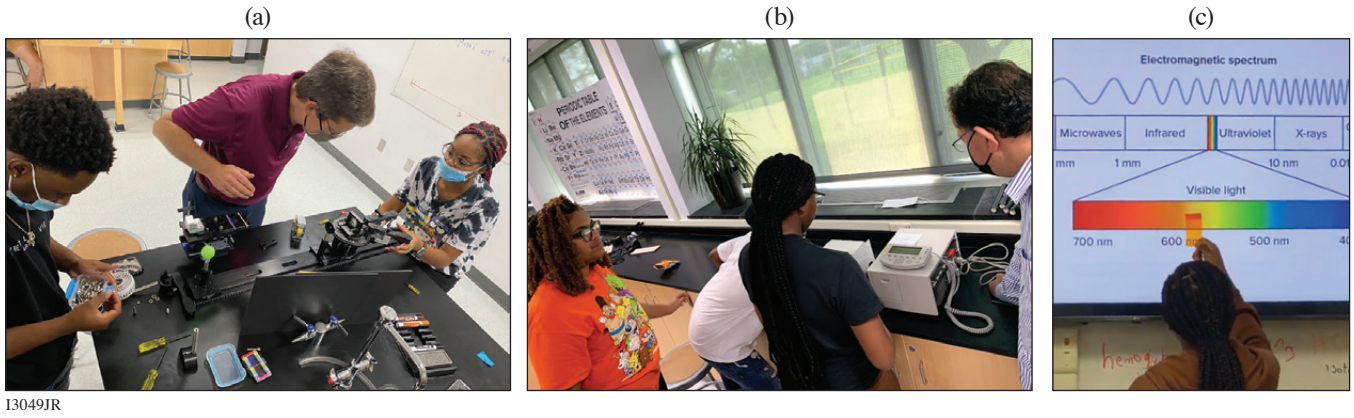

Figure 6
(a) Brian Kruschwitz, System Science Group Leader, is shown working with Ramir Wearen and Taiasia Gibson to construct a grating spectrometer. (b) Stavros Demos, Optical Materials Technology Group Leader, is shown demonstrating the procedure for operating a spectrometer to measure the wavelength transmission of optical filter glass. (c) Taiasia is shown visually comparing a glass filter to a large spectral scale.

Figure 7
The BEST students and teachers visited various LLE laboratories. (a) Amy Rigatti, Optical Manufacturing Group Leader, explains the work carried out in the coating facility. (b) Mike Campbell, LLE Director, discusses science and education with East High students Reganae Walters and Taiasia Gibson.

FY22 Q1 Laser Facility Report

J. Puth, M. Labuzeta, D. Canning, and R. T. Janezic

Laboratory for Laser Energetics, University of Rochester

During the first quarter of FY22, the Omega Facility conducted 233 target shots on OMEGA and 207 target shots on OMEGA EP for a total of 440 target shots (see Tables I and II). OMEGA averaged 10.4 target shots per operating day, averaging 91.3% Availability and 88.9% Experimental Effectiveness. OMEGA EP averaged 9.0 target shots per operating day, averaging 95.3% Availability and 94.9% Experimental Effectiveness.

Table I: OMEGA Laser System target shot summary for Q1 FY22.

Program	Laboratory	Planned Number of Target Shots	Actual Number of Target Shots
ICF	LLE	104.5	104
	LANL	11	12
	LLNL	11	6
ICF Subtotal		126.5	122
HED	LLE	11	8
	LANL	11	9
	LLNL	22	23
HED Subtotal		44	40
LBS	LLNL	22	21
LBS Subtotal		22	21
AIBS		22	17
APL		11	14
NLUF		22	19
Grand Total		247.5	233

AIBS: Academic and Industrial Basic Science
APL: Applied Physics Labs (Johns Hopkins University)
NLUF: National Laser Users Facility

Table II: OMEGA EP Laser System target shot summary for Q1 FY22.

Program	Laboratory	Planned Number of Target Shots	Actual Number of Target Shots
ICF	LLE	14	13
	LLNL	21	26
	NRL	7	9
ICF Subtotal		42	48
HED	LLE	14	16
	LANL	7	8
	LLNL	21	27
HED Subtotal		42	51
LBS	LLNL	10.5	18
	LLE	7	14
	PPPL	7	6
LBS Subtotal		24.5	38
CMAP		7	10
CEA		7	8
NLUF		31.5	39
Calibration	LLE	0	13
Grand Total		154	207

CMAP: Center for Matter at Atomic Pressures
CEA: Commissariat à l'énergie atomique et aux énergies alternatives

Publications and Conference Presentations

Publications

S.-W. Bahk, "Analytic Phase Solutions of Three-Wave Interactions," Opt. Lett. **46**, 5368 (2021).

I. A. Begishev, V. Bagnoud, S.-W. Bahk, W. A. Bittle, G. Brent, R. Cuffney, C. Dorrer, D. H. Froula, D. Haberberger, C. Mileham, P. M. Nilson, A. V. Okishev, J. L. Shaw, M. J. Shoup III, C. R. Stillman, C. Stoeckl, D. Turnbull, B. Wager, J. D. Zuegel, and J. Bromage, "Advanced Laser Development and Plasma-Physics Studies on the Multiterawatt Laser," Appl. Opt. **60**, 11,104 (2021).

M. D. Bergkoetter, B. E. Kruschwitz, S.-W. Bahk, and J. R. Fienup, "Measurement of Chromatic Aberrations Using Phase Retrieval," J. Opt. Soc. Am. A **38**, 1853 (2021).

A. F. A. Bott, L. Chen, G. Boutoux, T. Caillaud, A. Duval, M. Koenig, B. Khiar, I. Lantuéjoul, L. Le-Deroff, B. Reville, R. Rosch, D. Ryu, C. Spindloe, B. Vauzour, B. Villette, A. A. Schekochihin, D. Q. Lamb, P. Tzeferacos, G. Gregori, and A. Casner, "Inefficient Magnetic-Field Amplification in Supersonic Laser-Plasma Turbulence," Phys. Rev. Lett. **127**, 175002 (2021).

J. Bromage, S.-W. Bahk, M. Bedzyk, I. A. Begishev, S. Bucht, C. Dorrer, C. Feng, C. Jeon, C. Mileham, R. G. Roides, K. Shaughnessy, M. J. Shoup III, M. Spilatro, B. Webb, D. Weiner, and J. D. Zuegel, "MTW-OPAL: A Technology Development Platform for Ultra-Intense Optical Parametric Chirped-Pulse Amplification Systems," High Power Laser Sci. Eng. **9**, e63 (2021).

Y.-Y. Chang, X. Cheng, A. Hannasch, M. LaBerge, J. M. Shaw, K. Weichman, J. Welch, A. C. Bernstein, W. Henderson, R. Zgadzaj, and M. C. Downer, "Faraday Rotation Study of Plasma Bubbles in GeV Wakefield Accelerators," Phys. Plasmas **28**, 123105 (2021).

A. Colaïtis, I. Igumenshchev, J. Mathiaud, and V. Goncharov, "Inverse Ray Tracing on Icosahedral Tetrahedron Grids for Non-Linear Laser Plasma Interaction Coupled to 3D Radiation Hydrodynamics," J. Comput. Phys. **443**, 110537 (2021).

C. Feng, C. Dorrer, C. Jeon, R. Roides, B. Webb, and J. Bromage, "Analysis of Pump-to-Signal Noise Transfer in Two-Stage Ultra-Broadband Optical Parametric Chirped-Pulse Amplification," Opt. Express **29**, 40,240 (2021).

P. Franke, D. Ramsey, T. T. Simpson, D. Turnbull, D. H. Froula, and J. P. Palastro, "Optical Shock-Enhanced Self-Photon Acceleration," Phys. Rev. A **104**, 043520 (2021).

V. Gopalaswamy, R. Betti, J. P. Knauer, A. Lees, D. Patel, A. R. Christopherson, I. V. Igumenshchev, D. Cao, K. S. Anderson, A. Shvydky, D. H. Edgell, O. M. Mannion, C. Thomas, W. Theobald, C. Stoeckl, S. P. Regan, V. N. Goncharov, R. C. Shah, and E. M. Campbell, "Using Statistical Modeling to Predict and Understand Fusion Experiments," Phys. Plasmas **28**, 122705 (2021).

S. Heidtfeld, R. Adam, T. Kubota, K. Takanashi, D. Cao, C. Schmitz-Antoniak, D. E. Bürgler, F. Wang, C. Greb, G. Chen, I. Komissarov, H. Hardtdegen, M. Mikulics, R. Sobolewski, S. Suga, and C. M. Schneider, "Generation of Terahertz Transients from $CO_2Fe_{0.4}Mn_{0.6}Si$-Heusler-Alloy/Normal-Metal Nanobilayers Excited by Femtosecond Optical Pulses," Phys. Rev. Research **3**, 043025 (2021).

J. Jeet, A. B. Zylstra, M. Rubery, Y. Kim, K. D. Meaney, C. Forrest, V. Glebov, C. J. Horsfield, A. M. McEvoy, and H. W. Herrmann, "Inertial-Confinement Fusion-Plasma-Based Cross-Calibration of the Deuterium-Tritium γ-to-Neutron Branching Ratio," Phys. Rev. C **104**, 054611 (2021).

G. W. Jenkins, C. Feng, and J. Bromage, "Alignment Tolerance Analysis for Divided-Pulse Nonlinear Compression," J. Opt. Soc. Am. B **38**, 3199 (2021).

V. V. Karasiev, J. Hinz, S. X. Hu, and S. B. Trickey, "On the Liquid–Liquid Phase Transition of Dense Hydrogen," Nature **600**, E12 (2021).

D. I. Mihaylov, V. V. Karasiev, S. X. Hu, J. R. Rygg, V. N. Goncharov, and G. W. Collins, "Improved First-Principles Equation-of-State Table of Deuterium for High-Energy-Density Applications," Phys. Rev. B **104**, 144104 (2021).

S. F. Nwabunwanne and W. R. Donaldson, "Boosting the External Quantum Efficiency of AlGaN-Based Metal–Semiconductor–Metal Ultraviolet Photodiodes by Electrode Geometry Variation," IEEE J. Quantum Electron. **57**, 4000608 (2021).

A. M. Saunders, C. V. Stan, K. K. Mackay, B. Morgan, J. A. K. Horwitz, S. J. Ali, H. G. Rinderknecht, T. Haxhimali, Y. Ping, F. Najjar, J. Eggert, and H.-S. Park, "Experimental Observations of Laser-Driven Tin Ejecta Microjet Interactions," Phys. Rev. Lett. **127**, 155002 (2021).

A. Shvydky, A. V. Maximov, V. V. Karasiev, D. Haberberger, S. X. Hu, and V. N. Goncharov, "Ionization State and Dielectric Constant in Cold Rarefied Hydrocarbon Plasmas of Inertial Confinement Fusion," Phys. Rev. E **104**, 045207 (2021).

A. Tentori, A. Colaïtis, W. Theobald, A. Casner, D. Raffestin, A. Ruocco, J. Trela, E. Le Bel, K. Anderson, M. Wei, B. Henderson, J. Peebles, R. Scott, S. Baton, S. A. Pikuz, R. Betti, M. Khan, N. Woolsey, S. Zhang, and D. Batani, "Experimental Characterization of Hot-Electron Emission and Shock Dynamics in the Context of the Shock Ignition Approach to Inertial Confinement Fusion," Phys. Plasmas **28**, 103302 (2021).

W. Trickey, V. N. Goncharov, I. V. Igumenshchev, A. Shvydky, T. J. B. Collins, and E. M. Campbell, "Central Density and Low-Mode Perturbation Control of Inertial Confinement Fusion Dynamic-Shell Targets," Front. Phys. **9**, 784258 (2021).

C. A. Williams, R. Betti, V. Gopalaswamy, and A. Lees, "High Yields in Direct-Drive Inertial Confinement Fusion Using Thin-Ice DT Liner Targets," Phys. Plasmas **28**, 122708 (2021).

Forthcoming Publications

P. T. Campbell, C. A. Walsh, B. K. Russell, J. P. Chittenden, A. Crilly, G. Fiksel, L. Gao, I. V. Igumenshchev, P. M. Nilson, A. G. R. Thomas, K. Krushelnick, and L. Willingale, "Measuring Magnetic Flux Suppression in High-Power Laser–Plasma Interactions," to be published in Physics of Plasmas.

T. J. B. Collins, C. Stoeckl, R. Epstein, W. A. Bittle, C. J. Forrest, V. Yu. Glebov, V. N. Goncharov, D. R. Harding, S. X. Hu, D. W. Jacobs-Perkins, T. Z. Kosc, J. A. Marozas, C. Mileham, F. J. Marshall, S. F. B. Morse, P. B. Radha, S. P. Regan, B. Rice, T. C. Sangster, M. J. Shoup III, W. T. Shmayda, C. Sorce, W. Theobald, and M. D. Wittman, "Causes of Fuel–Ablator Mix Inferred from Modeling of Monochromatic Time-Gated Radiography in OMEGA Cryogenic Implosions," to be published in Physics of Plasmas.

M. F. Kasim, D. Watson-Parris, L. Deaconu, S. Oliver, P. Hatfield, D. H. Froula, G. Gregori, M. Jarvis, S. Khatiwala, J. Korenaga, J. Topp-Mugglestone, E. Viezzer, and S. M. Vinko, "Building High-Accuracy Emulators for Scientific Simulations with Deep Neural Architecture Search," to be published in Machine Learning: Science and Technology.

R. G. Kraus, R. J. Hemley, S. J. Ali, J. L. Belof, L. X. Benedict, J. Bernier, D. Braun, R. E. Cohen, G. W. Collins, F. Coppari, M. P. Desjarlais, D. Fratanduono, S. Hamel, A. Krygier, A. Lazicki, J. Mcnaney, M. Millot, P. C. Myint, M. G. Newman, J. R. Rygg, D. M. Sterbentz, S. T. Stewart, L. Stixrude, D. C. Swift, C. Wehrenberg, and J. H. Eggert, "Measuring the Melting Curve of Iron at Super-Earth Core Conditions," to be published in Science.

N. R. Shaffer and C. E. Starrett, "Dense Plasma Opacity via the Multiple-Scattering Method," to be published in Physical Review E.

R. Sobolewski, "Optical Detectors and Sensors," to be published in the Handbook of Superconducting Materials.

G. F. Swadling and J. Katz, "Novel Design for a Polarizing DUV Spectrometer Using a Wollaston Prism and Its Application as a Diagnostic for Measuring Thomson Scattering Data in the Presence of Strong Self-Emission Backgrounds," to be published in the Review of Scientific Instruments.

W. Theobald, D. Cao, R. C. Shah, C. A. Thomas, I. V. Igumenshchev, K. A. Bauer, R. Betti, M. J. Bonino, E. M. Campbell, A. R. Christopherson, K. Churnetski, D. H. Edgell, C. J. Forrest, J. A. Frenje, M. Gatu Johnson, V. Yu. Glebov, V. N. Goncharov, V. Gopalaswamy, D. R. Harding, S. X. Hu, S. T. Ivancic, D. W. Jacobs-Perkins, R. T. Janezic, T. Joshi, J. P.

Knauer, A. Lees, R. W. Luo, O. M. Mannion, F. J. Marshall, Z. L. Mohamed, S. F. B. Morse, D. Patel, J. L. Peebles, R. D. Petrasso, P. B. Radha, H. G. Rinderknecht, M. J. Rosenberg, S. Sampat, T. C. Sangster, W. T. Shmayda, C. M. Shuldberg, A. Shvydky, C. Sorce, C. Stoeckl, M. D. Wittman, and S. P. Regan, "Enhanced Laser-Energy Coupling with Small-Spot Distributed Phase Plates (SG5-650) in OMEGA DT Cryogenic Target Implosions," to be published in Physics of Plasmas.

D. Zhao, R. Betti, and H. Aluie, "Scale Interactions and Anisotropy in Rayleigh–Taylor Turbulence," to be published in the Journal of Fluid Mechanics.

Conference Presentations

The following presentations were made at Advanced Solid-State Lasers, Ontario, Canada, 3–7 October 2021:

C. Dorrer, I. A. Begishev, S.-W. Bahk, and J. Bromage, "Spatially Resolved Characterization of Partially Deuterated KDP Crystals for Parametric Amplification."

G. W. Jenkins, C. Feng, and J. Bromage, "Simultaneous Spectral Broadening and Contrast Improvement Using Divided-Pulse Nonlinear Compression."

M. Spilatro and C. Dorrer, "Versatile Spectral Shaping of Spectrally Incoherent Pulses in the IR and UV."

A. K. Schwemmlein, C. Fagan, W. T. Shmayda, M. Sharpe, C. Stoeckl, C. J. Forrest, S. P. Regan, and W. U. Schröder, "First Demonstration of a Triton Beam Using Target Normal Sheath Acceleration," presented at the American Physical Society Division of Nuclear Physics, Boston, MA, 10–14 October 2021.

D. A. Chin, P. M. Nilson, D. T. Bishel, E. Smith, X. Gong, M. K. Ginnane, B. J. Henderson, D. N. Polsin, T. R. Boehly, J. R. Rygg, G. W. Collins, D. Trail, A. Amouretti, M. Harmand, O. Mathon, R. Torchio, J. J. Ruby, F. Coppari, A. Coleman, and Y. Ping, "XANES and EXAFS Progress Studying Compressed Iron Oxides on OMEGA," presented at Matter in Extreme Conditions from Material Science to Planetary Physics, virtual, 12–13 October 2021.

The following presentations were made at Laser Damage, virtual, 12–15 October 2021:

D. Broege, S. G. Demos, C. Dorrer, K. R. P. Kafka, and M. Spilatro, "The Impact of Intensity Fluctuations on Laser Damage."

R. Dent, B. N. Hoffman, A. A. Kozlov, N. Liu, A. L. Rigatti, S. G. Demos, and A. A. Shestopalov, "Embedded Contamination Induced by Etching in E-Beam-Deposited Silica: A Possible Precursor to Laser Damage."

S. Elhadj, C. Gavin, A. Bayramian, W. Clauson, M. Murachver, J. Jarboe, D. Kissinger, C. LeBlanc, N. Urban, J. Wallace, S. Demos, and K. L. Marshall, "Large-Area, Multi-Pulse Laser Lifetime of Purified Nematic Liquid Crystals at Near-Infrared Wavelengths."

R. Jia, B. N. Hoffman, A. A. Kozlov, S. G. Demos, and A. A. Shestopalov, "Monolayer Organic Thin Films as Contamination-Resistant Coatings in Optical Elements."

K. R. P. Kafka, T. Z. Kosc, and S. G. Demos, "Methods and Apparatus for Laser Damage and Functional Performance Characterization of Ultrafast Laser Optics."

T. Z. Kosc, S. G. Demos, T. J. Kessler, H. Huang, A. Maltsev, R. Negres, and J. C. Lambropoulos, "Minimizing Risk for Laser Damage Due to Transverse Stimulated Raman Scattering in Large-Aperture KDP/DKDP Plates for Polarization Control at 3ω."

K. L. Marshall, K. R. P. Kafka, N. D. Urban, J. U. Wallace, and S. G. Demos, "The Effect of Incident Polarization Handedness and Ellipticity on the Laser-Damage Resistance of Oriented Liquid Crystals in the Nanosecond Regime."

P. Tzeferacos, "Big Computers and Big Lasers: How Concerted Numerical Simulations and Laser-Driven Laboratory Experiments Can Shed Light on Fundamental Astrophysical Processes in Turbulent Magnetized Plasmas," presented at CIRC Symposium, Rochester, 15 October 2021.

The following presentations were made at the Industrial Associates Meeting, Rochester, NY, 20–22 October 2021:

G. Chen, R. Adam, D. E. Bürgler, J. Cheng, D. Chaktraborty, I. Komissarov, S. Heidtfeld, D. Cao, H. Hardtdegen, M. Mikulics, A. Alostaz, F. Wang, M. Büscher, C. M. Schneider, L. Gladczuk, P. Przysłupki, and R. Sobolewski, "Ultrabroadband Spintronic THz Emitters Excited by Femtosecond Laser Pulse."

G. W. Jenkins, C. Feng, and J. Bromage, "Simultaneous Spectral Broadening and Contrast Improvement Using Divided-Pulse Nonlinear Compression."

E. M. Campbell, "A Vision for the Future for High-Power Laser Research and Applications," presented at OPTICSMEET 2021, Nice, France, 1–3 November 2021.

The following presentations were made at the 42nd Tritium Focus Group, Los Alamos, NM, 2–3 November 2021:

M. Sharpe and W. T. Shmayda, "Measurement of Palladium Hydride Isotherms Using H_2, D_2, and H_2/D_2 Mixtures."

W. T. Shmayda, H. Mutha, and K. Ryan, "The SPARC Tritium Fuel Cycle."

The following presentations were made at the 63rd Annual Meeting of the American Physical Society Division of Plasma Physics, Pittsburgh, PA, 8–12 November 2021:

M. B. P. Adams, P.-A. Gourdain, P. Tzeferacos, S. Feister, J. J. Pilgram, C. G. Constantin, and C. Niemann, "Exploration of Magnetic-Field Generation via Biermann Battery Using the *FLASH* Code to Model Experiments Performed at UCLA's Phoenix Laboratory."

M. V. Ambat, R. Boni, J. L. Shaw, P. Franke, K. R. McMillen, M. VanDusen-Gross, H. G. Rinderknecht, D. Ramsey, T. T. Simpson, J. P. Palastro, S.-W. Bahk, J. Bromage, and D. H. Froula, "Effects of Chromatic Aberration in a Dephasingless Laser Wakefield Accelerator."

K. S. Anderson, E. C. Hansen, J. A. Marozas, T. J. B. Collins, V. N. Goncharov, M. M. Marinak, and S. Sepke, "Computational Modeling of the Target Mounting Stalk in Direct-Drive Implosions."

A. Armstrong, A. Reyes, M. B. P. Adams, P. Farmakis, E. C. Hansen, Y. Lu, D. Michta, K. Moczulski, D. Q. Lamb, and P. Tzeferacos, "Implementation and Verification of Braginskii Viscosity in the *FLASH* Code."

J. Baltazar, R. C. Shah, D. Cao, V. Gopalaswamy, R. Betti, D. Patel, C. Stoeckl, W. Theobald, K. M. Woo, and S. P. Regan, "Diagnosing Low-Mode ($\ell \leq 6$) and Mid-Mode ($6 < \ell \leq 40$) Asymmetries in the Explosion Phase of Laser-Direct-Drive DT Cryogenic Implosions on OMEGA."

D. H. Barnak, R. Betti, V. Gopalaswamy, A. Lees, and A. Shvydky, "Understanding Shock-Release Experiments Using a Numerical Simulation of VISAR."

D. T. Bishel, P. M. Nilson, D. A. Chin, J. J. Ruby, E. Smith, S. X. Hu, J. R. Rygg, G. W. Collins, and E. V. Marley, "Utilizing Implosions to Constrain Atomic Physics of Gbar Materials."

G. Bruhaug, H. G. Rinderknecht, M. S. Wei, D. T. Bishel, G. W. Collins, J. R. Rygg, Y. E, K. Garriga, X. C. Zhang, R. Smith, A. Necas, and K. Zhai, "High-Power, High-Energy THz Generation with Joule and Kilojoule-Class Lasers."

M. Burns, R. K. Follett, A. Bowman, S. Zhai, A. Poudel, S. Dwarkadas, S. Pai, and A. B. Sefkow, "Heterogeneous Plasma Physics Codes in TriForce: Progress and Next Steps."

D. Cao, R. C. Shah, C. A. Thomas, A. Lees, V. Gopalaswamy, R. Betti, D. Patel, W. Theobald, J. P. Knauer, P. B. Radha, C. Stoeckl, S. P. Regan, W. Scullin, T. J. B. Collins, and V. N. Goncharov, "Understanding Origins of Observed Fusion-Yield Dependencies for Direct-Drive Implosions on OMEGA."

S. H. Cao, R. Betti, V. Gopalaswamy, H. Huang, D. Patel, C. Ren, M. J. Rosenberg, A. Shvydky, C. Stoeckl, and H. Wen, "Predicting Hot-Electron Generation in Inertial Confinement Fusion with Particle-in-Cell Simulations."

A. Casner, V. Bouffetier, L. Ceurvorst, G. Perez Callejo, T. Goudal, H. W. Sio, J. L. Peebles, P. Tzeferacos, V. Smalyuk, and O. A. Hurricane, "Mitigation of the Kelvin–Helmholtz Instability in HED Conditions by a Strong External Magnetic Field."

L. Ceurvorst, L. Masse, S. Khan, D. A. Martinez, N. Izumi, V. A. Smalyuk, T. Goudal, V. Bouffetier, A. Casner, B. Canaud, V. N. Goncharov, and I. V. Igumenshchev, "Effects of Ablation and Mode Coupling on the Deeply Nonlinear Stages of the Rayleigh–Taylor Instability."

D. A. Chin, P. M. Nilson, D. T. Bishel, E. Smith, R. S. Craxton, J. R. Rygg, G. W. Collins, J. J. Ruby, F. Coppari, A. Coleman, and Y. Ping, "Characterization of X-Ray Emission from Spherical Shells for X-Ray Absorption Spectroscopy Experiments on OMEGA 60."

S. Chowdry, S. Zhang, S. X. Hu, and G. Kagan, "Incorporating Quantum Electronics in Classical Calculations for Dense Plasmas."

K. Churnetski, K. M. Woo, W. Theobald, P. B. Radha, R. Betti, V. Gopalaswamy, I. V. Igumenshchev, S. T. Ivancic, M. Michalko, R. C. Shah, C. Stoeckl, C. A. Thomas, and S. P. Regan, "Three-Dimensional Hot-Spot Reconstruction from Cryogenic DT Polar-Direct-Drive Implosions on OMEGA."

A. Colaïtis, D. H. Edgell, I. V. Igumenshchev, D. Turnbull, J. P. Palastro, R. K. Follett, V. N. Goncharov, and D. H. Froula, "Low-Mode Asymmetry Induced by Polarized Cross-Beam Energy Transfer Interaction in Laser-Direct-Drive Spherical Implosions on OMEGA."

T. J. B. Collins, P. M. Nilson, R. Epstein, D. T. Bishel, D. A. Chin, J. J. Ruby, J. Kendrick, D. Guy, S. T. Ivancic, F. J. Marshall, C. Stoeckl, V. N. Goncharov, and D. H. Froula, "Theory and Modeling of Blast-Wave–Driven Interfacial Hydrodynamic Instability in OMEGA Planar Experiments."

R. S. Craxton, W. Y. Wang, M. A. Marangola, and E. M. Campbell, "A Dual Laser-Beam Configuration Compatible with Both Symmetric Direct Drive and Spherical Hohlraums."

J. R. Davies, D. H. Barnak, E. C. Hansen, P. V. Heuer, L. S. Leal, J. L. Peebles, and A. Birkel, "Evaluation of Direct Inversion of Proton Radiographs in the Context of Cylindrical Implosions."

A. Diaw, N. M. Cook, S. Coleman, J. P. Edelen, E. C. Hansen, and P. Tzeferacos, "Resistivity and Heat Conduction Modeling in Capillary Discharges."

D. H. Edgell, A. Colaitis, R. S. Craxton, R. K. Follett, M. J. Guardalben, A. Kalb, J. Katz, J. Kwiatkowski, O. M. Mannion, P. B. Radha, A. Shvydky, C. Stoeckl, D. Turnbull, and D. H. Froula, "Nonuniformity in Direct-Drive Implosions Caused by Polarization Smoothing" (invited).

R. Ejaz, V. Gopalaswamy, and R. Betti, "A Deep Learning Approach to Design Inertial Confinement Fusion Experiments."

R. Epstein, V. N. Goncharov, S. X. Hu, D. Cao, A. Shvydky, P. W. McKenty, G. W. Collins, D. Haberberger, J. L. Kline, and S. M. Finnegan, "Assessment of Radiation Trapping in Inertial Confinement Fusion Implosion Experiments with High-*Z*–Lined, Single-Shell Targets."

P. Farmakis, M. McMullan, A. Reyes, J. Laune, M. B. P. Adams, A. Armstrong, E. C. Hansen, Y. Lu, D. Michta, K. Moczulski, D. Lamb, and P. Tzeferacos, "Expanding the Tabulated Equation-of-State Implementations in the *FLASH* Code for the *SESAME* Database."

R. K. Follett, H. Wen, J. G. Shaw, D. H. Froula, A. V. Maximov, A. A. Solodov, D. Turnbull, J. P. Palastro, J. F. Myatt, and J. W. Bates, "A Local-Field Approach to Understanding Multibeam Laser–Plasma Instabilities."

C. J. Forrest, D. Cao, V. N. Glebov, V. N. Goncharov, V. Gopalaswamy, J. P. Knauer, O. M. Mannion, Z. L. Mohamed, S. P. Regan, R. C. Shah, C. Stoeckl, and K. M. Woo, "Inference of Isotropic and Anisotropic Flow in Laser Direct-Drive Cryogenic DT Implosions on OMEGA."

P. Franke, D. Ramsey, T. T. Simpson, D. Turnbull, D. H. Froula, and J. P. Palastro, "Optical Shock-Enhanced Self-Photon Acceleration."

F. García-Rubio, R. Betti, J. Sanz, and H. Aluie, "Magneto-hydrodynamic Instabilities in Ablation Fronts and Coronal Plasmas" (invited).

M. Gatu Johnson, P. J. Adrian, J. A. Frenje, T. M. Johnson, N. Kabadi, B. G. Lahmann, R. Petrasso, W. J. Garbett, R. S. Craxton, M. Hohenberger, H. D. Whitley, C. B. Yeamans, and A. B. Zylstra, "Measurement of Hot-Electron-Driven Fast Ions in Polar-Direct-Drive Exploding-Pusher Implosions on the NIF."

M. K. Ginnane, D. N. Polsin, X. Gong, M. C. Marshall, T. R. Boehly, J. R. Rygg, G. W. Collins, A. Lazicki, R. Kraus, J. H. Eggert, D. E. Fratanduono, J. P. Davis, C. A. McCoy, C. Seagle, and S. Root, "X-Ray Diffraction Measurements of Shocked and Shock-Ramped Platinum."

V. N. Goncharov, I. V. Igumenshchev, W. Trickey, N. Shaffer, K. M. Woo, T. J. B. Collins, E. M. Campbell, and Y. Lawrence, "Mitigating Deceleration Rayleigh–Taylor Growth in Inertial Confinement Fusion Designs."

X. Gong, D. N. Polsin, R. Paul, M. C. Marshall, M. K. Ginnane, B. J. Henderson, J. R. Rygg, G. W. Collins, and J. H. Eggert, "X-Ray Diffraction of Ramp-Compressed Silicon."

V. Gopalaswamy, R. Betti, J. P. Knauer, D. Patel, A. Lees, K. M. Woo, C. A. Thomas, D. Cao, O. M. Mannion, R. C. Shah, C. J. Forrest, Z. L. Mohamed, C. Stoeckl, V. N. Glebov, S. P. Regan, D. H. Edgell, M. J. Rosenberg, I. V. Igumenshchev, P. B. Radha, K. S. Anderson, J. R. Davies, T. J. B. Collins, V. N. Goncharov, K. Churnetski, W. Theobald, E. M. Campbell, R. T. Janezic, D. R. Harding, M. J. Bonino, S. Sampat, K. A. Bauer, S. F. B. Morse, M. Gatu Johnson, R. D. Petrasso, C. K. Li, and J. A. Frenje, "Advances Toward Hydro-Equivalent Ignition in OMEGA Direct-Drive Implosions" (invited).

D. Haberberger, A. Shvydky, S. T. Ivancic, V. N. Goncharov, C. Stoeckl, and D. H. Froula, "Schlieren Refraction Measurements of Implosion Density Profiles."

E. C. Hansen, M. B. P. Adams, A. Armstrong, J. R. Davies, P. Farmakis, F. García-Rubio, Y. Lu, D. Michta, K. Moczulski, C. Ren, A. C. Reyes, A. Sefkow, H. Wen, P. Tzeferacos, S. Langendorf, P. Ney, H. Rahman, and E. Ruskov, "Extended Magnetohydrodynamics in the *FLASH* Code."

B. J. Henderson, M. C. Marshall, J. R. Rygg, D. N. Polsin, L. E. Hansen, M. K. Ginnane, and G. W. Collins, "Thermal Emission and Reflectivity of Shocked SiO_2 Aerogel for Broadband Optical Probing."

P. V. Heuer, L S. Leal, J. R. Davies, E. C. Hansen, D. H. Barnak, J. L. Peebles, and A. Birkel, "Proton Radiography of Self-Generated Magnetic Fields in Laser-Driven Cylindrical Implosions."

P. V. Heuer, Y. Zhang, C. Ren, J. R. Davies, D. B. Schaeffer, M. S. Weidl, C. Niemann, W. Fox, and D. Caprioli, "Studying Quasi-Parallel Collisionless Shocks in the Laboratory."

S. X. Hu, P. M. Nilson, D. T. Bishel, D. A. Chin, V. V. Karasiev, I. E. Golovkin, M. Gu, T. Walton, and S. B. Hansen, "Probing Extreme Atomic Physics at Petapascal Pressures."

M. Huff, J. R. Rygg, G. W. Collins, T. R. Boehly, D. N. Polsin, M. Nakajima, B. J. Henderson, M. C. Marshall, T. A. Suer, D. E. Fratanduono, M. Millot, R. F. Smith, C. A. McCoy, and L. E. Hansen, "Measurements of Sound Speed in Iron Shock-Compressed Iron to ~3000 GPa."

I. V. Igumenshchev, V. N. Goncharov, E. M. Campbell, T. J. B. Collins, M. J. Rosenberg, N. Shaffer, W. Theobald, W. Trickey, R. C. Shah, A. Shvydky, A. Colaïtis, S. Atzeni, and L. Savino, "Dynamic Shell Stability to Low-Mode Perturbations."

S. T. Ivancic, W. Theobald, K. Churnetski, M. Michalko, R. Spielman, S. P. Regan, A. Raymond, J. D. Kilkenny, A. Carpenter, C. Trosseille, D. K. Bradley, J. D. Hares, A. K. L. Dymoke Bradshaw, G. Rochau, M. Sanchez, and D. Garand, "Design of the Third X-Ray Line of Sight for OMEGA."

T. R. Joshi, R. C. Shah, W. Theobald, I. V. Igumenshchev, J. Baltazar, D. Cao, and S. P. Regan, "Analysis of Modulations Observed in X-Ray Self-Emission Images of OMEGA Direct-Drive Inertial Confinement Fusion Implosions."

V. V. Karasiev, D. I. Mihaylov, S. X. Hu, S. B. Trickey, and J. W. Dufty, "Advancing the Accuracy of DFT Simulations for High-Energy-Density Plasmas by Developing Temperature-Dependent Exchange-Correlation Functionals" (invited).

J. Katz, A. L. Milder, D. Turnbull, S. T. Ivancic, D. H. Froula, M. Sherlock, P. Michel, L. Divol, D. Strozzi, and W. Rozmus, "Direct Measurements of Laser Absorption in Undersense Plasmas on OMEGA."

A. Kish, J. G. Shaw, M. Lavell, A. Sexton, and A. B. Sefkow, "Software Architecture Design for Modular Multiphysics Simulations."

J. P. Knauer, C. J. Forrest, Z. L. Mohamed, K. M. Woo, O. M. Mannion, I. V. Igumenshchev, R. Betti, V. Gopalaswamy, P. B. Radha, S. P. Regan, W. Theobald, M. Gatu Johnson, J. A. Frenje, A. J. Crilly, and B. D. Appelbe, "Effect of Mode-1 Perturbations on OMEGA Areal-Density Measurements."

M. J. Lavell, J. G. Shaw, A. Kish, A. Sexton, A. Srinivasan, S. Sikorski, and A. B. Sefkow, "Coulomb Collision Models for PIC Simulations of Field Reversed Configurations and Beam-Plasma Interactions."

Y. Lawrence, V. N. Goncharov, W. Trickey, I. V. Igumenshchev, K. Woo, and J. Carroll-Nellenback, "Deceleration Phase Rayleigh–Taylor Growth in Dynamic Shell ICF Designs."

Y. Lawrence, R. D. McBride, and A. B. Sefkow, "Transport Coefficient Sensitivities in a Semi-Analytic Model for MagLIF."

L. S. Leal, J. L. Peebles, D. H. Barnak, J. R. Davies, A. V. Maximov, E. C. Hansen, P. V. Heuer, A. B. Sefkow, and R. Betti, "Simulations of Ti-Layered Magnetized Liner Inertial Fusion Implosions on OMEGA Investigating the Effect of Mix."

A. Lees, D. Barnak, R. Betti, V. Gopalaswamy, A. Shvydky, and Z. K. Sprowal, "Measurements of Shock-Release Dynamics in Polystyrene Foils."

Y. Lu, S. Feister, J. Meinecke, F. Miniati, G. Gregori, A. Bott, A. Reyes, E. C. Hansen, J. T. Laune, B. Reville, J. S. Ross, D. Q. Lamb, and P. Tzeferacos, "Numerical Modeling of Laser-Driven Plasma Experiments Aiming to Study Turbulent Dynamo and Thermal Conduction at the National Ignition Facility."

O. M. Mannion, C. J. Forrest, V. Yu. Glebov, J. P. Knauer, P. W. McKenty, Z. L. Mohamed, S. P. Regan, C. Stoeckl, B. D. Appelbe, A. J. Crilly, W. T. Taitano, B. Keenan, P. Adrian, J. A. Frenje, N. Kabadi, and M. Gatu Johnson, "Fusion Neutron Energy Spectrum Measurements in Kinetic Plasmas."

M. J.-E. Manuel, M. Ghosh, R. Jonnalagadda, F. N. Beg, M. B. Adams, P. Tzeferacos, C. M. Huntington, B. Remington, J. S. Ross, D. D. Ryutov, H. W. Sio, G. F. Swadling, S. Wilks, and H.-S. Park, "Experimental Evidence of Early-Time Linear-Saturation of the Ion-Weibel Instability in Counter-streaming Plasmas."

J. A. Marozas, P. W. McKenty, T. J. B. Collins, M. J. Rosenberg, H. G. Rinderknecht, S. P. Regan, E. M. Campbell, C. B. Yeamans, B. E. Blue, L. Divol, G. E. Kemp, and H. D. Whitley, "National Ignition Facility Polar-Direct-Drive Exploding-Pusher Experiments—Improving Performance via Imprint Mitigation."

A. V. Maximov, D. Turnbull, R. K. Follett, D. H. Edgell, J. G. Shaw, H. Wen, D. H. Froula, and J. P. Palastro, "Absorption of Laser Light by Coupling to Incoherent Plasma Waves at Quarter-Critical Density."

P. W. McKenty, J. A. Marozas, T. J. B. Collins, M. J. Rosenberg, G. E. Kemp, C. B. Yeamans, and L. Divol, "Examining the Role of Cross-Beam Energy Transfer in NIF Direct-Drive Exploding-Pusher Experiments."

B. McLellan, S. Zhang, and S. X. Hu, "Revealing the Atomic Motion Composing the B1–B2 Structural Transformation of MgO Under High Pressures."

K. R. McMillen, M. V. Ambat, Z. Barfield, J. Pigeon, D. Haberberger, D. H. Froula, and J. L. Shaw, "Plasma Characterization for Raman Amplification."

D. Michta, P. Tzeferacos, F. Graziani, and G. W. Hammett, "A Many-Body Extension to Madelung Quantum Hydrodynamics."

D. I. Mihaylov, V. V. Karasiev, S. X. Hu, J. R. Rygg, V. N. Goncharov, and G. W. Collins, "Improved First-Principles Equation-of-State Table of Deuterium for High-Energy-Density Science Applications."

A. L. Milder, J. Katz, J. P. Palastro, D. H. Edgell, A. M. Hansen, D. Turnbull, D. H. Froula, M. Sherlock, and W. Rozmus, "Measurements of the Return-Current Instability with Ion-Acoustic Thomson Scattering."

S. C. Miller, V. N. Goncharov, T. J. B. Collins, and A. Shvydky, "Internal Perturbation Evolution and Amplification During the Early Phase of Inertial Confinement Fusion Implosions."

K. Moczulski, A. Reyes, M. B. P. Adams, A. Armstrong, P. Farmakis, E. C. Hansen, Y. Lu, D. Michta, D. Lamb, and P. Tzeferacos, "Implementation and Verification of LC Circuit for Z-Pinch *FLASH* Simulations."

Z. L. Mohamed, J. P. Knauer, A. Sorce, R. B. Brannon, R. T. Janezic, W. T. Shmayda, Y. H. Kim, K. Meaney, H. Geppert-Kleinrath, N. M. Hoffman, M. S. Rubery, A. B. Zylstra, and J. Jeet, "S-Factor Measurements for Gamma-Channel Fusion Reactions."

K. L. Nguyen, L. Yin, B. J. Albright, A. M. Hansen, D. Turnbull, R. K. Follett, D. H. Froula, and J. P. Palastro, "Cross-Beam Energy Transfer Saturation by Ion-Trapping–Induced Detuning."

K. Nichols, A. J. White, L. A. Collins, and S. X. Hu, "Investigating the Stopping Power of Warm Dense Plasmas Using Time-Dependent Mixed Density-Functional Theory."

P. M. Nilson, F. J. Marshall, T. J. B. Collins, R. Epstein, D. T. Bishel, D. A. Chin, J. J. Ruby, J. Kendrick, D. Guy, S. T. Ivancic, C. Stoeckl, V. N. Goncharov, and D. H. Froula, "High-Resolution X-Ray Imaging of Shock-Driven Interface Instabilities."

R. W. Paddock, R. H. Scott, W. J. Garbett, B. M. Haines, A. B. Zylstra, T. J. B. Collins, R. S. Craxton, and P. A. Norreys, "A Pathway Toward Burning Plasmas Through Low-Convergence-Ratio Direct-Drive ICF Implosions."

J. P. Palastro, P. Franke, D. H. Froula, L. Nguyen, D. Ramsey, and T. T. Simpson, "High Harmonic Generation Driven by a Flying Focus."

H. Pantell, L. E. Hansen, G. Tabak, M. F. Huff, G. Bruhaug, J. R. Rygg, and G. W. Collins, "Isotope Effects on High-Pressure Water."

D. Patel, R. Betti, C. Stoeckl, M. J. Rosenberg, V. Gopalaswamy, J. P. Knauer, S. P. Regan, W. Theobald, V. Yu. Glebov, and A. R. Christopherson, "Analysis of Hot-Electron Preheat of High-Performing OMEGA Cryogenic Implosions."

J. L. Peebles, J. R. Davies, D. H. Barnak, P. V. Heuer, L. S. Leal, F. J. Marshall, V. Yu. Glebov, and R. Betti, "Measurements of Laser-Preheat–Induced Mix in Scaled Magnetized Liner Inertial Fusion (MagLIF) Implosions."

D. N. Polsin, X. Gong, M. F. Huff, L. E. Hansen, B. J. Henderson, R. Paul, S. Burns, G. W. Collins, J. R. Rygg, A. Lazicki, F. Coppari, R. Smith, M. Millot, J. H. Eggert, M. I. McMahon, X. Wang, K. Hilleke, and E. Zurek, "Probing a New Regime of Extreme Chemistry at High-Energy-Density Conditions: Na as a Prototypical Example" (invited).

H. Poole, D. Cao, R. Epstein, I. Golovkin, T. Walton, S. X. Hu, M. Kasim, S. Vinko, J. R. Rygg, V. N. Goncharov, G. Gregori, and S. P. Regan, "A Feasibility Study of Using X-Ray Thomson Scattering to Diagnose the In-Flight Plasma Conditions of DT Cryogenic Implosions."

P. B. Radha, C. Stoeckl, W. Theobald, M. J. Rosenberg, M. Porcelli, R. Betti, E. M. Campbell, D. H. Edgell, V. N. Goncharov, J. P. Knauer, S. P. Regan, A. Shvydky, and A. A. Solodov, "Validation of Energy Coupling Models from kJ to MJ Scale."

D. Ramsey, P. Franke, D. H. Froula, T. T. Simpson, K. Weichman, J. P. Palastro, B. Malaca, M. Pardal, J. Vieira, A. Di Piazza, and M. Formanek, "Nonlinear Thomson Scattering with Ponderomotive Control."

S. P. Regan, O. M. Mannion, C. J. Forrest, H. McClow, Z. L. Mohamed, A. Kalb, J. Kwiatkowski, J. P. Knauer, C. Stoeckl, R. C. Shah, V. Yu. Glebov, W. Theobald, K. Churnetski, R. Betti, V. Gopalaswamy, H. G. Rinderknecht, I. V. Igumenshchev, P. B. Radha, V. N. Goncharov, D. H. Edgell, J. Katz, D. Turnbull, D. H. Froula, M. J. Bonino, D. R. Harding, C. M. Shuldberg, R. W. Luo, M. Hoppe, A. Colaïtis, and E. M. Campbell, "Systematic Trends of Hot-Spot Flow Velocity in Laser-Direct-Drive Implosions on OMEGA."

C. Ren, H. Wen, E. C. Hansen, S. J. Langendorf, D. Michta, and P. Tzeferacos, "PIC Simulations of Colliding Plasma Jets in Plasma Liner Experiment."

A. Reyes, M. B. P. Adams, A. Armstrong, K. Moczulski, P. Farmakis, E. C. Hansen, Y. Lu, D. Michta, P. Tzeferacos, J. Grove, and D. Q. Lamb, "Implementation of a 2-D Unsplit Volume of Fluid Interface—Capturing Method for Multifluid Compressible Flows in the *FLASH* Code."

H. G. Rinderknecht, M. S. Wei, G. Bruhaug, K. Weichman, J. P. Palastro, J. D. Zuegel, A. Arefiev, T. Wang, T. Toncian, A. Laso Garcia, D. Doria, K. Spohr, H. J. Quevedo, T. Ditmire, J. Williams, A. Haid, and D. Stutman, "Relativistically Transparent Magnetic Filament: A Laser-Plasma Platform for Efficient Electron Acceleration and MeV Photon Radiation."

M. J. Rosenberg, A. A. Solodov, A. R. Christopherson, R. Betti, P. B. Radha, C. Stoeckl, C. J. Forrest, V. Yu. Glebov, F. J. Marshall, S. P. Regan, T. J. B. Collins, D. H. Froula, J. P. Palastro, V. N. Goncharov, M. Hohenberger, B. Bachmann, G. N. Hall, P. Michel, and C. Krauland "Hot-Electron Preheat in Hydrodynamically Scaled Direct-Drive Implosions at the National Ignition Facility and OMEGA."

J. R. Rygg, G. W. Collins, and P. M. Celliers, "Plasma Waves and the Compressibility of Warm Dense Hydrogen."

M. J. Schmitt, B. S. Scheiner, D. Schmidt, L. Kot, B. Keenan, M. J. Rosenberg, P. W. McKenty, and R. S. Craxton, "Ablative Energetics of Large-Capsule, Low-Intensity Direct-Drive Implosions at the National Ignition Facility."

A. K. Schwemmlein, C. E. Fagan, W. T. Shmayda, M. Sharpe, C. Stoeckl, C. J. Forrest, S. P. Regan, and W. U. Schröder, "First Demonstration of a Triton Beam Using Target Normal Sheath Acceleration."

A. B. Sefkow, J. G. Shaw, A. Kish, M. Lavell, R. Masti, A. Sexton, S. Borve, A. Bowman, M. Burns, J. Carroll-Nellenback, S. Cohen, J. R. Davies, S. Dwarkadas, E. Evans,

R. K. Follett, M. Haddad, K. Hemsley, A. Kokash, Y. Lawrence, B. G. Logan, R. L. McCrory, A. Nahar, J. H. Nuckolls, S. Pai, A. Poudel, T. Seabourne, W. Scullin, S. Sikorski, A. Srinivasan, H. Stojkovic, A. Velberg, K. Yanik, and S. Zhai, "Overview of TriForce: Projects, Progress, and Plans."

N. R. Shaffer, A. V. Maximov, V. N. Goncharov, and M. Sherlock, "Impact of Bandwidth on the Electron Distribution Functions of Laser-Produced Plasmas."

R. C. Shah, D. Cao, R. Epstein, M. J. Rosenberg, W. Theobald, V. Gopalaswamy, R. Betti, S. P. Regan, P. Volegov, and B. Bachmann, "Mix, Temperature, and Compression of Statistical Model Optimized Cryogenic Implosions."

J. L. Shaw, G. Bruhaug, M. Freeman, F. Merrill, V. Geppert-Kleinrath, and C. Wilde, "Electron Radiography Based on Electron Beams from Laser-Plasma Accelerators."

A. Shvydky, J. L. Peebles, M. J. Rosenberg, A. V. Maximov, K. S. Anderson, V. N. Goncharov, J. A. Marozas, P. W. McKenty, P. B. Radha, S. P. Regan, T. C. Sangster, M. Hohenberger, J. M. Di Nicola, J. M. Koning, M. M. Marinak, L. Masse, M. Karasik, and L. Antonelli, "National Ignition Facility Planar Imprint Experiments."

T. T. Simpson, D. Ramsey, P. Franke, M. V. Ambat, K. Weichman, D. Turnbull, D. H. Froula, and J. P. Palastro, "Spatiotemporal Control of Laser Intensity Through Cross-Phase Modulation."

A. A. Solodov, M. J. Rosenberg, M. Stoeckl, R. Betti, W. Seka, R. Epstein, C. Stoeckl, R. K. Follett, P. B. Radha, S. P. Regan, D. H. Froula, J. P. Palastro, V. N. Goncharov, A. R. Christopherson, B. Bachmann, M. Hohenberger, P. Michel, and J. F. Myatt, "Hot-Electron Preheat and Mitigation in Polar-Direct-Drive Experiments at the National Ignition Facility."

Z. K. Sprowal, L. E. Hansen, M. Zaghoo, J. R. Rygg, T. R. Boehly, D. N. Polsin, M. Huff, G. W. Collins, D. G. Hicks, and P. M. Celliers, "Accessing High Density States in D_2 Using Double Shock."

C. Stoeckl, W. Theobald, P. B. Radha, T. Filkins, and S. P. Regan, "Energy-Coupling Experiments Using Solid Spheres in the Polar-Direct-Drive Configuration on OMEGA."

G. Tabak, M. A. Millot, S. Hamel, T. Ogawa, P. M. Celliers, D. E. Fratanduono, A. Lazicki, D. Swift, S. Brygoo, P. Loubeyre, T. R. Boehly, N. Dasenbrock-Gammon, R. Dias, L. E. Hansen, B. J. Henderson, M. Zaghoo, S. Ali, R. Kodama, K. Miyanishi, N. Ozaki, T. Sano, R. Jeanloz, D. G. Hicks, G. W. Collins, J. H. Eggert, and J. R. Rygg, "Equation of State and Metallization of Methane Shock Compressed to 400 GPa."

W. Theobald, M. J. Rosenberg, P. B. Radha, S. P. Regan, C. Stoeckl, L. Ceurvorst, R. Betti, K. S. Anderson, J. A. Marozas, V. N. Goncharov, E. M. Campbell, C. M. Shuldberg, R. W. Luo, W. Sweet, D. N. Kaczala, B. Bachmann, T. Döppner, M. Hohenberger, R. Scott, and A. Colaïtis, "Laser-Direct-Drive Energy Coupling at 4×10^{14} W/cm^2 to 1.2×10^{15} W/cm^2 from Spherical Solid-Plastic Implosions at the National Ignition Facility."

C. A. Thomas, W. Theobald, J. P. Knauer, C. Stoeckl, T. J. B. Collins, V. N. Goncharov, R. Betti, E. M. Campbell, K. S. Anderson, K. A. Bauer, D. Cao, R. S. Craxton, D. H. Edgell, R. Epstein, C. J. Forrest, V. Yu. Glebov, V. Gopalaswamy, I. V. Igumenshchev, S. T. Ivancic, D. W. Jacobs-Perkins, R. T. Janezic, T. Joshi, J. Kwiatkowski, A. Lees, F. J. Marshall, M. Michalko, Z. L. Mohamed, D. Patel, J. L. Peebles, P. B. Radha, S. P. Regan, H. G. Rinderknecht, M. J. Rosenberg, S. Sampat, T. C. Sangster, R. C. Shah, K. L. Baker, A. L. Kritcher, M. Tabak, M. C. Herrmann, A. R. Christopherson, and O. M. Mannion, "Laser-Direct-Drive Cryogenic Implosion Performance on OMEGA Versus Target and Laser-Spot Radius."

W. Trickey, V. N. Goncharov, E. M. Campbell, T. J. B. Collins, M. J. Rosenberg, N. Shaffer, W. Theobald, R. C. Shah, A. Shvydky, I. V. Igumenshchev, A. Colaïtis, S. Atzeni, and L. Savino, "Optimization of Beam-Port Configurations to Minimize Low-Mode Perturbations in High-Yield Inertial Confinement Fusion Targets."

W. Trickey, R. H. H. Scott, and N. Woolsey, "Shock-Augmented Ignition Using Indirect Drive."

P. Tzeferacos, A. Reyes, Y. Lu, A. Armstrong, K. Moczulski, G. Gregori, J. Meinecke, H. Poole, L. Chen, T. Campbell, A. Bell, S. Sarkar, F. Miniati, A. Schekochihin, D. Lamb, D. H. Froula, J. Katz, D. Haberberger, D. Turnbull, S. Fess, H.-S. Park, J. S. Ross, T. Doeppner, J. Emig, C. Goyon, D. Ryutov, B. Remington, A. Zylstra, C.-K. Li, A. Birkel, R. D. Petrasso, H. Sio, F. H. Séguin, A. F. A. Bott, C. Palmer, B. Khiar, S. Feister, A. Casner, D. Ryu, B. Reville, C. J. Forrest, J. Foster, Y. Sakawa, F. Fiuza, E. Churazov, R. Bingham, T. White, and E. Zweibel, "Strong Suppression of Heat Conduction in Laser-Driven Magnetized Turbulent Plasmas."

M. VanDusen-Gross, K. Weichman, D. R. Harding, A. Arefiev, J. Williams, A. Haid, and H. G. Rinderknecht, "Design of Experiments to Study Relativistically Transparent Magnetic Filaments Using OMEGA EP."

K. Weichman, A. V. Arefiev, H. Mao, F. N. Beg, J. P. Palastro, A. P. L. Robinson, M. Murakami, S. Fujioka, J. J. Santos, T. Toncian, T. Ditmire, H. Quevedo, Y. Shi, and V. V. Ivanov, "Effects of Kilotesla-Level Applied Magnetic Fields on Relativistic Laser–Plasma Interactions" (invited).

H. Wen, R. K. Follett, A. V. Maximov, and J. P. Palastro, "Mitigation of Inflationary Stimulated Raman Scattering with Laser Bandwidth."

C. A. Williams, R. Betti, V. Gopalaswamy, A. Lees, J. P. Knauer, C. J. Forrest, D. Patel, S. Sampat, R. T. Janezic, D. Cao, O. M. Mannion, P. B. Radha, S. P. Regan, R. C. Shah, C. A. Thomas, W. Theobald, and K. M. Woo, "Improving Performance and Understanding of Direct-Drive Inertial Fusion Implosions Using Statistical Modeling of Experimental Data."

K. M. Woo, R. Betti, C. A. Thomas, C. Stoeckl, K. Churnetski, C. J. Forrest, Z. L. Mohamed, B. Zirps, S. P. Regan, T. J. B. Collins, W. Theobald, R. C. Shah, O. M. Mannion, D. Patel, D. Cao, J. P. Knauer, V. N. Goncharov, P. B. Radha, H. G. Rinderknecht, R. Epstein, V. Gopalaswamy, and F. J. Marshall, "Three-Dimensional Hot-Spot Reconstruction in Inertial Fusion Implosions."

S. Zhang, M. C. Marshall, J. R. Rygg, A. Shvydky, D. Haberberger, V. N. Goncharov, T. R. Boehly, G. W. Collins, S. X. Hu, D. E. Fratanduono, and A. Lazicki, "Species Separation in Polystyrene Shock Release Evidenced by Molecular-Dynamics Simulations and Laser-Drive Experiments."

Y. Zhang, P. V. Heuer, J. R. Davies, and C. Ren, "Magnetized Collisionless Shock Formation Mediated by the Modified-Two-Stream Instability."

D. E. Keller and V. V. Karasiev, "VASP 6.2.1 Runtime Comparison for Extreme Thermodynamic Condition Simulations Using Graphics-Processing Units," presented at the 12th IEEE Workshop on Performance Modeling, Benchmarking, and Simulation of High-Performamce Computer Systems, virtual, 14–19 November 2021.

C. Deeney, "The Laboratory for Laser Energetics: An Overview," presented at the L3Harris visit, Rochester, NY, 15 November 2021.

E. M. Campbell, "Inertial Fusion Energy: Opportunities and Challenges," presented at the Inertial Fusion Energy Workshop, Livermore, CA, 16 November 2021.

C. Deeney, "The Laboratory for Laser Energetics: An Overview," presented at the Danny Lowe visit, Rochester, NY, 16 November 2021.

The following presentations were made at the OES Annual Meeting, virtual, 17–18 November 2021:

E. M. Campbell, "ICF-Facility Operations LLE 10.7."

S. P. Regan, "ICF Diagnostics and Instrumentation: LLE."

T. C. Sangster, "MTE 10.8."

M. Wang and D. R. Harding, "Mechanical Properties of Micrometer-Size Foam-Like Auxetic Structures," presented at the MRS Fall Meeting, Boston, MA, 28 November–3 December 2021.

E. M. Campbell, "Principles of Inertial Confinement Fusion," presented at the NROTC visit, Rochester, NY, 1 December 2021.

The following presentations were made at the Cooperative Agreement Review Meeting, Rochester, NY, 6–7 December 2021:

E. M. Campbell, "The Laboratory for Laser Energetics: An Overview of the FY19–FY23 Cooperative Agreement."

G. W. Collins, "HEDS Curriculum and Mentoring at the University of Rochester."

G. W. Collins, S. X. Hu, and J. R. Rygg, "Laboratory for Laser Energetics Contributions to the Stockpile Stewardship Mission."

C. Deeney and E. M. Campbell, "The Laboratory for Laser Energetics: Our Cooperative Agreement Going Forward."

V. N. Goncharov, "Review of Ignition Science Campaigns."

V. Gopalaswamy, R. Betti, J. P. Knauer, D. Patel, A. Lees, K. M. Woo, C. A. Thomas, D. Cao, O. M. Mannion, R. C. Shah, C. J. Forrest, Z. L. Mohamed, C. Stoeckl, V. Yu. Glebov, S. P. Regan, D. H. Edgell, M. J. Rosenberg, I. V. Igumenshchev, P. B. Radha, K. S. Anderson, J. R. Davies, T. J. B. Collins, V. N. Goncharov, E. M. Campbell, R. T. Janezic, D. R. Harding, M. J. Bonino, S. Sampat, K. A. Bauer, S. F. B. Morse, M. Gatu Johnson, R. D. Petrasso, C. K. Li, and J. A. Frenje, "OMEGA DT Cryogenic Implosion Progress."

D. R. Harding, A. Behlok, M. J. Bonino, T. Cracium, S. Fess, J. Fooks, S. Karim, I. Knudsen, K. Lintz, N. Redden, D. Wasilewski, M. Wittman, Y. Lu, P. Fan, and X. Huang, "Target Production and Development at LLE."

S. X. Hu, "Highlights of Recent Progress in High-Energy-Density Physics Theory/Computation at LLE."

S. F. B. Morse, "Omega Facility Performance FY19–FY23."

S. P. Regan, "DOE Cooperative FY19–FY23 Agreement: Diagnostic Development (10.3)."

J. R. Rygg, D. N. Polsin, X. Gong, M. C. Marshall, G. W. Collins, J.-P. Davis, C. McCoy, C. Seagle, A. Lazicki, R. Kraus, J. H. Eggert, and D. E. Fratanduono, "High-Energy-Density Experiments: Case Studies."

C. Sorce, "Engineering, Information Technology and Cybersecurity, and Safety."

S. Stagnitto, "University of Rochester Support of the Laboratory for Laser Energetics' Research Portfolio."

D. Turnbull, "Laser–Plasma Instabilities: Deep Dive."

M. S. Wei, "Education and User Access."

J. D. Zuegel, "Laser and Materials Technology Division and Major Projects."

The following presentations were made at the National Diagnostic Workshop, virtual, 7–9 December 2021:

S. T. Ivancic, W. Theobald, K. Churnetski, M. Michalko, R. Spielman, S. P. Regan, A. Raymond, J. D. Kilkenny, A. Carpenter, C. Trosseille, D. K. Bradley, J. D. Hares, A. K. L. Dymoke-Bradshaw, G. Rochau, M. Sanchez, and D. Garand, "Design of the Third X-Ray Line of Sight for OMEGA."

A. L. Milder, J. Katz, R. Boni, D. Nelson, J. P. Palastro, P. Franke, J. L. Shaw, S. T. Ivancic, A. M. Hansen, D. Turnbull, I. A. Begishev, K. Daub, Z. Barfield, R. K. Follett, D. H. Froula, M. Sherlock, H. P. Le, T. Chapman, and W. Rozmus, "Measurements of Non-Maxwellian Electron Distribution Functions Using Angularly Resolved Thomson Scattering."

J. P. Palastro, P. Franke, M. Lim Pac Chong, K. L. Nguyen, J. Pigeon, D. Ramsey, H. G. Rinderknecht, J. L. Shaw, T. T. Simpson, D. Turnbull, K. Weichman, D. H. Froula, M. Formanek, A. Di Piazza, B. Malaca, M. Pardal, and J. Vieira, "Advanced Radiation Sources Enabled by Spatiotemporal Control of Laser Intensity."

J. L. Peebles, "Magnetized Target Capabilities and Diagnostic Needs at LLE."

H. G. Rinderknecht, J. P. Knauer, W. Theobald, R. Fairbanks, B. Brannon, V. Kobilansky, R. Peck, J. Armstrong, M. Weisbeck, J. Brown, P. B. Radha, S. P. Regan, J. Kunimune, P. Adrian, M. Gatu Johnson, J. A. Frenje, F. H. Séguin, and B. Bachmann, "An Introduction to Knock-on Deuteron Imaging for Diagnosing the Fuel and Hot Spot in Direct-Drive ICF Implosions."

The following presentations were made at the 2021 IEEE Pulsed Power Conference and Symposium on Fusion Engineering, Denver, CO, 12–16 December 2021:

M. Sharpe, W. T. Shmayda, and J. J. Ruby, "Influence of Heat Treatments on the Near-Surface Tritium Concentration Profiles."

W. T. Shmayda, H. Mutha, and K. Ryan, "Tritium Recovery from SPARC."

C. A. Thomas, E. M. Campbell, and M. Tabak, "Review of Inertial Confinement Fusion: Physics and Engineering Challenges" (invited).

The following presentations were made at the American Geophysical Union Fall Meeting, New Orleans, LA, 13–17 December 2021:

M. Ghosh, S. Zhang, and S. X. Hu, "Mechanism of Cooperative Diffusion in bcc Iron Under Earth and Super-Earth's Inner Core Conditions."

R. Paul, K. Nichols, S. Zhang, S. X. Hu, and V. V. Karasiev, "Melting, Acoustic Properties, and Thermal Conditions of FeO_2 Near Core–Mantle Boundary Conditions."

E. M. Campbell, "ICF Research at the University of Rochester's Laboratory for Laser Energetics," presented at the 42nd Annual Meeting of Fusion Power Associates, virtual, 15–16 December 2021.

E. M. Campbell, "University of Rochester and the Laboratory for Laser Energetics: An Overview," presented at the 3rd INFUSE Workshop, virtual, 16–17 December 2021.

R. Betti, "Thermonuclear Ignition in Laser-Driven Inertial Confinement Fusion," presented at the Centro Ricerche Frascati, Frascati, Italy, 17 December 2021.

UNIVERSITY OF ROCHESTER
LABORATORY FOR LASER ENERGETICS

Volume 170
January–March 2022
DOE/NA/3856-1736

LLE Review

Quarterly Report

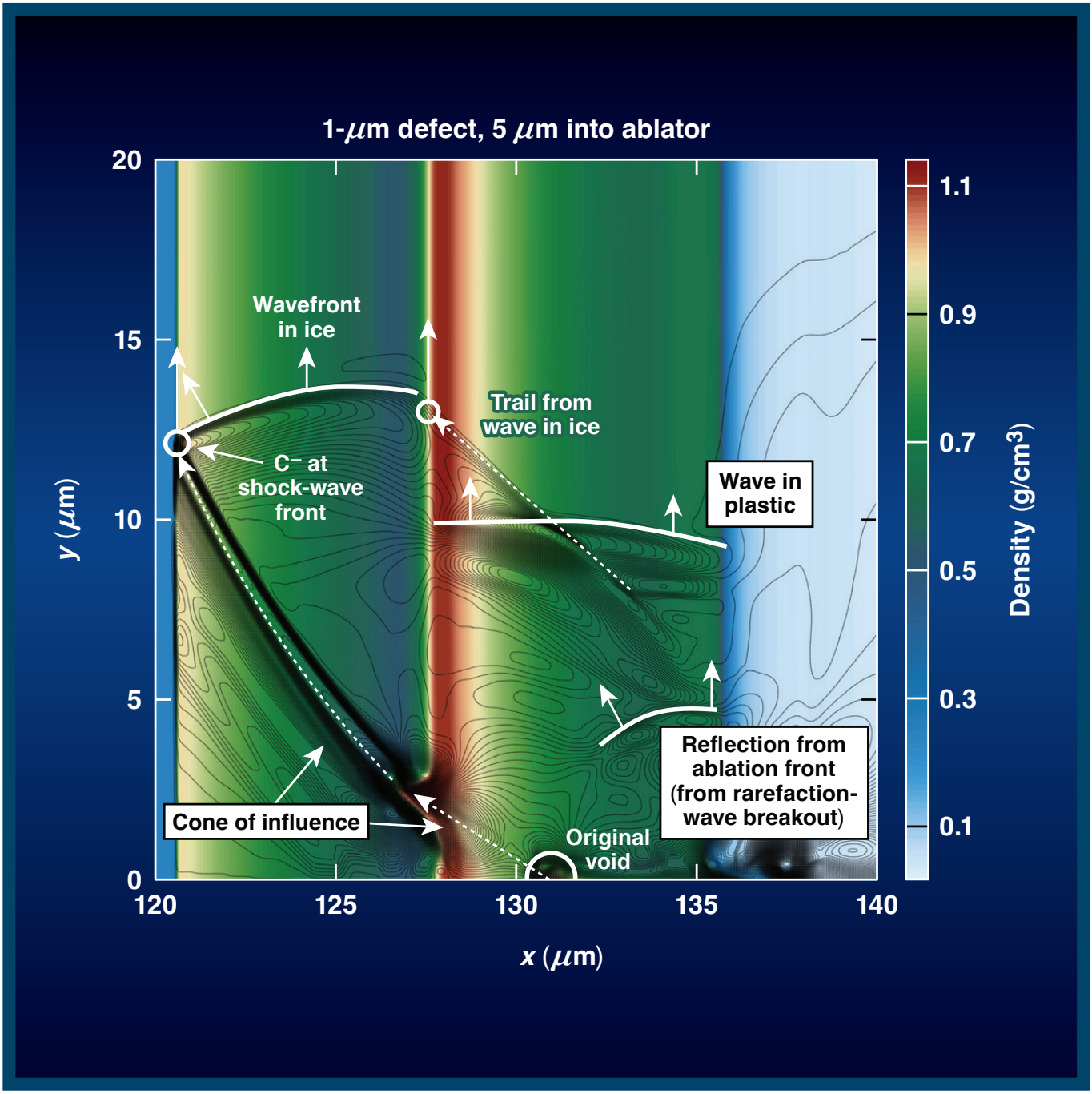

About the Cover:

The cover photo shows the density contour from a *Cygnus* simulation of a 2-D planar foil that contains a 1-μm defect located in the ablator (5 μm from the CH–DT interface). The color corresponds to density and the black lines correspond to y-velocity contours. The target accelerates from right to left, and the axis of symmetry is at $y = 0$. This shows the target after the first shock has passed through the CH–DT interface and into the ice. The shock front is located near $x = 121$ μm and the CH–DT interface is near $x = 128$ μm. The 1-D entropy wave that originates with the defect is labeled in the image just behind the CH–DT interface [near $(x, y) = (131, 0)$ μm]. In the image, perturbation information can be seen propagating along various ripples, after the shock has passed through the defect. When the shock interacts with the defect, the shock front becomes locally deformed. Since the perturbation wave has both x and y components, this deformation spreads laterally along the shock front, leaving a "trail" of vorticity in a cone-like manner, with its origin at the fluid trajectory of the original defect. The extent of this vorticity cone (labeled in the image by the dashed white line) is determined by the material sound speed, shock strength, and defect placement. As the original perturbation cone from the first shock front expands into the target, new waves (such as rarefaction waves) carry this updated information back to the ablation front. Additionally, the distortion laterally expands along the surface of the ablation front due to the 2-D nature of the flow.

Internal target defects create complex wave phenomena, yet simple single-mode (cosine) perturbations can provide clues as to how these complex wave dynamics evolve. In the image on the right, four different single-mode perturbations (λ = wavelength) are applied at different locations (x_p) relative to the interface within the ice or ablator material of a planar 2-D foil. This image shows that distortion growth is larger for large-wavelength modes that originate closer to the outer surface of the target due to shock transit time and the rarefaction wave created by the material interface.

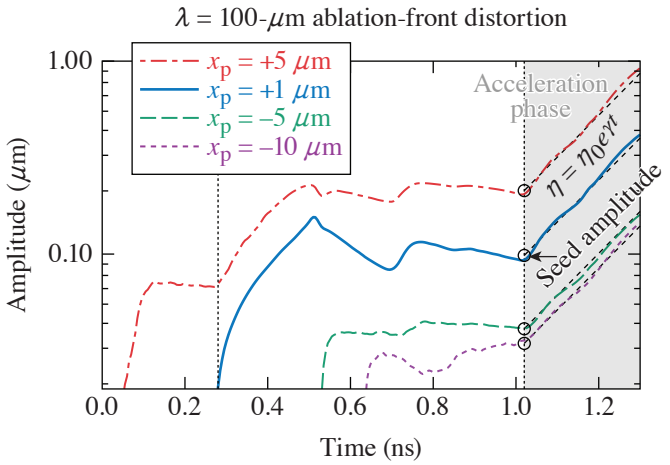

E30033JR

The work described in this volume includes current research at the Laboratory for Laser Energetics, which is supported by New York State Energy Research and Development Authority, the University of Rochester, the U.S. Department of Energy Office of Inertial Confinement Fusion under Cooperative Agreement No. DE-NA0003856, and other agencies.

Printed in the United States of America
Available from
National Technical Information Services
U.S. Department of Commerce
5285 Port Royal Road
Springfield, VA 22161
www.ntis.gov

For questions or comments, contact Milton J. Shoup III, Editor, Laboratory for Laser Energetics, 250 East River Road, Rochester, NY 14623-1299, (585) 275-9636.

www.lle.rochester.edu

UNIVERSITY OF ROCHESTER
LABORATORY FOR LASER ENERGETICS

Volume 170
January–March 2022
DOE/NA/3856-1736

LLE Review

Quarterly Report

UR LLE

Contents

In Brief

This volume of LLE Review 170 covers the period from January–March 2022. Articles appearing in this volume are the principal summarized results for long-form research articles. Readers seeking a more-detailed account of research activities are invited to seek out the primary materials appearing in print, detailed in the publications and presentations section at the end of this volume.

Highlights of research presented in this volume include:

- S. C. Miller and V. N. Goncharov model instability seeding mechanisms caused by internal defects in inertial confinement fusion targets (p. 1).
- A. Colaïtis *et al*. present detailed calculations that capture the persistent low-mode asymmetries evident in laser-direct-drive implosions on the OMEGA Laser System (p. 5).
- V. Gopalaswamy *et al.* present an analysis of limited coverage effects on areal-density measurements in inertial confinement fusion implosions on the OMEGA Laser System (p. 10).
- P. V. Heuer *et al.* report on diagnosing magnetic fields in cylindrical implosions with oblique proton radiography on the OMEGA Laser System (p. 16).
- L. S. Leal *et al.* model the effect of laser preheat in magnetized liner inertial fusion at the Omega Laser Facility (p. 19).
- K. M. Woo *et al.* present an analysis of core asymmetries in inertial confinement fusion implosions using 3-D hot-spot reconstruction of experimental data from the OMEGA Laser System (p. 21).
- J. R. Davies and P. V. Heuer conduct an evaluation of the direct inversion of proton radiographs in the context of cylindrical implosions (p. 24).
- H. Wen *et al.* report particle-in-cell modeling of plasma-jet merging in the large-Hall-parameter regime (p. 27).
- K. Weichman *et al.* present progress in modeling relativistic laser–plasma interaction with kilotesla-level applied magnetic fields (p. 30).
- G. Bruhaug *et al.* report the first single-shot electron radiography images using an electron beam from a 100-J-class laser-plasma accelerator (p. 35).
- G. Bruhaug *et al.* present on the development of a hardened THz energy meter for use on the kilojoule-scale, short-pulse OMEGA EP laser (p. 38).
- C. Dorrer and J. L Shaw demonstrate a single-shot cross-correlator based on the sum–frequency generation of counter-propagating beams in SBN61 ($Sr_xBa_{1-x}Nb_20_6$ with $x = 0.61$) using the Multi-Terawatt laser ($\lambda_A = 1053$ nm) and the idler of the MTW-OPAL laser ($\lambda_B = 1170$ nm) (p. 41).
- K. L. Marshall *et al.* report on the multiparameter laser performance characterization of liquid crystals for polarization control devices in the nanosecond regime (p. 44).
- M. Sharpe, W. T. Shmayda, and J. Ruby report on the experimentally determined influence of heat treatments on the near-surface tritium concentration profiles in 316 stainless steel (p. 47).
- G. Chen *et al.* experimentally determine the electron effective mass in highly resistive GaAs by exploiting the influence of a magnetic field on optically excited transient THz surface emissions (p. 50).

- J. L. Peebles *et al.* provide an assessment of generating quasi-static magnetic fields using laser-driven "capacitor" coils (p. 53).
- R. B. Spielman discusses pulsed-power innovations for next-generation, high-current drivers (p. 57).
- J. Puth *et al*. summarize operations of the Omega Laser Facility during the second quarter of FY22 (p. 60).

Milton Shoup III
Editor

Instability Seeding Mechanisms due to Internal Defects in Inertial Confinement Fusion Targets

S. C. Miller and V. N. Goncharov

Laboratory for Laser Energetics and Department of Mechanical Engineering, University of Rochester

Performance degradation in laser-driven inertial confinement fusion implosions is caused by several effects, one of which is Rayleigh–Taylor instability growth. Target imperfections from manufacturing processes create instability seeds in the form of roughness or isolated "dome" features on the outer surface, gaps or separation between material layers, ice-layer roughness, and internal defects such as voids and bubbles. Additionally, tritium decay from the DT fuel can deposit energy into the ablator and DT ice layers and cause localized swelling in the plastic ablator material.1 A comprehensive understanding of seeding mechanisms is essential to characterize the impact of target defects on in-flight shell integrity and mass injection into the central, lower-density vapor region. An analysis of early-time behavior of both single-mode shell mass modulations and isolated voids is performed by examining the evolution of the acoustic waves launched by these target imperfections. A systematic study of localized perturbation growth as a function of defect placement and size is presented. The use of low-density ablator materials (such as foams) is suggested as a potential mitigation strategy to improve target robustness against the impact of defect-initiated growth.

A new parallel high-order multiphysics code (*Cygnus*[2]) is used to simulate internal ("bulk") perturbations inside the solid-density DT ice and plastic ablator materials. Perturbations are applied to planar 2-D foils (driven by a laser-like heat flux up to the start the acceleration phase) to study hydrodynamic wave propagation and seeding mechanisms at the ablation front. Convergence effects are not significant in early-time evolution, and the use of planar foils simplifies the analysis.

The foils used in this work are defined by three fluid regions: a 100-μm-thick, low-density $\rho = 0.001$-g/cm^3 layer representing the vapor region; a 40-μm-thick, $\rho = 0.25$-g/cm^3 layer representing DT ice; and an 8-μm-thick, heavier-density $\rho = 1$-g/cm^3 layer to mimic the plastic (CH) ablator. Density perturbations are applied in two forms: single-mode sinusoidal (to study basic seeding mechanisms) and isolated Gaussian voids (to closer mimic a realistic defect).

Figure 1 shows the trajectories of the ablation front, CH–DT interface, DT gas–ice interface, and two shocks created by the single-picket laser pulse (plotted in the lower pane). When shocks pass through an internal perturbation, such as a defect, a void in the material, or an interfacial gap, perturbation waves are launched that travel along characteristic hypersurfaces. For small perturbations decomposed into Fourier harmonics, each wave harmonic travels along characteristics defined as $(\mathrm{d}x/\mathrm{d}t)_{C^+} = U + c_s$ (the C^+ characteristic), as $(\mathrm{d}x/\mathrm{d}t)_{C^-} = U - c_s$ (the C^- characteristic), and $(\mathrm{d}x/\mathrm{d}t)_e = U$ (the entropy wave that travels with the local fluid velocity), where U is local fluid velocity and c_s is local sound speed. These characteristic trajectories define how perturbations propagate throughout the target and deposit seeds for instability growth. In the event of a shock-perturbation interaction, the C^+ characteristic wave carries the information back to the ablation front, the C^- characteristic wave catches up to and perturbs the shock front, and the entropy wave travels with the original defect (and defines the trajectory of the shock-induced vorticity).

Figure 2 shows the results from single-mode sinusoidal perturbations applied at various depths in the ice and ablator material of the foil. These depths are reported as relative to the CH–DT interface (where a positive value denotes a position inside the ablator material). Figure 2 plots the evolution of the distortion amplitude (peak to valley) of the ablation front due to perturbations with a single-mode wavelength of 100 μm. The time history of the ablation-front distortion shows the arrival of particular hydrodynamics waves such as shocks, rarefaction waves, and other characteristic waves. The two perturbations that start in the

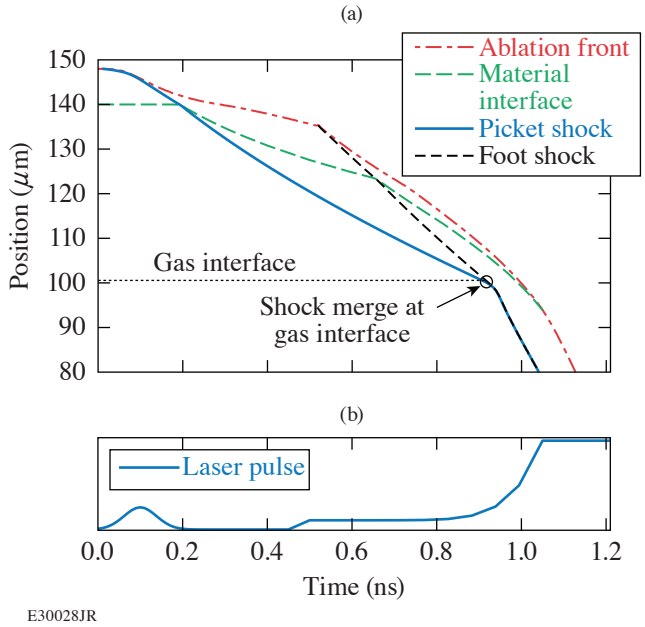

Figure 1
Interface and shock trajectories (position versus time) for the target and laser pulse.

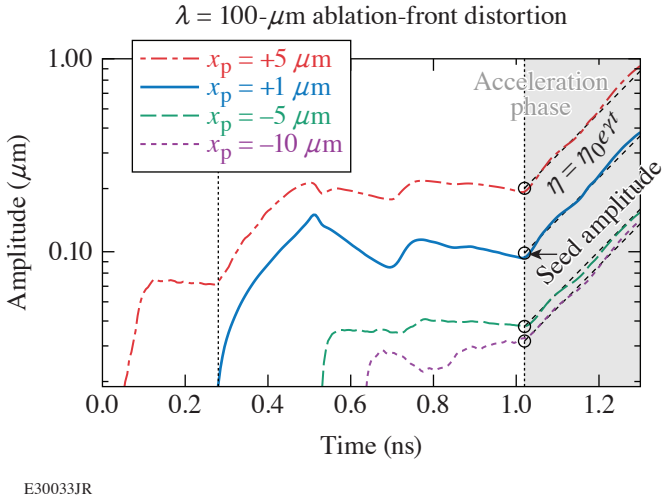

Figure 2
Ablation-front distortion history corresponding to perturbations at different locations in the ablator and DT ice. The acceleration phase is shaded in light gray. The dashed line is the exponential fit to $\eta = \eta_0 e^{\gamma t}$, and the seed amplitude is extracted from this curve. The initial perturbation depths (x_p) are +5, +1, –5, and –10 μm relative to the CH–DT interface for the red, blue, green, and purple lines, respectively. The vertical dotted black line near t = 0.3 ns indicae the arrival of the rarefaction wave at the ablation front.

ablator (red and blue curves) show significantly larger growth due to the rarefaction wave created by the interaction of the first shock (from the picket) and the CH-DT interface. This feedout growth process causes perturbations that start in the ablator to create larger seeds for instability growth when compared to those that originate in the ice. These seeds are defined as the amplitude of the distortion at the ablation front at the start of the acceleration phase (after which exponential RT growth occurs, or $\eta \sim \eta_0 e^{\gamma t}$, where γ is the growth rate and η is distortion). Figure 3 summarizes the seed amplitude (η_0) for perturbation wavelengths from 5 to 100 μm at different depths within the target material and shows the trend that perturbation seeds are largest when defects originate in the ablator and reduce as the initial position moves farther into the ice. As the wavelength reduces, however, interactions like destructive interference and phase change create wavelength-dependent behavior that complicates the position versus seed amplitude relationship. One region of particular interest [in Fig. 3(b)] is just inside of the CH–DT interface (near $x_p = -5$ μm). Here the interaction of the distorted CH–DT interface effectively cancels out or delays the onset of distortion growth at the ablation front (and reduces the acceleration-phase seed).

Simulations of isolated defects create complex wave interactions more likely to mimic target manufacturing defects, but much of the trends from single-mode perturbations apply. Figure 4(a) shows the density contour of the foil after the second shock has passed through a 1-μm defect (in the ablator). The black contour lines show velocity in the y direction and help to highlight

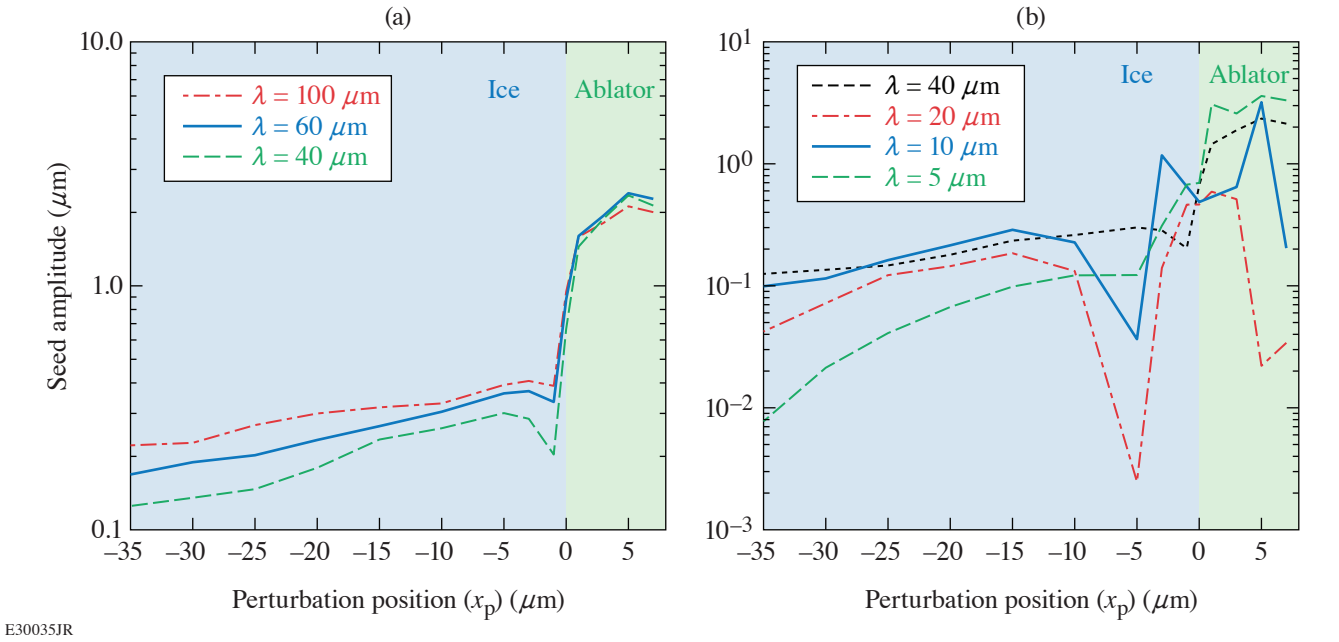

Figure 3
Scaled seed amplitudes as a function of perturbation position for (a) long-wavelength ($\lambda \geq 40$-mm) and (b) short wavelength ($\lambda < 40$-mm), single-mode perturbations.

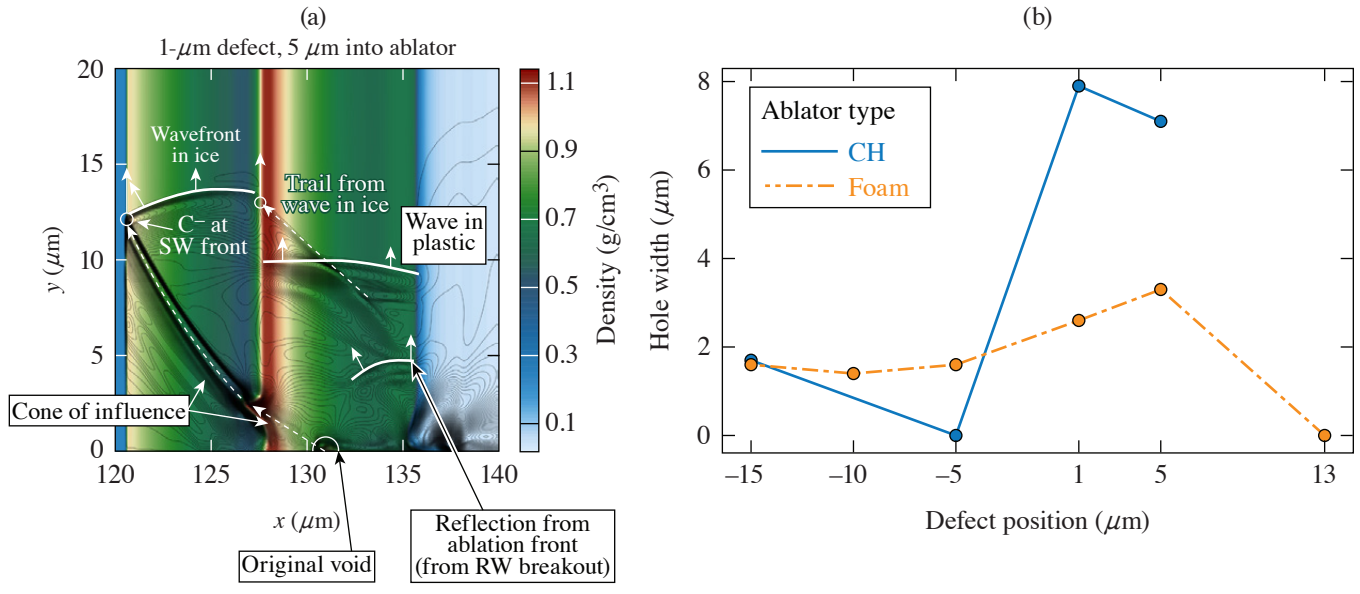

Figure 4
(a) Wave evolution for an isolated ablator defect (5 μm into the ablator from the CH–DT interface) at 0.5 ns after the first shock passage. Evolution in the y direction contributes to an extension of the maximum perturbation in y compared to the initial defect size. The contour colors show density and contour black lines show y velocity. (b) Hole sizes from shell punctures as a result of isolated defects in CH and wetted-foam targets approximately 300 ps after the start of the acceleration phase. RW: rarefaction wave; SW: shock wave.

particular wave features. These features include the wavefronts propagating through the different materials (ice and CH) and the lateral expansion of the defect perturbation. The lateral propagation is a unique feature of isolated defects (compared to sinusoidal perturbations). Isolated defect simulations show significant shell mass modulations and punctures at the start of the acceleration phase, depending on the position and size of the defect. Figure 4(b) shows the width of the hole due to a 1-μm defect located at various positions in the ice and ablator. Here, the degradation effects mimic the trend from short-wavelength, single-mode perturbations; ablator defects are more detrimental, and the effect is reduced just inward of the CH–DT interface.

A surrogate model that uses a wetted-foam ablator is proposed as a potential mitigation strategy to minimize the effects of manufacturing defects. In this design, the density is reduced from 1.0 (for CH) to 0.3 g/cm^3, and the shell thickness is increased to 26.7 μm (up from 8 μm) to conserve total shell mass compared to the CH ablator design. The smaller density reduces the strength of the rarefaction wave that travels from the ablator–ice interface (this rarefaction wave creates the large feedout growth shown in Fig. 1), and the increased thickness is beneficial because it isolates the defect perturbation (similar to how ice defects evolve). This effect can be seen in Fig. 4(b), where the foam ablator shows an overall reduction in hole width created by the defect.

Future work will examine internal defect evolution in 3-D and will include additional effects like convergent geometry along with and a more-detailed treatment of the materials (material-specific equations of state, radiation opacity, multiple materials, etc.). Additional work will seek to optimize shell thickness and continue to study alternative foam-like ablator designs.

This material is based upon work supported by the Department of Energy National Nuclear Security Administration under Award Number DE-NA0003856, the University of Rochester, and the New York State Energy Research and Development Authority.

1. D. R. Harding and W. T. Shmayda, Fusion Sci. Technol. **63**, 125 (2013).
2. S. C. Miller, "Hydrodynamic Instabilities in Inertial Confinement Fusion: Physics, Numerical Methods, and Implementation," Ph.D. Thesis, University of Rochester, 2022.

Three-Dimensional Simulations Capture the Persistent Low-Mode Asymmetries Evident in Laser-Direct-Drive Implosions on OMEGA

A. Colaïtis,[1] I. V. Igumenshchev,[2] D. H. Edgell,[2] D. Turnbull,[2] R. C. Shah,[2] O. M. Mannion,[2] C. Stoeckl,[2] D. W. Jacobs-Perkins,[2] A. Shvydky,[2] R. T. Janezic,[2] A. Kalb,[2] D. Cao,[2] C. J. Forrest,[2] J. Kwiatkowski,[2] S. P. Regan,[2] W. Theobald,[2] V. N. Goncharov,[2] and D. H. Froula[2]

[1]Université de Bordeaux, Centre Lasers Intenses et Applications, France
[2]Laboratory for Laser Energetics, University of Rochester

In this summary, detailed calculations are presented that include the first 3-D hydrodynamic simulations with sufficient physics models included to reproduce and quantify the anomalies observed in direct-drive implosions on OMEGA. When including all the known effects [polarized cross-beam energy transfer (CBET), mispointing, target offset], the simulations reproduce the measurements for bang time, yield, hot-spot flow velocity, and direction. To quantify these effects within the integrated experiments and describe the complex physical processes of polarized CBET and its interplay with multidimensional plasma hydrodynamics, an inline CBET model capable of accounting for polarization was implemented in a 3-D hydrodynamic code with a 3-D laser propagation solver. These integrated simulations were used to assess the effect of unpolarized and polarized CBET, explore the sensitivity of current direct-drive experiments to the various low-mode sources, and assess the predictive capabilities of such detailed 3-D modeling tools—an important component of the inertial confinement fusion program. Notably, current levels of beam mispointing, imbalance, target offset, and asymmetry from polarized CBET were found to degrade yields by more than 40%. Finally, mitigation strategies are explored: attempting to compensate the mode-1 asymmetry with a preimposed target offset and redesigning the double polarization rotators. These results were summarized in Ref. 1 and detailed in Refs. 2 and 3.

For the past few years, direct-drive implosion experiments conducted on the OMEGA Laser System[4] have reached a sufficient degree of control such that the errors induced by beam power imbalance, beam pointing inaccuracy, and target offset are relatively small. Despite these improvements, a large flow anomaly is still observed across many experiments, with a flow direction that appears systematic[5] (Fig. 1). Recently, it was proposed in Ref. 6 that a potential source of systematic low modes on the OMEGA laser[4] originates from polarized CBET. According to the authors of Ref. 6, the polarization dependency of CBET induces a significant low-mode anomaly in the laser drive, with its direction (in terms of spherical harmonics mode $\ell = 1$) being consistent with typical measured flow velocities from neutron diagnostics. Conclusions were reached, however, using post-processing of 1-D hydrodynamics simulations, which do not allow for a quantitative assessment of the final influence of polarized CBET on measured flow velocity and direction, for which inline modeling is required. Moreover, accounting for the compounded effect of beam balance, beam pointing error, and target offset in addition to polarized CBET requires a 3-D modeling of both the laser and hydrodynamics.

This lead to the development of the first inline-capable polarized CBET model, implemented within the inverse ray-tracing framework of the *IFRIIT*[7] code. Inline simulations were performed using a heterogeneous multiple-data, multiple-program framework coupling the *ASTER*[9,10] 3-D radiation-hydrodynamic code with the *IFRIIT*[7,10] 3-D laser propagation solver, running on 6000 cores of the French Commission for Atomic Energy and Alternative Energies' Très Grand Centre de Calcul (CEA TGCC) supercomputer, making it possible to describe the complex physical processes of polarized CBET and its interplay with plasma hydrodynamics. These integrated simulations were used to (1) quantify the sensitivity of current target designs to the best setup performances of the OMEGA Laser System, (2) assess if the source of the systematic flow can be identified, and (3) test various strategies for mitigation of the low-mode asymmetries.

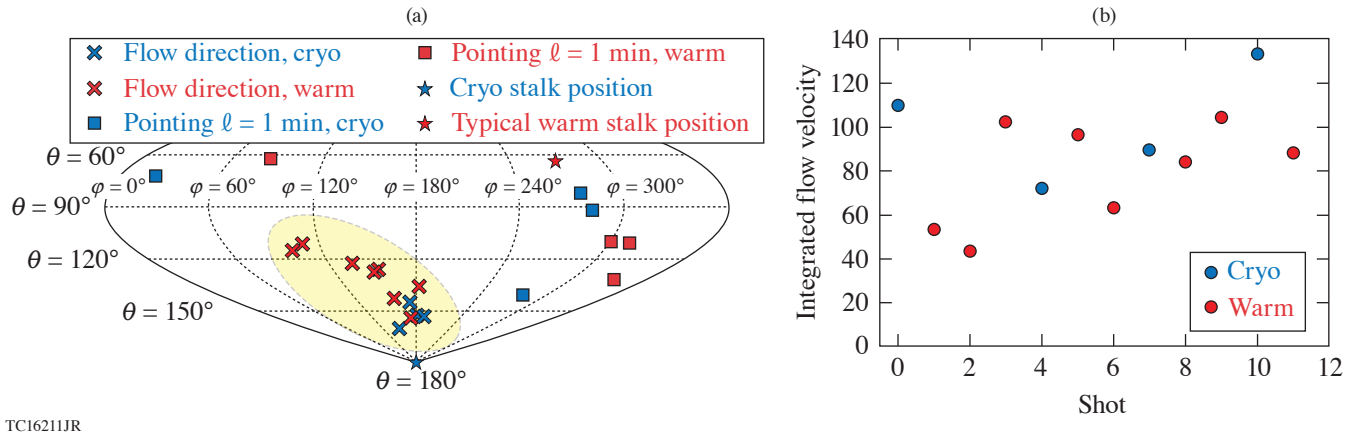

Figure 1
(a) Fusing DT flow direction shown in a sinusoidal projection of the OMEGA chamber and (b) associated flow magnitude in km/s in best-setup implosions (see also Refs. 5 and 11). The yellow region highlights the systematic anomaly.

The inline polarization model proposed here was developed within the field formulation of geometrical ray optics. The ray electric field is written $a = A\exp k_0\psi$, where k_0 is the vacuum wave number, A is the field swelling due to refraction, and ψ is a phase that includes the effects of absorption and energy exchange. The field at caustics is described using an etalon integral method,[12] which allows reconstruction of the Airy pattern without introducing free parameters. The ray field is then described onto the Frenet reference frame,[13] an orthogonal basis associated with the ray and defined at every point by a tangent $\mathbf{1} = \mathbf{k}/|\mathbf{k}|$, a normal $\boldsymbol{\nu}$ parallel to the permittivity gradient component transverse to the ray, and a binormal $\mathbf{b} = 1 \times \boldsymbol{\nu}$. The Frenet frame rotates with the ray, which allows for local accounting of polarization transport through refraction. The exchange of amplitude between the ray-field components in the Frenet frame, denoted $(A_n)^{\mathrm{T}} = (a_{n,\nu_n}, a_{n,b_n})$ for field n, can be written[13] as $\partial_{1_n} A_n = \underline{\underline{D_n}} A_n$ with $\underline{\underline{D_n}}$ a tensor that accounts for three polarization effects: polarization rotation due to refraction, polarization rotation of the probe beam toward the pump beam, and ellipticity induced in the initially linear polarizations due to CBET-induced plasma birefringence.

In the final model, the ray amplitude A is computed according to ray theory from a single inverse ray-tracing step,[14] while the ray phase is obtained by integrating the permittivity along the ray trajectory, $\psi = \int \varepsilon''[\mathbf{r}(\hat{\tau})\mathrm{d}\hat{\tau}/2]$, which includes ε'', the effect of polarized CBET from $\underline{\underline{D_n}}$, as well as collisional absorption and Langdon effect.[10,15] Pump depletion is obtained by iterating the ray phase computation until convergence. The final formulation of the laser propagation model has no free parameters, contrary to what is commonly used in inline CBET models to either limit caustic fields or tune the CBET interaction.[16–19] This polarized CBET model was validated against academic test cases and against the *BeamletCrosser* post-processor[2,6] and is now used in inline 3-D *ASTER/IFRIIT*[9,10] simulations. The full polarized CBET model and its validation are presented in Ref. 2.

The 12 shots reported in Fig. 1 span 19 months of operation and were obtained with good performance metrics for beam pointing, beam balance, offset error, target quality, and diagnostic quality. Out of these 12, three shots were modeled; 94343, 98755, and 98768. Among those, 94343 and 98768 are cryogenic shots, whereas 98755 is a warm plastic shot. Shot 98768 is a large-diameter shot with $D_t = 1012$ μm, while the others are smaller targets with $D_t \sim 980$ μm. To this set, we also add shot 94712 (Ref. 11), which was a cryogenic shot with poor pointing performances, contrary to the other three noted above. For these experiments, the beam pointing was measured at the beginning of the shot day. In addition, for shot 98755, pointing was also measured at the end of the shot day, providing two references. Finally, the ice-thickness uniformity was characterized using optical measurements prior to the shots. For the targets of interest, the ice layer nonuniformity was estimated to be less than the instrument resolution, i.e., <1% for the mode $\ell = 1$.

An extensive set of simulations was executed while varying the CBET model and/or the number of low-mode sources, which are included. The CBET model was toggled from off, to the commonly used unpolarized model[20] where the polarization effect for polarization-smoothed beams [e.g., distributed polarization rotation (DPR)] is modeled with fixed polarization and without any

rotation or ellipticity effects to the fully polarized model presented here. In all simulations, the Spitzer–Härm[21] heat conduction model was used at all times except in the first picket where the flux was limited with $f_{\text{lim}} = 0.1$ (Ref. 8).

The inline simulations are compared to various measurements: peak rise time of the neutron rate, yield, flow velocity magnitude, and direction. Several conclusions can be drawn from the simulations results for neutron data, some of which are reported in Fig. 2: (1) The CBET model alone gets nuclear bang time correctly, implying that the zero-order drive energetics are correct and well described by the model [Fig. 2(a)]. This also suggests that other effects not accounted for here, such as two-plasmon decay, do not significantly modify the total drive.[22] (2) Unpolarized and polarized CBET simulations with power balance and pointing variations get the neutron yield correct because both drive energetics and symmetry are important for the yield [Fig. 2(b)]. (3) Both CBET models with power balance and pointing variations match the flow velocity correctly for shot 94712 because the large pointing error dominates the low-mode sources. (4) Polarized CBET with power balance and pointing is needed to get the flow velocity correct for the more-accurately pointed shot 94343 (the low offset of 3.5 μm is seen to play a minor role). This indicates that the polarization effect becomes more important as other low-mode sources become smaller. The flow direction is reproduced correctly in all simulations as long as the effects of polarized CBET, beam imbalance, and beam pointing are accounted for. The full comparison to experiments is reported in Ref. 3.

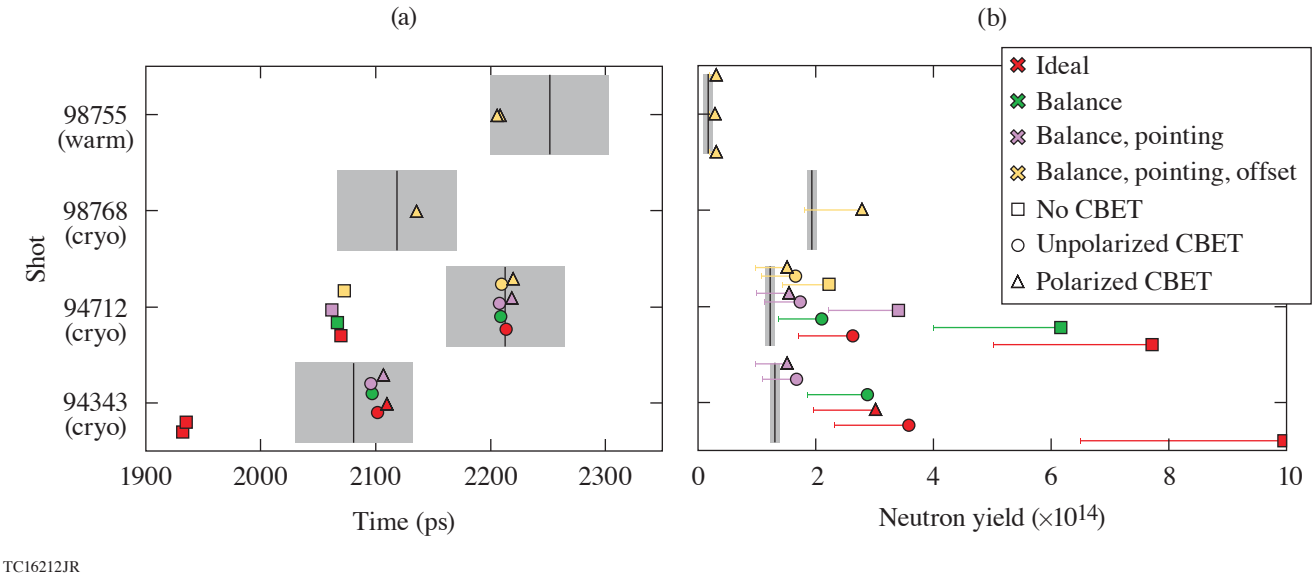

Figure 2
[(a),(b)] Comparison of the simulated (colored symbols) and measured (gray-shaded areas) (a) peak neutron rise time and (b) neutron yield. Simulations include a variety of low-mode sources and were conducted with and without CBET (see legends). Error bars on the simulated neutron yield account for the effect of small-scale mixing. Experimental yields are corrected for tritium aging.[23]

By examining the various simulations, it is observed that these best-setup OMEGA implosions lose ~40% in yield due to effects of balance, pointing, and offset alone [Fig. 3(a)]. In that framework, the polarization effect of CBET causes only a small drop in yield, by about 6%. However, in cases where there is no prior low-mode asymmetry from balance or pointing, the polarized CBET alone reduces the yield by 18% and induces an ~90-km/s flow anomaly compared to an unpolarized CBET case. In addition, the effect of unpolarized CBET alone reduces the yield by ~65% and amplifies the mode-10 anomaly by a factor of 2 to 3, leading to target perforation [Fig. 3(c)]. This is a strong argument for mitigation of the polarized CBET anomaly. It is observed, however, that the yield's dependency on low modes is more severe in cases without CBET because the latter was acting to mitigate drive asymmetries. These results highlight how CBET is a coupling loss mechanism that should be mitigated altogether in future driver designs.

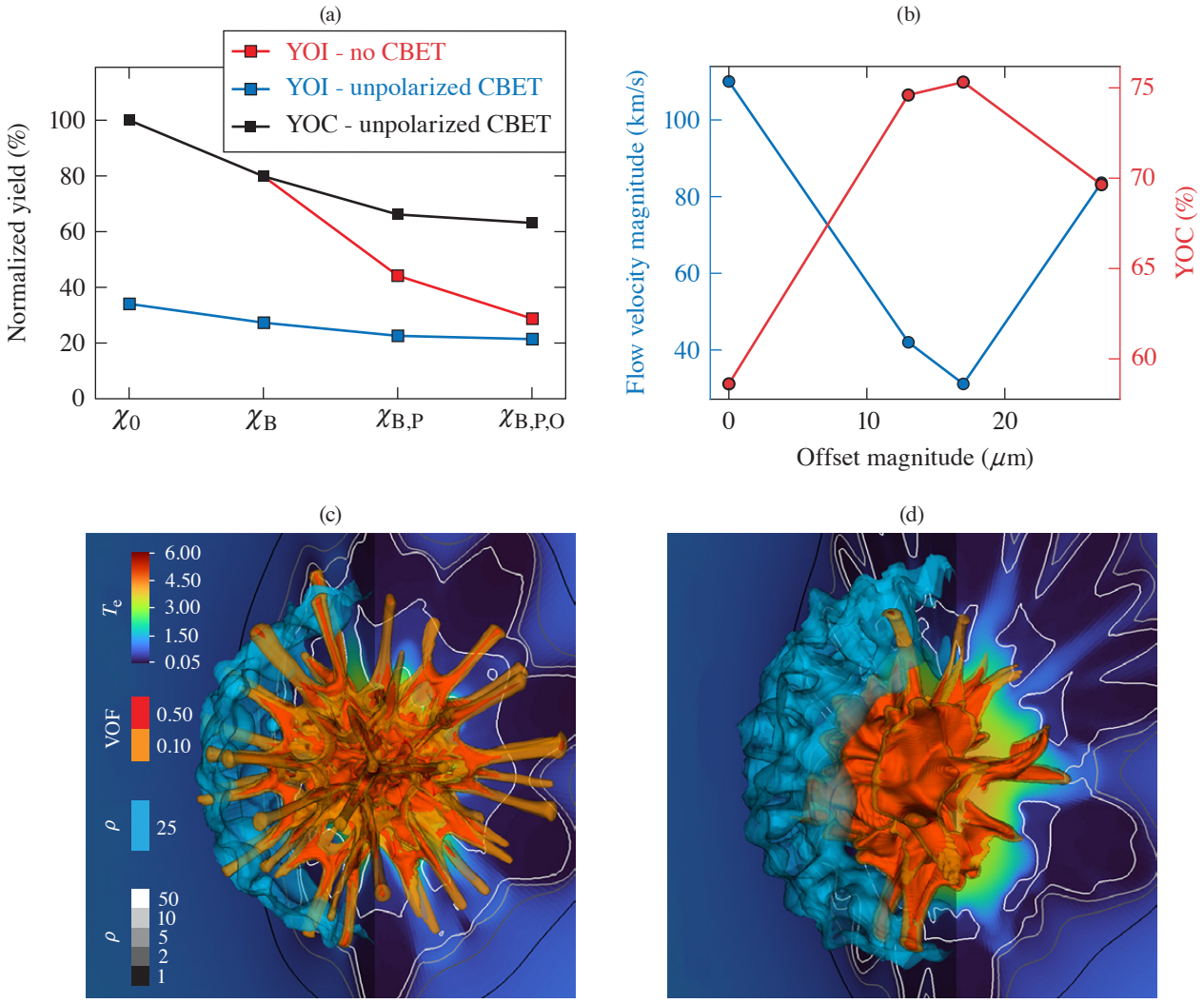

TC161213JR

Figure 3

(a) Scaling of the YOI (yield-over-ideal case in the absence of CBET) and YOC (yield-over-clean case in the presence of CBET) for simulations with and without unpolarized CBET, as a function of low-mode asymmetry sources (cases are labeled with a χ on the x axis; subscript 0 refers to the ideal case; B, P, and O indicate that beam balance, pointing, and offset were accounted for, respectively). (b) Flow anomaly (blue) and YOC (red) as functions of offset magnitude for a case with measured power balance and beam pointing ($\chi_{B,P}$). The target offset is in the opposite direction of the measured flow without offset. [(c),(d)] Target hot-spot electron temperature [colored background (keV)], 10% and 50% volume fraction of DT gas (orange and red volume contours, respectively), 25-g/cm^3 density isovalue (light blue volume contour), and 1-, 2-, 5-, 10-, and 50-g/cm^3 isocontours (black to white contour lines), for (c) an ideal case (χ_0) with unpolarized CBET. (d) A "real-setup" implosion accounting for power balance and beam pointing ($\chi_{B,P}$), with polarized CBET, is shown for comparison. All figures here relate to shot 94343.

Finally, two mitigation strategies are explored to compensate for the low-mode polarized CBET anomaly: offset compensation and DPR redesign. The offset compensation is able to increase the yield by ~15% [Fig. 3(b)] and reduce the modal $\ell = 1$ anomaly from the polarization effect by a factor of ~3. The offset compensation is not able to further improve the performances, however, due to the presence of other modes, notably from the polarized CBET anomaly but also from pointing and balance errors. Alternatively, considering a design of the DPR with only a 10-μm spot separation and half the smoothing by spectral dispersion (SSD) bandwidth, the simulations show that the flow direction and magnitude anomaly from the polarization effect disappear, and the unpolarized result is recovered. It is noted that halving the SSD bandwidth must be done in consideration of the potential effect on high mode-growth (not modeled here).

This work was granted access to the HPC resources of TGCC under the allocation 2020-A0070506129, 2021-A0090506129 made by GENCI, and PRACE grant number 2021240055. This work has been carried out within the framework of the EUROfusion Consortium, funded by the European Union via the Euratom Research and Training Programme (Grant Agreement No 101052200—EUROfusion). Views and opinions expressed are however those of the author(s) only and do not necessarily reflect those of the European Union or the European Commission. Neither the European Union nor the European Commission can be held responsible for them. The involved teams have operated within the framework of the Enabling Research Project: ENR-IFE.01.CEA "Advancing shock ignition for direct-drive inertial fusion." The software used in this work was developed in part at the University of Rochester's Laboratory for Laser Energetics. This material is based upon work supported by the Department of Energy National Nuclear Security Administration under Award No. DE-NA0003856, the University of Rochester, and the New York State Energy Research and Development Authority.

1. A. Colaïtis *et al.*, Phys. Rev. Lett. **129**, 095001 (2022).
2. A. Colaïtis *et al.*, "3-D Simulations of Implosions in Presence of Low Mode Asymmetries Part 1: Inline Polarized Cross Beam Energy Transfer Modeling," submitted to Plasma Physics and Controlled Fusion.
3. A. Colaïtis *et al.*, "3-D Simulations of Implosions in Presence of Low Mode Asymmetries Part 2: Systematic Flow Anomalies and Low Modes Impact on Performances on OMEGA," submitted to Plasma Physics and Controlled Fusion.
4. T. R. Boehly *et al.*, Opt. Commun. **133**, 495 (1997).
5. S. P. Regan *et al.*, Bull. Am. Phys. Soc. **66**, CO04.00011 (2021).
6. D. H. Edgell *et al.*, Phys. Rev. Lett. **127**, 075001 (2021).
7. A. Colaïtis *et al.*, Phys. Plasmas **26**, 072706 (2019).
8. I. V. Igumenshchev *et al.*, Phys. Plasmas **23**, 052702 (2016).
9. I. V. Igumenshchev *et al.*, Phys. Plasmas **24**, 056307 (2017).
10. A. Colaïtis *et al.*, J. Comput. Phys. **443**, 110537 (2021).
11. O. M. Mannion *et al.*, Phys. Plasmas **28**, 042701 (2021).
12. Yu. A. Kravtsov and Yu. I. Orlov, *Caustics, Catastrophes and Wave Fields*, 2nd ed., Springer Series on Wave Phenomena (Springer-Verlag, Berlin, 1993).
13. Yu. A. Kravtsov and N. Y. Zhu, *Theory of Diffraction: Heuristic Approaches*, Alpha Science Series on Wave Phenomena (Alpha Science International Ltd., Oxford, United Kingdom, 2010).
14. A. Colaïtis *et al.*, Phys. Plasmas **26**, 032301 (2019).
15. A. B. Langdon, Phys. Rev. Lett. **44**, 575 (1980).
16. I. V. Igumenshchev *et al.*, Phys. Plasmas **17**, 122708 (2010).
17. J. A. Marozas *et al.*, Phys. Plasmas **25**, 056314 (2018).
18. D. H. Edgell *et al.*, Phys. Plasmas **24**, 062706 (2017).
19. R. K. Follett *et al.*, Phys. Rev. E **98**, 043202 (2018).
20. P. Michel *et al.*, Phys. Plasmas **16**, 042702 (2009).
21. L. Spitzer, Jr. and R. Härm, Phys. Rev. **89**, 977 (1953).
22. D. Turnbull *et al.*, Phys. Rev. Lett. **124**, 185001 (2020).
23. A. Lees *et al.*, Phys. Rev. Lett. **127**, 105001 (2021).

Analysis of Limited Coverage Effects on Areal-Density Measurements in Inertial Confinement Fusion Implosions

V. Gopalaswamy,[1,2] R. Betti,[1,2,3] P. B. Radha,[1] A. J. Crilly,[4] K. M. Woo,[1] A. Lees,[1,2] C. A. Thomas,[1]
I. V. Igumenshchev,[1] S. C. Miller,[1,2] J. P. Knauer,[1] C. Stoeckl,[1] C. J. Forrest,[1] O. M. Mannion,[1,3,5] Z. L. Mohamed,[1,3]
H. G. Rinderknecht,[1] and P. V. Heuer[1]

[1]Laboratory for Laser Energetics, University of Rochester
[2]Department of Mechanical Engineering, University of Rochester
[3]Department of Physics and Astronomy, University of Rochester
[4]Imperial College London
[5]Sandia National Laboratories

To assess the quality of an inertial confinement fusion (ICF) experiment, various performance metrics based on the Lawson triple product[1–8] have been devised. These performance metrics must exceed a critical number to provide net energy gain. In direct-drive ICF implosions at the Omega Laser Facility,[9] the performance metric of interest is the so-called no-alpha normalized Lawson parameter χ

$$\chi = \rho R^{0.6} \left(0.12 \frac{Y_{16}}{M}\right)^{0.34}. \tag{1}$$

In an experiment, the areal density and yield can be diagnosed directly, while the stagnated DT mass can be estimated from simulations or from experimental data to infer χ. When χ is close to unity, alpha heating dominates the energetics of a hot spot, leading to ignition, which is a prerequisite for high-gain implosions. Due to the strong dependence of χ on the ρR, an accurate diagnosis is of critical importance. On OMEGA, an approach that synthesizes experiments and simulations[10–12] to create predictive models has led to dramatic increases in experimental performance, primarily through increases in neutron yield. References 10–12 present highly accurate predictive models for the neutron yield, but do not address the ρR—primarily because these models are not sufficiently accurate to drive experimental design. Achieving a comparable quality of predictive capability for ρR as exists for the yield is a necessary prerequisite for the predictive-model–driven campaign on OMEGA to optimize ρR since the effective "step-size" of an iterative scheme to improve the ρR is roughly bounded below by the prediction uncertainty.

One reason for the lack of predictive capability for ρR is that it is an inherently 3-D measurement with different diagnostics integrating over varying regions of the sphere relative to a fixed line of sight. A predictive model for the 1-D–equivalent ρR, which is what we are attempting to optimize in experiments, will have an uncertainty that is at least as large as this limited coverage error, which in turn sets the minimum step-size of the iterative scheme to improve the ρR in experiments.

To generate physically reasonable 3-D configurations for use in *IRIS*, the 3-D radiation-hydrodynamic simulation *ASTER*[13] is used. Three configurations are considered. In the first, the effect of illumination asymmetry arising from the beam geometry is considered. In the second and third configurations, the illumination resulting from a fixed beam size of $R_b = 330\ \mu$m is modulated with varying $\ell = 1$, $m = 0$ and $\ell = 2$, $m = 0$ perturbations, respectively, both aligned along the $+z$ axis. The detectors used are specified in Table I, and the detector permutations are specified in Table II. The MRS virtual detector simulates the action of the magnetic recoil spectrometer,[14] while the P7/H10 BS virtual detectors simulate the action of the neutron-time-of-flight (nTOF) backscatter measurement.[15] The P7/H10 FW virtual detectors simulate the action of a hypothetical forward scatter measurement

Table I: Detector configurations used in this work. See Table II for the permutations used. The P7 and H10 nTOF detectors are located at the center of P7 and H7 in the OMEGA target chamber, respectively. At the present time, the nTOF's are only capable of backscatter (BS) measurements. The forward scatter (FW) measurement on the nTOF's is under investigation.

Detector	θ_{det} (rad)	ϕ_{det} (rad)
P7 FW	2.03	2.83
P7 BS	2.03	2.83
H10 FW	1.35	2.83
H10 BS	1.35	5.27

Table II: Detector perumutations that are considered in this work. Note that the MRS + P7BS permutation is the one that is currently used in OMEGA experiments. Due to the unique details of each detector and experiment, it is possible that some measurements may be compromised on certain experiments.

Configuration	P7 FW	P7 BS	H10 FW	H10 BS	MRS FW
MRS Only					
MRS + P7BS					
MRS + H10BS					x
MRS + P7/H10BS		x			x
MRS + P7/H10BS + P7FW		x		x	x
MRS + P7/H10BS + H10FW	x	x		x	x
All	x	x	x	x	x

from the nTOF's that are under investigation on OMEGA. Note that the "MRS + P7BS" permutation represents the currently used permutation on OMEGA to assess the 1-D–equivalent ρR. For each simulation, each permutation of detectors is evaluated for each pair of (θ', ϕ'). The 1-D–equivalent ρR [that is, the areal density of a perturbed implosion that is appropriate to use in Eq. (1)], $\langle \rho R \rangle$, is calculated by a harmonic average over the observed ρL by virtual detectors that are distributed uniformly over the sphere, where the ρL of a particular virtual detector is the neutron-averaged path length integral of the density for all primary (i.e., not scattered) virtual particles binned in that virtual detector and is the best estimate of the "real" areal density that would be seen by that detector.

First, consider the highest ℓ-mode simulation case of the beam mode. At stagnation, the shell can be moderately to severely perturbed due to the driven mode.[12] However, ρR is inferred in experiments from integrals over the neutron spectrum, which corresponds (assuming a point source) to sampling over conical sections of the shell. Combined with the distributed source of a real hot spot, the inferred ρR from either the backscatter or forward-scatter measurement is found to be uniform over the sphere (although it may still be degraded with respect to 1-D), as seen in Fig. 1.

Next, consider the effect of the $\ell = 1$ mode. The strength of the mode is parametrized by the effective ion-temperature asymmetry $R_T = T_{\text{max}}/T_{\text{min}}$ it generates, and bin configurations belonging to similar R_T together to visualize the results. It is found that as the number of detectors used to infer an average ρR increases, the error in that inference decreases, although some detectors are more valuable than others (e.g., P10 backscatter is more valuable than P7 backscatter), as visualized in Fig. 2. This is due to the fixed positions of the diagnostics with respect to each other. With sufficient detectors, the error due to the mode 1 for high-performance–relevant implosions (i.e., $R_T \rightarrow 1$) approaches the acceptable limit of 5%.

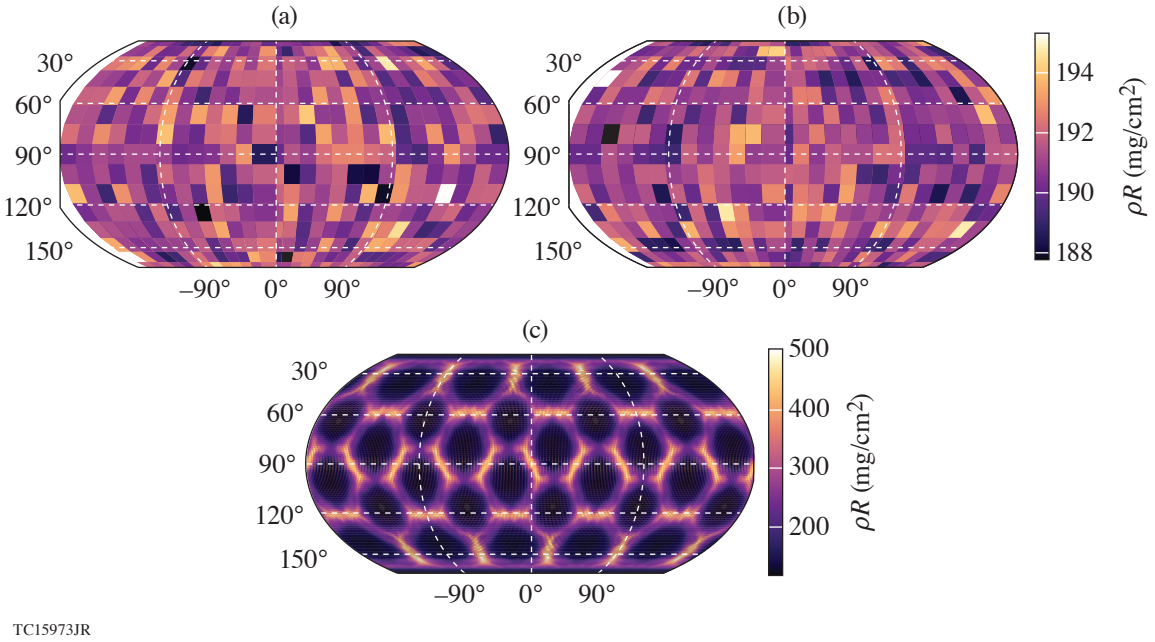

Figure 1
A projection of (a) the inferred ρR from the backscatter edge, (b) the inferred ρR from the forward-scatter edge for a simulation, and (c) $\int \rho \mathrm{d}r$ at bang time for a simulation with a target of radius 490 μm and a laser beam with radius 330 μm. Despite a rather large perturbation being driven, the effects of distributed source and integration over the edge result in no observable structured variation.

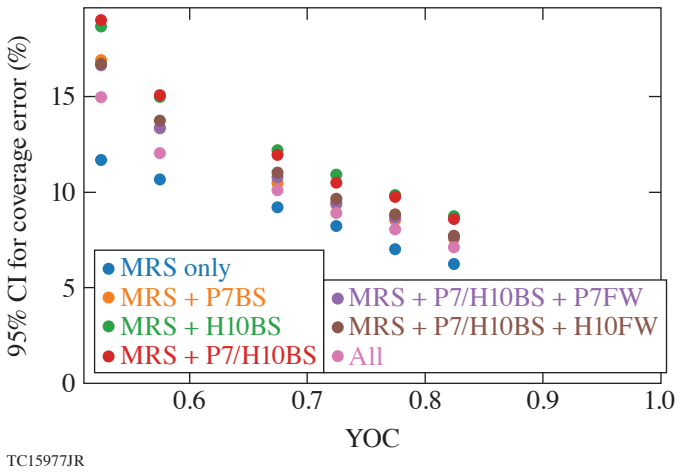

Figure 2
The 2σ upper bound on the coverage error for each detector permutation for simulations with similar yield over clean (YOC), over a range of YOC's. Unlike with the $\ell = 1$ case, there is no observable parameterizing the degradation due to $\ell = 2$, and so the YOC is used directly. Unlike the $\ell = 1$ case, adding any one backscatter detector increases the error rather than decreasing it. Although the addition of the forward-scatter measurements on the nTOF's does decrease the error relative in the case where only backscatter nTOF measurements are considered, they nevertheless are not reduced below the level when only the MRS is considered. Since this is a result of the relative orientations of the nTOF and MRS detectors on OMEGA, this is a result specific to the OMEGA setup, and not a general observation. CI: confidence interval.

In the $\ell = 2$ mode case, the strength of the mode is parametrized by its yield degradation YOC = $Y_{3\text{-D}}/Y_{1\text{-D}}$, and bin the various configurations accordingly, as before. The results are visualized in Fig. 3. First, using only the MRS forward-scatter measurement results in a lower error than combining the MRS with any backscatter measurement. This counterintuitive result can be understood when the relative orientations of various integration regions are considered. In the $\ell = 1$ case considered above, the orientations meant that the H10 backscatter measurement was strongly anticorrelated with the MRS (since the ρR varied with an $\ell = 1$ pattern), while the P7 backscatter measurement was only weakly correlated with the MRS. Since the $\langle \rho R \rangle$ lies in between the maxima and minima, an average (by whatever mechanism) of measurements best reproduces the $\langle \rho R \rangle$ if some measurements are greater than $\langle \rho R \rangle$, and some are less. In the $\ell = 2$ case, H10 and P7 backscatter measurements are, due to their specific orientations on the

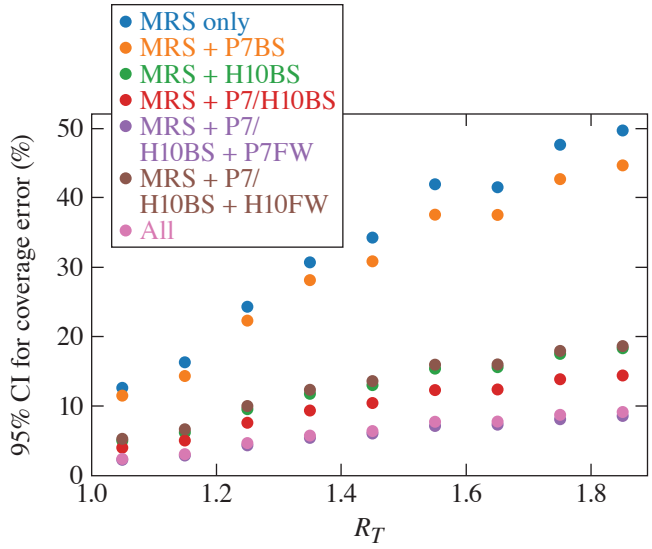

Figure 3
The 2σ upper bound on the coverage error for each detector permutation for all simulations with similar R_T over a range of R_T. First, note that having only the MRS (blue circles) has an extremely high error for even small values of R_T. Adding the P7 nTOF (orange circles) is not as valuable as adding the H10 nTOF (green circles) since the P7 backscatter and MRS forward-scatter regions are nearer to each other than the H10 backscatter and MRS forward scatter, and vice versa for the hypothetical P7 and H10 forward-scatter measurement. Nevertheless, adding all five detector configurations significantly reduces error from the currently used detector configuration.

OMEGA system, well correlated with the MRS (H10 more so than P7). In addition, the backscatter measurements sample a much smaller region of the shell than the forward scatter and, thus, have a higher probability of measuring an extremely different ρR from the MRS (again, H10 more than P7). Therefore, when including them in an average, it is possible to move the average further away from the $\langle \rho R \rangle$, and thereby increase the composite error. From there, including additional forward-scatter measurements either from P7 or H10 detectors reduces the error since a larger region of the shell is sampled. However, it is insufficient to correct for the bias induced by the backscatter measurement.

Finally, having established a measure of the likely values of how the measured ρR deviates from $\langle \rho R \rangle$ that can be expected under reasonable conditions, one considers whether it is possible to recover $\langle \rho R \rangle$, even if only in restricted cases. Here, the only case considered will be where the $\ell = 1$ mode dominates. The reason for choosing only this case is that the $\ell = 1$ case is the only one where the yield degradation due to the mode can be inferred on OMEGA at this time. Defining $R_{\rho R} = \rho R / \langle \rho R \rangle$ as the deviation of the measured ρR at some line of sight from the true 4π average $\langle \rho R \rangle$, it is noted that since the orientation of the mode with respect to each detector is known and deterministic, it is reasonable to presume that there ought to be a relationship between the $R_{\rho R}$ at the detector location and both a measure of the mode amplitude and the central angle y between the mode maximum and detector position. The mode amplitude can be parametrized either by the R_T, or by the ratio of the bulk flow to the implosion velocity $\tilde{v}$. A suggested ansatz for $R_{\rho R}$ is given by

$$R_{\rho R} \cdot (R_T, \psi) = R_T \alpha + A(R_T - 1)\beta \cos(\psi - \psi_0), \tag{2}$$

$$R_{\rho R} \cdot (\tilde{v}, \psi) = \exp(\alpha \tilde{v}) + A\tilde{v}\beta \cos(\psi - \psi_0), \tag{3}$$

where A, α, β, and ψ_0 are constants that differ for forward and backward scatter and will be determined by fitting to the data, and are summarized in Table III. A graphic presentation the quality of the fits is shown in Fig. 4 and indicates that Eqs. (2) and (3) accurately represent the modulation of ρR over the sphere.

Using the coefficients in Table I, it is also possible to calculate a final "prediction" of the ρR that would be used in experiments, assuming only the existing OMEGA detectors are used. This is shown in Fig. 5, where the arithmetic average of the detector predictions using the coefficients in Table III is shown for each simulation in the $\ell = 1$ dataset. If such a reconstruction could be performed on OMEGA, the uncertainty from the $\ell = 1$ modes can be made sufficiently low (<3.5%) for incremental iterative schemes to be successful on OMEGA. This suggests that generating such procedures for $\ell = 2$ should be a high priority since these modes are known to exist on OMEGA.

Table III: Fit parameters of Eqs. (2) and (3) for the forward and backscatter detectors.

Detector	α	β	ψ	A
Forward scatter (R_T)	0.34	0.62	–0.21	0.65
Backscatter (R_T)	0.46	0.64	–0.24	–0.78
Forward scatter ($\tilde{v}$)	0.32	1.09	–0.24	1.07
Backscatter ($\tilde{v}$)	0.44	1.05	0.37	–1.22

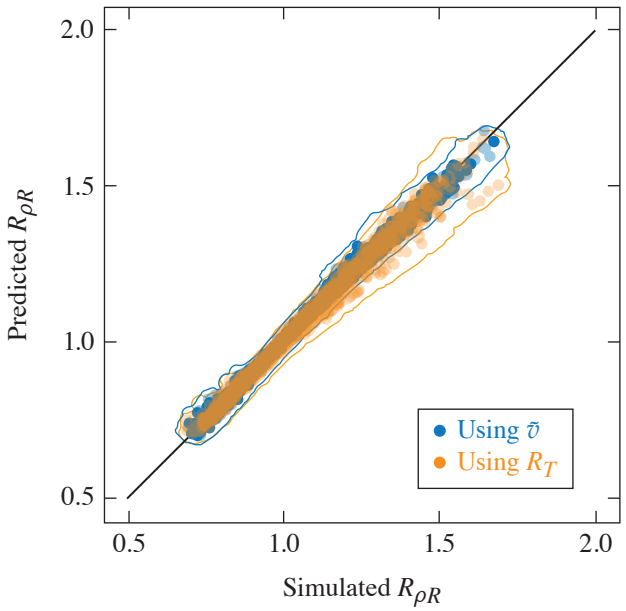

TC15980JR

Figure 4
The accuracy of Eq. (2) (orange circles) and Eq. (3) (blue circles) in reconstructing the $R_{\rho R}$ across the entire dataset for each detector separately, assuming the orientation and amplitude of the $\ell = 1$ mode is known. Due to the large number of points in the full dataset, 10% are selected randomly and plotted. The solid line shows the extent of the full dataset for both cases. The $R_{\rho R}$ calculated from the simulations is on the horizontal axis, while the prediction from Eqs. (2) and (3) is on the vertical axis.

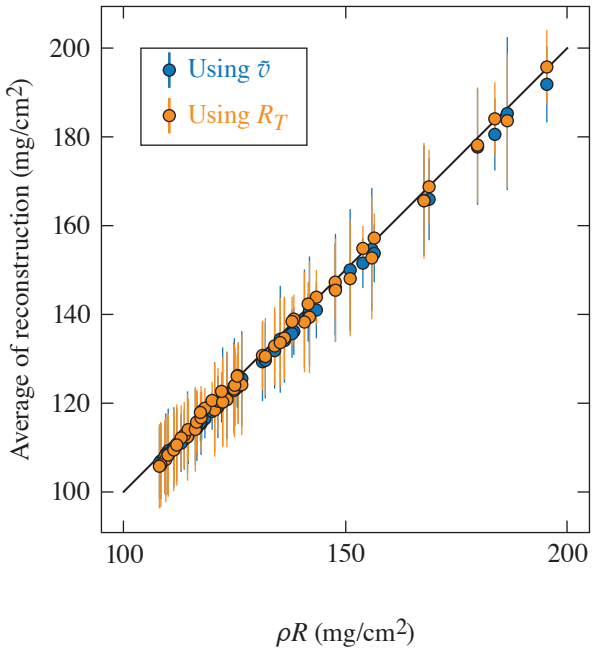

TC15981J1

Figure 5
The accuracy of harmonically averaging the reconstructed ρR inferred using Eq. (2) (blue circles) and Eq. (3) (orange circles) in predicting $\langle \rho R \rangle$ for all simulations in the dataset using only the MRS and P7/H10 backscatter detectors, assuming the orientation and amplitude of the $\ell = 1$ mode is known. Error bars represent the 2σ range of the reconstruction when varying mode orientations with respect to fixed detector locations. The method is clearly accurate across the full range of conditions, with an rms error of roughly 3.5% for both the R_T and ($\tilde{v}$) models.

Accurate measurements of the ρR are integral to an accurate understanding of the performance of cryogenic direct-drive ICF experiments on OMEGA. Quantifying and rectifying the errors that are incurred by incomplete coverage are a necessary step toward achieving the accuracy necessary to design OMEGA experiments that will scale to hydrodynamically equivalent ignition. Quantifying this error is also a step toward a quantification of the total uncertainty in the 1-D–equivalent ρR that arises as a combination of coverage and measurement uncertainty. Considered here are the effects of limited detector coverage over a range of core conditions using *ASTER* simulations, post-processed with *IRIS* with varying $\ell = 1$ and 2 modes, for a number of permutations of existing and hypothetical detectors used on OMEGA. The expected uncertainty is quantified due to the induced asymmetry over the credible range of expected perturbations on OMEGA. It is then found that the error due to limited detector coverage tends to decrease as additional detectors are added in the $\ell = 1$ case, but find that due to the specific detector geometry on OMEGA, the $\ell = 2$ coverage uncertainty can increase as additional backscatter measurements are made. The coverage error due to the $\ell = 1$ mode is robustly eliminated if the existing nTOF detectors on OMEGA were capable of forward-scattering measurements. After postulating that the orientation and yield degradation caused by a mode could be used to reconstruct the 1-D–equivalent ρR, it is shown that this is indeed possible in cases that are dominated by large $\ell = 1$ modes, and that the error in reconstructing the true 1-D–equivalent ρR can be made acceptably low with existing OMEGA diagnostics.

This material is based upon work supported by the Department of Energy National Nuclear Security Administration under Award Number DE-NA0003856, the University of Rochester, and the New York State Energy Research and Development Authority.

1. J. D. Lawson, Proc. Phys. Soc. Lond. B **70**, 6 (1957).
2. R. Betti and O. A. Hurricane, Nat. Phys. **12**, 435 (2016).
3. A. R. Christopherson *et al.*, Phys. Plasmas **25**, 012703 (2018).
4. R. Betti *et al.*, Phys. Plasmas **17**, 058102 (2010).
5. P. Y. Chang *et al.*, Phys. Rev. Lett. **104**, 135002 (2010).
6. B. K. Spears *et al.*, Phys. Plasmas **19**, 056316 (2012).
7. R. Betti *et al.*, Phys. Rev. Lett. **114**, 255003 (2015).
8. C. D. Zhou and R. Betti, Phys. Plasmas **14**, 072703 (2007).
9. T. R. Boehly *et al.*, Opt. Commun. **133**, 495 (1997).
10. V. Gopalaswamy *et al.*, Nature **565**, 581 (2019).
11. A. Lees *et al.*, Phys. Rev. Lett. **127**, 105001 (2021).
12. V. Gopalaswamy *et al.*, Phys. Plasmas **28**, 122705 (2021).
13. I. V. Igumenshchev *et al.*, Phys. Plasmas **23**, 052702 (2016).
14. M. Gatu Johnson *et al.*, Rev. Sci. Instrum. **89**, 10I129 (2018).
15. C. J. Forrest *et al.*, Rev. Sci. Instrum. **83**, 10D919 (2012).

Diagnosing Magnetic Fields in Cylindrical Implosions with Oblique Proton Radiography

P. V. Heuer,[1] L. S. Leal,[1] J. R. Davies,[1] E. C. Hansen,[1] D. H. Barnak,[1] J. L. Peebles,[1] F. García-Rubio,[1] B. Pollock,[2] J. Moody,[2] A. Birkel,[3] and F. H. Séguin[3]

[1]Laboratory for Laser Energetics, University of Rochester
[2]Lawrence Livermore National Laboratory
[3]Plasma Science and Fusion Center, Massachusetts Institute of Technology

Cylindrical implosions can be used to amplify an applied axial magnetic field via flux compression, which can be used to study fundamental plasma physics in high magnetic fields[1] and is a key feature of the magnetized liner inertial fusion (MagLIF) energy scheme.[2] Previous experiments on the OMEGA Laser System have measured flux compression in cylindrical implosions using proton radiography.[3,4] These experiments were followed by the development of the laser-driven MagLIF platform,[5] which uses smaller-diameter cylindrical targets with a higher maximum convergence that reach maximum convergence more quickly. However, attempts to use proton radiography with this platform to measure the compressed axial magnetic field in the same manner as previous work have so far been unsuccessful, primarily due to the impact on the radiographs of other strong electric and magnetic fields near the target. This summary analyzes the results of two recent experiments that attempted to measure the compressed magnetic field in a cylindrical implosion using the laser-driven MagLIF platform and demonstrate how the measurement is obscured by the presence of self-generated magnetic fields.

Two experiments were conducted [hereinafter Exp. 1 and Exp. 2 using the setup shown in Fig. 1(a)]. In both experiments, the target is a plastic (CH) cylinder imploded using 40 beams (1.5-ns square-shaped pulse, total energy 16 kJ) with an overlapped intensity of 10^{14} W/cm^2. In Exp. 1 the target is gas filled (14 atm H_2), which is preheated by an axial beam prior to compression as in MagLIF. In Exp. 2 the cylinder interior is initially vacuum but soon fills with CH plasma when the shock driven by the compression beam breaks out into the interior. A set of external coils driven by MIFEDS (magneto-inertial fusion electrical discharge system)[6] provides an axial magnetic field (9 T in Exp. 1, 5 T in Exp. 2). An unmagnetized shot (with the coils in place but not energized) was taken in Exp. 1. Experiment 2 was identical except for the thickness of the cylinder and the addition of a foil to block some of the protons [visible in Fig. 1(d)].

Proton radiography[7] is used to diagnose the fields. A D^{3}He backlighter capsule 11 mm from the cylinder is imploded by 16 beams to produce 3-MeV and 15-MeV protons. The protons pass through the target cylinder walls with negligible scattering (verified on the unmagnetized shot) but are deflected by electric and magnetic fields in the vicinity of the target. The protons are then recorded on two CR-39 plates (shielded by 7.5 μm of tantalum and separated by 200 μm of aluminum to differentiate between the two proton energies) at a distance of 270 mm. In both experiments, the timing of the proton source is chosen to match the peak convergence of the implosion (which is also the peak of neutron production, or "bang time") at $t = 1.5 \pm 0.1$ ns. Due to the target chamber geometry, in both experiments the proton radiography axis is tilted relative to the target normal by an angle θ_T, making this "oblique" proton radiography.

To directly compare simulations to experimental results, synthetic proton radiographs are generated using an open-source particle-tracing algorithm that was developed for the PlasmaPy project as part of this work.[8] Three-dimensional simulations of the experiment, including the coronal plasma produced by the compression beams, were performed using the multiphysics

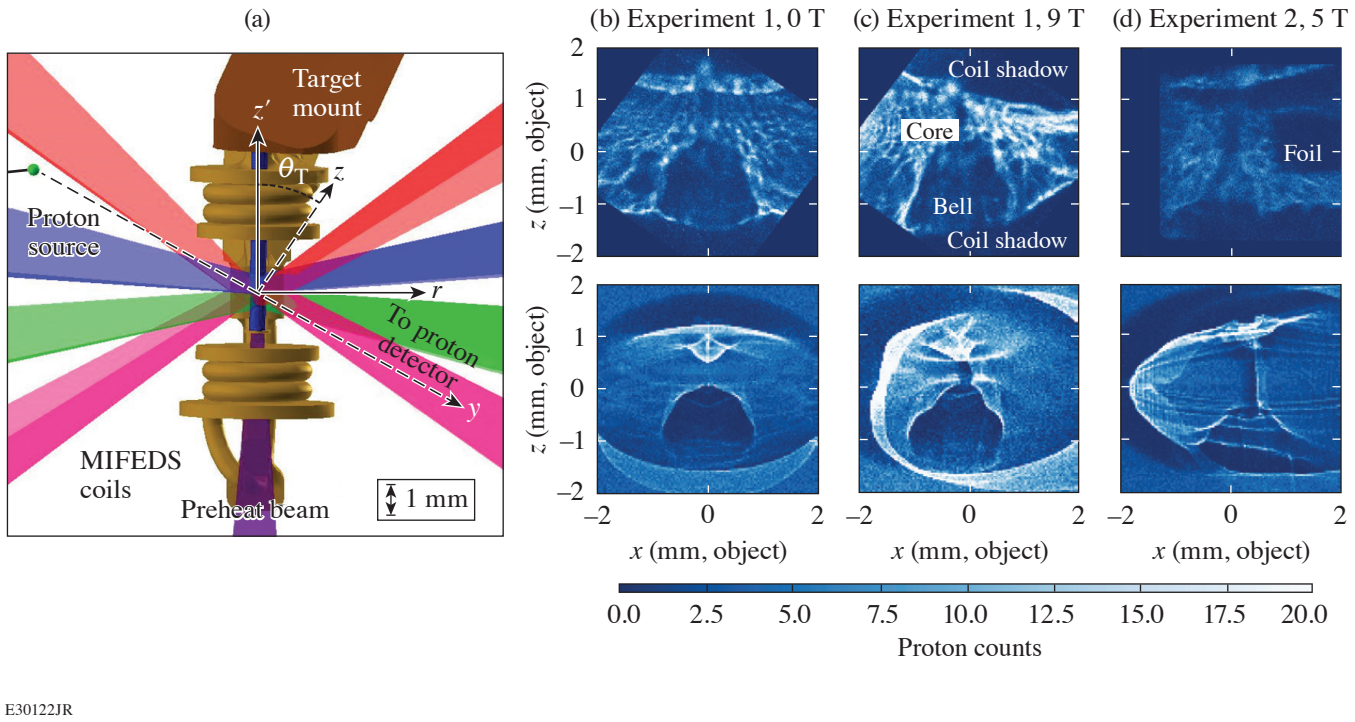

Figure 1
(a) A diagram of the setup for Exp. 1, with only a subset of the compression beams shown for clarity. (The setup for Exp. 2 is similar.) [(b)–(d)] Experimental proton radiographs (top row) for both experiments and the corresponding synthetic radiographs (bottom row) show good agreement.

radiation-hydrodynamic code *HYDRA*. A population of test protons was then traced through the simulated electric and magnetic fields and onto a detector to create synthetic radiographs. The resulting radiographs for Exp. 1 are shown in Figs. 1(b)–1(c) and Fig. 1(d) shows the radiograph for Exp. 2. All radiographs contain similar features. The "bell"-shaped feature is created by self-generated azimuthal magnetic fields in the coronal plasma produced by the drive beams, while the "core" feature visible on the magnetized radiographs is due to the compressed axial field. Small ripple features on the experimental data are not reproduced in the synthetic radiographs: this "small-scale structure" is likely due to kinetic effects such as instabilities or charge-separation fronts. Shadows are visible at the top and bottom of the experimental radiographs where protons are blocked by the MIFEDS coils.

Several approaches, including direct inversion algorithms, are applied to try and recover the line-integrated magnetic field from the experimental radiographs. However, while these techniques work reasonably well with the synthetic data, the loss of protons in the shadows of the MIFEDS fields and the presence of the small-scale structure prevent them from working with the experimental data. It is concluded that these experimental radiographs are consistent with the presence of a compressed axial field, but that a measurement of the compressed field is prevented by the self-generated azimuthal magnetic fields in the coronal plasma and the small-scale structure fields.

These results are compared to previous experiments on the OMEGA Laser System,[3,4] which successfully measured the compressed axial magnetic field in a similar cylindrical implosion. Comparing the design of this experiment to the current work provides guidance for the design of future work, suggesting that the radiography angle θ_T, target dimensions, laser pulse duration, and coil geometry are important parameters that determine the feasibility of this type of measurement. In many experiments, the ability to change these features is limited by other design considerations. However, future attempts to measure compressed axial magnetic fields in cylindrical implosions should include among these considerations the potential impact of self-generated fields on the measurement.

This material is based upon work supported by the Advanced Research Projects Agency-Energy (ARPA-E) under Award Number DE-AR0000568, the Department of Energy National Nuclear Security Administration under Award Numbers DE-NA0003856 and DE-SC0020431, the University of Rochester, and the New York State Energy Research and Development Authority.

1. C. A. Walsh *et al.*, Plasma Phys. Control. Fusion **64**, 025007 (2022).
2. S. A. Slutz *et al.*, Phys. Plasmas **17**, 056303 (2010).
3. O. V. Gotchev *et al.*, Phys. Rev. Lett. **103**, 215004 (2009).
4. J. P. Knauer *et al.*, Phys. Plasmas **17**, 056318 (2010).
5. J. R. Davies *et al.*, Phys. Plasmas **24**, 062701 (2017).
6. G. Fiksel *et al.*, Rev. Sci. Instrum. **86**, 016105 (2015).
7. N. L. Kugland *et al.*, Rev. Sci. Instrum. **83**, 101301 (2012).
8. PlasmaPy Community *et al.*, PlasmaPy (Version 0.8.1), Zenodo, Accessed 14 September 2022, https://doi.org/10.5281/zenodo.6774350.

The Effect of Laser Preheat in Magnetized Liner Inertial Fusion at the Omega Laser Facility

L. S. Leal,[1,2] A. V. Maximov,[1,3] E. C. Hansen,[1,2] J. R. Davies,[1] D. H. Barnak,[1] J. L. Peebles,[1] K. M. Woo,[1] P. V. Heuer,[1] A. B. Sefkow,[1,2,3] and R. Betti[1,2,3]

[1]Laboratory for Laser Energetics, University of Rochester
[2]Department of Physics and Astronomy, University of Rochester
[3]Department of Mechanical Engineering, University of Rochester

An important effect in magnetized transport is represented by the Nernst term in Ohm's law that advects magnetic fields down electron temperature gradients.[1–3] This term has been shown to be dominant over the fluid motion in plasmas below the critical density of the preheating laser. It is also possible that magnetic-flux transport in the hot spot is dominated by Nernst advection.[4] The preheat laser can also lead to material from the window or wall of the targets mixing with the fuel region.[5] This summary is focused on modeling the effect of preheat on the dynamics of the fuel in magnetic liner inertial fusion (MagLIF) experiments and the importance of certain terms in the magnetohydrodynamics model, specifically the Nernst effect, as well as the effect of wall material being mixed with the fuel within the capsule. Three-dimensional simulations are used to characterize the effects on yield and implosion characteristics when varying the preheat laser energy.

Three-dimensional radiation-hydrodynamic simulations show there is an optimal laser preheat energy for laser-driven MagLIF on OMEGA, with a 27-T initial magnetic field, resulting in a peak in neutron yield. A similar peak in neutron yield as a function of laser preheat energy was observed in experiments; however, the experimental yield and the optimal laser preheat energy were lower than predicted in simulations. By comparing simulations that do or do not include the Nernst effect, it was found that the Nernst effect is necessary to properly model how laser preheat affects the field dynamics in the fuel region of MagLIF. The drop from the peak in neutron yield with increasing laser preheat energy past the optimal value is larger with the Nernst effect. It is noted that with increasing preheat laser energy, there is less magnetic-field enhancement due to compression and the radial profile of the density becomes less dominated by edge effects.

A 2-D slice of the magnetic field was normalized to the initial seed magnetic field with and without Nernst effect at bang time where the fuel region is outlined. In the case without the Nernst effect, the magnetic field peaks at the radial edge of the fuel region in the center of the z axis. The magnetic field at the edges is convected with the blast wave during the preheat stage, remains at the edge throughout the implosion, and experiences flux compression. In Fig. 1(a) where the simulation includes the Nernst effect, flux compression occurs at the overdriven ends; however, the magnetic field at the center of the z axis has largely been advected out of the fuel region.

Simulations using a mix model show that including mix in implosions leads to yield degradation and can also shift the optimal laser preheat energy to a lower value. The use of premixed region limits the simulation's ability to exactly match the material penetrations occurring in experiments, but gives some insight to the effects of mix. Unlike MagLIF at Sandia National Laboratories, the primary-yield degradation mechanism from mix in MagLIF on OMEGA is not only from radiative losses (since neutron-averaged ion temperatures are not consistently lower between clean simulation and simulations with mix). The added mass from mix lowers the convergence ratios and the Hall parameter across the capsule fuel region, modifying plasma transport coefficients. Simulations also suggest that higher seed magnetic fields available from upcoming generations of MIFEDS (magneto-inertial fusion electrical discharge system) will further enhance yield in D–D cylindrical implosions. A future expanded study

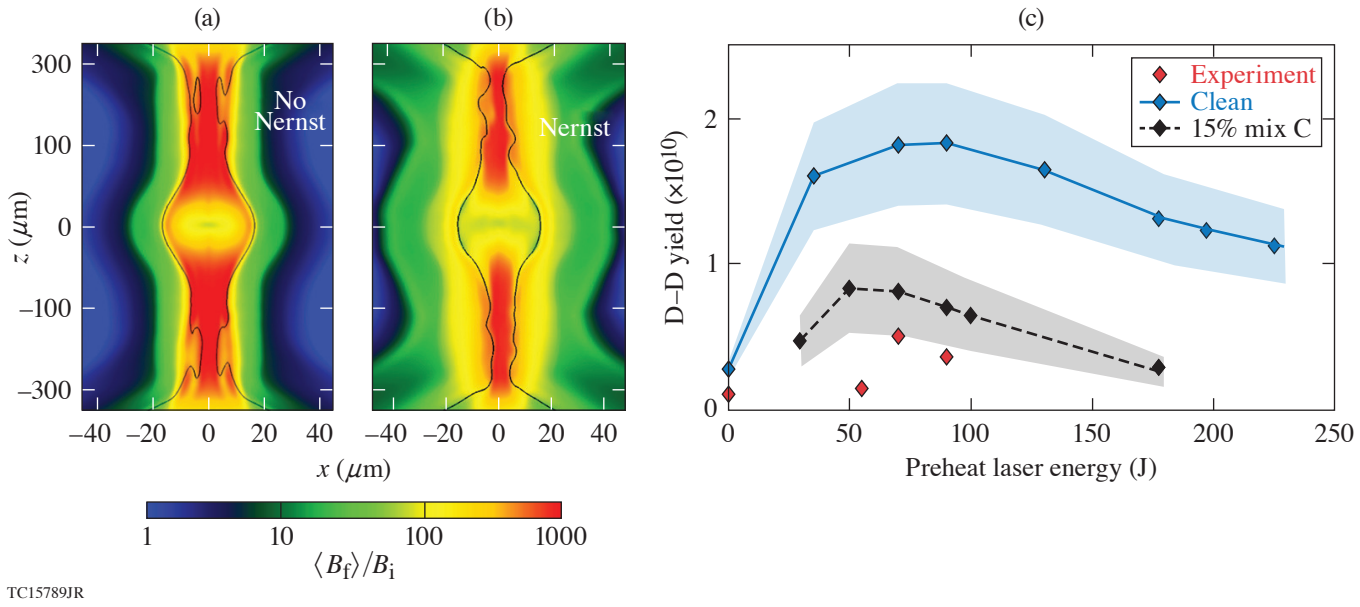

Figure 1
Two-dimensional slice of log scale magnetic-field enhancement (magnetic field over the initial seed field) at bang time for 90-J preheat laser energy and 27-T seed magnetic field from simulations (a) without the Nernst effect and (b) with the Nernst effect where the fuel region is outlined in black. (c) D–D neutron yield over varying preheat laser energies from experiments (red), clean simulations (blue), and simulations mixed with 15% C in the fuel region (black) with 27-T seed field including the Nernst effect.

of the mix effect will be needed to ascertain the degree to which mix products may penetrate the core, as well as its behavior at different preheat laser energies. Simulations can then attempt to model mix nonuniformly to study the impact on transport in the fuel region. As simulations with the mix model see a large drop in yield, they can lead to estimates on when yield degradation from increasing preheat laser energy could impact future experiments.

This material is based upon work supported by the Department of Energy National Nuclear Security Administration under Award Number DE-NA0003856, the University of Rochester, and the New York State Energy Research and Development Authority.

1. S. I. Braginskii, Sov. Phys. JETP **6**, 358 (1958).
2. E. M. Epperlein and M. G. Haines, Phys. Fluids **29**, 1029 (1986).
3. D. H. Froula *et al.*, Phys. Rev. Lett. **108**, 125003 (2012).
4. A. L. Velikovich, J. L. Giuliani, and S. T. Zalesak, Phys. Plasmas **26**, 112702 (2019).
5. A. J. Harvey-Thompson *et al.*, Phys. Plasmas **25**, 112705 (2018).

Analysis of Core Asymmetries in Inertial Confinement Fusion Implosions Using Three-Dimensional Hot-Spot Reconstruction

K. M. Woo,[1] R. Betti,[1] C. A. Thomas,[1] C. Stoeckl,[1] K. Churnetski,[1] C. J. Forrest,[1] Z. L. Mohamed,[1] B. Zirps,[2] S. P. Regan,[1] T. J. B. Collins,[1] W. Theobald,[1] R. C. Shah,[1] O. M. Mannion,[1] D. Patel,[1] D. Cao,[1] J. P. Knauer,[1] V. Yu. Glebov,[1] V. N. Goncharov,[1] P. B. Radha,[1] H. G. Rinderknecht,[1] R. Epstein,[1] V. Gopalaswamy,[1] F. J. Marshall,[1] S. T. Ivancic,[1] and E. M. Campbell[1]

[1]Laboratory for Laser Energetics, University of Rochester
[2]Department of Mechanical Engineering, University of Rochester

Three-dimensional effects play a crucial role during the hot-spot formation in inertial confinement fusion implosions. To characterize effects of low modes on hot-spot formations, a data-analysis technique for 3-D hot-spot reconstruction from experimental observables was developed. In summary, the effective flow direction, governed by the maximum eigenvalue in the velocity variance of apparent ion temperatures, was found to agree with the measured hot-spot flows for implosions dominated by mode $\ell = 1$. Asymmetries in areal-density (ρR) measurements were found to be characterized by a unique cosine variation along the hot-spot flow axis. A 3-D hot-spot x-ray emission tomography method was developed to reconstruct the 3-D hot-spot plasma emissivity using a generalized spherical-harmonic Gaussian function. The mapping between the projections from the 3-D hot-spot emission model and the measured x-ray images along multiple views is obtained by a gradient descent optimization algorithm.

Spherically symmetric flows,[1,2] turbulences,[3] and 3-D flows[4] are sources of velocity variances in neutron velocity spectra. Non-stagnating hot-spot flows kinematically boost the velocity of neutrons, produced from deuterium (D) and tritium (T) nuclear fusion reactions. The hot-spot residual fluid motion modifies the neutron velocity distribution so that the width of a neutron velocity spectrum is broadened according to a unique function of the velocity variance $\sigma = \mathrm{var}\left[v_{\mathrm{flow}} \cdot d_{\mathrm{LOS}}\right]$, where v_{flow} is the hot-spot flow velocity measured in the laboratory frame and d_{LOS} is the line of sight (LOS) unit vector, pointing from the target chamber center to the position of a detector. The velocity variance is a measurement for the hot-spot flow residual kinetic energy (RKE) since it measures the square of hot-spot flow velocity fluctuations. It contains six independent components $\sigma_{ij} = \left\langle\left(v_i - \bar{v}_i\right)\cdot\left(v_j - \bar{v}_j\right)\right\rangle$, including three directional variances with $i = j$ and three covariances with $i \neq j$. Indices i and j go from 1 to 3, representing x, y, and z Cartesian coordinates, respectively. Since covariances are unchanged upon exchanging i and j indices, the velocity variance matrix is Hermitian. This implies that σ is diagonalizable with real eigenvalues λ_i, which are the components of the hot-spot RKE along three orthonormal eigenvector directions e_i. This behavior is consistent with the fact that the trace of σ, the total hot-spot residual kinetic energy, is invariant under the special orthogonal SO(3) transformation in the 3-D Euclidean space. Hence, an apparent ion temperature measured at a given LOS is related to the hot-spot RKE's along the three eigenvector directions through the SO(3) transformation

$$T_{\mathrm{LOS}} = T_{\mathrm{thermal}} + M_{\mathrm{DT}} \sum_{i=1}^{3} \lambda_i \left\langle d_{\mathrm{LOS}} \middle| e_i \right\rangle^2, \tag{1}$$

where T_{thermal} is the ion thermal temperature in the center of mass frame of D–T nuclear reactions, and the bracket notation represents the inner product between the LOS unit vector and the ith eigenvector. Equation (1) is a generalized result to explain variations in apparent ion temperatures nonrelativistically. When implosions are dominated by mode 1, Eq. (1) implies a cosine-square variation along the eigenvector direction with the maximum eigenvalue, i.e., the hot-spot RKE of the jet. The extrapolation

for the cosine-square variation in OMEGA ion-temperature measurements using Eq. (1) is illustrated in Fig. 1(a). When implosions contain mode 2, the difference between eigenvalues parallel $\lambda_{\parallel}$ and perpendicular $\lambda_{\perp}$ to the rotational axis implies a nonvanishing ion-temperature asymmetry. Even the measured hot-spot flow velocity is zero since symmetric mode-2 hot-spot flows do not change the first moment of neutron velocity spectra. This phenomenon is illustrated by Fig. 1(b). A good agreement between the trend of experimental data and *DEC3D* simulations with a uniform 2% initial velocity perturbation of mode 2 on varying mode-1 perturbations is obtained. A semi-analytic model is derived to explain the mode-1 ρR degradation. Both 4π averaged and variations in ρR are found to be a function of the ion-temperature ratio $R_T = T_{\max}/T_{\min}$,

$$\frac{(\rho R)\mathrm{LOS}}{(\rho R)1\text{-D}} = R_T^{\alpha} + \sqrt{R_T^{2\alpha} - R_T^{2\beta}}\,\cos\theta_{\mathrm{LOS\text{-}flow}}\,, \tag{2}$$

where $\alpha = -0.3$ and $\beta = -0.47$ are parameters obtained from *DEC3D* mode-1 simulations, and $\theta_{\mathrm{LOS-flow}}$ is the inclination angle between the LOS and the measured hot-spot flow vectors. The extrapolation for the mode-1 angular-dependence in areal density measurements is illustrated by Fig. 1(c). The 3-D kernel as stated by Eq. (2) is shown to accurately fit the H10 ρR measurements. A 3-D x-ray emission tomography method was devised to reconstruct arbitrary hot-spot shapes using a generalized spherical harmonic Gaussian function,

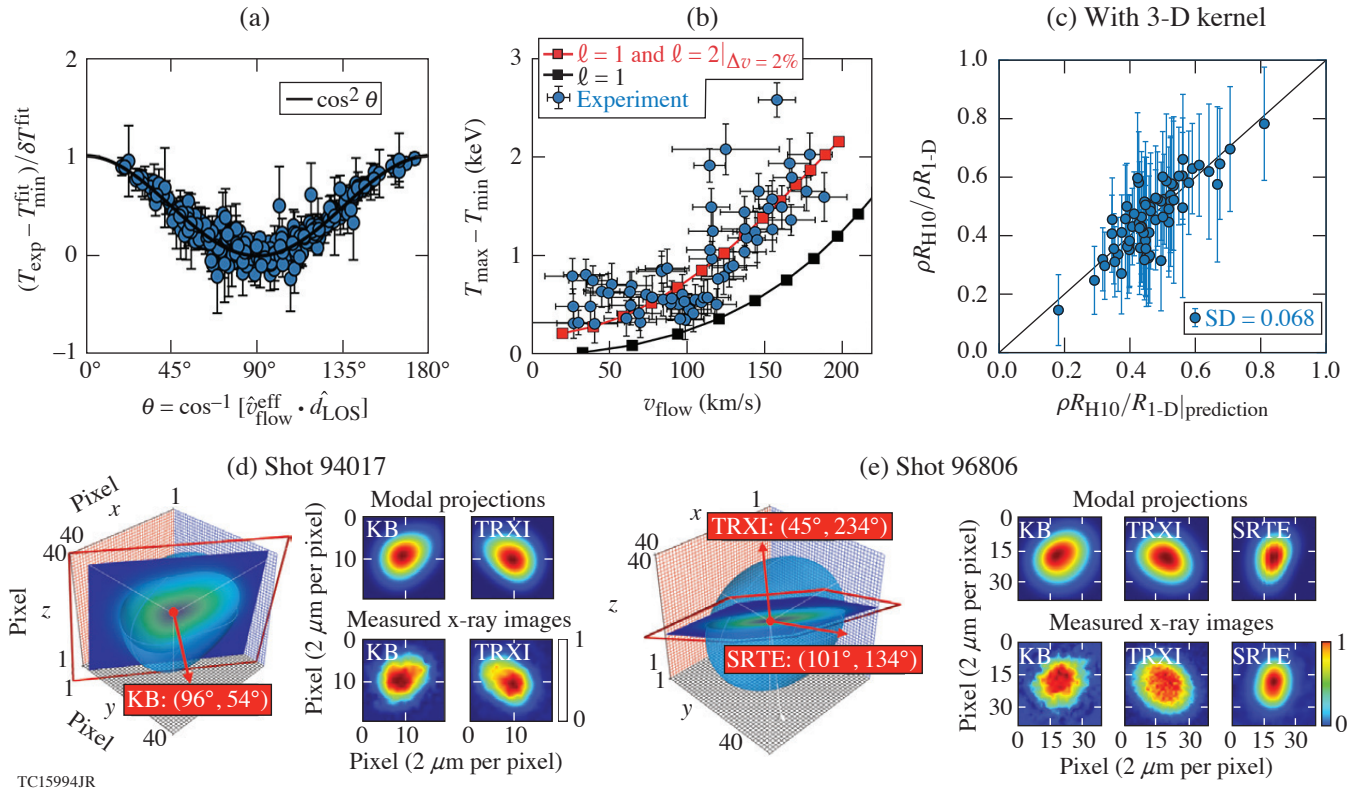

Figure 1
Analysis of core asymmetries in OMEGA implosion experiments. (a) The extrapolation for the cosine-square variation in ion-temperature measurements using Eq. (1). (b) The reconstruction for the trend of T_i and flow relation using *DEC3D* simulations. (c) The extrapolation for the mode-1 angular-dependence in areal density measurements using the 3-D kernel in Eq. (2). [(d),(e)] Three-dimensional hot-spot reconstructions for shots 94017 and 96806 using the generalized spherical-harmonic Gaussian model in Eq. (3). SD: standard deviation; KB: Kirkpatrick–Baez; TRXI: time-resolved x-ray imager; SRTE: spatially resolved x-ray imager.

$$\ln \varepsilon_{\nu} = \sum_{n=0}^{\infty} \sigma_n R^n \left[1 + \sum_{\ell=1}^{\infty} \sum_{m=-\ell}^{\ell} \sum_{k=0}^{\infty} A_{\ell mk} R^k Y_{\ell m}(\theta, \phi) \right]^n . \tag{3}$$

Expansion coefficients in Eq. (3) are determined by minimizing the root-mean-square deviations between modal projections and measured x-ray images measured at multiple views using the gradient descent optimization algorithm. Three-dimensional hot-spot reconstructions are illustrated in Fig. 1(d) and 1(e). The mode-1 skew signature and the mode-2 ellipticity are well reconstructed for shots 94017 and 96806, respectively.

This material is based upon work supported by the Department of Energy National Nuclear Security Administration under Award No. DE-NA0003856, the University of Rochester, and the New York State Energy Research and Development Authority and DOE grant DE-SC0022132.

1. R. E. Chrien, K. A. Klare and T. J. Murphy Rev. Sci. Instrum. **68**, 607 (1997).
2. T. J. Murphy, R. E. Chrien and K. A. Klare Rev. Sci. Instrum. **68**, 614 (1997).
3. T. J. Murphy, Phys. Plasmas **21**, 072701 (2014).
4. K. M. Woo *et al.*, Phys. Plasmas **25**, 102710 (2018).

Evaluation of Direct Inversion of Proton Radiographs in the Context of Cylindrical Implosions

J. R. Davies and P. V. Heuer

Laboratory for Laser Energetics, University of Rochester

Proton radiography is frequently used on OMEGA and OMEGA EP to infer electric and magnetic fields. If proton energy loss and scattering are negligible, proton deflection at the detector will be determined by the path-integrated transverse Lorentz force experienced by the protons. The most common technique used to infer fields from intensity modulations on the detector has been proton tracing in given fields, either assumed or obtained from simulations. Recently, a number of authors have used direct inversion to infer the fields,[1–6] and many of these direct inversion routines are publicly available on GitHub.[1–5] Direct inversion provides a solution independent of biases; particle tracing in specified forces is subject to user biases, and tracing in forces determined from simulations is limited by knowledge of the experimental conditions to be simulated and the physics included in the simulations. Publicly available direct inversion routines were applied to proton radiography data from cylindrical implosion experiments on OMEGA. As a first step, a series of test problems is generated using proton tracing to evaluate the routines.[7] These test problems are publicly available[8] as hdf5 files in pradformat.[9] The test results are summarized here.

Direct inversion determines deflections at the detector that map the source intensity (I_0) to the measured intensity (I). There is no unique solution to this problem, as demonstrated by the trivial case of simply swapping two particles on the detector. There is a unique solution, however, that minimizes total deflection and does not allow particles to be moved over one another. If proton trajectories to the detector do not cross, direct inversion will give the solution. If proton trajectories do cross, direct inversion will give one out of an infinite family of solutions, which is still useful information. In mathematics, direct inversion is known as the optimal transport problem, first described in a paper by Monge published in 1781 (Ref. 10), which derives what is now known as the Monge–Ampère equation. All but one of the publicly available direct inversion routines solve the Monge–Ampère equation.[1–4] The other routine[5] uses iterative methods to construct power diagrams (weighted Voronoi diagrams) of the source and measured intensities with equal flux in each cell, determining the deflections from the movement of cell centroids. Direct inversion can be applied to radiography with any charged particle, and to shadowgraphy where photons are deflected by gradients in refractive index.[5] In order to relate the deflections obtained at the detector to the forces in the object, one must assume a small angle deflection in the object ($\ll$1 rad or 57.3°) so that the deflections are proportional to the line-integrated force along the original trajectory. In practice, this is not a major restriction since the proton radiography and shadowgraphy setups used on OMEGA and OMEGA EP subtend a small angle at the target. If there are regions where large angle deflections occur, information on the forces in these regions will be lost.

Test radiographs or, equivalently, shadowgraphs, were generated by particle tracing through purely radial force profiles in cylinders and spheres for a range of force amplitudes with uniform source intensities. In cylinders a Gaussian potential [$F_r \propto r \exp(-r^2/R_2)$], a linear profile ($F_r \propto r$ for $r \leq R$)], and a top-hat profile (F_r = constant for $r \leq R$) were used. The linear profile was chosen to represent the electric field in an isothermal, cylindrical expansion,[11] ignoring the rapidly decaying field in the electron sheath beyond the ion front. The top-hat profile was chosen to represent the axial magnetic field in a cylindrical implosion, which is discontinuous at the inner surface of the shell. For spheres, a Gaussian potential was used. Force is expressed as a dimensionless parameter

$$\mu = \frac{2LF}{Mpv},$$

where L is object-to-detector distance, M is magnification, F is Lorentz force, p is particle momentum, and v is particle velocity, or

$$\mu = \frac{L}{\mathrm{M}} \frac{\mathrm{d}\left(n_\mathrm{e}/n_\mathrm{c}\right)/\mathrm{d}r}{\sqrt{1-n_\mathrm{e}/n_\mathrm{c}}}$$

for shadowgraphy, where n_e is electron density and n_c is the critical density of the probe. All distances are expressed in terms of the object size R. Trajectories cross in all cases for the linear and top-hat profiles and for both cylindrical and spherical Gaussian potentials when $\mu_{\max} \geq 1.08$ or $\mu_{\max} \leq -0.484$, negative values indicating a focusing force.

Five direct inversion routines were found on GitHub.[1–5] Two of the routines, both Monge–Ampère solvers, did not run.[1,2] The other two Monge–Ampère solvers were found to be essentially identical, which is not surprising considering they are implementations of the same algorithm by the same author.[3,4] Therefore, one Monge-Ampère routine and one power-diagram routine[5] was available to evaluate. The Monge–Ampère routine could not solve the cylindrical problems because it uses fixed deflection potential boundary conditions, which would also cause issues with any problem that has modulations near the boundary. The correct boundary conditions to obtain a minimum deflection from the Monge–Ampère equation are to set the deflections across the boundaries to zero.[2] The Monge-Ampère routine accurately inverted the spherical Gaussian tests when trajectories did not cross and did so roughly 1000× faster than the power-diagram routine, but failed when trajectories crossed. The failure was obvious from the poor reproduction of the measured intensity. The failure appears to be caused by the adaptive time step, which rapidly falls to the specified minimum value for tests where deflected trajectories cross. The power-diagram routine successfully inverted all but two of the test problems. The power diagram failed for the top-hat profile with $\mu_{\max} = 2$ and a smaller bin width (0.015R) than the final value we settled on (0.025R); however, for the coarser bin width an adequate solution was obtained. The power-diagram routine failed for a spherical Gaussian with $\mu_{\max} = -0.5$ and the issue was not resolved by coarser binning, the bin width of 0.052R already being too coarse to resolve the sharp peak. The power-diagram routine moves the sites closest to the corners into the corners in order to interpolate the deflections to all points on the original grid, which, for this strongly focusing test, leads to significant distortion of the entire region. Examples of the line-integrated forces obtained by the power-diagram routine for the cylindrical tests are given in Fig. 1. In all cases the measured intensity was accurately reproduced. The inversion underestimates the original line-integrated forces when trajectories cross because it gives a minimum deflection solution. It should be remembered that when trajectories cross, there exists an infinite family of solutions for the line-integrated force. As a result of these tests, only the power-diagram routine was used to analyze the proton radiographs of cylindrical implosions.[12]

This material is based upon work supported by the U. S. Department of Energy's Advanced Research Projects Agency-Energy under Award Number DE-AR0000568 and National Nuclear Security Administration under Award Number DE-NA0003856, the University of Rochester, and the New York State Energy Research and Development Authority.

1. C. Graziani *et al.*, Rev. Sci. Instrum. **88**, 123507 (2017).
2. A. F. A. Bott *et al.*, J. Plasma Phys. **83**, 905830614 (2017); PROBLEM Solver (PROton-imaged B-field nonLinear Extraction Module), Accessed 12 July 2021, https://github.com/flash-center/PROBLEM.
3. M. F. Kasim, Invert Shadowgraphy and Proton Radiography, Accessed 8 July 2021, https://github.com/mfkasim1/invert-shadowgraphy.
4. M. F. Kasim *et al.*, Phys. Rev. E **100**, 033208 (2019); M. F. Kasim, PRNS (Proton Radiography with No Source), Accessed 12 July 2021, https://github.com/OxfordHED/proton-radiography-no-source.
5. M. F. Kasim *et al.*, Phys. Rev. E **95**, 023306 (2017); M. F. Kasim, Invert Shadowgraphy and Proton Radiography, Accessed 8 July 2021, https://github.com/mfkasim1/invert-shadowgraphy.
6. N. F. Y. Chen *et al.*, Phys. Rev. E **95**, 043305 (2017).
7. J. R. Davies and P. V. Heuer, "Evaluation of Direct Inversion of Proton Radiographs in the Context of Cylindrical Implosions," Physics Archive: https://doi.org/10.48550/arXiv.2203.00495 (2022).
8. J. Davies and P. Heuer, Synthetic Proton Radiographs for Testing Direct Inversion Algorithms, Zenodo, Accessed 3 August 2022, https://doi.org/10.5281/zenodo.6632986.

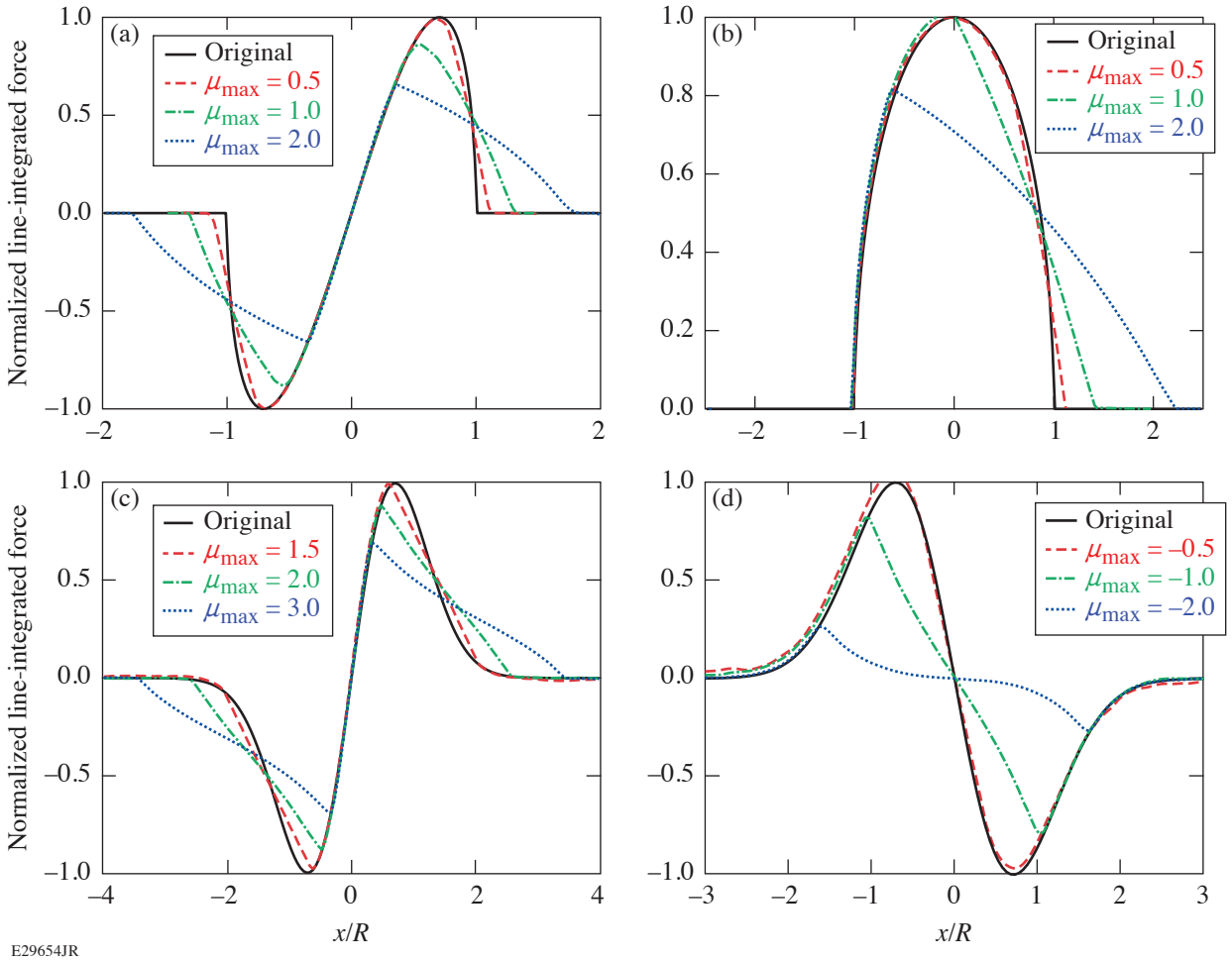

Figure 1

Line-integrated forces from the power-diagram routine for cylindrical test problems from (a) the linear profile, (b) the top-hat profile, and [(c),(d)] the Gaussian potential, normalized so that the maximum of the original is 1.

9. Pradformat (Proton Radiography File Format Tools), Accessed 12 July 2021, https://github.com/phyzicist/pradformat.
10. G. Monge, Mém. de l'Ac. R. des. Sc. An., 666 (1781).
11. M. Murakami and M. M. Basko, Phys. Plasmas **13**, 012105 (2006).
12. P. V. Heuer *et al.*, Phys. Plasmas **29**, 072708 (2022).

Particle-in-Cell Modeling of Plasma-Jet Merging in the Large-Hall-Parameter Regime

H. Wen,[1] C. Ren,[2,3] E. C. Hansen,[2] D. Michta,[2] Y. Zhang,[3] S. Langendorf,[4] and P. Tzeferacos[1,2]

[1]Laboratory for Laser Energetics, University of Rochester
[2]Department of Mechanical Engineering, University of Rochester
[3]Department of Physics and Astronomy, University of Rochester
[4]Physics Division, Los Alamos National Laboratory

Plasma-jet–driven magneto-inertial fusion (PJMIF) offers a novel "reactor-friendly" alternative approach to fusion energy that assembles targets by launching magnetized plasma jets from plasma guns at large standoff distances.[1] Fusion reactions take place in an all-gas/plasma architecture, avoiding repetitive hardware destruction. Furthermore, magnetic fields in the assembled target reduce thermal conduction and facilitate ignition. Most of the previous studies on this concept focused on the hydrodynamics,[2–5] while possible kinetic physics,[6] especially in target formation and compression, have not been well explored. Presented here are particle-in-cell (PIC) simulations with the code *OSIRIS* of two colliding counter-propagating magnetized jets to study the kinetic physics in the target formation process. The *OSIRIS* simulation results show that the fuel plasma jets can be stopped due to a microinstability—the modified two-stream instability (MTSI)[7,8]—rather than coulomb collisions. A comparison of 2-D simulations with *OSIRIS* and the single-fluid magnetohydrodynamic code *FLASH* shows that the codes predict similar macroscopic behaviors of the jets stopping and their subsequent expansion, despite the lack of kinetic physics in the *FLASH* simulations. The results provide validation for using *FLASH* to model target formation and beyond for plasma liner experiments (PLX's).

The total ion $v_x - x$ phase space and the spectrum of the longitudinal electric field E_x are shown in Fig. 1 to illustrate the two dominant MTSI modes identified in the simulation. One of the MTSI modes corresponded to the interaction between the incoming ions and the interpenetrated ions from the counter-propagating jet. This MTSI mode is localized in region 1 [locations between the two solid black vertical lines in the ion phase space as shown in Figs. 1(a)–1(c)]. The incoming and interpenetrating jets can be easily identified since the distribution within region 1 has two distinct peaks on the v_x axis. Using the parameters obtained in region 1, we found that the MTSI growth rate was $\gamma_{\mathrm{MTSI}} = 0.1\ \mathrm{ns}^{-1}$ for the fastest growing mode at $k = 0.65\omega_{\mathrm{pe}}/c$, where ω_{pe} is the local plasma frequency and c is the speed of light. The MTSI mode in region 1 initiated a shock that propagated to the left. A localized electrostatic field started to build up across the shock front as the MTSI grew. The interpenetrated ions were accelerated by this field to a longitudinal velocity of about 240 km/s (the sum of the plasma jet velocity and the shock velocity) and sustained that velocity afterward, as illustrated by the phase space features in region 1 in Figs. 1(b) and 1(c). The fastest-growing modes evaluated using parameters obtained from region 1 at different times are overlaid as the black solid line in Fig. 1(d), which agrees reasonably well with the dominant MTSI mode (the bright feature started around $k = 0.7\omega_{\mathrm{pe}}/c$ at $t \approx 70$ ns), including the shift to lower k at a later time. The other MTSI mode (first appeared around $t \approx 85$ ns with $k = 1.2\omega_{\mathrm{pe}}/c$) in Fig. 1(d) corresponded to the interaction between the incoming ions and the reflected ions. This MTSI mode was localized in region 2, locations between the two dashed vertical lines in Figs. 1(b) and 1(c), which tracked the shock-front propagation. Figure 1(d) plots the fastest-growing MTSI mode as a dashed black line that agreed well with the bright feature to the right of the initial MTSI mode corresponding to region 1. As evident in Fig. 1(d), this MTSI mode occurred later than the initial MTSI mode because the shock was generated by the initial MTSI mode. The wave number k_x of these two MTSI modes both shifted to smaller values over time, mainly due to the decreasing density and magnetic field in regions 1 and 2.

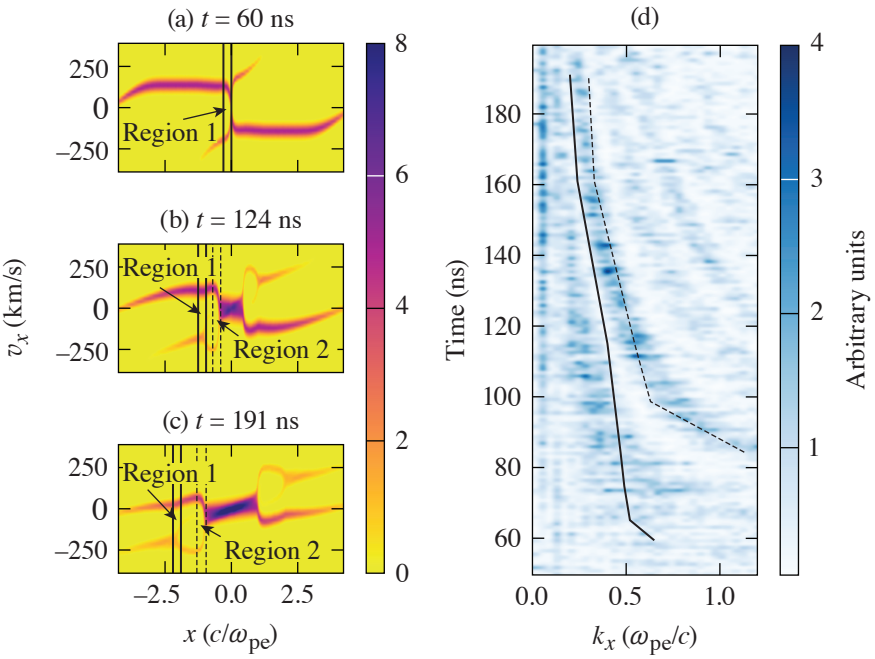

TC16003JR

Figure 1
Ion v_x–x phase space at (a) $t = 60$ ns, (b) $t = 124$ ns, and (c) $t = 191$ ns; (d) the spectrum of longitudinal electric field E_x. The solid and dashed black lines in the plot (d) correspond to the fastest-growing MTSI modes with parameters obtained from the regions 1 and 2 [plots (a)–(c)], respectively.

Figure 2 shows the time evolution of the plasma β, the electron Hall parameter χ_e, and the ion Hall parameter χ_i in the central merging region obtained from *OSIRIS* and *FLASH* simulations. The dimensionless parameters predicted by the two codes were on the same order of magnitude. During the jet-merging process and before the merged plasma expansion, i.e., between 50 and 200 ns, χ_e, and χ_i were greater than unity; the plasma β was close to unity. This is the desired characteristic of planned PLX. The same level of agreement between the two codes was achieved for the electron and ion Hall parameters. The plasma β differed more in the antiparallel-B case: β in *OSIRIS* was consistently larger than in *FLASH*. This is likely due to the interpenetrated species carrying magnetic fields to the other jet, leading to the enhanced magnetic-field cancellation.

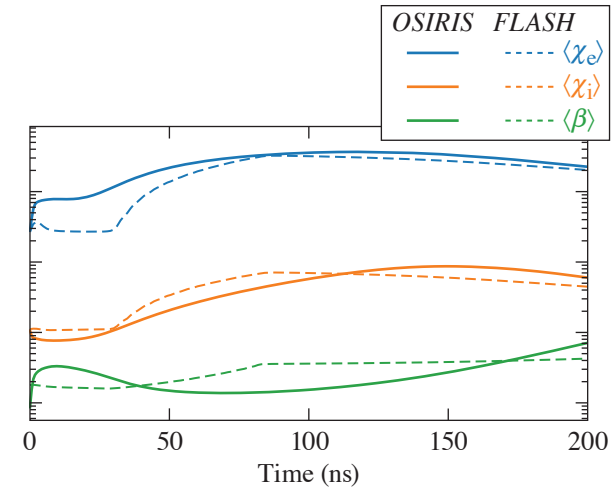

TC16011JR

Figure 2
The dimensionless parameters near the merging region obtained in *OSIRIS* (solid lines) and *FLASH* (dashed lines) simulations of a 5-eV plasma jet collision: electron Hall parameter $\langle\chi_e\rangle$ parameter (blue lines), ion Hall parameter $\langle\chi_i\rangle$ (orange lines), and plasma $\langle\beta\rangle$ (green lines). The angle bracket corresponds to spatial average.

In summary, the MTSI is identified to be the main mechanism responsible for stopping the plasma jets and preventing species interpenetration. The 2-D PIC simulations validate the results of the radiation magneto-hydrodynamics code *FLASH*, which will be the primary tool for modeling various stages of future PJMIF experiments.

This material was based upon the work supported, in part, by the Advanced Research Projects Agency-Energy (ARPA-E), U.S. Department of Energy (DOE), under Award Nos. DE-AR0001272and DE-SC0020431; by the U.S. DOE National Nuclear Security Administration (NNSA) under Award No. DE-NA0003856; the University of Rochester; and the New York State Energy Research and Development Authority. This manuscript has been authored in collaboration with Los Alamos National Laboratory/Triad National Security, LLC, Contract No. 89233218CNA000001, with the U.S. Department of Energy/National Nuclear Security Administration. This research used resources of the National Energy Research Scientific Computing Center (NERSC), a U.S. Department of Energy Office of Science User Facility located at the Lawrence Berkeley National Laboratory, operated under Contract No. DE-AC02-05CH11231 using NERSC Award No. FES-ERCAP0017949.

1. S. C. Hsu and S. J. Langendorf, J. Fusion Energy **38**, 182 (2019).
2. J. S. Davis *et al.*, Phys. Plasmas **19**, 102701 (2012).
3. J. T. Cassibry, M. Stanic, and S. C. Hsu, Phys. Plasmas **20**, 032706 (2013).
4. W. Shih *et al.*, Phys. Plasmas **26**, 032704 (2019).
5. K. Schillo and J. Cassibry, Phys. Plasmas **27**, 042707 (2020).
6. C. Thoma, D. R. Welch, and S. C. Hsu, Phys. Plasmas **20**, 082128 (2013).
7. J. B. McBride *et al.*, Phys. Fluids **15**, 2367 (1972).
8. S. P. Gary, *Theory of Space Plasma Microinstabilities*, Cambridge Atmospheric and Space Science Series (Cambridge University Press, Cambridge, 1993).

Progress in Relativistic Laser–Plasma Interaction with Kilotesla-Level Applied Magnetic Fields

K. Weichman,[1] A. P. L. Robinson,[2] M. Murakami,[3] J. J. Santos,[4] S. Fujioka,[3] T. Toncian,[5] J. P. Palastro,[1] and A. V. Arefiev[6,7]

[1]Laboratory for Laser Energetics, University of Rochester
[2]Central Laser Facility, STFC Rutherford Appleton Laboratory
[3]Institute of Laser Engineering, Osaka University, Japan
[4]University of Bordeaux, CNRS, CEA, CELIA, France
[5]Institute for Radiation Physics, Helmholtz-Zentrum Dresden-Rossendorf, Germany
[6]Department of Mechanical and Aerospace Engineering, University of California, San Diego
[7]Center for Energy Research, University of California, San Diego

Recent advances in vacuum magnetic-field–generation techniques[1–6] have renewed interest in the fundamentals of laser–plasma interaction in the presence of strong magnetic fields. In part, this interest has been motivated by the potential for applied magnetic fields to benefit applications of laser–plasma interaction at relativistic intensity ($I_0 \sim 10^{18}$ W/cm^2 for ~1-μm wavelength), including ion acceleration, inertial fusion energy, and the laboratory study of astrophysical phenomena. This summary builds on recent progress in understanding the basic physics of relativistic laser–plasma interaction with kilotesla-level applied magnetic fields: surface magnetic fields and the diamagnetic effect in laser–solid interaction, the effect of embedded magnetic fields on plasma expansion and ion acceleration, and magnetic-field–associated changes in the direct laser acceleration of electrons.

First, although plasma is conventionally considered diamagnetic and often acts to exclude magnetic fields, laser–plasma interactions have long been known to self-generate strong fields[7] and amplify applied magnetic fields.[8] The spatial localization of hot-electron production from an overdense target and the presence of a neutralizing cold return current offer additional opportunities for magnetic-field generation and amplification associated with kinetic electron dynamics, among which is surface magnetic-field generation arising from the inability of the hot-electron current to change the applied field in a conductive opaque target.[9] This surface magnetic field can influence later plasma dynamics including target expansion[9] and may reverse the sign of the magnetic field generated by laser-driven implosions when it is destabilized.[10] The latter case is of particular interest as a platform for extreme magnetic-field amplification. However, the process underlying the sign reversal phenomenon[10,11] has yet to be conclusively settled. This work introduces a computationally efficient model that is predictive of the sign of the magnetic field produced in implosions. This model demonstrates correlation between sign reversal in cylindrical implosions and instability of the surface magnetic field in a simplified planar configuration (Fig. 1).

Second, until recently, the effect of applied magnetic fields on laser-driven plasma expansion and ion acceleration has primarily been studied in the context of astrophysical jet dynamics[12] involving long time-scale (~nanosecond) evolution in sub-100-tesla magnetic fields, which necessitates magnetohydrodynamic modeling and eliminates the consideration of kinetic effects. The sheath-based ion-acceleration regime driven by short, relativistic intensity laser pules, on the other hand, is conducive to multidimensional kinetic modeling. Recent work in this regime has revealed the possibility of using an applied magnetic field to reverse the typical outward divergence associated with target normal sheath acceleration into focusing and improving the ion energy and number.[13,14] In this case, ion focusing, which is highly desirable and much studied under nonmagnetized conditions, is produced by eventual magnetization of the electron sheath as the plasma expands.[14] Observing ion focusing experimentally, however, will require the spatial scale of the applied magnetic field to be comparable to or greater than the focal length. This work introduces

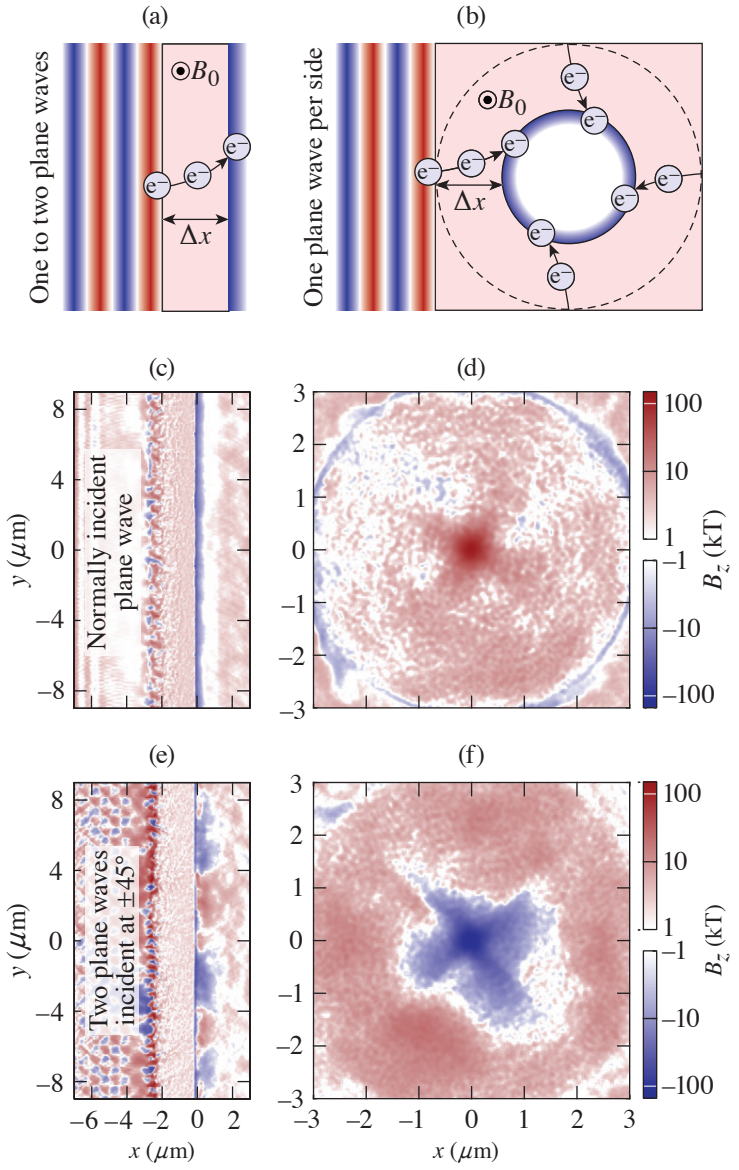

Figure 1
Planar model capturing surface magnetic-field stability and sign of the amplified field in implosions. [(a),(b)] Schematic of surface magnetic-field generation in (a) a planar target and (b) an implosion target with either square (solid line) or circular (dashed line) outer cross section. (c) Stable surface magnetic field in a planar target with normally incident plane wave pulse and (d) seed-aligned amplified magnetic field in a square implosion target. (e) Unstable surface magnetic field in a planar target with two obliquely incident pulses and (f) an amplified field in a circular implosion target.

a simple scaling model for sheath magnetization and subsequent ion focusing (Fig. 2). From this, realistic ion focal lengths are predicted that are likely compatible with the spatial extent of currently available applied magnetic fields.

Finally, while conventional electron acceleration mechanisms typically leave the majority of electrons cold either spectrally or spatially after the laser pulse has passed, direct laser acceleration (DLA) with an applied magnetic field is capable of volumetrically heating electrons to relativistic energy.[15–17] In the regime where the applied magnetic field affects the acceleration dynamics in a single accelerating laser half-cycle,[18] even modestly relativistic laser pulses can deliver significantly relativistic electron energy ($\gamma \sim 10$ or more). A configuration employing a secondary laser pulse prior to the main accelerating pulse (to provide the preheating necessary to enter this regime) was recently demonstrated to heat the majority of electrons in a large plasma volume to nonperturbatively relativistic energy.[18] The resulting optically diagnosable, relativistically thermal plasma is highly desirable for fundamental experimental studies in basic plasma physics, astrophysics and laboratory astrophysics, and laser-plasma physics. This work obtains an estimate for the average electron energy generated via magnetically assisted DLA (Fig. 3), which suggests plasma heating is most efficient for long, low (relativisitic)-intensity laser pulses.

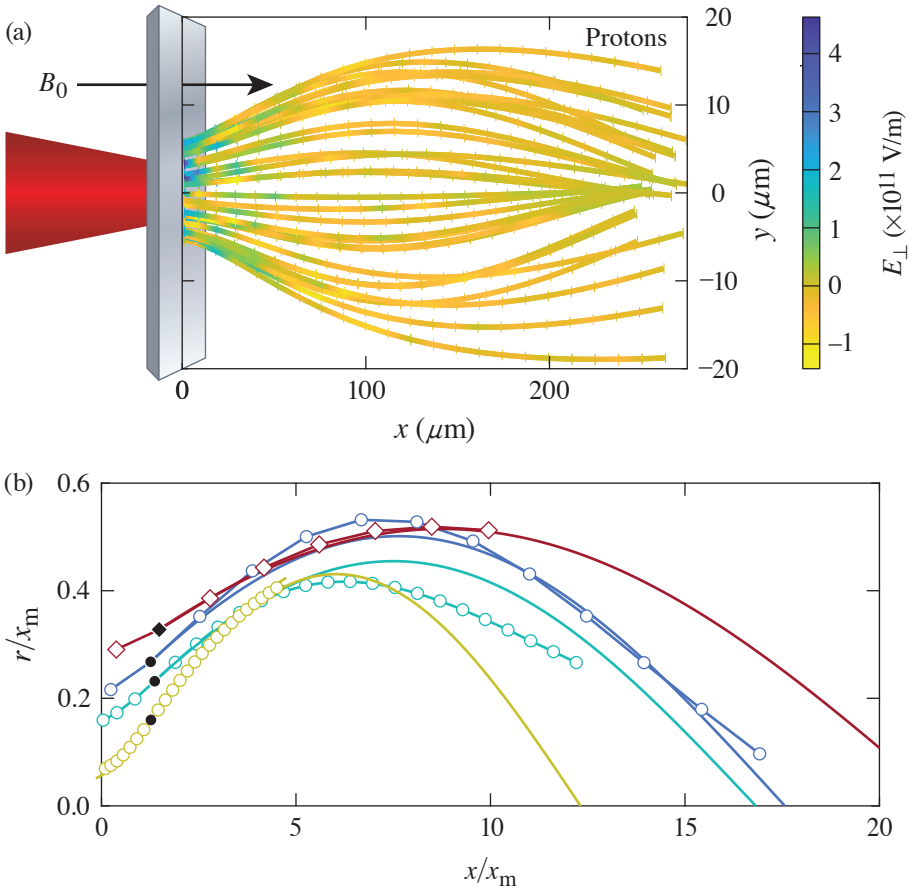

Figure 2
Model of ion focusing in magnetized electron sheath acceleration. (a) Schematic of ion acceleration with a target-normal applied magnetic field with proton trajectories. (b) Average high-energy proton trajectories from simulations keeping the laser waist divided by B_0 constant. $x_m \equiv (2\varepsilon_i T_e)^{1/2}/|e|B_0$.

Together, these results highlight the promise of applied magnetic fields in relativistic laser–plasma interactions. Current magnetic-field capabilities can already enable novel and highly desirable phenomena relevant to laser-plasma applications. The continual development of magnetic-field–generation techniques supports these efforts by opening new parameter regimes to exploration.

This material is based upon work supported by the Department of Energy National Nuclear Security Administration under Award Number DE-NA0003856, the University of Rochester, and the New York State Energy Research and Development Authority. A.V.A. was supported by NSF Grant No. 1903098. A.V.A. was supported by NSF Grant No. 1903098. The support of DOE does not constitute an endorsement by DOE of the views expressed in this paper. Particle-in-cell simulations were performed using *EPOCH*,[19] developed under UK EPSRC Grant Nos. EP/G054940, EP/G055165, and EP/G056803. This work used HPC resources of the National Energy Research Scientific Computing Center (NERSC), a U.S. Department of Energy Office of Science User Facility operated under Contract No. DE-AC02-05CH11231 using NERSC award FES-ERCAP-0021627, and the Extreme Science and Engineering Discovery Environment (XSEDE),[20] which is supported by National Science Foundation grant number ACI-1548562, under allocation TG-PHY210072 on the Texas Advanced Computing Center (TACC) at The University of Texas at Austin.

1. S. Fujioka *et al.*, Sci. Rep. **3**, 1170 (2013).
2. J. J. Santos *et al.*, New J. Phys. **17**, 083051 (2015).
3. L. Gao *et al.*, Phys. Plasmas **23**, 043106 (2016).
4. C. Goyon *et al.*, Phys. Rev. E **95**, 033208 (2017).
5. V. V. Ivanov *et al.*, Rev. Sci. Instrum. **89**, 033504 (2018).
6. G. Fiksel *et al.*, Rev. Sci. Instrum. **86**, 016105 (2015).
7. Z. M. Sheng and J. Meyer-ter Vehn, Phys. Rev. E **54**, 1833 (1996).

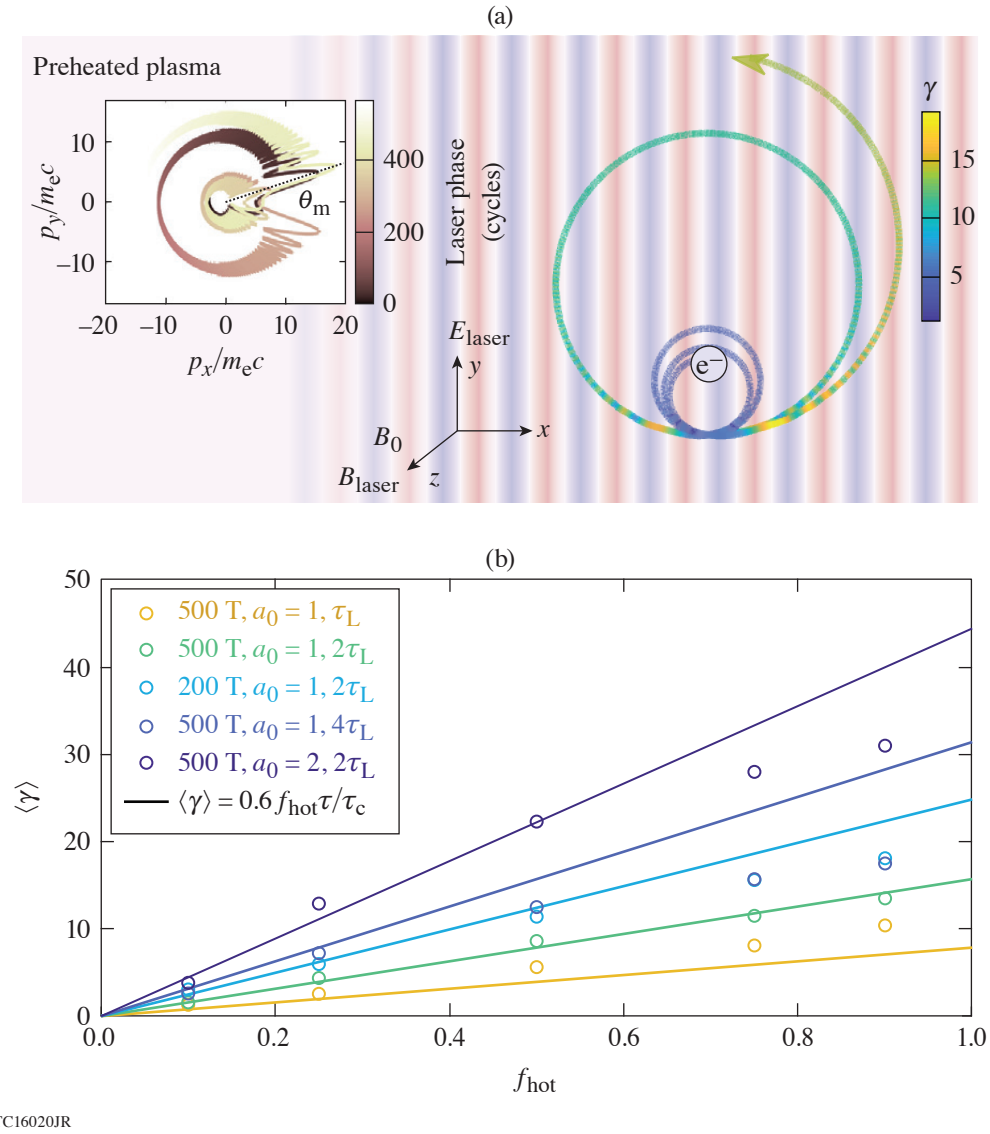

Figure 3
Half-cycle magnetically assisted direct laser acceleration in a preheated plasma. (a) Example of the many-kick electron acceleration process. (b) Average electron energy from particle-in-cell simulations varying the initial fraction of electrons above the the threshold for energy gain (f_{hot}). τ, τ_L, and τ_C are the pulse duration, the maximum Larmor period after a single kick, and the non-relativistic cyclotron period, respectively.

8. O. V. Gotchev *et al.*, Phys. Rev. Lett. **103**, 215004 (2009).
9. K. Weichman *et al.*, New J. Phys. **22**, 113009 (2020).
10. K. Weichman *et al.*, Appl. Phys. Lett. **117**, 244101 (2020).
11. Y.-J. Gu and M. Murakami, Sci. Rep. **11**, 23592 (2021).
12. B. Albertazzi *et al.*, Science **346**, 325 (2014).
13. A. Arefiev, T. Toncian, and G. Fiksel, New J. Phys. **18**, 105011 (2016).
14. K. Weichman *et al.*, Sci. Rep. **10**, 18966 (2020).
15. A. V. Arefiev, A. P. L. Robinson, and V. N. Khudik, J. Plasma Phys. **81**, 475810404 (2015).
16. A. P. L. Robinson and A. V. Arefiev, Phys. Plasmas **27**, 023110 (2020).

17. K. Weichman *et al.*, "Underdense Relativistically Thermal Plasma Produced by Magnetically Assisted Direct Laser Acceleration," Physics Archive: https://doi.org/10.48550/arXiv:2202.07015 (2022).
18. A. Arefiev, Z. Gong, and A. P. L. Robinson, Phys. Rev. E 101, 043201 (2020).
19. T. D. Arber *et al.*, Plasma Phys. Control. Fusion **57**, 113001 (2015).
20. J. Towns *et al.*, Comput. Sci. Eng. **16**, 62 (2014).

Single-Shot Electron Radiography Using a Laser-Plasma Accelerator

G. Bruhaug,[1,2] M. S. Freeman,[3] H. G. Rinderknecht,[1] L. P. Neukirch,[3] C. H. Wilde,[3] F. E. Merrill,[3] J. R. Rygg,[1,2,4] M. S. Wei,[1] G. W. Collins,[1,2,4] and J. L. Shaw[1]

[1]Laboratory for Laser Energetics, University of Rochester
[2]Department of Mechanical Engineering, University of Rochester
[3]Los Alamos National Laboratory
[4]Department of Physics and Astronomy, University of Rochester

To investigate the physical structure of compressed targets, laser-generated x-ray[1,2] or proton radiography[3–5] is typically used, with protons providing the extra feature of electromagnetic field sensitivity. Although x-ray and proton probes are the standard laser-generated diagnostic, there is another laser-generated probe that has seen little use: namely, relativistic electrons. Small-scale high-energy-density (HED) research facilities have performed electron radiography of ultrafast laser–plasma interactions,[6] but this capability has never before been extended to kJ- or MJ-class facilities. The work presented in this summary builds upon previous electron radiography (eRad) work using radio-frequency (rf) linear accelerators[7–9] and small-scale lasers[6–10] and extends it to kJ-class facilities via the already available picosecond lasers for electron-beam generation using a laser-plasma accelerator (LPA).[11,12]

Here, we report the first single-shot eRad images using an electron beam from a 100-J-class LPA. Both contact and projection radiography images of static targets were obtained in materials ranging from plastic to tungsten, and resolutions as good as 90-μm were achieved. This work lays the foundation for future electron radiography of laser-driven targets at kJ- and MJ-class facilities.

Radio-frequency–powered linear accelerators generate monochromatic, low-emittance electron beams suitable for high-quality electron radiography.[7–9] Such systems are rarely available, however, at the same facilities as large HED drivers and cannot easily be installed for experiments due to cost and space constraints. Nevertheless, these HED facilities often have ps lasers available, such as the OMEGA EP, NIF-ARC, PETAL, and Z-Petawatt lasers, which can be used to efficiently generate relativistic electron beams via LPA techniques.[11] This method could allow electron beams to be generated for radiography without needing to add a large and costly rf linear accelerator to an HED facility. A laser-driven eRad system also possesses the temporal characteristics that could make it an ideal diagnostic of other picosecond-scale processes for which linear accelerators do not provide sufficient instantaneous electron flux.

Electron radiography provides a complementary probe to existing x-ray and proton radiography techniques. Unlike laser-generated protons, laser-generated electrons are able to penetrate more material at a given energy. For example, a typical laser-generated 15-MeV proton will be fully stopped by ~2 mm of plastic at standard density and temperature, while a 15-MeV electron will require multiple centimeters of plastic to be fully stopped.[13] Relativistic electrons are also more sensitive to magnetic fields than protons for a given energy, but less sensitive to electric fields. This makes electrons an excellent complement to protons for radiography of electromagnetic fields.

The experiments were performed using the OMEGA EP LPA electron beam[11] and performed in both contact and projection radiography configurations (see Fig. 1).

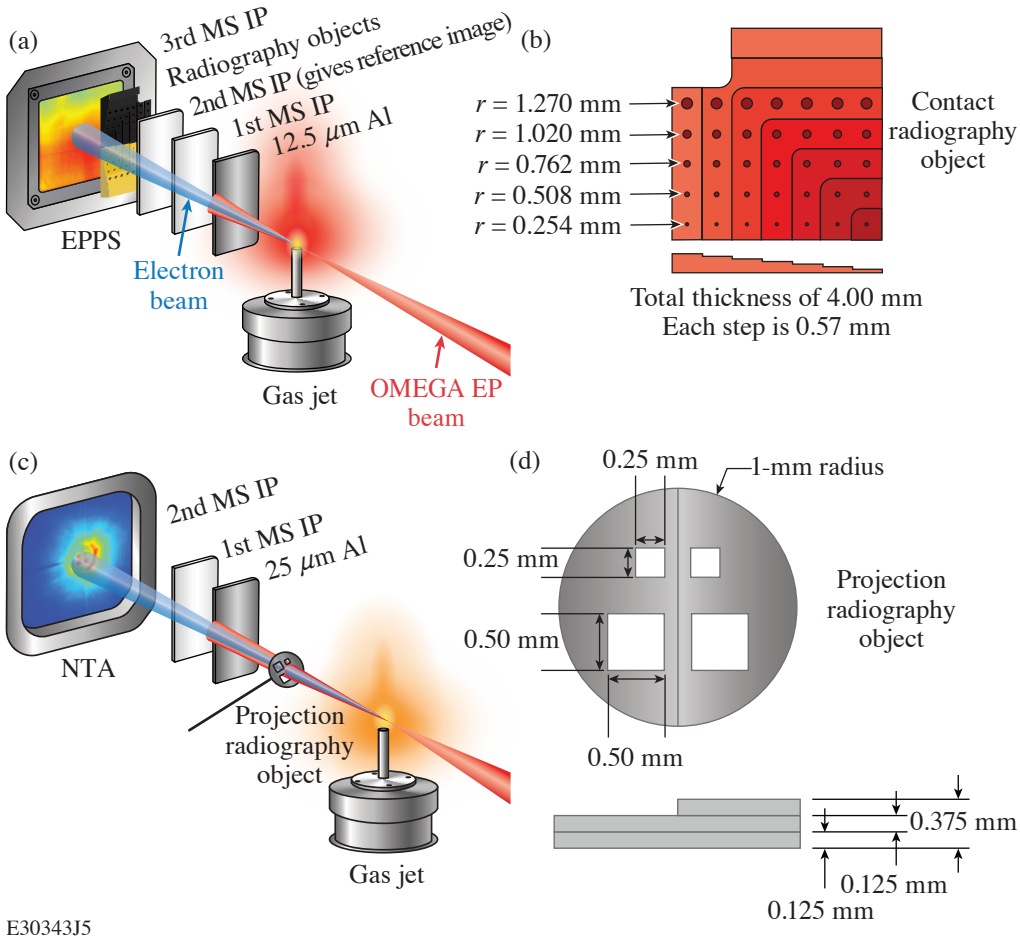

Figure 1
(a) Experimental setup for contact LPA eRad using radiography test objects (b) placed directly onto image plates and (c) projection LPA eRad using 2-mm-diam radiography test objects (d) offset from the image plates by distances ranging from 3.58 to 33.58 cm. MS IP: MS image plate; EPPS: electron–positron–proton spectrometer; NTA: near target arm.

Objects ranging from plastic to tungsten were radiographed at a wide variety of distances and thicknesses. This allowed testing the effect of target Z, density, thickness, and target magnification. The results of contact radiography can be seen in Fig. 2 and projection radiography in Fig. 3.

Resolutions nearing 90 μm were seen, but with little variation in magnification or target material. The resolution degraded with target thickness as expected, but nearly 4 mm of tungsten were able to be radiographed successfully. This shows the extreme penetrative capability of this new diagnostic platform. Laser-induced electric fields in projection radiography were also measured and found to be ~1 GV/m, which is in line with previous literature on the topic.[14]

This material is based upon work supported by the Department of Energy National Nuclear Security Administration under Award Number DE-NA0003856, the University of Rochester, and the New York State Energy Research and Development Authority.

1. E. L. Dewald *et al.*, Rev. Sci. Instrum. **89**, 10G108 (2018).
2. C. Courtois *et al.*, Phys. Plasmas **18**, 023101 (2011).
3. J. R. Rygg *et al.*, Science **319**, 1223 (2008).

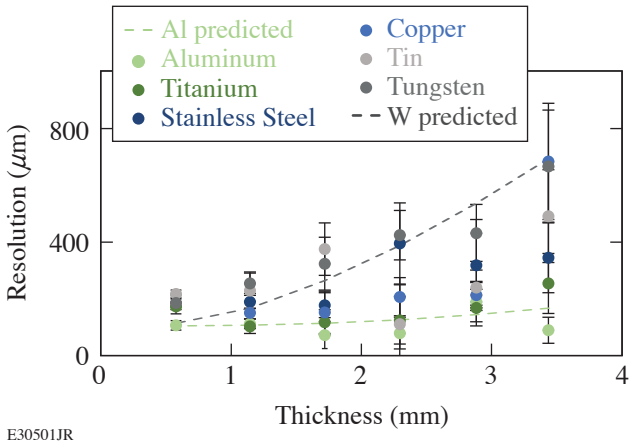

Figure 2
Average measured resolution of contact radiography test object versus target thickness. Theoretical predictions[15] for the tungsten and aluminum are included to guide the eye at the extremes of contact radiography test object *Z* numbers. The error bars are calculated using standard deviation between any repeat radiographs of the same target.

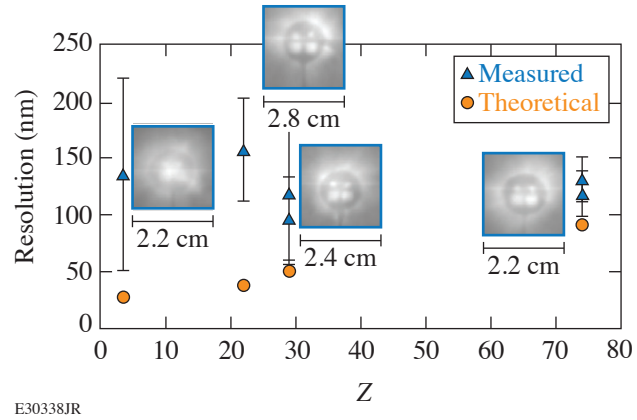

Figure 3
Resolution versus atomic number (*Z*) of the target material for the projection configuration when the image plate was 8 cm from the location of the best laser focus. Each data point has the radiograph recorded on the image plate next to it. Resolution is measured at the edges of each hole in the object as well as the outer edge. Error bars were calculated via the standard deviation between the resolution measurements on the same object.

4. A. B. Zylstra *et al.*, Rev. Sci. Instrum. **83**, 013511 (2012).
5. C. K. Li *et al.*, Phys. Plasmas **16**, 056304 (2009).
6. W. Schumaker *et al.*, Phys. Rev. Lett. **110**, 015003 (2013).
7. F. E. Merrill, Laser Part. Beams **33**, 425 (2015).
8. F. E. Merrill *et al.*, Appl. Phys. Lett. **112**, 144103 (2018).
9. F. Merrill *et al.*, Nucl. Instrum. Methods Phys. Res. B **261**, 382 (2007).
10. D. Hazra *et al.*, Phys. Rev. Accel. Beams **22**, 074701 (2019).
11. J. L. Shaw *et al.*, Sci. Rep. **11**, 7498 (2021).
12. F. Albert *et al.*, Nucl. Fusion **59**, 032003 (2018).
13. M. J. Berger *et al.*, (2017), *ESTAR*, *PSTAR*, and *ASTAR*: Computer Programs for Calculating Stopping-Power and Range Tables for Electrons, Protons, and Helium Ions (Ver. 2.0.1). [Online] Available: https://www.nist.gov/pml/stopping-power-range-tables-electrons-protons-and-helium-ions [17 August 2018].
14. J. L. Dubois *et al.*, Phys. Rev. E **89**, 013102 (2014).
15. A. Nassiri, Argonne National Laboratory, Urbana, IL, Report LA-165 (1991).

Development of a Hardened THz Energy Meter for Use on the Kilojoule-Scale, Short-Pulse OMEGA EP Laser

G. Bruhaug,[1,2] H. G. Rinderknecht,[1] Y. E,[3] M. S. Wei,[1] R. B. Brannon,[1] D. Guy,[1] R. G. Peck,[1] N. Landis,[1] G. Brent,[1] R. Fairbanks,[1] C. McAtee,[1] T. Walker,[1] T. Buczek,[1] M. Krieger,[1] M. H. Romanofsky,[1] C. Mileham,[1] K. G. Francis,[3] X. C. Zhang,[3] G. W. Collins,[1,2,4] and J. R. Rygg[1,2,4]

[1]Laboratory for Laser Energetics, University of Rochester
[2]Department of Mechanical Engineering, University of Rochester
[3]The Institute of Optics, University of Rochester
[4]Department of Physics and Astronomy, University of Rochester

Terahertz radiation occupies the frequency range between microwave and infrared radiation, making it a unique pump and probe of matter that interacts with matter in neither a purely photonic nor a bulk electronic fashion.[1–3] Because of the unique nature of THz radiation, there is a large interest in high-power sources for nonlinear time-domain spectroscopy and relativistic light–matter interactions at the extremes of low frequency;[1,3] however, the generation of such THz pulses is extremely difficult with traditional methods. Recent work with laser-plasma THz generation has shown great promise in scaling THz pulses to the terawatt and >100-mJ scale using ps, kJ-scale lasers to drive solid, liquid, or gaseous targets.[1] To maximize the THz power and pulse energy, lasers with both high energy (kJ) and high intensity (>10^{18} W/cm^2) must be used. These lasers are most commonly single shot and are well known for their immense electromagnetic pulse (EMP),[4] hard x-ray,[5] and charged-particle generation.[6] The OMEGA EP laser is especially challenging due to the peak EMP field measured being one of the highest seen on any laser (~500 kV/m) (Ref. 4). This adds to the already challenging task of THz detection due to the low efficiency (average of 0.1%) of laser THz generation in these systems. All available THz detection methods rely on electronics,[2] further compounding the EMP noise issue in these experiments.

This summary outlines the development of a ten-inch manipulator (TIM)–mounted THz energy meter, known as a THz background/energy meter (TBEM), for use on the kilojoule-class OMEGA EP laser and the associated challenges with the development of this detector. The TBEM is a broadband (0.3- to 10-THz or 1-mm to 30-μm) energy meter based on THz-sensitive pyrometers and capable of detecting broadband THz pulses as weak as ~50 μJ emitted in 4π or as strong as ~2 J emitted in 4π before suffering saturation of the detection element.

TBEM is a 112.5-cm-long, 20.9-cm-wide, TIM-mounted diagnostic weighing 33.1 kg primarily due to the inclusion of 19.8 kg of tungsten radiation shielding. As shown in Fig. 1, the diagnostic consists of a light-tight aluminum chassis with a front-mounted TPX[7] (THz and optical light transmissive) lens and filter pack extending 36.8 cm from the main body. This front lens allows for THz radiation to be collected 15 cm from target chamber center, maximizing the sensitivity of the detector. In front of the lens is a removable high-resistivity silicon wafer that acts as a THz-transmissive blast shield. The filter pack attached to the front lens can hold THz filters to alter the portion of the spectrum sampled and irises to reduce the amount of THz radiation sampled while operated in the forward position. This lens and filter assembly can also be removed and the detector operated while retracted from target chamber to further protect the electronics from EMP and radiation. A schematic of the detector and the THz transmission spectrum of the optical components can be seen in Fig. 2.

THz detection is accomplished by using commercially available nanojoule-sensitive pyrometers,[8] which are commonly used for commercial and scientific THz detection. A pyrometer is a broadband-sensitive energy meter that relies on the pyroelectric

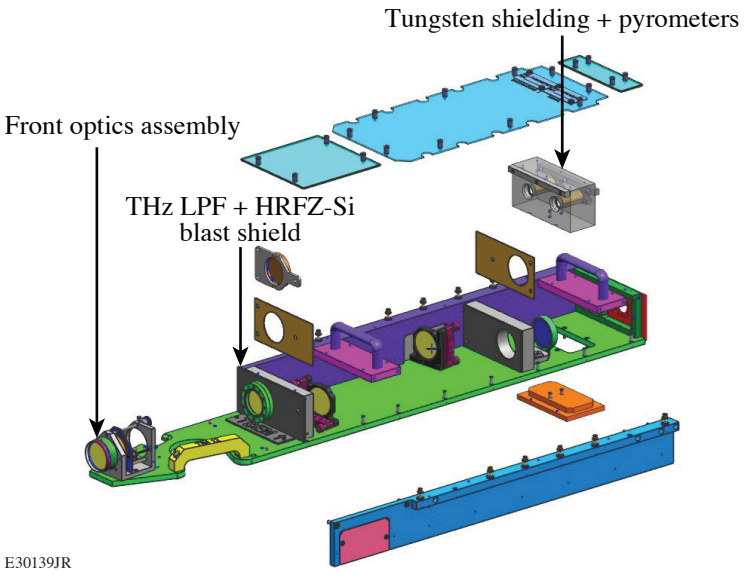

Figure 1
Expanded view of a TBEM detector assembly. LPF: low-pass filter; HRFZ: high-resistivity silicon.

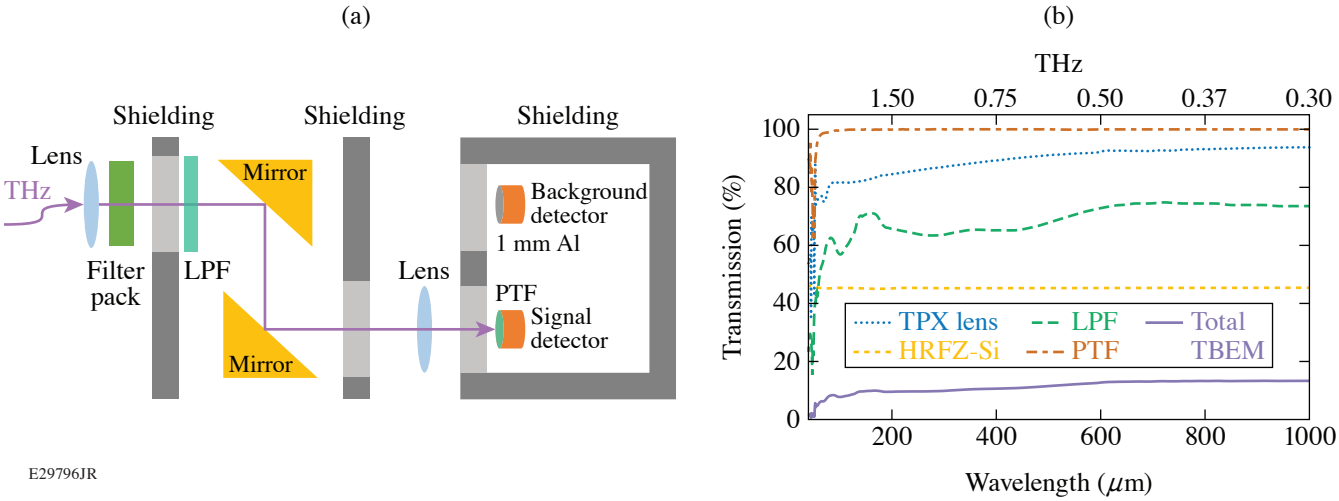

Figure 2
(a) Full optical path of the TBEM detector and (b) THz transmission of the optical components and full detector.[7,9] PTF: polytetrafluoroethylene.

effect to detect a change in energy deposition.[2,8] The sensor is built in a series of layers similar to a capacitor with two electrodes around an inner layer of pyroelectric material. One electrode is darkened to best absorb the wavelength range of interest. Upon pulsed irradiation, the pyrometer will heat up and the polarization direction in the pyroelectric material will change. A charge disparity then develops across the pyroelectric crystal, and a voltage pulse is generated that is proportional to the amount of energy deposited into the sensor.

The initial concept for TBEM was built and tested for use on the Multi-Terawatt (MTW) laser to support THz target design campaigns. The results have been extremely promising. Four campaigns were then undertaken on OMEGA EP to test the TBEM detectors with the final two campaigns showing repeatable THz detection. The first campaign did not have the full complement of radiation shielding in place and suffered from massive x-ray and EMP noise problems (Fig. 3.). The second campaign had the radiation and EMP shielding upgraded and showed more-promising results. As with MTW, it was found that using plastic target stalks reduced the noise, but in this case the reduction was not enough to observe THz signal above the background.

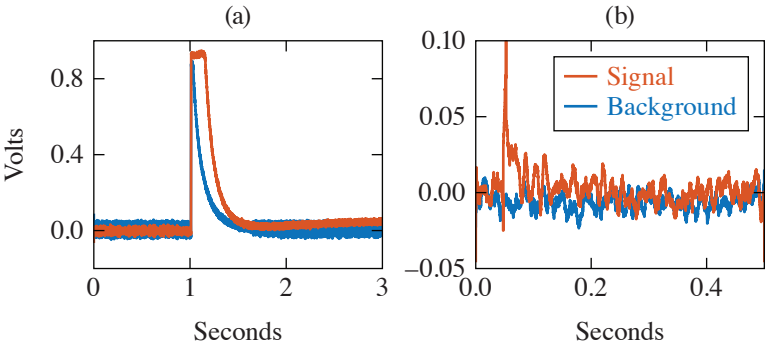

Figure 3
Example of data taken from one TBEM on the (a) first and (b) second OMEGA EP THz campaigns with ~100 J of laser energy used (July 2021 and March 2022, respectively). EMP and x rays, caused by extremely high background noise, can be seen in (a) when there was less shielding present on the detector.

For the third and fourth campaigns, the detectors were upgraded with the full complement of tungsten shielding described above, as well as improved cable EMP shielding. THz generation was reliably detected on both foil and microchannel targets with laser energies ranging from 100 to 500 J. Example THz detections from these experiments can be seen in Fig. 4.

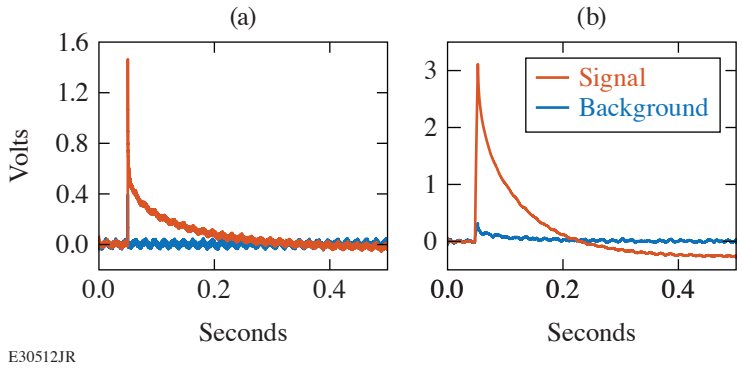

Figure 4
Example of data taken from one TBEM on third and fourth OMEGA EP campaign (June 2022): (a) from a foil irradiated with ~100 J of laser energy and (b) from a microchannel target irradiated with ~300 J of laser energy.

The THz yields were estimated to be ~130 mJ from the foil target and ~300 mJ from the microchannel target, which are in line with the estimated generation efficiencies of these target types for the given laser energy.[1,10] The additional EMP shielding on the pyrometer wiring was found to be crucial for the most energetic laser shots.

This material is based upon work supported by the Department of Energy National Nuclear Security Administration under Award Number DE-NA0003856, the University of Rochester, and the New York State Energy Research and Development Authority.

1. G. Liao *et al.*, Proc. Natl. Acad. Sci. **116**, 3994 (2019).
2. F. Sizov, Opto-Electronics Rev. **18**, 10 (2009); 223(E) (2010).
3. H. A. Hafez *et al.*, J. Opt. **18**, 093004 (2016).
4. S. Mondal *et al.*, J. Opt. Soc. Am. B **35**, A93 (2018).
5. C. Courtois *et al.*, Phys. Plasmas **18**, 023101 (2011).
6. J. L. Shaw *et al.*, Sci. Rep. **11**, 7498 (2021).
7. V. E. Rogalin, I. A. Kaplunov, and G. I. Kropotov, Opt. Spectrosc. **125**, 1053 (2018).
8. Gentec-EO, Accessed 23 March 2022, https://www.gentec-eo.com/products/qs5-thz-bl.
9. M. S. Kitai *et al.*, Radiophys. Quantum Electron. **57**, 881 (2015).
10. L. Yi and T. Fülöp, Phys. Rev. Lett. **123**, 094801 (2019).

Single-Shot Cross-Correlation of Counter-Propagating, Short Optical Pulses Using Random Quasi-Phase Matching

C. Dorrer and J. L. Shaw

Laboratory for Laser Energetics, University of Rochester

A single-shot cross-correlator based on the sum–frequency generation (SFG) of counter-propagating beams in SBN61 ($Sr_xBa_{1-x}Nb_2O_6$ with $x = 0.61$) has been demonstrated.[1] Random quasi-phase matching in disordered ferroelectric crystals such as SBN61 allows for nonlinear interactions in nonstandard geometries, e.g., the observation of a transverse second-harmonic–generation signal resulting from two co-propagating or counter-propagating pulses.[2,3] This diagnostic measures the cross-correlation between two laser facilities, leading to the relative delay between the pulses generated by each facility on every shot. It supports their precise co-timing and the study of their relative jitter with high precision over a time range larger than 150 ps.

The cross-correlation of optical pulses with instantaneous power profile $P_A(t)$ and $P_B(t)$ generated by the Multi-Terawatt (MTW) laser ($\lambda_A = 1053$ nm) and the idler of the MTW-OPAL laser ($\lambda_B = 1170$ nm) [Fig. 1(a)] were measured. The two beams are focused in a counter-propagating configuration in the underdense-plasma target chamber designed for Raman-amplification studies. Transverse SFG in an SBN61 maps out the cross-correlation signal $C_{AB}(\tau) = \int P_A(t)P_B(t-\tau)\mathrm{d}t$, where τ is the relative delay between the two pulses onto the longitudinal spatial coordinate. The generated transverse signal is re-imaged onto a camera, therefore allowing for single-shot cross-correlation acquisition over a range of relative delay set by the crystal length and group velocity of the two pulses, resulting in more than 150 ps for the 10-mm crystal used in these experiments. Both pulses generate a time-integrated transverse second-harmonic–generation signal at 526.5 nm and 585 nm, respectively, adding a background on the cross-correlation signal of interest [Fig. 1(b)]. Background-free acquisition with enhanced signal-to-noise ratio is obtained using a bandpass filter at the SFG wavelength (~550 nm). The cross-correlator has been used to co-time the two laser facilities at the common focal region where Raman-amplification in a gas jet are conducted. It has also provided valuable information on the relative jitter between the two laser facilities and for pulse-shape optimization.

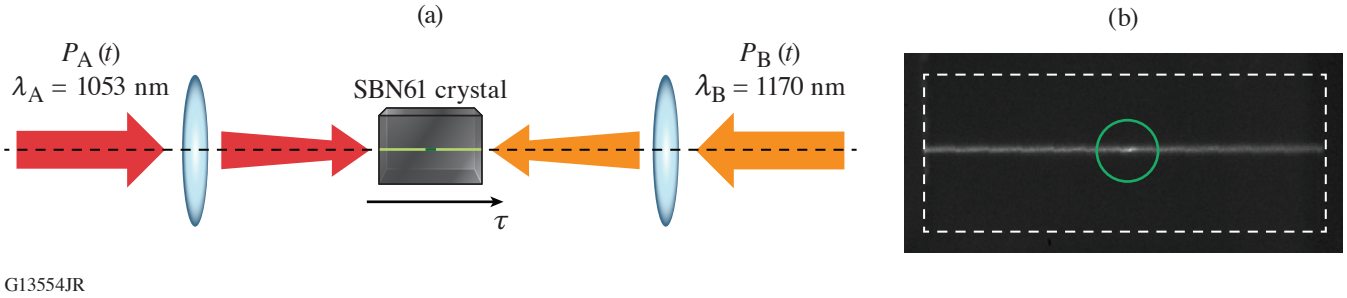

Figure 1
(a) Experimental setup. (b) Example of a signal acquired by the camera, without spectral filtering. The green circle identifies the cross-correlation signal, which is the only signal acquired by the camera when a bandpass filter at the SFG wavelength is used to remove the time-integrated SHG signals.

Fourier processing of the measured cross-correlation trace allows for extraction of its delay relative to reference and retiming for averaging purposes (Fig. 2). The collection of relative delays over a large number of shots represents the statistics of the jitter between the two laser facilities. As an example of application, Fig. 3(a) displays histograms of the relative delay between the two

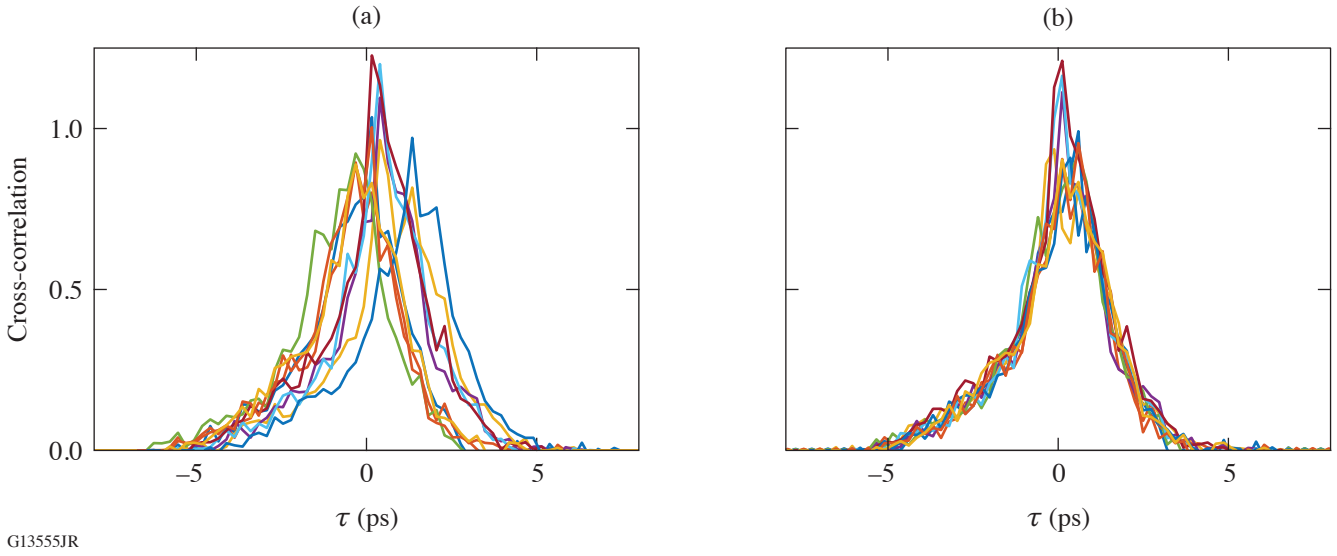

Figure 2
A set of ten measured single-shot cross-correlations (a) before and (b) after retiming.

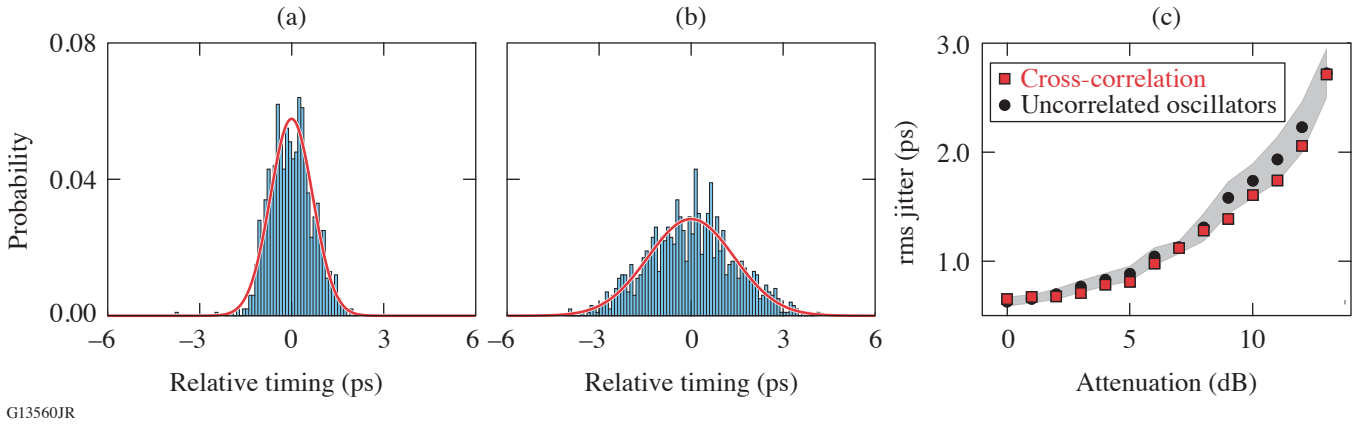

Figure 3
Probability histograms of the delay between the two laser sources measured (a) with a nominal synchronization-photodiode signal and (b) with a 9-dB attenuation. The bin size is 0.1 ps in all cases. A normal distribution with identical standard deviation has been added to (a) and (b) (red lines). On (c), the rms jitter determined from the measured cross-correlations (red squares) is compared to the rms jitter calculated from the jitter reported by the synchronization unit of the two mode-locked lasers (black circles, with confidence interval indicated by the shaded area).

facilities measured for three different synchronization configurations of the mode-locked laser seeding the MTW laser. Attenuation of its reference signal leads to poorer synchronization of that laser to the LLE reference frequency, thereby inducing a higher jitter for that particular laser and for the relative delay between the two facilities. The rms jitter calculated from the measured cross-correlations is in good agreement with the jitter calculated from the jitter of each mode-locked oscillator [Fig. 3(b)].

This simple approach supports the determination of the relative timing between two laser sources on a single shot, which is particularly important for low-repetition-rate sources. It also offers a direct approach to single-shot determination of the time-varying instantaneous power of an optical pulse by cross-correlation with a shorter ancillary pulse. Such determination is important for the development and optimization of chirped-pulse–amplification systems delivering pulses close to their Fourier transform–limited duration, but also for systems delivering pulses with a coherence time much shorter than their duration, e.g.,

incoherent pulses. Accurate single-shot temporal characterization with high resolution and long record length is paramount for safe operation and optimal interaction with the targets. SBN crystals as long as 20 mm are commercially available, leading to a 300-ps temporal window. Longer acquisition windows can be obtained by combining multiple crystals or implementing multiple passes in a single crystal with different relative delays between the two sources. Cross-correlations in disordered nonlinear crystals can also support the optimization of spatial overlap and timing in complex experiments involving multiple laser beams, such as the counter-propagating geometry used for Raman amplification and the crossing of beams at large angles used for Compton scattering.

This material is based upon work supported by the Department of Energy National Nuclear Security Administration under Award Number DE-NA0003856, the Department of Energy Office of Science under Award Number DE-SC0016253, the University of Rochester, and the New York State Energy Research and Development Authority. The authors thank I. A. Begishev, S. Bucht, R. Roides, M. V. Ambat, and K. McMillen for experimental assistance during this campaign.

1. C. Dorrer and J. L. Shaw, Opt. Express **30**, 16,677 (2022).
2. J. Trull *et al.*, Opt. Express **15**, 15,868 (2007).
3. R. Fischer *et al.*, Appl. Phys. Lett. **91**, 031104 (2007).

Multiparameter Laser Performance Characterization of Liquid Crystals for Polarization Control Devices in the Nanosecond Regime

K. L. Marshall,[1] K. R.P. Kafka,[1] N. D. Urban,[1] J. U. Wallace,[1,2] and S. G. Demos[1]

[1]Laboratory for Laser Energetics, University of Rochester
[2]Department of Chemistry, D'Youville College

The interactions of liquid crystals (LC's) with polarized light have been studied widely and have spawned numerous device applications, including the fabrication of optical elements for high-power and large-aperture laser systems. Such devices have numerous advantages that include scalability to large apertures, cost effectiveness, high optical quality and contrast, broad angular tolerance, and laser-induced–damage thresholds (LIDT's) for optimized materials at 1054 nm of >30 J/cm^2, 3 J/cm^2, and 1 J/cm^2 at 1-ns, 10-ps, and 600-fs pulse durations, respectively.[1,2] Evaluation of the LIDT of LC materials has been performed historically in long-path-length LC cells (50 to 100 μm) to gain an understanding of the LC material's behavior under exposure to high-energy laser pulses without competing physicochemical interactions with surface-anchoring layers and conditions (LC elastic constants, boundary molecular tilt angle, alignment materials chemistry and application methods[2,3]). Although useful for screening LC materials by chemical class to determine general laser survivability, such long-path-length testing gives very little insight on how the LC's LIDT may be affected in device applications where the LC molecules are constrained in a monodomain alignment state induced by contact with substrates bearing a polymer alignment layer (e.g., wave plates, mirrors, and beam shapers). In such cases, variations in optical behavior as a function of laser beam polarization due to molecular orientation, chemical interactions, or generation of electric-field enhancements in the LC material are a distinct possibility.[4–6] This summary reports on the first study of the nanosecond-pulsed LIDT's dependence on incident polarization for several optical devices employing nematic and chiral-nematic LC's oriented by surface alignment layers. Accelerated lifetime testing was also performed to characterize the ability of these materials and devices to maintain their performance under multi-pulse irradiation with increasing laser fluence at both 1053 nm and 351 nm (Ref. 7).

Figure 1 shows generic molecular structures of LC components with differing degrees of π-electron density (saturation) that were evaluated for their multipulse laser damage behavior in optical element configurations typically used in high-peak-power lasers (e.g., circular polarizers and wave plates), where the LC molecular director, which defines the average long-range orientation of the LC molecular axes in the bulk, is constrained to adopt a monodomain or nearly monodomain orientation.

A pulsed nanosecond laser system operated at either its fundamental wavelength (1053 nm) or the third harmonic (351 nm) was used along with a novel detection system employing a polarization-sensitive camera to detect both the onset of performance degradation and classical LIDT of several LC mixture compositions in both circular polarizers and wave-plate device geometries. These measurements were designed to explore a "laser-induced functional threshold" (LIFT), defined as a reduction in one or more system-defined, key device functional parameters (e.g., transmission, reflection, birefringence, polarization rotation, contrast) that may occur at fluences lower than those required to produce the visible and permanent evidence of material modification typically defined as laser-induced damage. The point at which the value of LIFT drops below a system-defined tolerance metric is taken as the LIFT "trigger point." For the purposes of this study, the LIFT trigger pointy was a reduction in transmission to <98% (Ref. 7).

Testing of these LC materials at 1053 nm and 351 nm showed that their LIDT behavior depends significantly on the incident polarization state for laser light encountering the input surface of the LC test device at near-normal incidence (7°). For LC circular polarizer devices, the LIDT varied as a function of incident circular-polarization handedness by a factor of 30% to 80% for a given sample (Fig. 2). It appears that an angular dependence of high-peak-power LIDT on incident polarization in LC materials

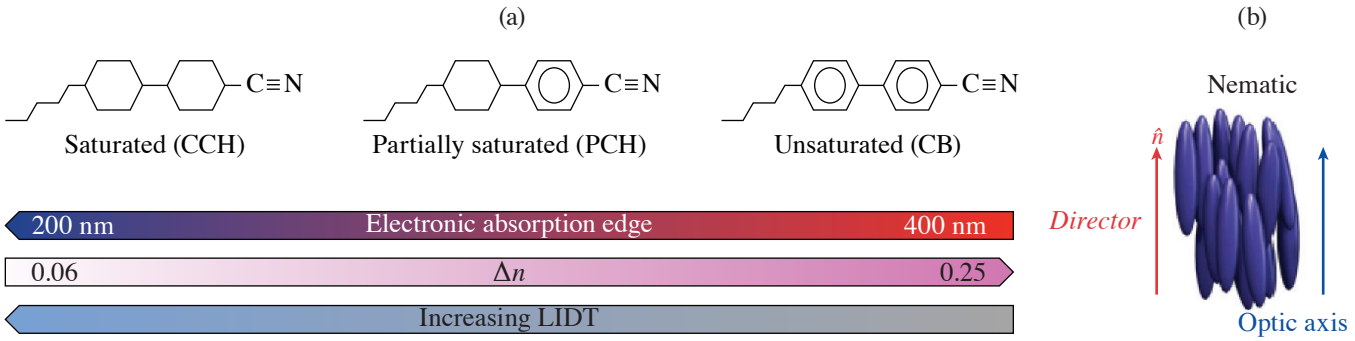

Figure 1
(a) Molecular structures for the three classes of LC compounds evaluated and a graphical representation of the dependence of optical absorbance, birefringence, and laser damage with respect to these classes. (b) Molecular ordering in the nematic LC phase. For this class of LC materials, both the LC director and the optic axis are parallell to the molecular axis.

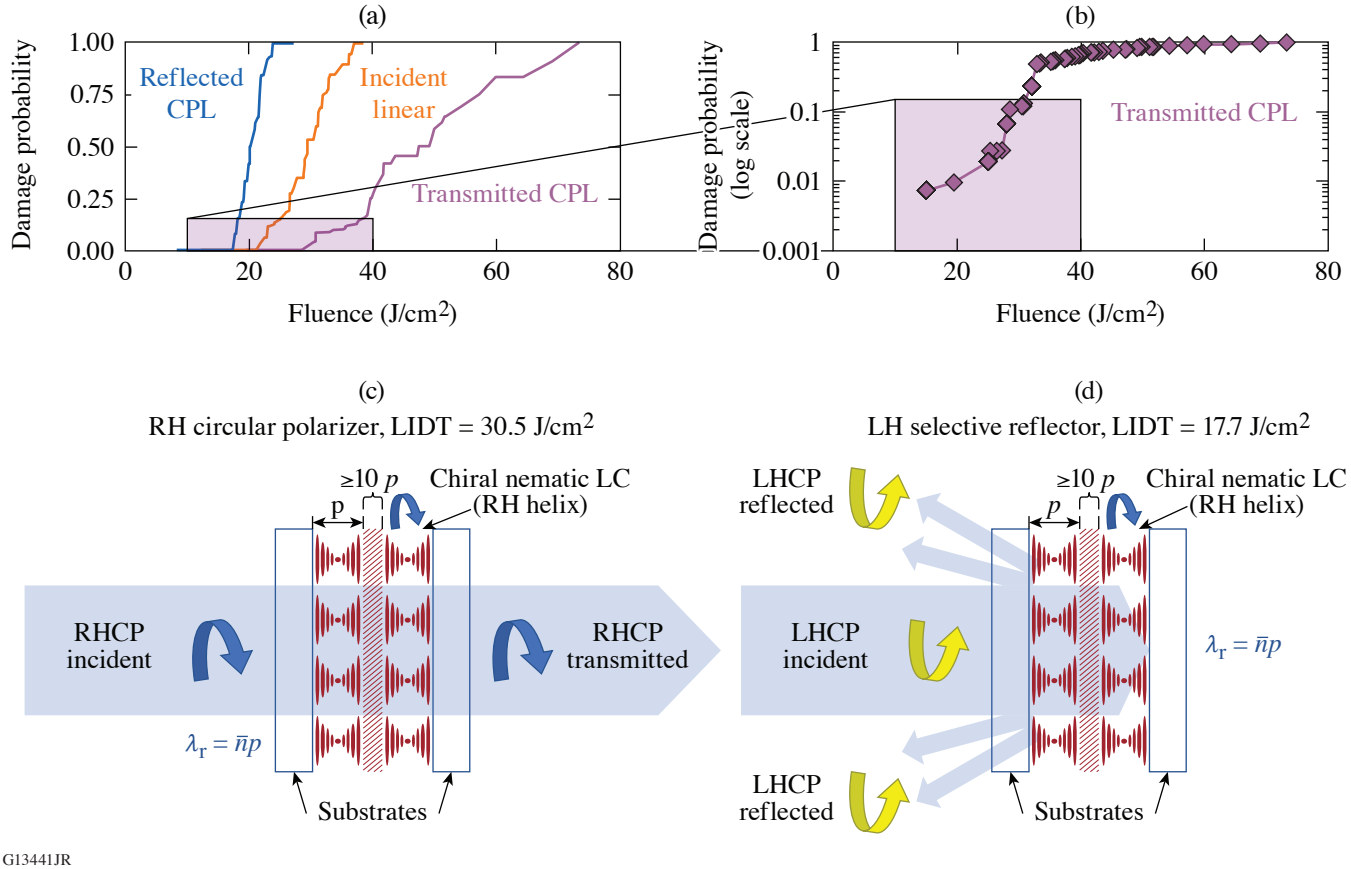

Figure 2
(a) Damage probabilities for the chiral-nematic LC circular polarizer/isolator device as a function of 1053-nm, 1.4-ns laser fluence and incident polarization; (b) damage probabilities for transmitted circularly polarized light pulses incident on the device at low fluence [corresponding to the inset in Fig. 2(a)]. The data, plotted on a logarithmic scale, represent an additional 250 sites of 1-on-1 damage data collected by line-scanning the sample; [(c),(d)] the interaction of circularly polarized light of opposite handedness on the LC structure, along with the representative LIDT thresholds. For (c), incident circular polarized light with the same twist sense as the LC helix (right-handed) is transmitted, whereas in (d) for the same device, incident circular polarization of the opposite handedness (left-handed) is selectively reflected due to Bragg scattering. A cell thickness of at least ten pitch lengths (p), indicated by the area filled with diagonal slashes near the center of the cell, is required to observe these effects with sufficient magnitude for device applications.

has not been reported previously. The results suggest that multipulse functionality was best preserved in LC devices having the highest degree of saturation.

Certain compositions of saturated, UV transparent nematic LC mixtures evaluated in a wave-plate geometry displayed remarkable robustness in LIFT testing at 351 nm, with one CCH-based LC mixture (LLE1202) being able to survive as many as 1000 1-ns pulses at 2 J/cm^2 (5-Hz repetition rate) before displaying any significant change in its functional performance (Fig. 3). The LIDT was seen to vary as a function of input polarization by 30% to 80% within the same device, while the multi-pulse LIFT depends on irradiation conditions such as laser fluence and wavelength.

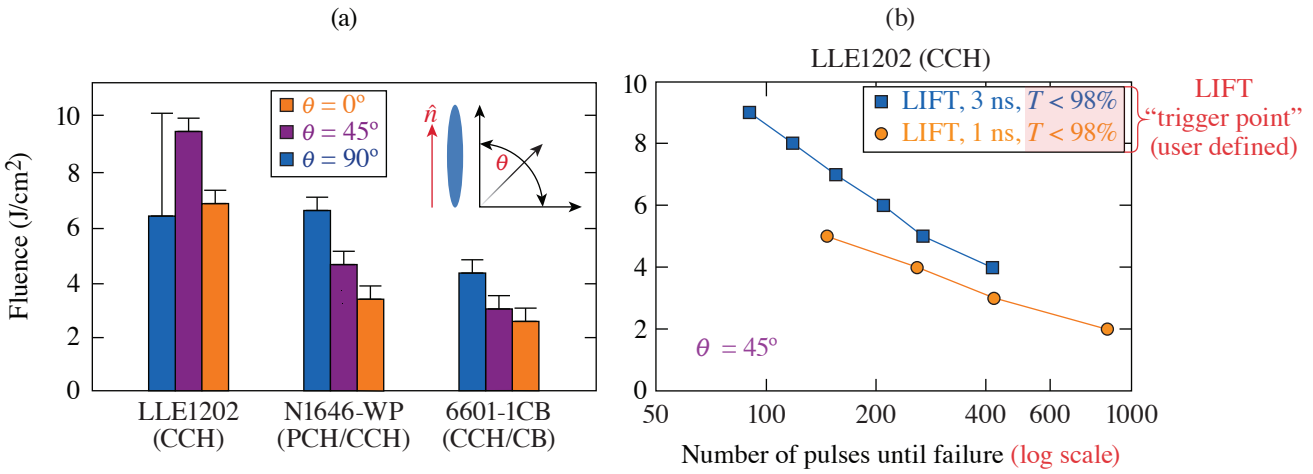

Figure 3
(a) LIDT at 351-nm, 1-ns pulse duration as a function of incident linear polarization angle with respect to the LC director. Uncertainty bars extend to the nominal 0% and 100% damage probability fluences. (b). LIFT results for LLE1210 at 351 nm for both 1-ns and 3-ns laser pulses delivered at a 5-Hz repetition rate. The high saturation of this CCH-based LC material allows it to withstand nearly 1000 pulses at 2 J/cm^2. The inset in (a) shows the orientation of the LC director with respect to the incident laser polarization.

These promising results highlight the potential of this class of LC materials in nanosecond-regime, high-peak-power lasers such as OMEGA for applications as polarization control and polarization-smoothing optics. Another distinct advantage of LC optics is that in the event they do sustain damage, they can be refurbished and reinstalled in a laser system with a relatively low cost of materials and effort. The results also illustrate the necessity of taking the molecular structure and electron delocalization of LC mesogens into account when designing new materials for such emerging applications.

This material is based upon work supported by the Department of Energy National Nuclear Security Administration under Award Number DE-NA0003856, the University of Rochester, and the New York State Energy Research and Development Authority.

1. S. D. Jacobs *et al.*, J. Opt. Soc. Am. B **5**, 1962 (1988).
2. T. Z. Kosc *et al.*, Sci. Rep. **9**, 16435 (2019).
3. A. Schmid *et al.*, Mol. Cryst. Liq. Cryst. **207**, 33 (1991).
4. J. Lu *et al.*, J. Appl. Phys. **80**, 5028 (1996).
5. C.-H. Wen, S. Gauza, and S.-T. Wu, J. Soc. Inf. Disp. **13**, 805 (2005).
6. Y. H. Wang *et al.*, IEICE Trans. Electron. **E-83-C**, 1553 (2000).
7. K. L. Marshall *et al.*, Sci. Rep. **12**, 10969 (2022).

Influence of Heat Treatments on Near-Surface Tritium Concentration Profiles

M. Sharpe, W. T. Shmayda, and J. J. Ruby

Laboratory for Laser Energetics, University of Rochester

At room temperature, tritium interacts with all metals (aluminum, copper, stainless steel, etc.) to some extent.[1] Such interactions can lead to a buildup of tritium on the metal's surface and just under the surface of the metal.[2–4] The presence of high tritium concentrations in these locations is a large concern for all tritium-handling facilities. These facilities contain a large quantity of metals that routinely come in contact with tritium gas. Over time, tritium buildup in these metals can lead to radiological hazards and high waste disposal costs. To mitigate tritium contamination in metals, it is common to heat the metal to high temperatures.[5,6] The details of this thermal desorption method (maximum temperature, dwell time, etc.) depend on the contaminated metal as well as the expected tritium dosing. To date, however, no systematic study has been performed showing how tritium migrates within the metal as a result of a chosen thermal desorption temperature and time. The current work addresses this gap in knowledge by showing how the tritium distribution within stainless steel, type 316 (SS316) responds to temperatures between 100°C and 300°C. The surface and near-surface concentrations were measured using a combination of a $ZnCl_2$ wash and sequential acid etching to reveal a high-resolution tritium concentration profile. Tritium deeper within the metal was measured using high-temperature thermal desorption to remove residual tritium from the bulk metal.

To measure the effect of heating on the tritium distribution within SS316, a series of samples were first exposed to tritium gas for 8 h at 25°C. Each sample was then heated to temperatures between 100°C and 300°C for 120 min under a stagnant, dry argon atmosphere. The tritium distribution was then measured by performing a $ZnCl_2$ wash first to remove surface tritium. Following this wash, the samples were then acid etched to reveal the tritium concentrations immediately under the surface (<100 μm). Finally, the residual tritium deeper in the samples was measured using high-temperature thermal desorption (550°C for 4 h). For comparison, several control samples were not heated prior to the $ZnCl_2$ wash, acid etching, and high temperature thermal desorption procedures.

The resulting concentration profiles (Fig. 1) show two notable deviations from the control samples. First, the surface activity decreases significantly with increasing preheating temperature as expected. Second, the near-surface (1 nm to 1 μm) tritium concentrations differ for only the 200°C and 300°C cases; the 100°C and 150°C preheating appears to have had no influence on the near-surface concentrations. Heating to temperatures greater than or equal to 200°C resulted in decreased concentrations in the near surface (~0.1 μm).

Integrating the concentration profiles shown in Fig. 1 reveals the total tritium remaining within each region of the SS316 sample. These integrals (Fig. 2) show that surface-bound tritium decreases with increasing preheating temperature, while tritium deeper in the metal (>1 μm) increases. Tritium quantities in the intermediate region (<1 μm) remain constant until the sample is heated to 200°C or greater. Above 200°C, the quantity of tritium decreases to a new, lower value.

These data indicate how tritium migrates within SS316 in response to moderate heating. Heating SS316 causes tritium to desorb from the surface and migrate deeper into the metal. Taking the median values of the data shown in Fig. 2, the quantity of tritium "lost" from the surface is greater than the tritium activity released from the surface. This indicates that tritium preferentially migrates into the metal as opposed to desorbing from the surface. Desorption from the surface is possibly not as favorable due to the gas conditions. The samples were kept under dry argon during the preheating phase. Past studies have shown that tritiated

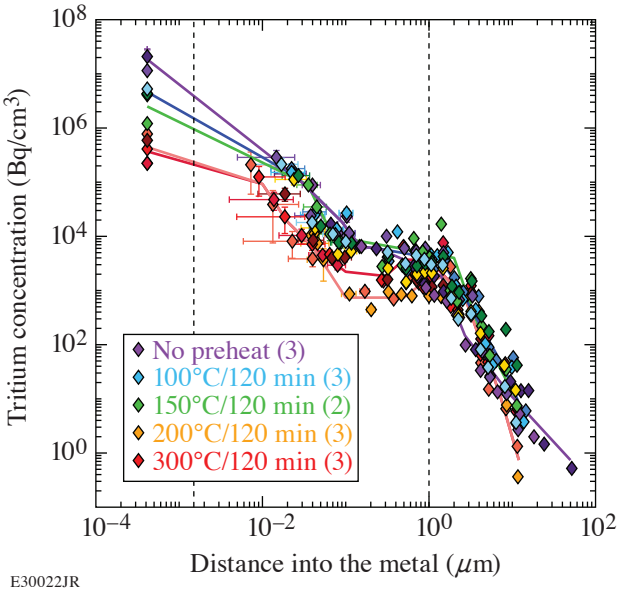

Figure 1
Tritium concentration profiles in the near surface of SS316 samples. Five preheating conditions are shown: no heating (purple), 100°C (blue), 150°C (green), 200°C (orange), and 300°C (red). Vertical dashed lines indicate different regions of the sample: surface (<1 nm), near-surface (<1 μm), and bulk (>1 μm). Each preheating condition was repeated with different SS316 samples that were exposed to tritium at the same time.

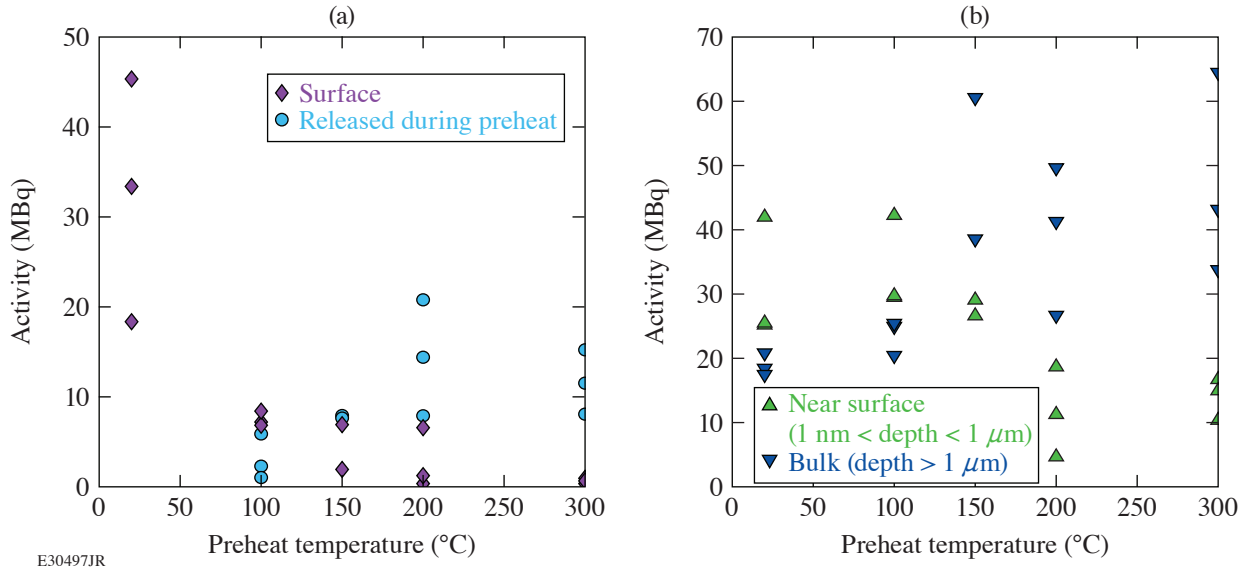

Figure 2
(a) Integrated tritium remaining on the surface and released during preheating and (b) tritium remaining in the near surface and bulk with respect to the preheating temperatures. Results from control samples are shown at 20°C.

water desorption is the primary release mechanism of tritium from SS316.[7–9] By limiting this mechanism for tritium desorption from the surface, tritium will preferentially migrate in the direction of the concentration gradient deeper into the metal.

Tritium quantities in the near surface do not appreciably change until the preheat temperature reaches 200°C (Fig. 1). These results indicate that a minimum temperature of 200°C is required to trigger near-surface tritium mobility for migration deeper into the substrate or desorption from the surface. Previous work has also demonstrated that heating SS316 to at least 200°C is required for the onset of desorption.[10,11] The increase in migration above 200°C indicates that tritium immediately below the surface is not bound at octahedral sites. The depletion of the near surface tritium and the increased desorbed tritium quantities by heating to 200°C suggests that tritium is bound in a hydrated iron (III) oxide: FeO(OH). Such binding explains three observations: First, hydrogen isotopes can be bound strongly to oxygen impurities in metals. Korzhavyi and Sandström used a density functional

theory calculation to simulate hydrogen interacting with an oxygen defect in copper.[12] Their results show a fourfold increase in the binding energy, as compared to a site without oxygen. Assuming oxygen in stainless steel has a similar effect, such deep trap states may explain the observed lack of tritium migration during the lengthy storage periods. Second, dehydration of hydrated iron (III) oxide occurs at 200°C (Ref. 13). Because tritium would be bound in the hydrate, dehydration would remove tritium from the near-surface region. Finally, dehydration may supply the oxygen and hydrogen/tritium necessary for tritiated water desorption from the surface. In this scenario, the primary pathway for tritium desorption is present even for dry inert gas atmospheres: the metal effectively supplies the water molecules for desorption.

The effect of heat treatments on the tritium distribution in SS316 samples was measured. It was found that the heating causes tritium to migrate both out of the sample and deeper into the bulk of the material. Tritium preferentially migrates deeper into the metal for temperatures less than 200°C, with very little desorbing from the surface. On reaching 200°C or above, dehydration of the hydrated iron (III) oxide occurs. The dehydration process reduces the tritium inventory in the near surface by allowing tritium to either desorb from the surface as tritiated water or diffuse deeper into the metal.

This material is based upon work supported by the Department of Energy National Nuclear Security Administration under Award Number DE-NA0003856, the University of Rochester, and the New York State Energy Research and Development Authority.

1. M. Nishikawa *et al.*, J. Nucl. Mater. **277**, 99 (2000).
2. A. Perevezentsev *et al.*, Fusion Sci. Technol. **41**, 746 (2002).
3. M. D. Sharpe *et al.*, Fusion Eng. Des. **130**, 76 (2018).
4. M. Sharpe, C. Fagan, and W. T. Shmayda, Fusion Sci. Technol. **75**, 1053 (2019).
5. A. N. Perevezentsev *et al.*, Fusion Sci. Technol. **52**, 84 (2007).
6. S. Rosanvallon *et al.*, Fusion Sci. Technol. **60**, 855 (2011).
7. K. Akaishi *et al.*, J. Vac. Sci. Technol. A **26**, 321 (2008).
8. M. J. Quinlan *et al.*, Fusion Sci. Technol. **54**, 519 (2008).
9. Y. Torikai *et al.*, Fusion Sci. Technol. **41**, 736 (2002).
10. W. T. Shmayda *et al.*, Fusion Sci. Technol. **68**, 766 (2015).
11. R.-D. Penzhorn *et al.*, Fusion Sci. Technol. **64**, 45 (2013).
12. P. A. Korzhavyi and R. Sandström, Comput. Mater. Sci. **84**, 122 (2014).
13. N. N. Greenwood and A. Earnshaw, eds. *Chemistry of the Elements*, 2nd ed. (Elsevier, New York, 1997).

Effective Mass Determination in Highly Resistive GaAs by Exploiting the Influence of a Magnetic Field on Optically Excited Transient THz Surface Emissions

G. Chen,[1,2] D. Chakraborty,[1,2] J. Cheng,[1,2] M. Mikulics,[3] C. Chimera,[4] I. Komissarov,[4] R. Adam,[5] D. E. Bürgler,[5] C. M. Schneider,[5,6] H. Hardtdegen,[3] and R. Sobolewski[1,2,4]

[1]Laboratory for Laser Energetics, University of Rochester
[2]Materials Science Graduate Program, University of Rochester
[3]Research Centre Jülich, Ernst Ruska Centre for Microscopy and Spectroscopy with Electrons, Germany
[4]Department of Electrical and Computer Engineering, University of Rochester
[5]Research Centre Jülich, Peter Grünberg Institute (PGI-6), Germany
[6]Department of Physics, University of California Davis

Generating broadband, free-space terahertz transients by pumping the surface of a semiconductor with femtosecond optical laser pulses is a well-established technique, generally called THz surface emission.[1] Several radiation models have been proposed to explain the THz surface emission such as surface depletion created by the internal electric field perpendicular to the sample surface,[2–5] nonlinear optical rectification,[6,7] and photocurrent generated by the photo-Dember effect.[8–10] It was also demonstrated that an external magnetic field applied in the plane of a semiconductor can tune the amplitude of the surface-emitted THz radiation. The enhancement of the THz amplitude was ascribed to the Lorentz force, induced by the applied magnetic field, which introduced an additional acceleration to the photocarriers.[11,12] Time-domain, nonequilibrium carrier relaxation dynamics can be characterized by an optical pump–probe spectroscopy technique,[13] which allows one to further analyze how the Lorentz force affects photocarriers and to determine the relationship between the THz transient amplitude enhancement and the semiconductor carrier mobility.

For these studies, five different, highly resistive (111)-oriented GaAs samples characterized by different mobilities and crystalline conditions were used. Namely, a standard semi-insulating GaAs wafer (SI GaAs), a semi-insulating GaAs wafer annealed at 300°C (annealed GaAs), and three nitrogen-ion–implanted GaAs specimens, implanted at an energy of 191 keV with a dose of $\sim 8 \times 10^{11}$ ions/cm^2 (Refs. 14 and 15), and, subsequently, annealed at 300°C, 350°C, and 400°C, denoted as N-GaAs 300, N-GaAs 350, and N-GaAs 400, respectively.

Experiments were performed using THz time-domain spectroscopy (THz-TDS) and optical femtosecond pump–probe spectroscopy (F-PPS). In both cases, a commercial Ti:sapphire laser that generated a train of nominal, 100-fs-wide laser pulses at 800-nm wavelength and 76-MHz repetition rate was used. In the THz-TDS setup,[16] the laser beam was split into two branches with a 90:10 power ratio. The high-power branch, after bouncing from a retroreflector mounted on a delay stage, was focused on our test GaAs sample to generate bursts of electromagnetic radiation, i.e., single-picosecond transients with the frequency spectrum extending into THz, while the low-power branch was used for the THz transient detection and focused on a commercial low-temperature–grown GaAs photoconductive (PC) THz detector with z-axis polarization sensitivity (perpendicular to the optical table).[17] A 5-mm-diam and ~10-mm-focal-length Teflon™ (polytetrafluoroethylene) lens, located between the test sample and the THz detector, collimated the transmitted THz radiation. In addition, an external magnetic field **B** was applied in the sample plane along the x axis, while the surface-emitted THz radiation was collected along the y direction, as indicated in Fig. 1. The F-PPS system was implemented to measure the nonequilibrium carrier dynamics in the samples. In this setup[18,19] optical pulses were split into two beams by a 60/40 beam splitter. Pump pulses had the higher power, and the beam was modulated with an acousto-optic modulator. The lower-power probe beam was delayed with respect to the pump by reflection from a retroreflector

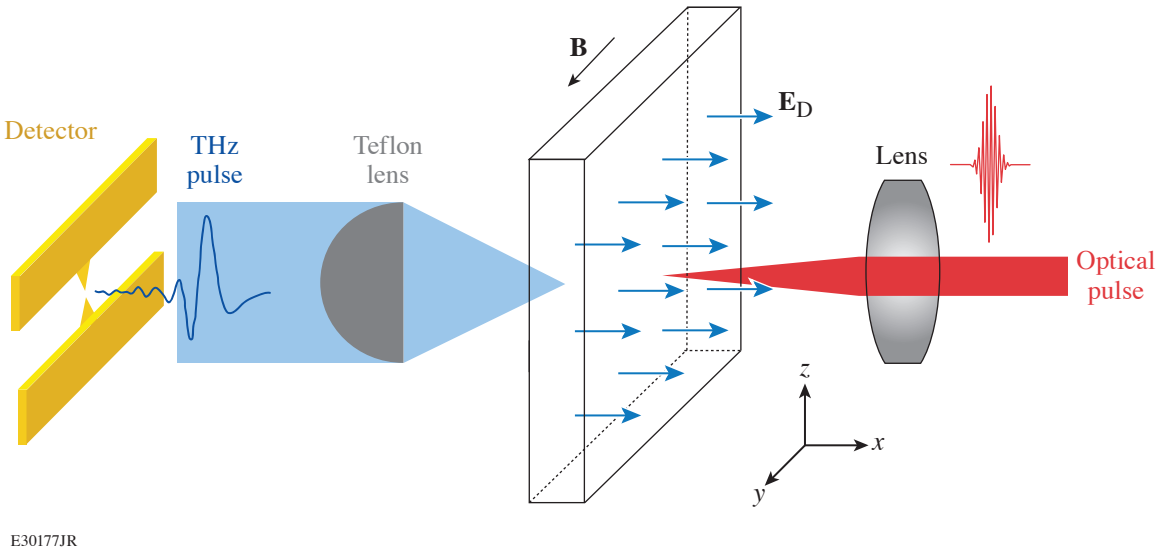

Figure 1
Schematics of the basic experimental geometry. The surface of the sample is parallel to the x–z plane. The built-in depletion electric field $\mathbf{E}_D$ is along the y axis and perpendicular to the sample surface. A lens is used to focus a laser beam at the surface of the sample, and a Teflon lens placed after the sample collimates the emitted THz radiation toward a PC THz detector aligned in such a way that it can only sense the z component of the THz transient. An external magnetic field applied along the x axis was used in the **B**-field enhancement experiments.

mounted on a delay stage. Both pump and probe beams were focused on the same spot of the sample; the beam size of the probe (~20 μm in diameter) was kept slightly smaller than that of the pump beam (~30 μm in diameter) to ensure probing only the optically excited area of the sample. To limit the probe-related electron heating to a minimum and to ensure a decent signal-to-noise ratio, the power ratio of the pump to probe beams was set to ~10:1. The probe beam was reflected at the sample surface and directed toward a photodetector connected to a lock-in amplifier to record the normalized reflectivity change ($\Delta R/R$) waveforms as a function of the time delay between the pump and probe pulses.

Figure 2 shows the dependence $k = (q/m^*)\tau_1$, where q is the elementary charge, m^* is the electron effective mass, and τ_1 is the relaxation time, for all five types of GaAs samples (black circles) and reveals a universal linear relationship (black solid line). This indicates that τ_1, derived based on the Drude model, is the trapping time for the samples. During this time, the Lorentz force accelerates electrons before they get trapped by defect states. Therefore, a high density of defects/traps in a semiconductor, e.g., in case of the N-GaAs samples, leads to a shorter carrier lifetime, which, in turn, limits the impact of the magnetic field on the THz transient.

The next important conclusion from Fig. 2 is that within the linear fit, the effective mass $m^* = q/(k/\tau_1)$ for all samples is exactly the same and the extracted value is $m^*/m_0 = 0.059$ (m_0 is the electron mass), which is close to the accepted value of 0.063 for GaAs single crystals,[20] and illustrated by the dashed line corresponding to the k dependence for $m^*/m_0 = 0.063$. The latter is an interesting result and shows that despite the large differences in the crystallinity of the test samples, the effective mass derived from our magnetic-field experiments remains constant and very close to the effective mass of electrons in GaAs with a perfect crystalline structure. The only deviation from the ideal m^* value observed was for the annealed GaAs sample. Contrary to the other samples, the clear distinction between trapping and recombination processes is somewhat difficult to establish.

In conclusion, we exhaustively analyzed the transient emission of THz signals, emitted from highly resistive GaAs samples with different crystallinity, excited by femtosecond optical pulses. The observed magnetic field impacted the THz transient generation, and the corresponding enhancement factor was directly proportional to the applied **B** field. Interestingly, the slope of the enhancement factor dependence was directly proportional to the samples' nonequilibrium trapping time measured using

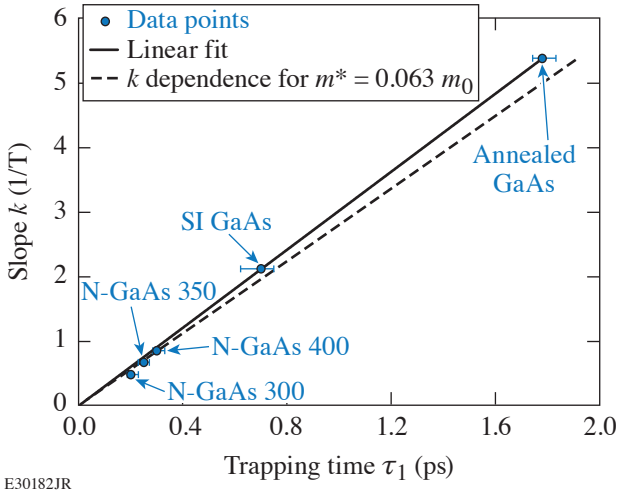

Figure 2
Dependence of the slope k on the trapping time τ_1. The circles are experimental data, and the black line is the best linear fit yielding $m^*/m_0 = 0.059$. The dashed line corresponds to the k dependence for the literature $m^*/m_0 = 0.063$.

femtosecond optical pump–probe spectroscopy. The latter enabled the determination of the electron effective mass $m^*/m_0 = 0.059$ that was very close to the literature m^* value for GaAs single crystals. The latter reveals that GaAs samples with very different crystallinity, including highly defected, N-implanted samples, all have an m^* value essentially equal to that of the ideal crystal.

This material is based upon work that was supported in Rochester in part by the National Science Foundation Grant Number 1842712. The work at the Research Center Jülich was performed within JuSPARC (Jülich Short-pulse Particle Acceleration and Radiation Center), a strategy project funded by the Federal Ministry of Education and Research (Bundesministerium für Bildung und Forschung).

1. X.-C. Zhang *et al.*, Appl. Phys. Lett. **56**, 1011 (1990).
2. X.-C. Zhang and D. H. Auston, J. Appl. Phys. **71**, 326 (1992).
3. R. Kersting *et al.*, Phys. Rev. B **58**, 4553 (1998).
4. J. N. Heyman *et al.*, Phys. Rev. B **64**, 085202 (2001).
5. J. S. Hwang *et al.*, Appl. Phys. Lett. **87**, 121107 (2005).
6. S. L. Chuang *et al.*, Phys. Rev. Lett. **68**, 102 (1992).
7. M. Reid, I. V. Cravetchi, and R. Fedosejevs, Phys. Rev. B **72**, 035201 (2005).
8. K. Liu *et al.*, Phys. Rev. B **73**, 155330 (2006).
9. R. Mendis *et al.*, J. Appl. Phys. **98**, 126104 (2005).
10. A. Reklaitis, J. Appl. Phys. **108**, 053102 (2010).
11. X.-C. Zhang *et al.*, Appl. Phys. Lett. **62**, 2003 (1993).
12. C. Weiss, R. Wallenstein, and R. Beigang, Appl. Phys. Lett. **77**, 4160 (2000).
13. A. Othonos, J. Appl. Phys. **83**, 1789 (1998); **84**, 1708(E) (1998).
14. M. Mikulics *et al.*, Appl. Phys. Lett. **87**, 041106 (2005).
15. M. Mikulics *et al.*, Appl. Phys. Lett. **88**, 041118 (2006).
16. R. Adam *et al.*, Appl. Phys. Lett. **114**, 212405 (2019).
17. A. Geižutis *et al.*, Opt. Mater. **30**, 786 (2008).
18. J. Zhang *et al.*, J. Appl. Phys. **110**, 113112 (2011).
19. J. Serafini *et al.*, Semicond. Sci. Technol. **31**, 045006 (2016).
20. G. Margaritondo, in *Encyclopedia of Condensed Matter Physics*, edited by F. Bassani, G. L. Liedl, and P. Wyder (Elsevier, Oxford, 2005), pp. 311–321.

An Assessment of Generating Quasi-Static Magnetic Fields Using Laser-Driven "Capacitor" Coils

J. L. Peebles, J. R. Davies, D. H. Barnak, F. Garcia-Rubio, P. V. Heuer, G. Brent, R. Spielman, and R. Betti

Laboratory for Laser Energetics, University of Rochester

Over the previous decade, numerous experiments have been performed using a laser to drive a strong, quasi-static magnetic field. Field strength and energy density measurements of these experiments have varied by many orders of magnitude, painting a confusing picture of the effectiveness of these laser-driven coils (LDC's) as tools for generating consistent fields. At the higher end of the field energy spectrum, kilotesla field measurements have been used to justify future experimental platforms, theoretical work, and inertial confinement fusion concepts. In this work we present the results from our own experiments designed to measure magnetic fields from LDC's as well as a review of the body of experiments that have been undertaken in this field. We demonstrate how problems with prior diagnostic analyses have led to overestimates of the magnetic fields generated from LDC's.

The first aspect of these experiments that must be addressed is conversion of laser energy to magnetic-field energy. While it is easy to claim results are feasible as long as energy in the magnetic field is less than the energy in the driving laser, the reality is that no laser experiment has a significant amount of free energy to generate a magnetic field. For certain experiments, the total laser absorption can be as high as 90%, but for the majority of experiments using drivers similar to those in most LDC experiments, it is much lower (50%). Hot-electron production is a potential source of free energy. Up to ~30% of the laser energy could be converted to hot electrons at the higher values of $I\lambda^2$ used.[1] For the parameters of most LDC experiments with lower $I\lambda^2$, however, a smaller percentage of the laser energy would be converted into hot electrons.[2] When considering that all the potential energy sinks for this conversion, at most half the energy put into hot electrons can be converted to current. Therefore, a physically reasonable upper limit on laser-energy conversion to magnetic energy would appear to be 15% and, in most cases, should be much less. Examining each LDC experiment's energy conversion by integrating the field energy density ($B^2/2\mu_0$) over a $10 \times 10 \times 10$-mm^3 volume produces the results in Fig. 1.[3–15]

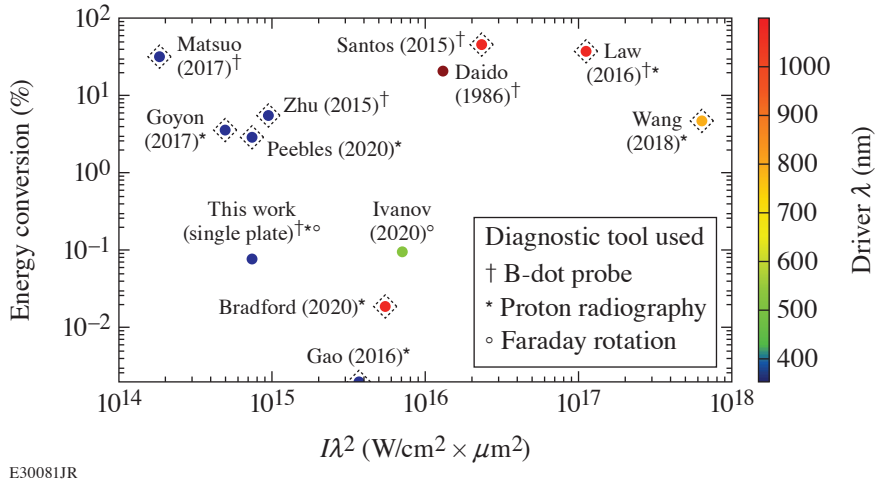

Figure 1
The calculated energy conversion from laser energy to field energy for the variety of LDC experiments.[3–15] Superscripts denote the diagnostic tool used to arrive at the result, while dotted diamonds around a shot indicate the presence of a short-pulse beam on the experiment. Experiments with conversion over 10% stand out because they have suspiciously high energy conversion.

Looking at the body of experiments, a trend emerges: several experiments measured fields that contained energy equal to 30%–40% of the energy of the driving laser. These experiments also coincidentally measured the primary result using the B-dot while a short-pulse, high-intensity laser was present. This is highly indicative that the B-dot probe responds differently to these experiments than other diagnostics. To address this, we performed our own experiments with LDC's using the entire battery of magnetic-field diagnostics: axial and transverse proton probing, Faraday rotation, and B-dot probes, as shown in Fig. 2. Two types of coils were tested to examine the effect of having the second plate on the target and were driven by a 1-ns, up-to-1.25-kJ, long-pulse UV beam.

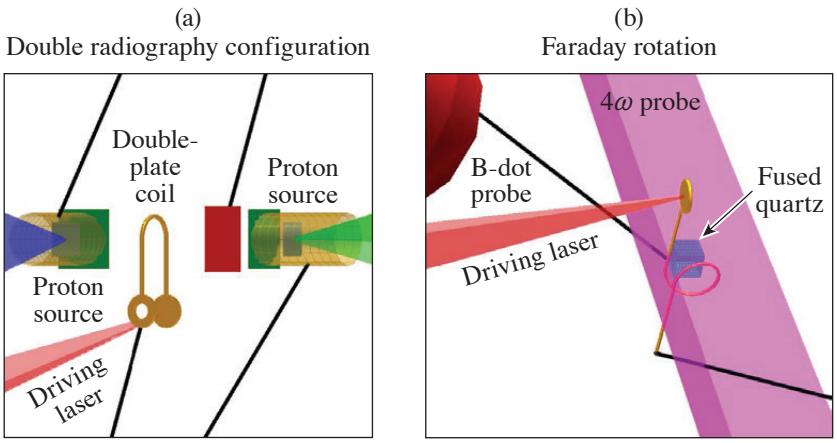

Figure 2
Experimental platform used to study the fields generated by LDC targets using a battery of diagnostics. (a) One campaign used both the sidelighter and backlighter beams to simultaneously probe the coil transverse and axially with protons. (b) A setup used the 4ω probe with a piece of fused quartz for Faraday rotation (polarimetry). All experiments had a B-dot probe placed roughly 2 cm from the loop attached to a 6-GHz-bandwidth balun and scope.

Several results from our experiments are shown in Fig. 3. A 40-T reference magnetic field was generated by MIFEDS (magneto-inertial fusion electrical discharge system) and probed by the axial proton probe [Fig. 3(a)]. As protons travel through the magnetic field, a secondary deflection from the radial magnetic field induces a rotation of the reference mesh. This rotation increases with field strength and decreases with proton energy. The same proton probe was applied to our LDC's and produced no measurable rotation. This indicates that the magnetic field in the LDC is below the measurement threshold (20 kA in the coil) for the axial probe. Using the more-sensitive transverse proton probe on the LDC produces a bulge near the top of the LDC, indicative of a small current of 2.5 kA. This current is far below that measured by most of the experiments shown in Fig. 1 and indicates a much poorer laser-to-field-energy conversion ratio.

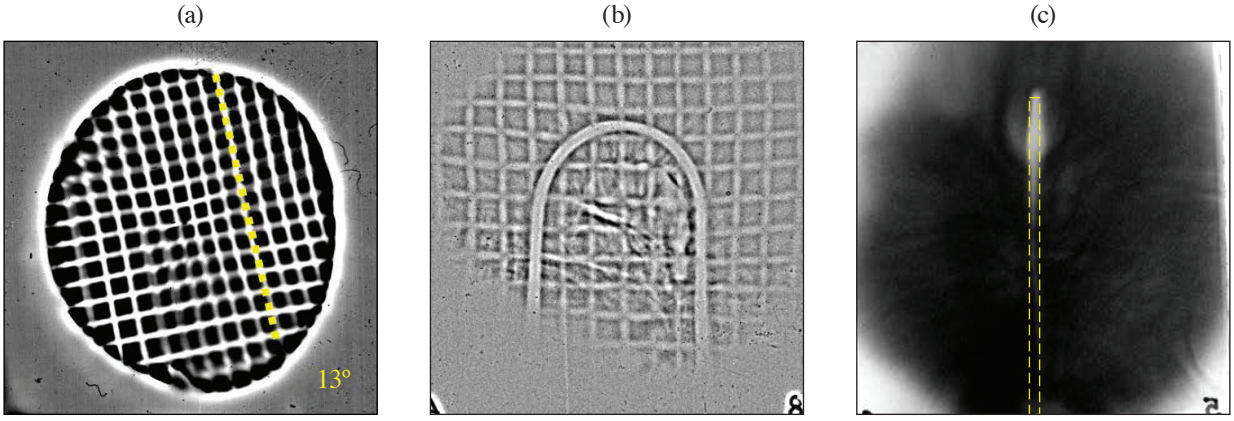

Figure 3
Axial proton probes of a known magnetic field generated by (a) MIFEDS and (b) a double-plate LDC. In (a) MIFEDS generated a 40-T field that induced an apparent rotation of the mesh fiducial dependent on the proton energy. This diagnostic technique is sensitive to fields generated by currents greater than 20 kA. In (b) no such rotation is measured, indicating that any current must be less than 20 kA. (c) A transverse proton probe of the same LDC shows a slight bulge near the top of the coil, indicating a current of ~2.5 kA.

Supplementing the proton radiography measurements were the Faraday rotation and B-dot probe diagnostics. Faraday rotation measures the magnetic field in a medium by comparing the rotation difference between orthogonal polarizations as they pass through the medium in the presence of a magnetic field. In the case of our LDC experiment, no significant rotation was measured in the two polarizations of the 4ω probe. The error in the measurement between the two polarizations is ±2%, which corresponds to a measurement limit of a 7.5-kA current in our coil, consistent with a 2.5-kA measurement of the proton probe. The B-dot probe acquired measurements in all experimental configurations, both with and without the short-pulse beams. When comparing the data in Fig. 4 it is clear that the B-dot probe is heavily influenced by the presence of the short-pulse beam. Since the short pulse-beams were timed 1 ns after the long-pulse drive beam in order to probe the interaction after the drive, the signal contributions between the two types of beams can be differentiated on the scope. When we account for the scope and cable attenuation based on assumed signal frequency, the signal from the long-pulse beam implies a current of 62.5 kA, much higher than all other diagnostics. The signal from the short pulse is roughly an order of magnitude higher than that of the long pulse, implying a very unrealistic current of over 600 kA.

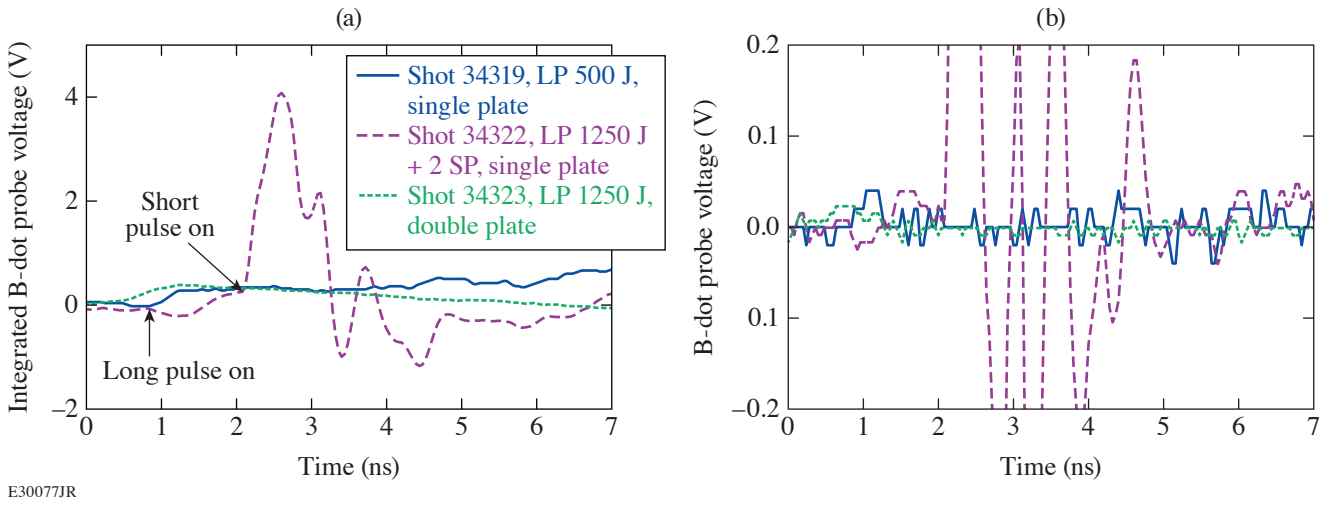

Figure 4

(a) Integrated B-dot probe signals for three different shots: two without short-pulse beams with different coil types and one with the short-pulse beams. The signal with the short-pulse beams is over 10× higher (4 V compared to 0.34 V) than that of the long-pulse beam drive only. The spike in signal from the short pulse is delayed compared to the long pulse due to the beam timings used on the experiment and time of flight from target to B-dot probe. (b) Raw data for the same shots, demonstrating the poor signal-to-noise ratio on the experiments without the short pulse. The signal is varying as quickly as the diagnostic can measure, indicating that the majority of signal is oscillating faster than 6 GHz.

While a B-dot probe (with differentiation) is designed in theory to measure only a changing magnetic field, in reality the entire probe and cabling is subject to effects that are not completely neutralized, such as capacitive coupling, where electric fields can induce significant voltage. The signal generated on the B-dot probe by the short-pulse beam clearly indicates current that is unphysical from a conservation of energy perspective; however, this effect explains the conclusions of many previous LDC experiments shown in Fig. 1. The "highest performing" experiments also utilized a B-dot probe in conjunction with proton radiography using a short-pulse, high-intensity beam. Similar to our experiment, other diagnostics (proton radiography or Faraday rotation) typically indicated field values far lower than the B-dot probe; however, in most of these experiments the B-dot probe result is given preference because of its larger value, despite the poorer accuracy of the method. When we account for this short-pulse interference of the B-dot probe, the majority of results fall into more-reasonable energy conversion ratios of, at most, a few percent.

We began experiments on laser-driven coils to develop a consistent platform for applying and measuring external magnetization of an experiment. In some regards we were successful: a field was measured that was relatively consistent across all diagnostics; however, the field values we measured departed severely from those in other publications. These experiments comprehensively demonstrated that laser-driven coils are not well described by a circuit or capacitor model nor do they produce

uniform consistent fields. Our experiments at best could convert less than a percent of driving laser energy into the magnetic field at the coil, far less than the optimistic conclusions of other experiments. B-dot probes and Faraday rotation were found to be ineffective at measuring magnetic fields in our higher-power LDC experiments because they were subject to the extreme radiation and electric-field environment. Proton radiography produced a precise and detailed picture of electrostatic and magnetic fields around the LDC, but a higher degree of confidence in our conclusions drawn from radiographs was obtained only by probing in two directions simultaneously.

This material is based upon work supported by the Department of Energy National Nuclear Security Administration under Award Numbers DE-NA0003856 and DE-NA0003868, the Office of Fusion Energy Sciences Award Number DE-SC0021072, the University of Rochester, and the New York State Energy Research and Development Authority.

1. J. R. Davies, Plasma Phys. Control. Fusion **51**, 014006 (2009).
2. C. Garban-Labaune *et al.*, Phys. Rev. Lett. **48**, 1018 (1982).
3. H. Daido *et al.*, Phys. Rev. Lett. **56**, 846 (1986).
4. J. J. Santos *et al.*, New J. Phys. **17**, 083051 (2015).
5. K. F. F. Law *et al.*, Appl. Phys. Lett. **108**, 091104 (2016).
6. C. Courtois *et al.*, J. Appl. Phys. **98**, 054913 (2005).
7. A. Tarifeño, C. Pavez, and L. Soto, J. Phys.: Conf. Ser. **134**, 012048 (2008).
8. L. Gao *et al.*, Phys. Plasmas **23**, 043106 (2016).
9. C. Goyon *et al.*, Phys. Rev. E **95**, 033208 (2017).
10. W. Wang *et al.*, Phys. Plasmas **25**, 083111 (2018).
11. B. J. Zhu *et al.*, Appl. Phys. Lett. **107**, 261903 (2015).
12. K. Matsuo *et al.*, Phys. Rev. E **95**, 053204 (2017).
13. V. V. Ivanov *et al.*, Phys. Plasmas **27**, 033102 (2020).
14. P. Bradford *et al.*, High Power Laser Sci. Eng. **8**, e11 (2020).
15. J. L. Peebles *et al.*, Phys. Plasmas **27**, 063109 (2020).

Pulsed-Power Innovations for Next-Generation, High-Current Drivers

R. B. Spielman

Laboratory for Laser Energetics, University of Rochester

Recent proposals to build larger high-current drivers to be used for high-energy-density physics, inertial confinement fusion, radiation effects testing, and basic science will present challenges.[1] Drivers significantly larger than the Z Machine at Sandia National Laboratories encounter increasing difficulties in water power flow, insulator performance, and vacuum power flow. The physics requirements of imploding loads limit a designer's flexibility in choosing machine parameters such as current rise time, driving impedance, and total inductance. This summary enumerates these physics constraints and shows how they impact driver design. This leads to the conclusion that advances in pulsed-power understanding and pulsed-power capabilities are needed to control risk and to build a cost-effective driver at peak currents of ~60 MA.

The Z machine, driving an imploding load, requires a peak insulator voltage of ~4 MV while delivering up to 25 MA to the load.[2] The current rise time is ~100 to 110 ns and the overall implosion times are 100 ns to 120 ns (Refs. 3–5). Scaling Z today at 25 MA to a new next-generation pulsed-power facility (NGPPF) at 60 MA requires that the driving voltage scale proportionally with the increased peak current (other parameters held constant). This results in a driver with a peak voltage at least ~2.4× larger than Z.[6,7] These scaled voltages will exist at all locations in the driver for all times during the pulse. This summary describes the physics constraints on driver parameters, discusses the pulsed-power impact on the pulsed-power design, and finally asks if advances in pulsed-power physics understanding and pulsed-power engineering can reduce the risk and cost of an NGPP driver.

Magneto-Rayleigh–Taylor (MRT) physics drives *Z*-pinch drivers to implosions times of 100 ns or less.[2,8,9] In the case of an NGPPF driver, implosion quality is paramount. It becomes difficult to justify a significant increase in the implosion time (current rise time) to reduce the voltage (and power) risk beyond 100 ns unless MRT can be stabilized to some extent.

Electrical coupling efficiency to the load is a huge part of driver optimization. Simplistically, the electrical coupling (to stored magnetic energy) is optimized when $L/Zt \sim 1$, where L is the total inductance of the load, Z is the impedance of the driver, and t is the rise time of the current. Given from MRT consideration that the current rise time t is constrained, we see that increases in the load inductance L must be accompanied by an increase in driver impedance Z. However, the coupling efficiency to the load is $\sim\Delta L/L$, where ΔL is the change in inductance due to the dynamic load and L here is the total final inductance. For a convergence ratio of ~10:1, the change in inductance of a 2-cm-long load is ~9.4 nH. We see that coupling to the load is optimized for lower total inductances. As a result, the overall coupling efficiency from available driver energy drives us to a lower inductance and lower impedance driver. The driver inductance and impedance are not free parameters.

Higher-voltage NGPP drivers force larger gaps in the water section of any driver because, for a voltage rise time of ~100 ns, the threshold for electrical discharges in water is 300 kV/cm. The only ways to increase the gap in the water section near the load are to increase the radius of the insulator stack (height scales with radius at constant impedance) and increase the impedance of the water lines. Both of these approaches will be required.

The largest-diameter parts that can be built and shipped across the country are roughly 6 m in diameter. With this assumption, the only additional way to increase the driver voltage is by using multiple levels of insulators and magnetically insulated

transmission lines (MITL's). (See Fig. 1 for a four-level example.) The key advantage of increasing the number of MITL levels is an increase in the water transmission-line gap for a given insulator stack radius because the levels are driven in parallel. A secondary impact is the paralleling of the MITL inductances at the post-hole convolute. Inductance is a secondary impact because the reduced current per MITL level forces an increase in MITL inductance to hold the electron vacuum flow nearly constant. The number of MITL levels and the insulator stack radius effectively determine the maximum current for a given design.

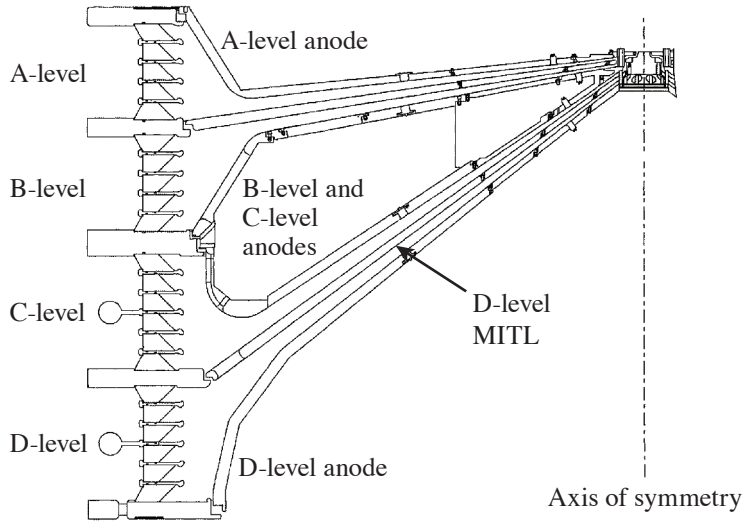

Figure 1
Schematic of a double-disk MITL that shows the insulator stack, the vacuum flare region, the MITL's, the post-hole convolute, the inner disk MITL, and the load region.

An impedance of $Z = 6.67\ h/r\ \Omega$ per level for a four-level MITL is used to estimate the peak current of a Z machine–like design. One potential design impedance is 0.180 Ω, so the individual level impedance is now increased to 0.72 Ω. This results in a water-transmission line gap of 32.4 cm at a radius of 3 m. Following the arguments of maximum electric field above, the peak allowed voltage is ~4.8 MV and the peak current is ~50 MA. Higher-current drivers will require a larger-radius insulator stack, a higher driving impedance, and/or more MITL levels.

The increased voltage on NGPPF (everywhere and at all times) will create difficulties in pulsed-power design and result in increased current losses and reduced coupling efficiency to dynamic loads. Mitigating losses by increasing physical gap results in an increase in inductance that reduces peak current and decreases coupling efficiency. Further increases in driving voltage are required to obtain the design load current. This is a strong feedback effect that can limit the overall magnitude of a potential NGPP driver. Kinetic energy delivered to a relevant load becomes the key metric for comparing various driver designs. It is possible to design a pulsed-power driver that achieves 60 MA at the load that couples insufficient energy to a dynamic load.

It is likely that there is an effective limit to the peak current and kinetic energy of a pulsed-power driver that is based on cost, shot rate, and programmatic impact. A 60-MA-class driver can be built but such a driver, based on today's pulsed-power understanding, will be costly and inefficient.

This material is based upon work supported by the Department of Energy National Nuclear Security Administration under Award Number DE-NA0003856, the University of Rochester, the New York State Energy Research and Development Authority.

1. D. B. Sinars *et al.*, Phys. Plasmas **27**, 070501 (2020).
2. T. W. Hussey and N. F. Roderick, Phys. Fluids **24**, 1384 (1981).
3. E. A. Weinbrecht *et al.*, in *2005 IEEE Pulsed Power Conference*, edited by J. Maenchen and E. Schamiloglu (IEEE, Monterey, CA, 2005), pp. 170–173.

4. M. E. Savage *et al.*, in *16th IEEE International Pulsed Power Conference*, edited by E. Schamiloglu and F. Peterkin (IEEE, New York, 2007), Vol. 2, pp. 979–984.
5. M. E. Savage *et al.*, in 2011 IEEE Pulsed Power Conference, edited by R. P. Joshi (IEEE, Piscataway, NJ, 2011), pp. 983–990.
6. W. A. Stygar *et al.*, Phys. Rev. Spec. Top., Accel. Beams **10**, 030401 (2007).
7. W. A. Stygar *et al.*, Phys. Rev. ST Accel. Beams **18**, 110401 (2015).
8. N. F. Roderick and T. W. Hussey, J. Appl. Phys. **56**, 1387 (1984).
9. T. W. Hussey *et al.*, Phys. Plasmas **2**, 2055 (1995).

FY22 Q2 Laser Facility Report

J. Puth, M. Labuzeta, D. Canning, and R. T. Janezic

Laboratory for Laser Energetics, University of Rochester

During the second quarter of FY22, the Omega Facility conducted 322 target shots on OMEGA and 238 target shots on OMEGA EP for a total of 570 target shots (see Tables I and II). OMEGA averaged 9.9 target shots per operating day, averaging 90.8% Availability and 95.6% Experimental Effectiveness. OMEGA EP averaged 8.8 target shots per operating day, averaging 94.8% Availability and 96.9% Experimental Effectiveness.

Table I: OMEGA Laser System target shot summary for Q2 FY22.

Program	Laboratory	Planned Number of Target Shots	Actual Number of Target Shots
ICF	LLE	110	111
	LANL	11	12
	SNL	11	8
ICF Subtotal		132	131
HED	LLE	33	25
	LANL	22	27
	LLNL	55	43
	SNL	11	11
HED Subtotal		121	106
LBS	LLE	22	18
	LLNL	27.5	29
LBS Subtotal		49.5	47
NLUF		22	23
Calibration		0	25
Grand Total		324.5	332

NLUF: National Laser Users Facility

Table II: OMEGA EP Laser System target shot summary for Q2 FY22.

Program	Laboratory	Planned Number of Target Shots	Actual Number of Target Shots
ICF	LLE	24.5	38
	LLNL	14	11
ICF Subtotal		38.5	49
HED	LLE	7	7
	LANL	14	16
	LLNL	28	29
HED Subtotal		49	52
LBS	LLE	14	22
	LLNL	14	23
LBS Subtotal		28	45
CMAP		14	16
LaserNetUS		14	18
NLUF		28	38
Calibration	LLE	0	20
Grand Total		171.5	238

CMAP: Center for Matter at Atomic Pressures

Publications and Conference Presentations

Publications

C. H. Allen, M. Oliver, L. Divol, O. L. Landen, Y. Ping, M. Scholmerich, R. Wallace, R. Earley, W. Theobald, T. G. White, and T. Döppner, "Toward an Integrated Platform for Characterizing Laser-Driven, Isochorically Heated Plasmas with 1 mm Spatial Resolution," Appl. Opt. **61**, 1987 (2022).

P. T. Campbell, C. A. Walsh, B. K. Russell, J. P. Chittenden, A. Crilly, G. Fiksel, L. Gao, I. V. Igumenshchev, P. M. Nilson, A. G. R. Thomas, K. Krushelnick, and L. Willingale, "Measuring Magnetic Flux Suppression in High-Power Laser-Plasma Interactions," Phys. Plasmas **29**, 012701 (2022).

T. J. B. Collins, C. Stoeckl, R. Epstein, W. A. Bittle, C. J. Forrest, V. Yu. Glebov, V. N. Goncharov, D. R. Harding, S. X. Hu, D. W. Jacobs-Perkins, T. Z. Kosc, J. A. Marozas, C. Mileham, F. J. Marshall, S. F. B. Morse, P. B. Radha, S. P. Regan, B. Rice, T. C. Sangster, M. J. Shoup III, W. T. Shmayda, C. Sorce, W. Theobald, and M. D. Wittman, "Causes of Fuel–Ablator Mix Inferred from Modeling of Monochromatic Time-Gated Radiography of OMEGA Cryogenic Implosions," Phys. Plasmas **29**, 012702 (2022).

C. Dorrer and M. Spilatro, "Spectral and Temporal Shaping of Spectrally Incoherent Pulses in the Infrared and Ultraviolet," Opt. Express **30**, 4942 (2022).

M. Formanek, D. Ramsey, J. P. Palastro, and A. Di Piazza, "Radiation Reaction Enhancement in Flying Focus Pulses," Phys. Rev. A **105**, L020203 (2022).

A. M. Hansen, K. L. Nguyen, D. Turnbull, B. J. Albright, R. K. Follett, R. Huff, J. Katz, D. Mastrosimone, A. L. Milder, L. Yin, J. P. Palastro, and D. H. Froula, "Cross-Beam Energy Transfer Saturation: Ion Heating and Pump Depletion," Plasma Phys. Control. Fusion **64**, 034003 (2022).

G. W. Jenkins, C. Feng, and J. Bromage, "Energy Scaling Beyond the Gas Ionization Threshold with Divided-Pulse Nonlinear Compression," Opt. Lett. **47**, 1450 (2022).

V. V. Karasiev, D. I. Mihaylov, and S. X. Hu, "Meta-GGA Exchange-Correlation Free Energy Density Functional to Increase the Accuracy of Warm Dense Matter Simulations," Phys. Rev. B **105**, L081109 (2022).

M. F. Kasim, D. Watson-Parris, L. Deaconu, S. Oliver, P. Hatfield, D. H. Froula, G. Gregori, M. Jarvis, S. Khatiwala, J. Korenaga, J. Topp-Mugglestone, E. Viezzer, and S. M. Vinko, "Building High Accuracy Emulators for Scientific Simulations with Deep Neural Architecture Search," Mach. Learn.: Sci. Technol. **3**, 015013 (2022).

R. G. Kraus, R. J. Hemley, S. J. Ali, J. L. Belof, L. X. Benedict, J. Bernier, D. Braun, R. E. Cohen, G. W. Collins, F. Coppari, M. P. Desjarlais, D. Fratanduono, S. Hamel, A. Krygier, A. Lazicki, J. Mcnaney, M. Millot, P. C. Myint, M. G. Newman, J. R. Rygg, D. M. Sterbentz, S. T. Stewart, L. Stixrude, D. C. Swift, C. Wehrenberg, and J. H. Eggert, "Measuring the Melting Curve of Iron at Super-Earth Core Conditions," Science **375**, 202 (2022).

M. C. Marshall, M. G. Gorman, D. N. Polsin, J. H. Eggert, M. K. Ginnane, J. R. Rygg, G. W. Collins, and L. D. Leininger, "Diamond Formation in Double-Shocked Epoxy to 150 GPa," J. Appl. Phys. **131**, 085904 (2022).

J. Meinecke, P. Tzeferacos, J. S. Ross, A. F. A. Bott, S. Feister, H.-S. Park, A. R. Bell, R. Blandford, R. L. Berger, R. Bingham, A. Casner, L. E. Chen, J. Foster, D. H. Froula, C. Goyon, D. Kalantar, M. Koenig, B. Lahmann, C.-K. Li, Y. Lu, C. A. J. Palmer, R. D. Petrasso, H. Poole, B. Remington, B. Reville, A. Reyes, A. Rigby, D. Ryu, G. Swadling, A. Zylstra, F. Miniati, S. Sarkar, A. A. Schekochihin, D. Q. Lamb, and G. Gregori, "Strong Suppression of Heat Conduction in a Laboratory Replica of Galaxy-Cluster Turbulent Plasmas," Sci. Adv. **8**, eabj6799 (2022).

S. F. Nwabunwanne and W. R. Donaldson, "Interdigitated Electrode Geometry Variation and External Quantum Effi-

ciency of GaN/AlGaN–Based Metal–Semiconductor–Metal UV Photodetectors," Proc. SPIE **12001**, 120010F (2022).

J. J. Pilgram, M. B. P. Adams, C. G. Constantin, P. V. Heuer, S. Ghazaryan, M. Kaloyan, R. S. Dorst, D. B. Schaeffer, P. Tzeferacos, and C. Niemann, "High Repetition Rate Exploration of the Bierman Battery Effect in Laser Produced Plasmas Over Large Spatial Regions," High Power Laser Sci. Eng. **10**, e13 (2022).

N. R. Shaffer and C. E. Starrett, "Dense Plasma Opacity via the Multiple-Scattering Method," Phys. Rev. E **105**, 015203 (2022).

T. T. Simpson, D. Ramsey, P. Franke, K. Weichman, M. V. Ambat, D. Turnbull, D. H. Froula, and J. P. Palastro, "Spatiotemporal Control of Laser Intensity Through Cross-Phase Modulation," Opt. Express **30**, 9878 (2022).

G. F. Swadling and J. Katz, "Novel Design for a Polarizing DUV Spectrometer Using a Wollaston Prism and Its Application as a Diagnostic for Measuring Thomson Scattering Data in the Presence of Strong Self-Emission Backgrounds," Rev. Sci. Instrum. **93**, 013501 (2022).

W. Theobald, D. Cao, R. C. Shah, C. A. Thomas, I. V. Igumenshchev, K. A. Bauer, R. Betti, M. J. Bonino, E. M. Campbell, A. R. Christopherson, K. Churnetski, D. H. Edgell, C. J. Forrest, J. A. Frenje, M. Gatu Johnson, V. Yu. Glebov, V. N. Goncharov, V. Gopalswamy, D. R. Harding, S. X. Hu, S. T. Ivancic, D. W. Jacobs-Perkins, R. T. Janezic, T. Joshi, J. P. Knauer, A. Lees, R. W. Luo, O. M. Mannion, F. J. Marshall, Z. L. Mohamed, S. F. B. Morse, D. Patel, J. L. Peebles, R. D. Petrasso, P. B. Radha, H. G. Rinderknecht, M. J. Rosenberg, S. Sampat, T. C. Sangster, W. T. Shmayda, C. M. Shuldberg, A. Shvydky, C. Sorce, C. Stoeckl, M. D. Wittman, and S. P. Regan, "Enhanced Laser-Energy Coupling with Small-Spot Distributed Phase Plates (SG5-650) in OMEGA DT Cryogenic Target Implosions," Phys. Plasmas **29**, 012705 (2022).

A. J. White, L. A. Collins, K. Nichols, and S. X. Hu, "Mixed Stochastic-Deterministic Time-Dependent Density Functional Theory: Application to Stopping Power of Warm Dense Carbon," J. Phys.: Condens. Matter **34**, 174001 (2022).

S. Zhang, D. E. Fratanduono, M. C. Marshall, J. R. Rygg, A. E. Lazicki, A. Shvydky, D. Haberberger, V. N. Goncharov, T. R. Boehly, G. W. Collins, and S. X. Hu, "Species Separation in Polystyrene Shock Release Evidenced by Molecular-Dynamics Simulations and Laser-Drive Experiments," Phys. Rev. Research **4**, 013126 (2022).

S. Zhang, M. A. Morales, R. Jeanloz, M. Millot, S. X. Hu, and E. Zurek, "Nature of the Bonded-to-Atomic Transition in Liquid Silica to TPa Pressures," J. Appl. Phys. **131**, 071101 (2022).

D. Zhao, R. Betti, and H. Aluie, "Scale Interactions and Anisotropy in Rayleigh–Taylor Turbulence," J. Fluid Mech. **930**, A29 (2022).

Forthcoming Publications

S.-W. Bahk, I. A. Begishev, R. Roides, C. Mileham, R. Cuffney, C. Feng, B. M. Webb, C. Jeon, M. Spilatro, S. Bucht, C. Dorrer, and J. Bromage, "Effect of the Pump Beam Profile and Wavefront on the Amplified Signal Wavefront in Optical Parametric Amplifiers," to be published in Optics Express.

A. Bose, J. Peebles, C. A. Walsh, J. A. Frenje, N. V. Kabadi, P. J. Adrian, G. D. Sutcliffe, M. Gatu Johnson, C. A. Frank, J. R. Davies, R. Betti, V. Yu. Glebov, F. J. Marshall, S. P. Regan, C. Stoeckl, E. M. Campbell, H. Sio, J. Moody, A. Crilly, B. D. Appelbe, J. P. Chittenden, S. Atzeni, F. Barbato, A. Forte, C. K. Li, F. H. Séguin, and R. D. Petrasso, "Effect of Strongly Magnetized Electrons and Ions on Heat Flow and Symmetry of Inertial Fusion Implosions," to be published in Physical Review Letters.

G. W. Jenkins, C. Feng, and J. Bromage, "Simultaneous Contrast Improvement and Temporal Compression Using Divided-Pulse Nonlinear Compression," to be published in Optics Express.

D. Kim, R. F. Smith, I. K. Ocampo, F. Coppari, M. C. Marshall, M. K. Ginnane, J. K. Wicks, S. J. Tracy, M. Millot, A. Lazicki, J. R. Rygg, J. H. Eggert, and T. S. Duffy, "Structure and Density of Silicon Carbide to 1.5 TPa and Implications for Extrasolar Planets," to be published in Nature Communications.

T. Z. Kosc, H. Huang, T. J. Kessler, and S. G. Demos, "Angular Dependence of the Transverse Raman Scattering in KDP and DKDP in Geometries Suitable for Beam Polarization Control," to be published in Optics Express.

L. S. Leal, A. V. Maximov, E. C. Hansen, J. R. Davies, D. H. Barnak, J. L. Peebles, K. M. Woo, P. V. Heuer, A. B. Sefkow, and R. Betti, "The Effect of Laser Preheat in Magnetized Liner Inertial Fusion at OMEGA," to be published in Physics of Plasmas.

R. W. Paddock, H. Martin, R. T. Ruskov, R. H. H. Scott, W. Garbett, B. M. Haines, A. B. Zylstra, E. M. Campbell, T. J. B. Collins, R. S. Craxton, C. A. Thomas, V. N. Goncharov, R. Aboushelbaya, Q. S. Feng, M. W. von der Leyen, I. Ouatu, B. T. Spiers, R. Timmis, R. H. W. Wang, and P. A. Norreys, "Pathways Towards Break Even for Low Convergence Ratio Direct-Drive Inertial Confinement Fusion," to be published in the Journal of Plasma Physics.

D. N. Polsin, A. Lazicki, X. Gong, S. J. Burns, F. Coppari, L. E. Hansen, B. J. Henderson, M. F. Huff, M. I. McMahon, M. Millot, R. Paul, R. F. Smith, J. H. Eggert, G. W. Collins, and J. R. Rygg, "Structural Complexity in Ramp-Compressed Sodium to 480 GPa," to be published in Nature Communications.

G. F. Swadling, C. Bruulsema, W. Rozmus, and J. Katz, "Quantitative Assessment of Fitting Errors Associated with Streak Camera Noise in Thomson Scattering Data Analysis," to be published in Review of Scientific Instruments.

Conference Presentations

E. M. Campbell, "Perspectives on Inertial Fusion Energy," presented at LLE Research and Review, 14 January 2022.

S. F. Nwabunwanne and W. R. Donaldson, "Interdigitated Electrode Geometry Variation and External Quantum Efficiency of GaN/AlGaN-Based Metal–Semiconductor–Metal UV Photodetectors," presented at Photonics West 2022, San Francisco, CA, 22–27 January 2022.

P. V. Heuer, S. Feister, N. A. Murphy, and J. R. Davies, "Open Source Software and Data Formats for High-Energy-Density Physics," presented at Laser-Plasma–Accelerator Control Systems and Machine Learning, virtual, 24–28 January 2022.

R. B. Spielman, E. M. Campbell, C. Deeney, P. Tzeferacos, and J. D. Zuegel, "Short-Pulse Lasers for Directed-Energy Hypersonic Defense, Swarms, and More," presented at the Visit of J. Stiles, Rochester, NY, 26 January 2022.

The following presentations were made at the National Ignition Facility and Jupiter Laser Facility User Meeting, Livermore, CA, 7–9 February 2022:

A. Armstrong, A. Reyes, M. B. P. Adams, P. Farmakis, E. C. Hansen, Y. Lu, D. Michta, K. Moczulski, D. Q. Lamb, and P. Tzeferacos, "Implementation and Verification of Braginskii Viscosity in the *FLASH* Code."

L. Ceurvorst, L. Masse, S. F. Khan, D. Martinez, N. Izumi, V. Smalyuk, T. Goudal, V. Bouffetier, A. Casner, B. Canaud, V. N. Goncharov, and I. V. Igumenshchev, "Observing the Effects of Ablation and Perforation on the Deeply Nonlinear Rayleigh–Taylor Instability."

G. W. Collins, "Extreme Matters: Pressure to Explore New Worlds and Revolutionary States of Matter."

P. Farmakis, M. McMullan, A. Reyes, J. Laune, M. B. P. Adams, A. Armstrong, E. C. Hansen, Y. Lu, D. Michta, K. Moczulski, D. Q. Lamb, and P. Tzeferacos, "Expanding the Tabulated Equation-of-State Implementations in the *FLASH* Code of the *SESAME* Database."

Y. Lu, S. Feister, J. Meinecke, F. Miniati, G. Gregori, A. Bott, A. Reyes, E. C. Hansen, J. T. Laune, B. Reville, J. S. Ross, D. Q. Lamb, and P. Tzeferacos, "Numerical Modeling of Laser-Driven Plasma Experiments Aiming to Study Turbulent Dynamo and Thermal Conduction at the National Ignition Facility."

K. Moczulski, A. Reyes, M. B. P. Adams, A. Armstrong, P. Farmakis, E. Hansen, Y. Lu., D. Michta, D. Q. Lamb, and P. Tzeferacos, "Implementation and Verification of LC Circuit for *Z*-Pinch *FLASH* Simulations."

D. N. Polsin, G. W. Collins, J. R. Rygg, X. Gong, M. Huff, M. K. Ginnane, M. McMahon, E. Zurek, A. Lazicki, S. Bonev, M. Gorman, R. Briggs, J. H. Eggert, and J. Wark,

"Transforming Simple Metals to Topological Insulators: Sodium to 18 Mbar."

V. Gopalaswamy, R. Betti, J. P. Knauer, D. Patel, A. Lees, A. R. Christopherson, K. M. Woo, C. A. Thomas, D. Cao, O. M. Mannion, R. C. Shah, C. J. Forrest, Z. L. Mohamed, C. Stoeckl, V. Yu. Glebov, S. P. Regan, D. H. Edgell, M. J. Rosenberg, I. V. Igumenshchev, P. B. Radha, K. S. Anderson, J. R. Davies, T. J. B. Collins, V. N. Goncharov, E. M. Campbell, R. Janezic, D. R. Harding, M. J. Bonino, S. Sampat, S. F. B. Morse, M. Gatu Johnson, R. D. Petrasso, C. K. Li, and J. A. Frenje, "Fusion Energy via Laser-Driven Inertial Confinement," presented at Reed College Physics Seminar, virtual, 9 February 2022.

E. M. Campbell, "Perspectives on Inertial Fusion Energy," presented at the Rochester Institute of Technology Spring Seminar, Rochester, NY, 10 February 2022.

W. Theobald, "LLE is Leading Innovative ICF/IFR Diagnostic Development, which is Amplified Through Participation in the National Diagnostics Working Group," presented at the Workshop on New Inertial Fusion Energy/ High-Energy-Density Physics Laser Facility, virtual, 10 February 2022.

V. V. Karasiev, D. I. Mihaylov, S. X. Hu, S. B. Trickey, and J. W. Dufty, "Meta-GGA Exchange-Correlation Free-Energy Density Functional: Achieving Unprecedented Accuracy for Warm-Dense-Matter Simulations," presented at the 61st Sanibel Symposium, St. Simons Island GA, 13–18 February 2022.

J. D. Zuegel, "High-Energy Lasers for Driving Dynamic Materials Experiments," presented at the NNSA Advanced Photon Sources Sector Opportunities Workshop, virtual, 15–17 February 2022.

E. M. Campbell, "Perspectives on Inertial Fusion Energy," presented at the PB11 Science Seminar, virtual, 17 February 2022.

C. Deeney, "National Nuclear Security: 21st Century Science and Technology Perspectives," presented at the World Affairs Council, West Palm Beach, FL, 21 February 2022.

D. H. Froula, "Thomson Scattering from a Different Perspective," presented at the Oxford Seminar, Oxford, UK, 21 February 2022.

J. D. Zuegel, "Kilojoule Lasers for Dynamic Compression Studies," presented at Science with High-Power Lasers, PETRA IV Workshop, virtual, 22–23 February 2022.

The following presentations were made at the Inertial Fusion Energy Science and Technology Workshop, virtual, 22–24 February 2022:

V. N. Goncharov, "Inertial Fusion Energy Target Designs with Advanced Laser Technologies."

J. D. Zuegel, "A Broad View of Solid-State Laser Drivers for Inertial Fusion Energy."

E. M. Campbell, "LLE Perspective," presented at the Office of Experimental Sciences Executives Meeting, virtual, 24 February 2022.

J. P. Palastro, "Research at the Laboratory for Laser Energetics," presented at the Physical Sciences and Astronomy Recruitment Event, Rochester, NY, 25 February 2022.

E. M. Campbell, "Perspectives on Inertial Fusion Energy," presented at the Plasma Science and Fusion Center Seminar, virtual, 7 March 2022.

The following presentations were made at the Ecosystem for Collaborative Leadership and Inclusive Innovation in Plasma Science and Engineering, Alexandria, VA, 9–11 March 2022:

G. W. Collins, "Extreme Matters: Pressures to Explore New Worlds and Revolutionary States of Matter."

P. Tzeferacos, "Laser-Driven Experiments Shed New Light on Magnetized Turbulence and Fluctuation Dynamo in Astrophysical Plasmas."

J. D. Zuegel, "Multi-Petawatt Physics Prioritization (MP3) Workshop."

The following presentations were made at Matter in Extreme Conditions from Material Science to Planetary Physics, Montgenevre, France, 12–19 March 2022:

D. A. Chin, P. M. Nilson, D. T. Bishel, R. Paul, E. Smith, X. Gong, M. K. Ginnane, B. J. Henderson, D. N. Polsin, S. X. Hu, J. R. Rygg, G. W. Collins, D. Trail, A. Amouretti, M. Harmand, O. Mathon, R. Torchio, J. J. Ruby, F. Coppari, A. Coleman, and Y. Ping, "X-Ray Absorption Spectroscopy Temperature Measurements at High-Energy-Density Conditions."

D. H. Froula, "Thomson Scattering from a Different Perspective."

S. X. Hu, V. V. Karasiev, P. M. Nilson, D. T. Bishel, D. A. Chin, K. Nichols, R. Paul, R. Goshadze, M. Ghosh, J. Hinz, S. Zhang, D. I. Mihaylov, G. W. Collins, N. Shaffer, L. A. Collins, A. J. White, V. Recoules, N. Brouwer, M. Torrent, I. E. Golovkin, M. Gu, T. Walton, and S. B. Hansen, "Understanding Matter in Extreme Conditions with *ab initio* Calculations."

Z. K. Sprowal, L. E. Hansen, M. F. Huff, D. N. Polsin, D. G. Hicks, T. R. Boehly, J. R. Rygg, and G. W. Collins, "Accessing High Density States in D_2 Using Double Shock."

The following presentations were made at the APS March Meeting, Chicago, IL, 14–18 March 2022:

M. Ghosh, S. Zhang, and S. X. Hu, "*Ab Initio* Investigation of the Cooperative Diffusion in Body-Centered-Cubic Iron Under Inner-Core Conditions of Earth and Super-Earth Exoplanets."

R. M. N. Goshadze, V. V. Karasiev, D. I. Mihaylov, and S. X. Hu, "Equation of State of Metallization of CH Along the Principal Hugoniot."

B. J. Henderson, M. C. Marshall, J. R. Rygg, D. N. Polsin, L. E. Hansen, M. K. Ginnane, and G. W. Collins, "Silica Aerogel as a Bright Optical Source for High-Energy-Density Experiments."

M. Huff, J. R. Rygg, G. W. Collins, T. R. Boehly, D. N. Polsin, M. Nakajima, B. J. Henderson, M. C. Marshall, T. A. Suer, D. E. Fratanduono, M. Millot, R. F. Smith, C. A. McCoy, and L. E. Hansen, "Measurements of Sound Speed in Iron Shock Compressed to ~3000 GPa."

R. Paul, S. Zhang, V. V. Karasiev, and S. X. Hu, "Thermal-Induced Evolution of Magnetic Properties of FeO_2 Under High Pressures."

S. Zhang, M. A. Morales, R. Jeanloz, M. Millot, S. X. Hu, and E. Zurek, "Nature of the Bonded-to-Atomic Transition in Liquid Silica at Extreme Conditions."

M. Ghosh, S. Zhang, and S. X. Hu, "An Exotic Phase of Iron in Earth's Inner Core: A First-Principles–Based Study on the Mechanism of Cooperative Diffusion in Body-Centered-Cubic Iron," presented at the University of Rochester Graduate Education and Postdoctoral Affairs Research Symposium, Rochester, NY, 23 March 2022.

C. Deeney, "The Laboratory for Laser Energetics: Progress in Science and Technology," presented at the Plasma Science and Fusion Center Seminar, virtual, 28 March 2022.

UNIVERSITY OF ROCHESTER
LABORATORY FOR LASER ENERGETICS

Volume 171
April–June 2022
DOE/NA/3856-1752

LLE Review

Quarterly Report

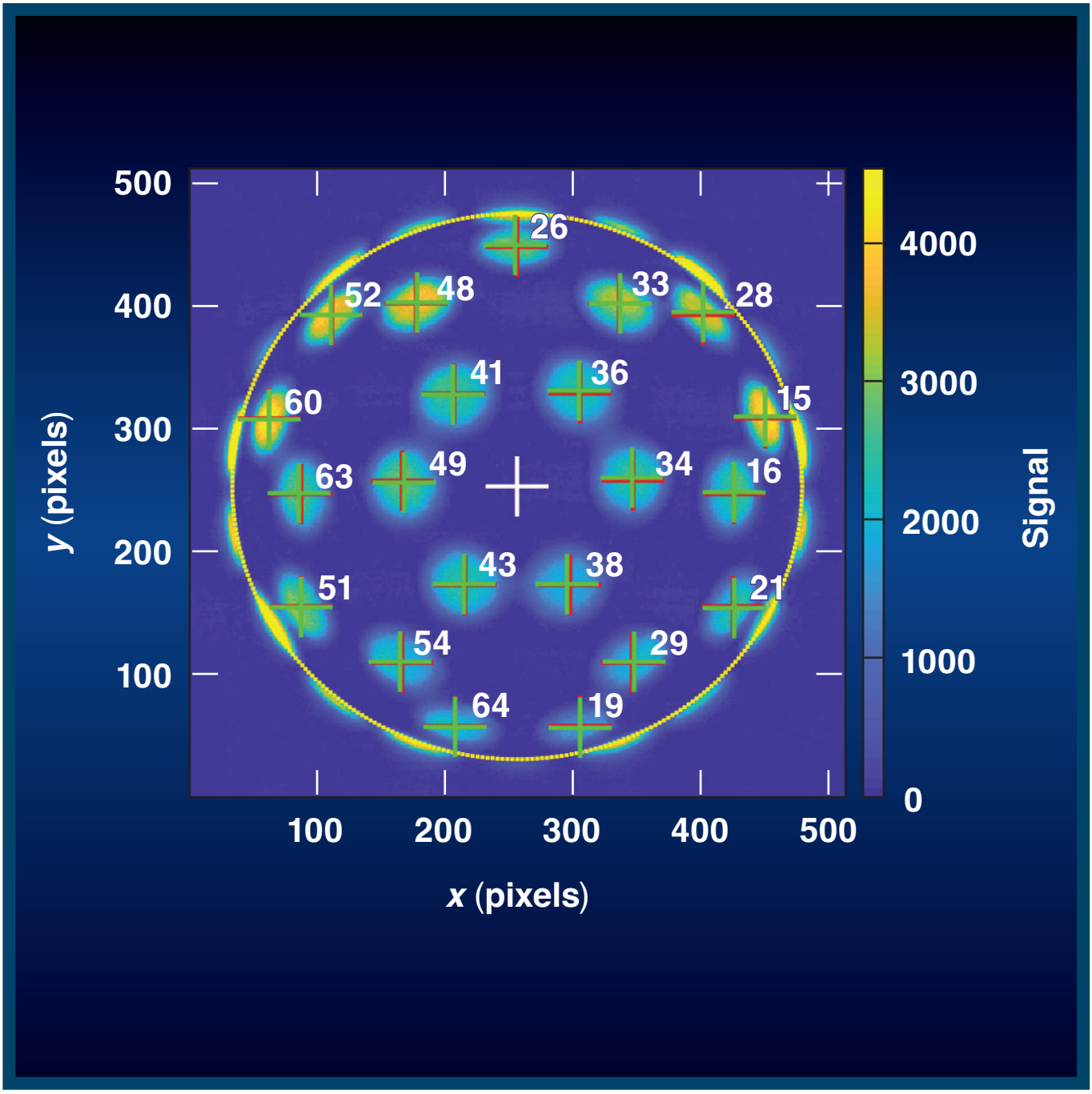

About the Cover:

The cover picture shows an x-ray image recorded on a charge-injection–device electronic sensor by one of the ten x-ray pinhole cameras located in TIM-5 in during a pointing shot. Beam-pointing accuracy is verified on the OMEGA Laser System by irradiating a 4-mm-diam Au-coated spherical target with ~23 kJ of laser energy. The large target diameter is used to separate the individual ~850-μm-diam laser spots that are typically overlapped on the ~1-mm-diam implosion targets. The spatial intensity distribution of the individual laser beams is carefully shaped and smoothed using distributed phase plates (DPP's), polarization wedges, and smoothing by spectral dispersion. A well-defined edge of the target can also be observed from the shadow of the beams behind the horizon of the sphere (yellow circle), which can be used to evaluate the location of the center of the sphere (white cross). The position of up to 21 beams can be evaluated from this image (red crosses) and compared to the desired locations (green crosses).

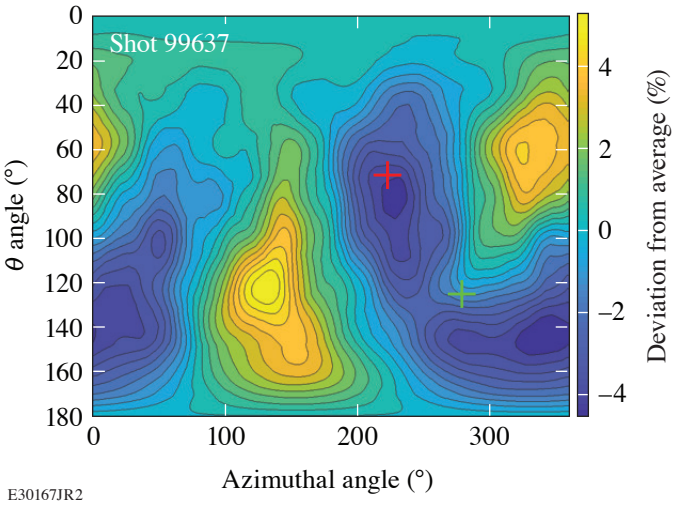

E30167JR2

To assess the impact of the pointing errors on the illumination uniformity, the on-target intensity distribution is calculated by overlapping all 60 beams onto a sphere of the typical diameter of an implosion target of ~870 μm. The pointing of the beams is set according to the evaluation of the data from the pointing shots. Identical beam profiles are assumed for all 60 beams, with a super-Gaussian intensity profile as set by the DPP. The resulting intensity map is shown in the figure on the right. Additionally, a modal decomposition into ℓ modes is performed, with the inferred direction of the $\ell = 1$ mode (red cross) and $\ell = 2$ mode (green cross) indicated in the above image.

The work described in this volume includes current research at the Laboratory for Laser Energetics, which is supported by New York State Energy Research and Development Authority, the University of Rochester, the U.S. Department of Energy Office of Inertial Confinement Fusion under Cooperative Agreement No. DE-NA0003856, and other agencies.

Printed in the United States of America
Available from
National Technical Information Services
U.S. Department of Commerce
5285 Port Royal Road
Springfield, VA 22161
www.ntis.gov

For questions or comments, contact Milton J. Shoup III, Editor, Laboratory for Laser Energetics, 250 East River Road, Rochester, NY 14623-1299, (585) 275-9636.

www.lle.rochester.edu

UNIVERSITY OF ROCHESTER
LABORATORY FOR LASER ENERGETICS

Volume 171
April–June 2022
DOE/NA/3856-1752

LLE Review

Quarterly Report

Contents

In Brief

This volume of LLE Review 171 covers the period from April–June 2022. Articles appearing in this volume are the principal summarized results for long-form research articles. Readers seeking a more-detailed account of research activities are invited to seek out the primary materials appearing in print, detailed in the publications and presentations section at the end of this volume.

Highlights of research presented in this volume include:

- C. Stoeckl *et al.* present beam-pointing verification using x-ray pinhole cameras on the 60-beam OMEGA Laser (p. 1).
- C. J. Forrest *et al.* describe measurements of low-mode asymmetries in the areal density of laser-direct-drive DT cryogenic implosions on OMEGA using neutron spectroscopy (p. 3).
- F. García-Rubio *et al.* discuss the theory of the magnetothermal instability in coronal plasma flows (p. 6).
- N. Acharya, H. Aluie, and J. K. Shang discuss a numerical investigation of a laser-driven shock interaction with a deformable particle (p. 9).
- S. X. Hu *et al.* describe probing extreme atomic physics at Gbar pressures (p. 11).
- H. Yin *et al.* report on the effective drift velocity from turbulent transport by vorticity (p. 13).
- L. Ceurvorst *et al.* report on the development of an x-ray radiography platform to study laser-direct-drive energy coupling at the National Ignition Facility (p. 15).
- D. H. Edgell *et al.* present on the use of a scattered-light uniformity imager for diagnosing laser-absorption asymmetries on OMEGA (p. 18).
- K. Churnetski *et al.* present three-dimensional hot-spot x-ray emission tomography results from cryogenic deuterium–tritium direct-drive implosions on OMEGA (p. 20).
- V. Yu. Glebov *et al.* demonstrate a new neutron time-of-flight detector for deuterium–deuterium yield and ion-temperature measurements on OMEGA (p. 24).
- H. G. Rinderknecht *et al.* report on a knock-on deuteron imager used for measurements of fuel and hot-spot asymmetry in direct-drive inertial confinement fusion implosions (p. 26).
- D. Weiner *et al.* discuss the design and implementation of a digital optical microscope for measuring submicron defects on cryogenic DT targets (p. 29).
- S. F. Nwabunwanne and W. R. Donaldson discuss the performance of a new class of tunable picosecond AlGaN UV photodiodes (p. 32).
- J. Katz *et al.* report on the measurement of laser absorption in underdense plasmas using near-field imaging of the incident and transmitted beams (p. 35).
- S. T. Ivancic *et al.* discuss the design of the high-yield time-gated x-ray hot-spot imager for OMEGA (p. 38).
- C. Dorrer *et al.* demonstrate high-resolution mapping of phase-matching conditions in second-order nonlinear crystals (p. 40).

- S. Bucht *et al.* report on achieving 100-GW idler pulses from an existing petawatt optical parametric chirped-pulse amplifier (p. 43).
- J. Zhang, W. R. Donaldson, and G. P. Agrawal discuss the impact of Raman scattering on the temporal reflection from a short soliton (p. 46).
- S. Zhang *et al.* report on a the first-principles equation of state of CHON resin for inertial confinement fusion applications (p. 49).
- B. J. Henderson *et al.* present measurements of the shocked-silica aerogel radiance transition (p. 52).
- R. M. N. Goshadze *et al.* present an analysis of shock-induced metallization of polystyrene along the principal Hugoniot investigated by advanced thermal density functionals (p. 54).
- J. A Frenje *et al.* report on the 13th Omega Laser Facility Users Group Workshop, held in person and virtually from 27–29 April 2022 (p. 57).
- J. Puth *et al.* summarize operations of the Omega Laser Facility during the third quarter of FY22 (p. 66).

Milton Shoup III
Editor

Beam-Pointing Verification Using X-Ray Pinhole Cameras on the 60-Beam OMEGA Laser

C. Stoeckl, D. Cao, L. Ceurvorst, A. Kalb, J. Kwiatkowski, A. Shvydky, and W. Theobald

Laboratory for Laser Energetics, University of Rochester

On the OMEGA Laser System, the beam-pointing accuracy is verified by irradiating a 4-mm-diam Au-coated spherical target with ~23 kJ of laser energy.[1] Up to ten x-ray pinhole cameras record the emission from all 60 beam spots [see Fig. 1(a)]. A new set of algorithms has been developed to improve the accuracy of the pointing evaluation. An updated edge-finding procedure allows one to infer the center of the sphere with subpixel accuracy. A new approach was introduced to back-propagate the pixel locations on the 2-D image to the 3-D surface of the sphere. A fast Fourier transform-based noise reduction method significantly improves the signal-to-noise ratio of the data. Based on the beam-pointing analysis, hard-sphere calculations of the laser-drive illumination uniformity on the target surface and the decomposition of the illumination distribution into lower order modes (1 to 10) are evaluated.

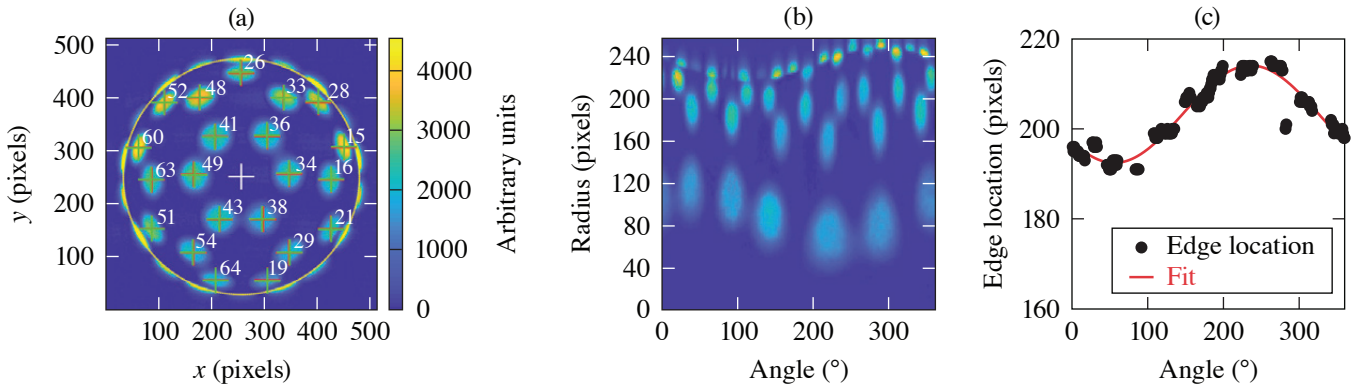

Figure 1
(a) X-ray image from one of the ten x-ray pinhole cameras acquired during a pointing shot. The position of up to 21 beams can be evaluated (red crosses) and compared to the desired locations (green crosses). The white cross shows the evaluated center of the sphere and the yellow circle is the outside radius. (b) Angular lineouts from a first guess of the center of the image of the sphere. (c) Evaluated location of the edge of the sphere compared to a cosine fit.

To infer the location of the center of the sphere, radial lineouts starting from a first estimate of the center (x_e, y_e) of the image are taken in 1° angular increments. Figure 1(b) shows a composite of these lineouts in the form of a 2-D image. The edge feature from the self-shadowing of the beams behind the horizon can be clearly seen at the top of the image. The location of the edge is determined as the position of the maximum of the gradient of each lineout and plotted in Fig. 2(c). Lines with low signal or high noise are discarded. A cosine function of the form $r = r_0 + a * \cos(t + b)$ is fitted to the data, with t as the angle, b as the phase offset, and a as the amplitude of the radial variation. From simple geometry, two offsets (dx, dy) can be computed that correct the estimated center to provide a better fit of the center $x_f = x_e + dx$; $y_f = y_e + dy$. Depending on the magnitude of the radial variation, this process can be repeated to get the best fit of the center.

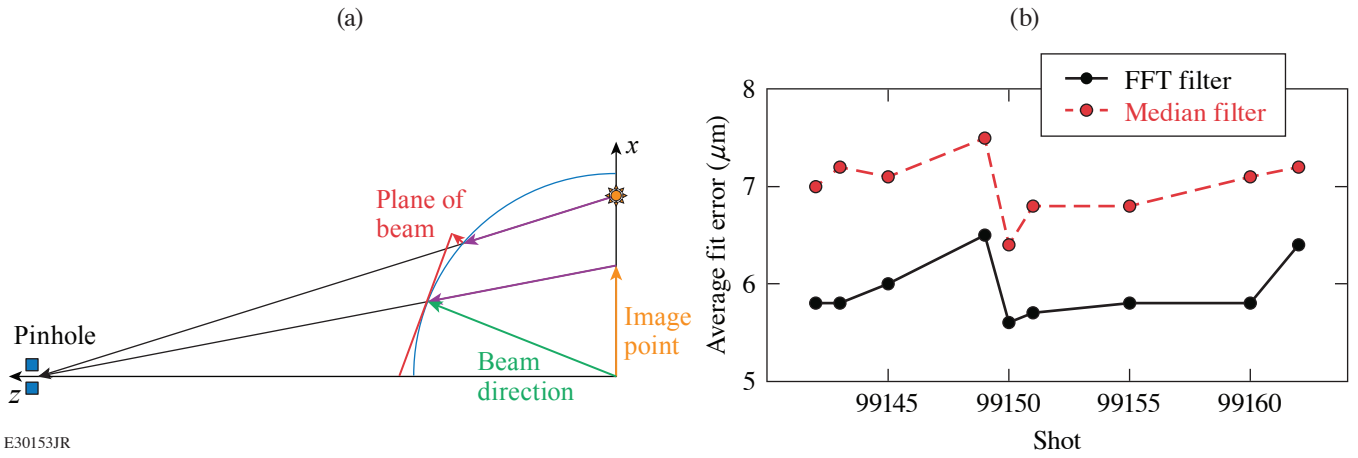

Figure 2
(a) Sketch of the geometry used to project the emission recorded from the individual beams into the planes perpendicular to the beam propagation direction. (b) Average pointing error evaluated from a median filtered image compared to a fast Fourier transform (FFT)-filtered image.

The x-ray pinhole camera image is a 2-D projection of the emission from a 3-D sphere. To infer the intensity distribution on the sphere, the image from the sensor is mapped to the object plane through the pinhole, and then each pixel location is projected onto the sphere [see purple arrow in Fig. 2(a)]. Since the intensity distribution of the laser focus is defined in a plane perpendicular to the laser propagation direction, the pixel locations on the sphere for a single beam are further projected onto the plane perpendicular to the laser direction tangent to the surface of the sphere [red arrow in Fig. 2(a)]. This procedure corrects all geometric effects of the imaging and compensates the ellipticity of the beams close to the edge of the image very well.

Simple median filters are typically used to clean up the raw charge-injection–device (CID) images under the assumption that the noise seen is purely statistical and uncorrelated. Upon more-detailed inspection of the images, it became obvious that there are medium- and large-scale correlations in the noise mostly caused by imperfections in the readout system. To clean up these correlated features a 2-D FFT is generated from the image and the regions in the FFT corresponding to high spatial frequencies or clearly identifiable background features are set to zero. A cleaned-up image is then reconstructed using the inverse FFT. The evaluation of the pointing with the FFT filtered images show a significant improvement in fit error [see Fig. 2(b)].

The limiting factors on the accuracy of the pointing evaluation, which are currently of the order of 5 μm, are most likely the quality of the pointing targets, noise (especially correlated features) in the CID readout, and imperfections in the intensity distribution of the laser beam focus. A more-uniform coating for of targets would reduce the artifacts in the image, like the “holes” [as seen in Fig. 1(a)], and lead to better fits. It is also likely that the FFT filter can be further improved by using an evolutionary algorithm or a machine learning approach.

This material is based upon work supported by the Department of Energy National Nuclear Security Administration under Award Number DE-NA0003856, the University of Rochester, and the New York State Energy Research and Development Authority.

1. R. A. Forties and F. J. Marshall, Rev. Sci. Instrum. **76**, 073505 (2005).

Measurements of Low-Mode Asymmetries in the Areal Density of Laser-Direct-Drive Deuterium–Tritium Cryogenic Implosions on OMEGA Using Neutron Spectroscopy

C. J. Forrest,[1] A. Crilly,[2] A. Schwemmlein,[1] M. Gatu Johnson,[3] O. M. Mannion,[4] B. Appelbe,[2] R. Betti,[1] V. Yu. Glebov,[1] V. Gopalaswamy,[1] J. P. Knauer,[1] Z. L. Mohamed,[1] P. B. Radha,[1] S. P. Regan,[1] C. Stoeckl,[1] and W. Theobald[1]

[1]Laboratory for Laser Energetics, University of Rochester
[2]Centre for Inertial Fusion Studies, the Blackett Laboratory, Imperial College London
[3]Plasma Science and Fusion Center, Massachusetts Institute of Technology
[4]Sandia National Laboratories

The OMEGA laser is used to study direct-drive inertial confinement fusion (ICF) by symmetrically irradiating a thin shell target with nominally identical laser beams. The shell is comprised of an outer plastic ablator (<10 μm) and a layer of cryogenic deuterium–tritium (DT) ice (~50 μm) encapsulating a vapor region DT gas. In these target designs, the incident laser ablates the thin shell, which then launches one or multiple shocks through the remaining converging shell and into the vapor region. The shock-transit stage of the implosion is followed by a deceleration phase, where the kinetic energy of the converging shell is converted to the internal energy of the hot spot. To achieve conditions relevant for ignition implosion designs, the hot-spot size must exceed the mean free path of the fusing ions and alpha particles in order to remain confined in the dense plasma. This requirement is essential to maximize the energy deposition of the alpha particle in the hot spot and surrounding dense fuel. Targets that are not compressed symmetrically will be unable to fully convert their shell kinetic energy to hot-spot thermal energy.

Areal density is one of the key parameters that determines the confinement time in ICF experiments, and low-mode asymmetries in the compressed fuel are detrimental to the implosion performance. The energy spectra from scattering of the primary DT neutrons off the compressed cold fuel assembly are used to investigate low-mode nonuniformities in direct-drive cryogenic DT implosions. For spherically symmetric implosions, the shape of the energy spectrum is primarily determined by the elastic and inelastic scattering cross sections for both neutron–deuterium (nD) and neutron–tritium (nT) kinematic interactions given by

$$\frac{\mathrm{d}N}{\mathrm{d}E} = Y_\mathrm{n}\left\{\left[\mathrm{DT} + \frac{1}{2}\frac{f_\mathrm{d}}{f_\mathrm{t}}\frac{\langle\sigma\nu_\mathrm{dd}\rangle}{\langle\sigma\nu_\mathrm{dt}\rangle}\,\mathrm{DD} + \frac{f_\mathrm{t}}{f_\mathrm{d}}\frac{\langle\sigma\nu_\mathrm{tt}\rangle}{\langle\sigma\nu_\mathrm{dt}\rangle}\,\mathrm{TT}\right]\right.$$

$$\left. + \rho L N_\mathrm{a}\left[\frac{\left(\mathrm{d}\sigma_\mathrm{nD}/\mathrm{d}E\right)f_\mathrm{d} + \left(\mathrm{d}\sigma_\mathrm{nT}/\mathrm{d}E\right)f_\mathrm{t}}{f_\mathrm{d}m_\mathrm{d} + f_\mathrm{t}m_\mathrm{t}} + \frac{\left(\mathrm{d}\sigma^\mathrm{d}_{\sigma_\mathrm{n2n}}/\mathrm{d}E\right)f_\mathrm{d}}{f_\mathrm{d}m_\mathrm{d} + f_\mathrm{t}m_\mathrm{t}} + \frac{\left(\mathrm{d}\sigma^\mathrm{t}_{\sigma_\mathrm{n2n}}/\mathrm{d}E\right)f_\mathrm{t}}{f_\mathrm{d}m_\mathrm{d} + f_\mathrm{t}m_\mathrm{t}}\right]\right\},$$

where Y_n is the primary DT yield, f_d and f_t are the fuel fraction of the fuel, and $\langle\sigma\nu\rangle$ is the reactivity rate with the associated fusing pair of ions. In the above expression DT, DD, and TT represent the shape of the primary neutron energy spectra for each reaction. The differential and double-differential cross-sections require a term to better describe this variation in the cold fuel, assuming a low-mode ($\ell = 1$) distribution as given by

$$\frac{\mathrm{d}\sigma}{\mathrm{d}E} = \int \left(\frac{\mathrm{d}\sigma}{\mathrm{d}\Omega}\right)\left(1 + \frac{\Delta\rho L}{\rho L} * \cos\theta\right)\mathrm{d}E,$$

$$\frac{\mathrm{d}\sigma_{\mathrm{n,2n}}}{\mathrm{d}E} = \int 2\pi\left(\frac{\mathrm{d}^2\sigma}{\mathrm{d}E\mathrm{d}\Omega}\right)\left(1 + \frac{\Delta\rho L}{\rho L} * \cos\theta\right)\mathrm{d}\cos\theta.$$

Experimental observations shown in Fig. 1 of the low-mode variations cold fuel assembly ($\rho L_0 + \rho L_1$) show good agreement with this recently developed model, indicating a departure from a spherical symmetry of the compressed DT fuel assembly.

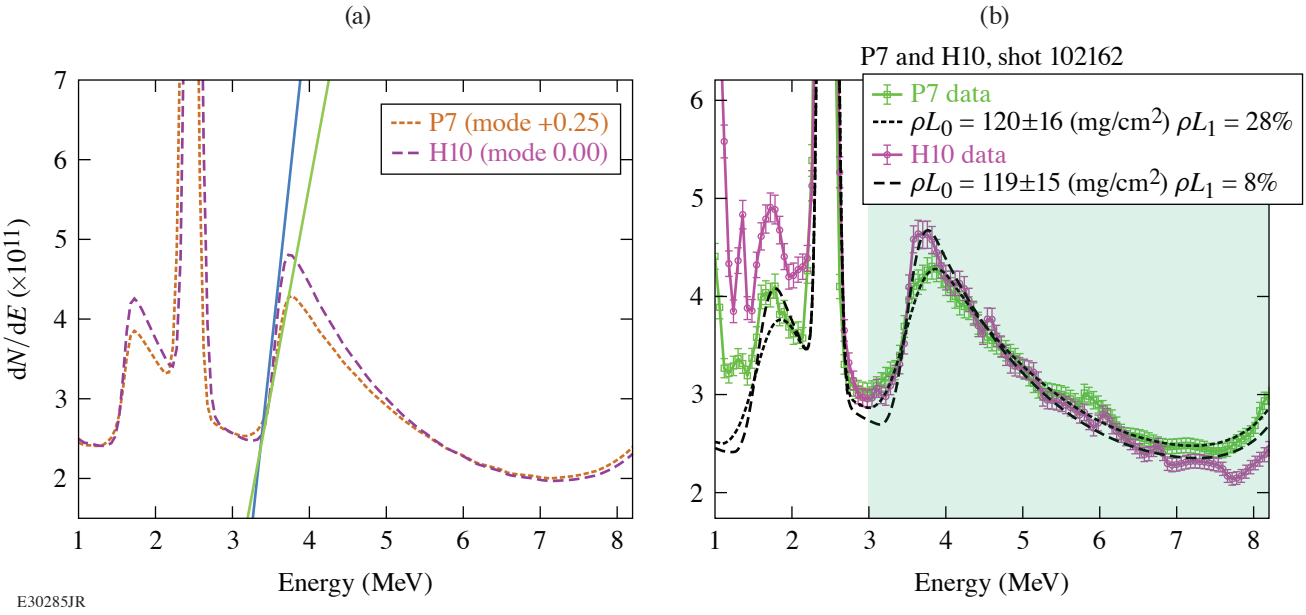

Figure 1
(a) An example of a cryogenic implosion with a significant mode 1 that shows qualitative agreement with the broadening of the kinematic edge due to the anisotropy of the cold fuel depending on the spectrometer's line of sight as predicted by the model. (b) A model illustrates the broadening of the kinematic edge due to the anisotropy of the cold fuel depending on the spectrometer's line of sight. Straight lines tangent to the nT edges are included to emphasize the difference in slopes. An example of a cryogenic implosion with a significant mode 1 shows qualitative agreement with the broadening of the kinematic edge due to the anisotropy of the cold fuel depending on the spectrometers line of sight as predicted by the model.

Another key signature in the presence of a low-mode variation is the broadening of the kinematic end point due to anisotropy of the dense fuel conditions has been observed. Recent theoretical[1] and experimental[2] studies have showed that the neutron-backscatter edge presents a novel measurement of the hydrodynamic conditions at stagnation. The spectral shape of the edge is determined by the velocity distribution of the scattering ions. When there is a large mode-1 variation in areal density, hydrodynamic models predict that the higher areal density side will decelerate slower than the lower areal density side.[3] The lower areal density side will therefore exhibit a larger variation in scattering ion velocities and consequently will produce a broader backscatter edge; the opposite is true for the higher areal density side.

More-recent hydrodynamics simulations of OMEGA implosions perturbed by a mode 1 were post-processed with a neutron transport code to obtain synthetic spectra on the P7 and H10 OMEGA lines of sight showing the anisotropic edge broadening. This anisotropy has been predicted in simulation to appear (Fig. 1) in the backscatter edge shape along different lines of sight. Measurements on the broadening of the kinematic edges show qualitative agreement with the anisotropy of the dense fuel conditions from separate lines of sight given by the model prediction. The anisotropy is also correlated with the observed mode-1

areal-density asymmetry. The P7 line of sight observes a positive mode-1 areal-density asymmetry and therefore backscatter occurs in a lower areal-density region for this line of sight.

This material is based upon work supported by the Department of Energy National Nuclear Security Administration under Award Number DE-NA0003856, the University of Rochester, and the New York State Energy Research and Development Authority.

1. A. J. Crilly *et al.*, Phys. Plasmas **27**, 012701 (2020).
2. O. M. Mannion *et al.*, Phys. Rev. E **105**, 055205 (2022).
3. B. K. Spears *et al.*, Phys. Plasmas **21**, 042702 (2014).

The Theory of Magnetothermal Instability in Coronal Plasma Flows

F. García-Rubio,[1,2] R. Betti,[1,2,3] J. Sanz,[4] and H. Aluie[1,2]

[1]Laboratory for Laser Energetics, University of Rochester
[2]Department of Mechanical Engineering, University of Rochester
[3]Department of Physics and Astronomy, University of Rochester
[4]Escuela Técnica Superior de Ingeniería Aeronáutica y del Espacio, Universidad Politécnica de Madrid, Spain

In this summary, the theory of the magnetothermal instability (MTI) is revisited through the lens of the stability of uniform systems, and its implication in the corona dynamics of direct-drive implosions is discussed. The underlying mechanism of this instability corresponds exclusively to the interplay between the Biermann battery generating magnetic (B) fields and the Righi–Leduc term bending the heat flux lines, as shown in Fig. 1. In its most simple configuration, a temperature perturbation δT results in B-field generation $\delta\vec{B}$ via the Biermann battery. This allows the Righi–Leduc heat flux, $\vec{q}_{\mathrm{RL}} \propto \left(T_0^4/n_0\right)\nabla T_0 \times \delta\vec{B}$, to pump heat into the hotter regions of the fluid, thereby driving the MTI by amplifying the δT perturbation.

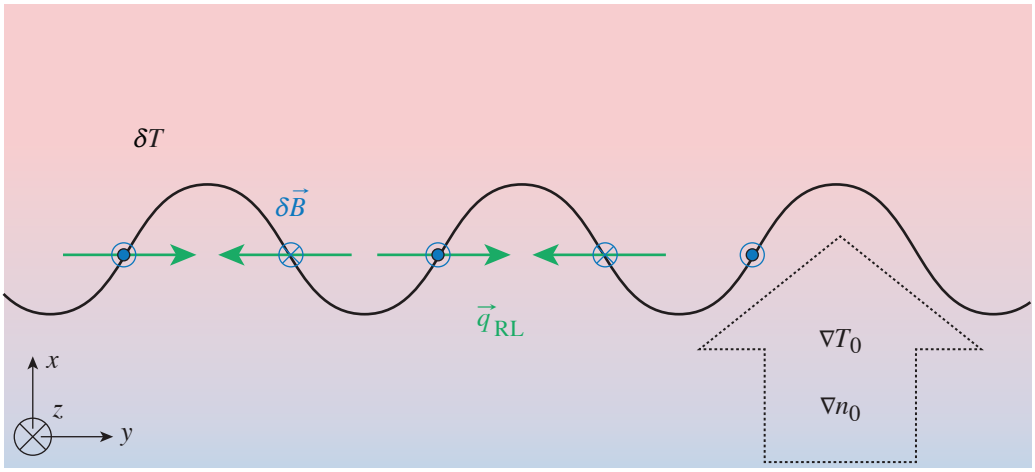

Figure 1
Schematic of the magnetothermal instability as first explained in Ref. 1. It relied on the background ∇T_0 and ∇n_0 being aligned.

The main novelty in the linear stability analysis performed in this summary corresponds to the distinction between the convective and the absolute nature of the perturbation growth. Previous analyses[1–3] identified the MTI as a convective instability and observed significant suppression of its growth rate caused by Nernst convection.[3] In the present linear analysis, we have applied the instability criteria derived by Briggs[4] to prove that, in the region where the Nernst and plasma blowoff velocities cancel, the MTI can be absolute and wave-packet perturbations grow *in situ*. The growth rate thereby derived becomes

$$\gamma \mathrm{MTI}_{\mathrm{ns}^{-1}} = 0.19 i\overline{\omega}_{M_2} \frac{10}{\log \Lambda} \frac{\gamma_0''}{\gamma_0 \delta_0 Z} \frac{T_{\mathrm{keV}}^{5/2}}{n_{10^{22}\mathrm{cm}^{-3}}} \left(\frac{\mathrm{d} \log T}{\mathrm{d}x_{100\,\mu\mathrm{m}}} \right)^2,$$

where γ_0'', γ_0, and δ_0 are coefficients that depend on the atomic number Z given in Braginskii,[5] and the dimensionless frequency $i\overline{\omega}_{M_2}$ depends on the isothermal Mach number (Ma) of the section in the corona in consideration and the pressure-to-temperature gradient ration (δ), Fig. 2.

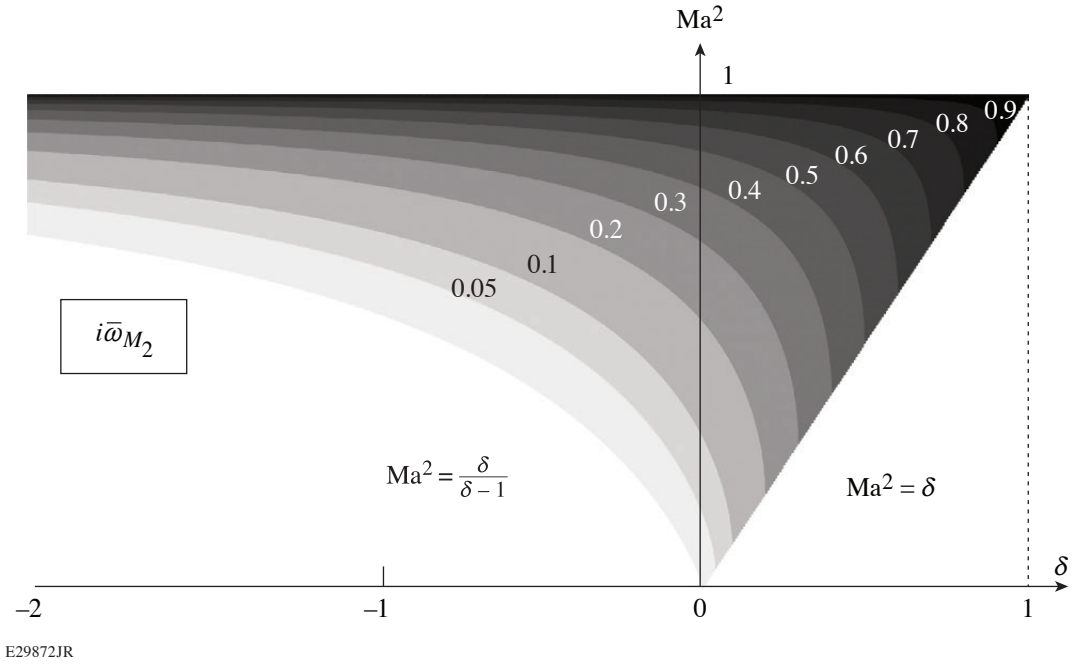

Figure 2
Isocontours of the temporal growth rate $i\overline{\omega}_{M_2}$ in the phase space isothermal Mach number Ma and pressure-to-temperature gradient ratio δ.

The analysis has been extended to derive the dispersion relation for short-wavelength perturbations developing in nonuniform profiles with application to coronal plasmas. It is found that the condition for MTI requires the net B-field convection velocity to be small at the isothermal sonic section, and the plasma conditions in this section govern the dynamics of the instability. This theory reveals a picture of the MTI where the conduction layer is the dynamically active region of the corona. Here is found the spatial resonance that causes perturbations to grow *in situ*, hence traveling with the imploding shell and potentially altering its dynamics. The structure of the unstable perturbations tends to elongate filaments in the azimuthal direction, in agreement with the observations made in Ref. 6. They can spread out to regions of outflowing convection velocity, being subsequently stretched radially and filling the outer corona. This picture is in qualitative agreement with the proton radiographs of imploding fast-ignition capsules performed by Rygg *et al.*,[7] who observed striated fields that originate close to the capsule surface, and conjectured that the vast spatial extent of these fields reflects an outward convection of filamentary structures originally produced inside the critical surface.

Applying this theory to direct-drive inertial confinement fusion implosions provides an MTI growth rate in the range of a fraction to few gigahertz (see Fig. 3), which is milder than the ones discussed by Manuel *et al.*[8] and Bissell *et al.*[9] (several to tens of gigahertz). This is mainly due to authors employing growth rate expressions derived from a convective instability analysis, which favors lower-density, higher-temperature regions (outer corona) as more-unstable regions. The outer corona indeed supports unstable waves, but we deem we must impose the requirement for absolute instability to account how the MTI affects the dynamics of the implosion. This holds the plasma state at the conduction layer responsible for the growth rate of the MTI. Finally, analysis of hydro-equivalent implosions suggests that unstable perturbations undergo more *e* foldings of growth in larger-size targets.

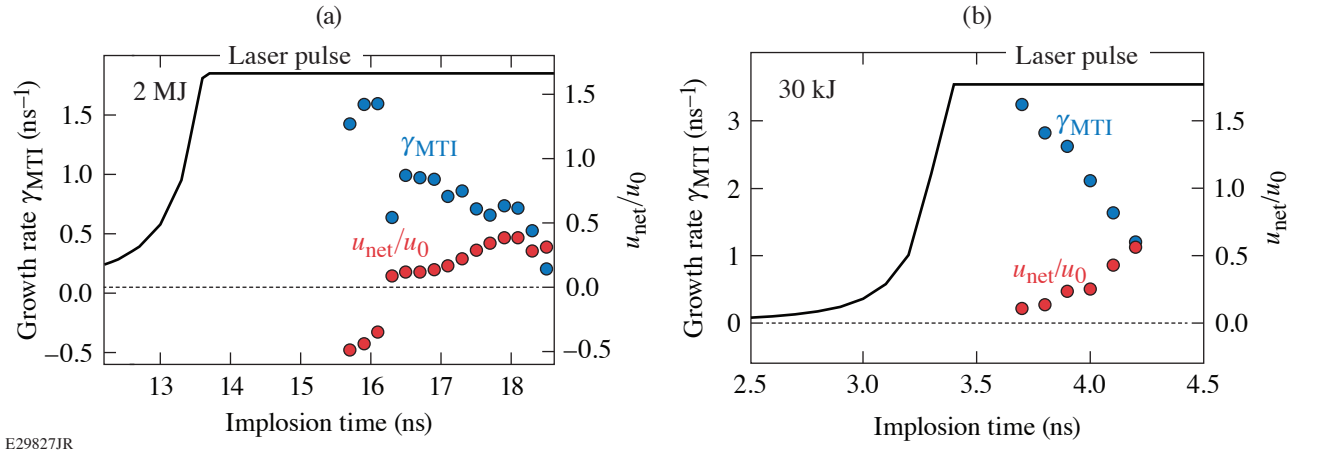

Figure 3
Maximum growth rate γ and velocity ratio u_{net}/u_0 at the isothermal sonic point for(a) 2-MJ and (b) 30-kJ direct-drive implosions. The laser power pulse shape is plotted for reference.

This work is supported by the Department of Energy Office of Science, Fusion Energy Sciences program grants DE-SC0016258, DE-SC0014318 and DE-SC0021072. F. García-Rubio was also supported by the Advanced Research Projects Agency-Energy (ARPA-E), U.S. Department of Energy, under Award No. DE-AR0001272. J. Sanz was also supported by the Spanish Ministerio de Economía y Competitividad, Project No. RTI2018-098801-B-I00. H. Aluie was also supported by U.S. DOE grants DE-SC0020229 and DE-SC0019329, U.S. NASA grant 80NSSC18K0772, U.S. NSF grants OCE-2123496 and PHY-2020249, and U.S. NNSA grants DE-NA0003856 and DE-NA0003914. This material is based upon work supported by the University of Rochester and the New York State Energy Research and Development Authority.

1. D. A. Tidman and R. A. Shanny, Phys. Fluids **17**, 1207 (1974).
2. J. J. Bissell, C. P. Ridgers, and R. J. Kingham, Phys. Rev. Lett. **105**, 175001 (2010).
3. M. Sherlock and J. J. Bissell, Phys. Rev. Lett. **124**, 055001 (2020).
4. R. J. Briggs, *Electron-Stream Interaction with Plasmas* (MIT Press, Cambridge, MA, 1964).
5. S. I. Braginskii, in *Reviews of Plasma Physics*, edited by M. A. Leontovich (Consultants Bureau, New York, 1965), Vol. 1, pp. 205–311.
6. I. V. Igumenshchev *et al.*, Phys. Plasmas **21**, 062707 (2014).
7. J. R. Rygg *et al.*, Science **319**, 1223 (2008).
8. M. J.-E. Manuel *et al.*, Phys. Plasmas **20**, 056301 (2013).
9. J. J. Bissell, R. J. Kingham, and C. P. Ridgers, Phys. Plasmas **19**, 052107 (2012).

Numerical Investigation of Laser-Driven Shock Interaction with a Deformable Particle

N. Acharya,[1,2] H. Aluie,[1,2] and J. K. Shang[1,2]

[1]Department of Mechanical Engineering, University of Rochester
[2]Laboratory for Laser Energetics, University of Rochester

To accurately simulate material behavior at relatively low temperatures, i.e., in the sub-eV range, we require models with strength properties in the solid/liquid regime. Such models are not often included in most radiation-hydrodynamics simulation codes including *FLASH*,[1] which are used as tools to design high-energy-density (HED) experiments. In addition, high-temperature equation-of-state (EOS) models used for simulations become less predictive of the thermodynamic material properties necessary for describing the hydrodynamic processes taking place at low temperatures. For instance, in *FLASH*, only thermal pressure contributes to the computation of the local sound speed. This entirely neglects the existence of nonthermal pressure, which is a property that determines the behavior of shock-compressed solids. Theoretically, this leads to higher material compressibility even at low shock pressures. Veification was carried out in 2-D *FLASH* simulations of an ~50-GPa ablation-driven shock propagating over an Al particle embedded in epoxy (CH) and observed ~3.5× compression and significant deformation of the particle in Fig. 1(a). The predicted evolution of the particle modeled with *IONMIX* EOS did not reproduce the experimental shock Hugoniot.[2] Hence, a technique was developed to implement a modified form of ideal gas EOS to model the materials (including Al, Ti, and W) and study the dynamics of the embedded particle. The simulated shock Hugoniots of multiple materials modeled using this technique compared well with experimental data. Examination of the flow field [see Fig. 1(b)] demonstrated that the unsteady drag coefficient for the particle featured a peak drag due to an unsteady interaction with the transmitted shock and a drag minimum due to shock focusing on the rear end of the particle. However, unlike previous studies performed without laser drives, the particle drag coefficient featured a second minimum due to rarefaction stretching associated with laser shutoff.

Numerous simulations were conducted that investigated the particle response for a range of particle densities, sizes, and acoustic impedances. These results revealed that lighter particles, such as Al, gained significant momentum up to 96% from the shocked CH compared to 29% in the case of heavier W. Finally, the effect of particle acoustic impedance on the bulk particle response was studied. Despite differences observed in the early stage of shock interaction, the acoustic impedance did not influence the peak particle velocity. This identified particle-to-host density ratio as a dominant factor in determining the inviscid terminal velocity of the particle. Time-scale analysis in previous works has pointed out that the shock–particle interaction time scale could be of the same order as the viscous time scale, particularly for condensed-matter systems.[3] Therefore, viscous effects coupled with rarefaction stretching effect could be important for particle drag calculation in the intermediate to later stages of shock interaction.

Finally, the simplified approach of modeling materials for hydrodynamic simulations presented in this work could be useful in studying propagation of shock waves through condensed media, in particular, dispersal of particles in multiphase explosives. The method could also be applied to understand the particle dynamics of tracers for their potential applications to x-ray particle image velocimetry in HED flows.

This work was performed under the auspices of the U.S. Department of Energy under Grant No. DE-SC0019329 within the joint HEDLP program and was supported by the Laboratory Basic Sciences program administered by UR/LLE for DOE/NNSA. H. Aluie was also supported by U.S. DOE Grant Nos. DE-SC0014318 and DE-SC0020229, NSF Grant Nos. PHY-2020249 and OCE-2123496, U.S. NASA Grant No. 80NSSC18K0772, and U.S. NNSA Grant Nos. DE-NA0003856 and DE-NA0003914. J. K.

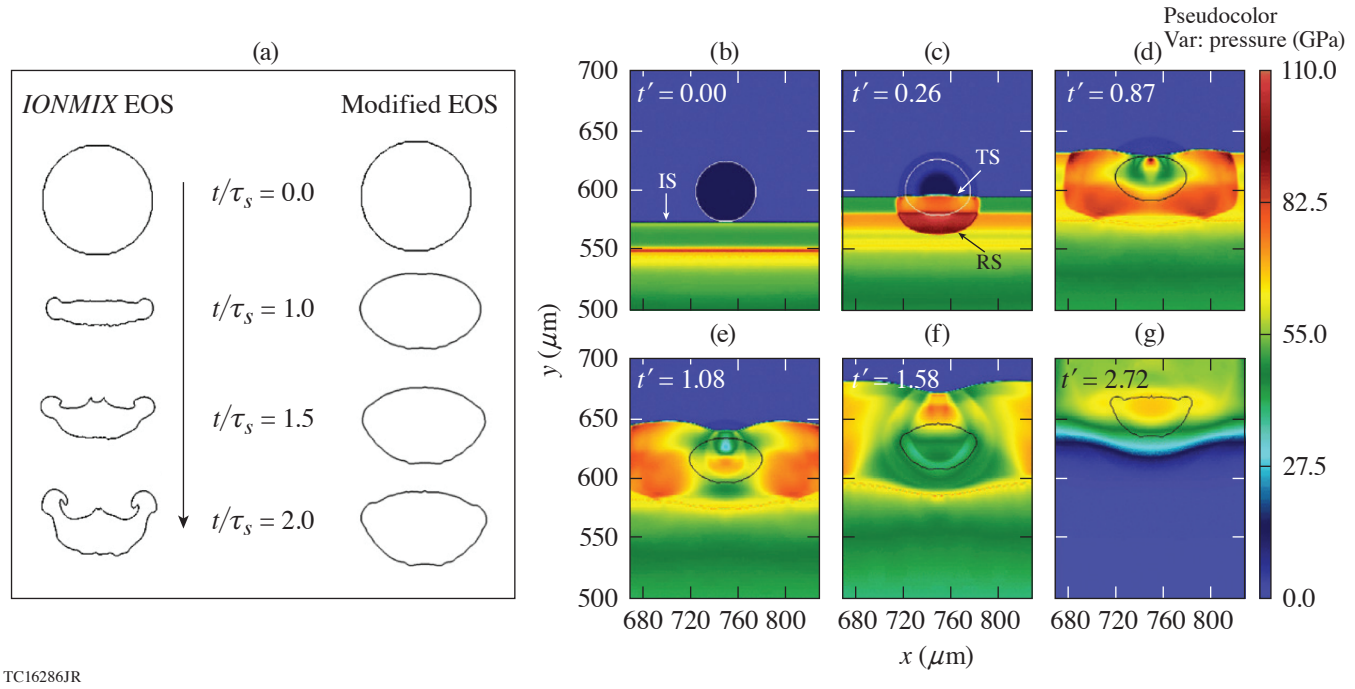

Figure 1
(a) Deformation of an Al particle in CH subjected to a 55-GPa shock with materials modeled using *IONMIX* EOS and a modified ideal gas EOS. τ_s is the shock–particle interaction time based on the particle diameter d_p and shock speed u_s. (b) Contour plots of pressure at increasing times for the post-shock pressure of 55 GPa in CH. Computational domain near the Al particle (modeled using modified EOS) is shown. The white curve [in (b) and (c)] or black curve [in (d)–(g)] is a particle interface constructed using cells around the particle with 25% mass-fraction cutoff. IS, TS, and RS denote incident, transmitted and reflected shock, respectively.

Shang was also supported by NSF Grant No. PHY2020249 and NNSA Grant No. DE-NA0003914. The software used in this work was developed in part by the DOE NNSA- and DOE Office of Science-supported Flash Center for Computational Science at the University of Chicago and the University of Rochester.

1. B. Fryxell *et al.*, Astrophys. J. Suppl. Ser. **131**, 273 (2000).
2. S. P. Marsh, ed. *LASL Shock Hugoniot Data*, Los Alamos Series on Dynamic Material Properties (University of California, Berkeley, CA, 1980).
3. F. Zhang, P. A. Thibault, and R. Link, Proc. Roy. Soc. A **459**, 705 (2003).

Understanding Extreme Atomic Physics at Gbar Pressure

S. X. Hu,[1,2] D. T. Bishel,[1,3] D. A. Chin,[1,3] P. M. Nilson,[1] V. V. Karasiev,[1] I. E. Golovkin,[4] M. Gu,[4] S. B. Hansen,[5] D. I. Mihaylov,[1] N. R. Shaffer,[1] S. Zhang,[1] and T. Walton[4]

[1]Laboratory for Laser Energetics, University of Rochester
[2]Department of Mechanical Engineering, University of Rochester
[3]Department of Physics and Astronomy, University of Rochester
[4]Prism Computational Sciences
[5]Sandia National Laboratories

Spectroscopic measurements of dense plasmas at billions of atmospheres (i.e., Gbar = billions of times the pressure at the Earth's surface) provide tests of the fundamental understanding of how matter behaves at extreme conditions, and by extension, the interpretation of dense astrophysical objects such as white dwarf stars. Developing reliable atomic physics models at these conditions, benchmarked by experimental data, is crucial to an improved understanding of radiation transport in both stars and inertial fusion targets. However, detailed spectroscopic measurements at these conditions are rare, and traditional collisional-radiative-equilibrium (CRE) models,[1] based on isolated-atom calculations and *ad hoc* continuum lowering models, have proved questionable at and beyond solid density, leaving open the possibility for more-accurate methods.

Reported here are x-ray spectroscopy measurements at gigabar pressures using laser-driven implosions. These measurements are used to test a density functional theory (DFT)-based multiband kinetic model (*VERITAS*), which was developed in this work. The *VERITAS* model uses DFT-derived band (atomic level) information to compute the radiative transition rates that can be coupled to the radiation transfer equation to describe the radiation generation and transport processes in a dense plasma. With Cu (as a witness element) doped inside a 30-μm-thick plastic shell implosion, time-integrated and time-resolved Cu K_α emission and 1*s*–2*p* absorption measurements during shell stagnation were performed. These observations are directly connected to the time-dependent atomic ionization balance in the assembled dense plasma. The system is further constrained by integrated measurements of the compressed areal density (ρR), neutron yield, bang time, and ion temperature, allowing the spectroscopic data to differentiate the DFT-based kinetic model from traditional treatments based on isolated-atom calculations and *ad hoc* continuum-lowering models.

DRACO-simulated dynamic plasma conditions was used to investigate x-ray generation and transport through the target using two CRE models (*ATBASE* and *FAC*) and the DFT-based kinetic code *VERITAS*. The predicted time-integrated spectra are compared with the experimental measurements in Fig. 1, in which the x-ray signal is plotted as a function of photon energy (all normalized to the continuum signal level at 7800 eV). The experimental spectra [Fig. 1(b); target is shown as inset in Fig. 1(b)] show both the pronounced K_α emission peaked at ~8042 eV and the 1*s*–2*p* absorption of Cu in the higher-photon energy range of 8100 to 8250 eV. Both the location and amplitude of the emission and absorption features are appropriately captured by *VERITAS* [Fig. 1(a)].

Figures 1(c) and 1(d) show the *Spect3D* simulation results in which either the atomic database (*ATBASE*) or the flexible atomic code (*FAC*) calculations are combined with the Ecker–Kroll and Stewart–Pyatt continuum-lowering models. When these CRE results are compared to experiments, they give a conflicting conclusion about the continuum-lowering model. Namely, the experimental emission and absorption features are qualitatively reproduced by the two CRE simulations of "*ATBASE* + Stewart–Pyatt" and "*FAC* + Ecker–Kroll" in Figs. 1(d) and 1(e) (although the emission peaks are too high), while the other two combinations

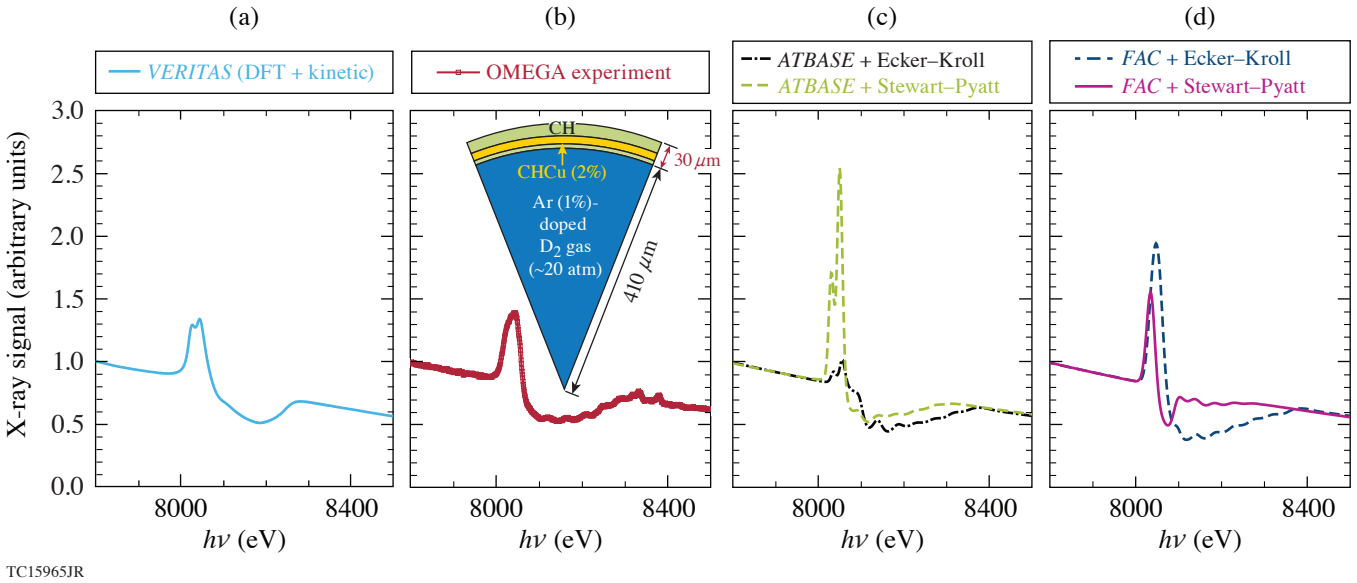

Figure 1
Comparisons of time-integrated x-ray spectra: (a) *VERITAS* DFT model prediction for the time-integrated K_α emission and 1*s*–2*p* absorption signals from a laser-driven implosion with a Cu-doped plastic layer. The model prediction is compared to (b) OMEGA experimental data, (c) CRE model predictions using the atomic database *ATBASE* in combination with Stewart–Pyatt and Ecker–Kroll continuum-lowering models, and (d) CRE model predictions using the *FAC* code with two different continuum-lowering models.

drastically disagree with experiments. This illustrates again the dilemma of the traditional spectroscopic treatment for warm dense plasmas: which *ad hoc* continuum-lowering model works better depends on the atomic physics model that is invoked. The resemblance between the *FAC* + Ecker–Kroll model [Fig. 1(d)] and experiments is likely coincidental since other recent measurements of ionization-potential depression have defied the Ecker–Kroll model. Overall, the DFT-based *VERITAS* model,[2] without invocation of an *ad hoc* continuum lowering model, better resembles the observed x-ray signal in the experiments. Nonetheless, one can see that the *VERITAS*-predicted continuum slope, the K_α-emission amplitude, and the 1*s*–2*p* absorption width are still slightly mismatched with respect to the experiment.

To summarize, a theoretical and experimental study of atomic physics in Cu-doped plastic at several billion atmospheres of pressure has been performed. Overall, a DFT-based approach reproduces many of the emission and absorption features that are observed in the experiment, while traditional plasma spectroscopy treatments show sensitivity to the combination of atomic physics and continuum-lowering models that are implemented. This sensitivity contributes to the present open questions on the validity of *ad hoc* continuum-lowering models. This work indicates the necessity for a self-consistent treatment of dense plasma effects on altering atomic energy levels/bands and their populations at ultrahigh pressures. The DFT-based *VERITAS* approach, with potential future benchmarks using other buried metal and metal-alloy layers, could provide a reliable way for simulating radiation generation and transport in dense plasmas encountered in stars and inertial fusion targets. The experimental scheme reported here, based on a laser-driven implosion, can be readily extended to a wide range of materials in single- and multishell geometries, opening the way for far-reaching investigations of extreme atomic physics and DFT models at tremendous pressures.

This material is based upon work supported by the Department of Energy National Nuclear Security Administration under Award Number DE-NA0003856, the University of Rochester, and the New York State Energy Research and Development Authority.

1. J. J. MacFarlane *et al.*, High Energy Density Phys. **3**, 181 (2007).
2. S. X. Hu *et al.*, Nat. Commun. **13**, 6780 (2022).

Effective Drift Velocity from Turbulent Transport by Vorticity

H. Yin,[1] H. Aluie,[1,2] S. Rai,[1] A. Lees,[1,2] D. Zhao,[1] S. M. Griffies,[3] A. Adcroft,[3] and J. K. Shang[1,2]

[1]Department of Mechanical Engineering, University of Rochester
[2]Laboratory for Laser Energetics, University of Rochester
[3]NOAA/Geophysical Fluid Dynamics Laboratory and Princeton University Program in Atmospheric and Oceanic Sciences

Highlighted here are the differing roles of vorticity and strain in the transport of coarse-grained scalars at length-scales larger than l by smaller-scale (subscale or subgrid or unresolved) turbulence. We use the first term in a multiscale gradient expansion due to Eyink,[1] which exhibits excellent correlation with the exact subscale physics when the partitioning length l is any scale smaller than that of the spectral peak. We show that unlike subscale strain, which acts as an anisotropic diffusion/anti-diffusion tensor, subscale vorticity's contribution is solely a conservative advection of coarse-grained quantities by an eddy-induced non-divergent velocity, $\mathbf{v}_*$, that is proportional to the curl of vorticity. Therefore, material (Lagrangian) advection of coarse-grained quantities is accomplished not by the coarse-grained flow velocity, $\bar{\mathbf{u}}_l$, but by the effective velocity, $\bar{\mathbf{u}}_l + \mathbf{v}_*$, the physics of which may improve hydrodynamic modeling.

Basic considerations from fluid dynamics indicate that the distance between particles in a laminar flow is determined by the strain.[2] Vorticity merely imparts a rotation on their separation vector $\mathbf{r}$ without affecting its magnitude. This behavior can be seen by considering the velocity, $\mathbf{u}$, difference between particles P and Q at positions $\mathbf{x}$ and $\mathbf{x} + \mathbf{r}$, respectively,

$$\mathbf{u}_Q - \mathbf{u}_P = \delta\mathbf{u} = \mathbf{u}(\mathbf{x}+\mathbf{r}) - \mathbf{u}(\mathbf{x}) = \mathbf{r}\cdot\nabla\mathbf{u}\,\big|_{\mathrm{x}} + ..., \tag{1}$$

where a Taylor-series expansion is justified for short distances $|\mathbf{r}|$ over which the flow is sufficiently smooth. In the Lagrangian frame of P at $\mathbf{x}$, the separation from Q evolves as

$$\frac{D\mathbf{r}}{Dt} = \delta\mathbf{u} = \mathbf{r}\cdot\mathbf{S} + \underbrace{\mathbf{r}\cdot\boldsymbol{\Omega}}_{\frac{1}{2}\boldsymbol{\omega}\times\mathbf{r}}, \tag{2}$$

where the velocity gradient tensor, $\nabla\mathbf{u} = \mathbf{S} + \boldsymbol{\Omega}$, has been decomposed into the symmetric strain rate tensor $\mathbf{S} = \left[\nabla\mathbf{u} - (\nabla\mathbf{u})^T\right]/2$ and the antisymmetric vorticity tensor $\boldsymbol{\Omega} = \left[\nabla\mathbf{u} - (\nabla\mathbf{u})^T\right]/2 = -1/2\epsilon_{ijk}\omega_k$. Here, $\boldsymbol{\omega} = \nabla \times \mathbf{u}$ is vorticity and ϵ_{ijk} is the Levi–Civita symbol. Taking an inner product of Eq. (2) with $\mathbf{r}$,

$$\frac{1}{2}\frac{D|\mathbf{r}|^2}{\mathrm{d}t} = \mathbf{r}\cdot\mathbf{S}\cdot\mathbf{r}, \tag{3}$$

shows that the distance is determined by the strain. Vorticity in Eq. (2) only acts to rotate $\mathbf{r}$ without changing its magnitude.

These considerations hinge on the critical assumption that the flow is sufficiently smooth over separation $\mathbf{r}$, which is patently invalid in a turbulent flow for $\mathbf{r}$ at inertial scales.[3] However, a version of this story survives due to the property of scale locality,[4] which justifies an expansion in scale. The main result of this research is Eq. (4),

$$\partial_t \overline{C}_l + \nabla \cdot \left[\left(\overline{\mathbf{u}}_l + \mathbf{v}_* \right) \overline{C}_l \right] = -\nabla \cdot \left[\mathbf{J}(C) \right], \tag{4a}$$

$$\mathbf{v}_* = \frac{1}{2} A l^2 \nabla \times \left(\nabla \times \overline{\mathbf{u}}_l \right), \tag{4b}$$

where Eq. (4a) shows us that coarse-grained simulations in general, including those from radiation-hydrodynamics inertial confinement fusion codes, may need to solve this equation to represent the unresolved (subgrid) vorticity physics self-consistently. Equation (4b) is an expression for the eddy-induced advection velocity $\mathbf{v}_*$ affecting length scales larger than l, which may be the grid cell size in a simulation. In Eq. (4a), $\mathbf{J}(C)$ can represent traditional subgrid models such as turbulent diffusion,[5] $\mathbf{J}(C) = -\alpha_{\text{turb}} \nabla \overline{C}_l$.

In summary, it is shown that unlike subscale strain, which acts as an anisotropic diffusion/anti-diffusion tensor, subscale vorticity's contribution at leading order is solely a conservative advection of coarse-grained scalars by an eddy-induced velocity $\mathbf{v}_*$ proportional to the curl of vorticity. Evidence of excellent agreement between the leading order terms and the exact ones from a 3-D compressible turbulence simulation are shown in Fig. 1. While the focus of this summary was on the transport of scalars, a similar analysis may also apply to the transport of momentum. Since the convergence of Eyink's expansion and, therefore, the dominance of the leading order term relies on ultraviolet scale locality,[4] these results and conclusions may not hold at length scales larger than those of the spectral peak. In other words, for coarse-grained simulations to use this modeling framework, they need to directly resolve the most energetic scales. Otherwise, some of the assumptions may not be valid. Note that the unresolved (subgrid) scales can still have the dominant vorticity contribution since energy and vorticity can occupy different scale ranges.

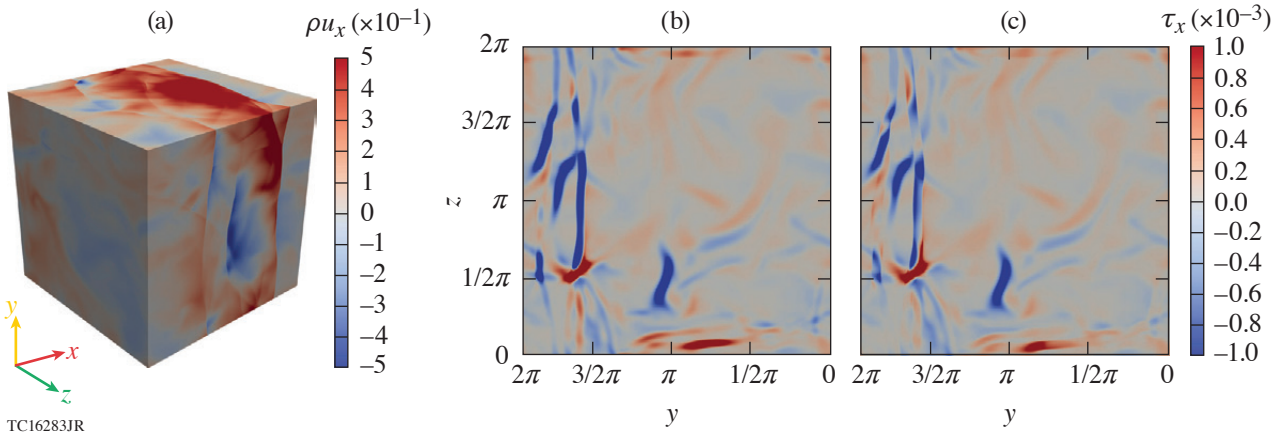

Figure 1
(a) Visualization of x component of momentum, ρu_x, in physical space from the 1024^3 compressible turbulence direct numerical simulation (DNS). The image is shown at an instant of time after the flow has reached steady state. Shocks can be seen as discontinuities. [(b),(c)] A 2-D slice at $x = 0$ from a snapshot of the 3-D compressible turbulence DNS, comparing the (b) exact $\overline{\tau}_l(u_x, \rho)$ at $l = 0.19635$ with (c) its approximation $\tau_m = 1/3 M_2 l^2 \partial_k \overline{\rho} \partial_k \overline{u}_x$.

This research was funded by U.S. DOE grant DE-SC0020229. Partial support from U.S. NSF grants PHY-2020249, OCE-2123496, U.S. NASA grant 80NSSC18K0772, and U.S. NNSA grant DE-NA0003856 is acknowledged.

1. G. L. Eyink, J. Fluid Mech. **549**, 159 (2006).
2. P. K. Kundu, I. M. Cohen, and D. R. Dowling, *Fluid Mechanics*, 6th ed. (Elsevier, 2016).
3. S. B. Pope, *Turbulent Flows* (Cambridge University Press, Cambridge, 2000).
4. H. Aluie, Phys. Rev. Lett. **106**, 174502 (2011).
5. J. Smagorinsky, Mon. Weather Rev. **91**, 99 (1963).

Development of an X-Ray Radiography Platform to Study Laser-Direct-Drive Energy Coupling at the National Ignition Facility

L. Ceurvorst,[1] W. Theobald,[1,2] M. J. Rosenberg,[1] P. B. Radha,[1] C. Stoeckl,[1] R. Betti,[1,2] K. S. Anderson,[1] J. A. Marozas,[1] V. N. Goncharov,[1,2] E. M. Campbell,[1] C. M. Shuldberg,[3] R. W. Luo,[3] W. Sweet,[3] L. Aghaian,[3] L. Carlson,[3] B. Bachmann,[4] T. Döppner,[4] M. Hohenberger,[4] K. Glize,[5] R. H. H. Scott,[5] A. Colaïtis,[6] and S. P. Regan[1,2]

[1]Laboratory for Laser Energetics, University of Rochester
[2]Department of Mechanical Engineering, University of Rochester
[3]General Atomics
[4]Lawrence Livermore National Laboratory
[5]Central Laser Facility, STFC Rutherford Appleton Laboratory
[6]Centre Lasers Intenses et Applications, Université de Bordeaux-CNRS-CEA

The coupling of laser energy to an imploding target in direct-drive inertial confinement fusion (ICF) is a key parameter that determines the ablation pressure and the implosion velocity of the shell. According to current models, cross-beam energy transfer (CBET) is a major factor that limits the ablation pressure on National Ignition Facility (NIF)-scale targets, reducing implosion velocity and shell kinetic energy. Hence, accurate measurements of the laser coupling efficiency for NIF-scale implosions are an important aspect of direct-drive ICF research. To obtain these measurements, a platform was developed on the NIF using x-ray radiography and self-emission imaging to diagnose the evolution of a directly driven solid spherical target. This plastic (CH) sphere was driven by 184 NIF beams in polar direct drive at three different intensities using a 7-ns ramp pulse. The remaining eight NIF beams were focused onto a copper backlighting foil to generate x rays that probed the target before being collected by a pinhole array coupled to a gated x-ray detector. This summary details the analysis technique used to reconstruct the target's density profile from these radiographs.

In the paraxial approximation, where the x rays are roughly parallel to the optical axis, the transmission T of x rays passing through a plasma is given by:

$$T(x,y) = e^{-\tau(x,y)}$$
$$\tau(x,y) = \int \mu(x,y,z)\rho(x,y,z)\mathrm{d}z, \tag{1}$$

where τ is the optical depth, μ is the opacity, and ρ is the density. The implosions performed in these experiments are expected to remain roughly spherically symmetric, meaning that both the opacity and density should primarily be radial functions. In this limit, Eq. (1) shows that the optical depth is simply the Abel transformation of the attenuation, equal to the opacity times the density. Therefore, the radiographs can be converted to optical depth images, azimuthally averaged, and Abel inverted to yield the attenuation profiles.

To convert radiographs to optical depth images, the transmission of the target must first be inferred by dividing the raw signal by a fitted backlighter profile. Typically, this is done by fitting the unobstructed portions of the backlighter emission with an appropriate function, in this case, the superposition of two super-Gaussians. As can be seen in Fig. 1(a), however, the backlighter was largely eclipsed by the target itself, leaving little unobstructed data with which to perform the fit. Instead, the entire image was used in the calculations by multiplying the backlighter emission profile by a simplified transmission function, resulting in fits such as the one shown in Fig. 1(b). The transmission images were then obtained by dividing the raw image by the fitted backlighter emission as displayed in Fig. 1(d).

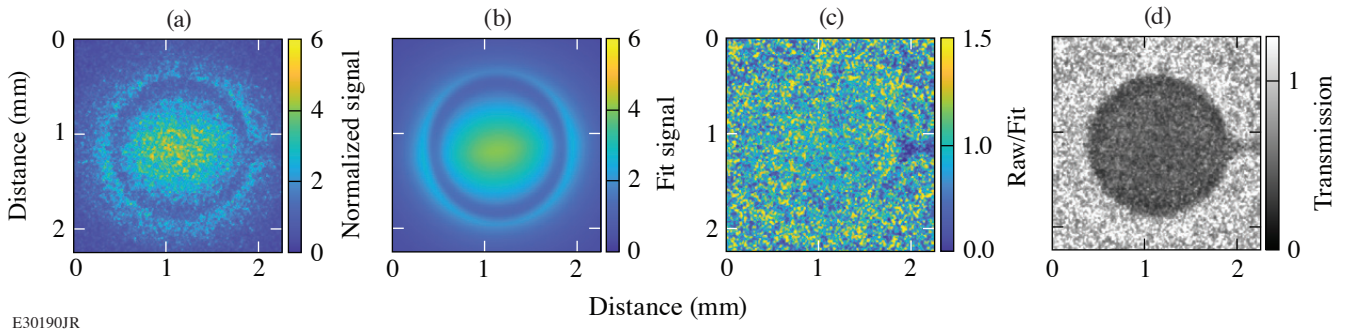

Figure 1
Converting radiographs into transmission images. (a) A single radiographic sub-image is taken from shot N210519-001 7.1 ns after the start of the drive. (b) This image is then fit with a simplified backlighter and transmission profile. (c) Dividing the raw radiograph by its fitted profile produces a flat image composed primarily of noise, confirming the quality of the fit. Note the stalk is not included in the fit and thus appears on the right side of this image. (d) The raw image is divided by the fitted backlighter profile to produce the final transmission image.

The resulting transmission was then converted to optical depth using Eq. (1), and the azimuthally averaged optical depth profiles were Abel inverted to obtain the system's radial attenuation. The final step of analysis was to separate the density and opacity profiles. Ahead of the shock, the target should not be significantly heated, maintaining its cold opacity value. After the shock, however, the material can be heated and ionized enough to reduce its overall opacity. A crude approximation was made that the opacity should be roughly constant in this shocked region, and its value was determined by matching the calculated target mass in the experiment to the accompanying *DRACO*[1] simulations. This yielded a hot opacity of 2.5±0.2 cm^2/g, similar to the 2.7 cm^2/g calculated by post-processing the simulations with *Spect3D*.[2]

Using this step function for the opacity, the final density profiles were inferred and compared to the simulations as shown in Fig. 2. The shock trajectories were in rough agreement, indicated by the rise in density. However, the subsequent fall in density corresponding to the ablation front occurred at a larger radius in the experiment compared to the simulations. This is similar to the trends seen previously with thin-shell targets.[3] At the time, the thicker observed shocked region was suspected to be caused by hydrodynamic instabilities. However, the ablation front is not accelerating here, largely eliminating this possibility.

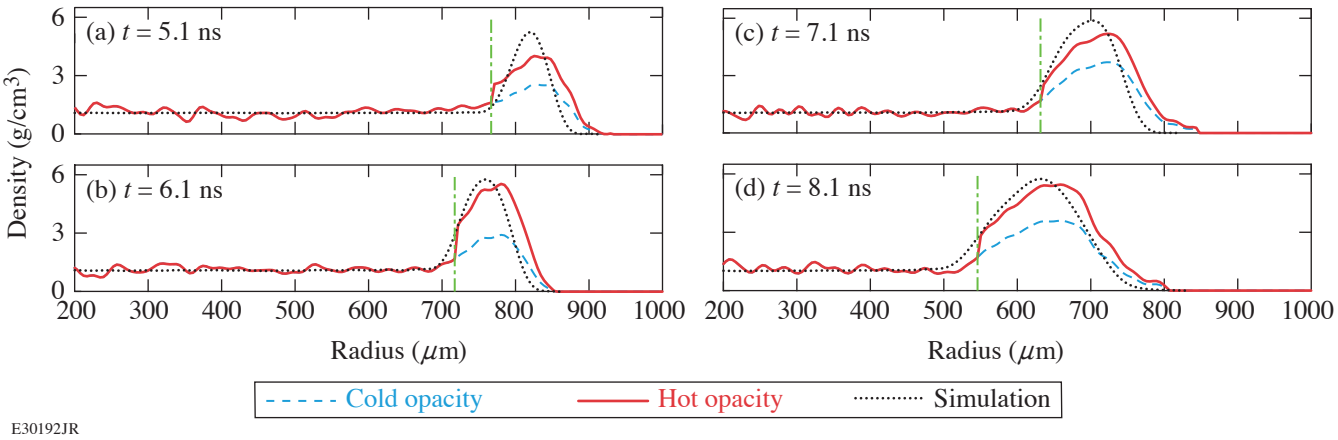

Figure 2
Inferred azimuthally averaged density profiles. The initial density calculation using only cold opacity (dashed blue curve) and mass conserving calculation using a stepped opacity profile (solid red curve) are compared to the simulated density profile convolved with the instrument response function of the system (dotted black curve) (a) 5.1 ns, (b) 6.1 ns, (c) 7.1 ns, and (d) 8.1 ns after the start of the drive. Vertical (dashed–dotted green) lines indicate the shock position beyond which the calculated hot opacity was applied.

To confirm that this discrepancy was not caused by the analysis technique, the same algorithm was applied to artificial radiographs calculated using *Spect3D*. The results of this analysis showed a 0.06 g/cm^3 rms error caused largely by the Abel inversion algorithm. As shown in Fig. 3, no shift to the reconstructed shock and ablation fronts was detected. The analysis also investigated the role of noise, which showed no systematic shift to these trajectories. The discrepancy in ablation front trajectory, therefore, appears to be physical. A comparison to simulations at all explored intensities and pulse shapes is now underway to distinguish between various effects such as preheat, CBET, and nonlocal heat-transport models. The results of this ongoing investigation will be published in a future manuscript.

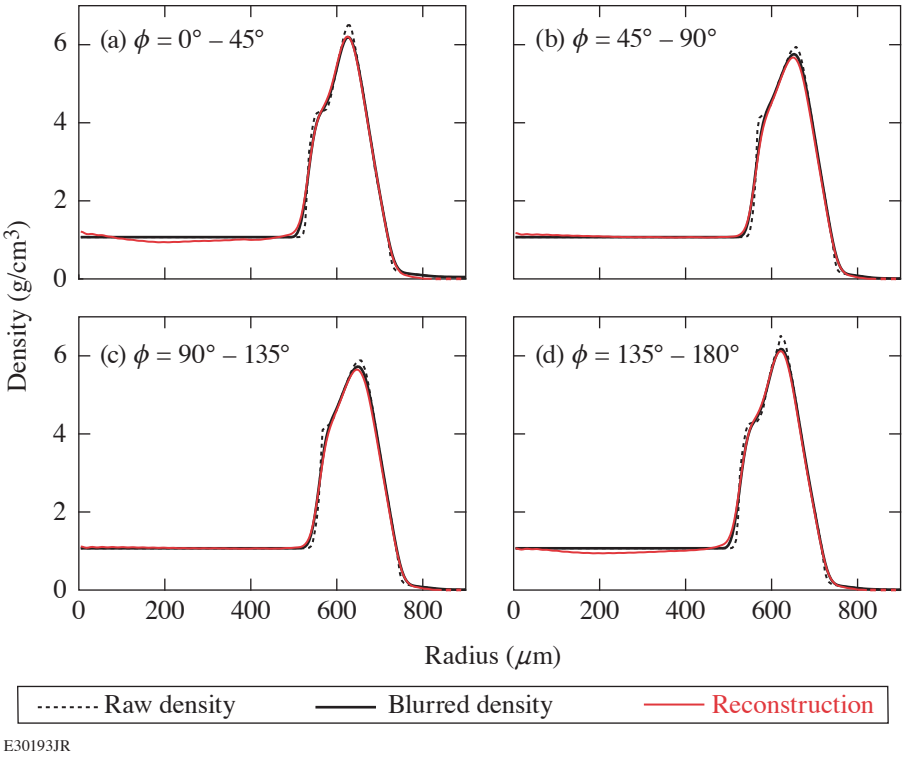

Figure 3
Validation of technique. Transmission images are calculated using *Spect3D*, and azimuthally dependent density profiles are reconstructed using this analysis technique. The data were calculated using azimuthal bins of (a) 0° to 45°, (b) 45° to 90°, (c) 90° to 135°, and (d) 135° to 180°. The reconstructed profiles (solid red curves) closely align with the original density profiles after accounting for the instrument response (solid black curves). The rms error between these two curves is 0.06 g/cm^3. Compared to the original density profile (dashed black curve), more features are lost because of imaging resolution than because of the reconstruction technique.

This material is based upon work supported by the Department of Energy National Nuclear Security Administration under Award Number DE-NA0003856, the University of Rochester, and the New York State Energy Research and Development Authority.

1. P. B. Radha *et al.*, Phys. Plasmas **23**, 056305 (2016).
2. J. MacFarlane *et al.*, High Energy Density Phys. **3**, 181 (2007).
3. M. Hohenberger *et al.*, Phys. Plasmas **22**, 056308 (2015).

A Scattered-Light Uniformity Imager for Diagnosing Laser-Absorption Asymmetries on OMEGA

D. H. Edgell, J. Katz, R. Raimondi, D. Turnbull, and D. H. Froula

Laboratory for Laser Energetics, University of Rochester

Successful implosions require efficient and highly uniform deposition of laser energy. Simulations suggest that the nonuniformity must be below the 1% rms level to achieve ignition.[1] Accurate measurement of the laser absorption is essential to evaluate implosion performance, including various schemes to mitigate laser–plasma instability losses. Laser light scattered from a target is the most direct measurement for diagnosing laser absorption in a direct-drive implosion. Observations from OMEGA implosions have shown much larger scattered-light asymmetries than standard predictions.[2,3] To address the insufficiencies of the existing scattered-light instruments, a new diagnostic, the scattered-light uniformity imager (SLUI), has been designed and deployed on OMEGA to absolutely measure the scattered-light intensity and nonuniformity for the purpose of diagnosing the asymmetry and determining its effect on laser drive uniformity. SLUI's collect a much larger portion of the scattered light around the target than other diagnostics.

SLUI measures the angularly discriminated scattered-light intensity distribution over a collection cone area by imaging a translucent transmission diffuser plate using a charge-coupled–device (CCD)/lens assembly There are two major assemblies in each SLUI: the diffuser plate front-end ten-inch manipulator (TIM)-based payload and a rear-end imaging assembly [Fig. 1(a)]. The main component of the front end is the 0.5-mm-thick translucent white spectralon diffuser plate. A stray light baffle, debris shield, and antireflection absorbing filter are also incorporated into the diagnostic payload inserted into the target chamber. The imaging part of the diagnostic (light baffle, vacuum window, filters, lens, and CCD camera) is located outside the target chamber. A sample diffuser image is shown in Fig. 1(b). Fine-scale structures, such as highlighted by the inset, are believed to be caused by structure in the diffuser plate. Some large-scale variances over the image may also be caused by the diffuser plate nonuniformity. The fine- and large-scale diffuser effects will be clarified by upcoming flat-fielding measurements. Each SLUI instrument sensitivity is absolutely calibrated offline using a National Institute of Standards and Technology traceable photodiode.

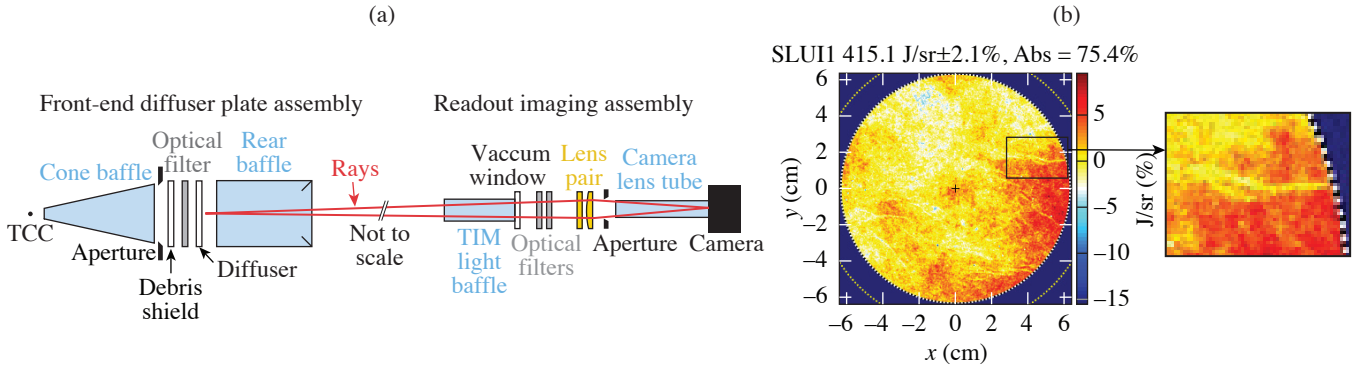

Figure 1
(a) The SLUI diagnostic. (b) Sample SLUI image of the diffuser plate for an OMEGA implosion. The inset highlights one of the small-scale features that are caused by the interior structure of the diffuser plate. TCC: target chamber center.

The standard operating position of the SLUI's places the diffuser plate standoff distance (SOD) at 31.5 cm from target chamber center (TCC) to avoid any chance of beam interference and helps reduce sputtering of baffle material on high-power shots. At this SOD, a SLUI has an effective *f* number of 2.5 and records the scattered light over a cone angle of 11.3° or ~0.97% of the total 4π emission area. Based on the measured point spread function, this effective area provides over 20K independent intensity measurements, enabling the study of the intensity and distribution of the scattered light over this area. Five SLUI's have been built and deployed in OMEGA's TIM diagnostic ports, covering almost 5% of the emission surface, enabling an absolute scattered-light measurement that according to modeling should be within a few percent of the global average. Five SLUI positions allowed resolution of the lowest modes (ℓ = 1,2) in the distribution. The large solid-angle image from each SLUI records the large local slopes in the distribution due to higher modes. Work is underway using these measured variations to evaluate the accuracy of the predicted scattered-light distributions and identify whether additional physics or other considerations need to be included.

The accuracy of the SLUI's measurements are sufficient to distinguish the effects of a 12-μm offset in target position. The green squares in Fig. 2 show the laser absorption inferred from each SLUI for an implosion that was centered at TCC within a couple of microns. The variation between the SLUI's is indicative of the scattered-light variation over the target chamber. The mean absorption for this shot is shown by the dotted black line. The blue diamonds are the laser absorptions inferred from SLUI from a similar implosion except that the target was intentionally offset 12 μm toward one of the SLUI's. The difference between the two implosions is illustrated by the red line. A consistent trend is found with a delta of about 5% absorption difference between the SLUI toward the offset and the SLUI away from the offset.

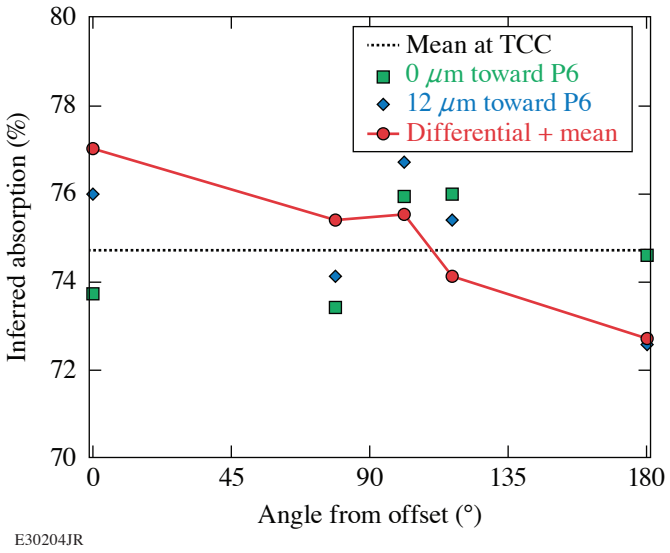

Figure 2
SLUI experimental measurements show the effect of a target offset. Shown is the laser absorption inferred for individual SLUI's for two similar implosions, one well centered at TCC (green squares) and the other intentionally offset ~12 μm toward one of the SLUI's (blue diamonds). The red line shows the difference between the two measurements centered on the mean overall absorption for the case at TCC (dotted black line).

The SLUI diagnostic is now available for deployment on OMEGA implosions, providing an absolutely calibrated platform to study the global laser absorption and sources of scattered-light and absorption asymmetries such as beam pointing, target offset, power balance, and polarization effects on cross-beam energy transfer.

This material is based upon work supported by the Department of Energy National Nuclear Security Administration under Award Number DE-NA0003856, the University of Rochester, and the New York State Energy Research and Development Authority.

1. V. N. Goncharov *et al.*, Plasma Phys. Control. Fusion **59**, 014008 (2017).
2. D. H. Edgell *et al.*, Phys. Rev. Lett. **127**, 075001 (2021).
3. O. M. Mannion *et al.*, Phys. Plasmas **28**, 042701 (2021).

Three-Dimensional Hot-Spot X-Ray Emission Tomography from Cryogenic Deuterium–Tritium Direct-Drive Implosions on OMEGA

K. Churnetski,[1,2] K. M. Woo,[1] W. Theobald,[1,2] P. B. Radha,[1] R. Betti,[1,2,3] V. Gopalaswamy,[1] I. V. Igumenshchev,[1] S. T. Ivancic,[1] M. Michalko,[1] R. C. Shah,[1] C. Stoeckl,[1] C. A. Thomas,[1] and S. P. Regan[1,2]

[1]Laboratory for Laser Energetics, University of Rochester
[2]Department of Mechanical Engineering, University of Rochester
[3]Department of Physics and Astronomy, University of Rochester

In direct-drive inertial confinement fusion (ICF),[1] laser beams are focused onto a spherical target to implode a thin shell composed of an outer ablation layer (typically plastic) and an inner layer of solid cryogenic deuterium–tritium (DT) fuel. The laser-direct-drive ICF concept is studied on the 60-beam, 30-kJ, 351-nm OMEGA laser,[2] which has produced high-performing implosions with hot-spot pressures exceeding 50 Gbar, described in Ref. 3. The recent application of statistical modeling significantly improved the implosion performance and the neutron yield.[4] Low-mode drive variations in the driver illumination and from target perturbations can significantly impact implosions.[5–7] The goal over the next several years is to further optimize OMEGA implosions and to demonstrate ignition-relevant implosions that when scaled to 2 MJ of laser energy, would enter the burning-plasma regime.[8,9] Three-dimensional hot-spot x-ray emission tomography is a powerful tool to diagnose low-mode asymmetries, which will help to mitigate low-mode perturbations and improve implosion performance. This work is embedded in a long-term project that aims to understand the physics and multidimensional effects that currently limit the hot-spot pressure in ICF implosions on OMEGA and to help to develop strategies to increase the hot-spot pressure.

OMEGA currently has a combination of time-gated and time-integrated x-ray diagnostics for hot-spot imaging along four lines of sight (LOS), which enable a 3-D interpretation of the hot-spot shape. These diagnostics include KBframed,[10] the single line-of-sight, time-resolved x-ray imager (SLOS-TRXI),[11] KB (formerly GMXI),[12] and a spatially resolved electron temperature diagnostic (SR-TE).[13] The diagnostics have different spatial and temporal resolutions, as well as slightly different spectral sensitivities. These four diagnostics are quasi-orthogonal from each other, allowing for a 3-D view of the imploding ICF core. Figure 1 shows the locations of the detectors on the OMEGA target chamber and example data from each detector.

A 3-D hot-spot emission model was developed to reconstruct the hot-spot emission profile of direct-drive implosions on OMEGA by combining the measured x-ray emission data from multiple LOS.[14] The radiation transfer equation along a single LOS is considered for a steady-state plasma in which the temperature and density distributions and the radiation field are independent of time.[15] The hot-spot plasma of cryogenic DT target implosions on OMEGA is optically thin for photon energies >2.5 keV. All of the x-ray imagers considered here satisfy this condition and absorption can be neglected.[13] Neither the absolute signal nor the temporal evolution of the hot-spot emission are taken into account in this simplified model. The spectral response is assumed to be the same for all the x-ray imagers. Using those simplifications and dropping the frequency dependence on the plasma emissivity ε, the projected x-ray image $I_{\hat{s}}$ along an observation direction $\hat{s}$ over a path length s is given by $I_{\hat{s}} \sim \int_{\hat{s}} \varepsilon \mathrm{d}s$.

A method described in Woo *et al.*[14] has been developed to reconstruct ε through a complete expansion set using both non-orthogonal polynomial and orthogonal polynomial expansions. The complex shape of the hot-spot emission can be described in terms of a model of generalized spherical-harmonic Gaussian functions,

$$\ln \varepsilon(r,\theta,\varphi) = \sum_{n=0}^{\infty} \sigma_n R^n \left[1 + \sum_{\ell=1}^{\infty} \sum_{m=-\ell}^{\ell} \sum_{k=0}^{\infty} A_{\ell m k} R^k Y_{\ell m}(\theta,\varphi)\right]^n. \quad (1)$$

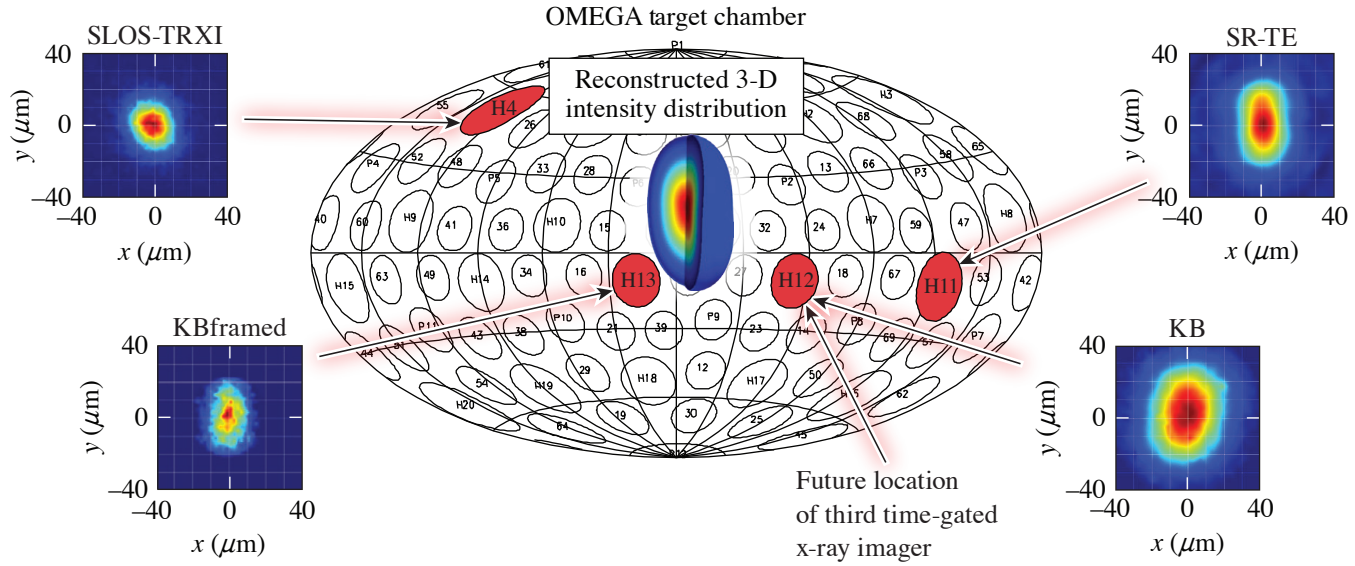

Figure 1
The locations of the existing four hot-spot x-ray imaging detectors on the OMEGA target chamber are indicated by the red circles. SLOS-TRXI is located in port H4 (45°, 234°), KBframed in port H13 (105°, 342°), KB in port H12 (96°, 54°), and SR-TE in port H11 (101°, 134°). The future third time-gated x-ray imager will also be located in port H12 (96°, 54°). Example data are shown for each diagnostic and the reconstructed 3-D hot-spot emission is displayed in the target chamber center. The polar and azimuthal angles for each detector are denoted in parenthesis.

The emissivity is described in spherical coordinates (r, θ, φ), where the origin of the coordinate system coincides with the peak of ε. In Eq. (1), R is the radius and $Y_{\ell,m}$ are the real spherical harmonic functions. The expansion coefficients, φ_n and $A_{\ell,m}$, are determined by a gradient-descent, machine-learning algorithm that minimizes a loss function, which is the fit error between the model and the normalized measured x-ray images.

To reconstruct the emission profile, an initial estimate is made for the solution of of ε, which is a 1-D Gaussian profile. This model is projected into the LOS of the x-ray detectors using a ray-tracing routine and the projections are compared with the experimental x-ray images from each diagnostic. The error between the model and the experimental images is calculated as the sum of the root-mean-square (rms) difference over the multiple lines of sight. The coefficients of the model are slightly perturbed, and this process is repeated for several iterations until the rms error is minimized.

Proof-of-principle simulations with the hydrodynamic code *DEC3D*[16] assuming a mode-2 perturbation were used to validate the 3-D reconstruction procedure. The result of the simulation was post-processed with the detector resolutions and spectral sensitivities using *Spect3D*[17] to create simulated x-ray images along the four lines of sight. Normally distributed random noise was added to the simulated x-ray images, and the hot-spot emission was reconstructed multiple times in a Monte Carlo simulation by varying the noise. The resulting 3-D reconstructions were projected along the detector lines of sight and the major and minor radii were calculated at the 1/e contour level for the reconstruction projections and simulated x-ray images. The radii agreed within the error bars, which gives confidence in the viability of this technique.

A direct-drive ICF campaign on OMEGA was conducted with deliberate laser-drive asymmetries to study the effect of hot-spot shape asymmetries on implosion performance. The polar-direct drive (PDD)[18] beam illumination geometry was applied by using 40 of the 60 OMEGA beams, switching off 20 beams around the equator. The 40 beams are grouped in three beam rings in the upper and lower hemisphere according to their polar angles.[18] The partition of beam energies in rings 1 and 3 was varied while keeping the total laser energy constant. The magnitude of the laser-drive asymmetry was varied to produce hot spots that

ranged from oblate to prolate in shape. Figure 2 shows data from three shots at stagnation from KBframed, which has an equatorial view of the capsule. Reconstructions were done for each shot during this campaign and compared to the experimental inputs.

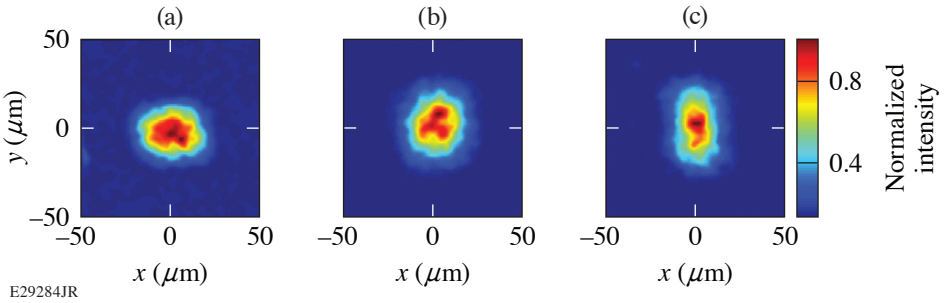

Figure 2
Experimental x-ray images from the KBframed diagnostic at stagnation of cryogenic DT target implosions performed with the PDD illumination geometry. The beam-energy balance was varied from a stronger drive on (a) the poles (shot 96578), to (b) a balanced drive (shot 96575), to (c) a stronger drive on the equator (shot 96581), while keeping the total laser energy conserved.

The reconstruction of shot 96581 is shown in Fig. 1. Data from SLOS-TRXI and KBframed are chosen to be from the time of peak emission, and data from KB channel 3 and SRTE channel 1 are used due to the similar energy ranges to those of SLOS-TRXI and KBframed. The differences in hot-spot size between the different diagnostics can be attributed to differences in time resolution. With a higher intensity of laser energy incident at the equator of the capsule, a prolate shape is expected in the hot-spot emission with the major axis aligned with the z axis of the target chamber. Spherical harmonic modes up to $\ell = 3$ were used in the reconstruction. The large $A_{2,0} = -0.47 \pm 0.03$ expansion coefficient indicates a strong mode $\ell = 2$ in the reconstruction, which can be seen in the experimental x-ray images. The $A_{2,0}$ coefficient is negative, which indicates a prolate shape and is consistent with what we expect from the laser-drive asymmetry. Reconstructions of other shots from this campaign also show the expected overall shape and orientation of the hot spot based on the laser-drive asymmetry and will be further discussed in a future publication.

This material is based upon work supported by the Department of Energy National Nuclear Security Administration under Award Number DE-NA0003856, the University of Rochester, and the New York State Energy Research and Development Authority.

1. R. S. Craxton *et al.*, Phys. Plasmas **22**, 110501 (2015).
2. T. R. Boehly *et al.*, Opt. Commun. **133**, 495 (1997).
3. S. P. Regan *et al.*, Phys. Rev. Lett. **117**, 025001 (2016); 059903(E) (2016).
4. V. Gopalaswamy *et al.*, Nature **565**, 581 (2019).
5. B. K. Spears *et al.*, Phys. Plasmas **21**, 042702 (2014).
6. O. M. Mannion *et al.*, Phys. Plasmas **28**, 042701 (2021).
7. H. G. Rinderknecht *et al.*, Phys. Rev. Lett. **124**, 145002 (2020).
8. O. A. Hurricane *et al.*, Phys. Plasmas **26**, 052704 (2019).
9. A. B. Zylstra *et al.*, Nature **601**, 542 (2022).
10. F. J. Marshall *et al.*, Rev. Sci. Instrum. **88**, 093702 (2017).)
11. W. Theobald *et al.*, Rev. Sci. Instrum. **89**, 10G117 (2018).
12. F. J. Marshall and J. A. Oertel, Rev. Sci. Instrum. **68**, 735 (1997).
13. D. Cao *et al.*, Phys. Plasmas **26**, 082709 (2019).
14. K. M. Woo *et al.*, Phys. Plasmas **29**, 082705 (2022).
15. Ya. B. Zel'dovich and Yu. P. Raizer, *Physics of Shock Waves and High-Temperature Hydrodynamic Phenomena*, edited by W. D. Hayes and R. F. Probstein (Dover, Mineola, NY, 2002).

16. K. M. Woo *et al.*, Phys. Plasmas **25**, 102710 (2018).
17. J. J. MacFarlane *et al.*, High Energy Density Phys. **3**, 181 (2007).
18. P. B. Radha *et al.*, Phys. Plasmas **19**, 082704 (2012).

A New Neutron Time-of-Flight Detector for Yield and Ion-Temperature Measurements at the Omega Laser Facility

V. Yu. Glebov,[1] C. J. Forrest,[1] J. Kendrick,[1] J. P. Knauer,[1] O. M. Mannion,[2] H. McClow,[1] S. P. Regan,[1] C. Stoeckl,[1] B. Stanley,[1] and W. Theobald[1]

[1]Laboratory for Laser Energetics, University of Rochester
[2]Sandia National Laboratories

A new neutron time-of-flight (nTOF) detector for deuterium–deuterium (D–D) fusion yield and ion-temperature measurements was designed, installed, and calibrated for the OMEGA Laser System. This detector provides an additional line of sight for D–D neutron yield and ion-temperature measurements for yields exceeding 1×10^{10} with higher precision than existing detectors. The nTOF detector consists of a 90-mm-diam, 20-mm-thick BC-422 scintillator and a gated Photek[1] photomultiplier tube (PMT240). This PMT has a 40-mm-diam photocathode, two microchannel plates, and provides a gain of up to 1×10^6. For DD measurements the PMT240 is operated at a bias voltage of –4.4 kV, corresponding to a PMT gain of 2×10^5. The PMT collects scintillating light through the 20-mm side of the scintillator without the use of a light guide. There is no lead shielding from hard x rays in order to allow the x-ray instrument response function of the detector to be easily measured. Instead, hard x-ray signals generated in implosion experiments are gated out by the PMT. The design provides a place for glass neutral-density (ND) filters between the scintillator and the PMT to avoid PMT saturation at high yields. The nTOF detector is installed in the OMEGA Target Bay along the P8A sub-port line of sight (LOS) with $\theta = 109.57°$ and $\phi = 90.00°$ (where θ and ϕ are the polar and azimuthal angles of the port in the target chamber coordinate system) at a distance of 5.3 m from the target chamber center. This detector is named P8A 5.3-m nTOF.

Until recently only two nTOF detectors on OMEGA [5.4-m nTOF (Ref. 2) located at 5.4 m from target chamber center (TCC) in sub-port H10G LOS with $\theta = 84.98°$ and $\phi = 311.76°$ and 12-m nTOFL (Ref. 3) located at 12.4 m from TCC in sub-port H8A LOS with $\theta = 87.86°$ and $\phi = 161.24°$] measured the D–D yield and ion temperature above the 2×10^{10} yield. The P8A 5.3-m nTOF detector provided an additional line of sight and increased the yield range of DD measurements on OMEGA. The P8A nTOF has a larger scintillator volume and records more neutron interactions than the other two detectors. The DD yield calibration of the P8A nTOF against the 12-m nTOFL detector is shown in Fig. 1. Only shots with yields exceeding 1×10^{10} were selected for the calibration. Figure 1(a) shows the charge of the neutron signal from P8A nTOF plotted versus the DD yield from the 12-m nTOF. The line in Fig. 1(a) is the linear fit of the data that is forced to go through the point (0,0). Figure 1(a) demonstrates a good linearity of the P8A nTOF detector signal for D–D yields up to 4×10^{11}. The data in Fig. 1 were recorded without an ND filter. When an ND filter is used there is practically no upper limit in D–D yield measurement for the P8A nTOF detector. Figure 1(b) shows the ratio of the yields from the two detectors as a function of the shot number.

Most of the LLE implosion campaigns are designed for DT yields in the range from 1×10^{13} to 1×10^{14} and recently for yields above 3×10^{14}. Therefore, the DT nTOF detectors on OMEGA were designed for such high yields. External OMEGA users, however, sometimes require DT yield measurements from 5×10^{10} to 1×10^{12}. The PMT high-voltage setting of P8A nTOF is adjusted from –4.4 kV for DD operation to –3.6 kV, corresponding to a PMT gain of 6×10^3 for the DT operation. The P8A nTOF was calibrated in DT yield against Cu activation. Figure 2(a) shows the charge of the neutron signal from P8A nTOF plotted versus the DT yield from Cu activation. The straight line in Fig. 2(a) is the linear fit of the data that is forced to go through the point (0,0). Figure 2(a) demonstrated that P8A nTOF is linear in desired DT yield range from 5×10^{10} to 1×10^{12}. Figure 2(b) shows the ratio of the yields from the two detectors as a function of shot number.

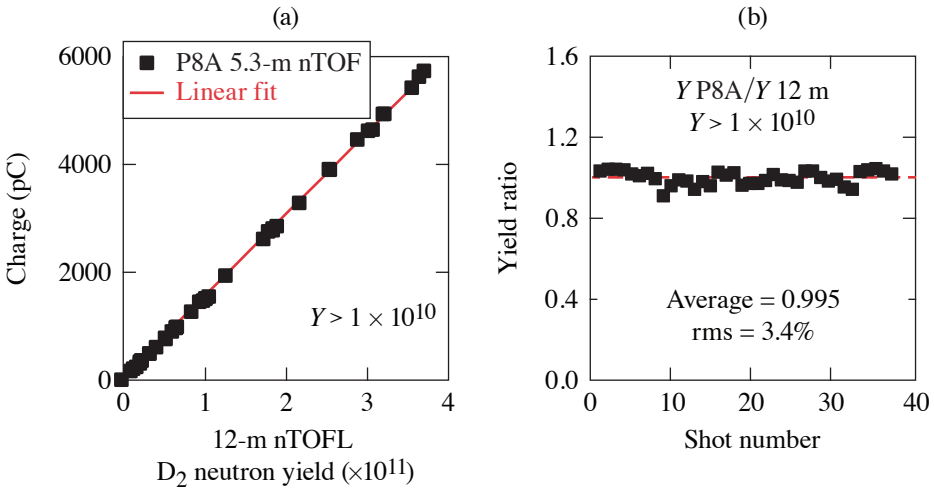

TC16083JR

Figure 1
(a) DD neutron calibration of P8A 5.3-m nTOF against 12-m nTOFL detector and (b) the ratio of DD yield measured by P8A 5.3-m nTOF and 12-m nTOFL detectors.

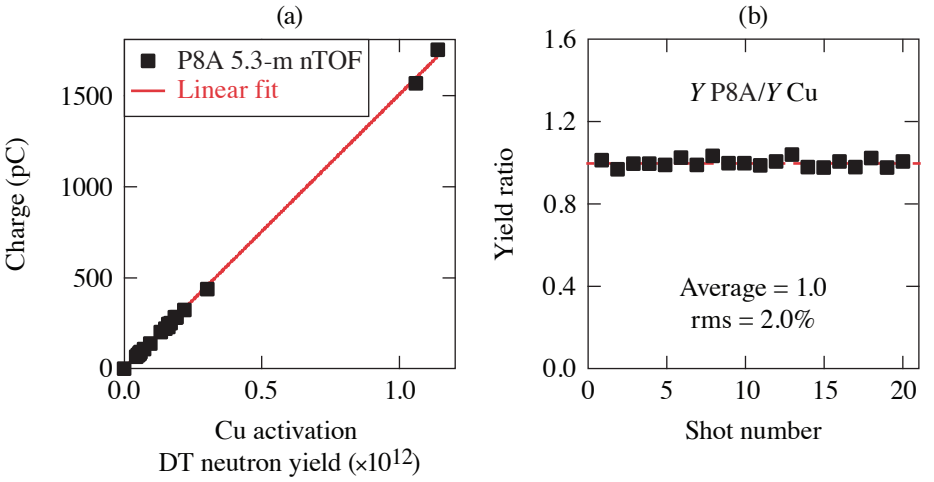

TC16085JR

Figure 2
(a) DT neutron calibration of P8A 5.3-m nTOF against copper activation and (b) the ratio of DT yield measured by P8A 5.3-m nTOF and copper activation.

A new nTOF detector was installed and calibrated on the OMEGA Laser System. This detector is now a standard OMEGA diagnostic for D–D yields above 1×10^{10} and DT yields from 5×10^{10} to 2×10^{12}.

This material is based upon work supported by the Department of Energy National Nuclear Security Administration under Award Number DE-NA0003856, the University of Rochester, and the New York State Energy Research and Development Authority. Sandia National Laboratories is a multimission laboratory managed and operated by National Technology & Engineering Solutions of Sandia, LLC, a wholly owned subsidiary of Honeywell International Inc., for the U.S. Department of Energy's National Nuclear Security Administration under contract DE-NA0003525. This paper describes objective technical results and analysis.

1. Photek Ltd., St. Leonards on Sea, East Sussex, TN38 9NS, United Kingdom, Accessed 9 September 2020, http://www.photek.com/.
2. M. A. Russotto and R. L. Kremens, Rev. Sci. Instrum. **61**, 3125 (1990).
3. V. Yu. Glebov *et al.*, Rev. Sci. Instrum. **75**, 3559 (2004).

A Knock-On Deuteron Imager for Measurements of Fuel and Hot-Spot Asymmetry in Direct-Drive Inertial Confinement Fusion Implosions

H. G. Rinderknecht,[1] P. V. Heuer,[1] J. Kunimune,[2] P. J. Adrian,[2] J. P. Knauer,[1] W. Theobald,[1] R. Fairbanks,[1] B. Brannon,[1] L. Ceurvorst,[1] V. Gopalaswamy,[1] C. A. Williams,[1] P. B. Radha,[1] S. P. Regan,[1] M. Gatu Johnson,[2] F. H. Séguin,[2] and J. A. Frenje[2]

[1]Laboratory for Laser Energetics, University of Rochester
[2]Plasma Science and Fusion Center, Massachusetts Institute of Technology

A knock-on deuteron imager (KoDI) has been implemented to measure the hot spot and fuel asymmetry of cryogenic inertial confinement fusion implosions on OMEGA. Energetic neutrons produced by D–T fusion elastically scatter ("knock-on") deuterons from the fuel layer with a probability that depends on ρR. Deuterons above 10 MeV are produced by near-forward scattering, and imaging them is equivalent to time-integrated neutron imaging of the hot spot. Deuterons below 6 MeV are produced by a combination of sidescattering and ranging in the fuel, and encode information about the spatial distribution of the dense fuel.

The KoDI instrument consists of a multi-penumbral aperture positioned 10 to 20 cm from the implosion using a ten-inch manipulator (TIM) and a detector pack at 350 cm from the implosion to record penumbral images with magnification of up to 35×. Range filters and the intrinsic properties of CR-39 (Ref. 1) are used to distinguish different charged-particle images by energy along the same line of sight. Image plates fielded behind the CR-39 record a 10-keV x-ray image using the same aperture.

Differential filtering is used to distinguish between high- and low-energy deuteron populations. The left half of the CR-39 is filtered by 135 μm tantalum, transmitting only deuterons initially above 10 MeV. The right half is filtered by 10 μm tantalum, transmitting deuterons initially above 2 MeV. The diameter of tracks is used to further discriminate the data into rough energy bins to interpret the images. While the exact diameter–energy relationship varies from sample to sample, the energy order and approximate energy range can be inferred. The analysis of the x-ray data is described in Ref. 2.

Penumbral imaging maximizes the statistics of the recorded signal. Each penumbral aperture is made by laser drilling a 200-μm-thick tantalum or 175-μm-thick tungsten substrate, producing a conical hole with an opening angle of 10°. Two effects cause the point-spread function (PSF) of the penumbral apertures to differ from the ideal knife edge: charged-particle scattering in the substrate and electrical charging of the array. Because of the high magnification of the camera, even a small amount of straggle is sufficient to produce a uniform background and the effect of scattering on the PSF blur is negligible. Electrical charging of the aperture array is more significant. A semi-analytic form of the charged-aperture PSF was derived using a numerically integrated electric field inside the array, $E(r)$:

$$\mathrm{PSF} = \left[\frac{\mathrm{d}r_\mathrm{i}'}{\mathrm{d}r_\mathrm{a}'}\right]^{-1}, r_\mathrm{i}' = r_\mathrm{a}' + \frac{e\Delta z}{4\pi\varepsilon_0}\left[\frac{Q}{K}\frac{D}{R_\mathrm{a}}\frac{M-1}{M^2}\right]E'\left(r_\mathrm{a}'\right), \tag{1}$$

where r_a and r_i are radial position in the aperture and image plane, R_a is the aperture radius, D the detector distance to target chamber center (TCC), Δz is the aperture thickness, M is the camera magnification, Q is the aperture charge density, K is the deuteron kinetic energy, and primes indicate normalized quantities $\left\{r_\mathrm{a}' = r_\mathrm{a}/R_\mathrm{a},\ r_\mathrm{i}' = r_\mathrm{i}/R_\mathrm{a}M,\ E' = E'/\left[Q/2\pi\varepsilon_0\right]\right\}$. The charged-aperture PSF is a family of curves that depends only on the value of the coefficient in square brackets, which we call V. [We select

$\Delta z = 200\ \mu$m and V has units of (coulomb/cm^2)/MeV.] Charging effects are negligible for values $V \lesssim 10^{-7}$, but become dominant for $V \gtrsim 3 \times 10^{-5}$. For accurate reconstructions using a charged aperture, the amount of charging must be known and the blurring caused by charging effects must not dominate the structure caused by the object. The PSF radius at 50% of maximum increases monotonically with the charging coefficient. The amount of charging from the data is inferred by comparing the projected radius of the deuteron aperture images with x-ray measurements of the camera magnification. Since V depends on particle energy, low-energy deuterons are more susceptible to the effects of charging than high-energy deuterons.

The images of the source are encoded in the recorded penumbral images and are recovered using the iterative reconstruction algorithm described by Gelfgat *et al.* in the limit of Poisson statistics.[3] We include a uniform background and begin with a uniform prior. Numerical testing shows that for N total tracks, the required number of iterations to converge grows as roughly $N^{0.33}$ for a fixed image size. The asymptotic reconstructions are overfit, concentrating numerical noise into high variations between neighboring pixels. To avoid overfitting, a condition for when to terminate the reconstruction is desirable and is under investigation.

The KoDI system was fielded on a series of direct-drive cryogenic implosions on OMEGA during 2021 and 2022. In the majority of the experiments, the diagnostic was fielded in TIM-1 with a magnification of 25 or 35. In one shot series (102560–102571), multiple KoDI instruments were fielded at different magnifications on each shot. Figure 1 shows the (a) deuteron and (b) x-ray data recorded on shot 102568. Analysis of the raw x-ray data indicated a magnification of 35.70±0.10. The deuteron data were analyzed to infer a charge-induced magnification increase of 5.4±0.3%. These values were used to calculate the point-spread function for reconstructing the data. A reconstruction of a high-energy deuteron image is shown in Fig. 1(c), and the corresponding reconstructed x-ray image in Fig. 1(d). The inferred shape and size of the hot spot is comparable between the x rays and deuterons. The 50% radius (P0) of the deuteron image was fit as 30 μm, with a significant mode-2 (P_2/P_0) of 30%. The axis of the mode-2 matches that seen in the reconstructed x-ray image. The camera was fielded in TIM-5, observing the implosion nearly perpendicularly to the stalk axis, and the observed mode-2 is elongated in the stalk direction.

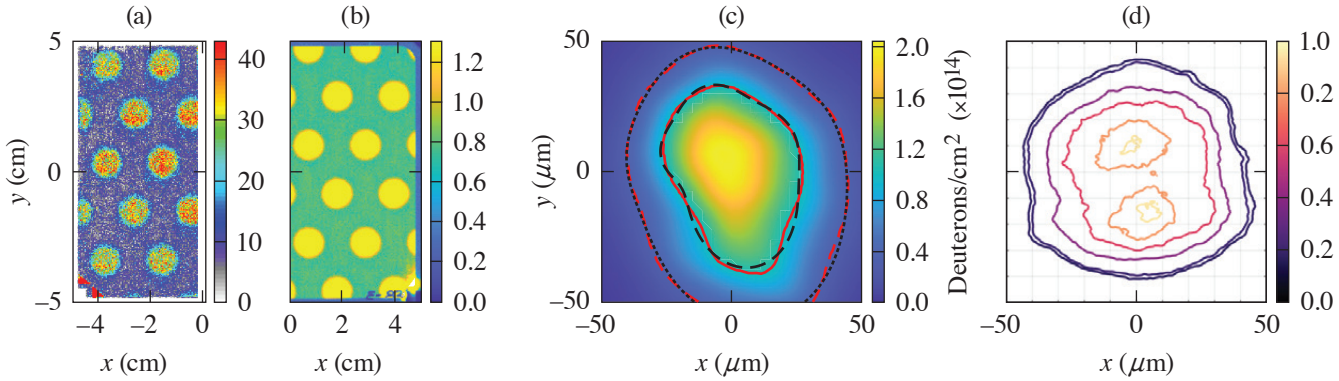

Figure 1
KoDI data recorded on OMEGA cryogenic implosion 102568. (a) High-energy deuteron image (>10 MeV, tracks per 400-μm square pixel); (b) 10-keV x-ray image (PSL per 100-μm square pixel); (c) reconstructed deuteron source with 50% and 17% intensity contours (red curves) and Legendre polynomial fits to $n = 4$ (black curves); and (d) reconstructed x-ray source.

Aperture charging was observed on the majority of the experiments and appears to show increased charging with aperture distance from TCC. The observed trend is not consistent with a prompt charging source that originates at TCC, which should fall off as R^2. The data are roughly consistent with a model in which the electromagnetic pulse (EMP) radiation produced by the laser–target interaction drives currents in the TIM body, for which farther distance from TCC allows a greater amount of time for the aperture to charge before being sampled by the deuterons.

While the charged-aperture PSF is, in principle, sufficient to interpret the diagnostic data, in practice, the reduction or elimination of aperture charging will significantly benefit the experiments by reducing analysis error and maximizing camera resolution,

and is necessary for low-energy deuteron images that are more severely distorted. Several approaches to controlling the aperture charging are being investigated, including replacing the front 30 cm of the diagnostic with a nonconductive material; fabricating the aperture from a nonconductive material such as silicon dioxide; and reducing the EMP source by changing the target mounting stalk.[4] These solutions will be tested in upcoming campaigns to assess their effects on the recorded data.

The data recorded by the KoDI diagnostic will enable detailed studies of the hot spot and assembled cold fuel on OMEGA. Comparisons of the high-energy deuteron and x-ray images will be used to infer the profiles of temperature and density to localize mix in the hot spot. Up to six lines of sight will be used to reconstruct the 3-D profiles of neutron emission and cold dense fuel. These data will provide unprecedented constraints on fuel assembly in direct-drive implosions, which will assist in the goals of reaching improved symmetry and hydro-equivalent ignition conditions on OMEGA.

This material is based upon work supported by the Department of Energy National Nuclear Security Administration under Award Number DE-NA0003856, the University of Rochester, and the New York State Energy Research and Development Authority.

1. N. Sinenian *et al.*, Rev. Sci. Instrum. **82**, 103303 (2011); **85**, 119901(E) (2014).
2. P. J. Adrian *et al.*, Rev. Sci. Instrum. **94**, 043548 (2021).
3. V. I. Gelfgat, E. L. Kosarev, and E. R. Podolyak, Comp. Phys. Commun. **74**, 335 (1993).
4. P. Bradford *et al.*, High Power Laser Sci. Eng. **6**, e21 (2018).

Design and Implementation of a Digital Optical Microscope for Measurement of Submicron Defects on Cryogenic DT Targets

D. Weiner, D. Bredesen, J. Bender, D. H. Edgell, C. Fella, V. N. Goncharov, D. W. Jacobs-Perkins, R. T. Janezic, M. W. Koch, S. F. B. Morse, S. P. Regan, S. Scarantino, M. J. Shoup III, M. D. Wittman, and J. Zou

Laboratory for Laser Energetics, University of Rochester

Submicron particles on the exterior surface of cryogenic deuterium–tritium (DT) target shells may contribute to hydrodynamic instability during target implosions that reduce predicted performance. Particles that originate from pre-existing shell defects or foreign material present within the target Fill/Transfer Station and are observed to exist on the surface after filling with a DT gas. Currently available imaging tools are limited to resolution of the order of 3 μm (Ref. 1). A digital optical microscope system has been developed that provides *in-situ* capability to image 0.5- to 1.0-μm features that are within a critical size range identified by physics considerations. The system design is described and initial results are presented.[2] Initial results indicate that the fill cycle process results in a statistically minor increase in defect count (+10%) and affected area (+4%), and that the pre-to-post fill particle distribution is unchanged.

The Fill/Transfer Station (FTS) is an existing system that houses a target during its fill cycle. Current target evaluation is done at a separate characterization station that is incompatible with cryogenic temperatures. Close examination of a target requires removal of the thermal shroud, which requires that the imaging system exist in a cryogenic environment. The target is held at a temperature of 40 to 50 K during observation.

A commercially available 40×, 0.60 N.A. long-working-distance microscope objective meets the 0.5-μm resolution goal. The projected 20-μm feature size implies that a camera sensor with pixel size less than 10 μm is required to avoid aliasing. A room-temperature test bed was designed and built to verify proof-of-concept using identical optics and illumination to enable comparison of pre- and post-fill images. A quasi-collimated illuminator was designed to reduce the formation hot spots in the target region that originate from LED source points and provide uniform irradiance in the target plane.

The prototype system is shown in Fig. 1. The mechanical design is comprised of three sections: an illuminator, the microscope holder and motion stage, and the charge-coupled–device camera. The microscope and illuminator assemblies are compatible with cryogenic temperatures while the camera is housed within a vacuum bubble to provide isolation from the cold environment. Heat sinks were included to provide for dissipation of thermal sources (LED and camera power supply). With the microscope located outside of the thermal shroud, the microscope translation stage is motorized with a range sufficient to move the objective to the target. Limit switches connected to the controls interface prevent inadvertent collisions between components. A prototype system was installed on the FTS.

The control system provides the ability to remotely power and adjust the LED illumination level, regulate the camera vacuum bubble temperature, and deliver motion control to the microscope and camera stages. To reduce the impact of target vibration and thermal load, the illumination is pulsed and synchronized with the camera's electronic shutter setting. The acquisition pulse width is adjusted to provide optimal integration time on the sensor. Interlocks prevent interference between the microscope, the FTS shroud puller, and the moving cryostat. A software interface is included for image acquisition, display, analysis, and storage. All major component controls are deliverable over an Ethernet connection.

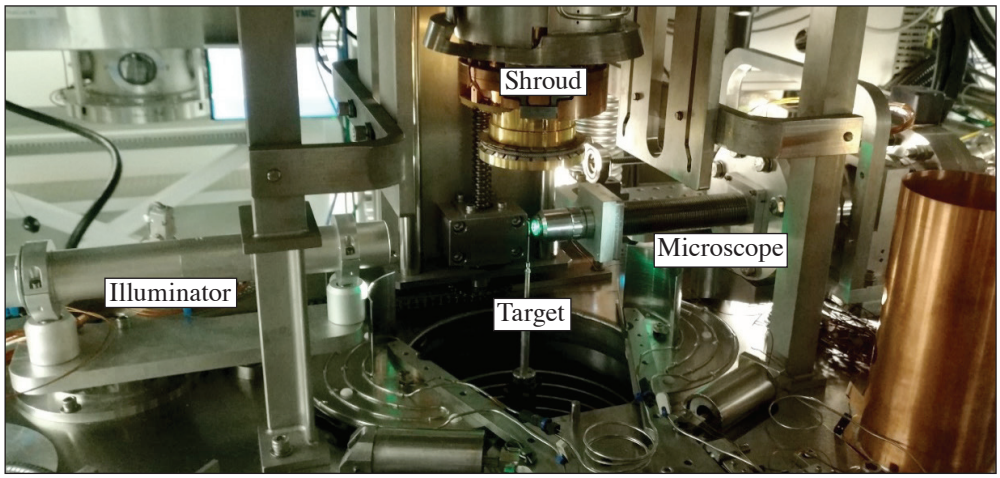

G13604JR

Figure 1
Installed FTS system showing key components.

A set of 12, 178 × 210-μm locations using pre-existing fiducial markers were established about the equator of the target shell, each of which was characterized under pre- and post-fill conditions. The warm temperature pre-fill and cryogenic post-fill optical systems used the same design with similar performance but separate systems. Each area was analyzed using all-in-focus (AIF)[3,4] and maximally stable extremal region (MSER)[5] image-processing techniques to detect and characterize micron-scale shell features. Images were pre-processed to normalize the bright-field background and optimize contrast. The AIF images were generated from a stack of eight to ten through-focus positions, which were then subject to an MSER algorithm for defect detection and statistical computation. A single target was used with a shell made from a glow-discharge polymer (GDP) process. Approximately 1% of the total shell area was analyzed and the results extrapolated. Figure 2 shows a side-by-side image comparison of one location for pre- and post-fill conditions.

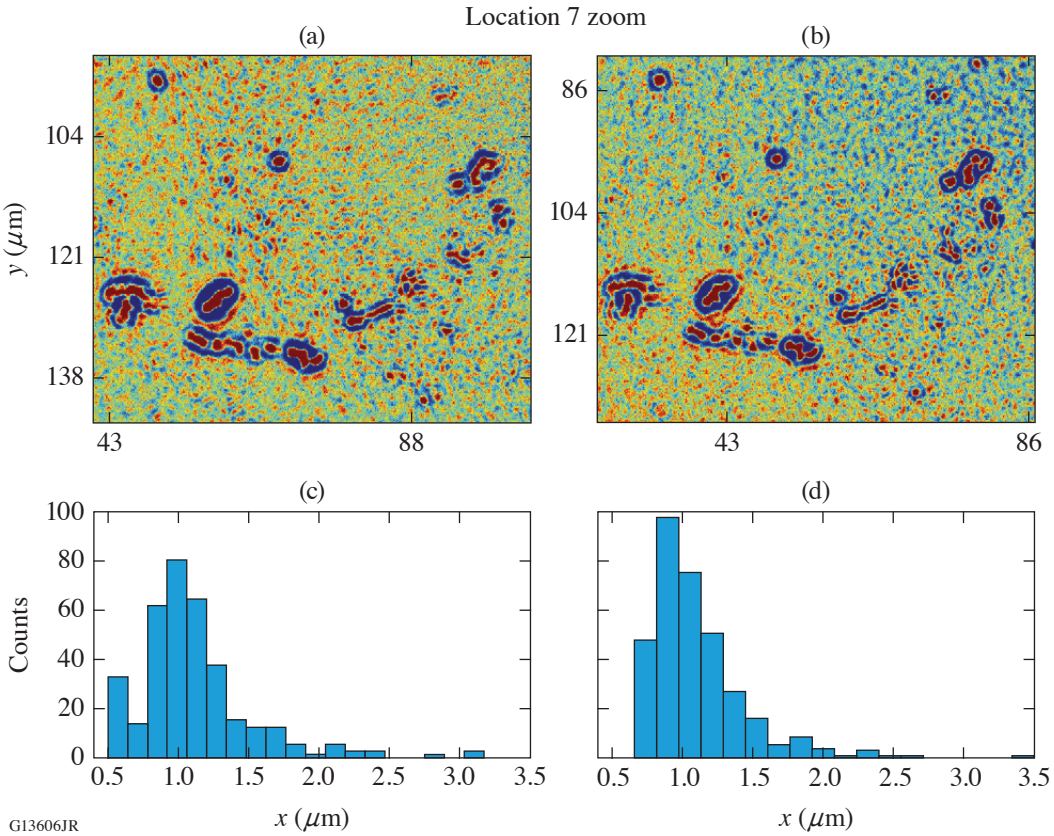

G13606JR

Figure 2
Image comparison for one of the 12 analyzed target areas.

The AIF/MSER techniques used found a 10% increase in feature counts and a 4% increase in feature area upon completion of the fill process (Fig. 3). While the plots suggest good agreement between the pre-fill and post-fill analysis, at present there is no assignment of error or degree of confidence assigned to the measurements.

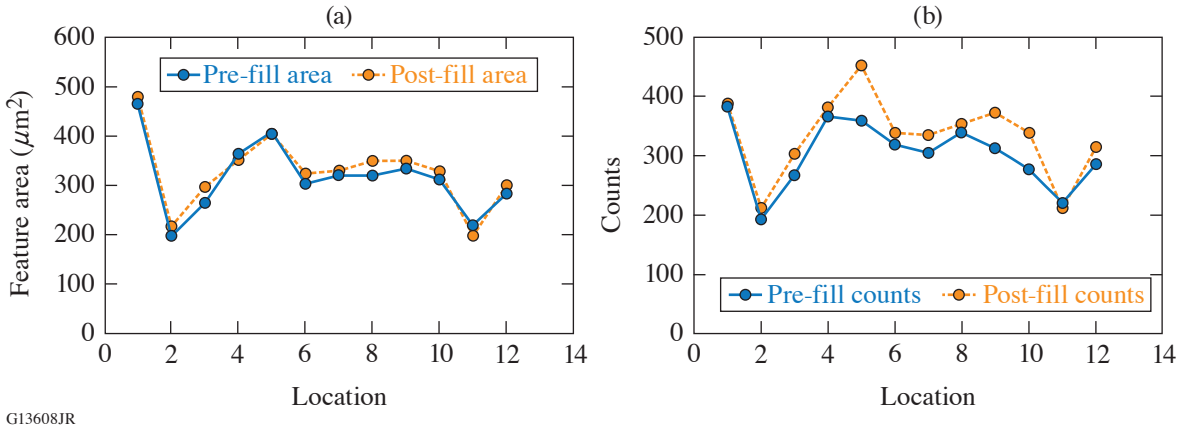

Figure 3
AIF/MSER analysis summary.

No new defects were identified between pre- and post-fill observations with the prototype system. Equivalent diameter size distribution for observed particles was between 0.5 to 2 μm (identified most significant for seeding hydrodynamic instabilities). Initial results indicate that the fill process does not significantly add to defect contribution, and that pre- and post-observation defect distributions are unchanged.

Future work is anticipated to include the testing of target shells made from materials other than GDP (e.g., polystyrene) containing fewer pre-existing defects and the collection of larger data sets to strengthen the statistical significance of results that are obtained. Periodic recharacterization of the platform using a surrogate target is also planned to monitor possible long time-scale system drift.

This material is based upon work supported by the Department of Energy National Nuclear Security Administration under Award Number DE-NA0003856, the University of Rochester, and the New York State Energy Research and Development Authority.

1. *LLE Review Quarterly Report* **104**, 169, Laboratory for Laser Energetics, University of Rochester, Rochester, NY, NTIS Order No. PB2006-108481 (2005).
2. D. R. Harding *et al.*, Matter Radiat. Extremes **3**, 312 (2018).
3. S. Pertuz *et al.*, IEEE Trans. Image Process. **22**, 1242 (2013).
4. F. Pérez Nava and J. P. Luke, in *2009 3DTV Conference: The True Vision - Capture, Transmission and Display of 3D Video* (IEEE, New York, 2009), pp. 1–4.
5. P. P. Ramya and J. Ajay, in *2019 1st International Conference on Innovations in Information and Communication Technology (ICIICT)* (IEEE, Chennai, India, 2019), pp. 1–4.

Tunable Picosecond AlGaN UV Photodiodes

S. F. Nwabunwanne and W. R. Donaldson

Laboratory for Laser Energetics and Department of Electrical and Computer Engineering, University of Rochester

Efficient and ultrafast UV photodetection is needed when characterizing high-temperature plasmas and ultrashort UV laser pulses. Semiconductor-based photodetectors (PD's) have not been widely used for these applications because of their reduced absorption depths in the UV spectrum, making streak cameras the dominant choice in the industry. A new category of photosensors built on $Al_xGa_{(1-x)}N$ (where x varies from 0 to 1) alloy provide tunable band gaps in the entire UV spectrum. Changing x varies from 0 to 1 and adjusts the band gap from 361 nm to 200 nm. Consequently, one can select the spectral window of interest for photosensing.

Laterally oriented AlGaN thin films were used to fabricate photodetectors with interdigitated electrodes.[1] These detectors recorded <30-ps response times, making them suitable for diagnosing ultrafast UV laser pulses and laser–plasma interactions.

This summary reports the outcomes of the spectral studies of detectors fabricated on different $Al_xGa_{(1-x)}N$ thin films where x is 0 to 0.3 (Ref. 1). Measured spectral responsivities are in the range of 0.43 A/W, which is comparable to other semiconductor-based detectors in the visible and infrared regions like silicon and InGaAs. High-quality semiconductors are critical for achieving these results, hence material characterization with x-ray diffraction is recommended prior to fabrication. The University of Rochester is in collaboration with Sydor Technologies to make these detectors available to the public. Some of the AlGaN PD's reported in Refs. 1 and 2, as well as newly fabricated GaN ($x = 0$) PD's with the same design parameters given in Ref. 1, were investigated for a comparison of their spectral selectivity profiles. The objective of this investigation was to determine the spectral responsivity and the ultrafast characteristics of our $Al_xGa_{(1-x)}N$ detectors with x ranging from 0 to 0.3

Figure 1 portrays the temporal response of a Au intrinsic $Al_{0.1}Ga_{0.9}N$ circular asymmetric (CA) device under study and a silicon reference PD at 260 nm under 20-V bias voltage. The voltage response of the AlGaN detector was 1.4 V with a 33-ps rise time

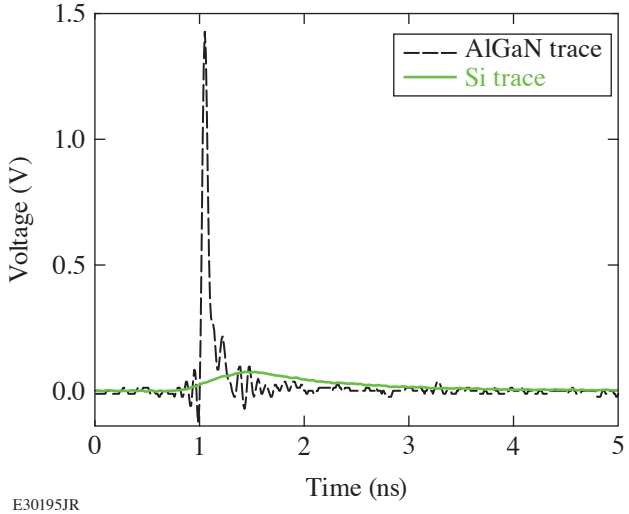

Figure 1
Au intrinsic $Al_{0.1}Ga_{0.9}N$ CA device response (black curve) under 20-V bias and Si reference detector (green curve) at 260 nm with rise times of 33 ps and 430 ps, and FWHM of 60 ps and 1.2 ns for AlGaN and Si PD's, respectively.

and a 60-ps full width half maximum. The pulse width of the device's temporal response increased from 26 ps (the resolution of the 12.5-GHz Tektronix oscilloscope) to 60 ps because of the delays introduced by the measurement system.[3]

The spectral responsivity of another AlGaN device that had 10% Al and rectangular asymmetric (RA) Pt (Ref. 1) metal contacts is depicted in Fig. 2. This detector's responsivity peaked at 315 nm with 0.43 A/W and a rapid cut off at 360 nm. The high responsivity supports the recorded external quantum efficiency of these photodiodes reported in Ref. 1. The responsivity dropped at shorter wavelengths because the absorption depth of photons within the AlGaN thin film reduced from 77 nm at 280 nm to 48 nm at 240 nm.

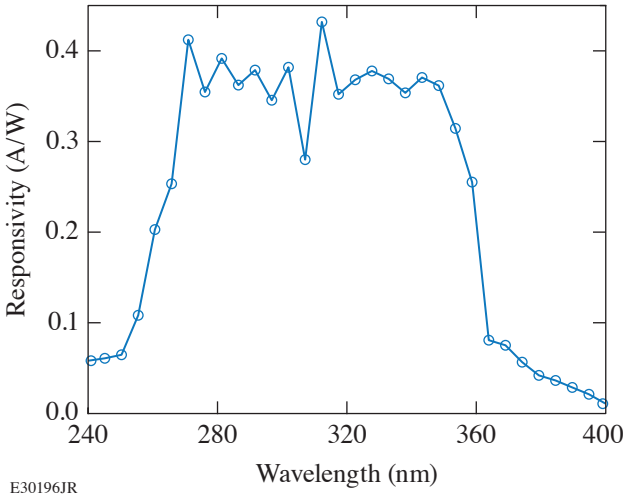

Figure 2
Pt intrinsic $Al_{0.1}Ga_{0.9}N$ RA device with spectral responsivity at 10-V bias voltage with peak responsivity of 0.43 A/W at 315 nm.

The spectral responsivity properties of another AlGaN UV PD that has 20% Al with CA Au metal is presented in Fig. 3. The data were measured under a 10-V bias voltage. This detector exhibited a maximum spectral responsivity of 0.033 A/W at 280 nm and a rapid cut off at 300 nm. The rising Al content implies that this diode will sense only deep UV wavelengths but a factor of 10 decrease in responsivity is recorded at 280 nm.

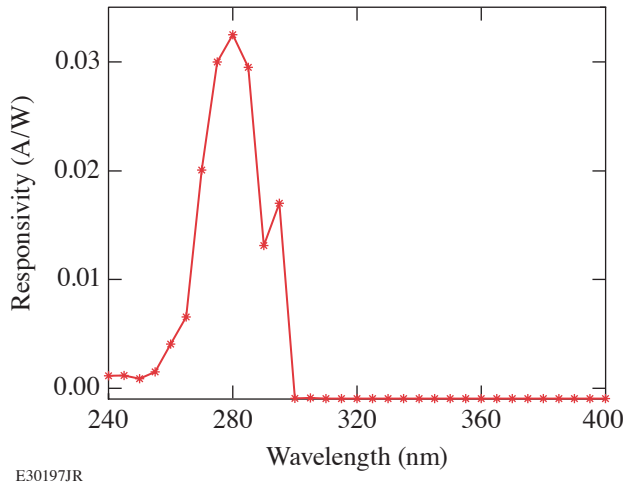

Figure 3
Au intrinsic $Al_{0.2}Ga_{0.8}N$ CA device with spectral responsivity at 10-V bias voltage with maximum responsivity of 0.033 A/W at 280 nm.

Summing up, the spectral responsivity of our AlGaN UV detectors in a metal–semiconductor–metal configuration was discussed. The results demonstrated that the applicability of AlGaN-based UV detectors in high-energy investigations of laser–plasma interactions, which have multiple sources of light in close proximity, require ultrafast and efficient UV photodetection. Finally,

it is necessary to carefully select the Al composition that meets the spectral window that needs to be sensed as this determines if the realized PD will meet the application requirements.

This material is based upon work supported by the Department of Energy National Nuclear Security Administration under Award Number DE-NA0003856, the University of Rochester, and the New York State Energy Research and Development Authority.

1. S. F. Nwabunwanne and W. R. Donaldson, IEEE J. Quantum Electron. **57**, 4000608 (2021).
2. S. Nwabunwanne and W. Donaldson, Proc. SPIE **12001**, 120010F (2022).
3. Y. Zhao and W. R. Donaldson, J. Mater. Res. **33**, 2627 (2018).

Measurement of Laser Absorption in Underdense Plasmas Using Near-Field Imaging of the Incident and Transmitted Beams

J. Katz,[1] D. Turnbull,[1] S. T. Ivancic,[1] A. L. Milder,[1] and D. H. Froula[1,2]

[1]Laboratory for Laser Energetics, University of Rochester
[2]Department of Physics and Astronomy, University of Rochester

Measurements of laser absorption in high-temperature, underdense plasmas produced at the Omega Laser Facility are made using two near-field imaging detectors that diagnose the spatial profile and energy of the port P9 beam before and after it transmits through the plasma. By comparing the signal ratios of these detectors for shots with and without plasma, absorption is measured without the need for absolute energy calibration of either detector. Complementary diagnostics monitor laser backscatter and spatially resolve key plasma parameters,[1] including ion and electron temperature and electron density, along the beam propagation length. Simultaneous measurements of the plasma conditions and total beam absorption provide means to experimentally validate physics models used to predict absorption in plasmas relevant to inertial confinement fusion.

The experimental platform, shown in Fig. 1, utilizes a set of 351-nm heater beams to ionize a 2-mm-diam, cylindrical column of neutral gas that is injected into target chamber center (TCC) using a gas-jet delivery system. The 527-nm P9 probe beam is then fired into the plasma. Experimental conditions can be varied by adjusting the 351-nm heater-beam energies and timings or by changing the gas type and initial neutral gas density. Total absorption in these high-temperature (>100-eV), millimeter-scale-length plasmas are often a few percent or less. As such, high-precision measurements of the input and transmitted beam energies are required. It is also important to confirm that any potential energy loss to the transmitted beam from mechanisms other than absorption remain energetically insignificant.

The input beam is sampled using a partial reflection from a full-aperture, 30-cm-diam uncoated-wedge pickoff located before the target chamber vacuum window and final-focus lens assembly. An uncoated, concave mirror focuses the reflected beam at *f*/10, allowing it to be recorded directly with a 13 × 13-mm sensor. The P9 transmitted-beam diagnostic (P9TBD)[2] characterizes the transmitted light by terminating the expanded beam on a semi-transparent diffuser and imaging the illuminated surface using a lens and charge-coupled–device (CCD) camera. The near-field image measures both the transmitted beam energy and the degree of any potential beam filamentation or whole beam refraction. The nominal diameter of the expanded beam at the diffuser plane is 28 cm. The 45-cm (*f*/4) acceptance aperture of the P9TBD allows energy of the beam to be measured even in the presence of moderate levels of beam refraction or filamentation.[3]

For an ideal detector, the total signal recorded on the CCD images is proportional to the amount of energy present at TCC. The proportionality constant, K, given in analog-to-digital units (ADU) per joule of photon energy, is influenced by a number of factors including the optical throughput between the sample point and TCC, the sensor quantum efficiency, the camera digitizer gain, and the throughput of any optical filtration used to adjust signal levels. It is difficult to accurately quantify all of these components individually. If the energy loss in the transmitted beam is limited to absorption alone, however, knowledge of the individual instrument sensitivities is not required to determine absorption since the measurement depends only on the ratio of the instrument sensitives K and the total signals.

$$\mathrm{ABS} = 1 - \frac{c_{\mathrm{Trans}}}{\underbrace{c_0}_{K}} \frac{\sum \mathrm{CCD}e^{-}_{\mathrm{Trans}}}{\sum \mathrm{CCD}e^{-}_{0}},$$

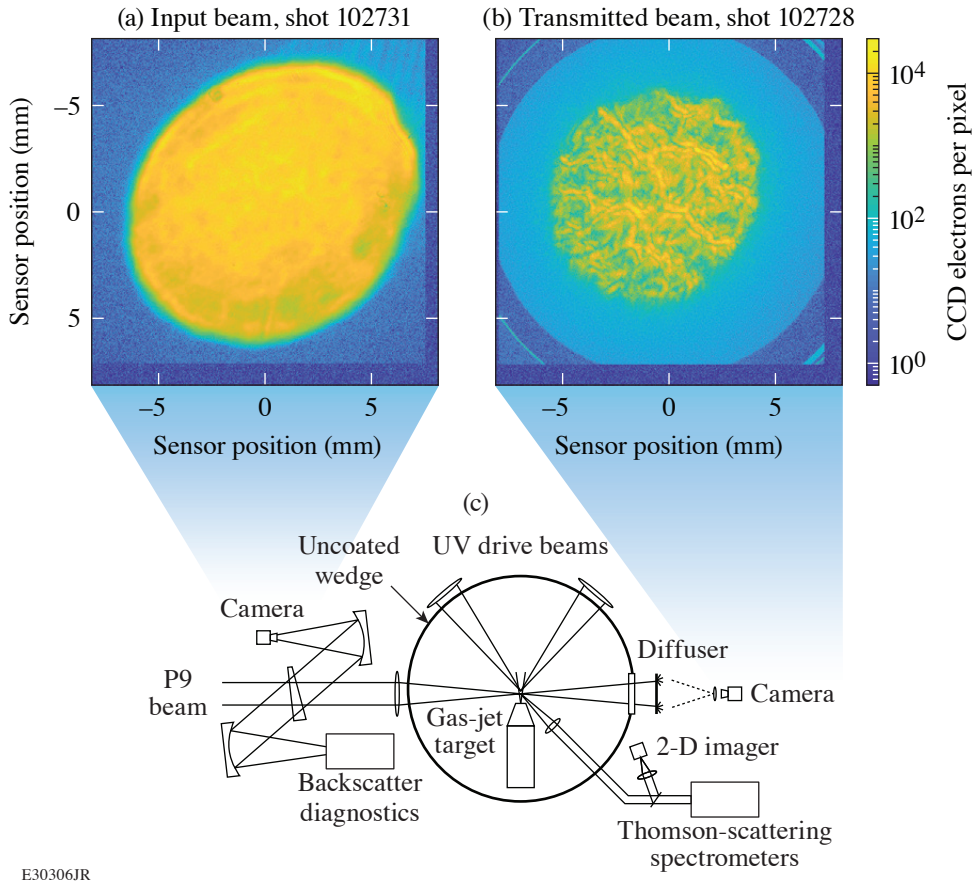

Figure 1
The amount of laser energy deposited in the plasma from a single beam is inferred by comparing input and output energies. Two CCD cameras measure the incident and transmitted beam spatial profiles and energies with high precision. Back and sidescatter diagnostics are used to verify that energy losses from laser–plasma instabilities are energetically insignificant.

where K is measured experimentally by taking a calibration shot with no plasma present. In this case, there is no absorption, $E_0 = E_{\text{Trans}}$, and K is given by the ratio of the input to transmitted signals. To the extent that c_0 and c_{Trans} remain stable over time, the accuracy of the absorption measurement is driven by the measurement precision of the two detectors. Two calibration shots are normally taken during a shot day to confirm the measurement stability and typically agree to within ±0.01%. Additionally, the measurement stability and precision of the two detectors was benchmarked using a full-aperture, Q-switched laser propagated along the P9 beamline through TCC. Synchronized images were recorded at 5-min intervals over a period of 8 h and the ratio of the detector sensitivities was measured. The measurement variation followed a normal distribution with a standard deviation of ±0.014% and showed no noticeable drifts as a function of time.

The amount of stray 2ω light from the other OMEGA drive beams that scatters into the P9 energy detectors is also measured. For these calibration shots, the plasma is heated by the drive beams but the P9 probe beam is turned off and the background level is measured directly. If a variety of beam energies are fielded during the shot day, the magnitude of the background subtraction is scaled by the total 2ω light present in the experiment, as measured by the harmonic energy diagnostic.[4] Baffling and optical filtration help limit the background signal levels to less than 0.05% of the primary signal.

Propagating the expected errors present in the calibrations and the statistical noise in the signal summations, the overall uncertainty of a typical absorption measurement is estimated to be ±0.07%. With these capabilities, the mechanics of inverse bremsstrahlung heating can be explored experimentally with exceptional quantitative detail.

This material is based upon work supported by the Department of Energy National Nuclear Security Administration under Award Number DE-NA0003856, the University of Rochester, and the New York State Energy Research and Development Authority.

1. J. Katz *et al.*, J. Instrum. **8**, C12009 (2013).
2. J. Katz *et al.*, Rev. Sci. Instrum. **92**, 033526 (2021).
3. D. Turnbull *et al.*, Phys. Rev. Lett. **129**, 025001 (2022).
4. *LLE Review Quarterly Report* **63**, 110, Laboratory for Laser Energetics, Rochester, NY, NTIS Order No. DE96000767 (1995).

Design of the High-Yield, Time-Gated X-Ray Hot-Spot Imager for OMEGA

S. T. Ivancic,[1] W. Theobald,[1] K. Churnetski,[1] M. Michalko,[1] D. Willistein,[1] W. A. Bittle,[1] S. P. Regan,[1] A. Carpenter,[2] C. Trosseille,[2] J. D. Kilkenny,[3] A. Raymond,[3] J. D. Hares,[4] A. K. L. Dymoke Bradshaw,[4] G. Rochau,[5] and D. Garand[6]

[1]Laboratory for Laser Energetics, University of Rochester
[2]Lawrence Livermore National Laboratory
[3]General Atomics
[4]Kentech Instruments Ltd., UK
[5]Sandia National Laboratories
[6]Sydor Technologies

Low-mode 3-D nonuniformities of the compressed core in inertial confinement fusion (ICF) implosions are important to diagnose because they represent inefficiency in the conversion of kinetic to internal energy of the core.[1] X-ray projection to infer 3-D shape is incisive for understanding drive nonuniformities and their potential mitigations.[2] Demonstration of using time-integrated x-ray imaging has been developed,[3,4] which is transferrable to time-resolved analysis with a suite of time-synchronized detectors with sufficient signal. Drift-tube imagers[5,6] coupled to high-speed hybrid complementary metal-oxide semiconductor (hCMOS) detectors[7] have a number of advantages over framing cameras[8] especially for being fieldable in a harsh neutron environment such as those found near the target chamber during high-yield implosions. Radiation-hardened electronic readout is essential to provide real-time data. A third, time-gated x-ray line of sight is proposed for OMEGA to provide an additional view to allow for time-resolved 3-D tomographic reconstruction of the hot-spot shape. The simultaneous operation of this new imager with the existing time-gated x-ray imaging lines of sight on OMEGA[9,10] will enable a time-resolved reconstruction of the low-mode shape of the ICF hot spot.

The x-ray hot-spot imager consists of three distinct subassemblies illustrated schematically in Fig. 1: A 22.5× magnification pinhole-array imager provides a multitude of images at an intermediate plane located outside of the OMEGA tank wall on a large-format photocathode. The x rays are converted to photoelectrons, which are imaged by a demagnifying, dilation drift tube that reduces the photoelectron image by 2× on a detector plane while providing temporal magnification of 100 to 350×. The demagnification serves two purposes, first it allows the imager to operate at a larger magnification that serves to lower the current at the photocathode. Demagnification is required in order to form the image to a suitable size to be detected by available solid-state detectors. In this case the photoelectron images are recorded by two side-by-side hCMOS[10] sensors, which are capable of recording eight sequential frames with an adjustable integration time in the range of 1 to 10 ns. The temporal magnification maps eight 20-ps sequential frames onto the hCMOS with a varying duration from 2 to 7 ns. This magnification allows the entire x-ray emission history of the hot spot to be captured.

The photoelectrons are constrained by a homogeneous axial magnetic field to move helical orbits along the axis of the drift tube, providing an upright photoelectron image onto the hCMOS detector. The design of the tube is segmented with the magnetic-field strength increasing in the latter two segments to provide the 2:1 demagnification of the drifting photoelectron signal as it traverses the tube. Simulations using magnetostatic modeling using the field solver *COMSOL* have been performed to measure the effect of segmentation of the solenoidal field into four separate tube parts working together. The overall effect is negligible relative to the sizes of the imager point-spread function and blurring caused by the drift tube.

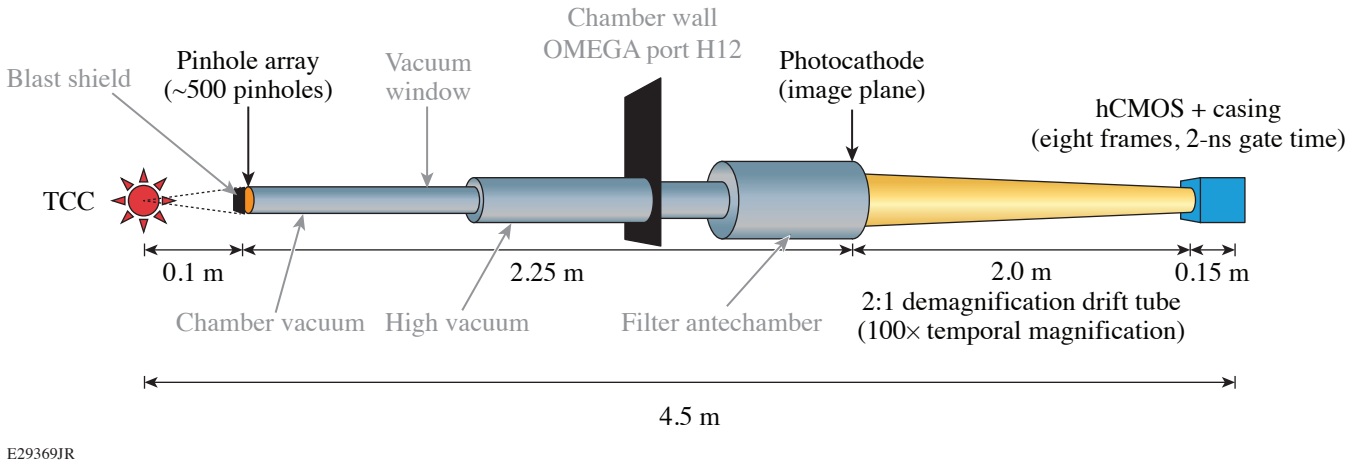

Figure 1
Schematic of the overall x-ray imaging system. A pinhole array is situated 100 mm from the target chamber center (TCC). The x-ray images pass through a beryllium vacuum window located in a re-entrant tube inside the tank that separates the tritium-contaminated tank vacuum from a separate clean vacuum volume that includes the instrument inclusive of the drift tube. The x-ray image emerges from the target chamber out of OMEGA port H12 to an intermediate image plane located 2.25 m from the pinhole array. An access hatch forward of the image plane allows for x-ray filters to be introduced over some or all of the x-ray images. The x-ray imager casts >500 images onto a 50-mm × 50-mm intermediate image plane.

This material is based upon work supported by the Department of Energy National Nuclear Security Administration under Award Number DE-NA0003856, the University of Rochester, and the New York State Energy Research and Development Authority.

1. K. M. Woo *et al.*, Phys. Plasmas **25**, 102710 (2018).
2. O. M. Mannion *et al.*, Phys. Plasmas **28**, 042701 (2021).
3. K. Churnetski *et al.*, Rev. Sci. Instrum. **93**, 093530 (2022).
4. S. M. Glenn *et al.*,, Rev. Sci. Instrum. **83**, 10E519 (2012).
5. T. J. Hilsabeck *et al.*, Rev. Sci. Instrum. **81**, 10E317 (2010).
6. K. Engelhorn *et al.*, Rev. Sci. Instrum. **89**, 10G123 (2018).
7. L. Claus *et al.*, Proc. SPIE **10390**, 103900A (2017).
8. D. K. Bradley *et al.*, Rev. Sci. Instrum. **66**, 716 (1995).
9. W. Theobald *et al.*, Rev. Sci. Instrum. **89**, 10G117 (2018).
10. F. J. Marshall *et al.*, Rev. Sci. Instrum. **88**, 093702 (2017).

High-Resolution Mapping of Phase-Matching Conditions in Second-Order Nonlinear Crystals

C. Dorrer, I. A. Begishev, S.-W. Bahk, and J. Bromage

Laboratory for Laser Energetics, University of Rochester

Nonlinear crystals are widely used for frequency conversion of lasers and optical parametric amplification. Phase matching between the interacting waves is required for efficient operation.[1] This can generally be achieved by temperature or angle tuning, which both allow precise control the optical index. Such global tuning is sufficient when the interacting beams and the crystal have spatially uniform properties. This is a reasonable assumption for relatively small nonlinear crystals. However, the local crystals properties are impacted by environmental stability during growth, stress within the boule, and impurities in the growth solution. These issues are particularly important for the large-aperture ($\sim 40 \times 40$-cm^2) KDP and partially deuterated KDP (DKDP) that are required to support doubling and tripling of inertial confinement fusion laser systems.[2,3] Variations in axis angle θ and deuteration level X can decrease the frequency-conversion efficiency and uniformity. Large-aperture deuterated KDP crystals will be required for optical parametric chirped-pulse–amplification systems delivering ultrashort optical pulses with peak power well beyond 1 PW (Ref. 4).

While x-ray techniques, optical interferometry, and spectroscopy can be used to spatially resolve the physical characteristics of nonlinear crystals, mapping the local phase-matching conditions is a more-direct approach to performance quantification for an actual laser system. This work demonstrates the high-resolution characterization of local phase-matching conditions for second-harmonic generation of a beam at 1053 nm in several laser crystals, including partially deuterated KDP crystals used for broadband optical parametric amplification of pulses at 920 nm by a pump pulse at 526.5 nm (Ref. 5).

A test bed capable of characterizing crystals over apertures as large as 50×50 mm^2 has been developed [Fig. 1(a)]. A Nd:YLF regenerative amplifier seeded by a fiber front end delivers 1053-nm (λ_1) 350-ps pulses collimated to an ~1-mm diameter. The crystal under test (length L) is mounted on two translation stages that provide transverse scanning in front of the static laser beam. The phase-mismatch $\Delta k_{SHG}L$ for second-harmonic generation (SHG) is proportional to the normalized energy variation $S(x,y) = [\eta(x,y)/(1/2)]-1$, where η is measured at 526.5 nm (λ_2) for the crystal angularly detuned from ideal phase matching [(θ_+) and (θ_-) in Fig. 1(b)]. The nonideal translation stages induce small position-dependent angular rotations of the crystal that can impact phase matching. To alleviate this, the 1053-nm beam is stabilized by a piezo-actuated mirror using the feedback signal from a four-quadrant photodetector on which the beam reflected by the crystal's input face is incident.

As an example of application, the normalized energy variation S is shown in Fig. 2 for a crystal with a deuteration level equal to 98%. For the first two measurements, the input face is the same [labeled as (A) on the figure], whereas the input face is the opposite face for the third measurement [labeled as (B) on the figure]. This crystal has variations in normalized energy up to 25%. Anticorrelated variations of S are obtained when operating at θ_- and θ_+ [Figs. 2(a) and 2(b)]. The high-frequency variations, e.g., in the upper-right corner on Fig. 2(a), are not measurement artifacts. They consistently correspond to a sign change between Figs. 2(a) and 2(b), indicating that they are caused by a local change in phase matching instead of another effect such as low local transmission. This is confirmed by the measured energy variations after a 180° rotation along the vertical axis [Fig. 2(c)]. The low-frequency variations in S are symmetric along the x axis for the two crystal orientations differing by the 180° crystal rotation [Figs. 2(a) and 2(c)]. This indicates that they are caused by bulk variations and do not depend on the propagation direction within the crystal. The observed 25% variations in S are consistent with 20-μrad angular variations and 0.025% deuteration variations.

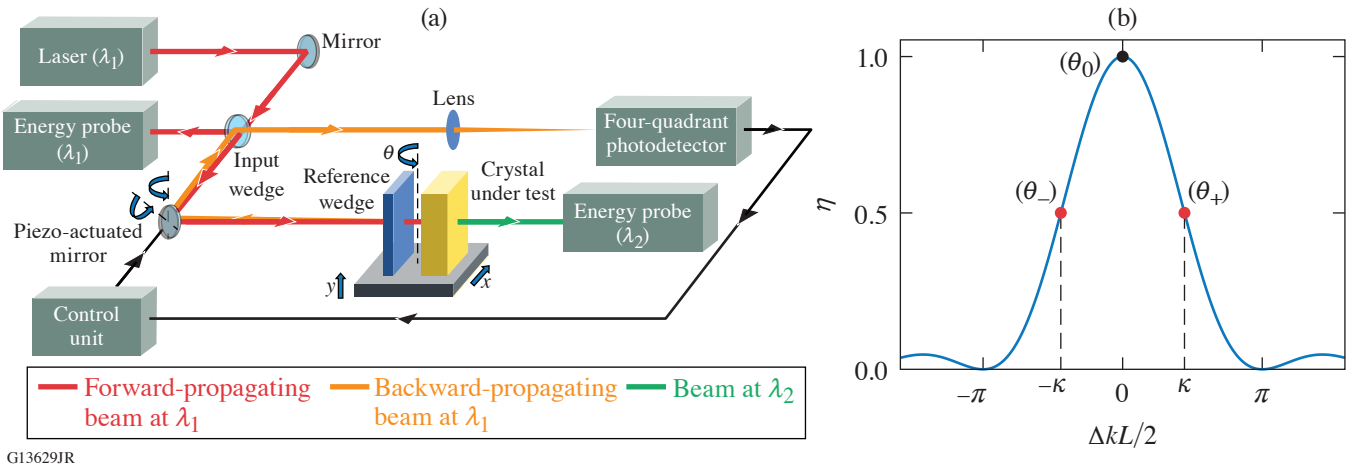

Figure 1
(a) Setup for spatially resolved measurement of the SHG energy, indicating the forward-propagating beam at λ_1 (red line), the backward-propagating beam at λ_1 (orange line), and the beam at λ_2 (green line). (b) Relative SHG efficiency η as a function of the phase mismatch ΔkL.

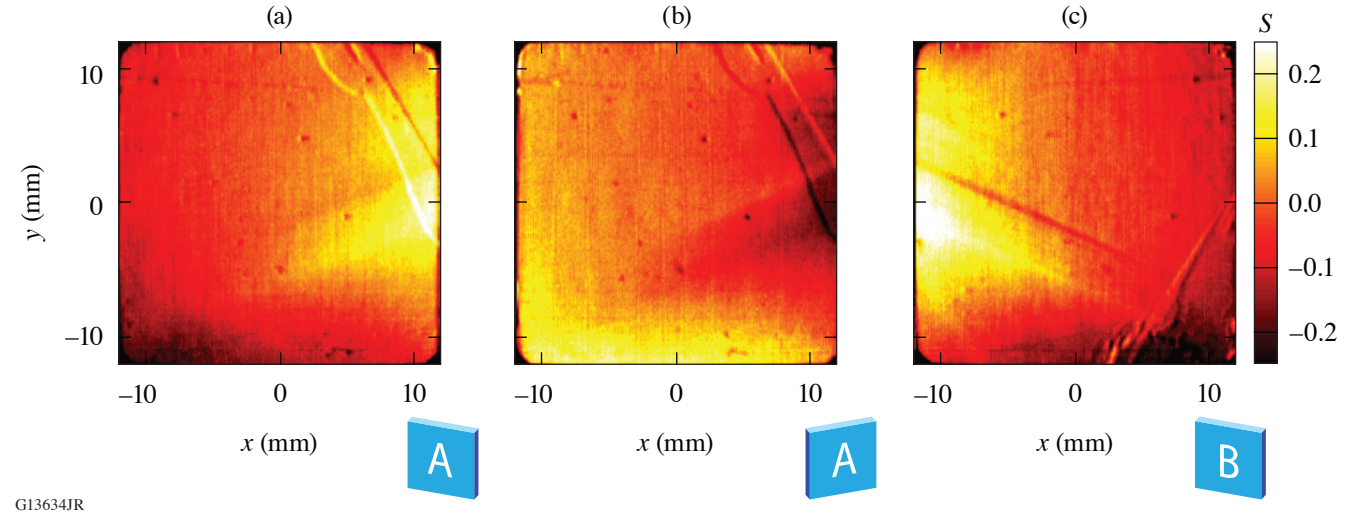

Figure 2
Normalized energy variation S for a crystal with a deuteration level equal to 98%. (a) and (b) correspond to characterization with the same face (A) at the input, and different phase-matching angles θ_- and θ_+, respectively. (c) corresponds to a 180° rotation of the crystal, i.e., characterization with the other face (B) at the input, and phase matching angle θ_-.

The high-frequency variations in S observed in the upper right corner of Fig. 2(a) are, however, not observed in the upper left corner of Fig. 2(c), indicating that these variations are caused by disruptions in phase matching occurring at or close to the input surface. Analytical derivations and experimental results obtained on other crystals confirm that surface variations, such as those introduced by irregularities in sol-gel antireflection coatings, can impact the phase-matching conditions.

A novel approach to the characterization of transverse variations in phase-matching conditions in nonlinear crystals has been demonstrated. SHG in the detuned crystal under test unambiguously converts the local phase mismatch onto energy at the upconverted frequency. Transverse scanning of the crystal combined with beam stabilization maps out phase-matching variations over an aperture only limited by the scanning range of the translation stages. The characterization of partially deuterated

KDP crystals with submillimeter resolution over a 50×50-mm^2 aperture has revealed the impact of spatially nonuniform crystal properties and high-frequency surface variations due to coating imperfections.

The authors thank A. Bolognesi, M. Barczys, T. McKean, and M. Spilatro for experimental assistance with the 1053-nm source. This material is based upon work supported by the Department of Energy National Nuclear Security Administration under Award Number DE-NA0003856, the University of Rochester, and the New York State Energy Research and Development Authority.

1. R. Boyd, *Nonlinear Optics*, 3rd ed. (Academic Press, Amsterdam, 2008), pp. 217–221.
2. J. J. De Yoreo, A. K. Burnham, and P. K. Whitman, Int. Mater. Rev. **47**, 113 (2002).
3. J. M. Auerbach *et al.*, Appl. Opt. **40**, 1404 (2001).
4. C. N. Danson *et al.*, High Power Laser Sci. Eng. **7**, e54 (2019).
5. C. Dorrer *et al.*, Opt. Mater. Express **12**, 3679 (2022).

Utilizing the MTW-OPAL Idler to Seed a Raman Plasma Amplifier

S. Bucht, R. G. Roides, B. Webb, D. Haberberger, C. Feng, D. H. Froula, and J. Bromage

Laboratory for Laser Energetics, University of Rochester

A Raman plasma amplifier (RPA) promises to overcome the damage limitations of chirped-pulse–amplification (CPA)[1] compression gratings by using a "damage-free" plasma to transfer energy from a multipicosecond high-energy pulse to a longer-wavelength femtosecond seed pulse.[2] This technology promises to achieve focused intensities exceeding 10^{23} W/cm^2 if pumped with the output of an Nd:glass-based CPA system laser[3] but requires a 1100- to 1250-nm seed pulse. Simulations show that to achieve an efficient amplifier, a high-intensity (10^{15} W/cm^2), sub-200-fs duration seed pulse is required.[4,5]

One technique for creating such a laser is by using the idler of an optical parametric chirped-pulse–amplification (OPCPA) system.[6] OPCPA systems produce two broadband pulses: a signal, which is seeded, and an idler, which has a wavelength that is red shifted. The Multi-Terawatt optical parametric amplifier line (MTW-OPAL) Laser System,[7,8] which produces 7-J, 20-fs pulses at 910 nm, consists of an ultrabroadband front end (UFE), a cylindrical Offner stretcher (COS), a power amplifier (N4), and a final DKDP amplifier (N5) as shown in Fig. 1(b). The idler that exits the N4 power amplifier has a bandwidth that ranges from 1100 to 1500 nm and 70 mJ of energy; if compressed and focused it would provide an ideal laser to seed an efficient RPA.

Using this idler requires overcoming two disadvantages that are a result of phase matching and energy conservation. First, phase matching in N4 produces an idler that is angularly dispersed, which hampers pulse focusing and compression.[9] Second, energy conservation inverts the spectral phase of the idler relative to the signal,[10] significantly changing the typical stretch–amplify–compress process of CPA.[1] Here we address both the phase reversal and angular dispersion of the MTW-OPAL idler with the addition of several optical subsystems to achieve 100-GW pulses at 1170 nm with 120-fs durations.

For ease of switching between the conventional MTW-OPAL configuration [Fig. 1(b)] and an idler OPAL configuration [Fig. 1(a)], many of the subsystems were left unchanged between the two modes of operation. No changes were made to the UFE or the N4 pump laser. The differences include switching from the COS to an alternate grism stretcher (GrS), operating at a reduced bandwidth, and bypassing the final amplifier (N5). This GrS accounts for the inversion of the idler spectral phase and allows for a standard grating compressor to be used to compress the idler (IGC). Angular dispersion was compensated with an angular dispersion compensator (ADC) prior to compression.

The design of the GrS is the result of compromise between a full compression of the pulse and optic manufacturing limitations.[11] Each grism is made from a 45°, N-SF57 prism mounted 1 mm away from a 1480-lp/mm gold grating. This design fully compensates for the two lowest orders of spectral phase (group-delay dispersion and third-order dispersion) but has some residual fourth-order dispersion. The stretcher also reduces bandwidth of OPAL to wavelengths that correspond those of interest for an RPA and a roof mirror double passes the pulse to a duration of 1 ns.

The idler exiting N4 is imaged with a 3× achromatic image relay onto two custom prisms to reduce angular dispersion from 123 μrad/nm to <0.5 μrad/nm. The idler is then compressed with a pair of parallel 1285-lp/mm gratings (PGL) and a roof mirror. Slant distance and input angle are selected to maximize peak power as measured with a custom IR-SPIDER (APE).[12] The compressed pulse was measured to have a full-width-half-maximum (FWHM) pulse duration of 120±10 fs (Fig. 2).

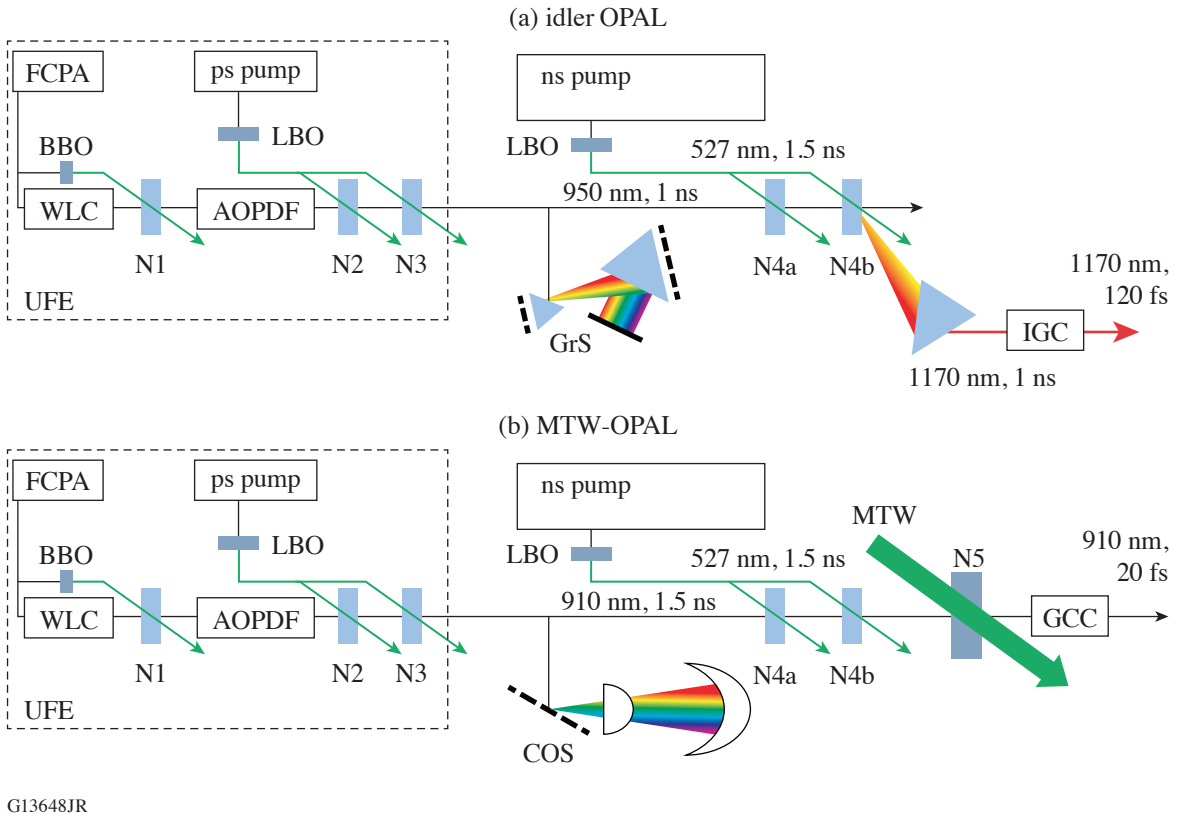

Figure 1

(a) A schematic of the idler OPAL and (b) standard MTW-OPAL configurations shows that they share many components including the UFE, the pre- and power amplifiers (N4a and N4b), and a nanosecond pump laser. (a) Systems added to operate the OPAL idler include an alternate grism stretcher (GrS), ADC, and an IGC. (b) The components of MTW-OPAL that are unused are the final amplifier, which is pumped by the MTW laser (N5), a COS, and grating compressor chamber (GCC). FCPA: fiber chirped pulse amplifier; WLC: white-light continuum; AOPDF: acoustic-optic-programable dispersive filter.

The focused and compressed idler had an average peak intensity of 5×10^{15} W/cm^2, which is about an order of magnitude lower than the transform-limited and diffraction-limited (TL-DL) intensity. The diffraction- and transform-limited intensity is based on the measured near-field beam profile and spectrum (row 1 in Table I). Reduction of this peak intensity is calculated from a subset of spatiotemporal effects: linear angular dispersion (AD), residual spectral phase, and monochromatic wavefront. Residual spectral phase was measured with the IR-SPIDER described above, while monochromatic wavefront was measured with a focal-spot diagnostic. This diagnostic was also used to measure residual angular dispersion by blocking all but two wavelengths in the GrS. How each of these spatiotemporal effects individually impact the achievable peak intensity is calculated in rows 2–4 in Table I. In the fifth row of Table I, all three spatiotemporal effects are applied.

Table I: Contributions to peak intensity.

	FWHM Pulse duration	Spot radii (μm)	AD$_x$,AD$_y$ (μrad/nm)	Intensity (W/cm^2)
TL-DL	50.2	19.6	0,0	56×10^{15}
Spectral phase	120	–		$14.1 \pm 0.8 \times 10^{15}$
Monochromatic wavefront	–	21.5 to 70		$18 \pm 3.7 \times 10^{15}$
Linear angular dispersion	–	–	<0.5, 0.5	35 to 56×10^{15}
Combined	120	21.5 to 70	<0.5, 0.5	$4.7 \pm 1 \times 10^{15}$

TL-DL: transform-limited; AD: angular dispersion

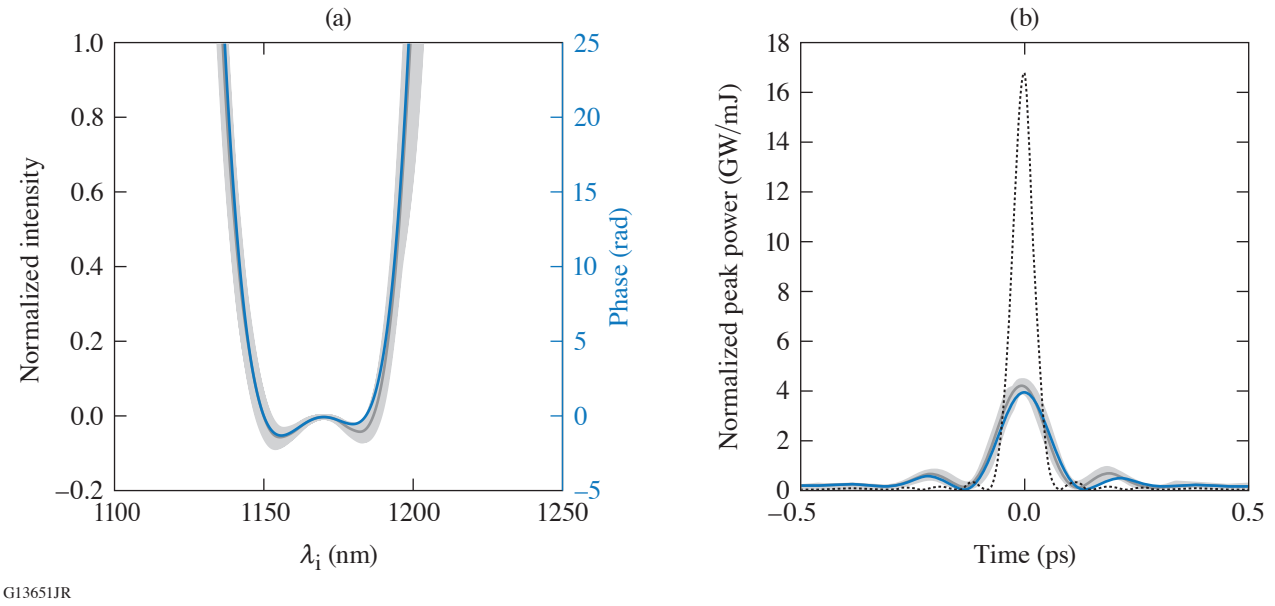

Figure 2
(a) The idler phase is measured over 100 shots by the IR-SPIDER and is denoted by the shaded area. The average phase and spectrum are shown by the solid gray and dotted curves, respectively, and closely matches the expected phase (blue curve). (b) The measured peak power is 4× lower than transform limited (black dotted curve), but matches the temporal pulse predicted by the design of the grism stretcher/grating compressor pair.

In conclusion, the compression of the idler to 100-GW peak powers from an existing OPCPA system has been demonstrated. While operating at a reduced peak intensity from the transform and diffraction limit, the idler from high-peak-power OPCPA systems achieves 100-GW pulses and provides a unique opportunity to further study the limits of laser technology.

This material is based upon the work supported by the Department of Energy Office of Science under Award No. DE-SC0016253, the Department of Energy National Nuclear Security Administration under Award No. DE-NA0003856, the University of Rochester, and the New York State Energy Research and Development Authority.

1. D. Strickland and G. Mourou, Opt. Commun. **56**, 219 (1985).
2. V. M. Malkin, G. Shvets, and N. J. Fisch, Phys. Rev. Lett. **82**, 4448 (1999).
3. J. H. Kelly *et al.*, J. Phys. IV France **133**, 75 (2006).
4. J. D. Sadler, "Optimisation and Applications of Raman Plasma Amplifiers," Ph.D. thesis, University of Oxford, 2017.
5. D. Haberberger *et al.*, Phys. Plasmas **28**, 062311 (2021).
6. A. Dubietis, G. Jonusauskas, and A. Piskarskas, Opt. Commun. **88**, 437 (1992).
7. J. Bromage *et al.*, High Power Laser Sci. Eng. **7**, e4 (2019).
8. J. Bromage *et al.*, High Power Laser Sci. Eng. **9**, e63 (2021).
9. T. Wilhelm, J. Piel, and E. Riedle, Opt. Lett. **22**, 1494 (1997).
10. I. N. Ross *et al.*, J. Opt. Soc. Am. B **19**, 2945 (2002).
11. S. Bucht *et al.*, J. Opt. Soc. Am. B **36**, 2325 (2019).
12. "APE Angewandte Physik & Elektronik GmbH," Ultrafast Laser Diagnostics & Tuneable Laser Solutions, Berlin, Germany.

Impact of Raman Scattering on Temporal Reflection from a Short Soliton

J. Zhang,[1] W. R. Donaldson,[2] and G. P. Agrawal[1]

[1]The Institute of Optics, University of Rochester
[2]Laborotary for Laser Energetics, University of Rochester

An optical pulse can be reflected at a temporal boundary across which the refractive index changes with time.[1] The reflected pulse is frequency shifted by an amount set by the law of momentum conservation. While a temporal boundary where the refractive index changes everywhere at the same time is hard to create in practice, reflection can also happen at a moving boundary. Such a boundary can be created through the optical Kerr effect by injecting an intense pump pulse into a dispersive nonlinear medium. This configuration has been studied in optical fibers when a weak pulse collides with an optical soliton.[2–4]

When a femtosecond soliton is formed inside an optical fiber, intrapulse Raman scattering between its different spectral components leads to a continuous red shift that decelerates the soliton as it propagates. This work considers the situation where a weak pulse reflects from such a decelerating soliton. It is shown that the reflected pulse can be much shorter than the input pulse, involving a new type of temporal focusing. The effect is explained using space–time duality and derive an approximate transformation law for Gaussian-shape input pulses.

Using the generalized nonlinear Schrödinger equation, the temporal reflection of a probe pulse from a soliton (called the pump pulse) is numerically simulated. Results are shown in Fig. 1 for a realistic set of parameters for silica fibers. In the time domain,

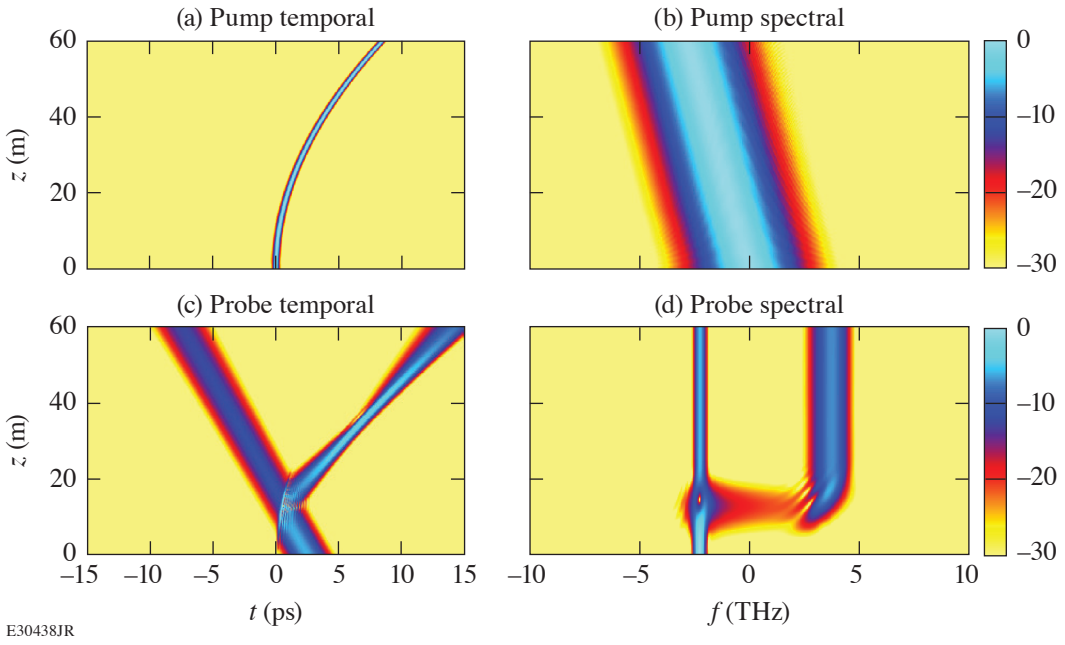

Figure 1
Simulation of temporal reflection of a probe pulse on a pump soliton. The pump soliton continuously red shifts because of Raman scattering.

the trajectory of the soliton has a parabolic shape because of its Raman-induced deceleration. When the probe pulse hits the pump pulse, it splits into a reflected pulse and a transmitted pulse.

The reflected pulse undergoes a frequency shift and its spectrum becomes broader than the incident spectrum. The reflected pulse also becomes narrower before it broadens again. This is an example of temporal focusing induced by the decelerating soliton. This effect can be explained using the concept of space–time duality.[5] The decelerating soliton forms a temporal boundary with a parabolic trajectory. A probe pulse reflected from this boundary is analogous to an optical beam being reflected by a parabolic-shaped mirror. It has been found that temporal focusing is more significant for longer incident pulses.

An approximate analytic theory has been developed that describes how the spectrum of an incident Gaussian pulse is modified when the pulse is reflected by a decelerating soliton. Figure 2 compares the analytical prediction with the numerical results. Both the reflected pulse spectrum and the rms pulse width of the reflected pulse agree well with the numerical simulations. The analytical approximation can be used to understand the temporal focusing effect.

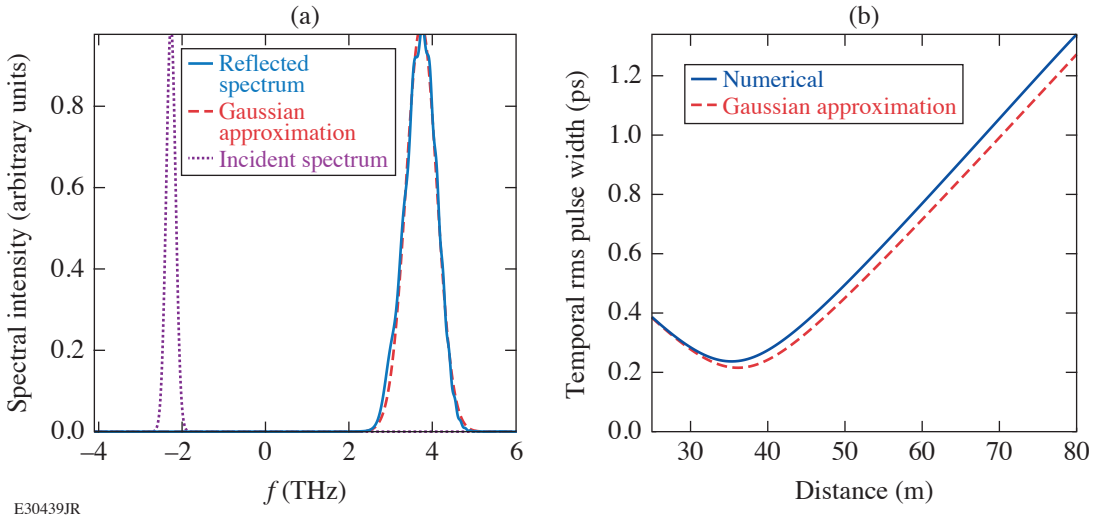

Figure 2
Comparison of analytical formula with numerical result. (a) Reflected pulse spectrum; (b) rms pulse width of a reflected pulse as it propagates.

This work is supported by National Science Foundation (ECCS-1933328). This material is based upon work supported by the Department of Energy National Nuclear Security Administration under Award Number DE-NA0003856, the University of Rochester, and the New York State Energy Research and Development Authority.

1. B. W. Plansinis, W. R. Donaldson, and G. P. Agrawal, Phys. Rev. Lett. **115**, 183901 (2015).
2. T. G. Philbin *et al.*, Science **319**, 1367 (2008).
3. K. E. Webb *et al.*, Nat. Commun. **5**, 4969 (2014).
4. L. Tartara, IEEE J. Quantum Electron. **48**, 1439 (2012).
5. B. H. Kolner, IEEE J. Quantum Electron. **30**, 1951 (1994).

A First-Principles Equation of State of CHON for Inertial Confinement Fusion Applications

S. Zhang,[1] V. V. Karasiev,[1] N. R Shaffer,[1] S. X. Hu,[1] D. Mihaylov,[1] K. Nichols,[1] R. Paul,[1] R. M. N. Goshadze,[1] M. Ghosh,[1] J. Hinz,[1] R. Epstein,[1] and S. Goedecker[2]

[1]Laboratory for Laser Energetics, University of Rochester
[2]Department of Physics, University of Basel, Switzerland

In laser-direct-drive (LDD) inertial confinement fusion (ICF) targets, a foam layer or ablator materials with radial density gradients can mitigate laser imprint and reduce hydrodynamic instabilities during ablation.[1,2] This can be realized by taking advantage of the two-photon polymerization (TPP) technique, which can precisely fabricate CHON polyacrylate resin into shell structures with superb lateral structure uniformity (to the level of 1 μm) (Ref. 3). To test the new ideas and optimize designs to improve target performance in relevant ICF and high-energy-density experiments, high-quality equations of state (EOS) of the target materials are required. In contrast to CH, however, which has been a widely used ablator material with relatively well understood EOS,[4–7] an EOS for CHON is still missing.

For this study, a wide-range (0 to 1044 g/cm^3 and 0 to 10^9 K) EOS table was constructed for a C-H-O-N quaternary compound ($C_{16}H_{27}O_6N_1$, stoichiometry that matches the resin material used in the laboratory for TPP printing) from first-principles simulations. The calculations combine two state-of-the-art approaches: Kohn–Sham density functional theory molecular dynamics (KS-DFT-MD) with an accurate meta-generalized gradient approximation (GGA)-level thermal exchange-correlation functional (T-SCAN-L) and orbital-free (OF) DFT-MD with lately developed Luo–Karasiev–Trickey γ Thomas–Fermi (LKTγTF) tunable noninteracting free-energy functionals. The thermal functional LKTγTF is constructed through a convex combination of LKT GGA[8] and Thomas–Fermi (TF)[9] functionals, where γ is determined for each density by matching the pressure from our OF-DFT-MD calculations at a high temperature (1 to 3×10^5 K) to the corresponding value from the KS-DFT-MD calculations; energies from OF-DFT-MD are uniformly shifted along each isochore to align with the KS-DFT-MD values at the matching temperature. This approach is similar but superior to previous EOS studies that stitch KS and OF but use TF functional in the OF calculations.[5,10,11] The first-principles EOS calculations are performed along 27 isochores (between 0.05 and 1044 g/cm^3) at 24 different temperatures (between 1000 and 10^9 K). The data have been extrapolated to lower densities and temperatures to produce a wide-range EOS table.

The EOS results show smooth bridging of KS and OF data at the matching condition. Figure 1 shows the EOS data approach the fully ionized ideal gas values in the limit of high temperatures (10^6 to 10^7 K, higher at higher densities). At lower temperatures, the energies and pressures for isochores of up to 4 to 7.5 g/cm^3 are below the ideal gas values because of the weaker ion and electron thermal contributions; for higher densities, the EOS increasingly exceeds the ideal gas values because of the increased degeneracy of electrons. The slope variations in the energy plots between different densities reflect changes in heat capacity; the differences between energy and pressure plots define the profile of the Grüneisen parameter. Both are caused by the joint effects of ion thermal vibration and electron thermal excitation.

Based on the calculated EOS, the predicted Hugoniot of CHON resin [Fig. 2(a)] shows a sharper profile and larger compression maximum by ~2% than that of pure CH polystyrene because of the coexistence of nitrogen and oxygen. Calculations of thermodynamic properties show overall consistency with that of CH along their respective Hugoniots [Figs. 2(b) and 2(c)]. Both exhibit a local minimum in heat capacity and maximum in the Grüneisen parameter at 2 to 3×10^4 K, which corresponds to

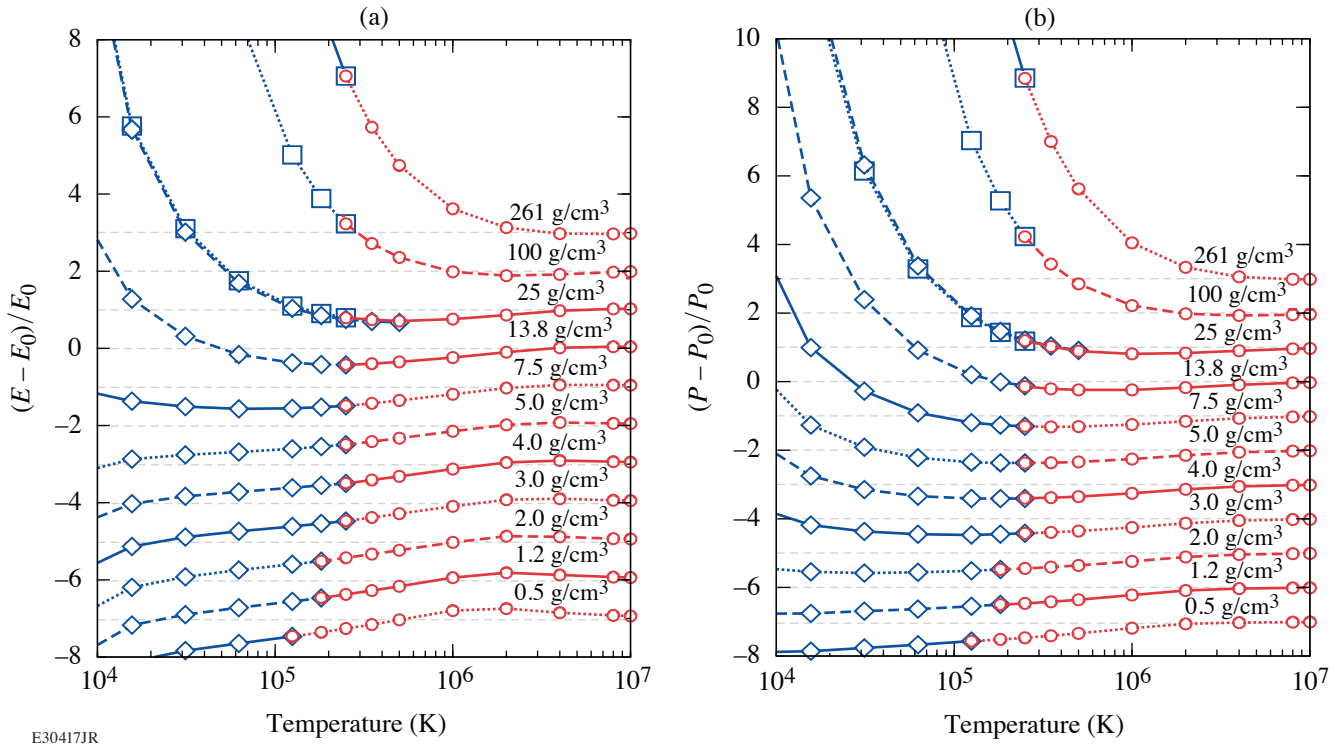

Figure 1
Matching KS (blue) and OF (red) (a) energies and (b) pressures along selected isochores. Data shown are relative to values of fully ionized ideal gas (denoted by E_0 and P_0 and shown with dashed gray horizontal lines). Blue diamonds and squares denote calculations using projector-augmented-wave and bare-coulomb potentials, respectively, which agree well with each other. Different isochores have been shifted apart for clarity.

bonded-to-atomic transition,[12] and a peak in heat capacity and a basin in the Grüneisen parameter at 10^6 K, corresponding to ionization of the K shell. The heat capacity and the Grüneisen parameters are found to reach the fully ionized ideal gas limit at 10^7 K. It is also found that the thermal expansion coefficient and the bulk sound velocity show independence of the isochore once the temperature exceeds 10^6 K.

To test the laser absorption and hydrodynamic efficiency of CHON resin as a potential ablator material for LDD targets, radiation-hydrodynamic simulations were performed of cryogenic DT implosion targets by using the 1-D radiation-hydrodynamics code *LILAC*.[13] The CHON results are compared with the conventional CH ablator. Results from the simulations show CHON outperforms CH as the ablator for LDD target designs (Fig. 3) due to a slight increase in the laser absorption fraction, which should further prompt the fabrication of the CHON shell with a foam layer for laser-imprint mitigation.

This material is based upon work supported by the Department of Energy National Nuclear Security Administration under Award Number DE-NA0003856, the University of Rochester, and the New York State Energy Research and Development Authority. V. V. Karasiev, D. I. Mihaylov, R. M. N. Goshadze, and S. X. Hu also acknowledge support by the U.S. NSF PHY Grant No. 1802964.

1. N. Metzler, A. L. Velikovich, and J. H. Gardner, Phys. Plasmas **6**, 3283 (1999).
2. S. X. Hu *et al.*, Phys. Plasmas **25**, 082710 (2018).
3. O. Stein *et al.*, Fusion Sci. Technol. **73**, 153 (2018)
4. M. A. Barrios *et al.*, Phys. Plasmas **17**, 056307 (2010).
5. S. X. Hu *et al.*, Phys. Rev. E **92**, 043104 (2015).
6. S. Zhang *et al.*, Phys. Rev. E **96**, 013204 (2017); S. Zhang *et al.*, J. Chem. Phys. **148**, 102318 (2018).

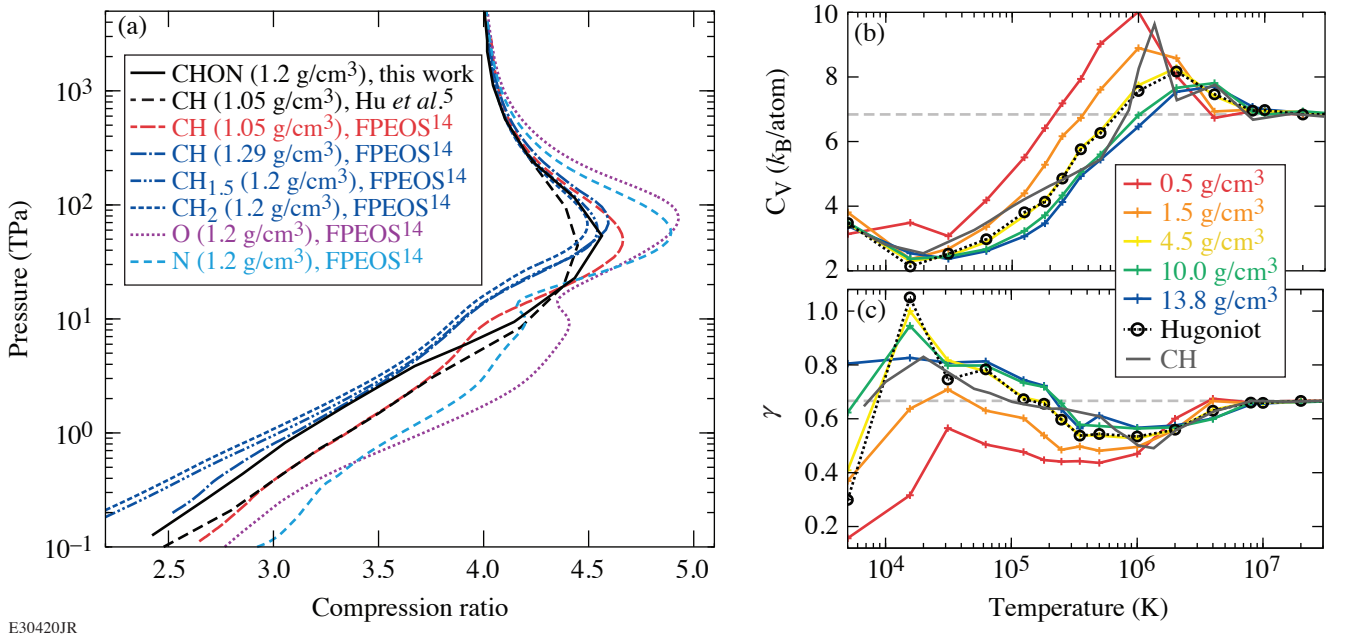

Figure 2
(a) Pressure-compression ratio Hugoniot, (b) heat capacity, and (c) Grüneisen parameter of CHON compared with that of CH. In (a), results of C–H compounds[5,6] and of O and N from first-principles EOS[14] are shown for comparison. In (b) and (c), the horizontal gray dashed lines denote the corresponding values of a fully ionized ideal gas.

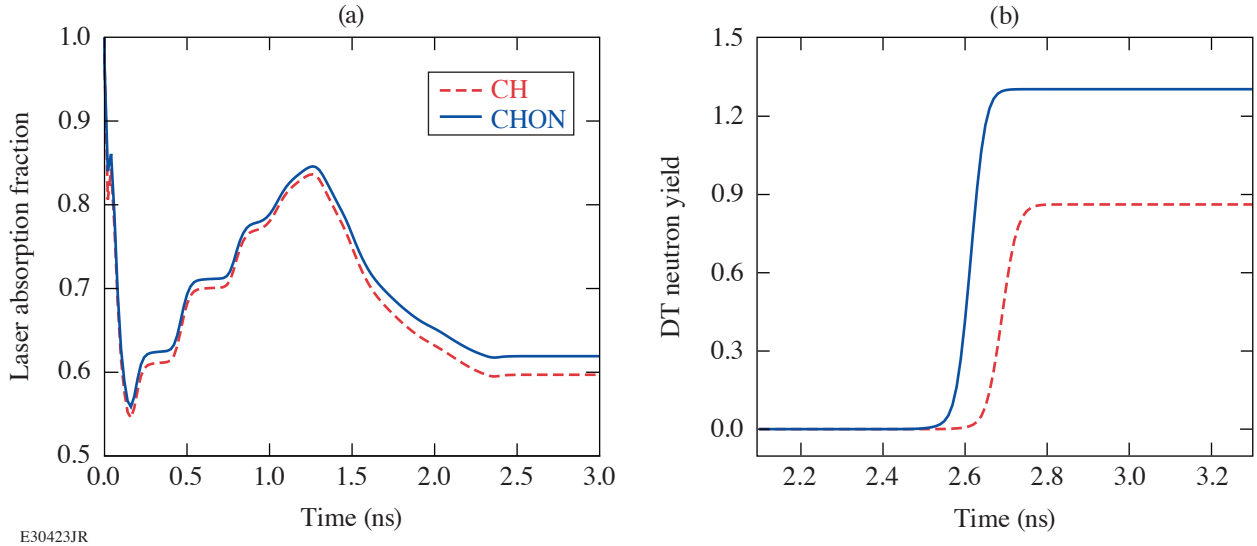

Figure 3
Comparison in (a) the time evolution of laser absorption fraction and (b) neutron yield at later time of the implosion when using targets with CH or CHON ablators. The simulations are based on a typical OMEGA-scale cryo-DT target with a 50-μm-thick DT-ice layer covered by 8-μm-thick CH ablator (ρ_0 = 1.05 g/cm^3) or 7-μm-thick CHON ablator (ρ_0 = 1.2 g/cm^3) to have equivalent target mass. The simulations employ the same laser pulse (total UV laser energy of ~27 kJ, shape optimized for the CH target assembly on OMEGA).

7. A. L. Kritcher *et al.*, Nature **584**, 51 (2020).
8. K. Luo, V. V. Karasiev, and S. B. Trickey, Phys. Rev. B **101**, 075116 (2020).
9. R. P. Feynman, N. Metropolis, and E. Teller, Phys. Rev. **75**, 1561 (1949).
10. S. X. Hu *et al.*, Phys. Rev. B **94**, 094109 (2016); Phys. Rev. E **95**, 043210 (2017).
11. Y. H. Ding and S. X. Hu, Phys. Plasmas **24**, 062702 (2017).
12. S. Zhang *et al.*, J. Appl. Phys. **131**, 071101 (2022).
13. J. Delettrez *et al.*, Phys. Rev. A **36**, 3926 (1987).
14. B. Militzer *et al.*, Phys. Rev. E **103**, 013203 (2021).

Shocked-Silica Aerogel Radiance Transition

B. J. Henderson,[1,2] J. R. Rygg,[1,2,3] M. C. Marshall,[1] M. K. Ginnane,[1] L. E. Hansen,[4] E. Davies,[5] P. M. Celliers,[5] and G. W. Collins[1,2,3]

[1]Laboratory for Laser Energetics, University of Rochester
[2]Department of Physics and Astronomy, University of Rochester
[3]Department of Mechanical Engineering, University of Rochester
[4]Sandia National Laboratories
[5]Lawrence Livermore National Laboratory

The objective of this work was to measure the radiance of shock fronts in SiO_2 aerogel at various initial densities. The optical properties of shock-compressed fused silica, quartz,[1] and stishovite[2] have been characterized and used as standards for temperature and reflectance measurements.[3] This work measures the optical radiant behavior of shock-compressed SiO_2 aerogel, which is expected to be significantly hotter, and thus brighter, at comparable shock pressures, than shock-compressed SiO_2 starting at solid density.[4,5] These measurements can be used to constrain radiative-hydrodynamics in inertial confinement fusion simulations of implosions using aerogel liners and to generate an optimally bright broadband source for high-energy-density–physics experiments.

Experiments were performed on the OMEGA EP Laser System. Targets were irradiated by one to four laser beams (λ = 351 nm) on a polystyrene (CH) ablator, producing strong shock waves that compress the planar samples. These experiments used laser irradiance between 10 and 200 TW/cm^2 produced by 2-, 2.5-, and 4-ns temporally square and ramp-top laser pulses with spatially uniform spot diameters of approximately 1100 or 1800 μm through the use of distributed phase plates. The targets were composed of a 40-μm CH ablator (refractive index n = 1.59 at λ = 532 nm, ρ_0 = 1.05 g/cm^3), a 50-μm quartz pusher (n = 1.547, ρ_0 = 2.65 g/cm^3), and a 250-μm SiO_2 aerogel sample (n = 1.02 to 1.06, ρ_0 = 0.1 to 0.3 g/cm^3). Shock velocity, reflectivity, and radiance were measured using a velocity interferometer for any reflector (VISAR) and a streaked optical pyrometer (SOP).

Brightness temperature of the shocked aerogel was determined by measuring the radiance of the shock front using the SOP. The SOP collects time- and spatially resolved thermal emission from the shock front integrated over wavelengths between 590 and 850 nm, with a peak efficiency at 600 nm. The SOP signal is converted to brightness temperature using an absolute calibration of the OMEGA EP SOP, which follows the procedure described in Ref. 6.

SiO_2 aerogel exhibits behavior that is starkly different from its higher-density counterparts (Fig. 1). Specifically, the exponent of the power law fit a is ~2 with no observed slope change for fused silica, quartz, and stishovite. For SiO_2 aerogel, a is 2 below the change in slope and ~1 above the change in slope. Below the change in slope observed in aerogel, the six T_{bright}–P curves for SiO_2 form a set of parallel lines. Some possible causes for this behavior include: (a) radiative precursor ahead of the shock, (b) a conductive precursor, and (c) shock propagation in aerogel microstructure.

This material was based upon work supported by the Department of Energy National Nuclear Security Administration under Award No. DE-NA0003856, the University of Rochester, and the New York State Energy Re-search and Development Authority. A portion of this work was performed under the auspices of NSF Physics Frontier Center Award No. PHY-2020249, and under the auspices of the U.S. Department of Energy by Lawrence Livermore National Laboratory under Contract No. DE-AC52-07NA27344.

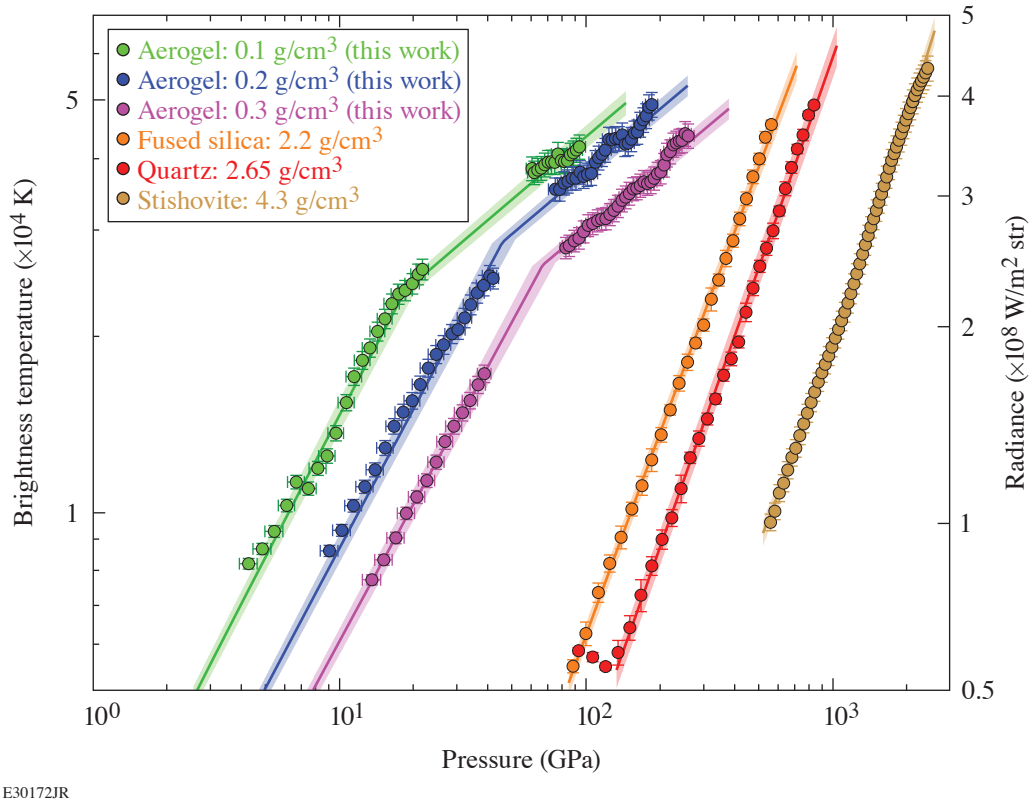

Figure 1
Brightness temperature (and integrated radiance in the 590- to 850-nm band) versus inferred pressure for shock compressed SiO_2 aerogel (green, blue, and pink circles) and their two-part power-law fits (green, blue, and pink curves). Shaded regions represent 1σ confidence intervals. Measurements of fused silica (orange circles),[1] quartz (red circles),[1] and stishovite (brown circles)[2] are fit with a single power-law function (orange, red, and brown curves).

1. D. G. Hicks *et al.*, Phys. Rev. Lett. **97**, 025502 (2006).
2. M. Millot *et al.*, Science **347**, 418 (2015).
3. S. Brygoo *et al.*, J. Appl. Phys. **118**, 195901 (2015).
4. J. C. Boettger, Los Alamos National Laboratory NM, New Mexico, Report LA-11488-MS (1989).
5. Ya. B. Zel'dovich and Yu. P. Raĭzer, in *Physics of Shock Waves and High-Temperature Hydrodynamic Phenomena*, edited by W. D. Hayes and R. F. Probstein (Academic Press, New York, 1966), Vol. I, Chap. II, pp. 107–175.
6. M. C. Gregor *et al.*, Rev. Sci. Instrum. **87**, 114903 (2016).

Shock-Induced Metallization of Polystyrene Along the Principal Hugoniot Investigated by Advanced Thermal Density Functionals

R. M. N. Goshadze, V. V. Karasiev, D. I. Mihaylov, and S. X. Hu

Laboratory for Laser Energetics, University of Rochester

Use of a recently developed thermal strongly constrained and appropriately normed Laplacian (T-SCAN-L)-dependent meta-generalized gradient approximation exchange correlation (XC) density functional[1] and thermal hybrid XC density functional (KDT0)[2] within the framework of density functional theory as implemented in Vienna *ab-initio* simulation package (VASP) to show that the inclusion of thermal and inhomogeneity effects is crucial for accurate prediction of structural evolution and corresponding insulator–metal transition (IMT) during shock compression. Optical reflectivity calculated as an indicator of IMT is in perfect accord with experimental data.[3] The discrepancy between experiment and *ab-initio* simulation results was reported several times during last decade.[4–6]

The equation of state (EOS) of shocked material just behind the shock front satisfies the Rankine–Hugoniot equation

$$E_1 - E_0 + \frac{1}{2}(P_1 + P_0)\left(\frac{1}{\rho_1} - \frac{1}{\rho_0}\right) = 0,$$

where the subscripts "0" and "1" stand for unshocked and shocked sides, respectively. The unshocked side of the ablator (CH) is in ambient conditions. At ambient conditions (T = 300 K and ρ = 1.055 g/cm^3), the pressure P_0 can be approximated by zero since it is orders of magnitude lower than the pressure at ~10^3 K. Based on the results from the *ab-initio* molecular dynamics (AIMD) calculations, E_0 is set to be –93 kJ/g.

Figure 1 shows the comparison between various experimental and theoretical studies of principal Hugoniot on the pressure–density plane. Both Perdew–Burke–Ernzerhof (PBE)[5] and T-SCAN-L AIMD calculations overestimate shock pressure compared

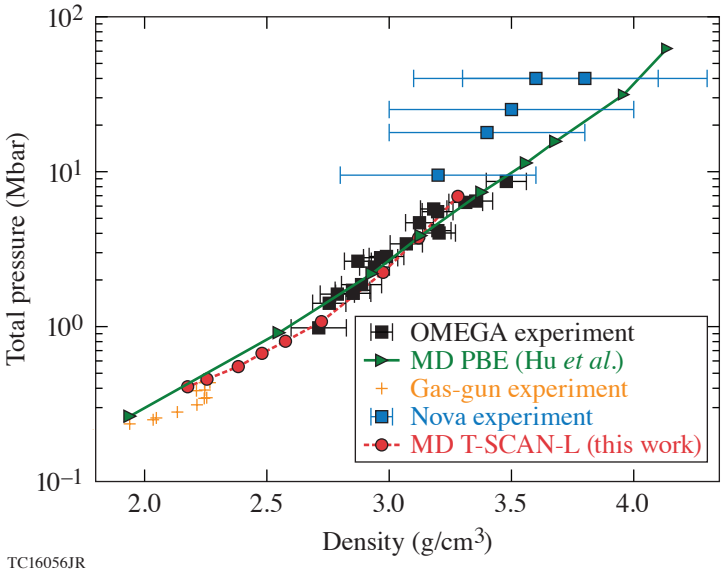

Figure 1
CH pressure as a function of density along the principal Hugoniot. The T-SCAN-L results are compared with PBE calculations by Hu *et al.*,[5] the Nova experiment,[7] gas-gun experiment,[8] and the OMEGA experiment[3] based on latest quartz EOS (black rectangles).

to a gas-gun[8] experiment below 1 Mbar. In the mid-pressure range (1 to 10 Mbar), T-SCAN-L shows concave behavior opposing more-linear PBE results. Apart from using a higher-rung XC functional with explicit temperature dependence, this change might also be associated with the proper treatment of structural characteristics of shocked CH. We carefully run structural relaxation until no structure remains, observing melting/dissociation exactly at these mid-range pressures.

Optical calculations are performed within the Kubo–Greenwood formalism, obtaining CH reflectivity by averaging the uncorrelated snapshots of ionic configurations from the AIMD simulations. The details of the process can be found in Ref. 5. A comparison of the results from the calculations with the OMEGA experiment and PBE-based AIMD study[5] is shown in Fig. 2. Note that the reflectivity turn-on point is shifted to higher pressures and the jump is much sharper, making it in perfect agreement with the OMEGA experiment. By separately plotting the results obtained by T-SCAN-L and KDT0 on top of the T-SCAN-L–generated ionic configurations in Fig. 2, we demonstrate that the improved results are the consequence of not only accurate ionic configurations, but also accurate electronic structure calculations. There are several factors that contribute to this enhancement. Foremost, our PBE calculations show that it underestimates the drop in density of states (DOS) as compared to T-SCAN-L at exactly the same conditions as shown in Fig. 3, which shows a comparison of DOS in the temperature range from 3500 to 5000 K along the principal Hugoniot. The second aspect is the shift in Hugoniot data. At lower densities, T-SCAN-L gives lower Hugoniot pressures compared to PBE calculations. As a result, the Hugoniot points at a fixed density predicted by T-SCAN-L have much less molecular dissociation and consequently exhibit a deeper drop in DOS, leading to smaller reflectivity.

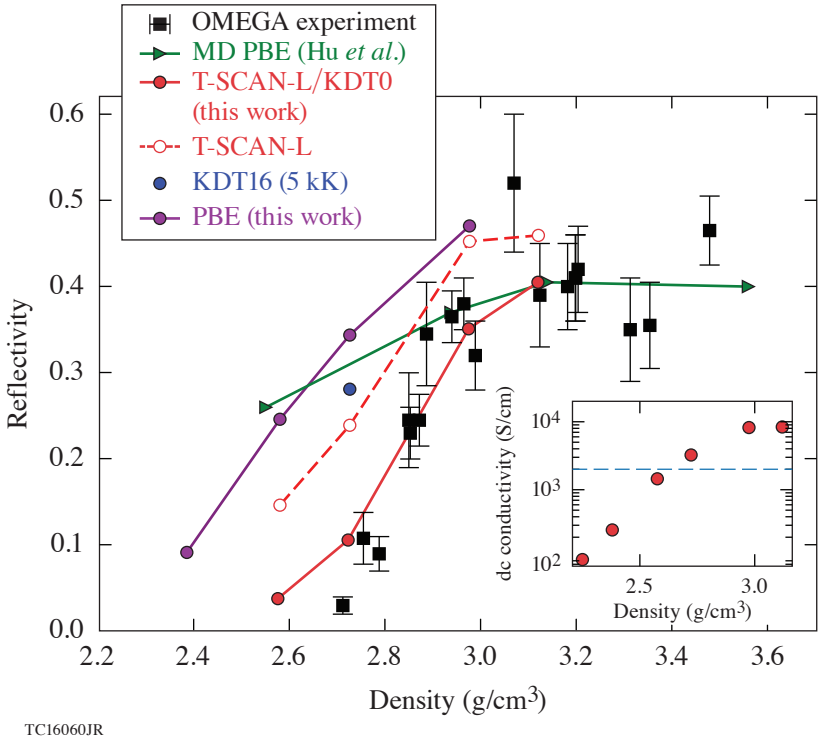

Figure 2
Reflectivity of shocked CH along the principal Hugoniot at 532-nm VISAR (velocity interferometer system for any reflection) light.

This material is based upon work supported by the Department of Energy National Nuclear Security Administration under Award Number DE-NA0003856 and US National Science Foundation PHY Grant No. 1802964.

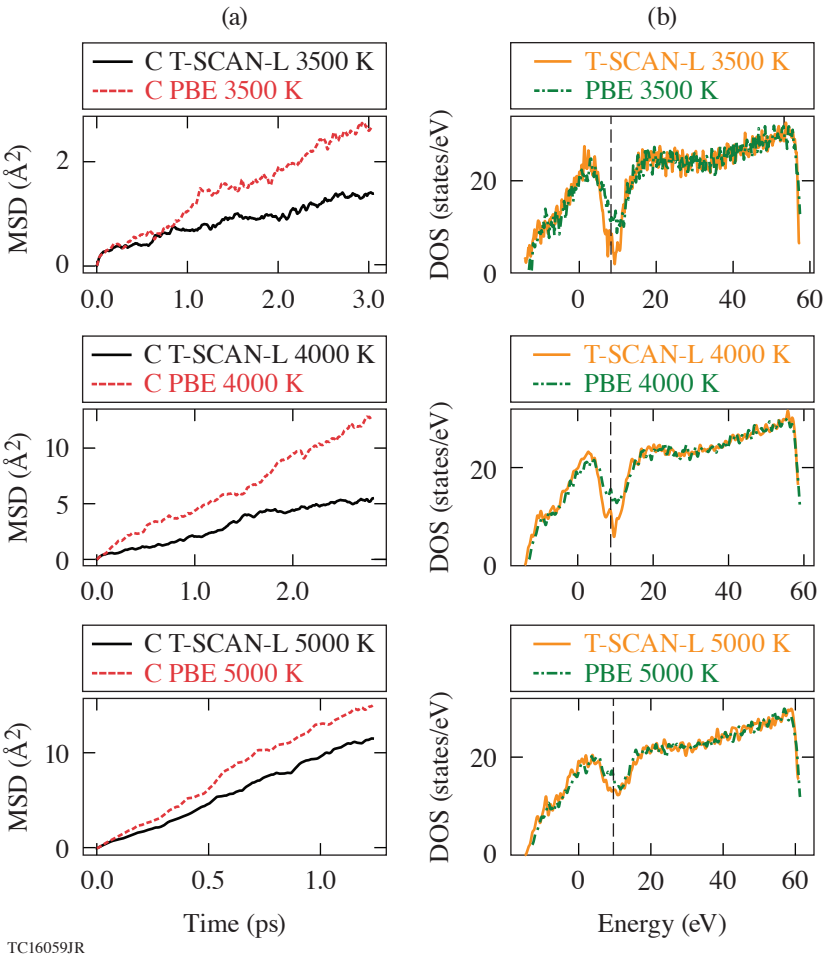

Figure 3
(a) Comparison of mean square displacement predicted by PBE versus TSCAN-L XC functionals and (b) comparison of corresponding DOS in the temperature range of 3500 to 5000 K. MSD: mean squared displacement.

1. V. V. Karasiev, D. I. Mihaylov, and S. X. Hu, Phys. Rev. Lett. **105**, L081109 (2022).
2. D. I. Mihaylov, V. V. Karasiev, and S. X. Hu, Phys. Rev. B **101**, 245141 (2020).
3. M. A. Barrios *et al.*, Phys. Plasmas **17**, 056307 (2010).
4. C. Wang, X.-T. He, and P. Zhang, Phys. Plasmas **18**, 082707 (2011).
5. S. X. Hu, T. R. Boehly, and L. A. Collins, Phys. Rev. E **89**, 063104 (2014).
6. N. J. Hartley *et al.*, Matter Radiat. Extremes **5**, 028401 (2020).
7. R. Cauble *et al.*, Phys. Plasmas **4**, 1857 (1997).
8. S. P. Marsh, ed. LASL Shock Hugoniot Data, Los Alamos Series on Dynamic Material Properties (University of California, Berkeley, CA, 1980).

The 13th Omega Laser Facility Users Group Hybrid Workshop

J. A. Frenje,[1] S. Ali,[2] E. Merritt,[3] K. Falk,[4] S. Finnegan,[3] M. Gatu Johnson,[1] J. P. Knauer,[5] M. P. Valdivia,[6] and L. Willingale

[1]Massachusetts Institute of Technology
[2]Lawrence Livermore National Laboratory
[3]Los Alamos National Laboratory
[4]Helmholtz-Zentrum Dresden-Rossendorf, Germany
[5]Laboratory for Laser Energetics, University of Rochester
[6]University of California, San Diego
[7]University of Michigan

Overview

On 27–29 April 2022, 158 researchers from more than 40 universities and laboratories and 13 countries gathered at LLE for the 13th Omega Laser Facility Users Group (OLUG) Hybrid Workshop (Fig. 1). Of these researchers, 103 had registered to attend the workshop in person and 55 had registered to attend the workshop virtually. The main goal of the three-day workshop was to facilitate a continuing dialog among the Omega users, the users and LLE management, and the users and the broader scientific community along with providing an opportunity for students and postdoctoral fellows to present their research at LLE in an interactive and informal atmosphere. What makes the annual OLUG Workshop unique is that it brings users together from all over the world, facilitating a vibrant dialog among them about their experiences running experiments at Omega, as can be seen in photographs shown in this summary.

U2877JR

Figure 1
In-person attendees at the 13th OLUG Hybrid Workshop.

A major part of OLUG's responsibility is to enhance the Omega Laser Facility and its capabilities by defining a set of Findings and Recommendations (F&R's) each year. In this year's workshop, the F&R discussions were stimulating and lively. As shown at the end of this report, 25 F&R's were defined and grouped into several categories. LLE management use these F&R's as a guide for making decisions about the Omega Laser Facility operations, priorities, and future changes.

The workshop included five science talks given by leading world authorities that described the breadth and excitement of high-energy-density (HED) science undertaken at Omega and other facilities in U.S. Two facility talks about the future of Omega proved especially enlightening to the OLUG participants. The workshop attendees also had a chance to hear the National Nuclear Security Administration's (NNSA's) and National Science Foundation's (NSF's) perspectives on the research conducted at Omega and how it fits into their national programs. A summary of this year's OLUG Executive Committee (ExCom) election was also presented. Another workshop highlight was the evening tutorial session given by LLE, in which the gas-jet platform, the MIFEDS (magneto-inertial fusion electrical discharge system) experimental platform, and as the *PlasmaPy* and *Fiducia* open-source codes were presented.

A student/postdoctoral-panel discussion was held to focus on their experiences at Omega and present their thoughts and recommendations on facility improvements. Several discussions were sparked by this forum, which resulted in the student/postdoctoral report summarized at the end of this summary. Another important event was the discussion on careers in HED science, which brought students together with potential future employers.

A total of 51 students and postdoctoral fellows (Fig. 2), 36 of whom were supported by travel grants from NNSA, attended the workshop and presented three sessions of posters. The presentations involved a large range of topics including target fabrication, inertial confinement fusion (ICF) experiments and simulations, and laboratory astrophysics, all of which generated spirited discussions, probing questions, and many suggestions. An award ceremony for the best student and postdoc posters was also held.

U2878JR

Figure 2
A total of 51 students and postdoctoral fellows attended the workshop and made engaging poster presentations.

The Workshop Presentations

A wide-ranging series of presentations and posters were presented during the workshop. The invited presentations covered facility, government, and science. The science talks focused on several interesting topics, including high-energy-density plasmas, laboratory astrophysics, and burning plasmas in ICF. Two facility talks—"The Renewal of the Five-Year LLE Cooperative Agreement" by Acting LLE Director Dr. Chris Deeney and "The LLE Sustainment Plan" by Omega Laser Facility Division Director Mr. Samuel Morse—presented important details on the status, performance, and path forward of the Omega Laser Facility. Mr. Morse also gave an enlightening talk on the "OMEGA Facility Update and Progress on OLUG Recommendations." Dr. Sarah Nelson, Acting Director of the NNSA Office of Experimental Sciences, presented an excellent perspective on the importance of the Omega facility within her program, and Dr. Slava Lukin, the Director for Plasma Physics at NSF, provided an informative overview of his program and the importance of training and educating the next-generation scientist in the area of plasma physics. In addition to the invited presentations, 63 contributed posters, presented in three sessions, covered a wide spectrum of work at Omega including target fabrication, ICF experiments, diagnostics, HED-plasma theory and simulations, laboratory astrophysics, material science, and laser–plasma interactions along with diversity, equity, and inclusion. Out of these posters, 51 were presented by graduate students, postdocs, and undergraduate students. These poster sessions offered ample opportunities for informal discussions about Omega experiments and their connections to work at other facilities. A set of four exciting facility talks were also given by LLE in an evening tutorial session. Figures 3–8 provide a representative sampling of the workshop's presentations and ambience.

Figure 3
In the plenary sessions, authorities spoke about science opportunities, government perspectives, and the evolving capabilities of the Omega Laser Facility to enable new science frontiers. (a) Dr. Chris Deeney, the Acting LLE Director, kicked off the workshop with a perspective on the renewal of the five-year LLE Cooperative Agreement; (b) Prof. Petros Tzeferacos of the University of Rochester (UR) gave an inspiring presentation on the Flash Center for Computational Science at the UR, and (c) Dr. Sarah Nelson, the Acting Director of the NNSA Office of Experimental Sciences, provided a bigger-picture perspective on the importance of the Omega Laser Facility within her program.

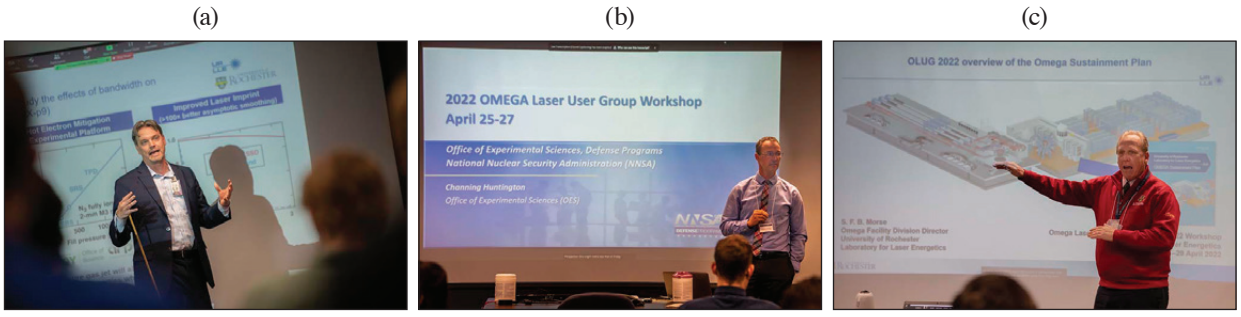

Figure 4
(a) UR Prof. Dustin Froula gave an exciting talk on the science that can be done on the Fourth-Generation Laser for Ultra-broadband eXperiments (FLUX); (b) Dr. Channing Huntington provided a wonderful personal account on his journey from a graduate student at University of Michigan (UM), conducting experiments at Omega, to working at the NNSA Office of Experimental Sciences; and (c) Samuel Morse (LLE) discussed the Omega sustainment plan, which is critical to the future of the laboratory and to the OLUG community. Mr. Morse's extensive knowledge of the facility is invaluable to those planning Omega experiments.

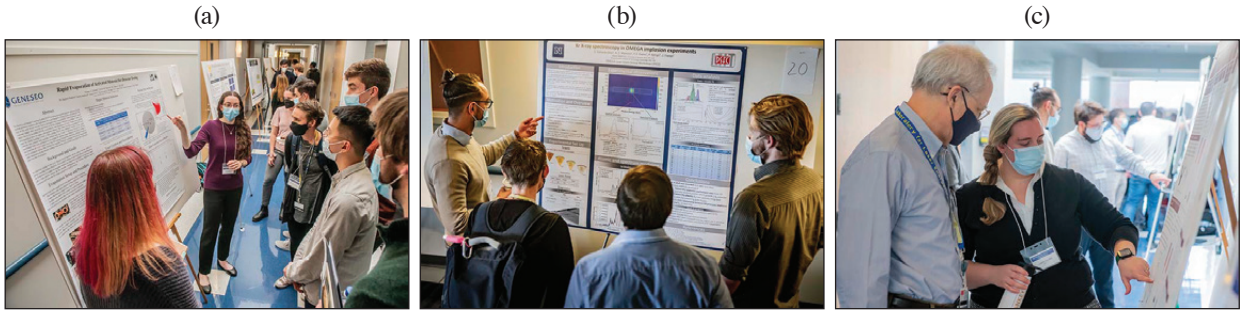

Figure 5
Sixty-three posters were presented in three sessions on a wide spectrum of work at Omega. Out of these posters, 51 were presented by graduate students, postdocs, and undergraduate students. In an interactive yet informal setting, these poster sessions provided opportunities for students and young researchers to present their research from Omega experiments and their connections to work at other facilities. (a) Undergraduate students Vizma Leimanis and Jessica Dawson [State University of New York (SUNY) Geneseo] discussed their work on "Rapid Evaporation of Activated Material for Detector Testing" with OLUG ExCom member Dr. Maria Gatu Johnson (MIT) and other students; (b) graduate student Enac Gallardo-Villaseca (University of Nevada, Reno) presented his work on "Krypton X-Ray Spectroscopy in OMEGA Implosion Experiments;" and (c) graduate student Camille Samulski (Virginia Tech) discusses her poster with LLE Senior Scientist Dr. Reuben Epstein on "Single-Feature Perturbation Seeded Rayleigh–Taylor Instability Studied in Planar Geometry."

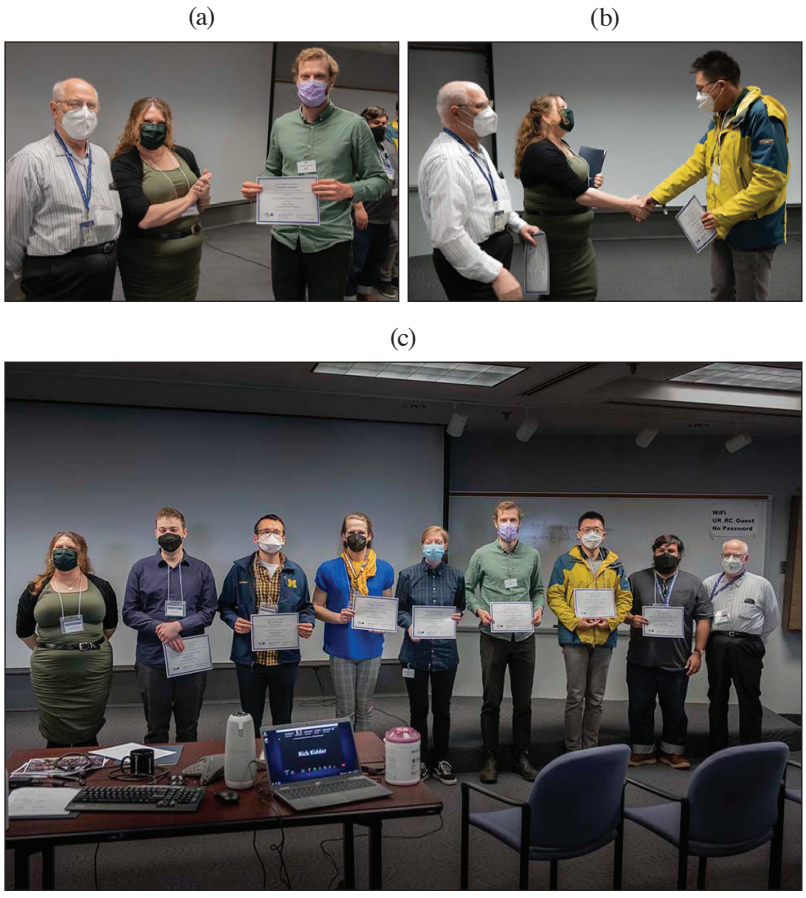

Figure 6
An award ceremony chaired by Drs. Liz Merritt and Jim Knauer was held for the best student and postdoctoral posters. (a) Graeme Sutcliffe (MIT) won the graduate student category; (b) Shu Zhang (Princeton) won the postdoctoral category. (c) Dr. Liz Merritt, Cameron Frank (graduate student at the University of Delaware), Michael Wadas [graduate student at UM (University of Michigan)], Abigail Armstrong (graduate student at UR), Skylar Dannhoff (graduate student at MIT), Graeme Sutcliffe (graduate student at MIT), Shu Zhang (postdoc at Princeton), Neel Kabadi (postdoc at MIT), and Dr. Jim Knauer. Not shown in the picture are Justin Kunimune (graduate student at MIT), Adam Brown (Houghton College) who won the undergraduate student category, and Jovahn Roumell (undergraduate student at SUNY Geneseo).

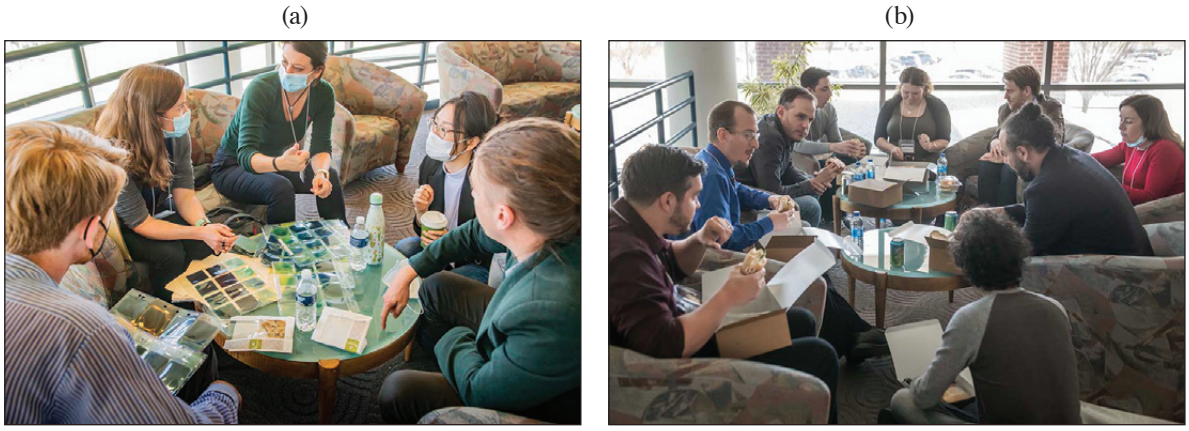

U2883JR

Figure 7
Productive discussions among researchers from around the world occurred in several informal settings.

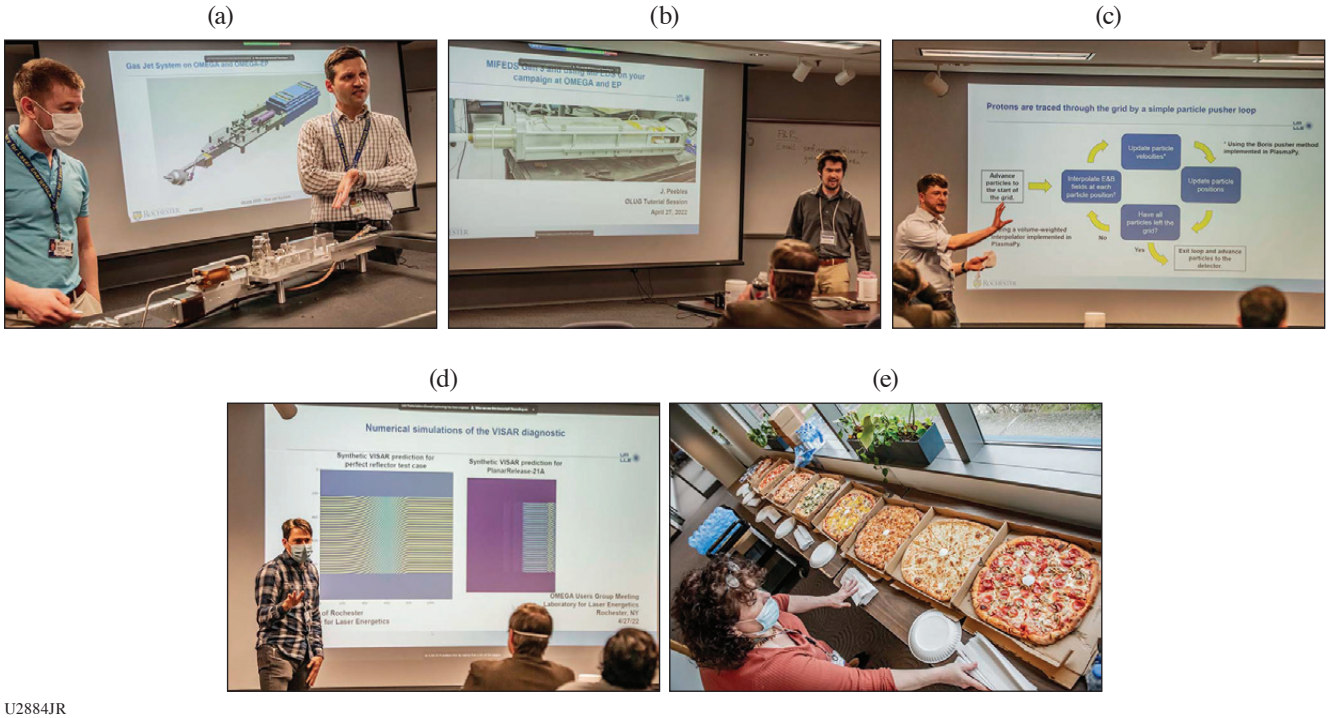

U2884JR

Figure 8
An evening tutorial session given by LLE highly regarded by the OLUG workshop participants. (a) Dr. Steven Ivancic and Tim Filkins discussed the "Gas-Jet System on OMEGA and OMEGA EP," which helped the external users get a better idea of what can be done with the system; (b) Dr. Jonathan Peebles gave an informative presentation on the "MIFEDS Generation-3 and Using It on Users' Experimental Campaign on OMEGA and OMEGA EP;" (c) Dr. Peter Heuer gave an inspiring talk on the "*PlasmaPy* Open-Source Code," which truly engaged the younger audience; (d) Dr. Daniel Barnak presented "*Fiducia* Open-Source Code and Analysis Software for the Dante-Diagnostic Data;" and (e) Mrs. Kim Truebger arranged for pizza to be served during the evening's tutorial session.

U2885JR

Figure 9
The student/postdoctoral panel presented important insights from young researchers working at the Omega facility. (a) Suzanne Ali (LLNL), not shown, Heath LeFevre (UM), Ellie Tubman (LLNL), Gabriel Perez-Callejo (University of Valladolid, Spain), and Brandon Russel (UM) led the discussion. (b) Graduate student Hongmei Tang (UM) brought her thoughts and recommendations.

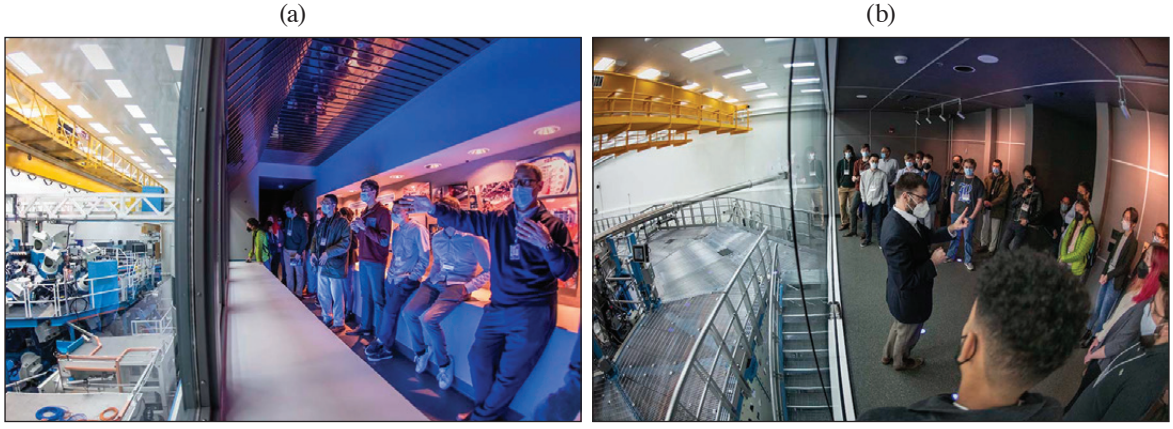

U2886JR

Figure 10
Mark Labuzeta and David Canning led tours of OMEGA and OMEGA EP, respectively. For many of the younger researchers, this was a great opportunity to learn about the facilities.

Summary of Findings and Recommendations

A big part of OLUG's responsibility is to enhance the Omega facility and its capabilities by defining a set of F&R's each year. Drs. Maria Gatu Johnson (MIT) and Sean Finnegan [Los Alamos National Laboratory (LANL)] led this year's F&R session, As shown below, 25 F&R's were defined and grouped into several categories at this workshop, i.e., general (1), documentation (2), calibration (3), diagnostics (4–15), target capability (16–18), laser systems (19–22), and data management (23–25). The LLE management is using these F&R's as a guide for making decisions about the operations of the Omega Laser Facility, priorities, and future changes. An update on the implementation of these F&R's will be presented by the LLE management at the OLUG satellite meeting on 18 October 2022 at the American Physical Society Division of Plasma Physics (APS-DPP) Conference in Spokane, WA.

1. Add equipment for improved hybrid workshop execution.
2. Ensure that users have access to detailed up-to-date documentation on diagnostics.
3. Make calibration data readily available on the PI portal.

4. Add a third VISAR (velocity interferometer system for any reflector) leg on the active shock breakout (ASBO) diagnostic on OMEGA EP and/or OMEGA.
5. Increase VISAR etalon support thickness for improved ASBO resolution.
6. Add a timing fiducial to Dante, noted in the Sustainment Plan (requires modern digitizers).
7. Add an optical Thomson-scattering diagnostic to OMEGA EP (multiple submissions).
8. Add the capability to infer directional flow vector on D_2 gas-filled or low-DT yield implosions.
9. Add the capability for neutron time-of-flight detectors to measure secondary DT-neutron spectra.
10. Reduce min/max camera timing jitter.
11. Improve Dante maintenance and documentation.
12. Create the ability to run streaked x-ray diagnostics with a gas jet.
13. Add gated spatially resolved x-ray spectroscopy.
14. Provide an additional Target Positioning System, more (mini) ten-inch manipulators (TIM's) and/or nuclear diagnostic inserters for OMEGA.
15. Add a diagnostic for forward-scattered light on OMEGA EP.
16. Characterize gas-jet nozzles (a TIM lab nozzle characterization test bench is now available to users).
17. Provide planar cryo on OMEGA EP.
18. Enable the ability to change MIFEDS leads on shot day
19. Increase UV power on OMEGA EP.
20. Enable 20-ns pulse duration on OMEGA EP.
21. Increase the quantity of tight-focus circular super-Gaussian distributed phase plates.
22. Extend backlighter beam delay.
23. Update HDF5 and utilize standard meta-data formats (multiple submissions).
24. Enable instant analysis of data on shot day.
25. Develop more open-source analysis software.

Findings and Recommendations from the Student/Postdoctoral Panel

Every year at the OLUG Workshop, a group of early career scientists, mainly students and postdocs, lead a discussion with the community on topics relevant to young researchers, including issues specific to the pandemic effects on early career scientists, the organization of the OLUG Workshop, and recommendations for the facility. Suzanne Ali [Lawrence Livermore National Laboratory (LLNL)] and Heath LeFevre (UM) led the discussion together with Ellie Tubman (LLNL), Gabriel Perez-Callejo (University of Valladolid, Spain), and Brandon Russel (UM). From these discussions, the following F&R were identified:

1. Develop a better framework for mentorship and guidance for early career scientists.
2. Facilitate cross-institution mentorship, matching up new researchers doing work at Omega with more-experienced mentors.
3. Form something like a journal club for topics related to experimental planning and analysis (monthly or biweekly, with a pre-meeting poll on the discussion topic).
4. Improve and modernize the web-based resources available to users.
5. Continue to improve documentation for diagnostic systems and targets.
6. Better advertise the existing online forum. A Microsoft Teams channel (or similar) is recommended specifically for users to ask questions to other users.
7. Record tutorials for some of the online resources for data access.
8. Enable access to calibration information for diagnostics via an online database.

Nominations and Election of Members for the OLUG ExCom

An OLUG ExCom election was held this year to elect three new members. A nominating committee was formed in November 2021 to request January nominations for the February 2022 election. Pia Valdivia [Chair, University of California, San Diego (UCSD), Hui Chen (LLNL), and Lan Gao (Princeton Plasma Physics Laboratory) formed the election committee. From a three-candidate ballot, Derek Schaeffer (Princeton) was elected as university representative to replace Maria Gatu Johnson (MIT); Verena Geppert-Kleinrath (LANL) was elected as national lab representative to replace Liz Merritt (LANL); and Heath LeFevre

(UM) was elected as the junior representative to replace Suzanne Ali (LLNL). In addition, Jim Knauer stepped down as the LLE ex-officio after 13 years of service. Jessica Shaw is the new LLE ex-officio.

For the May 2022–April 2023 period, the OLUG ExCom members are (a) four from U.S. university/small business: Johan Frenje (MIT, Chair), Maria-Pia Valdivia (UCSD, Vice Chair), Derek Schaeffer (Princeton), and Louise Willingale (UM); (b) three from national laboratory/major business: Verena Geppert-Kleinrath (LANL), Sean Finnegan (LANL), and Alison Saunders (LLNL); (c) one non-U.S. researcher: Katerina Falk [Helmholtz-Zentrum Dresden-Rossendorf (HZDM), Germany); (d) one from the junior researcher list: Heath LeFevre (UM); and (e) LLE ex-officio: Jessica Shaw. The OLUG ExCom thanks Maria Gatu Johnson, Liz Merritt, Suzanne Ali, and Jim Knauer for their service and excellent work making OLUG such a vibrant community.

U2887JR

Figure 11
Dr. Pia Valdivia (UCSD) presented the results from the 2022 OLUG ExCom elections.

(a)

(b)

(c)

(d)

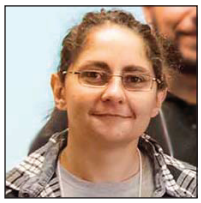

U2888JR

Figure 12
Members of the 2022 OLUG ExCom. (a) Back row (left to right): Jim Knauer (LLE), Liz Merrit (LANL), Katerina Falk (HZDR), Sean Finnegan (LANL), and Pia Valdivia (UCSD). Front row (left to right): Johan Frenje (MIT) and Maria Gatu Johnson (MIT); (b) Alison Saunders (LLNL); (c) Louise Willingale (UM); and (d) Suzanne Ali (LLNL) attended the workshop virtually.

Conclusions and Future Workshops

This OLUG Workshop, with 158 attendees, was part of a process that will keep members of the community involved in conversations and collaborations with each other and with the Omega Laser Facility. In addition, OLUG ExCom members and LLE management have an ongoing dialog to assess progress, compatibility with facility resources, and impact toward the implementation of the F&R's. An update on the implementation of these F&R's will be presented by the LLE management at the OLUG satellite meeting on 18 October 2022 at the APS-DPP Conference in Spokane, WA, and in depth at the 2023 OLUG Workshop.

Acknowledgment

This OLUG workshop was made possible in part by LLE at the University of Rochester for the use and availability of critical resources and support. In addition, OLUG thanks the LLE management for their exceptional responsiveness to our F&R's. For capturing the ambience and spirit of the workshop through his camera lens, we thank Eugene Kowaluk. To NNSA, we gratefully acknowledge the financial assistance for student/postdoctoral travel expenses. We also thank Kim Truebger for her incredible work setting up and executing the workshop.

FY22 Q3 Laser Facility Report

J. Puth, M. Labuzeta, D. Canning, and R. T. Janezic

Laboratory for Laser Energetics, University of Rochester

During the third quarter of FY22, the Omega Facility conducted 337 target shots on OMEGA and 242 target shots on OMEGA EP for a total of 579 target shots (see Tables I and II). OMEGA averaged 10.5 target shots per operating day, averaging 94.9% Availability and 94.7% Experimental Effectiveness. OMEGA EP averaged 8.3 target shots per operating day, averaging 95.4% Availability and 98.8% Experimental Effectiveness.

Table I: OMEGA Laser System target shot summary for Q3 FY22.

Program	Laboratory	Planned Number of Target Shots	Actual Number of Target Shots
ICF	LLE	66	61
	LANL	11	11
	LLNL	16.5	17
	SNL	5.5	6
ICF Subtotal		99	95
HED	LLE	33	38
	LANL	22	22
	LLNL	27.5	31
	SNL	11	12
HED Subtotal		93.5	103
LBS	LLNL	22	24
LBS Subtotal		22	24
NLUF		60.5	67
CEA		5.5	6
APL		11	12
CMAP		11	8
Calibration	LLE	0	22
Grand Total		302.5	337

APL: Applied Physics Labs (Johns Hopkins University)
CEA: Commissariat à l'énergie atomique aux énergies alternatives
CMAP: Center for Matter at Atomic Pressures
NLUF: National Laser Users Facility

Table II: OMEGA EP Laser System target shot summary for Q3 FY22.

Program	Laboratory	Planned Number of Target Shots	Actual Number of Target Shots
ICF	LLE	35	49
	LLNL	7	7
	SNL	7	6
ICF Subtotal		49	62
HED	LLE	14	17
	LANL	14	22
	LLNL	49	68
	SNL	7	10
HED Subtotal		84	117
CMAP		7	11
LaserNetUS		7	9
NLUF		28	25
Calibration	LLE	0	18
Grand Total		175	242

Publications and Conference Presentations

Publications

N. Acharya, H. Aluie, and J. K. Shang, "Numerical Investigation of Laser-Driven Shock Interaction with a Deformable Particle," Phys. Plasmas **29**, 052302 (2022).

S.-W. Bahk, I. A. Begishev, R. Roides, C. Mileham, R. Cuffney, C. Feng, B. M. Webb, C. Jeon, M. Spilatro, S. Bucht, C. Dorrer, and J. Bromage, "Effect of the Pump Beam Profile and Wavefront on the Amplified Signal Wavefront in Optical Parametric Amplifiers," Opt. Express **30**, 12,995 (2022).

A. Bose, J. Peebles, C. A. Walsh, J. A. Frenje, N. V. Kabadi, P. J. Adrian, G. D. Sutcliffe, M. Gatu Johnson, C. A. Frank, J. R. Davies, R. Betti, V. Yu. Glebov, F. J. Marshall, S. P. Regan, C. Stoeckl, E. M. Campbell, H. Sio, J. Moody, A. Crilly, B. D. Appelbe, J. P. Chittenden, S. Atzeni, F. Barbato, A. Forte, C. K. Li, F. H. Séguin, and R. D. Petrasso, "Effect of Strongly Magnetized Electrons and Ions on Heat Flow and Symmetry of Inertial Fusion Implosions," Phys. Rev. Lett. **128**, 195002 (2022).

A. F. A. Bott, L. Chen, P. Tzeferacos, C. A. J. Palmer, A. R. Bell, R. Bingham, A. Birkel, D. H. Froula, J. Katz, M. W. Kunz, C.-K. Li, H.-S. Park, R. Petrasso, J. S. Ross, B. Reville, D. Ryu, F. H. Séguin, T. G. White, A. A. Schekochihin, D. Q. Lamb, and G. Gregori, "Insensitivity of a Turbulent Laser-Plasma Dynamo to Initial Conditions," Matter Radiat. Extremes **7**, 046901 (2022).

S. J. Burns, J. R. Rygg, D. Polsin, B. Henderson, M. Marshall, S. Zhang, S. X. Hu, and G. Collins, "Planar, Longitudinal, Compressive Waves in Solids: Thermodynamics and Uniaxial Strain Restrictions," J. Appl. Phys. **131**, 215904 (2022).

D. A. Chin, J. J. Ruby, P. M. Nilson, D. T. Bishel, F. Coppari, Y. Ping, A. L. Coleman, R. S. Craxton, J. R. Rygg, and G. W. Collins, "Emission Phases of Implosion Sources for X-Ray Absorption Fine Structure Spectroscopy," Phys. Plasmas **29**, 052702 (2022).

A. Diaw, S. J. Coleman, N. M. Cook, J. P. Edelen, E. C. Hansen, and P. Tzeferacos, "Impact of Electron Transport Models on Capillary Discharge Plasmas," Phys. Plasmas **29**, 063101 (2022).

C. Dorrer and J. L. Shaw, "Single-Shot Cross-Correlation of Counter-Propagating, Short Optical Pulses Using Random Quasi-Phase-Matching," Opt. Express **30**, 16,677 (2022).

R. K. Follett, H. Wen, D. H. Froula, D. Turnbull, and J. P. Palastro, "Independent-Hot-Spot Approach to Multibeam Laser-Plasma Instabilities," Phys. Rev. E **105**, L063201 (2022).

G. W. Jenkins, C. Feng, and J. Bromage, "Simultaneous Contrast Improvement and Temporal Compression Using Divided-Pulse Nonlinear Compression," Opt. Express **30**, 13,968 (2022).

D. Kim, R. F. Smith, I. K. Ocampo, F. Coppari, M. C. Marshall, M. K. Ginnane, J. K. Wicks, S. J. Tracy, M. Millot, A. Lazicki, J. R. Rygg, J. H. Eggert, and T. S. Duffy, "Structure and Density of Silicon Carbide to 1.5 TPa and Implications for Extrasolar Planets," Nat. Commun. **13**, 2260 (2022).

Y.-J. Kim, B. Militzer, B. Boates, S. Bonev, P. M. Celliers, G. W. Collins, K. P. Driver, D. E. Fratanduono, S. Hamel, R. Jeanloz, J. R. Rygg, D. C. Swift, J. H. Eggert, and M. Millot, "Evidence for Dissociation and Ionization in Shock Compressed Nitrogen to 800 GPa," Phys. Rev. Lett. **129**, 015701(2022).

R. K. Kirkwood, P. L. Poole, D. H. Kalantar, T. D. Chapman, S. C. Wilks, M. R. Edwards, D. P. Turnbull, P. Michel, L. Divol, N. J. Fisch, P. Norreys, W. Rozmus, J. Bude, B. E. Blue, K. B. Fournier, B. M. Van Wonterghem, and A. MacKinnon, "Production of High Fluence Laser Beams Using Ion Wave Plasma Optics," Appl. Phys. Lett. **120**, 200501 (2022).

T. Z. Kosc, H. Huang, T. J. Kessler, and S. G. Demos, "Angular Dependence of the Transverse Raman Scattering in KDP and DKDP in Geometries Suitable for Beam Polarization Control," Opt. Express **30**, 12,918 (2022).

L. S. Leal, A. V. Maximov, E. C. Hansen, J. R. Davies, D. H. Barnak, J. L. Peebles, K. M. Woo, P. V. Heuer, A. B. Sefkow, and R. Betti, "Effect of Laser Preheat in Magnetized Liner Inertial Fusion at OMEGA," Phys. Plasmas **29**, 042703 (2022).

S. Malko, W. Cayzac, V. Ospina-Bohórquez, K. Bhutwala, M. Bailly-Grandvaux, C. McGuffey, R. Fedosejevs, X. Vaisseau, An. Tauschwitz, J. I. Apiñaniz, D. De Luis, G. Gatti, M. Huault, J. A. Perez Hernandez, S. X. Hu, A. J. White, L. A. Collins, K. Nichols, P. Neumayer, G. Faussurier, J. Vorberger, G. Prestopino, C. Verona, J. J. Santos, D. Batani, F. N. Beg, L. Roso, and L. Volpe, "Proton Stopping Measurements at Low Velocity in Warm Dense Carbon," Nat. Commun. **13**, 2893 (2022).

O. M. Mannion, A. J. Crilly, C. J. Forrest, B. D. Appelbe, R. Betti, V. Yu. Glebov, V. Gopalaswamy, J. P. Knauer, Z. L. Mohamed, C. Stoeckl, J. P. Chittenden, and S. P. Regan, "Measurements of the Temperature and Velocity of the Dense Fuel Layer in Inertial Confinement Fusion Experiments," Phys. Rev. E **105**, 055205 (2022).

K. L. Marshall, K. R. P. Kafka, N. D. Urban, J. U. Wallace, and S. G. Demos, "Multiparameter Laser Performance Characterization of Liquid Crystals for Polarization Control Devices in the Nanosecond Regime," Sci. Rep. **12**, 10969 (2022).

J. Musgrave and J. Bromage, "Impact of the Optical Parametric Amplification Phase on Laser Pulse Compression," Appl. Opt. **61**, 3838 (2022).

R. W. Paddock, H. Martin, R. T. Ruskov, R. H. H. Scott, W. Garbett, B. M. Haines, A. B. Zylstra, E. M. Campbell, T. J. B. Collins, R. S. Craxton, C. A. Thomas, V. N. Goncharov, R. Aboushelbaya, Q. S. Feng, M. W. von der Leyen, I. Ouatu, B. T. Spiers, R. Timmis, R. H. W. Wang, and P. A. Norreys, "Pathways Towards Break Even for Low Convergence Ratio Direct-Drive Inertial Confinement Fusion," J. Plasma Phys. **88**, 905880314 (2022).

D. N. Polsin, A. Lazicki, X. Gong, S. J. Burns, F. Coppari, L. E. Hansen, B. J. Henderson, M. F. Huff, M. I. McMahon, M. Millot, R. Paul, R. F. Smith, J. H. Eggert, G. W. Collins, and J. R. Rygg, "Structural Complexity in Ramp-Compressed Sodium to 480 GPa," Nat. Commun. **13**, 2534 (2022).

D. Ramsey, B. Malaca, A. Di Piazza, M. Formanek, P. Franke, D. H. Froula, M. Pardal, T. T. Simpson, J. Vieira, K. Weichman, and J. P. Palastro, "Nonlinear Thomson Scattering with Ponderomotive Control," Phys. Rev. E **105**, 065201 (2022).

G. F. Swadling, C. Bruulsema, W. Rozmus, and J. Katz, "Quantitative Assessment of Fitting Errors Associated with Streak Camera Noise in Thomson Scattering Data Analysis," Rev. Sci. Instrum. **93**, 043503 (2022).

K. Weichman, A. P. L. Robinson, M. Murakami, J. J. Santos, S. Fujioka, T. Toncian, J. P. Palastro, and A. V. Arefiev, "Progress in Relativistic Laser–Plasma Interaction with Kilotesla-Level Applied Magnetic Fields," Phys. Plasmas **29**, 053104 (2022) (invited).

H. Wen, C. Ren, E. C. Hansen, D. Michta, Y. Zhang, S. Langendorf, and P. Tzeferacos, "Particle-in-Cell Modeling of Plasma Jet Merging in the Large-Hall-Parameter Regime," Phys. Plasmas **29**, 062706 (2022).

J. Zhang, W. R. Donaldson, and G. P. Agrawal, "Temporal Reflection of an Optical Pulse from a Short Soliton: Impact of Raman Scattering," J. Opt. Soc. Am. B **39**, 1950 (2022).

Forthcoming Publications

A. F. Antoniadis, D. Drikakis, P. S. Farmakis, L. Fu, I. Kokkinakis, X. Nogueira, P. A. S. F. Silva, M. Skote, V. Titarev, and P. Tsoutsanis, "UCNS3D: An Open-Source High-Order Finite-Volume Unstructured CFD Solver," to be published in Computer Physics Communications.

Z. Chen, S. X. Hu, and N. P. Bigelow, "Imprinting a Three-Dimensional Skyrmion in a Bose–Einstein Condensate Via a Raman Process," to be published in the Journal of Low Temperature Physics.

V. Gopalaswamy, R. Betti, P. B. Radha, A. J. Crilly, K. M. Woo, A. Lees, C. Thomas, I. V. Igumenshchev, S. C. Miller, J. P. Knauer, C. Stoeckl, C. J. Forrest, O. M. Mannion, Z. L. Mohamed, H. G. Rinderknecht, and P. V. Heuer, "Analysis of Limited Coverage Effects on Areal Density Measurements in Inertial Confinement Fusion Implosions," to be published in Physics of Plasmas.

S. S. Harilal, M. C. Phillips, D. H. Froula, K. K. Anoop, R. C. Issac, and F. N. Beg, "Optical Diagnostics of Laser-Produced Plasmas," to be published in the Reviews of Modern Physics.

P. V. Heuer, L. S. Leal, J. R. Davies, E. C. Hansen, D. H. Barnak, J. L. Peebles, F. García-Rubio, B. Pollock, J. Moody, A. Birkel, and F. H. Séguin, "Diagnosing Magnetic Fields in

Cylindrical Implosions with Oblique Proton Radiography," to be published in Physics of Plasmas.

M. P. Jeske, W. Zhang, and M. Anthamatten "Two-Photon Printing of Shape-Memory Microstructures and Metasurfaces via Radical-Mediated Thiol-Vinyl Hydrothiolation," to be published in Advanced Materials Technologies.

K. R. P. Kafka, T. Z. Kosc, and S. G. Demos, "Methods and Apparatus for Comprehensive Characterization of Performance Attributes and Damage Thresholds of Ultrafast Laser Optics," to be published in Optical Engineering.

H. Poole, D. Cao, R. Epstein, I. Golovkin, T. Walton, S. X. Hu, M. Kasim, S. M. Vinko, J. R. Rygg, V. N. Goncharov, G. Gregori, and S. P. Regan, "A Case Study of Using X-Ray Thomson Scattering to Diagnose the In-Flight Plasma Condition of DT Cryogenic Implosions," to be published in Physics of Plasmas.

A. K. Schwemmlein, C. Stoeckl, C. J. Forrest, W. T. Shmayda, S. P. Regan, W. U. Schröder, "First Demonstration of a Triton Beam Using Target Normal Sheath Acceleration," to be published in Nuclear Instruments and Methods in Physics Research B.

R. C. Shah, D. Cao, L. Aghaian, B. Bachmann, R. Betti, E. M. Campbell, R. Epstein, C. J. Forrest, A. Forsman, V. Yu. Glebov, V. N. Goncharov, V. Gopalaswamy, D. R. Harding, S. X. Hu, I. V. Igumenshchev, R. T. Janezic, L. Keaty, J. P. Knauer, D. Kobs, A. Lees, O. M. Mannion, Z. L. Mohamed, D. Patel, M. J. Rosenberg, W. T. Shmayda, C. Stoeckl, W. Theobald, C. A. Thomas, P. Volegov, K. M. Woo, and S. P. Regan, "Bound on Hot-Spot Mix in High-Velocity, High-Adiabat Direct-Drive Cryogenic Implosions Based on Comparison of Absolute X-Ray and Neutron Yields," to be published in Physical Review E.

S. Singh, A. L. Coleman, S. Zhang, F. Coppari, M. G. Gorman, R. F. Smith, J. H. Briggs, and D. E. Fratanduono, "Quantitative Analysis of Diffraction by Liquids Using a Pink-Spectrum X-Ray Source," to be published in the Journal of Synchrotron Radiation.

R. Sobolewski, "Optical Detectors and Sensors," to be published in the Handbook of Superconducting Materials.

D. Turnbull, J. Katz, D. E. Hinkel, P. Michel, T. Chapman, L. Divol, E. Kur, S. MacLaren, A. L. Milder, M. Rosen, A. Shvydky, G. B. Zimmerman, and D. H. Froula, "Beam Spray Thresholds in ICF-Relevant Plasmas," to be published in Physical Review Letters.

N. D. Urban, K. R. P. Kafka, K. L. Marshall, and S. G. Demos, "Laser-Induced Damage Characteristics of Fused Silica Surfaces Polished to Different Depths Using Fluid Jet Polishing," to be published in Optical Engineering.

K. M. Woo, R. Betti, C. A. Thomas, C. Stoeckl, K. Churnetski, C. J. Forrest, Z. L. Mohamed, B. Zirps, S. P. Regan, T. J. B. Collins, W. Theobald, R. C. Shah, O. M. Mannion, D. Patel, D. Cao, J. P. Knauer, V. Yu. Glebov, V. N. Goncharov, P. B. Radha, H. G. Rinderknecht, R. Epstein, V. Gopalaswamy, F. J. Marshall, S. T. Ivancic, and E. M. Campbell, "Analysis of Core Asymmetries in Inertial Confinement Fusion Implosions Using Three-Dimensional Hot-Spot Reconstruction," to be published in Physics of Plasmas.

D. Zhang, J. Li, J. Xin, R. Yan, Z. Wan, H. Zhang, and J. Zheng, "Self-Generated Magnetic Field in Ablative Rayleigh–Taylor Instability," to be published in Physics of Plasmas.

Conference Presentations

The following presentations were made at the 2022 Panchanatan Visit, Rochester, NY, 11 April 2022:

C. Deeney, "An Overview of the Laboratory for Laser Energetics: Always 'Reaching for the Brightest Light.' "

V. Gopalaswamy, "Data-Driven Experimental Design at LLE."

E. M. Hill, "LLE is a Word Leader for Designing, Innovating, and Constructing State-of-the-Art Lasers for a Wide Range of Scientific Applications for Ourselves and the Broader Scientific Community."

M. F. Huff, "Measuring Sound Speed in Shocked Iron."

J. Katz, "Diagnostic Development and Advanced Instrumentation for Fundamental Physics."

Z. K. Sprowal, L. E. Hansen, M. F. Huff, D. N. Polsin, T. R. Boehly, J. R. Rygg, G. W. Collins, and D. G. Hicks, "Accessing High-Density States in D_2 Using Double Shocks."

M. S. Wei, "User Community."

C. A. Williams, "Convergence Research in Inertial Confinement Fusion."

J. D. Zuegel, "Laser Materials Technology Division and Major Projects," presented at the NNSA–OES Visit, virtual, 12 April 2022.

R. B. Spielman, "The Design of Self-Magnetically Insulated Transmission Lines for a 10-MA Intermediate-Scale Facility," presented at the Cornell University Seminar, Cornell, NY, 13 April 2022.

J. Bromage, S.-W. Bahk, M. Bedzyk, I. A. Begishev, S. Bucht, C. Dorrer, C. Feng, B. N. Hoffman, C. Jeon, C. Mileham, J. B. Oliver, R. G. Roides, E. M. Schiesser, K. Shaughnessy, M. J. Shoup III, M. Spilatro, B. Webb, D. Weiner, and J. D. Zuegel, "Development of Ultra-Intense OPCPA Technologies on the MTW-OPAL System," presented at the 11th Advanced Lasers and Photon Sources, Yokohama, Japan, 18–21 April 2022 (invited).

S. X. Hu, P. M. Nilson, D. T. Bishel, D. A. Chin, V. V. Karasiev, D. I. Mihaylov, N. R. Shaffer, S. Zhang, V. Recoules, N. Brouwer, M. Torrent, I. E. Golovkin, M. Gu, T. Walton, and S. B. Hansen, "Probing Atomic Physics at Extreme Conditions," presented at the International Conference on High-Energy-Density Sciences, Yokohama, Japan, 18–22 April 2022 (invited).

J. D. Zuegel, J. Bromage, D. H. Froula, E. M. Hill, J. P. Palastro, J. C. Puth, H. G. Rinderknecht, J. L. Shaw, C. J. Forrest, and L. J. Waxer, "Proposed EP-OPAL Laser Facility," presented at the MP3 Workshop, Paris, France, 20–22 April 2022.

C. Deeney, "Pulsed-Power Research at LLE," presented at the ZNetUS Workshop, virtual, 21–22 April 2022.

The following presentations were made at the 2022 ARPA-E Fusion Programs Annual Meeting, San Francisco, CA, 26–27 April 2022:

J. R. Davies, H. Berger, C. J. Forrest, V. Yu. Glebov, H. McClow, M. Sharpe, and W. T. Shmayda, "The LLE Diagnostic Resource Team for Innovative Fusion Concepts."

V. N. Goncharov, I. V. Igumenshchev, W. Trickey, R. K. Follett, N. Shaffer, A. Pineau, Y. Lawrence, M. Tobin, W. Meier, S. Woodruff, C. Dorrer, and J. D. Zuegel, "Advanced Inertial Fusion Energy Target Designs with Next-Generation Laser Technologies."

P. Tzeferacos, A. Sefkow, C. Ren, R. Betti, J. R. Davies, H. Wen, J. G. Shaw, E. C. Hansen, D. Michta, F. García-Rubio, and K. M. Woo, "A Simulation Resource Team for Innovative Fusion Concepts in the BETHE Program."

The following presentations were made at the 2022 Omega Laser Facility Users Group, Rochester, NY, 27–29 April 2022:

A. Armstrong, A. Reyes, M. B. P. Adams, P. Farmakis, E. C. Hansen, Y. Lu, D. Michta, K. Moczulski, D. Q Lamb, and P. Tzeferacos, "Implementation and Verification of Spitzer Viscosity in the *FLASH* Code."

D. H. Barnak, "Self-Optimizing Savitzky–Golay Filter for Generalized Signal Denoising."

D. H. Barnak, R. Betti, V. Gopalaswamy, A. Lees, and A. Shvydky, "Numerical Simulations of the VISAR Diagnostic."

D. H. Barnak, J. R. Davies, J. P. Knauer, and P. M. Kozlowski, "*FIDUCIA*: A New User's Course into the Wonderful World of Cubic Spline Unfolding."

G. Bruhaug, H. G. Rinderknecht, M. S. Wei, B. Brannon, D. Guy, R. Peck, N. Landis, G. Brent, R. Fairbanks, C. McAtee, T. Walker, T. Buczek, M. Krieger, M. Romanofsky, Y. E, K. Garriga, X. C. Zhang, G. W. Collins, and J. R. Rygg, "High-Power, High-Energy THz Generation Using Joule- and Kilojoule-Class Lasers."

C. Deeney, "The Next Cooperative Agreement: FY24–FY28."

P. Farmakis, M. McMullan, A. Reyes, J. Laune, M. B. P. Adams, A. Armstrong, E. C. Hansen, Y. Lu, D. Michta,

K. Moczulski, D. Lamb, and P. Tzeferacos, "Expanding the Tabulated Equationof-State Implementations in the *FLASH* Code for the *SESAME* Database."

D. H. Froula, "Fourth-Generation Laser for Ultra-Broadband Experiments."

E. C. Hansen, P. Farmakis, D. Michta, C. Ren, A. C. Reyes, H. Wen, S. Langendorf, and P. Tzeferacos, "Simulating the Plasma Liner Experiment (PLX) with the *FLASH* Code."

P. V. Heuer, J. R. Davies, D. Stanczak, E. Everson, and N. Murphy, "Synthetic Diagnostics for High-Energy-Density Physics in *PlasmaPy*."

S. T. Ivancic, "Gas-Jet System on OMEGA and OMEGA EP."

T. J. Kessler and M. Romo-Gonzalez, "Inclusion, Diversity, and Equity at the Laboratory for Laser Energetics."

Y. Lu, S. Feister, J. Meinecke, F. Miniati, G. Gregori, A. Bott, A. Reyes, E. C. Hansen, J. T. Laune, B. Reville, J. S. Ross, D. Q. Lamb, and P. Tzeferacos, "Numerical Modeling of Laser-Driven Plasma Experiments Aiming to Study Turbulent Dynamo and Thermal Conduction at the National Ignition Facility."

D. Michta, P. Tzeferacos, S. Bolanos, and M. Manuel, "*FLASH* Simulations of the Magnetized Quasi-Parallel Collisionless Shock Experiments on OMEGA EP."

K. Moczulski, A. Reyes, M. B. P. Adams, A. Armstrong, P. Farmakis, E. C. Hansen, Y. Lu, D. Michta, D. Q. Lamb, and P. Tzeferacos, "Implementation and Verification of LC Circuit for *Z*-Pinch *FLASH* Simulations."

S. F. B. Morse, "Omega Facility OLUG 2022 Update: Progress on Recommendations and Items of General Interest."

S. F. B. Morse, "The Sustainment Plan for the Omega Laser Facility."

J. L. Peebles, "Generating Magnetic Fields Using MIFEDS on Your Campaign at OMEGA/OMEGA EP."

A. Reyes, M. B. P. Adams, A. Armstrong, K. Moczulski, P. Farmakis, E. C. Hansen, Y. Lu, D. Michta, J. Grove, and P. Tzeferacos, "Volume-of-Fluid Representation of Multifluid Compressible Hydrodynamics in the *FLASH* Code."

P. Tzeferacos, "Big Lasers and Big Computers: The Flash Center for Computational Science and the *FLASH* Code at UR."

A. Bowman, M. Burns, A. Poudel, S. Zhai, S. Dwarkadas, A. B. Sefkow, and S. Pai, "Cross-Beam Energy Transfer on Graphics Processing Units," presented at Senior Design Day, Rochester, NY, 29 April 2022.

D. Mihaylov, "Improving the Accuracy of Density Functional Theory Simulations of Warm Dense Matter by Including Exchange-Correlation Thermal Effects," presented at the Center for Advanced Systems Understanding Seminar, virtual, 3 May 2022.

The following presentations were made at the 17th Direct Drive and Fast Ignition Workshop, Madrid, Spain, 3–5 May 2022:

E. M. Campbell, "Perspective on Inertial Fusion Energy."

L. Ceurvorst, W. Theobald, M. J. Rosenberg, P. B. Radha, S. P. Regan, C. Stoeckl, R. Betti, K. S. Anderson, J. A. Marozas, V. N. Goncharov, E. M. Campbell, C. M. Shuldberg, R. W. Luo, W. Sweet, L. Aghaiain, D. N. Kaczala, B. Bachmann, T. Döppner, M. Hohenberger, K. Glize, R. H. H. Scott, and A. Colaïtis, "Laser-Direct-Drive Energy-Coupling Experiments Using Solid Spheres at the National Ignition Facility."

V. N. Goncharov, W. Trickey, I. V. Igumenshchev, N. Shaffer, Y. Lawrence, S. Atzeni, and L. Savino, "Advanced Target Designs for Laser-Direct-Drive Inertial Confinement Fusion."

S. X. Hu, L. Ceurvorst, J. L. Peebles, V. N. Goncharov, Y.-F. Lu, A. Pineau, G. Duchateau, K. R. P. Kafka, S. G. Demos, W. Theobald, S. P. Regan, A. Shvydky, T. J. B. Collins, V. V. Karasiev, S. Zhang, D. R. Harding, R. C. Shah, E. M. Campbell, and C. Deeney, "Review on Laser Imprint for Direct-Drive Inertial Confinement Fusion Implosions."

S. P. Regan, V. N. Goncharov, E. M. Campbell, R. Betti, P. Adrian, K. S. Anderson, B. Appelbe, J. Baltazar, D. H. Barnak, J. Bates, K. A. Bauer, R. Boni, M. J. Bonino, D. Cao, A. Colaïtis, D. Canning, K. Churnetski, T. J. B. Collins, G. W.

Collins, A. J. Crilly, J. R. Davies, S. G. Demos, C. Dorrer, R. F. Earley, R. Epstein, M. Farrell, R. K. Follett, C. J. Forrest, J. A. Frenje, D. H. Froula, M. Gatu-Johnson, V. Yu. Glebov, V. Gopalaswamy, A. M. Hansen, D. R. Harding, P. V. Heuer, E. M. Hill, S. X. Hu, H. Huang, J. Hund, I. V. Igumenshchev, S. T. Ivancic, D. W. Jacobs-Perkins, R. T. Janezic, M. Karasik, J. Katz, J. P. Knauer, B. Kruschwitz, J. Kunimune, M. Labuzeta, A. Lees, O. M. Mannion, J. A. Marozas, P. W. McKenty, S. F. B. Morse, P. M. Nilson, J. P. Palastro, D. Patel, J. L. Peebles, P. B. Radha, H. G. Rinderknecht, M. J. Rosenberg, J. R. Rygg, S. Sampat, T. C. Sangster, R. C. Shah, M. Sharpe, W. T. Shmayda, M. J. Shoup III, C. Shuldberg, A. Shvydky, A. A. Solodov, Z. K. Sprowal, C. Sorce, A. Sorce, C. Stoeckl, C. A. Thomas, W. Theobald, D. Turnbull, L. J. Waxer, M. D. Wittman, K. M. Woo, and J. D. Zuegel, "Accomplishments of the 100-Gbar Campaign on OMEGA."

R. C. Shah, S. X. Hu, I. V. Igumenshchev, J. Baltazar, D. Cao, C. J. Forrest, V. N. Goncharov, V. Gopalaswamy, D. Patel, W. Theobald, S. P. Regan, and F. Philippe, "Anomalous X-Ray Emission at Early Stages of Hot-Spot Formation in Deuterium–Tritium Cryogenic Implosions."

W. Trickey, V. N. Goncharov, E. M. Campbell, Y. Lawrence, M. J. Rosenberg, N. Shaffer, W. Theobald, R. C. Shah, A. Shvydky, I. V. Igumenshchev, A. Colaïtis, S. Atzeni, and L. Savino, "Multidimensional Modeling of Low-Mode Perturbations in the Dynamic-Shell Inertial Confinement Fusion Design."

The following presentations were made at the 2022 Center for Matter at Atomic Pressures, Rochester, NY, 5–6 May 2022:

D. Bishel, P. M. Nilson, D. A. Chin, E. Smith, S. X. Hu, V. V. Karasiev, J. R. Rygg, G. W. Collins, J. J. Ruby, and E. V. Marley, "Interrogating the Atomic Structure of Dense Plasmas by X-Ray Absorption Spectroscopy of Implosion Shells."

D. A. Chin, P. M. Nilson, D. T. Bishel, R. Paul, E. Smith, X. Gong, M. K. Ginnane, B. J. Henderson, D. N. Polsin, S. X. Hu, J. R. Rygg, G. W. Collins, D. Trail, A. Amouretti, M. Harmand, O. Mathon, R. Torchio, J. J. Ruby, F. Coppari, A. Coleman, and Y. Ping, "X-Ray Fine Absorption Fine Structure Spectroscopy Measurements of High-Energy-Density Matter."

Z. K. Sprowal, L. E. Hansen, M. F. Huff, D. N. Polsin, D. G. Hicks, T. R. Boehly, J. R. Rygg, and G. W. Collins, "Accessing High-Density States in D_2 Using Double Shock."

S. Zhang, "Isentrope and Equation of State of Solid Hydrogen."

C. Jeon, "Smart Cities and Lasers: Connecting the Dots," presented at the Han Yang University Seminar, virtual, 6 May 2022.

The following presentations were made at the 2022 Materials Research Society Spring Meeting, Honolulu, HI, 8–25 May 2022:

S. M. Fess, D. R. Harding, M. J. Bonino, R. F. Earley, P. Fan, X. Huang, Y.-F. Lu, S. P. Regan, and E. M. Campbell, "Fabrication of Shells and Foams via Two-Photon Polymerization for Laser-Fusion Experiments."

D. R. Harding, S. M. Fess, M. Bonino, R. F. Earley, Y.-F. Lu, X. Huang, P. Fan, S. P. Regan, and E. M. Campbell, "Multiphoton Applications in Laser Fusion Research: From Printing Fusion-Fuel Targets with Sub-150-nm Features to Acquiring Three-Dimensional Structural and Elemental Information of the Target."

M. P. Jeske and M. Anthamatten, "Thermally Responsive Resins for Free-Radical and Base-Catalyzed Two-Photon Polymerization."

P. Tzeferacos, "*FLASH* for *Z*-Pinch Experiments and Extended MHD," presented at the 2022 Center for Matter Under Extreme Conditions Review, San Diego, CA, 10–11 May 2022.

The following presentations were made at the 24th High-Temperature Plasma Diagnostic Conference, Rochester, NY, 15–19 May 2022:

J. Baltazar, R. Betti, K. Churnetski, V. Gopalaswamy, J. P. Knauer, D. Patel, H. G. Rinderknecht, R. C. Shah, C. Stoeckl, C. A. Willliams, and S. P. Regan, "Diagnosing Low-Mode ($\ell < 6$) and Mid-Mode ($6 \leq \ell \leq 20$) Asymmetries in the

Explosion Phase of Laser-Direct-Drive Deuterium–Tritium Cryogenic Implosions on OMEGA."

G. Bruhaug, H. G. Rinderknecht, M. S. Wei, B. Brannon, D. Guy, R. G. Peck, N. Landis, G. Brent, R. Fairbanks, C. McAtee, T. Walker, T. Buczek, M. Krieger, M. Romanofsky, Y. E, K. Garriga, X. C. Zhang, G. W. Collins, and J. R. Rygg, "Development of a Hardened THz Energy Meter for Use on the Kilojoule-Scale, Short-Pulse OMEGA EP Laser."

L. Ceurvorst, W. Theobald, M. J. Rosenberg, P. B. Radha, S. P. Regan, C. Stoeckl, R. Betti, K. S. Anderson, J. A. Marozas, V. N. Goncharov, E. M. Campbell, C. M. Shuldberg, R. W. Luo, W. Sweet, L. Aghaian, D. N. Kaczala, B. Bachmann, T. Döppner, M. Hohenberger, K. Glize, R. H. H. Scott, and A. Colaïtis, "Development of an X-Ray Radiography Platform to Study Laser-Direct-Drive Energy Coupling at the National Ignition Facility."

J. Cheng, G. Chen, D. Chakraborty, S. Kutcher, J. Wen, H. Chen, S. Trivedi, and R. Sobolewski, "(Cd,Mg)Te for Picosecond Response Optical to X-Ray Radiation Detectors."

K. Churnetski, K. M. Woo, W. Theobald, P. B. Radha, R. Betti, V. Gopalaswamy, I. V. Igumenshchev, S. T. Ivancic, M. Michalko, R. C. Shah, C. Stoeckl, C. A. Thomas, and S. P. Regan, "Three-Dimensional Hot-Spot X-Ray Emission Tomography from Cryogenic Deuterium–Tritium Direct-Drive Implosions on OMEGA."

R. Cuffney, J. Shamlian, M. Sharpe, T. Lewis, M. J. Shoup III, J. Bromage, B. Golick, N. Palmer, A. Golod, B. Hatch, and M. Miller, "4ω Fiducial Generator: Provides Optical Timing Reference Marks for Streak Cameras."

D. H. Edgell, J. Katz, R. Raimondi, D. Turnbull, and D. H. Froula, "Scattered-Light Uniformity Imager for Diagnosing Laser Absorption Asymmetries on OMEGA."

T. Filkins, M. J. Rosenberg, R. Bahr, J. Katz, and S. T. Ivancic, "Calibration of the Sub-Aperture Backscatter System on OMEGA EP."

C. J. Forrest, R. Betti, J. P. Knauer, V. Yu. Glebov, V. Gopalaswamy, O. M. Mannion, Z. L. Mohamed, P. B. Radha, S. P. Regan, A. Schwemmlein, C. Stoeckl, W. Theobald, J. A. Frenje, M. Gatu Johnson, B. Appelbe, and A. J. Crilly, "Measurements of Low-Mode Asymmetries in Areal Density of Laser-Direct-Drive DT Cryogenic Implosions on OMEGA Using Neutron Spectroscopy" (invited).

V. Yu. Glebov, C. J. Forrest, J. Kendrick, J. P. Knauer, H. McClow, S. P. Regan, C. Stoeckl, B. Stanley, W. Theobald, and O. M. Mannion, "A New Neutron Time-of-Flight Detector for D_2 Yield and Ion-Temperature Measurements on OMEGA."

D. Haberberger, A. Shvydky, and D. H. Froula, "Fresnel Zone Plate Calculations for the Application to Laser-Plasma Experiments."

P. V. Heuer, D. Stanczak, E. T. Everson, N. A. Murphy, and J. R. Davies, "Open-Source Analysis Software for High-Temperature Plasma Diagnostics."

S. T. Ivancic, W. Theobald, K. Churnetski, M. Michalko, D. Willistein, W. Bittle, S. P. Regan, A. Carpenter, C. Trosseille, J. D. Kilkenny, A. Raymond, J. D. Hares, A. K. L. Dymoke-Bradshaw, G. Rochau, and D. Garand "Design of the High-Yield Time-Gated X-Ray Hot-Spot Imager (XRHSI) for OMEGA."

T. R. Joshi, R. C. Shah, W. Theobald, K. Churnetski, P. B. Radha, D. Cao, C. A. Thomas, J. Baltazar, and S. P. Regan, "Diagnosis of the Imploding Shell Asymmetry in Polar-Direct-Drive DT Cryogenic Target Implosions on OMEGA."

J. Katz, D. Turnbull, S. T. Ivancic, A. L. Milder, and D. H. Froula, "Measurement of Laser Absorption in Underdense Plasmas Using Near-Field Imaging of the Incident and Transmitted Beams."

J. P. Knauer, C. J. Forrest, V. Gopalaswamy, and Z. L. Mohamed, "Normalized Time Axis for Neutron Time-of-Flight Analysis."

S. Kostick, M. J. Rosenberg, W. Theobald, J. Katz, N. Lemos, E. Tubman, J. S. Ross, N. Butler, G. Swadling, R. Sommers, J. D. Moody, R. S. Craxton, A. Sharma, and S. P. Regan, "Assessment of the Calibration of the Scattered-Light Time-History Diagnostic at the National Ignition Facility."

H. McClow, H. Berger, J. R. Davies, C. J. Forrest, G. Gates, S. T. Ivancic, J. Katz, J. Ruby, A. Sorce, and W. Theobald, "First Measurements with a Single-Hit Neutron Spectrometer."

S. F. Nwabunwanne and W. R. Donaldson, "Tunable, Picosecond AlGaN UV Photodiodes."

H. Poole, M. K. Ginnane, J. Topp-Mugglestone, R. Saha, D. N. Polsin, G. W. Collins, S. X. Hu, T. White, S. P. Regan,

G. Gregori, and J. R. Rygg, "Measurements of Warm-Dense-Matter Silicon Based on Angularly and Spectrally Dispersed X-Ray Scattering."

H. G. Rinderknecht, P. V. Heuer, V. Gopalaswamy, J. P. Knauer, C. A. Williams, W. Theobald, R. Fairbanks, B. Brannon, V. Kobilansky, R. Peck, J. Armstrong, M. Weisbeck, J. Brown, L. Ceurvorst, P. B. Radha, S. P. Regan, J. Kunimune, P. Adrian, M. Gatu Johnson, J. A. Frenje, F. Séguin, A. J. Crilly, B. Appelbe, and B. Bachmann, "A Knock-On Deuteron Imager for Measurements of Fuel and Hot-Spot Asymmetry in Direct-Drive Inertial Confinement Fusion Implosions" (invited).

M. Romo-Gonzalez and R. Boni, "Free-Standing Thin Membrane Zero *B*-Integral Beam Splitters."

B. Stanley, C. J. Forrest, and S. T. Ivancic, "Nuclear Activation Analysis of Zirconium-90 Isomeric and Ground-State Reactions at the Omega Laser Facility."

C. Stoeckl, D. Cao, L. Ceurvorst, A. Kalb, J. Kwiatkowski, A. Shvydky, and W. Theobald, "Beam Pointing Verification Using X-Ray Pinhole Cameras on the 60-Beam OMEGA Laser."

The following presentations were made at CLEO 2022, San Jose, CA, 15–20 May 2022:

C. Dorrer and J. L. Shaw, "Single-Shot Cross-Correlation of Counter-Propagating Pulses in a Disordered Nonlinear Crystal."

C. Dorrer and M. A. Spilatro, "Spectral and Temporal Shaping of Spectrally Incoherent UV Pulses by Sum-Frequency Generation."

G. W. Jenkins, C. Feng, and J. Bromage, "Energy Scaling Beyond Gas-Ionization Thresholds with Divided-Pulse Nonlinear Compression."

J. P. Palastro, "Laser–Plasma Interactions Driven by Flying Focus Pulses."

J. Zhang, W. R. Donaldson, and G. P. Agrawal, "Theory and Applications of Temporal Reflection in a Dispersive Medium."

The following presentations were made at the 49th International Conference on Plasma Science, Seattle, WA, 22–26 May 2022:

C. Deeney, E. M. Campbell, V. N. Goncharov, R. Betti, J. D. Zuegel, S. P. Regan, G. W. Collins, S. F. B. Morse, C. Sorce, D. H. Froula, and M. S. Wei, "Laboratory for Laser Energetics: Progress in Science and Technology."

J. Katz, R. Boni, A. L. Milder, D. Nelson, K. Daub, and D. H. Froula, "A High-Numerical-Aperture, Angularly Resolved Thomson-Scattering Spectrometer" (invited).

V. N. Goncharov, W. Trickey, N. Shaffer, A. Peneau, I. V. Igumenshchev, R. K. Follett, T. J. B. Collins, C. Dorrer, J. D. Zuegel, M. Tobin, W. Meier, and Y. Lawrence, "Advanced Inertial Fusion Energy Target Designs with Next-Generation Laser Technologies," presented at the ARPA-E Summit, Denver, CO, 23–25 May 2022.

V. N. Goncharov, W. Trickey, I. V. Igumenshchev, N. Shaffer, T. J. B. Collins, R. K. Follett, C. Stoeckl, R. C. Shah, C. Dorrer, J. D. Zuegel, D. R. Harding, S. Fess, E. M. Campbell, C. Deeney, S. Atzeni, L. Savino, F. Barbato, and A. Colaïtis, "Direct-Drive Designs and Experiments on OMEGA," presented at the EUROfusion Science Meeting, virtual, 27 May 2022.

The following presentations were made at the 50th Anomalous Absorption Conference, Skytop, PA, 5–10 June 2022:

Z. Barfield, J. L. Peebles, P. Tzeferacos, D. Mastrosimone, J. Katz, P. V. Heuer, and D. H. Froula, "Measurements of Anisotropic Temperatures in Magnetized Gas-Jet Plasmas."

S. H. Cao, D. Patel, A. Lees, V. Gopalaswamy, C. Stoeckl, M. J. Rosenberg, H. Wen, H. Huang, A. Shvydky, R. Betti, and C. Ren, "Predicting Hot-Electron Generation in Inertial Confinement Fusion with Particle-in-Cell Simulations."

D. H. Edgell, A. Colaïtis, M. J. Guardalben, A. Kalb, J. Katz, J. Kwiatkowski, O. M. Mannion, A. Shvydky, C. Stoeckl, D. Turnbull, and D. H. Froula, "Cross-Beam Energy Transfer-Induced Nonuniformity in Direct-Drive Implosions on OMEGA."

R. Epstein, V. N. Goncharov, S. X. Hu, D. Cao, A. Shvydky, P. W. McKenty, G. W. Collins, and D. Haberberger, "Assessment of Radiation Trapping in Inertial Confinement Fusion Implosion Experiments with High-*Z*-Lined, Single-Shell Targets."

V. N. Goncharov, W. Trickey, I. V. Igumenshchev, N. Shaffer, T. J. B. Collins, R. K. Follett, W. Theobald, C. Stoeckl, R. C. Shah, C. Dorrer, J. D. Zuegel, D. R. Harding, S. Fess, E. M. Campbell, C. Deeney, S. Atzeni, L. Savino, F. Barbato, and A. Colaïtis, "Physics Requirements for High-Gain Inertial Confinement Fusion Target Designs."

D. Haberberger, A. Shvydky, C. Stoeckl, V. N. Goncharov, and D. H. Froula, "Schlieren Refraction Imaging for Cryo Implosions."

L. S. Leal, A. V. Maximov, F. García-Rubio, R. Betti, and V. V. Ivanov, "Modeling of Laser-Driven Ablative Magneto-thermal Instability."

A. V. Maximov, D. Turnbull, D. H. Edgell, R. K. Follett, H. Wen, J. P. Palastro, and D. H. Froula, "Nonlinear Laser–Plasma Coupling Caused by Two-Plasmon Decay and Cross-Beam Energy Transfer."

K. L. Nguyen, A. M. Hansen, D. Turnbull, R. K. Follett, D. H. Edgell, D. H. Froula, J. P. Palastro, L. Yin, and B. J. Albright, "Cross-Beam Energy Transfer Saturation by Ion-Trapping-Induced Detuning."

J. P. Palastro, D. Ramsey, M. Ambat, P. Franke, D. H. Froula, J. Pigeon, J. L. Shaw, T. T. Simpson, K. Weichman, B. Barbosa, B. Malaca, M. Pardal, J. Vieira, M. Vranic, M. Formanek, A. Di Piazza, J. Pierce, and W. Mori, "Nonlinear Thomson Scattering with Ponderomotive Control."

D. Ramsey, A. Di Piazza, M. Formanek, P. Franke, D. H. Froula, W. Mori, J. Pierce, T. T. Simpson, K. Weichman, and J. P. Palastro, "Exact Analytic Solutions Yielding Flying Focus Pulses (EASYFFP)."

H. G. Rinderknecht, G. Bruhaug, K. Weichman, M. Van Dusen-Gross, J. P. Palastro, M. S. Wei, A. Arefiev, T. Wang, T. Toncian, A. Laso Garcia, D. Doria, K. Spohr, H. J. Quevedo, T. Ditmire, J. Williams, A. Haid, and D. Stutman, "Relativistically Transparent Magnetic Filaments: a Short-Pulse Path to MegaTesla Fields and Efficient Gamma Radiation."

N. R. Shaffer, V. N. Goncharov, A. V. Maximov, and M. Sherlock, "An Extended Vlasov–Foller–Planck Approach to Laser Absorption and Ponderomotive Effects."

T. T. Simpson, J. Pigeon, M. Lim Pac Chong, D. Ramsey, K. Weichman, D. H. Froula, and J. P. Palastro, "High-Energy Two-Color Terahertz Generation."

A. A. Solodov, M. J. Rosenberg, M. Stoeckl, R. Betti, W. Seka, R. Epstein, C. Stoeckl, R. K. Follett, P. B. Radha, S. P. Regan, D. H. Froula, J. P. Palastro, E. M. Campbell, V. N. Goncharov, A. R. Christopherson, B. Bachman, M. Hohenberger, P. Michel, and J. F. Myatt, "Hot-Electron Preheat and Mitigation in Polar-Direct-Drive Experiments at the National Ignition Facility."

D. Turnbull, J. Katz, A. L. Milder, A. Shvydky, D. H. Froula, D. E. Hinkel, P. Michel, T. Chapman, L. Divol, E. Kur, S. MacLaren, M. Rosen, and G. B. Zimmerman, "Beam Spray Thresholds in ICF-Relevant Plasmas."

K. Weichman, J. P. Palastro, A. P. L. Robinson, and A. V. Arefiev, "Relativistically Thermal Plasma Generation by Magnetically Assisted Direct Laser Acceleration."

H. Wen, R. K. Follett, A. V. Maximov, and J. P. Palastro, "Mitigation of Inflationary Stimulated Raman Scattering with Laser Bandwidth."

The following presentations were made at the 24th Target Fabrication Specialist meeting, virtual, 6–9 June 2022:

J. M. García-Figueroa and D. R. Harding, "Observations on Smooth Diamond-Like Composition Films Deposited at Low Temperature via an Electron Cyclotron Resonance-Microwave-Chemical Vapor Deposition One-Step Process."

M. Wang and D. R. Harding, "Mechanical Properties of Micrometer-Size Foam Structures."

C. Deeney, "LLE Strategy," presented at the Office of Experimental Sciences Executives Meeting, Washington, DC, 8–9 June 2022.

The following presentations were made at Technology of Fusion Energy, Anaheim, CA, 12–16 June 2022:

M. Sharpe, C. Fagan, and W. T. Shmayda, "Influence of Microstructure on the Absorption of Tritium into Gold-Plated 316 Stainless Steel."

W. T. Shmayda, E. Dombrowski, and H. K. Mutha, "Pumping and Purifying the SPARC Tokamak Exhaust."

D. A. Chin, P. M. Nilson, J. J. Ruby, D. T. Bishel, R. Paul, M. Signor, A. Amouretti, A. Coleman, F. Coppari, M. K. Ginnane, X. Gong, M. Harmand, B. J. Henderson, S. X. Hu, O. Mathon, D. N. Polsin, E. Smith, R. Torchio, D. Trail, Y. Ping, J. R. Rygg, and G. W. Collins, "X-Ray Absorption Fine Structure Spectroscopy of Iron Compounds at High-Energy-Density Conditions," presented at the DOE NNSA Stewardship Science Graduate Fellowship, Santa Fe, NM, 20–23 June 2022.

E. M. Campbell, "Overview of Inertial Confinement Fusion History, Challenges, and Prospects for Driver-Target Concepts," presented at the Basic Research Needs Workshop, virtual, 21–23 June 2022.

R. B. Spielman and T. Joshi, "Annual Technical Review," presented at the Materials Science in Extreme Environments Annual Technical Review Meeting, Baltimore, MD, 22–24 June 2022.

C. Deeney, "The Laboratory for Laser Energetics: Progress in Science and Technology," presented at the Washington State University Institute for Shock Physics, Pullman, WA, 27 June 2022 (invited).

R Betti, A. Casner, X. Ribeyre, and W. Theobald, "Progress in Laser Direct Drive: Conventional and Shock Ignition," presented at the 48th European Physical Society Conference on Plasma Physics, virtual, 27 June–1 July 2022.

UNIVERSITY OF ROCHESTER
LABORATORY FOR LASER ENERGETICS

Volume 172
July–September 2022
DOE/NA/3856-1775

LLE Review

Quarterly Report

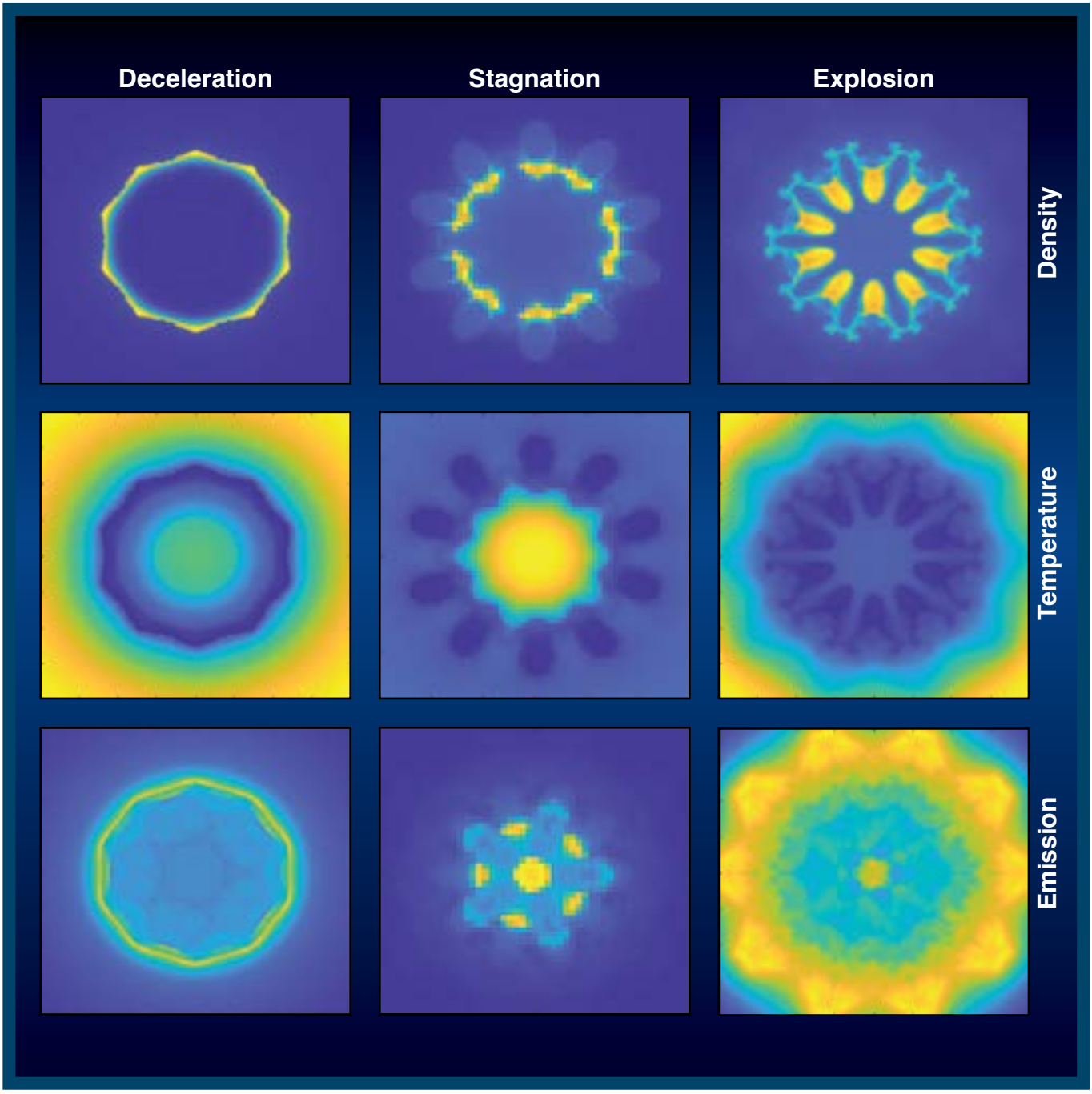

About the Cover:

The cover picture shows density (top row) and temperature (middle row) maps from 3-D *ASTER* simulations of a DT cryogenic implosion with a beam-to-target ratio of $R_b/R_t = 0.75$, and post-processed synthetic x-ray images (bottom row) for three different phases of the implosion: deceleration (left column), stagnation (middle column), and post-stagnation (explosion) (right column). These maps cover an area of 400 μm × 400 μm. The low-density regions in the shell in the deceleration phase correspond to the regions of the shell that are broken during the stagnation and post-stagnation phases. The post-stagnation x-ray image correlates well with the density profile, where the brightest regions in the image correspond to the shell locations where material is being ejected. Compared to the deceleration and stagnation phases, the structures in the post-stagnation x-ray image are spatially larger and are easier to analyze.

Simulations predict that the coupling of the laser energy to the target can be increased by lowering R_b/R_t. This change, however, also increases beam-overlap perturbations that cause distortions in the dense shell and lead to shell breakup at stagnation. To diagnose the shell breakup, the x-ray self-emission from the implosions was recorded during the post-stagnation phase with a filtered 16-pinhole array imager and x-ray framing camera using an exposure time of ~40 ps. The figure below shows experimental images obtained in implosions with different R_b/R_t. A Fourier decomposition is applied to the outer peak signal of the images to diagnose the low- and mid-mode asymmetries in the implosion. The images and modal analysis show higher low- and mid-mode amplitudes for the implosion with $R_b/R_t \sim 0.77$ compared with the implosion with $R_b/R_t \sim 0.95$, which indicates a better hydrodynamic instability for the implosion with higher R_b/R_t.

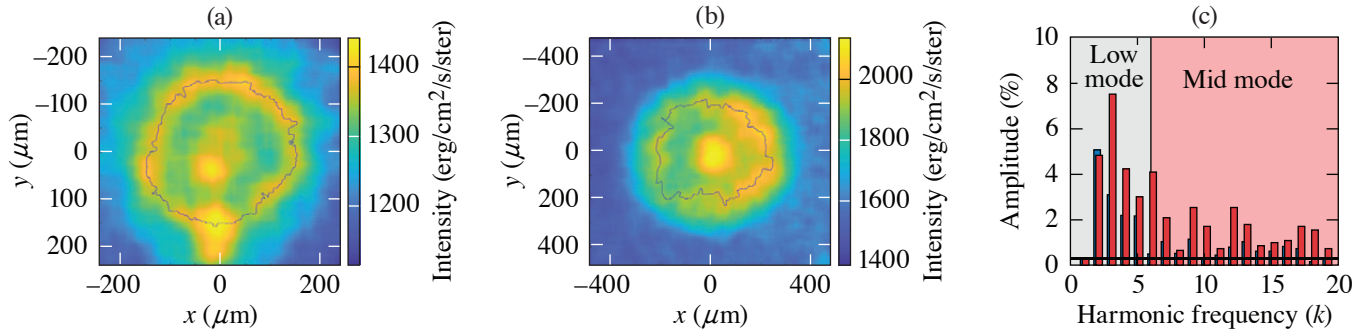

E30231JR

The work described in this volume includes current research at the Laboratory for Laser Energetics, which is supported by New York State Energy Research and Development Authority, the University of Rochester, the U.S. Department of Energy Office of Inertial Confinement Fusion under Cooperative Agreement No. DE-NA0003856, and other agencies.

Printed in the United States of America
Available from
National Technical Information Services
U.S. Department of Commerce
5285 Port Royal Road
Springfield, VA 22161
www.ntis.gov

For questions or comments, contact Nickolaos Savidis, Editor, Laboratory for Laser Energetics, 250 East River Road, Rochester, NY 14623-1299, (585) 275-3413.

www.lle.rochester.edu

UNIVERSITY OF ROCHESTER
LABORATORY FOR LASER ENERGETICS

Volume 172
July–September 2022
DOE/NA/3856-1775

LLE Review

Quarterly Report

UR LLE

Contents

Director's Remarks

C. Deeney

Director, Laboratory for Laser Energetics

The Laboratory for Laser Energetics (LLE) is funded primarily by the U.S. Department of Energy (DOE) National Nuclear Security Administration's (NNSA's) Office of Experimental Sciences Inertial Confinement Fusion (ICF) Program through a five-year Cooperative Agreement. The fiscal year ending September 2022 (FY22) comprised the fourth year of work under DOE/NNSA Cooperative Agreement No. DE-NA0003856. The Laboratory is also sponsored by the New York State Energy Research Development Authority and other federal agencies such as the DOE Office of Science and the National Science Foundation. I was honored to become the fifth Director of LLE, succeeding Dr. E. Michael Campbell who retired in March 2022.

The year 2022 was exciting for the National ICF Program and LLE. Ignition was achieved at the National Ignition Facility for the first time, producing more energy out of the implosion than the input laser energy to the target. LLE has made many contributions to the pursuit of ignition, including laser technologies, diagnostics, simulation capabilities, physics understanding, and student education. Groundbreaking for the construction of a new $42M addition to the LLE Complex (funded by the University of Rochester) occurred in August 2022. LLE submitted a proposal to renew the Cooperative Agreement with DOE/NNSA for FY24–FY28.

This report summarizes work conducted at LLE during FY22 that includes research on the ICF and High-Energy-Density (HED) science campaigns; laser, optical materials and advanced technology development; operation of the Omega Laser Facility for the ICF and HED campaigns, the National Laser Users' Facility, Laboratory Basic Science Program, and other external users, including the newly established LaserNetUS supported by the DOE Office of Fusion Energy Sciences; and programs focusing on the education of high school, undergraduate, and graduate students.

- The Omega Laser Facility conducted 2110 target shots in FY22, close to the average annual number of shots since FY14 with nearly 60% of the shots performed for external users. These experiments are critical to LLE and the national community achieving progress in the ICF/HED Physics mission, in advancing science, and in training students.

- Mission Impact: All of the completion criteria for the 15 NNSA Level II milestones were achieved.

- Scientific Output: One hundred and one technical manuscripts were published in peer-reviewed scientific journals during FY22.

- Sixteen Ph.D. degrees were conferred on graduate students during 2022 whose primary research was performed at the Laboratory either as students of the University of Rochester or as students of other collaborating user institutions who performed experiments or worked with scientists at the Omega Laser Facility.

- One University of Rochester Ph.D. graduate (Alison Christopherson) won the American Physical Society Division of Plasma Physics Marshall N. Rosenbluth Outstanding Doctoral Thesis Award.

- Radha Bahukutumbi, a Distinguished Scientist in the Theory Division, received the Leadership Award at the annual meeting of the Fusion Power Associates.

- Steve Ivancic, head of the Diagnostic Development and Integration Group, received a Defense Programs Award of Excellence from Lawrence Livermore National Laboratory.

Key technical highlights included:

- A series of high in-flight aspect ratio and high-velocity implosions on OMEGA produced yields between 2.6×10^{14} and 3.1×10^{14}, all above the previous yield record. The highest yield implosion, when corrected for ^{3}He buildup using statistical modeling, would have produced a yield of nearly 1 kJ, roughly the same as the shell kinetic energy. These direct-drive implosions enable Ph.D. research on ICF and open opportunities for future ICF optimization.

- Layered DT implosions with silicon dopants performed significantly better (higher yields) than comparable targets without dopants, confirming that the dopant suppresses imprint while only modestly increasing the shell adiabat via x-ray preheat.

- The Lawrence Livermore National Laboratory (LLNL)/LLE Neutron Sources collaboration conducted a polar-direct-drive exploding-pusher experiment at the National Ignition Facility that produced a record laser-direct-drive (LDD) yield of 1.6×10^{16} with a laser pulse of 1.6 MJ.

- The proof-of-concept for the LLE dynamic-shell ignition design, where pulse shaping dynamically creates a high-density shell with a DT wetted-foam target, was demonstrated using 3-D–printed foam capsules.

- Constrained by integrated implosion measurements, spectroscopic observables revealed that a density functional theory (DFT)-based kinetic model developed by LLE scientists (*VERITAS*) reproduces a majority of the emission and absorption features observed in experiments, while the traditional collisional-radiative-equilibrium treatment with *ad hoc* continuum lowering does not, suggesting that self-consistent treatment of dense plasma effects is needed at very high pressures.

- In collaboration with LLNL, LLE scientists showed that diamond can precipitate from twice-shocked CH polymers (e.g., ICF ablators) in the presence of oxygen, nitrogen, and chlorine.

- An LLE–LLNL team conclusively demonstrated species separation in the release of strongly shocked CH, finding that the hydrogen ions carry 10 to 100× more mass than the carbon ions to large distances, confirming a hypothesis developed to understand the seeds of instability growth in plastic ICF ablators.

- Based on x-ray diffraction measurements of sevenfold compressed sodium, a team from LLE and LLNL observed the *hP4* electride phase at a pressure of 480 GPa and a temperature of 3000 K (a regime where core electron overlap was thought to stabilize against this phase), indicating that electride formation is possible on nanosecond time scales at high temperatures.

- A decades-old discrepancy between theory and measurement on the shock-induced metallization of polystyrene was resolved using a new exchange correlation functional that properly captures the shock-induced dissociation of carbon and correctly predicts the band-gap closing behavior at 1 to 2 Mbar.

- New DFT calculations of Fe and Cr opacity at stellar interior densities and temperatures did not resolve the iron opacity "mystery" identified some time ago at Sandia National Laboratories' Z Pulsed Power Facility. The new calculations showed good agreement with the measured Cr opacity but did not agree with Z's measurements of the Fe opacity.

- Recent experiments showed that micron-scale x-ray radiography is possible for a wide range of flow visualizations at ultrahigh pressures using a new LLE-developed Fresnel zone plate imaging diagnostic.

- The first electron radiographs of a test object were acquired (in collaboration with Los Alamos National Laboratory) using a laser-plasma accelerator platform on OMEGA EP.

- The 13th Omega Laser Facility Users Group (OLUG) Workshop, held 27–29 April 2022 at LLE, attracted nearly 200 researchers from around the world.

- The 24th Topical Conference on High-Temperature Plasma Diagnostics (HTPD), hosted by LLE in Rochester, NY, attracted 370 registered participants. The HTPD conference showcased the latest in advanced instrumentation in the fields of magnetic confinement fusion, inertial confinement fusion, high-energy-density plasmas, space plasmas, astrophysics, and industrial applications.

- The 50th Anomalous Absorption Conference 2022 hosted and organized by LLE was held 5–10 June in Skytop, PA. Conference topics included theoretical and experimental studies in parametric instabilities, radiation hydrodynamics, particle acceleration, HED physics, short-pulse laser–matter interactions, and ICF.

- A classified report on the scope of applications within the Stockpile Stewardship Program for platforms that rely on LDD was submitted to the NNSA Office of Experimental Science, completing one of the milestones in the ICF five-year plan.

As the fifth Director working with the senior leadership team, we have set our vision to be "the leading academic institution advancing laser technologies, inertial confinement fusion, and high-energy-density science at scale." I hope you agree that FY22 met this vision.

In Brief

This volume of LLE Review 172 covers the period from July–September 2022. Articles appearing in this volume are the principal summarized results for long-form research articles. Readers seeking a more-detailed account of research activities are invited to seek out the primary materials appearing in print, detailed in the publications and presentations section at the end of this volume.

Highlights of research presented in this volume include:

- J. Baltazar *et al.* develop a technique to diagnose the low- and mid-mode asymmetries in the post-stagnation phase of a deuterium–tritium (DT) cryogenic implosion with the aim of relating the post-stagnation phase measurement to the shell breakup caused by an increase in beam overlap perturbations due to a lower R_b/R_t (p. 1).

- M. J. Rosenberg *et al.* analyze laser–plasma instability mitigation techniques for direct-drive inertial confinement fusion (ICF) by examining stimulated Raman scattering and two-plasmon–decay instabilities, assessing their dependence on density scale length and overlapping laser beam geometry critical to ICF ignition/fusion gain (p. 4).

- A. Shvydky *et al.* propose a new approach in producing uniform beam intensity distributions applied on a sphere for laser-direct-drive ICF system configurations based on mathematical spherical *t* designs to find optimal beam configurations, targeting a reduction of spherical harmonics and nonuniformity modes (p. 7).

- R. K. Follett *et al.* develop a series of test cases for validation of ray-based cross-beam energy transfer (CBET) models against wave-based calculations. Comparisons between various ray-based models show that an etalon integral field reconstruction with a coherent caustic correction and caustic gain truncation is the preferred ray-based CBET model, with equal to improved performance without increasing compuational cost (p. 10).

- T. R. Joshi *et al.* extend the application of the x-ray self-emission imaging technique to polar-direct-drive ICF implosions with cryogenically layered DT targets on OMEGA, diagnosing in-flight asymmetries (p. 13).

- J. R. Davies, P. V. Heuer, and A. F. A. Bott develop an electrostatic particle-in-cell (PIC) algorithm that was compared to algorithms for charged-particle radiography and shadowgraphy used in laser-plasma experiments, deducing a Monge–Ampère code applied as first order, and a PIC code if the Monge–Ampère code fails or requires a subsequent, more-accurate inversion (p. 18).

- A. L. Milder *et al.* present first measurements of the threshold and linear growth rate of the return-current instability driven by electron heat flux, where characterization of the plasma conditions show that the return-current instability occurs concurrently with nonlocal transport (p. 22).

- G. Bruhaug *et al.* present a method to determine the resolution for laser-plasma acceleration electron radiography that include accounting for drive laser image distortions, quantifying plasma-generated electric fields in laser-ablated targets by measuring electron radiography image feature sizes, and estimating field strength needed to produce those features (p. 25).

- V. V. Karasiev *et al.* apply first-principles density functional theory to calculate optical properties (mass-absorption coefficient and opacity) of Cr and Fe at stellar interior temperatures to explore whether *ab initio* calculations can resolve the disagreement between previous atomic physics calculations and measured data (p. 28).

- D. A. Chin *et al.* designed and built two extended x-ray absorption fine structure (EXAFS) flat crystal x-ray spectrometers (EFX's) for high-resolution x-ray spectroscopy over a large energy range with flexible, on-shot energy dispersion calibration capabilities, enabling x-ray absorption near-edge spectroscopy measurements to be made on OMEGA (p. 31).

- J. Cheng *et al.* demonstrate a promising candidate for ultrafast optical/near-infrared to x-ray radiation detector applications with a photodetector sensitive to both optical and x-ray picosecond pulses based on in-house grown cadmium magnesium telluride (Cd,Mg) Te single crystal (p. 34).
- D. Ramsey *et al.* derive exact solutions to Maxwell's equations for the electromagnetic fields of a constant-velocity flying-focus pulse and identified small differences to the paraxial solutions for a wide range of parameters, justifying paraxial solutions for many applications in many regimes, such as a spatiotemporal pulse-shaping technique (p. 38).
- K. R. P. Kafka, T. Z. Kosc, and S. G. Demos assess operational performance limits of optics and aspects required for the development of improved optic designs/reliable operational fluence limits for ultrashort optical performance characterization beyond the standard laser-induced–damage threshold testing system specifications that only characterize the damage-initiation threshold (p. 41).
- E. P. Power *et al*. design, simulate, fabricate, and test a prototype flow-cell, integrated-cooling substrate built using cordierite ceramic and demonstrate average power handling up to 3.88-W/cm^2 absorbed power density with 54-nm peak-to-valley deformation in a sub-aperture test, with a <30 s observed mechanical stabilization time scale (p. 44).
- M. Romo-Gonzalez and R. Boni test a zero *B*-integral pellicle beam splitter composed of uncoated nitrocellulose, having a maximum reflectivity of ∼30% with negligible absorption in the near-infrared (p. 48).
- L. J. Waxer, J. Bromage, and B. E. Kruschwitz provide an overview of the various topics they wrote in the SPIE Spotlight series e-book on petawatt laser systems, introducing the reader to the laser science and technology underpinning petawatt laser systems and technological advances required for state-of-the-art high-intensity laser performance (p. 51).
- R. S. Craxton summarizes the 33rd LLE Summer High School Research Program (p. 54). Sixteen students were invited from Rochester-area high schools to participate in the lab's state-of-the art research environment.
- T. J. Kessler, M. Romo-Gonzalez, and R. Ghosh report on the Broad Exposure to Science and Technology (BEST) Program, a research program designed to engage teachers and students from historically marginalized experiences in various aspects of science and technology that support LLE's laser science and applications research (p. 57).
- J. Puth *et al.* summarize operations of the Omega Laser Facility during the fourth quarter of FY22 (p. 62).
- M. J. Shoup III highlights the groundbreaking and early days of the LLE building expansion (p. 64).
- This volume concludes with the FY22 Laser Facility Report, the FY22 Education Summary, and overviews of the National Laser Users' Facility, Laboratory Basic Science, and LaserNetUS Programs.

Nickolaos Savidis
Editor

Diagnosing Low-Mode ($\ell < 6$) and Mid-Mode ($6 \leq \ell \leq 60$) Asymmetries in the Post-Stagnation Phase of Cryogenic Implosions on OMEGA

J. Baltazar,[1,2] R. Betti,[1,2] K. Churnetski,[1,2] V. Gopalaswamy,[1] J. P. Knauer,[1] D. Patel,[1] H. G. Rinderknecht,[1] R. C. Shah,[1] C. Stoeckl,[1] C. A. Williams,[1] and S. P. Regan[1,2]

[1]Laboratory for Laser Energetics, University of Rochester
[2]Department of Mechanical Engineering, University of Rochester

In order to achieve ignition-relevant conditions in direct-drive inertial confinement fusion (ICF) implosions, the hot spot must reach pressures exceeding ~100 Gbar (Ref. 1). Simulations of 1-D implosions predict that these pressures can be achieved by driving low- ($\alpha < 3$) to mid-adiabat ($\alpha > 4$) implosions, where mid-adiabat implosions require mitigation of cross-beam energy transfer (CBET) losses.[2] The performance of low-adiabat implosions is sensitive to ablation-surface modulations caused by target features and laser nonuniformity imprint, which becomes the seed for the Rayleigh–Taylor instability.[3] On some high-performance implosions[4] with $\alpha > 4$, CBET losses are mitigated by reducing the laser beam size, which reduces the ratio of the beam radius (R_b) to the initial target radius (R_t) below one and increases the laser coupling. Simulations predict that by increasing the on-target laser coupling, the hydrodynamic efficiency increases. However, this change also increases beam-overlap perturbations that causes distortions in the dense shell and leads to shell breakup at stagnation.[2] An interesting approach to diagnose the shell breakup was inspired by previous work at Lawrence Livermore National Laboratory,[5] where low modes were diagnosed by self-emission imaging in the explosion phase of DT cryogenic indirectly driven ICF implosions that were not diagnosed in the stagnation phase.

In this study, x-ray self-emission from the implosions is recorded with a filtered 16-pinhole array imager and an x-ray framing camera (XRFC) to produce gated-images of x-ray emission.[3,6] A 0.3-μm aluminum and 1-μm polypropylene filter is employed to record x rays with energies >800 eV. The framing camera is timed to record images in the explosion phase. A 3-D *ASTER*[2] simulation of a DT cryogenic implosion has been post-processed through *Spect3D*[7] to produce synthetic x-ray images that are analyzed to investigate x-ray signatures of the shell breakup. The synthetic images are integrated over 40 ps and blurred with 20-μm FWHM to match the instrument response function of the XRFC. The 3-D *ASTER* simulation was run with phase plates to produce a smaller beam radius compared to the radius of the target ($R_b/R_t \sim 0.75$) The evolution of the density, temperature, and emission from the deceleration phase to the post-stagnation (explosion) phase is shown in Fig. 1. The reduced R_b/R_t leads to an increase in beam-mode perturbations that evolve throughout the deceleration, stagnation, and explosion phase, where in the explosion phase the perturbed features are more apparent compared to the previous stages.

Figure 2 shows experimental images obtained in implosion using setups with different R_b/R_t. A Fourier decomposition is applied to the outer peak signal of the images to diagnose the low- and mid-mode asymmetries in the implosion. The images are first mapped onto a radius and angle coordinate system, where the radius is the distance from the center and the angle corresponds with the angle with respect to the x axis. The modal analysis for two implosions with different R_b/R_t is shown in Fig. 2(c). The implosion with $R_b/R_t \sim 0.77$ shows higher low- and mid-mode amplitudes compared with the implosion with $R_b/R_t \sim 0.95$. At a larger R_b/R_t, more beams overlap at the target surface, which leads to a more-uniform laser-intensity profile, less hydro instability seeds in the low/mid spatial modes, and lower measured mode amplitudes.

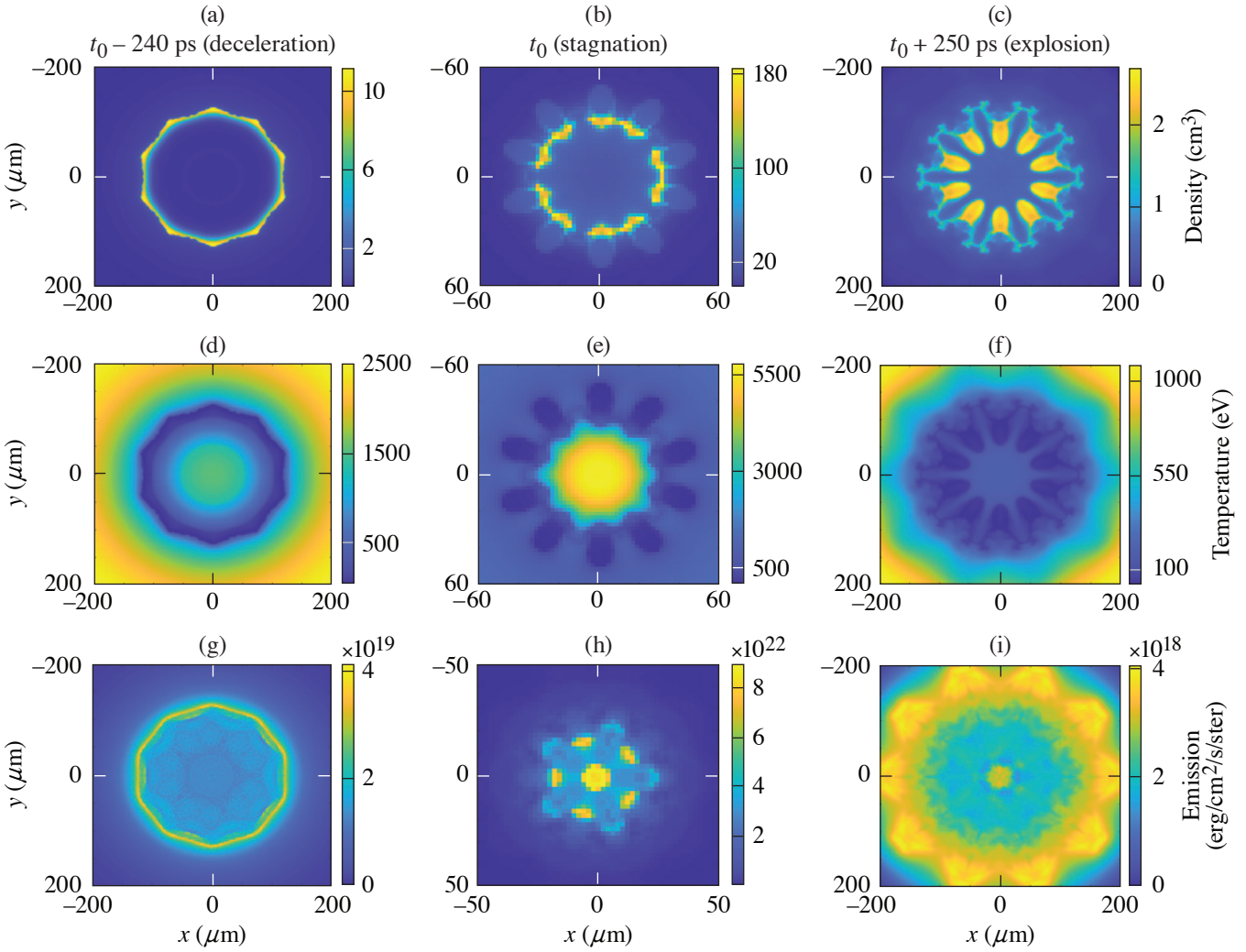

Figure 1
Evolution of the [(a)–(c)] density, [(d)–(f)] temperature, and [(g)–(i)] x-ray emission during the deceleration, stagnation, and explosion phases of a cryogenic DT implosion with a $R_b/R_t \sim 0.75$ (3-D *ASTER* simulation). The low-density regions in the shell in the deceleration phase correspond to the regions of the shell that are broken during the stagnation and post-stagnation phases. Therefore, the shell nonuniformity is seeded by the beam perturbation and leads to the breakup of the shell. The post-stagnation phase x-ray image resembles the density profile and the brightest regions in the image correspond to the broken shell locations where material is being ejected. Compared to the deceleration and stagnation phase, the signature in the post-stagnation phase x-ray measurement is spatially larger and is easier to analyze.

In conclusion, a technique was developed to diagnose the low- and mid-mode asymmetries in the explosion phase of a DT cryogenic implosion. This technique is developed with the aim of relating the explosion phase measurement to the shell breakup caused by an increase in beam overlap perturbations due to a lower R_b/R_t. An R_b/R_t sensitivity analysis from explosion phase measurements on OMEGA shows that the mid-mode rms value increases as the R_b/R_t value decreases, which is expected due to an increase in nonuniformity from the reduced beam overlap. A Monte Carlo simulation is underway to determine the error in the measurements and to guide the necessary changes in experimental setup to obtain better measurements.

This material is based upon work supported by the Department of Energy National Nuclear Security Administration under Award Number DE-NA0003856, the University of Rochester, and the New York State Energy Research and Development Authority.

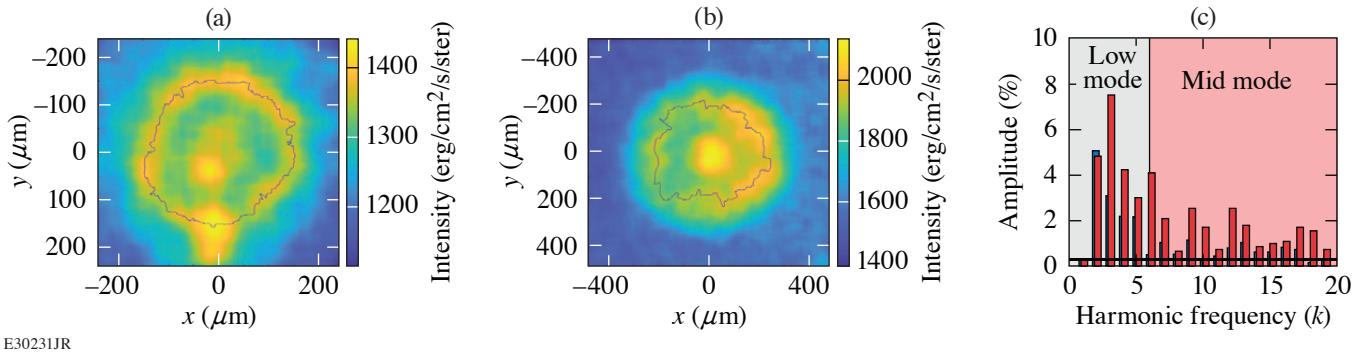

Figure 2
Experimental measurements for implosions with an R_b/R_t of (a) 0.95 and (b) 0.77. (c) The mode spectrum is plotted for both implosions [red is the analysis for the image shown in (a) and blue is the analysis for the image shown in (b)] and shows higher low- and mid-modes for the implosion with a lower R_b/R_t.

1. V. N. Goncharov *et al.*, Phys. Plasmas **21**, 056315 (2014).
2. I. V. Igumenshchev *et al.*, Phys. Plasmas **23**, 052702 (2016).
3. S. X. Hu *et al.*, Phys. Plasmas **23**, 102701 (2016).
4. V. Gopalaswamy *et al.*, Nature **565**, 581 (2019); A. Lees *et al.*, Phys. Rev. Lett. **127**, 105001 (2021).
5. A. Pak *et al.*, Phys. Plasmas **20**, 056315 (2013).
6. D. T. Michel *et al.*, Rev. Sci. Instrum. **83**, 10E530 (2012).
7. Prism Computational Sciences, Inc., Madison, WI 53711.

Effect of Overlapping Laser Beams and Density Scale Length in Laser–Plasma Instability Experiments on OMEGA EP

M. J. Rosenberg,[1] A. A. Solodov,[1] J. F. Myatt,[2] S. Hironaka,[2] J. Sivajeyan,[2] R. K. Follett,[1] T. Filkins,[1] A. V. Maximov,[1] C. Ren,[1,3,4] S. Cao,[1,3] P. Michel,[5] M. S. Wei,[1] J. P. Palastro,[1] R. H. H. Scott,[6] K. Glize,[6] and S. P. Regan[1]

[1]Laboratory for Laser Energetics, University of Rochester
[2]Department of Electrical and Computer Engineering, University of Alberta
3Department of Mechanical Engineering, University of Rochester
[4]Department of Physics and Astronomy, University of Rochester
[5]Lawrence Livermore National Laboratory
[6]Central Laser Facility, STFC Rutherford Appleton Laboratory

Laser–plasma instabilities (LPI's) are a concern in inertial confinement fusion (ICF) experiments because of the reduction in laser energy and potential generation of hot electrons, which can limit compression of the imploding capsule. Stimulated Raman scattering (SRS) and two-plasmon decay (TPD) can occur at densities at and below the quarter-critical density of the laser [$n_e = n_c/4$, where n_e is the electron density and n_c is the critical density for the laser wavelength λ_0 (in μm) (with $n_c \approx 1.1 \times 10^{21}\ \lambda_0^{-2}$ cm^{-3}), and have been observed at ICF-relevant intensities. Understanding these instabilities and their dependence on density scale length and overlapping laser beam geometry is critical to the pursuit of ICF ignition and fusion gain.

Planar- and spherical-geometry experiments were conducted on OMEGA EP to systematically explore SRS and TPD at scale lengths intermediate between previous experiments, at shorter scale length on OMEGA and longer scale length at the National Ignition Facility (NIF), and with different overlapped laser geometry. Solid 700-μm-diam CH spheres and 250-μm-thick CH slabs were irradiated with one or four beams and 750-μm spot size or with one beam and a 400-μm spot in a 2-ns square pulse or 4-ns ramp pulse with total laser energy of 8.2 to 9.3 kJ.

Figure 1 shows the 2-D *DRACO*-simulated quarter-critical density scale length, temperature, intensity, and threshold parameters for SRS and TPD for four-beam planar [Figs. 1(a)–1(d)] and spherical experiments [Figs. 1(e)–1(h)] with 750-μm phase plates and a 2-ns square pulse. Planar four-beam experiments were predicted to reach density scale lengths on axis of around 300 μm, electron temperatures of 2.8 keV, and overlapped laser intensities of 8×10^{14} W/cm^2. In contrast, four-beam spherical experiments were predicted to reach scale lengths of only 150 μm and similar electron temperatures (2.7 keV) and overlapped laser intensities (8.5×10^{14} W/cm^2). Planar one-beam experiments with the 750-μm spot had reduced intensity, temperature, and scale length, while one-beam experiments with the 400-μm spot size had a 190-μm scale length and laser intensity (4×10^{14} W/cm^2) between the 750-μm one-beam and four-beam experiments.

Time-resolved scattered-light spectra between wavelengths of 400 and 750 nm were measured for a variety of experiments driven by the 2-ns square pulse, as shown in Fig. 2. TPD is evident in a doublet feature corresponding to half-harmonic ($\omega/2$) emission around 702 nm, while SRS appears as a singlet red-shifted $\omega/2$ feature from absolute backscatter at quarter-critical density or as a broad-wavelength feature <680 nm generated in the underdense region. TPD is most prominent in the four-beam planar and spherical experiments, while SRS is generally favored in one-beam experiments, especially at high intensity with the small distributed phase plates (DPP's).

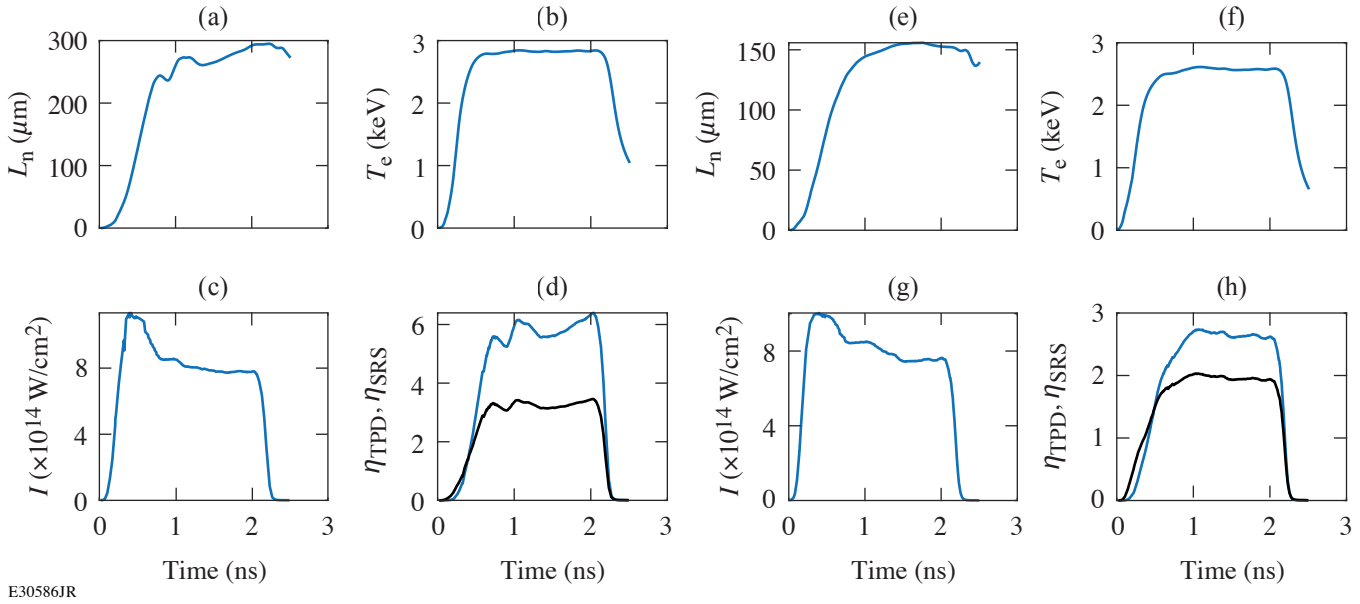

Figure 1
Two-dimensional *DRACO*-simulated plasma conditions at the quarter-critical density along the axis of symmetry for [(a)–(d)] a planar experiment and [(e)–(i)] a spherical experiment, driven by four beams in a 2-ns square pulse. The [(a),(e)] density scale length, [(b),(f)] electron temperature, [(c),(g)] overlapped laser intensity, and [(d),(h)] SRS (blue curves) and TPD (black curves) threshold parameters η are shown.

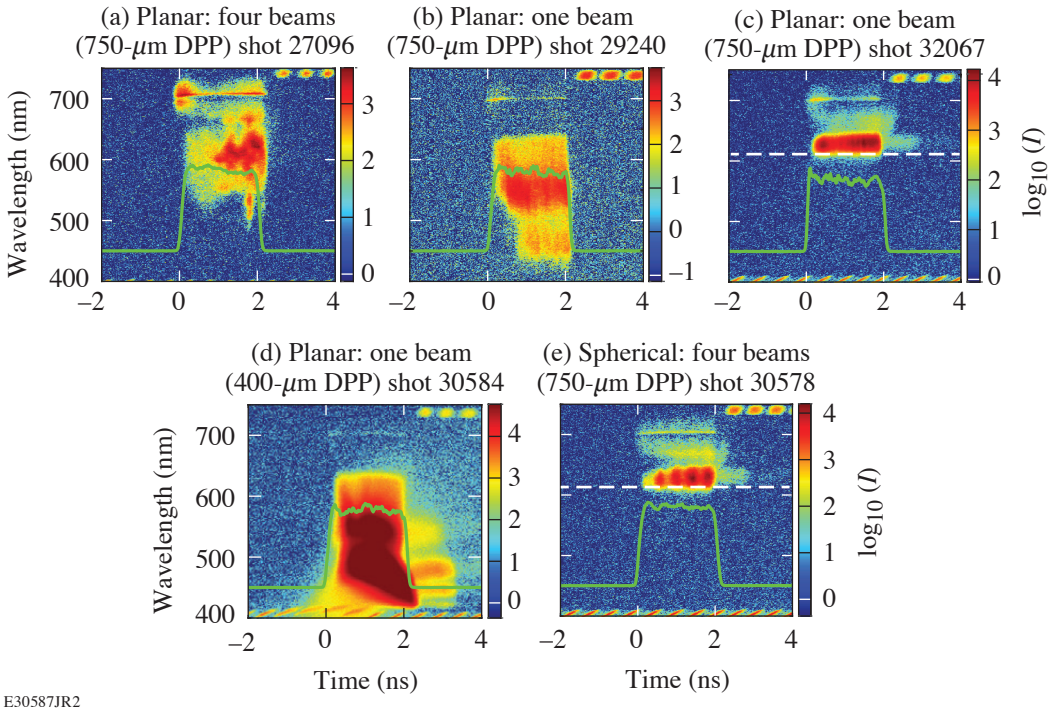

Figure 2
Measured time-resolved scattered-light spectra for experiments with a 2-ns square pulse (green line) and (a) a planar target irradiated by four beams, [(b),(c)] a planar target irradiated with one beam with a 750-μm spot size, (d) a planar target irradiated by one beam with a 400-μm spot size, and (e) a 700-μm-diam spherical target irradiated by four beams. [(c),(e)] The dashed white line represents the 630-nm cutoff of a long-pass filter, with (b) showing data from a nominally identical experiment as (c), but without the long-pass filter. The green line represents the laser pulse. The signal is strongly saturated in the 450- to 550-nm range in (d). Different neutral density filters and sub-aperture backscatter diagnostic throughput for each shot limits comparison of absolute signal levels.

Comparison to previous experiments on OMEGA[1] and the NIF[2] elucidate the effect of scale length and single-beam versus overlapped laser intensity on the prevalence of SRS and TPD. Typical OMEGA 60-beam spherical experiments at ∼150-mm scale length and low ($<10^{14}$ W/cm^2) single-beam intensity show evidence only of TPD and not SRS. Planar and spherical experiments at ∼400- to 600-μm scale length on the NIF are dominated by SRS and show negligible TPD. In combination with these experiments on OMEGA EP, it is evident that shorter density scale lengths and lower single-beam intensities (at sufficient overlapped intensity) are relatively favorable for TPD, while longer density scale lengths and higher single-beam intensities are relatively more favorable for SRS. These results are generally consistent with absolute TPD and SRS threshold considerations and the prevailing theory that TPD is more of a multibeam instability than SRS. This work will contribute to LPI mitigation techniques for direct-drive ICF.

This material is based upon work supported by the Department of Energy National Nuclear Security Administration under Award Number DE-NA0003856, the University of Rochester, and the New York State Energy Research and Development Authority.

1. W. Seka *et al*., Phys. Plasmas **16**, 052701 (2009)
2. M. J. Rosenberg *et al*., Phys. Rev. Lett. **120**, 055001 (2018); M. J. Rosenberg *et al*., Phys. Plasmas **27**, 042705 (2020).

Optimization of Irradiation Configuration Using Spherical *t* Designs for Laser-Direct-Drive Inertial Confinement Fusion

A. Shvydky, W. Trickey, A. V. Maximov, I. V. Igumenshchev, P. W. McKenty, and V. N. Goncharov

Laboratory for Laser Energetics, University of Rochester

In laser-direct-drive inertial confinement fusion (ICF), a cryogenically cooled spherical shell of deuterium–tritium (DT) fuel covered with a plastic layer on the outside is irradiated by a number of laser beams. The laser irradiation ablates the outer plastic (ablator) layer, compressing the fuel to reach ignition conditions.[1–3] Because of the finite number of beams (e.g., 60 on the OMEGA Laser System[4]) the laser irradiation nonuniformity on the target surface leads to a nonuniform shell compression and reduction in the implosion performance.

The beam-overlap uniformity improves with increasing the number of beams N. Optimization of beam port locations to minimize drive asymmetries for a given number of beams is an important consideration in designing an ICF implosion facility. There have been two basic methodologies of obtaining beam configurations presented in literature. One is based on either augmenting or composing together regular polyhedrons.[4,5] Advantages of this method include a symmetric intensity distribution with minimized nonuniformity for a few select values of N. A disadvantage is the lack of a systematic extension to an arbitrary N. The other method is the charged-particle method, which uses a system of N particles constrained to a sphere that repel each other with a coulomb force (or another distance-dependent force). The beam configurations are chosen to correspond to particle configurations that minimize the potential energy.[6–8] The advantage of the method is its simplicity in obtaining beam configurations for arbitrary N. The disadvantage is a slow decay of nonuniformity with the number of beams as, e.g., $1\sqrt{N}$ in Ref. 8. Neither of the above methods offer a way of finding beam configurations that simultaneously eliminate spherical harmonic modes below a certain number, which has been recognized as an important strategy in designing the irradiation system.[5]

In this summary, we propose new beam configurations based on spherical t designs, which are studied in the area of mathematics known as spherical designs.[9] New configurations have the advantage of combining the following properties: all of the nonuniformity modes with $\ell \leq t$ are zero, nonuniformity amplitudes decrease strongly with the number of beams, and intensity distribution on spherical targets exhibit symmetric patterns. Computational methods developed in the field of spherical designs (see, e.g., Refs. 10 and 11) offer a systematic approach of obtaining such configurations for any number of beams[10] feasible for a direct-drive ICF facility.

The beam configuration of the OMEGA Laser System[4] is practically a 60-beam 9-design (a spherical t design with $t = 9$). It has all $\ell \leq 9$ exactly equal to zero, except for mode 6, which is close to zero. OMEGA is not a regular truncated icosahedron "soccer ball," which is only a 5-design, but rather a "stretched soccer ball" whose hexagonal faces have unequal sides A and B with the stretch factor $A/B = 1.2$ [see Fig. 1(a)]. The ratio $A/B = 1.21$ is quoted in Ref. 5 to eliminate mode $\ell = 6$ in the stretched soccer ball configuration. Values of the stretch factor in both OMEGA and Ref. 5 are within 0.5% from the exact value $A/B = 1.205285...$ that can be calculated following the method from Ref. 12, where it was recognized that the stretched soccer ball with the optimal stretch factor is a better approximation for a sphere than the regular soccer ball.

Remarkably, a 10-design exists for a set of 60 points,[13] which we will call $T60$. The $T60$ configuration eliminates ℓ modes up to and including mode 10 and is shown in Fig. 1(b) along with the $M60$ configuration [Fig. 1(c)] obtained in Ref. 6 using the charged-particle method. Although $T60$ has [3,3]+ symmetry group and is the union of five snub tetrahedrons,[13] there are no

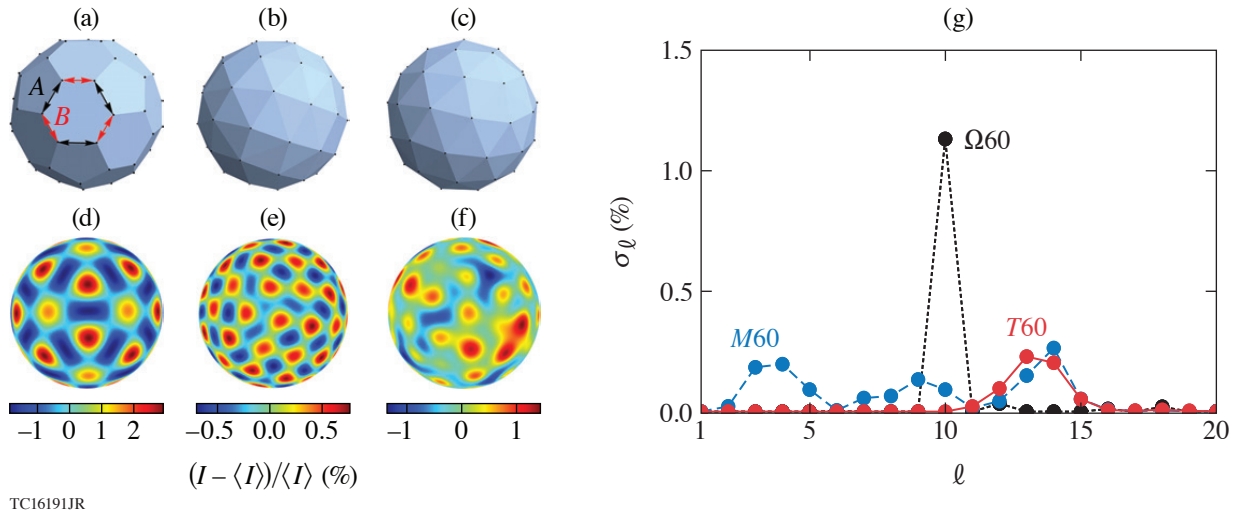

Figure 1
Beam configurations of (a) OMEGA, (b) *T*60, and (c) *M*60. Absorbed intensity distributions for (d) OMEGA, (e) *T*60, and (f) *M*60 configurations. (g) Plot of rms nonuniformity σ_ℓ as a function of mode number ℓ for OMEGA (black curve), *T*60, (red curve), and *M*60 (blue curve) configurations.

visually discernible symmetries in *T*60 point locations (much like in *M*60) in comparison to the aesthetically pleasing OMEGA laser. Figures 1(d)–1(f) show the intensity distributions produced by 60 laser beams from the OMEGA, *T*60, and *M*60 configurations, respectively. As an example, for Fig. 1, the beams were chosen to have the following profiles,

$$I_a(\theta) = I_0 \exp\left[-(\sin\theta/0.635)^{4.19}\right] \cdot \max(\cos\theta, 0), \tag{1}$$

which correspond to profiles produced by SG5-650 phase plates[14] on 450-μm-diam targets on the OMEGA Laser System. Similar to OMEGA, *T*60 produces a symmetric illumination pattern [compare Figs. 1(d) and 1(e)], while *M*60 produces less-regular illumination pattern [see Fig. 1(f)]. Out of the three configurations, the 10-design configuration produces the lowest intensity variation amplitude. Figure 1(g) shows the ℓ-mode spectra, σ_ℓ versus ℓ, corresponding to configurations in Figs. 1(a)–1(c). One can see dominant mode 10 and zero modes $\ell < 10$ for OMEGA. *M*60 has significant amplitude in a broad range of modes from $\ell = 2$ to $\ell = 14$. *T*60 has modes $\ell =$ (11 to 15) with amplitudes that are similar to that of *M*60 but, as expected, has zero modes $\ell < 11$.

Future direct-drive ICF laser systems will look to improve uniformity, which means increasing t in t-design configurations using the least number of beams N. Finding t designs with the smallest N for a given t happens to be one of the main problems in spherical design theory. It was conjectured that the spherical t designs exist for any t and require at least number of points $N \approx (1/2)t^2$ (see Ref. 13), where t designs are listed for every $N \leq 100$. The authors' website in Ref. 13 also contains point coordinates for t designs when $N = 12m$, $m = 1,2,3...$ with the number of points up to $N = 240$ and $t = 21$. Below, we will use these designs as an example. It is worth noting that numerical methods have been developed that make it possible to calculate t designs with $t \leq 1000$ and corresponding $N \leq 10^6$ (see, e.g., Ref. 10).

Figures 2(a)–2(d) show the intensity distribution for four $N = 12m$ spherical t designs with $t = 11$, 13, 16, and 21 and $N = 72$, 96, 144, and 240, which we call *T*72, *T*96, *T*144, and *T*240, respectively. Similar to *T*60, the $N = 12m$ configurations with a higher number of beams have intrinsic symmetry groups and show symmetric intensity distribution patterns. Note a dramatic reduction of the nonuniformity amplitude with t. Figure 2(e) shows ℓ-mode spectra σ_ℓ for the five $N = 12m$ t designs, four designs from Figs. 2(a)–2(d), and *T*60 from Fig. 1(b). One can see zero amplitude of modes $\ell \leq t$ and a sharp decrease of the σ_ℓ for large ℓ for all t designs.

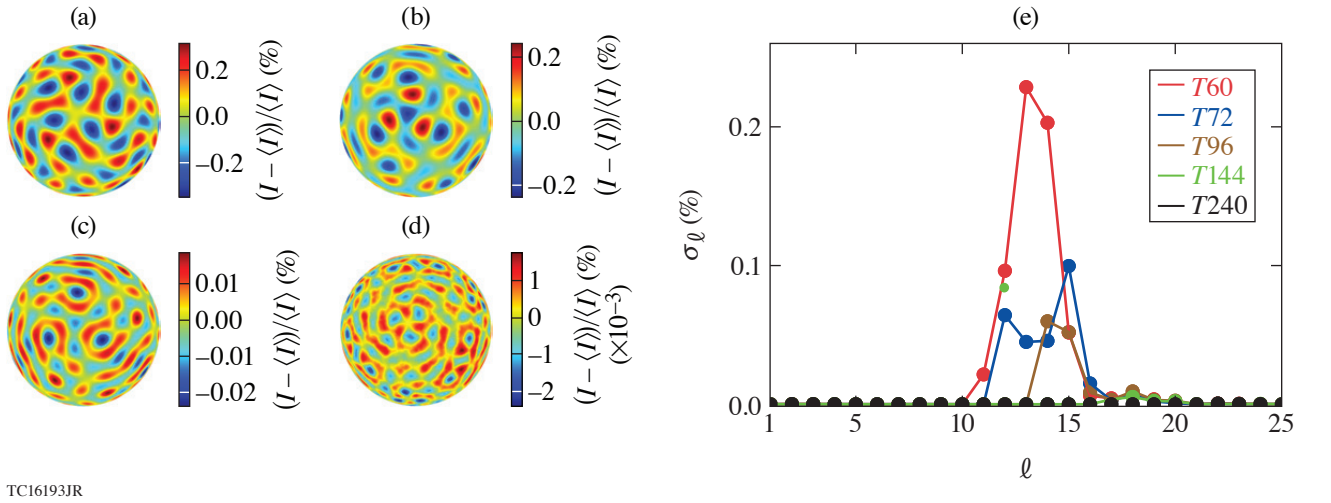

Figure 2
Intensity distributions for (a) $T72$, (b) $T96$, (c) $T144$, and (d) $T240$ configurations. (e) Plot of rms nonuniformity σ_ℓ as a function of mode number ℓ for $T60$ (red), $T72$ (blue), $T96$ (brown), $T144$ (green), and $T240$ (black) configurations.

In this summary, we have proposed a new approach to systematically obtain beam configurations for laser-direct-drive ICF systems that are based on t designs from the area of mathematics known as spherical designs. The t-design beam configurations offer the following advantages: (a) they eliminate all nonuniformity modes $\ell \leq t$, where t increases with the number of beams as $\sim\sqrt{2N}$; (b) the rms nonuniformity drops rapidly with the number of beams as a high power of N or close to exponentially with N; and (c) t designs with intrinsic symmetries show symmetric intensity-distribution patterns (although, it may have only aesthetic benefits). We envision that future laser-direct-drive ICF facilities will use t-design beam configurations with a number of beams that will be determined by the nonuniformity requirements. As a final note, spherical t designs can be used, more generally, in applications where a uniformity of an action on a sphere applied at discrete points is required, e.g., a uniformity of pressure applied with a system of identical actuators.

Funding was provided by the ARPA-E BETHE Grant No. DEFOA-0002212. This material is based upon work supported by the Department of Energy National Nuclear Security Administration under Award No. DE-NA0003856, the University of Rochester, and the New York State Energy Research and Development Authority.

1. J. Nuckolls *et al.*, Nature **239**, 139 (1972).
2. J. D. Lindl, Phys. Plasmas **2**, 3933 (1995).
3. R. S. Craxton *et al.*, Phys. Plasmas **22**, 110501 (2015).
4. *LLE Review Quarterly Report* **39**, 113 (1989).
5. M. Murakami, Appl. Phys. Lett. **66**, 1587 (1995).
6. M. Murakami *et al.*, Phys. Plasmas **17**, 082702 (2010).
7. M. Murakami and D. Nishi, Matter Radiat. Extremes **2**, 55 (2017).
8. W. Trickey *et al.*, Front. Phys. **9**, 784258 (2021).
9. P. Delsarte, J. M. Goethals, and J. J. Seidel, Geom. Dedicata **6**, 363 (1977).
10. M. Gräf and D. Potts, Numer. Math. **119**, 699 (2011).
11. R. S. Womersley, in *Contemporary Computational Mathematics–A Celebration of the 80th Birthday of Ian Sloan*, edited by J. Dick, F. Y. Kuo, and H. Woźniakowski (Springer, Cham, 2018), pp. 1243–1285.
12. J. M. Goethals and J. J. Seidel, Nieuw Archief voor Wiskunde **XXIX**, 50 (1981).
13. R. H. Hardin and N. J. A. Sloane, Discrete Comput. Geom. **15**, 429 (1996).
14. W. Theobald *et al.*, Phys. Plasmas **29**, 012705 (2022).

Validation of Ray-Based Cross-Beam Energy Transfer Models

R. K. Follett,[1] A. Colaïtis,[2] D. Turnbull,[1] D. H. Froula,[1] and J. P. Palastro[1]

[1]Laboratory for Laser Energetics, University of Rochester
[2]Centre Lasers Intenses et Applications

This summary presents a series of comparisons between ray- and wave-based CBET calculations that highlight the essential physics that must be included in a ray-based CBET model. The comparison cases are designed to aid in the validation of ray-based CBET models by including precise input parameters and quantitative comparison metrics and/or wave-based field data.[1] The cases vary in complexity from simple 2-D two-beam interactions in a linear density gradient to 60 beams interacting in a 3-D spherical plasma profile. We have found that in all cases the most sophisticated algorithm (etalon integral field reconstruction[2] with a coherent caustic correction and caustic gain truncation[3]) performed at least as well as its more-simplistic counterparts without increasing the overall computational cost and should be the preferred algorithm for use in ray-based CBET codes. A particular emphasis is placed on energy conservation because ray-based CBET models typically do not conserve energy explicitly and require artificial correction. We show that the intrinsic lack of energy conservation inherent to ray-based algorithms significantly affects the accuracy and that artificially correcting energy-conservation errors can have a large impact on results.

In direct-drive inertial confinement fusion (ICF), a millimeter-scale spherical capsule is illuminated by symmetrically oriented laser beams.[4–6] The lasers ablate the outer layer of the capsule, which generates pressure to implode the fuel. In addition to depositing thermal energy in the ablator, the lasers can resonantly drive various laser–plasma instabilities (LPI's) that can degrade the quality of the implosion. One of the predominant LPI's that impacts ICF implosions is cross-beam energy transfer (CBET), where laser beams exchange energy through a ponderomotively driven ion-acoustic wave.[7,8] CBET reduces the overall laser absorption in direct-drive ICF because it tends to transfer energy from the incoming lasers to outgoing reflected/refracted light.

Many of the radiation-hydrodynamics codes used to design ICF implosions include CBET models, but implementation details vary significantly between codes and artificial multipliers are often required to reproduce experimental results.[2,3,8–16] One of the underlying reasons for the prevalence of artificial multipliers is that it is not clear what level of accuracy is even possible with ray-based codes because there are very few analytic results available for use as test cases. An excellent way to validate ray-based CBET models, however, is with wave-based calculations. Wave-based CBET models naturally include all of the physics that can only be approximately included in ray-based models. Due to the much higher computational cost, it is not currently possible to run 3-D wave-based CBET calculations at the scale of ICF experiments, but all of physics required for ray-based CBET models can be studied in subscale simulations.

The *LPSE* results are compared to ray-based results from two different codes. The first is a relatively simple test-oriented code that was developed in conjunction with *LPSE* for the specific purpose of making comparisons between ray-based CBET algorithms and *LPSE* results.[3] We also include results from the *IFRIIT*[2,13] laser deposition code implemented in 3-D *ASTER* (Ref. 17). *IFRIIT* provides an interesting comparison point because it implements some of the algorithms detailed in this summary for the electromagnetic-field calculation, while it differs significantly on other points—most notably on the use of inverse ray tracing versus forward ray tracing. Finally, it is an inline model, implying that contrary to the test-oriented ray-based code, it was formulated for speed while still being able to reproduce the *LPSE* results.

Figure 1 shows the laser absorption as a function of grid resolution for 2-D 16-beam simulations in an azimuthally symmetric plasma profile that is based on fits to a *LILAC* simulation of an OMEGA implosion. The various subfigures correspond to scaled versions of the original hydro profile ranging from 1/64th scale to full scale (S = 1/64 to S = 1). The various ray-based CBET models that were used are as follows: (1) "FL, no CGT" corresponds to field-limiter treatment of the caustic without caustic gain truncation (which leads to slow convergence); (2) "FL, no CC" corresponds to a field-limiter treatment of the caustic without using a coherent treatment of the fields in the caustic region (which leads to poor energy conservation); (3) "FL" corresponds to a field-limiter treatment with both CGT and a coherent caustic treatment; (4) "EI" corresponds to an etalon integral field reconstruction with both CGT and a coherent caustic treatment; (5) "*IFRIIT*" corresponds to results from the *IFRIIT* code that uses the same physical model as "EI" but with a different numerical implementation.

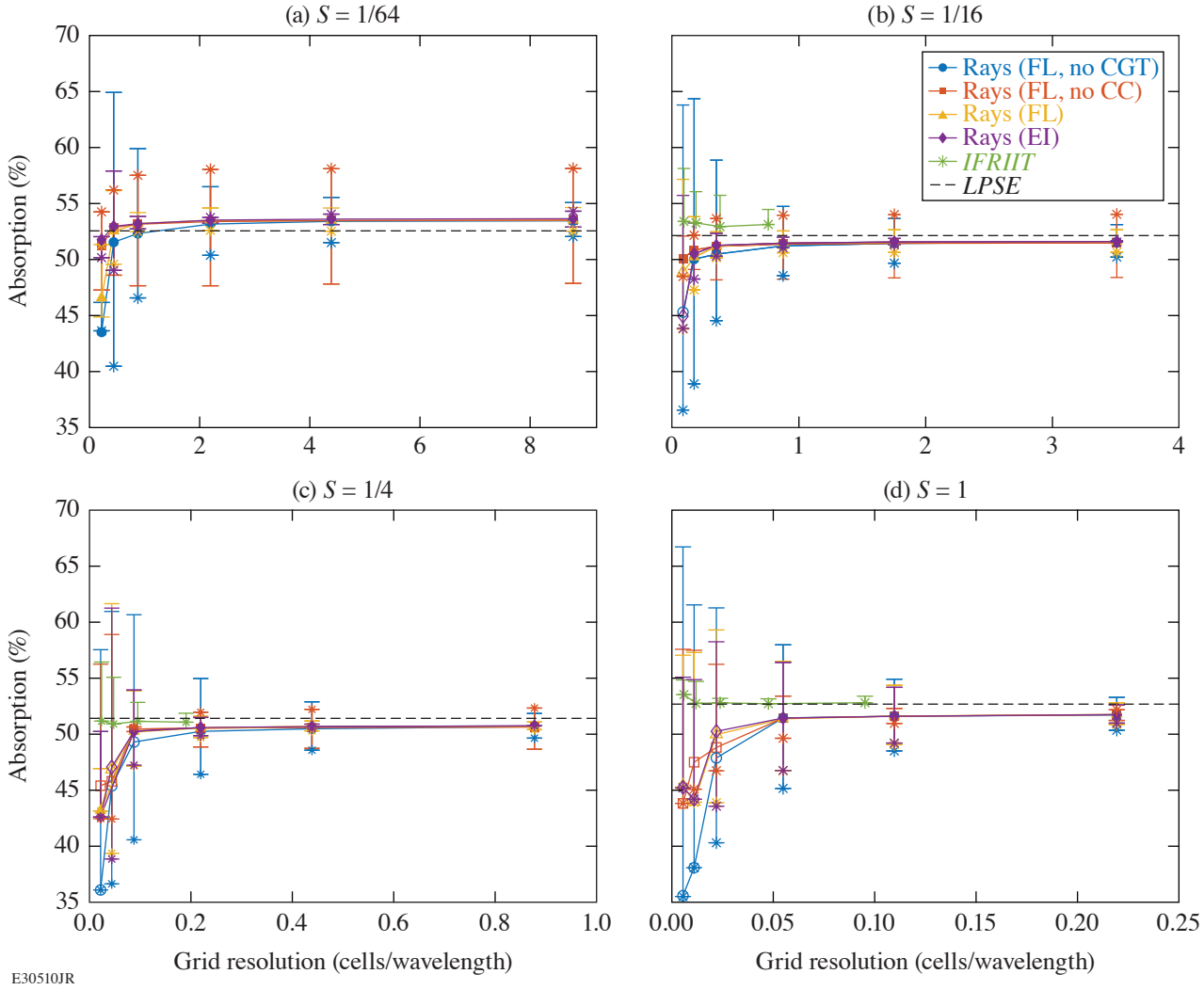

Figure 1
Laser absorption as a function of grid resolution for 16-beam 2-D simulations at (a) 1/64 scale, (b) 1/16 scale, (c) 1/4 scale, and (d) full scale. *LPSE* results are shown with horizontal black dashed lines. The stars represent the ray-based results without enforcing energy conservation, and the solid markers represent the energy-conserving results (open markers correspond to cases where energy conservation could not be achieved). The error bars show the size of the uncorrected energy-conservation error. The various ray-based approaches are FL without CGT (blue circles), FL without the coherent caustic correction (red squares), FL (yellow triangles), and EI (purple diamonds). The *IFRIIT* results are shown with green stars.

In all cases the converged ray-based results are in good agreement with the *LPSE* simulations ($\lesssim$1% difference in absorption). The ray-based results are plotted in a way that displays the absorption results and the energy-conservation properties on the same axes. Specifically, stars show the uncorrected absorption (energy conservation not enforced), and the solid markers show the absorption after enforcing energy conservation (open markers are used in cases where energy conservation could not be achieved). The range of the error bars corresponds to the range of absorption that could be achieved if all of the missing (extra) energy is added to (subtracted from) absorption or scattered (unabsorbed) light. Accordingly, any reasonable approach to enforcing energy conservation will result in an absorption within the error bar. Alternatively, a reasonable approach exists to enforcing energy conservation that would lead to any result between the error bars. An ideal algorithm would have the star on top of the solid marker (and vanishing error bounds), meaning that energy was conserved without any artificial correction. The results are plotted in this way because it is critically important to consider the impact of the somewhat arbitrary approach that is used to enforce energy-conservation ray-based CBET codes.

The "FL, no CC" model with $S = 1/64$ [Fig. 1(a)] provides a good example of why it is important to consider the uncorrected energy-conservation error. By simply comparing the converged solutions after correcting for energy conservation, the "FL, no CC" model gives the same result as the more-sophisticated models. However, the uncorrected energy-conservation error is greater than 10%, suggesting that the somewhat arbitrary choice of algorithm for enforcing energy conservation was a huge lever on the final result (the star being at the top of the error bar implies that extra energy was created). Conversely, the error bars using the EI method are much smaller ($\sim$1%), meaning that artificially enforcing energy conservation does not have a significant impact on those results. Note that the energy-conservation error (in the converged solution) tends to improve with increasing scale because a smaller fraction of the CBET is occurring in the caustic region. Achieving convergence at large scales can, however, be difficult because it becomes harder to resolve the caustics.

This material is based upon work supported by the Department of Energy National Nuclear Security Administration under Award Number DE-NA0003856, ARPA-E BETHE grant number DE-FOA-0002212, the University of Rochester, and the New York State Energy Research and Development Authority.

1. R. K. Follett, *LPSE* Data for Ray-Based CBET Test Cases (1.0.0) [Data set]. Zenodo (2022), Accessed 7 March 2023, http://dx.doi.org/10.5281/zenodo.6962934.
2. A. Colaïtis *et al.*, Phys. Plasmas **26**, 032301 (2019).
3. R. K. Follett *et al.*, Phys. Rev. E **98**, 043202 (2018).
4. J. Nuckolls *et al.*, Nature **239**, 139 (1972).
5. R. S. Craxton *et al.*, Phys. Plasmas **22**, 110501 (2015).
6. S. Atzeni and J. Meyer-ter-Vehn, *The Physics of Inertial Fusion: Beam Plasma Interaction, Hydrodynamics, Hot Dense Matter*, 1st ed., International Series of Monographs on Physics, Vol. 125 (Oxford University Press, Oxford, 2004).
7. C. J. Randall, J. R. Albritton, and J. J. Thomson, Phys. Fluids **24**, 1474 (1981).
8. P. Michel *et al.*, Phys. Plasmas **20**, 056308 (2013).
9. I. V. Igumenshchev *et al.*, Phys. Plasmas **19**, 056314 (2012).
10. A. Colaïtis *et al.*, Phys. Plasmas **23**, 032118 (2016).
11. J. A. Marozas *et al.*, Phys. Plasmas **25**, 056314 (2018).
12. A. Colaïtis *et al.*, Phys. Plasmas **25**, 033114 (2018).
13. A. Colaïtis *et al.*, J. Comput. Phys. **443**, 110537 (2021).
14. D. H. Edgell *et al.*, Phys. Plasmas **24**, 062706 (2017).
15. A. K. Davis *et al.*, Phys. Plasmas **23**, 056306 (2016).
16. D. J. Strozzi *et al.*, Phys. Rev. Lett. **118**, 025002 (2017).
17. I. V. Igumenshchev *et al.*, Phys. Plasmas **23**, 052702 (2016).

Diagnosis of the Imploding Shell Asymmetry in Polar-Direct-Drive Deuterium–Tritium Cryogenic Target Implosions on OMEGA

T. R. Joshi, R. C. Shah, W. Theobald, K. Churnetski, P. B. Radha, D. Cao, C. A. Thomas, J. Baltazar, and S. P. Regan

Laboratory for Laser Energetics, University of Rochester

The polar-direct-drive (PDD)[1–6] approach has been developed for performing laser-direct-drive inertial confinement fusion (ICF) experiments at the National Ignition Facility (NIF)[7] using the current configuration of laser beams customized for indirect-drive implosions. The NIF lacks beams near the equator for a symmetric illumination; therefore, the beams must be repointed to adequately irradiate the equator for direct-drive experiments.[8,9] The repointed beams have decreased energy coupling with the target, thereby requiring higher drive energies and unique pulse shapes to prevent reduced drive uniformity.[4] The irradiation nonuniformity caused by the PDD geometry reduces the implosion performance of OMEGA[10] ambient target implosions,[3,6] but it has never been evaluated in cryogenic target implosions. There is an ongoing effort on OMEGA to understand the hydrodynamic scaling of the best-performing symmetrically irradiated cryogenic target implosions,[11] as well as to study the impact of a PDD illumination geometry in order to improve our understanding of scaling from OMEGA to future NIF direct-drive cryogenic target implosions. The 40-beam PDD configuration on OMEGA provides a good approximation to the NIF PDD conditions.[1] However, differences remain in terms of the beams' angle of incidence, number of beams, number of rings, flexibility in laser pulse shaping, and laser smoothing.[4]

X-ray[2–4] radiography and self-emission imaging[12–14] techniques have been widely used to measure shell asymmetries and trajectories of imploded shells on OMEGA and the NIF. In this summary, we have extended the application of the x-ray self-emission imaging technique to PDD ICF implosions with cryogenically layered deuterium–tritium (DT) targets on OMEGA. The in-flight shell asymmetries were diagnosed at various times during the implosion, which were caused by the beam-pointing geometry and pre-imposed variations in the energy partition between the different groups of laser beams.

PDD ICF experiments with cryogenically layered DT targets were performed for the first time on OMEGA. The PDD illumination was achieved by using 40 of the 60 OMEGA[10] UV beams by switching off 20 beams around the equator. Figure 1(a) shows a schematic map of the OMEGA target chamber with the blue circles indicating the used beam ports. The 40 beams are grouped in three beam rings in the upper and lower hemisphere according to their polar angles. The beams were repointed to achieve the best possible illumination uniformity.[6] In each group of six rings, there were five, five, and ten laser beams, respectively. Figure 1(b) shows the beam pointing scheme, which was fixed during the experiment. The dashed lines indicate the repointing locations for the beams from the upper hemisphere. The beams from rings 1, 2, and 3 were repointed by 123 μm, 157 μm, and 219 μm, respectively. The displacement represents the distance from the target center along the direction perpendicular to the beam axis. The pointing condition was optimized with pre-shot *DRACO*[15] simulations.

All targets contained a DT ice shell overcoated by a thin plastic (CD) ablator layer, and the core of the shell was filled with DT vapor. The outer diameter of the CD shell was 767 μm and the thicknesses of the CD ablator and the DT ice layer were 6.2 μm and 33.5 μm, respectively. The laser pulse consisted of a picket that launched a shock controlling the shell adiabat ($\alpha \approx 4$, ratio of plasma pressure to the Thomas–Fermi pressure at peak density) and then gradually rose to a 1.4-ns dual-step main drive pulse [see Fig. 1(c)]. The total UV laser energy on target was 12.7$\pm$0.2 kJ, where the average was calculated for a set of five shots (three shots are discussed here) and the error represents the standard deviation. All 40 beams were outfitted with small-spot distributed phase plates (SG5-650),[16–18] polarization smoothing,[19] and 2-D smoothing by spectral dispersion[20] at 0.3-THz bandwidth and

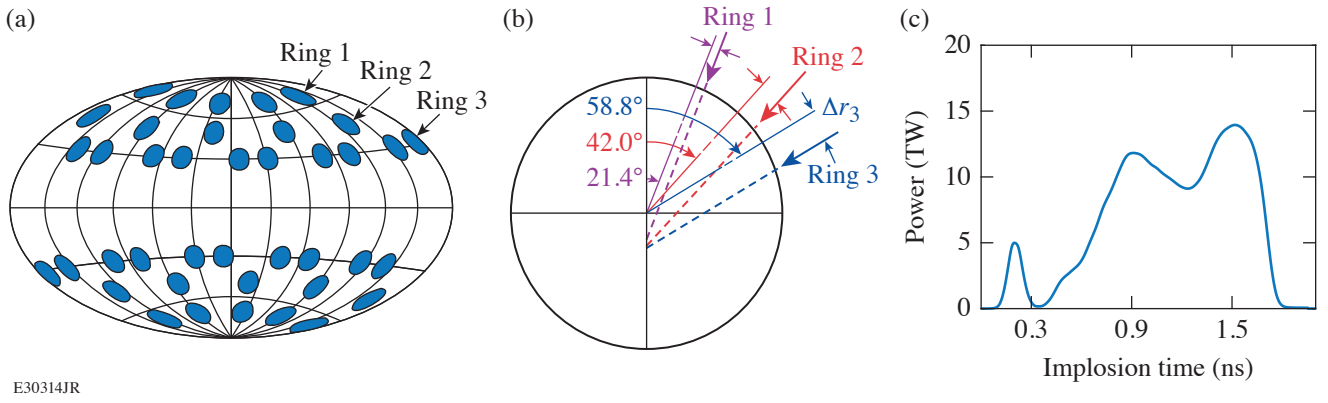

Figure 1
(a) Beam-port configuration for a PDD implosion on OMEGA. (b) Beam-pointing schemes and target geometry. The dashed lines show the shifted beams for OMEGA PDD geometry. (c) Pulse shape used for the implosions.

three-color cycles.[21,22] The partition of beam energies in rings 1 and 3 was varied while keeping the total laser energy constant. By denoting with ΔE_3 the change in energy of ring 3 (irradiating closer to the equator) and with ΔE_1 the change in energy of ring 1 (irradiating closer to the pole), the change in ring energy ratio is defined as $\Delta D = (\Delta E_3 - \Delta E_1)/E_{\text{tot}}$, where E_{tot} is the total energy on target. The nominal ring energy partition for a balanced drive ($\Delta D = 0$) is $E_1/E_{\text{tot}} = 0.25$, $E_2/E_{\text{tot}} = 0.25$, and $E_3 E_{\text{tot}} = 0.5$. Table I shows a summary of the discussed shots with drive imbalance condition, parameter ΔD, total laser energy on target, energy in each ring, and the measured neutron yield.

Table I: Summary of the shot number, drive imbalance condition, drive imbalance parameter, total laser energy on target, energy in each ring, and the measured neutron yield from DT fusion reactions.

Shot number	Drive	ΔD	E_{tot}(kJ)	E_1 (J)	E_2 (J)	E_3 (J)	Neutron yield (10^{13})
96575	Balanced	1.0%	12.7	3132	3155	6433	1.32±0.09
96578	Strong on poles	−4.6%	12.9	3522	3203	6173	1.93±0.07
96581	Stronger on equator	−10.6%	12.9	2560	3190	7158	1.34±0.09

The x-ray emission from the shell was recorded temporally and spatially resolved during the acceleration phase of the implosion with two pinhole cameras coupled to x-ray framing cameras in TIM-1 ($\theta = 63.44°$, $\varphi = 126°$ and in TIM-5 ($\theta = 101.81°$, $\varphi = 270°$), where TIM stands for ten-inch manipulator and θ and φ, respectively, are the polar angle and azimuthal angle coordinates of the OMEGA target chamber ports. An array of sixteen 15-μm-diam pinholes were used to produce 16 temporally resolved x-ray self-emission images[12,13,23] of the target on a four-strip x-ray framing camera.[24,25] Figure 2 shows x-ray self-emission images from the TIM-1 camera after the laser burned through the outer CD layer. The outer and inner rings in the images come from the emission at the CD–DT interface and the DT ice layer ablation front, respectively.[13] Here only the DT ablation front is analyzed because of its close proximity to the dense DT shell. The emission from the outer CD–DT interface layer is quickly diminishing in time due to the evaporation and rarefaction of the material in the plasma corona. Images in Figs. 2(a)–2(c) were acquired from shots 96578, 96575, and 96581, respectively, and at roughly the similar times relative to the start of their laser pulses. In shot 96578, the target is driven stronger on the poles with $\Delta D = -4.6\%$ and the shape of the DT ablation front in the measured image in Fig. 2(a) is oblate. In shot 96581, the target is driven stronger on the equator with $\Delta D = 10.6\%$ and the shape of the DT ablation front becomes prolate as shown in Fig. 2(c). In shot 96575, the drive was more balanced, and consequently a rounder shape can be seen in Fig. 2(b). Similar images were obtained from the TIM-5 camera. The shape of the DT ablation front was determined by tracking the peak x-ray emission in the inner ring with respect to the polar angle in the image plane.

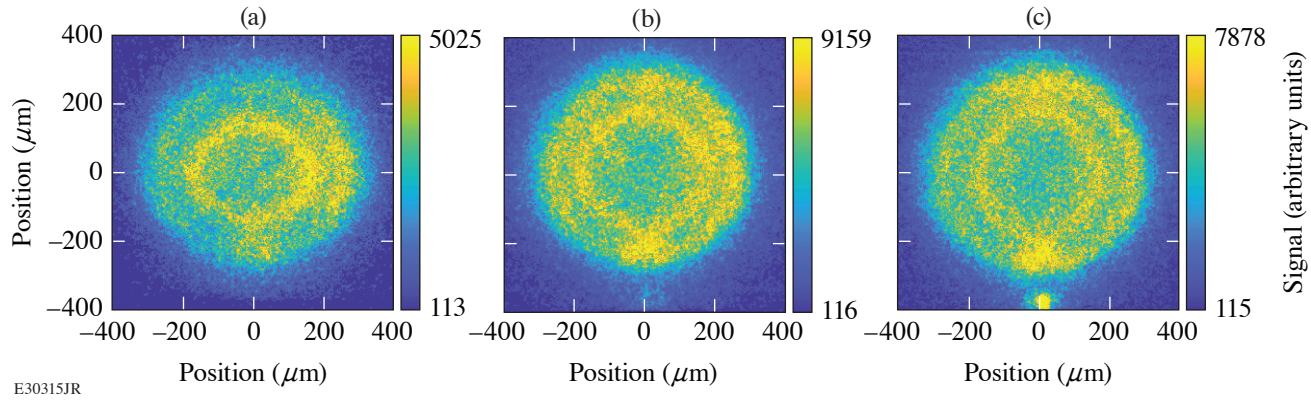

Figure 2
Measured x-ray self-emission images from three shots with different laser drive balance. Images from shots (a) 96578 ($\Delta D = -4.6\%$), (b) 96575 ($\Delta D = 1.0\%$), and (c) 96581 ($\Delta D = 10.6\%$). The camera was positioned in TIM-1 ($\theta = 63.44°$, $\varphi = 126°$). The x-ray self-emission images in (a)–(c) were recorded at 1.67±0.1 ns, 1.62±0.1 ns, and 1.58±0.1 ns, respectively, relative to the start of the laser pulse in their implosions.

Figure 3 shows the temporal evolution of P_2 from the three shots with different drive imbalance from the two different lines of sight (TIM-1 and TIM-5). The normalized mode amplitude is plotted along the ordinate versus the ablation-front radius on the abscissa. Since the ablation-front radius decreased with time during the compression phase, the corresponding time axis progresses from right to left. The P_2 amplitude magnitude at a large radius of ~350 μm (early time) is similarly small (<2%) for all the shots. The P_2 amplitude of the targets before the shots was measured to be <0.3% (Ref. 26). Both views show similar trends, although there are slight differences in the P_2 amplitude, which might indicate a systematic error in the data analysis. The temporal evolution of modes 4 and 6 from the three shots with different drive imbalance remain similar within the measurement uncertainty, and modes higher than 6 are negligible. The sign of the P_2 amplitude indicates whether the shell is oblate (negative) or prolate (positive).[3,14] In Fig. 3, the P_2 amplitude of two different shots (96578 and 96581) have opposite signs, particularly in the later phase of the implosions. The P_2 amplitudes in shot 96575 are close to zero (slightly negative) and always lie in between the amplitudes from shots 96578 and 96581. Errors for each mode are estimated by the difference in extracted mode amplitude when fitting to the left and right halves of the ablation surface in the self-emission images separately. We recall here that the energy of each beam in ring 1 (close to pole) in shot 96578 was increased ($\Delta D = -4.6\%$) and that the energy of each beam in ring 3 (close to equator) in shot 96581 was increased ($\Delta D = 10.6\%$).

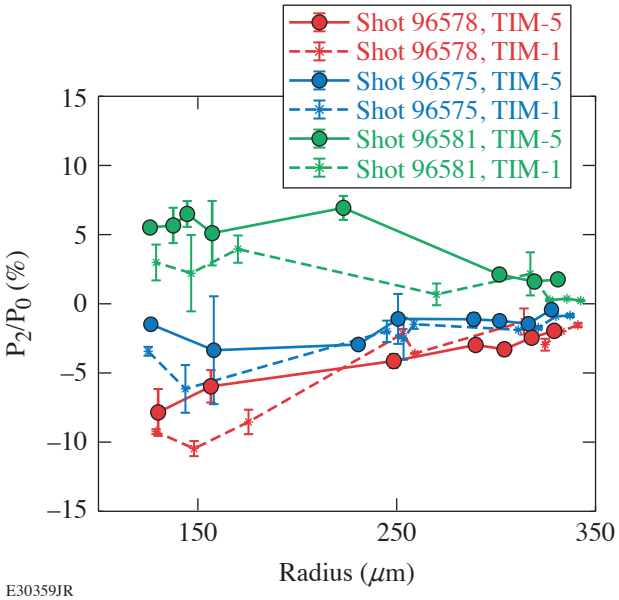

Figure 3
Comparisons of the temporal evolution of ℓ-mode 2 inferred from the shots 96578, 96575, and 96581 from the TIM-1 camera (star symbols, dashed lines) and the TIM-5 camera (circle symbols, solid lines).

Figure 4 shows that the extremum P_2 amplitude inferred from the TIM-1 and TIM-5 cameras varies linearly with the drive imbalance parameter ΔD. The dashed line represents a linear fit through all the data points. The slight vertical offset between the TIM-1 and the TIM-5 data set might indicate a systematic error in the data analysis. The P_2 amplitude is minimized for $\Delta D \sim 5\%$ and not as expected for $\Delta D = 0$. This might indicate that the energy coupling of non-normal laser rays in the equatorial region is over predicted in the current models. This trend also correlates with a 30% reduction in neutron yield (see Table I) for the shot with the largest ℓ-mode 2 amplitude. Future experiments will test the hypothesis of a minimal P_2 amplitude for a drive imbalance parameter of $\Delta D \sim 5\%$ for the current design and will perform similar experiments for designs with different shell adiabats. The observations of higher P_2 amplitudes in shot 96578 suggest that the shell asymmetry is higher when we increase the energies of the beams closer to the poles compared to the increase of the energies of the beams closer to the equator. This work will help to improve the understanding of the degradation mechanisms from the PDD beam geometry.

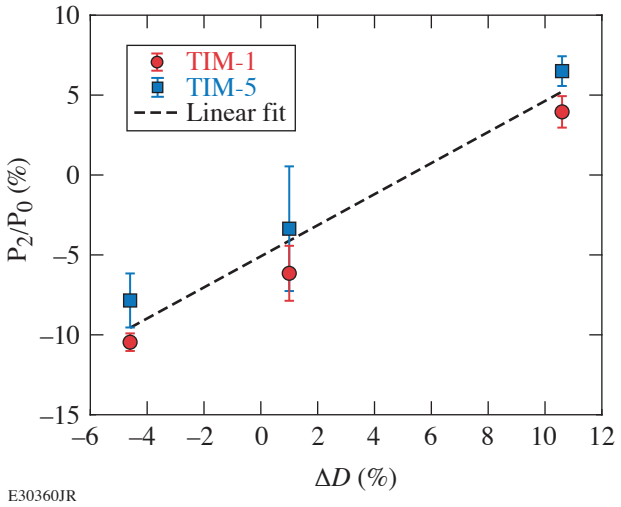

Figure 4
Inferred extremum P_2 amplitude versus drive imbalance parameter ΔD.

This material is based upon work supported by the Department of Energy National Nuclear Security Administration under Award Number DE-NA0003856, the University of Rochester, and the New York State Energy Research and Development Authority.

1. S. Skupsky *et al.*, Phys. Plasmas **11**, 2763 (2004).
2. R. S. Craxton *et al.*, Phys. Plasmas **12**, 056304 (2005).
3. F. Marshall *et al.*, J. Phys. IV France **133**, 153 (2006).
4. J. A. Marozas *et al.*, Phys. Plasmas **13**, 056311 (2006).
5. T. J. B. Collins *et al.*, Phys. Plasmas **19**, 056308 (2012).
6. P. B. Radha *et al.*, Phys. Plasmas **19**, 082704 (2012).
7. E. I. Moses, IEEE Trans. Plasma Sci. **38**, 684 (2010).
8. M. Hohenberger *et al.*, Phys. Plasmas **22**, 056308 (2015).
9. P. B. Radha *et al.*, Phys. Plasmas **23**, 056305 (2016).
10. T. R. Boehly *et al.*, Opt. Commun. **133**, 495 (1997).
11. V. Gopalaswamy *et al.*, Nature **565**, 581 (2019).
12. D. T. Michel *et al.*, Rev. Sci. Instrum. **83**, 10E530 (2012).
13. D. T. Michel *et al.*, Phys. Rev. Lett. **114**, 155002 (2015).
14. Y. Dong *et al.*, Plasma Sci. Technol. **22**, 084003 (2020).
15. P. B. Radha *et al.*, Phys. Plasmas **12**, 032702 (2005).
16. Y. Kato *et al.*, Phys. Rev. Lett. **53**, 1057 (1984).
17. T. J. Kessler *et al.*, Proc. SPIE **1870**, 95 (1993).
18. W. Theobald *et al.*, Phys. Plasmas **29**, 012705 (2022).

19. J. E. Rothenberg, J. Appl. Phys. **87**, 3654 (2000).
20. S. Skupsky *et al*., J. Appl. Phys. **66**, 3456 (1989).
21. *LLE Review Quarterly Report* **80**, 197 (1999).
22. S. P. Regan *et al*., J. Opt. Soc. Am. B **22**, 998 (2005).
23. A. K. Davis *et al*., Rev. Sci. Instrum. **87**, 11E340 (2016).
24. D. K. Bradley *et al*., Rev. Sci. Instrum. **63**, 4813 (1992).
25. D. K. Bradley *et al*., Rev. Sci. Instrum. **72**, 694 (2001).
26. D. H. Edgell *et al*., Fusion Science and Technology **49**, 616 (2006).

Quantitative Proton Radiography and Shadowgraphy for Arbitrary Intensities

J. R. Davies,[1] P. V. Heuer,[1] and A. F. A. Bott[2]

[1]Laboratory for Laser Energetics, University of Rochester
[2]Clarendon Laboratory, University of Oxford

Charged-particle radiography, most commonly with protons, and shadowgraphy are widely used in laser-plasma experiments to infer electric and magnetic fields and electron density, respectively. For many experiments of interest, intensity modulations due to absorption and scattering of the charged particles or photons can be neglected; therefore, intensity modulations are caused by deflections in the plasma. Deflection at the detector can then be expressed in terms of a path-integrated transverse Lorentz force for charged-particle radiography and a path-integrated transverse refractive index gradient for shadowgraphy. We will adopt the generic term deflectometry to describe both charged-particle radiography and shadowgraphy in the regime where intensity modulations are due principally to deflection.

A number of papers in plasma physics have used direct inversion of deflectometry data to obtain a path-integrated Lorentz force or refractive index gradient. These direct inversion algorithms find a minimum deflection solution where trajectories do not cross. Therefore, if trajectories did cross, the direct inversion may not reproduce the actual profiles. Direct inversion, however, does provide one possible solution to what is then a degenerate problem, subject to known constraints, which can be useful information. Most of these direct-inversion codes are publicly available.[1–5] These papers concentrate on proton radiography, with only one explicitly considering shadowgraphy,[1] and none considering the possibility of radiography with a relativistic particle, which is possible in laser-plasma experiments using electrons from a laser-plasma accelerator.

From a mathematical point of view, the direct-inversion problem was first formulated in a paper by Monge published in 1781,[6] and then in a modern mathematical manner by Kantorovich in 1942,[7] leading to the name Monge–Kantorovich problem or, more descriptively, the optimal transport problem. Monge and Kantorovich both considered finding the minimum cost for leveling a land area as an application of the theory. Kantorovich added "location of consumption stations with respect to production stations" as a second application of the theory. Since then, numerous applications have been found, of which direct inversion of deflectometry data by minimizing total deflection is perhaps the most recent.

The majority of the publicly available direct-inversion codes[3–5] solve the Monge–Ampère equation first derived by Monge and then stated in a more-general form by Ampère in 1819, although the numerical algorithm used in these codes was only published in 2011.[8] The Poisson equations considered by some authors,[1,2] and frequently mentioned in texts discussing shadowgraphy, can be considered special cases of the Monge–Ampère equation, valid in the limit of very small deflections.

If we consider the problem in terms of the data, then direct inversion comes down to determining the movement of counts in detector bins that map the source intensity I_0 (the signal on the detector in the absence of an object) to the measured intensity I, or vice versa. From this point of view, and from the perspective of a plasma physicist, it occurred to us that an algorithm based on an electrostatic plasma model should always be able to obtain a solution. The source or measured intensity can be treated as an initial electron distribution and the other intensity as a fixed ion distribution. Electrostatic forces will then cause the electron distribution to evolve to the ion distribution. The displacement of the electrons from their initial to their equilibrium positions will give the deflections at the detector. Oscillations about the desired equilibrium positions can be damped by applying drag to

the electrons. Electrostatic plus kinetic energy will decay steadily and go to zero in equilibrium since drag removes energy from the system, providing a simple convergence criterion.

The first scheme that occurred to us was an electrostatic particle-in-cell (PIC) code with the addition of electron drag; because this is a common type of code in plasma physics, efficient, robust algorithms exist, and it could make use of existing codes. We then considered a fluid code as a potentially faster, less memory-intensive alternative. A Lagrangian scheme, where the numerical grid moves with the fluid, provides the most direct method of determining the deflections. A Eulerian scheme, where the numerical grid is fixed, would require tracking the center of mass of the initial fluid elements in every cell, and so could require more calculations than a PIC code. Therefore, we also implemented a Lagrangian fluid scheme. We started with 1-D codes as a quick method to test the algorithms before writing 2-D codes.

To make a fair comparison of the electrostatic algorithm to the Sulman, Williams, and Russell algorithm for solving the Monge–Ampère equation,[3–5,8] we returned to the original *MATLAB* script of *PROBLEM*, which is not provided on GitHub, and added an inbuilt convergence criterion and an adaptive time step. We also compared our codes to the power-diagram algorithm,[1] which uses weighted Voronoi, or power diagrams of the intensities to determine the deflections at the detector.

Our codes output what we refer to as a dimensionless line-integrated transverse force. For charged-particle radiography,

$$\mathcal{F}_x = \frac{L}{Mw_x}\frac{q}{p\overline{v}}\int E_x - vB_y \mathrm{d}z, \quad \mathcal{F}_y = \frac{L}{Mw_y}\frac{q}{p\overline{v}}\int E_y - vB_x \mathrm{d}z,$$

which is valid for a relativistic particle. For shadowgraphy,

$$\mathcal{F}_x = \frac{L}{Mw_x}\frac{1}{2}\int \frac{\partial n'_\mathrm{e}/\partial x}{1-n'_\mathrm{e}}\mathrm{d}z, \quad \mathcal{F}_y = \frac{L}{Mw_\mathrm{y}}\frac{1}{2}\int \frac{\partial n'_\mathrm{e}/\partial y}{1-n'_\mathrm{e}}\mathrm{d}z,$$

where L is the object-to-detector distance, M is magnification, w is the detector pixel width in the object plane, q is the charge, p is momentum, v is velocity, z is the probing axis, and $n'_\mathrm{e} = n_\mathrm{e}/n_\mathrm{c}$, where n_e is electron density and n_c is critical density for the shadowgraphy probe.

Our codes are written in *MATLAB* and are publicly available.[9] Python versions of the 2-D PIC code and the Monge–Ampère code are under development.[10]

To test the codes, we used synthetic radiographs that we had generated previously by proton tracing in specified radial forces in cylindrical and spherical geometry for a range of profiles and amplitudes,[11] which are publicly available as hdf5 files in prad-format.[12] The force is expressed as a dimensionless parameter μ

$$\mu = \frac{2LF}{Mpv}, \quad \mu = -\frac{L}{M}\frac{\mathrm{d}n'_\mathrm{e}/\mathrm{d}r}{1-n'_\mathrm{e}}$$

for charged-particle radiography and shadowgraphy, respectively. Results for cylindrical Gaussian potentials with $\mu_\mathrm{max} = 0.5$ (defocusing) and –0.25 (focusing), values where trajectories do not cross, are shown in Fig. 1. All of our codes accurately reproduced the measured intensity and the line-integrated transverse force to within the noise level of the original intensity. We carried out an extensive range of tests intended to push the limits of the codes.

Only the PIC code obtained a solution for every case. The 2-D Lagrangian code failed for large-intensity modulations, but was faster than the 2-D PIC code without massively parallel processing, which would be possible with a PIC code. The Monge–Ampère code was considerably faster than the electrostatic codes in 2-D without massively parallel processing, but failed for intensities with extensive regions of zero signal, high contrast ratios, or large deflections across the boundaries, and could not obtain the

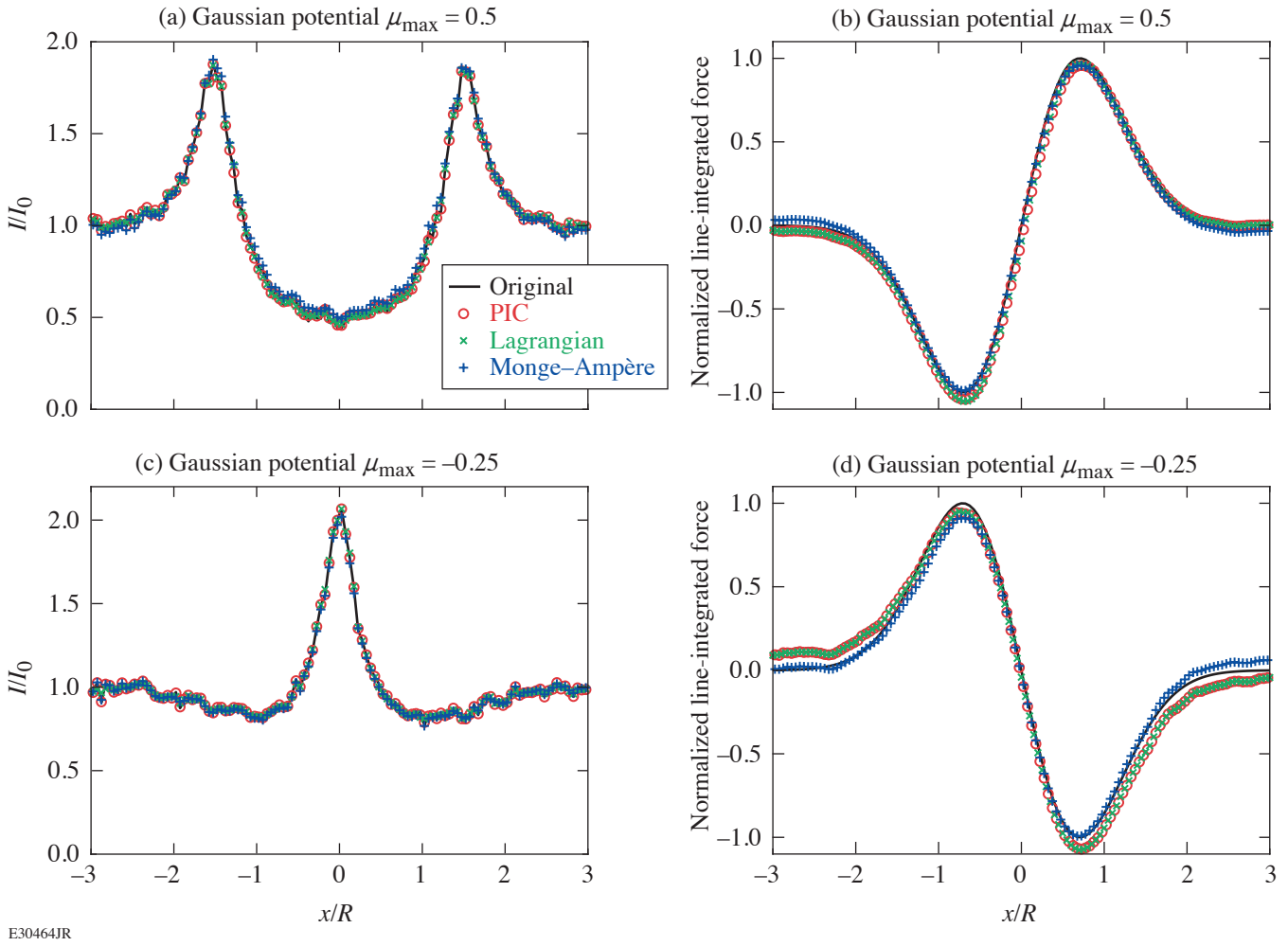

Figure 1
Results for a cylindrical Gaussian potential [(a),(c)] intensity profiles and [(b),(d)] line-integrated transverse force normalized so that the maximum of the original is 1 for μ_{max} = 0.5 and –0.25, respectively.

same degree of convergence to the measured intensity as the electrostatic codes. The power-diagram code was by far the slowest and failed for large peaks in the intensity. In 1-D, however, the Lagrangian code was the fastest and always obtained a solution.

Our final recommendations are to use the Monge–Ampère code to take a quick first look at data, and to use the PIC code if the Monge–Ampère code fails or a more-accurate inversion is desired. In the rare case of 1-D problems, the Lagrangian code is the best option.

This material is based upon work supported by the Department of Energy, under Award Number DE-SC0020431, by the Department of Energy National Nuclear Security Administration under Award Number DE-NA0003856, the University of Rochester, and the New York State Energy Research and Development Authority.

1. M. F. Kasim *et al.*, Phys. Rev. E **95**, 023306 (2017).
2. C. Graziani *et al.*, Rev. Sci. Instrum. **88**, 123507 (2017); PRaLine Code (Proton Radiography Linear Reconstruction, the "reconstruction" is silent), Accessed 03 March 2023, https://github.com/flash-center/PRaLine.

3. M. F. Kasim, Invert Shadowgraphy and Proton Radiography, Accessed 03 March 2023, https://github.com/mfkasim1/invert-shadowgraphy.
4. A. F. A. Bott *et al.*, J. Plasma Phys. **83**, 905830614 (2017); PROBLEM Solver (PROton-imaged B-field nonLinear Extraction Module), Accessed 03 March 2023, https://github.com/flash-center/PROBLEM.
5. M. F. Kasim *et al.*, Phys. Rev. E **100**, 033208 (2019); M. F. Kasim, PRNS (Proton Radiography with No Source), Accessed 03 March 2023, https://github.com/OxfordHED/proton-radiography-no-source.
6. G. Monge, Mém. de l'Ac. R. des. Sc. An. **1**, 666 (1781).
7. L. Kantorovitch, Manage. Sci. **5**, 1 (1958).
8. M. M. Sulman, J. F. Williams, and R. D. Russell, Appl. Numer. Math. **61**, 298 (2011).
9. J. R. Davies, A 1-D Electrostatic PIC Code for Direct Inversion of Deflectometry Data (Version 2), Zenodo, Accessed 7 March 2023, http://doi.org/10.5281/zenodo.6638904; J. R. Davies, A 2-D Electrostatic PIC Code for Direct Inversion of Deflectometry Data (Version 1), Zenodo, Accessed 7 March 2023, http://doi.org/10.5281/zenodo.6638812; J. R. Davies, A 1-D Electrostatic, Lagrangian Two-Fluid Code for the Direct Inversion of Deflectometry Data (Version 1), Zenodo, Accessed 7 March 2023, http://doi.org/10.5281/zenodo.6638911; J. R. Davies, A 2-D Electrostatic Lagrangian Two-Fluid Code for the Direct Inversion of Deflectometry Data (Version 1), Zenodo, Accessed 7 March 2023, https://doi.org/10.5281/zenodo.6638929; J. R. Davies and A. F. A. Bott, A Matlab Function to Solve the Monge–Ampere Equation Using the Sulman, Williams and Russell Algorithm (Version 1), Zenodo, Accessed 7 March 2023, (https://doi.org/10.5281/zenodo.6685314.
10. P. Heuer, InvertDeflectPy: A Collection of Algorithms for Inverting Deflectometry Data, Accessed 7 March 2023, https://github.com/pheuer/InvertDeflectPy.
11. J. Davies and P. Heuer, Synthetic Proton Radiographs for Testing Direct Inversion Algorithms, Zenodo, Accessed 7 March 2023, https://doi.org/10.5281/zenodo.6632986.
12. P. Feister, Pradformat (Particle Radiography File Format Tools)-MATLAB Package, Accessed 7 March 2023, https://github.com/sfeister/pradformat/blob/f9b95d1d87f26d01e59ab7f145d414e7043fe488/MATLAB/README.md.

Direct Measurement of the Return-Current Instability

A. L. Milder,[1,2,3] J. Zielinski,[3] J. Katz,[1] W. Rozmus,[3] D. H. Edgell,[1] A. M. Hansen,[1] M. Sherlock,[4] C. Bruulsema,[3] J. P. Palastro,[1] D. Turnbull,[1] and D. H. Frolua[1,2]

[1]Laboratory for Laser Energetics, University of Rochester
[2]Department of Physics and Astronomy, University of Rochester
[3]Department of Physics, University of Alberta
[4]Lawrence Livermore National Laboratory

Measurements were made of the return-current instability growth rate, demonstrating its concurrence with nonlocal transport. Thomson scattering was used to measure a maximum growth rate of 5.1×10^9 Hz, which was 3× less than classical Spitzer–Härm theory predicts. The measured plasma conditions indicate the heat flux was nonlocal and Vlasov–Fokker–Planck (VFP) simulations that account for nonlocality reproduce the measured growth rates. Furthermore, the threshold for the return-current instability was measured ($\delta_T = 0.017 \pm 0.002$) to be in good agreement with previous theoretical models.

Significant progress has been made in understanding laboratory and astrophysical plasmas through the use of fluid approximations,[1] but recently an increasing amount of work has been dedicated to understanding the kinetic effects and how the microscale physics impacts the larger macroscopic systems. In particular, kinetic effects associated with nonlocal transport have impacted the interpretation of inertial confinement fusion implosions, laboratory astrophysics, and high-energy-density experiments. Understanding transport and transport-driven instabilities often starts with the classical theories of Spitzer and Härm[2] or Braginskii.[3] Historically, challenges in accounting for kinetic effects, particularly in heat transport, have been addressed with *ad hoc* corrections to the Spitzer–Härm theory in order to match experimental observables.

In a plasma, heat-carrying electrons travel down the temperature gradient (q_{flux}), generating a neutralizing return current (j_{return}) consisting of slower counter-propagating electrons. When the return current is large enough to shift the peak of the electron distribution function beyond the phase velocity of the ion-acoustic waves, the slope of the distribution function becomes inverted and the electrons transfer energy to the waves (inverse Landau damping). These transport-driven waves become absolutely unstable when the inverse Landau damping rate exceeds the ion damping rate.[1] This return-current instability (RCI) is predicted to drive a broad turbulent spectrum of ion-acoustic waves that limit the return current, inhibit heat transport,[4,5] modify laser absorption,[6,7] and alter the fluctuation spectrum from which other ion instabilities grow.[8–10] Previous experimental work has shown anomalous absorption linked to ion turbulence[6] and evidence of reduced heat flux.[5]

In this summary, we present the first measurements of the threshold and linear growth rate of the return-current instability driven by electron heat flux. The thorough characterization of the plasma conditions show that the return-current instability occurs concurrently with nonlocal transport. Thomson scattering was used to measure a maximum RCI growth rate of 5.1×10^9 Hz, which was 3× less than classical Spitzer–Härm theory predicts, but the RCI threshold was measured ($\delta_T = 0.017 \pm 0.002$) to be in good agreement with previous theoretical models.[4,9] Measured plasma conditions indicate that the heat flux was nonlocal and electron velocity distribution functions from VFP simulations, which treat this nonlocality kinetically, reproduce the measured growth rates. These experiments provide a thorough description of the plasma conditions and the associated return-current instability, which enabled detailed comparison with theory and simulations and can now be used to better understand the impact of return-current instability in laboratory and astrophysical plasmas.

A supersonic Mach-3 gas jet with an exit diameter of 2 mm produced an argon gas plume. Eleven 351-nm ultraviolet beams of the OMEGA Laser System were focused 2 mm above the nozzle to heat the plasma. Each beam delivered 200 J in a 1-ns duration full-width at half-maximum (FWHM) flattop pulse. The beams used distributed phase plates, polarization smoothing, and smoothing by spectral dispersion and achieved a peak overlapped intensity of $I_{\text{total}} = 1.1 \times 10^{15}$ W/cm^2.

The overlapped beams produced a hot region of plasma surrounded by a colder region. The overlapped intensity profile created an electron temperature gradient that drove "fast" electrons from the hot region to the cold region. The Thomson-scattered light was collected from various radial locations in the plasma by moving the heater beams and gas jet. The configuration maintained the probed ion-acoustic wave vector parallel to the direction of the heat flux. A distributed phase plate was used on the Thomson-scattering probe beam ($\lambda_0 = 526.5$ nm) to produce a 200-μm FWHM flattop focal spot. This beam was used with ~4 J in a 300-ps FWHM flattop pulse ($I_{2\omega} = 4.2 \times 10^{13}$ W/cm^2) delayed 700 ps from the start of the heater beams to measure spatially resolved Thomson scattering or with ~5 J in a 2-ns FWHM flattop pulse, co-timed with the beginning of the heating beams, and a 100-μm phase plate ($I_{2\omega} = 3.2 \times 10^{13}$ W/cm^2) to measure temporally resolved Thomson scattering. The Thomson-scattering diagnostic, both temporally and spatially resolved, collects light with a 60° scattering angle.

Figure 1 shows the measured temporally resolved ion-acoustic wave amplitudes while the plasma conditions were quasi-stationary (500 to 1000 ps). At 475 μm [Fig. 1(a)], the ion-acoustic wave grows as a function of time consistent with the return-current instability. This is further supported by comparison with growth-rate calculations from the Spitzer–Härm theory and from VFP simulations. The growth rate in the Spitzer–Härm theory was found to be significantly larger than observed in the plasma, which is attributed to the nonlocality of the heat transport. VFP simulations, which include these effects kinetically, show excellent agreement with the data. At a radius of 200 μm [Fig. 1(b)], the ion-acoustic wave decays as a function of time, indicating that the plasma was stable to the return-current instability. The ion-acoustic wave was driven above the thermal fluctuation level at early time, likely by transient RCI or ponderomotive and thermal effects as the plasma was being formed.

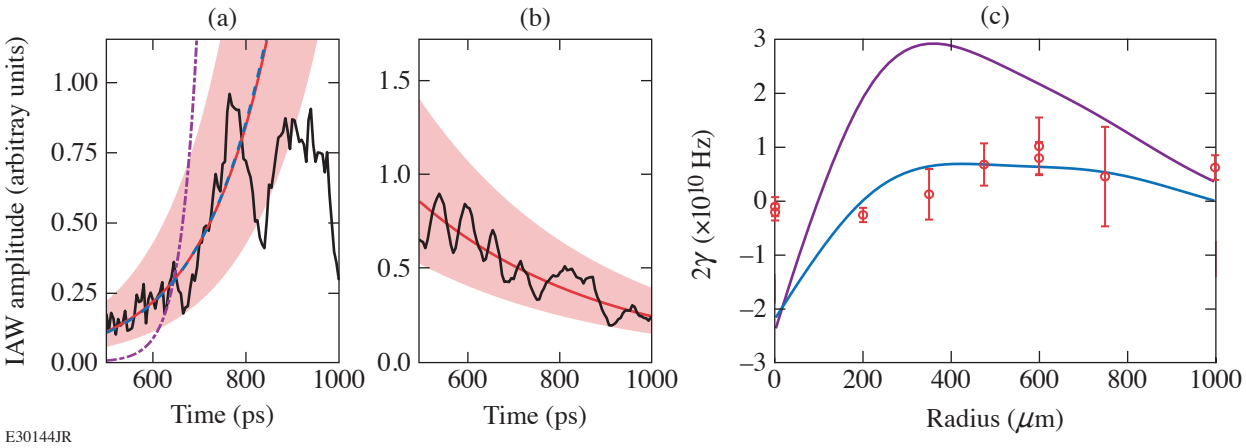

Figure 1
The ion-acoustic wave amplitude (black curves) at a radius of (a) 475 μm and (b) 200 μm are matched with an exponential model (red curves) with a shaded 90% confidence interval. (a) Exponential models with growth rates from the Spitzer–Härm theory (purple curve) and VFP simulations (blue curve) are compared to the data. (c) Measured growth rates (red) are compared to growth rates from the Spitzer–Härm theory (purple curve) and VFP simulations (blue curve) as a function of the radius.

Figure 1(c) compares the ion-acoustic growth rates from simulation and experiment as a function of space. As with the case at 475 μm, the Spitzer–Härm theory overpredicts the growth rate at all spatial locations. Nonlocal transport, included in VFP, was needed to match the measured growth rates. Experiment and simulation showed the return-current instability occurred over a large spatial extent from ~300 to 1000 μm but is maximized around 600 μm where the temperature gradient is large. This association with the temperature gradient helps identify this instability as a transport-driven instability. Simulations predicted the instability

threshold was crossed around 200 μm, while experimental data show the threshold between 200 μm and 350 μm. VFP simulations were performed with the code K2 (Ref. 11) and the resulting distribution functions were used to determine the growth rate.

Calculating the Knudsen number as a function of radius indicates that the return-current instability has a threshold of $\delta_T = 0.017 \pm 0.002$. The Knudsen number is within this range between $r = 200$ μm and $r = 350$ μm where the threshold was noted in Fig. 1(c). The Knudsen number (δ_T) is the scale parameter for the heat-flux distribution function perturbation, and therefore the return-current instability. An analytical threshold for the instability from Tikhonchuk *et al.*[5] is a reliable estimate for the return-current instability threshold. The threshold for the instability is also very close to the threshold for thermal transport nonlocality given by $\delta_T > 0.06/\sqrt{Z}$ (Ref. 12), i.e., RCI will occur where the transport relations are nonlocal.

Heat transport is a ubiquitous process in plasma physics that is impacted by nonlocality and the instabilities it causes. This work has demonstrated the need to account for this nonlocality in the calculation of growth rates for instabilities involving ion-acoustic waves, such as the return-current instability, and to account for the return-current instability under conditions of nonlocal transport. Large spatial extents have been found for both the nonlocal transport and the return-current instability. This can result in changes to instabilities and plasma conditions at a significant distance from the most unstable region. The threshold for the return-current instability was found and is in good agreement with a simple temperature- and density-based model that can be used predictively in future work.

This material is based upon work supported by the Department of Energy National Nuclear Security Administration under Award Number DE-NA0003856, the Office of Fusion Energy Sciences under Award Number DE-SC0016253, the University of Rochester, and the New York State Energy Research and Development Authority. The work of M. Sherlock was performed under the auspices of the U.S. Department of Energy by Lawrence Livermore National Laboratory under Contract DE-AC52-07NA27344.

1. D. W. Forslund, J. Geophys. Res., Space Phys. **75**, 17 (1970).
2. L. Spitzer, Jr. and R. Härm, Phys. Rev. **89**, 977 (1953).
3. S. I. Braginskii, in *Reviews of Plasma Physics*, edited by M. A. Leontovich (Consultants Bureau, New York, 1965), Vol. 1, pp. 205–311.
4. V. T. Tikhonchuk *et al.*, Phys. Plasmas **2**, 4169 (1995).
5. D. R. Gray and J. D. Kilkenny, Plasma Phys. **22**, 81 (1980).
6. S. H. Glenzer *et al.*, Phys. Rev. Lett. **88**, 235002 (2002).
7. W. M. Manheimer, D. G. Colombant, and B. H. Ripin, Phys. Rev. Lett. **38**, 1135 (1977).
8. W. Rozmus *et al.*, Plasma Phys. Control. Fusion **60**, 014004 (2018).
9. A. V. Brantov, V. Yu. Bychenkov, and W. Rozmus, Phys. Plasmas **8**, 3558 (2001).
10. J. D. Moody *et al.*, Phys. Plasmas **7**, 2114 (2000).
11. M. Sherlock, J. P. Brodrick, and C. P. Ridgers, Phys. Plasmas **24**, 082706 (2017).
12. V. Yu. Bychenkov *et al.*, Phys. Rev. Lett. **75**, 4405 (1995).

Analysis Methods for Electron Radiography Based on Laser-Plasma Accelerators

G. Bruhaug,[1,2] M. S. Freeman,[3] H. G. Rinderknecht,[1] L. P. Neukirch,[3] C. H. Wilde,[3] F. E Merrill,[3] J. R. Rygg,[1,2,4] M. S. Wei,[1] G. W. Collins,[1,2,4] and J. L. Shaw[1]

[1]Laboratory for Laser Energetics, University of Rochester
[2]Department of Mechanical Engineering, University of Rochester
[3]Los Alamos National Laboratory
[4]Department of Physics and Astronomy, University of Rochester

Electron radiography (eRad) is a proven, highly penetrative radiography technique that has typically been performed with traditional linear accelerators (LINAC's).[1,2] Recent work has extended electron radiography techniques into the laser-plasma acceleration (LPA) regime[3,4] with an emphasis on the radiography of laser-driven dynamics systems.

To compare LPA eRad to traditional LINAC eRad and other radiography methods, the resolution and transmission of said source must be determined. In addition, LPA-based eRad can modify the properties of the object being radiographed via a laser-generated plasma if the drive laser is not dumped.[4] Here we present analysis methods to determine the resolution for LPA eRad that include accounting for image distortion caused by the drive laser.

A polychromatic electron beam generated via LPA with an average energy of ~20 MeV and a bunch charge of up to 700 nC was used to radiograph various test objects in both contact and projection radiography.[4,5] All radiographs were taken using MS (multipurpose standard) image plates with 12.5 μm of aluminium in front to dump the laser. MeV-scale electrons have been found to have a relatively flat energy response in image plates and are detected at high efficiency.[6] All images were then analyzed via the software ImageJ[7] and the final scans were gray-scale balanced to make the clearest images.

It should be noted that the majority of the LPA drive laser is transmitted through the LPA plasma source. In the projected configuration the laser impacts the front face of the projection radiography object with ~10^{15} W/cm^2 intensity and ~20 to 100 J of laser energy depending on drive specifics. This excess laser energy will impact the target ~100 fs before the electron beam arrives and will generate plasma on the front surface of the object.[4] Consequently, even these supposedly "static" radiography objects were, in reality, laser-ablated dynamic radiography objects.

Contact radiography provided the ability to remove the transverse structure of the electron beam using the image plate placed in front of the radiography object to record the beam transverse structure before the beam passes through the radiography object. Transverse structure from the beam adds additional blurring to the radiograph that can be eliminated via image division using the software ImageJ.[7] Using these adjusted images, image resolution was determined by creating a box lineout tens of pixels wide across the edges generated by the thickness steps in the radiography object [see Fig. 1(a)] and across the edges of the holes in each thickness step. An error function of the form shown in Eq. (1) was then fitted to the lineout as shown in Fig. 1(b).

$$y = a + b\,\mathrm{erf}\left(\frac{x-c}{d}\right). \tag{1}$$

Variables a, b, c, and d are fitting parameters for the error function with d giving the resolution. This procedure was repeated across all edges of holes, all edges of the object, and all thickness steps on the object. The results were then averaged for each thickness of material to produce a final resolution at each thickness of material.

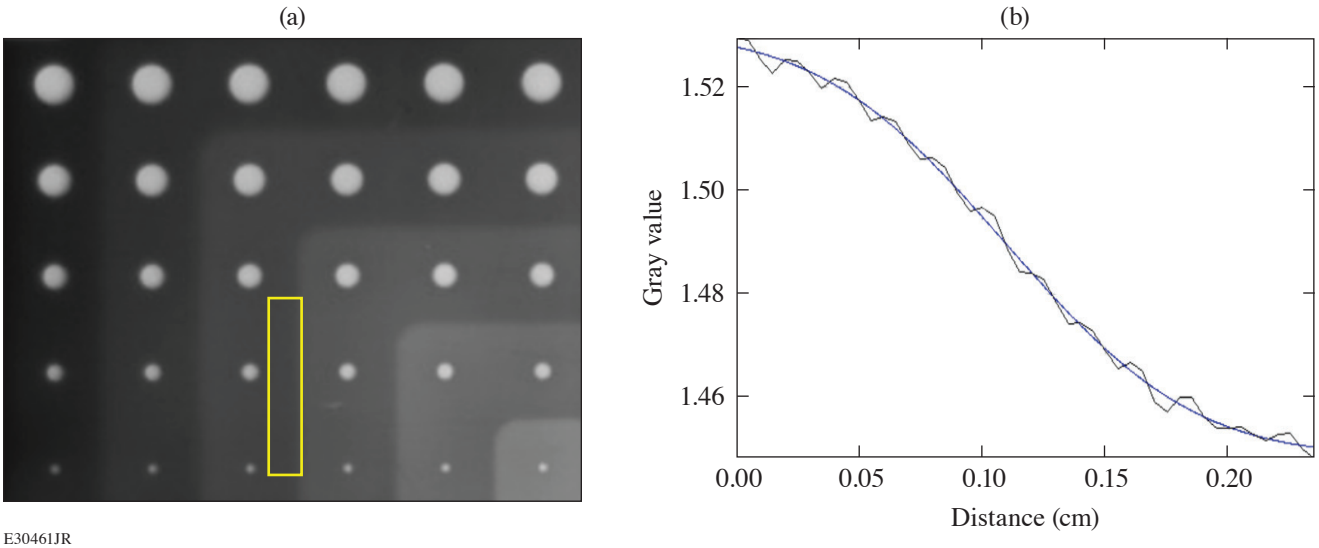

Figure 1
(a) Example of a resolution measurement across thickness step edge for tungsten contact radiography object. The yellow box across the thickness step edge shows the outline of the data used to make the measurement. (b) Lineout of boxed region from (a) (black curve) and error function fit (blue curve).

To determine the resolution in projection radiography, the final image plate scan is taken and gray scale is balanced for maximum clarity. Box lineouts tens of pixels wide are then taken across the central step in object thickness as well as the object outer edges and hole edges. An error function is fitted to the lineouts and the resolution taken from that function is shown in Fig. 2. These measurements are performed multiple times around the resolution measurement point of interest (i.e., an edge or a step-in material thickness) and then averaged to determine a final value.

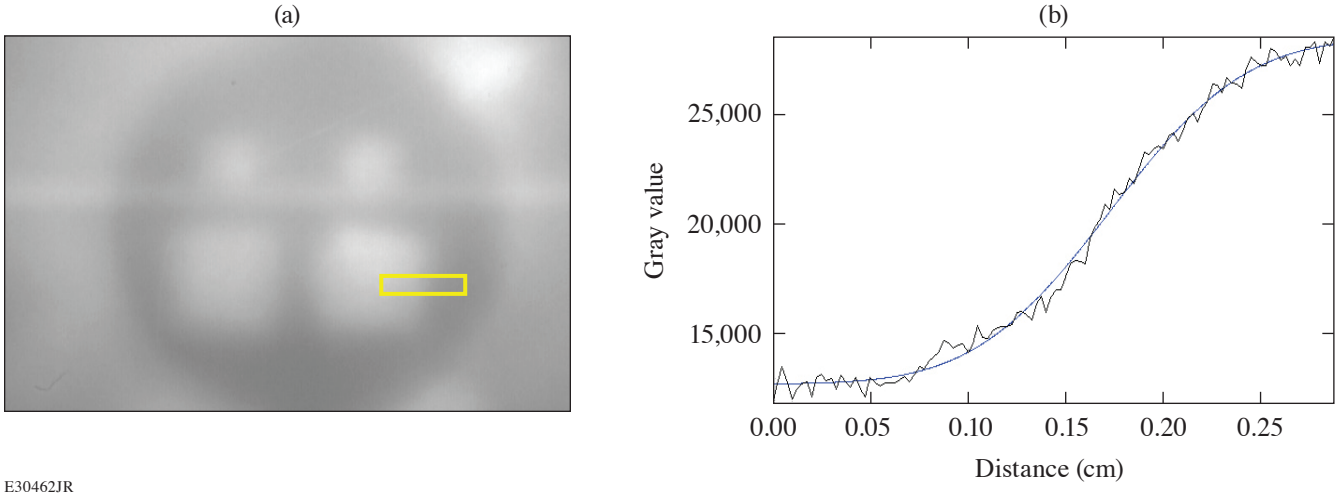

Figure 2
(a) Example of a resolution measurement across a hole for tungsten projection radiography object. The yellow box across the thickness step edge shows the outline of the data used to make the measurement. (b) Lineout of boxed region from (a) (black curve) and error function fit (blue curve).

Plasma-generated electric fields in laser-ablated targets can be roughly measured by measuring the size of features in the eRad image and estimating the field strength needed to produce those features. When measuring the sizes of the static projection radiography objects, it was noticed that the resulting radiographs were ∼1.5× smaller than expected, as illustrated in Fig. 3. Previous data suggest that this size discrepancy was caused by plasma-generated electric fields acting like an electrostatic lens on the electron beam.[8] Using the average electron beam energy of ∼20 MeV (Ref. 5), it was determined that the electric field that corresponded to ∼1 GV/m (Ref. 4) would generate the magnification discrepancies seen. This is well in line with previous laser-plasma electric-field strengths at this laser intensity.[8]

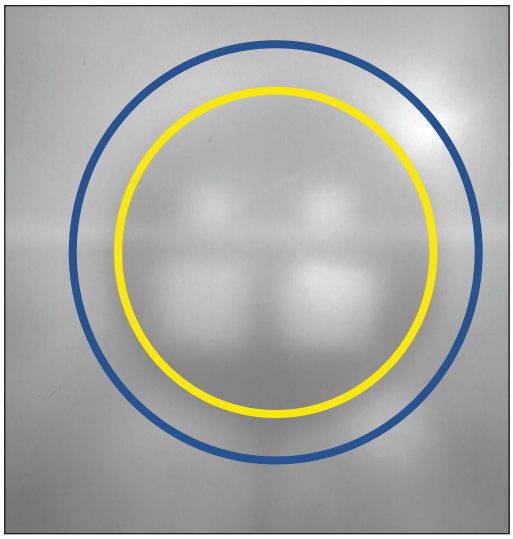

E30463JR

Figure 3
Projected radiograph of tungsten radiography object showing the size discrepancy caused by the plasma electric field focusing of the electron beam. The blue outline shows the expected image size of ∼1.8 cm if there was no plasma focusing, and the yellow circle shows the measured diameter of ∼1.2 cm.

This material is based upon work supported by the Department of Energy National Nuclear Security Administration under Award Number DE-NA0003856, the U.S. Department of Energy under Awards DE-SC00215057, the University of Rochester, and the New York State Energy Research and Development Authority.

1. F. Merrill *et al.*, Nucl. Instrum. Methods Phys. Res. B **261**, 382 (2007).
2. F. E. Merrill *et al.*, Appl. Phys. Lett. **112**, 144103 (2018).
3. W. Schumaker *et al.*, Phys. Rev. Lett. **110**, 015003 (2013).
4. G. Bruhaug *et al.*, Sci. Rep. **13**, 2227 (2023).
5. J. L. Shaw *et al.*, Sci. Rep. **11**, 7498 (2021).
6. G. Boutoux *et al.*, Rev. Sci. Instrum. **86**, 113304 (2015).
7. C. A. Schneider, W. S. Rasband, and K.W. Eliceiri, Nat. Methods **9**, 671 (2012).
8. J. L. Dubois *et al.*, Phys. Rev. E **89**, 013102 (2014).

A First-Principles Study of L-Shell Iron and Chromium Opacity at Stellar Interior Temperatures

V. V. Karasiev,[1] S. X. Hu,[1] N. R. Shaffer,[1] and G. Miloshevsky[2]

[1]Laboratory for Laser Energetics, University of Rochester
[2]Department of Mechanical and Nuclear Engineering, Virginia Commonwealth University

Accurate prediction of optical properties of matter across a wide range of material densities and temperatures is of great importance in planetary science, astrophysics, and inertial confinement fusion.[1–4] Building a reliable opacity model for materials under extreme conditions is one of the grand challenges in high-energy-density physics, especially across the most complicated warm-dense-matter (WDM) domain of thermodynamic conditions when both the coulomb coupling parameter and the electron degeneracy are close to unity. The traditional opacity models based on physics of isolated atoms when the important plasma density and temperature effects such as Stark broadening, ionization potential depression (IPD), and continuum lowering are incorporated via corrections often become unreliable beyond the ideal plasma conditions.

In this work we use a first-principles density functional theory (DFT)-based methodology to calculate optical properties (mass-absorption coefficient and opacity) of Cr and Fe at stellar interior temperatures corresponding to recent experiments.[5,6] The purpose is to explore whether or not such *ab initio* calculations can resolve the reported disagreement between previous atomic physics calculations and measured data.[5,6] Our DFT results are compared to the real-space Green's function (RSGF) method[7–9] and to the radiative emissivity and opacity of dense plasmas (REODP) atomistic model.[10]

A free-energy DFT-based methodology for optical property calculations in the WDM domain presented in Ref. 11 handles deeply bounded core electrons on an equal footing with free electrons in the system and self-consistently takes into account effects such as quasistatic pressure broadening due to interaction with neighboring ions [in case of calculations on molecular dynamics (MD) multi-ion supercell snapshots], the IPD, continuum lowering, and Fermi surface rising. The methodology incorporates a combination of the Kubo–Greenwood (KG) optical data, evaluated on a set of the *ab initio* molecular dynamics (AIMD) snapshots, with a periodic single-atom-in-a-cell calculation at the same thermodynamic conditions. KG calculations on snapshots account for the influence of the local plasma environment, which is important for photon energies near the L and K edges. Kubo–Greenwood data from periodic calculations with single atom cover the tail regions beyond the L and K edges.

The Kubo–Greenwood formulation implemented in the post-processing code *KGEC* (Kubo–Greenwood electronic conductivity) for use with the *Quantum-Espresso* large-scale DFT-based simulation package, *KGEC@Quantum-Espresso*,[12,13] calculates the frequency-dependent real and imaginary parts of electric conductivity, $\sigma_1(\omega)$ and $\sigma_2(\omega)$; the real part of the index of refraction, $n(\omega)$; the absorption coefficient, $\alpha(\omega) = \sigma_1(\omega)\,[4\pi/n(\omega)c]$; and the mass-absorption coefficient $\alpha m(\omega) = \alpha(\omega)/\rho$ (where c is the speed of light, ρ is the material density, and the photon energy is $\hbar\omega = h\nu$). The optical properties were calculated for a single-atom-in-a-cell and as an average over a selected set of uncorrelated two-atom MD snapshots. Eventually the grouped Rosseland mean opacities for a narrow 4-eV group of photon energies are calculated.

In this study we are focused on the L-shell absorption and opacity calculations at temperatures when the deep 1*s* bands remain fully populated. Therefore, 1*s* frozen-core projector augmented wave (PAW) data sets for Fe and Cr are generated using the *ATOMPAW* code.[14] A small augmentation sphere radius $r_{\mathrm{PAW}} = 0.35$ bohr requires a relatively high cutoff energy of $E_{\mathrm{cut}} = 800$ Ry to converge electronic pressure. The optical properties are calculated using the Kubo–Greenwood formulation implemented within

the PAW formalism in *KGEC@Quantum-Espresso*[12,13,15] packages. The Gaussian broadening was done with relatively large δ = 15 eV due to the sparsity of states in the case of the single-atom-in-a-cell calculations.

Table I shows free-electron densities of chromium and iron calculated at T = 182 eV and ρ = 0.161 g/cm^3 and 0.165 g/cm^3, respectively. Theoretical predictions by all three methods are in very good agreement; relative differences of the REODP and RSGF values with respect to the DFT data do not exceed 2% and 4%, respectively, matching the experimental value of 3 × 10^{22} cm^{-3} from measurements for Cr and Fe.

Table I: Free-electron density (in cm^{-3} units) for chromium and iron at T = 182 eV and ρ_{Cr} = 0.161 g/cm^3, ρ_{Fe} = 0.165, respectively, as predicted by the DFT, REODP, and RSGF methods.

System	DFT	REODPe	RSGF
Cr	3.00 × 10^{22}	2.95 × 10^{22}	3.12 × 10^{22}
Fe	3.00 × 10^{22}	2.95 × 10^{22}	3.12 × 10^{22}

Figure 1 shows our main results for opacity of chromium and iron calculated at T = 182 eV and material density of 0.161 g/cm^3 and 0.165 g/cm^3, respectively, alongside with experimental measurements. At short wavelengths below ~9.5 A [the L-shell bound-continuum region for photon energies above ~1.2 keV], the agreement between all three theoretical data and experiments is very good for chromium: the REODP curve goes straight through the experimental data, while the DFT and RSGF data are located slightly below, touching the yellow-shaded experimental error bars. The situation for iron is different; opacity predicted by theoretical methods in the L-shell bound-continuum region is underestimated by about 50% as compared to the experimental data. The REODP curve is slightly closer to the experimental data as compared to the DFT single-atom-in-a-cell and RSGF simulations.

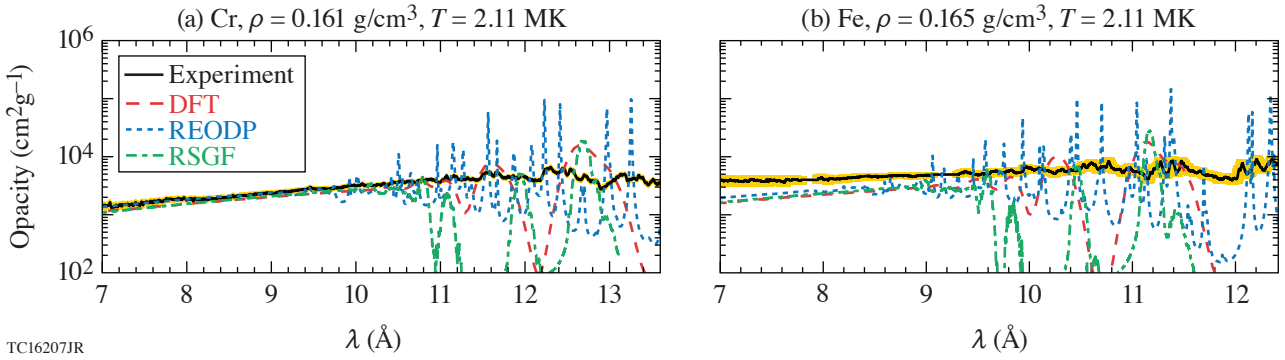

Figure 1
Opacity of iron and chromium at 0.165 g/cm^3 and 0.165 g/cm^3, respectively. A comparison is made between the experimental measurements (solid black curve, the yellow-shaded area corresponds to the experimental measurements error) and three theoretical predictions at T = 182 eV.

In the wavelength range above 9.5 A, opacity is dominated mostly by the bound–bound absorption lines. The DFT and RSGF calculations predict a small set of smooth and strong discrete lines separated by deep windows. The REODP method predicts a richer spectrum of sharp peaks. The REODP-calculated opacities represent the detailed all-line spectra without any kind of averaging into spectral groups. The peaks and wings of the lines are resolved with a high accuracy. The spectral lines are roughly centered on the experimental opacity curves. However, none of our theoretical predictions is close to the measured bound–bound opacity in that range. The DFT predictions for the bound–bound absorption can be improved by performing the Kubo–Greenwood optical calculations on top of the AIMD snapshots for larger supercells including more than two atoms by considering more-realistic charge-state distributions. However, such demanded calculations, on both memory and time, are currently out of reach.

This material is based upon work supported by the Department of Energy National Nuclear Security Administration under Award Number DE-NA0003856, U.S. National Science Foundation PHY Grants No. 1802964 and No. 2205521, Defense Threat

Reduction Agency under Grants No. HDTRA1-19-1-0019 and HDTRA1-20-2-0001, the University of Rochester, and the New York State Energy Research and Development Authority. This research used resources of the National Energy Research Scientific Computing Center, a DOE Office of Science User Facility supported by the Office of Science of the U.S. Department of Energy under Contract No. DE-AC02-05CH11231 using NERSC award FES-ERCAP0021234.

1. J. J. Fortney and N. Nettelmann, Space Sci. Rev. **152**, 423 (2010).
2. C. A. Iglesias, F. J. Rogers, and D. Saumon, Astrophys. J. Lett. **569**, L111 (2002).
3. S. X. Hu *et al.*, Phys. Rev. E **90**, 033111 (2014).
4. S. X. Hu *et al.*, Phys. Plasmas **22**, 056304 (2015).
5. J. E. Bailey *et al.*, Nature **517**, 56 (2015).
6. T. Nagayama *et al.*, Phys. Rev. Lett. **122**, 235001 (2019).
7. J. J. Rehr and R. C. Albers, Rev. Mod. Phys. **72**, 621 (2000).
8. Y. Wang *et al.*, Phys. Rev. Lett. **75**, 2867 (1995).
9. N. Shaffer and C. E. Starrett, Phys. Rev. E **150**, 015203 (2022).
10. G. Miloshevsky and A. Hassanein, Phys. Rev. E **92**, 033109 (2015).
11. V. V Karasiev and S. X. Hu, Phys. Rev. E **103**, 033202 (2021).
12. L. Calderín, V. V. Karasiev, and S. B. Trickey, Comput. Phys. Commun. **221**, 118 (2017).
13. P. Giannozzi *et al.*, J. Phys.: Condens. Matter **21**, 395502 (2009).
14. N. A. W. Holzwarth, A. R. Tackett, and G. E. Matthews, Comp. Phys. Commun. **135**, 329 (2001).
15. V. V. Karasiev, T. Sjostrom, and S. B. Trickey, Comput. Phys. Commun. **185**, 3240 (2014).

High-Resolution X-Ray Spectrometer for X-Ray Absorption Fine Structure Spectroscopy

D. A. Chin,[1,2] P. M. Nilson,[2] D. Mastrosimone,[2] D. Guy,[2] J. J. Ruby,[3] D. T. Bishel,[1,2] J. F. Seely,[4] F. Coppari,[3] Y. Ping,[3] J. R. Rygg,[1,2,5] and G. W. Collins[1,2,5]

[1]Department of Physics and Astronomy, University of Rochester
[2]Laboratory for Laser Energetics, University of Rochester
[3]Lawrence Livermore National Laboratory
[4]Syntek Technologies
[5]Department of Mechanical Engineering, University of Rochester

Two extended x-ray absorption fine structure (EXAFS) flat crystal x-ray spectrometers (EFX's) were designed and built for high-resolution x-ray spectroscopy over a large energy range with flexible, on-shot energy dispersion calibration capabilities. EFX uses a flat silicon [111] crystal in the reflection geometry as the energy dispersive optic covering the energy range of 6.3 to 11.4 keV and achieving a spectral resolution of 4.5 eV with a source size of 50 μm at 7.2 keV. A shot-to-shot configurable calibration filter pack and Bayesian inference routine were used to constrain the energy dispersion relation to within $\pm$3 eV. EFX was primarily designed for x-ray absorption fine structure (XAFS) spectroscopy and provides significant improvement to the OMEGA XAFS experimental platform at the Laboratory for Laser Energetics. EFX is capable of performing EXAFS measurements of multiple absorption edges simultaneously on metal alloys and x-ray absorption near-edge spectroscopy to measure the electron structure of compressed 3*d* transition metals.

Two EFX spectrometers were designed and built for OMEGA. Diagrams of the physical housing of EFX are shown in Fig. 1, where Fig. 1(a) highlights the different components of EFX and Fig. 1(b) shows a photograph of EFX. The primary components of the spectrometer are a flat silicon [111] crystal and flat image-plate detector, which is loaded into EFX through the back of the housing, opposite the x-ray source. The crystal and detector are held in an aluminum housing with an entrance port for the x rays on one side, as shown in Fig. 1(a). Four crystals were built for EFX: three 170-mm-long Si [111] crystals and one 110-mm-long Si [111] crystal. A blast shield to protect the crystal and a filter pack to characterize the energy dispersion are held in the front of EFX. To reduce noise, EFX has a 3.175-mm-thick, external tungsten shell and a 12.7-mm-thick, tungsten line-of-sight block that protects the detector from the x-ray source.

The performance of EFX was tested on OMEGA by simultaneously measuring EXAFS from multiple K edges of an alloy material. Invar ($Fe_{64}Ni_{36}$) foil was placed in the front-end filter pack of the EFX and the EXAFS spectrum from the Fe and Ni K edges was measured. The resulting spectra are shown in Fig. 2(a). By measuring two edges simultaneously, we are able to analyze both the iron and nickel K edges, allowing for more information to be extracted from a single shot.

The improved spectral resolution of EFX allows for x-ray absorption near-edge spectrometry (XANES) measurements to be made on OMEGA. Figure 2(b) shows the XANES from an iron foil in the front end of the EFX. A spectrum measured by an x-ray spectrometer (XRS) on the same shot is also shown for reference. XRS has been previously used to measure EXAFS on OMEGA[1] but was not able to perform XANES measurements. To highlight the key XANES features, the spectrum from iron measured at a synchrotron[2] is shown in the inset. The improved resolution of EFX is shown in the spectrum's steeper slope and ability to begin to capture the white line (point A) and central modulation (point B), which can be used to distinguish structural changes and melting in iron.[3] XANES pre-edge features have also been shown to increase with increasing compression,[4] meaning

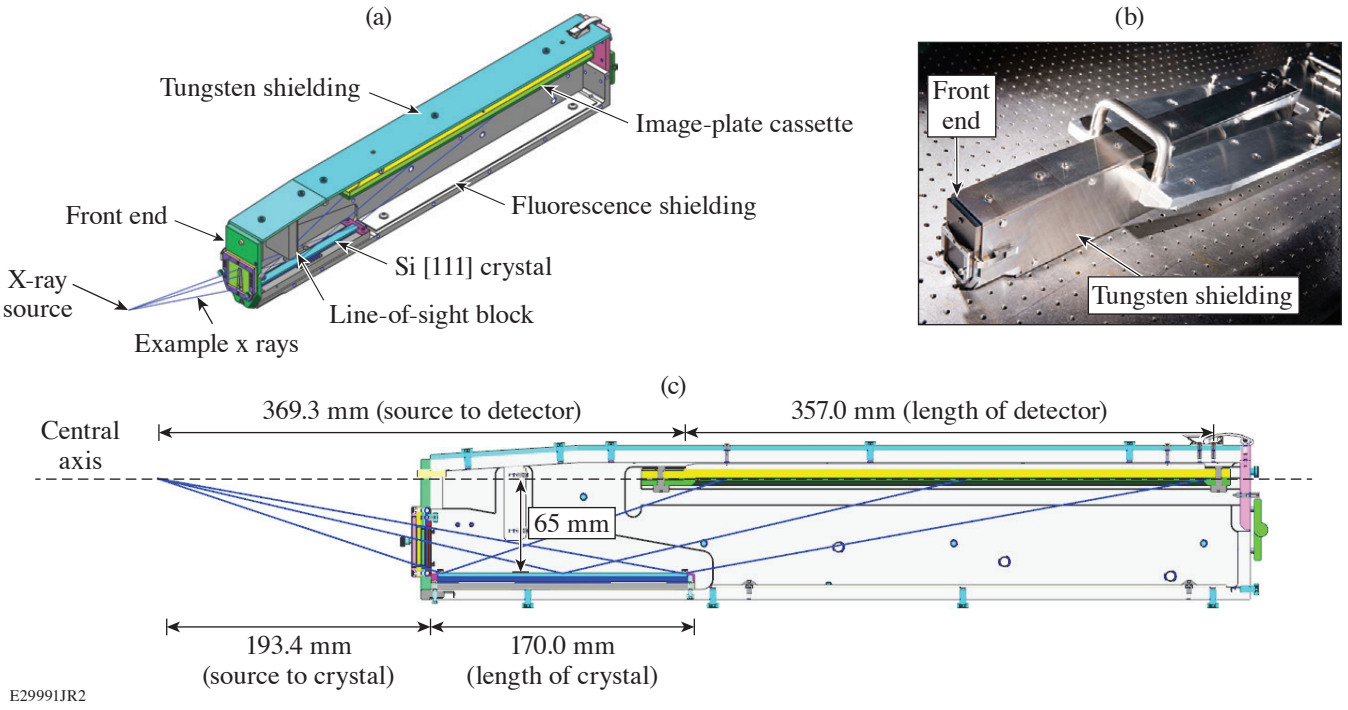

Figure 1
(a) Schematic of EFX showing the positions of the Si [111] crystal, the front end, and image-plate detector. (b) Photograph of EFX. (c) Cross section of EFX, highlighting the relevant distances for energy-dispersion calculations.

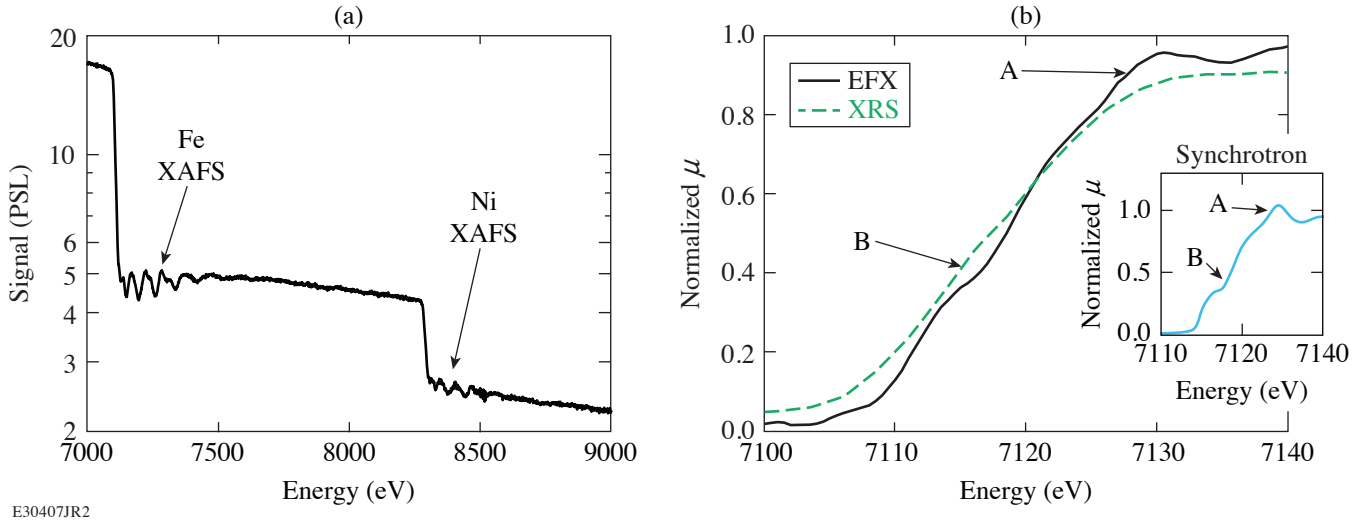

Figure 2
(a) Measured EXAFS spectra from Invar ($Fe_{64}Ni_{36}$) showing the Fe and Ni K edges from shot 100646. The figure demonstrates the capability of EFX to perform EXAFS on multiple edges of the same alloy simultaneously. (b) Comparison of iron XANES data between an EFX spectrum (black solid line) and an XRS spectrum (green dashed line), both taken on shot 97178. The higher resolution of EFX allows it to capture more detail in the white line (point A) and the central modulation (point B). Inset: An iron synchrotron spectrum,[2] where the same A and B points are highlighted similar to (b).

that these features may become more apparent during laser-driven experiments. This improved resolution in the XANES region of the spectrum will allow for future electron structure measurements of compressed materials.[4]

This material is based upon work supported by the Department of Energy National Nuclear Security Administration under Award Number DE-NA0003856. D. A. Chin acknowledges DOE NNSA SSGF support, which is provided under Cooperative Agreement No. DE-NA0003960. This collaborative work was partially supported under the auspices of the U.S. Department of Energy by Lawrence Livermore National Laboratory under Contracts No. DE-AC52-07NA27344.

1. Y. Ping *et al.*, Rev. Sci. Instrum. **84**, 123105 (2013).
2. International X-Ray Absorption Society: Fe Data, IXAS X-Ray Absorption Data Library, Accessed 10 May 2021, https://xaslib.xrayabsorption.org/elem/.
3. M. Harmand *et al.*, Phys. Rev. B **92**, 024108 (2015).
4. A. Sanson *et al.*, Phys. Rev. B **94**, 014112 (2016).

(Cd,Mg)Te Crystals for Picosecond-Response Optical-to-X-Ray Radiation Detectors

J. Cheng,[1,2] G. Chen,[1,2] D. Chakraborty,[1,2] S. Kutcher,[3] J. Wen,[3] H. Chen,[3] S. Trivedi,[3] and Roman Sobolewski,[1,2,4]

[1]Materials Science Graduate Program, University of Rochester
[2]Laboratory for Laser Energetics, University of Rochester
[3]Brimrose Technology
[4]Departments of Electrical and Computer Engineering and Physics and Astronomy, University of Rochester

We demonstrate a photodetector sensitive to both optical and x-ray picosecond pulses based on our in-house grown cadmium magnesium telluride (Cd,Mg)Te single crystal. Specifically, we developed In-doped $Cd_{0.96}Mg_{0.04}Te$ material and discuss its femtosecond optical photoresponse, as well as the detector performance, like <100-pA dark current and up to 0.22-mA/W responsivity for 780-nm-wavelength optical radiation. The detector exposed to Ti fluorescence (K_α) x-ray pulses at 4.5 keV, generated by a free-electron laser beam with a central energy of 9.8 keV and <100-fs pulse width, exhibited readout-electronics–limited 200-ps full-width-at-half-maximum photoresponse, demonstrating that it is suitable for coarse timing in free-electron laser x-ray/optical femtosecond pump–probe spectroscopy applications.

Ultrafast, solid-state detectors covering the optical/near-infrared to x-ray radiation spectrum are in high demand due to their versatile applications, including optical/x-ray subpicosecond pump–probe spectroscopy. Only a few available photodetectors can adequately do this job. Si-based photodetectors cover a wide range of wavelengths and can operate in the x-ray range; however, they degrade due to environmental effects as well as radiation damage.[1] Photodetectors based on metal–semiconductor–metal (MSM) structures with interdigitated electrodes, fabricated on low-temperature–grown GaAs (LT-GaAs), such as, e.g., a HAMAMATSU G4176-03 photodetector, are typically designed for picosecond temporal response for optical signals.[2]

We demonstrate that (Cd,Mg)Te (CMT) is a very promising candidate as a dual-optical/x-ray ultrafast detector. CMT is a ternary compound with a tunable direct energy gap from ~1.5 eV to 3.1 eV by changing the Mg content.[3] At the same time, due to the presence of a high-stopping-power Te element, crystals very effectively absorb high-energy x-ray photons [for a 1-mm-thick (Cd,Mn)Te crystal, the 1/*e* absorption drop occurs at 94.2 keV; Ref. 4]. The carrier lifetime of doped CMT can be comparable to that of LT-GaAs, which is critical in ultrafast temporal resolution. Ultralow device leakage current is another essential criterion, and CMT can have a lower leakage current than GaAs in the same MSM arrangement because of its larger band gap.

The $Cd_{1-x}Mg_xTe$ (x is between 0 to 0.45) crystal exhibits the zinc blende structure and it is the latest member of ternary alloys that include (Cd,Zn)Te and (Cd,Mn)Te, both well known for x-ray detection applications.[4,5] (Cd,Mg)Te possesses all the necessary qualities for an optimal radiation detector, like high material density (5.83 g/cm^3), high effective mass (49.5), ultrahigh resistivity (~10^{10} Ωcm), and good electron mobility lifetime ($\mu\tau$) product (>10^{-4} cm^{2}V^{-1}) (Ref. 6). In addition, the CMT "parent" crystals, CdTe and MgTe, exhibit very close lattice constants, 6.48 Å and 6.42 Å, respectively,[7] leading to a high-quality growth of CMT single crystals. At room temperature, the band gap of $Cd_{1-x}Mg_xTe$ is a linear function of x, increasing at a rate of around 15 meV per Mg atomic percent.[3] At $x = 0$, the CdTe band gap is 1.503 eV (Ref. 3).

Brimrose developed an innovative in-house procedure to purify magnesium to the highest achievable level. This proprietary technique involves sublimation under dynamic vacuum. The process uses two ampoules—the inner pyrolytic boron nitride (PBN)

ampoule is placed inside the graphitized fused-silica ampoule of a length a little longer than the PBN ampoule. Thus Mg (in molten or vapor phase) is prevented from reacting with the outer fused-silica ampoule, which is connected to the high-vacuum system.

The vertical Bridgman method was used to grow high-purity CMT single crystals.[8] Approximately 1-in.-diam ingots are grown, sliced into 1-mm-thick wafers (Fig. 1), and, finally, cut into suitably sized samples (from 4 × 4 mm^2 to 10 × 10 mm^2). During the growth process, the content of Mg can be modified and selective dopants can be added. Additionally, post-growth annealing can be optimized in order to engineer a material that will exhibit characteristics required for a given application. We determined that 3% to 8% Mg and 2% to 5% In doping led to CMT crystals with a suitable band gap and acceptable electron mobility times lifetime ($\mu\tau$) product (>10^{-4} cm^{2}V^{-1}), as well as a large enough resistivity (>10^{10} W-cm) for detector applications.[9]

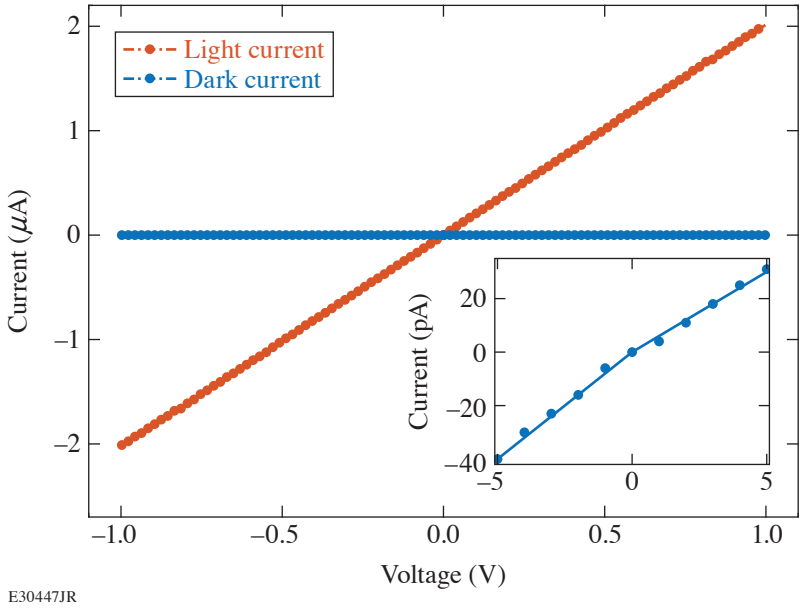

Figure 1
Current–voltage (I–V) characteristics under light (orange) and dark (blue) conditions for a tested CMT device. The inset shows the dark current I–V in detail (bulk measurement across a CMT sample).

We selected the Mg concentration in (Cd,Mg)Te the way that the crystal should have the band gap compatible for an optical photodetector operation within the tunability of a Ti:sapphire femtosecond pulsed laser. For this purpose, we performed optical reflection and transmission spectra measurements using a PerkinElmer Lambda 900 spectrometer with samples placed at normal incidence. The Tauc plot for direct-band-gap material[10] combines the collected experimental spectra and presents the crystal absorption spectrum. We observed a sharp optical transition edge and the band gap E_G = 1.57 eV, with a small absorption tail below E_G that is typically related to shallow sub-gap trap states. For photons with energies above E_G we see the full absorption. In-doped, $Cd_{0.96}Mg_{0.04}Te$ crystals were used in the subsequent detector fabrication.

Photoresponse measurements were carried out in the surface-mode configuration with an optical beam, generated by a Ti:sapphire laser (780-nm wavelength) focused between the electrodes. A bank of neutral-density filters was used to control the laser intensity and the current–voltage (I–V) characteristics were collected using a digital sourcemeter. Figure 1 demonstrates a strong photoconductive effect of our CMT MSM diode. Under optical excitation (orange curve; 20-mW laser power) a photocurrent reaches ~2 μA at a 1-V bias. The I–V dependence is linear, indicating an absence of Schottky barriers. At the same time, the dark current (blue curve) is completely negligible. In the measurements above, we used the bias voltage only up to 1 V in order to avoid a possible breakdown between the electrodes separated by just 25 μm.

Further systematic photoresponse characterization was carried out on our CMT diodes, including the photocurrent and responsivity dependencies on voltage for a wide range of incident optical powers. Figure 2 shows a family of the responsivity traces as a function of detector bias voltage for incident power in the 20-μW to 20-mW range. We note that for our device, the responsivity increases as the decrease of incident power. This phenomenon is related to the intrinsic gain mechanism in semiconductors characterized by a substantial disparity in electron and hole mobilities. The greatest responsivity obtained is 0.22 mA/W, but we

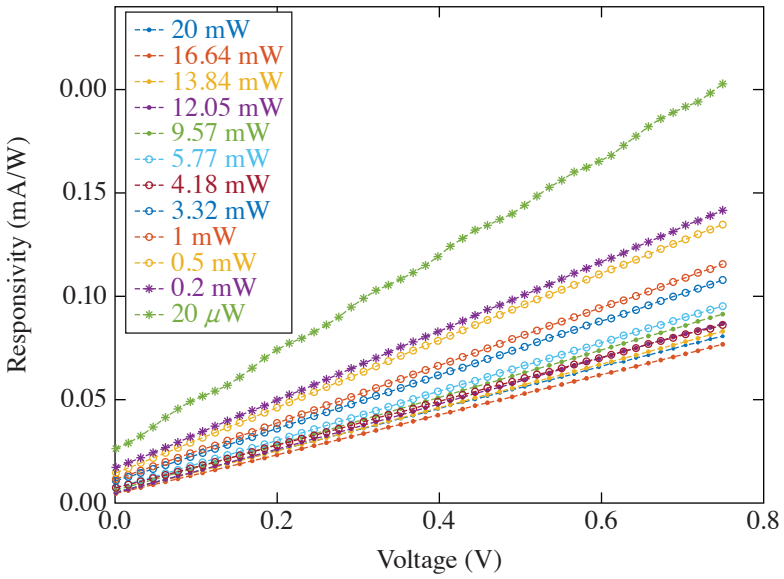

Figure 2
CMT diode responsivity versus bias voltage for several incident power levels of the 780-nm-wavelength radiation (bulk measurement across a CMT sample).

expect to increase it very substantially when the surface detector structure is fabricated in a form of a large-area interdigitated-electrode configuration to increase the collection of carriers generated by the light/x-ray radiation.

The CMT diode was also a subject of preliminary tests at the SLAC National Accelerator Laboratory. Figure 3 presents an actual oscilloscope image of the diode response to an x-ray pulse. To prevent damage to the detector, a <100-fs-wide, 9.8-keV central energy, and 120-Hz repetition rate train of x-ray pulses from a free-electron laser were directed onto a titanium target, so the signal shown in Fig. 3 is actually the x-ray fluorescence at the Ti K_α edge (4.5 keV). The observed signal has an ~0.2-ns FWHM and a <100-ps rise time, limited by the detection electronics. The above parameters make our device suitable for course timing of optical/x-ray subpicosecond pump–probe spectroscopy experiments.

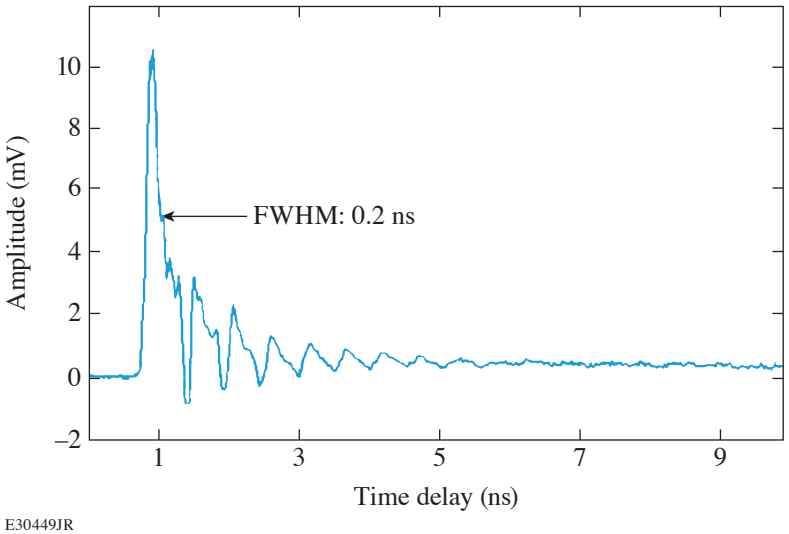

Figure 3
Oscilloscope plot of the time-resolved CMT detector response to a pulsed x-ray signal generated at the SLAC National Accelerator Laboratory. After-pulse oscillations are due to the impedance mismatch in the electronics detection channel.

We demonstrate that (Cd,Mg)Te is a very promising candidate for ultrafast optical/near-infrared to x-ray radiation detector applications. We selected the In-doped $Cd_{0.96}Mg_{0.04}Te$ crystal for our detectors, so its optical bandwidth made it sensitive to the Ti:sapphire light, while In doping resulted in an ultrahighly resistive material characterized by a <100-pA leakage dark current and 2.4-ps electron relaxation time. The detector was tested at the SLAC National Accelerator Laboratory and exhibited a

response signal of 200-ps FWHM (electronics limited) when exposed to Ti fluorescence (K_α) x-ray pulses at 4.5 keV, generated by a free-electron laser beam with the central energy of 9.8 keV and <100-fs pulse width. The latter confirms CMT suitability for the free-electron laser pump–probe spectroscopy timing applications.

The authors thank Drs. Takahiro Sato and David Fritz from the SLAC National Accelerator Laboratory for providing Fig. 3. This work was supported in part by the Department of Energy Phase I SBIR program under Award: DE-SC0021468 and monitored by Dr. Eliane S. Lessner and Dr. Yiping Feng (DOE/SLAC).

1. M. Shanmugam *et al.*, J. Instrum. **10** (2015).
2. Hamamatsu Preliminary Data, Ultrafast Response of Several Tens Picosecond; G4176-03, Accessed 27 February 2023, https://www.datasheet.cloud/pdfviewer?url=https%3A%2F%2Fpdf.datasheet.cloud%2Fdatasheets-1%2Fhamamatsu_photonics_k.k.%2FG4176-03.pdf.
3. E. G. LeBlanc *et al.*, J. Electron. Mater. **46**, 5379 (2017).
4. A. S. Cross *et al.*, Nucl. Instrum. Methods Phys. Res. A **624**, 649 (2010).
5. Y. Eisen, A. Shor, and I. Mardor, IEEE Trans. Nucl. Sci. **51**, 1191 (2004).
6. S. B. Trivedi *et al.*, *Next Generation Semiconductor-Based Radiation Detectors Using Cadmium Magnesium Telluride (Phase I Grant—DE-SC0011328)*, U.S. Department of Energy, Washington, DC, Report DOE/11172015-Final (2017).
7. J.-H. Yang *et al.*, Phys. Rev. B **79**, 245202 (2009).
8. S. B. Trivedi *et al.*, J. Cryst. Growth **310**, 1099 (2008).
9. J. Serafini *et al.*, Semicond. Sci. Technol. **34**, 035021 (2019).
10. J. Tauc, R. Grigorovici, and A. Vancu, Phys. Stat. Sol. (B) **15**, 627 (1966).

Exact Solutions for the Electromagnetic Fields of a Flying Focus

D. Ramsey,[1] A. Di Piazza,[2] M. Formanek,[3] P. Franke,[1] D. H. Froula,[1] B. Malaca,[4] W. B. Mori,[5] J. R. Pierce,[5] T. T Simpson,[1] J. Vieira,[4] M. Vranic,[4] K. Weichman,[1] and J. P. Palastro[1]

[1]Laboratory for Laser Energetics, University of Rochester
[2]Max-Planck-Institut für Kernphysik
[3]ELI-Beamlines, Institute of Physics of Czech Academy of Sciences
[4]GoLP/Instituto de Plasmas e Fusão Nuclear, Instituto Superior Técnico, Universidade de Lisboa
[5]University of California Los Angeles

All focused laser fields exhibit a moving focus in some frame of reference. In the laboratory frame, an ideal lens focuses every frequency, temporal slice, and annulus of a laser pulse to the same location. The pulse moves through the focus at its group velocity and diffracts over a Rayleigh range. In any other Lorentz frame, the focus moves. "Flying-focus" techniques recreate these moving foci in the laboratory frame by modifying the focal time and location of each frequency, temporal slice, or annulus of a pulse. The intensity peak formed by the moving focus can travel at any arbitrary velocity while maintaining a near-constant profile over many Rayleigh ranges. All of these features make the flying focus an ideal spatiotemporal pulse-shaping technique to enhance a vast array of laser-based applications.

Assessing the extent to which a flying focus can enable or enhance these applications requires an accurate description of the electromagnetic fields. With the exception of the special case $v_I = -c$, all of the aforementioned applications were modeled using approximate solutions for the electromagnetic fields of flying-focus pulses. In the case of conventional pulses with stationary foci, improving the accuracy of approximate solutions has been found to impact models of phenomena ranging from direct laser acceleration to optical trapping. Methods for obtaining accurate solutions to Maxwell's equations for conventional laser pulses come in three forms: a "Lax"-like series expansion in which corrections to paraxial fields can be calculated recursively; a series expansions of exact spectral integrals for each field component; and the complex source-point method (CSPM), which exploits the invariance of Maxwell's equations under a translation in the complex plane to transform multipole solutions into beam-like solutions. Of these three, the CSPM is unique in its ability to provide closed-form solutions that exactly satisfy Maxwell's equations.[1] As a result, the solutions can be Lorentz transformed without introducing additional error.

In this summary, we derive exact solutions to Maxwell's equations for the electromagnetic fields of a constant-velocity flying-focus pulse. Figure 1 illustrates a schematic of the theoretical approach. The approach combines the CSPM with a Lorentz transformation from a frame in which the focus is stationary to a frame in which the focus is moving. The vector solutions are inherently non-paraxial, can have arbitrary polarization, and are generalized to higher-order radial and orbital angular momentum modes. Subluminal ($|v_I < c|$) and superluminal ($|v_I > c|$) solutions are constructed from multipole spherical and hyperbolic wave solutions, respectively. Propagating the fields backward in space reveals that each solution corresponds to a pulse that was focused by a lens with a time-dependent focal length. Thus, these solutions can be experimentally realized using the flying-focus X (Ref. 2). For a wide range of parameters, the differences between the exact solutions and simpler paraxial solutions are small, justifying the use of paraxial solutions for theoretical or computational studies of flying-focus applications in many regimes.

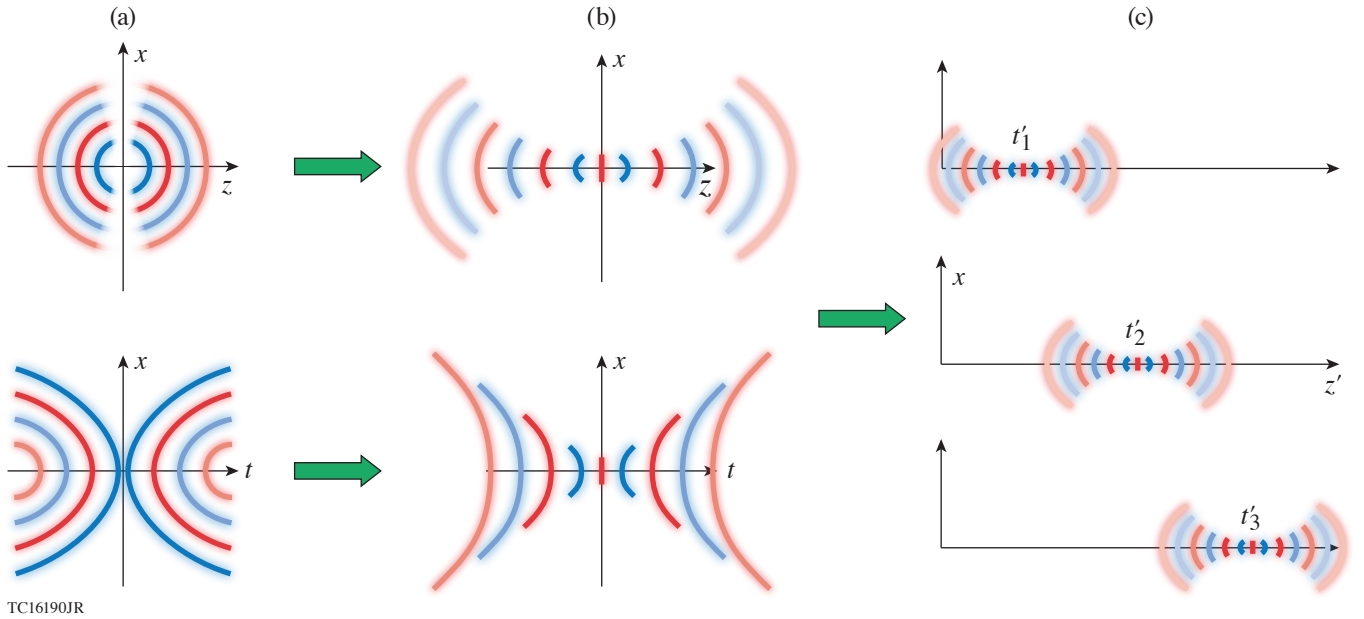

Figure 1
A schematic of the theoretical approach. (a) The approach starts with a multipole spherical (top) or hyperbolic (bottom) solution. (b) A displacement of the coordinate z (top) or t (bottom) into its complex plane transforms the multipole solution into a beam-like solution with a stationary focus in space (top) or time (bottom). (c) A Lorentz transformation of either beam-like solution from a frame of reference in which the foci appear stationary to the laboratory frame produces the exact electromagnetic fields of a flying focus.

As an example, the lowest-order mode electromagnetic fields with polarization vector $\hat{\mathbf{x}}$ are generated by the electric Hertz vector

$$\mathbf{\Pi}_e(\mathbf{x},t) = \frac{1}{2}\alpha_{00} j_0(\omega R/c) e^{i\omega t}\hat{\mathbf{x}} + \text{c.c.} \tag{1}$$

and magnetic Hertz $\mathbf{\Pi}_m = \hat{\mathbf{z}} \times \mathbf{\Pi}_e$ [Fig. 1(a)], where ω is the angular frequency and α_{00} is an arbitrary constant. After computing the corresponding four potential, the coordinate R is translated into the complex domain as $R \rightarrow \sqrt{x^2 + y^2 + (z - iZ_R)^2}$, where Z_R is the Rayleigh range of the resulting beam-like solution [Fig. 1(b)]. Finally, a Lorentz boost in the axial direction results in a flying focus [Fig. 1(c)]. All of these operations preserve the resulting electromagnetic fields as solutions to Maxwell's equations.

Figures 2(a)–2(f) display cross sections of the resulting electric and magnetic fields at the location of the moving focus $z' = v_I t'$ for $v_I = 0.5c$ and $\omega w_0/c = 20$, where the primed terms are as observed in the laboratory frame and w_0 is the spot size at focus. The predominant electric and magnetic fields, E'_x and B'_y have equal amplitudes and Gaussian-like transverse profiles. The remaining vector components exhibit more-complex spatial structure, but are much smaller in amplitude. Figure 2(g) illustrates the motion of the focus in the laboratory frame. The cycle-averaged longitudinal component of the Poynting vector $S'_z = c\hat{\mathbf{z}} \cdot \mathbf{E}' \times \mathbf{B}'/4\pi$ is plotted as a function of z' and t' at $x = y = 0$. For comparison, the dashed black line demarcates the speed of light trajectory $z' = ct'$.

This material is based upon work supported by the Office of Fusion Energy Sciences under Award Number DE-SC0019135 and DE-SC00215057, the Department of Energy National Nuclear Security Administration under Award Number DE-NA0003856, the University of Rochester, and the New York State Energy Research and Development Authority.

1. A. L. Cullen and P. K. Yu, Proc. Roy. Soc. A **366**, 155 (1979).
2. T. T. Simpson *et al.*, Opt. Express **30**, 9878 (2022).

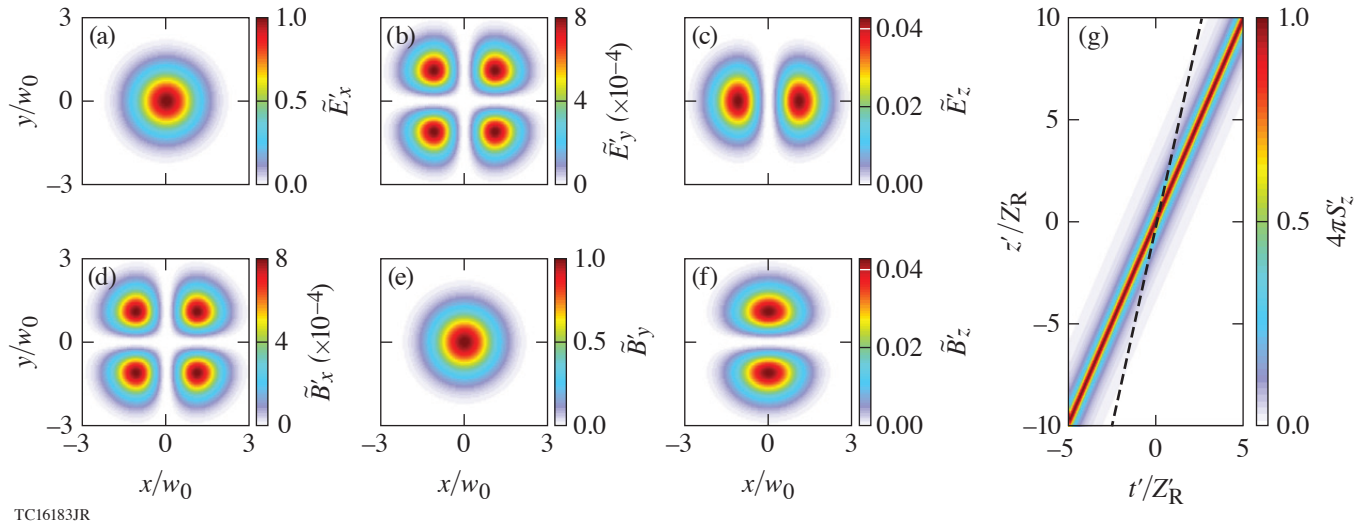

Figure 2

The lowest mode subluminal focus with $v_f = 0.5c$ and $\kappa' w_0 = 20$. [(a)–(f)] Cross sections of the electromagnetic-field amplitudes at the location of the moving focus $z' = v_f t'$. Here $\widehat{E}' = \langle E'^2 \rangle^{1/2}$, where $\langle\ \rangle$ denotes a cycle average. The amplitudes are normalized to the $(\widetilde{E}'_x)$. (g) The longitudinal component of the cycle-averaged Poynting vector S'_z at $x = y = 0$, showing the motion of the focus. The dashed black line demarcates the trajectory $z' = ct'$ for reference.

Methods and Apparatus for Comprehensive Characterization of Performance Attributes and Limits of Ultrafast Laser Optics

K. R. P. Kafka, T. Z. Kosc, and S. G. Demos

Laboratory for Laser Energetics, University of Rochester

The output power of ultrashort-pulse laser systems can be affected by the ability of the constituent optical components to withstand the generated laser intensity, typically defined by the laser-induced–damage threshold (LIDT). However, large-aperture optics employed in the most powerful laser systems can operate using optics that have sustained some damage with limited performance degradation. In this regime, the operational lifetime of an optic then begins to be governed by the rate of damage growth (increase in size of the damaged area) under subsequent exposure to system laser pulses. Furthermore, recent reports have shown that the optical properties of materials exposed to ultrashort laser pulses can be transiently modified by the high electric-field intensities that can still be below the LIDT fluences. This in turn may cause the modification of the functionality of a device without the initiation of damage.[1] The vast majority of literature to date has focused primarily on measuring the LIDT under single- and multipulse excitation. There is clearly a need to expand the characterization protocols for such optics to include evaluation for the laser-induced–damage growth and functional failure thresholds. The present work describes a system that was developed to provide comprehensive performance characterization, including damage initiation, damage growth, and laser-induced functional degradation for near-infrared, femtosecond-pulsed applications.

A schematic of the testing apparatus developed as part of this work is shown in Fig. 1, with the main components consisting of an ultrafast laser and the experimental damage-testing platform located inside a vacuum chamber. It employs a custom-built optical parametric chirped-pulse–amplification laser system ("Ultraflux," EKSPLA) with 20-fs pulse duration, 820-nm to 970-nm tunable central wavelength, 5-Hz repetition rate, and up to 2-mJ output pulse energy. An *in-situ* dark-field microscope monitors the sample surface to detect damage initiation and/or growth. The reflected beam from the surface of the sample is imaged onto a camera located outside the chamber (L and M7, respectively, in Fig. 1) for laser-induced functional threshold (LIFT) characterization.

Since accurate measurements of damage-growth parameters require the test beam to be significantly larger than the initial and subsequently growing damage site, this system is designed to provide beam area variation of more than one order of magnitude. This was achieved by mounting the beam-focusing optic [off-axis parabolic mirror (OAP) in Fig. 1] on a translation stage together with folding mirror M4 to control the distance from the sample. As these two optics move in tandem, the beam size on the sample changes without disturbing the beam alignment. To facilitate utilization of near-LIDT fluences across a wide range of beam sizes, many of the necessary system features required considerations for management of B-integral (nonlinear phase) that is introduced at high energies in the large-beam configuration. These considerations impacted the design of pulse energy control, polarization control, vacuum window, and beam sampling for diagnostics after all resulting in a calculated total of about $B \approx 1$ at maximum pulse energy.

The operation of the system is demonstrated by the testing of a low-group-delay-dispersion metal-dielectric mirror coating that is designed for broadband enhanced reflection in the near-infrared. This sample was tested at 890-nm central wavelength using 22-fs pulses at a 45°angle of incidence under vacuum environment. The damage-growth measurements were carried out by first initiating damage sites using the smallest beam with a single pulse at a fluence 10% to 15% above the LIDT. This formed a damage site with a diameter of approximately 20 to 30 μm, a precursor from which to measure damage growth. Then the beam size was increased to a 350-μm Gaussian diameter, and each precursor was irradiated by 50 pulses at a fixed fluence. Figure 2(a)

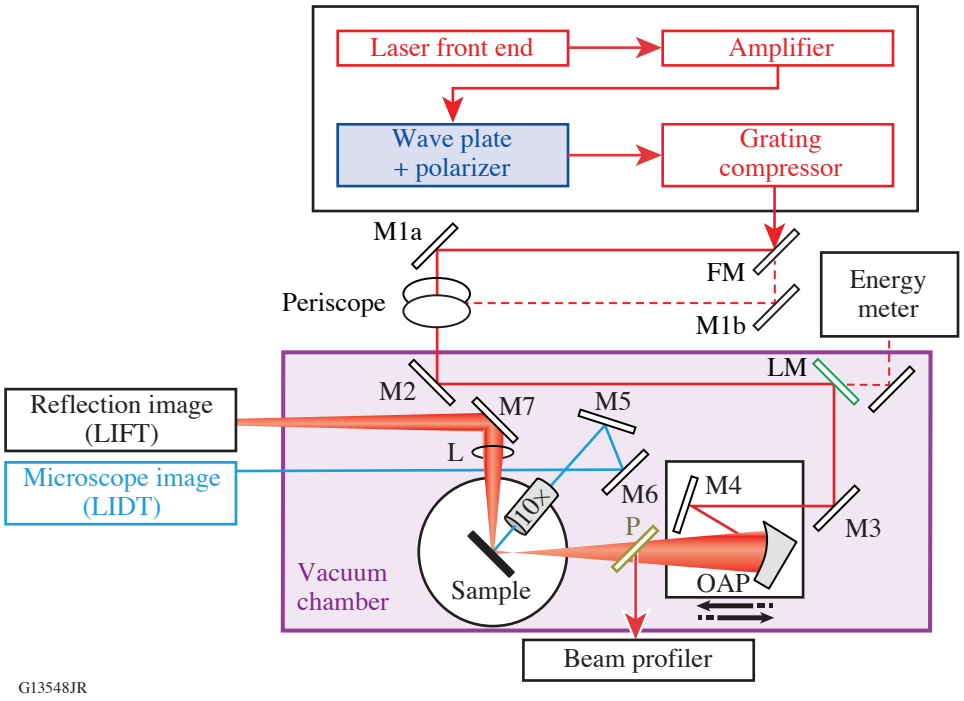

Figure 1
Schematic of performance characterization apparatus. FM: flip mirror; M#: mirror; LM: leaky mirror; OAP: off-axis parabolic mirror; P: pickoff; 10×: 10× microscope objective lens; L: lens.

depicts the size of the single-pulse damage initiation site with respect to the enlarged test beam. The remainder of Fig. 2 shows examples of non-growing and growing sites with each test polarization, imaged off-line using differential interference contrast microscopy. By comparing images of the sample before and after multipulse irradiation, the presence or absence of damage growth was determined for each site, making it possible to calculate the fluence thresholds.

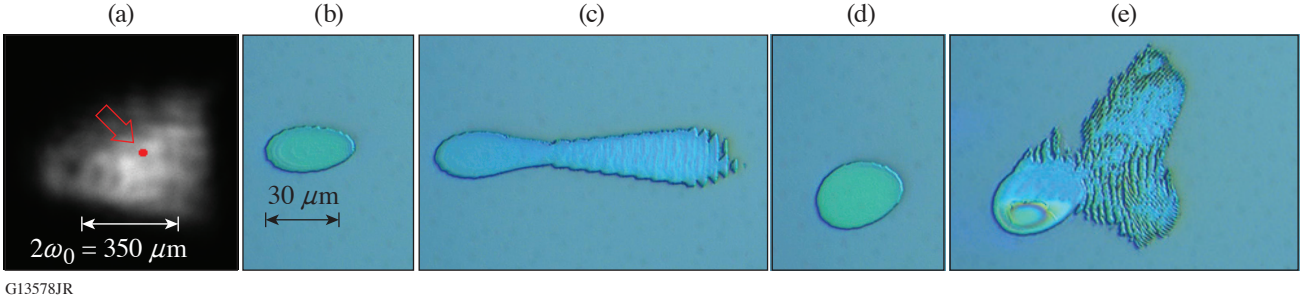

Figure 2
Example morphologies of a damage-growth experiment in optical microscopy. (a) The 30-μm damage initiation site (purposely generated to become the "seed" site for damage-growth experiments) is shown in red overlaid on an example beam profile. For *s* polarization: (b) non-growing site, (c) growing site at 0.34 J/cm^2. For *p* polarization: (d) non-growing site, and (e) growing site at 0.43 J/cm^2. The laser is incident from the left.

The functional performance (a change of the reflection) can be observed by calculating the ratio of reflected beam images from different pulses after first normalizing those images to the total energy. Specifically, reflected beam images represent the ratio between (1) a given test pulse and (2) a previous pulse that did not initiate damage. An example sequence of ratio images showing a detected functional change is depicted in Fig. 3, alongside the concurrent images from *in-situ* dark-field microscopy that show damage has formed. The lineouts across the respective interaction regions are shown in Fig. 3(f). Starting with the

pulse in Fig. 3(a), no damage is initiated, and the lineout shows a constant value. In Fig. 3(b), there is clearly a measurable drop of reflectance in the center of the laser beam (indicating functional modification), consistent with energy loss and the onset of damage. The dark-field images shown before and after damage initiation [Figs. 3(d) and 3(e), respectively]. Because in this example the LIFT occurred concurrently to the initiation of damage, the ratio image from the next pulse [Fig. 3(c)] has severely reduced central reflectance (from 1.0 to 0.3) due to low reflectivity of the ablation site. This suggests that a system designed to measure LIFT could simultaneously be a sensitive *in-situ* diagnostic for LIDT measurement with *S*-on-1 or *R*-on-1 protocols.

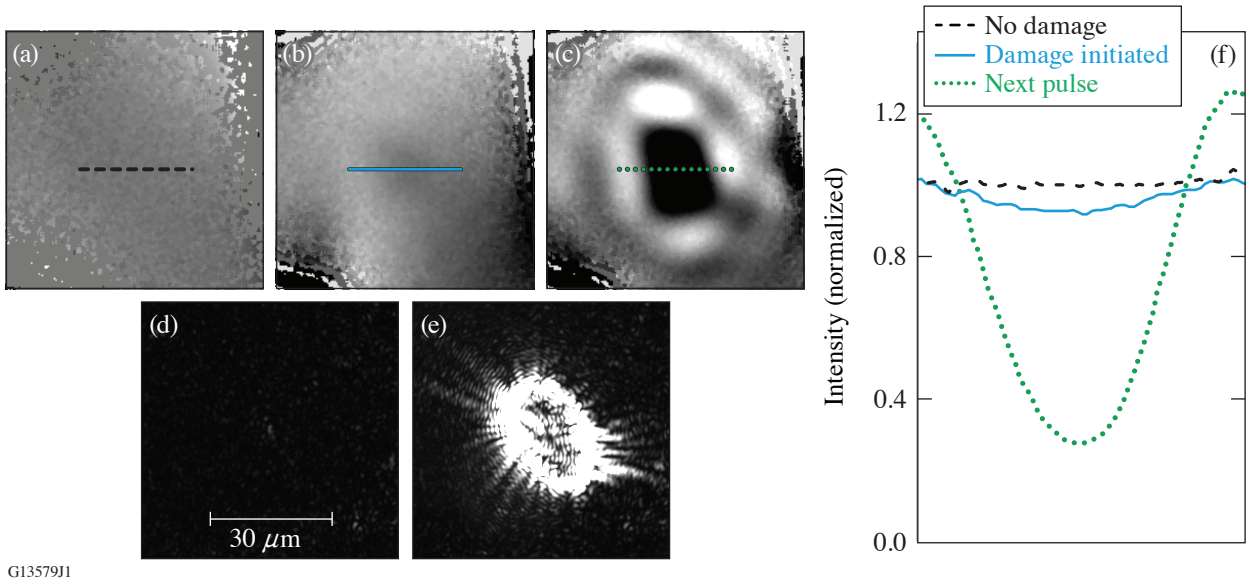

Figure 3
In-situ microscopy of damage formation using [(a)–(c),(f)] functional performance characterization and [(d),(e)] dark-field microscopy. Reflected beam images of (a) a pulse that did not damage, (b) the pulse that initiated damage, (c) the next pulse after damage initiation. Each image in (a)–(c) was normalized by a reflected beam image of a previous pulse that did not initiate damage. (f) The lineouts of the respective reflection images. Dark-field microscope image of the sample, collected (d) before damage initiation, (e) after damage initiation but before the next pulse.

The system and methodology for the characterization of optical components for large-aperture, ultrashort pulse laser systems aims to address current and future needs to support the development of next-generation 100-PW-class laser systems. Achieving the technical objectives required novel implementation of the testing system to avoid problematic nonlinear beam-propagation effects. Initial results underscore that precise damage-testing measurements of optical elements using ultrashort pulses with an expanded and multifaceted definition of damage is important to provide a wide range of information regarding the processes involved that can aid development of improved optic designs and reliable operational fluence limits.

This material is based upon work supported by the Department of Energy National Nuclear Security Administration under Award Number DE-NA0003856, the University of Rochester, and the New York State Energy Research and Development Authority.

1. O. Razskazovskaya *et al.*, Proc. SPIE **9237**, 92370L (2014).

Design and Demonstration of the "Flow-Cell" Integrated-Flow, Active-Cooling Substrate for High-Average-Power Substrates

E. P. Power, S. Bucht, K. R. P. Kafka, J. Bromage, and J. D. Zuegel

Laboratory for Laser Energetics, University of Rochester

We designed, fabricated, and tested a prototype flow-cell integrated-cooling substrate built using cordierite ceramic and demonstrated average power handling up to 3.88-W/cm^2 absorbed power density with 54-nm peak-to-valley deformation in a subaperture test.[1,2] Mechanical stabilization was observed to occur on a time scale <30 s. Model predictions indicate a full-aperture performance limit of 2.6-W/cm^2 absorbed power density with <λ/10 deformation and <90-s stabilization time, equivalent to 100-mJ/cm^2 fluence per pulse with a 1-kHz repetition rate on an optic with 2.6% absorption. Chirped-pulse–amplification lasers commonly use gold-coated compressor gratings operating with beam-normal fluences of ~100 mJ/cm^2 to stay below the short-pulse damage-fluence limit. Existing multiterawatt and petawatt femtosecond lasers operate at relatively low repetition rate (Hz and slower); thermal effects are not experienced by gratings located in vacuum chambers at these low-average powers. Thermal expansion of gratings under high-average-power conditions will cause wavefront deformation (focusing errors) and modify the frequency-dependent path lengths through the system (compression errors), leading to unacceptable spatial and temporal degradation of the focused laser spot and compressed pulse, respectively. Joule-class lasers operating at kilowatt average powers would require large beam sizes (~300 cm^2 or ~20 cm diam) with current gratings given their ~10-W/cm^2 average power (~10 mJ/cm^2 at 1 kHz) handling capacity. Simulations show that new gratings fabricated on thermally stable and actively cooled substrates can reduce pulse width, improve temporal contrast, and decrease focal-spot degradation,[3] but significantly better thermal management of diffraction gratings is needed for future high-average-power lasers for accelerator and beam-combining applications.

The flow-cell integrated active-cooling design is built around a hexagonal unit cell. The close-packed structure of cells is similar to lightweighted optics for aerospace applications, the primary differences being a closed back and integrated fluid input/output channels. The final prototype design uses a hexagon inscribed in a 13-mm diameter with 8-mm pocket depth and cell-to-cell wall thickness of 2 mm. Exterior dimensions for the prototype are 130.18 × 63.5 × 47.29 mm^3, with a defined clear aperture of 101.6 × 50.8 mm^2 centered on the front surface. The front boundary of each cell is located 5 mm behind the optical surface. Figure 1 shows the interior structure of the fabricated prototype.

COMSOL modeling was performed using unidirectional coupling between pressure in the fluid domain and deformation in the solid domain. That is, it was assumed that the small nanometer-scale motion of the fluid–solid boundaries would not impact fluid flow, which is defined by millimeter-scale geometric features. Therefore, as discussed in more detail in Ref. 1, steady-state isothermal turbulent flow was computed once, and the resulting fluid velocities and pressures were used as static input to the follow-up thermomechanical computation. The predicted temperature rise of <1° C in the fluid is assumed insufficient to require a fully coupled model including non-isothermal flow. Input and output coolant baths were computed only in the fluid domain; we are uninterested in the response of the steel plenum pieces fabricated as dual-purpose optic mount/fluid baths.

Figure 2 shows the heater beam delivery and metrology for testing thermally loaded samples. The device under test was held under vacuum in a custom-built cylindrical vacuum chamber. The heater beam entrance and exit ports were arranged 90° apart, allowing 45° incidence on the test optic. The heater source available in our setup was a 976-nm cw source with a maximum on-target power of ~100 W. A commercial Fizeau interferometer (Zygo Dynafiz) was used at normal incidence using a 632.8-nm

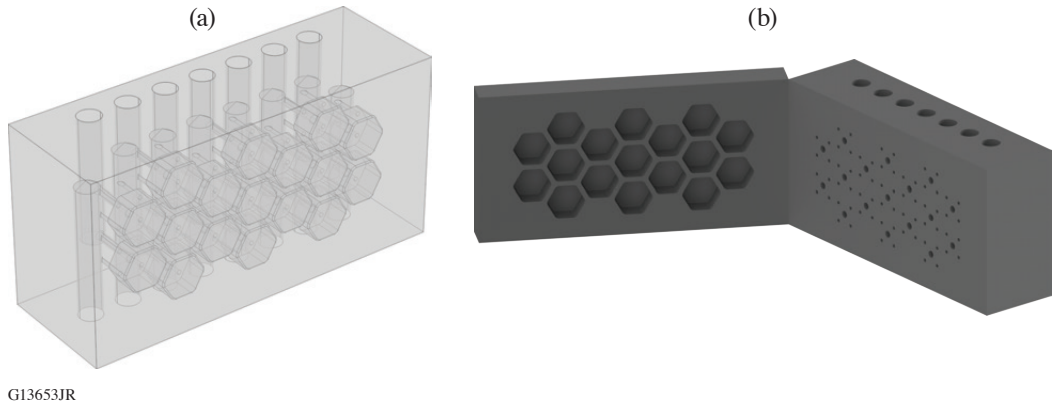

Figure 1
(a) Transparent rendering of the prototype optic used in modeling. The optical surface is toward the front, fluid input is through the top columns, and coolant drainage is through the bottom (obscured). (b) Opaque rendering of the prototype optic cut open at the back plane of the flow cells to aid visualizing input and output channels for individual unit cells.

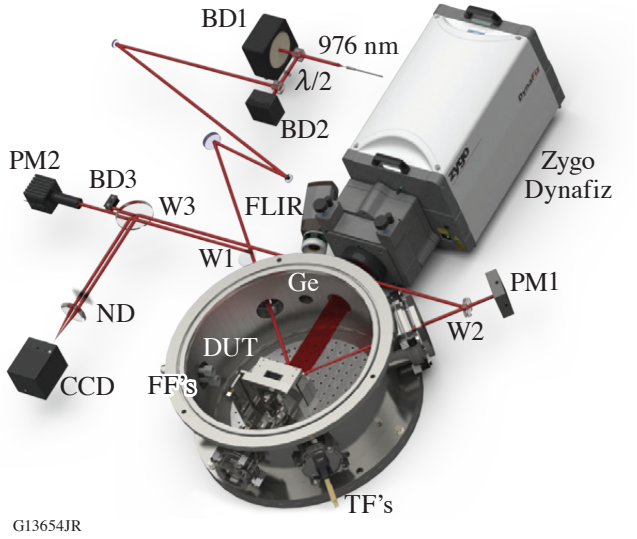

Figure 2
Thermal loading test stand layout using the 976-nm heater source. BD1: water-cooled beam dump; BD2, BD3: air-cooled beam dumps; W1, W2, W3: uncoated wedges; PM1: water-cooled thermopile; PM2: air-cooled Si diode + integrating sphere; FF: fluid feedthrough; TF: thermocouple feedthrough; ND: neutral-density filter; CCD: charge-coupled device; DUT: device under test. A Ge window for the FLIR thermal imaging camera is shown; all other windows are V-coated for the appropriate wavelength (976-nm heater or 632.8-nm Fizeau).

stabilized HeNe laser. A small Ge window placed near the interferometer window allows a thermal imaging camera (FLIR) to view the heated area. Eight type-K thermocouple feedthroughs allowed for spot measurement of temperature in a variety of locations on the sample, mount, or chamber. Two fluid feedthroughs allowed coolant flow for in vacuum liquid-cooled components.

Cordierite ceramic was selected as the material for the flow-cell prototype due to its superior thermomechanical properties: 4.0 W/m-K thermal conductivity and $<0.02 \times 10^{-6}$ K^{-1} thermal expansion coefficient. Steady-state and time-dependent testing of a flow-cell prototype was performed using 97.1 W of optical power, corresponding to 3.88 W/cm^2 absorbed power density. The incidence angle in the COMSOL model was set to 45° to match laboratory conditions. Unfortunately, the 976-nm laser source does not have additional power available; therefore, the beam size could not be increased to cover a larger portion of the clear aperture. Results measured when heating the flow-cell with 3.88 W/cm^2 absorbed power density are shown in Figs. 3(a) and 3(c), with COMSOL model results in Fig. 3(b). Agreement between the modeled and measured steady-state response in Figs. 3(b) and 3(c) is excellent, differing by 0.2 nm peak-to-valley (p–v). Also in excellent agreement is the time-dependent response in Fig. 3(a); stabilization dynamics measured in the laboratory are well matched by model predictions, and the observed mechanical stabilization time is <30 s to reach >99% of the steady-state deformation.

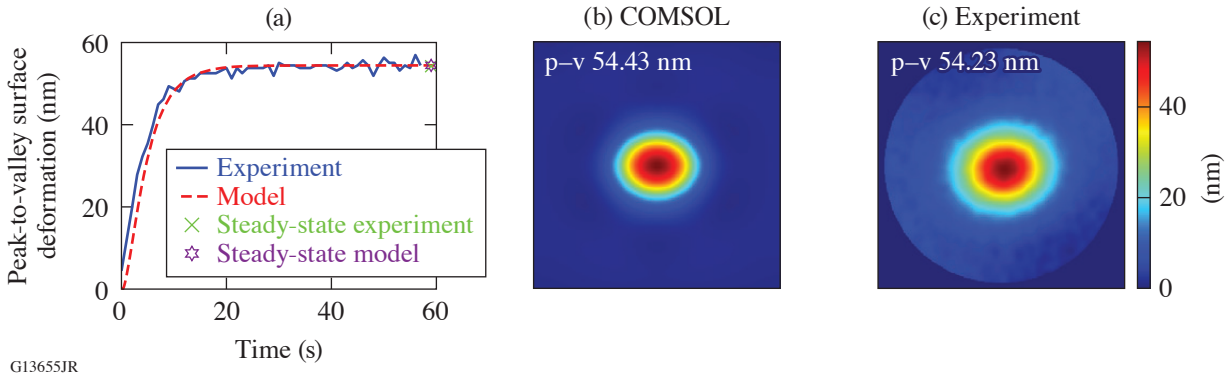

Figure 3
(a) Stabilization dynamics of the flow-cell prototype as indicated by the measured p–v surface deformation (blue curve): the sample was heated with a 1.3-cm-diam beam with absorbed power density of 3.88 W/cm^2. Surface maps were acquired in fast Fizeau mode at 1 Hz; $t = 0$ marks the initiation of the heater beam. Model results for the same conditions (red curve) are an excellent match; the dynamics and stabilization time scales are well reproduced. Mechanical stabilization was observed to occur in <30 s. (b) COMSOL steady-state model prediction for surface deformation, and (c) measured surface deformation after 5 min of continuous heating.

We used the same COMSOL model that successfully predicted sub-aperture behavior to predict full-aperture performance. The only model parameters changed were beam diameter (increased to 5 cm) and optical power (increased to 1 kW). The resulting absorbed power density was 2.6 W/cm^2, slightly above our 2.5-W/cm^2 design target. Figure 4 shows the results from this modeling effort: (a) shows that the thermal profile is qualitatively similar to the sub-aperture case we tested in the laboratory, with peak temperature on the surface slightly lower in this scenario due to the lower absorbed power density, and (b) shows the surface deformation dynamics: surface deformation reaches >99% of the steady-state value in <90 s. The steady-state model predicts 80-nm deformation for 2.6-W/cm^2 absorbed power density, meeting the $\lambda/10$ limit at 800 nm.

We simulated the dynamic response of a passively cooled cordierite brick with identical outer dimensions and beam geometry as the flow-cell prototype and found an upper limit of ~0.1 W/cm^2 absorbed power density to maintain p–v deformation $<\lambda/10$. As expected, stabilization was orders of magnitude slower, reaching the >99% threshold for p–v deformation required 4.75 h, as shown in the inset of Fig. 4(b).

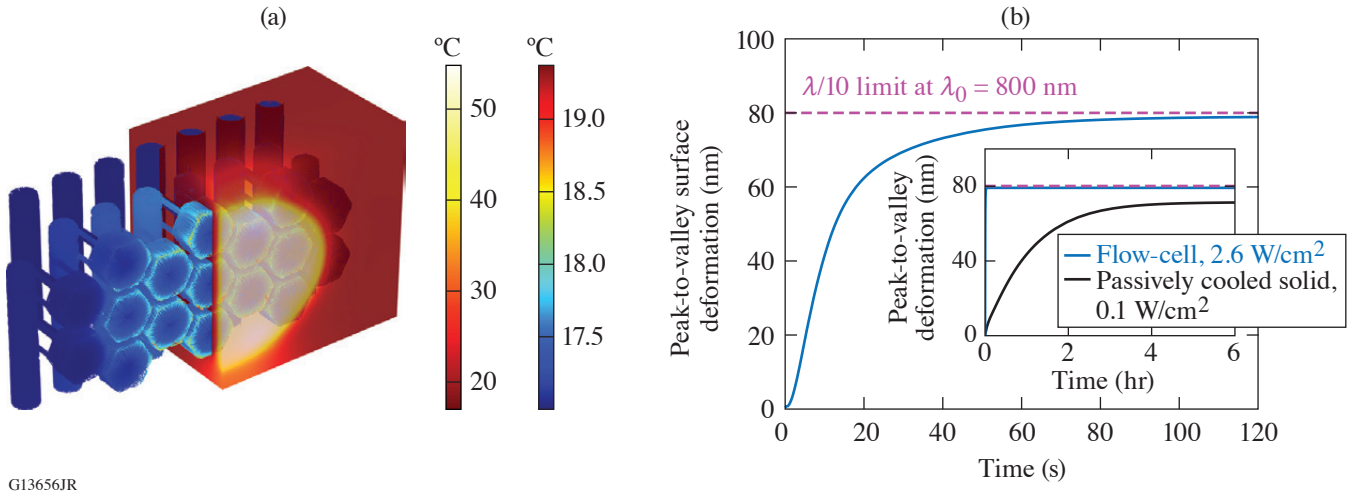

Figure 4
COMSOL results for the flow-cell prototype heated with a 5-cm-diam beam. (a) Temperature profile using 2.6-W/cm^2 absorbed power density; the solid domain is semi-transparent. (b) Predicted heating dynamics: the mechanical stabilization time was <90 s. Inset: dynamic response of a passively cooled cordierite brick heated with 0.1 W/cm^2.

In separate testing, Plymouth Grating Labs fabricated four Au-coated gratings on cordierite coupons, as well as two reference gratings on fused silica. Diffraction efficiency and laser-damage–threshold measurements for test gratings fabricated on cordierite coupons reveal no red flags, with average efficiencies of 88.4%, 89.9%, 91.5%, and 91.7%; all measurements were made at 799 nm. Despite higher-amplitude content in polished cordierite 1-D power spectral densities, diffraction efficiency measurements of the best two gratings on cordierite are within 1% of witness gratings on glass, and 50-on-1 laser-damage threshold is identical at 250 mJ/cm^2 for both glass and cordierite gratings.

This material is based upon work supported by the Department of Energy Office of Science under Award Number DE-SC0019496, the University of Rochester, and the New York State Energy Research and Development Authority.

1. E. P. Power *et al.*, Opt. Express **30**, 42,525 (2022).
2. E. P. Power *et al.*, "Demonstration of the "Flow-Cell" Integrated-Flow Active Cooling Substrate for High-Average-Power," submitted to Optics Letters.
3. D. A. Alessi *et al.*, Opt. Express **24**, 30,015 (2016).

Free-Standing Thin-Membrane, Zero *B*-Integral Beam Splitters

M. Romo-Gonzalez and R. Boni

Laboratory for Laser Energetics, University of Rochester

Uncoated nitrocellulose pellicles have a maximum reflectivity of ~30% with negligible absorption in the near-infrared (NIR). Our application used nitrocellulose pellicle beam splitters with a pulse of 30 ps and 135 fs for 1053-nm and 1170-nm beams, at a damage threshold of 1.3 J/cm^2 for 500 fs, λ = 1053-nm pulses[1] for nitrocellulose; our requirements were not limited by the material. Typical pellicle thickness of 2 μm to 5 μm effectively eliminates the *B*-integral, whose minimization is critical for propagating high-power laser pulses through an optical medium. Alternatively, a typical uncoated glass beam splitter can be made thin to control *B*-integral contribution while maintaining optical flatness imaging in reflection for these applications. These glass beam-splitter substrates are limited by ratios greater than the ~4% yielded from the uncoated surface of the glass and as a result, require at least one thin-film dielectric coating to be applied. The application of dielectric coatings introduces mechanical stress, which can significantly warp the substrate, rendering it unsuitable for imaging in reflection.

Pellicles (125-mm-diam, 2.2-μm- and 1.56-μm-thick λ/4 flat nitrocellulose membranes) were used to replace the 3-mm-thick dielectric coated NBK-7 glass plates used as λ = 1053-nm and λ = 1170-nm beam splitters that became warped upon coating.

A generalized multilayer thin-film modeling program was written to determine the thickness of the pellicle film that yields the desired reflectivity at the wavelength, angle of incidence, and polarization of interest following the matrix method described by Thelen.[2] The solution used by Thelen expresses a system of equations that solve Maxwell's equation for *s* and *p* polarization at the interface boundaries Z_1 and Z_2 in Fig. 1 into a matrix form in Eqs. (1) and (2).

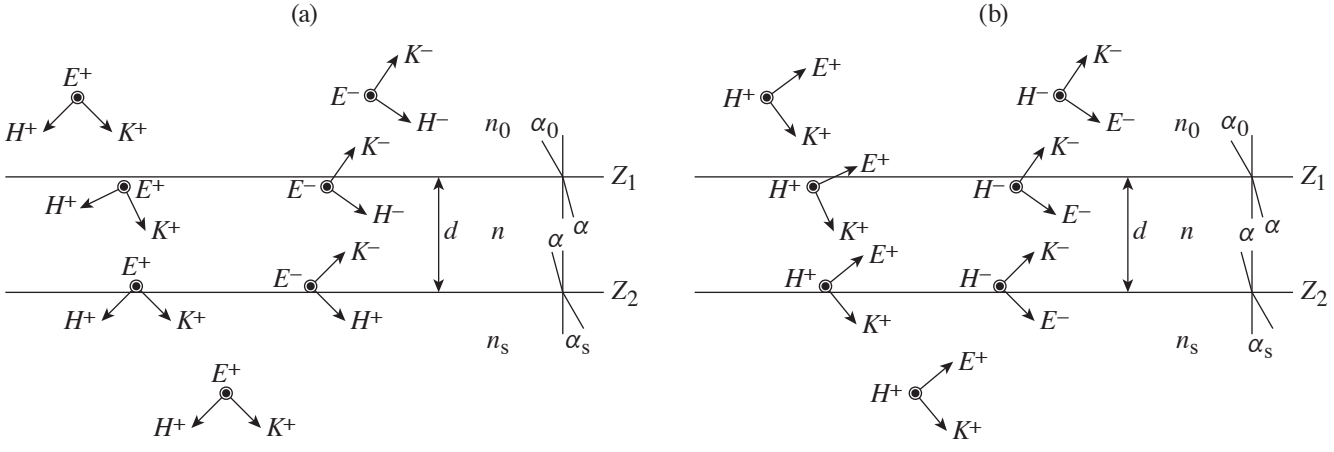

Figure 1
The electromagnetic fields at the boundaries of a thin film: (a) *s* polarization, where $\vec{E}$ is perpendicular to the plane of incidence and (b) *p* polarization, where $\vec{E}$ is parallel to the plane of incidence.

$$\begin{bmatrix} E(Z_1) \\ Z_0 H(Z_1) \end{bmatrix} = \begin{bmatrix} \cos\phi & \frac{i\sin\phi}{n} \\ in\sin\phi & \cos\phi \end{bmatrix} \begin{bmatrix} E(Z_2) \\ Z_0 H(Z_2) \end{bmatrix}, \tag{1}$$

$$\begin{bmatrix} E \\ ZH \end{bmatrix} = \begin{bmatrix} 1 & 1 \\ n & -n \end{bmatrix} \begin{bmatrix} E^+ \\ E^- \end{bmatrix}. \tag{2}$$

Equations (1) and (2) provide the matrix transfer function [Eq. (3)] of the electric fields across the layer, where δ is an infinitesimal distance from the boundary layer and M_{11} through M_{22} are the elements of the 2×2 matrix in Eq. (1). A compact matrix transfer can be written as seen in Eq. (4) for a multilayer of thin films.

$$\begin{bmatrix} E^+(z_1-\delta) \\ E^-(z_1-\delta) \end{bmatrix} = \begin{bmatrix} 1 & 1 \\ n & -n \end{bmatrix}^{-1} \begin{bmatrix} M_{11} & M_{12} \\ M_{21} & M_{22} \end{bmatrix} \begin{bmatrix} 1 & 1 \\ n & -n \end{bmatrix} \begin{bmatrix} E^+(z_2-\delta) \\ E^-(z_2-\delta) \end{bmatrix}, \tag{3}$$

$$\begin{bmatrix} E^+(z_1-\delta) \\ E^-(z_1-\delta) \end{bmatrix} = \begin{bmatrix} Q_{11} & Q_{12} \\ Q_{21} & Q_{22} \end{bmatrix} \begin{bmatrix} E^+(z_2-\delta) \\ E^-(z_2-\delta) \end{bmatrix}. \tag{4}$$

Since there is no reflected wave in the exit medium, $E^-(z_2 + \delta) = 0$, the amplitude of the reflectance $\vec{R}$ is shown in Eq. (5) and the reflected and transmitted energy coefficients **R** and **T** in Eq. (7) are yielded by Eqs. (5) and (6) in the absence of absorption, where $\vec{R}^*$ is the complex conjugate

$$\vec{R} = \frac{E^-(z_1-\delta)}{E^+(z_1-\delta)} = \frac{Q_{21}}{Q_{11}}, \tag{5}$$

$$\mathbf{R} = \vec{R}\vec{R}^*, \tag{6}$$

$$\mathbf{T} = 1 - \boldsymbol{R}. \tag{7}$$

In our implementation of Thelen's matrix equations, we found solutions that correctly solve for the reflected and transmitted energy coefficients **R** and **T** while considering absorption as a factor in the thin-film layers.

Spectrophotometer measurements of various pellicles and illumination configurations agree well with the model predictions. Figure 2(a) shows agreement between the predicted and measured transmission of a 2.2-μm-thick pellicle at a 45° angle of incidence with unpolarized light. Figure 2(b) results led to the replacement of one of the coated BK7 substrate beam splitters.

The imaginary component of the index for nitrocellulose was included in the model so the effect of absorption on reflectivity and transmission at shorter wavelengths could be investigated. The transmission measurement of a 2.5-μm-thick nitrocellulose pellicle was used in conjunction with modeling to estimate the absorption coefficient, κ. These results are shown in Fig. 3.

A thin-film model was used in conjunction with transmission and reflection measurements of pellicles at UV and visible wavelengths to determine the absorption coefficient for nitrocellulose from 220 nm to 1.2 μm. When exploring the experimental setup of propagating high-power laser pulses through optical mediums, such as a pellicle beam splitter, understanding the absorption is crucial to understanding the properties in the UV to NIR. Future applications and explorations include a more-accurate determination of the complex index of refraction and its performance.

This material is based upon work supported by the Department of Energy National Nuclear Security Administration under Award Number DE-NA0003856, the Department of Energy Office of Science under Award Numbers DE-SC0016253 and DE-SC0021057, the University of Rochester, and the New York State Energy Research and Development Authority.

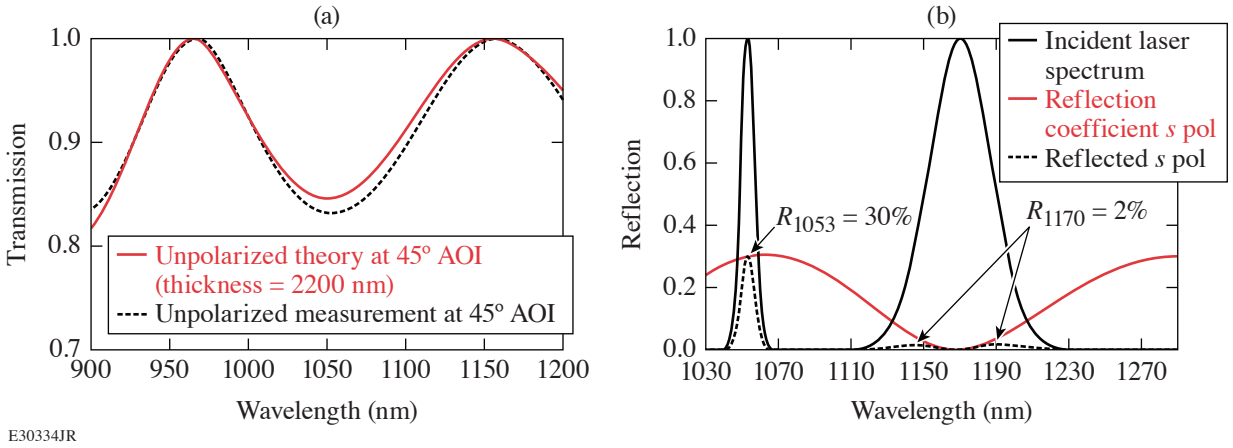

Figure 2
(a) Model prediction and measurement. Transmission of unpolarized light at a 45° angle of incidence (AOI) through a 2.2-μm-thick nitrocellulose pellicle. (b) Pellicle beam-splitter replacement. Reflection of *s*-polarized light at a 45° AOI through a 2.2-μm-thick nitrocellulose pellicle.

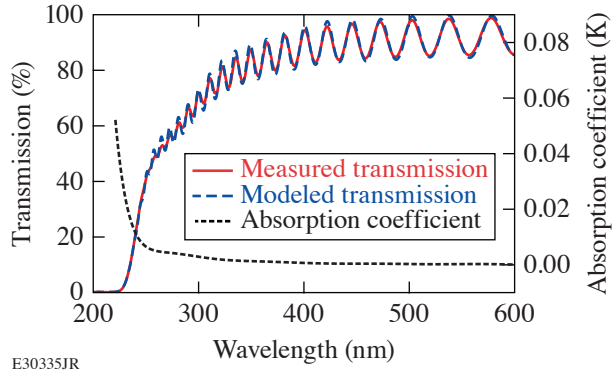

Figure 3
Measured and modeled pellicle transmission with absorption. Transmission of unpolarized light at normal incidence through a 2.2-μm-thick nitrocellulose pellicle and the absorption coefficient κ used in the modeling.

1. M. Kimmel *et al.*, Proc. SPIE **7132**, 71321O (2008).
2. A. Thelen, *Design of Optical Interference Coatings*, McGraw-Hill Optical and Electro-Optical Engineering Series (McGraw-Hill, New York, 1989).

Petawatt Laser Systems

L. J. Waxer, J. Bromage, B. E. Kruschwitz

Laboratory for Laser Energetics, University of Rochester

Since lasers were first demonstrated,[1] researchers have endeavored to increase their focused intensity (power/unit area). Within a few years, the demonstration of Q-switching[2] and then mode locking[3–7] significantly increased the peak power of lasers. However, the following two decades saw little progress in achieving substantially higher peak powers. Then, in 1985, the first demonstration of chirped-pulse amplification (CPA)[8] paved the way for dramatic increases in the peak power of lasers and their accompanying focused intensity. Today, peak powers as high as 10^{16} W or 10 PW (Ref. 9) and focused intensities of 10^{23} W/cm^2 (Ref. 10) have been demonstrated in the laboratory.

The ability to achieve these intensities in the laboratory creates extreme conditions that make possible, for example, the study of high-density laser–plasma interactions, the generation of beams of particles (electrons, positrons, neutrons, protons) and radiation (x ray, gamma ray), particle acceleration, the study of quantum vacuum interactions, and science on an attosecond time scale.[11] These opportunities have spurred an enormous international effort to build high-intensity laser facilities that support a large variety of scientific endeavors.[12] The authors have written an e-book for the SPIE Spotlight Series that introduces the reader to the laser science and technology underpinning petawatt laser systems, hopefully providing an appreciation of the substantial technological advances required to achieve today's state-of-the-art high-intensity laser system performance. This summary provides an overview of the various topics covered by the Spotlight e-book.

An overview of the building blocks of a petawatt laser system is shown in Fig. 1. CPA-based petawatt laser systems begin with seed pulses that are generated from mode-locked laser cavities employing broadband gain media such as titanium-doped sapphire or neodymium-doped glass. Depending on the performance requirements and the specific architecture of the petawatt laser system, conditioning that improves pulse contrast, shapes the spectrum to overcome gain narrowing, or uses the pulse itself to generate ultrabroadband light via nonlinear processes that serve as the seed for the system are employed prior to amplification. This work reviews broadband materials, common mode-locking methods, and various pulse-conditioning techniques utilized in petawatt laser systems.

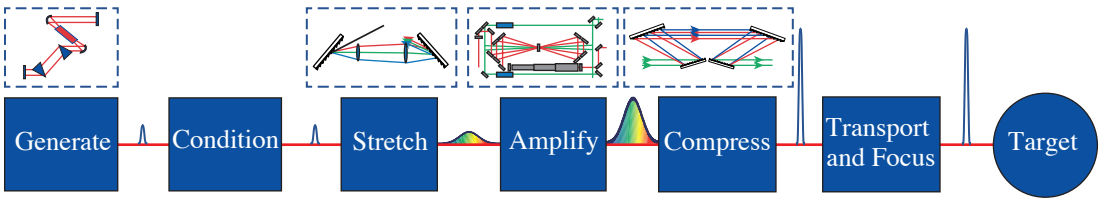

Figure 1
Building blocks of a petawatt laser system incorporating the CPA architecture.

To reach petawatt-level peak powers, these seed pulses require eight to nine orders of magnitude of amplification. Nonlinear optical effects and optical damage, however, significantly limit the ability to directly amplify ultrashort laser pulses. CPA first stretches a broadband pulse in time so that the peak power inside the amplifier is significantly reduced, thus avoiding destructive

nonlinear effects. Then after amplification, the pulse is recompressed back to near its original duration, generating a high-energy ultrashort pulse. We introduce the reader to the effects of dispersion on ultrashort pulses and how dispersion is used to stretch and compress the duration of these pulses. Nonlinear effects relevant to high-power laser systems are described along with a discussion of how one determines the minimum stretched pulse width required to safely achieve a particular output energy. Finally, we review the design of pulse stretchers, compressors, and considerations necessary to minimize the final output pulse width.

There are currently two approaches that have been demonstrated for generating petawatt laser pulses. One produces 150- to 1000-J pulses with durations between 150 and 1000 fs (10^{-15} s). The other generates much shorter pulses (~20 to 30 fs) with tens to hundreds of joules of energy. In either case, broadband amplifiers are required to safely generate the required energy while simultaneously maintaining sufficient bandwidth of the pulse. Two basic types of amplifiers have been developed; one uses energy-storage laser media that are optically energized or "pumped," and the other uses nonlinear crystals to mediate the exchange of energy from a high-energy narrowband pump pulse to a weaker broadband seed. We describe the principles of both types, how they can be combined using the relative strengths of each to form "hybrid" systems, and considerations for scaling to higher *average* powers (e.g., increased repetition rates) and future approaches.

Delivering petawatt laser peak powers to a target would not have been possible without large-aperture optics that have both broadband reflectivity (or diffraction efficiency) and high damage thresholds. This necessitated significant technological development to produce compressor diffraction gratings and transport mirrors that met these requirements while maintaining high wavefront quality for tight focusing. Even with high damage thresholds, the highest-energy petawatt laser systems motivated the development of fabrication techniques that could deliver the above qualities at meter-scale apertures. Since they are critical components of these laser systems, gold and broadband multi-dielectric coating development, large-aperture manufacturing, and issues of damage are reviewed.

Equally important is the ability to control and diagnose the performance of the laser system. Optimal recompression of the amplified pulse requires accurate *characterization* of the output pulse and fine *control* of the relative phase of the spectral components based on these measurements. Realizing the maximum intensity on target requires near-diffraction-limited focusing. Achieving this entails accurate focal-spot characterization, preferably at the target location, and the ability to manipulate the wavefront of the on-target beam. We review techniques for phase measurement and control in both the spectral and spatial domains, and introduce the reader to spatiotemporal couplings, which span both domains.

For most of the science enabled by petawatt laser systems, it is the peak *intensity* on target that is the critical parameter, not the peak power. This makes the final focusing of the laser a key consideration in the system design. Although minimizing wavefront aberrations and spatiotemporal couplings in the front end, amplifiers, and pulse compressor is critical to preserve the focusability of the laser beam, ultimately the focal spot size is defined by the parameters and performance of the final focusing optics. We discuss large-aperture, low-*f*-number off-axis parabolas that are used to achieve small focal areas, schema to protect high-value final optics from target debris, methods for improving on-target pulse contrast at the back end of the system, techniques to characterize the *in-situ f*ocal spot size at the target location, and future prospects for increasing on-target intensity.

The journey from the first demonstration of lasing action to the realization of 10-PW laser pulses took 60 years and significant technological development. Today, there are petawatt-class laser facilities all over the world (see ICUIL website[13]) with many more in the design and construction phase. These facilities make possible scientific explorations that were previously unachievable in the laboratory. This work introduces the reader to the laser science, engineering, and technology required to successfully deliver the highest focused intensities on Earth.

This material is based upon work supported by the Department of Energy National Nuclear Security Administration under Award Number DE-NA0003856, the University of Rochester, and the New York State Energy Research and Development Authority.

1. T. H. Maiman, Nature **187**, 493 (1960).
2. F. J. McClung and R. W. Hellwarth, J. Appl. Phys. **33**, 828 (1962).

3. A. Yariv, J. Appl. Phys. **36**, 388 (1965).
4. A. J. DeMaria, D. A. Stetser, and H. Heynau, Appl. Phys. Lett. **8**, 174 (1966).
5. M. DiDomenico, Jr., J. Appl. Phys. **35**, 2870 (1964).
6. L. E. Hargrove, R. L. Fork, and M. A. Pollack, Appl. Phys. Lett. **5**, 4 (1964).
7. H. W. Mocker and R. J. Collins, Appl. Phys. Lett. **7**, 270 (1965).
8. D. Strickland and G. Mourou, Opt. Commun. **56**, 219 (1985).
9. C. Radier *et al*., High Power Laser Sci. Eng. **10**, e21 (2022).
10. J. W. Yoon *et al*., Optica **8**, 630 (2021).
11. The National Academies of Sciences, Engineering, and Medicine, *Opportunities in Intense Ultrafast Laser: Reaching for the Brightest Light* (The National Academies Press, Washington, DC, 2018), p. 346.
12. C. N. Danson *et al*., High Power Laser Sci. Eng. **7**, e54 (2019).
13. Intense Laser Labs World Wide, Accessed 27 March 2023, https://www.icuil.org/activities/laser-labs.html.

LLE's Summer High School Research Program

R. S. Craxton

Laboratory for Laser Energetics, University of Rochester

During the summer of 2022, 16 students from Rochester-area high schools participated in the Laboratory for Laser Energetics' Summer High School Research Program (Fig. 1). This was the 33rd year of the program, which started in 1989. The 2020 program was unfortunately canceled because of the pandemic. In 2021, LLE held a fully virtual program for students who had applied and been interviewed for the 2020 program, and in 2022 LLE was able to return to a normal, in-person program.

I3194JR

Figure 1
Front Row: Cameron Ryan, Alisha Upal, Dr. Stephen Craxton, Grace Wu, Rick Zhou; Middle Row: Jackson McCarten, John Giess, Elizabeth Norris, Jenny Zhao, Samuel Gray, David Villani, Jayden Roberts, Olivia Fietkiewicz; Back Row: Arjun Patel, Sara Davies, Vinay Pendri, and Micah Kim.

The goal of LLE's program is to excite a group of highly motivated high school students about careers in the areas of science and technology by exposing them to research in a state-of-the-art environment. Too often, students are exposed to "research" only through classroom laboratories, which have prescribed procedures and predictable results. In LLE's summer program, the students experience many of the trials, tribulations, and rewards of scientific research. By participating in research in a real environment, the students often become more excited about careers in science and technology. In addition, LLE gains from the contributions of the many highly talented students who are attracted to the program.

The students spent most of their time working on their individual research projects with members of LLE's technical staff. The projects were related to current research activities at LLE and covered a broad range of areas of interest including experimental

diagnostic development, computer modeling of implosion physics, physical and computational chemistry, laser physics, optical engineering, terahertz radiation, future laser system design, and scientific data management (see Table I).

The students attended weekly seminars on technical topics associated with LLE's research. Topics this year included laser physics, fusion, nonlinear optics, fission energy, pulsed power, fiber optics, and LLE's cryogenic target program. The students also received safety training, learned how to give scientific presentations, and were introduced to LLE's computational resources.

Table I: High School Students and Projects—Summer 2022.

Name	High School	Supervisor	Project Title
Sara Davies	Pittsford Sutherland	R. S. Craxton	Direct-Drive Uniformity Calculations for a Future High-Gain Laser Facility
Olivia Fietkiewicz	Mercy	S. Bucht	Measuring the Mode Field Diameter of Single-Mode Fibers Using the Knife-Edge Technique
John Giess	McQuaid	V. N. Goncharov and K. M. Woo	Mitigating Hydrodynamic Instabilities in the Deceleration Phase of Inertial Confinement Fusion
Samuel Gray	Brighton	W. T. Shmayda and E. Dombrowski	Characterizing a Cryosorption Pump for Collecting Tokamak Exhausts
Michah Kim	Home School	D. W. Jacobs-Perkins	Design, Fabrication, and Testing of a 3-D–Printed Optomechanical Assembly for the MIFEDS Coil Characterization Station
Jackson McCarten	Webster Schroeder	B. N. Hoffman and K. R. P. Kafka	Viability Testing of Polymer Coating for Optical Cleaning Applications
Elizabeth Norris	Brighton	M. D. Wittman	Determining the Absorption Efficiency of a Flow-Through Pd-Bed as a Function of Initial $^4He:D_2$ Ratio and Flow Rate
Arjun Patel	Brighton	D. Chakraborty and R. Sobolewski	Terahertz Time-Domain Characterization of Biological Tissues Modeled Using COMSOL Multiphysics
Vinay Pendri	Pittsford Mendon	K. L. Marshall	Computational Modeling of Electron Density Polarization in Liquid Crystals Using Time-Dependent Density Functional Theory
Jayden Roberts	Brockport	S. T. Ivancic	Investigation of Microwave-Induced Chemical Etching
Cameron Ryan	McQuaid	R. W. Kidder	Containerized Application Management for Cloud-Based Scientific Analysis
Alisha Upal	Pittsford Sutherland	R. S. Craxton	Development of a National Ignition Facility Laser Configuration with X-Ray Backlighting of a Foam Ball Target
David Villani	Harley School	M. J. Guardalben	Energy Prediction on the OMEGA EP Laser System Using Neural Networks
Grace Wu	Pittsford Mendon	I. A. Begishev	Measurement of the Refractive Index of KDP and ADP Crystals at Low Temperatures
Jenny Zhao	Pittsford Mendon	K. L. Marshall and N. D. Urban	Chiroptical Properties and Mesophase Stability of Saturated Chiral Dopants for High-Peak-Power Liquid Crystal Device Applications
Rick Zhou	Brighton	W. T. Shmayda and M. Sharpe	Measuring the Performance of Molecular Sieve Driers

The program culminated on 24 August with the "High School Student Summer Research Symposium," at which the students presented the results of their research to an audience including parents, teachers, and LLE staff. The students' written reports will be made available on the LLE Website and bound into a permanent record of their work that can be cited in scientific publications.

Four hundred and fifteen high school students have now participated in the program. This year's students were selected from just under 40 applicants.

At the symposium, LLE presented its 24th annual William D. Ryan Inspirational Teacher Award to Mrs. Dawn Knapp, a mathematics teacher at Victor High School. This award is presented to a teacher who motivated one of the participants in LLE's Summer High School Research Program to study science, mathematics, or technology and includes a $1000 cash prize. Teachers are nominated by alumni of the summer program. Mrs. Knapp was nominated by Semma Alfatlawi, a participant in the 2021 program. In her nomination letter, Semma recalled her first encounter with Mrs. Knapp: "As I enter her room for the first time, I am immediately greeted with elation and a smile. I look around at all the perseverance posters and math jokes... her voice echoing through the room as she excitedly welcomes her new students... and immediately conclude that this is going to be a life-changing class. I have never seen another teacher like Mrs. Knapp." She observed that Mrs. Knapp noticed her yearning for math knowledge and "broadened it like no one had before." She found that "the combination of her devotion to teaching and fascination with math makes her an immediate role model to all her students." She cited open discussions in class about math problems that "brought laughter and human connections along with it, and showed me how community and education go hand in hand to reward people through cooperation as well as increasing intelligence and the ability to problem solve." In conclusion, Semma stated: "Thinking about my experiences with Mrs. Knapp never ceases to brighten my day… I will carry the life lessons that Mrs. Knapp has taught me as I continue to grow, and will never forget how much a warm smile and excitement for education can brighten the future."

This material is based upon work supported by the Department of Energy National Nuclear Security Administration under Award Number DE-NA0003856, the University of Rochester, and the New York State Energy Research and Development Authority.

2022 BEST Student and Teacher Research Program

T. J. Kessler, M. Romo-Gonzalez, and R. Ghosh

Laboratory for Laser Energetics, University of Rochester

The primary goal of the Broad Exposure to Science and Technology (BEST) Research Program is to engage teachers and students from historically marginalized experiences in various aspects of science and technology that support LLE's laser science and applications research.[1] This broad exposure helps guide students in their pursuit of science, technology, engineering, and math (STEM) fields and encourages them to explore the next generation of related jobs and careers. The BEST Program was carried out at East High School within the Rochester City School District (RCSD) during the summer of 2022. Five students and two teachers participated in this research experience over a six-week period during the months of July and August. Students were also given credit toward high school graduation through the Work-Based Learning Program sponsored by the RCSD.

I3187JR

Figure 1
The students and teachers who participated in the 2022 BEST program included (left to right); Terry Kessler [LLE DEI (Diversity, Equity, and Inclusion) Manager], Nigel Copeland (East High), Tiketa Thomas (Rochester Early College), Isis Wearing (Johanna Perrin Middle School), Olivia Galloway [YWCP (Young Women's College Prep)], Chavon Phelps (YWCP, teacher), Bre'Ay'zha White (YWCP), Trent Russell (East High teacher), and Marco Romo-Gonzalez (LLE DEI Deputy Manager).

Multi-faceted scientific institutions, such as UR/LLE, employ a wide variety of professionals to carry out a diverse set of research and development activities. Each of these research activities requires support teams consisting of professionals who

contribute their expertise to ensure a thriving research program. Exposure to the members of the LLE community provides the students and teachers with an understanding of the broad range of research activities as well as the rich diversity of individual professionals that enable successful research programs.

A team of LLE volunteers worked with the BEST students and teachers in a variety of science, technology, skilled trade, and technical communication fields. Twenty volunteers spent between one and two days at East High school over the six-week period. These volunteers, experts in their field, were able to bring detailed information, coupled with hands-on opportunities, into the high school laboratory environment.

The teachers and students were exposed to many different areas of science and technology research including laboratory safety, optical microscopy, spectroscopy, magnetic technology, illustrations and graphic design, light polarization and liquid crystal applications, high-energy-density physics (HEDP), diffraction grating applications, electrical technology, building operations and maintenance, optical system alignment, database applications, acoustics, code development, and laser holography. The importance of engineering support for research, including chemical, electrical, mechanical, optical, and computer engineering, together with support from facilities groups and graphics experts, were emphasized to highlight the extensive teamwork required to make scientific advancements and be able to communicate the results (see Fig. 2).

I3191JR

Figure 2
Members of the Publications and Illustrations department at LLE, Heather Palmer (near monitor), Mike Franchot (near board at right), and Jenny Hamson (far right) are shown instructing the BEST students and teachers on the principles of technical communication through graphical illustrations.

One of the areas of science that is central to fusion science is electricity and magnetism, especially electromagnetic waves or light. Both laser fusion and magnetic fusion are studied around the world to eventually harness the vast resource of nuclear energy. In addition, many technological applications involve electromagnetic systems and the electromagnetic spectrum. Bob Boni, research engineer, taught the BEST group to use the magnetic compasses in their cell phones to locate magnets hidden around the classroom and to build and test electric motors (Fig. 3).

(a) (b)

I3188JR

Figure 3
(a) Deputy Diversity Manager, Marco Romo-Gonzalez and research engineer, Bob Boni are shown working with students Isis Wearing and Bre'Ay'zha White to construct electric motors. (b) Bre'Ay'zha is shown examining the operation of a completed motor.

Spectrometers are used to study of the absorption and emission of light and other radiation by matter. There are numerous applications of spectroscopy at LLE, including optical material composition analysis, light-scattering investigations, and the study of laser–matter interaction. Jeremy Pigeon, scientist in the Plasma and Ultrafast Laser Science and Engineering Group, worked with students and teachers to construct a cell-phone spectrometer. Stavros Demos, Group Leader of Optical Materials Technology, activated a spectrometer for the students to measure the wavelength transmission of optical filter glass. Spectroscopy reliably engages the curious mind into the many wonders of light (Fig. 4).

(a) (b)

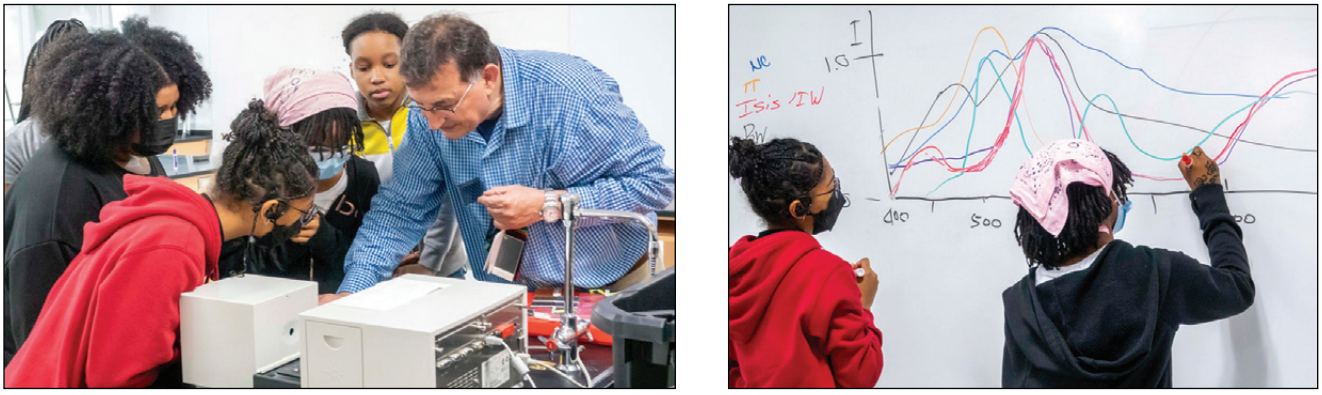

I3189JR

Figure 4
(a) Senior scientist, Stavros Demos, is shown demonstrating use of a spectrometer to measure the wavelength-dependent transmission of glass filters. (b) BEST students Tiketa Thomas and Isis Wearing are shown plotting the observed transmitted spectra for one of the color filters.

In this second year of LLE's BEST Program, aspects of theoretical physics and computation were introduced in ways that engaged the students and teachers. Theoretical physicist, Duc Cao, provided instructive examples of computer code development while Suxing Hu, Group Leader of HEDP Theory, shared his personal career path from grade school to graduate school and his professional experiences. In addition, graduate students from the University of Rochester's physics department developed a series of demonstrations to simulate superconductivity and compressed matter without the danger associated with very cold and very hot conditions (Fig. 5).

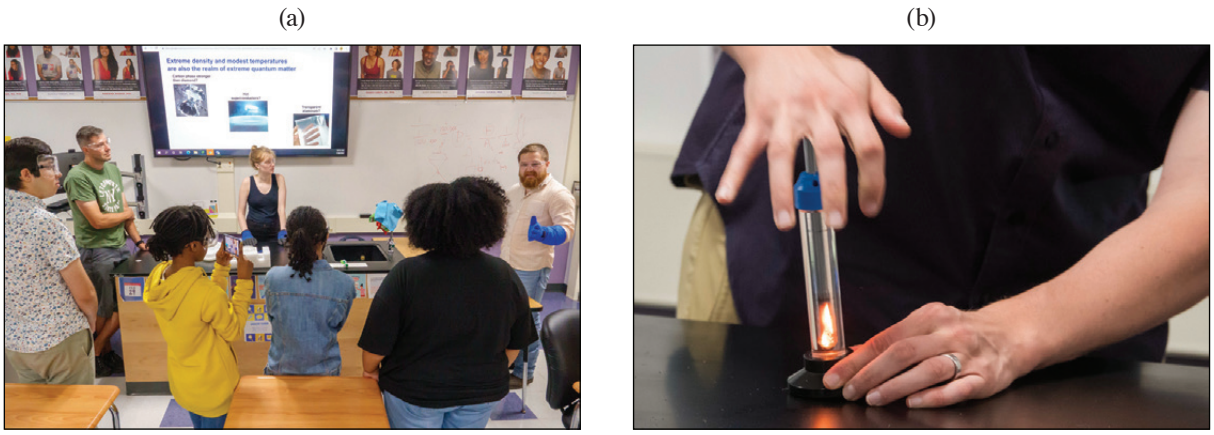

Figure 5
(a) Graduate students Maggie Huff and Gerrit Bruhaug (wearing blue gloves) demonstrate magnetic effects under extremely cold temperatures. (b) Graduate student David Bishel is shown igniting cotton strands by compressing the air with a plunger in a sealed glass cylinder.

The BEST participants visited LLE three times during the summer program to tour the OMEGA lasers, optical manufacturing facilities, and other support laboratories (Fig. 6). Together, the students and teachers were exposed to elements of science and technology that underscored the importance of their STEM high school curricula. Laboratory Director, Chris Deeney, emphasized the importance of STEM education and the numerous areas of employment in the DOE/NNSA complex. In addition, the BEST group participated in tours of optics and imaging related departments at Monroe Community College, the Rochester Institute of Technology, and the University of Rochester.

Figure 6
(a) During one of the visits to LLE, the BEST program participants met with the LLE Director, Chris Deeney (left), to learn about the scientific mission of the laboratory and the variety of staff careers that form a successful research team. (b) During another visit to LLE, the students and teachers were exposed to many of the trades needed to build and maintain a large laboratory complex. Nate Heckman (Facilities Group) is shown bending an electrical conduit with student Olivia Galloway.

Throughout the following school year, the students and teachers of the BEST Program serve as ambassadors for outreach to other students enrolled at RCSD high schools. They created a PowerPoint presentation showing the broad range of science and technology topics included in the program. In addition, a photomontage video was created to show the relationship between the BEST Program experiences and the wide variety of work activities carried out at LLE. The images for the photomontage were generated by LLE photographer, Eugene Kowaluk, and by several of the program participants.

On the last day of the six-week schedule, LLE mentors joined the students and teachers to celebrate completion of the 2022 BEST research program and to share their broad exposure to science and technology with family members (Fig. 7). The attendees had the opportunity to describe their roles in the program and to highlight their area of interest. In planning for the 2023 BEST program, students from several additional RCSD high schools are being invited to participate in this unique learning experience.

I3193JR

Figure 7
Members of the LLE staff, students, teachers, and parents assembled in front of the teaching monitor and "Google Board" on which questions are posted each day for further investigation.

1. T. J. Kessler, LLE Review Quarterly Report **169** (2021).

FY22 Q4 Laser Facility Report

J. Puth, M. Labuzeta, D. Canning, and R. T. Janezic

Laboratory for Laser Energetics, University of Rochester

During the fourth quarter of FY22, the Omega Facility conducted 331 target shots on OMEGA and 202 target shots on OMEGA EP for a total of 533 target shots (see Tables I and II). OMEGA averaged 10.3 target shots per operating day, averaging 91.1% Availability and 94.1% Experimental Effectiveness. OMEGA EP averaged 7.7 target shots per operating day, averaging 92.8% Availability and 93.1% Experimental Effectiveness.

Table I: OMEGA Laser System target shot summary for Q4 FY22.

Program	Laboratory	Planned Number of Target Shots	Actual Number of Target Shots
ICF	LLE	88	70
	LLNL	22	23
ICF Subtotal		110	93
HED	LLE	22	20
	LANL	44	48
	LLNL	27.5	20
HED Subtotal		93.5	88
LBS	LLE	22	16
	PPPL	11	10
	SLAC	11	7
LBS Subtotal		44	33
APL		11	10
CEA		27.5	29
NLUF		44	44
OFES		11	14
Calibration	LLE	0	20
Grand Total		341	331

APL: Applied Physics Labs (Johns Hopkins University)
CEA: Commissariat à l'énergie atomique aux énergies alternatives
NLUF: National Laser Users Facility
OFES: Office of Fusion Energy Sciences

Table II: OMEGA EP Laser System target shot summary for Q4 FY22.

Program	Laboratory	Planned Number of Target Shots	Actual Number of Target Shots
ICF	LLE	17.5	19
	LLNL	21	23
	NRL	7	8
ICF Subtotal		45.5	50
HED	LLE	21	27
	LANL	7	7
	LLNL	31.5	33
HED Subtotal		59.5	67
LBS	LLE	3.5	3
	LLNL	7	13
LBS Subtotal		10.5	16
CMAP		7	10
LaserNetUS		7	7
NLUF		35	42
Calibration	LLE	21	10
Grand Total		185.5	202

CMAP: Center for Matter at Atomic Pressures

Groundbreaking for the LLE Building Expansion

M. J. Shoup III

Laboratory for Laser Energetics, University of Rochester

Groundbreaking to celebrate the construction of the new addition to the LLE Complex occurred on 17 August with representatives from federal, state, and local offices; University senior leadership; and LLE (Fig. 1).

Figure 1
(a) Artist rendering of LLE building expansion. (b) Groundbreaking ceremony. Shown from left to right: Senior Associate Vice President for Facilities and Services, Michael Chihoski; Provost, David Figlio; Brighton Town Supervisor, Bill Moehle; New York State Senator, Jeremy Cooney; Executive Vice President of Administration and Finance and CFO, Elizabeth Milavec; University Trustee, Larry Kessler; University Trustee, Wayne LeChase; New York State Representative, Sarah Clark; LLE Director, Chris Deeney; University of Rochester President, Sarah Mangelsdorf; U.S. Congressman, Joe Morelle; Deputy State Director for U.S. Senator Kirsten Gillibrand, Jarred Jones; Director of Economic Development, New York State Energy Research and Development Authority (NYSERDA), Kevin Hale; and University of Rochester Interim Vice President for Research, Stephen Dewhurst.

Initial planning work for the project began in 2019. In January 2020, the Board of Trustees Committee on Facilities approved entering into a contract for the design of the addition at a cost of $3,538,700. Design work kicked off in November 2020 and was completed in March 2022. For construction, four bids were solicited and two competitive bids were received, with LeChase Construction being the lowest bidder. The University entered into a Guaranteed Maximum Price contract with LeChase Construction for the addition. The total cost of this project will not exceed $42,265,736, inclusive of previously approved design costs.

Achieving permitting approval for the project with the Town of Brighton was an unexpectedly difficult and drawn out process. A primary sticking point was a conservation easement to accommodate a vernal pond on the LLE site. Diligent efforts by LLE

staff, Nixon Peabody, and the Office of Government and Community Relations were ultimately successful in finding a mutually agreeable solution; however, the start of construction was slightly delayed. The final approval for this project also accounts for a potential future EP-OPAL expansion.

The new 66,600-sq.-ft, three-floor building will house laboratory and office space for approximately 110 scientists and LLE personnel and includes a class-1000 target fabrication laboratory and thin-film coating laboratory, a laser computing facility, and several other wet laboratory and general laboratory spaces. The largest laboratory space will house the AMICA Laser System—a state-of-the-art, high-energy, long-pulse laser that scientists at LLE are assembling for Stanford University's SLAC National Accelerator Laboratory Matter at Extreme Condition Upgrade (MEC-U).

A team consisting of 23 local companies was contracted and mobilized to start the building construction project. Site clearing began on 5 July 2023 and progressed into foundation work through September 2023 (see Figs. 2–4). Over that three-month period the site was cleared and graded, and foundation work was started. Exceptional weather allowed the team to perform better than originally scheduled. Although it is early in the construction project, the team is still on track for a March 2024 completion.

Figure 2
The second day of site clearing on 6 July 2023.

Figure 3
Foundation work in full swing at the end of September 2023.

Figure 4
Footers being poured for the perimeter of the new building.

FY22 Laser Facility Report

J. Puth, M. Labuzeta, D. Canning, R. T. Janezic, G. Pien, and S. T. Ivancic

Laboratory for Laser Energetics, University of Rochester

Under the facility governance plan, experimental time at the Omega Laser Facility is allocated to four NNSA-supported programs: Inertial Confinement Fusion (ICF), High-Energy Density (HED), National Laser Users' Facility (NLUF), and Laboratory Basic Science (LBS). FY22 will be the final year under these programs; beginning in FY23 the allocation will be determined by the combined HED Council per guidance from the NNSA Office of Experimental Science.

During FY22, the Omega Laser Facility conducted 1233 target shots on OMEGA and 889 target shots on OMEGA EP, with a total of 2122 target shots (see the shot summaries for OMEGA and OMEGA EP in Tables I and II, respectively). The ICF and HED Programs conducted 60% of the NNSA-supported facility shots in FY22. More than half of these experiments were conducted by scientists from Lawrence Livermore National Laboratory (LLNL), Los Alamos National Laboratory (LANL), Sandia National Laboratories (SNL), and the Naval Research Laboratory (NRL). About 6% of the facility shots were used to maintain operational effectiveness. The NLUF and LBS programs described below conducted 15% of the NNSA target shots. The facility also delivered 199 shots ($\sim$9% of the total) for external users who purchased the shot time. Overall, externally led investigators used 59% of the facility time. (See Figs. 1 and 2 for the fractional use by the various programs, including shot time that was purchased by outside users for OMEGA and OMEGA EP, respectively).

OMEGA investigators rated the overall experimental effectiveness of the facility at 93.4%, while OMEGA EP was rated at 94.2%. OMEGA averaged 11 target shots per day, averaging 91.9% Availability. OMEGA EP averaged nine target shots per day, averaging 92.5% Availability.

During Q4, construction of the new laboratory and office space at LLE required additional effort to mitigate the effects of construction vibrations that will continue in FY23. The Shot Director was able to contact the construction manager to halt problematic vibrations for the final preparations and shot cycle. Construction can occasionally impact availability but has been effectively minimized by planning and procedure.

In FY22, the facility continued to evolve to meet the needs of the scientific community.

To achieve higher uniformity in the pulse power balance, LLE built a laser diagnostic to passively measure the transmission of each beamline. This diagnostic has helped to identify degraded optics and will be systematically employed in the future to decrease the effort required to balance beamline energetics.

The magneto-inertial fusion electrical discharge system (MIFEDS) was significantly redesigned to improve the high-voltage safety and increase reliability and efficiency of operations.

Table I: OMEGA Laser System target shot summary for FY22.

Program	Laboratory	Number of Campaigns	Planned Number of Target Shots	Actual Number of Target Shots
ICF	LLE	33.5	368.5	346
	LANL	3	33	35
	LLNL	4.5	49.5	46
	SNL	1.5	16.5	14
ICF Subtotal		42.5	467.5	441
HED	LLE	9	99	91
	LANL	9	99	106
	LLNL	12	132	117
	SNL	2	22	23
HED Subtotal		32	352	337
LBS	LLE	4	44	34
	LLNL	6.5	71.5	74
	PPPL	1	11	10
	SLAC	1	11	7
LBS Subtotal		12.5	137.5	125
NLUF		13.5	148.5	153
AIBS		2	22	17
CEA		3	33	35
APL		3	33	36
CMAP		1	11	8
OFES		1	11	14
Calibration		0	0	67
Grand Total		110.5	1215.5	1233

AIBS: Academic and Industrial Basic Science
APL: Applied Physics Labs (Johns Hopkins University)
CEA: Commissariat à l'énergie atomique aux énergies alternatives
CMAP: Center for Matter at Atomic Pressures
NLUF: National Laser Users Facility
OFES: Office of Fusion Energy Sciences
PPPL: Princeton Plasma Physics Laboratory

New diagnostics and upgrades to diagnostics in the LLE inventory continue to increase the breadth of measurements that can be achieved. Many of these projects are conceived and led by external laboratory researchers. Ten diagnostic upgrade projects were completed in FY22 including:

- Talbot–Lau x-ray deflectometer upgrade [led by Johns Hopkins University (JHU)]
- Applied Physics Lab fast accumulating radiometer diagnostic suite upgrades (led by JHU)
- gas Cherenkov detector modified with Ti puck (led by LANL)
- copper activation sampling (led by LLNL)
- scattered-light diode (led by LLNL)
- vacuum Cherenkov detector (led by LLNL)
- MiniDMX upgrade (data acquisition system and detector array) (led by CEA)

Table II: OMEGA EP Laser System target shot summary for FY22.

Program	Laboratory	Number of Campaigns	Planned Number of Target Shots	Actual Number of Target Shots
ICF	LLE	13	91	119
	LLNL	9	63	67
	NRL	2	14	17
	SNL	1	7	6
ICF Subtotal		25	175	209
HED	LLE	8	56	67
	LANL	6	42	53
	LLNL	18.5	129.5	157
	SNL	1	7	10
HED Subtotal		33.5	234.5	287
LBS		3.5	24.5	39
		4.5	31.5	54
		1	7	6
LBS Subtotal		9	63	99
NLUF		17.5	122.5	144
CEA		1	7	8
LaserNetUS		4	28	34
CMAP		5	35	47
Calibration	LLE	3	21	61
Grand Total		98	686	889

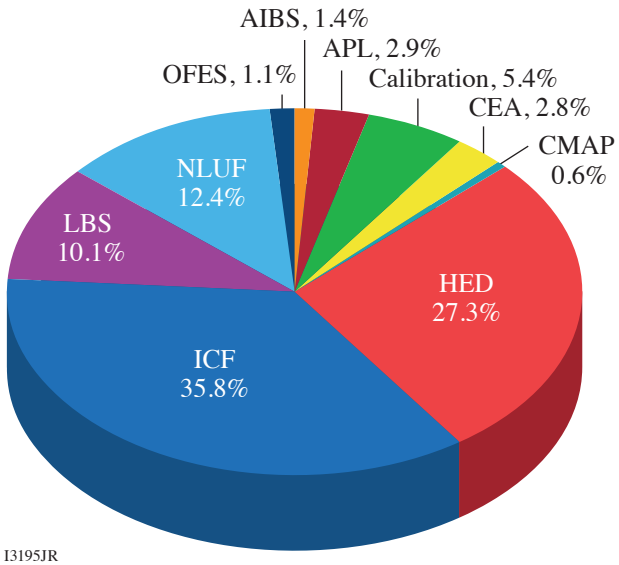

Figure 1
Fractional breakdown of FY22 shots on OMEGA by NNSA-supported programs.

- transmission grating spectrometer image-plate modification (led by NRL)
- scattered-light uniformity instrument (led by LLE)
- THz background energy measurement diagnostic (led by LLE)

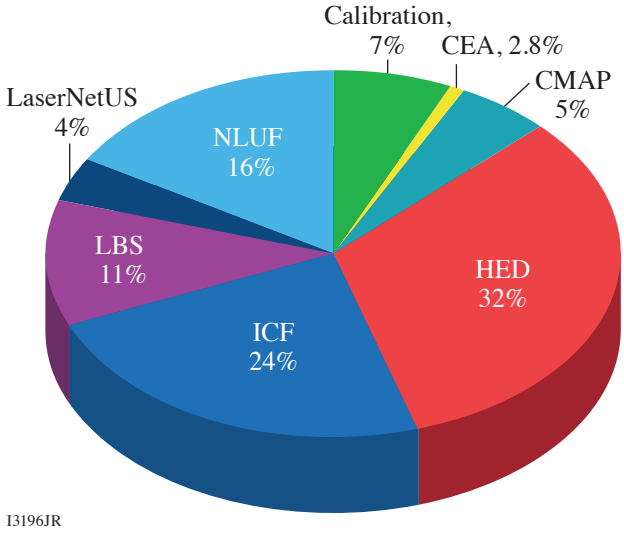

Figure 2
Fractional breakdown of FY21 shots on OMEGA EP by NNSA-supported programs.

Education Summary

M. S. Wei

Laboratory for Laser Energetics, University of Rochester

Education/training is a primary technical mission for LLE. LLE is the only place where students can be trained at scale for careers in national security related to the science of Stockpile Stewardship. The education programs at LLE include a high school research program that exposes students to a professional environment where they work alongside scientists and engineers for a summer; undergraduate programs where students conduct research or work part-time with scientists and engineers often in the summer with some throughout an academic year (or longer) to understand how classroom education is applied to real world problems; graduate education where students are immersed in the science of high energy density (HED) physics and lasers to earn MS and Ph.D. degrees; and a new high school program for underrepresented minority students and their teachers in the local Rochester area. This report provides a summary of these activities in FY22.

Summer High School Research Program

Since 1989, LLE has held the annual Summer High School Research Program for Rochester-area high school students who have just completed their junior year. The eight-week program provides an exceptional opportunity for highly motivated students to experience scientific research in a professional environment. Sixteen students participated in the 2022 program (see p. 54). Four hundred and fifteen students from 55 high schools have participated in the program to date including 143 students who identify as female. Thirty-nine students have become Scholars in the prestigious Regeneron Science Talent Search based on the research projects they carried out at LLE. Many of the students progress to major in science-related disciplines at nationally recognized universities, and more than 100 have now received their doctoral degrees, which was a featured news article by the University of Rochester.[1]

Broad Exposure to Science and Technology Student and Teacher Research Program

Started during FY20 by T. J. Kessler, the LLE Diversity Manager, the goal of the Broad Exposure to Science and Technology (BEST) initiative is to engage underrepresented high school students and their teachers from the Rochester City School District (RCSD) in various aspects of science and technology that support laser science and applications research at LLE. Two RCSD high school science and technology teachers and five high school students participated in this second year of LLE's BEST Program carried out at the RCSD's East High School over the six-week period during the summer of 2022 (see p. 57). A team of 20 LLE volunteers worked with the BEST students and teachers in a greater number of fields, including HED physics, magnetics, acoustics, theoretical physics, database management, graphic design, and the technology trades that support all research activities at LLE. The BEST participants visited LLE three times during the summer program to tour the OMEGA lasers, optical manufacturing facilities, and other support laboratories. The teachers and students of the BEST Program serve as ambassadors for outreach to other students at RCSD high schools, assisting in expanding the number of BEST candidates for the following year. Both an RCSD teacher and student from the 2021 BEST program participated in a visit by the director of the National Science Foundation to UR/LLE during the spring of 2022.

Undergraduate Student Program

Although LLE does not have a formal undergraduate student program, it has provided unique work-study opportunities for undergraduate research and co-op internships by involving undergraduate and community college students in its research activi-

ties. These students come from the University of Rochester, the Rochester Institute of Technology (RIT), the State University of New York (SUNY) at Geneseo, Cornell University, Monroe Community College, and other institutions. LLE scientists also host and mentor students participating in the Research Experience for Undergraduate Program funded by the National Science Foundation, and from 2022 the new Plasma and Fusion Undergraduate Research Opportunity (PFURO) Program funded by the Office of Fusion Energy Sciences. During FY22, 49 undergraduates including 17 co-op students and three PFURO students conducted research and work-study at LLE. To meet increased needs, LLE's undergraduate student program will be expanded into a formal program from FY23 and coordinated by a dedicated new program director.

Graduate Student Program

Graduate students use the Omega Laser Facility as well as other LLE facilities to conduct inertial confinement fusion (ICF) and high-energy-density–physics research to earn advanced degrees. These students make significant contributions to the LLE research output (e.g., they write a large fraction of the manuscripts published annually by LLE). Thirty-five UR faculty members across eight academic departments hold secondary appointments with LLE, increasing the breadth of leadership in science and technology. Sixteen scientists and research engineers at LLE hold secondary faculty appointments with the University in five different academic departments. The large number of faculty and LLE staff enable the Laboratory to pull together a new high-energy-density science (HEDS) curriculum and educate a large number of graduate students. More than 80 UR graduate students were involved in research at LLE in FY22 (see Table I), among which 67 students were directly funded by LLE via the NNSA-supported University of Rochester Frank Horton Fellowship Program. Their research includes theoretical and experimental plasma physics and fusion science, HED physics, x-ray and atomic physics, nuclear physics, material properties under extreme pressure, astrophysics, ultrafast optoelectronics, high-power laser development and applications, nonlinear optics, optical materials and optical fabrication technology, and target fabrication.

In FY22, LLE directly funded graduate/undergraduate research with twelve external academic partners including SUNY Geneseo, RIT, the University of Delaware, Massachusetts Institute of Technology's Plasma Science and Fusion Center, the University of Michigan, the University of Nebraska-Lincoln, the University of Nevada at Reno, Stony Brook University, the University of California at Los Angeles, the University of Alberta, Imperial College London, and Oxford University. These programs involved 22 undergraduate students including 20 from SUNY Geneseo, 19 graduate students, six postdoctoral researchers, eight scientists and research staff, and 17 faculty members.

In addition, LLE has significantly facilitated the education and training of several hundred students and postdoctoral researchers in the HEDP and ICF science areas from other universities through their participation in the National Laser Users' Facility, Laboratory Basic Science, LaserNetUS, and collaborations with LLE and DOE national laboratories. More than 70 graduate students (including 16 mentioned above) from 28 universities (see Table I in the **External Users' Program**, p. 80) and over 40 postdoctoral researchers were involved in these external user-led research projects with experiments conducted at the Omega Laser Facility in FY22.

Sixteen graduate students, including nine from the University of Rochester and seven from other academic institutions have successfully completed their thesis research and obtained Ph.D. degrees in calendar year 2022. Table II lists their name, university, and current employer. Seven of them (44% of the total), including three from UR, joined the NNSA laboratories, five stayed within academia, and four work in the private sector.

1. L. Valich, University of Rochester, Laser Lab Springboards 100-Plus High Schoolers to Doctoral Degrees, Accessed 3 July 2023, https://www.rochester.edu/newscenter/laser-lab-springboards-100-plus-high-schoolers-to-doctoral-degrees-517662/.

Table I: More than 80 graduate students, including 67 LLE-funded UR Frank Horton Fellows (marked by *), conducted research at LLE during FY22.

Student Name	Department	Faculty Advisor	LLE Advisor (if different)	Research Area	Notes
N. Acharya*	ME	J. Shang	D. N. Polsin	Viscosity Measurements in High-Energy-Density Fluids	New Horton Fellow
M. Adams	PA	P.-A. Gourdain/ P. Tzeferacos		Elucidation of Magnetic-Field Generation via Laser-Target Illumination in the Magnetohydrodynamic Framework	Former Horton Fellow; graduated in 2022
M. V. Ambat*	ME	D. H. Froula	J. L. Shaw	First-Light Laser Wakefield Acceleration Experiments on MTW-OPAL	
A. Anand*	PA	J. Carroll-Nellenback		The Role of Exoplanetary Magnetic Fields in Atmospheric Evolution and Habitability	
A. Armstrong*	PA	P. Tzeferacos		Radiative, High-Energy-Density Magnetized Turbulence: Charting the Uncharted Plasma Regimes of Fluctuation Dynamo	
B. Arnold*	PA	S. X. Hu		Developing a Finite-Element Discrete-Variable-Representation–Based Real-Space Density-Function-Theory Code for High-Energy-Density Physics	New Horton Fellow
J. Baltazar*	ME	S. P. Regan	R. C. Shah	Inertial Confinement Fusion Implosion Physics	
Z. Barfield*	PA	D. H. Froula		Heat Transport in High Magnetic Fields	
D. T. Bishel*	PA	G. W. Collins/ J. R. Rygg	P. M. Nilson	X-Ray Spectroscopy of Hot Dense Matter: Plasma Screening of Atomic Orbitals at Atomic Pressures	
G. Bruhaug*	ME	G. W. Collins/ J. R. Rygg	H. G. Rinderknecht/ M. S. Wei	Short-Pulse Laser-Generated Probes for High-Energy-Density Experiments	
S. Cao*	ME	C. Ren	R. Betti	Predicting Hot Electrons for Inertial Confinement Fusion	
D. Chakraborty	ECE	R. Sobolewski		Optics and Imaging	
G. Chen	ECE	R. Sobolewski		Novel Terahertz Sources and Terahertz Time-Domain Spectroscopy: Characterization of Novel Materials	
J. Cheng	MS	R. Sobolewski		Terahertz and Optical Pump–Probe Spectroscopy	
D. A. Chin	PA	G. W. Collins/ J. R. Rygg	P. M. Nilson	X-Ray Absorption Spectroscopy for the Study of Materials Under Extreme Conditions	NNSA Stockpile Stewardship Graduate Fellow (a former Horton Fellow)

Table I: More than 80 graduate students, including 67 LLE-funded UR Frank Horton Fellows (marked by *), conducted research at LLE during FY22 (continued).

Student Name	Department	Faculty Advisor	LLE Advisor (if different)	Research Area	Notes
K. Churnetski*	ME	S. P. Regan	W. Theobald	Three-Dimensional Hot-Spot X-Ray Emission Reconstruction for Mitigation of Low-Mode Asymmetries on OMEGA	
C. Danly	ME	R. Betti		Spatial Measurements of Ion Temperatures of Inertial Confinement Fusion Hot Spots	Technical Advisor: V. Geppert-Kleinrath (LANL)
R. Dent*	CHE	A. Shestopalov	S. G. Demos	Next-Generation Gratings for High-Power Lasers	
J. D'Souza*	PA	P.-A. Gourdain	S. Zhang	Large-Scale High-Energy-Density Simulations with *ab initio* Quality	New Horton Fellow
R. Ejaz*	ME	R. Betti		Understanding the Physics of Areal-Density Degradation in Direct-Drive OMEGA Implosions Through Dedicated Experiments and Statistical Modeling	
I. N. Erez*	PA	P.-A. Gourdain		Achieving High Magnetization with Cylindrically Converging Plasma Flows	New Horton Fellow
M. Evans*	PA	P.-A. Gourdain		The Study of Warm Dense Matter Generated by Pulsed-Power Generators	
P. Farmakis*	ME	R. Betti	R. Betti/ P. Tzeferacos	Three-Dimensional Reconstruction of the Compressed Core in OMEGA Direct-Drive Implosions	
P. Franke*	PA	D. H. Froula		Measuring the Dynamics of Electron Plasma Waves with Thomson Scattering	Graduated in 2022
J. García-Figueroa	CHE	D. R. Harding		Electron Cyclotron Resonance Microwave Chemical Vapor Deposition Method and Its Influence over the Properties of Vapor-Deposited Hydrocarbon Films	Former Horton, graduated in 2022
K. Garriga	OPT	X. C. Zhang		Terahertz Research	
M. Ghosh*	CHE	D. McCamant	S. Zhang	Chemistry of Planetary Materials Under Extreme Pressure and Temperature Conditions	
M. K. Ginnane*	ME	G. W. Collins/ J. R. Rygg		Compressibility, Structure, and Melting of Platinum to 500 GPa	
X. Gong*	ME	G. W. Collins/ J. R. Rygg		Structure and Electronic Properties of Sodium and Potassium at High Pressure	

Table I: More than 80 graduate students, including 67 LLE-funded UR Frank Horton Fellows (marked by *), conducted research at LLE during FY22 (continued).

Student Name	Department	Faculty Advisor	LLE Advisor (if different)	Research Area	Notes
R. Goshadze*	ME	Y. Gao	V. V. Karasiev	Deep Neural Network for Learning Noninteractive Free-Energy Density Functional to Enhance Density Functional Theory-Based Simulations Relevant to High-Energy-Density Physics	New Horton Fellow
S. Gupta*	OPT	P. S. Carney/ J. M. Zavislan	M. D. Wittman	Quantitative Confocal Phase Imaging for the Inspection of Target Capsules	
H. Hasson*	PA	P.-A. Gourdain		Understanding the Transition from Accretion Flows to Magnetized Turbulent Jets Using Pulsed-Power Drivers	New Horton Fellow
S. K. Harter	EES	M. Nakajima	D. N. Polsin	Planetary Science	
B. J. Henderson*	PA	G. W. Collins/ J. R. Rygg		Hugoniot Measurements of Silicon and Radiance Transition in Shocked Silica Aerogel	
J. Hinz*	PA	S. Rajeev	V. V. Karasiev	Developing Accurate Free-Energy Density Functionals via Machine Learning for Warm-Dense-Matter Simulations	
R. Holcomb*	OPT	J. Bromage		Machine-Learning Control of High-Average-Power Lasers for Ultrafast Applications	
M. F. Huff*	PA	G. W. Collins/ J. R. Rygg		The Equation of State of Shocked Iron and Bridgmanite	
G. W. Jenkins*	OPT	J. Bromage		Divided-Pulse Coherent Combination for Scaling High-Power Nonlinear Processes	Graduated in 2022
M. Jeske*	CHE	D. R. Harding		Engineering Resins for Two-Photon Polymerization	
R. Jia*	CHE	A. Shestopalov	S. G. Demos	Effects of Organic Monolayer Coatings on Optical Substrates	
A. Kish*	PA	A. B. Sefkow		Algorithms for Long-Time-Scale Plasma Simulation	
S. Kostick*	ME	W. Theobald	M. J. Rosenberg	Laser–Energy Coupling in Direct-Drive Experiments at the National Ignition Facility and Omega	New Horton Fellow
K. Kotorashvili*	PA	E. G. Blackman		Magnetic-Field Generation, Mass Transport, and Spin Evolution in Hydrogen Burning Stars and White Dwarfs	
A. LaPierre	CH	G. W. Collins/ J. R. Rygg		Development of Raman Spectroscopy for Dynamic Compression Experiments on OMEGA	

Table I: More than 80 graduate students, including 67 LLE-funded UR Frank Horton Fellows (marked by *), conducted research at LLE during FY22 (continued).

Student Name	Department	Faculty Advisor	LLE Advisor (if different)	Research Area	Notes
M. Lavell*	ME	A. B. Sefkow		The Development of Hybrid Fluid-Kinetic Numerical Models for Simulating Fusion-Relevant Plasmas	
L. S. Leal*	PA	R. Betti	A. V. Maximov	Simulations and Studies of Inertial Confinement Fusion Relevant Laser-Generated Plasmas in External Magnetic Fields	Graduated in 2022
A. Lees*	ME	R. Betti		Understanding the Fusion Yield Dependencies in OMEGA Implosions Using Statistical Modeling	
Y. Liu*	OPT	B. E. Kruschwitz		Development of an Electro-Optical–Based Ultraviolet Pulse Measurement System	
R. Markwick*	PA	A. Frank		Laboratory Astrophysics Studies of Colliding Radiative Magnetized Flows	New Horton Fellow
J. Martinez	ME	S. P. Regan	C. J. Forrest	Measurements of the Scattered Neutron Energy Spectrum from OMEGA Cryogenic Implosions	
T. Mason	CHE	R. B. Spielman		Pulsed-Power Technology	
M. M. McKie*	PA	D. H. Froula	J. L. Shaw	Wave Breaking of Electron Plasma Waves as it Applies to Hot-Electron Generation and Laser-Plasma Amplifiers	
B. McLellan*	PA	P. Tzeferacos	S. X. Hu/ S. Zhang	A Theoretical Study of Structural Transformations, Hydrodynamic Motion, and Optical Properties of Crystals and Amorphous High-Energy-Density Materials	
K. R. McMillen*	PA	D. H. Froula	J. L. Shaw	Filamentation of Picosecond Pulses Through Underdense Plasmas	
S. C. Miller*	ME	V. N. Goncharov		Hydrodynamic Instabilities of Inertial Confinement Fusion Implosions	Graduated in 2022
K. Moczulski*	ME	P. Tzeferacos		Characterization of Magnetized Turbulence and Fluctuation Dynamo Through *FLASH* Simulations and OMEGA Experiments	
K. L. Nguyen*	PA	J. P. Palastro		Nonlinear Saturation of Cross-Beam Energy Transfer	
K. A. Nichols*	PA	S. X. Hu		*Ab initio* Investigations of Nonlocal Electron and Ion Transport in High-Energy-Density Plasmas	
S. F. Nwabunwanne*	ECE	W. R. Donaldson		Design, Fabrication, and Characterization of AlGaN-Based Ultrafast Metal–Semiconductor–Metal Photodiodes	

Table I: More than 80 graduate students, including 67 LLE-funded UR Frank Horton Fellows (marked by *), conducted research at LLE during FY22 (continued).

Student Name	Department	Faculty Advisor	LLE Advisor (if different)	Research Area	Notes
H. Pantell*	PA	G. W. Collins/ J. R. Rygg		Thermodynamic and Mass Transport Properties of Planetary Materials at Extreme Conditions	
S. Paramanick*	PA	E. G. Blackman		Multiscale Study of Supersonic Plasma Wind Interacting with a Magnetized Earth-Like Planet	New Horton Fellow
H. Pasan*	PA	R. Dias	G. W. Collins	Novel Hydrogen Rich Materials at High-Energy-Density Conditions: Route to "Hot" Superconductivity	
D. Patel*	ME	R. Betti		High- and Mid-Mode Number Stability of OMEGA Cryogenic Implosions	
R. Paul*	ME	S. X. Hu		High-Pressure Phase Diagram of Ramp-Compressed Materials	Graduated in 2022
D. Ramsey*	PA	J. P. Palastro		Electron Dynamics and Radiation Generation in a Flying Focus	
J. Ruby*	CH	W. U. Schroeder	W. T. Shmayda	Effects of Surfaces on Superpermeation	
A. Sexton*	ME.	A. B. Sefkow		Advanced Graphics Processing Units Algorithms for Simulations of Inertial Confinement Fusion and High-Energy-Density Physics	New Horton Fellow
M. Signor*	PA	G. W. Collins/ J. R. Rygg		Using X-Ray Spectroscopy to Study Material Properties at High Energy Densities	New Horton Fellow
T. T. Simpson*	PA	J. P. Palastro		A Flying Focus Driven by Self Focusing	
E. Smith*	PA	G. W. Collins/ J. R. Rygg		Understanding Materials Assembled to Extreme States via Laser-Driven Implosions Using Bayesian Inference	
Z. K. Sprowal*	PA	G. W. Collins/ J. R. Rygg		Off-Hugoniot Studies in Hydrogen and Hydrocarbons	
R. Swertfeger*	OPT	J. Bromage		High-Power Ultrafast Amplifiers Using Cryogenically Cooled, Diode-Pumped Fluoride Crystals	New Horton Fellow
A. Syeda	ME	J. Shang/ H. Aluie		Particle Tracking with X-Ray Radiography in Shock-Driven Flows and Viscometry Using Shocked Particles	
G. Tabak*	PA	G. W. Collins/ J. R. Rygg		Experimental Investigation of Warm Dense Matter	
M. VanDusen-Gross*	PA	H. G. Rinderknecht		Electron and Gamma Signatures of Relativistically Transparent Magnetic Filament Experiments	

Table I: More than 80 graduate students including 67 LLE-funded UR Frank Horton Fellows (marked by *) conducted research at LLE during FY22 (continued).

Student Name	Department	Faculty Advisor	LLE Advisor (if different)	Research Area	Notes
M. Wang*	CHE	D. R. Harding		Using Two-Photon Polymerization to "Write" Millimeter-Size Structures with Micron Resolution	
C. A. Williams*	PA	R. Betti		High-Yield Cryogenic Implosions on OMEGA	
J. Young*	PA	P.-A. Gourdain		Laser-Triggered X Pinches	
J. Zhang	OPT	G. Agrawal	W. R. Donaldson	Slow Light in Photonic Crystal Fiber	
Y. Zhang*	ME	J. R. Davies		Kinetic Study of Magnetized Collisionless Shock Formation and Particle Acceleration	

ME: Mechanical Engineering
PA: Physics and Astronomy
CH: Chemistry
CHE: Chemical Engineering
OPT: Institute of Optics
ECE: Electrical and Computer Engineering
EES: Earth and Environmental Sciences
MS: Material Science

Table II: Sixteen students successfully defended their Ph.D. theses in calendar year 2022.

Name	Ph.D. Institution	Current Position, Employer
M. Adams	University of Rochester	Postdoc, Sandia National Laboratories
G. Chen	University of Rochester	System Engineer, KLA
P. Franke	University of Rochester	Scientist, Tau Systems Inc.
J. García-Figueroa	University of Rochester	Postdoc, Johns Hopkins University
B. J. Henderson	University of Rochester	Specialist in Optical Design, L3Harris Technologies
G. Jenkins	University of Rochester	Senior Optical Design Engineer, ASML
L. S. Leal	University of Rochester	Postdoc, Lawrence Livermore National Laboratory (LLNL)
S. Miller	University of Rochester	Assistant Scientist, LLE
R. Paul	University of Rochester	Postdoc, LLNL
M. Khan	University of York	Postdoc, University of York
D. Kim	Princeton University	Postdoc, Carnegie Institute of Science
G. Righi	University of California, San Diego	Postdoc, LLNL
B. Russell	University of Michigan	Postdoc, University of Michigan
R. Simpson	Massachusetts Institute of Technology (MIT)	Lawrence Fellow, LLNL
G. Sutcliffe	MIT	Postdoc at MIT, to join LLNL (HEDS Center Postdoc Fellow)
R. Vandervort	University of Michigan	Postdoc, Los Alamos National Laboratory

External Users' Program

M. S. Wei

Laboratory for Laser Energetics, University of Rochester

Under the facility governance plan implemented in FY08 to formalize the scheduling of the Omega Laser Facility as a National Nuclear Security Administration (NNSA) User Facility, Omega Facility shots are allocated by programs following NNSA guidance. NNSA funds about 190 shot days each year on the OMEGA and OMEGA EP Laser Systems for experiments. The principal uses of Omega are for NNSA-supported research and development in high-energy-density physics recommended by the HED Council and basic science through peer-reviewed proposals. The majority (~68%) of these shot days are committed to the national Inertial Confinement Fusion (ICF) Program and the High-Energy-Density Program with shots conducted by scientists from Lawrence Livermore National Laboratory (LLNL), Los Alamos National Laboratory (LANL), Sandia National Laboratories (SNL), the Naval Research Laboratory (NRL), and LLE. In FY22, the Omega Laser Facility delivered a total of 2110 shots over 207 days, among which 1390 target shots (including 128 calibration shots) were conducted for the ICF and HED campaigns, which are ~65.9% of the overall facility shots. The successful completion of the large number of experiments at the Omega Laser Facility during the COVID-19 global pandemic is attributed to the "RemotePI" operation protocol that enabled experimental principal investigators (PI's) and collaborators to safely and effectively conduct experiments via remote access.

The Basic Science Program at the Omega Laser Facility, with projects selected through open-call and peer-reviewed processes, is typically allotted between 25% to 29% of the total NNSA-funded Omega Facility shot days. The program has two distinct components: (1) the National Laser Users' Facility (NLUF) experiments (~18% of the NNSA-funded shot time) led by researchers from U.S. academia and business; and (2) the Laboratory Basic Science (LBS) experiments (with ~11% of the NNSA-funded shot time) that are led by the NNSA HED laboratories including LLNL, LANL, SNL, NRL, and LLE and the Office of Science laboratories such as SLAC National Accelerator Laboratory, and Princeton Plasma Physics Laboratory (PPPL). In FY22, the NLUF and LBS programs obtained 314 and 224 target shots, respectively, and together accounted for ~25.5% of the overall facility shots.

Since FY20, LLE has provided a few additional shot days each year on OMEGA EP to the users of the newly established LaserNetUS network funded by the DOE Office of Fusion Sciences (FES) with user experimental proposals annually solicitated and selected by a fully independent proposal review panel process. The LaserNetUS program obtained 34 target shots on OMEGA EP in FY22.

Since FY21, a few additional shot days each year at the Omega Laser Facility have also been made available to the University of Rochester (UR)-hosted Center for Matter at Atomic Pressure (CMAP), a new Physics Frontier Center funded by the National Science Foundation (NSF). CMAP is a collaboration among faculty, scientists, researchers, and students at UR, Massachusetts Institute of Technology (MIT), Princeton University, the University of California at Berkeley and Davis, the University of Buffalo, and LLNL. CMAP researchers conduct laboratory-based exploration of planets and stars throughout the universe and obtained 55 target shots in FY22.

During FY22, the Omega Laser Facility was also used to support research grants led by LLE scientists and funded by FES (14 target shots on OMEGA) and for other externally funded programs led by teams from the Johns Hopkins University's (JHU's) Applied Physics Laboratory (APL) (36 target shots on OMEGA) and the French le Commissariat à l'énergie atomique et aux énergies alternatives (CEA) (43 target shots on OMEGA and OMEGA EP). These externally funded experiments are conducted at the facility on the basis of special agreements put in place by UR/LLE and participating institutions with the endorsement of NNSA.

The facility users who conducted experiments during this year included 23 collaborative teams participating in the NLUF Program, 20 teams led by scientists from LLNL, LANL, LLE, SLAC, and PPPL participating in the LBS Program; three project teams participating in the LaserNetUS Program; six project teams from CMAP; many collaborative teams from the national laboratories (LLNL, LANL, SNL, NRL) and LLE conducting ICF experiments; investigators from LLNL, LANL, SNL, and LLE conducting experiments for HED campaigns; and researchers from APL and CEA.

A critical part of the Omega external users' programs is the training of graduate students and postdoctoral researchers in HED and plasma physics. In total, over 70 graduate students (see Table I) from 28 other universities,18 undergraduate students, and more than 40 postdoctoral researchers participated in these external user-led research projects with experiments at the Omega Laser Facility during FY22, among which seven students successfully defended their Ph.D. theses in calendar year 2022 (see the highlighted names in Table I). It is worth noting that 25 of these graduate students are new to the Omega Laser Facility.

Table I: More than 70 graduate students from 28 universities have conducted research utilizing the Omega Laser Facility through NLUF, LBS, and LaserNetUS, and/or via collaborations with national labs and LLE during FY22. Seven students successfully defended their Ph.D. theses in calendar year 2022 (see shaded cells).

Name	Institution	Advisor(s)	Notes
A. Aghedo	Florida A&M University	Albert (LLNL)	LLNL collaboration including LBS projects
E. Grace	Georgia Tech (GT)	Trebino (GT)/ Ma (LLNL)	LLNL collaboration (PI: Swadling)
J. Gonzalez Quiles	JHU	Wicks	
Y. Li	JHU	Wicks	
T. Perez	JHU	Wicks	
Z. Ye	JHU	Wicks	
P. J. Adrian	MIT	Frenje	
C. Chang	MIT	Li/Frenje	
S. Danhoff	MIT	Frenje	
T. Evans	MIT	Frenje	
T. M. Johnson	MIT	Li	
J. Kunimune	MIT	Frenje	NNSA Laboratory Residency Graduate Fellow
J. Pearcy	MIT	Li	
B. Reichelt	MIT	Li	NNSA Laboratory Residency Graduate Fellow
R. Simpson	MIT	Winslow (MIT)/ Ma (LLNL)	LLNL collaboration; graduated in 2022; joined LLNL as Lawrence Postdoc Fellow
G. Sutcliffe	MIT	Li	Defended Ph.D. thesis in October 2022; to join LLNL as the High-Energy-Density Science Center Postdoc Fellow
J. Copley	Princeton University	Duffy	New
S. Han	Princeton University	Duffy	
C. Johnson	Princeton University	–	LBS (PI: Malko); new
D. Kim	Princeton University	Duffy	Graduated in March 2022; Postdoc at Carnegie Science
I. Ocampo	Princeton University	Duffy	

Table I: More than 70 graduate students from 28 universities have conducted research utilizing the Omega Laser Facility through NLUF, LBS, and LaserNetUS, and/or via collaborations with national labs and LLE during FY22. Seven students successfully defended their Ph.D. theses in calendar year 2022 (see shaded cells) (continued).

Name	Institution	Advisor(s)	Notes
B. Cage	Rice University	Liang	New
W. Riedel	Stanford University	Cappelli	
S. You	Stanford University	Edwards	LLNL collaboration–LBS; new
W. Gammel	University of Arizona	–	LANL collaboration (PI: Palaniyappan); new
D. Lioce	University of California, Berkeley	–	LANL collaboration (PI: Kozlowski); new
M. Harwell	University of California, Davis (UC Davis)	Stewart	CMAP
A. Postema	UC Davis	Stewart	CMAP; new
R. Lee	University of California, Los Angeles (UCLA)	Mori	
M. Sinclair	UCLA	Joshi	LLNL collaboration including LBS (PI: Albert)
K. Bhutwala	University of Califonia, San Diego (UC San Diego)	Beg	
A. Bogale	UC San Diego	Beg	
T. Cordova	UC San Diego	Beg	LLNL collaboration
A. Li	UC San Diego	Meyers	
M. Postornik	UC San Diego	Arefiev	LLNL collaboration (PI: Smith); new
G. Righi	UC San Diego	Meyers	LaserNetUS and LLNL collaboration; graduated in July 2022; postdoc at LLNL
J. Saret	UC San Diego	Beg	NLUF (PI: McGuffey, General Atomics); new
I-L. Yeh	UC San Diego	Arefiev	NLUF (PI: Willingale, UM); new
C. Frank	University of Delaware	Bose	Princeton Plasma Physics Laboratory-LBS (PI: Malko); new
K. Bolduc	University of Massachusetts, Amherst	–	LLNL collaboration (PI: Smith); new
A. Angulo	University of Michigan (UM)	Kuranz	
K. Bryant	UM	Kuranz	
S. Coffing	UM	Drake	LANL collaboration (PI: Kozlowski)
C. Fiedler-Kawaguchi	UM	Kuranz	LANL collaboration (PI: Rasmus)
K. Kelso	UM	Kuranz	
J. Kinney	UM	Kuranz	New
J. Latham	UM	Krushelnick	New

Table I: More than 70 graduate students from 28 universities have conducted research utilizing the Omega Laser Facility through NLUF, LBS, and LaserNetUS, and/or via collaborations with national labs and LLE during FY22. Seven students successfully defended their Ph.D. theses in calendar year 2022 (see shaded cells) (continued).

Name	Institution	Advisor(s)	Notes
S. Miller	UM	McBride	SNL collaboration (PI: Gomez); new
B. Russell	UM	Willingale	Graduated in Sept. 2022; postdoc at UM
M. Springstead	UM	Kuranz	NLUF and LLNL collaboration (PI: Swadling)
H. Tang	UM	Willingale	
R. Vandervort	UM	Drake/Kuranz	Graduated in July 2022; postdoc at LANL
M. Wadas	UM	Johnsen	LaserNetUS and LLNL collaboration
C. Allen	University of Nevada (UNR)	White	
J. Clapp	UNR	Mancini	new
E. Gallardo-Diaz	UNR	Mancini	
T. Griffin	UNR	White	new
J. Rowland	UNR	Mancini	
J. King	University of New Mexico	–	SNL collaboration (PI: Aguirre); new
E. Smith	University of Notre Dame	–	LANL collaboration (PI: Kozlowski); new
C. Danley	UR/LANL	–	LANL collaboration
I. Pagano	University of Texas, Austin	Downer	LLNL collaboration including LBS (PI: Albert)
C. Samulski	Virginia Tech	Srinivasan	
M. Vescovi	Helmholtz-Zentrum Dresden-Rossendorf	–	NLUF collaboration (PI: Valdivia); new
V. Valenzuela	Imperial Collage	–	LLNL collaboration including LBS (PI: Swadling); new
F. Barbato	Sapienza Università di Roma	Atzeni	LLE collaboration–LBS (PI: Igumenshchev); new
L. Savino	Sapienza Università di Roma	Atzeni	LLE collaboration–LBS (PI: Igumenshchev); new
C. Bruulsema	University of Alberta	Rozmus	LLE and LLNL collaborations
R. Loitard	University of Bordeaux	–	LLE collaboration–LBS (PI: Igumenshchev); new
S. Iaquinta	University of Oxford	Gregori	NLUF and LLE collaboration
H. Poole	University of Oxford	Gregori	NLUF and LLE collaboration
M. Khan	University of York	Woolsey	Rutherford Appleton Laboratory/York (PI: Scott) and LLE collaboration (PI: Theobald); graduated in May 2022; postdoc at York

FY22 National Laser Users' Facility Program

M. S. Wei

Laboratory for Laser Energetics, University of Rochester

The Office of Experimental Sciences of the National Nuclear Security Administration within the U.S. Department of Energy funds the operations of LLE and specifically, of the National Laser Users' Facility (NLUF), thus making it possible for users from universities and industry in the United States to conduct basic science experiments without a direct facility charge. To better serve a growing, diverse user community and streamline the process, the NLUF Program has evolved into a facility-access-only program starting from FY22. During FY21, LLE completed a call for proposals, review, and selection process for the NLUF experiments to be conducted at the Omega Laser Facility during FY22 and FY23. After peer review by an independent proposal review panel for scientific merit and broad impact and the feasibility and executability review by the Omega facility and experimental support team, LLE selected 27 proposals for Omega shot allocation with a total of 25.5 and 34 shot days for experiments in FY22 (Q2–Q4) and FY23, respectively.

FY22 was the first of a two-year period of performance for these 27 NLUF projects (Table I). In addition, a few FY21 NLUF projects as carryover also completed experiments during FY22. In total, 314 target shots were conducted for NLUF projects during FY22. The NLUF experiments conducted during FY22 are summarized in this section.

Table I: Four FY21 carryover projects (in gray) conducted shots during FY22. Twenty-one (in blue) of the 27 new NLUF projects approved for the FY22–FY23 Omega Laser shot allocation conducted shots during FY22. The remaining six (in yellow) are scheduled for FY23.

Principal Investigator	Institution	NLUF Project Title/Article Title
F. N. Beg	University of California, San Diego	Charged-Particle Transport and Energy Deposition in Warm Dense Matter with and without an External Magnetic Field/ Measurements of Temperature Evolution in Copper from Intense Proton Beam Energy Deposition
W. Fox	Princeton University	Magnetic Reconnection in High-Energy-Density Plasmas
H. Ji/L. Gao	Princeton University/Princeton Plasma Physics Laboratory	Study of Particle Acceleration from Magnetically Driven Collisionless Reconnection at Low Plasma Beta Using Laser-Powered Capacitor Coils/Electron Exhaust Jets and Current-Driven Kinetic Instabilities in Laser-Powered Magnetic Reconnection
C. K. Li	Massachusetts Institute of Technology	Inertial Confinement Fusion Interface
M. Bailly-Grandvaux	University of California, San Diego	Effects of an External Magnetic Field on Laser–Plasma Instabilities
T. Duffy	Princeton University	Dynamic Compression of Exoplanetary Materials: Pressure-Induced B1–B2 Phase Transition in ZnO Under Laser-Driven Ramp Compression

Table I: Four FY21 carryover projects (in gray) conducted shots during FY22. Twenty-one (in blue) of the 27 new NLUF projects approved for the FY22–FY23 Omega Laser shot allocation conducted shots during FY22. The remaining six (in yellow) are scheduled for FY23 (continued).

Principal Investigator	Institution	Title
J. A. Frenje	Massachusetts Institute of Technology	Advanced Studies of Kinetic and Multi-Ion-Fluid Effects, Electron-Heat Conduction, Ion–Electron Equilibration, and Ion-Stopping Power in High-Energy-Density Plasmas/Multi-Ion Campaign: Studies of Multi-Ion and Kinetic Effcts in Shock and Ablatively Driven Implosions
M. Gatu Johnson	Massachusetts Institute of Technology	Study of Diffusion, Interpenetration, Instability, and Dynamics at the Ablator–Gas Interface in Inertial Confinement Fusion-Relevant Conditions/Ablator–Gas Interface Dynamics and Mix in Confinement Fusion-Relevant Conditions
R. Jeanloz/G. Tabak	University of California, Berkeley/LLE	Search for Immiscibility in Hydrogen–Neon Mixtures at Jupiter-Interior Conditions/Report for DACPlanet-22A/B
K. Krushelnick	University of Michigan	The Dynamics and Reconnection of Strong Magnetic Fields Using OMEGA EP/Plasmoid Magnetic Reconnection Between Long-Pulse Laser-Driven Plasmas Perturbed by a Short-Pulse Laser
C. C. Kuranz/ H. LeFevre	University of Michigan	Radiation Transport in Strongly Coupled Plasmas/Achieving Neutron Star Envelope Relevant Conditions Through a Radiative Shock in Strongly Coupled Plasmas
C. C. Kuranz/ H. LeFevre	University of Michigan	Photoionization Fronts on the OMEGA Laser/Observation of a Radiative Heat Front in Ar Using the Omega Gas-Jet System
D. Lamb/P. Tzeferacos	University of Chicago/ LLE	Onset, Subsistence, and Decay of Magnetized Turbulence and Fluctuation Dynamo
E. Liang	Rice University	Collision of Magnetized Jets Created by Hollow-Ring Lasers Irradiating High-*Z*–Doped CH Targets
R. C. Mancini	University of Nevada, Reno	X-Ray Heating and Ionization of Photoionized Plasmas in a Steady State
W. L. Mao	Stanford University	Low-Entropy Diamond Formation Pathways for Reactive H Chemistry/Shock-Induced Hydrogen Chemistry for Hydride Formation
C. McGuffey	General Atomics	Opacity of Ionized Iron Under Broad Pressure and Temperature Conditions/Driving Iron to Dense, Hot Conditions Using the Long- and Short-Pulse Beams of OMEGA EP
J. Shang	University of Rochester	Tracking Rarefaction with Particle Image Velocimetry
B. Srinivasan	Virginia Tech	Rayleigh–Taylor Evolution of Isoloated-Feature Perturbations in a Background Magnetic Field
S. Tochitsky/N. Lemos	University of California, Los Angeles/LLNL	Control of Laser–Plasma Interactions in Three-Dimensional–Printed Foam Structures with Graded Density
S. J. Tracy	Carnegie Institute for Science	Dynamic Compression of Iron Carbide at Exoplanetary Core Conditions

Table I: Four FY21 carryover projects (in gray) conducted shots during FY22. Twenty-one (in blue) of the 27 new NLUF projects approved for the FY22–FY23 Omega Laser shot allocation conducted shots during FY22. The remaining six (in yellow) are scheduled for FY23 (continued).

Principal Investigator	Institution	Title
P. Valdivia	University of California, San Diego/Johns Hopkins University	Phase-Contrast Imaging of Inner Shell Release Through Talbot–Lau X-Ray Interferometry/Monochromatic Talbot–Lau X-Ray Deflectometer for the OMEGA EP and Multi-Terawatt Lasers
T. White	University of Nevada, Reno	Experimental Measurement of Thermal Conductivity in Warm Dense Matter
J. Wicks	Johns Hopkins University	Exploration of Decomposition Kinetics in the Warm-Dense-Matter Regime: Orientation and Melting Effects
L. Willingale	University of Michigan	Direct Laser Acceleration of Electrons for Bright, Directional Radiation Sources/Relativistic Intensity Laser Channeling and Direct Laser Acceleration of Electrons from an Underdense Plasma
G. Fiksel	University of Michigan	Study of a Self-Generated Magnetic Field in Imploding D^3He Backlighter Capsules and Its Effect on the Properties of the Diagnostic Proton Beams
H. Ji	Princeton University	Thomson-Scattering Measurement of Non-Maxwellian Electrons and Current-Driven Instabilities During Low-Beta Magnetically Driven Reconnection
J. Kim	University of California, San Diego	Efficient Ion Acceleration by Continuous Fields in the Target Transparency Regime
D. Schaeffer	Princeton University (now at University of California, Los Angeles)	Detailed Measurements of Electric and Magnetic Fields in Laser-Driven, Ion-Scale Magnetospheres
D. Schaeffer	Princeton University (now at University of California, Los Angeles)	Particle Heating by High-Mach-Number Collisionless Shocks in Magnetized HED Plasmas
F. H. Séguin	Massachusetts Institute of Technology	Study of Magnetized Plasmas in Shock-Driven Inertial Confinement Fusion Implosions and in Laser-Driven Hohlraums

Measurements of Temperature Evolution in Copper from Intense Proton Beam Energy Deposition

M. Bailly-Grandvaux,[1] C. McGuffey,[2] J. Kim,[1] K. Bhutwala,[1] J. Saret,[1] D. Mariscal,[3] T. Ma,[3] P. M. Nilson,[4] T. Filkins,[4] W. Theobald,[4] A. Haid,[2] S. T. Ivancic,[4] and F. N. Beg[1*]

[1]Center for Energy Research, University of California, San Diego

[2]General Atomics

[3]Lawrence Livermore National Laboratory

[4]Laboratory for Laser Energetics, University of Rochester

[*]Principal Investigator

OMEGA EP can deliver intense proton and ion beams with tens of joules that can then rapidly deposit their energy in bulk samples, leading to isochoric heating of materials into the warm-dense-matter regime. Our group previously studied proton beam transport in thick plastic foams on OMEGA EP, a work that was published recently.[1] Following results from our previous shot day,[2] the FY22 NLUF shot day examined the bulk heating resulting from laser-generated proton beams focused onto solid Cu disks (10- or 25-μm thick $\times$ 200-μm diameter). To quantify the heating, the K_α fluorescence emitted by the Cu was measured with a high-resolution streaked spectrometer (HiResSpec). This diagnostic was used successfully for the first time with proton-heated samples. The Cu temperature was obtained with a few picoseconds resolution and it reached ~50 eV in ~35 ps (Ref. 3).

In the recent FY22 shot day, a steep-walled hollow plastic cone with 100-μm openings at its tip was added where the Cu sample was attached. These cones were used to focus the proton beam into a small spot.[4] The target and diagnostic lines of sight for these shots are shown in Figs. 1(a) and 1(b).

On the primary target configurations discussed above and shown in Figs. 1(a) and 1(b), we collected time-resolved spectra of the K_{α_1} and K_{α_2} and line emissions using the HiResSpec diagnostic in the range of 7.97 to 8.11 keV with a spectral resolution of $E/\Delta E \sim 5000$ and time resolution of ~2 ps. Experimental spectra are compared with spectra calculated using the collisional-radiative spectral analysis code *PrismSPECT*, which together describe the evolution of temperature in the sample and are shown in Fig. 2(a). These spectra are complemented with time-dependent simulations performed with the 1-D radiation-hydrodynamics code *HELIOS*, shown in Fig. 2(b), using as an input the proton beam characteristics inferred from the Thompson parabola ion energy (TPIE) analyzer, radiochromic film diagnostics (RCF), and results from previous work.[4]

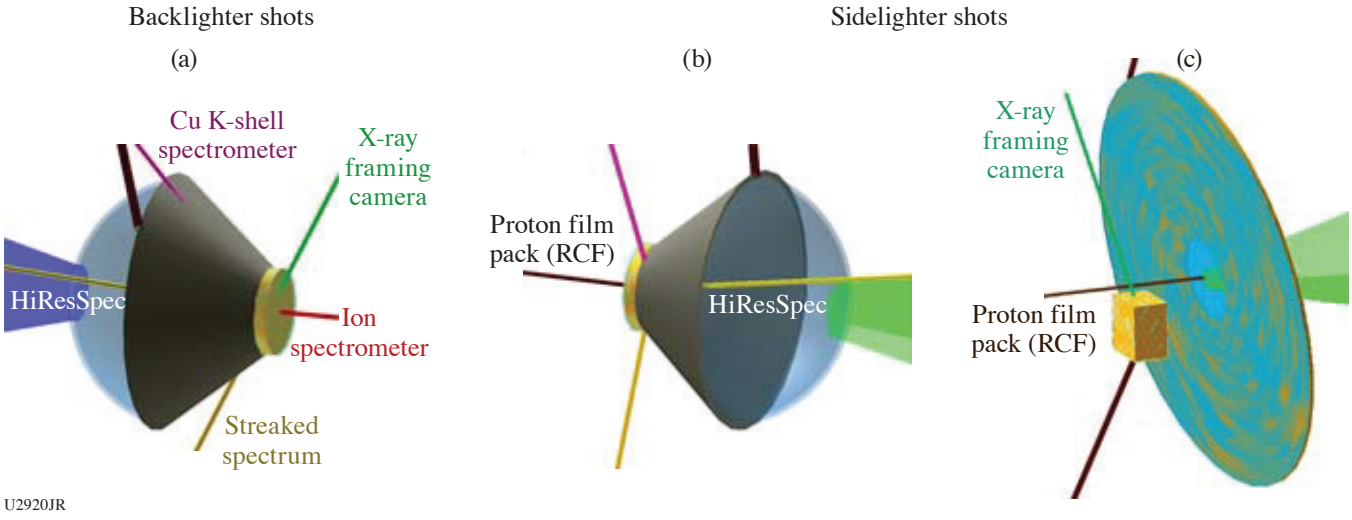

Figure 1
[(a),(b)] Experimental configurations for the Cu disk proton heating experiment. Configurations (a) and (b) used the same laser and target conditions but had complementary diagnostics for the proton beam characterization, an ion spectrometer, or a film pack. Configuration (c) provided a measurement of energy deposition as well as time-resolved images of the top Cu face, giving a cross-sectional view of the emission profile.

The temperature evolution inferred from the *PrismSPECT* analysis and simulated in *HELIOS* are shown in Fig. 2(c). A good agreement was obtained once the sample was heated above 20 eV, into the regime where K_α lines shifts start to be measured.

Remaining analysis includes continued construction of synthetic K_α spectra with more-advanced atomic models to improve comparison with the measured spectra, especially at late times (>50 ps) where the K_α spectra are significantly broadened by spatial gradients and a possible hydrodynamic expansion. Hybrid particle-in-cell simulations using the *LSP* code are also being performed to model the proton and electron transport through the cone and energy deposition into the sample.

We also performed a shot where the proton beam was generated by a thin foil, directed unfocused onto a Cu half block, as shown in Fig. 1(c). Due to the absence of a focusing structure, the measured temperatures were low (<20 eV). With the Cu block intersecting only part of the beam, radiochromic films provided the unblocked and transmitted beam's energy distribution, hence potentially extracting energy deposition. However, significant charging of the Cu block was observed, affecting the measurement.

The experiment was conducted on the OMEGA EP Laser System at the University of Rochester's Laboratory for Laser Energetics with the beam time through the National Laser Users' Facility (NLUF) program. This material is based upon work supported by the Department of Energy, National Nuclear Security Administration under Award Number DE-NA0003943, the University of Rochester, and the New York State Energy Research and Development Authority.

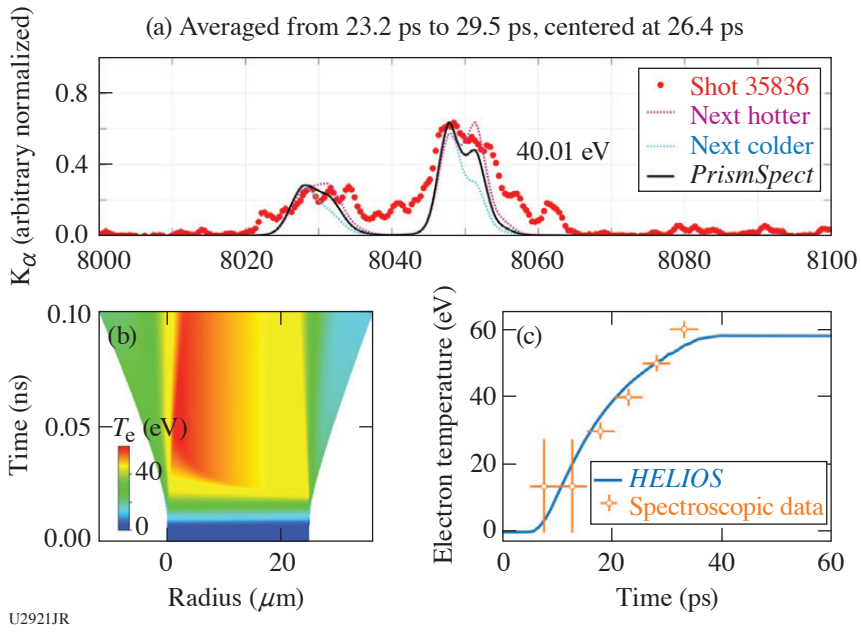

Figure 2
Experimental and simulation results collectively describing temperature evolution in Cu disks. Sample time-integrated spectrum with corresponding iterated time-dependent (a) *PrismSPECT* simulations describe measured temperature evolution and (b) *HELIOS* simulates 1-D temperature evolution. (c) A good agreement in the evolution of sample temperature is obtained once $T > 20$ eV, where K_α line shifts occur.

Magnetic Reconnection in High-Energy-Density Plasmas

W. Fox,[1,2*] D. B. Schaeffer,[2] S. Malko,[1] G. Fiksel,[3] and M. J. Rosenberg[4]
[1]Princeton Plasma Physics Laboratory
[2]Princeton University, Department of Astrophysical Sciences
[3]University of Michigan
[4]Laboratory for Laser Energetics, University of Rochester
[*]Principal Investigator

Magnetic reconnection[5] is a fundamental process in astrophysical plasmas that can convert magnetic energy to plasma kinetic energy, and it underlies processes in cosmic plasmas such as solar flares and substorms in the Eartth's magnetotail. In this project, we conducted laboratory experiments using OMEGA to study how magnetic reconnection proceeds under the conditions of laser-produced plasmas.[5] In these plasmas, magnetic fields are self-generated in the plasma by the Biermann battery effect. Creating two neighboring plumes produces a collision of two magnetized plasmas, driving together the oppositely directed magnetic-field lines and driving magnetic reconnection, which can be observed using the OMEGA suite of plasma diagnostics including x-ray imaging, Thomson scattering, and proton radiography. Laser-produced plasmas are an exciting platform for magnetic reconnection experiments because they can reach a large normalized system size regime, where the plasma is much larger than intrinsic plasma scales such as the electron and ion gyro radius, while simultaneously maintaining low particle collisionality due to high temperature (see Fig. 3). Our recent campaign has conducted experiments at National Ignition Facility and OMEGA, where the range of experiments allows scanning parameters such as the size, temperature, and density of the plasma.[6]

For these particular experiments on OMEGA, we determined that an important and necessary milestone for the project was to improve and validate techniques for analyzing proton radiography data to infer experimental magnetic fields. We therefore devoted several shots to conducting proton radiography measurements of a single expanding plasma plume, which is the simplest possible system to analyze, but which has several pitfalls uncovered in other recent experiments. In particular, our recent work has identified the importance of obtaining and applying boundary conditions on the magnetic field, and second that it is important to deal with intrinsic nonuniformities in the probing proton beam.[6] These new data will allow us to validate techniques for dealing with both issues. Over the rest of the experimental day we obtained additional experimental data on reconnecting plasmas, including Thomson scattering, x-ray images, and proton radiographs. The single-plume experiments, however, are particularly interesting and we present them here in this report.

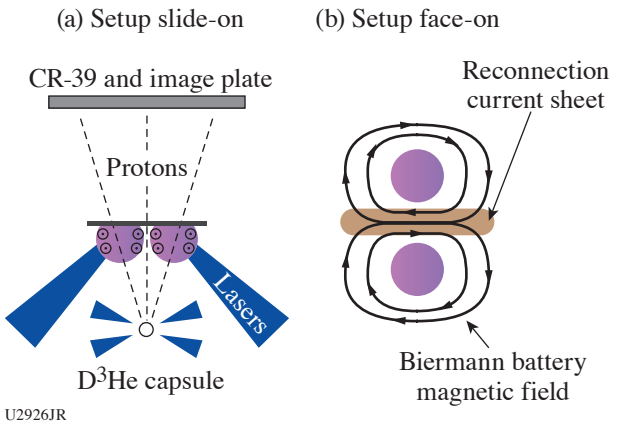

Figure 3
The general setup of laser-driven magnetic reconnection experiments. (a) Side-on view, showing self-generated Biermann-battery magnetic fields in expanding plasmas, and probing of fields by monoenergetic protons from a driven D–^{3}He fusion implosion. (b) Face-on view, showing self-generated Biermann battery fields and formation of a magnetic reconnection current sheet where the two plasmas collide.

For this shot sequence, shown in Fig. 4, we radiographed the evolution of a single plasma plume, driven by two overlapped beams with near-normal incidence, with an on-target energy near 900 J in 1 ns, using standard OMEGA phase plates. The plumes were radiographed after 1.5 ns of evolution, using 15-MeV protons from a imploding D^{3}He capsule. We conducted experiments with three different probing techniques. First, we used a full mesh behind the target [Fig. 4(a)], which breaks the proton beam into multiple beamlets. The magnetic-field strength and direction can be directly inferred from the deflection of the beamlets, albeit at reduced spatial resolution (one data point per beamlet). In addition to the proton data shown here, we additionally obtained an x-ray shadow of the mesh using an image-plate detector at the back of the proton detector stack.[7] The x-ray mesh image provides a direct location of the "undeflected" location of each beamlet.

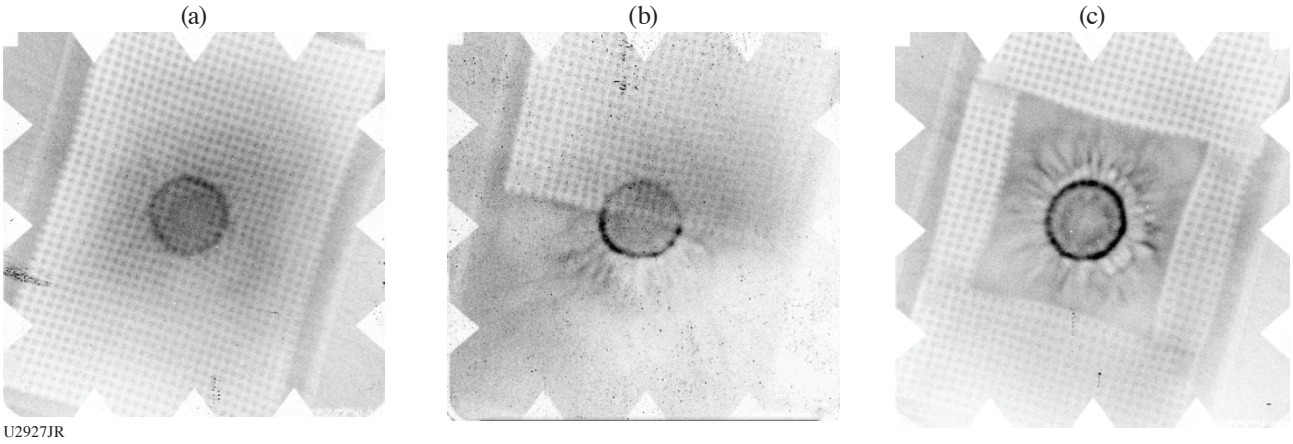

Figure 4
Shown are 15-MeV proton radiographs of expanding plasma plumes. The different experiments show the identical point of evolution of an isolated expanding plume, with three different probing techniques: (a) full mesh behind the foil, (b) half-mesh, and (c) boundary mesh.

We additionally obtained data using a half-mesh [Fig. 4(b)], or boundary mesh [Fig. 4(c)]. In the half-mesh, half of the plume is covered with a mesh, while the other half is a pure-proton-fluence image. In the pure-fluence image, we can observe several features that we commonly see in these plasmas, namely dark circular ring, which is produced by the proton focusing by the global Biermann battery magnetic field wrapping around the plume. Second, we now also observe fine-scale magnetic structures in the plume, which are obscured in the mesh image due to the sacrificed resolution. The pure-fluence data will be analyzed using reconstruction techniques.[6,8] In the half-mesh image, the results can be directly validated against the mesh data, assuming symmetry. Finally, in the boundary mesh case, we will conduct a fluence reconstruction of the central plume, using "help" from outer boundary conditions on the magnetic field, as inferred from the boundary mesh data.

We thank the support of the facility scientists. Experimental time at OMEGA was provided through the LLE Academic and Industrial Basic Science Program. Funding support was provided through Joint FES-NNSA Program in HEDP.

Electron Exhaust Jets and Current-Driven Kinetic Instabilities in Laser-Powered Magnetic Reconnection

S. Zhang,[1] A. Chien,[1] L. Gao,[2] H. Ji,[1,2*] E. G. Blackman,[3] R. K. Follett,[4] D. H. Froula,[4] J. Katz,[4] W. Daughton,[5] C. K. Li,[6] A. Birkel,[6] R. D. Petrasso,[6] J. D. Moody,[7] and H. Chen[7]
[1]Princeton University
[2]Princeton Plasma Physics Laboratory
[3]Department of Physics and Astronomy, University of Rochester
[4]Laboratory for Laser Energetics, University of Rochester
[5]Los Alamos National Laboratory
[6]Massachusetts Institute of Technology
[7]Lawrence Livermore National Laboratory
[*]Principal Investigator

Magnetic reconnection is a ubiquitous phenomenon in space and astrophysical plasmas that rapidly converts magnetic energy into particles and flows. Current-driven instabilities may play an important role in facilitating magnetic energy dissipation. Using two Academic and Industrial Basic Science (AIBS) campaigns on OMEGA, we combined the laser-driven capacitor-coil experiments with time-resolved collective Thomson scattering to study the kinetic physics in the collisionless reconnection, including the evolution of the non-Maxwellian velocity distribution function, electron jets, and kinetic instabilities. Thomson scattering reveals electron-acoustic waves (EAW's) with phase velocities near the electron thermal speed, indicating a non-Maxwellian distribution overcoming Landau damping. We also observed bursty and asymmetric ion-acoustic waves (IAW's), confirming the existence of the electron jet and the current-driven ion-acoustic instabilities (IAI's). The IAW bursts are followed by EAW bursts and electron heating. One- and two-dimensional particle-in-cell (PIC) simulations show that current-driven IAI can form double layers, which induce an electron two-stream instability generating EAW bursts in accordance with the measurements. Our experiments and simulations demonstrate that the electron outflow jet is unstable and can dissipate energy via the nonlinear development of the current-driven instabilities involving electron–ion coupling. We have submitted our findings to Nature Physics and the manuscript is now under review.[9]

The experimental platform is shown in Fig. 5. The capacitor-coil target is made of a 50-μm-thick Cu foil. The coils have a 600-μm diameter and 500-μm-length legs and are separated by 600 μm. The magnetic field generated by the capacitor-coil targets

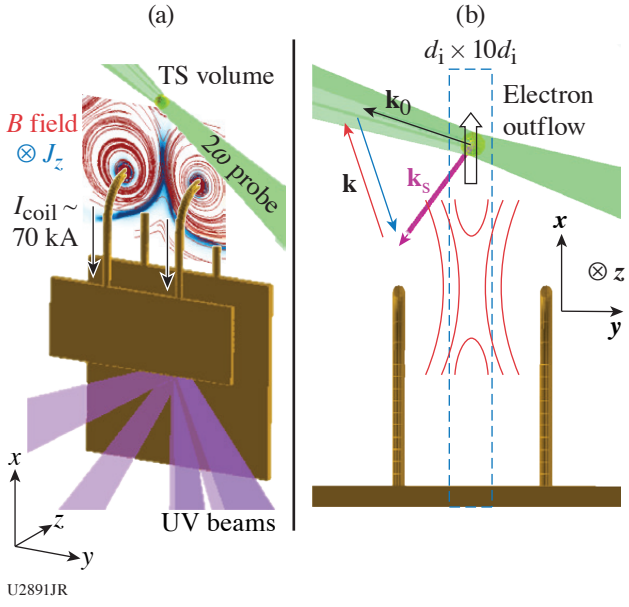

Figure 5
Experimental setup. Six beams of 500-J, 1-ns UV lasers are used to irradiate the back plate of the capacitor, driving current in the coils with $I_{coil} \sim 70$ kA. (a) *FLASH* magnetohydrodynamic (MHD) simulation results are overlapped to show the structure of the magnetic field (red lines) and the out-of-plane current density (blue) in the z direction. A 2ω (527-nm) Thomson-scattering (TS) beam (green) probes the reconnection exhaust region, 600 μm above the center point between the top of the coils. (b) $\mathbf{k}_0$ and $\mathbf{k}_s$ are the wave vectors of the probe beam and the collected scattered light. The red and blue arrows indicate wave vectors ($\mathbf{k}$) of waves in plasma that scatter the probe light to the collector. These $\mathbf{k}$'s are in the x–y plane and 17° off the outflow direction.

is profiled by proton radiography.[10–12] The upstream magnetic field strength is ~40 T at 6 ns after the lasers' onset. The proton radiography also shows the center feature, indicating the reconnection current sheet.

The non-Maxwellian distribution and the kinetic instabilities of the reconnection exhaust are shown in the Thomson-scattering spectrogram . As shown in Fig. 6(a), the IAW-resonant scattering is bursty and asymmetric. The asymmetric IAW spectrum before the bursts can be reproduced in the synthetic TS spectrum with relative drift between electrons and ions as shown in Fig. 6(c). The bursts confirm the existence of the current-driven IAI's. Figure 6(b) shows that the asymmetric IAW peaks are accompanied by an electron-acoustic wave resonant peak, which needs a two-stream distribution as shown in Fig. 6(d) to reproduce.

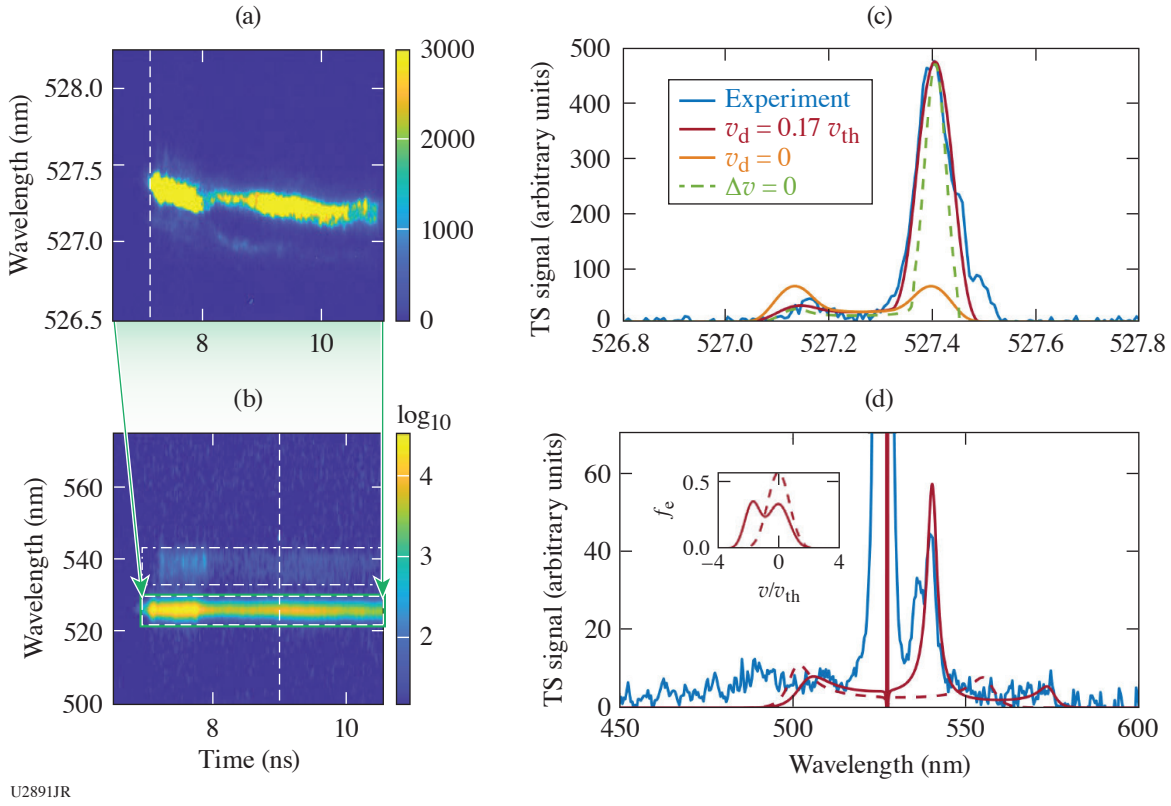

Figure 6
[(a),(b)] Time-resolved Thomson scattering (TS) at $t = 7$ to 10 ns. The IAW resonant peaks in (a) are highly asymmetric (10:1 to 100:1). (c) The spectrum along the vertical dashed line of (a) before the IAW bursts and the comparison with the synthetic TS spectra. The highly asymmetric IAW's can be reproduced with electrons streaming relative to ions with $v_d \sim 0.17\ v_{th}$. (b) The EAW peak along with the IAW feature. (d) The spectrum at 9 ns [along vertical dashed line of (b)] with a fitted synthetic spectrum (red solid line). A two-stream electron distribution is needed to reproduce the strong EAW signal. The distribution is shown as the solid line in the inserted plot. For reference, the synthetic TS spectrum from a Maxwellian distribution is shown as the dashed line.

We acknowledge the Omega Laser Facility staff at the Laboratory for Laser Energetics. This work was performed under the auspices of U.S. DOE NNSA under the AIBS program, and the DOE Office of Science under the HEDLP program with award number DE-SC0020103.

Inertial Confinement Fusion Interface 22A

B. Reichelt and C. K. Li*
Massachusetts Institute of Technology
*Principal Investigator

Inertial Confinement Fusion (ICF) Interface 22A was a makeup shot day for ICF Interface 21A, a separated reactant type shot day from 2021 that had a target assembly issue with out-of-spec glue spots. Like the original experiment, this day aimed to study the issue of interface mix for an 8-μm-thick target using a CD ablator separated from a ^{3}He gas fill by an inert CH layer of varying thickness. Thus, D^{3}He protons and D_2 protons/neutrons provide information about mix since their ratio is proportional to $n_{^3\mathrm{He}}/n_{\mathrm{D}}$. Further, the use of reactions that produce charged particles enables the use of the nuclear-imaging diagnostic proton core imaging spectrometer, which sheds further insight into the region that is producing reactions and how localized the mix is.

This shot day utilized targets that were significantly thinner than previous campaigns in the hopes of probing a regime more dominated by kinetic effects. Of particular interest is determining the accuracy of various mixing models in systems where strong shocks exist, which has become more programmatically relevant as OMEGA cryo shots have worked to increase implosion velocity. Both hydrodynamic and fully kinetic models are being interrogated using the LANL codes *xRAGE* and *iFP*, respectively.

Early analysis of nuclear data has been done to determine the charged-particle spectra emitted from the implosion shown in Fig. 7. As shown, the relationship between the CH buffer layer thickness and the spectral peak/width is not immediately apparent, but might be possible to relate to implosion ρR through stopping power and straggling formulas. There are interesting trends seen in the yields, however, which show an inversion effect as a function of offset thickness similar to past experiments for thicker capsules with lower temperatures.[13] Work is ongoing to analyze the time and spatially resolved nuclear diagnostic data collected by this experiment and to compare to predictions from hydrodynamic and kinetic simulations.

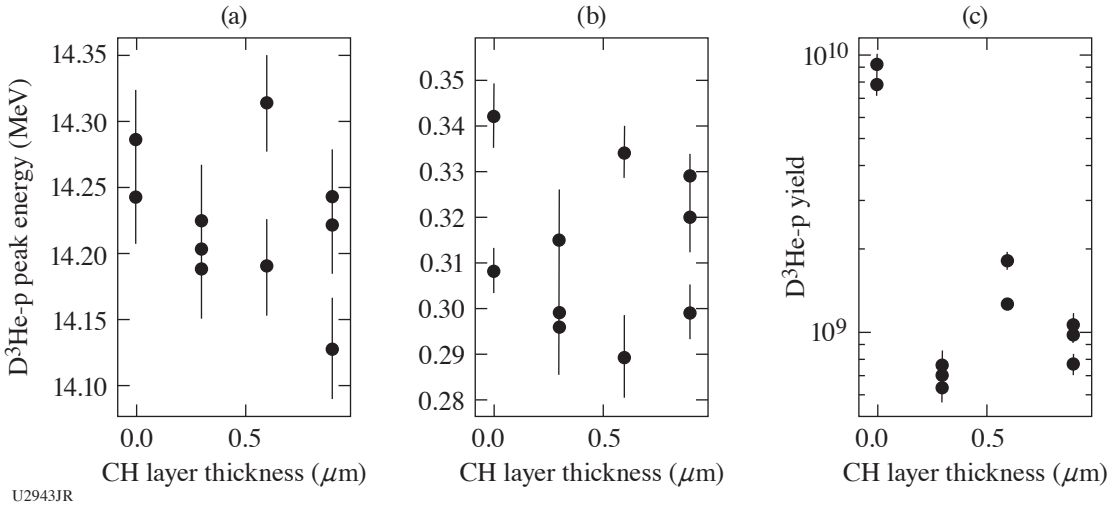

Figure 7
Analysis of D^{3}He proton spectra data from ICF Interface 22A using the wedge-range-filter array diagnostic.

This work is funded by DOE/NNSA Center of Excellence Contract DE-NA0003868. B. Reichelt is supported by NNSA Stewardship Science Graduate Fellowship Contract DE-NA0003960.

Effects of an External Magnetic Field on Laser–Plasma Instabilities

M. Bailly-Grandvaux,[1*] S. Bolaños,[1] R. Lee,[2] M. J.-E Manuel,[3] W. B. Mori,[2] F. Tsung,[2] B. Winjum,[4] and F. N. Beg[1]
[1]Center for Energy Research, University of California, San Diego
[2]Physics and Astronomy Department, University of California, Los Angeles
[3]General Atomics
[4]Office of Advanced Research Computing, University of California, Los Angeles
[*]Principal Investigator

Laser–plasma instabilities (LPI's) play a detrimental role in energy coupling to the target in inertial confinement fusion (ICF). This fundamental constraint of energy coupling of high-power lasers to plasma has been studied extensively over the last couple of decades under a wide variety of laser and plasma parameters. The recent development of applied strong magnetic fields for use in ICF and laboratory astrophysics experiments, however, has opened opportunities to investigate the role of external magnetic fields on LPI's. Recent numerical studies have shown that stimulated Raman scattering (SRS)[14] can be mitigated by external magnetic fields in the kinetic regime of the instability and warrant systematic experimental studies to validate modeling.

With this aim, we developed a platform for OMEGA EP to investigate the effect of an external magnetic field on SRS. A first shot day experiment was carried out in FY20, where we successfully demonstrated the feasibility to investigate backward-SRS (BSRS) in the kinetic regime and in a magnetized environment.[15] The experiment relied on the ability to measure the BSRS light when a laser pulse propagated through a magnetized gas-jet target, as sketched in Fig. 8(a). To measure the backscattered light, we used the sub-aperture backscatter (SABS) diagnostic, which provided a temporal and spectral resolution. The dual magneto-inertial fusion electrical discharge system (MIFEDS) ten-inch manipulator (TIM)-based pulsed-power device was fielded to embed the gas jet in a quasi-perpendicular and uniform magnetic field of ~22 T. The Rowland x-ray spectrometer and the 4ω-probe diagnostics suite were fielded in order to estimate the plasma conditions by comparing them with radiation-magnetohydrodynamic simulations (using *FLASH* and *GORGON* codes). We modified the platform in light of the first shot day experience: the MIFEDS axis was oriented in the same direction as the gas flow [Fig. 8(a)]. We also modified the laser profile of the interaction beam [orange curve in Fig. 8(b)] and added a heater beam. The main benefit of the heater beam is to prepare the plasma prior to the excitation beam interaction with improved uniformity. Its larger size reduces gradients within the smaller excitation beam spot size and lowers the intensity on target to avoid filamentation during heating. The SRS driver (Beam 4) utilized a special laser shape (a train of short pulses) to aid the interpretation of the BSRS signal by drastically reducing temporal variations of plasma conditions within the interaction of a 100-ps pulse.

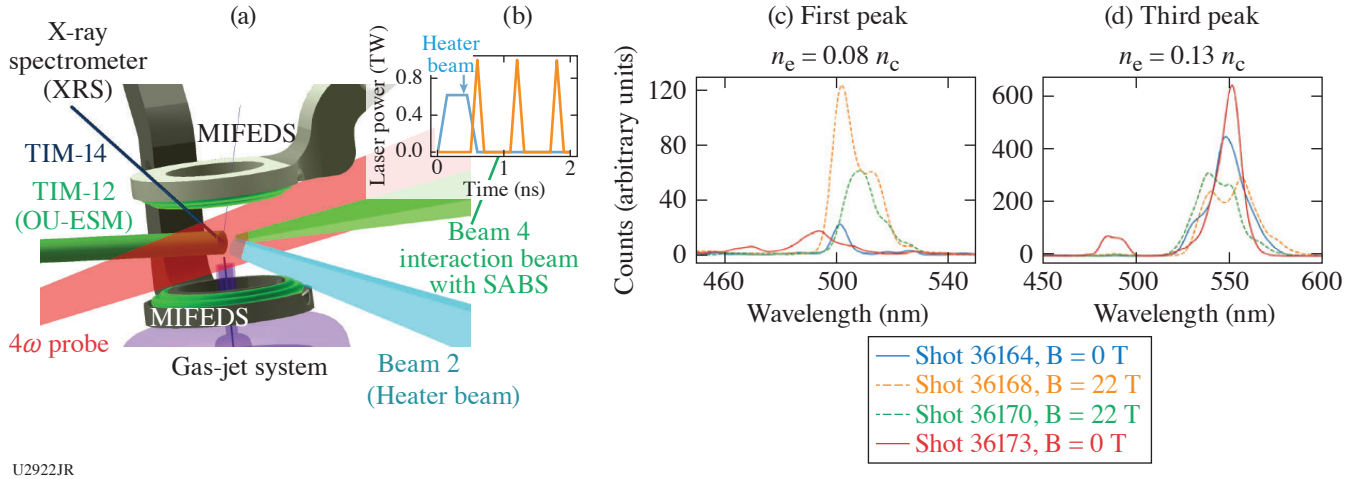

Figure 8
(a) *VISRAD* schematic of the experimental platform. (b) Temporal profiles of the laser power at target chamber center. [(c),(d)] Spectra of the backscattered light measured with SABS. Solid lines are shots without an external B field, and dashed lines are shots with an applied B field of 22 T. Spectra of the (c) first peak (d) the third peak. Note that the density is estimated according to the wavelength shift. OU-ESM: Osaka University electron spectrometer.

In the latest MagSRS-22A campaign, seven shots were performed. The first two shots of the day were performed with an argon pressure of 550 psi. The following shots were performed with a pressure of 880 psi in order to reach a higher density and thus reach the desired kinetic regime ($k\lambda_D \sim 0.2$ to 0.35). Three out of the five 880-psi shots were magnetized shots. We note that in one magnetized shot, MIFEDS failed, likely due to an arcing effect.

The SRS emission excited by a train of short 100-ps pulses is separated in the streaked spectral measurements, making it possible to correlate the spectra to specific plasma conditions for each pulse, as illustrated in Figs. 8(c) and 8(d). Since the time between pulses (~600 ps) is larger than the hydrodynamic time scale, the SRS excitation occurs in different conditions, meaning we diagnose the magnetic effect in various regimes. Figures 8(c) and 8(d) show the spectra measured with the SABS diagnostic for the first and third pulses where we observe contradictory behavior in the presence of the applied B field. For the third peak [$n_e \sim 13\%\ n_c$, see Fig. 8(d)], we observe mitigation of SRS reflectivity in the presence of the external B field, as expected. This is the first experimental evidence of SRS mitigation with B field. On the other hand, for the first peak [$n_e \sim 8\%\ n_c$, see Fig. 8(c)], we observe an apparent enhancement of the SRS reflectivity when applying an external magnetic field. We suspect that this enhancement is due to a rescattering mechanism. For the second peak (not shown) the backscattered light spectra are shifted to a wavelength corresponding to lower densities of $n_e \sim 5\%\ n_c$, although the data were not reproducible for repeated shots. As seen by the shift of the BSRS wavelength, shot-to-shot variations are related to hydrodynamic fluctuations that seem to be significant ~1 ns after the laser–plasma interaction (heater beam) and averaged out later in time.

We estimate the electron density from the backscatter wavelength. Indeed, the backscatter wavelength is strongly dependent on electron density. The electron temperature also induces a small shift. We fielded the Rowland x-ray spectrometer to estimate an average temperature of ~800 eV. Figure 9(a) shows the time-integrated K-shell emissions from the Ar gas jet and the synthetic spectra calculated by the collisional-radiative spectral analysis code *PrismSPECT*. With this measurement, we were able to correct the estimation of the electron density from the wavelength shifts in the backscatter spectra.

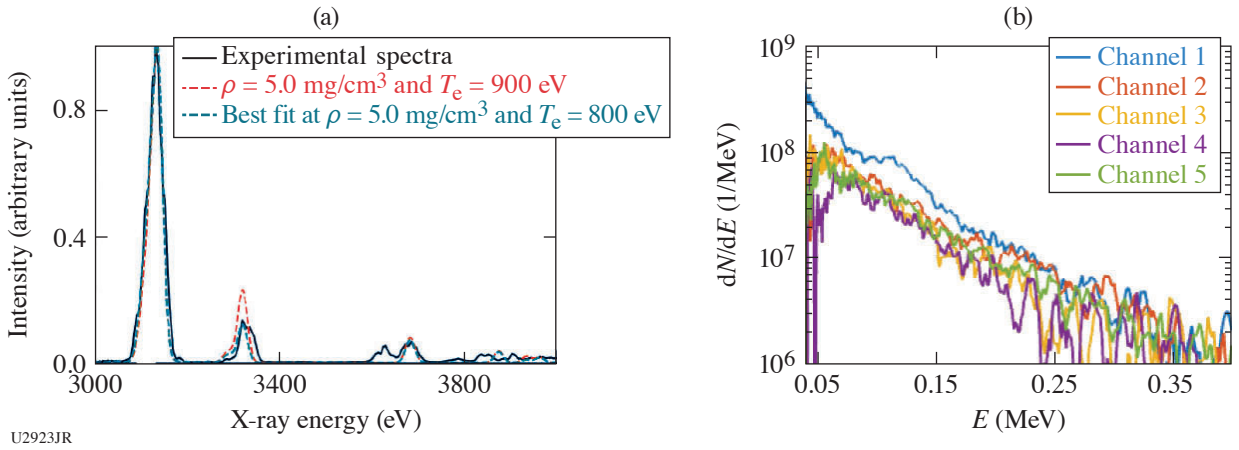

Figure 9
(a) XRS signal with a fit using *PrismSPECT*, giving an average electron temperature of ~800 eV. (b) Electron spectra measured at various angles via the OU-ESM.

In the studied regime, the wave-particle interaction plays a crucial role. A part of the electrons become trapped in the electron plasma wave and are accelerated at the phase velocity of the electron plasma wave in the direction of the laser. We fielded the OU-ESM electron spectrometer to measure the energy distribution of hot electrons. When unmagnetized, these hot electrons reduce the Landau damping and enable the growth of the SRS at $k\lambda_D \sim 0.3$. Figure 9 shows the electron spectra measured on one of the unmagnetized shots with a pressure of 880 psi. It reveals the presence of hot electrons with a temperature reaching ~300 keV, while no electrons were detected at the lower pressure of 550 psi. The OU-ESM is angularly resolved, such that each of the channels collects a sample of the electron beam at a different angle. Here, channel 1 is the channel the most aligned with the SRS driver

beam (Beam 4). We note an increase in the number of electrons (×2) for $E < 150$ keV, suggesting they were probably accelerated by the electron plasma wave induced by the SRS driver. Yet, the measured temperature is above our expectation and suggests that other LPI's occurred.[16] More particle-in-cell simulations will be run to understand the origin of such hot electrons. We did not detect any electrons in magnetized shots due to the deflections by the large-volume B field generated by the MIFEDS coils.

The experiment was conducted on the OMEGAG EP Laser System at the University of Rochester's Laboratory for Laser Energetics with the beam time through the NLUF Program. This material is based upon work supported by the Department of Energy, National Nuclear Security Administration under Award Numbers DE-NA0003842 and DE-NA0003856, the University of Rochester, and the New York State Energy Research and Development Authority.

Pressure Induced B1–B2 Phase Transition in ZnO Under Laser-Driven Ramp Compression

I. K. Ocampo,[1] D. Kim,[1] F. Coppari,[2] R. F. Smith,[2] and T. S. Duffy[1*]
[1]Department of Geosciences, Princeton University
[2]Lawrence Livermore National Laboratory
[*]Principal Investigator

ZnO is a wide-band-gap semiconductor (3.37 eV) well suited for use in electronic and optoelectronic devices (UV emission lasers and detectors, chemical sensors, and solar cells).[17] At ambient conditions, ZnO crystallizes in the wurtzite-type structure (B4, $P6_3mc$). Under quasi-hydrostatic loading, ZnO undergoes a phase transition from a B4-type to a B1-type structure (*Fm-3m*) at ~10 GPa (Ref. 18). Although no further phase transitions have been observed in ZnO experimentally up to ~209 GPa, density functional theory calculations predict that the B2 phase (*Pm-3m*) will become stable at high pressures. The calculated B1–B2 transition pressure varies by approximately 25% between two existing computational studies.[19,20] A tetragonal phase (B10, *P4/nmm*) has also been predicated to become thermodynamically stable over a narrow pressure region (236 to 316 GPa). In this study, we utilized the pulse-shaping capabilities of the OMEGA laser to ramp compress ZnO up to ~800 GPa and probe the atomic level structure of highly compressed ZnO using the powder x-ray diffraction image-plate (PXRDIP) diagnostic. These experiments allow us to directly test theoretical predictions of phase stability and equations of state.

Polycrystalline ZnO foils were synthesized by cold-pressing ZnO powders at 1.7 GPa in a diamond-anvil cell with 800-μm culets. Scanning electron microscope images of the foils were used to estimate the porosity of the foils (~3%). The ZnO foils were sandwiched between an ablator and a single-crystal diamond (SCD) tamper. The ablator for these experiments consisted of two SCD plates with a thin gold coating deposited in between, which acts to shield heat generated at the ablation surface. The ablator–ZnO–tamper target package was then centered over a Ta foil with a 300-μm pinhole and mounted onto the front of the PXRDIP diagnostic box. A 7- to 10-ns ramp shaped pulse was used to ablate the surface of the target package and quasi-isentropically compress the sample. When the target was expected to be at peak stress according to pre-shot hydrocode simulations, a 1-ns laser pulse was used to irradiate a Cu backlighter foil, generating quasi-monochromatic x rays (8.37 keV) that were diffracted from the target and recorded using the PXRDIP diagnostic. A line-VISAR (velocity interferometer system for any reflector) was used to monitor the planarity of the laser drive as well as the particle velocity at the SCD tamper-free surface. We used a Monte Carlo backward-propagating characteristics algorithm to infer the stress history in the sample and estimate the uncertainty in the achieved stress during the x-ray flash.

We have previously reported a series of laser-driven, ramp-compression experiments on ZnO with peak stresses from 260 to 620 GPa where we observed the onset of the B1–B2 phase transition between 299 and 332 GPa. This result is in very good agreement with theoretical predictions. Preliminary analyses of these data also suggest that the B1 and B2 phases remain in coexistence from 330 to 620 GPa. This shows that ramp compression can produce a remarkably large mixed-phase region. In our recent campaign, XRDEOS-22A-NLUF, we conducted four new experiments on OMEGA, extending the pressure–density data for this material up to 800 GPa. At 650 GPa, only the B2 phase was observed. To test the repeatability of this result, another experiment was conducted at 651 GPa and again, only the B2 phase was observed. This provides a high accuracy constraint on the extent of the B1–B2 mixed-phase region under ramp compression (300 to 650 GPa). The extreme metastability of the B1-type structure under the nanosecond time scales of our experiments suggests a kinetic limitation to the B1–B2 transition, yet further experi-

ments are required to evaluate the role of non-hydrostaticity and material strength on this fundamental phase transformation. The diffraction results from our experiment at 800 GPa are shown in Fig. 10. Two sample diffraction peaks could be indexed as corresponding to the (010) and (011) reflections of the B2-type structure. At this stress, ZnO has experienced a more than 2.6-fold increase in its ambient density. This work is ongoing and further experiments will be conducted to develop a pressure–density equation of state of the high-pressure B2 phase.

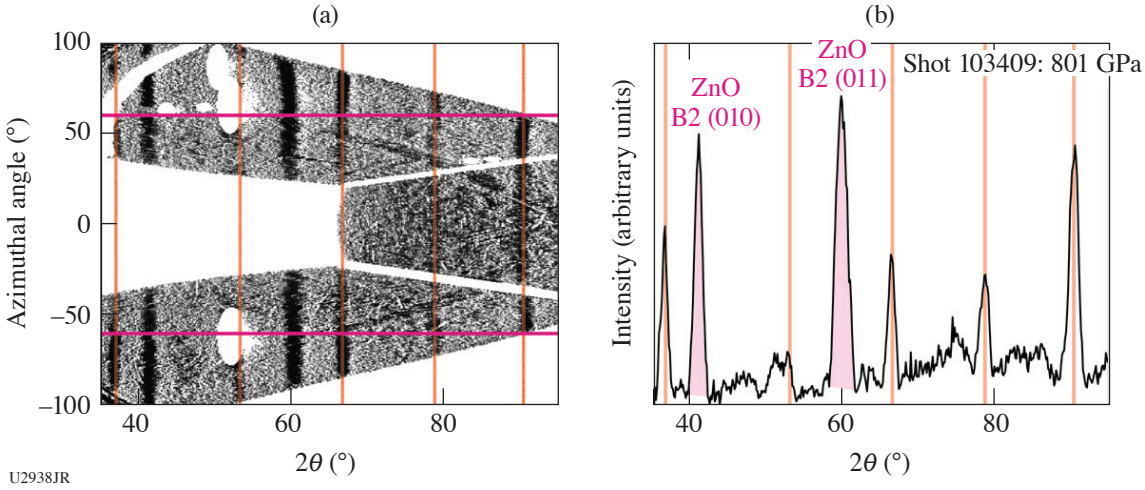

Figure 10
Diffraction results from shot 103409, our highest stress experiments (801 GPa). (a) The dewarped image plates projected into 2θ–ϕ space. Orange vertical lines highlight diffraction from the Ta pinhole. (b) The 1-D diffraction pattern integrated over the azimuthal angles specified by the horizontal magenta lines.

This work was supported by DOE Office of Science, Fusion Energy Sciences under Contract No. DE-SC0020005, the LaserNetUS initiative at the Omega Laser Facility, NNSA Contract No. DE-NA0003957, and National Science Foundation (NSF) EAR-1644614.

MultiIon Campaign: Studies of Multi-Ion and Kinetic Effects in Shock and Ablatively Driven Implosions

T. Evans,[1] N. V. Kabadi,[2] P. Adrian,[1] J. Kunimune,[1] E. Gallardo-Diaz,[3] R. C. Mancini,[3] C. Stoeckl,[2] V. N. Glebov,[2] and J. A. Frenje[1*]
[1]Plasma Science and Fusion Center, Massachusetts Institute of Technology
[2]Laboratory for Laser Energetics, University of Rochester
[3]University of Nevada, Reno
*Principal Investigator

MultiIon-22A and MultiIon-22B focused on studying the impact of multi-ion and kinetic effects on several observables during the shock-burn phase and subsequent compression phase in both shock- and ablatively driven implosions. Previous work demonstrated the presence of thermal decoupling and a significant deviation from hydrodynamic behavior of implosions with low initial gas-fill density (or pressure).[21,22] Yield, ion temperature, emission histories of x rays, neutrons, and protons were measured simultaneously in each implosion experiment. The measured data set is being compared to both hydrodynamic and kinetic simulations to understand the influence of multi-ion and kinetic effects at different stages of an ICF implosion.

As shown in Fig. 11, the MultiIon-22A experiment featured 2.8-μm Hoppe-glass capsules with four different initial gas-fill densities, ranging from 0.5 mg/cm^3 to 3.5 mg/cm^3. The variation in initial gas-fill density was selected to obtain a range of Knudsen numbers (K_n) spanning the transition from kinetic to hydro-like behavior. K_n is defined as the ratio of the ion–ion mean free path to the system size (radius of the shell), and is proportional to the square of the temperature over density:

$$K_n = \frac{\lambda_{ii}}{R_{\text{shell}}} \propto \frac{T^2}{n}.$$

Data demonstrate a large discrepancy between the yield in the lower-density cases and that predicted by hydrodynamic theory alone, even where hydrodynamic simulations effectively match other key implosion parameters, including bang time and ion temperature (see Fig. 12). Further analysis of data from this shot day will include comparison to fully kinetic simulations, which are expected to recreate the observed discrepancy.

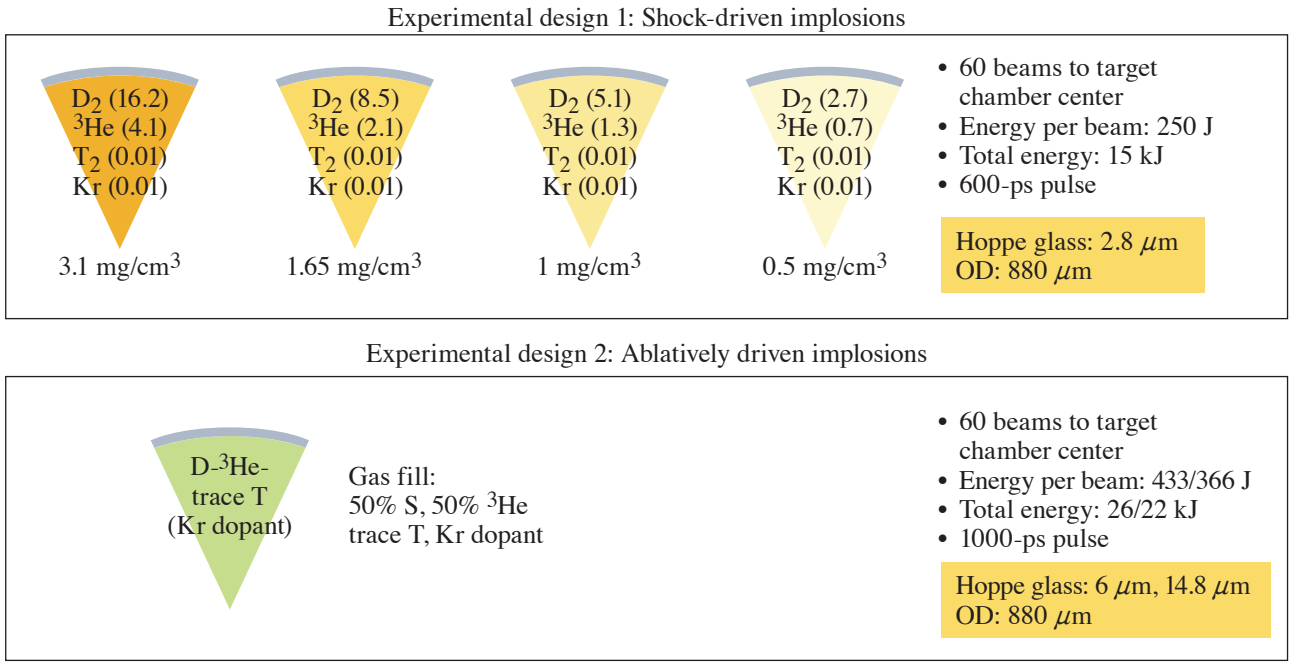

Figure 11
Capsule and laser specifications for both MultiIon-22A and MultiIon-22B experiments.

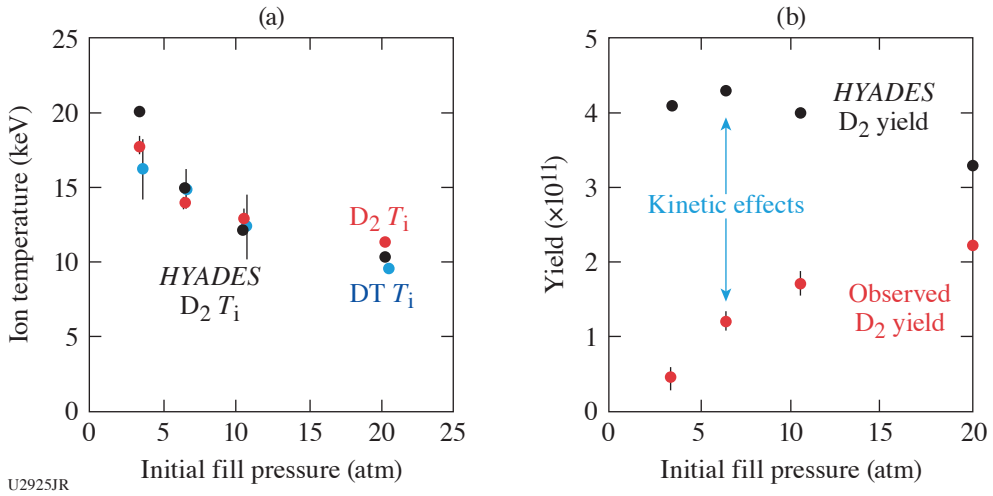

Figure 12
(a) Measured and hydro-simulated D_2 and DT ion temperature versus initial gas-fill pressure. A preliminary evaluation suggests a good agreement between data and simulation is observed. (b) Measured and hydro-simulated D_2 yield versus initial gas-fill pressure. The yield shows a large discrepancy at lower fill pressures, clearly indicating the impact kinetic effects, which will be further analyzed.

The MultiIon-22B experiment featured 6-μm and 15-μm-thick Hoppe-glass capsules that were illuminated by two different laser driver energies. The purpose with these capsule and laser configurations was to generate compression-driven implosions and study how kinetic effects persist from the shock-burn phase to the subsequent compression phase. In addition, the different shell thicknesses and laser energies provide different shock strengths. The analysis of the resulting data is ongoing and will involve both hydrodynamic and kinetic simulations with the intention of linking key implosion parameters to those observed in MultiIon-22A.

In summary, excellent data were obtained with the primary particle x-ray temporal diagnostic[23] and neutron temporal diagnostic in both the MultiIon-22A and MultiIon-22B experiments. The analysis of the resulting data is underway. Continued analysis will link the results of the two shot days and inform a dynamic model of the impact of shock-burn phase kinetic effects on the subsequent compression phase.

This work was supported by DOE/NNSA contracts DE-NA0003868, DE-NA0003856, and DE-NA0003938. Thank you to collaborators at MIT and LLE for support and guidance.

Ablator–Gas Interface Dynamics and Mix in Inertial Confinement Fusion-Relevant Conditions

J. Kunimune,[1] B. Reichelt,[1] P. Adrian,[1] S. Anderson,[2] B. Appelbe,[3] A. Crilly,[3] T. Evans,[1] C. J. Forrest,[4] J. A. Frenje,[1] V. Yu. Glebov,[4] B. M. Haines,[2] T. M. Johnson,[1] C. K. Li,[1] H. G. Rinderknecht,[4] G. D. Sutcliffe,[1] W. Taitano,[2] and M. Gatu Johnson[1*]
[1]Massachusetts Institute of Technology
[2]Los Alamos National Laboratory
[3]Imperial College, London
[4]Laboratory for Laser Energetics, University of Rochester
[*]Principal Investigator

The main goal of this NLUF campaign is to validate and confirm the impact of "kinetic mix,"[24] where fast streaming ions generated during the shock phase of an ICF implosion impact core plasma conditions. Reaching this goal also requires quantifying the relative impact of other mix effects (hydro-instabilities, diffusion, and localized mix) as a function of implosion conditions (to isolate the kinetic mix effect, these other effects must be mitigated or understood). During FY22, two initial experiments were executed as part of this project: LocMix-22A (0.5 shot days, PI MIT Ph.D. student Justin Kunimune) and KinMix-22A (one shot day, PI MIT Ph.D. student B. Reichelt).

Targets for LocMix-22A and KinMix-22A are shown in Fig. 13. All were filled to the same number density and had the same outer diameter, and both campaigns used both 6-μm and 15-μm-thick plastic shells to vary implosion conditions from more kinetic (6 μm) to more hydro-like (15 μm), with the anticipation that kinetic and diffusion mix will dominate at 6 μm with hydro (instability) mix starting to play more of a role at 15 μm.

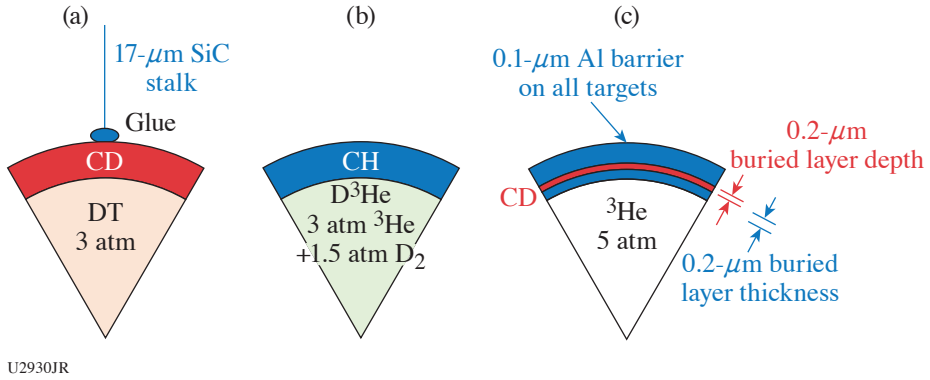

Figure 13
Pie diagrams for targets used for (a) LocMix-22A and [(b),(c)] KinMix-22A. For each experiment, total shell thickness of 6 μm and 15 μm were used to vary implosion conditions from strongly shock driven and thus highly kinetic (6-μm shell) to more compressively driven and hence more hydro-like (15-μm shell). The goal of LocMix-22A was to quantify localized mix due to stalk impact by using imaging diagnostics and one to two stalks, while the goal of KinMix-22A was to study the balance of diffusion/kinetic/hydro mix as a function of implosion conditions using nuclear observables with time-resolved nuclear burn-history measurements as the primary diagnostic.

The specific goal of LocMix-22A was to measure impact of localized mix due to the capsule stalk mount. To this end, half of the implosions used a single stalk, while half used two stalks in opposing geometry. The primary diagnostics were three-axis x-ray and knock-on deuteron (KOd) imaging (Fig. 14). Three x-ray images in different energy bands were obtained in each of three near-orthogonal viewing directions; these data will be used to reconstruct spatial electron temperature profiles. *xRAGE* simulations predict that the effect of the stalk mix will be a region of less x-ray emission due to injection of material that is ~2 keV colder than the surrounding fuel;[25] if correct, this should be clearly visible in the x-ray data. The KOd come from DT neutrons scattering off of D in the fuel or CD shell. By imaging deuterons in different energy bands, differences in morphology of the fuel (high-energy, forward-scattered deuterons) and shell (lower-energy, side-scattered deuterons) should be discernible. Analysis of both x-ray and KOd images are still in the early stages; preliminary images from the TIM-4 viewing angle are also shown in Fig. 14.

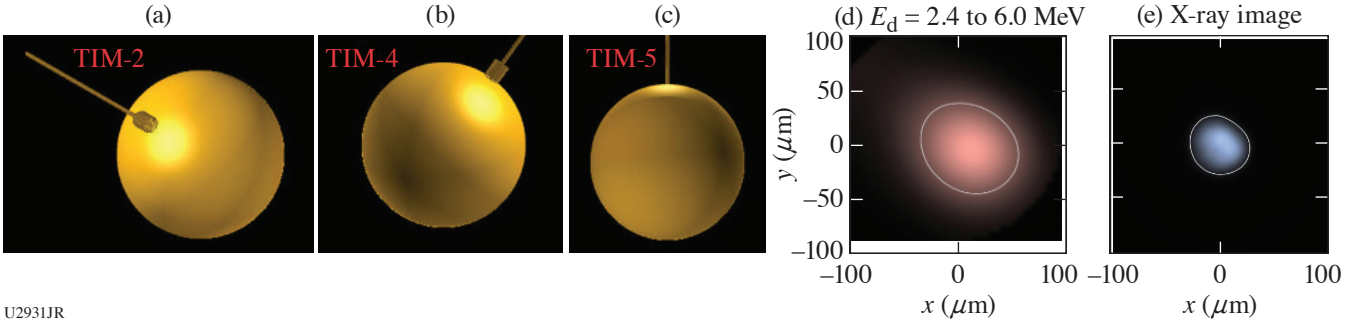

Figure 14
[(a)–(c)] LocMix-22A used three near-orthogonal penumbral imaging detectors in OMEGA TIM-2, -4, and -5 set up to measure (d) knock-on deuterons and (e) x rays in three different energy bands. (d) The TIM-4 deuteron image in the 2.4- to 6.0-MeV energy band, and (e) the x-ray image recorded in the same location. Analysis is in progress to infer stalk impact through reconstruction of the spatial electron temperature distribution from the x-ray images in different energy bands, and through the study of asymmetries in the knock-on deuteron emission.

KinMix-22A used directly comparable buried-layer targets, with a CD tracer layer and pure ^{3}He gas fill, and reference targets, with CH shells and 50:50 D^{3}He fill, to study the level (through integrated nuclear signatures) and timing (through nuclear burn history measurements) of mix. Detailed analysis of the data is in progress; preliminary D^{3}He yields show substantially more mixing for the thin shell (6 μm) than thick shell (15 μm) targets (Table II). The particle x-ray temporal diagnostic (PXTD) also recorded good data on this experiment, which will be used to address the relative timing of proton emission versus peak convergence for the two shell thicknesses, thus helping constrain the mix mechanisms responsible for injecting deuterium into the fuel as a function of implosion conditions.

Table II: Highly preliminary results from KinMix-22A suggest substantially more shell mixing (D^{3}He signal) for the 6-μm shells than for the 15-μm shells (10% of the control versus 2% of the control D^{3}He yield, respectively). CR-39 etching and scanning is still in progress to finalize these numbers. nTOF: neutron time of flight.

Total shell thickness (μm)	Capsule fill	Laser pulse	YDD$_n$ estimated (nTOF)	YD^{3}He$_P$ estimated (nTOF)	DD$_n$ temperature (nTOF)
14.3	4.5 atm D^{3}He	SG010	1×10^{10}	6×10^9	6 keV
14.6	5 atm ^{3}He	SG010	2.5×10^8	1×10^8	2.5 keV
6.3	5 atm ^{3}He	SG006	4×10^7	1×10^9	Uncertain (5 to 15 keV)
5.8	4.5 atm D^{3}He	SG006	1.5×10^{10}	1×10^{10}	15 keV

The KinMix-22A and LocMix-22A datasets will be completed with further buried-layer data from KinMix-23A, and with measurements of the ion release from 6-μm and 15-μm flat foils in opposing geometry with a gas jet in between, using Thomson scattering and x-ray imaging, on FoilGasDist-23A.

This material is based upon work supported by the National Nuclear Security Administration, Stewardship Science Academic Alliances, under Award Number DE-NA0003868. The experiments were conducted at the Omega Laser Facility with the beam time through the NLUF under the auspices of the U.S. DOE/NNSA by the University of Rochester's Laboratory for Laser Energetics under Contract DE-NA0003856. B. Reichelt is supported by NNSA SSGF Contract DE-NA0003960.

Report for DACPlanet-22A/B

G. Tabak,[1,2*] G. W. Collins,[1,2,3] J. R. Rygg,[1,2,3] R. Dias,[2,3] N. Dasenbrock-Gammon,[2] T.-A. Suer,[1,3] S. Brygoo,[4] P. Loubeyre,[4] and R. Jeanloz[5*]
[1]Laboratory for Laser Energetics, University of Rochester
[2]Department of Physics and Astronomy, University of Rochester
[3]Department of Mechanical Engineering, University of Rochester
[4]Commissariat à l'énergie atomique et aux energies alternatives
[5]University of California, Berkeley
[*]Principal Investigators

The purpose of this campaign was to study a hydrogen–neon gas mixture with planetary science applications in mind. Hydrogen and neon are present in gas giants such as Saturn and the two are predicted to be immiscible at certain pressure–temperature conditions inside these planets. Documenting the exact location of the demixing boundary has implications for planetary modeling. This study is a follow-up on similar experiments performed on hydrogen–helium mixtures.[26]

The experimental approach was to precompress H_2–Ne mixtures (20% Ne by mole) in diamond-anvil cells (DAC's) to 4 GPa and shock compress them using the high-power lasers at LLE. At the 4-GPa precompression, hydrogen and neon are liquid and miscible, making it possible to prepare a homogeneous sample at liquid initial densities. The resulting Hugoniot curve is predicted to span pressure–temperature conditions relevant to planets and cross the demixing boundary, beyond which (i.e., at the most extreme conditions) the hydrogen and neon are miscible. A quartz layer was inserted into the DAC chamber to serve as a material standard. The filled DAC's were characterized to measure the sample pressure and chamber thickness. The targets were then driven with a 1-ns square pulse drive on the OMEGA 60-beam laser, driving a shock wave through the samples. VISAR and SOP (streaked optical pyrometry) were used to measure the shock velocity, reflectivity, and self-emission.

Excellent velocimetry and pyrometry data were obtained using VISAR and SOP (see Fig. 15). Impedance matching with quartz will be used to infer the pressure and density of the gas mixture. The self-emission and VISAR fringe amplitude will be referenced to quartz to measure the reflectivity and temperature of the shocked gas mixture. The expected signature of the demixing boundary is a discontinuity in the reflectivity along the Hugoniot. Such a signature has been observed for hydrogen–helium mixtures.[26]

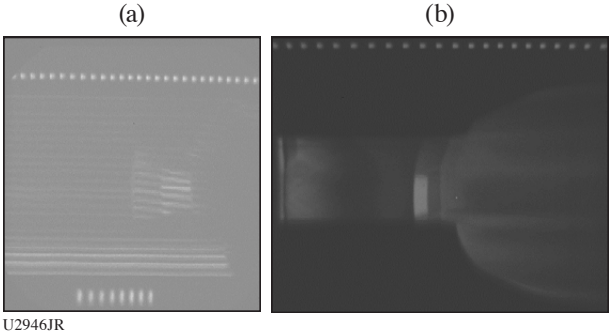

U2946JR

Figure 15
(a) VISAR and (b) SOP data for shot 103818. The two fringe events at the spatial center of the streak camera image indicate shock breakout into quartz and then into the gas mixture. The self-emission of the quartz standard is clearly seen as the small rectangular region on the SOP image, after which the gas mixture self-emission is recorded.

Several data points on the hydrogen–neon mixture have been obtained, providing the first step to understanding the mixture. Additional data will be obtained in FY23 that should provide definitive evidence of the expected reflectivity discontinuity in order to demarcate the demixing threshold. In particular, more shots at lower pressures (<150 GPa) are needed to study the region of interest. The resulting impedance match with quartz would entail a quartz sample that is either absorbing or transparent at the

VISAR probe frequency (532 nm), so some targets will be prepared instead with a fused-silica window. The fused silica becomes reflective at lower pressures than quartz, so this will facilitate lower shock pressure experiments with a reflective material standard.

Plasmoid Magnetic Reconnection Between Long-Pulse, Laser-Driven Plasmas Perturbed by a Short-Pulse Laser

J. L. Latham,[1] B. K. Russell,[1] L. Willingale,[1] P. T. Campbell,[1] G. Fiksel,[1] P. M. Nilson,[2] and K. M. Krushelnick[1*]
[1]Center for Ultrafast Optical Science, University of Michigan
[2]Laboratory for Laser Energetics, University of Rochester
[*]Principal Investigator

To understand magnetic reconnection in high-energy-density plasmas,[27] this campaign studied the magnetic fields of a three-pulse geometry, where a short-pulse laser illuminated the interaction region between two expanding plasma plumes, each driven by a long-pulse laser. Pre-shot studies anticipated that the reconnection rate would increase with the temperature of the interaction region, à la plasmoid reconnection theory,[28] but that the outflowing plasma from the short-pulse laser would inhibit reconnection.

In the experiment, plastic targets were irradiated by two UV beams with an intensity of 1.1×10^{14} W/cm^2 for 2.5 ns ("long-pulse lasers"). Some of the targets were also irradiated by an IR beam with an intensity of 2×10^{19} W/cm^2 for 10 ps ("short-pulse laser"). The resulting magnetic (and electric) fields were recorded in radiochromic film (RCF), using a proton beam created by a second short-pulse laser incident at a copper foil located 8 mm away from the target. The data show dark rings around each of the laser spots, and in several cases a highly complicated structure (Fig. 16).

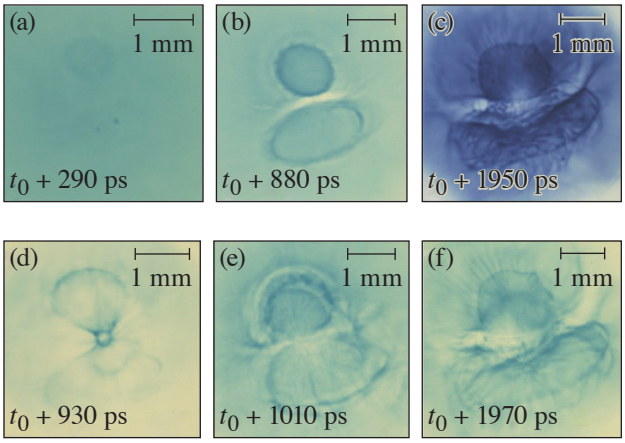

Figure 16
Scans of RCF irradiated by 24-MeV protons that passed through the main laser target. The time that the proton beam passed through the target is indicated on each film where t_0 is the onset of the UV beams. For shots (a)–(c) there was no short-pulse laser on the main target. For films (d)–(f), the short-pulse laser arrived at times t_0 + 360 ps, t_0 + 940 ps, and t_0 + 950 ps, respectively.

Plasmoid reconnection theory alone is not sufficient to explain the dynamics of the magnetic fields in this experiment. The discontinuities in the dark regions of the film indicate that reconnection may have been inhibited rather than enhanced. A future experiment is required to capture the dynamics in between the time windows captured in this experiment. The laser–plasma interaction is also being investigated using computer simulations.

The experiment was conducted at the Omega Laser Facility with the beam time through NLUF under the auspices of the U.S. DOE/NNSA by the University of Rochester's Laboratory for Laser Energetics under Contract DE-NA0003856.

Achieving Neutron Star Envelope-Relevant Conditions Through a Radiative Shock in a Strongly Coupled Plasma

C. C. Kuranz,* H. J. LeFevre,* S. D. Baalrud, and J. Kinney
Nuclear Engineering and Radiological Sciences, University of Michigan
*Principal Investigators

Compact objects are some of the most extreme environments in the universe. The temperatures and densities inside a neutron star can reach truly extraordinary values of 10^9 K and 10^{14} g/cm^3, respectively, at masses of around one solar mass. This makes these objects extremely small (tens of kilometers diameter), which make them difficult to directly observe.[29] In the envelope of a neutron star, in the more-outer portions, radiation dominates the heat transport, and the plasma is not fully stripped, which makes the opacities difficult to model.[30] The strong ion coupling (with the coupling parameter ~10) is a challenging regime for theory and radiation is not typically considered in these systems.[31] Additionally, the strongly coupled nature of this plasma will affect the contributions of bremsstrahlung to the emissivity and opacity, which is not currently adequately modeled. The dimensionless parameter to determine if a shock is radiative is

$$R_F = \frac{2\sigma T^4}{\rho u_s^3},$$

where σ is the Stefan–Boltzmann coefficient, T is the immediate post-shock temperature, ρ is the mass density, and u_s is the shock velocity. If R_F is greater than or about one, then the radiative energy fluxes are significant in the system and the shock is radiative. The coupling parameter determines if the microphysics or bulk physics drives the evolution of the system and one writes it as

$$\Gamma_{ii} = \frac{q^2 Z^2}{4\pi\varepsilon_0 \bar{d} T},$$

where q is the fundamental charge, Z is the ionization, ε_0 is the permittivity of free space, d is the Wigner–Seitz radius, and T is the plasma ion temperature. If Γ_{ii} is greater than one, then the plasma is strongly coupled.

The SCRaP Campaign addresses these problems with a novel capsule implosion experiment. It uses an 860-μm-outer-diam capsule with a 7-μm outer plastic layer and a mid-Z metal layer on the interior surface. The experiments described here used three capsule designs with three different material layers: 0.2 μm of nickel, 0.4 μm of titanium, or 0.7 μm of aluminum. The different layer thicknesses provide capsules of equal mass, so the drive energy can remain unchanged between the different capsule designs. The drive consisted of 60 beams with SG5-650 phase plates and 1-ns square pulses using about 120 J per beam. This resulted in an average irradiance of 3×10^{14} W/cm^2 over the surface of the capsule. The primary diagnostics used to measure the conditions in these experiments were x-ray framing cameras and a time-integrated spectrometer. The framing cameras used 8× magnification and a 50-ps pulse forming module. The Henway spectrometer uses four convex crystals with image-plate detectors covering a spectral range of about 3 to 13 keV.

Figure 17(a) shows contrast-enhanced framing camera data of a nickel-lined capsule implosion. These images have a pair of 20-μm-thick copper and 12.5-μm-thick nickel foils at the rear filter to act as an imager of K-shell emission from nickel. This makes the images show where only the nickel is during the implosion. The regions labeled 1, 2, and 3 in Fig. 17(a) show the imploding shell, the accretion of matter at the center of the shell, forming a shock, and the shock reaching the plastic resulting in rapid cooling, respectively. Figure 17(b) shows the measured velocity of the rebounding shock as about 180 km/s. Figure 17(c) shows the line emission from the highly ionized Ni and an absorption feature at lower energies due to the absorption of bremsstrahlung produced in the hot, dense core of the capsule implosion along the radial gradient in conditions.

This shock velocity is lower than what 1-D radiation hydrodynamics predict, and 2-D simulations are in progress to determine if structure in the imploding material leads to these effects. Further analysis of the spectra will provide the ionization of the pre-shock material and the volume-averaged density, which will be useful for constraining the dimensionless parameters described above.

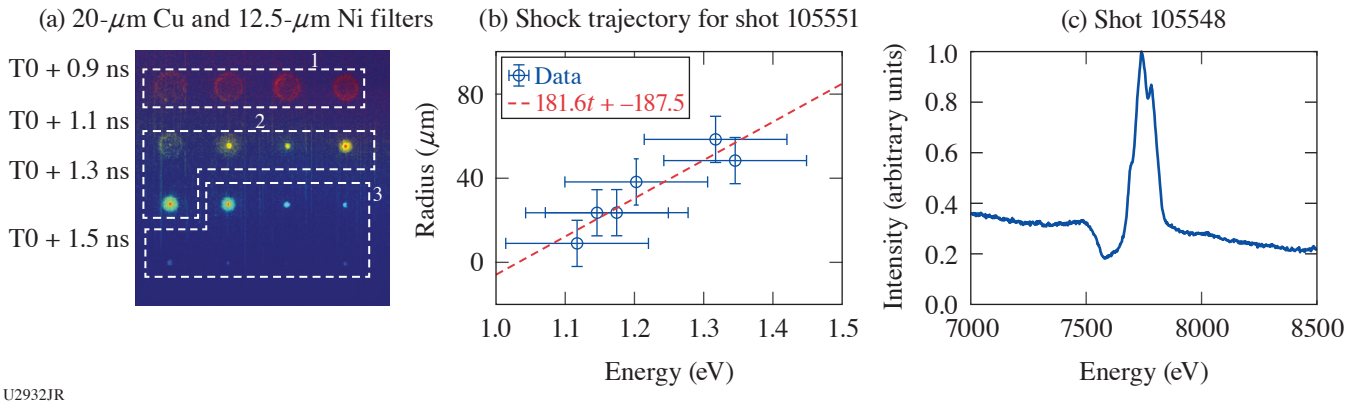

Figure 17
(a) Contrast enhanced framing camera data of a Ni-lined capsule implosion showing region 1 where the Ni shell is imploding and decreasing in radius, region 2 where mass begins accreting at the center of the capsule and forms a rebounding shock, and region 3 where the shock reaches the plastic then expands and cools. (b) The trajectory of the rebounding shock from (a). The linear fit to the data shows a shock velocity of about 180 μm/ns. (c) Spectroscopic data showing the 2 ≥ 1 emission features of Li, Be, and B-like emission features of Ni with an absorption feature to the red of the emission lines due to gradients in the plasma.

This material is based upon work supported by the National Science Foundation MPS-Ascend Postdoctoral Research Fellowship under Grant No. 2138109. This work is supported by SSAA Grant 13432116, and the NLUF Program, grant number DE-NA0002719, and through LLE/NNSA Cooperative Agreement No. DE-NA0003856.

Observation of a Radiative Heat Front in Ar Using the OMEGA Gas-Jet System

C. C. Kuranz,[1*] H. J. LeFevre,[1*] and K. V. Kelso[2]
[1]Department of Nuclear Engineering and Radiological Sciences, University of Michigan
[2]Department of Applied Physics, University of Michigan
[*]Principal Investigators

Radiation from hot, massive stars in star-forming regions can heat the surrounding nebula, heating it and producing an HII region, which consists of ionized hydrogen.[32] This heating propagates as a radiation-driven heat front and this may influence the development of clumps in the nebula, which is an open question in astrophysics.[33,34] The PIonFront Campaign on OMEGA creates a radiative heat front to study the radiation hydrodynamics of this system and understand the ionizing radiation–matter interactions that drive its evolution. The goal of this work is to produce a radiative heat front where photoionization dominates the energy deposition. To determine if that is the case and the front is in the desired physics regime, the dimensionless parameters α and β define the physics regime. The parameter α is the ratio of recombination to photoionization

$$\alpha = \frac{^{n}(\mathrm{i}+1)^{n_\mathrm{e}} R_{\mathrm{i}+1,\mathrm{i}}}{n_\mathrm{i}\Gamma_{\mathrm{i},\mathrm{i}+1}},$$

where n_i is the number density of the ith ionization state, n_e is the electron number density, $R_{\mathrm{i}+1,\mathrm{i}}$ is the recombination rate coefficient, and $\Gamma_{\mathrm{i}+1,\mathrm{i}}$ is the photoionization rate. If α is less than one, then photoionization dominates over recombination. The parameter β is one plus the ratio of electron collisional ionization to recombination

$$\beta = 1 + \frac{n_\mathrm{i}\langle\sigma v\rangle_{\mathrm{i},\mathrm{i}+1}}{n_{\mathrm{i}+1}R_{\mathrm{i}+1,\mathrm{i}}},$$

where $\langle\sigma v\rangle_{\mathrm{i},\mathrm{i}+1}$ is the electron collisional ionization rate coefficient, and all the other values are the same as for α.

To conduct these experiments, it is necessary to have a driving x-ray source and a propagation medium. These experiments use a 500-nm-thick gold foil, irradiated with a 5-ns laser pulse with an irradiance of 10^{14} W/cm^2 to create a bright, quasi-blackbody source. The OMEGA gas-jet system using argon gas with a 2-mm-diam, Mach 5 nozzle and a backing pressure of 750 psi acts as the propagating medium.[35] Figure 18(a) demonstrates the experimental geometry. A capsule implosion using 17 beams with 1-ns square pulses creates a bright, short-lived (~200-ps) probe source for absorption spectroscopy of the argon K shell. The spectroscopic measurement uses a flat, pentaerithritol crystal using an MS image plate as a detector with the backlighter duration self-gating the signal. Figure 18(b) shows the time series of the absorption spectroscopy measurements, indicating a cold plasma with minimal changes to the spectrum until after 2.5 ns after the drive turns on when $n = 1 \rightarrow 3$ and $n = 1 \rightarrow 2$ transitions in argon appear. Additionally, the argon K edge shifts to higher energy due to ionization from the heat front. This indicates a delay in the arrival of the heating at the probe location in the center of the gas jet, 3 mm from the initial driving source position, relative to the speed of light. The appearance of $n = 1 \rightarrow 2$ transitions also indicates that the source ionizes the argon the neon-like state and likely stops at the chlorine-like state. Figure 18(b) shows the time series of spectra over several shots that demonstrates the increase in ionization as the radiative heat front passes the measurement volume.

Currently, the radiation-hydrodynamics simulations of these experiments overpredict the velocity of the heat front. This makes it difficult to compare synthetic spectra to the measured results. Efforts are underway to improve the model of the driving source used in the experiment to address this discrepancy between simulation and experiment. These combined efforts will result in a determination of α and β using the measured and simulated results with models for the atomic rate coefficients.

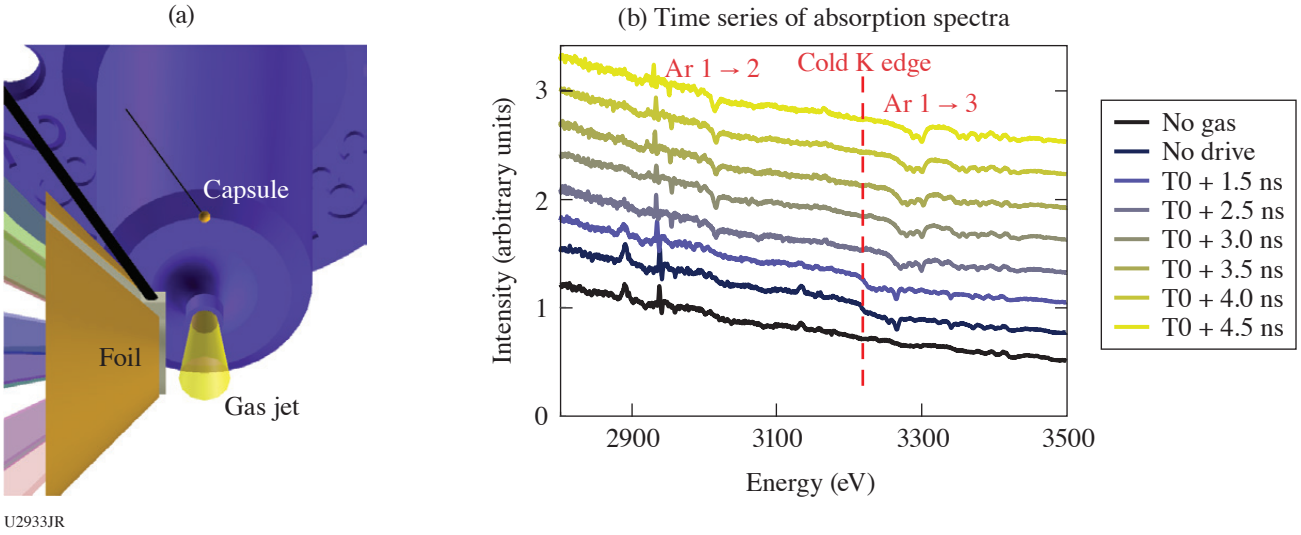

Figure 18
(a) A *VISRAD* model of the gold foil target, the capsule backlighter, and the gas jet. (b) A series of spectra with one spectrum collected during a single shot progressing upward from the bottom. The first (bluest) spectrum is from a capsule backlighter only and the next spectrum has a capsule backlighter with undriven Ar gas. The following spectra moving upward show a delayed onset of a blue shifting of the K edge, which indicates ionization. This is indicative of a heat front propagating through the gas column.

This material is based upon work supported by the National Science Foundation MPS-Ascend Postdoctoral Research Fellowship under Grant 2138109. This work is funded by the U.S. Department of Energy NNSA Center of Excellence under cooperative agreement number DE-NA0003869, and through the LLE/NNSA Cooperative Agreement No. DE-NA0003856.

Onset, Subsistence, and Decay of Magnetized Turbulence and Fluctuation Dynamo

H. Poole,[1] A. F. A. Bott,[1,2] C. A. J. Palmer,[3] Y. Lu,[4] S. Iaquinta,[1] S. Zhang,[1] K. Moczulski,[4,5] P. Farmakis,[4,5] A. Reyes,[4] A. Armstrong,[4,5] D. H. Froula,[5] J. Katz,[5] T. Johnson,[6] C. K. Li,[6] R. D. Petrasso,[6] J. S. Ross,[7] H.-S. Park,[7] P. Tzeferacos,[1,4,5*] G. Gregori,[1] and D. Lamb[8*]
[1]Department of Physics, University of Oxford
[2]Department of Astrophysical Sciences, Princeton University
[3]Centre for Plasma Physics, School of Mathematics and Physics, Queen's University Belfast
[4]Flash Center for Computational Science, Department of Physics and Astronomy, University of Rochester
[5]Laboratory for Laser Energetics, University of Rochester
[6]Plasma Science and Fusion Center, Massachusetts Institute of Technology
[7]Lawrence Livermore National Laboratory
[8]Department of Astronomy and Astrophysics, University of Chicago
[*]Principal Investigators

Magnetic fields are ubiquitous in the universe and are salient agents in numerous astrophysical processes;[36] their origin, however, is not fully understood. Guided by high-fidelity *FLASH*[37,38] simulations, the TDYNO collaboration has conceived, designed,[39] and successfully executed experimental campaigns at the Omega Laser Facility through the NLUF Program that demonstrated turbulent dynamo in the laboratory for the first time,[40] establishing laboratory experiments as a component in the study of turbulent magnetized plasmas.[41] Our more-recent experimental results on OMEGA were able to realize a time-resolved characterization of the evolution of magnetized turbulence in the magnetic Prandtl number (*Pm*) order-unity regime,[42] which is directly relevant to that of idealized fluctuation dynamo simulations and demonstrated the insensitivity of the dynamo achieved in the experiments to initial conditions.[43] The TDYNO platform was also successfully deployed to create an experimental analogue for transport of ultrahigh energy cosmic rays in stochastic magnetic fields.[44] The success of past OMEGA campaigns enabled the launch of a concerted effort to study and characterize turbulent dynamo in various plasma regimes and for different astrophysical environments, springboarding sister experimental campaigns at world-class laser facilities. Using large-scale *FLASH* simulations, we ported the TDYNO platform to the National Ignition Facility at Lawrence Livermore National Laboratory, where the hundredfold increase in available energy enabled us to demonstrate turbulent dynamo in a regime relevant for magnetized turbulence in galaxy clusters. The strong magnetization of the turbulent plasma resulted in prominent reduction of local heat transport and highly structured temperature distributions[45] seen in intracluster medium plasmas and explaining hot galaxy cluster cores. In experiments at the French Laser Mégajoule Facility (the first academic experiment there) we demonstrated, for the first time, magnetic-field amplification in supersonic turbulence[46] relevant to the star-forming interstellar medium. As a result, we can now critically assess dynamo theory and numerical predictions through dedicated experiments with the TDYNO platform. Under the auspices of the NLUF Program, we are building on our recent work and achievements, and are executing an experimental campaign on OMEGA to answer key fundamental questions pertinent to the onset, subsistence, and decay of magnetized turbulence and turbulent dynamo: (1) What is the range of critical magnetic Reynolds numbers for the onset of subsonic fluctuation dynamo in the *Pm* order-unity regime, where most resistive-MHD driven-turbulence simulations in the literature lie? (2) How does the magnetic energy of the saturated dynamo state depend on *Pm*? Can we reach larger magnetic fields if high plasma temperatures are sustained? (3) How, why, and at what rate do magnetized turbulence and its magnetic energy decay?

The first shot day of our ongoing OMEGA campaign was carried out 3 June 2022 and was geared toward measuring the decay rate of magnetized turbulence and characterizing the dissipation of magnetic energy at late times, i.e., question 3 above. To date, our OMEGA experimental campaigns have focused on the onset and saturation of the fluctuation dynamo mechanism but have not studied how the magnetic energy and plasma turbulence eventually decay. While the hydrodynamic case of how the kinetic energy decays was solved by Kolmogorov[47] in 1941, theories for the decay of nonhelical stochastic magnetic fields have only recently been proposed, predicting specific decay power laws ($\propto t^{-10/9}$ and $\propto t^{-20/17}$ in the fast- and slow-reconnection regimes, respectively). The platform deployed is shown in Fig. 19(a) and is similar to the one we fielded on OMEGA for our previous successful TDYNO campaigns[42] with diagnostics trained at late times of the plasma evolution. The assembly is comprised of two composite targets and two grids that are connected by a pair of cylindrical shields. The composite targets are 3 mm in diameter and consist of a 50-μm-thick polystyrene foil (CH) and a 230-μm-thick polystyrene washer. The polystyrene

washers were machined to have a 400-μm-diam cylindrical "well" in their centers. The two targets are mounted 8 mm apart and the pair of grids is placed between them. The two grids are made of polyimide and are mounted 4 mm apart—each of them 2 mm away from the respective proximate face of the foil target. The grids have a diameter of 3 mm, a thickness of 250 μm, and consist of 300-μm-wide holes and 100-μm wires, offset with respect to each other to break the mirror symmetry of the assembly: grid A (red) has a hole in the center, while grid B (blue) does not. Rectangular cones on each target shield the diagnostics from the intense x-ray emission produced when a sequence of ten 1-ns-duration laser beams coming from different angles illuminate each target. The two targets are driven for 10 ns, delivering a total of 5 kJ per target on an area defined by the laser SG5 phase plates. The temporal profile of the drive is a flattop profile. As shown in the *FLASH* simulation we performed for the platform design, the beams drive a pair of counter-propagating, high-magnetic Reynolds number *Rm*, plasma flows that carry the seed magnetic fields generated by Biermann battery. The flows propagate through a pair of grids [Fig. 19(b)] that destabilize the flow and define the driving scale of the turbulence (*L*). The flows then meet at the center of the chamber to form a hot, turbulent interaction region where the magnetic fields are amplified to saturation values [Fig. 19(c)].

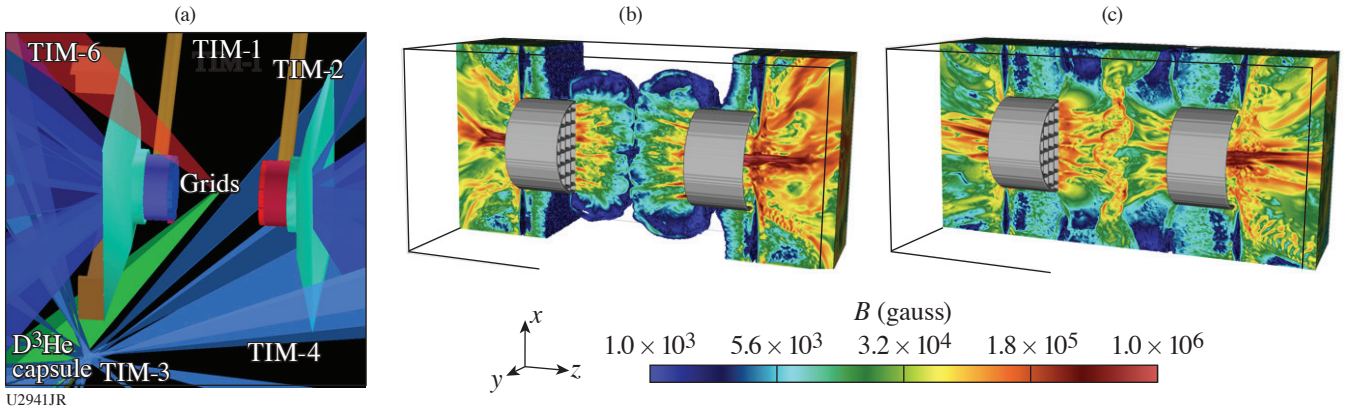

Figure 19
Turbulent dynamo experiments on OMEGA. (a) *VISRAD* schematic of the TDYNO platform for OMEGA to study the decay of the turbulence and its kinetic and magnetic energy. (b) *FLASH* simulation of experiment showing the flows carrying seed magnetic fields to the center where the turbulent interaction is established. (c) Same as (b) but after the establishment of the turbulent interaction region. There, fluctuation dynamo action amplifies the magnetic fields to saturation values prior to their subsequent decay at $t > 30$ ns.

To fully characterize the properties of the magnetized turbulent plasma at late times (>28 ns after the laser drive), we fielded our mature suite of experimental diagnostics [Fig. 19(a)] that consists of (1) an x-ray framing camera (TIM-1: XRFC3) to measure the x-ray fluctuations [Fig. 20(a)] associated with the turbulent spectrum; (2) the 4ω optical Thomson-scattering diagnostic (TIM-4: alignment cart and TIM-6: collection cone) to characterize plasma temperatures, density, and velocities by measuring the ion-acoustic wave (IAW) signal and the electron plasma wave (EPW) signal; and (3) proton radiography (TIM-3: target positioner for the D^3He capsule and TIM-2: CR-39 film pack) to record the 3-MeV and the 15-MeV [Fig. 20(b)] protons generated by the implosion of a D^3He MIT capsule, which are subsequently deflected by the stochastic magnetic field of the turbulent plasma. The proton radiographs are being post-processed to recover the path-integrated magnetic-field maps using the inversion techniques we developed.[8]

The shots yielded a wealth of experimental data and preliminary analysis indicates that we were in fact able to capture the decay rates of the turbulence. The temporal decay of the x-ray intensity fluctuations, and therefore in the turbulent kinetic energy, is clearly visible in the x-ray images we recorded [Fig. 20(a)]. Moreover, the 4ω Thomson-scattering diagnostic (not shown) yielded detailed information on the plasma state (ion and electron temperatures, bulk flow velocity, turbulent velocity, and electron density). Finally, the proton-radiography diagnostic performed perfectly, and the magnetic-field decay was captured in a sequence of proton radiographs [Fig. 20(b)]. We are grateful to the MIT team for their careful etching and development. In the radiographs, we see the gradual reduction in time of the stochastic features but also a reduction in their sharpness, both indica-

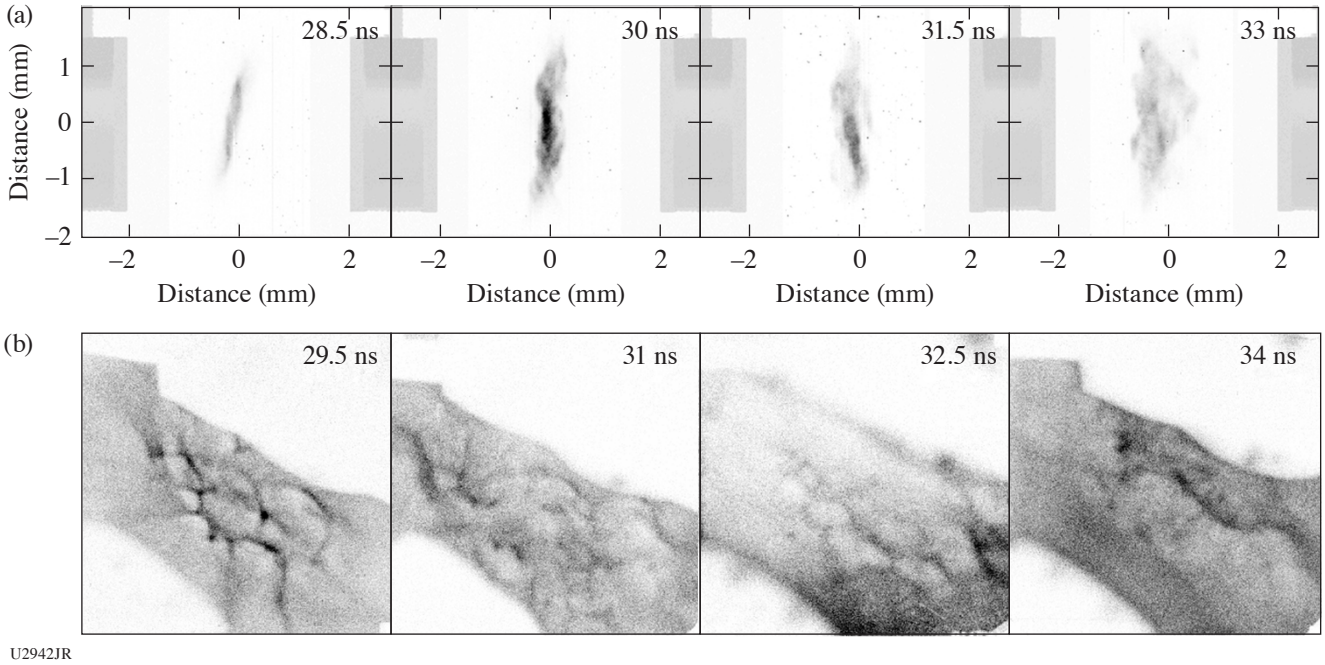

Figure 20

Experimental results. (a) Self-emission x-ray images of the turbulent interaction region from the 2× magnification framing camera at 28.5 ns, 30 ns, 31.5 ns, and 33 ns. The images were taken using a mylar-vanadium filter and can also be used to recover electron temperature information using the method we developed for our National Ignition Facility campaign.[45] Both emission and stochastic features decay in time, which can furnish the decay rate for the kinetic energy. (b) Late-time 15.0-MeV proton images of interaction-region plasma. The D^3He capsule is imploded using 17 270-J beams, each with a 600-ps pulse length and 1.82-mm defocus. This results in the generation of ~109 3.3- and 15.0-MeV protons via nuclear fusion reactions. These protons pass through the stochastic magnetic field and are deflected before reaching the CR-39 detector. The proton images are now being post-processed to recover path-integrated magnetic-field measurements[8] that will quantify the decay rate of the magnetic energy. The gradual reduction in time of the stochastic features and their sharpness is visible, indicative of magnetic energy decay.

tive of a measurable reduction in magnetic energy values. The quantitative analysis of these results will furnish the decay rates that we sought to characterize in this shot day. Despite the complexity of the experimental platform, with the help of personnel from the Laboratory for Laser Energetics, we were able to perform 12 shots during our first shot day. The experimental data are currently being analyzed and promise to further our understanding of how astrophysical magnetized turbulence decays.

The research leading to these results received funding from the U.K. EPSRC (grant numbers EP/M022331/1 and EP/N014472/1); the European Research Council under the European Community's Seventh Framework Programme (FP7/2007-2013)/ERC grant agreements nos. 256973 and 247039; the U.S. DOE under Contract No. B591485 to LLNL; Field Work Proposal No. 57789 to ANL and Awards DE-SC0016566, DE-NA0003605, and DE-NA0003934 to the University of Chicago; DE-NA0003868 to the Massachusetts Institute of Technology; DE-NA0001808, 89233118CNA000010, and 89233119CNA000063 to General Atomics; subcontract nos. 536203 and 630138 (LANL) and B632670 (LLNL) and Award DE-SC0021990 to the Flash Center for Computational Science, University of Rochester; and Cooperative Agreement DE-NA0003856 to the Laboratory for Laser Energetics (LLE), University of Rochester. LLNL work was performed under the auspices of the U.S. Department of Energy by Lawrence Livermore National Laboratory under Contract DE-AC52-07NA27344. We acknowledge support from the NSF under grants PHY-1619573 and PHY-2033925. Awards of compute time were provided by the U.S. DOE ALCC program. Compute time was provided by the U.S. DOE ALCC and ERCAP programs, and the LLE High-Performance Computing group. We acknowledge funding from grants 2016R1A5A1013277 and 2020R1A2C2102800 of the NRF of Korea. Support from AWE plc. and the STFC of the UK is also acknowledged. The Omega shots were allocated through the U.S. DOE NNSA NLUF Program at LLE. The software used in this work was developed in part by the DOE NNSA- and DOE Office of Science-supported Flash Center for Computational Science at the University of Chicago and the University of Rochester.

Collision of Magnetized Jets Created by Hollow Ring Lasers Irradiating High-Z-Doped CH Targets

E. P. Liang,[1*] L. Gao,[2,3] and H. Ji[2,3]
[1]Rice University
[2]Princeton University
[3]Princeton Plasma Physics Laboratory
[*]Principal Investigator

In our 2022 NLUF experiment we investigated the effects of radiative cooling on magnetized, high-beta shocks by colliding head-on two supersonic magnetized jets created by irradiating Fe-doped flat CH targets using a hollow ring of laser beams.[48,49] In earlier OMEGA experiments we successfully demonstrated the creation of such shocks with two opposing jets by using 19 beams from each hemisphere of OMEGA to irradiate flat pure CH targets in a hollow ring pattern. We have characterized the properties of these magnetized jets and shocks and investigated the role of electron thermal conductivity. In the 2022 experiment we explored the effects of radiative cooling by adding 1% to 2% (atomic) Fe dopants to the CH targets to increase the radiative cooling and systematically compare the results with those from pure CH targets. This project is in progress since we only received the first half of proton radiography (Prad) data from MIT at the writing of this report. The preliminary data from all diagnostics appear excellent. We are confident of achieving our original scientific objectives. Our next experiment of this NLUF project, currently scheduled for May 2023, will use Sn-doped CH targets to further increase the effects of radiative cooling. The final results of both experiments will have broad applications to magnetized radiative shocks in both astrophysics and magnetized high-energy-density science, including magnetized ICF.

Experiment Setup and Diagnostics

In the 27 April 2022 experiment, 19 beams from each hemisphere of OMEGA were configured to form an 800-μm-radius hollow ring pattern, irradiating a 1% to 2%-Fe-doped flat CH disk. Two such disks face each other at a separation of 6.4 mm. MG magnetized jets launched from each target collide head-on at mid-plane centered near target chamber cebter (TCC). Strongly magnetized shocks were created and propagated upstream into the jet body. Radiative cooling from the Fe dopants is expected to affect the magnetic-field strength, electron transport, and shock strength, structure, and evolution. We plan to systematically compare the results of Fe-doped CH targets with those of pure-CH targets to quantify the effects of high-Z dopants and compare with 3-D *FLASH* simulation results. The primary diagnostics are the same as those used in our earlier experiments: Thomson scattering (TS) at both TCC and off-TCC locations, x-ray framing camera time-lapse x-ray imaging, and proton radiography using D^{3}He protons for OMEGA shots. Figure 21 is a sketch of the experimental setup and diagnostics.

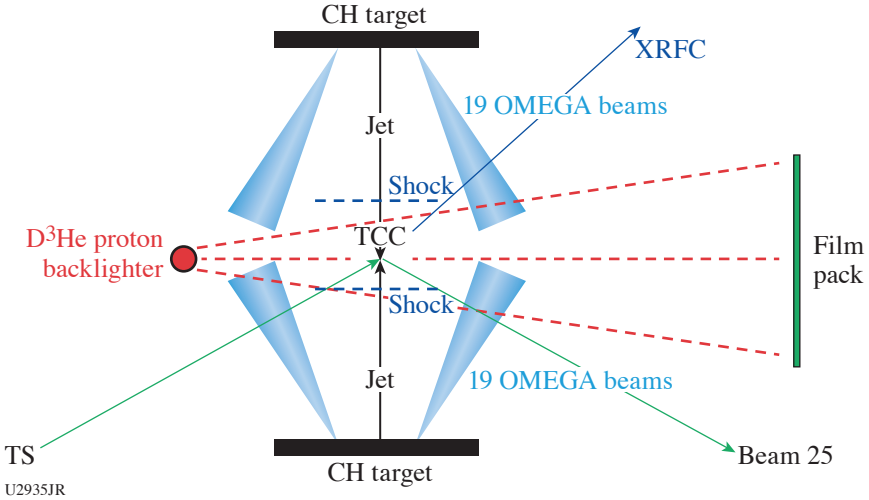

Figure 21
Sketch of experimental setup of colliding MG jets experiment using 38 OMEGA beams to irradiate two opposite flat CH disks separated by 6.4 mm. Locations of the main diagnostics are also indicated. In the 2022 experiment the CH disks were doped with 1% to 2% (atomic number) Fe.

Preliminary Results of the 220427 Experiment

We successfully completed nine shots on 27 April 2022 and obtained excellent data from all three diagnostics. Sample data are shown below even though we have not had the time to complete the detailed analysis, modeling, and comparison with earlier experiments. These tasks are in progress.

Figure 22 shows Prad images that are consistent with the conceptual picture of strong poloidal fields parallel to the jet axis, while strong transverse fields are created and amplified near the contact surface by the collision. Even though these images resemble those of earlier experiments with pure-CH targets, we expect the detailed field configurations and evolution will vary with radiative cooling. This will be investigated after the fields are fully deconvolved from the Prad images and compared with 3-D *FLASH* simulations, which are ongoing. The magnetic fields will strongly impact electron thermal conduction.

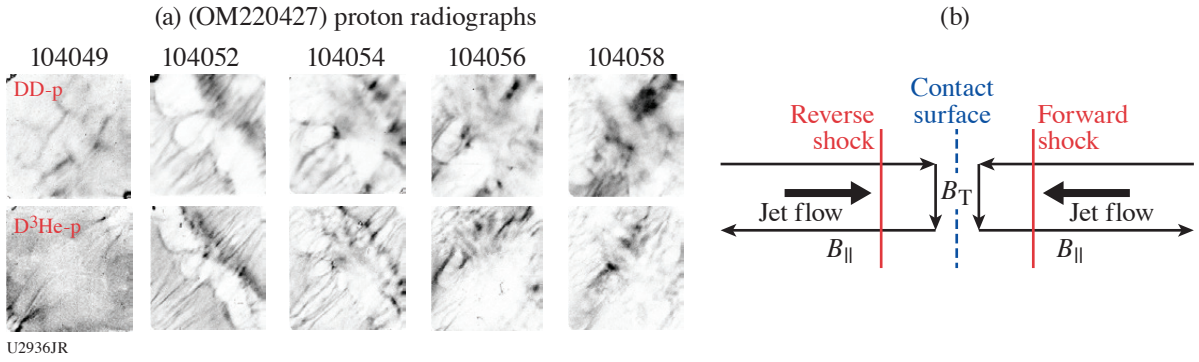

Figure 22
(a) Prad images of the 220427 experiment showing the evolution of ordered poloidal fields along jet axis and transverse fields along the contact surface, consistent with the conceptual picture below. Jet axis lies at 45° from lower left to upper right.

Figure 23 compares the TS data at TCC from 2021 (pure-CH) and 2022 (Fe-doped) experiments. They suggest that the electron temperature and density are lower, but the ion temperature and flow velocity are higher in the Fe-doped cases. These results will be compared with 3-D *FLASH* results before we can provide physical interpretations because the effects of radiative cooling are complex and highly nonlinear. All these results will be used to design and optimize our next NLUF experiment scheduled for May 2023.

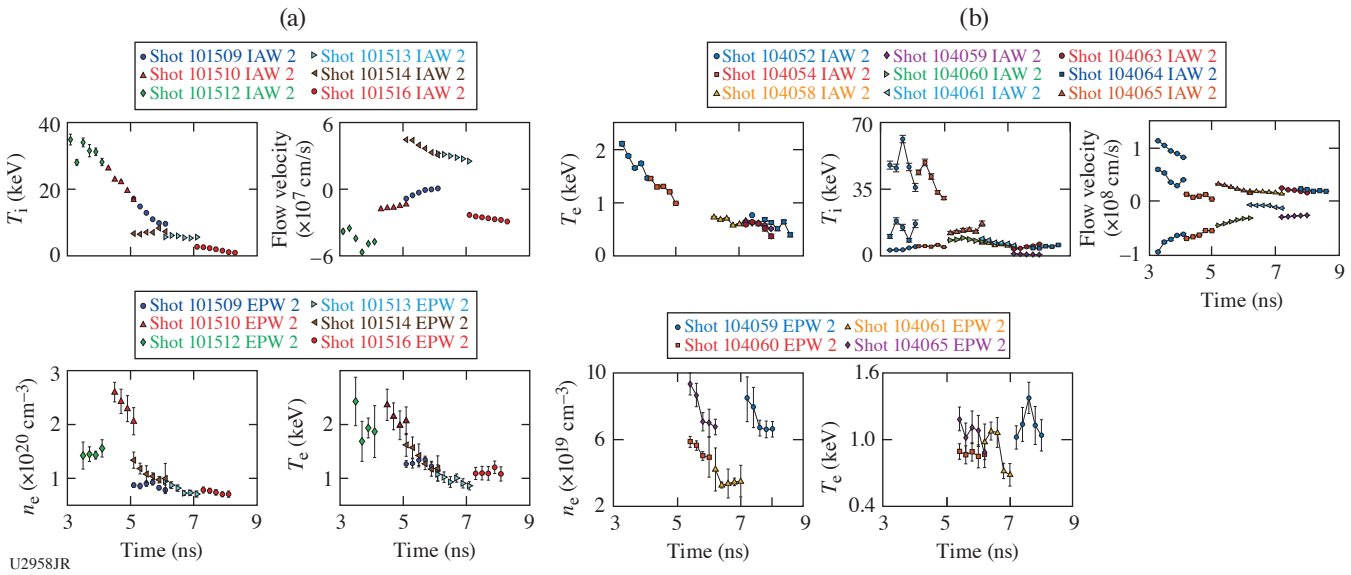

Figure 23
Comparison of TS data at TCC from (a) 210811 (pure CH) and (b) 220427 (Fe-doped CH) show that T_e and n_e are lower, while T_i and flow velocity are higher, for the Fe-doped targets.

Rice University graduate students Yingchao Lu (Ph.D., 2021, current University of Rochester postdoc) and Brandon Cage (second year) and undergraduate student Jackson White (BS, 2021), Princeton University graduate student Abe Chen and postdoc Sue Zhang, contributed to these experiments.

This work was supported by DOE DE-NA0003942.

X-Ray Heating and Ionization of Photoionized Plasmas in Steady State

R. C. Mancini,[1*] R. F. Heeter,[2] D. Liedahl,[2] and S. P. Regan[3]
[1]University of Nevada, Reno
[2]Lawrence Livermore National Laboratory
[3]Laboratory for Laser Energetics, University of Rochester
[*]Principal Investigator

The goal of this project is to study the x-ray heating, temperature, and ionization properties of plasmas produced and sustained by a broadband intense x-ray flux, i.e., photoionized plasmas, with experiments on OMEGA EP. Most laboratory work performed to date on high-energy-density laboratory physics pertains to collisional plasmas, i.e., plasmas where electron collisional processes play a dominant role in the plasma ionization and atomic physics. Relatively little attention has been paid, however, to studying and understanding the basic properties of laboratory photoionized plasmas where both photoionization and photoexcitation, driven by an external broadband x-ray flux, become dominant. These relatively low-density plasmas are important for understanding a myriad of astrophysical phenomena including x-ray binaries, warm absorbers in active galactic nuclei, and the accretion disks formed in the vicinity of compact objects. The quantitative information that we obtain from these systems is mainly based on the analysis of x-ray astronomy observations made by orbiting telescopes such as Chandra and XMM-Newton.

Given the time scales of astrophysics phenomena, the models implemented in astrophysical codes assume that the plasma is in steady state. In the case of photoionized plasmas, the type of steady state is photoionization equilibrium (PIE), where photon-driven photoionization is counterbalanced by electron-driven radiative and dielectronic recombination. Achieving PIE in the laboratory is challenging since it requires large driver energy and long times. We have established a new experimental platform on OMEGA EP that uses a plastic-tamped silicon sample driven by the 30-ns-duration, broadband x-ray flux produced by the "Gatling-gun" radiation source. This source is comprised of three copper hohlraums that are sequentially driven by three OMEGA EP beams, each one delivering 4 kJ of UV energy in a 10-ns square pulse shape. Each copper hohlraum has a length of 2.8 mm and an inner diameter of 1.4 mm, and is filled with TPX foam. The laser beams sequentially illuminate one hohlraum at a time, thus producing an x-ray flux characteristic of 90-eV radiation temperature for a time of 30 ns. The relatively long duration of the Gatling-gun radiation source is critical to produce a photoionized in steady state. The experiment setup is schematically illustrated in Fig. 24.

The experiment employs the four OMEGA EP beams and has three target components. Beams B3, B2, and B4 sequentially drive the "Gatling-gun" (GG) x-ray source. Each of these beams lasts for 10 ns. The 30-ns-duration x-ray flux of GG irradiates the photoionization sample, i.e., a plastic-tamped SiFe or SiO foil, to produce a photoionized plasma that undergoes a controlled expansion. Beam B1 is independently fired to drive a Ti laser-produced plasma source of backlit photons to probe the photoionized plasma at different times in nominally identical shots via transmission spectroscopy. This laser beam is 1 ns long and delivers 1 kJ of UV energy onto a Ti slab target in a 1-ns square pulse shape. The radiative recombination continuum emission photons of the Ti laser-produced plasmas backlight and probe the photoionized plasma via K-shell absorption spectroscopy. From this measurement, the charged-state distribution and electron temperature of the plasma can be extracted.

The combination of a 30-ns-long x-ray flux to produce and sustain the photoionized plasma and the possibility of performing transmission spectroscopy with a relatively short duration (i.e., 1-ns) source of backlit photons is key to demonstrating that the plasma is in steady state. In addition, gated imaging measurements of the plasma self-emission provide the density of the plasma. The GG performance is monitored with a VISAR package located on the back end of GG and the active shock breakout (ASBO) and SOP diagnostics, as well as a grating spectrometer to record the broadband spectral distribution GG x-ray flux. The GG x-ray source has a characteristic radiation temperature T_R = 90 eV and lasts for 30 ns.

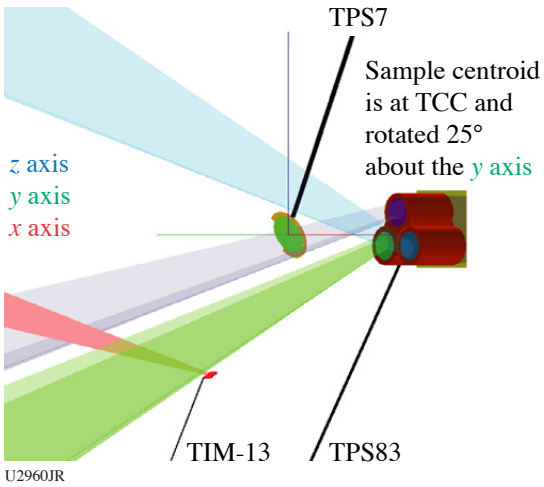

Figure 24
Schematic of the experiment setup. OMEGA EP beams B3, B2, and B4 fire sequentially in time to drive the three-hohlraum Cu Gatling-gun x-ray source, producing a 30-ns x-ray flux, while beam B1 is independently fired to drive the Ti backlight source. Details of Target Positioning Systems (TPS), TIM's, and diagnostics used in the experiment: TIM-10: SSCA/SXS streaked spectrometer for K-shell transmission spectrum of Si plasma; TIM-11: XRFC5/VSG_1 (variable speed grating) gated spectrometer for Cu x-ray flux; TIM-12: ASBO and SOP diagnostics for VISAR hohlraum radiation temperature; TIM-13: Ti backlighter (BL); TIM-14: SFC1 (Sydor framing camera 1)/VSG_2 gated spectrometer for imaging Si L-shell emission spectroscopy.

The spatial extension of the blowoff TPX/copper plasma from the copper hohlraums is monitored with the 4ω probe laser to make sure that it does not reach the silicon sample. The silicon photoionized plasma is probed with self-emission spectra recorded with a grating spectrometer, and K-shell line absorption spectra are recorded with a KAP crystal streaked spectrometer.

Figure 25 displays measurements recorded in three nominally identical OMEGA EP shots, i.e., 32980, 32981 and 32982, where the Ti backlighter was fired at three different times to monitor the evolution of the plasma-charged distribution via transmission spectroscopy. Everything else in the experiments remained the same. The earliest observation at t = 8 ns shows weak n = 1 to 2 line absorption in F- and O-like Si ions and n = 1 to 3 in Ne-like Si; this indicates that the Si ionization is just breaking into the L-shell range of ions. Later in time, at t = 18 ns and t = 25 ns, the transmission spectrum is dominated by n = 1 to 2 in Ne transitions in F-, O-, N-, and C-like Si ions and it is very similar at both times. This is an indication that the charge-state distribution is the same and thus in steady state. These observations are the first experimental evidence of having achieved a steady-state charged-state distribution in a laboratory photoionized plasma, i.e., PIE.

Shock-Induced Hydrogen Chemistry for Hydride Formation

S. Pandolfi,[1] C. Mcguire,[2] R. Smith,[2] M. C. Marshall,[3] D. Kraus,[4] W. Mao,[5*] A. Gleason,[1] and J. H. Eggert[2]
[1]SLAC National Accelerator Laboratory
[2]Lawrence Livermore National Laboratory
[3]Laboratory for Laser Energetics, University of Rochester
[4]University of Rostock
[5]Stanford University
[*]Principal Investigator

Recent work showing diamond formation in nonreactive polymers under laser-driven compression[50–52] has demonstrated that it is possible to initiate and characterize controlled reactive chemistry over ultrafast (i.e., nanosecond) time scales. Here, we use a novel approach that builds on previous work to: (a) extend previous studies to low-entropy pathways at multi-Mbar pressures; and (b) use shock-induced polymer dissociation and diamond formation as a source of reactive hydrogen (H) atoms to initiate reactive chemistry and hydrides formation.

In this experiment, we used a new sample fabrication procedure that has been recently developed by part of the group, and that allows us to embed particles of selected heteroatoms, in this case iron (Fe), in a polymer matrix, specifically Stycast epoxy.[53] This sample design ensures that, as the dissociation of the polymer takes place under dynamic compression, the heteroatoms are

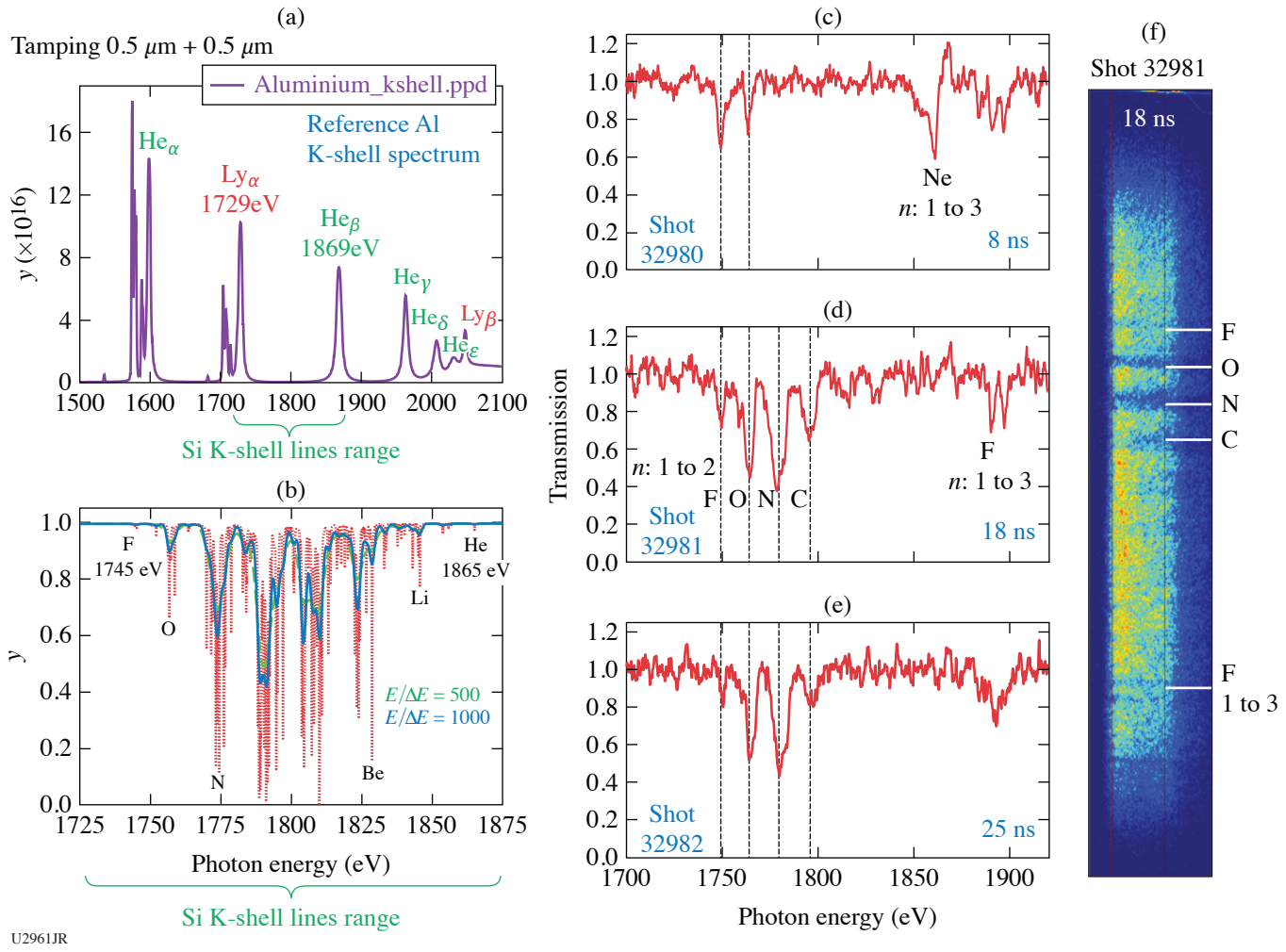

Figure 25

(a) Reference Al K-shell line emission spectrum used to calibrate the photon energy axis, (b) range of Si K-shell line absorption spectrum bounded by the Al Ly_α and He_β lines, and [(c)–(e)] experimental transmission from three nominally identical experiments using 0.5-μm plastic-tamped samples that show steady-state charged distribution in the Si photoionized plasma at t = 18 ns and t = 25 ns (right). (f) The image data is the streaked spectrum recorded with TIM-10/streaked x-ray camera A/streaked x-ray spectrometer (see Fig. 24) from which the transmission is extracted.

surrounded by a carbon- and H-rich environment, promoting eventual chemical reaction. We used the PXRDIP diagnostic and a Fe backlighter to collect x-ray diffraction (XRD) data to characterize the structural evolution of the sample as it undergoes compression; changes in the structure and eventual chemical reaction leading to hydride (or carbide) formation can be readily detected by studying the arrangement of the Fe atoms. Results from our first day of experiments are reported in Fig. 26.

Data analysis shows that single-shock compression yields to polymer dissociation and crystallization of the FeH hydride with double hexagonal close-packed (dhcp) structure [Fig. 26(b)]. This structure differs from the stable one for pure Fe, i.e., a hcp (hexagonal close-packed) structure, demonstrating that the mobility and energy of the H atoms released by polymer dissociation is sufficient to extensively react with the embedded Fe particles. Data collected under ramp compression (i.e., isentropic, low-entropy compression pathways) show a markedly different pattern, compatible with pure hcp Fe, and no signature of diamond formation. This result and other runs performed on pure epoxy show that the low-energy pathways achievable under ramp compression do not lead to diamond crystallization, most likely due to energetic barriers. During FY23, our efforts will focus on exploiting the pulse-shaping capabilities on OMEGA EP to realize a combined shock + ramp compression profile. The initial shock-compression will provide the necessary energy to initiate polymer decomposition, while the following ramp compression will allow us to characterize the hydrides forming at multi-Mbar pressure.

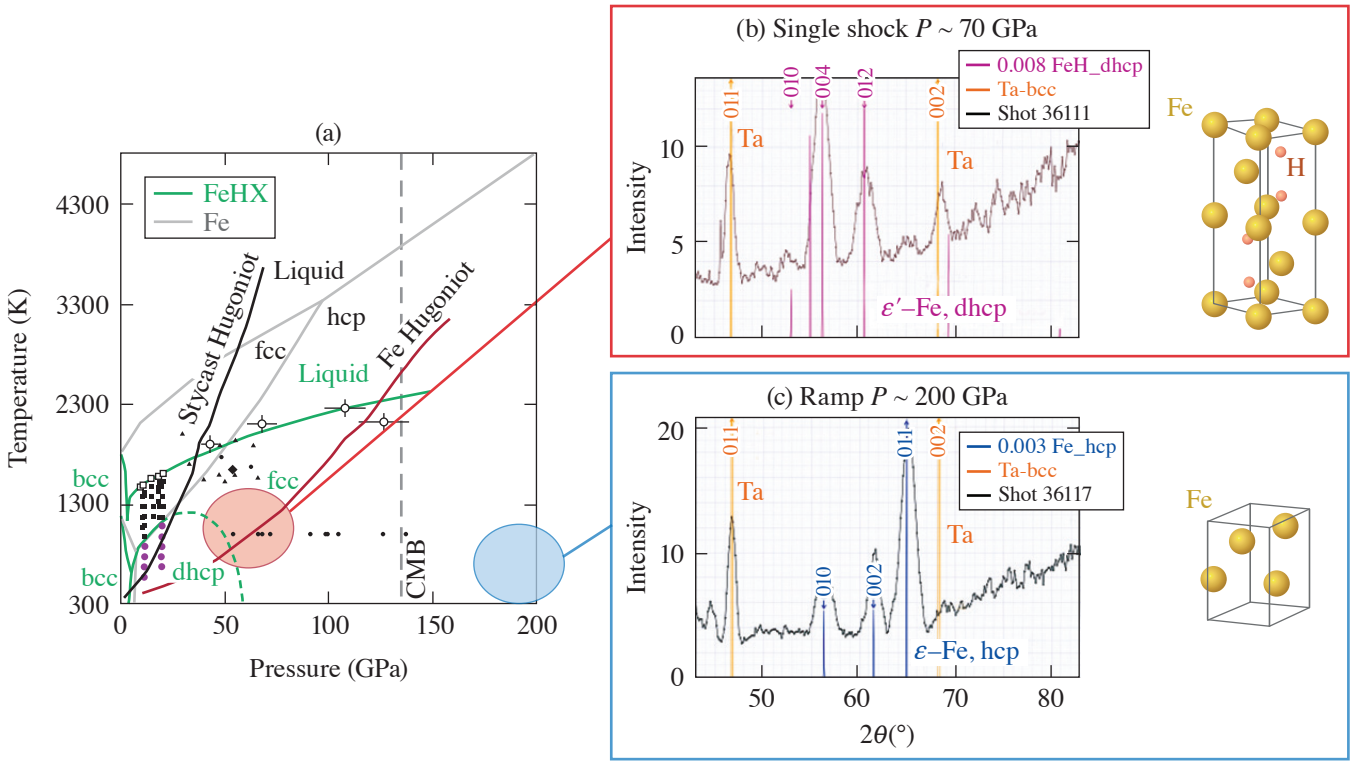

Figure 26
XRD diffraction data collected using different compression profiles. (a) Phase diagram of Fe and iron hydrides, shown in gray and green, respectively, are overlaid with the Hugoniot curve for both pure Fe (red) and pure Stycast. Data obtained using (b) single-shock compression up to 70 GPa and (c) low-entropy ramp compression up to 200 GPa. bcc: body-centered cubic; fcc: face-centered cubic; CMB: core mantle boundary.

Furthermore, part of the experimental time has been dedicated to velocimetry studies to better characterize the samples' equation of state. With a specific target design, we have been able to simultaneously measure our samples and a known material used as reference, quartz in this case, as shown in Fig. 27. The results will be used to further refine the equation of state of the epoxy–Fe mixture and to inform theoretical models investigating epoxy–metal mixtures.

This work is funded through the NLUF Program at LLE. Parts of this work was performed under the auspices of the U.S. Department of Energy by Lawrence Livermore National Laboratory under Contract DE-AC52-07NA27344 and was supported by the LLNL-LDRD Program under Project No. 21-ERD-032. Travel was partially funded by the 2019 DOEFES ECA.

Driving Iron to Dense, Hot Conditions Using Long- and Short-Pulse Beams of OMEGA EP

C. McGuffey,[1*] M. A. Meyers,[2] F. N. Beg,[2] G. Righi,[2] A. Li,[2] M. Bailly-Grandvaux,[2] and J. Kim[2]
[1]General Atomics
[2]University of California, San Diego
[*]Principal Investigator

Iron is an abundant constituent of all burning stars. The opacity of iron is a critical parameter to the inner workings of sun-like stars, constraining the radiative flux leaving the interior, and thus the temperature and nuclear reaction rates. A material's opacity, κ_ν, at a certain frequency, ν, is defined such that

$$I(x) = I_0 e^{-i\kappa_\nu \rho x},$$

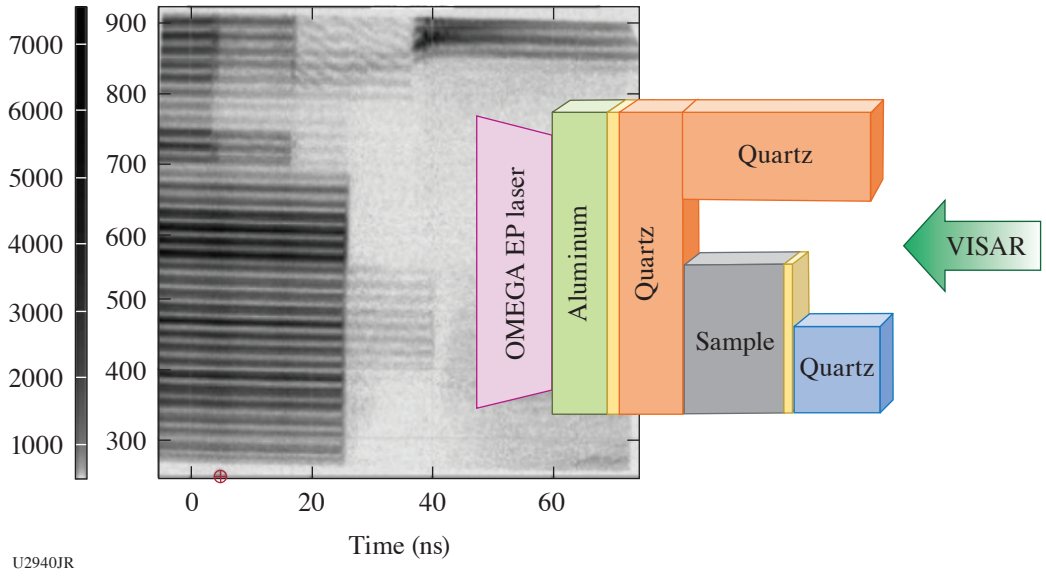

Figure 27
Velocimetry data obtained using the active shock breakout diagnostic and schematic view of the target assembly designed for equation-of-state measurements.

where $I(x)$ is the intensity, lower than the incident intensity I_0, after traveling a distance x through the material with mass density ρ. Opacity is cumulative of multiple contributions. For the materials present in high-energy-density (HED) systems, which are hot and partially or highly ionized, photoelectronic absorption develops multiplicity for all the ionic states present; Doppler broadening and continuum-lowering effects may be present, for example. High-atomic-number, opacity calculations can become intractable, even with large computational resources. This is to say that HED opacity is highly situationally dependent and challenging to model. That is why experimental opacity measurements are important, and in highly radiative HED systems including stars, hohlraums, and ICF capsules, opacity measurements are needed in a variety of conditions.

The FeHotCompress experiment, allocated through the NLUF Program, seeks a methodology for creating dense, hot Fe samples and measuring their opacity on the OMEGA EP Laser System. The methodology combines two common uses of large laser facilities: laser compression[54] and isochoric heating from a laser-driven proton beam.[1,4,55] Laser-direct-drive compression of planar materials has been used to apply well-controlled, high pressure on materials for decades, pushing beyond what diamond-anvil cells can do to study material properties at high pressure. When compressed by an appropriate ramp pulse shape, high density can be attained with minimal temperature increase. Separately, short-pulse laser drivers or the charged-particle beams they create can heat samples quickly enough for the material to retain its initial density ("isochorically"). This dual-drive approach provides flexibility in the conditions that can be attained and could offer a high data collection rate compared to other major iron opacity campaigns using flagship x-ray drivers.

In the FeHotCompress configuration, long-pulse beams irradiate an iron sample package using distributed phase plates for broad, quasi-1-D drive. Short-pulse Beam 1 irradiates a curved plastic foil to direct protons into the sample. Short-pulse Beam 2 serves as an x-ray continuum backlighter with a bare Ti wire target. The objective of the campaign is to collect absorption spectra of Fe in a hot, compressed condition. On the first shot day, x-ray signatures of the three beam types were collected, one by one, using two x-ray spectrometers, which presented challenges. The proton spectrum was recorded for future use in simulations of the target heating. Streaked, spectrally resolved x-ray emission measurements were also taken with the PJ-X streak camera + streaked x-ray spectrometer diagnostic. Figure 28 shows these data for a two-beam shot.

We acknowledge travel support to participate in this shot day provided by the National Nuclear Security Administration. Three students participated in the shot day.

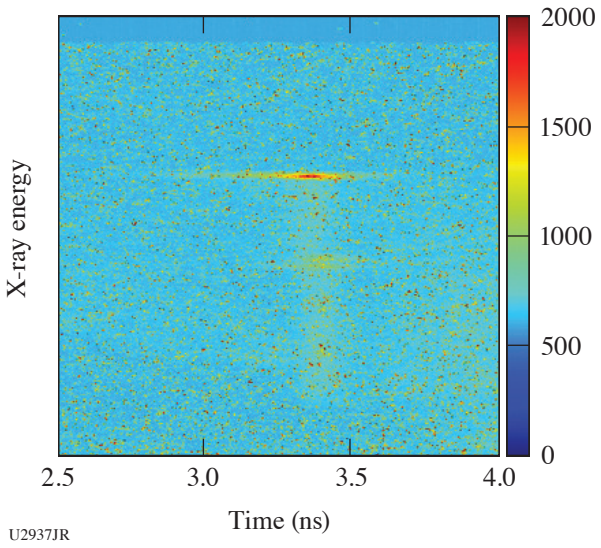

Figure 28
Streaked and spectrally resolved x-ray emission above 5.5 keV from Fe driven by a long-pulse beam and Ti irradiated by a short-pulse beam. Cold and hot Fe lines are seen late in the drive, as is a continuum from the short pulse arrival at 3.4 ns.

Tracking Rarefaction with Particle Image Velocimetry

J. Shang,[1,2*] H. Aluie,[1,2] D. N. Polsin,[1,2] and R. Betti[1,2]
[1]Department of Mechanical Engineering, University of Rochester
[2]Laboratory for Laser Energetics, University of Rochester
[*]Principal Investigator

Prior OMEGA experiments of a plasma releasing into a vacuum suggested that the released material travels more than twice the distance and spreads over 4× the range predicted by radiation-hydrodynamic codes, which could account for a reduction in target performance by a factor of 2 (Ref. 56). In this campaign, we sought to measure the evolution of the rarefaction wave from the leading to the trailing edge by imaging the position of particles embedded in the rear surface of an irradiated CH foil. At shock breakout, the particles would become entrained and move with the fluid.

In the experiment, we used titanium microspheres as the tracer particles and a framing camera to capture the backlit samples over time. A representative sequence of radiographs from the same shot is shown in Fig. 29, where the three particles can be seen in most frames as dark ellipsoids. After release, the particles appear to compress and then expand. Due to this expansion, it is not evident from the images whether the particles have moved appreciably.

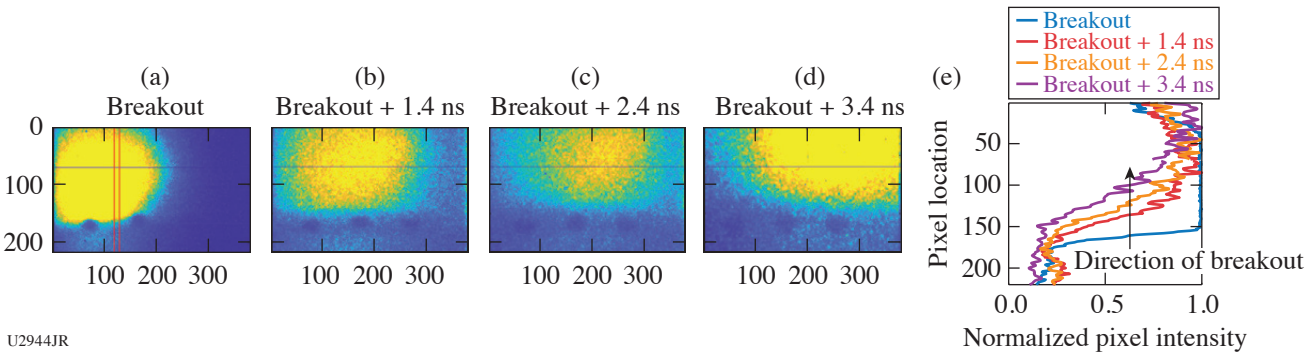

Figure 29
(a–d) Radiographs of the apex of a thin hemispherical plastic shell embedded with three titanium spherical particles (45-μm diameter, dark bodies) during and after shock breakout. The rarefaction wave travels from the bottom to the top of the image. The particles initially compress, and after 2.4 ns, appear to expand with the rarefaction wave. (e) Lineouts of normal pixel intensity in the area between two of the particles, outlined in the breakout image in red.

A qualitative analysis of the radiographs appears to show that the density gradient of the plasma decreases over time as the trailing edge of the rarefaction wave propagates into the vacuum. Further analysis is needed to determine if this is consistent with the angular filter refractometry data.

The experiment was conducted at the Omega Laser Facility at the University of Rochester's Laboratory for Laser Energetics with beam time through NLUF Program. This work was supported by the Department of Energy National Nuclear Security Administration under awards DE-SC0019329 and DE-NA0003914. Partial support from grants NSF PHY-2020249 and DE-SC0020229 and DE-NA0003914 is also acknowledged.

Rayleigh–Taylor Evolution of Isolated-Feature Perturbations in a Background Magnetic Field

B. Srinivasan,[1*] C. Samulski,[1] M. J.-E. Manuel,[2] and P. M. Nilson[3]
[1]Kevin T. Crofton Department of Aerospace and Ocean Engineering, Virginia Tech
[2]General Atomics
[3]Laboratory for Laser Energetics, University of Rochester
[*]Principal Investigator

The project aims to study magnetic-field effects on the Rayleigh–Taylor (RT) evolution of single-feature perturbations, such as those that exist in fill tubes, and to validate modeling which predicts reduced mix-width growth in the presence of magnetic fields. To achieve this, we developed a magnetized, shock-tube platform to study blast-wave–driven RT growth using the Fresnel zone plate (FZP) diagnostic.

On the first shot day, we tested the newly developed platform to explore whether the unmagnetized RT growth is detectable using the FZP diagnostic for two targets with different single-feature perturbations that were predicted to have significantly different evolution from simulations. We executed seven shots for the two targets by varying the timing of the diagnostic (0 ns, 3.5 ns, 5 ns, and 8 ns) to capture different stages of the RT evolution for each of the targets. Some raw FZP data from the shots are included to show a comparison between the two targets with different single-feature perturbations, where Fig. 30(a) is at 3.5 ns and Fig. 30(b) is at 5 ns.

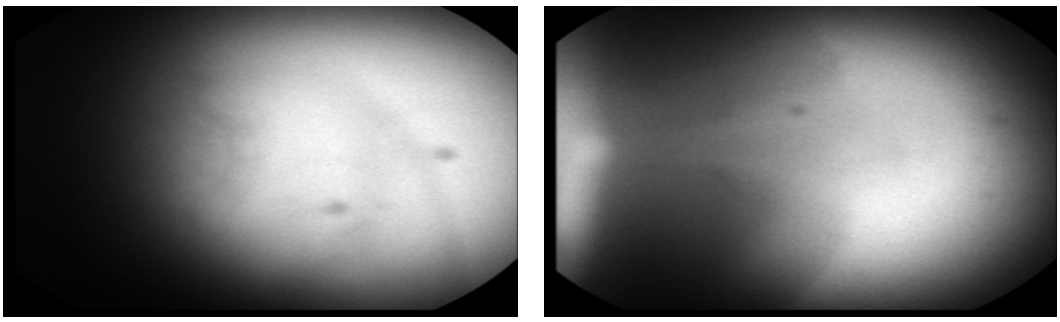

U2945JR

Figure 30
A quick analysis of the FZP images shows that (a) has multiple forks occurring with RT growth, whereas (b) has a more-uniform bubble growth, which is consistent with predictions from simulation.

Early analysis shows that our timing prediction from simulations needs a little refinement but there is generally good agreement of RT features between simulations and experiments. The features, however, were not captured with sufficient contrast to be clear and easily diagnosable for early and late times. These lessons are being applied toward the second shot day where further analysis is in progress to refine the timing in the simulations to improve the predictive capability. Additionally, the target is being redesigned due to the need for better contrast when using the FZP diagnostic. This was a successful shot day because it tested a new platform and provided very useful and relevant information to prepare for upcoming magnetized shots.

This work was supported by the DOE Office of Science under award number DE-SC0022319 and the NLUF Program for awarding and supporting the targets and the shot days.

Control of Laser–Plasma Interactions in Three-Dimensional–Printed Foam Structures with Graded Density

S. Tochitsky,[1*] N. Lemos,[2*] R. Simpson,[2] F. Fiuza,[3] A. Haid,[4] A. Pak,[2] D. Haberberger,[5] and C. Joshi[1]
[1]University of California, Los Angeles
[2]Lawrence Livermore National Laboratory
[3]Stanford Linear Accelerator Center
[4]General Atomics
[5]Laboratory for Laser Energetics, University of Rochester
[*]Principal Investigators

This work aimed to explore, through experiments and simulations, how laser-driven ion acceleration in a near-critical-density 3-D–printed target can be controlled by tailoring its density profile. We measured an enhancement up to 30%±20% of the maximum proton energy supported by a hotter electron distribution using a 3-D–printed target when compared with a simple 2-μm CH foil.

Intense research is being conducted into sources of laser-accelerated ions around the world (see e.g., a review by Macchi *et al*.[57] and the references therein). It is known that interactions of high-intensity lasers with solid-density targets can accelerate ion beams to tens of MeV/u by a well-studied target normal sheath acceleration (TNSA) mechanism or TNSA enhanced via radiation-induced transparency,[58,59] so-called breakout afterburner mechanisms.[60] Efforts to increase the maximum ion energy have largely focused on the development of novel acceleration mechanisms relying on ultrathin ($\leq$100-nm) targets that require utilization of single or double plasma mirrors to mitigate the effect of the laser prepulse to provide target survival. In this study we used special 3-D–printed targets in order to optimize the plasma density profile to maximize the laser absorption and proton/ion acceleration and minimize the sensitivity to laser prepulse. With the new 3-D printing technology, it is possible to fabricate complex structures with unprecedented geometric detail. Figure 31 shows an example of the targets that were fabricated by the General Atomics team who collaborated with us on the project and used this work as an opportunity to advance resolution of 3-D printing technology and metrology. We tested targets with different density gradients and maximum densities on the front and back surfaces, as well as targets with log-pile and stochastic low-density structures with densities in the range of 10^{20} to 10^{22} cm^{-3}.

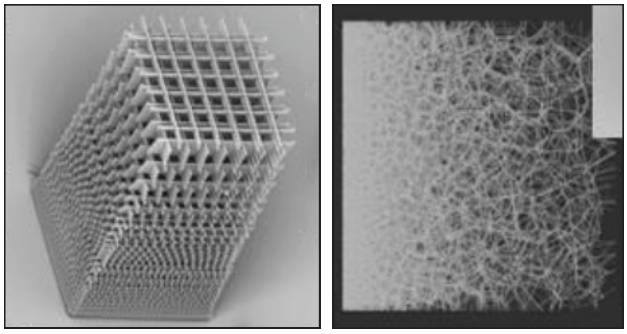

U2948JR

Figure 31
Examples of (a) a 3-D–printed log pile and (b) stochastic foam structure with graded density.

These targets were irradiated by the OMEGA EP laser with a pulse duration of 1 ps and maximum energy of 500 J. The spectrum of accelerated protons was measured using a Thomson parabola and a radiochromic film stack developed at LLNL (PROBIES). As a baseline, we used a 2-μm CH target that accelerated protons up to ~60 MeV from TNSA. Preliminary results show that an optimized 3-D–printed density profile target can accelerate protons up to at least 80-MeV energies. There targets showed good reproducibility that was relatively independent of the laser prepulse. Moreover, the log-pile targets seem to produce higher-energy protons than the stochastic targets.

Support by DOE Office of Science Early Career Research Program (Fusion Energy Sciences) under DOE-SC FWP 1651 and NNSA grant DE-NA0003842.

Dynamic Compression of Iron Carbide at Exoplanetary Core Conditions

S. J. Tracy,[1*] D. Kim,[1] S. Takagi,[1] I. I. Oleynik,[2] R. F. Smith,[3] F. Coppari,[3] M. Millot,[3] S. M. Clarke,[3] and J. H. Eggert[3]
[1]Carnegie Institution for Science
[2]University of South Florida
[3]Lawrence Livermore National Laboratory
[*]Principal Investigator

Our major scientific goal was to investigate the stable crystal structure of iron carbide (Fe_3C) at the pressure–temperature conditions of planetary cores. These results are highly sought after to establish improved models of structure, formation, and evolution of the cores of Earth and carbon-rich exoplanets. During our first shot day in September 2022, we utilized the unique capabilities of OMEGA EP to load Fe_3C samples along the principal isentrope to pressures between 250 and 600 GPa using a 10-ns ramped pulse. The compressed samples were probed with x-ray diffraction using the PXRDIP diagnostic [Fig. 32(d)][61] and pressures were determined using the ASBO diagnostic [Fig. 32(a)].[62] Figure 32 shows preliminary results for shot 37643 with a probe stress of 380 GPa. Early analysis of our results reveals that the orthorhombic Fe_3C structure is stable up to 600 GPa, placing new constraints on the Fe_3C phase diagram and equation of state.

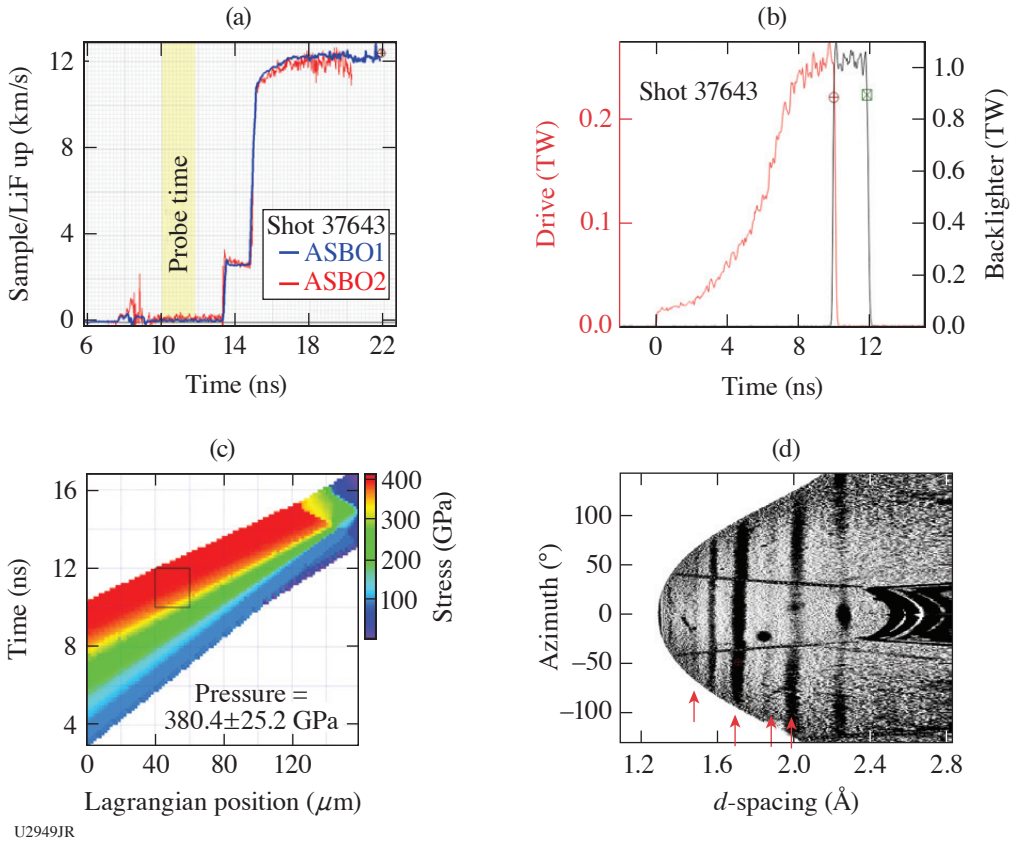

Figure 32
Preliminary analysis of results from shot 37643 for Fe_3C ramp compressed to a peak stress of 380 GPa. (a) VISAR data, Fe_3C–LiF interface velocity with 2-ns x-ray probe time in the yellow band. (b) Drive laser pulse (red trace). X rays are generated using a 2-ns square pulse (black trace). (c) Preliminary analysis of VISAR data showing a calculated map of stress distribution within the target assembly as a function of time. (d) De-warped x-ray diffraction data image plates with red arrows indicating compressed Fe_3C peaks.

The research is supported by the Department of Energy National Nuclear Security Administration under Award No. NA0004089.

Monochromatic Talbot–Lau X-Ray Deflectometer for the OMEGA EP and Multi-Terawatt Lasers

M. P. Valdivia[1,2*] C. Stoeckl,[3] T. Filkins,[3] C. Mileham,[3] M. Romanofsky,[3] I. A. Begishev,[3] V. Bouffetier,[4] G. Perez-Callejo,[5] A. Casner,[6] and D. Stutman[2,7]
[1]Center for Energy Research, University of California, San Diego
[2]Department of Physics and Astronomy, The Johns Hopkins University
[3]Laboratory for Laser Energetics, University of Rochester
[4]European XFEL GmbH, Germany
[5]Departamento de Física Teórica, Atómica y Óptica, Universidad de Valladolid, Spain
[6]CEA-CESTA, France
[7]ELI-NP, Institute for Physics and Nuclear Engineering, Romania
[*]Principal Investigator

The accurate diagnostic of density profiles in high-energy-density physics (HEDP) is an important but challenging task due to the high densities, small spatial scales, and short time scales encountered. In FY22, monochromatic 8-keV Talbot–Lau x-ray interferometry diagnostic capabilities were established for the OMEGA EP and Multi-Terawatt (MTW) lasers to increase HEDP phase-contrast diagnostic accuracy. Laterally graded multilayer mirrors were integrated to the design and the Talbot–Lau x-ray deflectometry (TXD) technique was improved based on previous results.[63] A new on-site x-ray calibration station reproduced vacuum chamber geometry, allowing for reliable instrument alignment. Preliminary experiments on MTW determined laser and target conditions, leading to optimal x-ray backlighter production for the 8-keV TXD (Table III). Additionally, a dedicated interferometry analysis code with a post-processing module was developed, delivering x-ray transmission, phase, and dark-field maps from moiré images.[64] Electron density retrieval methods were further enhanced by integrating phase-stepping capabilities to the analysis tool, making it possible to record *ex-situ* reference images on-site using the x-ray station in combination with x-ray backlighting from a copper x-ray tube.[65]

Monochromatic TXD (M-TXD) achieves high contrast (21% to 30%) close to the theoretical value (35%) for this configuration. Even with lower relative x-ray charge-coupled–device (CCD) counts, the signal-to-noise ratio (SNR) nearly doubles that of standard TXD, proving that monochromatic TXD successfully selects 8-keV contribution from Cu K_α emission, improving diagnostic performance by increasing electron density retrieval accuracy. Previously, alternative backlighter target configurations enhanced spatial resolution, albeit at the cost of reduced moiré fringe contrast due to increased high-energy emission (>8 keV) from hot-electron recirculation.[66] Therefore, x-ray backlighter quality from Cu wire targets and planar foils irradiated normal to the surface [i.e., edge-on from the TXD diagnostic line of sight (LOS)] and at standard 50° was evaluated for M-TXD.

Table III: Monochromatic TXD parameters for three MTW laser pulse lengths and standard TXD parameters for a matching laser pulse length.

Laser pulse length (ps)	Laser Intensity ($\times 10^{14}$ W/cm^2)	SNR	Contrast (%)	Relative CCD counts
25 (at 27 J)	7.3	6.0 to 7.9	24 to 25	1.00
60 (at 36 J)	4.1	6.9 to 7.2	21 to 24	1.30
80 (at 29 J)	2.5	6.0 to 8.6	27 to 30	0.71
Standard TXD				
24 (at 27 J)	4.4	3.5	19	1.85

Figure 33 shows M-TXD moiré images recorded using x-ray backlighting from Cu foil and wire targets irradiated at $I \sim 4 \times 10^{14}$ W/cm^2. Foils irradiated at 50° delivered a moiré fringe contrast of 24% and 6.9 SNR compared to a Cu wire contrast of 11% and 1.9 SNR for similar detector counts. Considering a Cu K_α conversion efficiency (CE) of $\sim 3 \times 10^{-5}$ for foils and $\sim 9 \times 10^{-6}$ for wires, it can be concluded that an overall photon count increase (higher laser intensity) could improve performance of wire x-ray backlighters, although additional data are needed to better determine their suitability for M-TXD diagnostics. Meanwhile, foils irradiated at 90° delivered 7% contrast and 1.2 SNR with reduced detector counts (~20%), which are inconsistent with CE measure-

ments. Lower photon counts can be attributed to diagnostic LOS and target misalignment, as observed on selected 50° foil shots. In the M-TXD configuration, a mirror alignment precision of ∼0.015° is required, which translates to extremely sensitive backlighter target and diagnostic LOS alignment. While x-ray emission from foils irradiated at 50° propagate toward the mirror unobstructed at 90°, x rays are obstructed by the foil itself. Since MTW's laser intensity was varied by displacing the target away from the laser focal spot, foils irradiated at 90° (edge-on to diagnostic) are most sensitive to alignment since the foil is displaced away from the mirror surface. Moreover, if the emission is highly directional, the total x rays reflected by the mirror would be further reduced. In turn, wire targets are less affected since the laser spot size is larger than their diameter and total x-ray emission is limited by the amount of material irradiated along the wire length. Consistent with the results shown, high moiré fringe contrast was measured (27% to 30%) for laser incidence angles of 50°, 70°, and 80° with similar detector photon counts. Respective spatial resolutions of ∼10.1 μm, ∼7.6 μm, and ∼5.6 μm, were measured with a 5.5-μm effective detector pixel size. Thus, 80° irradiation is an adequate compromise between spatial resolution and x-ray flux optimization, as is supported by previous results obtained in FY21.

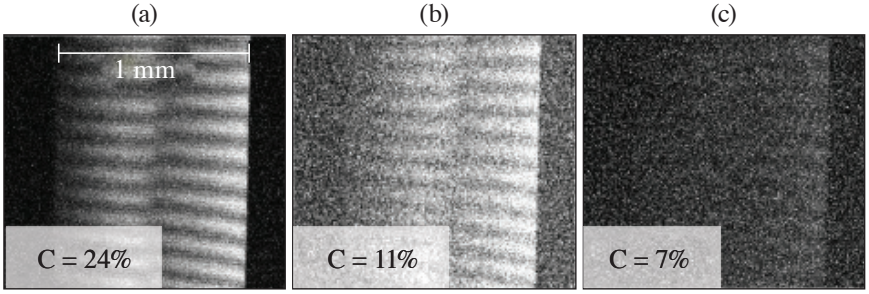

Figure 33
M-TXD moiré from Cu targets irradiated at $I \sim 4 \times 10^{14}$ W/cm^2: (a) foil at 50° from surface, (b) wire, and (c) foil at 90°. *The field of view is restricted due to mirror length. Contrast was enhanced to better showcase fringes. "Broken fringes" (middle of image) are due to grating imperfections.[67]

A 500-μm-diam CH rod was probed with M-TXD by laser irradiating ($I \sim 3 \times 10^{14}$ W/cm^2) foils at 50° (Fig. 34). The moiré images were analyzed with the newly developed Talbot numerical tool (TNT). Matching reference images were not available through experimental acquisition or *ex-situ* phase-stepping methods, hence, a reference was selected from images recorded with different laser parameters through correlation. Phase retrieval was enabled by the backlighter background removal feature included in TNT, included in consideration of data acquisition limitations encountered in most HEDP experiments. The feature allows for postprocessing using reference images recorded with different x-ray sources, which is a powerful resource for TXD diagnostics. Figure 34(d) shows the x-ray refraction angle profile retrieved with TNT (yellow). The G0 source grating background refraction profile (purple curve), obtained from the reference image and a flat field background reveals the grating structure imperfections that contribute to the overall x-ray refraction profile retrieved with TNT. In this case, grating imperfections are significant enough to prevent accurate phase retrieval in the "broken" fringe section. Nevertheless, outside this area, the x-ray refraction angle profile matches simulations within experimental error. Note that *IDEA*, a standard phase-retrieval code, could not deliver a phase map using this input, which proves TNT is a valuable advancement for TXD diagnostic techniques.

An NLUF OMEGA EP campaign was performed in FY22Q4. Multiple factors contributed to a total lack of M-TXD data. Ground vibrations due to building construction and imprecise source grating target fabrication/mounting affected M-TXD rail alignment. Laser beam source failure delayed shots and persistent x-ray CCD data acquisition failures, along with incorrect mounting of a collimator plate, caused further delays and data loss. Improvements and procedure changes have been made in response to these issues where appropriate. Note that x-ray backlighter spectral data were successfully acquired and will be used to complement data from previous campaigns, which will be the subject of a future publication. Further, in preparation for a second NLUF shot (FY23Q2), additional measures have been taken to ensure proper diagnostic performance. The previous OMEGA EP campaign goals to determine laser parameters for optimal x-ray backlighter considering moiré fringe contrast and spatial resolution will be pursued.

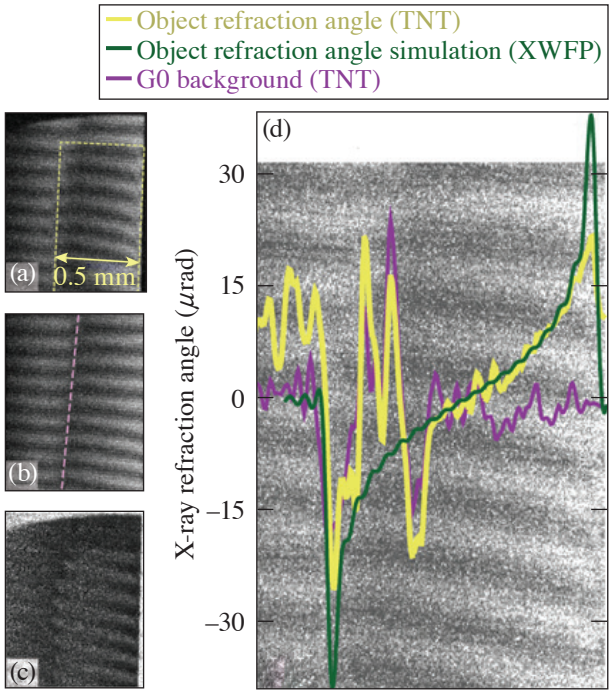

Figure 34
(a) CH rod moiré (yellow line) recorded with an ~36-J, 70-ps laser pulse. (b) Reference moiré from a 36-J, 60-ps laser pulse. The pink line marks grating imperfections. (c) Differential object/reference image. (d) X-ray refraction angle profile from TNT, simulations, and reference "background." XWFP: X-ray wavefront propagation.

This work was supported by NNSA Grant HEDLP DE-NA0003882. OMEGA EP laser beam time was awarded through NLUF by the University of Rochester's Laboratory for Laser Energetics under the auspices of the U.S. DOE/NNSA Contract DE-NA0003856.

Experimental Measurement of Thermal Conductivity in Warm Dense Matter

T. G. White,[1*] T. Doeppner,[2] C. H. Allen,[1] M. Oliver,[3] L. Divol,[2] A. Kemp,[2] E. Kemp,[2] O. Landen,[2] Y. Ping,[2] M. Schölmerich,[2] and W. Theobald[4]
[1]University of Nevada, Reno
[2]Lawrence Livermore National Laboratory
[3]Central Laser Facility, UK
[4]Laboratory for Laser Energetics, University of Rochester
[*]Principal Investigator

The thermal conductivity for materials at warm-dense-matter (WDM) conditions plays a vital role in planetary physics and ICF efforts. In the former, predictions of the power supplied by the geodynamo are utilized to constrain the Earth's evolution, while in the latter, heat transport between the layers plays an essential role in capsule implosions. As is typical for transport properties in the warm-dense-matter regime, however, a dearth of experimental measurements has led to a considerable body of theoretical and computational work that exhibit significant differences.

At the interface between two materials, initially at different temperatures, slow thermal conduction combined with rapid pressure equilibration produces gradients in the density profile on either side of the interface. On a nanosecond time scale, these density gradients typically have scale lengths of the order of 1 μm. We have developed a radiography platform for OMEGA that uses thin slits cut with a focused ion beam to perform micron-scale radiography—the highest spatial resolution achieved to date. Furthermore, due to the partially spatially coherent source, we observe significant diffractive and refractive effects in the radiograph; therefore, the technique is termed Fresnel diffractive radiography.

Initial data taken using plastic-coated tungsten wires are shown in Fig. 35. The data taken at 0 ns (i.e., no drive lasers) provided a measurement of the platform resolution,[68,69] which is less than 2 μm. A time sequence of the wire evolution after the drive was obtained, where we clearly see the outgoing shock wave launched from the expanding tungsten and the rarefaction wave traveling inward from the outside of the cylinder, both of which can be used to constrain the material equation of state and deposited energy. Most importantly, the high-resolution radiography captured information at the interface, with a well-characterized diffraction pattern observed in the 4-ns data at ~12 μm.

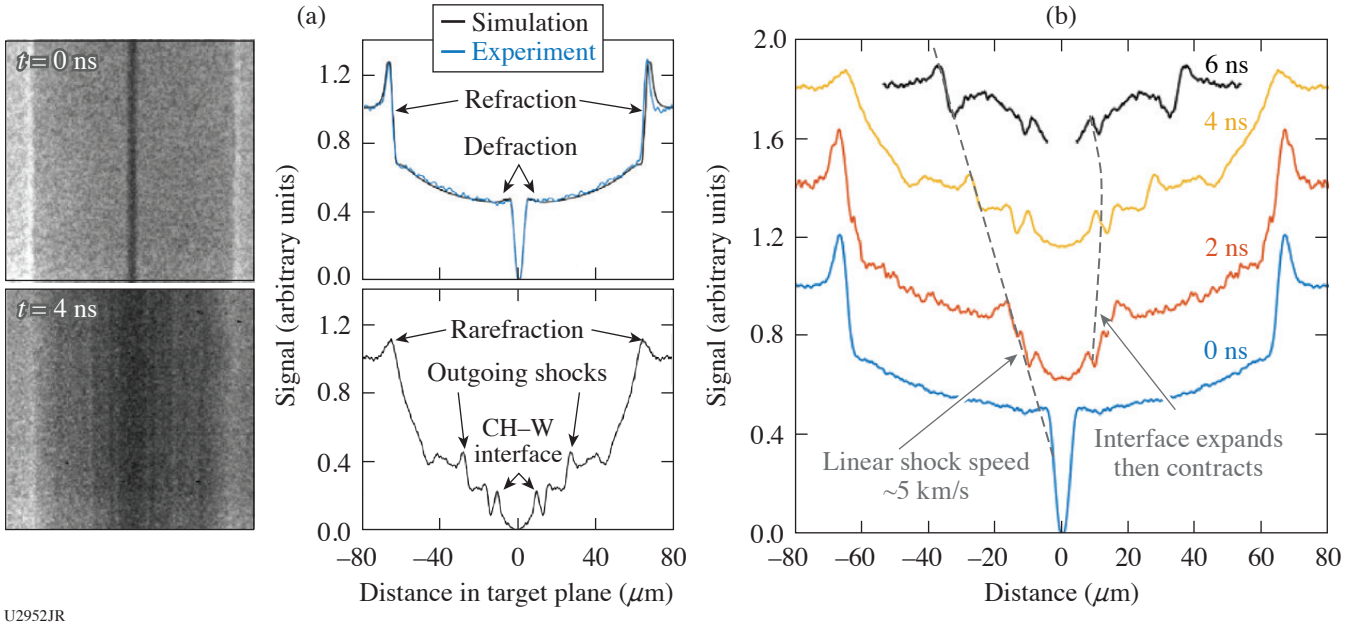

Figure 35
(a) Radiographs and lineouts of a cold target (top) and a driven target (bottom). A clear change in the features is evident in the lineouts, showing the expanded W–CH interface, as well as shock waves launched into the CH. (b) A plot showing the time evolution of our data over the course of the experiment. The signal lineouts are spread out vertically to better see the changes. The shock trajectory and interface evolution are highlighted by the dashed lines.

To analyze the driven data, we solve the Fresnel–Kirchoff integral[70] for a synthetic density profile, incorporating a parameterized material interface to resolve the features we see in the data. Specifically, we expect to see a discontinuity at the interface with a density slope on either side. As seen in Fig. 36, our simulated density profile reproduces the experimental diffraction pattern exceptionally well. We note, however, that the shock is additionally blurred in the experimental data due to its high velocity and the 250-ps gate time of the framing camera. We use Bayesian inference to sample parameter space to better constrain our results and provide error estimates. From this we have extracted the density scale lengths in each material, approximately 0.9±0.15 μm for the tungsten and 1.6±0.3 μm for the plastic.

In these initial experiments, we used tungsten wires due it the high opacity. However, we have now changed from plastic-coated tungsten to plastic-coated nickel and copper wires since as these materials are of broader interest. We are still in the process of analyzing the results and are simultaneously working to improve the platform for our next shot day. Thus far, this work has resulted in two publications (see Refs. 68 and 69). In addition, we are currently working toward a publication on our thermal conductivity measurement.

This work has been supported by the National Science Foundation under Grant No. PHY-2045718. The work of T. Doeppner, L. Divol, A. Kemp, E. Kemp, O. Landen, Y. Ping, and M. Schölmerich was performed under the auspices of the U.S. Department of Energy by Lawrence Livermore National Laboratory under Contract DE-AC52-07NA27344 and supported by Laboratory Directed Research and Development (LDRD) Grant No. 21-ERD-029.

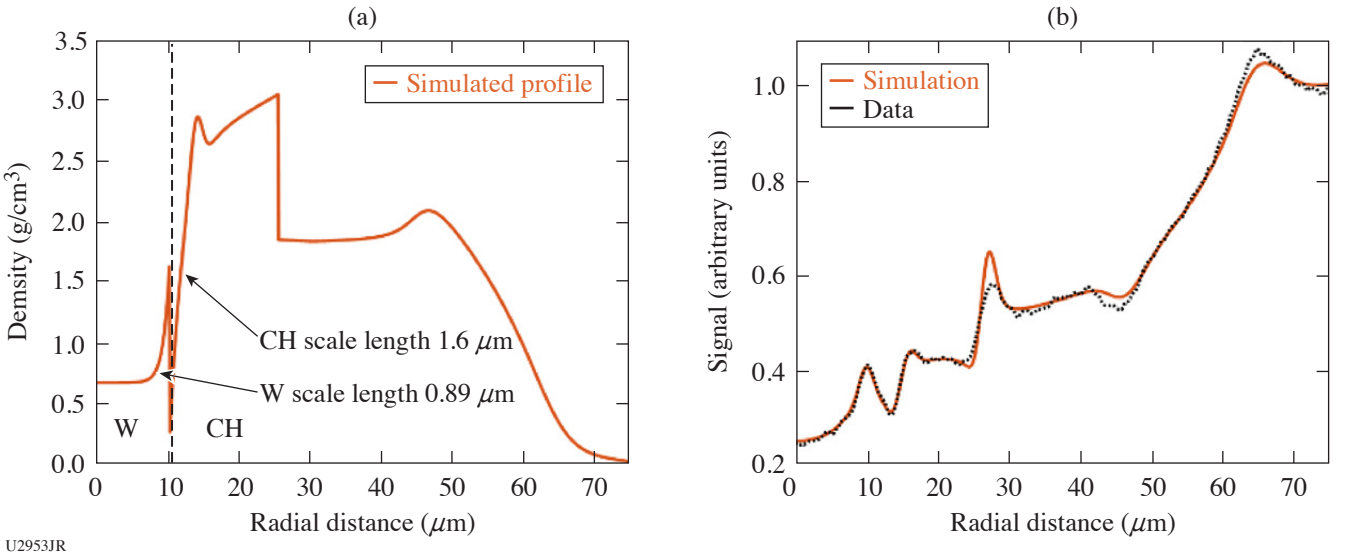

Figure 36
(a) Simulated radial density profiles that we have created to match our data, with a discontinuity at the interface, the outward-traveling shock wave, and the rarefaction of the outer plastic edge. The material interface is located at a radius of around 10 μm. The measured scale lengths of each material's density profile are given. (b) The simulated diffraction pattern from the density profile given in (a) is compared with the data at 4 ns from above. We see excellent fitting, especially in the region near the material interface at 10 μm. The shock wave at 27 μm has not considered any motion blurring, and as such diverges from the data.

Relativistic Intensity Laser Channeling and Direct Laser Acceleration of Electrons from an Underdense Plasma

H. Tang,[1] I.-L. Yeh,[2] P. T. Campbell,[1] F. Albert,[3] H. Chen,[3] Y. Ma,[1] A. McKelvey,[1] P. M. Nilson,[4] B. K. Russell,[1] J. L. Shaw,[4] A. G. R. Thomas,[1] A. V. Arefiev,[2] and L. Willingale[1*]
[1]University of Michigan
[2]University of California, San Diego
[3]Lawrence Livermore National Laboratory
[4]Laboratory for Laser Energetics, University of Rochester
[*]Principal Investigator

Laser–plasma interactions generate high-energy electrons, which have a number of potential applications, including generating secondary sources like bright x-ray radiation, electron–positron pairs, ion acceleration, or neutron generation. The direct laser acceleration (DLA) mechanism uses the laser's electric field, in the presence of an external field such as the channel fields, to produce a relativistic electron beam. Our experiments aim to understand the DLA dynamics and optimize the high-energy electron beam production. The experimental variables are plasma density, laser pulse duration, focusing geometry, and laser energy. For the FY22 shots, expanded the parameter space was explored, building on previous data; the secondary x-ray emission using a Ross pair filter was also investigated.

The apodized backlighter laser pulse was focused onto the edge of a 2-mm-diam helium gas-jet target with a plasma density of either $0.01n_c$ or $0.004n_c$, where n_c is the critical density. An *f*/5 apodizer was utilized for most shots. The laser energy was decreased from 110 J to 12 J to observe the acceleration mechanism in low a_0 regime. We also performed one shot using an *f*/8 apodizer to study the effect of a large beam. In order to study the effect of laser pulse duration on laser channeling, we used a 3-ps pulse for our final shot. The main diagnostics were EPPS3 Rad (electron–positron–proton spectrometer) and proton radiography, which employed the sidelighter beam, and a 50-μm Cu foil to generate the proton beam. Additionally, the 4ω probe was turned on, taking shadowgraphy and angular filter refractometry data to observe the channel.

As shown in Fig. 37(a), the proton radiography imaged the laser channel structure after a 3-ps laser pulse propagation through the gas column from left to right. The channel walls generate a bump in the center of the picture, implying the formation of

new laser modes when the laser travels through the plasma. The dark line segment inside the channel (shown by orange arrow) indicates the field reversal, which is due to the ion motion. Figure 37(b) shows the electron spectra. Electrons with energy up to 170 MeV were observed. The effective temperature decreases with the laser energy for a fixed laser focal spot size. Figure 37(c) shows the Ross pair filters and a raw image of the x ray on an image plate. The x-ray diagnostic was installed behind the EPPS. The Ross pair filters contain eight sections, which are made by different metal materials with varying thicknesses. A hole was on the back of the filter; therefore, eight small sections blocked the x ray with different cutoff energies, forming a round disk with eight sections of different brightnesses. A rough analysis estimated the x-ray energy to be in the 10- to 100-KeV range. Further calculation and calibration need to be performed for x-ray measurement.

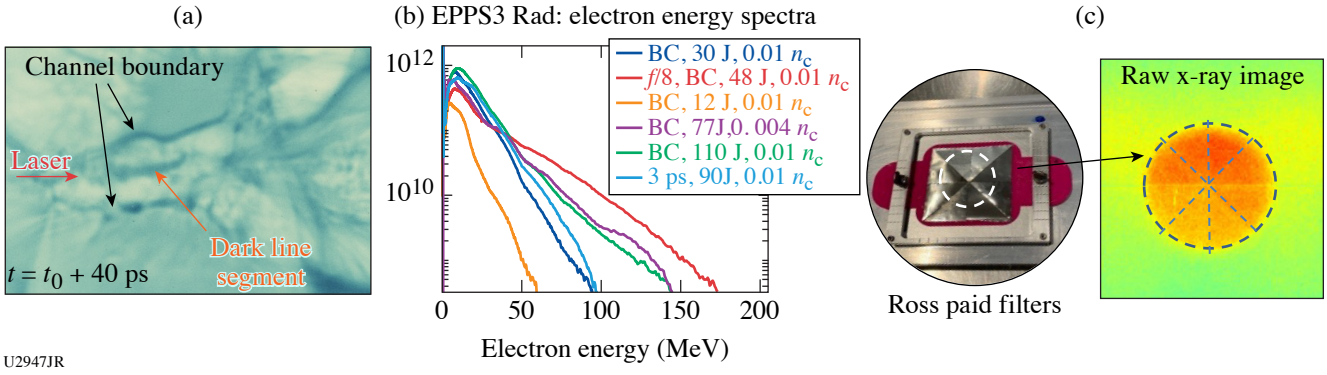

Figure 37
(a) Raw proton radiography image from shot 37147. The red arrow represents the laser propagation direction, the black arrows point at the channel walls, and the orange arrow points at the dark line segment inside the channel. The image was taken 40 ps after the interaction. (b) Electron spectra from the 16 June 2022 shot day. (c) Ross pair filters and raw x-ray image from shot 37147.

This material is based upon work supported by the Department of Energy/NNSA under Award Number DE-NA0004030.

1. K. Bhutwala *et al.*, Phys. Rev. E **105**, 055206 (2022).
2. C. McGuffey *et al.*, Bull. Am. Phys. Soc. **65**, VO05.00005 (2020).
3. J. Saret *et al.*, "Measurements of Temperature Evolution in Copper from Intense Proton Beam Energy Deposition," in preparation.
4. C. McGuffey *et al.*, Sci. Rep. **10**, 9415 (2020).
5. W. Fox, A. Bhattacharjee, and K. Germaschewski, Phys. Rev. Lett. **106**, 215003 (2011).
6. W. Fox *et al.*, submitted to Physical Review Letters, available arXiv:2003.06351 (2020).
7. C. L. Johnson *et al.*, Rev. Sci. Instrum. **93**, 023502 (2022).
8. A. F. A. Bott *et al.*, J. Plasma Phys. **83**, 905830614 (2017).
9. S. Zhang *et al.*, "Ion and Electron Acoustic Bursts During Anti-Parallel Reconnection Driven by Lasers," to be published in Nature Physics.
10. L. Gao *et al.*, Phys. Plasmas **23**, 043106 (2016).
11. A. Chien *et al.*, Phys. Plasmas **26**, 062113 (2019).
12. A. Chien *et al.*, Phys. Plasmas **28**, 052105 (2021).
13. K. D. Meaney, presented at the 64th Annual Meeting of the APS Division of Plasma Physics, Spokane, WA, 17–21 October 2022 (YI01.00002).
14. B. J. Winjum, F. S. Tsung, and W. B. Mori, Phys. Rev. E **98**, 043208 (2018).
15. M. Bailly-Grandvaux *et al.*, J. Plasma Phys. **89**, 175890201 (2023).
16. B. J. Winjum *et al.*, Phys. Rev. Lett. **110**, 165001 (2013).
17. X. Sha *et al.*, Sci. Rep. **5**, 11003 (2015).
18. H. Liu, J. S. Tse, and H. Mao, J. Appl. Phys. **100**, 093509 (2006).

19. J. E. Jaffe *et al.*, Phys. Rev. B **62**, 1660 (2000).
20. Z. Li *et al.*, Phys. Rev. B **79**, 193201 (2009).
21 N. V. Kabadi *et al.*, Phys. Rev. E **104**, L013201 (2021).
22. M. J. Rosenberg *et al.*, Phys. Rev. Lett. **112**, 185001 (2014).
23. H. Sio *et al.*, Rev. Sci. Instrum. **87**, 11D701 (2016).
24. B. Reichelt *et al.*, Bull. Am. Phys. Soc. **66**, UO04.00006 (2021).
25. M. Gatu Johnson *et al.*, Phys. Plasmas **27**, 032704 (2020).
26. S. Brygoo *et al.*, Nature **593**, 517 (2021).
27. P. M. Nilson *et al.*, Phys. Rev. Lett. **97**, 255001 (2006).
28. R. Samtaney *et al.*, Phys. Rev. Lett. **103**, 105004 (2009).
29. E. Greco *et al.*, Astrophys. J. Lett. **908**, L45 (2021).
30. J. E. Gudmundsson, C. J. Pethick, and R. I. Epstein, Astrophys. J. **272**, 286 (1983).
31. S. D. Bergeson *et al.*, Phys. Plasmas **26**, 100501 (2019).
32. B. Strömgren, Astrophys. J. **89**, 526 (1939).
33. R. P. Drake *et al.*, Astrophys. J. **833**, 249 (2016).
34. A. Mizuta *et al.*, Astrophys. J. **621**, 803 (2005).
35. A. M. Hansen *et al.*, Rev. Sci. Instrum. **89**, 10C103 (2018).
36. E. N. Parker, *Cosmical Magnetic Fields: Their Origin and Their Activity*, The International Series of Monographs on Physics (Clarendon Press, Oxford, 1979).
37. B. Fryxell *et al.*, Astrophys. J. Suppl. Ser. **131**, 273 (2000).
38. P. Tzeferacos *et al.*, High Energy Density Phys. **17**, 24 (2015).
39. P. Tzeferacos *et al.*, Phys. Plasmas **24**, 041404 (2017).
40. P. Tzeferacos *et al.*, Nat. Commun. **9**, 591 (2018).
41. *2019 John Dawson Award for Excellence in Plasma Physics Research Recipient*, Petros Tzeferacos, University of Chicago, (2019).
42. A. F. A. Bott *et al.*, Proc. Natl. Acad. Sci. **118**, e2015729118 (2021).
43. A. F. A. Bott *et al.*, Matter Radiat. Extremes **7**, 046901 (2022).
44. L. E. Chen *et al.*, Astrophys. J. **892**, 114 (2020).
45. J. Meinecke *et al.*, Sci. Adv. **8**, eabj6799 (2022).
46. A.F. A. Bott *et al.*, Phys. Rev. Lett. **127**, 175002 (2021).
47. A. Kolmogorov, Dokl. Akad. Nauk SSSR **30**, 301 (1941).
48. L. Gao *et al.*, Astrophys. J. Lett. **873**, L11 (2019).
49. Y. Lu *et al.*, Phys. Plasmas **26**, 022902 (2019).
50. Z. He *et al.*, Sci. Adv. **8**, eabo0617 (2022).
51. D. Kraus *et al.*, Nat. Astron. **1**, 606 (2017).
52. M. C. Marshall *et al.*, J. Appl. Phys. **131**, 085904 (2022).
53. R. F. Smith *et al.*, J. Appl. Phys. **131**, 245901 (2022).
54. R. F. Smith *et al.*, Nature **511**, 330 (2014).
55. P. K. Patel *et al.*, Phys. Rev. Lett. **91**, 125004 (2003).
56. D. Haberberger *et al.*, Phys. Rev. Lett. **123**, 235001 (2019).
57. A. Macchi, M. Borghesi, and M. Passoni, Rev. Mod. Phys. **85**, 751 (2013).
58. S. Palaniyappan *et al.*, Nat. Commun. **6**, 10170 (2015).
59. A. Higginson *et al.*, Nat. Commun. **9**, 724 (2018).
60. L. Yin *et al.*, Phys. Rev. Lett. **107**, 045003 (2011).
61. J. R. Rygg *et al.*, Rev. Sci. Instrum. **83**, 113904 (2012).
62. P. M. Celliers *et al.*, Rev. Sci. Instrum. **75**, 4916 (2004).
63. M. P. Valdivia *et al.*, Rev. Sci. Instrum. **92**, 065110 (2021).
64. G. Pérez-Callejo *et al.*, Phys. Plasmas **29**, 043901 (2022).

65. G. Pérez-Callejo *et al.*, "Phase Imaging of Irradiated Foils at the OMEGA EP Facility Using Phase-Stepping X-Ray Talbot–Lau Interferometry," in preparation.
66. M. P. Valdivia *et al.*, Rev. Sci. Instrum. **89**, 10G127 (2018).
67. M. P. Valdivia, D. Stutman, and M. Finkenthal, Rev. Sci. Instrum. **85**, 073702 (2014).
68. C. H. Allen *et al.*, Appl. Opt. **61**, 1987 (2022).
69. M. Oliver *et al.*, Rev. Sci. Instrum. **93**, 093502 (2022).
70. A. Pogany, D. Gao, and S. W. Wilkins, Rev. Sci. Instrum. **68**, 2774 (1997).

FY22 Laboratory Basic Science Program

M. S. Wei

Laboratory for Laser Energetics, University of Rochester

The Laboratory Basic Science (LBS) Program awarded 21 projects with a total allocation of 22 shot days for a full-year schedule at the Omega Laser Facility in FY22 including six carryover FY21 LBS projects with shots in Q1FY22. A total of 224 target shots were conducted for the LBS Program in FY22. These experiments were led by scientists from Lawrence Livermore National Laboratory (LLNL), SLAC, Princeton Plasma Physics Laboratory (PPPL), and LLE (see Table I). The LBS experiments conducted in FY22 are summarized in this section.

During FY22, LLE issued a solicitation for LBS proposals for beam time in FY23. A total of 20 proposals were submitted, requesting a total of 30 Omega shot days, which was about 150% of the notional allocation for the LBS Program. The reduced number of proposals compared to prior years was attributed to several factors including an early deadline (by a month due to the change of the annual Omega Scheduling meeting from June 2022 to May 2022) and many overlapping activities such as proposals to the High-Energy-Density (HED) Council for shots at the National Ignition Facility and white papers for the Laboratory Directed Research and Development (LDRD) Program at LLNL, among others. An independent LBS Proposal Review Panel (PRP) consisting of eight subject-matter experts from universities, national laboratories, and industry reviewed and ranked the proposals. Based on the LBS PRP's recommendation, 19 proposals were selected and allocated a total of 21.5 shot days for experiments at the Omega Laser Facility in FY23, as shown in Table II.

Table I: LBS Projets with experiments conducted at the Omega Laser Facility in FY22, including six carryovers from the FY21 LBS Program (gray shaded cells).

Principal Investigator	Lead Institution	Title
H. Chen/M. R. Edwards	LLNL/Stanford Univeristy	Developing a Magnetic Mirror Trap for Laser-Produced Relativistic Electron–Positron Pairs/Exploring Electron and Electron–Positron Plasma Dynamics
H. Chen/G. Gregori	LLNL/University of Oxford	Measuring Particle Transport in Turbulent Plasmas/Laboratory Model of Particle Acceleration in Supernova Shocks
F. Coppari/Y. Kim	LLNL	Measurements of Shock Equation of State and Melting Temperature of H:N:O and H:C:N:O Mixtures
L. Gao	PPPL	Particle Acceleration from Magnetically Driven Collisionless Reconnection Using Short-Pulse, Laser-Powered Capacitor Coils
H. G. Rinderknecht	LLE	Initial Relativistically Transparent Microchannel Experiments on OMEGA EP
A. Zylstra/J. Jeet	LLNL	Inertial Confinement Fusion Plasma-Based Measurements of the T + ^{4}He Cross Section
F. Albert	LLNL	High-Precision X-Ray Radiography Driven by Laser Wakefield Acceleration/X-Ray Sources from Laser Wakefield Acceleration on OMEGA EP

Table I: LBS Projets with experiments conducted at the Omega Laser Facility in FY22, including six carryovers from the FY21 LBS Program (gray shaded cells) (continued).

Principal Investigator	Lead Institution	Title
G. Bruhaug	LLE	Relativistic THz-Matter Interactions/Extreme THz Generation and Detection
G. W. Collins/ A. Schwemmlein	LLE	Quantum States of Hydrogen: Toward a Superconducting Superfluid
A. Gleason	SLAC	Viscosity Measurements Using Tracer Particles
I. V. Igumenshchev/ V. N. Goncharov	LLE	Formation of Dynamic Shells Using Foam Ball Targets
J. Jeet	LLNL	Cross-Calibration of the D–T γ-to-Neutron and D–^{3}He γ-to-Protron Branching Ratios Against the ^{12}C(n,n$'$)γ Reaction/Inertial Confinement Fusion Plasma-Based Measurements of the D–T γ-to-Neutron and D–^{3}He γ-to-Protron Branching Ratios
S. Malko	PPPL	Detailed Benchmarking of the Nernst Effect in a Magnetized High-Energy-Density Plasma
J. L. Peebles	LLE	Probing In-Flight Vacuum Magnetic-Field Compression on OMEGA
M. J. Rosenberg	LLE	Electron Energization in Colliding and Reconnecting Magnetized Plasmas
M. Schneider	LLNL	Using Isoelectronic Line Ratios to Measure Density in Nonlocal Thermodynamic Equilibrium Plasmas/Measuring Electron Densities in Nonlocal Thermodynamic Equilibrium Plasmas Using Isoelectronic Line Ratios
S. Singh/S. Clarke	LLNL	The Effect of Ni Concentration on Phase Transformation Dynamics in the Fe-Ni Binary System/Probing the Fe–Ni Phase Space Using Powder X-Ray Diffraction Image Plates
R. F. Smith	LLNL	Measuring the Viscosity of MgO at Lower-Mantle Conditions
C. Stoeckl/A. Schwemmlein	LLE	Development of a New Experimental Platform LIANS on OMEGA EP for Deuteron and Triton-Induced Nuclear Reactions—Studying the T–T Reaction at Energies Exceeding 2 MeV on OMEGA
G. Swadling	LLNL	Angular Momentum Transport in Disk-Jet Transitions

Table II: Nineteen projects from the FY23 LBS Program approved for target shots at the Omega Laser Facility in FY23.

Principal Investigator	Lead Institution	Title
F. Albert	LLNL	X-Ray Radiography of Laser-Driven Shocks Using Laser Wakefield Acceleration
L. Ceurvorst	LLE	Amplification of Laser Imprint with Strong Magnetic Fields
K. Churnetski	LLE	Evaluating Shock-Augmented Ignition and Late-Time Laser–Capsule Coupling in Laser Inertial Fusion
G. W. Collins	LLE	Quantum States of Hydrogen: Toward a Superconducing Superfluid
J. R. Davies	LLE	Measurement of a Self-Generated Magnetic Field in Laser–Foil Interactions with Oblique Proton Probing
C. J. Forrest	LLE	Multiple Reactant Implosions to Improve Cross-Section Measurements of Reactions Relevant to Nuclear Astrophysics
L. Gao	PPPL	Multi-Scale Reconnection and Particle Acceleration in Long Current Sheets During Magnetically Driven Collisionless Reconnection at Low Plasma β

Table II: Nineteen projects from the FY23 LBS Program approved for target shots at the Omega Laser Facility in FY23 (continued).

Principal Investigator	Institution	Title
F. García-Rubio	LLE	Driving Magnetized Collisionless Shocks with Solid Pistons on OMEGA EP
A. Gleason	SLAC	Particle Tracking in High-Energy-Density Flows
D. Haberberger	LLE	Raman Pump Propagation
P. V. Heuer	LLE	Benchmarking Nernst Advection in Local and Nonlocal Regimes
M. Holec	LLNL	Nonlocal Electron Transport in Collisional Magnetized Plasma Jets
Y. Kim	LANL	Development of an Ion Stopping-Power Platform at Low Projectile-to-Thermal Velocity Ratio
S. Malko	PPPL	Proton Radiography of a Bounded, Magnetized Plasma Relevant to MagLIF
J. L. Peebles	LLE	Measurement and Application of Short-Pulse Compressed Magnetic Field
M. Sherlock	LLNL	Study of Magnetization Effects in Cylindrically Imploded Hot Dense Plasmas Using Dopant Spectroscopy Techniques
R. Smith	LLNL	Novel Experiments to Measure Viscosity of Minerals at the Conditions of Planetary Interiors
C. Stoeckl	LLE	Investigating the Dynamics and Stability of Astrophysical-Relevant Plasma Jets
G. Swadling	LLNL	Effects of Collisionality in Angular Momentum Transport in Disk-Jet Transitions

Exploring Electron and Electron–Positron Plasma Dynamics

M. R. Edwards,[1*] S. You,[2] J. von der Linden,[3] J. L. Peebles,[4] L. Willingale,[5] G. Fiksel,[5] and H. Chen[2*]
[1]Stanford University
[2]Lawrence Livermore National Laboratory
[3]Max Planck Institute for Plasma Physics
[4]Laboratory for Laser Energetics, University of Rochester
[5]University of Michigan
[*]Principal Investigators

To explore instabilities of relativistic electron and electron–positron beams, this experiment aimed to collide a relativistic electron–positron jet with a low-density hydrocarbon plasma and examine the interaction region for the development of magnetic-field filaments. This work aims both to understand the fundamental properties of electron and electron–positron plasmas and to explore possible scaled experiments with astrophysical relevance.

In the experiment, electron–positron jets were produced by focusing the backlighter beam on specially designed large-diameter gold-copper targets that controlled the positron acceleration. A background plasma was generated using Beam 3 on a hydrocarbon disk target. The interaction zone was imaged with sidelighter-driven proton radiography and the properties of the jet were characterized with an electron–proton–positron spectrometer (EPPS). We used the magneto-inertial fusion electrical discharge system (MIFEDS) to control the focusing of low-energy electrons and positrons into the interaction zone.

Particle spectrometer measurements confirmed control over positron energy using large-diameter targets and control over low-energy electron and positron focusing using MIFEDS. We observed the development of large-scale instabilities (Fig. 1), suggesting the presence of an electron-driven instability. These results suggest progress toward a platform for studying relativistic electron jet instabilities using kilojoule-class lasers.

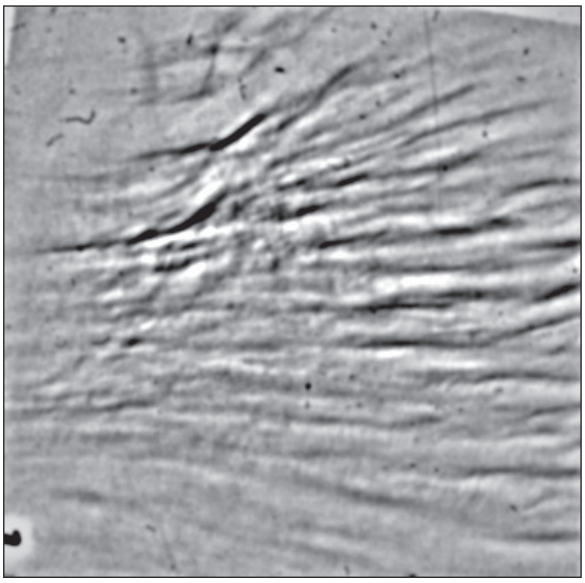

U2900JR

Figure 1
Filtered proton radiography image-plate data showing evidence of instability development in an electron beam crossing a background plasma.

Laboratory Model of Particle Acceleration in Supernova Shocks

H. Chen,[1*] C. A. J. Palmer,[2] H. Poole,[3] A. R. Bell,[3] A. Bott,[4] G. Gregori,[3*] O. Karnbach,[3] J. Matthews,[3] D. Lamb,[5] R. D. Petrasso,[6] P. Tzeferacos,[7] A. Birkel,[6] C. K. Li,[6] and H.-S. Park[1]
[1]Lawrence Livermore National Laboratory
[2]Queen's University, Belfast, UK
[3]University of Oxford, UK
[4]Princeton University
[5]University of Chicago
[6]Massachusetts Institute of Technology
[7]Laboratory for Laser Energetics, University of Rochester
[*]Principal Investigator

Magneto-collisional instabilities (MCI's) have been proposed as an explanation for the observation of acceleration of cosmic rays (CR's) to energies higher than those predicted by simple models in the turbulent magnetized plasmas surrounding supernova remnants. The instabilities, driven by high-intensity currents of CR's, can lead to amplification of the plasma magnetic fields, which results in prolonged trapping of the energetic CR in the turbulent plasma and, consequently, higher maximum energies. This is particularly true for a subset of these instabilities, the "nonresonant hybrid instability," which drives the growth of fields at the scale of the Larmor radius of the CR current. Due to the nature of this instability, covering a high dynamic range of spatial and temporal scales and requiring the inclusion of kinetic processes, computational simulations struggle to accurately model the process.

A joint shot day at LLE in 2019 aimed to explore this field amplification in the laboratory using the well-established turbulent dynamo target platform (TDYNO) to create a turbulent plasma embedded with stochastic magnetic fields, and a high-energy (2-kJ), short-pulse (100-ps) OMEGA EP laser beam to produce a high-intensity proton current that would drive the instability (Fig. 2). The results of this shot day indicated the generation of a >1-kA proton beam with a cutoff energy of approximately 3 MeV, which was only detected when the turbulent plasma was not present.

This may indicate MCI's inhibition of the proton propagation or disruption to the proton-generation mechanism due to the close proximity of the proton source to the turbulent plasmas. Follow-up experiments in 2021 aimed to directly compare the density and magnetic-field structure of the plasma turbulence with and without a high-current drive beam, as well as test for confirmation signatures of proton production using a modified target design. As in 2019, the main diagnostics included an x-ray framing camera to measure self-emission from the turbulent plasma, proton radiography using a D^3He capsule irradiated with 17 OMEGA beams

(450 J/beam, 1 ns) to probe the magnetic-field structure of the plasma, the EPPS to measure the energy spectrum of the target normal sheath acceleration (TNSA) proton beam, and the Zinc von Hamos spectrometer to measure protons induced x-ray emission from a tracer foil on the proton-generation target.

Data were obtained for a direct comparison on the proton radiography and x-ray self-emission with and without the high-current instability drive beam. This confirmed that a change in structure of the x-ray self-emission from the standard TDYNO plasma, observed in 2019, was not due to the presence of the proton beam, but likely due to a small change in ordering and therefore orientation of the TDYNO drive beam (Fig. 3). This is being investigated further using the radiation hydrocode *FLASH*.

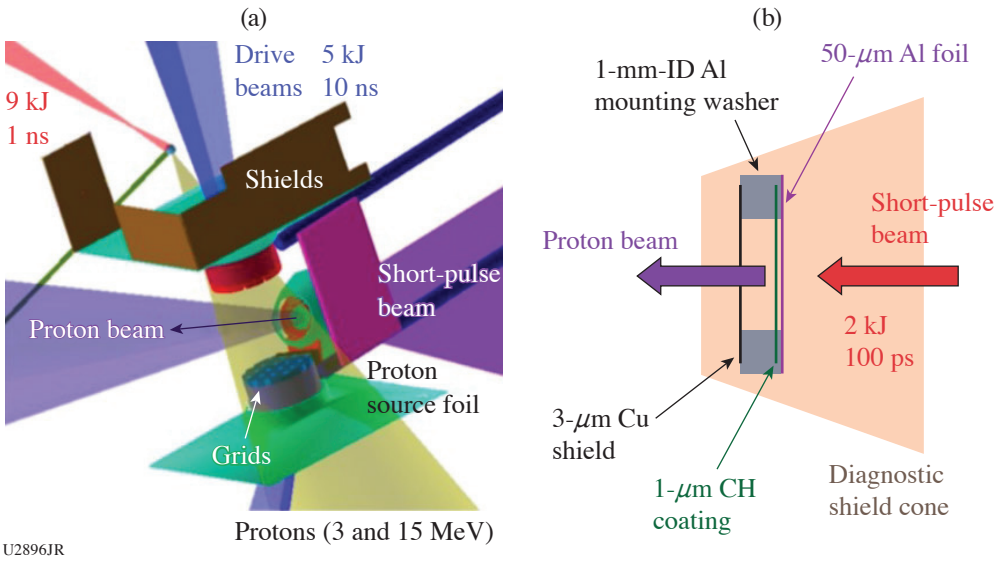

Figure 2
(a) Experimental configuration and (b) a TNSA target. The EPPS diagnostic sits along the axis of the marked proton beam.

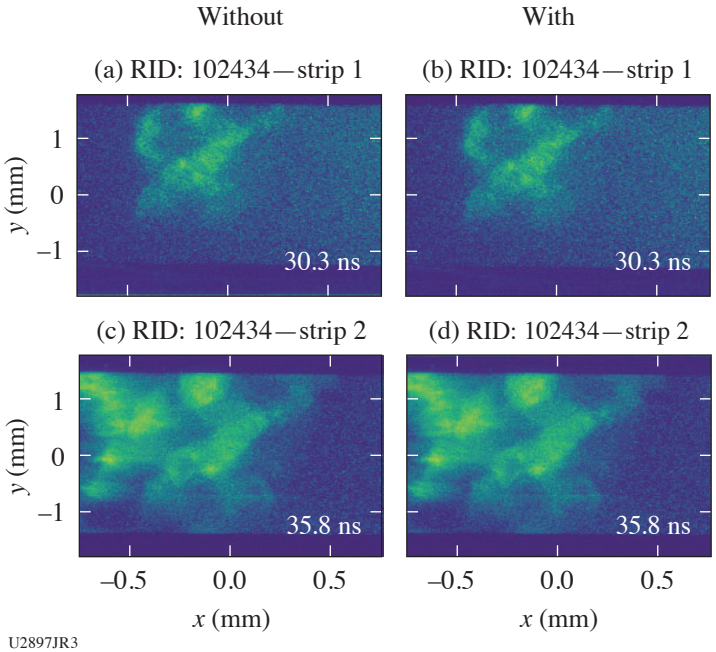

Figure 3
Comparison of the evolution of the plasma density structure via the x-ray self-emission measured at two times, 30.3 ns and 35.8 ns, respectively, for shots [(a) and (c)] without or [(b) and (d)] with the high-energy OMEGA EP interaction. While the structure is qualitatively different from typical TDYNO data, with a central hole, the two shots here do not indicate that structural changes are due to the propagation of a high-current proton beam.

The zinc von Hamos spectrometer suffered from strong continuum background due to the capsule drive, but the spectra indicated the presence of several lines consistent with copper emission, which is most clearly visible on shots without the D^3He backlighter capsule or turbulent plasma (Fig. 4). Analysis is ongoing to determine whether this diagnostic can confirm that proton-beam acceleration is not prevented by the presence of the turbulent plasma.

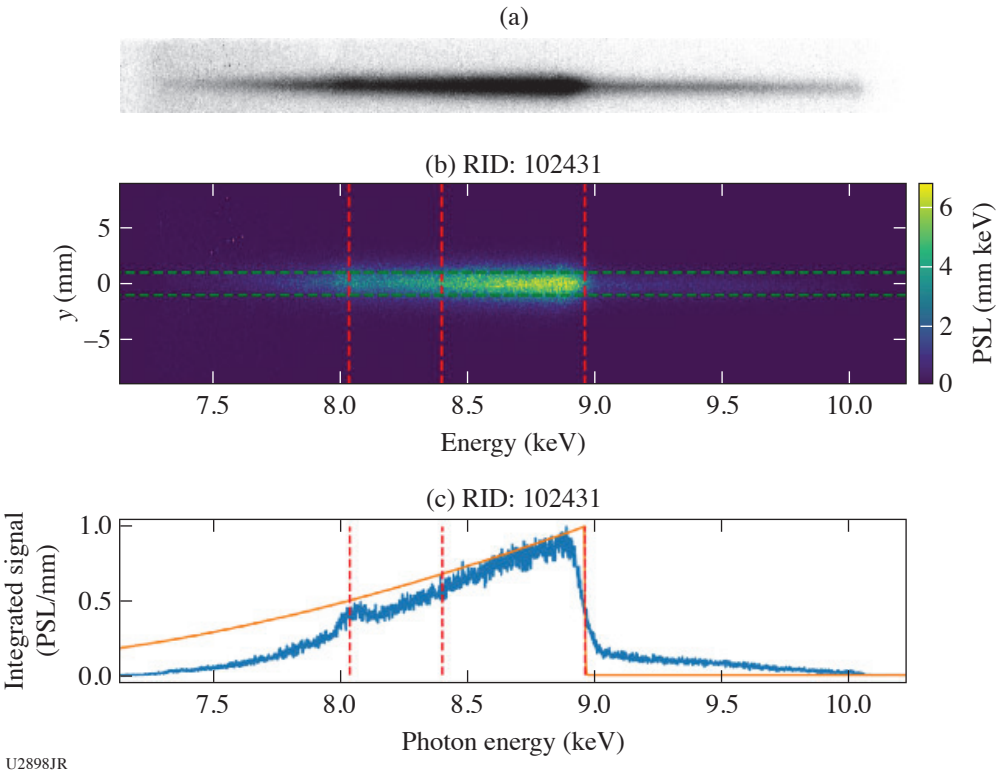

Figure 4
Zinc von Hamos spectra from an OMEGA EP shot showing (a) the raw data, (b) processed image, and (c) an integrated signal lineout, which indicates excess emission consistent with copper K_α emission with only the copper in the target included in the tracer layer of the OMEGA EP target.

Measurements of Shock Equation of State and Melting Temperature of H:N:O and H:C:N:O Mixtures

Y.-J. Kim,[1] M. Bethkenhagen,[2] S. Hamel,[1] M. Wadas,[3] S. Stanley,[4] M. Millot,[1] and F. Coppari[1*]
[1]Lawrence Livermore National Laboratory
[2]Rostock University, Germany
[3]University of Michigan
[4]Johns Hopkins University
[*]Principal Investigator

This ExtChmDAC-21 campaign under the support of the LBS Program aims at investigating the optical and thermodynamic properties of ammonia-rich H:N:O and synthetic Uranus (SU) H:C:N:O mixtures at the extreme pressure–temperature conditions that we expect in the deep interior of icy giant planets such as Uranus and Neptune. This work expands on our recent discovery of superionic water ice (or ice XVIII)[1–3] to reveal the possible existence of the superionic phase in the icy planet constituents as well as its melting temperature.

We prepared ammonia monohydrate (AMH, $NH_3{\cdot}H_2O$), ammonia hemihydrate (AHH, $2NH_3{\cdot}H_2O$), and SU mixtures, and documented their optical properties at the ambient condition.[4] These liquid mixtures were precompressed to 1 to 2 GPa in diamond anvil cells (DAC's) to increase their initial density at room temperature, achieve lower temperatures but higher compression under dynamic loading, and finally reach planetary interior conditions. With excellent laser performance and support, we collected 14 system shots in the one-day allocation. Doppler velocimetry (VISAR) and streaked optical pyrometry (SOP) were used to track the shock-wave propagation through the precompressed sample and to document the pressure–density–temperature shock equation of state as well as the evolution of the optical properties (reflectivity, absorption coefficient) along the shock Hugoniot curves using a quartz reference (see Fig. 5) (Refs. 5,6). The ongoing data analysis will be used to improve our understanding of chemical bonding changes in this regime and benchmark future improved equation-of-state and planetary models.

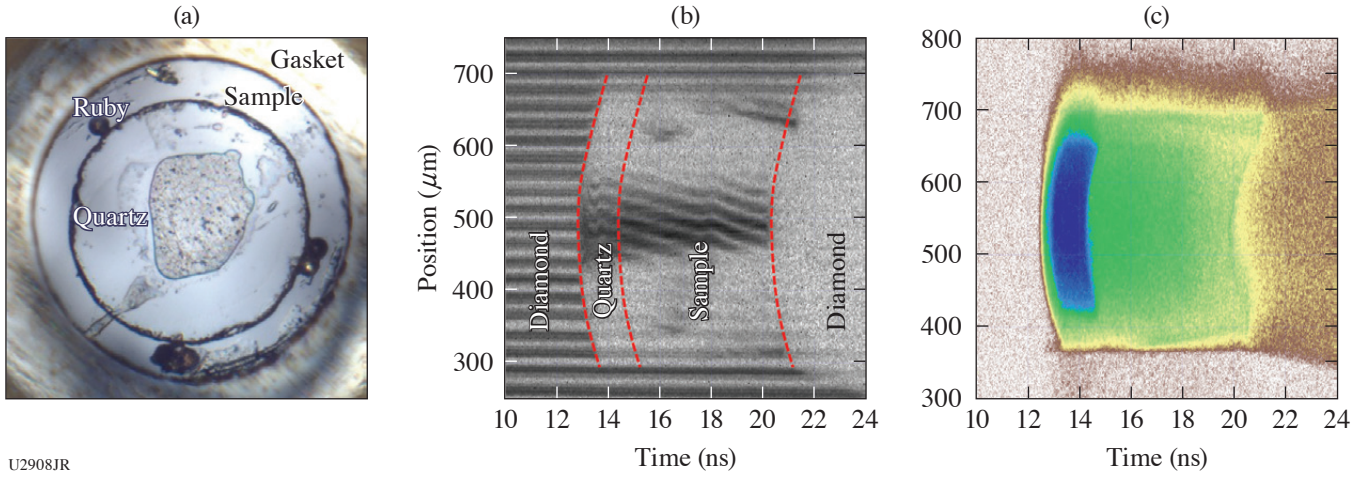

Figure 5
(a) Sample image. Example of (b) VISAR and (c) SOP data showing the decaying shock along the 100-mm-thick SU mixture on OMEGA.

This work was prepared by LLNL under Contract Number DE-AC52-07NA27344 and was supported by LLNL LDRD Program No. 19-ERD-031.

Particle Acceleration from Magnetically Driven Collisionless Reconnection Using Short-Pulse, Laser-Powered Capacitor Coils

L. Gao,[1*] S. Zhang,[2] A. Chien,[2] H. Ji,[1,2] E. G. Blackman,[3] and P. M. Nilson[4]
[1]Princeton Plasma Physics Laboratory
[2]Princeton University
[3]Department of Physics and Astronomy, University of Rochester
[4]Laboratory for Laser Energetics, University of Rochester
[*]Principal Investigator

Magnetic reconnection is a ubiquitous astrophysical process whereby magnetic energy is rapidly converted into plasma kinetic energy in the form of bulk flow, thermal energy, and nonthermal particles. The latter is often regarded as an observational signature of reconnection, which can be a more-efficient particle accelerator than other processes such as collisionless shocks. In the past ∼six years, our team has developed a platform to study acceleration of nonthermal electrons from magnetic reconnection at low plasma beta using UV laser-powered capacitor coils.[7] For the first time, nonthermal electrons accelerated by the reconnection electric field have been measured.[8] In our previous LBS campaigns, we have measured ultrastrong magnetic fields using short-pulse, laser-powered capacitor coils. The measured magnetic fields driven by the short-pulse lasers are ∼2 to 3× larger than those with UV lasers. In this new FY22 LBS shot day, we extended our platform to study particle acceleration by magnetically driven axisymmetric reconnection using short-pulse, laser-powered capacitor coils.

The experimental platform is shown in Fig. 6. The main target was composed of two Cu plates with an extended wing in the back plate, connected by a pair of parallel U-shaped coils. The OMEGA EP sidelighter (SL) was focused onto the wing section of the backplate, positively charging it up. The resulting voltage difference between the back and front plate drives currents in both coils for reconnection. Ultrafast protons generated by the backlighter (BL) probed through the coils to measure the magnetic-field distributions around the coils. The primary advantages of this target design were to (1) perform face-on proton radiography of the reconnection region, and (2) position multiple particle spectrometers around the coils to capture particles at various angles with respect to the reconnection region. The proton data, however, show very small magnetic-field generation for the new target. As a reference, our single-coil experiment used a capacitor coil target without the tiny wing and the SL was directly focused onto the back plate.

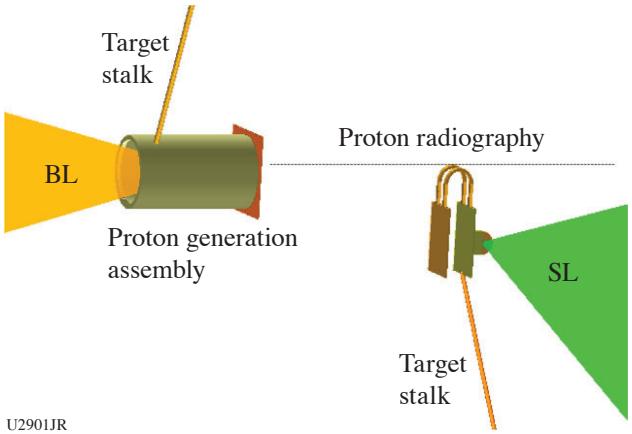

Figure 6
Experimental setup. The OMEGA EP SL was focused onto the wing section of the back plate, positively charging it up. The resulting voltage difference between the back and front plate drives currents in both coils, creating reconnection. Ultrafast protons generated by the BL probed through the coils and were collected by the proton film pack.

Two shots were dedicated to exploring magnetic-field evolution using the old single-coil target, where the SL was focused onto the back Cu plate. Figure 7 shows the proton images collected at 1 ns and 25 ps after the SL drive was turned off. Large and well-defined voids are observed for both cases, indicating a slow decay time of the coil current.

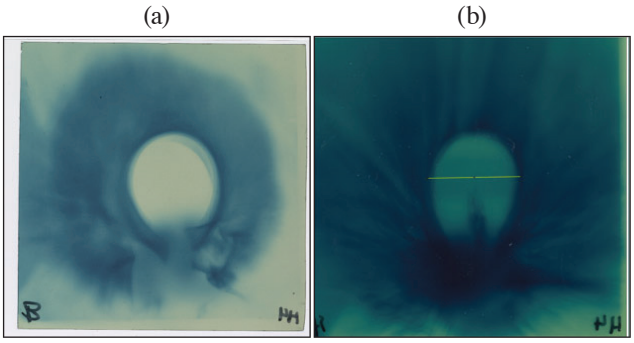

Figure 7
Proton radiographs of the single wire case at (a) 1 ns and (b) 25 ps, respectively, after the SL was turned off. The slight bubble is caused by magnetic fields around the wire deflecting incident protons.

In parallel to the LBS shot day, we conducted two LaserNetUS campaigns using the short-pulse, laser-powered coils for reconnection. Although the new target design with the tiny wing on the back plate did not work out, the data collected on this LBS day helped us with experiment designs for the two LaserNetUS campaigns where successful particle spectra were measured.

We acknowledge the Omega Laser Facility staff at the Laboratory for Laser Energetics. This work was performed under the auspices of U.S. DOE NNSA under the LBS Program, and the DOE Office of Science under the HEDLP Program No. DE-SC0020103.

Initial Relativistically Transparent Microchannel Experiments on OMEGA EP

H. G. Rinderknecht,* G. Bruhaug, M. VanDusen-Gross, and K. Weichman
Laboratory for Laser Energetics, University of Rochester
*Principal Investigator

In relativistically transparent interactions of high-intensity lasers with an overdense plasma, the ponderomotive force of the laser pulse is predicted to drive relativistic current filaments, which in turn produce an azimuthal magnetic filament strong enough to trap electrons.[9] The trapped electrons are predicted to be rapidly accelerated by direct laser acceleration (DLA) to high energies. In this campaign we studied magnetic filament acceleration using the OMEGA EP laser interacting with microchannel targets. The targets were arrays of 6-μm-ID microchannels filled with low-density CH foam, as shown in Figs. 8(a) and 8(b). From prior experiments and scaling laws,[10] we predicted that targets with lower density (3 mg/cm^3) would accelerate electrons more efficiently than targets with higher density (5 mg/cm^3); empty channel targets were also shot as a control.

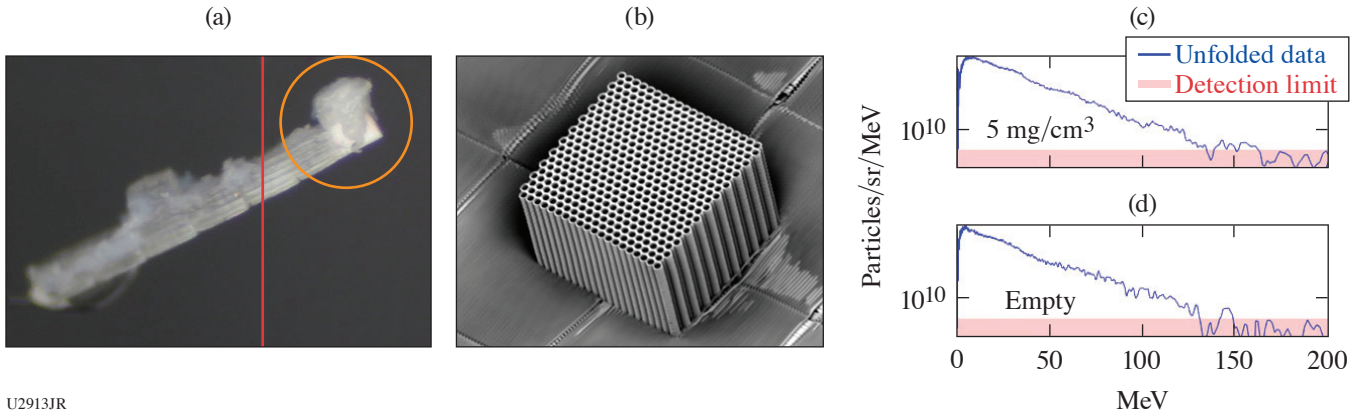

Figure 8
(a) Targets used in the experiment. The active component (orange) is an array of 6-μm-ID, 200-μm-long microchannels, either empty or filled with 3 mg/cm^3 or 5 mg/cm^3 CH foam. (b) Electron microscope image of an empty microchannel array. (c) Recorded electron spectrum from channels with 5-mg/cm^3 fill; (d) no fill. Recorded electron spectra were comparable for all target types.

The EPPS spectrometer recorded electron acceleration from all target types [Figs. 8(c) and 8(d)]. While both the fluence of electrons F and the average electron energy $\langle E\rangle$ increased significantly with higher peak laser amplitude $a_0\left(F \propto a_0^3,\ \langle E\rangle \propto a_0\right)$, no clear difference was observed between the three types of targets used. X-ray data recorded with the bremsstrahlung MeV x-ray spectrometer (BMXS) also did not show a significant difference in radiation between target types.

Post-shot 3-D particle-in-cell (PIC) simulations indicate that, for laser–channel interactions on the time scale of OMEGA EP, the initial channel fill is blown out of the channel within the first 300 fs of the interaction. Subsequently, plasma pulled from the channel wall fills the channels to a density of roughly 7× the plasma critical density in all cases, resulting in identical magnetic filament formation and electron acceleration in all cases. This supports the data interpretation that, on the time scale of OMEGA EP interactions, the magnetic filament acceleration is observed; however, initial plasma density does not determine the acceleration performance.

This material is based upon work supported by the DOE NNSA under Award Number DE-NA0003856, the University of Rochester, and the New York State Energy Research and Development Authority.

Inertial Confinement Fusion Plasma-Based Measurements of the T + ^{4}He Cross Section

J. Jeet,[1*] A. B. Zylstra,[1*] M. Rubery,[1] Y. Kim,[2] Z. L. Mohamed,[2] M. Gatu Johnson,[3] C. J. Forrest,[4] and V. Yu. Glebov[4]
[1]Lawrence Livermore National Laboratory
[2]Los Alamos National Laboratory
[3]Plasma Science and Fusion Center, Massachusetts Institute of Technology
[4]Laboratory for Laser Energetics, University of Rochester
[*]Principal Investigators

Inertial confinement fusion (ICF) implosions provide a relatively new platform for studying nuclear astrophysics. Unlike beam-target accelerator measurements, nuclear reactions occurring in these implosion experiments are a direct surrogate for astrophysical systems since the reactions occur at comparable plasma conditions. The tritium (T) + ^{4}He reaction is important for big-bang nucleosynthesis (BBN) production of ^{7}Li, which has a notable abundance anomaly. Observations of metal-poor halo stars[11] show approximately one-third of the ^{7}Li abundance from predictions that match the abundance inferred from the cosmic microwave background.[12] The important energy range for BBN is a center of mass energy (E_{CM}) between 60 and 160 keV (Ref. 13), corresponding to a range in temperature of 13 to 50 keV. The lower end of this range can be easily studied with implosions conducted at ICF facilities. The T + ^{4}He reaction produces ^{7}Li and a 2.4-MeV gamma, the latter of which can be measured using gamma detectors based on the Cherenkov mechanism. The gas Cherenkov detector (GCD-1) with a fused-silica radiator as well as the vacuum Cherenkov detector (VCD) are used to measure the gammas from this reaction. The implosions use all 60 of the OMEGA beams at 500 J per beam and a 1-ns square

pulse width. The capsules are 1-mm-diam, ~3-μm-thick Hoppe glass. The target fills consist of T + ^{4}He, as well as T_2 for a baseline comparison. Additionally, DT implosions are conducted along with a carbon puck attached to GCD-1 to calibrate both GCD-1 as well as the VCD.[14] Figure 9(a) shows the results of the calibration of the detector response, for both the GCD-1 and the VCD, to 4.4-MeV carbon gammas resulting from inelastic scattering of DT neutrons with the carbon puck. Figure 9(b) shows the gamma measurements made by GCD-1. These are average signals from multiple shots for each fuel type normalized to both the DT and TT neutron yields. The DT and TT yield-normalized signals measured for the T^{4}He fills (black solid and blue solid curves, respectively) are consistent and within 10%. These are significantly larger than the background measurements provided by the T_2 gas fills (dashed curves).

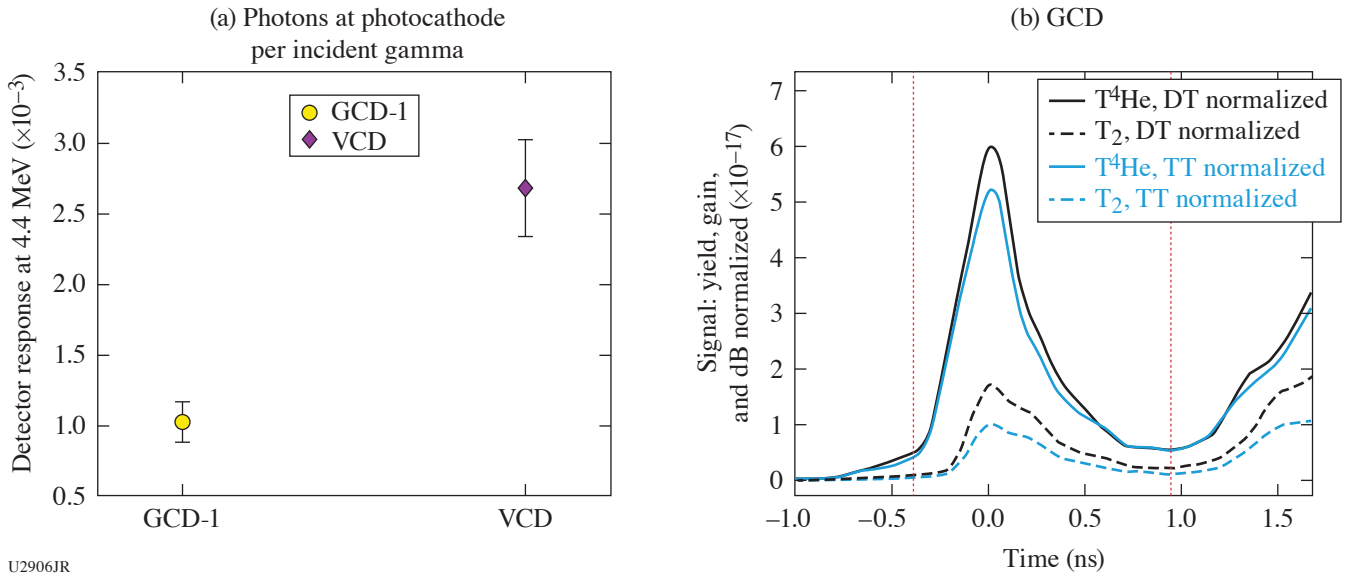

Figure 9
(a) The detector response, for both the GCD-1 with a fused-silica radiator as well as the VCD, is measured to 4.4-MeV gammas, resulting from inelastic scattering of DT neutrons with a carbon puck attached to the GCD-1. (b) Average gamma signals as measured by GCD-1 are shown for each fuel type, T^{4}He (solid) and T_2 (dashed), and normalized to the DT (black) and TT (blue) neutron yields. The excess gamma signal in the T + ^{4}He reaction relative to the T_2 gas fills, for each type of yield normalization, agree with one another within a factor of 10%.

The excess gamma signal, along with the detector calibrations, will be used to determine *S* factor for the T + ^{4}He reaction. The results of these experiments can potentially impact the BBN modeling community by improving confidence in the reaction rate at relevant energies.

We thank the operations crews and engineering staff at Omega for supporting these experiments. This work was performed under the auspices of the U.S. Department of Energy by Lawrence Livermore National Laboratory in part under Contract No. DE-AC52-07NA27344 and supported by the U.S. DOE Early Career Research Program (Fusion Energy Sciences) under FWP SCW1658.

X-Ray Sources from Laser Wakefield Acceleration on OMEGA EP

F. Albert,[1*] I. Pagano,[1,2] N. Lemos,[1] J. Williams,[1] H. Chen,[1] J. L. Shaw,[3] D. H. Froula,[3] C. Arrowsmith,[4] A. Aghedo,[5] M. Sinclair,[6] and C. Joshi[6]
[1]Lawrence Livermore National Laboratory
[2]University of Texas, Austin
[3]Laboratory for Laser Energetics, University of Rochester
[4]University of Oxford, UK
[5]Florida A&M University
[6]University of California, Los Angeles
*Principal Investigator

X-ray backlighting is one of the most used methods to look into the extreme temperatures, pressures, and densities created during laser-driven high-energy-density science (HEDS) experiments. Over the years, much effort has gone into developing backlighting techniques to look into these states of matter, with new sources and diagnostics. The properties of an x-ray backlighter (flux, source size, spectrum, duration) required for an experiment depend on the application being studied and on the quantity being measured. The goal of the Wakefield-EP shot series is to develop a new type of x-ray backlighter, which could be advantageous for applications requiring broadband spectra, small source sizes (sub-50 μm), short duration (less than 10 ps), and x rays extending beyond 100 keV. Our proposed x-ray sources are based on laser wakefield acceleration (LWFA) of electrons in the self-modulated regime (SMLWFA). Specifically, we aim to develop three different x-ray sources based on betatron radiation, Compton scattering, and bremsstrahlung emission.

The WakefieldLBS-EP-22A shot day was a continuation of our previous work, aimed at producing and detecting x-ray radiation produced by SMLWFA using a modified version of the EPPS diagnostic. We enlarged apertures to 5 mm (instead of 1 mm) and included a hole at the back of the magnet box, as well as a stack of nine image plates at the back of the ten-inch manipulator (TIM) boat to detect betatron radiation. In addition to betatron radiation, this year we also measured x rays produced by inverse Compton scattering, where the OMEGA EP laser pulse was reflected by a foil onto the accelerated electrons to produce high-energy x rays. We also implemented a new crosshair on the front end of the EPPS diagnostic to be able to measure the x-ray source size. The wakefield platform continued to produce robust electron beam data, recording a >100-nC charge electron beam at each shot, as well as two temperature spectra extending up to about 200 MeV (see Fig. 10).

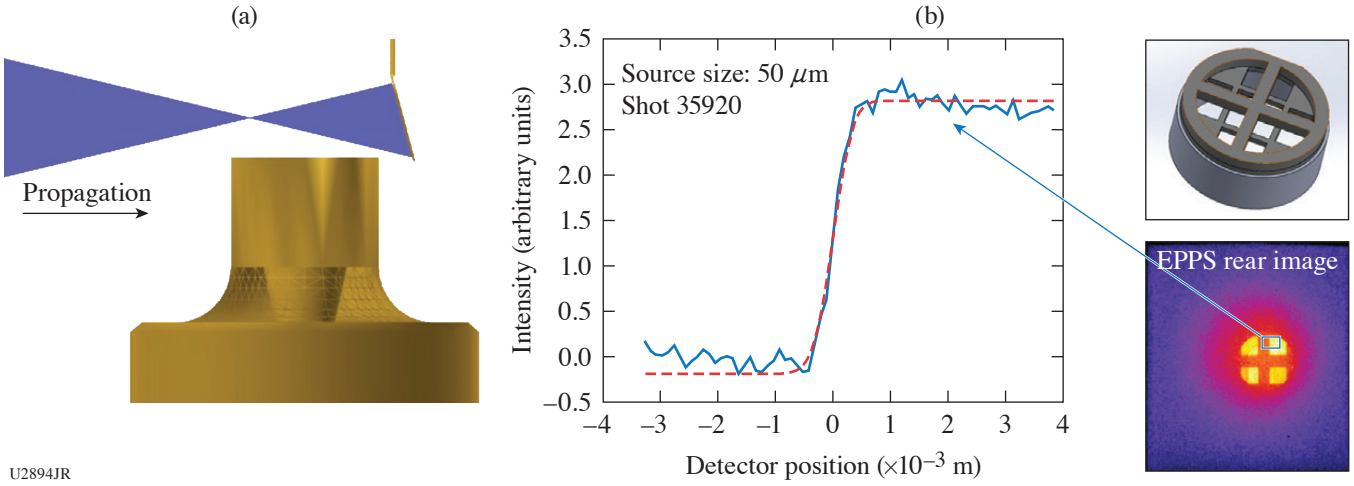

Figure 10
Results obtained during the WakefieldLBS-EP-22A shot day using the modified EPPS diagnostic. (a) Setup for an inverse Compton scattering x-ray source; (b) x-ray source size measurement and analysis.

Extreme THz Generation and Detection

G. Bruhaug,[1*] H. G. Rinderknecht,[1] Y. E,[2] M. S. Wei,[1] K. G. Francis,[2] X. C. Zhang,[2] G. W. Collins,[1] and J. R. Rygg[1]
[1]Laboratory for Laser Energetics, University of Rochester
[2]The Institute of Optics, University of Rochester
[*]Principal Investigator

For several decades, the creation of THz radiation was considered extremely challenging due to the frequency in question being too fast for classic electronic switching techniques and not efficiently generated via classic optical sources.[15] The first usable THz sources were based on large particle accelerators and were created via either synchrotron radiation or as free-electron lasers.[15,16] Later source development led to the creation of laser-based sources utilizing nonlinear crystals for frequency conversion.[15–18] Commercial laser-based sources of THz radiation are now widely available and utilized for homeland security applications, medical imaging, and traditional materials science research. However, these laser-based sources are limited in average and

peak THz power by the damage limits of nonlinear crystals.[15–18] This limits their applications in noisy environments and as drivers for pump–probe experiments. Newer laser-plasma–based THz sources have been developed using high-intensity lasers (>10^{18} W/cm^2) and have shown great promise as both experimental pumps and probes.[15,18] These THz generation methods involve irradiating foils, wires, and gas jets with high-intensity lasers.[15–20]

We performed the first laser-plasma THz generation experiments on OMEGA EP that tested our new THz background/energy meter (TBEM) detectors and showed extremely high THz yield from foil targets, similar to previous experiments on smaller lasers.[15] Analysis is still ongoing, but we estimate hundreds of mJ of THz were made from laser energies ranging up to 200 J. In addition, we performed the first ever attempts at THz/proton interferometry using TNSA protons. This measurement utilized OMEGA EP's unique dual-axis short-pulse capability and performed the first ever proton measurements of extreme THz fields, but not at the same time as the TBEM detectors due to background noise issues that have now been resolved in the detector design. A typical TNSA "proton tube" target was driven with a 10-ps, 900-J laser pulse and then ~90 ps later a THz generating foil was driven with a 0.7-fs, 500-J laser [Fig. 11(a)]. Both targets were positioned 5 mm from target chamber center, keeping each target out of the sheath field region of the resulting plasmas.

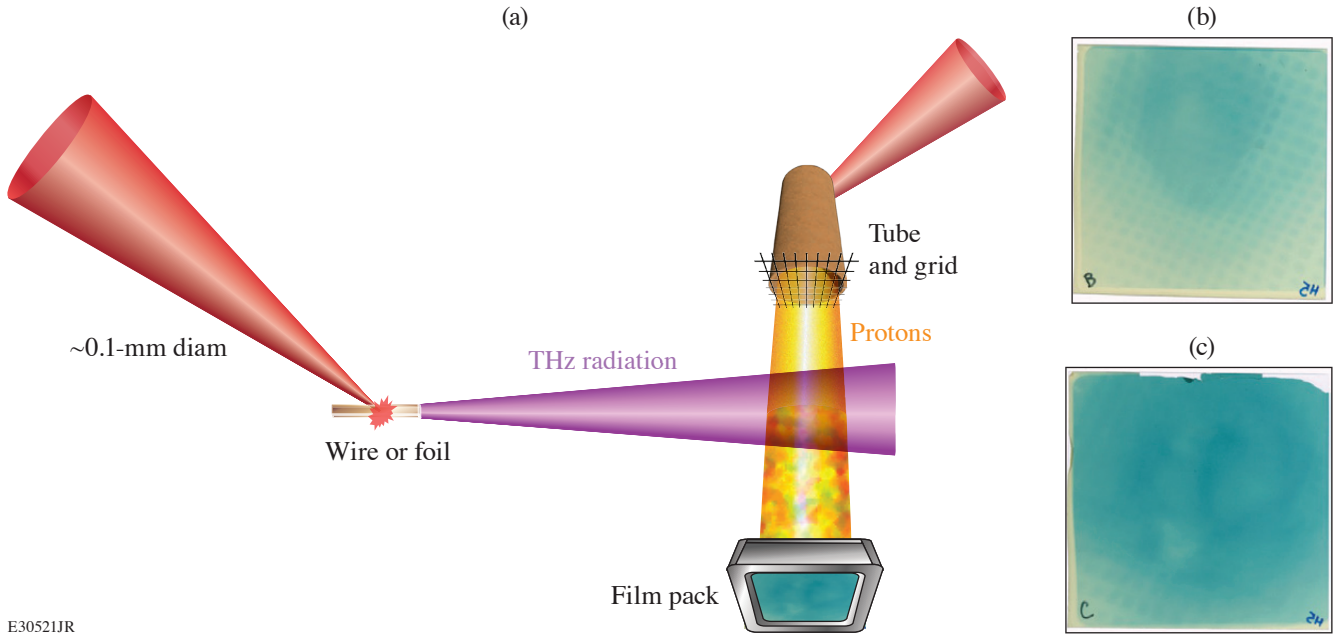

Figure 11
(a) Outline of the THz/proton interferometry experimental setup; (b) 15-MeV proton radiograph without any THz radiation present; and (c) 15-MeV proton radiograph with a THz pulse incident on the protons.

The THz pulse is believed to be single or even half-cycle, which allows the large (GV/m) electric fields in the pulse to provide net momentum to the protons. A test shot was taken [Fig. 11(b)] without a THz foil and a typical TNSA proton source is seen. The addition of a THz pulse altered the proton radiographs [Fig. 11(c)] in energies ranging from 10 to 28 MeV. These phenomena were repeatable between shots and became weaker with a lower-energy laser driver, as would be expected. Analysis is still ongoing but we believe GV/m electric fields generated this effect, requiring >100-mJ THz pulses. We anticipate that further analysis will allow exact discernment of the THz pulse energy and field strength, as well as provide a rough estimate as to the spectral distribution. The TBEM research and development performed during these experiments were also crucial for finalizing detector design and allowing for the detection of even higher THz yields on later OMEGA EP experiments.

This material is based upon work supported by the Department of Energy National Nuclear Security Administration under Award Number DE-NA0003856, the University of Rochester, and the New York State Energy Research and Development Authority.

Quantum States of Hydrogen: Toward a Superconducting Superfluid

A. Schwemmlein,[1*] G. W. Collins,[1*] R. Jeanloz,[2] S. Brygoo,[3] P. M. Celliers,[4] J. H. Eggert,[4] D. E. Fratanduono,[4] R. Hemley,[5] P. Loubeyre,[3] M. Millot,[4] J. R. Rygg,[1] Y. Kim,[4] J. Sater,[4] L. E. Hansen,[1] Z. K. Sprowal,[1] and R. Earley[1]
[1]Laboratory for Laser Energetics, University of Rochester
[2]University of California, Berkeley
[3]Commissariat à l'énergie atomique et aux énergies alternatives, France
[4]Lawrence Livermore National Laboratory
[5]University of Illinois, Chicago
[*]Principal Investigators

Crystalline metallic hydrogen has attracted significant theoretical interest since the 1930s (Ref. 21). Recent theoretical work suggests that its quantum nature gives rise to remarkable properties like high-temperature superconductivity.[22] In addition, metallic hydrogen is the predominant constituent of giant planets and stars; it is thus the most abundant form of condensed matter in the universe. Experimental studies of crystalline metallic hydrogen, however, have only recently become possible using dynamic-compression experiments at high-intensity laser facilities like Omega.

To reach the necessary low temperatures (<1000 K) and high pressures (>500 GPa), a low-temperature and entropy initial state is compressed using a custom OMEGA pulse shape approximating an isentropic drive. To reduce the entropy of the targets, only hydrogen molecules in the low-entropy solid and parastate, where the proton spins not aligned, are used. This special state of hydrogen was successfully produced in a newly developed target fill and diagnostic station, which confirmed >95% purity and stability of this state over hours in the standard planar cryo targets. These targets were cooled down in the target chamber to 10 K while observing the formation of a uniform solid using the VISAR field of view.

Raw data with a preliminary analysis of a representative shot is shown in Fig. 12. The VISAR fringes (background) were converted into the pusher velocity (green) that was subsequently matched using a hydrocode, which finally revealed a maximum

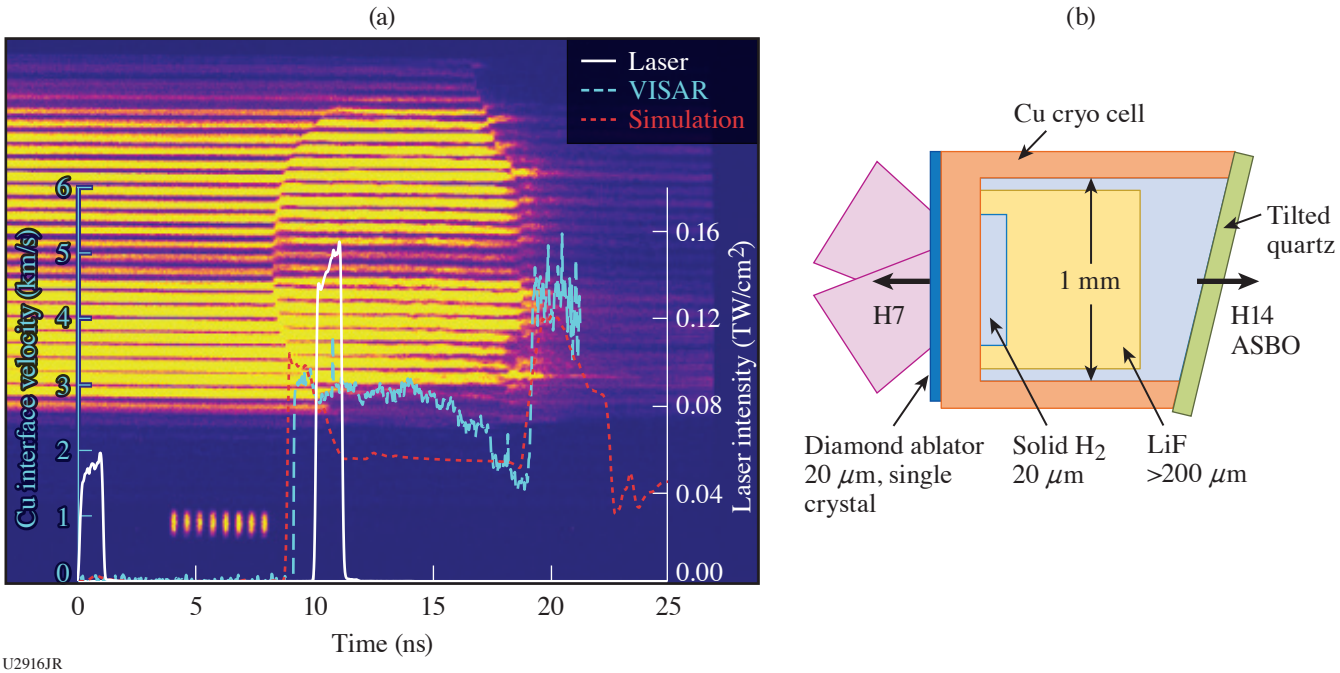

Figure 12
(a) VISAR raw data and analysis of (b) a 10-K parahydrogen target shot by a two pulse sequence. The VISAR sees the copper pusher in front of the 20-μm-thick hydrogen payload. The simulation revealed that a maximum pressure of 40 GPa was reached. Future experiments will use these two pulses in combination with a 12-ns ramp.

pressure of 40 GPa inside the 20-μm hydrogen payload. For this experiment, the first two pulses of a six-pulse sequence that was optimized using a hydrocode were tested. These two 1-ns square pulses initiate the ablation and reverberate inside the hydrogen to increase the pressure to several tens of GPa. A subsequent 12-ns ramp will be added in future experiments to increase the pressure to 700 GPa at a temperature around 1000 K. Simulations using the standard code *HYADES* indicate that these conditions can be met.

This experiment was conducted at the Omega Laser Facility at the University of Rochester's Laboratory for Laser Energetics with the beam time through the Laboratory Basic Science program.

Viscosity Measurements Using Tracer Particles

A. Gleason,[1*] J. Shang,[2,3] D. N. Polsin,[2,3] H. Aluie,[2,3] and J. R. Rygg[2,3]
[1]SLAC National Accelerator Laboratory, Stanford University
[2]Department of Mechanical Engineering, University of Rochester
[3]Laboratory for Laser Energetics, University of Rochester
[*]Principal Investigator

Any study of hydrodynamic flows in HED environments requires knowledge of material properties such as dynamic viscosity, and its inclusion in simulations can dramatically alter flows such as in inertial confinement fusion implosions.[23] Measurements of viscosity under HED conditions are sparse. In this campaign, we collected additional data to quantify the viscosity of epoxy, a surrogate for polystyrene and other commonly used ablator materials, to corroborate against a previous campaign. The method relies on measuring the acceleration of bluff bodies embedded in the material of interest since the hydrodynamic forces include viscous contributions; the viscosity can be estimated from the trajectory.[24]

In the experiment, the epoxy was embedded with titanium microspheres. The target was then shock compressed to ~215 GPa and we imaged the backlit target at different times after the shock had traversed the spheres. Figure 13 shows images of the instantaneous particle position and compression of two Ti spheres entrained in the flow behind the shock, and their displacement from their pre-shock location. Due to the lower mass of the spheres compared to the last experiment, we expect that our analysis will show they accelerate faster than the spheres in our last campaign.

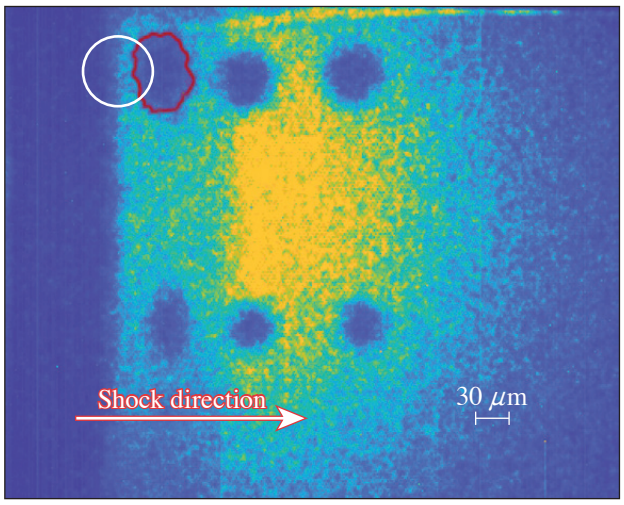

U2903JR

Figure 13
Radiograph of shocked and unshocked titanium particles for shot 105537 at t = 19.7 ns after the drive. The initial location of the larger sphere is outlined in white; the instantaneous particle position is shown in red, showing a displacement of about 40 μm after acceleration. Spheres are compressed behind the shock.

The experiment was conducted at the Omega Laser Facility at the University of Rochester's Laboratory for Laser Energetics with the beam time through the LBS Program. This work was supported by the DOE Office of Fusion Energy Sciences under the Early Career Award for A. Gleason. This work was also supported by US Department of Energy and NNSA under awards DE-SC0019329 and DE-NA0003914. Partial support from grants NSF PHY-2020249, DE-SC0020229 and DE-NA0003914 is also acknowledged.

Formation of Dynamic Shells Using Foam Ball Targets

I. V. Igumenshchev,[1*] W. Theobald,[1] C. Stoeckl,[1] R. C. Shah,[1] D. T. Bishel,[1] V. N. Goncharov,[1*] P. Adrian,[1] M. J. Bonino,[1] E. M. Campbell,[1] D. A. Chin,[1] T. J. B. Collins,[1] S. Fess,[1] D. R. Harding,[1] S. Sampat,[1] N. R. Shaffer,[1] A. Shvydky,[1] W. T. Trickey,[1] L. J. Waxer,[1] A. Colaïtis,[2] R. Loitard,[2] S. Atzeni,[3] F. Barbato,[3] and L. Savino[3]
[1]Laboratory for Laser Energetics, University of Rochester
[2]Centre Lasers Intenses et Applications, France
[3]University of Rome, Italy
[*]Principal Investigators

A dynamic-shell (DS) concept in direct-drive ICF utilizes the conventional hot-spot–ignition scheme and uses about 3-mm-diam sphere targets of liquid deuterium–tritium (DT) as a fuel.[25] Implosion shells of DT, which are required for hot-spot ignition, are developed dynamically from such sphere targets. This development and ignition are accomplished in four distinct evolution stages. In the first stage, a liquid DT sphere target is compressed by a few-Mbar convergent shock wave, which is launched by intense laser beams symmetrically irradiating the target. The second stage starts when this shock reaches the target center, reflects, and is transformed into a blast wave, causing the shock-compressed fuel, now becoming a plasma cloud, to expand. The third stage begins with launching convergent shocks at the outer edge of the expanding cloud. These shocks decelerate and reverse the expansion, resulting in a dynamic formation of a dense shell. In the fourth stage, this shell is imploded using a megajoule laser pulse similar to that in the conventional hot-spot–ignition scheme.

Proof-of-principle experiments on the OMEGA laser[26] have demonstrated, for the first time, the feasibility of DS formation and stability of DS's to low-mode perturbations (for Legendre modes less than about 10) using a scaled-down experimental setup to accommodate limitations in the available laser energy (<20 kJ) and pulse duration (<4 ns). The experiments used room-temperature surrogate sphere targets consisting of a CH foam and having an outer diameter of about 600 μm [see Fig. 14(a)]. Foam targets in the OMEGA experiments undergo the same evolution stages (compression, expansion, and shell formation) as in the ignition design, excluding the final implosion/ignition stage. Figure 14(b) illustrates these stages, showing a simulated shock diagram in gray scales for OMEGA shot 105251. The laser pulse is shown by a red line and has 11.2-kJ energy. The square pulse in the beginning of the pulse (see the red line) launches a shock that initially compresses the target. This shock reflects from the center at t = 1.4 ns, forming a blast wave and resulting in expansion of the compressed target mass. The second square pulse, which

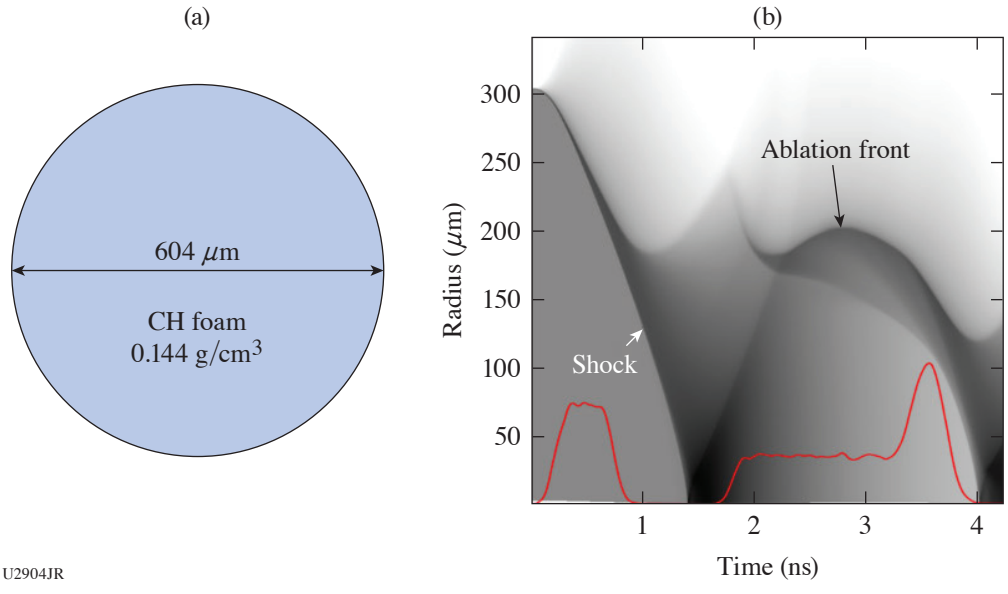

Figure 14
(a) Foam-ball target and (b) simulated log-density evolution, or "shock diagram," for OMEGA shot 105251. The red line in (b) shows the laser pulse in relative units.

starts at $t = 1.8$ ns, decelerates the expanding mass by sending convergent shocks and forms a dense shell. The outer shell radius, which is defined as the radius of the ablation front and seen as a density-contrast interface in Fig. 14(b), is initially reduced to about 180 μm at 2.15 ns, then increased, reaching about 200 μm at 2.8 ns, and then decreased again, approaching the minimum of about 120 μm at 4.0 ns [see Fig. 14(b)]. The power spike at the end of the pulse helps to additionally compress the shell mass, increasing the contrast in density at about 3.7 to 4 ns. This time interval is the most favorable for probing the formation of DS.

The experiments employed three x-ray diagnostics to evidence the DS formation. These include a streaked self-emission radiography,[27] backlighting radiography,[28] and framed shadowgraphy.[29] Figure 15(a) shows the streak data (the color map) aligned with the laser pulse (the white line) that were obtained in shot 105251. Two bright spots at $t \approx 1.4$ and 3.9 ns near $y = 0$ correspond to shock bounce events that were predicted in simulations [see Fig. 14(b)]. The bright region between $t \approx 1.9$ and 3.9 ns represents the emission at the ablation-front during the formation of DS. The rims bounding this region in the top and bottom show the ablation front trajectory. These data, while not directly indicating the formation of DS, make it possible to verify the simulations in Fig. 14(b), which show good quantitative agreements with inferred shock timing and ablation-front trajectory.

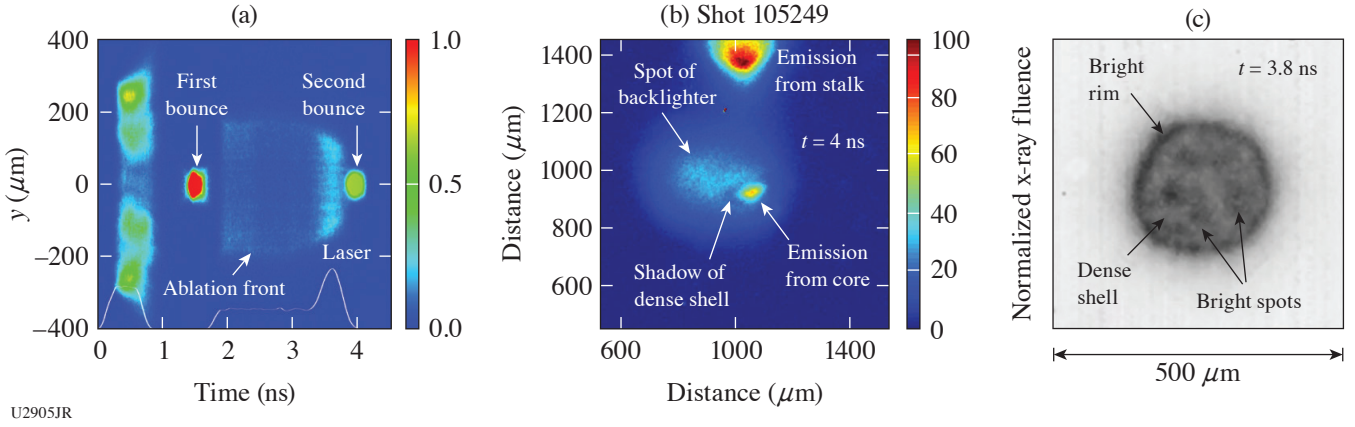

Figure 15
(a) X-ray streaked self-emission radiograph from shot 105251, (b) backlighting radiograph from shot 105249, and (c) framed shadowgraph from shot 105251.

Figure 15(b) illustrates results of backlighting radiography performed using joint OMEGA and OMEGA EP shot 105249. A 25-ps x-ray backlighter pulse (1.865 keV) was fired at $t \approx 4.0$ ns using the high-intensity OMEGA EP beam illuminating a Si foil target. This moment corresponds to the maximum convergence of DS, causing bright emission of the hot shell interior, or the core. The shadow on the background of backlighter and core emission is clearly visible in Fig. 15(b) and directly evidences the formation of a DS. Note the emission from remnants of a plastic (CH) stalk in the upper part of this figure. This stalk had a diameter of 50 μm and was used to mount the target. Its emission is observed far from the shell and without apparent influence of the formation of DS. This agrees with results of 3-D radiation-hydrodynamic simulations using the code *ASTER*,[30] which predict that the stalk is completely ablated off during earlier evolution (up to $t \approx 2$ ns) and does not significantly affect the shell dynamics.

The shadowgraph in Fig. 15(c) shows the DS at the late stage of its formation, $t \approx 3.8$ ns. The bright (dark in the image) circular rim in this figure corresponds to x-ray emission just outside the ablation front. The less-bright regions inside the rim represent the developed DS, which shadows x rays coming from the ablation front on the opposite side of the shell with respect to the viewing direction and from the hot shell interior. The five almost symmetric bright spots (again, darker in the image) inside the rim appear from perturbations in the shell coming from the OMEGA 60-beam illumination pattern. There are five of them because the viewing direction is projected through the center of a pentagon formed by the OMEGA beam ports. Three-dimensional *ASTER* simulations suggest that OMEGA beam overlapping can result in dips in the dense shell in the locations of maximum on-target intensity. This causes the emission from the shell interior to escape more efficiently through these dips resulting in imaging symmetric bright spots.

This material is based upon work supported by the Department of Energy National Nuclear Security Administration under Award Number DE-NA0003856 and ARPA-E BETHE Grant No. DE-FOA-0002212. The experiment was conducted at the Omega Laser Facility at the University of Rochester's Laboratory for Laser Energetics with the beam time through the Laboratory Basic Science program.

Inertial Confinement Fusion Plasma-Based Measurements of the D–T γ-to-Neutron and the D–^{3}He γ-to-Proton Branching Ratios

J. Jeet,[1*] A. B. Zylstra,[1] M. Rubery,[1] M. Eckart,[1] Y. Kim,[2] Z. L. Mohamed,[2] K. Meaney,[2] M. Gatu Johnson,[3] C. J. Forrest,[4] and V. Yu. Glebov[4]
[1]Lawrence Livermore National Laboratory
[2]Los Alamos National Laboratory
[3]Plasma Science and Fusion Center, Massachusetts Institute of Technology
[4]Laboratory for Laser Energetics, University of Rochester
[*]Principal Investigator

The D–T γ-to-neutron branching ratio [^{3}H(d,γ)^{5}He/^{3}H(d,n)^{4}He] has been previously determined in beam–target-based experiments as well as in ICF experiments.[31,32] In the latter case, neutron-induced backgrounds are significantly reduced compared to the former due to the short-pulse nature of ICF implosions and the use of gas Cherenkov γ-ray detectors. A benefit of ICF-based measurements is the ability to achieve lower center-of-mass energies as compared to accelerators. Previous ICF-based experiments, however, report a large uncertainty in the D–T γ-to-neutron branching ratio of ≈48%. A more-precise value for the branching ratio based on data taken at OMEGA has been determined. This relies on a cross-calibration against the better known ^{12}C neutron inelastic scattering cross section [^{12}C(n,n′)γ] in a puck-based experiment involving the gas Cherenkov detector (GCD-3). A D–T branching ratio value of $(4.6\pm0.6) \times 10^{-5}$ is determined by this method;[33] the results are shown in Fig. 16 and compared to values obtained in previous experiments. This campaign will improve this experiment to further reduce the uncertainty in the measurement. We will also provide a measurement of the D–^{3}He γ-to-proton branching ratio to significantly better precision than reported by previous experiments, which are limited to ≈33%. This is made possible due to an absolute detector calibration that relies on the inelastic scattering of DT neutrons in a carbon puck attached to the GCD-3 (Ref. 14). The resulting 4.4-MeV gammas are temporally separated from the primary gamma signal resulting from the D–T fusion and can be isolated by performing a yield-normalized subtraction of a background signal that does not field the carbon puck. Signals as measured by the VCD are shown in Fig. 17 for the D–T implosions.

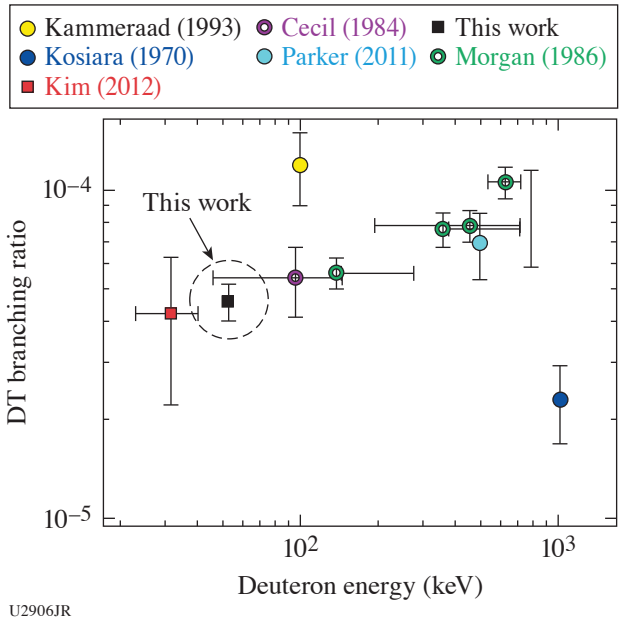

Figure 16
The D–T branching ratio measurement resulting from the work of Ref. 33 is shown (black square) along with other recent experiments (Refs. 31 and 32), which include both beam–target-based measurements (dark blue circle) as well as an ICF-based result (red square).

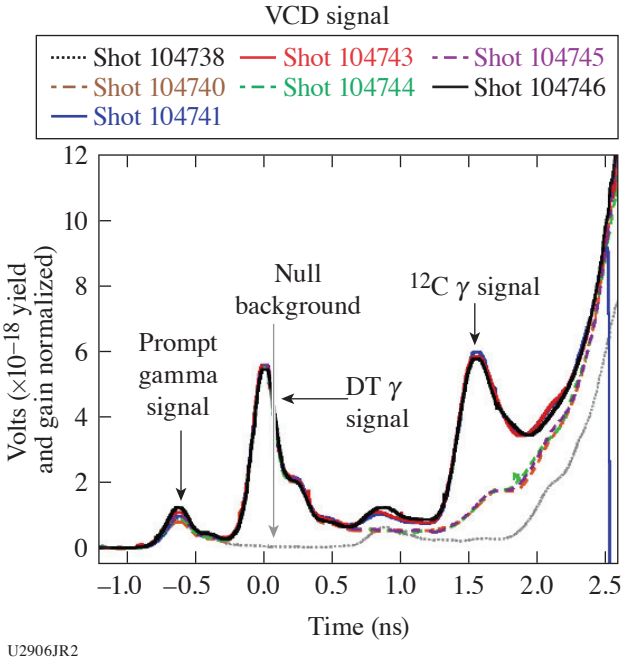

Figure 17
D–T implosion signals as measured by the VCD. Each signal is comprised of different features. The prompt gamma signal results from direct interaction of gammas with the photomultiplier tube inside the VCD. The DT gamma signal results from the fusion and is delayed with respect to the prompt gamma signal. The ^{12}C gamma signal results from the inelastic scattering of DT neutrons with a carbon puck attached to the GCD-3. The resulting 4.4-MeV gammas are temporally separated from the primary D–T fusion gammas.

Relative to the experimental data analyzed in Ref. 33, these experiments were optimized to improve the precision in the measurement. The TIM diagnostic loadout is kept minimal to reduce the extraneous neutron-induced noise that can coincide with the ^{12}C gamma signal. A thinner capsule shell is used to minimize shell areal-density contributions to the primary D–T fusion gamma signal. Measurements were taken with multiple gamma detectors, GCD-3 as well as the VCD, at different threshold energies. The ratio of the ^{12}C gamma signal to that of the DT gamma signal allows for extraction of the D–T branching ratio while eliminating the need for absolute detector calibrations and systematic yield uncertainties for the measured DT neutrons. D^{3}He shots were also conducted in this campaign to determine the gamma-to-proton branching ratio, which is measured to higher precision using the absolute detector calibration provided by the ^{12}C gamma measurement.

With improved measurements of the ^{12}C(n,n′)γ scattering cross section or the D–T γ spectrum, the data taken in this campaign can be revisited and systematic uncertainties in the D–T γ-to-neutron and D–^{3}He γ-to-proton branching ratios can be further reduced.

We thank the operations crews and engineering staff at Omega for supporting these experiments. This work was performed under the auspices of the U.S. Department of Energy by Lawrence Livermore National Laboratory in part under Contract No. DE-AC52-07NA27344 and supported by the U.S. DOE Early Career Research Program (Fusion Energy Sciences) under FWP SCW1658.

Detailed Benchmarking of the Nernst Effect in a Magnetized High-Energy-Density Plasma

S. Malko,[1*] W. Fox,[1,2] D. B. Schaeffer,[2] C. Walsh,[3] G. Fiksel,[4] A. J. Harvey-Thompson,[5] M. Weiss,[5] A. Hansen,[5] D. Ruiz,[5] A. Bose,[6] C. Frank,[6] P. Heuer,[7] and J. Davies[7]

[1]Princeton Plasma Physics Laboratory
[2]Princeton University
[3]Lawrence Livermore National Laboratory
[4]Center for Ultrafast Optical Science, University of Michigan
[5]Sandia National Laboratories
[6]University of Delaware
[7]Laboratory for Laser Energetics, U. Rochester
[*]Principal Investigator

Magnetic fields are known to affect and suppress heat flux through thermomagnetic effects in HED laser-produced plasmas.[34] In the high-beta and moderate collisionality regimes on HED plasmas, however, the heat flux can also feedback and drive advection of the magnetic field via the Nernst effect. This can be important for several applications of magnetized HED plasmas, including magnetized liner inertial fusion (MagLIF).[35] The heating laser creates a radial temperature and density gradient in the D_2 fuel perpendicular to the axial magnetic field. Simulations show that the Nernst effect significantly reduces the performance of the MagLIF preheat phase by advecting the applied axial magnetic field out of the fuel, thereby increasing energy losses due to thermal conduction.[36] Nernst transport can also strongly affect the dynamics of both externally applied and self-generated magnetic fields in hohlraums and ablation fronts in directly driven capsules in ICF and ICF hot spots. The detailed experimental benchmarking of numerical models that include the Nernst effect are crucial and required to further understand how to control such magnetized plasma systems. To identify the importance of this effect, one can introduce the "Nernst number" N_e, which gives the ratio of the characteristic velocity of the Nernst field advection v_N to the sonic plasma expansion v_s, $N_e = v_N/v_s$.

Here we report on novel experimental platform NerntEffect22A at the Omega Laser Facility for benchmark Nernst effect in the regime where the Nernst advection dominates the frozen-in plasma flow $0.1 < N_e < 1$. The platform is based on laser heating of a gas jet in a magnetic field and simultaneous direct measurement of the Nernst velocity and plasma conditions (density and temperature). In order to design this experiment and find the regime of interest, we performed a pre-shot parametric study with 1-D *GORGON*[37] by varying gas densities, gas type, laser energy, and magnetic field. In addition, *FLUKA*[38] Monte Carlo simulations were used to obtain expected proton signal level and design proton radiography diagnostics.

The setup of experiment is presented at Fig. 18. One OMEGA beam (heater) with 500-J energy is used to heat a H_2 gas jet in a cylindrically symmetric volume aligned parallel to an external magnetic field of approximately 5 T produced by MIFEDS. Proton radiography with 3- and 15-MeV monoenergetic protons produced from a D–^{3}He implosion was used to measure the magnetic fields at several expansion times. The plasma parameters (n_e, T_e) and radial bulk flow speed of plasma at different positions across cavity (0, +250 μm, +500 μm) were measured by time-resolved 2ω optical Thompson scattering (OTS).

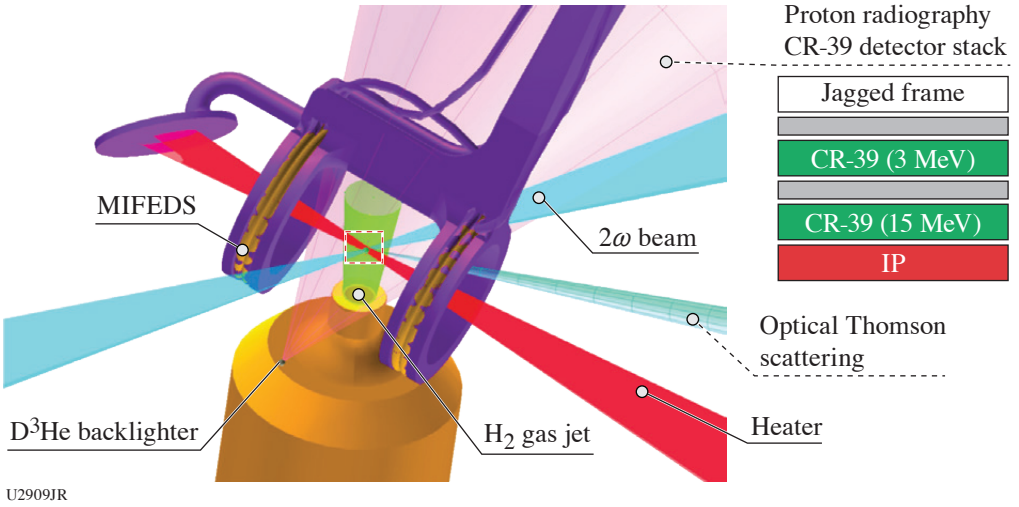

Figure 18
The experimental setup at the Omega Laser Facility. IP: image plate.

The example of obtained proton radiography data at 0.5- and 1-ns expansion time is shown in Fig. 19. We have observed a clear magnetic-field cavitation and pileup on the edges of the cavity as predicted by 1-D *GORGON* simulations. The measured time evolution of the cavity will allow us to calculate the cavitation rate and thus the Nernst velocity. The preliminary analysis of OTS electron plasmon wave (EPW) and ion-acoustic wave (IAW) spectra at the center of cavity provided electron temperature of $T_e \sim 400$ eV and electron density of 1×10^{20} cm^{-3} at 700-ps expansion time. Based on these measurements we have estimated $N_e \sim 0.28$ compared to 0.12 for the MagLIF preheat phase.[39] These experimental results will be compared with *GORGON*, *HYDRA*, and *LILAC* simulations.

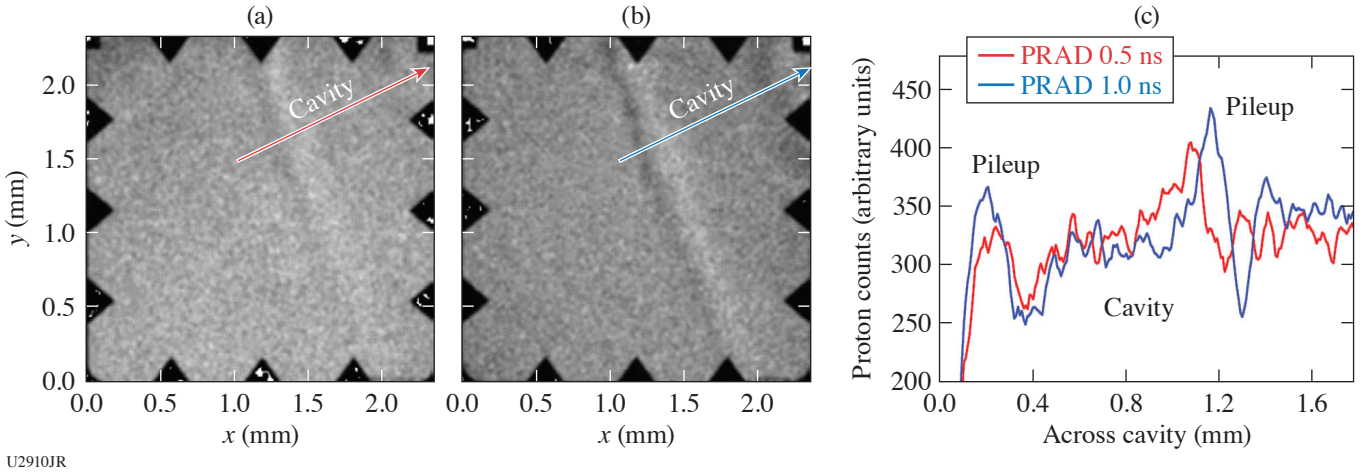

Figure 19
The raw proton radiography CR-39 images obtained with 15-MeV protons. PRAD acquired at (a) 0.5-ns and (b) 1-ns expansion time. (c) The lineout across the cavity obtained from at 0.5 ns (red curve) and 1 ns (blue curve). PRAD: proton radiography.

In summary, we have developed a novel experimental platform for benchmarking of Nernst effect in an open-geometry configuration at the Omega Laser Facility. We have successfully measured cavitation of magnetic fields by proton radiography and electron temperature and density, as well as bulk flow velocity at different positions across cavity by 2ω optical Thomson scattering. The preliminary analysis of proton radiography results indicates magnetic-field advection in time and pileup at the edges of the cavity. These results will be used for benchmarking extended magnetohydrodynamic codes. This platform can be also used to benchmark the Nernst effect in low- (high Nernst number $5 < N_e < 10$) and high-magnetization regimes ($0.1 < N_e$) by tuning magnetic field and gas-jet parameters.

Probing In-Flight Vacuum Magnetic-Field Compression on OMEGA

J. L. Peebles,* F. García-Rubio, J. R. Davies, D. H. Barnak, P. V. Heuer, and R. Betti
Laboratory for Laser Energetics, University of Rochester
*Principal Investigator

Measurements of the compression of a magnetic field have remained elusive in laser-driven magnetohydrodynamic (MHD) experiments. These measurements are required to validate simulations for field conservation and loss mechanisms. The primary goal of this campaign was to measure the magnetic field at different stages of compression in a cylindrical target, which would provide experimental feedback for MHD codes. To do this, an experiment was carried out where a strong magnetic field (>65 T) was applied to a cylindrical implosion with a large radius. This large radius (twice the size of a typical cylindrical implosion on OMEGA) was chosen to provide enough of a window for proton probing to be used. Prior issues with using proton probing to measure magnetic fields transverse to the primary field axis was that deflection was too large; to address this we probed down the axis of the cylinder, which has been proven to be a more-accurate measurement for fields of this magnitude. Ideally this probing could be done while the shell is in-flight, providing many data points on field strength and compression.

The experimental setup is shown in Fig. 20. The well-benchmarked cylindrical implosion setup used for MagLIF experiments was modified to drive a narrower portion of the cylinder. Since the cylinder was twice the radius of typical cylindrical experiments, intensity on target had to be maintained by doubling beams on a portion half the length of the typical MagLIF implosion. The tube was left empty of gas for ease of construction since field compression should occur regardless of fill. A D^3He exploding-pusher proton source was used to probe the interaction; since the drive for the exploding pusher and the cylinder needed to be the same pulse shape and the proton source benefits from shorter, higher-intensity pulses, there was a long coasting period for the compressing cylinder. An image plate placed on the wedge range filter module (WRFM) allowed for a simultaneous x-ray measurement of the mesh fiducial, which indicated the initial angle of the mesh without field deflections.

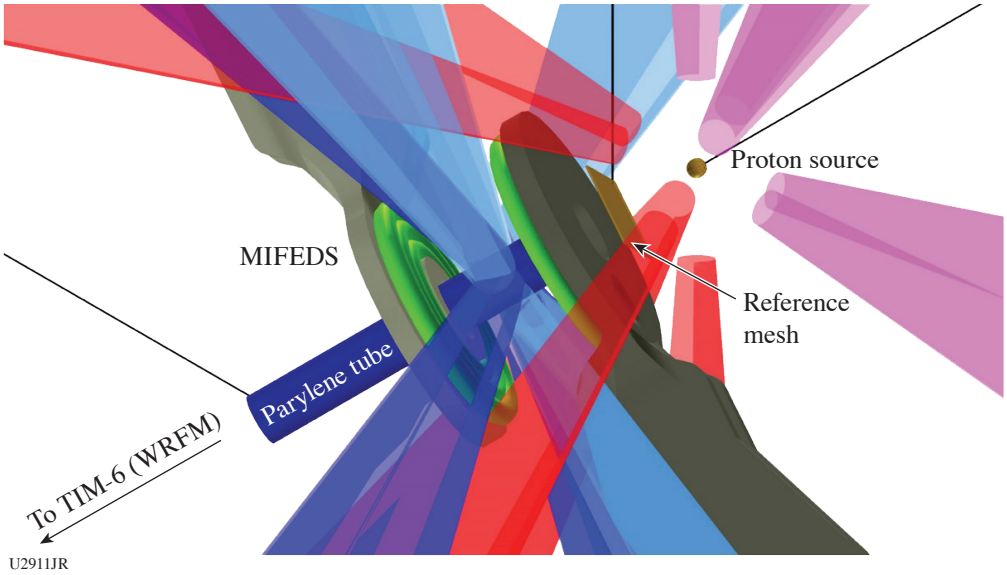

Figure 20
Schematic of the experimental setup. A large-radius cylindrical implosion is radiographed axially by protons, measuring the field applied by the MIFEDS coils.

Six shots were carried out in the campaign: three without the magnetic field and three shots with the magnetic field. The reference shots without the magnetic field were able to image the reference mesh at two different stages of compression. Since there was no field, the mesh appeared to be stable regardless of probe time, with the compressing shell scattering the protons later in time. As shown in Fig. 21, the mesh can be distinguished at nearly any stage of compression. X-ray framing camera data indicated that the shell coasts to full compression by 4.5 ns, where the probe at 3.5 ns can probe a region roughly 350 μm in diameter. Proton attenuation from scattering removes most of the signal from the regions where the shell has been in flight, although the proton signal appeared to decrease throughout the shot day (despite neutronics indicating otherwise).

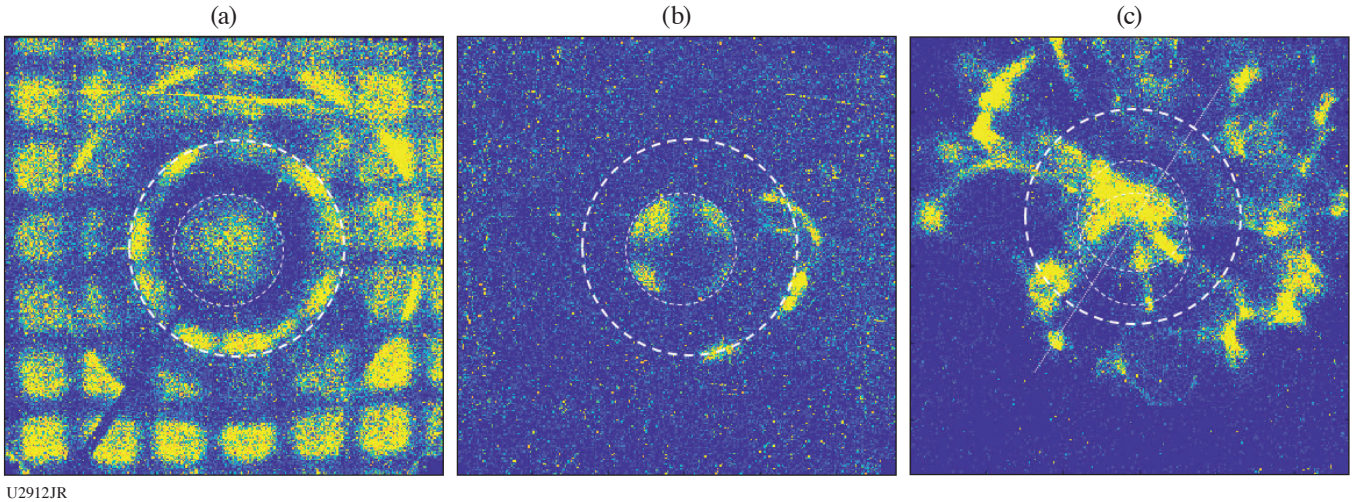

Figure 21
Proton probes of three different shots. The probes are timed at 1.0, 3.5, and 3.5 ns with the field off, off and on, and left to right, respectively. The grid is clearly distinguishable in the first two images, although at 3.5 ns the cylinder is nearly fully compressed. When the field is added, however, the mesh distorted beyond identifiability, even though the compression is at the same stage as the second image.

Difficulties with the MIFEDS led the diagnostic to be disqualified for use after the shot day since the unit entered a self-charge state when getting ready for the seventh shot and destroyed the target. For one of the magnetized shots, the reference mesh was apparently lost close to shot time (after the Target Viewing System was shuttered). Late timing of the proton probe for another magnetized shot led to missing the compressed field. This led to only one shot with usable magnetized data. Due to a mistiming of one of the MIFEDS units, the field was lower and asymmetric. Upon adding the external magnetic field, the very clear mesh was heavily distorted such that the angle of the mesh could not be identified. Fourier analysis indicated that some features may be aligned with a 37° rotation of the mesh; however, this appears unlikely since this would indicate much higher field compression than the shell at this stage could accomplish. While the field for this shot was not ideal, it alone does not explain the complete distortion of the radiograph. More likely, the ends of the field compression region are significantly more complex than an ideal compression.

For future shot days exploring field compression it would be of great benefit to have additional data points earlier in the compression. Presumably, field-distortion effects would not be so strong early into compression. By probing earlier in time, more of the mesh is visible on the probe, making the process of identifying mesh lines and angles much more likely. Other improvements would include shortening the length of the tube; the length of tube combined with the proximity to the proton source meant that two of the rings seen on the early time radiographs are the uncompressed regions of the tube close to and far away from the source. Shortening the tube to 1 to 2 mm (rather than 10+ mm) would shrink this feature substantially. Improvements made to the MIFEDS diagnostic since this shot day have also made its usage much more reliable.

This experiment was conducted at the Omega Laser Facility at the University of Rochester's Laboratory for Laser Energetics with the beam time through the Laboratory Basic Science program.

Electron Energization in Colliding and Reconnecting Magnetized Plasmas

M. J. Rosenberg,[1*] G. Fiksel,[2] W. Fox,[3] D. Schaeffer,[4] and C. K. Li[5]
[1]Laboratory for Laser Energetics, University of Rochester
[2]University of Michigan
[3]Princeton Plasma Physics Laboratory
[4]Princeton University
[5]Massachusetts Institute of Technology
[*]Principal Investigator

The MagRecon-22A shot day on OMEGA (17 February 2022) through the LBS Program successfully demonstrated an enhancement in the suprathermal electron population in laser-plasma experiments that drove the collision or reconnection of plasma plumes carrying self-generated magnetic fields. The energization of particles during the annihilation of magnetic fields is a common process in astrophysical plasmas, but is poorly understood and has rarely been investigated in the laboratory. The experiments use the interaction of 200-J, 0.5-ns laser pulses with 5-μm-thick CH foils to produce Biermann-battery magnetic fields that azimuthally encircle the expanding plasma created by each beam. While previous experiments[40] [illustrated schematically in Fig. 22(a)] showed that the interaction of two adjacent plasma plumes containing antiparallel magnetic fields, which undergo magnetic reconnection, enhanced the energetic electron population in the direction of the reconnection current sheet, it was not proven whether this was due to the collision or due to reconnection itself. To address this question, this shot day employed the configuration shown in Fig. 22(b), in which the experimental geometry is altered so that the magnetic fields are parallel in the collision region and do not reconnect.

The energized electron spectra are shown in Fig. 23. Preliminary analysis shows that experiments with colliding parallel fields produce significantly more than twice the energized electron population than experiments with only a single laser–foil interaction (and therefore no collision), indicating that the plasma plume collision contributes partially to the acceleration of electrons regardless of the magnetic-field orientation or any reconnection. In addition, the magnetic reconnection experiments show more electron energization than in experiments driving the collision of parallel magnetic fields, although there is significant shot-to-shot variation. These results suggest that the magnetized plasma plume collision causes some acceleration of electrons, possibly through a Fermi-like mechanism, but that magnetic reconnection is a significant contributor to electron energization. This platform can therefore be used in further experiments to study the dependence of magnetic reconnection-induced particle energization on reconnection parameters like collisionality.

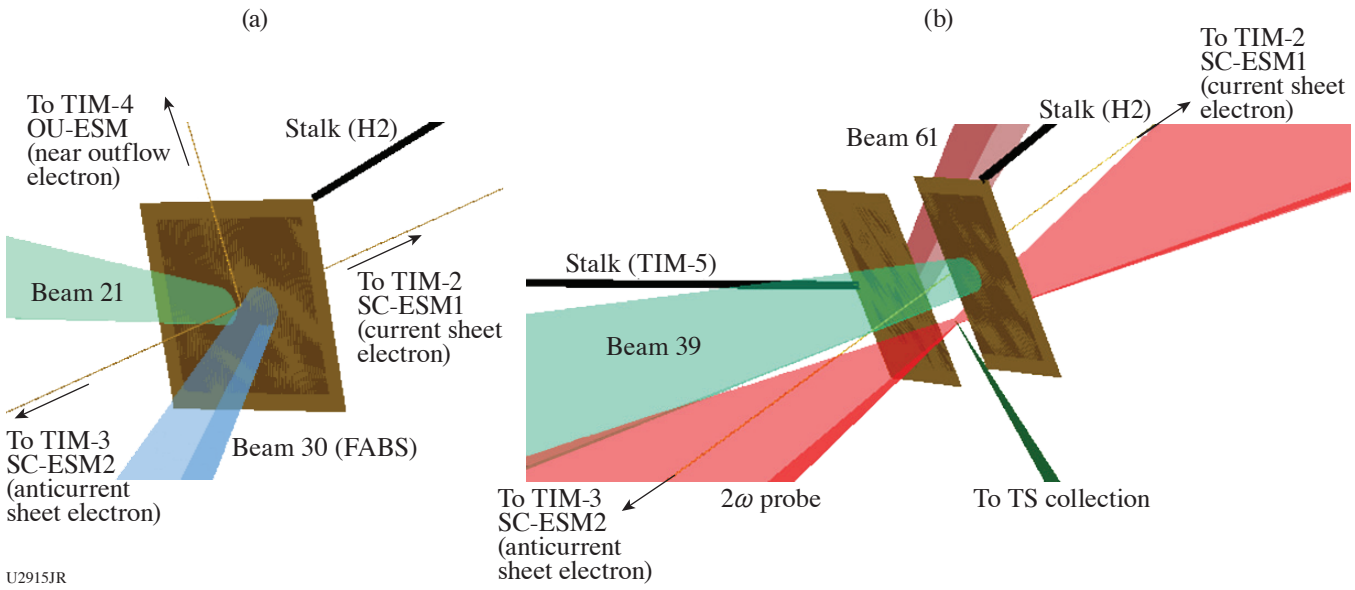

Figure 22
Experimental setup for (a) reconnection of anti-parallel magnetic fields and (b) collision (but no reconnection) of parallel magnetic fields. OU-ESM: Osaka University electron spectrometer; SC-ESM: single channel spectrometer; FABS: full-aperture backscatter station; TS: Thomson scattering.

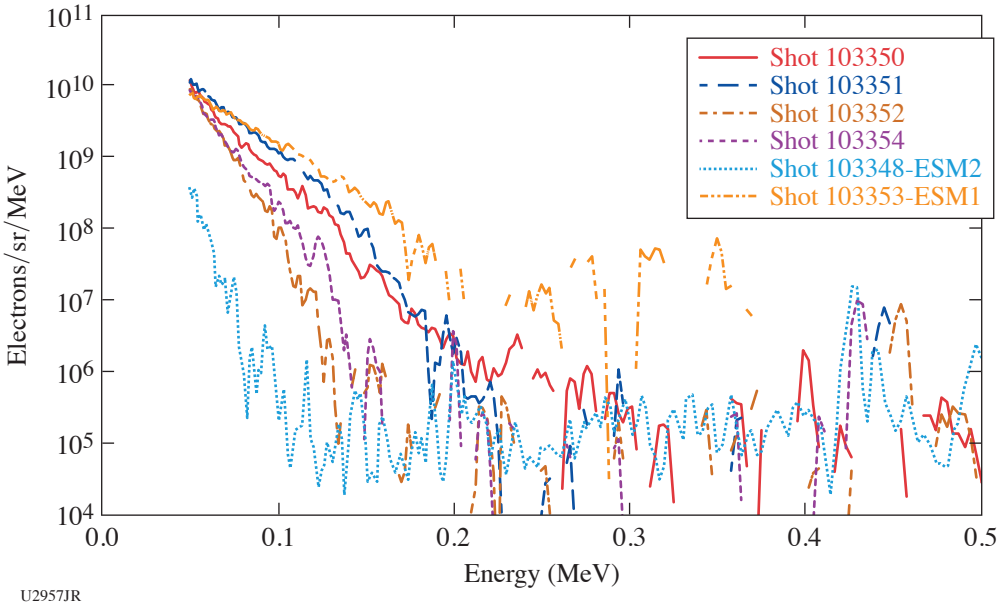

Figure 23
Measured energetic electron spectra for: one-beam experiments (no collision nor reconnection) (dashed curve), colliding parallel magnetic-field experiments (collision, but no reconnection) (thin solid curves), and reconnection (thick solid curves) experiments. The data have been background subtracted. The reconnection spectrum shows more energization than the parallel magnetic-field experiments (with significant variation).

These experiments were conducted at the Omega Laser Facility at the University of Rochester's Laboratory for Laser Energetics with the beam time through the Laboratory Basic Science Program.

Measuring Electron Densities in Nonlocal Thermodynamic Equilibrium Plasmas Using Isoelectronic Line Ratios

G. Pérez-Callejo,[1] E. V. Marley,[2] D. A. Liedahl,[2] J. A. Emig,[2] and M. B. Schneider[2*]
[1]Universidad de Valladolid, Spain
[2]Lawrence Livermore National Laboratory
[*]Principal Investigator

Measuring electron temperatures and densities in HED plasmas is no easy task. To that end, several different diagnostics have been designed, each exploiting one or several characteristics of these extreme plasmas, in order to extract information about their conditions. In particular, x-ray spectroscopy has proved to be a reliable diagnostic that can provide valuable information about the atomic structure of the elements in the plasma. A particularly bright component of the x-ray emission of HED plasmas is the He-like emission since He-like ions are present over a wide range of temperatures and densities. The brightest emission from these ions is, in most cases, the He_α complex, which comprises two He-like transitions and a significant contribution from Li-like ions. However, this complex is also heavily affected by optical depth effects, sensitive to gradients in the plasma, which makes it difficult to extract useful information (and usually other simpler lines are used).

In this experiment, we generated a uniform two-element plasma using a similar platform that was used in the past to characterize optical depth effects.[41] By placing a thin disk of CaS buried in a CH tamper, an axially expanding cylindrical plasma at 1 to 2 keV with $n_\mathrm{e} \sim 10^{21}$ cm^{-3} was generated. We recorded the x-ray emission spectra from both Ca and S, as well as the target size as a function of time. Since Ca and S are in the same proportion in the plasma, and at the same temperature and density conditions, the optical depth effects on their He_α emission are very similar and can be canceled out. This makes it possible to extract the electron density from the ratio $\left(w_\mathrm{s}/y_\mathrm{s}\right)/\left(w_{\mathrm{c}_\alpha}/y_{\mathrm{c}_\alpha}\right)$, where w and y are the two He-like transitions that make up the He_α emmission and the subindices are used to denote the element. All of the instruments obtained good data, which are currently being post-processed. Preliminary analysis of the data hints to the possibility that S dissolved into the target rather than staying confined to the buried layer (Fig. 24). This was a possibility since it was the first time that a salt-like component was used in this configuration, and target development was necessary. Careful post-processing of the spectral data is required to verify this possibility.

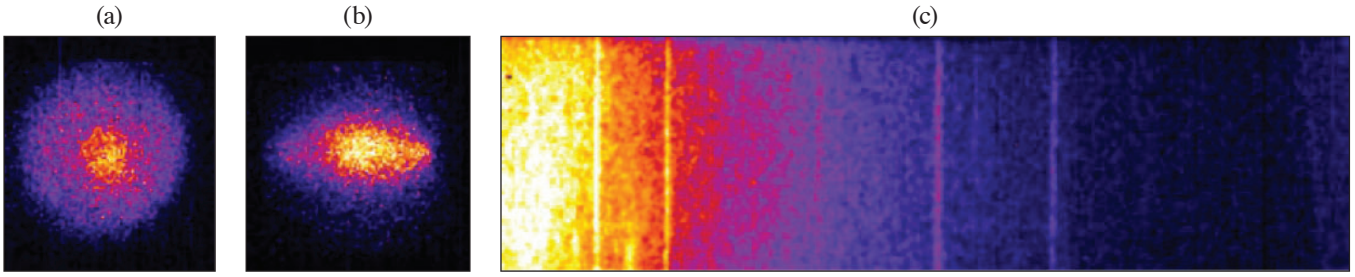

Figure 24
Example set of data from the experiment. (a) Top and (b) side view of the cylindrical plasma(c) S x-ray emission spectrum. The Ca spectrum was only obtained on film, which is currently being digitized.

This work was performed under the auspices of the U.S. Department of Energy by Lawrence Livermore National Laboratory under Contract DE-AC52-07NA27344. This document was prepared as an account of work sponsored by an agency of the United States government. Neither the United States government nor Lawrence Livermore National Security, LLC, nor any of their employees makes any warranty, expressed or implied, or assumes any legal liability or responsibility for the accuracy, completeness, or usefulness of any information, apparatus, product, or process disclosed, or represents that its use would not infringe privately owned rights. Reference herein to any specific commercial product, process, or service by trade name, trademark, manufacturer, or otherwise does not necessarily constitute or imply its endorsement, recommendation, or favoring by the United States government or Lawrence Livermore National Security, LLC. The views and opinions of authors expressed herein do not necessarily state or reflect those of the United States government or Lawrence Livermore National Security, LLC, and shall not be used for advertising or product endorsement purposes. The work has also been supported by the Research Grant No. PID2019-108764RB-I00 from the Spanish Ministry of Science and Innovation.

Probing the Fe–Ni Phase Space Using Powder X-Ray Diffraction Image Plates

S. M. Clarke,[1*] S. Singh,[1*] K. Bolduc,[2] and R. F. Smith[1]
[1]Lawrence Livermore National Laboratory
[2]University of Massachusetts, Amherst
[*]Principal Investigators

In this campaign we studied Fe–Ni, an alloyed material with geophysical relevance, under dynamic compression. The three goals to this experiment were to (1) determine the effect of Ni composition on the onset of melting on the Hugoniot, (2) understand the stability field of the γ [face-centered cubic (fcc)] phase within the alloy, and (3) develop a general methodology for investigating alloy materials under dynamic compression. Previous static compression experiments have shown that the incorporation of nickel expands the stability field of the fcc phase relative to the hexagonal close-packed (hcp) phase, thus changing the slope of the phase boundary.[42]

We successfully performed 13 shots: eight probing a shocked state and five probing a ramped state. For each shot we used one beam as a 2-ns x-ray backlighter and one beam to drive a shock- or ramp-compression wave in the sample. From the ramp-compression experiments, we found that alloying did not change the structure along the ramp quasi-isentrope. The Fe–Ni alloy maintained the hcp structure like the behavior of pure Fe. Preliminary analysis suggests we reached alloy densities over 15 g/cm^3. For the shock-compression samples, we targeted pressures near the melt line (see Fig. 25). Preliminary analysis suggests a diffraction signal consistent with melt in some shots, and a mixture of melt and high-pressure hcp phase in other shots. Pressure determination for these shots is ongoing, and when the analysis is complete, we will compare the onset of melt for the alloy to that of Fe to better understand the effect of alloying on the melt line. We do not observe the existence of a high-pressure bcc phase on the Hugoniot, in contrast to previous findings from other groups and theoretical predictions.[43] We hope to include all the data in a publication about the behavior of Fe–Ni alloys under dynamic compression.

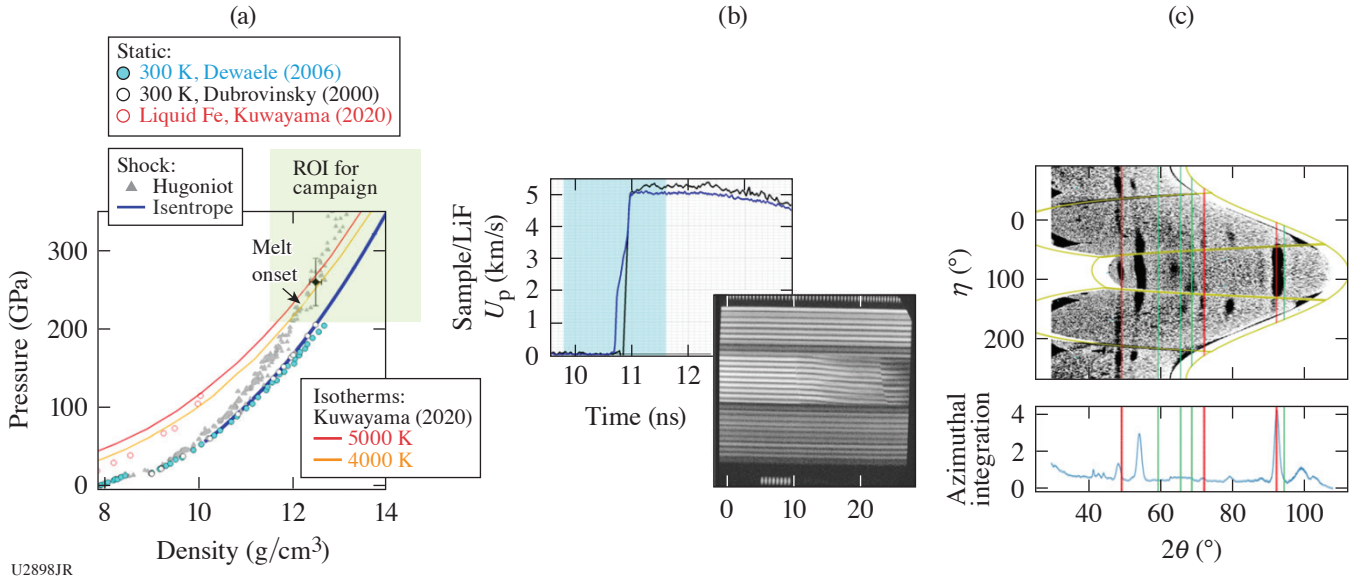

Figure 25
(a) Density versus pressure plot for Fe with the region of interest for this campaign highlighted in green. (b) Example of raw VISAR data and analyzed data showing the particle velocity at the sample/LiF interface, which can be used to determine the pressure in the sample. The blue highlighted region shows where the 2-ns x-ray pulse probed in time. (c) An example of analyzed data from the powder x-ray diffraction image-plate (PXRDIP) diagnostic. This diagnostic will provide information about the density and phase of the alloy on compression. ROI: region of interest.

This work was performed under the auspices of the U.S. Department of Energy by Lawrence Livermore National Laboratory under Contract DE-AC52-07NA27344.

Measuring the Viscosity of MgO at Lower-Mantle Conditions

R. F. Smith,[1*] T. Perez,[2] S. Ali,[1] P. M. Celliers,[1] F. Coppari,[1] J. H. Eggert,[1] and J. K. Wicks[2]
[1]Lawrence Livermore National Laboratory
[2]Department of Earth and Planetary Sciences, Johns Hopkins University
[*]Principal Investigator

The viscosity of MgO under high pressures and temperatures strongly influences a terrestrial planet's mantle dynamics, which impacts the planet's chemical and thermal evolution. Characterizing mantle dynamics is crucial in our understanding of the geologic history of planets in our solar system, as well as establishing habitability of exoplanetary systems. Despite the importance of MgO viscosity, there is currently no consensus from either theory or experiment on its value at mantle conditions. Here we use new experimental techniques to constrain the rheological properties of MgO at pressures and temperatures relevant to the Earth's mantle. The results of these experiments will constrain mantle dynamics models, aiding our understanding of planetary interior evolution and surface habitability.

The OMEGA EP laser ramp drive allows us to reach lower-mantle pressures over a wide range of strain rates while providing direct constraints of viscosity with the OMEGA EP active shock breakout (ASBO–VISAR) diagnostic. The target design for this experimental campaign is shown schematically in Fig. 26. Perturbed interfaces between ablation layer and sample create perturbed shock waves and Rayleigh–Taylor (RT) instabilities that can be tracked with VISAR to constrain rheological properties. An example of the data obtained is shown in Fig. 27. Our shot day was very successful and data analysis is ongoing.

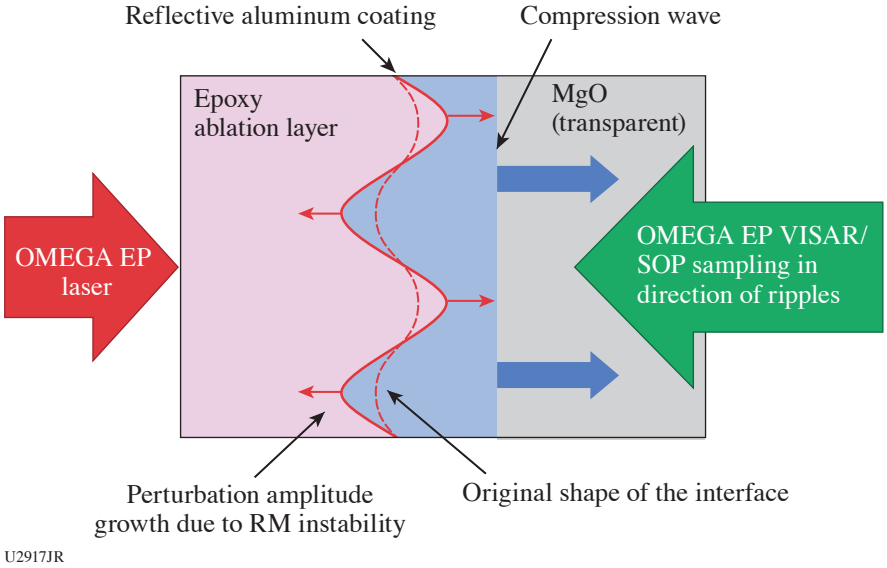

Figure 26
Conceptual design of viscosity measurements on OMEGA EP. The laser-ablated shock wave takes on sinusoidal shape after passing through rippled epoxy–MgO interface and undergoes damped oscillation controlled by viscosity. VISAR/SOP can track continuous breakout of ripple anti-node on wedged interface and therefore can constrain viscosity. RM: Richtmyer–Meskov.

This experiment was conducted at the Omega Laser Facility at the University of Rochester's Laboratory for Laser Energetics with the beam time through the Laboratory Basic Science program.

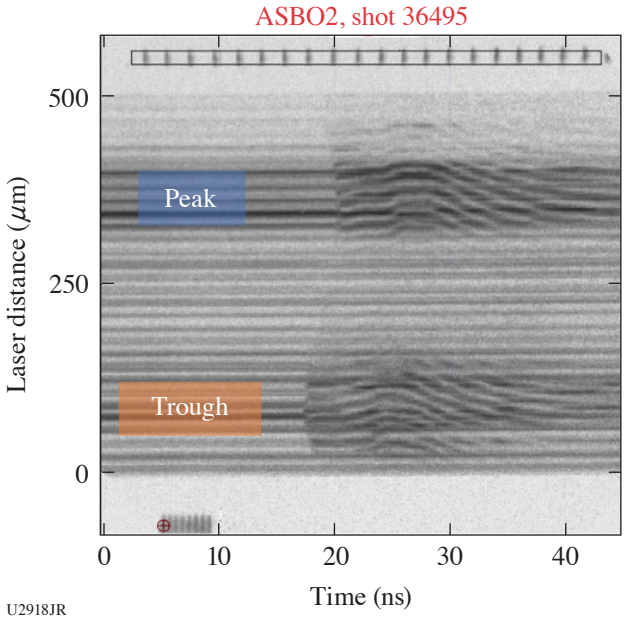

Figure 27
Example VISAR/ASBO data using the design from Fig. 26.

Studying the T–T Reaction at Energies Exceeding 2 MeV on OMEGA

A. Schwemmlein,[1*] C. Stoeckl,[1*] W. U. Schröder,[2] and W. T. Shmayda[1]
[1]Laboratory for Laser Energetics, University of Rochester
[2]Department of Chemistry, University of Rochester
[*]Principal Investigator

TNSA provides a unique opportunity to generate rare-isotope particle beams for nuclear-reaction experiments. Such experiments can be done at short-pulse laser facilities. In this technique, the surface of a small ($500 \times 500 \times 20$-μm^3) metallic converter foil is doped with the particle specie to be accelerated. When the foil is hit from the back with a high-power ($>10^{18}$ W/cm^2) laser pulse, particles from the foil surface layers are ejected and accelerated by the strong electric fields generated in the process. This approach is especially interesting for the generation of a beam of energetic tritons ($^3H^+$), which is presently not available anywhere. TNSA pilot studies on OMEGA EP[44,45] have generated beams of tritons capable of inducing nuclear reactions, for example, D–T fusion in a secondary, deuterated physics target. Utilizing this beam to study the tritium–tritium (T–T) reaction in a similar fashion can answer open questions about the predominant T–T reaction channel, as well as the structure of the compound nucleus ^{6}He. It is noteworthy that the tritium used in viable TNSA experiments is confined within small volumes of metal lattice and in amounts that are orders-of-magnitude smaller than in comparable accelerator experiments.

A follow-up experiment utilized improved converter and physics targets, each consisting of a stainless-steel substrate and an unpassivated 500-nm titanium layer. A radio-chemical analysis of the targets revealed a tritium content about 5× higher (670 μCi versus 130 μCi) compared to the pilot study. A control experiment with this type of converter foil and a secondary deuterated physics target produced the expected D–T fusion neutrons (see Fig. 28). However, the total neutron yield did not improve appreciably compared to the pilot study, suggesting that the additional tritium in the improved converter foil did not participate in the TNSA process.

A new experiment was conducted to study the triton-on-tritium (t–T) reaction. Here, the deuterated physics target was replaced with a tritiated physics target. The resulting spectrum of TT neutrons is compared in Fig. 28 with those of the D–T control reaction. The absence of neutrons above the background in the former spectrum is consistent with the much-lower T–T reaction cross section that was previously reported,[46] up to about $E_t \approx 1$ MeV. This new result is a first indication that the T–T reaction does not proceed via the third excited state of ^{6}He at 2.3 MeV above the T–T reaction threshold—an energy that could not be reached in past experiments. Like in the D–T reaction, which proceeds via ^{5}He, population of this ^{6}He state would noticeably increase the reaction cross section.

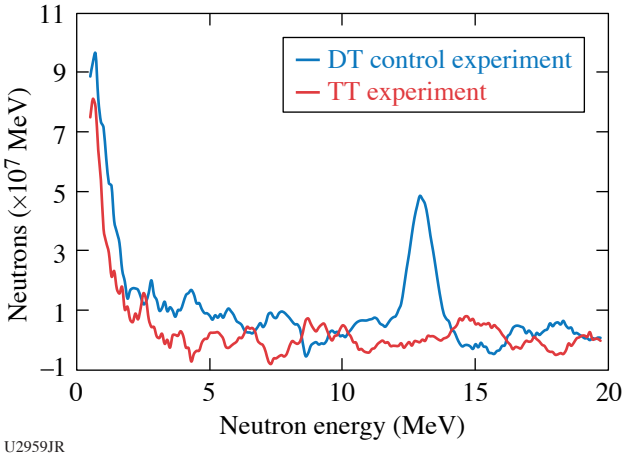

Figure 28
Neutron time-of-flight spectrum from the "8 × 4 nTOF" detector in energy space. While the TNSA triton beam generated a DT peak with a secondary deuterated target in the control experiment, no neutrons above the background were observed in the experiment with a secondary tritiated target.

These experiments were conducted at the Omega Laser Facility at the University of Rochester's Laboratory for Laser Energetics with the beam time through the Laboratory Basic Science Program.

Angular Momentum Transport in Disk-Jet Transitions

G. Swadling,[1*] F. Suzuki-Vidal,[2] V. Valenzuela-Villaseca,[2] M. Bailly-Grandvaux,[3] and C. Walsh[1]
[1]Lawrence Livermore National Laboratory
[2]Imperial College London, UK
[3]University of California, San Diego
[*]Principal Investigator

First experiments were performed on OMEGA looking at the formation of supersonic rotating plasmas as a platform to study fundamental HED hydrodynamics and laboratory astrophysics.[47] These experiments were part of the AngMomentumDisk-22A Campaign and were performed on 9 February 2022.

The experiments consisted of a target package made of six V-shaped apertures in a circular array with a diameter of ~12 mm [Fig. 29(a)], 3-D printed in CH. Each V-shaped target has a 5° tilt respect to the axis of the array, with each target "face" illuminated by a 3ω 500-ns, 1-ns square beam. This drives simultaneous radial plasma flows off-axis, injecting initial angular momentum and thus driving a rotating plasma.

The main diagnostic was optical Thomson scattering in spatially resolved mode, using 120 J with a duration of 3.7 ns. Scattered light was collected at 63° from the input **k** vector. Data consisted of IAW and EPW spectra. Example results are shown in Figs. 29(b) and 29(c) from 5 to 8.7 ns at a position −500 μm from the axis of the array. The results were very consistent for all shots. Analysis of the IAW spectra at 8 ns is shown in Fig. 29(d), which results in plasma parameters of the rotating plasma constrained by analysis of the EPW spectra at the same time. Plasma parameters are in line with 3-D numerical simulations with the *GORGON* code.[48]

The experiment was conducted at the Omega Laser Facility at the University of Rochester's Laboratory for Laser Energetics with the beam time through the Laboratory Basic Science (LBS) Program. Work was performed under the auspices of the U.S. DOE by LLNL under Contract DE-AC52-07NA27344. Research supported by The Royal Society through a University Research Fellowship.

1. M. Millot *et al.*, Nature **569**, 251 (2019).
2. M. Millot *et al.*, Nat. Phys. **14**, 297 (2018).
3. B. Cheng *et al.*, Nat. Phys. **17**, 1228 (2021).
4. Y.-J. Kim *et al.*, Sci. Rep. **11**, 5610 (2021).
5. S. Brygoo *et al.*, J. Appl. Phys. **118**, 195901 (2015).

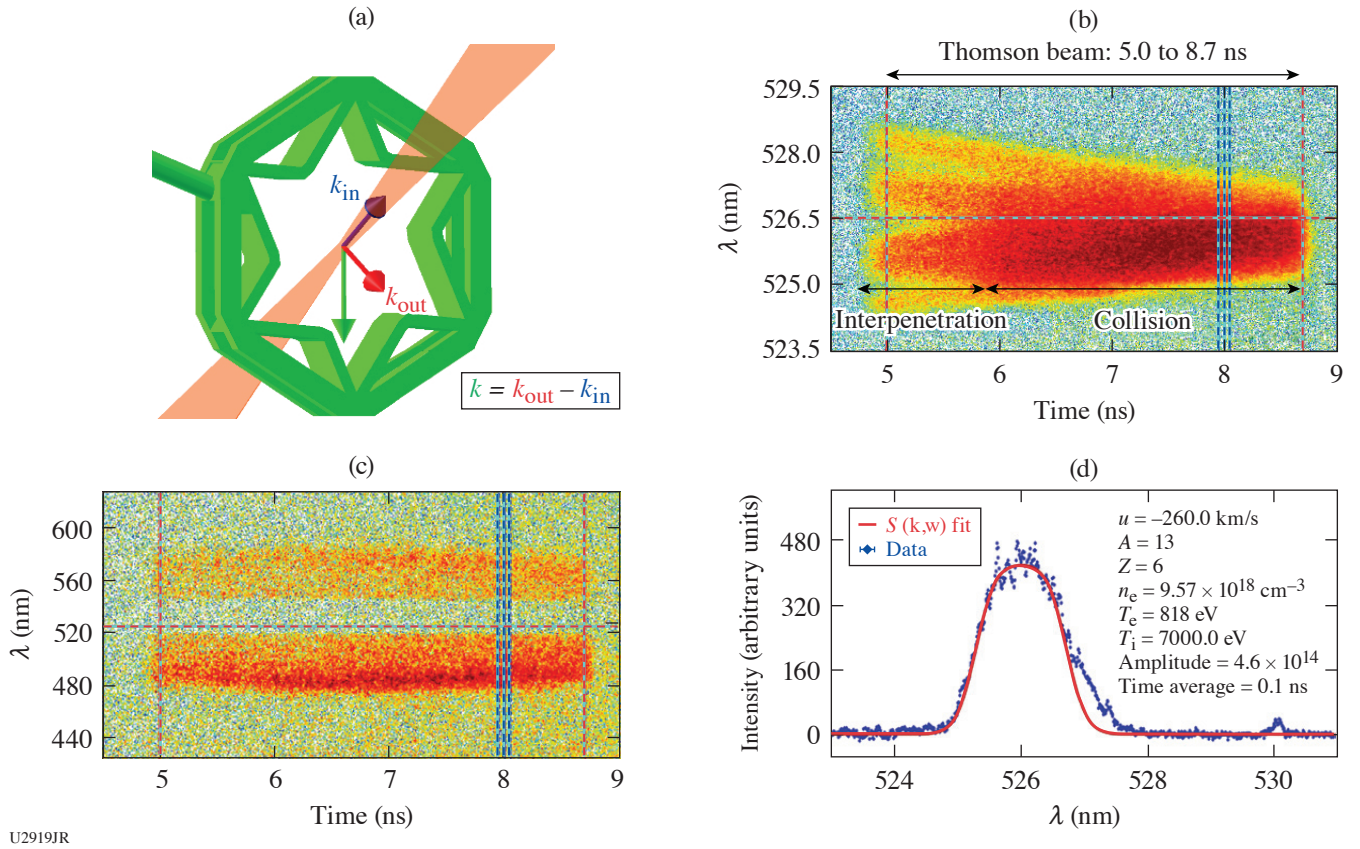

Figure 29
Overview of AngMomentumDisk-22A shot day. (a) *VISRAD* view of sixfold target with Thomson scattering geometry. [(b),(c)] Example results from Thomson scattering (shot 103212), EPW and IAW, respectively. Data were obtained from 5 to 8.7 ns after the beams illuminated the targets. (d) Lineout from IAW data at 8 ns, integrated over 100 ps together with a fit of the theoretical spectral density function $S(k,w)$, which allows measuring plasma parameters in the rotating plasma.

6. Y.-J. Kim *et al.*, Phys. Rev. Lett. **129**, 015701 (2022).
7. L. Gao *et al.*, Phys. Plasmas **23**, 043106 (2016).
8. A. Chien *et al.*, Nat. Phys. **19**, 254 (2023).
9. D. J. Stark, T. Toncian, and A. V. Arefiev, Phys. Rev. Lett. **116**, 185003 (2016).
10. H. G. Rinderknecht *et al.*, New J. Phys. **23**, 095009 (2021).
11. F. Spite and M. Spite, Astron. Astrophys. **115**, 357 (1982).
12. M. Tegmark *et al.*, Phys. Rev. D **69**, 103501 (2004).
13. S. Burles *et al.*, Phys. Rev. Lett. **82**, 4176 (1999).
14. A. B. Zylstra *et al.*, Rev. Sci. Instrum. **90**, 123504 (2019).
15. G. Q. Liao and Y. T. Li, IEEE Trans. Plasma Sci. **47**, 3002 (2019).
16. G. Liao *et al.*, Proc. Natl. Acad. Sci. **116**, 3994 (2019).
17. S. Herzer *et al.*, New J. Phys. **20**, 063019 (2018).
18. K. Y. Kim, University of Maryland, College Park, MD, Technical Report DOE-UMCP-3891 (5 May 2016).
19. G.-Q. Liao *et al.*, Phys. Rev. X **10**, 031062 (2020).
20. Y. Zeng *et al.*, Opt. Express **28**, 15258 (2020).
21. E. Wigner and H. B. Huntington, J. Chem. Phys. **3**, 764 (1935).
22. J. M. McMahon and D. M. Ceperley, Phys. Rev. B **84** (14), 144515 (2011); **85** (21), 219902(E) (2011).)
23. B. M. Haines *et al.*, Phys. Plasmas **21**, 092306 (2014).
24. L. V. Al'tshuler, S. E. Brusnikin, and E. A. Kuz'menkov, J. Appl. Mech. Tech. Phys. **28**, 129 (1987).

25. V. N. Goncharov *et al.*, Phys. Rev. Lett. **125**, 065001 (2020).
26. T. R. Boehly *et al.*, Opt. Commun. **133**, 495 (1997).
27. S. Ressel *et al.*, Phys. Plasmas **29**, 072713 (2022).
28. C. Stoeckl *et al.*, Rev. Sci. Instrum. **87**, 11E323 (2016).
29. D. T. Michel *et al.*, Rev. Sci. Instrum. **83**, 10E530 (2012).
30. I. V. Igumenshchev *et al.*, Phys. Plasmas **23**, 052702 (2016); A. Colaïtis *et al.*, J. Comput. Phys. **443**, 110537 (2021).
31. C. E. Parker, "The ^{3}H(d, γ) Reaction and the ^{3}H(d, γ)/^{3}H(d, n) Branching Ratio for $E_{\text{c.m.}} \leq 300$ keV," Ph.D. Thesis, Ohio University, 2016.
32. Y. Kim *et al.*, Phys. Rev. C **85**, 061601 (2012).
33. J. Jeet *et al.*, Phys. Rev. C **104**, 054611 (2021).
34. A. Nishiguchi *et al.*, Phys. Rev. Lett. **53**, 262 (1984).
35. S. A. Slutz *et al.*, Phys. Plasmas **17**, 056303 (2010).
36. M. R. Gomez *et al.*, Phys. Rev. Lett. **125**, 155002 (2020).
37. C. A. Walsh *et al.*, Phys. Rev. Lett. **118**, 155001 (2017).
38. C. Ahdida *et al.*, Front. Phys. **9**, 788253 (2022).
39. M. R. Weis *et al.*, Phys. Plasmas **28**, 012705 (2021).
40. G. Fiksel *et al.*, J. Plasma Phys. **87**, 905870411 (2021).
41. G. Pérez-Callejo *et al.*, Phys. Rev. Lett. **126**, 085001 (2021).
42. T. Komabayashi, K. Hirose, and Y. Ohishi, Phys. Chem. Miner. **39**, 329 (2012).
43. L. Dubrovinsky *et al.*, Science **316**, 1880 (2007).
44. A. K. Schwemmlein *et al.*, Nucl. Instrum. Methods Phys. Res. B **522**, 27 (2022).
45. C. Stoeckl *et al.*, Nucl. Instrum. Methods Phys. Res. B **453**, 41 (2019).
46. C. Wong, J. D. Anderson, and J. W. McClure, Nucl. Phys. **71**, 106 (1965).
47. D. D. Ryutov, Astrophys. Space Sci. **336**, 21 (2011).
48. A. Ciardi *et al.*, Phys. Plasmas **14**, 056501 (2007).

FY22 LaserNetUS Program

M. S. Wei

Laboratory for Laser Energetics, University of Rochester

UR/LLE is part of the LaserNetUS Collaborative Network established in 2018 and funded by the Department of Energy Fusion Energy Sciences within the Office of Science. The mission of LaserNetUS is to reestablish U.S. scientific competitiveness in high-energy-density physics and high-field optical science by advancing the frontiers of laser-science research, providing students and scientists with broad access to unique facilities and enabling technologies, and fostering collaboration among researchers and networks from around the world. During FY22, LaserNetUS facility nodes consisted of ten institutions including Colorado State University, Lawrence Berkeley National Laboratory, Lawrence Livermore National Laboratory (LLNL), SLAC, The Ohio State University, the University of Central Florida, the University of Nebraska-Lincoln, Institut National de la Recherche Scientifique, the University of Rochester, and the University of Texas at Austin. Through a coordinated annual call for proposals and an independent proposal review panel process, the LaserNetUS network makes available a variety of ultrafast, high-peak-power and high-energy, petawatt-class lasers including LLE's four-beam, high-energy and high-intensity OMEGA EP laser to users who do not have regular access to ultrahigh-intensity lasers.

UR/LLE provides an average of four shot days each year on OMEGA EP to LaserNetUS users. Since 2019, 18 projects have been awarded a total of 20 shot days on OMEGA EP, including 13 projects from the first three solicitations for shots in Cycle-1 (2019–2020), Cycle-2 (2020–2021), and Cycle-3 (2021–2022), and five new projects from the fourth solicitation completed during FY22 for experiments in Cycle-4 (2022–2023). During FY22, a total of 34 target shots were successfully conducted over four shot days for three LaserNetUS projects led by scientists from Princeton University, the University of California, San Diego (UCSD), and Lawrence Livermore National Laboratory (see Table I below). These three experiments involved three graduate students and four postdoctoral researchers. FY22 LaserNetUS user experiments are summarized below.

Table I: During FY22, three LaserNetUS Cycle-3 projects (blue-shaded cells) completed 34 target shots over four shot days and five new LaserNetUS projects selected from the Cycle-4 solicitation were approved with a total of five shot days for experiments on OMEGA EP in FY23.

Principal Investigator	Institution	Title	LaserNetUS beam-time cycle
M. R. Edwards	LLNL	Reaching an Electron–Positron Plasma with OMEGA EP	3
G. Righi	UCSD (now at LLNL)	Understanding Temperature Dependence of Iron Strength at High Pressure with Ramped Compression on OMEGA EP	3
S. Zhang	Princeton University	Study of Particle Acceleration in Magnetic Reconnection Using Laser-Powered Coils	3
M. Manuel	General Atomics	Characterization of Early-Stage, Quasi-Parallel, Collisionless-Shock Formation	4

Table I: During FY22, three LaserNetUS Cycle-3 projects (shaded cells) completed 34 target shots over four shot days and five new LaserNetUS projects selected from the Cycle-4 solicitation were approved with a total of five shot days for experiments on OMEGA EP in FY23 (continued).

Principal Investigator	Institution	Title	LaserNetUS beam-time cycle
I. Oleynik	University of South Florida	Exploring Metastability and Phase Transitions in Dynamically Compressed Amorphous Carbon	4
D. Schaeffer	Princeton University (now at University of California, Los Angeles)	Dependence of Particle Acceleration on Shock Structure in Magnetized Collisionless Shocks on OMEGA EP	4
M. Wadas	University of Michigan	Observation and Scaling of Vortex Rings Ejected from Shock-Accelerated Interfaces	4
J. Wicks	Johns Hopkins University	*In Situ* X-Ray Diffraction Study of Shock-Compressed Diamond: Improving Equation-of-State Models Through Data-Driven Experimental Designs	4

Controlling the Energy of Relativistic Positron Jets

M. R. Edwards,[1*] J. von der Linden,[2] J. L. Peebles,[3] L. Willingale,[4] G. Fiksel,[4] A. Link,[1] and H. Chen[1]
[1]Lawrence Livermore National Laboratory
[2]Max Planck Institute for Plasma Physics
[3]Laboratory for Laser Energetics, University of Rochester
[4]University of Michigan
[*]Principal Investigator

Creating a platform to study the physics of relativistic electron–positron plasmas requires control over the key parameters of laser-driven positron jets. Specifically, the positron beams produced by kilojoule-scale, 10-ps laser pulses focused on gold targets are too high in energy for efficient interactions at the electron and positron densities that we are currently able to achieve. The energy of generated positrons is dominated by their acceleration in the sheath field on the back surface of gold-disk targets. Here we examined two approaches for controlling the energy of these positron jets: (1) we increased the target diameter and (2) we generated a plasma using a long-pulse beam on the back surface of our primary target. Both approaches were designed to reduce the accelerating sheath field. Initial results indicate successful reduction in the average measured positron energy using both approaches. Figure 1 shows how the distribution of positron energies decreased for larger target diameters, following model expectations.

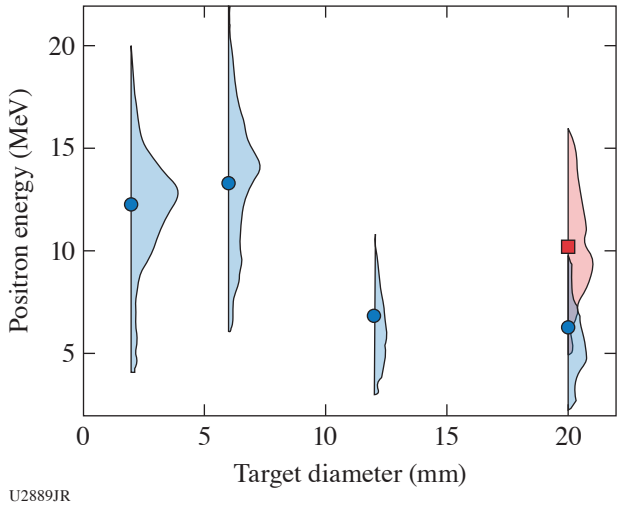

Figure 1
Measured positron energy distributions as a function of target diameter. Blue points are taken for targets under the same conditions. The red square corresponds to data taken with a microwire-coated target, producing enhanced yield and less energy reduction.

Initial analysis suggests scaling behavior follows expectations and that both mechanisms can, in principle, be used for energy control. The addition of microwires at the target front surface enhanced yield and reduced the effectiveness of the sheath field reduction.

Understanding Temperature Dependence of Iron Strength at High Pressure with Ramped Compression on OMEGA EP

G. Righi,[1*] Y.-J. Kim,[1] C. Stan,[1] M. Hill,[1] T. Lockard,[1] R. Rudd,[1] H.-S. Park,[1] and M. Meyers[2]
[1]Lawrence Livermore National Laboratory
[2]University of California, San Diego
[*]Principal Investigator

A fundamental material property—strength—is studied under high-stress and -temperature loading conditions (150 GPa, thousands of K) relevant to the interior of rocky planetary bodies. Experiments on OMEGA EP are well suited to probe this region of plastic deformation to better understand iron strength under these extreme conditions and to test physics-based constitutive models. Hydrodynamic simulations were used to design unique laser pulse shapes to probe iron samples at constant, high pressure, and different temperatures.

In the experiment, the Rayleigh–Taylor instability was used to infer the material's strength by analyzing the amount of growth of preimposed ripples and comparing to growth simulations. The VISAR (velocity interferometer system for any reflector) diagnostic was used to measure the pressure incident on the iron after laser irradiation of the custom 30-ns laser pulse. Radiography was used to image ripple iron samples at specific times (Fig. 2).

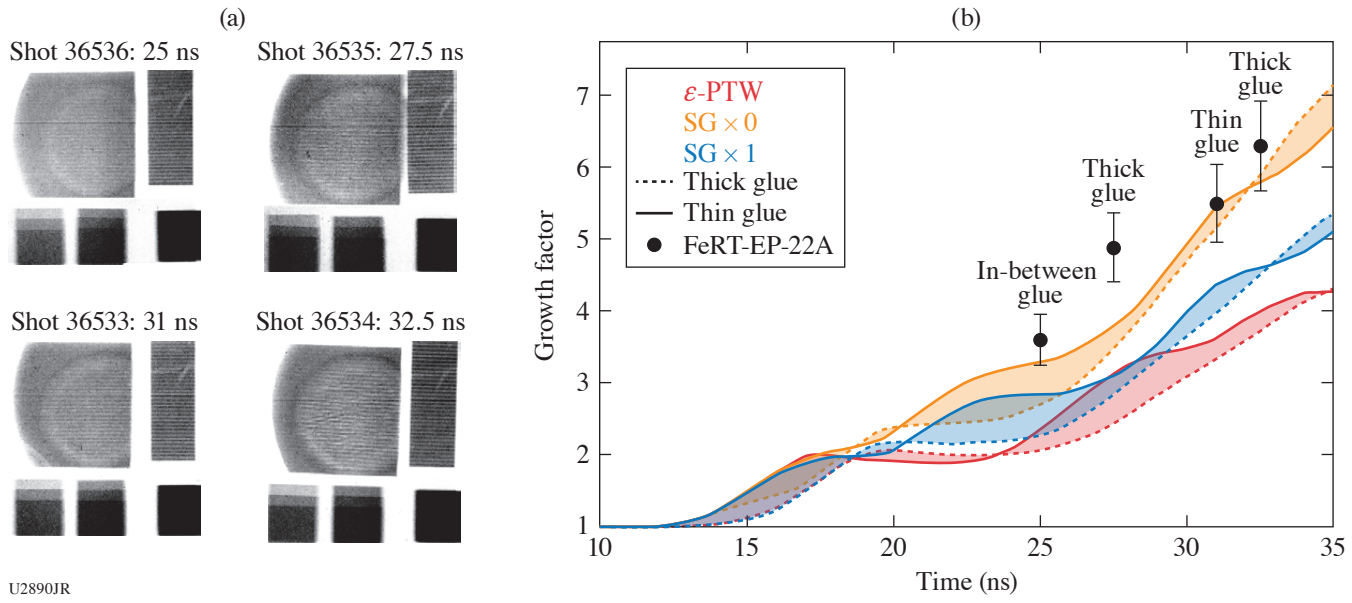

Figure 2
(a) High-quality radiographs taken at different delay times. The large, rippled sample shows clear evidence of laser spot size. Ripple material on the right side of each image is undriven material used for growth factor calculation. Steps and knife-edge on the bottom of each image are calibration metrics. (b) Growth factor predicted from hydrodynamic simulations compared to experimental data. Curves represent varying glue thicknesses according to target metrology. Data are consistent with low strength. PTW: Preston–Tonks–Wallace;[1] SG: Steinberg–Guinan.[2]

High-pressure, high-temperature shots (200 GPa, ~4000 K) were taken during one OMEGA EP shot day and preliminary results found that growth is larger than is predicted by the Preston–Tonks–Wallace[1] and Steinberg–Guinan[2] strength models. This suggests that iron is weaker than expected, contradictory to recent ultrahigh-pressure iron experiments at the National Ignition Facility. The differences between the experimental and simulated growth could be attributed to: (1) the high temperature allows

for easier deformation that the models and simulations are not accurately predicting or (2) the iron is unexpectedly melting. Further post-shot analysis and post-shot simulations will confirm results. An additional shot day is needed to probe the high-pressure, low-temperature regime of iron strength not discussed here.

The material is based upon work supported by the LLNL Academic Collaboration Team University Program (ACT-UP) award (subcontract B639114) and the Department of Energy, National nuclear Security Administration under Award Number DE-NA0003842. Part of this work was performed under the auspices of the U.S. Department of Energy by Lawrence Livermore National Laboratory under Contract DE-AC52-07NA27344.

Particle Acceleration Mechanisms in Magnetically Driven Reconnection Using Laser-Powered Capacitor Coils

S. Zhang,[1] A. Chien,[1] L. Gao,[2*] H. Ji,[1,2*] E. G. Blackman,[3] D. H. Froula,[4] D. Haberberger,[4] W. Daughton,[5] J. Moody,[6] and H. Chen[6]
[1]Princeton University
[2]Princeton Plasma Physics Laboratory
[3]Department of Physics and Astronomy, University of Rochester
[4]Laboratory for Laser Energetics, University of Rochester
[5]Los Alamos National Laboratory
[6]Lawrence Livermore National Laboratory
[*]Principal Investigators

Magnetic reconnection is a ubiquitous astrophysical process, whereby magnetic energy is rapidly converted into plasma kinetic energy in the form of bulk flow, thermal energy, and nonthermal particles. The latter is often regarded as an observational signature of reconnection, which can be a more-efficient particle accelerator than other processes such as collisionless shocks. In the past ~six years, our team has developed a platform to study acceleration of nonthermal electrons from magnetic reconnection at low plasma beta using UV laser-powered capacitor coils.[3] For the first time, nonthermal electrons accelerated by the reconnection electric field have been measured.[4] Using the short-pulse laser-powered capacitor coils newly developed by our group, we extended our platform to a new regime with tripled magnetic-field strength to achieve particle acceleration by magnetically driven axisymmetric reconnection with one order of magnitude higher energy. In FY22, under the LaserNetUS program, we successfully performed two shot days on OMEGA EP. The proton data show a clear signature of current sheet formation and evolution. Particle acceleration was also observed. Detailed analyses and particle-in-cell (PIC) simulations are underway.

The experimental setup shown in Fig. 3 built on our previous experiments using the short-pulse IR lasers. The main target is composed of two Cu plates with a laser entrance hole in the front plate, connected by a pair of parallel U-shaped coils. OMEGA EP backlighter Beam 2 was used to irradiate the back plate center at a 45° incidence angle, thereby positively charging up the back Cu

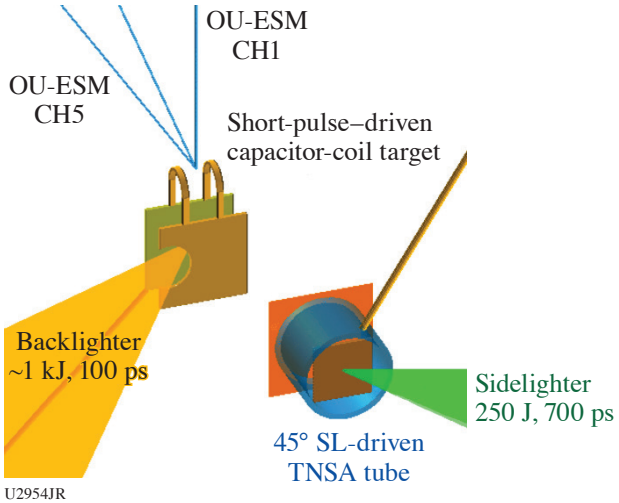

Figure 3
Experimental setup. The OMEGA EP BL was focused onto the back plate, positively charging it up. The resulting voltage difference between the back and front plate drives currents in both coils, creating reconnection. Ultrafast protons generated by the SL probed through the coils and was collected by a proton film back held by TIM-14. For shots aiming for particle acceleration, proton radiography was turned off, and OU-ESM, EPPS, and SC-ESM's were fielded at TIM-11, TIM-12, TIM-10, and TIM-13 to monitor particles at various angles.

plate. The voltage difference between the back and front plate drove the currents in both coils, creating reconnection in between. Face-on proton radiography was used to probe through the coils, capturing the magnetic-field topology change and associated fine structures. We positioned multiple particle spectrometers such as the Osaka University Electron Spectrometer (OU-ESM), single-channel electron spectrometer (SC-ESM), and electron–positron–proton spectrometer (EPPS) in TIM-10 to TIM-13 (ten-inch manipulators) to capture the energetic particles accelerated tangentially along the X-line, and compare the particle spectra at various distances and angles with respect to the reconnection region.

Figure 4 presents two examples of the proton images taken at 1 ns and 3 ns, with respect to the beginning of the sidelighter (SL) drive. Compared to the proton images obtained with UV lasers, these proton images see almost no plasma effects around the coils. Two prolate voids corresponding to magnetic-field generation around the coils are observed. In addition, at 3 ns a center feature developed between the voids corresponding to current sheet formation.

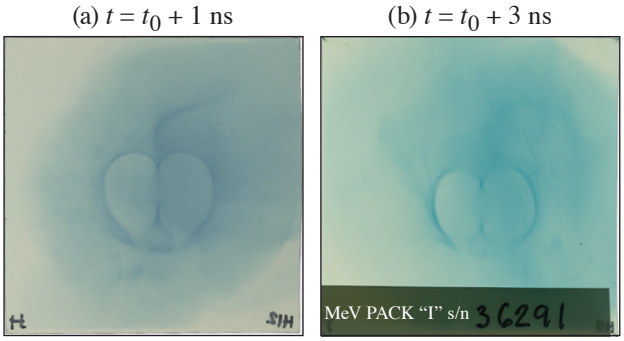

Figure 4
Photon radiographs taken at (a) 1 ns and (b) 3 ns with respect to the beginning of the SL.

Figure 5(a) presents the OU-ESM data for the reconnection case and Figs. 5(b) and 5(c) present two no-reconnection cases. The no-reconnection case had only one coil (either left or right), thereby no reconnection occurred. Compared to the data from the no-reconnection cases, the electron spectra for the reconnection case had much higher signals and a significant bump at ~80 keV is clearly seen. These data will be compared with in-depth PIC simulations as well as our previous observations using the UV drivers.

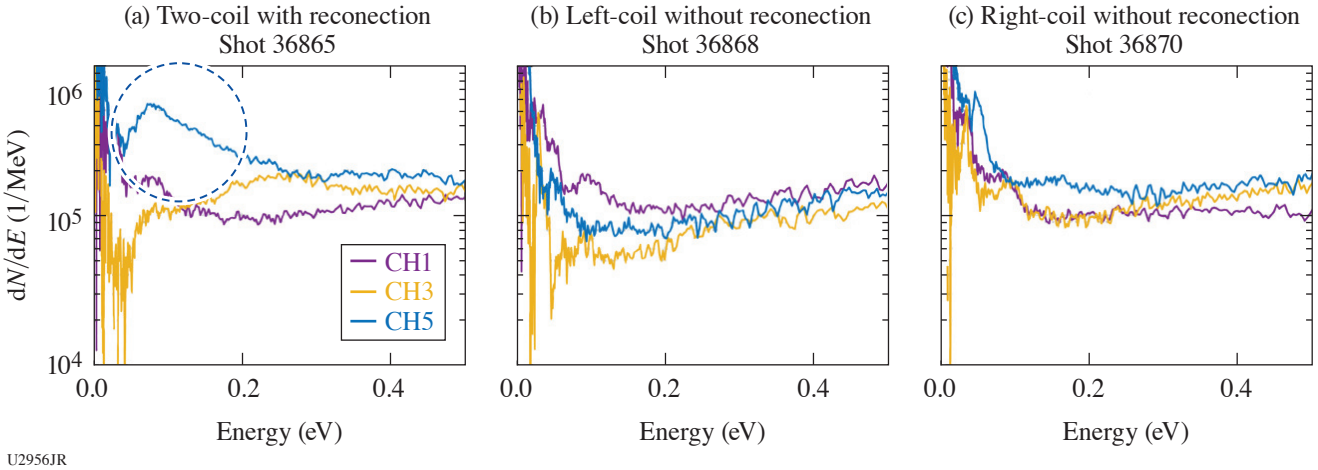

Figure 5
(a) OU-ESM data for the reconnection case and [(b),(c)] two no-reconnection cases.

We acknowledge the Omega Laser Facility staff at the Laboratory for Laser Energetics. This work was performed under the auspices of U.S. DOE Office of Science under the HEDLP program with award number DE-SC0020103 with beam time through LaserNetUS.

1. D. L. Preston, D. L. Tonks, and D. C. Wallace, J. Appl. Phys. **93**, 211 (2003).
2. D. J. Steinberg, S. G. Cochran, and M. W. Guinan, J. Appl. Phys. **51**, 1498 (1980).
3. L. Gao *et al.*, Phys. Plasmas **23**, 043106 (2016).
4. A. Chien *et al.*, Nat. Phys. **19**, 254 (2023).

Publications and Conference Presentations

Publications

H. Abu-Shawareb *et al.*, "Lawson Criterion for Ignition Exceeded in an Inertial Fusion Experiment," Phys. Rev. Lett. **129**, 075001 (2022).

D. Barlow, T. Goffrey, K. Bennett, R. H. H. Scott, K. Glize, W. Theobald, K. Anderson, A. A. Solodov, M. J. Rosenberg, M. Hohenberger, N. C. Woolsey, P. Bradford, M. Khan, and T. D. Arber, "Role of Hot Electrons in Shock Ignition Constrained by Experiment at the National Ignition Facility," Phys. Plasmas **29**, 082704 (2022).

G. Bruhaug, G. W. Collins, H. G. Rinderknecht, J. R. Rygg, J. L. Shaw, M. S. Wei, M. S. Freeman, F. E. Merrill, L. P. Neukirch, and C. H. Wilde, "Analysis Methods for Electron Radiography Based on Laser-Plasma Accelerators," in Proc. NAPAC2022 (JACoW Publishing, Geneva, Switzerland, 2022), pp. 274–277.

Z. Chen, S. X. Hu, and N. P. Bigelow, "Imprinting a Three-Dimensional Skyrmion in a Bose–Einstein Condensate Via a Raman Process," J. Low Temp. Phys. **208**, 172 (2022).

K. Churnetski, K. M. Woo, W. Theobald, P. B. Radha, R. Betti, V. Gopalaswamy, I. V. Igumenshchev, S. T. Ivancic, M. Michalko, R. C. Shah, C. Stoeckl, C. A. Thomas, and S. P. Regan, "Three-Dimensional Hot-Spot X-Ray Emission Tomography from Cryogenic Deuterium–Tritium Direct-Drive Implosions on OMEGA," Rev. Sci. Instrum. **93**, 093530 (2022).

S. X. Coffing, C. L. Fryer, H. F. Robey, C. J. Fontes, S. R. Wood, P. M. Kozlowski, H. M. Johns, D. D. Meyerhofer, T. Byvank, A. Liao, and T. J. Urbatsch, "Inferring the Temperature Profile of the Radiative Shock in the COAX Experiment with Shock Radiography, Dante, and Spectral Temperature Diagnostics," Phys. Plasmas **29**, 083302 (2022).

A. Colaïtis, D. P. Turnbull, I. V. Igumenshchev, D. Edgell, R. C. Shah, O. M. Mannion, C. Stoeckl, D. Jacobs-Perkins, A. Shvydky, R. Janezic, A. Kalb, D. Cao, C. J. Forrest, J. Kwiatkowski, S. Regan, W. Theobald, V. N. Goncharov, and D. H. Froula, "3D Simulations Capture the Persistent Low-Mode Asymmetries Evident in Laser-Direct-Drive Implosions on OMEGA," Phys. Rev. Lett. **129**, 095001 (2022).

T. Cordova, M. J. MacDonald, T. Döppner, F. N. Beg, M. Dozieres, B. Kozioziemski, N. A. Pablant, C. M. Sorce, and N. G. Whiting, "Absolute Calibration of the Conical Crystal Configuration of the Zinc Spectrometer (ZSPEC) at the OMEGA Laser Facility," Rev. Sci. Instrum. **93**, 083509 (2022).

C. Dorrer, I. A. Begishev, S.-W. Bahk, and J. Bromage, "High-Resolution Mapping of Phase-Matching Conditions in Second-Order Nonlinear Crystals," Opt. Mater. Express **12**, 3679 (2022).

F. García-Rubio, R. Betti, J. Sanz, and H. Aluie, "Theory of the Magnetothermal Instability in Coronal Plasma Flows," Phys. Plasmas **29**, 092106 (2022).

V. Yu. Glebov, C. J. Forrest, J. Kendrick, J. P. Knauer, O. M. Mannion, H. McClow, S. P. Regan, C. Stoeckl, B. Stanley, and W. Theobald, "A New Neutron Time-of-Flight Detector for Yield and Ion-Temperature Measurements on OMEGA Laser Facility," Rev. Sci. Instrum. **93**, 093522 (2022).

V. Gopalaswamy, R. Betti, P. B. Radha, A. J. Crilly, K. M. Woo, A. Lees, C. Thomas, I. V. Igumenshchev, S. C. Miller, J. P. Knauer, C. Stoeckl, C. J. Forrest, O. M. Mannion, Z. L. Mohamed, H. G. Rinderknecht, and P. V. Heuer, "Analysis of Limited Coverage Effects on Areal Density Measurements in Inertial Confinement Fusion Implosions," Phys. Plasmas **29**, 072706 (2022).

B. M. Haines, D. E. Keller, K. P. Long, M. D. McKay, Jr., Z. J. Medin, H. Park, R. M. Rauenzahn, H. A. Scott, K. S. Anderson, T. J. B. Collins, L. M. Green, J. A. Marozas, P. W. McKenty, J. H. Peterson, E. L. Vold, C. Di Stefano, R. S. Lester, J. P. Sauppe, D. J. Stark, and J. Velechovsky, "The Development of a High-Resolution Eulerian Radiation-Hydrodynamics Simulation Capability for Laser-Driven Hohlraums," Phys. Plasmas **29**, 083901 (2022).

S. S. Harilal, M. C. Phillips, D. H. Froula, K. K. Anoop, R. C. Issac, and F. N. Beg, "Optical Diagnostics of Laser-Produced Plasmas," Rev. Mod. Phys. **94**, 035002 (2022).

B. J. Henderson, J. R. Rygg, M. C. Marshall, M. K. Ginnane, L. E. Hansen, E. Davies, P. M. Celliers, and G. W. Collins, "Shocked Silica Aerogel Radiance Transition," J. Appl. Phys. **132**, 095902 (2022).

P. V. Heuer, L. S. Leal, J. R. Davies, E. C. Hansen, D. H. Barnak, J. L. Peebles, F. García-Rubio, B. Pollock, J. Moody, A. Birkel, and F. Séguin, "Diagnosing Magnetic Fields in Cylindrical Implosions with Oblique Proton Radiography," Phys. Plasmas **29**, 072708 (2022).

M. P. Jeske, W. Zhang, and M. Anthamatten, "Two-Photon Printing of Shape-Memory Microstructures and Metasurfaces via Radical-Mediated Thiol-Vinyl Hydrothiolation," Adv. Mater. Technol. **7**, 2101725 (2022).

T. R. Joshi, R. C. Shah, W. Theobald, K. Churnetski, P. B. Radha, D. Cao, C. A. Thomas, J. Baltazar, and S. P. Regan, "Diagnosis of the Imploding Shell Asymmetry in Polar-Direct-Drive Deuterium–Tritium Cryogenic Target Implosions on OMEGA," Rev. Sci. Instrum. **93**, 093524 (2022).

K. R. P. Kafka, T. Z. Kosc, and S. G. Demos, "Methods and Apparatus for Comprehensive Characterization of Performance Attributes and Damage Thresholds of Ultrafast Laser Optics," Opt. Eng. **61**, 071605 (2022).

J. H. Kunimune, H. G. Rinderknecht, P. J. Adrian, P. V. Heuer, S. P. Regan, F. H. Séguin, M. Gatu Johnson, R. P. Bahukutumbi, J. P. Knauer, B. L. Bachmann, and J. A. Frenje, "Knock-On Deuteron Imaging for Diagnosing the Morphology of an ICF Implosion at OMEGA," Phys. Plasmas **29**, 072711 (2022).

A. L. Milder, J. Zielinski, J. Katz, W. Rozmus, D. Edgell, A. Hansen, M. Sherlock, C. Bruulsema, J. P. Palastro, D. Turnbull, and D. H. Froula, "Direct Measurement of the Return Current Instability in a Laser-Produced Plasma," Phys. Rev. Lett. **129**, 115002 (2022).

S. C. Miller and V. N. Goncharov, "Instability Seeding Mechanisms Due to Internal Defects in Inertial Confinement Fusion Targets," Phys. Plasmas **29**, 082701 (2022).

M. Oliver, C. H. Allen, L. Divol, Z. Karmiol, O. L. Landen, Y. Ping, R. Wallace, M. Schölmerich, W. Theobald, T. Döppner, and T. G. White, "Diffraction Enhanced Imaging Utilizing a Laser Produced X-Ray Source," Rev. Sci. Instrum. **93**, 093502 (2022).

J. L. Peebles, J. R. Davies, D. H. Barnak, F. García-Rubio, P. V. Heuer, G. Brent, R. Spielman, and R. Betti, "An Assessment of Generating Quasi-Static Magnetic Fields Using Laser-Driven 'Capacitor' Coils," Phys. Plasmas **29**, 080501 (2022).

A. Pineau, K. R. P. Kafka, S. G. Demos, T. Z. Kosc, V. N. Goncharov, S. X. Hu, and G. Duchateau, "Benchmarking Solid-to-Plasma Transition Modeling for Inertial Confinement Fusion Laser-Imprint with a Pump-Probe Experiment," Phys. Rev. Research **4**, 033178 (2022).

H. Poole, D. Cao, R. Epstein, I. Golovkin, T. Walton, S. X. Hu, M. Kasim, S. M. Vinko, J. R. Rygg, V. N. Goncharov, G. Gregori, and S. P. Regan, "A Case Study of Using X-Ray Thomson Scattering to Diagnose the In-Flight Plasma Conditions of DT Cryogenic Implosions," Phys. Plasmas **29**, 072703 (2022).

S. Ressel, J. J. Ruby, G. W. Collins, and J. R. Rygg, "Density Reconstruction in Convergent High-Energy-Density Systems Using X-Ray Radiography and Bayesian Inference," Phys. Plasmas **29**, 072713 (2022).

H. G. Rinderknecht, P. V. Heuer, J. Kunimune, P. J. Adrian, J. P. Knauer, W. Theobald, R. Fairbanks, B. Brannon, L. Ceurvorst, V. Gopalaswamy, C. A. Williams, P. B. Radha, S. P. Regan, M. Gatu Johnson, F. H. Séguin, and J. A. Frenje, "A Knock-On Deuteron Imager for Measurements of Fuel and Hotspot Asymmetry in Direct-Drive Inertial Confinement Fusion Implosions," Rev. Sci. Instrum. **93**, 093507 (2022) (invited).

A. K. Schwemmlein, C. Stoeckl, C. J. Forrest, W. T. Shmayda, S. P. Regan, and W. U. Schröder, "First Demonstration of a Triton Beam Using Target Normal Sheath Acceleration," Nucl. Instrum. Methods Phys. Res. B **522**, 27 (2022).

R. C. Shah, D. Cao, L. Alghaian, B. Bachmann, R. Betti, E. M. Campbell, R. Epstein, C. J. Forrest, A. Forsman, V. Yu. Glebov, V. N. Goncharov, V. Gopalaswamy, D. R. Harding, S. X. Hu, I. V. Igumenshchev, R. T. Janezic, L. Keaty, J. P. Knauer, D. Kobs, A. Lees, O. M. Mannion, Z. L. Mohamed, D. Patel, M. J. Rosenberg, W. T. Shmayda, C. Stoeckl, W. Theobald, C. A. Thomas, P. Volegov, K. M. Woo, and S. P. Regan, "Bound on Hot-Spot Mix in High-Velocity, HighAdiabat Direct-Drive Cryogenic Implosions Based on Comparison of Absolute X-Ray and Neutron Yields," Phys. Rev. E **106**, L013201 (2022).

S. Singh, A. L. Coleman, S. Zhang, F. Coppari, M. G. Gorman, R. F. Smith, J. H. Eggert, R. Briggs, and D. E. Fratanduono, "Quantitative Analysis of Diffraction by Liquids Using a Pink-Spectrum X-Ray Source," J. Synchrotron Radiat. **29**, 1033 (2022).

H. Sio, O. Larroche, A. Bose, S. Atzeni, J. A. Frenje, N. V. Kabadi, M. Gatu Johnson, C. K. Li, V. Glebov, C. Stoeckl, B. Lahmann, P. J. Adrian, S. P. Regan, A. Birkel, F. H. Séguin, and R. D. Petrasso, "Fuel–Shell Mix and Yield Degradation in Kinetic Shock-Driven Inertial Confinement Fusion Implosions," Phys. Plasmas **29**, 072710 (2022).

R. Sobolewski, "Optical Detectors and Sensors," in *Handbook of Superconductivity: Characterization and Applications*, 2nd ed., edited by D. A. Cardwell, D. C. Larbalestier, and A. I. Braginski (Taylor & Francis, New York, 2022), Vol. III, Chap. H4.5, pp. 780–796.

R. B. Spielman, "Pulsed-Power Innovations for Next-Generation, High-Current Drivers," IEEE Trans. Plasma Sci. **50**, 2621 (2022).

B. A. Storer, M. Buzzicotti, H. Khatri, S. M. Griffies, and H. Aluie, "Global Energy Spectrum of the General Oceanic Circulation," Nat. Commun. **13**, 5314 (2022).

D. Turnbull, J. Katz, D. E. Hinkel, P. Michel, T. Chapman, L. Divol, E. Kur, S. MacLaren, A. L. Milder, M. Rosen, A. Shvydky, G. B. Zimmerman, and D. H. Froula, "Beam Spray Thresholds in ICF-Relevant Plasmas," Phys. Rev. Lett. **129**, 025001 (2022).

N. D. Urban, K. R. P. Kafka, K. L. Marshall, and S. G. Demos, "Laser-Induced Damage Characteristics of Fused Silica Surfaces Polished to Different Depths Using Fluid Jet Polishing," Opt. Eng. **61**, 071604 (2022).

K. M. Woo, R. Betti, C. A. Thomas, C. Stoeckl, K. Churnetski, C. J. Forrest, Z. L. Mohamed, B. Zirps, S. P. Regan, T. J. B. Collins, W. Theobald, R. C. Shah, O. M. Mannion, D. Patel, D. Cao, J. P. Knauer, V. Yu. Glebov, V. N. Goncharov, P. B. Radha, H. G. Rinderknecht, R. Epstein, V. Gopalaswamy, F. J. Marshall, S. T. Ivancic, and E. M. Campbell, "Analysis of Core Asymmetries in Inertial Confinement Fusion Implosions Using Three-Dimensional Hot-Spot Reconstruction," Phys. Plasmas **29**, 082705 (2022).

Y. Zou, L. Chamandy, J. Carroll-Nellenback, E. G. Blackman, and A. Frank, "Jets from Main Sequence and White Dwarf Companions During Common Envelope Evolution," Mon. Not. R. Astron. Soc. **514**, 3041 (2022).

Forthcoming Publications

H. Aluie, S. Rai, H. Yin, A. Lees, D. Zhao, S. M. Griffies, A. Adcroft, and J. K. Shang, "Effective Drift Velocity from Turbulent Transport by Vorticity," to be published in Physical Review Fluids.

A. F. Antoniadis, D. Drikakis, P. S. Farmakis, L. Fu, I. Kokkinakis, X. Nogueira, P. A. S. F. Silva, M. Skote, V. Titarev, P. Tsoutsanis, "UCNS3D: An Open-Source High-Order Finite-Volume Unstructured CFD Solver," to be published in Computer Physics Communications.

N. Birge, V. Geppert-Kleinrath, C. Danly, B. Haines, S. T. Ivancic, J. Jorgenson, J. Katz, E. Mendoza, A. T. Sorce, L. Tafoya, C. Wilde, and P. Volegov, "Instrument Design for an Inertial Confinement Fusion Ion Temperature Imager," to be published in Review of Scientific Instruments.

E. G. Blackman and S. V. Lebedev, "Persistent Mysteries of Jet Engines, Formation, Propagation, and Particle Acceleration: Have They Been Addressed Experimentally?" to be published in New Astronomy Reviews.

L. Ceurvorst, W. Theobald, M. J. Rosenberg, P. B. Radha, C. Stoeckl, R. Betti, K. S. Anderson, J. A. Marozas, V. N. Goncharov, E. M. Campbell, C. M. Shuldberg, R. W. Luo, W. Sweet, L. Aghaian, L. Carlson, B. Bachmann, T. Döppner, M. Hohenberger, K. Glize, R. H. H. Scott, A. Colaïtis, and S. P. Regan, "Development of an X-Ray Radiography Platform to Study Laser-Direct-Drive Energy Coupling at the National Ignition Facility," to be published in Review of Scientific Instruments.

F. Coppari, D. E. Fratanduono, M. Millot, R. G. Kraus, A. Lazicki, J. R. Rygg, R. F. Smith, and J. H. Eggert, "X-Ray Diffraction Measurements and Pressure Determination in Nanosecond Compression of Solids up to 600 GPa," to be published in Physical Review B.

D. H. Edgell, J. Katz, R. Raimondi, D. Turnbull, and D. H. Froula, "Scattered-Light Uniformity Imager for Diagnosing Laser Absorption Asymmetries on OMEGA," to be published in Review of Scientific Instruments.

C. J. Forrest, A. Crilly, A. Schwemmlein, M. Gatu-Johnson, O. M. Mannion, B. Appelbe, R. Betti, V. Yu. Glebov, V. Gopalaswamy, J. P. Knauer, Z. L. Mohamed, P. B. Radha, S. P. Regan, C. Stoeckl, and W. Theobald, "Measurements of Low-Mode Asymmetries in Areal Density of Laser-Direct-Drive Deuterium–Tritium Cryogenic Implosions on OMEGA Using Neutron Spectroscopy," to be published in Review of Scientific Instruments (invited).

H. Geppert-Kleinrath, Y. Kim, K. Meany, M. Rubery, J. Carrera, and E. Mariscal, "Gas Scintillation Mitigation in Gas Cherenkov Detectors for Inertial Confinement Fusion," to be published in Review of Scientific Instruments (invited).

R. Ghosh, X. Liu, and M. Z. Yates, "Flexible Copper Metal Circuits via Desktop Laser Printed Masks," to be published in Advanced Materials Technologies.

M. G. Gorman, S. Elatresh, A. Lazicki, M. M. E. Cormier, S. A. Bonev, D. McGonegle, R. Briggs, A. L. Coleman, S. D. Rothman, L. Peacock, J. V. Bernier, F. Coppari, D. G. Braun, J. R. Rygg, D. E. Fratanduono, R. Hoffmann, G. W. Collins, J. S. Wark, R. F. Smith, J. H. Eggert, and M. I. McMahon, "Experimental Observation of Open Structures in Elemental Magnesium at Terapascal Pressures," to be published in Nature Physics.

D. S. Hodge, A. F. T. Leong, S. Pandolfi, K. Kurzer-Ogul, D. S. Montgomery, H. Aluie, C. Bolme, T. Carver, E. Cunningham, C. B. Curry, M. Dayton, F.-J. Decker, E. Galtier, P. Hart, D. Khaghani, H. J. Lee, K. Li, Y. Liu, K. Ramos, J. Shang, S. Vetter, B. Nagler, R. L. Sandberg, and A. E. Gleason, "Multi-Frame, Ultrafast, X-Ray Microscope for Imaging Shockwave Dynamics," to be published in Optics Express.

N. Kabadi, P. Adrian, C. Stoeckl, A. Sorce, H. W. Sio, M. Bedzyk, T. Evans, S. Ivancic, J. Katz, J. Knauer, J. Pearcy, D. Weiner, R. Betti, A. Birkel, D. Cao, M. Gatu Johnson, S. P. Regan, R. D. Petrasso, and J. Frenje, "The Phase-2 Particle X-Ray Temporal Diagnostic for Simultaneous Measurement of Multiple X-Ray and Nuclear Emission Histories from OMEGA Implosions," to be published in Review of Scientific Instruments (invited).

A. Krygier, C. E. Wehrenberg, J. V. Bernier, S. Clarke, A. L. Coleman, F. Coppari, T. S. Duffy, M. G. Gorman, M. Hohenberger, D. Kalantar, G. E. Kemp, S. F. Khan, C. Krauland, R. G. Kraus, A. Lazicki, M. J. MacDonald, A. G. MacPhee, E. Marley, M. C. Marshall, M. May, J. M. McNaney, M. Millot, Y. Ping, P. L. Poole, J. R. Rygg, M. Schneider, H. Sio, S. Stoupin, D. Swift, C. Yeamans, T. Zobrist, R. F. Smith, and J. H. Eggert, "X-Ray Source Characterization and Sample Heating on X-Ray Diffraction Experiments at the National Ignition Facility," to be published in Physics of Plasmas.

R. N. Markwick, A. Frank, J. Carroll-Nellenback, E. G. Blackman, P. M. Hartigan, S. V. Lebedev, D. R. Russell, J. W. D. Halliday, and L. G. Suttle, "Morphology of Shocked Lateral Outflows in Colliding Hydrodynamic Flows," to be published in Physics of Plasmas.

S. Pandolfi, T. Carver, D. Hodge, A. F. T. Leong, K. Kurzer-Ogul, P. Hart, E. Galtier, D. Khaghani, E. Cunningham, B. Nagler, H. J. Lee, C. Bolme, K. Ramos, K. Li, Y. Liu, A. Sakdinawat, S. Marchesini, P. M. Kozlowski, C. B. Curry, F.-J. Decker, S. Vetter, J. Shang, H. Aluie, M. Dayton, D. S. Montgomery, R. L. Sandberg, and A. E. Gleason, "Novel Fabrication Tools for Dynamic Compression Targets with Engineered Voids Using Photolithography Methods," to be published in Review of Scientific Instruments.

J. J. Pigeon, S. Ya. Tochitsky, D. Tovey, G. J. Louwrens, I. Ben-Zvi, and C. Joshi, "Interferometric Measurements of the Resonant Nonlinearity of IR-Active Minor Air Constituents," to be published in the Journal of the Optical Society of America B.

L. Savino, V. N. Goncharov, I. V. Igumenshchev, and S. Atzeni, "Studies on Dynamical Shell Formation for Direct-Drive Laser Fusion," to be published in Il Nuovo Cimento.

M. Sharpe, W. T. Shmayda, and J. J. Ruby, "Influence of Heat Treatments on the Near-Surface Tritium Concentration Profiles," to be published in IEEE Transactions on Plasma Science.

C. Stoeckl, D. Cao, L. Ceurvorst, A. Kalb, J. Kwiatkowski, A. Shvydky, and W. Theobald, "Beam-Pointing Verification Using X-Ray Pinhole Cameras on the 60-Beam OMEGA Laser," to be published in Review of Scientific Instruments.

M. P. Valdivia, G. Perez-Callejo, V. Bouffetier, G. W. Collins IV, C. Stoeckl, T. Filkins, C. Mileham, M. Romanofsky, I. A. Begishev, W. Theobald, S. R. Klein, M. K. Schneider, F. N. Beg, A. Casner, and D. Stutman, "Current Advances on Talbot–Lau X-Ray Imaging Diagnostics for High-Energy-Density Experiments," to be published in Review of Scientific Instruments (invited).

K. Weichman, J. P. Palastro, A. P. L. Robinson, R. Bingham, and A. V. Arefiev, "Underdense Relativistically Thermal

Plasma Produced by Magnetically Assisted Direct Laser Acceleration," to be published in Physical Review Research.

S. Zhang, V. V. Karasiev, N. Shaffer, D. I. Mihaylov, K. Nichols, R. Paul, R. M. N. Goshadze, M. Ghosh, J. Hinz, R. Epstein, S. Goedecker, and S. X. Hu, "First-Principles Equation of State of CHON Resin for Inertial Confinement Fusion Applications," to be published in Physical Review E.

Conference Presentations

K. Churnetski, K. M. Woo, W. Theobald, P. B. Radha, R. Betti, V. Gopalaswamy, I. V. Igumenshchev, S. T. Ivancic, M. Michalko, R. C. Shah, C. Stoeckl, C. A. Thomas, and S. P. Regan, "Three-Dimensional Hot-Spot X-Ray Emission Tomography from Cryogenic Deuterium–Tritium Direct-Drive Implosions on OMEGA," presented at the 9th Plasmas in Super-Intense Laser Fields, Erice, Italy, 1–11 July 2022.

F. García-Rubio, R. Betti, J. Sanz, and H. Aluie, "Magneto-hydrodynamic Instabilities in Ablation Fronts and Coronal Plasmas," presented at the Plasma Science and Technology Seminar, Princeton, NJ, 5 July 2022.

W. T. Shmayda, "Fusion-Related Tritium Research and Development at the Laboratory for Laser Energetics," presented at the 20th Tritium Users Group, Culham, UK, 5–6 July 2022.

C. Deeney, "The Laboratory for Laser Energetics: An Overview," presented at the Jill Hruby Visit, Rochester, NY, 6 July 2022.

The following presentations were made at the 22nd Biennial Conference of the APS Topical Group on Shock Comprehension of Condensed Matter, Anaheim, CA, 10–15 July 2022:

M. K. Ginnane, D. N. Polsin, X. Gong, M. C. Marshall, T. R. Boehly, J. R. Rygg, G. W. Collins, A. Lazicki, R. Kraus, J. H. Eggert, D. E. Fratanduono, J.-P. Davis, C. A. McCoy, C. Seagle, and S. Root, "X-Ray Diffraction of Shocked Platinum."

X. Gong, M. C. Marshall, M. K. Ginnane, R. Boni, J. R. Rygg, and G. W. Collins, "Extending Optical Pyrometry for Temperature Measurements Below 5000 K."

E. Smith, D. T. Bishel, D. A. Chin, J. R. Rygg, G. W. Collins, and J. J. Ruby, "Shock-Wave Properties in High-Energy-Density Environments."

S. Zhang, S. X. Hu, M. C. Marshall, J. R. Rygg, A. Shvydky, D. Haberberger, V. N. Goncharov, T. R. Boehly, G. W. Collins, D. E. Fratanduono, and A. E. Lazicki, "Molecular-Dynamics Simulations and Laser-Drive Shock-Release Experiments on Polystyrene Under Inertial Confinement Fusion Conditions."

S. Zhang, R. Paul, M. Ghosh, T.-A. Suer, M. Millot, M. A. Morales, F. Malone, R. Jeanloz, E. Zurek, S. X. Hu, J. R. Rygg, and G. W. Collins, "Equations of State and Phase Transformations in Rocky Materials to TPa Pressures."

T. R. Joshi, R. B. Spielman, E. N. Hahn, M. Bailly-Grandvaux, T. Cordova, R. E. Turner, J. E. Garay, and F. N. Beg, "Investigation of Laser Ablation as a Function of Pulse Length in Silicon at 10^{15} W/cm^2 Intensities," presented at the Association of Nepali Physicists in America, virtual, 15–17 July 2022.

The following presentations were made at the Research at High Pressure, Holderness, NH, 17–22 July 2022:

D. A. Chin, P. M. Nilson, D. T. Bishel, B. J. Henderson, R. Paul, D. N. Polsin, M. Signor, S. X. Hu, M. K. Ginnane, X. Gong, E. A. Smith, A. Coleman, F. Coppari, Y. Ping, J. J. Ruby, D. Trail, A. Amouretti, M. Harmand, R. Torchio, J. R. Rygg, and G. W. Collins, "X-Ray Absorption Fine Structure Spectroscopy of Iron Compounds at High-Energy-Density Conditions."

H. Pantell, G. W. Collins, and J. R. Rygg, "The Rosenfeld Viscosity and Phase Changes in Silicates."

Z. K. Sprowal, L. E. Hansen, M. F. Huff, D. N. Polsin, D. G. Hicks, T. R. Boehly, J. R. Rygg, and G. W. Collins, "Accessing High-Density States in D_2 Using Double Shock."

T.-A. Suer, X. Gong, M. C. Marshall, S. Zhang, M. K. Ginnane, M. Huff, A. LaPierre, D. A. Chin, J. R. Rygg, and G. W. Collins, "A New Phase of Aluminum Oxide Observed at ~450 GPa."

T. J. B. Collins and P. Tzeferacos, "Computational Modeling at the University of Rochester's Laboratory for Laser Energetics and Flash Center: Advanced Simulation Tools for High-Energy-Density Physics," presented at Materials Science in Extreme Environments, virtual, 2 August 2022.

The following presentations were made at the J. Stiles Visit, Rochester, NY, 3 August 2022:

R. B. Spielman, P. Tzeferacos, S. G. Demos, S. P. Regan, and C. Deeney, "Pulsed Laser Lethality."

J. D. Zuegel, "The Laboratory for Laser Energetics: An Overview."

P. M. Nilson, F. J. Marshall, T. J. B. Collins, R. Epstein, D. T. Bishel, D. A. Chin, J. Kendrick, D. Guy, M. Krieger, W. J. Armstrong, D. Haberberger, S. M. Fess, D. Wasilewski, T. Cracium, M. J. Bonino, J. Katz, S. T. Ivancic, C. Stoeckl, V. N. Goncharov, D. H. Froula, J. J. Ruby, and R. Peters, "Flow Visualization at Ultrahigh Pressure," presented at the University of Michigan Talk, Ann Arbor, MI, 5 August 2022.

G. Bruhaug, J. L. Shaw, H. Rinderknecht, M. S. Wei, J. R. Rygg, G. W. Collins, M. Freeman, F. Merrill, L. P. Neukirch, C. Wilde, C. A. Walsh, and E. Tubman, "Laser-Plasma-Acceleration–Driven Electron Radiography on the OMEGA EP Laser," presented at the North American Particle Accelerator Conference, Albuquerque, NM, 7–12 August 2022.

The following presentations were made at the LaserNetUS User Group Meeting, Fort Collins, CO, 16–18 August 2022:

A. E. Raymond, S.-W. Bahk, I. A. Begishev, S. Bucht, C. Dorrer, C. Feng, C. Jeon, C. Mileham, R. G. Roides, M. Spilatro, B. Webb, and J. Bromage, "Status of the MTW-OPAL Laser System, a Prototype All-OPCPA System for Ultra-Intense Science."

H. G. Rinderknecht, G. Bruhaug, K. Weichman, M. VanDusen-Gross, J. P. Palastro, M. S. Wei, A. Arefiev, T. Wang, T. Toncian, A. Laso Garcia, D. Doria, K. Spohr, H. J. Quevedo, T. Ditmire, J. Williams, A. Haid, and D. Stutman, "Initial Experimental Results from Relativistically Transparent Magnetic Filament Experiments."

P. Tzeferacos, "*FLASH*—An Open Computational Tool for Laser-Driven High-Energy-Density Physics."

M. VanDusen-Gross, K. Weichman, D. R. Harding, A. Arefiev, A. G. MacPhee, A. Haid, and H. G. Rinderknecht, "Designing and Testing Optical Concentrator Targets for High-Intensity Lasers."

K. L. Marshall, J. U. Wallace, N. Urban, K. R. P. Kafka, and S. G. Demos, "The Impact of π-Electron Delocalization on the Chiroptical Properties, Mesophase Stability, and Laser-Damage Resistance of Chiral Dopants and Liquid Crystal Host Mixtures in High-Peak-Power Laser Applications," presented at Liquid Crystals XXVI, San Diego, CA, 21–25 August 2022 (invited).

D. Chakraborty, B. N. Mills, J. Cheng, S. A. Gerber, and R. Sobolewski, "Maximum A-Posteriori Probability THz Parameter Extraction for Pancreatic Ductal Adenocarcinoma," presented at the 47th International Conference on Infrared, Millimeter and Terahertz Waves, Delft, Netherlands, 28 August–2 September 2022.

The following presentations were made at the 13th International Laser Operations Workshop, Livermore, CA, 30 August–1 September 2022:

M. Barczys, D. Canning, M. J. Guardalben, B. E. Kruschwitz, T. McKean, J. O'Sullivan, N. Savidis, and L. J. Waxer, "OMEGA EP Updates from 2021–2022."

D. Canning, "Omega Facility Update."

A. Consentino, G. Pien, S. Householder, M. Labuzeta, D. Canning, J. Puth, and S. F. B. Morse, "LLE's Experience with Mix of Remote and In-Person PI."

M. Heimbueger, W. R. Donaldson, S. Sampat, and L. J. Waxer, "New Temporal Diagnostic Scheme Based on Semiconductor Technology."

E. M. Hill, C. Dorrer, J. D. Zuegel, S. Herman, A. Bolognesi, N. Ekanayake, K. Gibney, and M. Spilatro, "Overview of the Fourth-Generation Laser for Ultrabroadband eXperiments (FLUX) at the Laboratory for Laser Energetics."

S. T. Ivancic, R. B. Brannon, T. Filkins, J. Katz, A. Sorce, D. Mastrosimone, N. Pelepchan, M. Michalko, J. Tellinghuisen, B. Stanley, and J. Frelier, "Experimental Diagnostic Development and Integration at OMEGA."

M. Labuzeta, S. F. B. Morse, J. Puth, D. Canning, A. Consentino, and S. Householder, "The Role of Availability and Effectiveness Performance Metrics in the Omega Sustainment Plan."

C. Mileham, S.-W. Bahk, I. A. Begishev, S. Bucht, R. Cuffney, C. Dorrer, C. Feng, T. Filkins, C. Jeon, R. Roides, J. L. Shaw, M. Spilatro, C. Stoeckl, B. Webb, J. D. Zuegel, and J. Bromage, "An Overview of the Multi-Terawatt Facility Operational Paradigm."

S. Sampat, B. Ehrich, M. Heimbueger, S.-W. Bahk, J. Kwiatkowski, L. J. Waxer, B. E. Kruschwitz, and S. F. B. Morse, "Current Status of On-Target Uniformity Improvements on the OMEGA 60 Laser."

A. Sorce, G. Bogan, E. Power, R. Raimondi, D. Guy, M. Romanofsky, S. Ali, and P. M. Celliers, "OMEGA High-Resolution Velocimeter Laser Replacement Project: Considerations and Design Challenges for Integration at OMEGA."

S. Zhang, "Isentropes and Equations of State of Solid Hydrogen—Perspectives from Theory and Calculations," presented at the Center for Matter at Atomic Pressures Seminar, virtual, 2 September 2022.

The following presentations were made at the Laser-Induced Damage in Optical Materials 2022, Rochester, NY, 18–21 September 2022:

Z. S. Davidson, J. Wallace, Y. Sargol, N. Urban, S. G. Demos, K. L. Marshall, and S. Elhadj, "Laser Damage to Liquid Crystal Alignment Materials in Ordinary and Extraordinary Modes."

B. N. Hoffman, N. Savidis, S. Abbey, A. Kalb, A. L. Rigatti, and S. G. Demos, "Characterization of Particulate Contamination Inside the OMEGA EP Grating Compressor Chamber."

H. Huang, T. Z. Kosc, T. J. Kessler, and S. G. Demos, "Modeling of Transverse Stimulated Raman Scattering in KDP/DKDP Polarization Control Plates."

K. R. P. Kafka, "Cumulative Damage Probability Algorithm: Advantages and Limitations."

J. B. Oliver, A. A. Kozlov, J. Spaulding, C. Smith, S. MacNally, D. Coates, K. R. P. Kafka, A. L. Rigatti, and S. G. Demos, "Striated Composite Layers for High-Fluence Applications."

Y. Sargolzaeiaval, J. U. Wallace, N. D. Urban, S. G. Demos, K. L. Marshall, and S. Elhadj, "Optimized Liquid Crystals for High-Power Laser Beam Manipulation: An Evaluation and Feasibility Study."

N. D. Urban, K. R. P. Kafka, J.-M. Jang, K. L. Marshall, S. G. Demos, R. Emms, and D. Walker, "Laser-Damage Performance of Fused Silica and Potassium Dihydrogen Phosphate Surfaces Finished by Fluid Jet Polishing."

The following presentations were made at The International Committee on Ultrahigh-Intensity Lasers, Jeju, South Korea, 18–23 September 2022:

S.-W. Bahk, I. A. Begishev, R. Roides, C. Mileham, R. Cuffney, C. Feng, B. Webb, C. Jeon, M. Spilatro, S. Bucht, C. Dorrer, and J. Bromage, "Experimental Verification of Pump Wavefront Transfer in an Optical Parametric Amplifier."

S.-W. Bahk, S. Sampat, M. Heimbueger, J. Kwiatkowski, K. A. Bauer, and L. J. Waxer, "Single-Shot Wavefront Characterization of High-Energy Focal Spots in the OMEGA Target Chamber Using a Phase Diversity Grating."

J. Bromage, S.-W. Bahk, M. Bedzyk, I. A. Begishev, S. Bucht, C. Dorrer, C. Feng, B. N. Hoffman, C. Jeon, C. Mileham, J. B. Oliver, A. Raymond, R. G. Roides, E. M. Schiesser, K. Shaughnessy, M. J. Shoup III, M. Spilatro, B. Webb, D. Weiner, and J. D. Zuegel, "Commissioning and Performance of MTW-OPAL, an All-OPCPA System."

W. T. Shmayda, H. Mutha, E. Dombrowski, and K. Ryan, "SPARC Tokamak Tritium Processing Systems," presented at the 32nd Symposium on Fusion Technology, Dubrovnik, Croatia, 18–23 September 2022.

The following presentations were made at the 36th European Conference on Laser Interaction with Matter, Frascati, Italy, 19–23 September 2022:

R. Betti, V. Gopalaswamy, J. P. Knauer, D. Patel, A. Lees, K. M. Woo, C. A. Thomas, D. Cao, O. M. Mannion, R. C. Shah, C. J. Forrest, Z. L. Mohamed, C. Stoeckl, V. Yu. Glebov, S. P. Regan, D. H. Edgell, M. J. Rosenberg, I. V. Igumenshchev, P. B. Radha, K. S. Anderson, J. R. Davies, T. J. B. Collins, V. N. Goncharov, K. Churnetski, W. Theobald, A. A. Solodov, D. Turnbull, D. H. Froula, E. M. Campbell, R. T. Janezic, D. R. Harding, M. J. Bonino, S. Sampat, K. A. Bauer, S. F. B. Morse, M. Gatu Johnson, R. D. Petrasso, C. K. Li, and J. A. Frenje, "High-Performance Implosions on OMEGA and Prospects for Direct-Drive Ignition with Multimegajoule Lasers."

C. Dorrer, "The Fourth-Generation Laser for Ultrabroadband eXperiments (FLUX)."

D. Turnbull, C. Dorrer, D. H. Edgell, R. K. Follett, V. N. Goncharov, A. M. Hansen, A. L. Milder, K. L. Nguyen, J. P. Palastro, R. C. Shah, J. D. Zuegel, D. H. Froula, A. Colaïtis, and P. Michel, "Broadband Lasers will be a Game Changer for Inertial Confinement Fusion—Foundation for this Belief, Plans for Further Validation" (invited).

D. Haberberger, "Overview of Plasma Experiments and Diagnostics on Laser Facilities," presented at the HRMT-62 Collaboration Meeting at the European Council for Nuclear Research, Geneva, Switzerland, 26–27 September 2022.

The following presentations were made at the 8th Target Fabrication Workshop, Oxford, UK, 26-28 September 2022:

M. J. Bonino, D. R. Harding, A. Behlok, T. Cracium, S. Fess, S. Karim, I. Knudson, K. Lintz, N. Redden, D. Wasilewski, M. D. Wittman, J. Fooks, and K. Knolker, "Target Fabrication Capabilities at LLE."

D. R. Harding, S. M. Fess, M. J. Bonino, Y. Lu, and P. Fang, "3-D Printing Foam Targets."

D. R. Harding, J. D. Zuegel, T. B. Jones, R. Gram, M. Bobeica, Z. Bei, and W. Wang, "Technologies for Mass Producing IFE Targets and Determining Their Survival in an IFE Chamber."


1850
MELIORA
UNIVERSITY of
ROCHESTER